

JOURNAL OF THE ELECTROCHEMICAL SOCIETY

ELECTROCHEMICAL
SCIENCE AND TECHNOLOGY

SOLID-STATE
SCIENCE AND TECHNOLOGY

REVIEWS AND NEWS
Call for Papers—
Hollywood, Florida Meeting

INDEX TO VOLUME 126 (1979)



VOL. 126, NO.12

DECEMBER 1979

JESOAN 126 (12) 2047-2288, 479C-508C



FUTURE MEETINGS

ST. LOUIS, MISSOURI—MAY 11, 12, 13, 14, 15, & 16, 1980

Headquarters at the Chase-Park Plaza

The detailed Call for Papers published in July-November 1979 issues of *This Journal*. Final program published in March 1980 issue of *This Journal*.

Planned symposia for the St. Louis Meeting include the following Divisions, Group, Subcommittee, and subjects: **Battery/Energy Technology**—Load Leveling and Regenerative Braking for Transportation; **Corrosion**—General Session; **Corrosion/Electrothermics and Metallurgy/Industrial Electrolytic/Physical Electrochemistry/Energy Technology**—Industrial Electrolytic Processes in Molten Salts; **Corrosion/Physical Electrochemistry**—Substrate Morphology Effects in Electrode Processes; **Dielectrics and Insulation**—Electronic Devices for Chemical Analysis, General Session; **Dielectrics and Insulation/Electronics**—Conducting Polymers and Related Materials, Magnetic Bubble Materials and Device Processing, Packaging of Electronic Devices, Plasma Etching and Deposition; **Electronics**—Diffusion Processes in Semiconducting Materials, Processing of Solid-State Imaging Devices, Semiconductors and New Electronic Technologies General Session, Recent News Papers Session, Phosphor Depreciation, Phosphor Screening, Luminescence General Session; **Electronics/Electrothermics and Metallurgy**—Ninth International Conference on Electron and Ion Beam Science and Technology; **Electronics/Electrothermics and Metallurgy/Energy Technology**—Current Voltage Characteristics of Photovoltaic Devices, Electronic and Optical Properties of Polycrystalline or Impure Semiconductors, Novel Silicon Growth Methods; **Electrothermics and Metallurgy/Energy Technology**—Thermal Energy Storage and Transfer by Thermochemical Means; **Energy Technology**—General Session; **Energy Technology/Organic and Biological Electrochemistry**—Photobiological Energy Conversion; **Industrial Electrolytic**—Electrochemical Engineering of Industrial Electrolytic Processes, Electrochemical Methods of Waste Water Purification; **Organic and Biological Electrochemistry**—Electroorganic Synthesis (honoring Manuel M. Baizer), Electrochemical Mediation of Developmental Processes and Regeneration in Biological Systems, Electron Transfer and Interfacial Behavior of Molecules of Biological Importance, Electron Transfer in Inorganic and Organic Reactions; **Physical Electrochemistry**—General Session; and **New Technology Subcommittee**—Near Zero Gravity Phenomena and Materials Processing in Space, Supercritical Fluids.

HOLLYWOOD, FLORIDA—OCTOBER 5, 6, 7, 8, 9, & 10, 1980

Headquarters at The Diplomat

The detailed Call for Papers published in December 1979-May 1980 issues of *This Journal*. Final program published in August 1980 issue of *This Journal*.

Planned symposia for the Hollywood Meeting include the following Divisions, Group, Subcommittee, and subjects: **Battery**—Characteristics of Fuel Cell and Battery Electrodes, Lithium Battery, Rechargeable Alkaline Zinc Electrodes, Uninterruptible Power Supplies, General Session; **Battery/Corrosion/Electrothermics and Metallurgy/Energy Technology**—Molten Carbonate Fuel Cell Technology; **Battery/Corrosion/Energy Technology**—Energy Storage for Solar Applications; **Corrosion**—Corrosion in Organic Solvents, International Symposium on Atmospheric Corrosion, General Session; **Corrosion/Dielectrics and Insulation/Electronics/Electrothermics and Metallurgy/Energy Technology**—Materials and New Processing Technologies for Photovoltaics; **Corrosion/Electronics/Energy Technology/Physical Electrochemistry**—Materials Problems in Photoelectrochemical Devices; **Dielectrics and Insulation**—General Session; **Dielectrics and Insulation/Electronics**—Dielectric Isolation for VLSI and Other Devices, Fiber Optics: Materials and Devices, Ionic and Electronic Conduction in Glasses, Resist and Patterning Technology, Thin Films of Tunneling Dimensions; **Dielectrics and Insulation/Electronics/Electrothermics and Metallurgy**—Defects and Transport in Semiconductors and Dielectrics; **Electrodeposition**—General Session; **Electrodeposition/Physical Electrochemistry**—Electrocrystallization; **Electronics**—Annealing of Semiconductors, Electron Microscopy of Semiconductors, Semiconductor Materials and Technologies for High Speed Logic, Semiconductors and New Electronic Technologies General Session, Recent News Papers Session; **Electronics/Electrothermics and Metallurgy**—Process and Use Related Radiation Effects in Electronic Devices; **Electronics/Energy Technology**—Properties and Preparation of Amorphous Silicon for Electronic Devices; **Electrothermics and Metallurgy**—Science and Technology of Halide Lamps and Lasers; **Electrothermics and Metallurgy/Energy Technology**—Sulfur Removal from Fuels; **Energy Technology**—Fuels from Nonfossil Energy Storage Systems, General Session; **Energy Technology/Industrial Electrolytic/Physical Electrochemistry**—Ion Exchange: Transport and Interfacial Properties; **Industrial Electrolytic**—Regeneration of Chemicals; **Physical Electrochemistry**—Third International Symposium on Molten Salts; and **New Technology Subcommittee**—Electrochemical Aspects of Ocean Resource Development.

MINNEAPOLIS, MINNESOTA—MAY 10, 11, 12, 13, 14, & 15, 1981

Headquarters at the Raddison Hotel

The detailed Call for Papers published in July-November 1980 issues of *This Journal*. Final program published in March 1981 issue of *This Journal*.

Planned symposia for the Minneapolis Meeting include the following Divisions, Group, Subcommittee, and subjects: **Battery/Energy Technology**—Electric Hybrid Systems for Vehicle Propulsion; **Battery/Energy Technology/Industrial Electrolytic**—Porous Structure in Electrochemical Devices; **Corrosion**—General Session; **Corrosion/Dielectrics and Insulation**—Anodic Oxidation; **Corrosion/Dielectrics and Insulation/Electrothermics and Metallurgy**—Transport Under Electrical and Thermal Gradients; **Corrosion/Energy Technology**—Corrosion and Solar Energy Systems, Materials Problems in OTEC Devices; **Corrosion/Physical Electrochemistry**—Nonaqueous Electrolytes; **Dielectrics and Insulation**—Electrolytic Capacitor, General Session; **Dielectrics and Insulation/Electrothermics and Metallurgy**—Adhesion Aspects of Dielectrics, Insulating, and Resist Materials; **Electronics**—Semiconductors and New Electronic Technologies General Session, Recent News Papers Session, II-VI Luminescent Materials, Luminescence General Session; **Electronics/Dielectrics and Insulation**—Fourth International Symposium on Silicon Materials Science and Technology; **Electronics/Energy Technology**—Chemical Modification of Grain Boundaries in Photovoltaic Devices, New Concepts in Photovoltaic Devices; **Electrothermics and Metallurgy**—Thermochemistry of Intermetallics, Vibrational Spectroscopy (Laser Raman IR); **Electrothermics and Metallurgy/Energy Technology**—Thermionics and Thermoelectric Generation; **Energy Technology**—Second Law Economics of New Energy Devices, General Session; **Industrial Electrolytic**—Chlorine, Energy Conversion in the Electrochemical Industries; **Organic and Biological Electrochemistry**—Electrochemistry in the Study of Novel Organic Compounds, Mechanisms and Mechanistic Techniques in Organic Electrode Reactions; **Physical Electrochemistry**—Solid Electrolyte Interface, General Session; **Physical Electrochemistry/Energy Technology**—Electrocatalysis; and **New Technology Subcommittee**—Environmental Reactions of Ozone and Active Oxygen Compounds.

THE ELECTROCHEMICAL SOCIETY

BOOKS IN PRINT

Society Proceedings Series

The following softbound proceedings volumes are sponsored and published by The Electrochemical Society, Inc., P.O. Box 2071, Princeton, N.J. 08540. Orders filled at the list price given, subject to availability. Enclose payment with order.

High-Temperature Metallic Corrosion of Sulfur and Its Compounds. Z. A. Foroulis, Editor. A 1969 symposium. 276 pages, \$4.50.

Electron and Ion Beam Science and Technology, Fourth International Conference. R. Bakish, Editor. A 1970 symposium. 680 pages, \$7.50.

Fundamentals of Electrochemical Machining. C. L. Faust, Editor. A 1970 symposium. 365 pages, \$4.50.

Electron and Ion Beam Science and Technology, Fifth International Conference. R. Bakish, Editor. A 1972 symposium. 420 pages, \$5.50.

Electrochemical Contributions to Environmental Protection. T. R. Beck, O. B. Cecil, C. G. Enke, J. McCallum, and S. T. Wlodek, Editors. A 1972 symposium. 173 pages, \$4.00.

Oxide-Electrolyte Interfaces. R. S. Alwitt, Editor. A 1972 symposium. 312 pages, \$9.00.

Marine Electrochemistry. J. B. Berkowitz, M. Banus, M. J. Pryor, R. Horne, P. L. Howard, G. C. Whitnack, and H. V. Weiss, Editors. A 1972 symposium. 416 pages, \$15.00.

Electrochemical Bioscience and Bioengineering. H. T. Silverman, I. F. Miller, and A. J. Salkind, Editors. A 1973 symposium. 268 pages, \$8.00.

Chlorine Bicentennial Symposium. T. C. Jeffery, P. A. Danna, and H. S. Holden, Editors. A 1974 symposium. 404 pages, \$11.00.

Electron and Ion Beam Science and Technology, Sixth International Conference. R. Bakish, Editor. A 1974 symposium. 594 pages, \$16.00.

Properties of Electrodeposits—Their Measurement and Significance. R. Sard, H. Leidheiser, Jr., and F. Ogburn, Editors. A 1974 symposium. 430 pages, \$13.00.

Metal-Slag-Gas Reactions and Processes. Z. A. Foroulis and W. W. Smeltzer, Editors. A 1975 symposium. 1032 pages, \$20.00.

Chemistry and Physics of Aqueous Gas Solutions. W. A. Adams, G. Greer, J. E. Desnoyers, G. Atkinson, G. S. Kell, K. B. Oldham, and J. Walkley, Editors. A 1975 symposium. 522 pages, \$11.00.

Chemical Vapor Deposition, Fifth International Conference. J. M. Blocher, Jr., H. E. Hintermann, and L. H. Hall, Editors. A 1975 symposium. 848 pages, \$18.00.

Thermal and Photostimulated Currents in Insulators. D. M. Smyth, Editor. A 1975 symposium. 215 pages, \$7.00.

Energy Storage. H. P. Silverman and J. B. Berkowitz, Editors. A 1975 symposium. 258 pages, \$8.00.

Etching. H. G. Hughes and M. J. Rand, Editors. A 1976 symposium. 203 pages, \$7.00.

Electron and Ion Beam Science and Technology, Seventh International Conference. R. Bakish, Editor. A 1976 symposium. 632 pages, \$18.00.

International Symposium on Solar Energy. J. B. Berkowitz and I. A. Lesk, Editors. A 1976 symposium. 372 pages, \$10.00.

International Symposium on Molten Salts. J. P. Pemsler, J. Braunstein, K. Nobe, D. R. Morris, and N. E. Richards, Editors. A 1976 symposium. 632 pages, \$16.00.

Properties of High Temperature Alloys. Z. A. Foroulis and F. S. Pettit, Editors. A 1976 symposium. 851 pages, \$12.00.

Semiconductor Silicon 1977. H. R. Huff and E. Sirtl, Editors. A 1977 symposium. 1100 pages, \$15.00.

A History of The Electrochemical Society. The first 75 years. R. M. Burns with E. G. Enck. 160 pages, \$5.00.

Semiconductor-Liquid Junction Solar Cells. A. Heller, Editor. A 1977 symposium. 340 pages, \$7.00.

Load-Leveling. N. P. Yao and J. R. Selman, Editors. A 1977 symposium. 412 pages, \$13.00.

Chemical Vapor Deposition, Sixth International Conference. L. F. Donaghey, P. Rai-Choudhury, and R. N. Tauber, Editors. A 1977 symposium. 596 pages, \$14.00.

Electrode Materials and Processes for Energy Conversion and Storage. J. D. E. McIntyre, S. Srinivasan, and F. G. Will, Editors. A 1977 symposium. 1048 pages, \$20.00.

High Temperature Metal Halide Chemistry. D. L. Hildenbrand and D. D. Cubicciotti, Editors. A 1977 symposium. 678 pages, \$17.00.

Thin Film Phenomena—Interfaces and Interactions. J. E. E. Baglin and J. M. Poate, Editors. A 1977 symposium. 525 pages, \$14.00.

Semiconductor Characterization Techniques. P. A. Barnes and G. A. Rozgonyi, Editors. A 1978 symposium. 532 pages, \$16.00.

Industrial Water Electrolysis. S. Srinivasan, F. J. Salzano, and A. R. Landgrebe, Editors. A 1978 symposium. 297 pages, \$12.00.

Electron and Ion Beam Science and Technology, Eighth International Conference. Robert Bakish, Editor. A 1978 symposium. 684 pages, \$20.00.

Selected Topics in the History of Electrochemistry. George Dubpernell and J. H. Westbrook, Editors. A 1977 symposium. 523 pages, \$11.00.

Battery Design and Optimization. S. Gross, Editor. A 1978 symposium. 486 pages, \$14.00.

The Electrocatalysis of Fuel Cell Reactions. W. E. O'Grady, S. Srinivasan, and R. F. Dudley, Editors. A 1978 workshop sponsored by the Division of Fossil Fuel Utilization, United States Department of Energy. 228 pages, \$8.00.

Chemical Vapor Deposition, Seventh International Conference. T. O. Sedgwick and H. Lydtin, Editors. A 1979 symposium. 658 pages, \$16.00.

December 1979

ELECTROCHEMICAL SCIENCE AND TECHNOLOGY

EDITOR

Norman Hackerman
Jackie Bourne, Assistant to the Editor

DIVISIONAL AND GROUP EDITORS

BATTERY

R. J. Brodd
Elton J. Cairns
G. F. Nordblom

Boone B. Owens
C. Joseph Venuto
J. L. Weininger

CORROSION

J. W. Faust, Jr.
R. P. Frankenthal
Jerome Kruger
Florian Mansfeld

Ken Nobe
Earl S. Snavely, Jr.
Ellis D. Verink
J. Bruce Wagner

DIELECTRICS AND INSULATION

Robert S. Alwitt
Dennis Hess
T. W. Hickmott

George L. Schnable
Lawrence Young

ELECTRODEPOSITION

Ugo Bertocci
Huik Y. Cheh

Y. Okinaka
Mordechai Schlesinger

ELECTRONICS

Ephraim Banks
D. M. Brown
Ted F. Cizek
George R. Gronin
John A. DeLuca
Murray Gershenzon
James S. Harris
Simon Larach

Ernest Paskell
Bertram Schwartz
Frederic N. Schwettmann
A. K. Sinha
C. C. Wang
P. Wang
J. M. Woodall

ELECTROTHERMICS AND METALLURGY

William A. Adams
Joan B. Berkowitz
V. K. Kapur
W. E. Kuhn

R. A. Rapp
Gene F. Wakefield
Jack H. Westbrook

High Temperature Science and Technology

Leo Brewer
Daniel Cubicciotti

E. D. Cater

INDUSTRIAL ELECTROLYTIC

Richard C. Alkire

Scott Lynn

ORGANIC AND BIOLOGICAL ELECTROCHEMISTRY

Martin Blank
Arthur A. Pilla

Stanley Wawzonek

PHYSICAL ELECTROCHEMISTRY

M. J. Dignam
Larry R. Faulkner
Barry Miller
Keith B. Oldham

Robert A. Osteryoung
David K. Roe
C. W. Tobias
F. G. Will

News Editor—Jack H. Westbrook

Book Review Editor—Julius Klierer

JOURNAL OF THE ELECTROCHEMICAL SOCIETY

(USPS 284-140)

The JOURNAL OF THE ELECTROCHEMICAL SOCIETY (USPS 284-140) is published monthly by The Electrochemical Society, Inc. at 215 Canal St., Manchester, N.H. 03108. The address for the Executive Offices, Editorial and Advertising Office, and Circulation Department of The Electrochemical Society, Inc. is P.O. Box 2071, Princeton, N.J. 08540. Subscription to members as part of membership service; subscription to nonmembers \$60.00 plus \$5.00 for postage outside U.S. and Canada. Single copies \$3.25 to members, \$5.00 to nonmembers. © Copyright 1979 by The Electrochemical Society, Inc. Second Class Postage paid at Princeton, New Jersey and at additional mailing offices.

POSTMASTER: Send address changes to THE ELECTROCHEMICAL SOCIETY, INC., P.O. Box 2071, Princeton, N.J. 08540.

TECHNICAL PAPERS

E. Peled

... 2047

The Electrochemical Behavior of Alkali and Alkaline Earth Metals in Nonaqueous Battery Systems—The Solid Electrolyte Interphase Model

A. N. Dey

... 2052

Primary Li/SOCl₂ Cells

VIII. Effect of Type of Carbon on the Performance

P. Doig

P. E. J. Flewitt

... 2057

A Finite Difference Numerical Analysis of Galvanic Corrosion for Semi-Infinite Linear Coplanar Electrodes

E. J. Kelly

... 2064

Anodic Dissolution and Passivation of Titanium in Acidic Media

III. Chloride Solutions

B. Mazza

P. Pedefterri

D. Sinigaglia

A. Cigada

G. A. Mondora

G. Re

G. Taccani

D. Wenger

... 2075

Pitting Resistance of Cold-Worked Commercial Austenitic Stainless Steels in Solution Simulating Seawater

P. H. Melville

... 2081

Distribution of Potential Around a Scratch in a Passive Film

H. Feigenbaum

R. Weil

... 2085

Surface-Stress Phenomena at the Start of Epitaxial Electrodeposition of Nickel

J. C. Dabrowiak

F. S. Santillo

... 2091

The Redox Properties of Bleomycin and Tallysomyacin and a Series of Their Metalloderivatives

M. H. Brooker

... 2095

Kinetic Stability of Nitrate Ion in Molten Nitrate by Raman Spectroscopic Studies of ¹⁸O-Enriched KNO₃

N. R. Carmichael

S. N. Flengas

... 2098

Molar Volume and Electrical Conductivity Measurements in the Ternary Molten Salt System NaCl-CsCl-MnCl₂
I. Molar Volumes

N. R. Carmichael

S. N. Flengas

... 2104

Molar Volume and Electrical Conductivity Measurements in the Ternary Molten Salt System NaCl-CsCl-MnCl₂
II. Electrical Conductivities

D. C. Hamby

N. J. Hoover

J. Wirkkala

D. Zahnle

... 2110

Concentration Changes in Porous Zn Electrodes during Cycling

R. Alkire

P.-Y. Lu

... 2118

Effect of Hydrogen Evolution on Current Distribution during Electrodeposition at Vertical Electrodes

R. M. Gould

R. C. Alkire

... 2125

Effect of Multiple Reactions on Metal Deposition in Flow-Through Porous Electrodes

B. Reichman

A. J. Bard

... 2133

Semiconductor Electrodes

XXII. Electrochromism and Photoelectrochemistry at WO₃ Layers Prepared by Thermal and Anodic Oxidation of W

R. O. Lezna

N. R. de Tacconi

A. J. Arvia

... 2140

The Influence of H₂SO₄ Concentration on Hydrogen and Oxygen Electrosorption at Platinum

ELECTROCHEMICAL SOCIETY

Vol. 126 • No. 12

C. T. Moynihan
... 2144

C. G. Law, Jr.
J. Newman
... 2150

TECHNICAL NOTE

R. R. Dubin
S. Prochazka
... 2156

J. P. Franey
... 2159

A. D. Franklin
J. Epp
... 2162

D. S. Ginley
M. L. Knotek
... 2163

DISCUSSION SECTION

... 2167

Mixed Alkali Effect in Hydrate Melts

A Model for the Anodic Dissolution of Iron in Sulfuric Acid

Evaluation of Sintered SiC as an Electrode and Container Material in Sodium/Sulfur Cells

Trace Gas Flow Control Using Polymer Permeation

Preparation of Pt-Fe Alloy Foils by Electrodeposition of Fe

Hydrogen in TiO₂ Photoanodes

SOLID-STATE SCIENCE AND TECHNOLOGY

TECHNICAL PAPERS

T. Moroshi
H. Fujikawa
H. Makiura
... 2173

P. Fabry
M. Kleitz
... 2183

M. J. Dignam
... 2188

W. Primak
E. Monahan
... 2196

T. Takahashi
O. Yamada
... 2206

V. Novotny
M. A. Hopper
... 2211

T. C. Chandler, Jr.
J. W. Faust, Jr.
R. B. Hilborn
... 2216

M. Tomkiewicz
... 2220

J. Saraie
M. Kitagawa
T. Tanaka
... 2226

L. Jastrzebski
J. Lagowski
H. C. Gatos
... 2231

M. Doken
I. Miyata
... 2235

The Effect of Carbon, Zirconium, Niobium, and Titanium on the Oxidation Resistance of Chromium Stainless Steel

Electrochemical Characterization of the Point Defects Associated with Copper Dissolved in Stabilized Zirconia

High Field Intrinsic Ionic Conduction in Solids

Glow Discharge Tube Glass Electrodes

Luminescence of Terbium-Activated Alkali Rare Earth Metaphosphate Glasses

Optical and Electrical Characterization of Electrochromic Displays

Debris-Induced Effects from Spin-On Diffusion Sources

Relaxation Spectrum Analysis of Semiconductor-Electrolyte Interface-TiO₂

Effect of Excess Component Element during LPE on Electrical Properties of CdTe

Outdiffusion of Recombination Centers from the Substrate into LPE Layers; GaAs

Etching Uniformities of Silicon in CF₄ + 4% O₂ Plasma

DIVISION AND GROUP OFFICERS

Battery Division

Albert Himy, Chairman
John Pierson, Vice-Chairman
Gene Gagnon, Secretary-Treasurer
General Motors Corp.
Research Laboratories, Dept. 37
12 Mile and Mounds Rds.
Warren, Mich. 48090

Corrosion Division

Ken Nobe, Chairman
Robert P. Frankenthal, Vice-Chairman
Florian Mansfeld, Secretary-Treasurer
Rockwell International
Science Center
P.O. Box 1085
Thousand Oaks, Calif. 91360

Dielectrics and Insulation Division

Rudolf G. Frieser, Chairman
James A. Amick, Vice-Chairman
Alexis T. Bell, Treasurer
John S. Judge, Secretary
28 Columbus St.
Lexington, Mass. 02173

Electrodeposition Division

Richard Sard, Chairman
Thomas Franklin, Vice-Chairman
Lubomir Romankiw, Secretary-Treasurer
IBM T. J. Watson Research Center
P.O. Box 218
Yorktown Heights, N.Y. 10598

Electronics Division

Arnold Reisman, Chairman
Don W. Shaw, Vice-Chairman (Semiconductors)
Frederick M. Ryan, Vice-Chairman (Luminescence)
Ronald E. Enstrom, Vice-Chairman (General Materials and Processes)
William A. McAllister, Treasurer
Edward H. Nicollan, Secretary
Bell Laboratories
Murray Hill, N.J. 07974

Electrothermics and Metallurgy Division

H. Stephen Spall, Chairman
J. Bruce Wagner, Jr., Senior Vice-Chairman
William A. Auzens, Junior Vice-Chairman
Frederick S. Pettit, Secretary-Treasurer
Pratt and Whitney Aircraft
Materials Engineering and Research Laboratory
Middletown, Conn. 06457

Energy Technology Group

Sigurd Wagner, Chairman
James McGreen, Vice-Chairman
A. J. Appieby, Treasurer
Arthur J. Nozik, Secretary
Solar Energy Research Institute
Golden, Colo. 80401

Industrial Electrolytic Division

Richard C. Alkire, Chairman
Leonard Nanis, Vice-Chairman
M. P. Grotheer, Secretary-Treasurer
Hooker Chemical Corp.
P.O. Box 344
Niagara Falls, N.Y. 14302

Organic and Biological Electrochemistry Division

Larry L. Miller, Chairman
John H. Wagenknecht, Vice-Chairman
Martin Blank, Secretary-Treasurer
Dept. of Physiology
Columbia University
630 W. 168th St.
New York, N.Y. 10032

Physical Electrochemistry Division

Fritz G. Will, Chairman
Elton J. Cairns, Vice-Chairman
Robert A. Osteryoung, Secretary-Treasurer
Dept. of Chemistry
State University of New York
Buffalo, N.Y. 14214

SOCIETY OFFICERS AND STAFF

Joan B. Berkowitz, President
Arthur D. Little, Inc.
15 Acorn Park
Cambridge, Mass. 02140

Erik M. Pell, Vice-President
Xerox Corp.
Xerox Square—W105
Rochester, N.Y. 14644

Ralph J. Brodd, Vice-President
ESB Technology Inc.
19 W. College Ave.
Yardley, Pa. 19067

Frederick J. Strieter, Vice-President
Texas Instruments, Inc.
7814 Fallmeadow Lane
Dallas, Texas 75240

Paul C. Milner, Secretary
Bell Laboratories
Room 1D-259
Murray Hill, N.J. 07974

John L. Griffin, Treasurer
Research Laboratories
General Motors Corporation
General Motors Technical Center
Warren, Mich. 48090

V. H. Branneky, Executive Secretary
The Electrochemical Society, Inc.
P.O. Box 2071
Princeton, N.J. 08540

Donna Kimberlin, Administrative Assistant
The Electrochemical Society, Inc.
P.O. Box 2071
Princeton, N.J. 08540

PUBLICATION STAFF

Sarah A. Kilfoyle, Publication Editor
Annette R. Van Deusen, Assistant Publication Editor

PUBLICATION COMMITTEE

Newton Schwartz, Chairman
Paul C. Milner
Norman Hackerman
Richard C. Aikire
Robert T. Foley
Lawrence Young
Halina S. Wroblewska
Robert P. Frankenthal

Manuscripts submitted to the JOURNAL should be sent in triplicate to the Editorial Office at P.O. Box 2071, Princeton, N.J. 08540. They should conform to the revised "Instructions to Authors" available from Society Headquarters. Manuscripts so submitted, as well as papers presented before a Society technical meeting, become the property of the Society and may not be published elsewhere in whole or in part without written permission of the Society. Address such requests to the Editor. The Electrochemical Society does not maintain a supply of reprints of papers appearing in its JOURNAL. A photoprint copy of any particular paper may be obtained from University Microfilms, Inc., 300 N. Zeeb St., Ann Arbor, Mich. 48106. Inquiries regarding positive microfilm copies of issues should be addressed to University Microfilms, Inc., 300 N. Zeeb St., Ann Arbor, Mich. 48106.

Walter J. Johnson, Inc., 355 Chestnut St., Norwood, N.J. 07648, have reprint rights to out-of-print volumes of the JOURNAL, and also have available for sale back volumes and single issues with the exception of the last two calendar years.

The JOURNAL OF THE ELECTROCHEMICAL SOCIETY combines the JOURNAL and TRANSACTIONS OF THE ELECTROCHEMICAL SOCIETY. Statements and opinions given in articles and papers in the JOURNAL OF THE ELECTROCHEMICAL SOCIETY are those of the contributors, and The Electrochemical Society, Inc. assumes no responsibility for them.

Claims for a missing issue should be reported within 60 days of normal delivery date to the Circulation Dept., The Electrochemical Society, Inc., P.O. Box 2071, Princeton, N.J. 08540.

Notice of a change in address should be sent to the Circulation Dept., The Electrochemical Society, Inc., P.O. Box 2071, Princeton, N.J. 08540. Include the mailing label or the number from the mailing label from your previous issue of the JOURNAL to ensure proper identification.

SOLID-STATE SCIENCE (Cont.)

A. Murgai
H. C. Gatos
W. A. Westdorp
... 2240

Effect of Microscopic Growth Rate on Oxygen Micro-segregation and Swirl Defect Distribution in Czochralski-Grown Silicon

K. F. Galloway
S. Mayo
P. Roitman
... 2245

Radiation Levels Associated with Advanced Lithographic Techniques

K. Ehara
K. Sakuma
K. Ohwada
... 2249

Kinetics and Oxide Properties of Silicon Oxidation in O₂-H₂-HCl Mixtures

E. M. Jallouli
J. P. Larpin
M. Lambertin
J. C. Colson
... 2254

Fe-Cr-Al Alloy, High Temperature Corrosion in Sulfur Vapor

C. J. Wen
B. A. Boukamp
R. A. Huggins
W. Weppner
... 2258

Thermodynamic and Mass Transport Properties of "LiAl"

TECHNICAL NOTES

K. L. Chiang
C. J. Dell'Oca
F. N. Schwettman
... 2267

Optical Evaluation of Polycrystalline Silicon Surface Roughness

Y. Mishitani
T. Kotani
... 2269

Chemical Etching of InP by H₂O₂-H₂SO₄-H₂O Solution

Y. Tamaki
S. Isomae
A. Shintani
M. Maki
... 2271

Ge-Doped Si₃N₄ Film

DISCUSSION SECTION

... 2273

ACCELERATED BRIEF COMMUNICATIONS

A. J. Jacobson
R. R. Chianelli
M. S. Whittingham
... 2277

Amorphous Molybdenum Disulfide Cathodes

S. N. Shabde
K. Helliwell
... 2279

Arsenic Diffusion Through Thin Oxides

M. Paunovic
D. Vitkavage
... 2282

Determination of Electroless Copper Deposition Rate from Polarization Data in the Vicinity of the Mixed Potential

J. M. Bailey
I. M. Ritchie
... 2285

The Calculation of Polarization Curves in the Vicinity of the Limiting Current

D. W. Kirk
F. R. Foulkes
W. F. Graydon
... 2287

Electron Stoichiometry of Anodic Dissolution of Gold in Aqueous Alkaline Cyanide

REVIEWS AND NEWS

W. Cheng
... 483C

F. M. Becket Award Report—The Effects of Surface Additives on the Performance of Lithium-Aluminum Electrodes

NEWS
... 487C



The Electrochemical Behavior of Alkali and Alkaline Earth Metals in Nonaqueous Battery Systems—The Solid Electrolyte Interphase Model

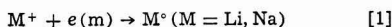
E. Peled*

Institute of Chemistry, Tel-Aviv University, Tel Aviv, Israel

ABSTRACT

It is suggested that in practical nonaqueous battery systems the alkali and alkaline earth metals are always covered by a surface layer which is instantly formed by the reaction of the metal with the electrolyte. This layer, which acts as an interphase between the metal and the solution, has the properties of a solid electrolyte. The corrosion rate of the metal, the mechanism of the deposition-dissolution process, the kinetic parameters, the quality of the metal deposit, and the half-cell potential depend on the character of the solid electrolyte interphase (SEI).

The electrochemical behavior of the alkali metals in nonaqueous systems was extensively studied in the last 15 years, mainly in connection with high energy battery systems. This work is summarized in Ref. (1-4). The electrode kinetics of the alkali metals in these systems were treated and analyzed following the Butler-Volmer equation. It was generally assumed (1-4) that the rate-determining step (rds) is the transfer of electrons from the metal to the ions in the solution. Some experimental results indicate that this assumption is oversimplified and the real situation is much more complex. For example, the anodic transfer coefficient (α_a) measured for the reaction



was in many cases 0.45-0.13 (1-5). In one case, α_a , (for reaction [1]) was found to be insensitive to the concentration of Li^+ ions in the solution (7) while in another case (6) it was extremely sensitive to the concentration of Na^+ in the solution. The most complex behavior of these systems is demonstrated in Table I. This table contains six similar nonaqueous systems. However, when these systems are electrolyzed, the first three yield aluminum as expected from thermodynamic considerations, while the other three yield lithium or magnesium in apparent contradiction to thermodynamics. Each of the first three systems is used as a bath for the electroplating of aluminum. The surfaces of the electrodes immersed in these systems are in direct contact with the solution either during electrolysis or under open-circuit conditions. The last three systems are examples of nonaqueous battery (NAB) systems. In these systems the electrodeposited metal is the more reactive one.

Recently, it was concluded by Dey (13), and Rauh and Brummer (14) that in some NAB systems the lithium metal is covered by a Li^+ conducting film. A more detailed model for such a film has been described for

the magnesium electrode in thionyl chloride solutions (12).

In this paper it will be emphasized that the electrode kinetics and the deposition-dissolution mechanism of the alkali and alkaline earth metals in NAB systems are entirely different from those characteristic of other nonaqueous or aqueous electrochemical systems. A model will be proposed aimed at explaining the complex and unique behavior of NAB systems.

The SEI model.—It is suggested that in practical NAB systems the alkali and alkaline earth metals are always covered by a surface layer at least 15-25 Å thick (12). This layer is formed instantly by the contact of the metal with the solution. The thickness of this freshly formed layer is determined by the electron tunneling range. This layer consists of some insoluble products of the reaction of the metal with the solution. It acts as an interphase between the metal and the solution and has the properties of solid electrolyte, through which electrons are not allowed to pass. Therefore, it is called "Solid Electrolyte Interphase (SEI)."

The existence of this electronic insulating layer on the anodes in NAB systems is the principle difference between NAB and aqueous-like systems such as, Examples 1-3 in Table I. It should be emphasized that

Table I. Electrolysis of nonaqueous systems

No.	Electrolyte	Solvent	Electrodeposited metal	Ref.
1	$AlBr_3 + LiBr$	Toluene	Al	(8)
2	$AlCl_3 + LiCl + LiAlH_4$	Diethyl ether	Al	(9)
3	$AlCl_3 + LiCl + LiAlH_4$	THF	Al	(10)
4	$AlCl_3 + LiCl$	Thionyl chloride	Li	(11)
5	$AlCl_3 + LiCl$	Propylene carbonate	Li	(1)
6	$FeCl_2 + MgCl_2$	Thionyl chloride	Mg	(12)

* Electrochemical Society Active Member.
Key words: battery, electrolyte, corrosion.

in NAB systems (according to this suggestion) there is never a direct and free contact between the metal and the solution. Thus, these batteries will be called SEI batteries. The electrochemical behavior of SEI electrodes will be governed by the properties of the SEI. The following properties of the SEI should be considered: its morphology (compact or porous, size of the crystals); its thickness (L); the type and the concentration of the lattice defects; the transference numbers of electrons (t_e), cationic defect (t_+), anionic defect (t_-); the mobility of these defects. The potential difference $\Delta\phi_{M/sol}$ contains three components (12)

$$\Delta\phi_{M/sol} = \Delta\phi_{M/SE} + \Delta\phi_{SE} + \Delta\phi_{SE/sol} \quad [2]$$

the total overpotential contains similar terms.

The simplest and most important case for NAB systems is a SEI electrode having $t_+ = 1$ and $t_e = 0$, i.e., the SEI is a pure cationic conductor. In this case, the electrode will be reversible for its own cations and thus will obey the Nernst law. The dissolution-deposition process for SEI electrode having Schottky lattice defects is schematically described in Fig. 1. It has three steps: (i) on cathodic polarization a metallic cation sheds its solvent molecules, crosses the solution/SE interface and enters inside a vacancy in the SEI; (ii) it migrates through the bulk of the SEI by Schottky vacancies mechanism; (iii) finally, it reaches the metallic surface and accepts an electron from the metal and becomes a member of the metallic lattice. On anodic polarization the metallic cation moves in

the opposite direction. The dissolution-deposition process in a real SEI electrode is more complicated as some of the following phenomena can be involved: crystallization; grain boundary effect; shorts through the SEI during prolonged deposition; breakdown and repair of the SEI during prolonged dissolution; adatoms formation in the M/SE interface; and adsorbed ions in the SEI/solution interface. Some of these phenomena will be discussed later.

It is possible to electrodeposit alkali or alkaline earth metals (12) from NAB systems on an inert cathode. However, in these cases the metal should start to deposit only after the electrode surface is completely covered by a passivating layer which acts as a SEI through which the electrons cannot pass (12).

Kinetics of the SEI electrode.—As it was mentioned the most important and simple case is $t_+ = 1$ ($t_-, t_e = 0$). In this case, the rds may be any one of the three steps described above. For highly conductive SEI at small thickness the charge transfer reaction at one of the SEI interfaces may be the rds. However, when the SEI is thick enough the migration of ions through it may be the rds. Moreover, it is known that the ionic conductivity of pure solid crystals is very low at room temperature (15), a fact which strengthens the last assumption. In this case it is possible to use Eq. [3] describing the migration of ions in a solid crystal under external field (16). It is assumed that L is larger than the space charge lengths in the SEI, and there is no change in the concentration or mobility of the mobile lattice defects through the SEI

$$i = 4ZF a n_+ \nu \exp(-W/RT) \sinh(aZF E/RT) \quad [3]$$

a = half-jump distance, ν = vibration frequency of the ion in the crystal, n_+ = concentration of the lattice cationic defect, Z = the valance of the mobile ion, W = a barrier energy for jumping, E = electric field. The assumption that the migration of the cation in the SEI is the rds means that the largest fraction of the electrode overpotential (η) will develop on the SEI, i.e.

$$\eta = EL \quad [4]$$

On the substitution of Eq. [4] in Eq. [3], one gets

$$i = 4ZF a n_+ \nu \exp(-W/RT) \sinh(aZF \eta /RTL) \quad [5]$$

At $\eta = 0$, the forward and backward ionic current through the SEI are equal and the ionic exchange current density (i_0') can be defined

$$i_0' = \vec{i} = \overleftarrow{i} \quad [6]$$

where i_0' is given by (7)

$$i_0' = 2ZF a n_+ \nu \exp(-W/RT) \quad [7]$$

and Eq. [5] becomes

$$i = 2i_0' \sinh(aZF \eta /RTL) \quad [8]$$

For high field conditions ($aZF \eta > RTL$) a Tafel-like equation is obtained

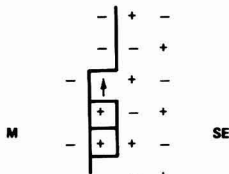
$$i = i_0' \exp(aZF \eta /RTL) \quad [9]$$

and the Tafel slope is

$$b = \frac{2.3 RTL}{aZF} \quad [10]$$

That means that one cannot expect to get a sole Tafel slope when measuring the kinetics of the alkali and the alkaline earth metals in NAB systems. The minimum value of b can roughly be estimated using Eq. [11]. For $z = 1$, $a = 3A$, $L = 20A$ one gets b 400 mV

$$b(\text{mV}) \sim \frac{60L}{aZ} \quad [11]$$



MIGRATION IN SE ($\Delta\phi_{SE}$)

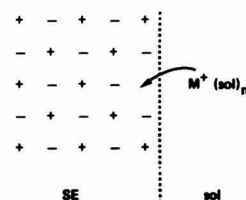
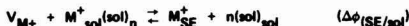
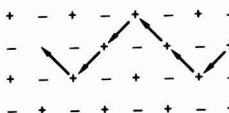


Fig. 1. A schematic description of the deposition-dissolution process (see text).

However, Tafel slopes of several volts can be measured for a thicker SEI electrode.

For low field conditions, Eq. [5] reduces to Ohm's law

$$i = \frac{4a^2 Z^2 F^2 \rho n_+ \exp(-W/RT)}{RT} \cdot \frac{\eta}{L} \quad [12]$$

or

$$i = \frac{1}{\rho} \cdot \frac{\eta}{L} \quad [13]$$

where ρ is the resistivity of the SEI. The reaction resistance of an electrode is defined as

$$R_r = \left(\frac{\eta}{i} \right)_{\eta \rightarrow 0} \quad [14]$$

thus

$$R_r = \rho L \quad [15]$$

The relation between i_0' and ρ is given by

$$i_0' = \frac{RT}{2\rho a Z F} \quad [16]$$

where

$$\rho = \frac{RT}{4a^2 Z^2 F^2 \rho n_+ \exp(-W/RT)} \quad [17]$$

The reaction resistance of SEI electrode increases linearly with the thickness of the SEI (Eq. [15]). Thus no sole value of R_r can be measured in these NAB systems.

Another interesting aspect is the way the concentration of the cation in the solution affects the reaction resistance. In the case of regular electrode kinetics regarding an electron transfer reaction the concentration effect is given by (18)

$$i_0(CT) = \text{const} \cdot C_M + \alpha_a \quad [18a]$$

or

$$R_r = \text{const} \cdot C_M + \alpha_a \quad [18b]$$

where α_a is the anodic transfer coefficient and i_0 is the exchange current density for the electron charge transfer (CT) reaction.

However, in the case of SEI electrodes two extreme cases can be identified: (i) $L \gg$ space charge length and the rds is migration through the SEI. In this case the concentration of the cation in the solution is not expected to affect R_r and the calculated apparent α_a should be close to zero; (ii) $L \approx$ space charge length. In this case the concentration of the ions in the solution may affect the concentration of the defects in the SEI and thus may affect R_r , i_0' , and ρ . It can be expected that the apparent transfer coefficient as defined in Eq. [18b] will be decreased to zero as L increases. The direction of this effect depends on the type of the lattice defects and on the pzc of the SEI.

Literature examples.—The double-layer capacitance in nonaqueous solutions has values of 10–30 $\mu\text{F cm}^{-2}$ (19). Any nonaqueous alkali or alkaline earth metal system which shows electrode interfacial capacitance smaller than 5 $\mu\text{F cm}^{-2}$ should be suspected for an anode being coated by SEI. Scarr (20) measured 2.4–5.2 $\mu\text{F cm}^{-2}$ in the Li/PC + LiClO₄ system. Values smaller than 1 $\mu\text{F cm}^{-2}$ were measured for the Mg/SOCl₂, Mg²⁺, and the Li/SOCl₂, Li⁺ systems (21). The anodic transfer coefficient (α_a) for the lithium electrode in nonaqueous solution was found to be smaller than 0.5 which means that the Tafel slope (b) is larger than 120 mV. The results are summarized in Table II. Scarr (20) found a smaller α_a value where the "double layer" capacity was smaller: α_a was 0.25 where C_{dl} was 2.4 $\mu\text{F cm}^{-2}$, α_a was 0.5 where C_{dl} was 5 $\mu\text{F cm}^{-2}$. This can be explained by different thicknesses of the SEI in these two experiments. If we assume that the dielectric coefficient of the SEI is 10, then in the first

Table II. The kinetic parameters for the Li electrode in nonaqueous system

$\alpha_a^{(1)}$	$\alpha_a^{(2)}$	$b^{(3)}$ (mV)	System	Ref.
0.25		250	Li (Hg), DMSO, LiCl	(22)
	0.2		PC, LiAlCl ₄	(7)
0.13		450	PC, LiAlCl ₄	(5)
	0.5		PC, LiClO ₄	(20)
	0.25		PC, LiClO ₄	(20)
	0.25		PC, LiAlCl ₄	(1)
	0.17–0.52 ⁽⁴⁾		TC, LiAlCl ₄	(23)

⁽¹⁾ From Tafel equation.

⁽²⁾ From Equation (18a).

⁽³⁾ Formally calculated using $b = 60/\alpha_a$ (mV).

⁽⁴⁾ Depending on the thickness of the SEI.

experiment L was about 40 Å and in the second one only 20 Å.

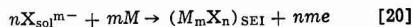
In other cases it was found that a linear relation between the overpotential and the current density is continuous beyond the expected value predicted by the Volmer-Butler equation. The lithium electrode in SOCl₂ shows ohmic behavior up to 600 mV (23). The Li electrode in pc exhibits ohmic behavior up to 200 mV (7). The value of the Tafel slope (b) should be at least five times larger than the highest overpotential value on the linear plot. Thus the expected Tafel slopes for these electrodes should be 3 and 1V (at least), respectively.

Complications associated with SEI batteries (SEI with $t_- > 0$).—So far the simplest SEI anodes having $t_+ = 1$ were discussed. These anodes are mostly desirable from a practical point of view. SEI anodes having $t_+ < 1$, $t_- > 0$ ($t_e = 0$) are undesirable for battery applications and may exhibit a much more complex behavior. The current through such SEI is carried both by cationic and anionic defects. As a result, on anodic polarization (discharge of the battery), anions will be injected from the solution into the SEI and will finally reach the M/SE interface. In such systems, especially where $t_- > t_+$, this process may lead to the increase of the thickness of the SEI and to increase in the polarization. In NAB having such SEI, the anode will be severely polarized and even blocked after a short period of discharge time.

Another disadvantage of such a system is the effect of t_- on the emf of the battery and on the anodic half-cell potential. These electrodes are not expected to follow a simple Nernst equation, but a more complicated one (19)

$$\Delta\phi_{M/\text{sol}} = t_+ \left(E^\circ - \frac{RT}{nF} \ln [M^{n+}]_{\text{sol}} \right) + \frac{t_-}{mF} (\Delta G \text{ side reaction}) \quad [19]$$

The over-all side reaction may be



where X^{m-} is an anion in the solution which is capable of migrating through the SEI.

It seems that this case is relevant to many NAB systems which use calcium or magnesium as the anode since in many magnesium or calcium compounds, the value of t_+ is smaller than 1 (15) (e.g., chlorides and oxides). This may be the reason we have no calcium or magnesium nonaqueous batteries.

It was found that calcium and magnesium SOCl₂ cells have less capacity than the lithium one (24–26). In addition, it was observed that the Ca anode in the SOCl₂ cell became coated by a white precipitate during discharge until it was completely blocked (25, 26).

A similar situation may exist in the Mg-MnO₂ dry cell (24). In this case the passivating layer on the surface of the anode (MgO or Mg(OH)₂) may have $t_{Mg+2} < 1$. As a result the OCP of this cell is lower than expected. A similar phenomenon was observed during cycling of Li in LiBF₄-PC solutions (27). The stripping overpotential rose with time and a buildup of a passivating layer on the top of the lithium deposit was observed by SEM. This type of behavior may be attributed to SEI having $t_{-} > 0$. An attempt to improve the electrochemical performance of Mg electrode in SOCl₂ solution by doping the SEI with higher valance cations was made but with no success yet (24).

Shorts during deposition.—The plating current efficiency of lithium in organic systems reaches 100% (2, 14, 28, 27). However, the stripping efficiency is much lower than 100% and declines with wet standing and with the plating current density (27, 28). The reason for this phenomenon seems to be the formation of shorts through the SEI during plating as a result of local excessive heating and the high electric field on the SEI. The increase of the plating rate should aggravate the formation of shorts. The formation mechanism of these shorts may be the dissolution and trapping of metallic atoms in the cationic vacancies and of electrons in the anionic vacancies. This type of phenomenon occurs during the electrolysis of solid alkali halides at elevated temperatures and it causes the increase of the electronic conductivity of the solid (29). A more detailed description of this problem can be seen in Fig. 2. As a result of local heating, some part of the SEI becomes an electronic conductor (Fig. 2a), and therefore, lithium metal begins to deposit in the bulk of the SEI (Fig. 2b). This process continues and a ball of lithium totally covered by SEI is formed (Fig. 2c). As the current diminishes, this short zone in the SEI dis-

appears and later, when the battery is discharged, this insulated lithium ball will not be dissolved (Fig. 2d). This results in a decrease in the discharge current efficiency. In order to alleviate this problem the ionic resistivity of the SEI should be decreased by doping. This way both the electric field, which will be developed on the SEI, and the electrical heating of the SEI will be reduced.

The growth rate of the SEI.—A slow corrosion rate, and therefore, a long shelf life is expected for systems in which, at least, one of the corrosion products is very insoluble and immediately precipitates on the anode surface to form a dense and hole-free SEI which is a very good insulator for electrons. However, even in this case, the thickness of the SEI will slowly increase with time of storage. The rds for this process will always be the cathodic reaction, i.e., the reduction of the solvent. The functional relation between the thickness of the SEI and the storage time is determined by the mechanism of the cathodic reaction. Two extreme cases can be identified. (i) The anode surface and the SEI are not completely homogeneous, i.e., the anode contains anodic areas in which metallic ions are dissolved and cathodic areas in which the electrons are migrating through the SEI and reducing the solvent. This case may be relevant to practical systems having impurities which are able to create cathodic zones. (ii) In an ultrapure system, the anode and the SEI are completely homogeneous and thus no well-defined cathodic areas can exist. In this case, the rds will be the diffusion of electrons through the SEI to the solution side.

For the first case, the growth rate of the SEI can be formulated as follows

$$V(\text{corrosion}) = V_{\text{eq,cell}} - \eta_c - \eta_a - iR = 0 \quad [21]$$

$V_{\text{eq,cell}}$ = OCP ($i = 0$), η_c , η_a = cathodic and anodic overpotential; R = resistance of the solution. In practical NAB systems both η_a and iR can be neglected. Thus

$$\eta_c = V_{\text{eq,cell}} \quad [22]$$

If we assume that (i) the corrosion current follows Ohm's law and (ii) the electronic resistivity of the SEI [$\rho(e)$] is constant with time then we get

$$i_{\text{corr}} = \frac{V_{\text{eq,cell}}}{\rho(e) \cdot L} \quad [23]$$

It was assumed that all the corrosion products precipitate on the anode, to give a homogeneous film thus

$$\frac{dL}{dt} = Ki_{\text{corr}} \quad [24]$$

where K is a constant.

From Eq. [23] and [24] one gets

$$\frac{dL}{dt} = \frac{KV_{\text{eq,cell}}}{\rho(e) \cdot L} \quad [25]$$

After integration of Eq. [25]

$$L = \left(L_0^2 + \frac{2KV_{\text{eq,cell}}}{\rho(e)} \cdot t \right)^{1/2} \quad [26]$$

where $L_0 = L$ at $t = 0$. This is a parabolic law of growth of the SEI.

The second mechanism involves the diffusion of electrons through the SEI as the rds for the corrosion of the anode. The corrosion current density will follow Eq. [27]

$$i_{\text{corr}} = \frac{FDC_0}{L} \quad [27]$$

where D is the diffusion coefficient of the electrons in the SEI and C_0 is the concentration of the electrons in

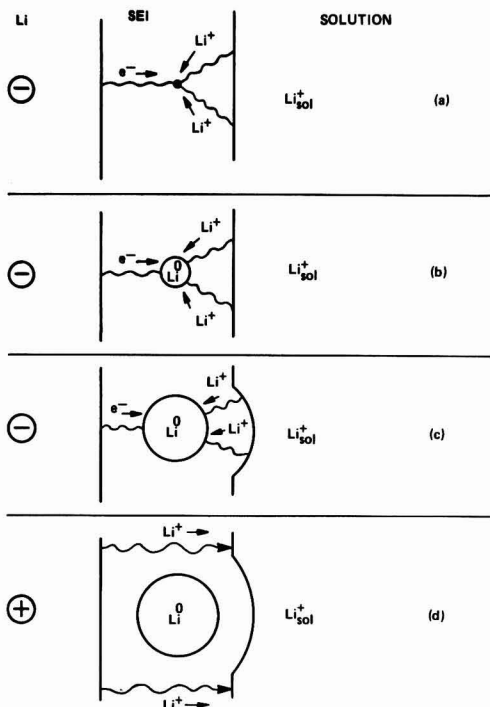


Fig. 2. The effect of a partial short on the deposition-dissolution process (see text).

the SEI near the M/SE interface. From Eq. [24] and [27]

$$\frac{dL}{dt} = \frac{KFDC_0}{L} \quad [28]$$

After integration a parabolic law of growth is obtained

$$L = (L_0^2 + 2KFDC_0 t)^{1/2} \quad [29]$$

Although the two corrosion mechanisms both lead to parabolic law of growth they should be considered as first approximation only. A practical system may be more complicated due to the following: $\rho(e)$ or D may change with L ; the SEI may contain cracks, holes, and grain boundaries at which the greatest part of the electronic leakage current may take place. The SEI may be nonhomogeneous and contain crystals of different sizes (21). Therefore deviations from the parabolic law of growth are expected.

The thickness of the SEI of Li in $\text{LiAlCl}_4\text{-SOCl}_2$ system was measured as a function of time at room temperature. The value of α in Eq. [30] was calculated for several Li electrodes (21)

$$L = \text{const} \cdot t^\alpha \quad [30]$$

Not all the Li electrodes exhibited the parabolic law of growth as values between 0.2 and 0.5 were obtained.

Summary

A model which is designed to explain the complex and unique electrochemical behavior of alkali and alkaline earth metals NAB systems was presented in this paper. This model is supported by many experimental results. It was indicated that the deposition-dissolution mechanism of alkali and alkaline earth metals in SEI-NAB systems is entirely different from that in aqueous or aqueous-like systems. Therefore the improvement or control of this process should be done by different means. It is concluded that a proper anodic SEI is the key for the operation of NAB. It seems that the controlling of the properties of the SEI, i.e., reducing t^- and t_e , increasing t^+ as close as possible to unity, and reducing ρ (by doping the SEI), will improve the performance of the SEI nonaqueous batteries.

Manuscript submitted Dec. 27, 1978, revised manuscript received April 9, 1979. This was Paper 4 presented at the Atlanta, Georgia, Meeting of the Society, Oct. 9-14, 1977.

Any discussion of this paper will appear in a Discussion Section to be published in the June 1980 JOURNAL. All discussions for the June 1980 Discussion Section should be submitted by Feb. 1, 1980.

Publication costs of this article were assisted by Tel-Aviv University.

REFERENCES

- J. Jorne and C. W. Tobias, *This Journal*, **121**, 994 (1974).
- R. Jasinski, in "Advances in Electrochemistry and Electrochemical Engineering," Vol. 8, C. W. Tobias, Editor, Wiley-Interscience, New York (1971).
- J. W. Butler, in "Advances in Electrochemistry and Electrochemical Engineering," Vol. 7, P. Delahay, Editor, Wiley-Interscience, New York (1970).
- W. H. Tiedemann and D. N. Bennion, *This Journal*, **120**, 1624 (1973).
- J. C. Cessna, *Corrosion (Houston)*, **27**, 244 (1971).
- S. G. Meibuhr, *This Journal*, **118**, 709 (1971).
- S. G. Meibuhr, *ibid.*, **118**, 1320 (1971).
- E. Peled and E. Gileadi, *Plating (East Orange, N.J.)*, **62**, 342 (1975).
- A. Brenner, in "Advances in Electrochemistry and Electrochemical Engineering," Vol. 5, C. W. Tobias, Editor, Wiley-Interscience, New York (1967).
- M. Yoshio and N. Ishibashi, *J. Appl. Electrochem.*, **3**, 321 (1973).
- J. J. Auborn, K. W. French, S. I. Lieberman, V. K. Shah, and A. Heller, *This Journal*, **120**, 1613 (1973).
- E. Peled and H. Straze, Extended Abstract No. 127 presented at the 27th ISE Meeting, Zurich, Switzerland, September (1976); *This Journal*, **124**, 1030 (1977).
- A. N. Dey, Paper 62 presented at The Electrochemical Society Meeting, Atlantic City, New Jersey, October 4-8, 1970.
- R. D. Rauh and S. B. Brummer, *Electrochim. Acta*, **22**, 75 (1977).
- L. Heyen, *ibid.*, **15**, 1251 (1970).
- L. Young, in "Anodic Oxide Films," Academic Press, New York (1961).
- M. J. Digman, in "The Anodic Behavior of Metals and Semiconductors Series," Vol. 1, J. W. Diggle, Editor, Marcel Dekker Inc., New York (1972).
- E. Gileadi, E. Kirova-Eisner, and J. Penciner, in "Interfacial Electrochemistry," Addison-Wesley Publishing Co., Inc., Reading, Mass. (1975).
- P. Payne, in "Advances in Electrochemistry and Electrochemical Engineering," Vol. 7, P. Delahay and C. W. Tobias, Editors, Wiley-Interscience, New York (1970).
- R. F. Scarr, *This Journal*, **117**, 295 (1970).
- E. Peled and H. Yamin, in "Proceedings of the 28th Power Sources Symposium," p. 237, Atlantic City, New Jersey, June 1978.
- D. R. Cogley and J. M. Butler, *J. Phys. Chem.*, **72**, 4568 (1968).
- E. Peled and H. Yamin, *Isr. J. Chem.*, **18**, 131 (1979).
- E. Peled and A. Meitav, Paper 554 presented at The Electrochemical Society Meeting, Seattle, Washington, May 21-26, 1978.
- M. Domeniconi, *et al.*, Interim Report No. N00014-76-C-0524, October 1977.
- J. R. Driscoll, *et al.*, ECOM Report No. 74-0030-12, April 1977.
- P. J. Rommer and J. R. V. Beck, Paper 1 presented at The Electrochemical Society Meeting, Atlanta Georgia, Oct. 9-14, 1977.
- R. Selim and P. Bro, *This Journal*, **121**, 1457 (1974).
- J. H. Schulman and W. D. Compton, in "Color Centers in Solids," Pergamon Press, New York (1962).

Primary Li/SOCl₂ Cells

VIII. Effect of Type of Carbon on the Performance

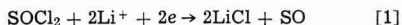
A. N. Dey*

P. R. Mallory & Company, Incorporated, Laboratory for Physical Science, Burlington, Massachusetts 01803

ABSTRACT

Twelve different carbons having a large variation in physical properties such as particle size, BET surface area, density, and electrical conductivity were evaluated as cathodes for Li/SOCl₂ hermetic D cells. The particle size, BET surface area, and density did not affect the performance of the cells in terms of delivered energy density except in extreme cases such as graphite, the particle size of which is larger by three orders of magnitude. At least five different types of carbon were found to be as good as Shawinigan Black at high rates.

The performance limiting process of the Li/SOCl₂ cells was found (1) to be the passivation of carbon cathode by the precipitation of LiCl, the product of SOCl₂ reduction on the porous carbon cathode according to the reaction



We examined (2) the cathode reaction profiles as well as the cathode expansion characteristics in an effort to optimize the cathode structures for maximum energy density, using Shawinigan Black carbon. It was felt that, in addition to the cathode structure, the type of carbon may also play an important role in determining the performance of the cathode. Only a few types of carbon other than Shawinigan Black were reported to be used (3-5) in Li/SOCl₂ cells so far. We selected twelve different types of carbon having diverse properties in terms of particle size, density, and electrical conductivity for evaluation as cathodes in the Li/SOCl₂ system. We chose a high rate hermetic D cell as a vehicle for this evaluation. The experimental details and the results are reported here.

Experimental

Carbons.—Of the twelve types of carbon selected, Neo Spectra AG, Raven-420, Raven 3500, Royal Spectra, and Conductex 950 were from Cities Service Company, Columbia Division; Elftex-12, Mogul L, Regal 660-R, Vulcan XC-72R, Monarch 700, and Sterling R were from Cabot Corporation; and Graphite KS10 was from Lonza Corporation. The above carbons were used as received without any pretreatment.

Specific resistivity of the carbons was measured by pressing pellets at 13,300 psi and measuring the electrical resistance of the pellets at 1 kHz using a General Radio Impedance Bridge.

Cathode fabrication.—The various carbons were mixed with colloidal Teflon binder in a 90:10 weight ratio and the mixture was pasted on expanded nickel current collector to make carbon cathodes. The finished cathodes were found to be quite different from carbon to carbon. The thickness of the cathodes varied from carbon to carbon. In cathodes with some types of carbon, there were visible cracks along the ribs of the expanded nickel current collector. The appearance of the cathodes made from the various types of carbon are shown in Fig. 1. Only the gross physical characteristics of the cathodes are visible from the photographs. Cathodes were also characterized using SEM (scanning electron microscope). The electrical resistance of the cathode across its thickness was also measured using two copper electrodes (0.71 cm²).

Cell fabrication and testing.—Hermetic D size (OD: 3.30 cm, Ht: 6.05 cm) cells were made using either (51 cm) or (38 cm) long (4.445 cm wide) cathodes made from the various carbons depending upon the thickness of the cathodes; 51 cm for thinner cathodes and 38 cm for thicker cathodes, respectively. The length and the width of the Li anode was the same as the cathode; only the thickness of the Li was varied depending upon the length; viz. 0.038 cm thick Li was used with 51 cm long electrodes and 0.051 cm thick Li was used for the 38 cm long cathodes.

The details of the cell construction and the electrolyte preparation are available elsewhere (6). The cells were filled with 1M LiAlCl₄-SOCl₂ electrolyte and then sealed hermetically. The performance characteristics of the cells were evaluated by discharging them at constant currents ranging from 0.03 to 3.0A at 25°C. The efficacy of the various carbons was determined from the capacities and the energy densities delivered by the cells.

Results and Discussion

Carbons.—The properties of the various carbons used are listed in Table I. The Shawinigan Black is made by the continuous thermal decomposition of acetylene at 800°C. The other blacks are made by the furnace process except for the Royal Spectra and Neo Spectra AG which are made by the Channel process. In the Channel process, the carbons are subjected to thermal oxidation, thereby incorporating oxygen on the carbon surface which in turn results in higher volatile matter content and a low pH, most likely due

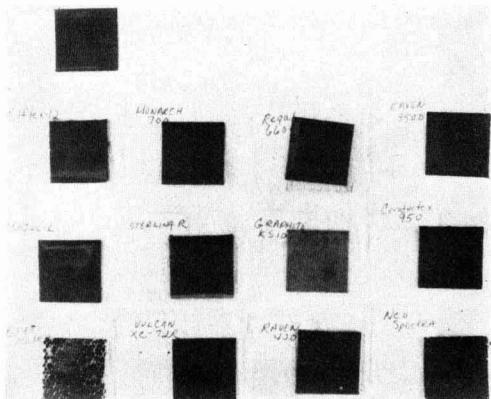


Fig. 1. Photograph of carbon cathode specimens made from the various types of carbon.

* Electrochemical Society Active Member.

Key words: inorganic, electrolyte, carbon, cathode.

Table I. Types of carbon and their properties

Carbon type	Supplier	Letter Designation	Particle size (m μ)	BET surface area (m ² /g)	Apparent density (lb/ft ³)	pH	Fixed carbon (%)	Volatile matter (%)	Specific resistance (Ω -cm)
Shawinigan Black	(Shawinigan)		43	60	1.2	—	99.5	—	0.022, 0.026
Neo Spectra AG	(Columbian)	G	13	900	8	3	86.0	14.0	0.276, 0.383
Elfex-12	(Cabot)	H	37	45	11	8.5	99.0	1.0	0.030, 0.033
Mogul-L	(Cabot)	J	24	138	15	3.4	95.0	5.0	0.075, 0.074
Raven-420	(Columbian)	K	28	70	17	9	99.6	0.4	0.044, 0.037
Raven-3500	(Columbian)	L	16	319	17	3	96.2	3.8	0.025, 0.111
Regal 660-R	(Cabot)	M	24	112	15	7.5	99.0	1.0	0.101, 0.042
Royal Spectra	(Columbian)	N	10	1125	6	4	83.5	16.5	1.10, 1.15
Conductex-950	(Columbian)	O	21	245	10	6.5	99.2	0.8	0.044, 0.051
Vulcan XC-72R	(Cabot)	P	30	254	6	7	98.0	2.0	0.021, 0.035
Monarch-700	(Cabot)	R	18	200	9	8	99.0	1.0	0.167, 0.054
Sterling R	(Cabot)	S	75	25	16	8.5	99.0	1.0	0.035, 0.034
Graphite KS10	(Lonz)	T	10 ^a	~20	140	7.6	99.9	0.1	~0.002

to the formation of carboxylic acid groups on the carbon surface.

The particle size of the various carbons varied from 10 m μ for Royal Spectra to 75 m μ for Sterling R. Graphite KS10 has the largest particle size of 10 microns. Correspondingly, the surface areas of the various carbons varied from 25 m²/g for Sterling R to 1125 m²/g for Royal Spectra. Shawinigan Black has the lowest apparent density of 1.2 lb/ft³ (0.0192 g/cm³). Among the other carbon types, the lowest apparent density was 6 lb/ft³ (0.0961 g/cm³) for Royal Spectra and Vulcan XC-72R. The highest apparent density was 17 lb/ft³ (0.272 g/cm³) for Raven 3500 and 420 (excluding graphite, the density of which is 140 lb/ft³ 2.24 g/cm³).

The electrical resistivity of the various carbons was measured by pressing the carbons in pellets at a pressure of 13,300 psi. The values shown in Table I were obtained while the pellets were under pressure. On releasing the pressure, the resistivity values increased significantly. It appears that the carbons with the highest surface areas *viz.* Royal Spectra and Neo Spectra AG have the highest electrical resistivities. Next to graphite, Shawinigan Black and Vulcan XC-72R have the lowest resistivity. The resistivities of Elfex-12, Sterling R, Conductex 950, and Raven 420 are slightly higher. The resistivities of Mogul-L and Raven 3500 were almost twice as much as the above carbons.

The measured electrical resistance of the cathodes made from the above carbons, across its thickness, also followed approximately the same pattern.

Cathodes.—The cathodes were characterized by scanning electron microscopy at 1000 and 10,000 magnifications. The photographs revealed the microstructure of the cathodes. The photographs of the cathodes made from the various types of carbon at 1000 magnification are shown in Fig. 2 and 3. The photographs were taken at or near a surface microcrack on the cathode. The filaments crossing over the cracks are Teflon filaments from the Teflon binder. They demonstrate the efficacy of Teflon in binding the carbon particles in a filamentary web. This allows the carbon cathode to expand (2) on discharge without losing its mechanical integrity. The filamentary nature of the binder also prevents mechanical blockage of the active sites on the carbon particle where the discharge of SOCl₂ occurs according to the reaction [1].

Note that the photograph of the Shawinigan Black cathode, shown in Fig. 4, was at 2000 magnification instead of 1000. The carbon particles of the Shawinigan Black cathode appear to be somewhat less conglomerated than the other types of carbon. This is reflected in the exceptionally low bulk density of the Shawinigan Black compared to the other carbons.

The microstructures of the cathode surface were further clarified at a magnification of 10,000 \times . The photographs are shown in Fig. 5 and 6. Again, the spacings

between the carbon particles appear to be much greater in cathodes made from Shawinigan Black than in the cathodes made from the other carbons. This is consistent with their bulk densities.

Cell performance.—The details of the relevant cell construction parameters and the test results of the D

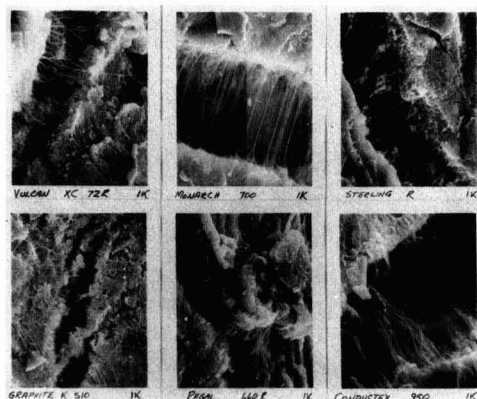


Fig. 2. SEM photographs of cathode specimens made from Mogul L, Raven 3500, Neo Spectra, Elfex 12, Raven 420, and Royal Spectra; original magnification 1000 \times .

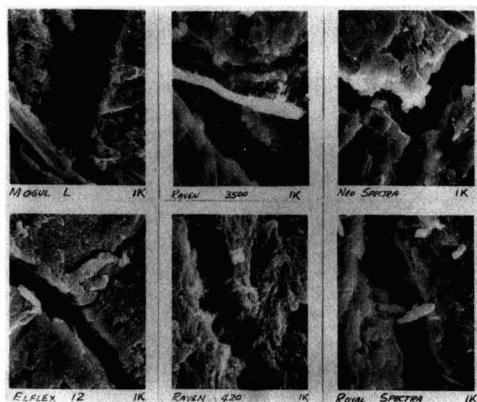


Fig. 3. SEM photograph of cathode specimens made from Vulcan XC72R, Monarch 700, Sterling R, Graphite KS10, Regal 660R, and Conductex 950; original magnification 1000 \times .

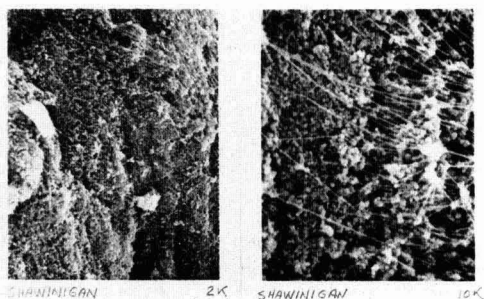


Fig. 4. SEM photograph of cathode specimens made from Shawinigan Black carbon; original magnification, 2000 \times and 10,000 \times .

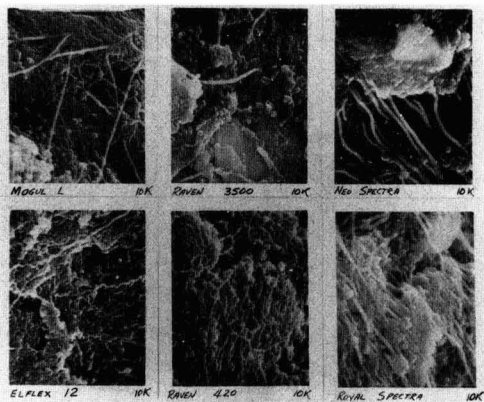


Fig. 5. SEM photograph of cathode specimens made from Mogul L, Raven 3500, Neo Spectra, Elfex 12, Raven 420, and Royal Spectra; original magnification 10,000 \times .

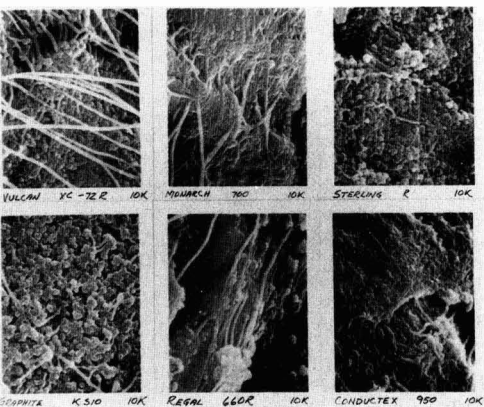


Fig. 6. SEM photograph of cathode specimens made from Vulcan XC72R, Monarch 700, Sterling R, Graphite KS10, Regal 660R, and Conductex 950; original magnification 10,000 \times .

cells with the carbons described above are summarized in Table II. The typical discharge curves of Li/SOCl₂ D cells made with the Sterling R carbon are shown in Fig. 7. Since we have chosen a practical hermetically sealed D cell structure instead of experimental bottle or bag type of cell (with excess electrolyte, etc.) for the evaluation of the various types of carbons, it is

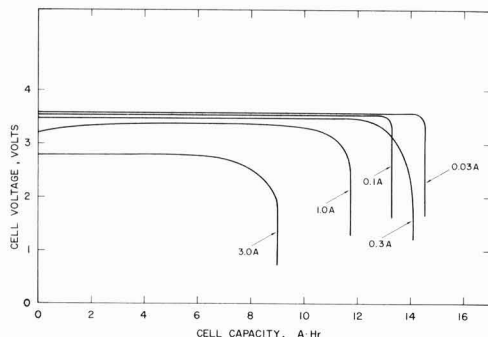


Fig. 7. Typical discharge curves of Li/SOCl₂ hermetic D cells with Sterling R carbon cathode.

possible to analyze the data with reference to actual, practical cell performance rather than in terms of criteria that cannot be translated to actual cell performance. The energy densities of all the cells made with various types of carbons and tested at various currents are plotted as a function of current and shown in Fig. 8. The data points are shown in letters G to T representing various types of carbons. The two solid lines represent the data points of D cells with Shawinigan Black; the line with shaded circles belongs to the cells with 38 cm long electrodes and the line with unshaded circles belongs to the cells with 51 cm electrodes. It is clear that almost all types of carbon with the exception of Mogul L (J), Raven 3500 (L), and Graphite KS10 (T) are as good as the Shawinigan Black carbon insofar as the performance of the Li/SOCl₂ cells is concerned. The five types of carbon which were found to be the most promising, particularly for high rate cells are Elfex-12 (H), Regal 660 R (M), Vulcan XC-72R (P), Monarch 700 (R), and Sterling R (S). In addition Conductex 950 (O) also performed very well.

The properties of Mogul L (J) were quite interesting in that the cells using it had a higher intrinsic energy density than did the other cells except Shawinigan Black although the rate capability was significantly poorer, most likely due to its low electrical conductivity. Graphite KS10 (T), on the other hand, has an excellent electrical conductivity, but a poor performance, due to its larger particle size and crystallinity. The poor performance of Royal Spectra and Raven 3500 may be due to their poor electrical conductivity and poor electrode integrity.

One may arrive at an altogether different conclusion if one compares the performance of the cells made with various types of carbon, based on normalizing the

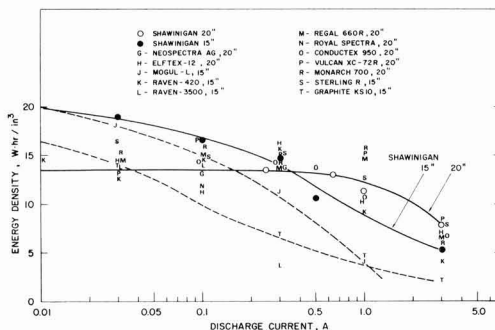


Fig. 8. Energy density of hermetic Li/SOCl₂ D cells made from various types of carbon at various currents at room temperature.

Table II. Performance characteristics of Li/SOCI₂ hermetic D cells with various carbons at 25°C

Cell No.	Electrode length (in.)	Carbon wt (g)	Electrolyte wt (g)	Li wt (g)	Cell wt (g)	Discharge current (A)	Capacity to 2.0V (A-hr)	Total energy (W-hr)	Energy density (W-hr/in. ³)
Neo Spectra AG; thickness: 0.020 in., resistance: 1.15Ω									
G-1	20	5.0	43.7	4.52	95	0.3	12.8	43.5	13.8
G-2	20	6.5	45.8	4.51	98	0.1	11.9	41.7	13.2
G-3	20	5.9	46.4	4.47	98	1.0	8.0	26.0	8.3
G-4	20	5.3	46.0	4.53	96	3.0	4.1	10.3	3.3
Elftex-12; thickness: 0.026 in., resistance: 0.71Ω									
H-2	20	11.6	41.3	4.49	100	0.03	12.8	45.4	14.4
H-1	20	11.8	42.5	4.51	101	0.1	9.9	34.8	11.1
H-3	20	12.4	42.1	4.51	100	0.3	14.8	51.8	16.4
H-6	20	9.8	43.5	4.55	101	1.0	10.0	33.0	10.5
H-4	20	9.9	44.1	4.50	101	3.0	7.5	21.8	6.9
Mogul-L; thickness: 0.037 in., resistance: 1.30Ω									
J-6	15	11.9	41.0	4.66	99	0.03	16.2	57.2	18.1
J-5	15	11.9	41.3	4.65	100	0.3	10.5	35.7	11.3
J-2	15	11.4	40.5	4.64	99	1.0	4.0	12.8	4.1
Raven-420; thickness: 0.038 in., resistance: 0.58Ω									
K-6	15	12.5	40.8	4.63	100	0.03	11.1	39.4	12.5
K-3	15	13.6	41.9	4.60	102	0.1	13.2	46.2	14.7
K-1	15	13.1	41.8	4.63	101	0.3	14.4	48.9	15.5
K-5	15	12.8	42.9	4.61	102	1.0	9.3	28.8	9.2
K-4	15	12.5	42.6	4.62	101	3.0	4.5	13.1	4.1
K-2	15	13.0	40.9	4.69	99	0.01	13.1	46.5	14.8
Raven-3500; thickness: 0.029 in., resistance: 1.0Ω									
L-2	15	7.8	44.6	4.70	97	0.1	12.5	43.8	13.9
L-3	15	7.9	43.2	4.69	96	0.3	3.5	11.7	3.7
L-4	15	7.9	47.0	4.70	96	1.0	—	—	Would not run
L-1	15	7.5	43.2	4.70	95	3.0	—	—	Would not run
L-6	15	7.9	45.1	4.70	98	0.03	12.3	43.1	13.7
Regal-660R; thickness: 0.024 in.									
M-5	20	10.8	43.1	4.52	101	0.1	13.5	47.3	15.0
M-1	20	10.5	44.0	4.55	101	0.03	13.0	46.1	14.6
M-4	20	11.0	42.5	4.50	101	0.3	12.4	43.0	13.7
M-2	20	10.3	43.2	4.50	101	1.0	13.5	45.9	14.6
M-3	20	10.4	42.1	4.52	99	3.0	7.5	21.0	6.7
Royal Spectra									
N-1	20	4.4	44.4	4.54	95	0.1	10.6	37.1	11.8
Conductex-950; thickness: 0.029 in., resistance: 0.70Ω									
O-1	20	7.6	43.4	4.54	98	1.0	10.8	34.6	11.0
O-2	20	7.6	46.1	4.53	99	0.3	13.2	44.9	14.2
O-3	20	7.6	46.2	4.50	100	3.0	7.5	21.0	6.7
O-4	20	8.1	46.2	4.52	100	0.1	12.7	45.1	14.3
O-6	20	7.6	45.9	4.52	100	0.5	13.0	42.9	13.6
Vulcan XC-72R; thickness: 0.028 in., resistance: 0.37Ω									
P-2	20	7.0	46.4	4.54	100	0.03	11.6	41.2	13.1
P-1	20	6.9	46.2	4.50	100	0.1	14.4	50.8	16.1
P-3	20	7.1	45.6	4.57	100	0.3	13.7	47.3	15.0
P-5	20	7.2	45.6	4.53	98	1.0	14.0	46.2	14.7
P-4	20	7.1	44.9	4.52	99	3.0	9.0	26.6	8.4
Monarch-700; thickness: 0.029 in., resistance: 0.82Ω									
R-5	20	10.6	44.1	4.51	102	0.1	13.5	47.5	15.1
R-1	20	10.1	44.3	4.51	100	0.3	12.8	44.4	14.1
R-6	20	10.4	45.1	4.54	102	1.0	14.0	47.6	15.1
R-2	20	10.5	44.1	4.55	102	3.0	6.8	19.7	6.3
R-3	20	10.2	44.0	4.53	101	0.03	13.8	49.0	15.5
Sterling R; thickness: 0.036 in., resistance: 0.81Ω									
S-1	15	11.5	42.5	4.64	100	0.1	13.3	46.8	14.9
S-3	15	11.3	42.6	4.66	100	0.3	14.1	48.6	15.4
S-2	15	11.9	41.8	4.65	100	1.0	11.8	38.9	12.4
S-5	15	11.6	42.5	4.60	101	0.03	14.6	51.8	16.4
S-4	15	11.5	42.8	4.60	101	3.0	9.0	24.3	7.7
Graphite KS10									
T-3	15	16.6	42.1	4.68	105	0.1	9.0	31.4	10.0
T-6	15	16.5	41.1	4.72	104	0.3	6.4	22.2	7.0
T-5	15	16.4	39.9	4.65	103	1.0	4.5	14.9	4.7
T-1	15	16.6	41.8	4.67	105	3.0	2.3	6.7	2.1
T-2	15	16.8	40.3	4.71	103	0.03	12.8	45.4	14.4
Shawinigan									
B-32	15	5.7	44.0	5.86	98	0.03	17.6	61.6	19.0
B-33	15	5.7	43.7	5.86	98	0.1	15.2	52.4	16.5
B-30	15	5.3	45.2	5.86	99	0.3	13.3	45.9	14.4
B-19	15	—	—	—	—	0.5	10.6	33.4	10.5
B-29	15	6.2	44.0	5.75	98	3.0	7.5	19.5	6.1
Shawinigan; thickness: 0.018 in., resistance: 0.30Ω									
103	20	—	—	—	—	0.25	12.7	42.5	13.4
108	20	—	—	—	—	0.75	13.2	40.9	12.9
95	20	—	—	—	—	1.0	12.0	36.0	11.3
109	20	—	—	—	—	3.0	10.0	28.0	8.8

data with respect to the carbon weight and the electrode areas. For example, if we plot the cell capacity/wt of carbon in the cathode (instead of energy density) vs. current density (current/electrode area) for the various types of carbon, we obtain a plot shown in Fig. 9. The various letters represent the various data points belonging to the various types of carbon. The solid lines represent the data points belonging to Shawinigan Black for cells with both the 38 and 51 cm electrodes. Based on this type of analysis, the obvious conclusion is that almost all types of carbon are inferior to Shawinigan Black since all data points fall below Shawinigan Black. The reason for this is that Shawinigan Black has the lowest bulk density of all the carbons, thus having the highest capacity/carbon wt value. We have shown already that this has little bearing on the volumetric energy density of an actual cell. The increase in the carbon weight (with the denser carbons) results in only 1% or less increase in the cell weight. Thus, the dense carbons do not significantly affect the gravimetric energy densities either.

It should be pointed out that the method of preparation of the cathode using Shawinigan Black has been thoroughly optimized whereas no such exhaustive optimization has been carried out for the other types

of carbon. It is reasonable to speculate that somewhat better performance may be obtained with the other carbons after suitable optimization of the method of preparation since the physical properties of the carbon mix were found to be quite different from carbon to carbon.

Conclusions

1. Of the twelve types of carbon (including graphite) tested, all except three types had almost as good a performance as the Shawinigan Black carbon in most cells manufactured today. It should be noted that the process for making the carbon-Teflon cathode mix has been developed for Shawinigan Black over a long time. This is not the case with the other carbons.
2. The most outstanding carbon types were Shawinigan Black, Elftex-12, Regal 660R, Vulcan XC-72R, Monarch 700, Sterling R, and Conductex 950.
3. Mogul L carbon has a low electrical conductivity and a poor rate capability but its intrinsic energy density was found to be as good as that of Shawinigan Black and significantly higher than that of all the other carbons. This type of carbon might be particularly suitable for low rate high energy density cells.
4. The particle size, BET surface area, and the bulk density of the various carbons do not appear to affect the performance of the cathodes except in the case of graphite.

Acknowledgment

The author wishes to thank P. Witalis, R. Granelli, and K. Beutler for experimental assistance.

Manuscript submitted Nov. 13, 1978; revised manuscript received May 30, 1979.

Any discussion of this paper will appear in a Discussion Section to be published in the June 1980 JOURNAL. All discussions for the June 1980 Discussion Section should be submitted by Feb. 1, 1980.

Publication costs of this article were assisted by P. R. Mallory & Company, Incorporated.

REFERENCES

1. A. N. Dey, *This Journal*, **123**, 1262 (1976).
2. A. N. Dey and P. Bro, *ibid.*, **125**, 1574 (1978).
3. W. K. Behl, J. A. Christopoulos, M. Ramirez and S. Gilman, *ibid.*, **120**, 1619 (1973).
4. J. J. Auborn, K. W. French, S. I. Lieberman, V. K. Shah, and A. Heller, *ibid.*, **120**, 1613 (1973).
5. J. Christopoulos and S. Gilman, *IECEC '75 Rec.*, p. 437 (1975).
6. A. N. Dey, *Electrochim. Acta*, **21**, 855 (1976).

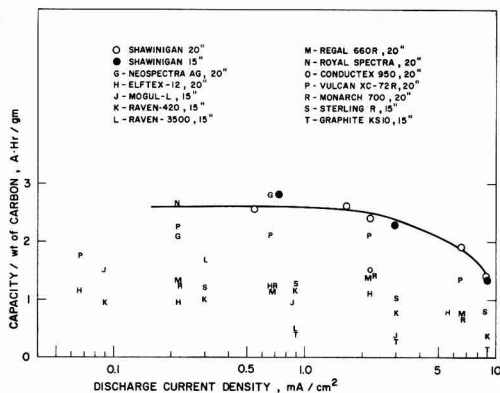


Fig. 9. Normalized plots of capacity per unit weight of carbon as a function of current density for the various type of carbon.

A Finite Difference Numerical Analysis of Galvanic Corrosion for Semi-Infinite Linear Coplanar Electrodes

P. Doig and P. E. J. Flewitt

Central Electricity Generating Board, South Eastern Region,
Scientific Services Department, Gravesend, Kent, England

ABSTRACT

A finite difference numerical analysis technique has been used to evaluate the distribution of the electrode potential within the electrolyte above a galvanic corrosion couple with linear, semi-infinite, coplanar electrodes. Corrosion reactions are assumed to be under activation control with logarithmic polarization behavior. The analysis accommodates any combination of electrochemical polarization parameters, corrosion current densities, solution conductivity, electrode dimensions, and depth of corrosion solution as variable parameters. Further, the analysis has been adapted to include the influence of an externally impressed polarization. The accuracy of the analysis procedure has been established by comparison with experimental results obtained from a model zinc-copper galvanic corrosion couple. The effects of various parameters on the electrode potential distribution at the surface of the corrosion couple have been examined and their significance discussed.

The distribution of electrode potential across the surface of heterogeneous corroding electrodes is of fundamental importance in describing the localization and kinetics of nonuniform corrosion phenomena. In general, corrosion of service components can occur under various operating conditions ranging from very shallow condensed layers to bulk volume solutions. Previous papers (1, 2) have evaluated analytically the distributions of electrode potential across coplanar corrosion couples in which the electrode reactions are subject to activation control. In order to achieve an analytical solution, ion current flows within the solution were restricted to the plane of the electrode surface. Although valid for shallow corrosion solutions with moderate conductivity, such a restriction is not adequate for the more general case of corrosion under bulk solutions where current flows normal to the corroding electrode surface become significant.

A number of other analyses have been developed which either are based on linear polarization kinetics (3-9) with or without the additional requirement of similar polarization parameters for the anodic and cathodic electrode reactions, or assume general Tafel kinetics (10) with equal anodic and cathodic polarization parameters. As discussed previously (1, 2), the assumption of linear polarization kinetics is not valid for many corrosion reactions where the electrode reactions are subject to activation control resulting in logarithmic polarization behavior which is rarely similar for both the anodic and cathodic reactions. At present there is no analytical procedure available which can generally accommodate different logarithmic polarizations such that it becomes necessary to adopt a numerical technique. There are two basic techniques available for such analysis. The earlier and perhaps simpler of these is based on the finite difference technique of solution by successive iteration or relaxation (11). This technique has been shown theoretically to be suitable for the evaluation of the electrode potential in two-dimensional electrochemical cells (12). More recently, the finite element technique has been developed (13) and shown to be particularly efficient when applied to electrochemical processes which result in significant changes in the electrode geometry (14). The relative simplicity of

the finite difference technique, however, recommends its application to general corrosion phenomena where such shape changes are not of prime significance and are small in relation to the over-all corrosion cell dimensions.

This paper describes the application of a numerical finite difference method to the evaluation of electrode potential distribution within the electrolyte above a coplanar, linear, semi-infinite corrosion couple in which the electrode reactions are subject to activation control with different polarization parameters. This corrosion couple geometry was chosen to simulate the phenomenon of intergranular corrosion which results from either second-phase precipitation or selective solute segregation to the grain boundaries brought about by strengthening heat-treatments, fabrication, or component service. Here, the grain boundary region may be either anodic or cathodic to the matrix and the distribution of the electrode reactions is of importance in creating surface defects which may develop into incubation sites for surface-initiated failure processes such as fatigue and stress corrosion cracking.

The present analysis considers not only the free corrosion condition but includes a facility for simulating the effects of an externally applied superimposed polarization. Results obtained from the free corrosion numerical analysis are compared with experimental results obtained from a model copper-zinc galvanic corrosion couple. The influence of the various experimental parameters, in particular the solution depth and applied polarization, on the distribution of electrode potential are discussed.

Analysis of the Electrode Potential Distribution

The present analysis is based on a model galvanic corrosion couple consisting of two semi-infinite, coplanar, strip elements shown schematically in Fig. 1. The electrode surface lies in the XY plane and is infinite in the $\pm Y$ directions. The couple consists of a cathodic element A of width a in the $-X$ direction and anode B of width b in the $+X$ direction covered by an electrolyte of depth w in the $+Z$ direction. The electrolyte is bounded by perfect insulators at $z = w$ and $x = -a$ and $+b$. The symmetry of the electrode configuration constrains all current flow to the XZ plane such that the analysis is reduced to a two-dimensional problem.

Key words: corrosion, copper, numerical analysis, cathodic protection, potentiostatic control, zinc.

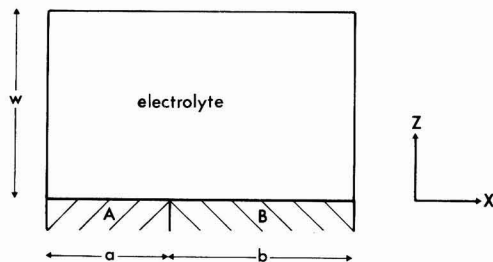


Fig. 1. Schematic diagram showing the arrangement of electrodes in the corrosion couple. Element A is the cathode and element B is the anode.

The various current *vs.* electrode potential relationships for the anodic and cathodic reactions are assumed to be subject to activation control with logarithmic (Tafel) polarization behavior. Polarization characteristics of the anodic and the cathodic reactions for each element of the corrosion couple are shown schematically in Fig. 2. Thus the net cathodic current density per unit length of corrosion couple, $i_{c(x)}$, on element A at an electrode potential E_x is

$$i_{c(x)} = i_{o(A)} \{ \exp((E_A - E_x)/\beta_A) - \exp((E_A - E_x)/-\alpha_A) \} \quad [1]$$

where E_A is the free corrosion potential of element A, $i_{o(A)}$ is the free corrosion current density, and α_A and β_A are the Tafel parameters for the anodic and cathodic reactions, respectively. Similarly for element B, the net anodic current density per unit length of corrosion couple, $i_{a(x)}$, on element B at an electrode potential E_x is

$$i_{a(x)} = i_{o(B)} \{ \exp((E_B - E_x)/-\alpha_B) - \exp((E_B - E_x)/\beta_B) \} \quad [2]$$

where E_B is the free corrosion potential of element B, $i_{o(B)}$ is the free corrosion current density, and α_B and β_B are the anodic and the cathodic Tafel parameters. Thus, anodic current flows within the electrolyte from the element B to element A following an electric potential gradient equal and opposite to the electrode potential gradient (dE_x/dx). The electrode potential distribution across the corrosion couple surface at

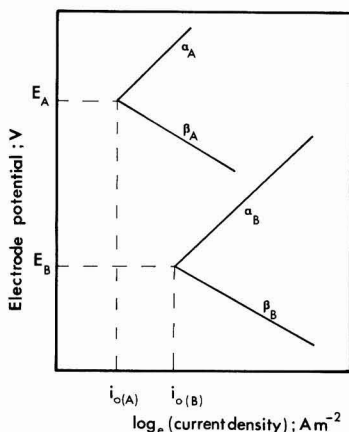


Fig. 2. Schematic polarization curves for the two elements of the corrosion couple shown in Fig. 1. α and β are the Tafel parameters for the respective anodic and cathodic reactions.

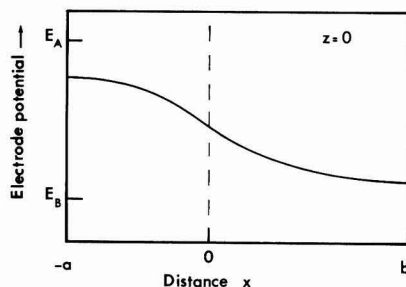


Fig. 3. Schematic diagram showing the electrode potential distribution in solution across the surface of the galvanic corrosion couple shown in Fig. 1.

$z = 0$ is illustrated schematically in Fig. 3. At distances $x < 0$, anodic current is complemented and effectively reduced by an excess cathodic current generated on element A.

Since there is no accumulation or loss of ions in the bulk of the electrolyte the distribution of electrode potential within the electrolyte must satisfy Laplace's equation

$$\nabla^2 E = 0 \quad [3]$$

subject to the following boundary conditions:

For $z = 0$ the normal derivative of electrode potential E is given by

$$\left. \begin{aligned} \frac{dE}{dz} &= i_{c(x)}/C \quad \text{for } -a < x < 0 \\ \frac{dE}{dz} &= i_{a(x)}/C \quad \text{for } 0 < x < b \end{aligned} \right\} \quad [4]$$

where C is the conductivity of the corrosion electrolyte.

Since there is no current flow normal to the insulating boundaries

$$\frac{dE}{dx} = 0 \quad \text{at } x = -a \text{ and } +b \quad [5]$$

$$\frac{dE}{dz} = 0 \quad \text{at } z = w \quad [6]$$

Equation [3] has been solved by the finite difference method of successive over-relaxation (15) using an iterative numerical procedure on an IBM 370 computer (11, 12, 16). This required a notional rectangular Cartesian grid to be established over the region defined by the electrolyte. The potential values at the nodal points, defined by the intersection of the grid lines, were then determined by iterative solution of the system of finite difference equations associated with the numerical solution of Laplace's equation. The present computer program (16) allows the experimental parameters a , b , w , $i_{o(A)}$, $i_{o(B)}$, E_A , E_B , α_A , α_B , β_A , β_B , and C to be specified by the user.

The program provides a graphical plot of equipotential lines across the XZ plane and the corresponding electrode potential *vs.* x values across selected grid lines parallel to the electrode surface including $z = 0$. Typical results for a hypothetical symmetrical corrosion couple with the given electrochemical parameters are shown in Fig. 4. Figure 4(a) shows the equipotential distribution in the XZ plane with the dimensional scales expanded for clarity of presentation. Figures 4(b) and (c) show the electrode potential *vs.* x plots for $z = 0$ (the electrode surface) and w (the solution surface), respectively. The symmetry of the solutions obtained for a range of similar parameters provides confidence in the application of the technique and confirms that the specified error of calculation was sufficiently small to give accurate results.

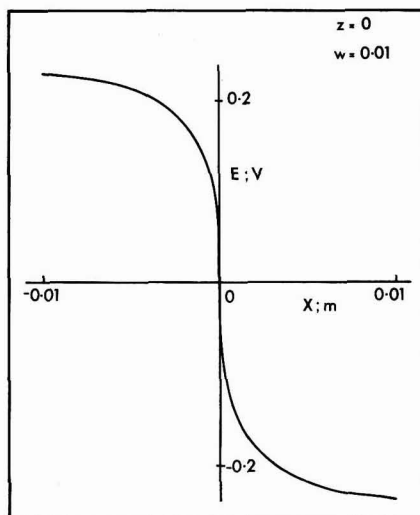
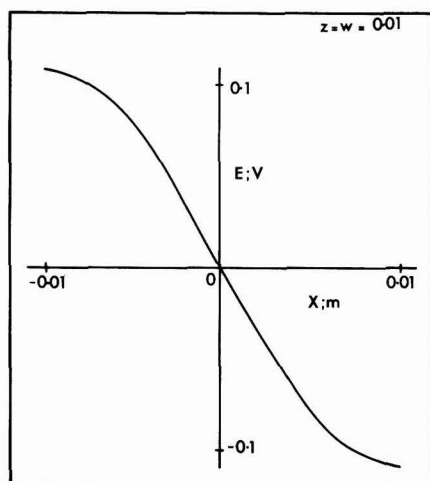
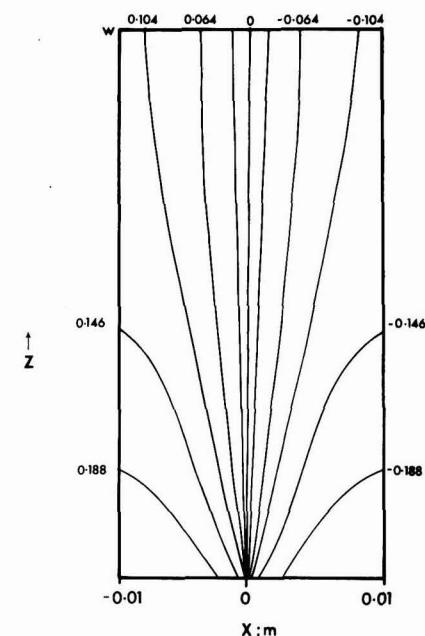


Fig. 4. Computer analysis results showing: (a, upper left) equipotential distribution, (b, upper right) electrode potential in solution vs. x at $z = 0$, and (c, lower left) electrode potential vs. x at $z = w = 0.01$ m for an electrode couple with $\alpha_A = \alpha_B = \beta_A = \beta_B = 0.05$, $C = 10 \Omega^{-1} \text{m}^{-1}$, $i_{0(A)} = i_{0(B)} = 1 \text{ A m}^{-2}$, $a = b = w = 0.01$ m, and $E_A = -E_B = 0.5$ V.

In practice there are many corrosion situations of technological interest in which the galvanic corrosion couple is subject to an external applied polarization, either galvanic or potentiostatic, where the mixed electrode potential of the corrosion couple is displaced from its equilibrium value. Common examples include cathodic protection and potentiostatic or galvanostatic polarization measurements. Under these circumstances the electrode potential distribution over the corrosion couple will be changed in a nonuniform, complex manner. This change will influence the distribution and intensity of the corrosion reactions on the electrode surfaces. Such applied polarization effects may be examined using the above analysis simply by modifying the boundary condition, Eq. [6]. For typical inert counterelectrodes, e.g., platinum, with very low polarization parameters and for values of w which are comparable or large with respect to the electrode dimensions, we can reasonably approximate the electrode

potential along the boundary $z = w$ to be a constant E_3 . This value E_3 is a user definable variable in the present computer program. This boundary plane simulates the position of the counterelectrode which passes that external current required to produce the polarization. The net external current flow may be deduced from an integration of the resulting electrode potential vs. x plot for $z = 0$ and the current density Eq. [1] and [2].

An example of this analysis with a value of $E_3 = 4.5$ V, is shown in Fig. 5 for the same variables as illustrated in Fig. 4. Figure 5(a) shows the equipotential distribution in the XZ plane, again with the Z axis expanded for clarity, and Fig. 5(b) shows the electrode potential across the surface of the galvanic couple, i.e., $z = 0$ when polarized and under free corrosion conditions. Clearly, the over-all distribution of electrode potential within the solution is significantly modified by the applied polarization. The distribution at the

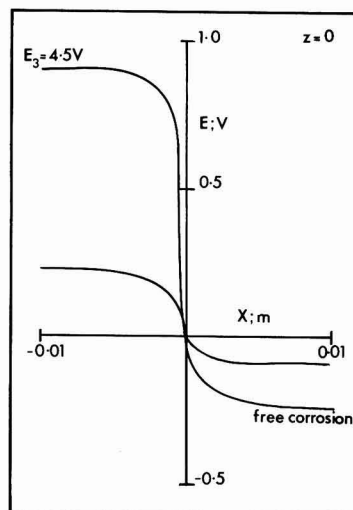
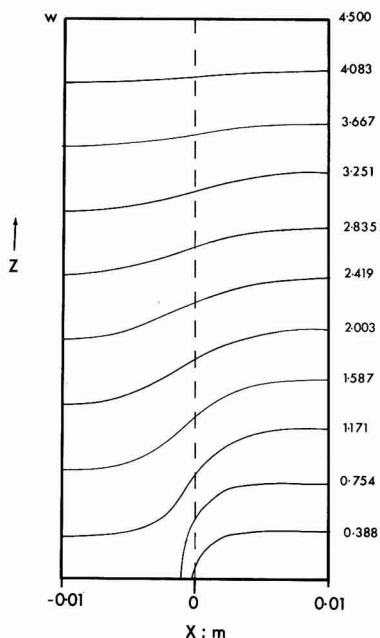


Fig. 5. Computer analysis results showing: (a, left) the equipotential distribution above the galvanic corrosion couple described in Fig. 4 with an applied anodic polarization $E_3 = +4.5V$, and (b, right) electrode potential in solution vs. x at $z = 0$ for both open-circuit free corrosion and applied anodic polarization.

surface is shifted in the direction of the applied polarization but its general form is preserved with the cathodic element remaining cathodic to the anodic element, however, in this case, the gradient dE/dx is increased in the region of the couple interface $x = 0$, when compared with the free corrosion condition, Fig. 5(b).

Experimental Test of the Numerical Solution

The analysis described above has been applied to a copper-zinc galvanic couple corroding in a 0.01M hydrochloric acid solution. The experimental cell, shown schematically in Fig. 6, comprises an open Perspex vessel placed across the copper-zinc couple and

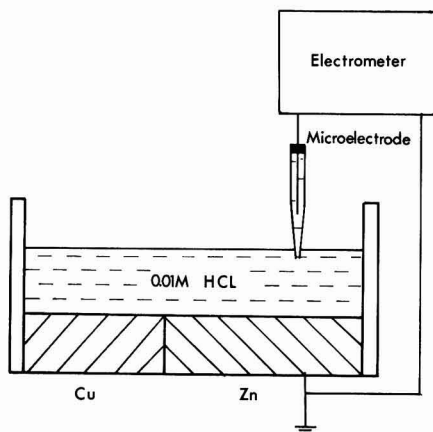


Fig. 6. Schematic diagram showing the experimental arrangement for measurement of electrode potential distribution above the copper-zinc corrosion couple.

filled with solution to depths of 2 and 20 mm. The distribution of electrode potential across the couple was measured using a reference microelectrode (Ag/AgCl) (1, 2, 17) with probe diameter ~ 0.1 mm, accurately positioned using a micromanipulator. Distributions were measured at solution depths corresponding to $z = 1$ mm and w . The electrode potential of the reference microelectrode was measured to be $+100 \pm 2$ mV with reference to a saturated calomel electrode. All measured potential values are reported with reference to the saturated calomel electrode scale.

The polarization parameters for zinc and copper in 0.01M hydrochloric acid have been measured (1) and these are listed in Table I together with the solution conductivity C . These values were used in the numerical analysis to calculate the equipotential distribution above the experimental corrosion couple and the results obtained for the two solution depths are shown in Fig. 7. Figure 8 shows the experimental results obtained for the electrode potential vs. x at $z = 1$ mm and w for both solution depths superimposed on the analysis results.

Both the calculated and measured equipotential distributions are different for the two solution depths. The equipotential distribution above the 2 mm depth [Fig. 7(a)] is almost independent of z , i.e., the current flow

Table I. Experimental values for the parameters used in the calculation of electrode potential distribution above the copper-zinc corrosion couple in 0.01M hydrochloric acid*

	Zn	Cu
Anodic Tafel parameter, α (V)	0.025	0.001
Cathodic Tafel parameter, β (V)	0.05	0.05
Corrosion current, i_c ($A \cdot m^{-2}$)	1.00	1.00
Free corrosion potential, E (V SCE)	-0.985	-0.845

* Solution conductivity, $C = 0.42 \Omega^{-1} m^{-1}$; cathode width, $a = 0.0075m$; anode width, $b = 0.02m$; solution depth, $w = 0.002$ and $0.02m$.

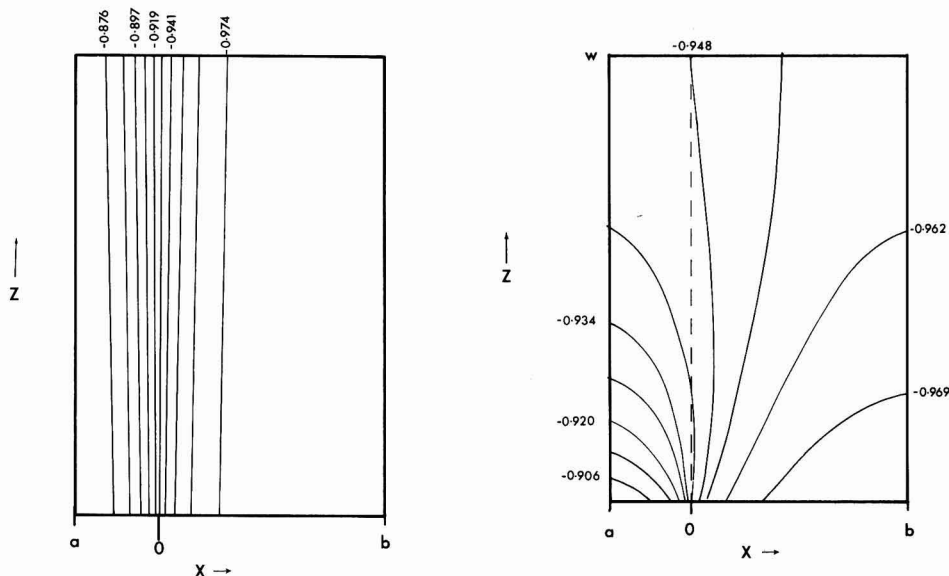


Fig. 7. Calculated equipotential distribution above the experimental copper-zinc corrosion couple for solution depths: (a, left) $w = 0.002\text{m}$ and (b, right) $w = 0.02\text{m}$.

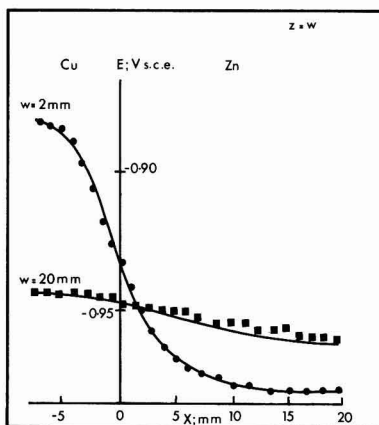
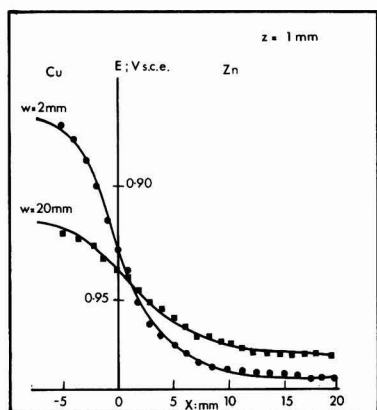


Fig. 8. Calculated curves and experimental points showing the electrode potential vs. x at: (a, left) $z = 1\text{ mm}$ and (b, right) $z = w$ for $w = 2$ and 20 mm .

in solution is primarily in the $\pm X$ direction, whereas the distribution above the 20 mm depth example [Fig. 7(b)] is highly dependent on z . The very good agreement observed between the measured and the calculated electrode potential vs. x plots in Fig. 8 support the accuracy and validity of this numerical analysis procedure.

Discussion

The experimental results show the present finite difference method of numerical analysis to be capable of evaluating the distribution of electrode potential above a coplanar galvanic corrosion couple in which the electrode reactions are subject to activation control. Application of such an analysis requires an experimental determination of the various electrochemical parameters describing the electrode reactions of each component of the couple, the value of any applied polarization, as well as the physical dimensions of the corrosion cell.

The distribution of electrode potential for $z > 0$ within the corrosion cell is important only insofar as it is this which can be measured directly with an external reference electrode via a Luggin probe. This volume distribution is a result of the electrode potential variation across the surface of the galvanic corrosion couple at $z = 0$. It is this latter distribution which describes the kinetics and localization of the corrosion reactions. Clearly, both the volume and associated surface distributions of electrode potential are dependent on all of the above electrochemical parameters and physical dimensions (Fig. 4-8).

The distribution of electrode potential across a galvanic corrosion couple describes the localization of the corrosion reaction; consequently, any consideration of corrosion behavior requires a knowledge of this distribution. The present analysis procedure allows this to be calculated using experimentally determined polarization behavior from any combination of elec-

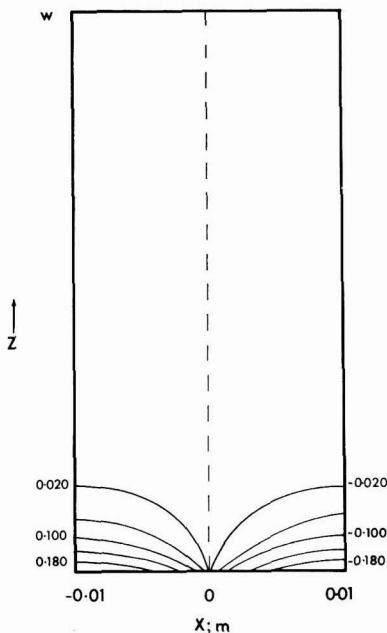
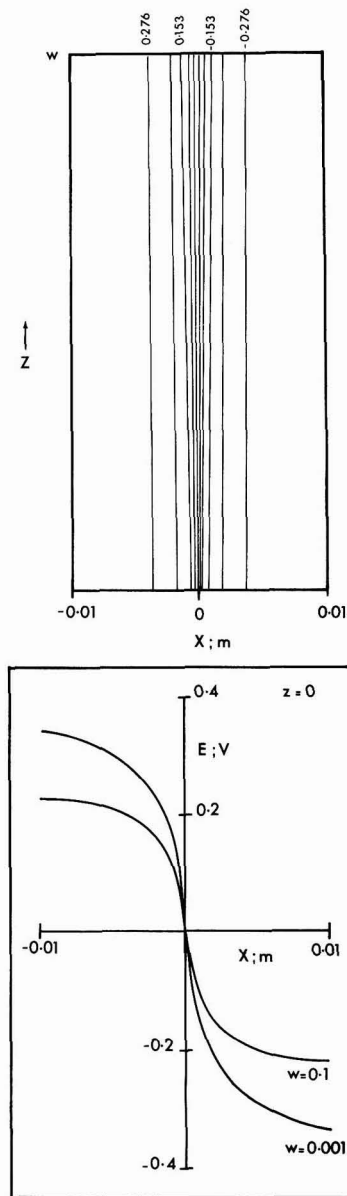


Fig. 9. Computer analysis results for the corrosion couple described in Fig. 4 showing the equipotential distribution for: (a, upper left) $w = 0.001\text{m}$, (b, upper right) $w = 0.1\text{m}$, and (c, lower left) the electrode potential in solution vs. x at $z = 0$.

trodes on which the reaction kinetics are subject to activation control. The infinite number of permutations of electrode polarization parameters, corrosion currents, conductivity, and electrode dimensions which can occur makes quantitative discussion of the separate influence of each variable on the resulting electrode potential distribution difficult. However, the qualitative effect of changes in each of these variables may be predicted intuitively and are not discussed further in this paper.

The influence of changes in solution depth, w , however, is not so readily envisaged. Clearly, for very small solution depths the earlier approximation to unidirectional current flow in the X direction remains valid and potential distributions may be obtained analytically (1, 2). However, for larger solution depths a

numerical method of analysis is required. Figure 9 shows calculated results obtained using the symmetrical model case shown in Fig. 4 for different values of $w = 1$ and 100 mm . Figures 9(a) and (b) show the equipotential distribution within the solution with the Z axes adjusted for clarity of presentation [c.f. Fig. 4(a) with $w = 10\text{ mm}$]. Figure 9(c) shows the calculated electrode potential vs. x at $z = 0$ for both values of w . Clearly, the case for $w = 1\text{ mm}$ [Fig. 9(a)] may be approximated to a unidirectional current flow, i.e., all equipotentials are nearly normal to the electrode surface. Figure 9(b), $w = 100\text{ mm}$, however, shows the case where w is large and the equipotentials at $z \rightarrow w$ are parallel to the electrode surface and the potential at $z = w$ is almost constant. The main point of interest in these results, however, is the observation

that the absolute values and shape of the electrode potential vs. x distributions at $z = 0$ are significantly different for the two values of w [Fig. 9(c)]. This results in a different distribution of anodic dissolution over the anodic element B. Such an effect is of particular interest when considering the relative corrosion behavior of galvanic couples under thin film and bulk solution environments. This may be of significance when attempting to reproduce service corrosion conditions in simulated laboratory tests. Previous analyses (1, 2) found the parameter $(i_0/wC)^{1/2}$ to be of fundamental significance in scaling distances over which potential changes were significant. Here, this parameter has values of 10 and $1 \text{ V}^{1/2}\text{m}^{-1}$ for $w = 1$ and 100 mm, respectively. Clearly, as the magnitude of this parameter increases the earlier approximation of unidirectional current flow becomes more accurate.

Similarly, changes in the electrode potential distribution above a corrosion couple resulting from an externally applied polarization are not readily predicted. Such polarization is effected by superimposing an additional external current flow normal to the surface of the corrosion couple. Changes in the local current density at the electrode surface must be reflected in a shift in the electrode potential, Eq. [1] and [2]. The additional current is supplied by some external source and is introduced via an additional, usually inert, counterelectrode located remote from, but usually parallel to, the surface of the corrosion couple. In the present analysis this position is defined as the plane $z = w$ and the electrode is polarized to a constant potential E_3 . When E_3 is fixed positive to the normal free corrosion potential a net anodic current is drawn from the corrosion couple which shifts the electrode potential everywhere in the anodic direction. Similarly a negative value for E_3 shifts the potential distribution in the cathodic direction. Thus, as shown in Fig. 5(b), the relative distribution of corrosion reactions is influenced by an externally applied polarization. Such changes may be of fundamental importance when considering electrochemically accelerated test methods for assessing the localization of corrosion in service components, e.g., crevice and pitting corrosion.

The present results clearly show that the localized corrosion behavior of a galvanic corrosion couple is dependent not only on the various electrochemical parameters, but also on the corrosion cell geometry and the magnitude of an externally applied polarization. The dependence cannot be described analytically but may be evaluated using the numerical finite difference procedure described above. The results to date indicate the need for caution in correlating localized corrosion behavior under different environmental conditions.

Conclusions

1. The electrode potential distribution above a semi-infinite, linear, coplanar, galvanic corrosion couple in which the electrode reaction kinetics are subject to activation control may be evaluated numerically using finite difference methods.

2. The absolute values and distribution of electrode potential and associated corrosion behavior are dependent not only on the electrochemical parameters but also on the corrosion cell dimensions.

3. Externally applied polarization of a galvanic corrosion couple preserves the over-all form of the electrode potential distribution at the couple surface but changes its precise shape and the relative absolute potential values.

Acknowledgments

The authors wish to thank Mr. F. A. J. Ford and Mr. A. J. Donovan (CEGB Computing Centre) for useful discussions and Mr. G. D. Elson (CEGB Computing Centre) for writing the computer program used in this work. This paper is published with the permission of the Director General, Central Electricity Generating Board, South Eastern Region.

Manuscript submitted March 2, 1979; revised manuscript received June 21, 1979.

Any discussion of this paper will appear in a Discussion Section to be published in the June 1980 JOURNAL. All discussions for the June 1980 Discussion Section should be submitted by Feb. 1, 1980.

LIST OF SYMBOLS

α_n	Tafel parameter describing the anodic dissolution behavior of element n (V)
β_n	Tafel parameter describing the cathodic reduction behavior of element n (V)
C	specific conductance of the solution ($\Omega^{-1}\text{m}^{-1}$)
E_n	the bulk corrosion potential of element n (V)
E_x	the electrode potential at position x (V)
E_3	the imposed electrode potential at the boundary $z = w$ (V)
$i_{o(n)}$	the free corrosion current density on element n (Am^{-2})
$i_{a(x)}$	the net anodic current density generated on the anode at potential E_x (Am^{-2})
$i_{c(x)}$	the net cathodic current density generated on the cathode at potential E_x (Am^{-2})
w	depth of solution above the corrosion couple surface (m)

REFERENCES

1. P. Doig and P. E. J. Flewitt, *Phil. Mag. B*, **38**, 27 (1978).
2. P. Doig and P. E. J. Flewitt, *Br. Corros. J.*, **13**, 118 (1978).
3. C. Wagner, *This Journal*, **98**, 116 (1951).
4. J. T. Waber and M. Rosenbluth, *ibid.*, **102**, 344 (1955).
5. J. T. Waber, *ibid.*, **102**, 420 (1955).
6. E. Kennard and J. T. Waber, *ibid.*, **117**, 880 (1970).
7. L. Gal-Or, Y. Raz, and J. Yahalom, *ibid.*, **120**, 599 (1973).
8. E. McCafferty, *Corros. Sci.*, **16**, 183 (1976).
9. E. McCafferty, *This Journal*, **124**, 1869 (1977).
10. W. H. Smyrl and J. Newman, *ibid.*, **123**, 1423 (1976).
11. G. E. Forsythe and W. R. Wasow, "Finite Difference Methods for Partial Differential Equations," John Wiley & Sons, Inc., New York (1960).
12. J. A. Klingert, S. Lynn, and C. W. Tobias, *Electrochim. Acta*, **9**, 297 (1964).
13. O. Zienkiewicz, "The Finite Element Method in Engineering Science," 2nd ed., McGraw-Hill Book Co., New York (1971).
14. R. Alkire, T. Bergh, and R. L. Sani, *This Journal*, **125**, 1981 (1978).
15. B. A. Carre, *Computer J.*, **4**, 73 (1961).
16. G. D. Elson, CEGB Report "GALVAN 1L, CC/P556, 6602P" (1978).
17. P. Doig and J. W. Edington, *Br. Corros. J.*, **9**, 88 (1974).

Anodic Dissolution and Passivation of Titanium in Acidic Media

III. Chloride Solutions

Eugene J. Kelly*

Oak Ridge National Laboratory, Chemistry Division, Oak Ridge, Tennessee 37830

ABSTRACT

The electrochemical behavior of titanium in deoxygenated acidic chloride solutions, with and without additions of Ti(III) and Ti(IV) ions, has been determined and compared with that observed in acidic sulfate media. A monolayer mechanism has been developed for the active-state dissolution and passivation of titanium in acidic media. According to this mechanism, the metal is oxidized in a sequence of one-electron charge-transfer reactions which results in the formation of adsorbed reaction intermediates corresponding to each of the relevant valence states of titanium (+1, +2, +3, +4) and which leads to Ti(III) ions in solution in the active and active-passive transition regions. The mechanism is in quantitative agreement with the experimental results for both chloride and sulfate media. In acidic chloride solutions, as well as in acidic sulfate solutions, the rates of oxidation at a passive titanium surface of Ti(III) ions in solution to Ti(IV) and of reduction at an active-state surface of Ti(IV) ions in solution to Ti(III) are directly proportional to the concentrations of Ti(III) and Ti(IV), respectively. The reduction of Ti(IV) at an active surface is responsible for the fact that, at a critical concentration of Ti(IV), an active-state surface passivates. In localized corrosion systems, active and passive surfaces are in simultaneous contact with the electrolyte within the occluded cell, and the aforementioned oxidation and reduction reactions serve to couple the active-state and passive-state electrochemical systems. Such electrolyte-coupled active-passive systems are capable of generating the critical concentration of Ti(IV) required to passivate the active-state surface, a fact which explains random spontaneous cessation of localized corrosion (self-healing). The critical concentration of Ti(IV) is much greater in chloride solutions than in sulfate media and takes much longer to attain. Consequently, the halide ion functions as a promoter of localized corrosion.

The results of a study of the electrochemical behavior of titanium in deoxygenated acidic chloride solutions, with and without additions of Ti(III) and Ti(IV) ions, are presented in this report. The work complements an earlier investigation of the mechanisms of active-state dissolution and passivation of titanium in acidic sulfate media (1). In addition, the comparative study of the effects of Ti(III) and Ti(IV) ions on the dissolution of titanium in acidic sulfate (2) and acidic chloride solutions provides a new rationale for the "random" spontaneous cessation of localized corrosion and for the role of chloride ion as a promoter of localized attack.

Although there have been numerous investigations of the electrochemical behavior of titanium in acidic media, mechanistic studies of the active-state dissolution and passivation (active-passive transition) processes have been extremely limited in number, i.e., few investigators have attempted to describe the electrochemical polarization data in a quantitative fashion and to relate the mathematical description of the polarization data to a specific reaction scheme (1, 3, 4).

According to a monolayer mechanism developed for the titanium/acidic sulfate system (1), the metal is oxidized in a sequence of one-electron charge-transfer reactions which results in the formation of adsorbed reaction intermediates corresponding to each of the relevant valence states of titanium (+1, +2, +3, +4) and which leads to Ti(III) ions in solution in the active and active-passive transition regions. The surface intermediates are analogous to the adsorbed (FeOH) and (NiOH) intermediates in the mechanism of active-state dissolution of iron (5) and nickel (6). A phase oxide, as opposed to monolayer species, is considered

to exist only in the passive state and, consequently, plays no role in the active-state dissolution and passivation processes. The monolayer model will be shown to apply to acidic chloride media as well as to acidic sulfate solutions and, therefore, it is examined in detail in the Discussion section of this paper. Here, it is sufficient to state that the equation which was derived on the basis of the monolayer model accurately describes the effects of both potential and pH on the steady-state current density in both the active and active-passive transition potential regions. It is particularly significant that the model accounts for the experimentally determined diagnostic relationships represented by Eq. [1]-[3]

$$a \log i_{m,d}/dpH = -2/3 \quad [1]$$

$$d \ln i_{m,d}/dE_{m,d} = F/2RT \quad [2]$$

$$dE_{m,d}/dpH = -(4/3)(2.303RT/F) \quad [3]$$

where $i_{m,d}$ and $E_{m,d}$ represent the maximum anodic current density arising from the metal dissolution reaction and the corresponding potential, respectively, i.e., the observed values, i_m and E_m (as shown, for example, in Fig. 2), corrected for the hydrogen evolution reaction (HER). Others have reported that $\log i_m$ and E_m are linear functions of pH, for acidic sulfate solutions, but no interpretations accompanied these reports (7, 8).

Several investigators, although relying on rather limited data, have subscribed to a monolayer concept. Caprani *et al.* (4) measured the apparent valence state of the dissolution product as a function of potential in the active, transition, and passive potential regions. On the basis of a schematic monolayer model, they derived an equation for the anodic current density/potential relationship which, although omitting pH as a

* Electrochemical Society Active Member.

Key words: corrosion, kinetics, passivity, polarization.

variable, was in accord with their data and closely resembled that given earlier by the author (1). Brynza *et al.* (9) employed an impedance technique to study the passivation of titanium in 5N H_2SO_4 and concluded that their results (capacitance and resistance as functions of potential and frequency) were consistent with a monolayer adsorption mechanism, but were not compatible with the hypothesis that a phase oxide was present in the active and active-passive transition potential regions. Similar capacitance data have been reported by others and also interpreted as a faradaic adsorption pseudocapacitance (1, 7). Armstrong *et al.* (10, 11), in rejecting the phase-oxide model (see below) and adopting a monolayer viewpoint, relied primarily on open-circuit potential/time curves observed during the spontaneous activation of passive titanium in sulfuric acid solutions.

Thomas and Nobe (3, 12) studied the electrochemical behavior of titanium in acidic sulfate solutions and developed a mechanism for the active-state dissolution process based on the assumption that an oxide layer is present on titanium not only in the passive state but also in the active state. This assumption was justified on the grounds that "the thermodynamic data on these oxides (Ti_2O_3 and TiO_2) indicate their possible presence even on active titanium." However, the fact that thermodynamic data do not preclude the existence of a particular oxide cannot be interpreted as evidence for its presence. The question of whether or not a phase oxide exists on titanium in the active and/or active-passive transition region will be considered below. In any event, the authors derived an equation which was comparable to their experimental rate expression, Eq. [4]

$$i_a = k[\text{H}^+]^{0.53} \exp(0.43FE/RT) \quad [4]$$

where i_a represents the current density corresponding to the active-state dissolution process and the other symbols have their conventional significance. There are difficulties with this equation. First, it not only fails to account for the diagnostic relationships given by Eq. [1]–[3], it indicates, contrary to fact, that there is no potential for which the anodic current density is a maximum, i.e., it does not account for i_m at E_m (see Fig. 2). Obviously, neither the equation nor the mechanism on which it is based address the question of the passivation mechanism, i.e., the active-passive transition potential region. Second, contrary to the indications of Eq. [4], neither $(\partial \log i_a / \partial \text{pH})_E$ nor $(\partial \log i_a / \partial E)_{\text{pH}}$ are constants. The fact that $(\partial \log i_a / \partial E)_{\text{pH}}$ is not constant corresponds to the well-established fact that titanium does not exhibit Tafel behavior in the active state (1, 4, 8, 11). All of the aforementioned limitations and errors can be traced to the authors' statement that Eq. [4] is only meant to apply in the "vicinity of the active corrosion potential." The anodic polarization measurements used in arriving at Eq. [4] were restricted to the linear polarization region (within 15 mV of the open-circuit potential) and, consequently, anodic Tafel behavior was not actually observed, but merely assumed. With the assumption that the anodic dissolution process exhibits Tafel behavior, the magnitude of the anodic Tafel slope was calculated using the measured values of the slope of the linear (small) polarization curve, the cathodic (HER) Tafel slope, and the corrosion current determined by extrapolation of the cathodic Tafel line to the corrosion potential. Even if it were known that the anodic process followed Tafel kinetics, this method for determining the magnitude of the diagnostically important anodic Tafel slope is inappropriate for mechanistic studies because small errors in the cathodic polarization data can lead to a large error in the calculated anodic slope. A more fundamental flaw exists in the fact that the small (linear) polarization method cannot distinguish between a linearized Tafel equation and any other current density/potential re-

lationship which can be linearized over the very narrow potential regions to which the method is applied. It is shown in the present paper that, as applied to titanium in the active state, the method merely evaluates the slope of the tangent to the partial anodic polarization curve ($\log i_a$ vs. E), a curve which does not exhibit Tafel behavior. One final difficulty with the mechanism proposed by Thomas and Nobe is that, in the presence of added Ti(III) ions, i_a is considered to be proportional to the square root of the concentration of Ti(III) . More recently (2), it has been proven that i_a is not a function of the concentration of Ti(III) (see Results and Discussion section).

The phase-oxide concept, according to which a phase oxide (as opposed to adsorbed monolayer species) exists on titanium in the active and/or active-passive transition potential regions, is frequently encountered in the literature on titanium. Some investigators have attempted to explain the most salient features of the electrochemical polarization curves on the basis of thermodynamic considerations, for example, by attempting (unsuccessfully) to identify E_m with a thermodynamic equilibrium potential corresponding to the formation of an oxide (13, 14). Others have invoked the concept in order to explain various singular observations, for example, the observation (15) that the initial anodic current density at a freshly fractured surface is much greater than the steady-state current density in the active-state potential region (obviously, there is no *a priori* reason to suppose that a monolayer concept could not account for this fact as readily as a phase-oxide concept). Studies of the type just cited are never mechanistic in the sense defined in the second paragraph of this paper, and are mentioned only because they illustrate the pervasive nature of the phase-oxide school of thought.

Although electron diffraction (16–18), electrochemical polarization (19–23), ellipsometric (24), reflectometric (24, 25), and photopotential (25, 26) measurements have provided useful information concerning the physical and electrochemical properties of oxide films formed on titanium in the passive state, they have not provided reliable evidence for the existence of oxide films (as opposed to adsorbed monolayer species) in either the active or active-passive transition potential regions. With decreasing potential within the passive potential region, the oxide film thickness decreases, and film thicknesses down to approximately 15–20 Å have been demonstrated at potentials clearly in the passive potential region. At still lower potentials, the theoretical limitations inherent in the ellipsometric (27), reflectometric (28), and photopotential techniques, i.e., the inability to unambiguously distinguish between a limitingly thin phase-oxide and adsorbed monolayer species, casts doubt on conclusions concerning the potential at which a phase oxide first forms. As an illustration of the interpretational difficulties which arise, consider the photopotential technique employed by Oshe *et al.* (26) in a study of titanium in sulfuric acid solutions. In the derivation of the photovoltage equation (29), one presupposes the existence of an oxide phase, and assumes that the transport of charge carriers (electrons or holes) within the oxide phase is properly described by classical concepts, i.e., by a diffusion flux represented by Fick's law and by a migration flux equal to the product of the charge carrier concentration and field-dependent drift velocity. It is unlikely that this description of charge transport is applicable to very thin oxide films where, for example, charge transport by electron tunneling has been demonstrated (24), and it obviously does not encompass the transition from the ultimately thin but finite phase-oxide to the monolayer species.

Experimental

The three-compartment cell assembly (test, reference, and counterelectrode compartments) was made

of Pyrex glass and Teflon and was so designed that solutions could be added to or removed from the cell without exposure to the atmosphere. All compartments were jacketed and maintained at a constant temperature ($\pm 0.02^\circ\text{C}$) which, except where noted, was 30°C . A stream of hydrogen was passed through all compartments at all times. The hydrogen source was a Matheson generator which produces ultrapure gas via diffusion of electrolytically generated hydrogen through a palladium membrane. Additional stirring in the test compartment was achieved with a Teflon-coated magnetic stirrer.

The titanium electrodes employed in this study were made from zone-refined, polycrystalline titanium (Materials Research Corporation). The cylindrical electrodes (diameter = 0.635 cm) were mounted on Teflon electrode holders which exposed either one planar surface or the cylindrical surface or both. All solutions were prepared from reagent grade chemicals and triply distilled water. Acidic chloride solutions having the desired pH were made by mixing 1M HCl and 1M NaCl solutions. Stock solutions of 0.1M Ti(III) in 1N HCl were prepared by dissolving 0.9593g of zone-refined titanium in 21.31 ml of 12.2N HCl at $65^\circ\text{--}70^\circ\text{C}$. The resultant solution was cooled to room temperature and diluted to 200 ml with water. The entire preparation was conducted under a helium atmosphere, using helium-saturated liquids. Stock solutions of 0.1M Ti(IV) in 1M HCl were prepared by adding hydrogen peroxide (30% solution) to stock Ti(III) solution until the purple color of the latter just disappeared. The next drop of H_2O_2 produced an orange color which was eliminated by addition of some Ti(III) solution. The final solution contained a negligible excess of Ti(III).

The electrochemical measurements were made with a PAR potentiostat (Model 173), a PAR programmable waveform generator (Model 175), an Aardvark potential scanner (Model SCAN-4), an Orion pH meter (Model 801-A), and a Hewlett-Packard/Moseley recorder (Model 7100B, Model 17501A plug-ins).

All electrode potentials (E) were measured against a saturated calomel reference electrode and, unless stated otherwise, all E values are given with reference to SCE.

The potential-step method was used to determine all of the polarization curves with the exception of those shown in Fig. 3 (curves I-IV) and Fig. 9. The term "steady state" is used in the operational sense to mean that there was no discernible change with time in the value of the current density at a given potential and that the indicated value was not dependent on whether the previous potential was more positive or more negative.

In this paper, by convention, net and partial anodic (oxidation) current densities are positive, while net and partial cathodic (reduction) current densities are negative.

Results and Discussion

A typical activation curve observed on immersing a titanium electrode into 1N HCl is shown in Fig. 1. Due to the presence of an air-formed oxide film on the metal following pretreatment (polishing with 300 nm $\alpha\text{-Al}_2\text{O}_3$ and rinsing with distilled water), the potential initially lies in the passive potential region. The slow decrease in the open-circuit potential in the region above -300 mV vs. SCE is attributed to slow dissolution of the oxide film, a process which, under steady-state conditions, is completed at approximately -300 mV vs. SCE with the transition from the limiting thin phase-oxide to adsorbed monolayer species. Below -300 mV, adjustment in the coverages of the adsorbed reaction intermediates is accompanied by the subsequent rapid decrease in potential. Ultimately, a stable active-state corrosion potential of -665 mV vs. SCE is attained. Since the surface state during activation is not in a steady-state condition, the transition

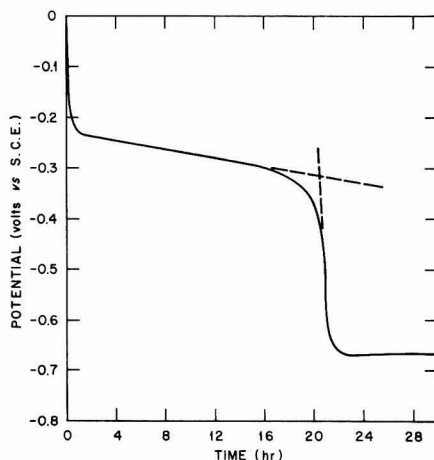


Fig. 1. Spontaneous activation of titanium in 1N HCl

at -300 mV is not abrupt. However, when the activation curve shown in Fig. 1 is correlated with the steady-state polarization curve shown in Fig. 2, the singular significance of the potential value of -300 mV is apparent. Similar activation curves have been reported by other investigators. Brauer and Nann (14) examined activation curves obtained in 6N H_2SO_4 and noted that for a variety of pretreatment processes the rapid decrease in potential always occurred at approximately -280 mV vs. SCE. Thomas and Nobe (7) observed a sudden decrease in potential at -300 mV vs. SCE for 1N H_2SO_4 (also observed by the present author). The presence of only one arrest in the activation curves observed for preanodized titanium in 10M H_2SO_4 was interpreted by Armstrong *et al.* (10) to mean that only one phase oxide forms during anodic

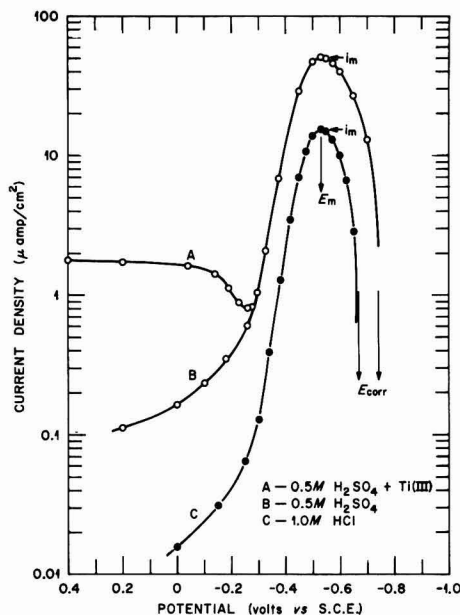


Fig. 2. Steady-state anodic polarization of titanium in 1N HCl and 1N H_2SO_4 .

polarization into the passive potential region, that it is removed during activation, and that only monolayer species exist on the surface after activation.

The steady-state anodic polarization curve for titanium in 1.0M HCl is shown in Fig. 2 (curve C). As the potential of the metal is made increasingly positive (noble) relative to the corrosion potential, the anodic current density rises to a maximum (i_m) at the critical potential ($E_m = -530$ mV vs. SCE) and then decreases as the metal is transformed from the active to the passive state. For comparison purposes, the steady-state anodic polarization curve observed in 1N H_2SO_4 is also shown in Fig. 2 (curve B). In acidic chloride and acidic sulfate solutions, the steady-state anodic polarization curves are completely unaffected by stirring. Moreover, it has been reported previously (for acidic sulfate media) that potentiostatic current/time transients spanning the time range from a few microseconds to steady state are totally unaffected by stirring (1).

The monotonic decrease in the anodic current density with increasing potential in the potential region positive (noble) to E_m is interrupted at approximately -300 mV vs. SCE, i.e., for any potential positive to -300 mV vs. SCE the steady-state current density exceeds that which would be expected from extrapolation of the polarization curve observed between E_m and -300 mV vs. SCE. This is the only discontinuity in the steady-state polarization curve in the potential region positive to E_m and represents the potential at which the transformation from an adsorbed monolayer system to a phase oxide occurs. Consequently, throughout this paper the term "active state" refers to the potential region negative to E_m , the term "passive state" refers to the potential region positive to the discontinuity potential (approximately -300 mV vs. SCE for 1M HCl or 1N H_2SO_4), and the active-passive transition potential region lies between the two defined states.

Effect of potential scan rate.—Anodic polarization curves for titanium in 1M HCl were measured with scan rates ranging from 0.01 to 10 mV/sec and are shown, together with the steady-state polarization curve, in Fig. 3. In each case, the potential scan origi-

nated from the steady state at -650 mV vs. SCE. Stirring had no effect on the curves, i.e., the chloride system like the sulfate system is entirely under activation control. The very large effect of scan rate on the polarization curves, an effect which may be attributed to the low rates of the interfacial reactions which determine the potential dependent steady-state coverages of the adsorbed reaction intermediates, argues against the application of the potentiodynamic technique to mechanistic studies of titanium dissolution. For example, with increasing scan rate, the maximum anodic current density (i_m) increases and the corresponding potential (E_m) becomes increasingly positive. Moreover, the disparity between the potentiodynamic and steady-state curves, at constant scan rate, is dependent on such variables as the pH and temperature. One consequence is that the value of i_m and E_m as diagnostically significant parameters is lost when the potentiodynamic method is used. The limited value of the potentiodynamic technique is all the more obvious when one considers that, with all other factors constant, the disparity between the potentiodynamic and steady-state polarization curves depends on the surface state at the start of the scan. Cyclic scanning, for example, always results in hysteresis loops the shapes of which depend on the initial surface conditions as reflected by the initial current density at the originating potential. Phase oxides, formed by scanning into the passive potential region, exhibit a transitory existence in the active and/or active-passive potential regions and can lead to erroneous mechanistic conclusions when the latter are based on potentiodynamic polarization curves (14) or on correlations thereof with optical data (25). The common practice (8, 30, 31) of waiting a fixed but inadequate time interval at each potential when using the potential-step method also results in a disparity between the observed and steady-state polarization curves, together with the attendant interpretational ambiguities, and is best avoided.

Effect of temperature.—The effect of temperature on the steady-state polarization data in 1N HCl is shown in Fig. 4. As the temperature increases, E_m (measured against a SCE at the same temperature as the test

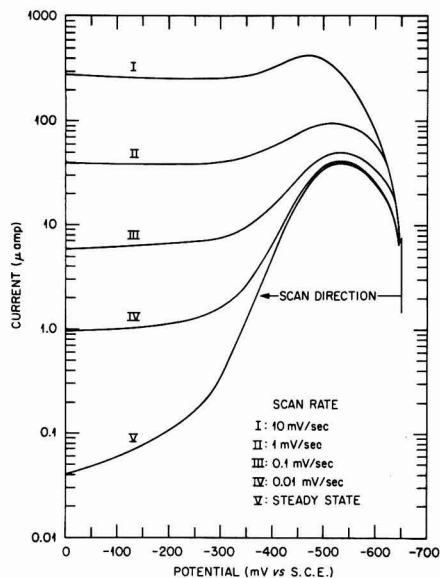


Fig. 3. Effect of scan rate on anodic polarization curves in 1N HCl.

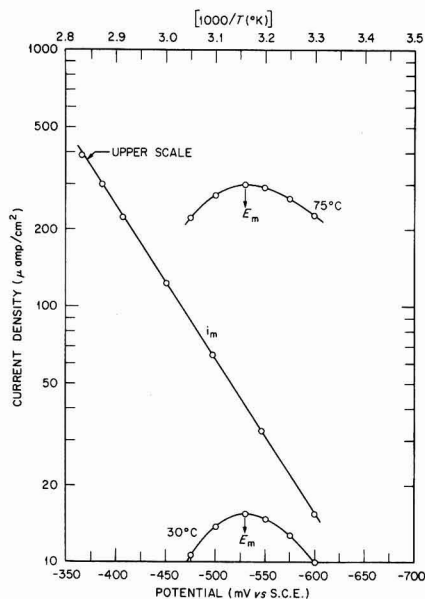


Fig. 4. Effect of temperature on E_m and i_m in 1N HCl

solution) remains constant (-530 mV vs. SCE), while i_m increases. The data show that $\log i_m$ is a linear function of $(1/T)$. The slope, $d \log i_m/d(1/T)$, leads to a calculated apparent activation energy of 57.3 kJ/mole (13.7 kcal/mole). Similar results have been reported earlier for $1N$ H_2SO_4 , for which it was found that E_m was independent of temperature and $d \log i_m/d(1/T)$ was constant (1). The apparent activation energy reported for $1N$ H_2SO_4 was 59.9 kJ/mole (14.3 kcal/mole). In a qualitative sense, it has been known for many years that E_m is independent of temperature and i_m increases with increasing temperature (32, 33). Typical of the apparent activation energies that have been reported for i_m are 14.6 kcal/mole in $6N$ H_2SO_4 (14), 20 kcal/mole in 20% HCl (34), and 11 kcal/mole in $(0.1M$ $HCl + 0.9M$ $NaCl)$ (31).

Coulometric weight-loss data.—Potentiostatic coulometric weight-loss experiments were performed at E_m (-530 mV vs. SCE) and $E_m + 90$ mV (-440 mV vs. SCE) with $1N$ HCl at $30^\circ C$. The apparent valence (z) was calculated according to the equation, $z = AQ/wF$, where A and F represent the atomic weight of titanium and the Faraday constant, respectively, and w represents the weight loss occurring during the passage of Q coulombs of charge. The following results were obtained: $z = 2.94$ ($Q = 18.88C$, $w = 3.192$ mg), $E = E_m$, $P = 2.21\%$; $z = 2.94$ ($Q = 36.47C$, $w = 6.164$ mg), $E = E_m$, $P = 2.15\%$; and $z = 2.97$ ($Q = 32.73C$, $w = 5.48$ mg), $E = E_m + 90$ mV, $P = 1.18\%$. Here, P represents the current corresponding to the hydrogen evolution reaction, expressed as a percentage of the observed current, if $z = 3.00$. For comparison, the results obtained (1) in $1N$ H_2SO_4 were as follows:

$$z = 2.97 (Q = 191.22C, w = 31.99 \text{ mg}),$$

$$E = E_m, T = 75^\circ C, P = 1.11\%;$$

$$z = 2.97 (Q = 229.48C, w = 38.37 \text{ mg}),$$

$$E = E_m, T = 75^\circ C, P = 1.06\%;$$

$$z = 3.00 (Q = 84.23C, w = 13.96 \text{ mg}),$$

$$E = E_m, T = 60^\circ C, P = 0.17\%;$$

and

$$z = 3.00 (Q = 24.04C, w = 3.98 \text{ mg}),$$

$$E = E_m + 160 \text{ mV}, T = 60^\circ C, P = 0.06\%.$$

These results clearly demonstrate the faradaic oxidation of the metal to $Ti(III)$, not only in the active state, but also in the active-passive transition region. This is true for both acidic chloride and acidic sulfate solutions. Additional proof of the quantitative faradaic oxidation of titanium to form $Ti(III)$ ions in solution has been presented earlier (2) for active-state dissolution in acidic sulfate solutions.

Effect of pH.—Steady-state anodic polarization curves for titanium in the active and active-passive transition regions have been determined for chloride solutions ($[Cl^-] = 1M$) having pH values ranging from -0.078 to 2.00 , and are shown in Fig. 5. The metal spontaneously activates in these solutions and exhibits an active-state corrosion potential (volts vs. SCE) given approximately by the expression, $E_{corr} \approx -0.667 - 0.023$ pH. The maximum pH for which there exists a stable active state was estimated to be 2.3 , and a stable active state was not attainable at $pH = 2.5$.

The curves shown in Fig. 5 demonstrate that as the pH decreases, i_m increases and E_m becomes increasingly positive (noble). These qualitative observations have been reported by many investigators for both chloride and sulfate solutions (31, 33-35). However, attempts to establish quantitative relationships among i_m , E_m , and pH have been very limited in number, and not successful. This situation can be attributed to the failure to obtain steady-state data, and/or to the failure to correct the anodic polarization curves for the effect

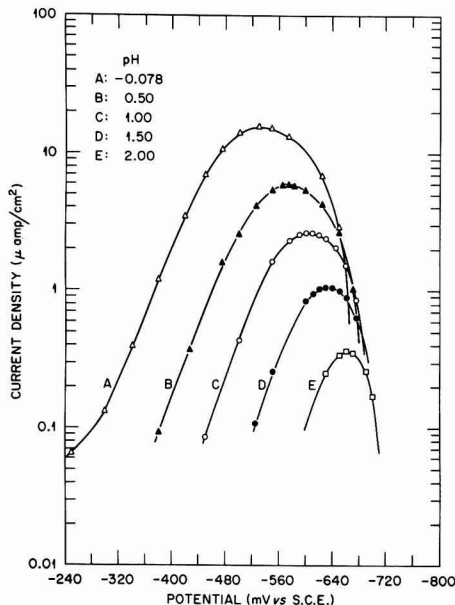


Fig. 5. Effect of pH on anodic polarization curves in chloride media ($[Cl^-] = 1M$).

of the HER. For sulfuric acid solutions ($1-10N$) at $22^\circ C$, Peters and Myers (8) reported that $(d \log i_m/dpH) = -0.77$, and $(dE_m/dpH) = -50$ to -60 mV/pH. Thomas and Nobe (7) reported that for acidic sulfate solutions ($pH = 0.25-2.0$) at $24^\circ C$, $(d \log i_m/dpH) = -0.84$ and $(dE_m/dpH) = -60$ mV/pH. In neither case were the data corrected for the HER. When corrected for the HER, the aforementioned values of $(d \log i_m/dpH)$ and (dE_m/dpH) approach those given by Eq. [1] and Eq. [3], respectively. In chloride solutions ($[Cl^-] = 1M$) ranging from $pH = -0.08$ to $pH = 1.58$, the data observed at $98^\circ C$ by Griess (31), uncorrected for the HER, gives $(dE_m/dpH) = -78.6$ mV/pH at $30^\circ C$ compared to the value of -80 mV/pH given by Eq. [3]. This agreement with Eq. [3] results from the fact that the correction for the HER becomes less important as the temperature increases. This is apparent from the fact that E_m is independent of temperature while E_{corr} becomes increasingly negative as the temperature increases (for example, $dE_{corr}/dT \approx -1.1$ mV/degree in $1N$ HCl).

In Fig. 6, the correction of i_m and E_m for the effect of the HER is shown for $pH = 1.00$. The cathodic Tafel line corresponding to the HER has a slope of -120 mV/decade, i.e., $(\partial \log i_H/\partial E) = -F/2$ ($2.303RT$), and gives the corrosion current density (i_{corr}) at the corrosion potential (E_{corr}). The partial anodic polarization curve (i_a) corresponding to just the oxidation of the metal to form $Ti(III)$ ions in solution is obtained by adding $|i_H|$ to the observed anodic polarization curve (i_a). The corrected value of the current density maximum ($i_{m,d}$) is greater than i_m , and the corrected corresponding potential ($E_{m,d}$) is more negative than E_m . As shown by the coulometric weight-loss data (see above), the correction of i_m and E_m for the HER is negligible in $1N$ HCl and $1N$ H_2SO_4 but becomes increasingly important as the pH increases. Moreover, at any specified pH, the correction is greater in chloride than in sulfate media. The latter fact is reflected in the greater difference between E_m and E_{corr} observed in sulfate solutions for any pH value.

The polarization curves shown in Fig. 6 clearly demonstrate that neither i_a nor i_d obey the Tafel equa-

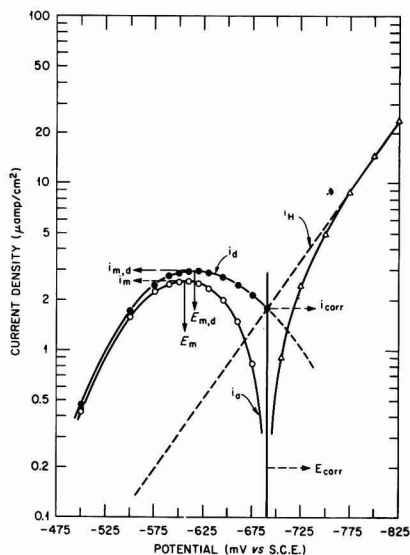


Fig. 6. Correction of E_m and i_m for the effect of the HER in 1M $[\text{Cl}^-]$ at pH = 1.00.

tion, i.e., $(\partial \log i_d / \partial E)_{\text{pH}}$ is not constant, an important mechanistic fact cited in the beginning of this paper.

In Fig. 7, $\log i_{m,d}$ is plotted against pH and against $E_{m,d}$. The results show that $\log i_{m,d}$ is a linear function of pH, and also a linear function of $E_{m,d}$, i.e.

$$d \log i_{m,d} / dpH = -2/3 \quad [5]$$

and

$$d \ln i_{m,d} / dE_{m,d} = F/2RT \quad [6]$$

where it should be noted that Eq. [5] and [6] are

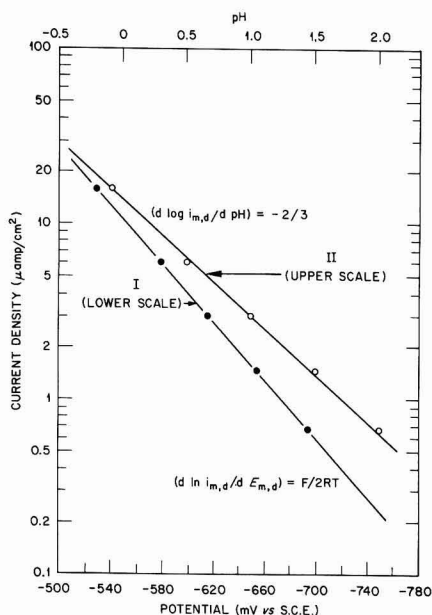


Fig. 7. Variation of $\log i_{m,d}$ with $E_{m,d}$ (curve I) and with pH (curve II) in 1M $[\text{Cl}^-]$.

exactly the same as those found for acidic sulfate solutions, Eq. [1] and [2].

The effect of pH on E_m and on $E_{m,d}$ is shown in Fig. 8. The results show that $E_{m,d}$, unlike E_m , is a linear function of pH, i.e.

$$dE_{m,d} / dpH = - (4/3) (2.303RT/F) \quad [7]$$

Again, the results for acidic chloride solutions are exactly the same as for acidic sulfate solutions, i.e., Eq. [7] is identical to Eq. [3]. Equation [7] also follows from the relationship

$$(dE_{m,d} / dpH) = (d \log i_{m,d} / dpH) / (d \log i_{m,d} / dE_{m,d}) \quad [8]$$

when the results shown by Eq. [5] and [6] are inserted into Eq. [8].

The existence of such simple functional relationships as those represented by Eq. [5]-[7], together with their mechanistically significant constants (i.e., $-2/3$ and simple multiples of RT/F), must be accounted for by any mechanism proposed for the dissolution of titanium.

Linear polarization.—In Fig. 9, the net active-state current density (i_a) is plotted against η , where η represents $(E - E_{\text{corr}})$. The results are shown for pH = 1.00

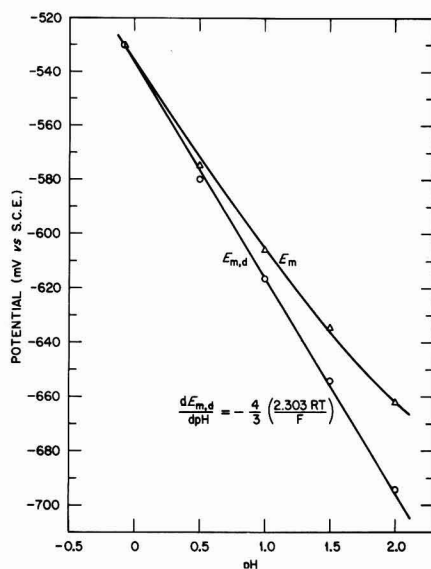


Fig. 8. Variation of E_m and $E_{m,d}$ with pH in 1M $[\text{Cl}^-]$

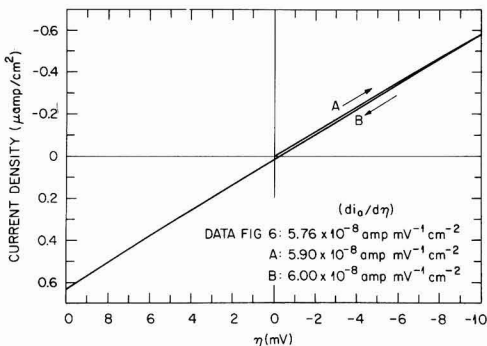


Fig. 9. Linear polarization of titanium in 1M $[\text{Cl}^-]$ at pH = 1.00; scan rate = 1.34×10^{-3} mV/sec.

and were obtained by continuous scanning (scan rate = 1.34×10^{-3} mV/sec) from an initial steady state at E_{corr} . Despite the extremely low scan rate, some hysteresis is evident. The slopes of the "linear" polarization curves, $(di_a/d\eta)_{\eta \rightarrow 0}$, for the scans in the negative and positive directions are 5.90×10^{-8} and 6.00×10^{-8} A mV $^{-1}$ cm $^{-2}$, respectively.

The net current density is given by Eq. [9]

$$i_a = i_d + i_H \quad [9]$$

where i_d and i_H represent the current densities corresponding to the metal dissolution and hydrogen evolution reactions, respectively. In accordance with the results shown in Fig. 6, Eq. [9] becomes

$$i_a = i_d - i_{\text{corr}} \exp(-\beta_c \eta) \quad [10]$$

where $\beta_c = F/2RT$, and where no *a priori* assumption has been made concerning the nature of the functional relationship between i_d and η . Then, for the linear polarization case, Eq. [10] gives the result

$$(di_a/d\eta)_{\eta \rightarrow 0} = (di_d/d\eta)_{\eta \rightarrow 0} + \beta_c i_{\text{corr}} \quad [11]$$

According to Eq. [11], the linear relationship between i_a and η observed in Fig. 9 merely requires that the functional relationship between i_d and η , whatever its actual form, may be linearized for small values of η , i.e., $(di_d/d\eta)_{\eta \rightarrow 0} \approx \text{constant}$. In particular, it does not require i_d to be an exponential function of η , i.e., to exhibit Tafel behavior, a fact cited earlier in the paper. Equation [11] may be rewritten in the form

$$(d \ln i_d/d\eta)_{\eta \rightarrow 0} = (1/i_{\text{corr}})(di_a/d\eta)_{\eta \rightarrow 0} - \beta_c \quad [12]$$

where use has been made of the fact that, at $\eta = 0$, $i_a = i_{\text{corr}}$. Equation [12] shows that it is merely the slope of the tangent to the $\log i_d$ vs. E curve at E_{corr} that is calculable from known values of i_{corr} , β_c , and $(di_a/d\eta)_{\eta \rightarrow 0}$. Conversely, if the values of $(d \ln i_d/d\eta)_{\eta \rightarrow 0}$, i_{corr} , and β_c taken from Fig. 6 are inserted into Eq. [12], the calculated value of $(di_a/d\eta)_{\eta \rightarrow 0}$ is 5.76×10^{-8} A mV $^{-1}$ cm $^{-2}$, i.e., virtually the same as that observed in Fig. 9. If i_d obeyed the Tafel equation, $i_d = i_{\text{corr}} \exp \beta_a \eta$, then, with $d \ln i_d/d\eta = \beta_a$, Eq. [12] would reduce to the usual linear polarization equation

$$\beta_a = (1/i_{\text{corr}})(di_a/d\eta)_{\eta \rightarrow 0} - \beta_c \quad [13]$$

and the slope, $(d \ln i_d/d\eta)_{\eta \rightarrow 0}$, calculated from known values of β_c , i_{corr} , and $(di_a/d\eta)_{\eta \rightarrow 0}$, would be mechanistically significant. However, as is evident in Fig. 6, $d \ln i_d/d\eta$ is not constant, i.e., i_d does not obey the Tafel equation, and, consequently, contrary to what has been assumed (3), the calculated (using Eq. [12]) value of $(d \ln i_d/d\eta)_{\eta \rightarrow 0}$ does not represent a mechanistically significant Tafel constant (see the beginning of this paper).

Effects of Ti(III) and Ti(IV) ions.—For acidic sulfate solutions, it has been shown (2) that Ti(III) ions in solution are oxidized at a passive titanium surface to form Ti(IV) ions in solution and that the oxidation reaction is first order with respect to the concentration of Ti(III) ions. The current density (i_3) corresponding to the oxidation of Ti(III) ions simply adds to the current density (i_p^*) corresponding to the dissolution of the substrate metal in the absence of Ti(III), i.e.

$$i_p = i_p^* + k_3 C_3 \quad [14]$$

where i_p is the observed anodic current density in the passive potential region, C_3 is the concentration of Ti(III) ions, and k_3 is the rate constant for the oxidation of Ti(III) ions, i.e., $k_3 = (i_3/C_3)$. The difference between curves A and B in Fig. 2 illustrates the effect of Ti(III). It should be noted that i_p^* , at con-

stant potential, is not affected by the presence of either Ti(III) or Ti(IV) ions. The effects of potential and pH on k_3 have been discussed earlier (2). In the present study, it has been found that Eq. [14] also applies to acidic chloride solutions. In Fig. 10, i_p is plotted against C_3 for a titanium electrode maintained at $E = 0$ mV vs. SCE in 1N HCl. Again, i_p is a linear function of C_3 , and from the slope, $(\partial i_p/\partial C_3)_{E=0}$, the calculated value of $(k_3)_{E=0}$ is 1.13×10^{-4} A cm $^{-2}$ liter mole $^{-1}$. The value of $(k_3)_{E=0}$ observed in 1N H₂SO₄ was 1.12×10^{-3} A cm $^{-2}$ liter mole $^{-1}$ (2), i.e., approximately ten times greater than the value observed in 1N HCl. It should be noted that the oxidation of Ti(III) is activation controlled, i.e., i_p is not affected by stirring.

In acidic sulfate solutions, Ti(IV) ions in solution are reduced at an active-state titanium electrode to form Ti(II) ions in solution, and the reduction reaction is first order with respect to the concentration of Ti(IV), i.e.

$$i_4 = -k_4 C_4 \quad [15]$$

where i_4 represents the current density associated with the reduction reaction, C_4 is the concentration of Ti(IV) ions in solution, and k_4 is the rate constant for the reduction reaction. The current density, i_a , simply adds to the current densities corresponding to the dissolution of the metal to form Ti(III) ions in solution and to the hydrogen evolution reaction, i_d and i_H , respectively, to yield the observed current density (i_a)

$$i_a = (i_d + i_H) - k_4 C_4 \quad [16]$$

Since, at constant potential, neither i_d nor i_H are affected by the presence of Ti(III) or Ti(IV) ions in solution, one may rewrite Eq. [16] in the form

$$i_a = i_a^* - k_4 C_4 \quad [17]$$

where i_a^* represents the value of i_a observed in the absence of Ti(IV), i.e., $(i_d + i_H)$. Equation [17] applies to acidic chloride solutions as well as to acidic sulfate media (2). The polarization curves shown in Fig. 11 show the decrease in i_a which accompanies the addition of Ti(IV) ions to 1N HCl. According to Eq. [17], the polarization curves shown in Fig. 11 may be used to evaluate k_4 at any specified potential by simply subtracting i_a from i_a^* and dividing the result by C_4 , i.e., $(k_4)_E = (i_a^* - i_a)/C_4$. Alternately, $(k_4)_E$ may be determined by adding Ti(IV) ions to the solution while maintaining a constant electrode potential. The results of such an experiment conducted in 1N HCl at $E = -530$ mV vs. SCE are shown in Fig. 12, where $-i_4$ (i.e., $i_a^* - i_a$) is plotted against C_4 . The results demonstrated the validity of Eq. [17], and from the slope, $[\partial(-i_4)/\partial C_4]$, yield a value of 1.80×10^{-4} A

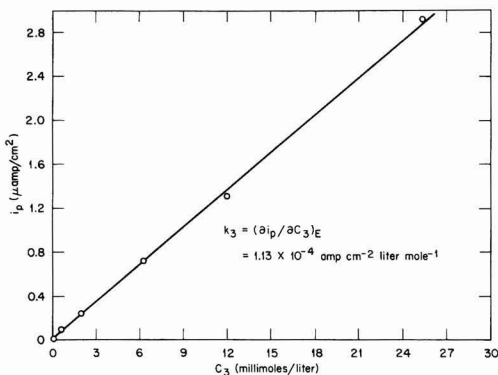


Fig. 10. Determination of the rate constant (k_3) for oxidation of Ti(III) to Ti(IV) at a passive titanium electrode in 1N HCl; $E = 0$ mV vs. SCE.

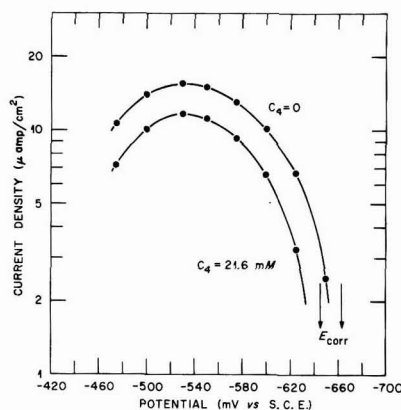


Fig. 11. Effect of Ti(IV) ions on the steady-state anodic polarization to titanium in 1N HCl.

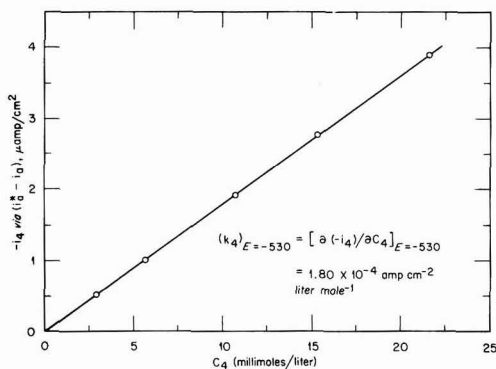


Fig. 12. Determination of the rate constant (k_4) for reduction of Ti(IV) to Ti(III) at an active titanium electrode in 1N HCl; $E = E_m = -530$ mV vs SCE.

cm^{-2} liter mole $^{-1}$ for $(k_4)_{E=-530}$ in 1N HCl. The value of $(k_4)_{E=-530}$ observed (2) in 1N H_2SO_4 was $6.31 \times 10^{-3} \text{A cm}^{-2}$ liter mole $^{-1}$, approximately 35 times greater than in 1N HCl. It should be noted that the reduction of Ti(IV) is activation controlled, i.e., i_4 is not affected by stirring.

Spontaneous cessation of localized corrosion and the role of chloride ion as a promoter of localized corrosion.—As shown in the preceding section, the partial anodic polarization curve ($\log i_4$ vs. E) is not affected by the presence of Ti(IV) ions in solution and, consequently, the intersection of the partial cathodic polarization curve ($\log |i_H - k_4 C_4|$ vs. E) with the partial anodic polarization curve is displaced to more positive (noble) open-circuit potentials and correspondingly greater corrosion current densities as C_4 increases, i.e., as $|i_H - k_4 C_4|$ increases. However, when $|i_H - k_4 C_4|$ just exceeds $i_{m,d}$, i.e., when C_4 exceeds a critical value (C_4^*) given approximately by the expression

$$C_4^* \approx (i_m)_{C_4=0} / (k_4)_{E=E_m} \quad [18]$$

then the partial cathodic polarization curve can no longer intersect the partial anodic polarization curve in the active-state potential region and, consequently, the active-state surface passivates. A detailed analysis of this phenomenon is given in Ref. (2).

In localized corrosion systems, both active and passive surfaces are in contact with the electrolyte within the occluded cell (36). Consider the case of

crevice corrosion of titanium in neutral or weakly acidic sulfate or chloride solutions. Acidification within the crevice, a consequence of hydrolysis of titanium dissolution products ($\text{Ti}^{4+} + 2\text{H}_2\text{O} = [\text{Ti}(\text{OH})_2]^{+2} + 2\text{H}^+$ and $\text{Ti}^{3+} + \text{H}_2\text{O} = (\text{TiOH})^{+2} + \text{H}^+$) coupled with mass transport limitations, can result in very low (<1) pH values in the innermost region of the crevice (31). The innermost surface of the crevice exists in the active state (low potential and low pH), whereas, nearer the entrance to the crevice, the titanium surface exists in the passive state (37-39).

In the course of their egress from the innermost region of the crevice, Ti(III) ions formed by active-state dissolution encounter conditions (i.e., a passive surface) under which they are known to be oxidized (i_3) to Ti(IV) ions in solution. The resultant Ti(IV) ions are transported back to the innermost region of the crevice where they encounter conditions (i.e., an active surface) under which they are known to be reduced (i_4) to Ti(III) ions in solution. The reduction of Ti(IV) has been shown to result in an ennobling of the active-state corrosion potential and a corresponding increase in the open-circuit (corrosion) dissolution rate of the active-state surface. Thus, Ti(IV) ions would adversely affect the rate of crevice corrosion, but only as long as C_4 remained below the critical concentration (C_4^*) required to passivate the active surface. The attainment of C_4^* , given by Eq. [18], is accompanied by the spontaneous cessation of localized corrosion. This phenomenon of spontaneous cessation of localized corrosion has long been recognized (36, 40), but not previously explained.

If one substitutes the values of i_m and $(k_4)_{E=E_m}$ observed for 1N HCl, i.e., $1.55 \times 10^{-5} \text{A cm}^{-2}$ and $1.80 \times 10^{-4} \text{A cm}^{-2}$ liter mole $^{-1}$, respectively, into Eq. [18], one obtains a value of 86 mmoles for the critical concentration of Ti(IV) required to passivate an active-state surface in 1N HCl, i.e., for $(C_4^*)_{1\text{N HCl}}$. On the other hand, the values of i_m and $(k_4)_{E=E_m}$ observed in 1N H_2SO_4 , $5.30 \times 10^{-5} \text{A cm}^{-2}$ and $6.31 \times 10^{-3} \text{A cm}^{-2}$ liter mole $^{-1}$, respectively, give a value of only 8.4 mmoles for $(C_4^*)_{1\text{N H}_2\text{SO}_4}$, i.e., it requires 10.3 times as large a concentration of Ti(IV) to passivate the active-state surface in the chloride solution as in the sulfate solution.

The fact that $(C_4^*)_{1\text{N HCl}}$ is ten times larger than $(C_4^*)_{1\text{N H}_2\text{SO}_4}$ suggests that spontaneous cessation of localized corrosion would be much less likely to occur in the chloride solution, i.e., the halide ion in effect acts as a promoter of localized corrosion. However, it is necessary to consider the relative times required for an electrolyte-coupled active-passive system to generate C_4^* in the chloride and sulfate solutions. Insight into this problem may be gained by considering a system consisting of an active-state surface (potentiostatically maintained at E_m) and a passive-state surface (potentiostatically maintained at, for example, 0 mV vs. SCE) in contact with v (liters) of stirred electrolyte initially ($t = 0$) free of Ti(III) and Ti(IV) ions. For such an electrolyte-coupled active-passive system, the increase in C_4 with time is given by Eq. [19]

$$C_4 = -\alpha[1 - \exp(-Kt/Fv)] + A_p k_3 \beta t \quad [19]$$

where, in order to simplify writing, α , β , and K represent the following

$$\alpha = (1/K) [(A_p k_3 A_a i_d / 3K) - (A_a k_4 A_p i_p^* / 4K)] \quad [20]$$

$$\beta = (1/KFv) [(A_a i_d / 3) + (A_p i_p^* / 4)] \quad [21]$$

$$K = (A_p k_3 + A_a k_4) \quad [22]$$

and A_a and A_p are the areas of the active and passive surfaces, respectively (2). The required values of k_3 , k_4 , and i_d have been given elsewhere in this paper, for both 1N HCl and 1N H_2SO_4 , and the values of i_p^* may be taken from Fig. 2. Using these values, it can be shown that the term, $-\alpha[1 - \exp(-Kt/Fv)]$, is

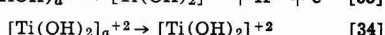
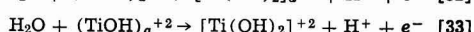
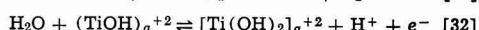
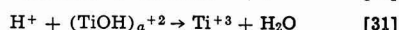
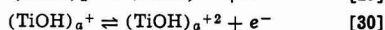
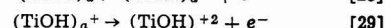
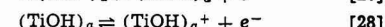
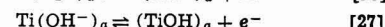
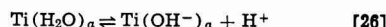
negligible compared to C_4^* , regardless of the values of A_a and A_p . Consequently, for the purpose of estimating the time (t^*) required to attain C_4^* , Eq. [19] reduces to the form

$$C_4^* \approx A_p k_3 \beta t^* \quad [23]$$

which, on inserting the value of C_4^* given by Eq. [18], gives t^*

$$t^* \approx i_m / A_p k_3 k_4 \beta \quad [24]$$

In order to simplify writing, symbols with a bar over them refer to 1N HCl and symbols without a bar refer to 1N H_2SO_4 . According to Eq. [24], the ratio, $(t^*)_{1N\ HCl} / (t^*)_{1N\ H_2SO_4}$, i.e., (\bar{t}^*/t^*) , exhibits a lower limit of 9.91, i.e., (k_3/\bar{k}_3) , corresponding to $A_a \gg A_p$, and increases as (A_p/A_a) increases. For example, (\bar{t}^*/t^*) increases to 13.8, i.e., to $(k_3/\bar{k}_3) (k_4/\bar{k}_4) [(k_3 + \bar{k}_4)/(k_3 + k_4)]$, when $A_p = A_a$. Finally, (\bar{t}^*/t^*) reaches an upper limit of 106, i.e., $(\bar{i}_m/i_m) (k_4/\bar{k}_4) (i_p/\bar{i}_p)$, for $A_p \gg A_a$. In localized corrosion (crevice corrosion or SCC), the case of interest is $(A_p \approx A_a)$ and, consequently, not only is the concentration of Ti(IV) required for spontaneous cessation of localized corrosion ten times greater in 1N HCl than in 1N H_2SO_4 , but, in addition, the time required to generate C_4^* is one or two orders of magnitude (more likely the latter since, generally, $A_p \gg A_a$) greater in the chloride media. The result is that the halide ion functions as a promoter of localized corrosion. It might be noted that, with $A_p \approx A_a$, the concentration of Ti(III) which exists when $C_4 = C_4^*$ is approximately equal



Among the requirements satisfied by the proposed mechanism are the following: the oxidation of the metal (as in the cases of the active iron, nickel, and cobalt electrodes) must occur in a sequence of single-electron transfer reactions (42); corresponding to each of the four valence states of titanium encountered in the oxidation of the metal to the Ti(IV) state, there exists a surface intermediate (indicated by subscript "a" in Eq. [25]–[34]); only one proton or water molecule is involved in any single reaction (43); and neither Ti(I) nor Ti(II) exist except as surface intermediates. In addition, it is recognized that in the pH region of interest, Ti(III) ions in solution exist as Ti_{aq}^{+3} and its first hydrolysis product, $(TiOH)^{+2}$, whereas, Ti(IV) ions in solution exist only as $[Ti(OH)_2]^{+2}$ (43).

For the reaction system represented by Eq. [25]–[34], the steady-state current density is given by Eq. [35]

$$i_d/F = \frac{3(\bar{k}_{29} + k_{31}a_{(H^+)}N) + 4N(\bar{k}_{33} + k_{34}M)}{[(1/PQR) + (1/PQ) + (1/P) + 1 + N + MN]} + [(k_{-25} + k_{26} - k_{-26}a_{(H^+)}R)/PQRk_{25}] \quad [35]$$

to $(A_a/A_p) (k_4/k_3) C_4^*$, i.e., to $4.74 \times 10^{-2} (A_a/A_p)$ and $1.37 \times 10^{-1} (A_a/A_p)$ mole/liter in 1N H_2SO_4 and 1N HCl, respectively, values too small to introduce any complications into the preceding analysis. According to Schmets *et al.* (41), the standard potential of the Ti(III)/Ti(IV) couple is approximately 0.10V vs. SHE. Consequently, if the open-circuit potential of the once active surface, on passivation at C_4^* , were determined primarily by the Ti(III)/Ti(IV) couple, then, with $(C_3^*/C_4^*) \approx (A_a/A_p) (k_4/k_3)$, the potential would lie in the passive potential region ($> -0.30V$ vs. SCE). This has been confirmed for sulfate solutions (2).

The electrolyte-coupled active-passive system just described contains all of the chemical and electrochemical elements present in localized corrosion and, consequently, serves to demonstrate in a quantitative fashion the critical roles played by Ti(III), Ti(IV), and Cl^- ions in determining the cessation or propagation of localized corrosion. In a true localized corrosion system, the time required to generate C_4^* increases as a consequence of mass transport limitations. However, if one assumes that the ratio of the diffusion coefficients of Ti(III) in chloride and sulfate media is approximately the same as that for the Ti(IV) ion, then there is obviously nothing in the mass transport process that could completely ameliorate against the above-described electrochemical kinetic factors responsible for the role of halide ions as promoters of localized corrosion.

Active-state dissolution and passivation mechanism.—The highly restrictive set of diagnostic relationships observed in both acidic sulfate and acidic chloride solutions, i.e.

$$d \log i_{m,d}/dpH = -2/3 \quad [5]$$

$$d \ln i_{m,d}/dE_{m,d} = F/2RT \quad [6]$$

$$dE_{m,d}/dpH = -(4/3) (2.303RT/F) \quad [7]$$

may be derived on the basis of the following mechanism



where, in order to simplify writing, the following definitions apply

$$M = (\theta_4/\theta_3) = \bar{k}_{32}/(\bar{k}_{-32}a_{(H^+)} + k_{34}) \quad [36]$$

$$N = (\theta_3/\theta_2) = \bar{k}_{30}/(\bar{k}_{-30} + k_{31}a_{(H^+)} + \bar{k}_{32} - \bar{k}_{-32}a_{(H^+)}M + \bar{k}_{33}) \quad [37]$$

$$P = (\theta_2/\theta_1) = \bar{k}_{28}/(\bar{k}_{-28} + \bar{k}_{29} + \bar{k}_{30} - \bar{k}_{-30}N) \quad [38]$$

$$Q = (\theta_1/\theta_{(OH^-)}) = \bar{k}_{27}/(\bar{k}_{-27} + \bar{k}_{28} - \bar{k}_{-28}P) \quad [39]$$

$$R = (\theta_{(OH^-)}/\theta_{H_2O}) = k_{26}/(k_{-26}a_{(H^+)} + \bar{k}_{27} - \bar{k}_{-27}Q) \quad [40]$$

In the preceding equations, θ_j represents the fraction of the available sites occupied by the j th species, with $j = 1, 2, 3$, and 4 indicating the valence state of titanium in the surface species. In addition, a bar over a rate constant indicates a potential dependent rate constant, i.e., $\bar{k}_{\pm} = k_{\pm} \exp(\pm FE/2RT)$. The rate constants, k_{\pm} , are assumed to be independent of θ_j values, i.e., Langmuir kinetics are assumed to prevail.

For the system of reactions indicated by Eq. [25]–[34], the general current density expression is given by Eq. [41]

$$i_d/F = (\bar{k}_{27}\theta_{(OH^-)} - \bar{k}_{-27}\theta_1) + (\bar{k}_{28}\theta_1 - \bar{k}_{-28}\theta_2) + \dots \quad [41]$$

where, for each of the electron-transfer reactions, a corresponding term appears on the right side of Eq. [41], as illustrated by $(\bar{k}_{27}\theta_{(OH^-)} - \bar{k}_{-27}\theta_1)$ for the reaction shown by Eq. [27]. Similarly, expressions are written for $(d\theta_{H_2O}/dt)$, $(d\theta_{(OH^-)}/dt)$, and $(d\theta_j/dt)_{j=1,2,3,4}$. For the steady-state case, all $(d\theta/dt)$ expressions equate to zero, and the resulting set of equations may be solved θ_{H_2O} , $\theta_{(OH^-)}$, and θ_j in terms of the rate constants (alone or, where indicated by the specific reaction, multiplied by $a_{(H^+)}$). Insertion of the steady-state θ values into Eq. [41] followed by re-

arrangement of terms, yield Eq. [35]. The systematic reduction of Eq. [35] to correspond to the results contained in Eq. [5]-[7] requires very few assumptions. Let θ_T represent the sum of all θ terms, i.e., $\theta_T = \theta_{H_2O} + \theta_{(OH)^-} + \theta_j$ ($j = 1, 2, 3, 4$). The first assumption is expressed by the condition

$$k_{25}(\theta_T/\theta_{H_2O}) \gg (k_{-25} + k_{26} - k_{-26}a_{(H^+)}R) \quad [42]$$

This condition simply means that $\theta_T = 1$, i.e., there is no significant "bare metal." Imposition of this condition immediately reduces Eq. [35] to Eq. [43]

$$i_d/F = \frac{3(\bar{k}_{29} + k_{31}a_{(H^+)}N) + 4N(\bar{k}_{33} + k_{34}M)}{[(1/PQR) + (1/PQ) + (1/P) + 1 + N + MN]} \quad [43]$$

In Eq. [43], the term, $4N(\bar{k}_{33} + k_{34}M)$, is related to the formation of Ti(IV) ions in solution and, on the basis of the coulometric weight-loss data in the vicinity of E_m , has been shown to be negligible compared to the term, $3(\bar{k}_{29} + k_{31}a_{(H^+)}N)$, which is related to the formation of Ti(III) ions in solution. Consequently, Eq. [43] reduces to the form

$$i_d/F = 3(\bar{k}_{29} + k_{31}a_{(H^+)}N)/[(1/PQR) + (1/PQ) + (1/P) + 1 + N + MN] \quad [44]$$

The second assumption is that $(1 + N + MN) \gg [(1/PQR) + (1/PQ) + (1/P)]$, which is equivalent to $(\theta_2 + \theta_3 + \theta_4) \gg (\theta_{H_2O} + \theta_{(OH)^-} + \theta_1)$. This is less an assumption than a necessity, i.e., if one examines all of the possible potential and pH dependencies of all of the terms in Eq. [44] (see Eq. [36]-[40]), it becomes evident that it is not possible to satisfy Eq. [5]-[7] unless this assumption is made. The assumption reduces Eq. [44] to the expression

$$i_d/F = 3(\bar{k}_{29} + k_{31}a_{(H^+)}N)/(1 + N + MN) \quad [45]$$

According to Eq. [36], there are two limiting values of M . According to Eq. [37], the two limiting values of M lead to five distinct limiting values of N . If these limiting values of M and N are inserted into Eq. [45], a total of eight distinct cases for the steady-state current density are generated, one of which is given by Eq. [46]

$$i_d/3F = \frac{(k_{29} + k_{30}) \exp(FE/2RT)}{[1 + (k_{30}/k_{31})a_{(H^+)}^{-1} \exp(FE/2RT) + (k_{30}k_{32}/k_{31}k_{-32})a_{(H^+)}^{-2} \exp(3FE/2RT)]} \quad [46]$$

Application of the condition, $(\partial \log i_d/\partial E)_{pH} = 0$ at $E = E_{m,d}$, to Eq. [46] gives the result

$$E_{m,d} = (2/3)(2.303RT/F) \log(k_{31}k_{-32}/2k_{30}k_{32}) - (4/3)(2.303RT/F)pH \quad [47]$$

i.e.

$$dE_{m,d}/dpH = -(4/3)(2.303RT/F)$$

which is identical to Eq. [7]. Substitution of $E_{m,d}$ from Eq. [47] into Eq. [46] gives Eq. [48]

$$i_{m,d} = (k_{31}k_{-32}/2k_{30}k_{32})^{1/3}(k_{29} + k_{30})(2/3)a_{(H^+)}^{2/3} \quad [48]$$

provided $(3/2) \gg (k_{31}k_{-32}/2k_{30}k_{32}a_{(H^+)}^{1/3})(k_{30}/k_{31})$, i.e., provided the second term in the denominator of Eq. [46] is negligible at $E_{m,d}$ compared to the first and third terms. From Eq. [48], one obtains the expression

$$d \log i_{m,d}/dpH = -2/3$$

which is identical to Eq. [6]. The denominator of Eq. [46] is equal to $[(\theta_2 + \theta_3 + \theta_4)/\theta_2]$ and therefore, the condition leading to Eq. [48] may be expressed in the form, $[(\theta_2 + \theta_3 + \theta_4)/\theta_2] = [(\theta_2 + \theta_4)/\theta_2] = 3/2$. However, since $(\theta_2 + \theta_4) = \theta_T = 1$, it follows that at $E_{m,d}$, $\theta_2 = 2/3$ and $\theta_4 = 1/3$. As E becomes increasingly positive relative to $E_{m,d}$, passivation occurs

as a consequence of the increase in θ_4 at the expense of θ_2 .

In addition to satisfying the diagnostic relations, Eq. [5]-[7], it should be noted that as E becomes increasingly positive in the active-passive transition region, Eq. [46] reduces to the limiting case

$$i_d/3F \rightarrow (k_{31}k_{-32}/k_{30}k_{32})(k_{29} + k_{30})a_{(H^+)}^{-2} \exp(FE/RT) \quad [49]$$

i.e., the polarization curve should approach a limiting Tafel line having a slope, $(\partial E/\partial \log i_d)_{pH}$, equal to $(-2.303RT/F)$, i.e., -60 mV/decade, and a second-order dependency on $a_{(H^+)}$, i.e., $(\partial \log i_d/\partial pH)_E = -2$. The limiting Tafel slopes observed for curves A, B, and C of Fig. 5 are -83 , -76 , and -61 mV/decade, respectively. From curves A and B, one obtains $(\partial \log i_d/\partial pH)_E = -400 = -1.89$, and from curves B and C (extrapolated limiting Tafel line), one obtains $(\partial \log i_d/\partial pH)_E = -400 = -2.0$. The small derivations from ideal values can be attributed to neglect of the term, $4N(\bar{k}_{33} + k_{34}M)$, in Eq. [43] and subsequent equations.

Of the eight distinct steady-state current density cases generated by substitution of the limiting values of M and N into Eq. [45], only that given by Eq. [46] satisfies the experimentally determined criteria represented by Eq. [5]-[7]. Suppose, however, that in writing the reaction scheme shown by Eq. [25]-[34], the natures of the adsorbed surface species and the solution species were left unspecified, i.e., if the surface species were simply represented by $Ti(I)_a$, $Ti(II)_a$, $Ti(III)_a$, and $Ti(IV)_a$, and the solution species by $Ti(III)_s$ and $Ti(IV)_s$. Then, proceeding as before, one would again obtain Eq. [35]-[45], unchanged except for omission of $a_{(H^+)}$. Again, insertion of the limiting values of M and N into Eq. [45] generates eight limiting cases for the steady-state current density. Three of the eight cases can be eliminated because they fail the test, $(\partial^2 \log i_d/\partial E^2)_{pH, E=E_m} = (-)$, i.e., they fail to exhibit a maximum in the polarization curve. For the remaining cases, one sets $(\partial \log i_d/\partial E)_{pH, E=E_m}$ equal to zero, solves for $E_{m,d}$, inserts $E_{m,d}$ into the current density equation and, thereby, obtains $i_{m,d}$. Then, $E_{m,d}$ and $i_{m,d}$ must satisfy Eq. [7] and Eq. [5], respectively. Only two cases survive these tests, case I and case II. If r_n represents the rate of the n th reaction,

then case I requires the following: $r_{29} \neq f(pH)$, $r_{30} \neq f(pH)$, $r_{31} = \bar{k}_{31}a_{(H^+)}$, $r_{32} \neq f(pH)$, and $r_{-32} = \bar{k}_{-32}a_{(H^+)}$. These requirements are precisely those satisfied by the reaction scheme given by Eq. [25]-[34]. Other reaction schemes which satisfy these requirements can be written, but only by invoking species not known to exist, or unlikely to exist at low pH. For example, if one substitutes $(TiO)_a$, $(TiOOH)_a$, $(TiO_2)_a$, TiO^+ , and TiO^{++} for the corresponding surface and solution species in Eq. [25]-[34], all requirements can be met (1), but such a sequence of basic species is less likely to exist in acidic media, if at all. For case II, the requirements are the following: $r_{29} \neq f(pH)$, $r_{30} \neq f(pH)$, $r_{-30} = \bar{k}_{-30}a_{(H^+)}$, $r_{32} \neq f(pH)$, and $r_{34} = k_{34}a_{(H^+)}$. Again, no reasonable reaction scheme, i.e., one involving only known species, can be devised to satisfy these requirements. In summary, the mechanism of active-state dissolution and passivation of titanium is rather uniquely represented by the reaction scheme given by Eq. [25]-[34].

Electron diffraction studies have shown that dark gray to black hydride layers can be formed on titanium by corrosion in concentrated H_2SO_4 or HCl , or by strong cathodic polarization in more dilute acids. For example, TiH has been observed after cathodic polariza-

zation for 100 hr in 6N H₂SO₄ (25°C) at -0.8V vs. SCE, and TiH_{0.9} after 100 hr in 1N H₂SO₄ (24°C) at a cathodic current density of 20 mA/cm² (44). Similarly, TiH has been observed after corrosion for 20 hr at 18°C in 15 weight percent HCl (45), and TiH₂ after corrosion for 20 hr at 15°C in 12N HCl (45), or after 16 hr in concentrated HCl at 20°C (44). Formation of hydride is dependent on pH, electrode potential, temperature, etc., and, for the systems described in the present study, would not be expected to occur except under strong cathodic polarization (46). Indeed, the only observation that could be considered to reflect the presence of hydride occurred under strong cathodic polarization, where it was found that the current density at constant potential increased with time to values much greater than expected on the basis of extrapolation of the cathodic Tafel line established at higher potentials. Thomas and Nobe observed this same phenomenon in 4N HCl at potentials below approximately -875 mV vs. SCE (47), and in acidic sulfate solutions at potentials more negative than approximately -1.0V vs. SCE (12), and noted the possibility of hydride formation as the cause. At one time, hydride was assigned a dominant role in the behavior of titanium in acidic media and, in fact, was assumed to be responsible for the passivity of the metal (45). This viewpoint was based on qualitative interpretations of corrosion tests and electrochemical polarization data in aerated solutions, interpretations which can no longer be considered valid when viewed in the light of present knowledge concerning the conditions under which oxide passivity or active-state dissolution occur, the effects of O₂, Ti(III), Ti(IV), pH, etc., and the interpretational ambiguities which are from nonsteady-state data. In addition to the present studies, the work of Mansfeld (48,49) clearly refutes the concept of "hydride passivity." His studies showed that passivation of titanium failed to occur in anhydrous methanol containing HCl or H₂SO₄, but occurred in the usual manner when traces of water were added. However, as indicated by the cathodic polarization curves, conditions for hydride formation were equally favorable with or without the added water.

Summary

The electrochemical behavior of titanium in deoxygenated acidic chloride solutions has been determined and compared with the results obtained earlier in acidic sulfate media.

A monolayer mechanism for the active-state dissolution and passivation of titanium in acidic media has been developed and shown to be in quantitative agreement with the experimental results.

A comparative study of the effects of Ti(III) and Ti(IV) ions on the electrochemical behavior of titanium in acidic chloride and acidic sulfate solutions has provided explanations for (i) the random spontaneous cessation of localized corrosion, and (ii) the role of halide ions as promoters of localized corrosion.

Acknowledgment

This research was sponsored by the Division of Materials Sciences, U.S. Department of Energy, under Contract W-7405-eng-26 with Union Carbide Corporation.

Manuscript submitted April 16, 1979; revised manuscript received May 16, 1979.

Any discussion of this paper will appear in a Discussion Section to be published in the June 1980 JOURNAL. All discussions for the June 1980 Discussion Section should be submitted by Feb. 1, 1980.

Publication costs of this article were assisted by Oak Ridge National Laboratory.

REFERENCES

1. E. J. Kelly, "Proceedings International Congress on Metallic Corrosion, 5th, Tokyo, 1972," p. 137, NACE, Houston (1974).
2. E. J. Kelly, *This Journal*, **123**, 162 (1976).
3. N. T. Thomas and K. Nobe, *ibid.*, **119**, 1450 (1972).
4. A. Caprani, I. Epelboin, and Ph. Morel, "Proceedings European Congress of Corrosion, 5th, Paris, 1973," p. 111.
5. E. J. Kelly, *This Journal*, **112**, 124 (1965).
6. J. R. Vilche and A. J. Arvia, *Corros. Sci.*, **18**, 441 (1978).
7. N. T. Thomas and K. Nobe, *This Journal*, **116**, 1748 (1969).
8. J. M. Peters and J. R. Myers, *Corrosion*, **23**, 326 (1967).
9. A. P. Brynza, V. P. Fedash, and V. N. Kovtun, *Prot. Met. Engl. Transl.*, **2**, 31 (1966).
10. R. D. Armstrong, R. E. Firman, and H. R. Thirsk, *Corros. Sci.*, **13**, 409 (1973).
11. R. D. Armstrong, J. A. Harrison, H. R. Thirsk, and R. Whitfield, *This Journal*, **117**, 1003 (1970).
12. N. T. Thomas and K. Nobe, *ibid.*, **117**, 622 (1970).
13. A. M. Sukhotin and L. I. Tungusova, *Prot. Met. Engl. Transl.*, **7**, 218 (1973).
14. E. Brauer and E. Nann, *Werkst. Korros.*, **20**, 676 (1969).
15. T. R. Beck, *Electrochim. Acta*, **18**, 815 (1973).
16. T. Koizumi and T. Nakayama, *Corros. Sci.*, **8**, 195 (1968).
17. E. E. Rider, V. I. Ovcharenko, V. Ya. Dudarev, and V. M. Novakovskii, *Prot. Met. Engl. Transl.*, **11**, 160 (1975).
18. N. D. Tomashov, R. M. Al'tovskii, and M. Ya. Kushnerev, *Proc. Acad. Sci. USSR*, **141**, 927 (1961).
19. N. D. Tomashov, Yu. S. Ruskol, and G. A. Ayuyan, *Prot. Met. Engl. Transl.*, **10**, 472 (1974).
20. N. D. Tomashov, G. P. Chernova, Yu. S. Ruskol, and G. A. Ayuyan, *Electrochim. Acta*, **19**, 159 (1974).
21. I. A. Ammar and I. Kamal, *ibid.*, **16**, 1539 (1971).
22. K. D. Allard, M. Ahrens, and K. E. Heusler, *Werkst. Korros.*, **26**, 694 (1975).
23. K. D. Allard and K. E. Heusler, *J. Electroanal. Chem.*, **77**, 35 (1977).
24. D. Laser, M. Yaniv, and S. Gottesfeld, *This Journal*, **125**, 358 (1978).
25. W. Paatsch, *Ber. Bunsenges. Phys. Chem.*, **79**, 922 (1975).
26. E. K. Oshe, I. L. Rozenfel'd, and Yu. V. Batrakova, *Prot. Met. Engl. Transl.*, **13**, 253, 266 (1977).
27. J. Kruger, "Advances in Electrochemistry and Electrochemical Engineering," Vol. 9, P. Delahay and C. W. Tobias, Editors, pp. 227-280, John Wiley & Sons, Inc., New York (1973).
28. J. D. E. McIntyre, *ibid.*, pp. 61-166.
29. E. K. Oshe and I. L. Rozenfel'd, *Prot. Met. Engl. Transl.*, **5**, 458 (1969).
30. M. Levy, *Corrosion*, **23**, 236 (1967).
31. J. C. Griess, Jr., *ibid.*, **24**, 96 (1968).
32. W. R. Fischer, *Werkst. Korros.*, **10**, 243 (1959).
33. M. Stern and H. Wissenberg, *This Journal*, **106**, 755 (1959).
34. M. Levy and G. N. Sklover, *ibid.*, **116**, 323 (1969).
35. D. Sinigaglia, G. Tacani, and B. Vicentini, *Werkst. Korros.*, **24**, 1027 (1973).
36. I. L. Rozenfel'd, "Proceedings International Congress on Metallic Corrosion, 5th, Tokyo, 1972," p. 53, NACE, Houston (1974).
37. Yu. S. Ruskol and I. Ya. Klinov, *Prot. Met. Engl. Transl.*, **2**, 544 (1966).
38. Zh. F. Solov'eva, M. N. Fokin, and V. A. Timonin, *ibid.*, **6**, 187 (1970).
39. B. Vicentini, *Werkst. Korros.*, **25**, 8 (1974).
40. E. J. Bohlmann and F. A. Posey, "Proceedings of the First International Symposium on Water Desalination, Washington, D.C., Oct. 3-9, 1965," Vol. 1, pp. 306-325.
41. J. Schmets, J. Van Muylder, and M. Pourbaix, "Atlas of Electrochemical Equilibria in Aqueous Solutions," p. 213, Pergamon Press, Inc., New York (1966).
42. J. O'M. Bockris and A. K. N. Reddy, "Modern Electrochemistry," Vol. 2, p. 1082, Plenum Press, New York (1970).
43. C. F. Baes, Jr. and R. E. Mesmer, "Hydrolysis of Cations," chap. 8, John Wiley & Sons, Inc., New York (1976).

44. E. Brauer and E. Nann, *Werkst. Korros.*, **25**, 481 (1974).
45. R. Otsuka, *Sci. Papers Phys. Chem. Res.*, **54**, 97 (1960).
46. N. D. Thomashov, V. N. Modestova, L. A. Plavich, and A. B. Averbukh, "Corrosion of Metals and Alloys," Coll. 2, 1965, Israel Program for Scientific Translations, 1966, pp. 66-84.
47. N. T. Thomas and K. Nobe, *Corrosion*, **29**, 188 (1973).
48. F. Mansfeld, *This Journal*, **118**, 1412 (1971).
49. F. Mansfeld, *ibid.*, **120**, 188 (1973).

Pitting Resistance of Cold-Worked Commercial Austenitic Stainless Steels in Solution Simulating Seawater

B. Mazza, P. Pedferri, D. Sinigaglia, A. Cigada, G. A. Mondora,

G. Re, G. Taccani,¹ and D. Wenger²

*Istituto di Chimica-fisica, Elettrochimica e Metallurgia del Politecnico di Milano,
Centro di Studio del CNR sui Processi Elettrodici, 20133 Milano, Italy*

ABSTRACT

This paper describes the results of an electrochemical investigation concerning the pitting resistance of cold-worked AISI 304 L and 316 L stainless steels in deaerated 3.5 weight percent (w/o) NaCl solutions of different pH's (pH = 2, 7, and 9). An anisotropic behavior of specimen surfaces with different orientations to the direction of deformation is shown and discussed in relation to characteristic structural aspects.

A systematic study of the influence of cold plastic deformation on the corrosion behavior of commercial austenitic stainless steels in different aggressive media has been carried out in our laboratory from 1970 onward (1-9), and is now coming to an end.

In this paper, a general view is given of the results concerning the pitting resistance of AISI Types 304 L and 316 L stainless steels cold-worked under various conditions, immersed in deaerated 3.5 w/o NaCl solutions of different pH's (pH = 2, 7, and 9).

Literature data on pitting corrosion of cold-worked stainless steels are scant and inconsistent (10-16). In particular, the critical pitting potential has been observed either to remain unaffected by cold work, or to shift to more negative values. This inconsistency should not arouse surprise: as a matter of fact, commercial steels are generally considered, and especially after cold plastic deformation their microstructure is neither simple, nor well controlled by the different authors (also in relation to the different working conditions).

¹ Present address: LTM-CNR, Cinisello Balsamo, Milano, Italy.

² Present address: CISE, Segrate, Milano, Italy.

Key words: corrosion, pitting, austenitic stainless steels, cold plastic deformation.

Experimental and Materials (Microstructure Analysis)

Materials were first annealed at 1050°C for 1 hr and water quenched (solution heat-treatment), then submitted to cold plastic deformation by either tension, drawing, or rolling, at room temperature (25°C) or at liquid nitrogen temperature (-196°C). Chemical compositions and some structure characteristics of the stainless steels under study (after the solution heat-treatment) are given in Table I. The microstructure analysis of the deformed materials was carried out by means of magnetic measurements, x-ray diffraction, and transmission electron microscopy.

Magnetic measurements (17) enable us to determine (following the scheme of Table II) the weight percentage of ferromagnetic α' -martensite in the deformed steels [the weight percentage of δ -ferrite in the non-deformed state being negligible (see Table III)].

Transmission electron microscopy shows the presence of the following: (i) dislocations, with a tendency to their arrangement in a cell structure; (ii) deformation bands, which can be resolved either as deformation twins or as ϵ -martensite, and (iii) platelets of α' -martensite (approximately one micron in length and

Table I. Chemical compositions and some structure characteristics of the commercial austenitic stainless steels under study (after the solution heat-treatment)

Steel type	Composition (w/o)										ASTM grain-size number ^a	M_{500}^b (°C)	M_s^c (°C)	Subsequent cold-working
	C	Si	Mn	P	S	Cr	Ni	Mo	Cu	N				
AISI 304 L	0.025	0.45	1.39	0.023	0.021	18.60	8.75	0.50	0.24	0.036	6-6.5	+22	<-196	Tension
	0.032	0.54	1.64	0.009	0.009	18.60	8.70	0.48	0.20	0.038	7-7.5	+16	<-196	Drawing
	0.020	0.41	1.40	0.032	0.013	18.10	10.30	0.32	0.24	0.039	4-5	+18	<-196	Rolling
AISI 316 L	0.022	0.43	1.51	0.033	0.023	16.80	10.65	2.90	0.07	0.033	5-5.5	-14	<-196	Tension
	0.023	0.40	1.45	0.034	0.021	16.60	10.90	3.00	0.08	0.037	5.5-6	-17	<-196	Drawing
	0.026	0.41	1.24	0.008	0.011	16.10	10.90	2.20	0.07	0.034	3.5-4.5	+7	<-196	Rolling

^a Determined according to ASTM Designation E 112.

^b Temperature at which 50% of martensite is formed in tension after a true strain of 0.30 [calculated according to Ref. (17) and (18)].

^c Martensite starting temperature.

Table II. Scheme showing how the w/o of ferromagnetic phase (M%) in the deformed austenitic stainless steels under study is determined (17)

σ_H = specific saturation magnetization (emu/g) measured at a given magnetic field strength H (as a rule in our measurements, $H = 20,000$ oe)

σ_s = specific saturation magnetization (emu/g) corrected for the austenite paramagnetic contribution as follows: $\sigma_s = \sigma_H - 2.5 \times 10^{-5} H$

$$100 \times \sigma_s = (M\%) \times \sigma_s^* \rightarrow (M\%)$$

σ_s^* constant calculated for each steel composition as follows (from Angel):

$$\sigma_s^* = 160.4 + \sum_i \Delta\sigma_i^* \times \Delta c_i$$

160.4 = specific saturation magnetization (emu/g) of a totally-martensitic reference heat whose chemical composition (w/o) is as follows (from Angel): C = 0.09; Si = 0.42; Mn = 0.42; Cr = 18.20; Ni = 8.6; Mo = 0.29; N = 0.053
 $\Delta\sigma_i^*$ = coefficients calculated from Angel's data. His values for each element are as follows: C = 8.34; Si = 3.38; Mn = -0.29; Cr = 2.77; Ni = -0.076; Mo = 0.33; N = 36
 Δc_i = difference between the weight percentages of the element "i" in a given steel and in the reference steel.

N.B.: The values of the different magnetic quantities are given in cgs units to allow an easy comparison with data of Ref. (17). Relation between SI units and cgs units is as follows:

Quantity	cgs unit	SI unit	Conversion factor for cgs to SI units
Magnetic field	Oersted (oe)	Ampere turns per meter (A/m)	$\times 10^4/4\pi$
Magnetic moment	emu	Weber meter (Wb m)	$\times 4\pi \cdot 10^{-10}$

a few tenths of a micron in width) at the intersections of the deformation bands; in all three cases the amounts increase with increasing degree of deformation. Dislocations or deformation bands prevail when the steels under study are deformed at room temperature, while deformation bands with platelets of α' -martensite prevail in the case of cold-working at liquid nitrogen temperature (Fig. 1a). In this latter case, the deformation structure at the higher degrees of deformation consists almost solely of small equiaxed grains of α' -martensite (Fig. 1b).

The results of the microstructural investigations are summarized in Table III. The phenomenological aspects previously described in the literature (17-23) are confirmed.

Specimens for the electrochemical experiments were cut so as to obtain different orientations of the surface exposed to the aggressive medium, with respect to the direction of deformation. Longitudinal (L) and transverse (T) surfaces in the cases of tension and drawing, and longitudinal (L), long-transverse (T_L), and short-transverse (T_S) surfaces in the case of rolling were considered.

A detailed description of the procedure for specimen surface preparation of the polarization cell and electrode assembly is given elsewhere (4-7). The testing solution temperature was maintained at 40°C, in order to compare the results with those obtained in a physiological saline solution in previous research work. Nitrogen was continuously bubbled to remove the air. Saturated calomel reference electrodes (SCE) were used.

The currently popular electrochemical techniques, i.e., the cyclic polarization (or electrochemical hystere-

Table III. Results of the microstructural investigations

Steel type	Deformation		Vickers hardness number ^b	X-ray diffraction Phases ^c	Magnetic measurements Ferro-magnetic phase (w/o)	Transmission electron microscopy					
	Type	Temperature (°C)				Degree ^a (%)	Dislocations density (× 10 ⁸ cm/cm ²)	Deformation bands ^c	α'-martensite ^c	Austenite ^c	
AISI 304 L	Tension	25	0	147	—	0.3	1.3	—	—	≈100%	
			10	202	γ + α' (v.l.)	0.7	15	l.	n.o.	≈100%	
			15	228	γ + α' (l.)	1.5	>20	m.q.	l.	l.p.	
			30	313	γ + α' (m.q.)	10.6	>20	m.	m.q.	p.	
			9	326	γ + α' (m.q.) + ε (v.l.)	37.5	—	m.	m.	m.	
			13	415	γ + α' (m.) + ε (v.l.)	66.5	—	l.p.	p.	l.	
			19	459	γ + α' (p.) + ε (v.l.)	73.0	—	v.l.	l.p.	n.o.	
			25	0	135	—	0.04	1.2	—	—	100%
			10	198	γ	0.04	10	n.o.	n.o.	100%	
			15	220	γ	0.04	>20	l.	n.o.	100%	
AISI 316 L	Tension	30	288	γ	0.25	>20	m.q.	n.o.	l.p.	—	
		9	274	γ + α' (m.q.) + ε (v.l.)	18.0	—	m.	m.q.	p.	—	
		13	355	γ + α' (m.) + ε (v.l.)	41.0	—	p.	m.	m.q.	—	
		19	425	γ + α' (m.) + ε (v.l.)	60.0	—	v.l.	p.	m.	—	
		25	0	143	—	0.30	0.90	—	—	≈100%	
			10	200	γ + α' (v.l.)	0.40	30	l.	n.o.	≈100%	
			30	292	γ + α' (m.q.)	9.2	—	m.	m.q.	l.p.	—
			50	366	γ + α' (m.)	35.7	—	p.	m.	p.	—
			10	298	γ + α' (m.) + ε (v.l.)	31.6	—	m.	m.	p.	—
			30	406	γ + α' (p.)	78.2	—	v.l.	p.	l.	—
AISI 304 L	Drawing	50	494	γ + α' (l.p.)	88.8	—	v.l.	l.p.	n.o.	—	
		25	0	136	—	0.04	1.0	—	—	100%	
			10	192	γ	0.04	20	l.	n.o.	100%	
			30	272	γ	0.20	—	m.	v.l.	l.p.	—
			50	331	γ	1.7	—	l.p.	l.	l.p.	—
			10	246	γ + α' (l.)	3.2	—	m.	l.	l.p.	—
			30	400	γ + α' (m.q.) + ε (v.l.)	54.8	—	v.l.	p.	m.q.	—
			50	413	γ + α' (p.)	75.6	—	v.l.	l.p.	l.	—
			25	0	135	—	0.05	1.0	—	—	100%
			10	203	γ + α' (v.l.)	0.14	17	m.q.	n.o.	l.p.	—
AISI 316 L	Rolling	30	272	γ + α' (v.l.)	0.60	>20	p.	n.o.	l.p.	—	
		50	307	γ + α' (l.)	2.35	>20	p.	n.o.	l.p.	—	
		10	272	γ + α' (m.q.) + ε (v.l.)	26.2	—	m.	m.q.	p.	—	
		30	417	γ + α' (p.) + ε (v.l.)	63.0	—	p.	m.	m.q.	—	
		50	466	γ + α' (l.p.) + ε (v.l.)	86.5	—	v.l.	l.p.	n.o.	—	
		25	0	142	—	0.06	1.6	—	—	100%	
			10	200	γ	0.06	>20	m.q.	n.o.	100%	
			30	280	γ	0.13	—	p.	n.o.	l.p.	—
			50	327	γ	0.70	—	p.	n.o.	l.p.	—
			10	260	γ + α' (m.q.)	26.6	—	m.	m.q.	p.	—
AISI 304 L	Rolling	30	421	γ + α' (p.) + ε (v.l.)	57.3	—	p.	m.	m.q.	—	
		50	476	γ + α' (l.p.)	62.6	—	v.l.	l.p.	l.	—	

^a Quantified as reduction in the cross-sectional area.

^b Values measured on transversal sections (in the case of rolling long-transverse sections) with respect to the deformation direction.
^c v.l. = very little (<1%); l. = little (1-10%); m.q. = medium quantity (10-40%); m. = much (40-60%); p. = prevailing (60-80%); l.p. = largely prevailing (>80%); n.o. = not observed.

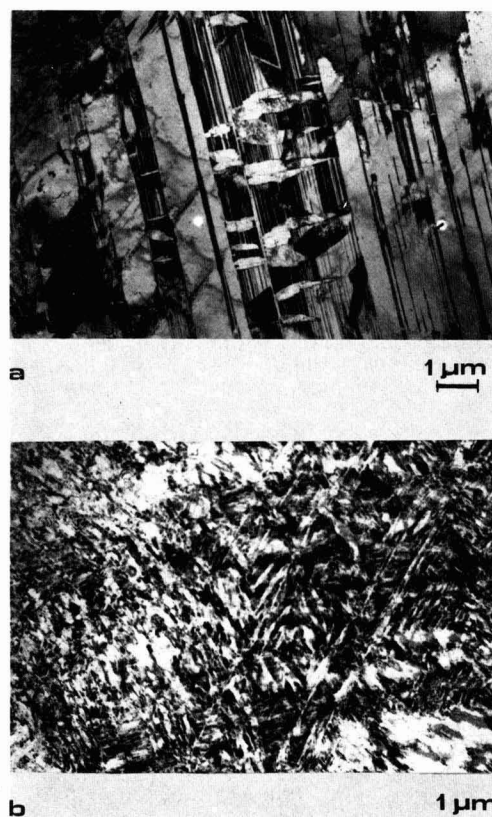


Fig. 1. Deformation structure of AISI Type 304 L stainless steel rolled at liquid nitrogen temperature: (a) deformation degree, 10%; (b) deformation degree, 50%.

sis) technique (16, 24-29) and the scratch method under potentiostatic conditions (30) were applied for investigating the pitting resistance of the stainless steels under study.

As is well known, cyclic anodic polarization (or electrochemical hysteresis) curves enable us to determine: (i) a critical pitting potential (E_c), at which pitting is initiated in the forward scan portion; and (ii) a protection potential against pitting (E_{prot}), more active than E_c , at which the growing pits are repassivated in the reverse scan portion. Pitting attack will initiate and propagate if the potential rises above E_c , while new pits will not initiate and existing pits will not propagate if the potential remains below E_{prot} . Inside the hysteresis loop the pitting attack will not initiate, but will propagate if initiated at other potentials. E_c and E_{prot} values were taken from the curves of potential vs. logarithm of current density, as shown for example in Fig. 2.³

The pitting susceptibility of the stainless steels under study was also tested by means of the scratch method according to the following procedure.⁴ The electrode was anodically polarized at a potential value about 200 mV below the critical pitting potential determined by the electrochemical hysteresis technique. Then the specimen surface was scratched with a sapphire point, and the current-time curve was recorded for a few

³ The sweep was always reversed at a current density of 100 $\mu\text{A}/\text{cm}^2$.

⁴ Before testing by this method, specimens were prepassivated in a 30 w/o HNO_3 solution at 55°C for 30 min (4-6).

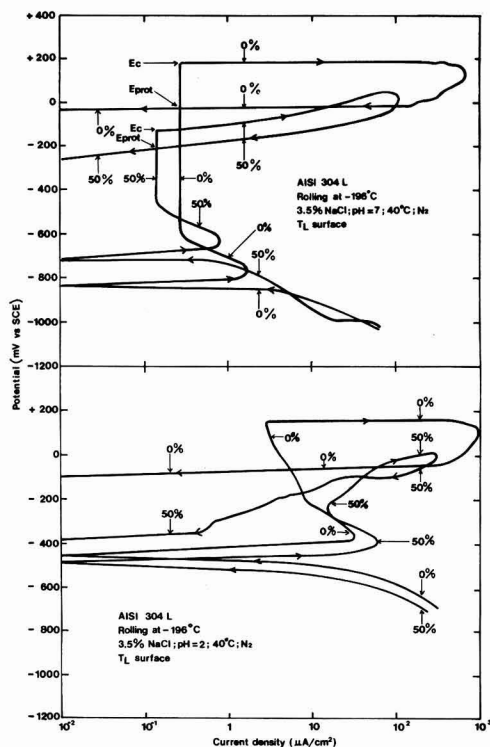


Fig. 2. Cyclic potentiodynamic anodic polarization curves (sweep rate 20 mV/min, sweep reversal current density 100 $\mu\text{A}/\text{cm}^2$) for AISI Type 304 L stainless steel in deaerated 3.5 w/o NaCl solution at 40°C, indicating the effect of the degree of deformation (0% and 50%) and of the pH (pH = 2 and 7). Deformation by rolling at liquid nitrogen temperature, long-transversal surfaces exposed. Potential values referred to a saturated calomel electrode (SCE). The upper curves show how E_c and E_{prot} values are determined. Cathodic branches of the polarization curves are also reported.

minutes until the scratch repassivated. This procedure was repeated with the electrode potential adjusted in 10 mV steps to more and more noble values, until a critical value E_c was reached at which the scratch failed to repassivate—a failure that was indicated by a gradual rise in current with time.

After the electrochemical tests, the specimens were removed from the assembly and examined under a metallographic microscope.

Results⁵

Both the cyclic polarization and the scratch methods show a decrease in critical pitting potential with increase in the degree of deformation (Fig. 3 and 4). Moreover, an anisotropic behavior of specimen surfaces with different orientations to the direction of deformation should be emphasized. In fact, for every given value of the degree of deformation, E_c decreases when passing from the longitudinal to the transversal surfaces. This anisotropic behavior may be shown also by steels not deformed by cold-work.

The values of E_c obtained by the scratch method are always less noble (with a maximum difference of about 100 mV) and more reproducible than the corre-

⁵ The results shown here refer only to cold-rolling; first, because this is the most widely used operation in the case of austenitic stainless steels, and second, because, for the sake of comparison, tests are in progress on cold-rolled austenitic stainless steels high purity, laboratory produced. Anyway, the results shown for the case of cold-rolling are quite similar to the ones obtained on materials cold-worked by tension or drawing.

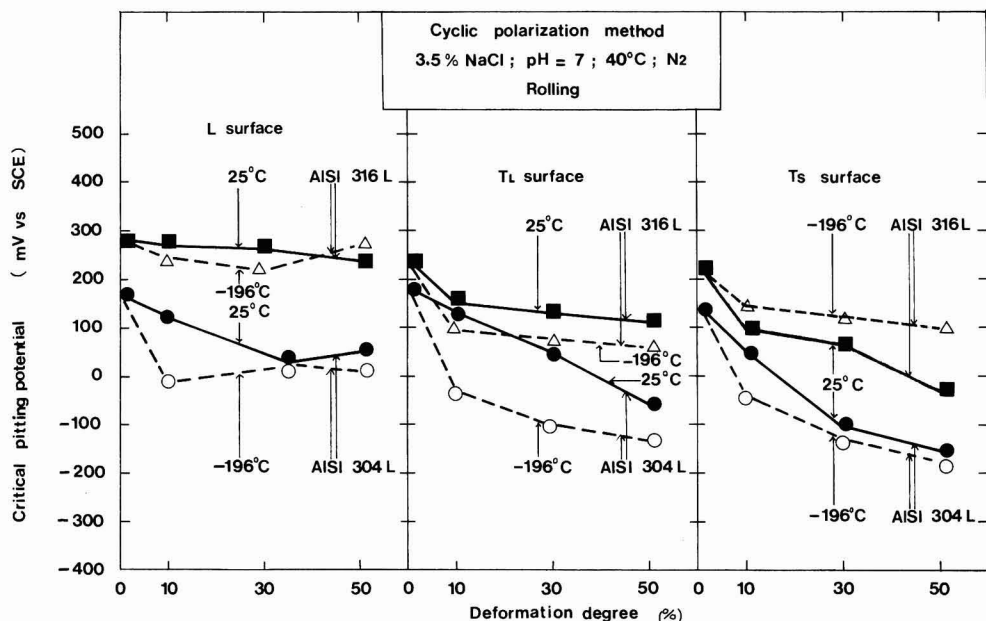


Fig. 3. Critical pitting potential (E_c , determined by the cyclic polarization method, sweep rate 20 mV/min) vs. degree of deformation for AISI Type 304 L and 316 L stainless steels deformed by rolling at both room and liquid nitrogen temperatures, and exposed to deaerated 3.5 w/o NaCl solution pH = 7, at 40°C, with different orientations of the specimen surface to the direction of deformation (L = longitudinal, T_L = long-transversal, and T_S = short-transversal surfaces). Potential values referred to a saturated calomel electrode (SCE).

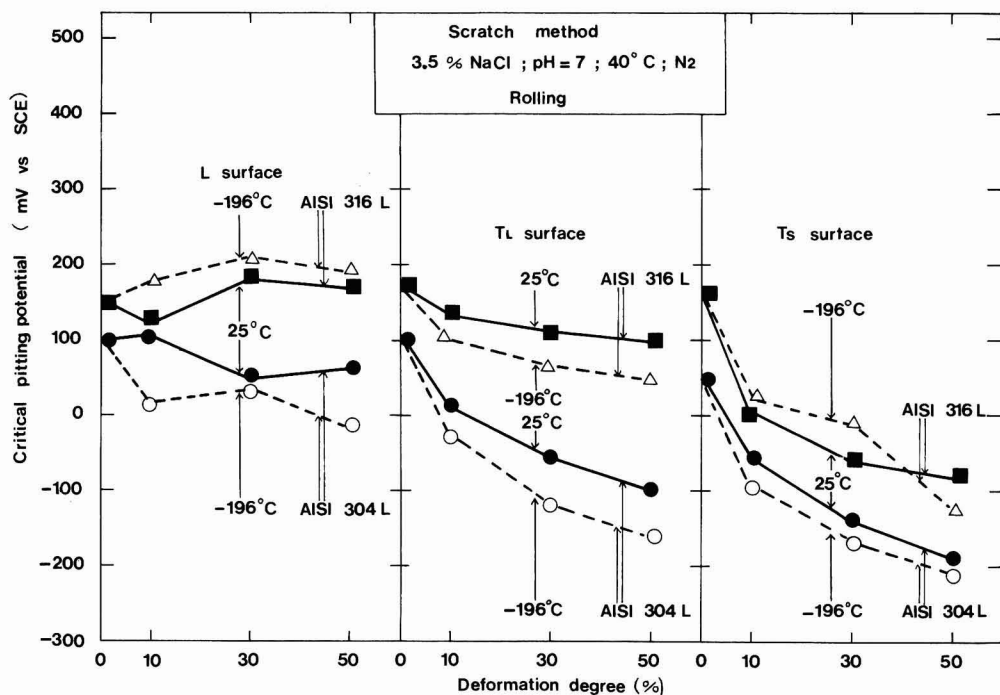


Fig. 4. Critical pitting potential (E_c , determined by the scratch method under potentiostatic conditions) vs. degree of deformation for AISI Types 304 L and 316 L stainless steels deformed by rolling at both room and liquid nitrogen temperatures, and exposed to deaerated 3.5 w/o NaCl solution pH = 7, at 40°C, with different orientations of the specimen surface to the direction of deformation (L = longitudinal, T_L = long-transversal, and T_S = short-transversal surfaces). Potential values referred to a saturated calomel electrode (SCE).

sponding values obtained by the cyclic polarization method.

Repassivation of pits in electrochemical hysteresis experiments occurs at potentials E_{prot} which are generally some hundred millivolts less than E_c (no matter how the E_c was obtained) (Fig. 5 and 6). In any case, the protection potential also decreases with increase in the degree of deformation.

On increasing the degree of deformation, especially for the acid pH's and the transversal surfaces, the passivity region and the hysteresis loop in the cyclic polarization curves tend to contract (Fig. 2).

As a whole, the results obtained in 3.5 w/o NaCl solution confirm those obtained in a physiological saline solution in previous research work (4-7).

Microscopic observation shows that the pit shape and general distribution over the specimen surface are unrelated to structural effects of cold plastic deformation such as dislocations, deformation bands, martensite transformation. Moreover, the pit location appears to be unrelated to structural features such as grain boundaries. The results of morphology studies recently described in the literature (15) are thus confirmed.

Discussion

In our opinion, an explanation of the detrimental effect of cold-work on the pitting resistance of the commercial stainless steels under study, and especially of the anisotropic pitting corrosion behavior of the specimen surfaces with different orientations to the direction of deformation, cannot neglect other structural aspects not included among those of the previously given microstructure analysis (i.e., dislocations, deformation bands, and martensite transformation). Thus, the role played by the nonmetallic inclusions

through their shape and space distribution should be considered.

It is widely acknowledged that in the case of stainless steels, sulfide inclusions and complex sulfide-oxide or sulfide-silicate inclusions are the most active sites for pit nucleation. Selective dissolution of sulfide inclusions, whether isolated, or surrounding oxide or silicate particles, results in microcavities from which the pit propagation can occur (pitting being thus understood as one kind of crevice corrosion) (14, 31-42).

During plastic deformation, fractures in the inclusions and/or cracks at the inclusion-matrix boundary can occur, mostly due to differences in deformability, with microcavities formation (43, 44).

Moreover, in the deformed state of the steel, the inclusions (which in the as-cast state are spherical and randomly distributed) deform to give triaxial ellipsoids with the major axis on the longitudinal sections (in relation to the direction of deformation) and with the minor axis on the transversal ones (45).

As a result, the transversal sections of the deformed steels show a greater density of inclusions and a geometric shape of the inclusions more favorable to pitting nucleation and propagation than the longitudinal sections (40). Thus, the anisotropic pitting corrosion behavior of deformed steels could remain reasonably explained.

Also, the anisotropic behavior shown by materials not deformed by cold-work could be explained through the influence of factory thermomechanical treatments such as hot-rolling, an influence that is not completely cancelled by the solution heat-treatment.

The presence of α' -martensite (even if it becomes far more prevalent, as shown in Table III for the cold-working at liquid nitrogen temperature) generally

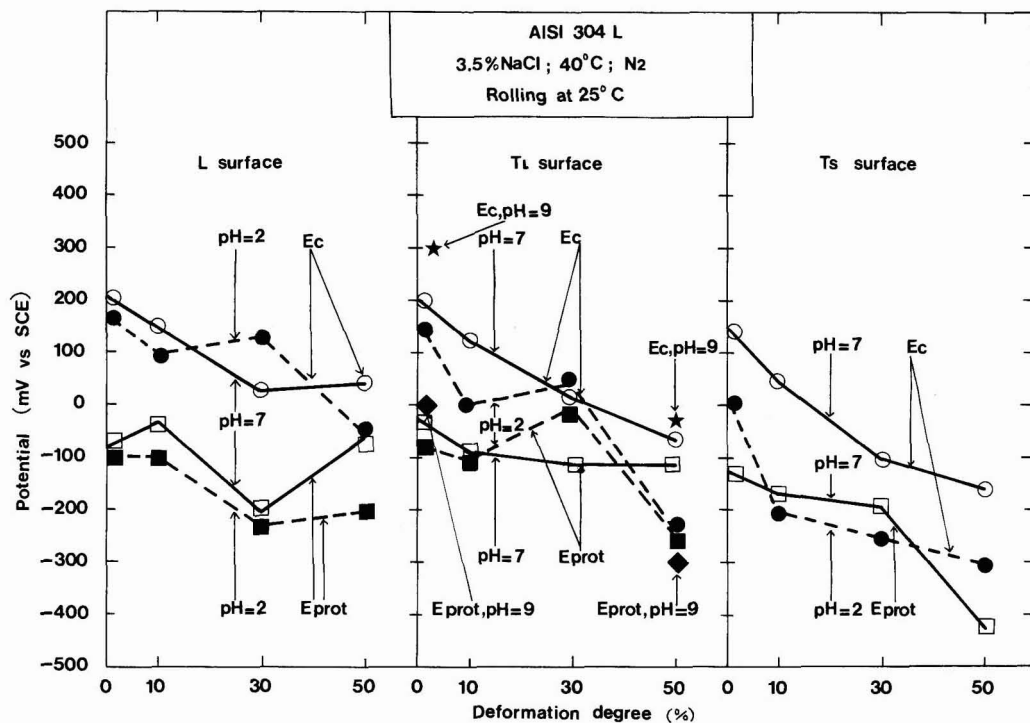


Fig. 5. Critical pitting potential and protection potential against pitting (E_c and E_{prot} , respectively, both obtained by the cyclic polarization method, sweep rate 20 mV/min, sweep reversal current density $100 \mu\text{A}/\text{cm}^2$) vs. degree of deformation (L = longitudinal, T_L = long-transversal, and T_S = short-transversal surfaces), in the case of AISI Type 304 L stainless steel deformed by rolling at room temperature, and exposed to deaerated 3.5 w/o NaCl solutions of different pH's (pH = 2, 7, and 9), at 40°C. Potential values referred to a saturated calomel electrode (SCE).

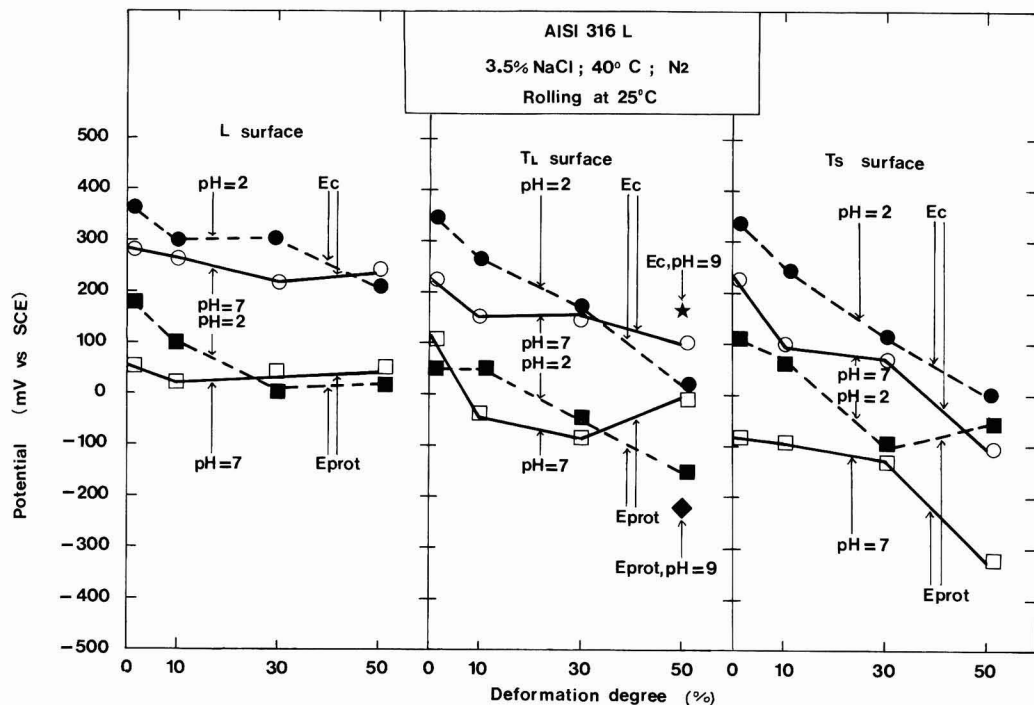


Fig. 6. Critical pitting potential and protection potential against pitting (E_c and E_{prot} , respectively, both obtained by the cyclic polarization method, sweep rate 20 mV/min, sweep reversal current density $100 \mu\text{A}/\text{cm}^2$) vs. degree of deformation for different orientations of the specimen surface to the direction of deformation (L = longitudinal, T_L = long-transversal, and T_S = short transversal surfaces), in the case of AISI Type 316 L stainless steel deformed by rolling at room temperature, and exposed to deaerated 3.5 w/o NaCl solutions of different pH's (pH = 2, 7, and 9), at 40°C . Potential values referred to a saturated calomel electrode (SCE). In the pH 9 solution, no pitting corrosion has been observed on the undeformed material.

does not seem to produce any significant beneficial effect on pitting resistance of the commercial stainless steels under study (e.g., see the critical pitting potential curves at room temperature and liquid nitrogen temperature in Fig. 3 and 4). This seems to disagree with the results of some authors concerning other types of stainless steel, e.g., the so-called TRIP steels, in which the transformation of austenite to martensite during cold-work at room temperature generally increases the pitting resistance (16).

In order to attain further confirmation of the hypothesis concerning the very important role played by the nonmetallic inclusions, the subsequent step in our research work will be the investigation of the pitting resistance of cold-worked high purity austenitic stainless steels prepared in the laboratory.

Manuscript submitted Feb. 2, 1979; revised manuscript received May 16, 1979.

Any discussion of this paper will appear in a Discussion Section to be published in the June 1980 JOURNAL. All discussions for the June 1980 Discussion Section should be submitted by Feb. 1, 1980.

Publication costs of this article were assisted by the Centro di Studio del CNR sui Processi Elettrodici.

REFERENCES

- W. Nicodemi, P. Pedferri, and D. Sinigaglia, *Metallurgia Italiana*, **63**, 23 (1971).
- D. Sinigaglia, P. Pedferri, B. Mazza, G. P. Galliani, and L. Lazzari, *ibid.*, **65**, 77 (1973).
- B. Mazza, P. Pedferri, D. Sinigaglia, U. Della Sala, and L. Lazzari, *Werkst. Korros.*, **25**, 239 (1974).
- A. Cigada and P. Pedferri, *Ann. Chim.*, **65**, 509 (1975).
- B. Mazza, P. Pedferri, D. Sinigaglia, A. Cigada, L. Lazzari, G. Re, and D. Wenger, *This Journal*, **123**, 1157 (1976).
- A. Cigada, B. Mazza, P. Pedferri, and D. Sinigaglia, *J. Biomed. Mater. Res.*, **11**, 503 (1977).
- A. Cigada, B. Mazza, G. A. Mondora, P. Pedferri, G. Re, and D. Sinigaglia, "Corrosion and Degradation of Implant Materials," ASTM STP 684, p. 144, ASTM, Philadelphia, Pa. (1979).
- B. Mazza, P. Pedferri, D. Sinigaglia, A. Cigada, G. Fumagalli, and G. Re, *Corros. Sci.*, in press.
- G. Re, D. Sinigaglia, D. Wenger, and A. Benvenuti, *Metallurgia Italiana*, in press.
- G. Herbsleb and W. Schwenk, *Stahl Eisen*, **87**, 709 (1967).
- S. Szklarska-Smialowska and M. Janik-Czachor, *Br. Corros. J.*, **4**, 138 (1969).
- P. Forchhammer and H. J. Engell, *Werkst. Korros.*, **20**, 1 (1969).
- A. Randak and F. W. Trautes, *ibid.*, **21**, 97 (1970).
- S. Szklarska-Smialowska, "Localized Corrosion," NACE-3, p. 312, NACE, Houston, Texas (1974).
- R. Stefanc and F. Franz, *Corros. Sci.*, **18**, 161 (1978).
- B. C. Syrett and S. S. Wing, *Corrosion*, **34**, 138 (1978).
- T. Angel, *J. Iron Steel Inst., London*, **177**, 165 (1954).
- F. C. Hull, *Weld. J. Suppl.*, **52**, 193s (1973).
- P. M. Kelly and J. Nutting, *J. Iron Steel Inst., London*, **197**, 199 (1961).
- R. Lagneborg, *Acta Metall.*, **12**, 823 (1964).
- F. Leroisey and A. Pineau, *Metall. Trans.*, **3**, 387 (1972).
- G. Blanc, R. Tricot, and R. Castro, *Mem. Sci. Rev. Metall.*, **70**, 527 (1973).
- G. B. Olson and M. Cohen, *Metall. Trans.*, **6A**, 791 (1975).

24. B. E. Wilde and E. Williams, *This Journal*, **117**, 775 (1970).
25. B. E. Wilde and E. Williams, *ibid.*, **118**, 1057 (1971).
26. B. E. Wilde and E. Williams, *Electrochim. Acta.*, **16**, 1971 (1971).
27. B. E. Wilde, *Corrosion*, **28**, 283 (1972).
28. M. Pourbaix, L. Klimzack-Mathieiu, C. Mertens, J. Meunier, A. Van Leugenhaghe, L. de Munck, J. Laureys, L. Neelemans, and M. Warzee, *Corros. Sci.*, **3**, 239 (1963).
29. E. D. Verink, Jr. and M. Pourbaix, *Corrosion*, **27**, 495 (1971).
30. N. Pessal and C. Liu, *Electrochim. Acta*, **16**, 1987 (1971).
31. A. Szummer, Z. Szklarska-Smialowska, and M. Janik-Czachor, *Corros. Sci.*, **8**, 833 (1968).
32. M. Smialowski, Z. Szklarska-Smialowska, A. Szummer, and M. Rychcik, *ibid.*, **9**, 123 (1969).
33. Z. Szklarska-Smialowska, A. Szummer, and M. Janik-Czachor, *Br. Corros. J.*, **5**, 159 (1970).
34. G. H. Wagner, A. Desestret, H. Coriou, and L. Grall, *Compt. Rend. Paris*, **270**, Serie C, 1093 (1970).
35. M. Janik-Czachor, A. Szummer, and Z. Szklarska-Smialowska, *Br. Corros. J.*, **7**, 90 (1972).
36. Z. Szklarska-Smialowska, *Corrosion*, **28**, 388 (1972).
37. J. L. Crolet and J. M. Defranoux, *Corros. Sci.*, **13**, 575 (1973).
38. A. Szummer and M. Janik-Czachor, *Br. Corros. J.*, **9**, 216 (1974).
39. P. Poyet, A. Desestret, H. Coriou, and L. Grall, *Mem. Sci. Rev. Metall.*, **72**, 133 (1975).
40. V. Scotto, G. Ventura, and E. Traverso, "The Influence of Non-metallic Inclusion Nature and Shape on Pitting Corrosion Susceptibility of 17Cr-11Ni-2Mo and 18Cr-9Ni Austenitic Stainless Steels," Laboratorio del CNR per la Corrosione Marina dei Metalli, Genova, Italy (1977).
41. I. L. Rosenfeld and I. S. Danilov, *Corros. Sci.*, **7**, 129 (1967).
42. W. D. France, Jr., "Localized Corrosion—Cause of Metal Failure," ASTM STP 516, p. 164, ASTM, Philadelphia, Pa. (1972).
43. S. Rudnik, *J. Iron Steel Inst., London*, **204**, 374 (1966).
44. E. Rozovsky, W. C. Hahn, Jr., and B. Avitzur, *Metall. Trans.*, **4**, 927 (1973).
45. A. Segal and J. A. Charles, *Met. Technol.*, **4**, 177 (1977).

Distribution of Potential Around a Scratch in a Passive Film

P. H. Melville

Central Electricity Research Laboratories, Materials Division, Leatherhead, Surrey, England

ABSTRACT

A Fourier analysis technique has been used to solve the problem of the potential distribution around a long narrow scratch in a passive film on an electrode surface. Analytic solutions have been obtained for situations where linear polarization kinetics may be assumed for the unscratched region, and where the current density is constant over the scratch and very much greater than the current density over unscratched regions. If the half-width l of the scratch is very much smaller than the Wagner polarization parameter for the unscratched region L_c , a simple expression is obtained for the potential distribution close to the scratch. There is a small additional increase in electrode potential at the scratch, but the main increase in potential is over a distance characterized by L_c and not by the size of the scratch. The potential within the electrolyte and along the electrode depends mainly on the logarithm of distance from the center of the crack. There is an angular dependence of the potential only for distances $\lesssim 2l$ from the center of the scratch.

The distribution of potential around coplanar cells consisting of parallel strips of cathode-anode-cathode has been solved by Waber and his associates (1-6) for linear polarization kinetics for a number of different situations. The solutions are obtained in the form of Fourier series for finite systems or as Fourier integrals for infinite ones. More recently a similar method of solution has been extended by Nanis and Kesselman (7), Gal-Or et al. (8), and McCafferty (9) for a circular cathode with a concentric central anode. Other problems of practical interest which may be approximated by this kind of model are the distribution of potential around a scratch in a passive film and the distribution of potential around a pit, when the electrode is submerged in a bulk electrolyte. In these systems the anode is very small compared with the cathode, which may be treated as infinite. One dimensional solutions [e.g., Ref. (10)] cannot be used for these systems since they are valid only when the depth of the electrolyte on the surface of the electrode is very much smaller than the width of the anode. As shown below for the case of a scratch analytic solutions may be obtained for the potential distribution, and since for most practical situations the width of the scratch is

very much smaller than any of the other dimensions of the system, the solutions reduce to a comparatively simple form (Eq. [42]). The potential around a pit will be considered elsewhere.

It is assumed that quasi steady-state conditions prevail and that there are no appreciable concentration gradients in the electrolyte, so that the problem reduces to the solution of the Laplace equation. These conditions may not be satisfied, if the scratch is repassivated very rapidly. The solutions are also restricted to those conditions where the potential is never very far from the free corrosion potential for the unscratched electrode, so that linear polarization may be assumed. The model may also be applied to other situations with similar geometry, e.g., the distribution of potential around the mouth of a stress corrosion crack.

Mathematical Model

The problem considered is shown in Fig. 1. An infinite plate in the x - y plane at $z = 0$ has a narrow scratch of infinite length and width $2l$ covering the region $-l < x < +l$. This is submerged in an infinite electrolyte. The electrostatic potential $P(x, z)$ in the

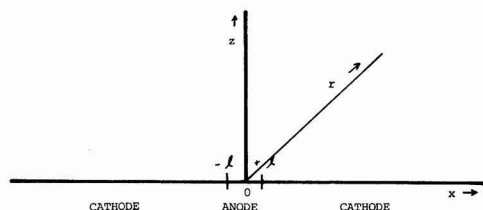


Fig. 1. Schematic representation of a scratch of width $2l$ on an infinite plate.

electrolyte is given by the Laplace equation. The boundary conditions require that P is zero or constant at $z = \infty$ and that the solution is symmetric about $x = 0$. This requirement is satisfied by solutions of the form $[\cos \nu x e^{-\nu z}]$, so that the general solution for an infinite system is a Fourier integral of the form

$$P = A_0 + \int_0^\infty A(\nu) \cos \nu x e^{-\nu z} d\nu \quad [1]$$

where the constant A_0 and the function $A(\nu)$ have to be determined.

If σ is the conductivity of the electrolyte, the current density j^* flowing across the surface of the electrode is given by

$$j^* = -\sigma \frac{\partial P}{\partial z} \bigg|_{z=0} \quad [2]$$

The electrode potential $E(x)$, measuring the drop in potential across the electrode surface is related to the electrostatic potential by

$$E(x) = V - P(x, 0) \quad [3]$$

where V is some constant. E and j^* are related by the electrochemical reactions at the electrode and may be described by some function $j^*(E)$, where different functions for $j^*(E)$ apply for the scratch (anode) and the rest of the electrode (cathode). If the changes in potential are small, so that linear kinetics may be assumed, as in Ref. (1-8), this becomes

$$j^*(E) = \frac{\sigma}{L_0} (E - E_0) \quad [4]$$

where E_0 is the free corrosion potential and where L_0 is Wagner's polarization parameter (11) and has the dimensions of length. L_0 and E_0 have the values L_a and E_a over the scratch (anode), and L_c and E_c over the rest of the electrode (cathode). From Eq. [2]-[4] the reactions at the electrode require that at $z = 0$

$$\begin{aligned} \frac{\partial P}{\partial z} = \frac{1}{L_c} [P + (E_c - V)] [1 - \phi(x/l)] \\ + \frac{1}{L_a} [P + (E_a - V)] \phi(x/l) \quad z = 0 \end{aligned} \quad [5]$$

where $\phi(x/l)$ is the step function

$$\begin{aligned} \phi(x/l) = 0, \quad (x/l) < -1, \quad +1 < (x/l) \\ = 1, \quad -1 < (x/l) < +1 \end{aligned} \quad [6]$$

Fourier analysis may be achieved most readily by substituting for the Fourier transform of $\phi(x/l)$

$$\phi(x/l) = \frac{2}{\pi} \int_0^\infty \frac{\sin \nu l \cos \nu x}{\nu} d\nu \quad [7]$$

avoiding the need for integration. Considerable simplification may be achieved, if it may be assumed that the current density across the scratch is constant and very large, i.e., over the region of the scratch

$$j_a^* = \frac{I}{2l} \gg \frac{\sigma}{L_c} [P + (E_c - V)] \quad [8]$$

where I is the total current flowing through a unit length of the scratch. Equation [3] then becomes

$$\frac{\partial P}{\partial z} = \frac{1}{L_c} [P + (E_c - V)] - \frac{I}{\sigma} \frac{1}{2l} \phi(x/l) \quad z = 0 \quad [9]$$

In this approximation there is a small additional current density

$$j_c^* = \frac{\sigma}{L_c} [P + (E_c - V)] \phi(x/l) \quad [10]$$

flowing through the scratch that has been neglected in Eq. [9] since this is small compared with $I/2l$. Waber and Rosenbluth (2) have considered a situation with similar geometry, i.e., an anode of finite width at the center of an infinite cathode. In their analysis the Wagner polarization parameter has the same value for both the anode and the cathode, and the current density flowing from the anode has to be calculated. In the present analysis the polarization parameter and the free corrosion potential for the anode are not specified, but the current density flowing from the anode is fixed. However, despite the very different assumptions the equations describing the two situations are similar, since substitution for $L_a = L_c = L$ into Eq. [5] to give the situation considered by Waber and Rosenbluth gives

$$\frac{\partial P}{\partial z} = \frac{1}{L} [P + (E_c - V)] - \frac{1}{L} (E_c - E_a) \phi(x/l) \quad z = 0 \quad [11]$$

which is identical to Eq. [9] except for a factor $(1/L)$ $(E_c - E_a)$ instead of $I/2l\sigma$. Substitution for the Fourier integrals for P and ϕ into Eq. [9] gives

$$\begin{aligned} \int_0^\infty -\nu A(\nu) \cos \nu x d\nu = \frac{1}{L_c} [A_0 + (E_c - V)] \\ + \frac{1}{L_c} \int_0^\infty A(\nu) \cos \nu x d\nu - \frac{I}{\sigma} \frac{1}{\pi l} \int_0^\infty \frac{\sin \nu l \cos \nu x}{\nu} d\nu \end{aligned} \quad [12]$$

from which

$$A_0 = - (E_c - V) \quad [13]$$

$$A(\nu) = \frac{I}{\sigma} \frac{1}{\pi l} \frac{\sin \nu l}{\nu [\nu + 1/L_c]} \quad [14]$$

The electrostatic potential is then given by substituting for A_0 and $A(\nu)$ in Eq. [1].

Distribution of Potential Along the Electrode

It is useful to define a reduced potential

$$p(x, z) = \frac{\sigma}{I} [P - (E_c - V)] \quad [15]$$

Along the electrode surface this is given from Eq. [1], [13], and [14] as

$$p(x, 0) = \frac{1}{\pi l} \int_0^\infty \frac{\sin \nu l \cos \nu x}{\nu [\nu + 1/L_c]} d\nu \quad [16]$$

This may be rearranged to give

$$\begin{aligned} p(x, 0) = \frac{L_c}{2l} \frac{2}{\pi} \int_0^\infty \frac{\sin \nu l \cos \nu x}{\nu} d\nu \\ - \frac{L_c}{l} \frac{1}{2\pi} \int_0^\infty \frac{\sin \nu (l + x) - \sin \nu (l - x)}{\nu + 1/L_c} d\nu \end{aligned} \quad [17]$$

where the first term may be recognized as the step function ϕ of Eq. [6] and [7], and the second term may be integrated using

$$\int_0^\infty \frac{\sin t}{t+w} dt = f(w) = \text{Ci}(w) \sin w - \left[\text{Si}(w) - \frac{\pi}{2} \right] \cos w \quad [18]$$

where $\text{Ci}(w)$ and $\text{Si}(w)$ are the cosine and sine integral functions. On substitution for $\xi = x/l$ and $\lambda = l/L_c$ this then gives

$$p(\xi, 0) = \frac{1}{2\lambda} \left\{ 1 - \frac{1}{\pi} f[\lambda(1+|\xi|)] - \frac{1}{\pi} f[\lambda(1-|\xi|)] \right\} |\xi| < 1 = \frac{1}{2\lambda} \left\{ \frac{1}{\pi} f[\lambda(|\xi|+1)] - \frac{1}{\pi} f[\lambda(|\xi|-1)] \right\} 1 < |\xi| \quad [19]$$

for the potential along the surface of the electrode in terms of the reduced potential p (see Eq. [15]) and the reduced dimensions ξ and λ . Equation [19] is essentially the solution obtained by Waber and Rosenbluth (2). In the case of a scratch further simplification may be made. If the scratch is narrow, and the half-width l is much less than the Wagner polarization parameter L_c for the unscratched electrode, so that $\lambda \ll 1$, and the region of interest is restricted that close to the scratch, i.e., $x \ll L_c$, an expansion of $f(w)$ for small w may be used. The sine and cosine integral functions have expansions

$$\text{Si}(w) = w - \frac{w^3}{3 \times 3!} + \frac{w^5}{5 \times 5!} - \frac{w^7}{7 \times 7!} + \dots \quad [20]$$

$$\text{Ci}(w) = \gamma + \ln w - \frac{w^2}{2 \times 2!} + \frac{w^4}{4 \times 4!} - \frac{w^6}{6 \times 6!} \quad [21]$$

where $\gamma = 0.5772 \dots$ is Euler's constant.

Expansion of $\text{Si}(w)$, $\text{Ci}(w)$, $\sin w$ and $\cos w$ and substitution into Eq. [18] then gives

$$f(w) = \frac{\pi}{2} - w(1 - \gamma - \ln w) + O w^2 \quad [22]$$

On substitution into Eq. [19] this then gives

$$p(\xi, 0) = p_0 - \frac{1}{2\pi} [(1+|\xi|) \ln(1+|\xi|) + (1-|\xi|) \ln|1-|\xi||] \quad [23]$$

where

$$p_0 = p(0, 0) = \frac{1}{\pi} [(1-\gamma) - \ln \lambda] \quad [24]$$

is the potential (in reduced units) at the center of the scratch.

The potential is shown as a function of position for different values of λ in the linear plot of Fig. 2 and with the logarithm of distance from the center of the scratch in Fig. 3. The full lines are results obtained by using the approximate form of Eq. [23] and the dashed lines are for the exact solution given by Eq. [19], where this differs from the approximate solution. The simple form of Eq. [23] gives a very close approximation for $\lambda \leq 0.1$ and for $\xi \leq 0.1/\lambda$, i.e., up to the value of ξ , where Eq. [23] would predict negative values for p . These curves show that there is a small additional increase in the potential at the scratch, but for small λ the distance over which there is increase in the potential is characterized by the polarization parameter L_c and not by the size of the scratch.

Variation of Potential in the Electrolyte

In their model Waber and Rosenbluth (2) considered only the potential along the electrode surface. However the potential at any point in the electrolyte may be evaluated from Eq. [1], [13], and [14]. The reduced

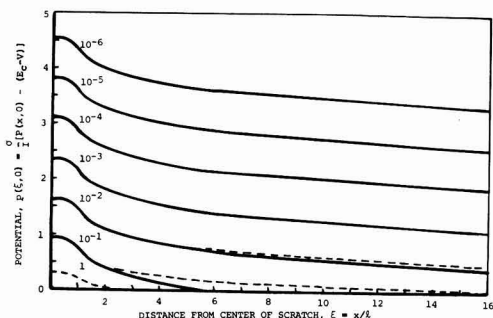


Fig. 2. Variation of potential along electrode with distance from center of scratch for different values of $\lambda = l/L_c$. Full lines are approximate solution (Eq. [23]). Dashed lines are full solution (Eq. [19]) where this differs from the approximate solution.

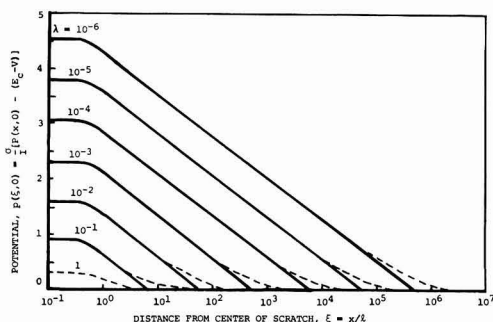


Fig. 3. Variation of potential along electrode with distance from center of scratch for different values of $\lambda = l/L_c$. Full lines are approximate solution (Eq. [23]). Dashed lines are full solution (Eq. [19]) where this differs from the approximate solution.

potential at a point (x, z) is given by

$$p(x, z) = \frac{1}{\pi l} \int_0^\infty \frac{\sin \nu l \cos \nu x e^{-\nu z}}{\nu(\nu + 1/L_c)} d\nu \quad [25]$$

which like Eq. [16] may be rearranged to give

$$p(x, z) = \frac{1}{2\pi} \frac{L_c}{l} \int_0^\infty \frac{[\sin \nu(l+x) + \sin \nu(l-x)] e^{-\nu z}}{\nu} d\nu - \frac{1}{2\pi} \frac{L_c}{l} \int_0^\infty \frac{[\sin \nu(l+x) + \sin \nu(l-x)] e^{-\nu z}}{\nu + 1/L_c} d\nu \quad [26]$$

The first term is readily integrated using

$$\int_0^\infty \frac{\sin \nu X e^{-\nu z}}{\nu} d\nu = \tan^{-1} \frac{X}{z} \quad [27]$$

and the second term may be integrated by writing

$$\int_0^\infty \frac{\sin \nu X e^{-\nu z}}{\nu + 1/L_c} d\nu = \int_0^\infty \frac{1}{2i} \left[\frac{e^{-\nu(z-iX)} - e^{-\nu(z+iX)}}{\nu + 1/L_c} \right] d\nu \quad [28]$$

and using

$$\int_0^\infty \frac{e^{-at}}{b+t} dt = h(ab) = e^{ab} E_1(ab) \quad [29]$$

where $E_1(w)$ is the exponential integral function.

On substitution for $\xi = x/l$, $\zeta = z/l$, and $\lambda = l/L_c$ this then gives

$$p(\xi, \zeta) = \frac{1}{2\pi} \frac{1}{\lambda} \left\{ \tan^{-1} \left(\frac{1+\xi}{\zeta} \right) - \frac{1}{2i} h[\lambda(\zeta - i(1+\xi))] + \frac{1}{2i} h[\lambda(\zeta + i(1+\xi))] + \tan^{-1} \left(\frac{1-\xi}{\zeta} \right) - \frac{1}{2i} h[\lambda(\zeta - i(1-\xi))] + \frac{1}{2i} h[\lambda(\zeta + i(1-\xi))] \right\} \quad [30]$$

$E_1(w)$ may be expanded in the form

$$E_1(w) = -\gamma - \ln w + w - \frac{w^2}{2 \times 2!} + \frac{w^3}{3 \times 3!} - \frac{w^4}{4 \times 4!} + \dots \quad [31]$$

so that for small w

$$h(w) = -(\gamma + \ln w) + w(1 - \gamma - \ln w) + O(w^2) \quad [32]$$

Thus for λ small and $(x^2 + z^2) \ll L_c$

$$p(\xi, \zeta) = p_0 - \frac{1}{2\pi} \left\{ (1+\xi) \ln[(1+\xi)^2 + \zeta^2]^{1/2} + \zeta \tan^{-1} \left(\frac{1+\xi}{\zeta} \right) + (1-\xi) \ln[(1-\xi)^2 + \zeta^2]^{1/2} + \zeta \tan^{-1} \left(\frac{1-\xi}{\zeta} \right) \right\} \quad [33]$$

where $p_0 = p(0,0)$ is the electrode potential at the center of the scratch given by Eq. [24]. Equation [33] reduces to Eq. [23] for $\zeta = 0$. The reduced potential p is shown in Fig. 4 in the form $(p - p_0)$ as a function of distance ρ from the center of the scratch, where

$$\rho = (\xi^2 + \zeta^2)^{1/2} = \frac{1}{l} (x^2 + z^2)^{1/2} \quad [34]$$

for different angles

$$\theta = \tan^{-1} \frac{\zeta}{\xi} = \tan^{-1} \frac{z}{x} \quad [35]$$

where $\theta = 0$ is in the plane of the electrode (see Fig. 1). Only very close to the scratch is there any angular dependence of p for the same distance ρ from the center of the scratch. For $\xi \gg 1$ and $\zeta \gg 1$ Eq. [33] and [23] give simply

$$p(\rho) = p_0 - \frac{1}{\pi} [1 + \ln \rho] \quad [36]$$

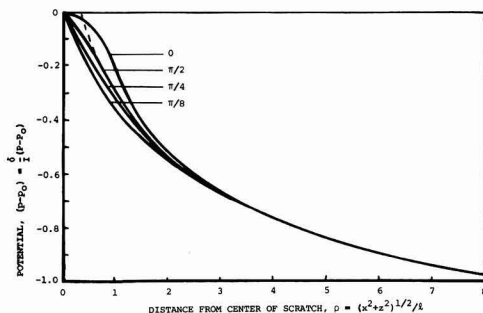


Fig. 4. Variation of potential in the electrolyte as a function of distance from center of the scratch for different values of the angle θ (Eq. [33] and [37]). Dashed line indicates logarithmic approximation (Eq. [36] and [39]).

As shown by the dashed line of Fig. 4, this is a good approximation to the potential distribution for $\rho \gtrsim 2$.

Discussion

As shown in the previous sections, provided that the scratch is narrow ($l \ll L_c$), a good approximation for the potential around the scratch is given by

$$P(x,z) = P_0 - \frac{1}{2\pi} \frac{I}{\sigma} \left\{ (1+x/l) \ln \left[\frac{(1+x)^2 + z^2}{l^2} \right]^{1/2} + \frac{z}{l} \tan^{-1} \left(\frac{1+x}{z} \right) + (1-x/l) \ln \left[\frac{(1-x)^2 + z^2}{l^2} \right]^{1/2} + \frac{z}{l} \tan^{-1} \left(\frac{1-x}{z} \right) \right\} \quad [37]$$

where the reduced potential and the reduced coordinates of Eq. [33] have been replaced by their true values, and where

$$P_0 = -(E_c - V) + \frac{1}{\pi} \frac{I}{\sigma} \left[\ln \frac{L_c}{l} + 0.423 \right] \quad [38]$$

is the potential at the center of the scratch. For larger distances from the center of the scratch, for $r = (x^2 + z^2)^{1/2} \gtrsim 2l$ Eq. [37] reduces to

$$P(r) = P_0 - \frac{1}{\pi} \left[1 + \ln \frac{r}{l} \right] \quad [39]$$

These equations are valid for $r \ll L_c$, or while the equations predict $P > (V - E_c)$. For larger values of r the full forms of Eq. [19] and [30] should be used. The electrode potential (see Eq. [3]) is given by

$$E(x) = V - P(x,0) \quad [40]$$

These equations predict $E(x) = E_c$ away from the scratch, as expected, with a minimum value for $E(x)$ at the center of the scratch given from Eq. [38] as

$$E_0 = E(0) = V - P_0 = E_c - \frac{1}{\pi} \frac{I}{\sigma} \left[\ln \frac{L_c}{l} + 0.423 \right] \quad [41]$$

The assumption of linear polarization kinetics is justified provided that the scratch is narrow and the current flowing from it is small, so that the potential is everywhere close to the free corrosion potential E_c for the unscratched electrode. Since for narrow scratches, $l \ll L_c$, the polarization parameter appears only as $\ln L_c$, accurate determination of the polarization curves is unnecessary, and the results are relatively insensitive to the assumption of linear kinetics. As shown in Fig. 2, there is little change in potential over the width of the scratch, provided $l \ll L_c$, and thus the assumption of a uniform current density j_a^* for the scratch is a reasonable approximation. A small contribution to the current from the scratch was neglected in the derivation of Eq. [9]. Substitution for the potential at the center of the scratch from Eq. [38] into Eq. [10] and substitution for j_a^* from Eq. [8] gives the value of this extra current density at the center of the scratch as

$$j_c^*(0) = \frac{2}{\pi} \frac{l}{L_c} j_a^* \left[\ln \frac{L_c}{l} + 0.423 \right] \quad [42]$$

However, provided $l \ll L_c$, the error made in neglecting this contribution is small.

Conclusions

1. A Fourier analysis technique has been used to solve the problem of the potential distribution around

a long narrow scratch in a passive film on an electrode surface.

2. Analytic solutions have been obtained for situations where linear polarization kinetics may be assumed for the unscratched region and where the current density is constant over the scratch and very much greater than the current density over unscratched regions.

3. These solutions are expressed as sine, cosine, and exponential integral functions, but if the half-width l of the scratch is very much smaller than the Wagner polarization parameter for the unscratched region L_c , as will generally be the case, a simple expression (Eq. [37]) is obtained for the potential distribution close to the scratch.

4. Under the conditions $l \ll L_c$ the potential depends only on $\ln L_c$, so that accurate determination of the polarization curve is unnecessary. The conditions imposed by 2 (above) are also satisfied for $l \ll L_c$.

5. There are two characteristic lengths, l and L_c , and provided $l \ll L_c$, there is a small additional increase in electrode potential at the scratch, but the main increase in potential is over a distance characterized L_c and not by the size of the scratch.

6. The potential within the solution and along the electrode depends on the logarithm of distance from the center of the crack. There is an angular dependence of the potential only for distances $\lesssim 2l$ from the center of the scratch.

Acknowledgments

This work was carried out at the Central Electricity Research Laboratories.

Manuscript submitted Nov. 6, 1978; revised manuscript received April 17, 1979.

Any discussion of this paper will appear in a Discussion Section to be published in the June 1980 JOURNAL. All discussions for the June 1980 Discussion Section should be submitted by Feb. 1, 1980.

REFERENCES

1. J. T. Waber, *This Journal*, **101**, 271 (1954).
2. J. T. Waber and M. Rosenbluth, *ibid.*, **102**, 344 (1955).
3. J. T. Waber, *ibid.*, **102**, 420 (1955).
4. J. T. Waber and B. Fagan, *ibid.*, **103**, 64 (1956).
5. E. Kennard and J. T. Waber, *ibid.*, **117**, 880 (1970).
6. J. T. Waber, in "Localized Corrosion," R. W. Staehle, B. F. Brown, J. Kruger, and A. Agrawal, Editors, p. 221, NACE, Houston (1974).
7. L. Nanis and W. Kesselman, *This Journal*, **118**, 454 (1971).
8. L. Gal-Or, Y. Raz, and J. Yahalom, *ibid.*, **120**, 598 (1973).
9. E. McCafferty, *ibid.*, **124**, 1869 (1977).
10. P. Doig and P. E. J. Flewitt, *Philos. Mag.*, **38**, 27 (1978).
11. C. Wagner, *This Journal*, **98**, 116 (1951).

Surface-Stress Phenomena at the Start of Epitaxial Electrodeposition of Nickel

H. Feigenbaum*¹ and R. Weil*

Department of Materials and Metallurgical Engineering,
Stevens Institute of Technology, Hoboken, New Jersey 07030

ABSTRACT

In studies to determine the internal stresses during epitaxial nickel electrocrystallization, bending of thin copper substrates was observed to occur upon application of the deposition potential but before any deposit had formed. This phenomenon was attributed to the changes in the surface tension upon application of the deposition potential. The sign of the internal stress in the discrete crystallites, which constitute the initial electrocrystallization, could only be determined in the absence of the otherwise overshadowing stress contribution due to the lattice mismatch between substrate and deposit. Deposition was interrupted, so that upon resumption of deposition now on a nickel substrate the mismatch-stress contribution was absent. Then it was found when a new layer of crystallites formed, that they were under a compressive stress. Such new crystallite layers formed when the nickel surface became passivated during a prolonged interruption or a polarity reversal. Sulfur from saccharin addition to the electrolyte prevented the passivation.

The relationships between structure, electrode potential, and internal stress in epitaxial nickel deposits up to thicknesses of 100 nm were reported in a previous paper (1). It was found that the initial stress was dominated by an extrinsic, tensile component due to the stretching of the nickel crystal lattice to fit that of the copper substrate. Then, as this extrinsic stress was relieved by the formation of interfacial dislocations, there developed an intrinsic tensile component due to the coalescence of the three-dimensional epitaxial crystallites (TEC), which were found (2, 3) to constitute the initial structure. However, two phenomena associated with the beginning of deposition were observed which have not yet been published.²

One of these phenomena is that the substrate, which was insulated so that only one side was plated, tried to bend upon the application of the deposition potential before any deposit had formed. The second phenomenon concerned the state of stress of the TEC before they coalesced. As the extrinsic stress overshadowed other contributions during the initial electrocrystallization of nickel on copper substrates, homoepitaxial deposition was necessary to determine the intrinsic stresses in the TEC. To eliminate the extrinsic contribution, deposition was interrupted so that upon resumption, there was now a nickel substrate. This communication deals, therefore, with substrate bending prior to deposition and the detailed investigation of the intrinsic stresses in TEC using plating-interruption techniques.

Experimental Procedure

The stresses were determined from the attempted bending of the substrate in the form of narrow strip plated on one side, the other one being insulated. An

* Electrochemical Society Active Member.

¹ Present address: Engelhard Industries, Edison, New Jersey.

Key words: electrodeposition, epitaxy, electrolyte.

² The paper by Feigenbaum and Weil (1) is an abridged version of an interim report submitted to the American Electroplaters' Society. The data reported here were included in the interim report, but left out of the published paper, which dealt primarily with the subjects most relevant to practical plating.

electrobalance, similar to one used previously for the same purpose by Klockholm (4), applied a force to one end of the substrate strip to prevent the bending. The force was applied by means of a glass rod which hooked through a small hole at the end of the substrate as schematically shown in Fig. 1. The other end of the glass rod was attached to the electrobalance. The force exerted by the electrobalance was calibrated immediately prior to each experiment by hanging known weights on the substrate strip.

The plating cell is also schematically shown in Fig. 1. It consisted of a small glass dish to which a nickel clamp was rigidly attached. The substrate strip (A, Fig. 1) was held in the nickel clamp between two glass slides (D, Fig. 1) which provided electrical insulation. A 99.99% nickel counterelectrode (B, Fig. 1) lay on the bottom. The substrate side to be plated faced downward. When a compressive stress developed in the deposit, the substrate tended to bend upward. In order that contact with the glass rod would not be lost when the substrate tried to deflect upward, an initial force was applied to the substrate by the electrobalance. The plating vessel was attached to the platform which in turn was rigidly connected to the electrobalance. The whole assembly was shock mounted.

The substrates were 55 mm long, 5.5 mm wide, and 75 μ m thick cube-textured, copper strips. The insulation for the side not to be plated was a photoresist layer. Other preplating treatments have been previously (1) described. The plating solution contained 112 g/liter $\text{NiSO}_4 \times 6\text{H}_2\text{O}$ and 30 g/liter H_3BO_3 and was prepared with water distilled so as to minimize inorganic and organic impurities (3). Further purification of the plating solution was the same as in previous experiments (3). The pH was 3.0 ± 0.1 , the temperature 20°C , and the current density 2.5 mA/cm^2 . To some plating solutions either 10^{-3} moles/liter saccharin or 6×10^{-6} moles/liter phenosafranine were added. A fresh solution was used for each experiment.

The potential of the cathode vs. SCE was monitored during each plating experiment. To increase the sensitivity, only the range from -800 to -1000 mV was recorded. The Luggin capillary (C in Fig. 1) was located in the nickel holder 5 mm below the substrate surface. The plating was interrupted for either 12 or 120 sec. In some experiments, the connections to the current source were reversed for approximately half the interruption time. Thus the nickel-plated strip became the anode in the cell. The magnitude of the current was not changed during this polarity reversal. After plating, the substrates were dissolved (3) and the deposits examined by transmission electron microscopy.

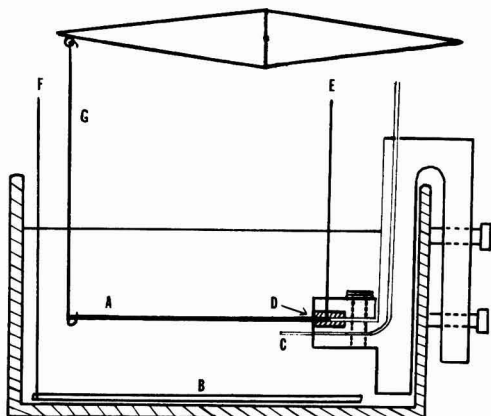


Fig. 1. Schematic drawing of plating cell, showing substrate (A), counterelectrode (B), Luggin capillary (C), glass insulators (D), electrical contacts (E and F), and glass rod attachment to electrobalance (G).

The instantaneous stress, S_1 was calculated from the restoring force, F , exerted by the electrobalance using the equation (1)

$$S_1 = \frac{4L}{3WT} \left[\frac{1}{1-\nu} \right] \frac{dF}{dt}$$

where L , W , T , and ν are the length, width, thickness, and Poisson's ratio of the substrate and t is the deposit thickness. The thickness of the deposit was calculated on the basis of 100% efficiency, uniform-layer formation, and bulk density.

Results and Discussion

Substrate bending before deposition.—The initial portion of the curve of the electrobalance restoring force vs. deposition time is shown in Fig. 2. When the current was turned on, the electrobalance exerted a force of about 0.2 mg marked OA in Fig. 2. There was also a peak in the magnitude of the electrode potential shown in Fig. 3 and marked P; it occurred after 1 sec of plating. It was previously (3) found by transmission electron microscopy and verified in this study that the first TEC are observed after the development of

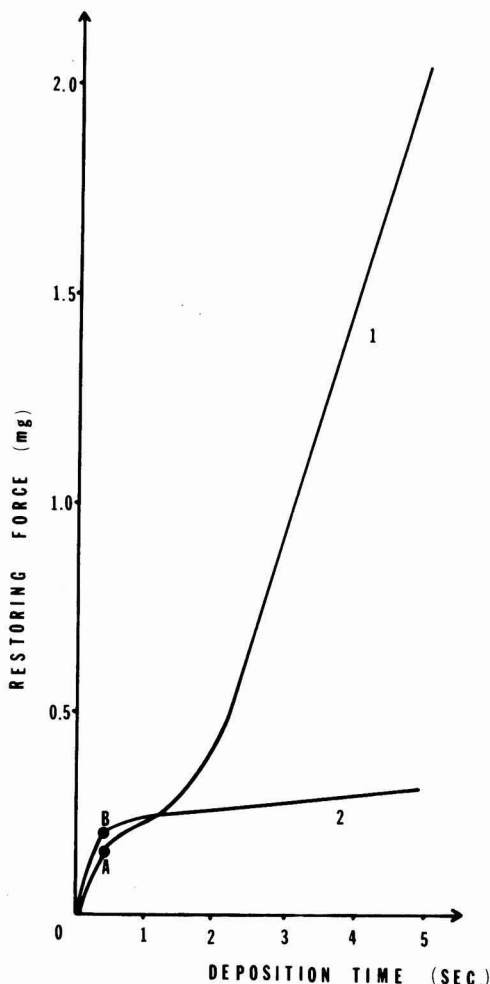


Fig. 2. Restoring force by electrobalance vs. deposition time. Curve 1 obtained in nickel-plating solution, curve 2 obtained in solutions in which sodium ions were substituted for nickel.

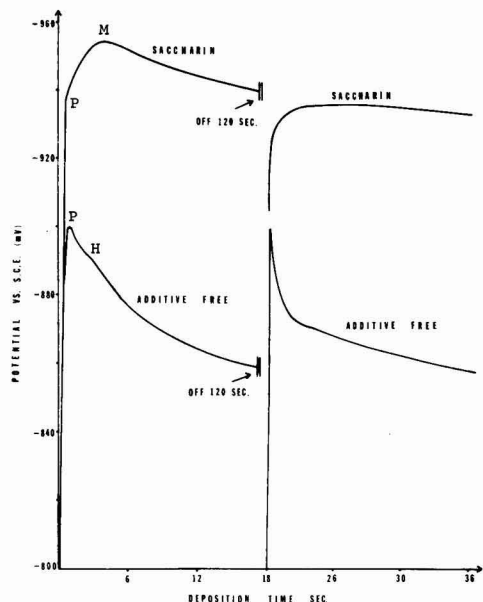


Fig. 3. Electrode potentials before and after 120 sec deposition interruption in additive-free and saccharin-containing electrolytes.

this electrode-potential peak. Hence the potential at P may represent the nucleation potential. Thus the initial electrobalance force segment OA, which was applied prior to the potential peak, was not due to TEC formation. The sharp rise in the electrobalance force in Curve 1 of Fig. 2 which starts after about 1.5 sec is due to the stress, primarily the extrinsic contribution, in the nickel deposit. The initial attempted bending of the substrate, which was counteracted by the force segment OA was not caused by buoyancy due to gas bubbles, which would have caused a deflection opposite to the observed one. Experiments in which the substrate was charged with hydrogen showed that this phenomenon did not cause the attempted bending either.

The cause of the attempted bending of the substrate was probably the change in surface tension due to the application of the deposition potential (5). This phenomenon is thus related to the electrocapillary effect on either side of the potential of zero charge. Fredlein, Damjanovic, and Bockris (6) observed a similar phenomenon when potentials were imposed on gold and platinum electrodes and provided a formula for calculating the change in the surface energy. Using this formula, a force of 0.2 mg under the conditions of this study is equivalent to a surface-tension change of 240 dynes/cm. It appeared relevant to check further whether the application of the deposition potential rather than metal plating caused the initial substrate bending. Approximately the same potential which was imposed initially for nickel deposition, i.e., about -900 mV with respect to SCE, was applied to a copper substrate in an electrolyte which contained the same normality of Na_2SO_4 as NiSO_4 in the plating solution. Thus no metal deposition could occur. The resulting graph of electrobalance force vs. time is Curve 2 in Fig. 2. There is very little difference in the magnitude of the restoring force OB and the segment OA, which resulted in the nickel-plating solution. This result shows that the initial restoring force is not due to a stress in the deposit. As the instantaneous stresses in this study were calculated from the slope of the electrobalance force vs. thickness, the initial segment did

not affect the subsequent results. There may have been small changes in the restoring force due to the changes of the potential with thickness and the gradual change from a copper to a nickel substrate. However, any such effects were smaller than the experimental uncertainty.

Deposition interruptions and polarity reversal.—Two graphs of instantaneous stress vs. thickness of epitaxial nickel deposits on copper substrates are shown in Fig. 4. The portions of the graphs prior to the interruptions were discussed in the earlier paper (1). It was found that there was a sharp rise in stress to the maximum plateau marked P1 in Fig. 4. The stress plateau corresponds to the steep slope in Curve 1 of Fig. 2. The plateau was caused primarily by the extrinsic contribution due to the mismatch between the crystal lattices of the deposit and substrate. The experimental stress values at the maximum plateau ranged from 1800 to 2200 MPa. This range of values was due primarily to the uncertainties in the deposit thickness at the very early stage. The extrinsic stress at a thickness of 5 nm which is on the plateau was calculated to be 1400 MPa by a formula due to van der Merwe (7). The difference between the extrinsic and experimental stress values was attributed (1) to an intrinsic, tensile contribution due to the coalescence of crystallites. The reason for postulating this cause of the intrinsic stresses was that it was in the range of values found (8) to be due to crystallite coalescence in homoepitaxial vapor deposits of nickel, in which there was, of course, no extrinsic contribution.

The sharp decrease in the stress after the maximum is due to the formation of misfit dislocations which results in a relaxation of the extrinsic contribution. The extrinsic stress then decreases inversely proportionally to the thickness. So when the stress tends to level off, the intrinsic contribution due to crystallite coalescence, which decreases only slightly with thickness, predominates.

The stress maxima were related to the deposition potential. In deposits from the additive-free solution, a hump, marked H in Fig. 3 occurs at the same thickness as the stress maxima. In nickel deposits produced in the electrolyte containing saccharin, which had the same initial portion of the stress vs. thickness as is shown in Fig. 4, the stress maximum corresponded to

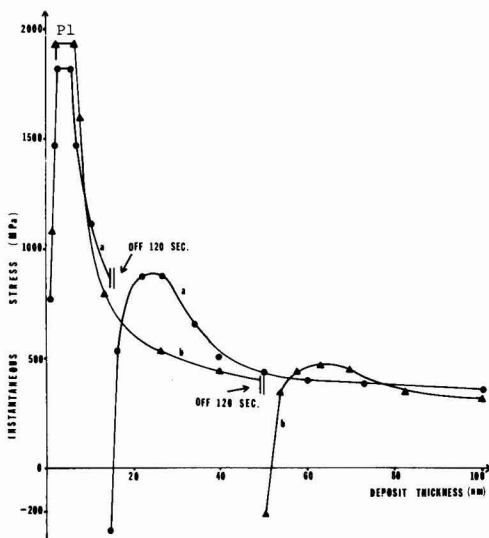


Fig. 4. Instantaneous stress in deposits from additive-free electrolytes. (a) Deposition interrupted for 120 sec at 15 nm thickness. (b) Deposition interrupted for 120 sec at 50 nm thickness.

the maximum in the magnitude of the potential marked M in Fig. 3.

When plating was interrupted, the nickel deposit was already continuous and covered the copper substrate. In the experiment represented by Curve a of Fig. 4, plating was interrupted at an average deposit thickness of 15 nm. The last stage of crystallite coalescence is shown in Fig. 5 specifically in the area marked B. It occurred at an average thickness slightly less than 15 nm. The region marked B is an epitaxial nickel deposit which had formed on an annealing twin in the substrate and had a {110} plane parallel to the surface as determined by selected-area electron diffraction. On both sides of Region B, which are marked A, a {100} plane was parallel to the surface. In Region A with the exception of a few rectangular pores, the deposit is a complete layer. The TEC were always nucleated and their coalescence was completed first on {100} substrate grains. Thus, the favored plane for epitaxial growth is the same as the one which preferentially develops in nonepitaxial nickel deposits from sulfate electrolytes or Watt's solutions and is perpendicular to the fiber axis. At a thickness of 15 nm, a complete deposit layer covered the whole substrate. Thus when plating was resumed after the interruption, the substrate was nickel. This condition was necessary for this study as already pointed out.

As soon as the deposition was interrupted, the electrobalance force *vs.* time graph became horizontal. So the instantaneous stress, which is proportional to the slope, was zero. After a 120 sec interruption, when plating resumed in the additive-free or phenosafranine-

containing electrolytes, the electrobalance force decreased from the horizontal value as can be seen at B in Fig. 6a. Figure 6a is the actual record of the electrobalance force *vs.* time which was proportional to deposit thickness. Because of the negative slope from B to C in Fig. 6a, the stress was compressive as shown in Fig. 4. At C in Fig. 6a the stress became tensile. The behavior of the electrobalance shown in Fig. 6a differs from that in Fig. 2. In Fig. 2, the slope remained positive so that the stress was tensile because of the mismatch in the lattice dimensions of the substrate and deposit which overshadowed all other contributing factors as already discussed. At the time corresponding to Point B in Fig. 6a, i.e., when plating resumed after a 120 sec interruption, the electrode potential also peaked as shown in Fig. 3.

After an interruption of only 12 sec, the stress did not become compressive and there was only a small peak of about -10 mV in the magnitude of the electrode potential compared to -40 mV above the steady-state value of Fig. 3. When the polarity was reversed during a 12 sec pause, a compressive stress and a -40 mV potential peak developed again when plating resumed.

In the electrolyte containing saccharin, no compressive stresses developed after an interruption of plating. Regardless of whether the polarity was reversed and even after interruptions as long as 10 min, the stress was tensile when deposition resumed. Also as seen in Fig. 3, the potential returned without a peak to the value it had before the pause. It is noteworthy that the shapes of the instantaneous-stress *vs.* thickness graphs for deposits plated in the presence of saccharin were the same before an interruption as those shown in Fig. 4 (1). The magnitudes of the maxima were also the same, but then the stress values became lower than those in deposits from the additive-free electrolyte and continued to decrease with increasing thickness. However, the stresses did not become compressive until a thickness of 800 nm was reached (1).

The initial force exerted by the electrobalance prior to the beginning of deposition, such as shown in Fig. 2, was sometimes observed after an interruption. When the stress did not become compressive upon the resumption of deposition, the initial electrobalance force was smaller than the 0.2 mg shown in Fig. 2. Thus, the effect is smaller on a nickel surface than on a copper one. The magnitude of the initial electrobalance force decreased with the electrode potential which was applied when plating resumed. The electrode potential and, therefore, the initial electrobalance force thus decreased with increasing thickness at which the interruption occurred.

When a compressive stress developed after a plating resumption, there was no observed initial electrobalance force. In Fig. 6a, there is no force increase before the decrease due to the compressive stress. The force was apparently absent in spite of the larger magnitude of the potential which was applied when plating resumed. The potential was greater when a compressive stress developed because of the larger peak seen in Fig. 3. It is thus indicated that the state of the surface upon which a compressively stressed deposit developed

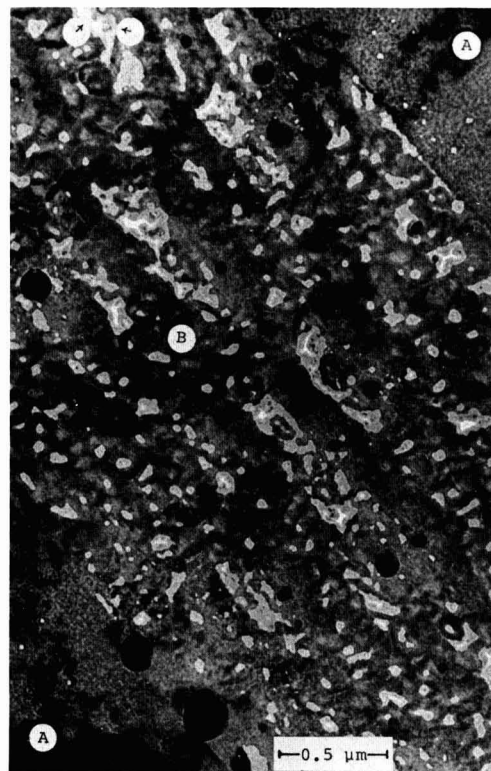


Fig. 5. Transmission electron micrograph showing incomplete crystallite coalescence in {110}-oriented deposit in area B and completed coalescence in {100}-oriented deposit in area A.

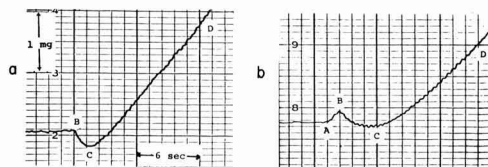


Fig. 6. Restoring force by electrobalance *vs.* deposition time after (a) 120 sec interruption of deposition in additive-free electrolyte, (b) 120 sec interruption of deposition during which polarity was reversed for 60 sec in phenosafranine-containing electrolyte.

after the interruption had a different potential of zero charge from that on which the stress remained tensile. When the polarity was reversed for about half of the 120 sec interruption in the electrolyte containing phenosafranine, a greater force of about 0.4 mg was applied by the electrobalance before the compressive stress developed as seen in Fig. 6b. As the potential peaked exactly at the point marked B in Fig. 6b where the electrobalance force reversed itself, nickel deposition resumed after the electrobalance force was applied. This experiment was not performed in an additive-free solution. There are strong indications of a difference in the states of the surfaces when a compressive stress developed after a prolonged polarity reversal as compared to a short one.

The transmission electron-microscopic examinations of the samples which experienced plating interruptions showed that they were still epitaxial. There was one exception, namely the one represented by Fig. 6b. In all other samples, deposits which formed on one substrate grain were single crystals as determined by selected-area electron diffraction. However, the dislocation density was two to three times greater in samples which developed a compressive stress after a plating interruption. In all the deposits from the saccharin electrolyte which never developed a compressive stress after a plating pause, the dislocation density was the same. The electron diffraction patterns of the deposits which experienced a polarity reversal of about 60 sec and are represented by Fig. 6b showed some rings meaning that they were no longer completely epitaxial. The structure is shown in Fig. 7. The small crystallites, some indicated by arrows, were found by dark-field electron microscopy to be non-epitaxial. There are also a number of twins visible in Fig. 7. Such profuse twinning is characteristic of deposits from phenosafranine-containing electrolytes.

During a 120 sec interruption or a polarity reversal which preceded the development of a compressive stress, the nickel surface undoubtedly became oxidized. When plating resumed new layers of crystallites were nucleated as indicated by the large potential peak. As was already mentioned, the potential peak was found (3) to be associated with TEC nucleation. The observed higher dislocation densities are also indicative of formation of new TEC and their coalescence (3). During a 12 sec interruption without polarity reversal, the oxidation was less severe. Thus, as indicated by the much smaller potential peak, it was not necessary to start a whole new layer of TEC. In the presence of sulfur from the saccharin which is known to prevent passivation of nickel anodes, it was also not necessary to start a new TEC layer as shown by the absence of the potential peak.

The new TEC were probably in compression. There is evidence that homoepitaxially vapor-deposited nickel (8) and silver (9) crystallites while still discrete before coalescence are in compression. Compressive stresses have also been observed initially when copper (10) and cobalt (11) were electrodeposited on platinum. These electrodeposits were probably non-epitaxial so that the extrinsic component was missing. Wilcock *et al.* (9) found that the lattice parameter of small, discrete crystallites was smaller than that of bulk due to surface-tension effects. As the crystallite size increased and the interatomic spacing tried to approach the bulk value, the substrate opposed it and thereby imposed the compressive stress. The compressive instantaneous stresses which developed after certain plating interruptions can therefore be attributed to the presence of a layer of not yet coalesced TEC which formed because of the oxide film on the nickel-deposit substrate. When there was no oxide or it was so thin as to be epitaxial so that most of the existing crystallites could continue to grow and coalesce, the resulting tensile stress probably offset the compressive one in the newly formed ones. Thus no compressive

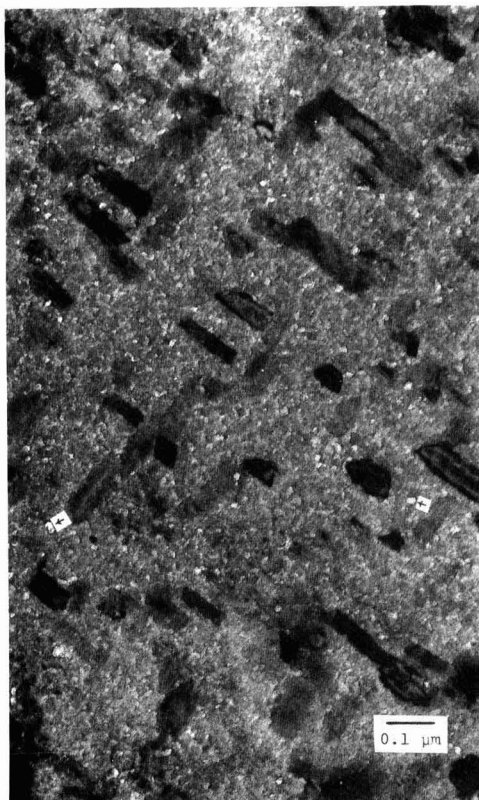


Fig. 7. Transmission electron micrograph showing non-epitaxial crystallites, some marked by arrows, which developed following a 60 sec polarity reversal during 120 sec deposition interruption.

stress was observed after a 12 sec interruption or in the saccharin-containing electrolyte.

It is not known whether the oxide which probably caused TEC nucleation after a plating pause was reduced first. As all electron-diffraction patterns showed the presence of NiO on the surfaces of the samples, it could not be determined whether there was an oxide layer within the specimens. During the prolonged anodization where the polarity was reversed for half of the 120 sec plating pause, a different oxide (12) was probably produced as was also indicated by the effect of the potential on the surface tension shown in Fig. 6b. This oxide, probably NiOOH, either prevented epitaxial growth or was partially reduced to Ni(OH)₂ before deposition was resumed (12). The relatively long delay before the potential peak and the development of the compressive stress shown in Fig. 6b could have been due to the partial oxide reduction and resulted in the non-epitaxial crystallites seen in Fig. 7.

As seen in Curve a of Fig. 4, the stress eventually returned to approximately the same value it had before the interruption. However, at the deposit thicknesses involved, the stress is higher than it would have been if there had not been an interruption. During continuous plating, the stress decreased with increasing deposit thickness because of the increase in the size of the coalescing crystallites (1). At thicknesses where the deposit is continuous, the extrinsic contribution becomes very small. The intrinsic stress was attributed (1) to a continued requirement for coales-

cence of existing crystallites at their pyramidal or dome-shaped tops. After a new layer of TEC was formed, the intrinsic stress is larger because the size of the coalescing units is smaller. Therefore the stress is greater than it would have been if there had been no pause and the size of the coalescing unit had not been reduced. When the pause occurred at a larger thickness as in Curve b of Fig. 4, the effect was more pronounced as the crystallites were larger before the interruption. Therefore the stress rose to a higher value than that which was prevalent before the pause. When the stress did not become compressive after a pause there was still a small time interval after plating resumed before the stress returned to the original value. The development of some new crystallites, which were in compression, was probably responsible for this effect.

It is interesting to speculate whether the lower stress of pulse-plated deposits is due to the formation of new crystallites which are in compression. Because of the much higher pulse frequency used commercially, it is unlikely that there is sufficient time for substrate oxidation during plating interruptions as was the case in this study. However, because of the larger current densities employed in pulse plating, the overpotentials are much higher than in this study. Thus the nucleation of a new layer of three-dimensional crystallites at the start of each pulse is probable. Such crystallites, which would probably not be epitaxial, are likely to be under compressive stress (10, 11). Upon coalescence, the instantaneous stress would become tensile. Such a cyclical stress pattern from compressive to tensile which corresponded to variations in the overpotential was observed by Schneider and Weil (13). The average stress, which is the integral of the instantaneous stress over the thickness would thus be reduced by pulse plating as has been frequently observed.

Conclusions

An initial deflection of the substrate which occurred prior to electrocrystallization was attributed to the change in surface tension when the deposition potential was applied.

Discrete TEC were in a state of compressive stress, which changed to tensile when they coalesced. However, when nickel was epitaxially deposited on copper, the compressive stress was overshadowed by the higher tensile misfit stress. When new TEC formed on nickel substrates, which had become slightly oxidized during a 120 sec interruption of deposition, or the application of an anodic pulse, the compressive stress was manifested.

No compressive stress was observed after an interruption of deposition when very few or no new TEC

formed as was the case in the presence of the passivation-inhibiting additive, saccharin, or when the pause was too short for sufficient oxidation of the nickel surfaces.

After the prolonged application of an anodic current during an interruption of deposition, when the sample was again made cathodic, some oxide reduction took place prior to the nucleation of new crystallites, some of which were no longer epitaxial.

Acknowledgments

This paper is based on work performed under Project 38 sponsored by the American Electroplaters' Society, incorporated. The permission by the Research Board of AES to publish this paper is gratefully acknowledged as is the advice of the Project Committee consisting of Messrs. A. Damjanovic, G. Fisher, D. Hardesty, F. Koch, R. Sanwald, and D. Shanefield. The work is part of a thesis submitted by H. Feigenbaum to Stevens Institute of Technology in partial fulfillment for the degree of Doctor of Philosophy.

Manuscript submitted April 19, 1979; revised manuscript received June 15, 1979.

Any discussion of this paper will appear in a Discussion Section to be published in the June 1980 JOURNAL. All discussions for the June 1980 Discussion Section should be submitted by Feb. 1, 1980.

Publication costs of this article were assisted by N.S.F. Grant SER77-06938.

REFERENCES

1. H. Feigenbaum and R. Weil, *Plating Surf. Finish.*, **66**, 64 (May 1979).
2. S. Nakahara and R. Weil, *This Journal*, **120**, 1462 (1977).
3. R. Weil, G. J. Stanko, and D. E. Moser, *Plating Surf. Finish.*, **62**, 34 (Sept. 1976).
4. E. Klockholm, *Rev. Sci. Instrum.*, **40**, 1054 (1969).
5. K. F. Lin and T. R. Beck, *This Journal*, **123**, 1145 (1976).
6. R. A. Fredlein, A. Damjanovic, and J. O'M. Bockris, *Surf. Sci.*, **24**, 261 (1971).
7. J. H. van der Merwe, in "Single-Crystal Films," M. H. Francombe and H. Sato, Editors, Pergamon Press, Oxford, England (1964).
8. R. W. Springer, AEC Tech. Report No. 70, Case-Western Reserve University (1972).
9. J. D. Wilcock, D. S. Campbell, and J. C. Anderson, *Thin Solid Films*, **3**, 14 (1969).
10. J. B. Kushner, *Plating (East Orange, N.J.)*, **60**, 1246 (1973).
11. S. A. Armanov and R. Weil, *Plating Surf. Finish.*, **63**, 49 (May 1976).
12. A. Damjanovic, Private communication.
13. R. Schneider and R. Weil, *Plating (East Orange, N.J.)*, **55**, 1063 (1968).

The Redox Properties of Bleomycin and Tallysomycin and a Series of Their Metalloderivatives

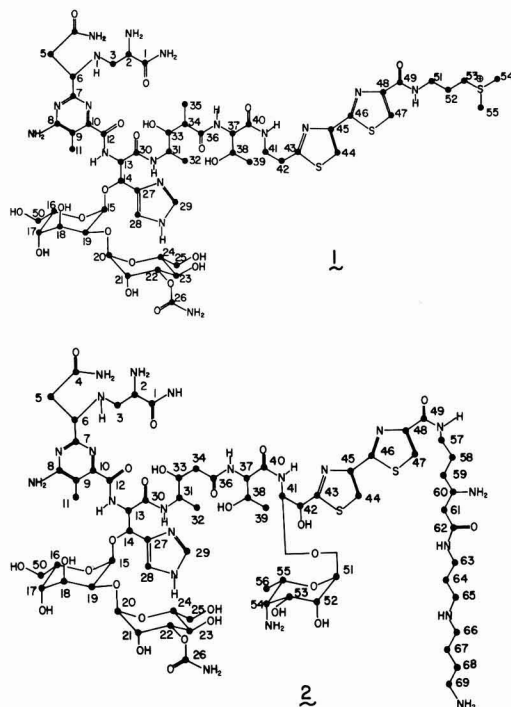
James C. Dabrowiak and Frank S. Santillo

Department of Chemistry, Syracuse University, Syracuse, New York 13210

ABSTRACT

D-c polarographic and cyclic voltammetric studies on bleomycin A₂ (BLM-A₂), tallysomycin A (TLM-A), a series of their metalloderivatives, and four of their components have been conducted. The antibiotics exhibit two reduction processes. The first, at -1.22V, has been assigned to the two electron reduction of the 4-amino pyrimidine moiety of the drugs. A second multielectron reduction process appears to be associated with the bithiazole portion of the antibiotics. The first polarographic wave, due to the pyrimidine moiety, is sensitive to metal binding phenomena. The binding of Fe(II), Co(II, III), Ni(II), and Zn(II) to the antibiotics, causes this wave to disappear from the polarogram of the metalloderivatives. Thus, for these metal ions the pyrimidine moieties of the drugs appear to be metal ligating sites. The involvement of this group in metal ligation in the case of Fe(III) is highly dependent on the mode of preparation of the complex, and Fe(III) complexes containing both bound and unbound pyrimidine residues are possible. The impact of the electrochemical results on the proposed mechanism of action of the pharmaceuticals is also discussed.

Bleomycin-A₂ (BLM), **1** and tallysomycin-A (TLM), **2** are fungus-produced glycopeptides which exhibit



antitumor properties (1, 2). Of the two antibiotics, bleomycin is an important anticancer drug, and it is clinically employed in the treatment of squamous cell carcinomas, lymphomas, and testicular carcinomas (3).

The mechanism of action of neither drug is completely understood. However, recent evidence suggests that both antibiotics operate by a metal mediated redox mechanism involving iron ions (2, 4-7). It has been proposed that BLM exists in the cancer cell as

Key words: polarography, cyclic voltammetry, antibiotic, bleomycin, tallysomycin, bithiazole, pyrimidine, metal complexes.

its Fe(II) complex, Fe(II)BLM, which is in turn bound to DNA, the drug receptor site. The Fe(II)-BLM complex is air sensitive and it can be readily air oxidized to Fe(III)BLM with the production of a radical (Eq. [1]) (8, 9)

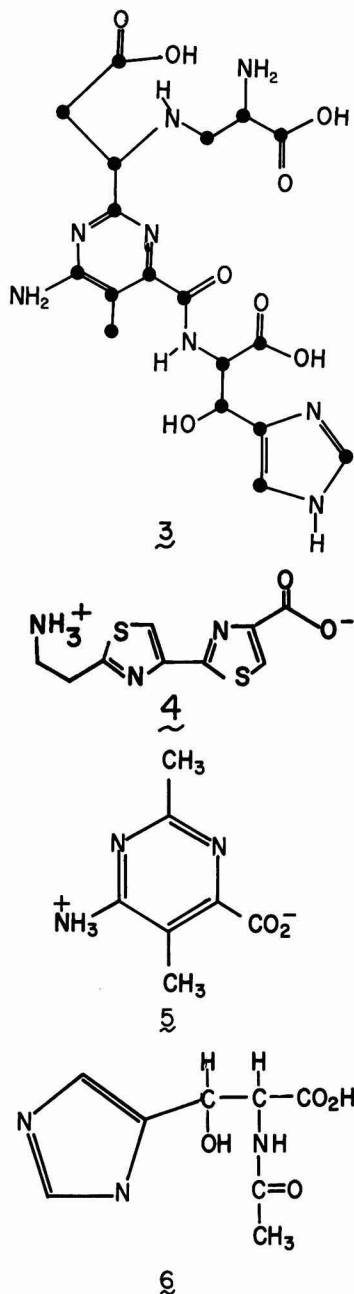


Apparently it is the radical which leads to DNA damage and ultimately to the death of the cancer cell. In view of the structural similarity of BLM and TLM, both antibiotics probably operate by the same biological mechanism.

In an effort to more clearly define the role of the metal ion in the mechanism of action of both antibiotics, we initiated a study of the physical and chemical properties of a group of metalbleomycins and metal-tallysomycins (10-12). An important aspect of the study is the delineation of the redox characteristics of the drugs and their metalloderivatives. This paper treats the electrochemical properties of bleomycin A₂, **1**, tallysomycin-A, **2**, and a series of their metal complexes. In order to understand the electrochemical behavior of the antibiotics it was also necessary to examine the redox characteristics of four model compounds. They were: peptide M of TLM, **3** (13), the amino acid bithiazole, **4**, the 4-amino pyrimidine **5**, and the hydroxy-imidazole, **6**.

Experimental

The drugs BLM-A₂·HCl and TLM-A·5HCl·9H₂O and peptide M of tallysomycin, **3**, were furnished by Bristol Laboratories. The amino acid bithiazole, **4**, the 4-amino pyrimidine, **5**, and the hydroxy-imidazole **6**, were kindly provided by S. Hecht, Department of Chemistry, Massachusetts Institute of Technology, Cambridge, Massachusetts 02139. U.V.-visible absorption and ESR measurements were done in the previously described manner (10). All polarographic studies were done in a standard H cell (at 25°C) using a microcomputer-controlled electrochemical station (14). The polarographic solutions (10⁻³M) were deaerated with a stream of water-saturated nitrogen gas 20 min prior to each run and were blanketed with nitrogen during the run. To scan the entire potential window, two types of working electrodes were used. A dropping mercury electrode (DME) covered the potential range from -1.8 to +0.15V, while a carbon paste electrode (CPNjl) covered potentials from -0.6 to +1.5V. The CPNjl was fabricated using the design described by Adams (15). Cyclic voltammetric studies were accom-



plished using a Metrohm micrometer type hanging mercury drop electrode (HMDE). The reference electrode was a Ag/AgCl saturated NaCl system, and the counterelectrode was a Pt wire. Determinations were done in pH 8 phosphate buffer (0.05M) that was 0.15M in NaCl and in doubly distilled deionized water that was 0.15M in NaCl. Unless otherwise noted, the pH of the unbuffered solutions was adjusted by addition of 0.1N NaOH or 0.1N HCl. The pH of the air-sensitive complexes, Fe(II), Co(II), Cu(I), was adjusted under nitrogen in an inert atmosphere box.

The polarographic behavior of bleomycin as a function of pH was studied in doubly distilled deionized water. The observed $E_{1/2}$ values in volts as a function of pH were: $E_{1/2}$ (pH); -0.81, (2.3); -0.90, -1.15, (3.4); -0.96, ~ -1.2 (4.2); -1.26 (5.3); -1.24 (7.5); -1.28 (9.2); -1.32 (11.0).

Using a mercury pool, controlled potential electrolysis (CPE) of the antibiotics, of any of their metal-loderivatives, or of the bithiazole, 4, was unsuccessful. The observed current decay as a function of time proved to be nonexponential and to terminate at a nonzero value of current. Calculation of the number of electrons transferred from the decay curve yielded a multielectron process. CPE of the 4-amino pyrimidine, 5, at -1.60V was successful and yielded a polarographic n value of 2.2. The d-c polarogram of 5 before reduction, showed a single reduction process at -1.36V. The polarogram of 5 after CPE showed the loss of the reduction wave at -1.36V. A check of the absorption properties of the solution containing the 4-amino pyrimidine before and after electrolysis revealed that of the two ultraviolet absorptions of 5 at 230 and 275 nm, only the lowest energy absorption band remained after reduction. The diffusion current associated with the Cu(II) \rightarrow Cu(I) reduction of Cu(II)-BLM and Cu(II)-TLM was found to be one-half the value observed for the pyrimidine-centered reduction of BLM and TLM.

The metal complexes were made by adding the appropriate amount of M(II)(ClO₄)₂ where M is Fe, Co, Ni, Cu, or Zn to a 10⁻³M solution of the drug in either a pH, 8.0 phosphate buffer or in water followed by the adjustment of the pH to 8.0. No difference in the electrochemical behavior between the two methods of complex preparation could be detected.

Two procedures were used for preparing the Fe(III) antibiotic complexes. In one, the solution containing the Fe(II)-drug complex was exposed to oxygen to yield the Fe(III)-drug complex. The second approach involved preparing the Fe(III)-drug compound by directly combining Fe(III)(ClO₄)₃ and the antibiotic. Buffered (phosphate) and unbuffered pH, 8.0 solutions were used for both preparations. Cu(I)Cl was used to prepare the Cu(I)-drug compounds in buffered and in unbuffered media.

Results and Discussion

The polarographic assignments.—The filtered d-c polarograms of BLM, 1, TLM, 2, peptide M, 3, the amino acid bithiazole, 4, and the 4-amino pyrimidine, 5, are shown in Fig. 1. The two drugs exhibit identical redox behavior and yield two reduction waves: a two electron wave at -1.22V and a multielectron wave (~16 electrons) at -1.48V. Cyclic voltammetric studies (CV) showed that both waves are electrochemically irreversible and that the irreversibility was independent of the CV scan rate (up to 3.2V sec⁻¹). In addition, the current associated with the multielectron wave (-1.48V) was found to vary with the length of time that the mercury drop was in contact with the polarographic solution. Neither BLM nor TLM exhibited an oxidation wave using a CPNjl electrode.

The polarographic assignments of the two reduction waves of BLM and TLM was accomplished using the model compounds 3-6. One of the model compounds, peptide M, exhibited a single irreversible reduction process at -1.22V (Fig. 1b). CV studies showed the absence of a reverse peak for this wave. The $E_{1/2}$ value and the irreversible characteristics of the wave were identical to the first reduction process of BLM and TLM (Fig. 1a). Thus, the moiety in BLM and TLM responsible for the reduction must also be present in peptide M. A check of the literature revealed that the reduction must be occurring at either the pyrimidine or the imidazole residue of the two drugs and peptide M (16). Since model compound 6, the hydroxy-imidazole, did not exhibit reduction behavior

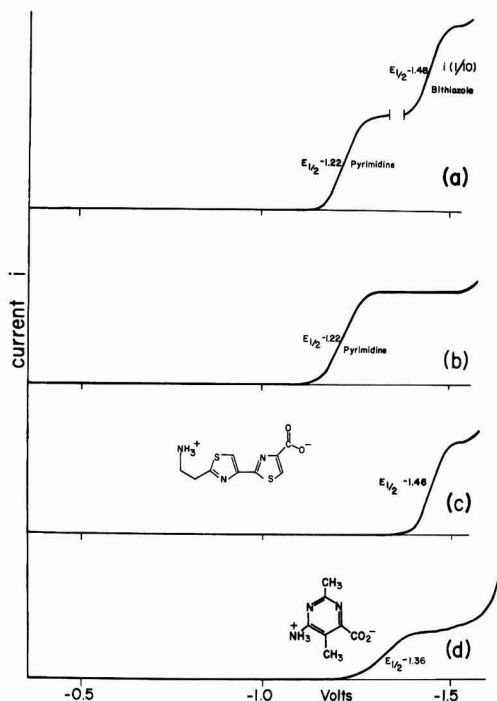
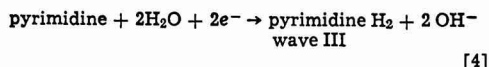
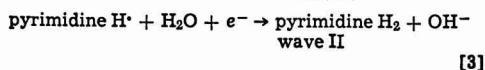
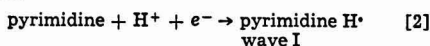


Fig. 1. The filtered d-c polarogram of (a) bleomycin A₂, 1, and tallysomyacin-A, 2; (b) peptide M of tallysomyacin; (c) the amino acid bithiazole, 4; and (d) the 4-amino pyrimidine, 5. $\nu = 1$ mV/sec, pH, 8 phosphate buffer.

in the polarographic window of observation, but the 4-amino pyrimidine, 5, did (Fig. 1d), the first reduction wave of BLM and TLM was assigned to the 4-amino pyrimidine moiety of the two antibiotics. Although CPE experiments with the drugs were not successful, electrolysis of 5 at -1.60 V showed the reduction to be a two electron process. At pH 8, 5 exhibited a reduction wave with the $E_{1/2}$ value of -1.36 V under the same experimental conditions that the antibiotics exhibited a single reduction wave at -1.22 V. As was earlier shown by Elving *et al.* (16-18), pyrimidines exhibit reduction behavior which is strongly dependent on pH. In acidic solution (pH ~ 3) pyrimidines generally yield two reduction waves which merge to form a single wave at high pH (pH ~ 9). The pH dependency of the first reduction waves of BLM and TLM is shown in Fig. 2. In acidic solution the drugs exhibit two reduction waves [Fig. 2 (waves I and II, which merge at pH ~ 5.5 to form a single wave, wave III)]. By analogy with pyrimidines, wave I is associated with the formation of the protonated one electron reduction product of the 4-amino pyrimidine moiety of 1 and 2 (Eq. [2]). Wave II, which exhibits less pH dependence than does wave I, corresponds to the production of the protonated one electron reduction



product of the previously formed species (Eq. [3]).

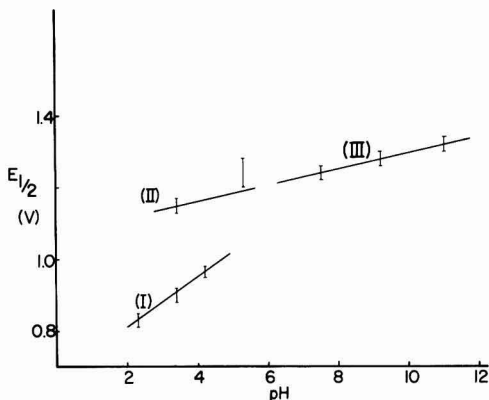


Fig. 2. A plot of $E_{1/2}$ as a function of pH for the pyrimidine reduction of bleomycin A₂ and tallysomyacin-A.

Above pH 5.5 a concerted two electron reduction occurs to give directly the dihydropyrimidine (Eq. [4]).

Both BLM and TLM exhibit a second, multielectron, reduction wave at -1.48 V (Fig. 1a). Since this wave is observed for the amino acid bithiazole, 4, at -1.46 V (Fig. 1c) and it is absent in the polarogram of peptide M, 3, and the 4-amino pyrimidine, 5, the wave must be associated with the bithiazole moiety of the antibiotics. The wave yielded an unusually high diffusion current for the drug concentrations employed (10^{-3} M). Furthermore, there appeared to be no linear relationship between concentration and the diffusion current. Multiple scan CV on a single drop shows that the current of the cathodic reaction ultimately decreased to zero (Fig. 3). If the HMDE is left in solution momentarily without an applied potential, and then scanned with CV, the current is found to be negligible. All of these features suggest that not only does the wave exhibit catalytic activity (17, 19) but that it reflects some sort of adsorption phenomenon between the drug (perhaps due to the sulfur atoms of the bithiazole) and the mercury working electrode. No further experiments were done to establish the mechanism of the catalytic activity.

The metal complexes.—Complexation of Fe(II), Co(II, III), Ni(II), and Zn(II) caused the pyrimidine wave to disappear from the polarogram of the antibiotic in both buffered and unbuffered media. In view of the fact that Ni(II) and Zn(II) are known to bind to the pyrimidine moiety of both drugs (8, 10-12, 20) the similar polarographic behavior of all of the metal-loderivatives infers that Co(II, III) and Fe(II) also utilize the pyrimidine moiety as a binding site. The electrochemical studies show that complexation to the heterocycle causes its reduction potential to be dramatically altered and to shift out of the window used for the polarographic studies ($+1.5$ to -1.8 V). The fact that all of the complexes studied exhibited an unaffected bithiazole reduction wave at -1.46 V is indica-

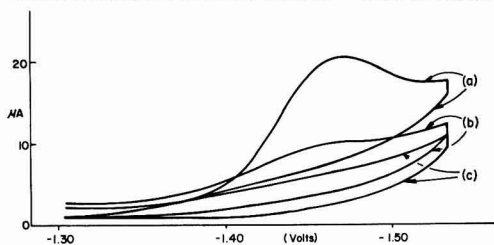


Fig. 3. Cyclic voltammograms as a function of the number of scans of the second reduction wave of BLM and TLM: (a) one scan, (b) five scans, (c) 100 scans, on a single drop. $\nu = 3.2$ V/sec.

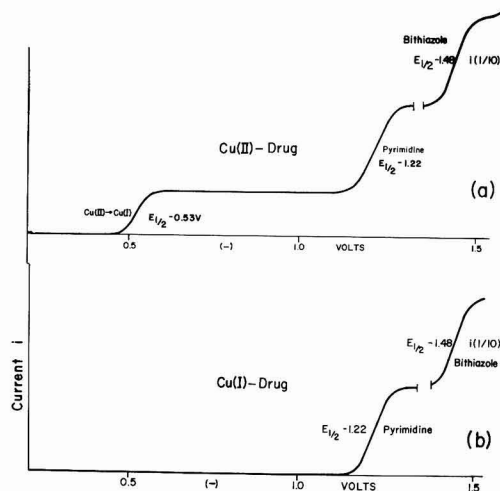


Fig. 4. The filtered d-c polarograms of (a) Cu(II)BLM-TLM and (b) Cu(I) BLM-TLM in a pH, 8.0 phosphate buffer.

tive that the nitrogen-sulfur heterocycle is not involved in metal binding.

The polarograms of the Cu(II) drug complexes (Fig. 4a) indicate that the pyrimidine wave is unaffected by complexation. Thus, the electrochemical data infer that the pyrimidine moiety is unbound in the Cu(II) complexes. However, this conclusion is at variance with the earlier established binding site of Cu(II) on BLM and TLM (10-12). The apparent contradiction is resolved by considering the reduction wave at $-0.53V$ (at $-0.43V$ in unbuffered media) to be due to the metal centered reduction, $Cu(II) \rightarrow Cu(I)$, of the copper(II) complexes. Thus, at potentials more negative than $\sim -0.6V$ the polarographic experiment is actually examining the Cu(I) antibiotic complexes. The unaffected pyrimidine wave implies that the Cu(I) drug complexes, and not the divalent compounds, contain an unbound moiety. Confirmation of this conclusion was obtained by studying the electrochemistry of the Cu(I) derivatives (Fig. 4b). As expected the polarograms of these complexes possess an unaffected pyrimidine wave indicating that Cu(I) does not bind to the 4-amino pyrimidine moiety of the antibiotic. The results were the same in buffered and unbuffered media. Although more detailed studies are necessary, Cu(I) does in fact appear to be bound to the antibiotic. While the dissolved CuCl is relatively passive to oxygen, the Cu(I)-drug complexes are very air sensitive, and they readily oxidize in the atmosphere to the Cu(II) derivatives. The polarographic, u.v. visible absorption, and ESR properties of the oxidation produced Cu(II)-drug complexes were identical to those of the compounds synthesized from the antibiotics and Cu(II) $(ClO_4)_2$. Efforts to observe Cu(I) bound to the pyrimidine moiety by studying the Cu(II)-Cu(I) couple of the Cu(II)-drug complex with CV failed. Electrochemical irreversibility was observed for the most rapid scan rates employed ($3.2V\ sec^{-1}$), indicating that the Cu(I)-pyrimidine bond-breaking step is more rapid than the time frame of the electrochemical measurement.

The polarographic behavior of the Fe(III)-drug complexes is dependent on the mode of preparation of the compound. If the trivalent complex is prepared by air oxidation of the Fe(II)-drug compounds with molecular oxygen, the pyrimidine moiety of the antibiotics remains bound to Fe(III) since polarographic analysis of the complexes shows the absence of a pyrimidine wave. The results obtained in buffered and unbuffered

solutions were the same. If the Fe(III)-drug complexes are synthesized by combining equal molar amounts of Fe(III) $(ClO_4)_3$ and the antibiotics in a phosphate buffer, the pyrimidine remains unbound. Carrying out the same synthesis in the absence of buffer ion results in an Fe(III)-drug complex containing a bound pyrimidine group.

The electrochemical results and their implication on the mechanism of action of the antibiotics.—At least two important points which bear on the proposed mechanism of action of the pharmaceuticals can be derived from the electrochemical studies. The first concerns the mechanism by which the air-sensitive drug complexes, Cu(I), Co(II), and the biologically important Fe(II) compounds are oxidized by molecular oxygen. The observation that none of these complexes exhibit a metal-centered oxidation process in the accessible potential range implies that the oxidation by molecular oxygen must be an inner sphere process (21), i.e., there is direct contact between the O_2 molecule and the antibiotic bound metal ion. The limiting voltage in the polarographic experiment, $+1.5V$, from a thermodynamic standpoint is a considerably stronger "oxidant" than is molecular oxygen (22). However, in no case was a metal-centered oxidation wave observed. This observation strongly implies that the species present at the electrode surface in the "electrochemical" experiment and the one ultimately oxidized by molecular oxygen in the "chemical" oxidation are different. The most logical explanation for this observation is that the chemical oxidation proceeds via an unstable dioxygen-drug complex. The electrochemical experiment is not examining that complex but is, in fact, examining a metal complex which does not contain bound dioxygen. Evidence that this type of inner sphere mechanism must be operating in the metalbleomycins has recently been given (23). In every case these complexes are relatively resistant to oxidation at the electrode surface (as is evidenced by the lack of an oxidation wave). All of the dioxygen complexes, on the other hand, are unstable and rapidly convert to metalbleomycins having the next higher oxidation state of the metal ion, and a radical. The radical which is produced by the redox process either remains bound to the now oxidized metal ion as it does in Co(III)-BLM- O_2^- (23), or it may be rapidly ejected as is the case for the iron and copper bleomycin systems. Although the DNA degrading ability of the Cu(I) complexes of BLM and TLM in the presence of oxygen has been unexplored, these complexes like the Fe(II) derivatives appear to be radical producers and as such should be capable of degrading DNA.

A second point evident from the electrochemical studies is that buffer ions can play an important role in the coordinating ability of at least one metal ligating site, the 4-amino pyrimidine moiety of TLM and BLM. While this group remains bound to divalent iron, components present in a phosphate buffer prevent it from binding to trivalent iron. In view of the fact that many experiments with the metallo-antibiotics have been carried out in buffered media and that buffer ions can significantly affect the metal binding site, closer attention should be paid to the effects that extraneous ions can have on the redox characteristics of the iron-drug complexes.

Acknowledgment

We acknowledge Dr. S. T. Crooke of Bristol Laboratories for supplying the bleomycin A_2 , tallsomycin-A and peptide M of tallsomycin. This investigation was supported by Grant Number CA 25112-01 awarded by the National Cancer Institute, DHEW, and an N.I.H. Institutional Award to Syracuse University.

Manuscript submitted Nov. 13, 1978; revised manuscript received ca. July 25, 1979.

Any discussion of this paper will appear in a Discussion Section to be published in the June 1980 JOURNAL. All discussions for the June 1980 Discussion Section should be submitted by Feb. 1, 1980.

Publication costs of this article were assisted by Syracuse University.

REFERENCES

1. H. Umezawa, *Biomedicine*, **18**, 459 (1973).
2. J. E. Strong and S. T. Crooke, *Cancer Res.*, **38**, 3322 (1978).
3. R. H. Blum, S. K. Carter, and K. A. Agre, *Cancer*, **31**, 903 (1973).
4. E. A. Sausville, J. Peisach, and S. B. Horwitz, *Biochem. Biophys. Res. Commun.*, **73**, 814 (1976).
5. E. A. Sausville, R. W. Stein, J. Peisach, and S. B. Horwitz, *Biochemistry*, **17**, 2740 (1978).
6. E. A. Sausville, R. W. Stein, J. Peisach, and S. B. Horwitz, *ibid.*, **17**, 2746 (1978).
7. W. J. Lown and S. Sims, *Biochem. Biophys. Res. Commun.*, **77**, 1150 (1977).
8. J. C. Dabrowiak, F. T. Greenaway, and F. S. Santillo, in "Bleomycin: Chemical, Biochemical and Biological Aspects," S. Hecht, Editor, Springer-Verlag, New York (1979).
9. Y. Sugiura and T. Kikuchi, *J. Antibiot.*, **31**, 1310 (1978).
10. J. C. Dabrowiak, F. T. Greenaway, W. E. Longo, M. Van Husen, and S. T. Crooke, *Biochim. Biophys. Acta*, **517**, 517 (1978).
11. J. C. Dabrowiak, F. T. Greenaway, and R. Grulich, *Biochemistry*, **17**, 4090 (1978).
12. F. T. Greenaway, J. C. Dabrowiak, M. Van Husen, R. Grulich, and S. T. Crooke, *Biochem. Biophys. Res. Commun.*, **85**, 1407 (1978).
13. M. Konishi, K. Saito, K. Numata, T. Tsuno, K. Asama, H. Tsukiura, T. Naito, and H. Kawaguchi, *J. Antibiot.*, **30**, 789 (1977).
14. D. J. Macero, L. W. Burgess, Jr., T. M. Banks, and F. C. McElroy, Proceedings, Symposium on Microcomputer Based Instrumentation, National Bureau of Standards, Gaithersburg, Maryland, p. 45, June, 1978.
15. R. N. Adams, "Electrochemistry at Solid Electrodes," p. 280, Marcel Dekker, New York (1969).
16. P. J. Elving, S. J. Pace, and J. E. O'Reilly, *J. Am. Chem. Soc.*, **95**, 647 (1973).
17. L. D. Smith and P. J. Elving, *ibid.*, **84**, 2741 (1962).
18. J. E. O'Reilly and P. J. Elving, *J. Electroanal. Chem.*, **21**, 196 (1969).
19. L. Meites, in "Polarographic Techniques," p. 182, Interscience Publishers, New York (1965).
20. J. C. Dabrowiak, W. Longo, M. Van Husen, F. T. Greenaway, and S. T. Crooke, Abstracts, 17th National Meeting of the American Chemical Society, Chicago, Illinois, September 1977, MED1, 051.
21. J. L. Tobe, in "Inorganic Reaction Mechanism," Thomas Nelson and Sons, Ltd., Ontario, Canada (1972).
22. W. M. Lattimer, in "The Oxidation States of the Elements and Their Potentials in Aqueous Solutions," Prentice-Hall, Inc., New York (1938).
23. Y. Sugiura, *J. Antibiot.*, **31**, 1206 (1978).

Kinetic Stability of Nitrate Ion in Molten Nitrate by Raman Spectroscopic Studies of ^{18}O -Enriched KNO_3

M. H. Brooker*

Chemistry Department, Memorial University of Newfoundland, St. John's, Newfoundland, Canada A1B 3X7

ABSTRACT

Raman spectra of nonrandom mixtures of ^{18}O -enriched potassium nitrate with normal ^{16}O -nitrate reveal that ^{18}O , ^{16}O interchange does not take place in the melt until the decomposition of nitrate occurs. The kinetic stability of the nitrate ion with respect to oxygen exchange processes is thus established for low temperature melts. At higher temperatures sodium from the glass was detected in the potassium nitrate. Possible oxygen exchange with the glass has been inferred from the decrease in total ^{18}O content.

The nature of the active species in molten nitrates has long been the subject of considerable controversy. Kerridge (1) has recently summarized the state of affairs and has pointed out the importance of small amounts of nitrite impurity and differences in thermal history to the results of chemical processes observed in molten nitrates. The importance of chemical reactions with the siliceous container can also explain some of the many discrepancies between results of different workers. Since the kinetic stability of the nitrate ion is an important parameter in establishing the reversibility of proposed chemical reactions it seemed desirable to attempt to measure the kinetic stability of the nitrate ion in nitrate melts. Previous studies have shown that Raman spectroscopy can provide useful information on ^{18}O exchange reactions with nitrate ion (2, 3).

Experimental

A nonrandom ^{18}O -enriched sample of KNO_3 was prepared by dissolving 50 mg of n- KNO_3 and 35 mg of 52% ^{18}O -enriched KNO_3 (Isomet) in about 1 ml of neutral distilled water and slowly evaporating the solution to dryness. In neutral solution ^{18}O from NO_3^- does not

exchange with water which means that the ^{18}O containing nitrate groups will be dispersed homogeneously but the ^{18}O atoms will remain with their original nitrogen and hence will not be randomly distributed. Samples of about 15 mg were placed in the 1 mm ID region of soft-glass Pascal dropping pipettes (Kimble) and dried under vacuum for about 2 hr at 150°C and then sealed off under vacuum.¹ One sample of the original mixture was left unmelted for comparison while the other samples were melted in a tube oven for about 15 min just above melting point. Although the solid mixture was white, the melts were at first rather gray, however, a small amount of gas trapped in the solid and released on melting (or a decomposition

¹ Soft-glass pipettes were used for convenience of sample manipulation, however, the low softening temperature ($\sim 500^\circ\text{C}$) would normally make them less than ideal. The major goal of the work was to determine the lifetime of NO_3^- with respect to oxygen exchange and the exchange with glass was not anticipated. A referee has suggested that oxygen diffusion would be negligible in glass since that is the case for fused silica at 470°C [E. L. Williams, *J. Am. Ceram. Soc.*, **48**, 190 (1965)]; G. H. Frischat, "Ionic Diffusion in Oxide Glasses," Diffusion and Defect Monograph Series, p. 28, Trans. Tech. Publications, Bay Village, Ohio (1975)]. This conclusion may not be valid since fused silica has a very high softening temperature and presumably a much higher activation energy for oxide diffusion than soft glass. A more detailed study with different containers and atmosphere is necessary to advance this topic.

* Electrochemical Society Active Member.

Key words: oxygen-exchange, nitrate decomposition nitrite.

product) caused the melt section to rise up the tube leaving the gray ring on the tube below. The lower part of the tube was removed and the tubes were resealed under vacuum. Raman spectra taken at this point revealed no difference from the unmelted sample so it appeared that decomposition of nitrate was not a problem. The samples were then remelted at different temperatures for appropriate times. Temperatures were measured with a Chromel-Alumel thermocouple placed near the samples and could be in error by as much as 10°C. The Raman spectra were obtained for the room temperature solids on a PHO spectrometer after sample excitation with the 488.0 nm line of a coherent Radiation Model 52 argon-krypton mixed gas laser. A narrow-band pass interference filter was used to remove unwanted laser lines. Peak intensities were measured from peak heights since the half-widths of all the peaks were equal within the experimental error. Slit widths of 1.0 cm^{-1} and laser power of about 200 mW at the sample gave spectra with suitable signal to noise to measure the intensities with an estimated error of 5%.

Occasionally the room temperature solids were obtained all or partly in the metastable $\text{KNO}_3(\text{III})$ phase which gave peak positions about 3 cm^{-1} higher than the $\text{KNO}_3(\text{II})$ room temperature phase. When this occurred it was necessary to wait until the solid naturally transformed to $\text{KNO}_3(\text{II})$ or to heat the sample to 120°C and cool slowly (4).

Results and Discussion

Raman spectra for the unmelted reference sample and the melted samples are shown in Fig. 1, while Raman intensities for each peak expressed as percentage of the total area are presented in Table I. Previously (2, 3) it has been shown that the peaks at 1050, 1030, 1010, and 990 cm^{-1} can be assigned to the symmetric stretching modes of the $\text{N}^{16}\text{O}_3^-$, $\text{N}^{16}\text{O}_2^{18}\text{O}^-$, $\text{N}^{18}\text{O}^{18}\text{O}_2^-$, $\text{N}^{18}\text{O}_3^-$ ions in KNO_3 and that the relative intensities of these peaks can be used quantitatively to measure the fraction of each ion present in the sample. The peak at 1070 cm^{-1} has been assigned to a NaNO_3 impurity. The $\text{N}^{16}\text{O}_2^{18}\text{O}^-$ peak for NaNO_3 may contribute slightly to the 1050 cm^{-1} KN^{16}O_3 peak but this has been neglected in the calculations. Assignment of the 1070 cm^{-1} peak to the NaNO_3 species was based on the following facts: (i) the peak position matches that of NaNO_3 (5), (ii) sample (d) was dissolved in water and the peak at 1070 cm^{-1} was not observed, only the peaks at 1050, 1030, 1010, and 990 cm^{-1} , which is consistent with both NaNO_3 (aq) and KNO_3 (aq) having identical dilute solution peak positions (6), (iii) the solution used in (ii) was evaporated to dryness and the Raman spectrum of the solid again showed the 1070 cm^{-1} peak. Raman spectra obtained in this laboratory for mixed NaNO_3 , KNO_3 solids obtained from solutions of the mixed salts gave peaks at 1070 and 1050 cm^{-1} , (iv) sodium ion from the glass seemed to be the only logical impurity. It should be pointed out that a weak 1070 cm^{-1} peak was also seen in the pure 51.5% ^{18}O KNO_3 thus its presence is not due to exchange in the preparation process. The increase in the intensity of the peak in sample (d) indicates considerable cation exchange between the melt and the glass at the higher temperature.

Over-all ^{18}O -enrichments of the samples calculated from peak intensities are given in Table I and averaged 21.5% excluding sample (d) which showed exchange with the glass. This value compares well with the 21.4% ^{18}O -enrichment expected from the mass measurements of the two forms of KNO_3 . Intensity calculations for the 51.5% ^{18}O -enriched sample employed in this work showed that the ^{18}O was distributed randomly over all the nitrate ions, e.g., an intensity ratio of about 1:3:3:1 was observed. Comparison of rows (a), (c), and (f) of Table I shows that the ^{18}O from the enriched KNO_3 did not exchange with the ^{16}O from the natural KNO_3 during the preparation. Even more

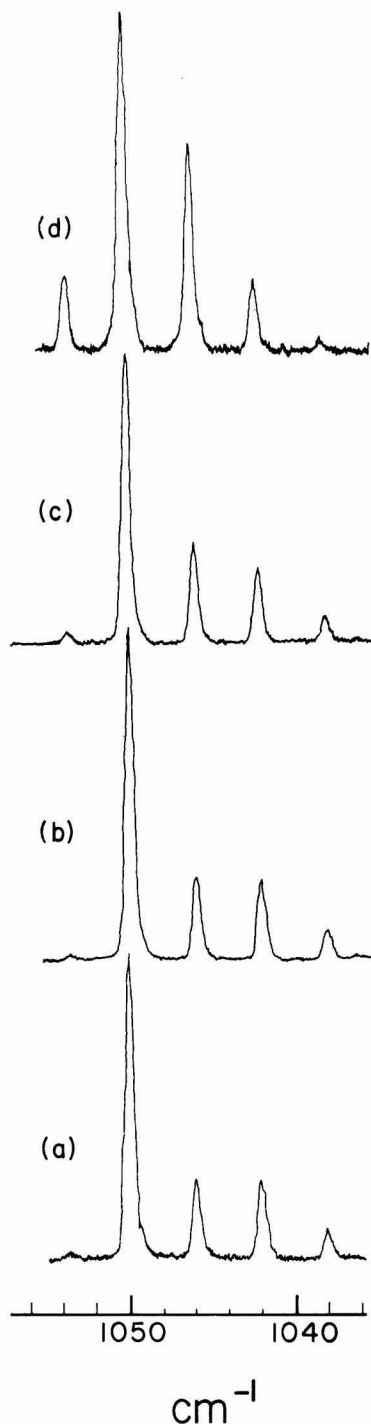


Fig. 1. Raman spectra of the symmetric stretching region of a mixture of natural- KNO_3 + 51.5% ^{18}O -enriched KNO_3 . From left to right the peaks are due to $\text{NaN}^{16}\text{O}_3$, KN^{16}O_3 , $\text{KN}^{18}\text{O}_2^{18}\text{O}$, $\text{KN}^{18}\text{O}^{18}\text{O}_2$, KN^{18}O_3 . (a) Never melted, (b) melted 8 hr at 360°C, (c) melted 2 hr at 410°C, (d) melted 2 hr at 470°C.

Table I. Raman intensities expressed as percentages of the total intensity in the symmetric stretching region of isotopic nitrate ions

Sample	NaN ¹⁸ O ₃ 1070 cm ⁻¹	KN ¹⁸ O ₃ 1050 cm ⁻¹	KN ¹⁸ O ₃ ¹⁸ O 1030 cm ⁻¹	KN ¹⁸ O ¹⁸ O ₂ 1010 cm ⁻¹	KN ¹⁸ O ₃ 990 cm ⁻¹	Calculated ¹⁸ O enrichments (%)
(a) Never melted	1.2	61.5	16.0	15.6	5.76	21.5
(b) Melted 8 hr at 360°C	1.2	62.9	15.8	15.2	5.76	21.2
(c) Melted 2 hr at 410°C	2.4	57.7	20.0	14.8	5.0	21.6
(d) Melted 2 hr at 470°C	10.1	47.7	30.2	10.2	1.75	18.6
(e) Calculated ^a for no ¹⁸ O exchange	1.2	58.7	16.2	16.9	5.98	average ¹ 21.5
(f) Calculated ^b for total exchange	1.2	47.1	39.7	10.9	0.99	(21.4)
(g) Calculated ^c for total exchange	10.1	43.8	37.0	8.4	0.64	(18.6)

¹ Sample (d) was omitted due to obvious ¹⁸O exchange with silicate.

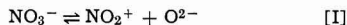
² Calculated for no exchange based on nonrandom 51.5% NO₃⁻ in natural NO₃⁻ for comparison to (a) and (b).

³ Calculated for total exchange based on random distribution of a 21.5% over-all enrichment for comparison to (a) and (b).

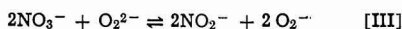
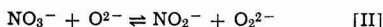
⁴ Calculated for total exchange based on random distribution of 18.6% over-all enrichment for comparison to (d).

important, comparison of rows (a), (b), (e), and (f) shows that the nitrate melt at 360°C did not show any measurable ¹⁸O exchange over an 8 hr period. The kinetic stability of NO₃⁻ in nitrate melts is thus established below the decomposition temperature. Decomposition temperatures for NO₃⁻ are not well established since some small decomposition can occur at rather low temperatures. For KNO₃ melt the onset of appreciable decomposition occurs at about 400°C (1, 6). At this temperature ¹⁸O exchange among the NO₃⁻ groups does occur (Fig. 1(c), Table I) but cation exchange with the glass does not seem too severe. At 470°C decomposition is more appreciable as indicated by the exchange of ¹⁸O among the NO₃⁻. The increase in the intensity of the peak at 1070 cm⁻¹ indicates that cation exchange with the glass was quite considerable (~10%). Although the ¹⁸O exchange was obviously considerable in sample d (Fig. 1) comparison of rows (d) and (g) indicate that complete exchange had not been obtained. The over-all decrease in ¹⁸O enrichment from 21.5 to 18.6% (sample d) suggests that ¹⁶O from an external source has exchanged with the nitrate oxygens at 470°C. The decrease is too large and in the wrong direction to be a kinetic isotope effect and since the tubes were vacuum sealed, atmospheric oxygen should not be present. It is also difficult to envisage an oxygen containing impurity of such magnitude. Oxygen exchange from the soft-glass container appears to be the most likely source of ¹⁶O (1). At 470°C the glass tube was on the verge of softening at which point the chemical exchange at the glass surface would be expected to be enhanced. Kerridge (1) has commented on the fact that results of electrochemical studies in molten nitrates appear to depend on container material. Attempts to search for ¹⁸O in the glass tubes was precluded by the broad weak character of the Raman spectrum of glass.

The above exchange results clearly indicate that NO₃⁻ is kinetically stable below the decomposition temperature for a long period of time. This greatly weakens self-dissolution mechanism of NO₃⁻

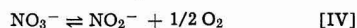


as proposed by Duke *et al.* (7) since not only must the equilibrium concentration of NO₂⁺ be small but its rate of formation must be extremely slow. The correspondence between the ¹⁸O-exchange rate and the decomposition temperature suggests that the active species in nitrate melts is more likely to come from decomposition products as proposed by Zambonin *et al.* (8, 9) and Kerridge (1). Decomposition of the form



as suggested by Zambonin and Jordan (8) could occur with O₂²⁻ coming from the glass (1). Nitrite can also

arise by direct thermal decomposition of nitrate



Kerridge has noted that although the forward reaction of [IV] may be very fast, the reverse reaction appears to be very slow which is consistent with the rather slow ¹⁸O exchange rates even above the decomposition temperature (sample c). By the exchange rate criterion the reverse reactions of [II] and [III] must also be slow at least for situations where the oxide apparently comes from silicate species. A search for peaks due to other species proved unsuccessful. Although undoubtedly some nitrite must have been present, a careful search of the 800 cm⁻¹ region did not reveal the expected peaks. Since it is felt that a 5% NO₂⁻ presence would be easily detectable it might be concluded that even for sample (d) relatively little KNO₃ actually decomposed during the exchange process. This implies that recombination of oxygen with NO₂⁻ to replace the decomposed NO₃⁻ occurs readily which is similar to that found in radiation decomposition studies (3).

The above methods should be generally useful for investigating effects of solutes, atmosphere, and container material on reactions of nitrate and other poly-Memorial University of Newfoundland.

Acknowledgment

This work was supported by the National Research Council of Canada.

Manuscript submitted Jan. 22, 1979; revised manuscript received June 22, 1979.

Any discussion of this paper will appear in a Discussion Section to be published in the June 1980 JOURNAL. All discussions for the June 1980 Discussion Section should be submitted by Feb. 1, 1980.

Publication costs of this article were assisted by the Memorial University of Newfoundland.

REFERENCES

1. D. H. Kerridge, in "Molten Salts as Nonaqueous Solvents in the Chemistry of Nonaqueous Solvents," Vol. 5B, J. J. Lagowski, Editor, chap. 5, Academic Press, London (1978).
2. A. J. Melveger, E. R. Johnson, and E. N. Ladov, *J. Inorg. Nucl. Chem.*, **32**, 337 (1970).
3. G. E. Boyd and M. H. Brooker, *J. Am. Chem. Soc.*, **95**, 4816 (1973).
4. M. H. Brooker, *J. Phys. Chem. Solids*, **39**, 657 (1978).
5. M. H. Brooker and D. E. Irish, *Can. J. Chem.*, **48**, 1183 (1970).
6. R. F. Bartholomew, *J. Phys. Chem.*, **70**, 3442 (1966).
7. R. N. Kust and F. R. Duke, *J. Am. Chem. Soc.*, **85**, 3338 (1963) and references therein.
8. P. G. Zambonin and J. Jordan, *J. Am. Chem. Soc.*, **89**, 6365 (1967).
9. P. G. Zambonin, *J. Electroanal. Chem. Interfacial Electrochem.*, **33**, 243 (1971).

Molar Volume and Electrical Conductivity Measurements in the Ternary Molten Salt System NaCl-CsCl-MnCl₂

I. Molar Volumes

N. R. Carmichael^{*1} and S. N. Flengas

Department of Metallurgy and Materials Science, University of Toronto, Toronto, Ontario, Canada M5S 1A4

ABSTRACT

Densities in the ternary system NaCl-CsCl-MnCl₂ have been measured by the Archimedian technique at temperatures varying between 550° and 1050°C. The molar volumes of the solutions show positive deviations from additivity which become more pronounced in the CsCl-rich melts. The behavior of the system is explained in terms of a complex ion model based on the presence of NaMn₂Cl₄ and Cs₂MnCl₄ complex species in these melts. It is shown theoretically and proven experimentally that the molar volumes in the ternary system may be predicted by the simple expression

$$V_{1,2,3} = tV_{1,2} + (1 - t)V_{1,3}$$

where $t = X_{\text{CsCl}}/(X_{\text{NaCl}} + X_{\text{CsCl}})$, $V_{1,2,3}$ is the molar volume of the ternary system, and $V_{1,2}$ and $V_{1,3}$ are the molar volumes of the binary system MnCl₂-CsCl and MnCl₂-NaCl, respectively, having the same MnCl₂ content as the ternary. This expression is valid along a composition path for which $y = \text{constant}$, where $y = 1 - X_{\text{MnCl}_2}$. It is of interest to note that the t -fraction average equation formulated herein was also found applicable to predicting the enthalpy of mixing and activities in several ternary systems (7) from data on their component binary systems.

There have been few systematic molar volume measurements on ternary solutions of transition metal chlorides with alkali chlorides, particularly on ternary systems. In the present investigation densities in the ternary system NaCl-CsCl-MnCl₂ have been measured over the entire composition range and for temperatures varying between 506° and 1050°C. This ternary system is of interest as the physicochemical properties of two of its component binary systems, namely, the systems NaCl-MnCl₂ and CsCl-MnCl₂, differ significantly.

The NaCl-MnCl₂ system is characterized by relatively low exothermic enthalpies of mixing which reach a maximum value of only -1900 cal/mole at a composition of about 35 mole percent (m/o) MnCl₂ (1,2). In this system, the change of volume on mixing shows slight positive deviations from additivity (3,4). On the contrary, in the CsCl-MnCl₂ system the enthalpies of mixing are strongly exothermic and reach their maximum value of -5400 cal/mole at a composition close to 33 m/o MnCl₂, representing the stoichiometric composition for the compound Cs₂MnCl₄. The change of volume on mixing in the CsCl-MnCl₂ system also indicates pronounced positive deviations from additivity which have their maximum value at about this same composition.

The thermodynamic properties of these solutions have been attributed to the presence of MnCl₄²⁻ type complex species whose strength is dependent on the size of the alkali metal cation (A⁺) present (5-7). In general, the thermodynamic stability of these complex species increases as the alkali metal cation is changed from Li⁺ to Cs⁺. Tetrahedrally coordinated complexes of this kind have also been suggested by Gruen and McBeth (8) from spectrophotometric work, from Raman spectra by Bues *et al.* (9), and more recently by Tanemoto and Nakamura (10).

Accordingly, one of the aims of the present investigation was to observe the effect of complex formation on densities and molar volumes in a ternary system which becomes progressively dominated by the stronger Cs₂MnCl₄ type complex species as NaCl is replaced by CsCl.

Experimental

Pure anhydrous MnCl₂ was prepared from reagent-grade material. The purification included first heating under vacuum and then subjecting the solid to a stream of gaseous HCl at temperatures about 100°C below the MnCl₂ melting point. Reagent-grade NaCl and reagent-grade CsCl, the latter containing 0.2% RbCl or less, were dehydrated by heating normally at about 130° under vacuum for about 10 hr.

The density measurement apparatus was similar to that used in previous work (3) in this laboratory, except that it contained a side arm used to introduce argon gas to the melt for stirring. The technique involved the measurement of the weight change of a fused quartz sinker having a volume of about 0.8 cm³ containing platinum. Weight changes were determined using a fused quartz spring-type thermobalance suspended from a pulley, the entire system being enclosed in glass tubing. A cathetometer which could be read to the nearest 0.005 cm was used to read spring extension changes. The lower part of the apparatus containing the salt was made of fused quartz and all measurements were taken in the presence of an argon gas atmosphere. An electrically heated tubular furnace allowed measurements to be taken up to about 1050°C, with a maximum uncertainty in the measured temperature of +3°C. Each run necessitated about 100 cm³ of salt mixture.

In the Archimedian density technique used herein, the sinker was calibrated to determine its volume by measuring the weight change before and after immersion in water at a specified temperature. The weight change of the same sinker, as measured before and after immersion in the molten salt, was used to

^{*} Electrochemical Society Active Member.

¹ Present address: Union Carbide Canada Limited, Toronto, Ontario, Canada.

Key words: fused salts, molar volumes, ternary systems, complexes.

determine the density (ρ) of the molten salt from the simple formula

$$\rho = \frac{F}{v} \quad [1]$$

where F is the buoyant force and v is the volume of the sinker.

The measurement could involve systematic sources of error, particularly at high temperatures. These errors included surface tension effects and salt condensation on the fused quartz fiber used to suspend the sinker. Surface tension errors depended on the diameter of the fiber at the liquid-gas interface and were minimized by using fibers having diameters of less than 0.1 mm. Salt condensation on the suspension fiber was minimized by measuring densities in the MnCl₂-rich solutions over short periods of time and by avoiding temperatures higher than 870°C.

The ternary compositions studied are given in the composition triangle shown in Fig. 1. In all, densities for about 41 different compositions were measured as functions of temperature.

The ternary composition parameters are defined as

$$t = \frac{X_{\text{CsCl}}}{X_{\text{NaCl}} + X_{\text{CsCl}}} \quad [2]$$

and

$$y = 1 - X_{\text{MnCl}_2} = X_{\text{NaCl}} + X_{\text{CsCl}} \quad [3]$$

where X_i represents the mole fractions of component i and $1.0 \geq t \geq 0$ and $1.0 \geq y \geq 0$. Then $t = 0$ and $t = 1$ represent, respectively, the binary MnCl₂-NaCl and MnCl₂-CsCl binary systems, and $y = 0$ and $y = 1$ are, respectively, pure MnCl₂ and the NaCl-CsCl binary system.

Constant values of t describe solutions having a constant mole ratio of CsCl to NaCl. Hence, at constant y , as t is increased from 0 to 1, the same moles of MnCl₂ are interacted with a salt mixture in which the CsCl content is increased at the expense of the NaCl component.

Results

For a given composition the measured densities were found to decrease linearly with increasing temperature. Accordingly, the results were fitted to the linear expression

$$\rho = A + BT \quad [4]$$

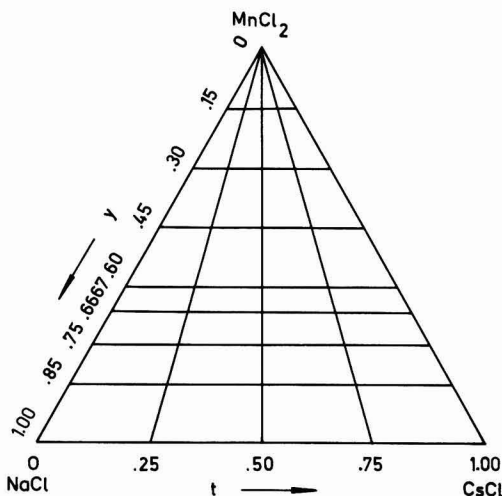


Fig. 1. MnCl₂-NaCl-CsCl ternary showing the pattern used for selection of compositions for experiments.

where A and B are constants and T is the temperature in degrees Kelvin. The coefficients A and B have been calculated by the method of least squares. These data are presented in Table I which also includes estimates of standard errors, maximum deviations, and correlation coefficients. Over-all errors in the density data were of the order of 0.3%. Reproducibility of the results was confirmed by measuring the densities over a complete temperature cycle.

The density data determined in this study may be compared with previously reported results for NaCl, CsCl, and MnCl₂. The data, calculated from fitted equations, were compared over an overlapping temperature range and absolute values of maximum departures are given to the nearest 0.1%.

For the density of NaCl, the departures are 0.3, 0.2, 0.3, and 0.2% in comparison with the values of Kucharski and Flengas (3), van Artsdalen and Yaffe (11) as reported by Janz *et al.* (12), Zuca and Ionescu-Vasu (13), and Grjotheim *et al.* (14), respectively.

For the density of CsCl the departures are 0.3, 0.6, 0.2, 0.7, and 0.3% in comparison with the data of Kucharski and Flengas (3), Yaffe and van Artsdalen (15) as reported by Janz *et al.* (12), Zuca and Olteanu (16), Grjotheim *et al.* (14), and of Markov *et al.* (17), respectively.

For the density of MnCl₂ the departures are 0.4, 0.8, and 0.2% in comparison with the data of Kucharski and Flengas (3), Murgulescu and Zuca (18) as reported by Janz *et al.* (12), and of Markov *et al.* (17), respectively.

It should be noted that Kucharski and Flengas (3) placed an accuracy of $\pm 0.3\%$ on their density data, and the values for NaCl and CsCl from Janz *et al.* (12) were given uncertainties of ± 0.4 and $\pm 0.1\%$, respectively.

The density data allow calculation of the molar volume, V , of the molten salt where

$$V = \frac{\bar{M}}{\rho} \quad [5]$$

and \bar{M} , the mean molecular weight, is given by

$$\bar{M} = X_{\text{MnCl}_2}M_{\text{MnCl}_2} + X_{\text{NaCl}}M_{\text{NaCl}} + X_{\text{CsCl}}M_{\text{CsCl}}$$

Figures 2 and 3 show the molar volumes for the MnCl₂-NaCl-CsCl ternary system as a function of composition. The significance of the linearity in Fig. 3 is discussed subsequently. Figure 4 shows the molar volume of the NaCl-CsCl binary system at three temperatures.

Discussion

In addition to the molar volume composition trends shown previously, it is of interest to compare the observed molar volume of the solution (V) with the ideal additive molar volume (V_{ideal}) given by

$$V_{\text{ideal}} = \sum X_i V_i^\circ \quad [6]$$

where, V_i° is the molar volume of pure component i . The difference between the measured molar volume of the molten salt and the ideal additive molar volume is the excess molar volume, ΔV^{xs}

$$\Delta V^{\text{xs}} = V - V_{\text{ideal}} \quad [7]$$

Figure 5 shows the excess molar volumes in the ternary MnCl₂-NaCl-CsCl system as a function of y for five constant t values at 1075°K. The trend of increased positive deviation with increasing y is apparent. A possible slight negative deviation exists at low values of both t and y for solutions rich in NaCl.

Figure 5 also shows the maximum positive deviations from additivity occurs at a mole fraction of MnCl₂ of about 0.33. This value corresponds to a ratio of total alkali chloride to MnCl₂ of about 2:1. It should be

Table I. Least squares fit of density vs. temperature ($^{\circ}\text{K}$) for various values of the composition parameters t and y for the MnCl_2 - NaCl - CsCl ternary molten salt system

$\rho = A + BT \text{ (g cm}^{-3}\text{)}$						
t	Temperature range ($^{\circ}\text{C}$)	A'	$-B \times 10^3$	Standard error	Maximum deviation	Correlation coefficient
$y = 0.0000$						
MnCl_2	694-845	2.8189	0.5080	0.0022	0.0038	-0.99661
$y = 0.1500$						
0.0000	672-861	2.8630	0.6151	0.0020	0.0036	-0.99900
0.2500	655-859	2.9283	0.6432	0.0010	0.0011	-0.99988
0.5000	640-861	2.9511	0.6406	0.0017	0.0022	-0.99961
0.7500	670-844	3.0110	0.6734	0.0021	0.0032	-0.99898
1.0000	663-803	3.0544	0.6839	0.0012	0.0013	-0.99975
$y = 0.3000$						
0.0000	610-860	2.8220	0.6597	0.0022	0.0051	-0.99912
0.2500	626-839	2.9329	0.7025	0.0010	0.0015	-0.99989
0.5000	574-869	3.0135	0.7264	0.0016	0.0019	-0.99980
0.7500	595-861	3.1145	0.7681	0.0021	0.0028	-0.99970
1.0000	613-860	3.1978	0.8065	0.0008	0.0010	-0.99995
$y = 0.4500$						
0.0000	577-849	2.7086	0.6551	0.0015	0.0020	-0.99974
0.2500	576-854	2.8693	0.7101	0.0019	0.0023	-0.99973
0.5000	603-853	3.0078	0.7577	0.0017	0.0021	-0.99977
0.7500	591-855	3.1272	0.7986	0.0012	0.0017	-0.99991
1.0000	646-861	3.2207	0.8230	0.0006	0.0006	-0.99997
$y = 0.6000$						
0.0000	506-869	2.5851	0.6449	0.0026	0.0042	-0.99955
0.2500	527-861	2.7897	0.7018	0.0025	0.0036	-0.99964
0.5000	597-865	2.9345	0.7222	0.0026	0.0038	-0.99942
0.7500	599-858	3.0903	0.7675	0.0012	0.0018	-0.99989
1.0000	623-861	3.2096	0.7916	0.0017	0.0029	-0.99979
$y = 0.6667$						
0.0000	684-849	2.4834	0.6001	0.0005	0.0005	-0.99995
0.2500	624-861	2.7397	0.6801	0.0009	0.0012	-0.99991
0.5000	576-861	2.9393	0.7327	0.0030	0.0054	-0.99914
0.7500	590-864	3.1063	0.7697	0.0026	0.0038	-0.99961
1.0000	613-861	3.2541	0.8053	0.0016	0.0025	-0.99981
$y = 0.7500$						
0.0000	757-870	2.4129	0.5930	0.0013	0.0015	-0.99929
0.2500	699-848	2.6464	0.6080	0.0039	0.0046	-0.99475
0.5000	660-861	2.9423	0.7280	0.0019	0.0029	-0.99582
0.7500	602-873	3.1625	0.7965	0.0015	0.0016	-0.99987
1.0000	597-862	3.3780	0.8725	0.0021	0.0037	-0.99975
$y = 0.8500$						
0.0000	790-914	2.2873	0.5565	0.0012	0.0016	-0.99895
0.2500	715-873	2.7002	0.6873	0.0021	0.0035	-0.99886
0.5000	666-850	3.0023	0.7712	0.0015	0.0021	-0.99969
0.7500	606-861	3.2844	0.8638	0.0018	0.0033	-0.99978
1.0000	616-864	3.5513	0.9681	0.0038	0.0070	-0.99920
$y = 1.0000$						
0.0000	812-1052	2.1328	0.5354	0.0020	0.0046	-0.99866
0.2500	762-881	2.7058	0.7191	0.0015	0.0020	-0.99907
0.5000	727-870	3.0964	0.8247	0.0025	0.0039	-0.99860
0.7500	647-871	3.4338	0.9311	0.0022	0.0031	-0.99959
1.0000	678-844	3.7459	1.0305	0.0020	0.0022	-0.99952

noted that this 2:1 ratio coincides to the stoichiometry of the reaction



where, Al , is an alkali metal.

The binary NaCl - CsCl system exhibits positive molar volume deviations which have also been observed by Zuca and Olteanu (19) and are of about the same magnitude as in the MnCl_2 - NaCl binary systems.

In addition to the excess molar volumes it is also of interest to examine the behavior of the partial molar volume of MnCl_2 (\bar{V}_{MnCl_2}).

Partial molar volumes are defined by the expression

$$\bar{V}_{\text{MnCl}_2} = \left(\frac{\partial V}{\partial n_1} \right)_{n_2, n_3, P, T} \quad [9]$$

where, n_1 , n_2 , n_3 represent the mole numbers for the components MnCl_2 , NaCl , and CsCl , respectively.

These values, shown in Fig. 6, have been determined graphically from the data, along constant t composition paths, by the method of tangents (20).

In the region where y is less than about 0.6, the values of the partial molar volumes of MnCl_2 are

similar to the molar volume of pure molten MnCl_2 , regardless of the value of t .

Coefficients of thermal expansion, α , where α is given by

$$\alpha = \frac{1}{V} \left(\frac{\partial V}{\partial T} \right)_p \quad [10]$$

may be determined from the density data.

Since $V = \bar{M}/\rho$, it may be shown that

$$\alpha = \frac{1}{\rho} \left(\frac{\partial \rho}{\partial T} \right)_p \quad [11]$$

Substituting $\rho = A + BT$ into Eq. [11] yields

$$\alpha = \frac{-B}{A + BT} \quad [12]$$

From the results of this study, the density decreases with increasing temperature and therefore α will be positive and will decrease with increasing temperature. Equation [12] was used to calculate the coefficient of thermal expansion at 1075°C and the results are shown in Fig. 7.

The coefficients of thermal expansion decrease as MnCl_2 is added to the NaCl - CsCl melts, exhibit a

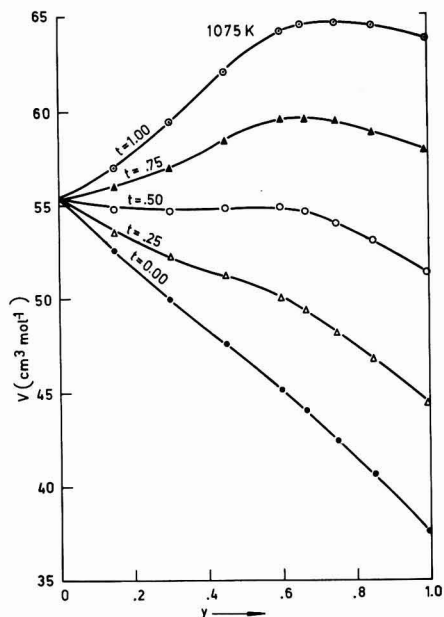


Fig. 2. Molar volume as a function of y for five values of constant t for the $\text{MnCl}_2\text{-NaCl-CsCl}$ ternary system at 1075°K .

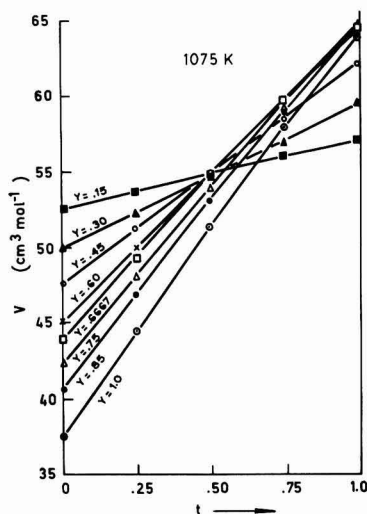


Fig. 3. Molar volume as a function of t for eight values of constant y for the $\text{MnCl}_2\text{-NaCl-CsCl}$ ternary system at 1075°K .

minimum at about $X_{\text{MnCl}_2} = 0.33$, then increase and finally decrease to a value representing pure MnCl_2 .

Application of the complex ion model to the calculation of molar volumes in the NaCl-CsCl-MnCl_2 system.—The existence of complex species in fused salt-ionic solutions should be compatible with the concept of the cation and anion interlocking quasi-lattices proposed by Temkin (21). Complex species appear to form in some charged asymmetric fused salt solutions in which mixing involves ions having different valences (5-7, 22). The application of an ionic model requires the following postulates (5-7):

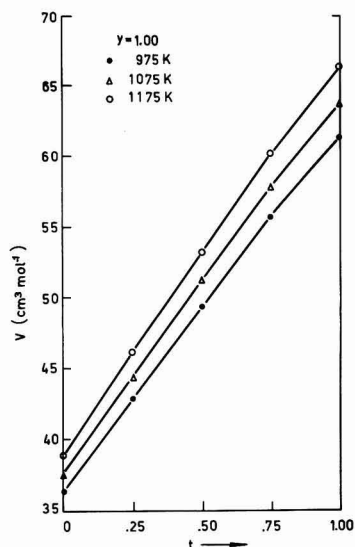


Fig. 4. Molar volume of the NaCl-CsCl system as a function of t at three temperatures.

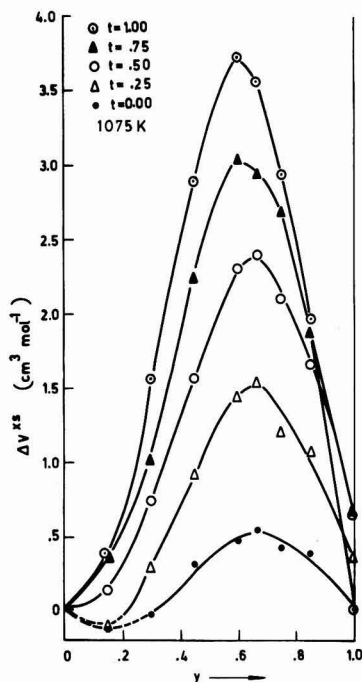


Fig. 5. Excess molar volume as a function of y for five values of constant t for the $\text{MnCl}_2\text{-NaCl-CsCl}$ ternary system at 1075°K .

1. The fused salt is taken as a continuous and highly electrified medium, so that interlocking anionic and cationic quasi-lattices exist to preserve local electrical neutrality.
2. The difference between a complexed and a noncomplexed state, involving a cation M^{+2} in a mixture containing A^+ , M^{+2} , and X^- species is sim-

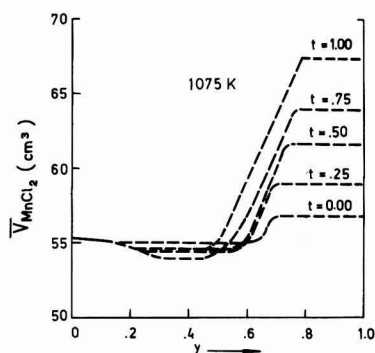


Fig. 6. Composition dependence of the partial molar volume of MnCl_2 in the MnCl_2 - NaCl - CsCl ternary system at 1075°K .

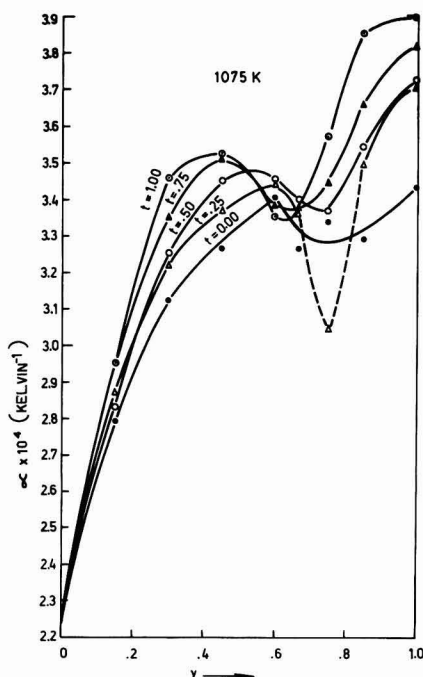
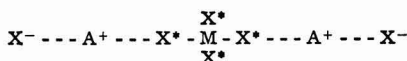


Fig. 7. Composition dependence of the coefficient of thermal expansion for the MnCl_2 - NaCl - CsCl ternary system at 1075°K .

ply defined by a characteristic "shorter" bond distance M-X^* for the complexed state, as compared to the M-X bond distance for the noncomplexed state.

3. Complexed ionic species must still belong to their respective quasi-lattices and not disrupt the continuity of the molten structure. Hence the ligands X^* in a complex MX_n^* interact with the surrounding A^+ cations in the sequence



whereby an anion X is always a cation "bridging" species.

4. Under such restrictions, the complex represents a coordinated configuration of the type MX_n^* which may be treated as a statistical entity.

5. The formation of a complex is favored by the presence of foreign cations which "compete" less favorably with the central cations M^{+2} for the same ligands X^- . Accordingly, the size of the foreign cation decides its capability for promoting or preventing the formation of complexes.

6. In the ternary system containing MnCl_2 and where two ligand donors are present, namely NaCl and CsCl , Mn^{2+} always has Cl^- ions in its first coordination shell. The strength of each Mn-Cl type bond will be expected to be influenced by the ions in the second coordination shell. Thus, if a Na^+ cation is replaced by a Cs^+ cation in the second coordination shell of Mn^{2+} cation, then the type of bonding in the Mn-Cl pair is expected to change and accordingly bond distances are also expected to differ. From this point of view, the smaller Na^+ cation would exert a stronger attraction for the Cl^- ions in the first coordination shell thereby relaxing the Mn-Cl bond, as compared to a situation where a Cs^+ cation is introduced.

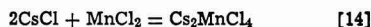
In this sense, when the formulas Na_2MnCl_4 and Cs_2MnCl_4 are written, it is not implied that they represent discrete complex ions or compounds within the molten salt structure. However, regardless of the nature of the bonds present in the NaCl - CsCl - MnCl_2 system, it is possible to select arbitrarily such melt components for the treatment of the results. This approach is often applied in describing the activities of components in condensed phases.

The effect of complexing on the molar volume shown in Fig. 3 may now be explained by a simple treatment. The melt components arbitrarily selected are MnCl_2 , NaCl , CsCl , Na_2MnCl_4 , and Cs_2MnCl_4 . These species will be used for the NaCl - MnCl_2 and CsCl - MnCl_2 binary melts and for the ternary NaCl - CsCl - MnCl_2 .

The amounts of the five components selected above may be determined if it is assumed that the following reactions occur in their respective binaries



and



It is further assumed that in the ternary system, MnCl_2 is distributed between the two possible complex species Na_2MnCl_4 and Cs_2MnCl_4 , in the same mole ratio as the ratio of NaCl to CsCl . The latter is readily found from Eq. [2] to be $1 - t/t$. The mass balance for the ternary system NaCl - CsCl - MnCl_2 may then be considered on the basis of the two regions $y \geq 0.6667$ and $y \leq 0.6667$; that is, $X_{\text{MnCl}_2} \leq 0.3333$ and $X_{\text{MnCl}_2} \geq 0.3333$.

The amounts of the components in the reacted system may also be expressed in terms of the composition parameters y and t which lead to the expressions

$$X_{\text{MnCl}_2} = 1 - y$$

$$X_{\text{NaCl}} = y(1 - t)$$

$$X_{\text{CsCl}} = ty$$

Table II gives the mass balances for the two regions of the ternary.

Considering the results on partial molar volumes given in Fig. 6 and the mass balances given in Table II, the ternary solutions at y values less than 0.6667 should contain both unreacted MnCl_2 and amounts of complex species. The amounts of the latter become progressively less as $y \rightarrow 1$.

However, as shown by the constant value of the partial molar volume \bar{V}_{MnCl_2} in this range (Fig. 6), the presence of the alkali chloride does not appear to affect the over-all packing ability of the MnCl_2 in these solutions to any significant extent and its partial molar volume remains at about the same value as for pure MnCl_2 ($\sim 55.5 \text{ cm}^3$). The situation changes at y values higher than 0.6667. In this concentration range, unreacted MnCl_2 should no longer be possible and the solutions, in addition to containing excess

Table II. Mass balance for the MnCl₂-NaCl-CsCl ternary system

Component	Primary composition	Reacted system composition
For $y \leq 0.6667$		
MnCl ₂	X_{MnCl_2}	$X_{MnCl_2} - (X_{NaCl} + X_{CsCl}) = \frac{2-3}{2}$
NaCl	X_{NaCl}	0
CsCl	X_{CsCl}	0
Na ₂ MnCl ₄	0	$\frac{X_{NaCl}}{2} = \frac{y(1-t)}{2}$
Cs ₂ MnCl ₄	0	$\frac{X_{CsCl}}{2} = \frac{ty}{2}$
For $y > 0.6667$		
MnCl ₂	X_{MnCl_2}	0
NaCl	X_{NaCl}	$X_{NaCl} - 2(1-t)X_{MnCl_2} = y(1-t) - 2(1-t)(1-y)$
CsCl	X_{CsCl}	$X_{CsCl} - 2tX_{MnCl_2} = ty - 2t(1-y)$
Na ₂ MnCl ₄	0	$2(1-t)X_{MnCl_2} = 2(1-t)(1-y)$
Cs ₂ MnCl ₄	0	$2tX_{MnCl_2} = 2t(1-y)$

alkali chlorides, also contain MnCl₂ in its complexed form.

In the NaCl-MnCl₂ system, at $t = 0$, the partial molar volume (~ 57 cm³) of MnCl₂ in Na₂MnCl₄ is only slightly larger than that corresponding to pure molten MnCl₂ (~ 55.5 cm³) at the same temperature. This probably is indicative of the weak nature of the Na₂MnCl₄ complex species. In the MnCl₂-CsCl binary system at $t = 1$, the partial molar volume of MnCl₂ (~ 67.5 cm³) is significantly larger and reflects the stronger CsMnCl₄ complex. This behavior suggests that these complex species accommodate themselves less efficiently within a melt structure.

The molar volume of the solution, V , may now be represented in terms of the partial molar volumes of the arbitrarily selected components in each composition range of the reacted system.

In the following treatment it is assumed that the partial molar volumes \bar{V}_i of the various species that have been arbitrarily selected are composition independent, and, therefore, the partial molar volume for any given component should be the same in corresponding binary and ternary systems.

Considering the portion of the ternary given by $y \leq 0.6667$, the molar volume may be expressed as

$$V = \frac{ty}{2} \bar{V}_{Cs_2MnCl_4} + \frac{(1-t)y}{2} \bar{V}_{Na_2MnCl_4} + \frac{(2-3y)}{2} \bar{V}_{MnCl_2} \quad [15]$$

The third term in expression [15] may be multiplied by the arbitrary term $[(1-t) + t]$ whereupon Eq. [15] may be rewritten as

$$V = (1-t) \left[\frac{y}{2} \bar{V}_{Na_2MnCl_4} + \frac{2-3y}{2} \bar{V}_{MnCl_2} \right] + t \left[\frac{y}{2} \bar{V}_{Cs_2MnCl_4} + \frac{2-3y}{2} \bar{V}_{MnCl_2} \right] \quad [16]$$

As the partial molar volumes (\bar{V}_i) have been assumed to be composition independent at constant y , the terms

$$\frac{y}{2} \bar{V}_{Na_2MnCl_4} + \frac{2-3y}{2} \bar{V}_{MnCl_2} = V_{1,2} \quad [17]$$

and

$$\frac{y}{2} \bar{V}_{Cs_2MnCl_4} + \frac{2-3y}{2} \bar{V}_{MnCl_2} = V_{1,3} \quad [18]$$

where $V_{1,2}$ and $V_{1,3}$ are, respectively, the molar volumes of the NaCl-MnCl₂ and CsCl-MnCl₂ binary systems, for the given y value.

Accordingly, the molar volume of the ternary system $V_{1,2,3}$ may be written as

$$V_{1,2,3} = (1-t) V_{1,2} + t V_{1,3} \quad [19]$$

at constant y .

Furthermore, for $y = 0.6667$, Eq. [15] reduces to

$$V = 0.3333 t \bar{V}_{Cs_2MnCl_4} + 0.3333 (1-t) \bar{V}_{Na_2MnCl_4} \quad [20]$$

Considering now the region of the ternary represented by $y > 0.6667$, the molar volume may be expressed as

$$V = 2(1-t)(1-y) \bar{V}_{Na_2MnCl_4} + 2t(1-y) \bar{V}_{Cs_2MnCl_4} + [y(1-t) - 2(1-t)(1-y)] \bar{V}_{NaCl} + [ty - 2t(1-y)] \bar{V}_{CsCl} \quad [21]$$

On rearrangement Eq. [21] may be written

$$V = (1-t) \cdot [(3y-2) \bar{V}_{NaCl} + 2(1-y) \bar{V}_{Na_2MnCl_4}] + t[(3y-2) \bar{V}_{CsCl} + 2(1-y) \bar{V}_{Cs_2MnCl_4}] \quad [22]$$

For this composition range in the ternary system, if it is assumed that all the partial molar volumes are composition independent at constant y , then the terms

$$(3y-2) \bar{V}_{NaCl} + 2(1-y) \bar{V}_{Na_2MnCl_4} = V_{1,2} \quad [23]$$

and

$$(3y-2) \bar{V}_{CsCl} + 2(1-y) \bar{V}_{Cs_2MnCl_4} = V_{1,3} \quad [24]$$

where, $V_{1,2}$ and $V_{1,3}$ are again the molar volumes of the NaCl-MnCl₂ and CsCl-MnCl₂ binary systems for the given y value. Hence, Eq. [19] is valid in this region of the ternary.

This treatment predicts a linear relationship between the molar volume and t for constant y values. In Fig. 3 graphs of V vs. t at constant y values are almost linear and therefore the theoretical treatment predicts the experimentally observed concentration dependence of the molar volumes in this system.

The integral enthalpy of mixing in the ternary systems NaCl-CsCl-MnCl₂ and the partial molar free energies of mixing in the systems CoCl₂-NaCl-KCl, NiCl₂-NaCl-KCl, NaCl-CsCl-MnCl₂, and in AgCl-NaCl-RbCl, have been shown (7) to vary approximately linearly with respect to t at constant y values. These results were explained by a "t-fraction average" relationship which was also derived from a theory based on complex forming reactions (7). This t-fraction average relationship may now be written in a general form as

$$\Delta Z_{1,2,3} = t \Delta Z_{1,3} + (1-t) \Delta Z_{1,2} \text{ at } y \text{ constant} \quad [25]$$

where Z represents a molar or partial molar thermodynamic property and the subscripts 1, 2, and 3 identify the three components in a ternary system. Then the ternary solution is described by the subscripts 1, 2, 3 and subscripts 1, 2 and 1, 3 represent two constituent binary systems of the ternary, while t is a concentration parameter of the form

$$t = \frac{X_2}{X_2 + X_3}$$

The application of Eq. [23] to a ternary charge asymmetrical system which contains a reactive component MCl_n and two alkali metal chlorides having low reactivity toward each other requires that the ternary composition triangle contains the reactive salt as component 1. Where applicable, the t-fraction average rule is extremely useful in predicting the thermodynamic properties of a ternary system from binary data.

Acknowledgments

The authors would like to acknowledge the financial assistance of the International Nickel Company of Canada Limited and of the National Research Council of Canada.

Manuscript submitted Aug. 9, 1978; revised manuscript received Feb. 24, 1979.

Any discussion of this paper will appear in a Discussion Section to be published in the June 1980 JOURNAL. All discussions for the June 1980 Discussion Section should be submitted by Feb. 1, 1980.

Publication costs of this article were assisted by the University of Toronto.

REFERENCES

- G. N. Papatheodorou and O. J. Kleppa, *J. Inorg. Nucl. Chem.*, **33**, 1249 (1971).
- A. S. Kucharski and S. N. Flengas, *This Journal*, **119**, 1170 (1972).
- A. S. Kucharski and S. N. Flengas, *ibid.*, **121**, 1298 (1974).
- L. S. Murgulescu and S. Zuca, *Acad. Rep. Populare Romine Studii Cercetari Chim.*, **7**, 325 (1959).
- S. N. Flengas and A. S. Kucharski, *Can. J. Chem.*, **49**, 3971 (1971).
- S. N. Flengas and J. M. Skeaff, *ibid.*, **50**, 1345 (1972).
- D. R. Sadoway and S. N. Flengas, *This Journal*, **122**, 515 (1975).
- D. M. Gruen and R. L. McBeth, *Pure Appl. Chem.*, **6**, 23 (1963).
- W. Bues, L. El-Sayed, and H. A. Oye, *Acta Chem. Scand.*, **A31**, 461 (1977).
- K. Tanemoto and T. Nakamura, *Chem. Lett.*, 351-356 (1975).
- E. R. van Artsdalen and I. S. Yaffe, *J. Phys. Chem.*, **59**, 118 (1955).
- G. J. Janz, F. W. Dampier, G. R. Lakshminarayanan, P. K. Lorenz, and R. P. T. Tomkins, "Molten Salts, Vol. 1, Electrical Conductance, Density and Viscosity Data," NSRDS-NBS15, National Bureau of Standards, Washington, D.C. (1968).
- S. Zuca and L. Ionescu-Vasu, *Rev. Roum. Chim.*, **12**, 1285 (1967).
- K. Grjotheim, J. L. Holm, B. Lillebuen, and H. A. Oye, *Trans. Faraday Soc.*, **67**, 640 (1971).
- I. S. Yaffe and E. R. van Artsdalen, *J. Phys. Chem.*, **60**, 1125 (1956).
- S. Zuca and M. Olteanu, *Rev. Roum. Chim.*, **13**, 1567 (1968).
- B. F. Markov, V. D. Prisyazhnyi, and G. P. Prikhod'ko, *Sov. Prog. Chem.*, **36**, 24 (1970).
- I. G. Murgulescu and S. Zuca, *Rev. Roum. Chim.*, **4**, 227 (1959).
- S. Zuca and M. Olteanu, *ibid.*, **15**, 357 (1970).
- L. S. Darken, *J. Am. Chem. Soc.*, **72**, 2909 (1950).
- M. Temkin, *Acta Physicoch. URSS.*, **20**, 411 (1945).
- S. N. Flengas and P. Pint, *Can. Met. Quart.*, **8**, 151 (1969).

Molar Volume and Electrical Conductivity Measurements in the Ternary Molten Salt System NaCl-CsCl-MnCl₂

II. Electrical Conductivities

N. R. Carmichael*¹ and S. N. Flengas

Department of Metallurgy and Materials Science, University of Toronto, Toronto, Ontario, Canada M5S 1A4

ABSTRACT

Electrical conductivities in the ternary molten salt system NaCl-CsCl-MnCl₂ have been measured in U-tube capillary-type cells over the entire ternary composition range and at temperatures varying between 510° and 1054°C. Molar conductivity and apparent activation energies for the process have been calculated. The "t-fraction average" relationship obeyed by some of the thermodynamic properties for this system (10) is not applicable to electrical conductivities. The concentration dependence of the molar conductivity indicates the presence of complex species in this system.

Electrical conductivity data on pure molten salt and on simple binary systems are numerous. These have been compiled critically by Tomlinson (1), Janz and Reeves (2), and Solomons (3) and in publications on conductivity and molar volumes (4).

The physicochemical properties of the binary molten salt solutions of MnCl₂ in alkali chlorides have been investigated extensively in this laboratory. Thus, the partial molar properties of the systems MnCl₂-LiCl, MnCl₂-NaCl, MnCl₂-KCl, and MnCl₂-CsCl have been obtained by emf measurements (5), and corresponding molar volumes and electrical conductivities have been measured over the entire composition range (6).

The concentration dependence of the molar volumes and of the electrical conductivities of these systems has been interpreted in terms of a complex ion model proposed previously (7, 8) for the purpose of understanding thermodynamic properties.

It has also been shown theoretically and proven experimentally (9) that in several ternary charge asymmetrical fused salt solutions the concentration dependence of an integral thermodynamic property ΔZ in a ternary system 1, 2, 3 may be calculated with reasonable accuracy from corresponding binary data using the expression

$$\Delta Z_{(1,2,3)} = (1 - t) \Delta Z_{(1,2)} + t \Delta Z_{(1,3)} \quad [1]$$

where t is a ternary concentration parameter defined as $t = X_3/(X_2 + X_3)$ and X 's are ternary mole fractions.

For this equation component 1 is always that component which forms a complex configuration, while components 2 and 3 may be considered as ligand donors.

A similar relationship was also found to be applicable (10) to the concentration dependence of the molar volumes, V , in the ternary system NaCl-CsCl-MnCl₂, which are given as

$$V_{(1,2,3)} = (1 - t) V_{1,2} + t V_{1,3} \quad [2]$$

where components 1, 2, and 3, were, respectively,

* Electrochemical Society Active Member.

¹ Present address: Union Carbide Canada Limited, Toronto, Ontario, Canada.

Key words: fused salts, electrical conductivities, ternary systems.

MnCl₂, NaCl, and CsCl. One of the aims of the present investigation was to test the applicability of the "t-fraction average" relationship to a transport property such as the electrical conductivity of a ternary system.

The test system chosen for this purpose was the ternary MnCl₂-NaCl-CsCl in which the two component binary systems MnCl₂-NaCl and MnCl₂-CsCl are characterized by pronounced differences in their thermodynamic behavior.

Comparison data are facilitated by selection of compositions in a suitable pattern. For the purposes of these experiments, a grid was constructed on the ternary field using the two composition parameters y and t , where

$$y = 1 - X_{\text{MnCl}_2} = X_{\text{NaCl}} + X_{\text{CsCl}} \quad [3]$$

and

$$t = \frac{X_{\text{CsCl}}}{X_{\text{NaCl}} + X_{\text{CsCl}}} \quad [4]$$

Compositions y and t are identical with those used in our previous work on molar volumes (10).

Experimental

The measurement of electrical conductivity in molten salts has been discussed by many investigators; for example Tomlinson (1), Janz and Reeves (2), Solomons (3).

The most commonly used approach for measuring molten salt electrical conductivity is the capillary cell technique. This technique was used in the present work. The capillary cell technique has several advantages; the cell is usually straightforward in design, widely applicable, and yields high cell constants.

When using this technique, the cell is calibrated to determine its cell constant L/A as given in the expression

$$R = \frac{1}{\kappa} \cdot \frac{L}{A} \quad [5]$$

where R is resistance, $1/\kappa$ is the electrical conductivity, L is length, and A is the area. Calibration consists of measuring the cell resistance when the cell contains a liquid of known specific resistivity and then using Eq. [3] to determine the cell constant.

The cell resistance is also measured when the cell contains the molten salt and, knowing the cell constant from calibration, the electrical conductivity of the molten salt may be calculated with the use of Eq. [5]. Capillary fused quartz electrical conductivity cells, calibrated at room temperature, were used to measure electrical conductivities. Resistances were measured as functions of frequency, composition of the molten salt, and temperature.

The electrical conductivity cell is shown in Fig. 1 and is similar to that used in this laboratory in previous work (6). The electrodes were platinum wire (0.095 cm diam) welded to lead rods of Inconel (0.125 cm diam) which passed through vacuum sliding seals at the top of the cell. Fused quartz was used for the lower portion of the cell.

Capillary fused quartz tubing having an internal diameter of about 0.15 cm was connected to standard fused quartz tubing of about 1.3 cm ID. Thus, the restricted path of the capillary was, by far, the largest contribution to the cell constant. Fused quartz is characterized by a very low thermal expansivity, hence, when a cell is calibrated at room temperature, the calibration value so determined may be expected to represent the cell constant at elevated temperatures used in this study with little loss in accuracy.

The cells were calibrated using 1 demal KCl solution and a commercial conductivity bridge (Model RC-18, Industrial Instruments) equipped with a Wagner ground and a series of variable capacitors. The bridge was limited to frequencies of 1 and 3 kHz. Null point could be seen on a built-in cathode ray oscilloscope. The frequency dependence of resistance was also investigated during the initial stages of this work using

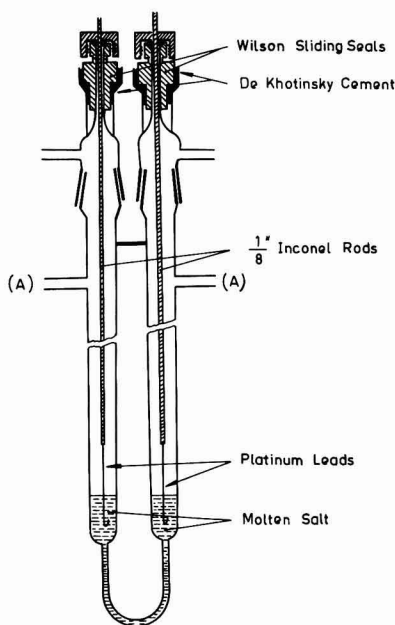
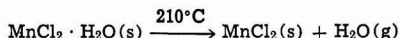
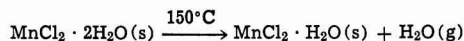


Fig. 1. Electrical conductivity cell

another a-c conductivity bridge equipped with a variable frequency generator.

Jones and Bradshaw's data (11) on the conductivities of the 1 demal KCl solution were used for calibration. During calibration, the cells were kept at constant temperature to within $\pm 0.1^\circ\text{C}$. Typical cell constants were of the order of 1000 cm^{-1} . During calibration and measurements, the electrode tips on both sides of the conductivity cells were kept at the same distance above the capillary tube openings. Reagent grade MnCl₂ · 4H₂O, NaCl, and CsCl were used as the starting materials.

Dehydration of MnCl₂ · 4H₂O reportedly proceeds according to the following steps (12, 13)



where s, l, and g are solid, liquid, and gas, respectively.

Reagent grade manganese chloride (hydrated) was obtained from the McArthur Chemical Company and A and K Petro Chem Industries Limited. In order to remove most of the water, the manganese chloride was partially dehydrated by heating under continuous evacuation, first, in an open container in a vacuum drying oven and then in a heated Pyrex tube. The pre-dried salt was loaded into one compartment of a two-compartment fused quartz purification unit and was heated under continuous evacuation. At approximately 400°C , dry argon and then dry HCl were allowed to flow through the cell. The salt was melted and held under dry HCl gas for about 1 hr. The system was then purged with dry argon gas. Following the argon purge, the MnCl₂ was distilled under continuous evacuation to the second, cooler compartment. Then the two-compartment purification unit was cooled and removed from the furnace.

In typical purification, reagent-grade NaCl (Shawinigan distributed by McArthur Chemical Company

Limited) or analar-grade CsCl (British Drug Houses Limited) was placed in one compartment of the two-compartment purification unit and purified following a procedure similar to that just outlined for predried MnCl_2 . Hence, all three salts were melted under HCl and sublimed. The purified salts were stored in bottles in dessicators.

During a typical experiment, the appropriate exact amounts of MnCl_2 , NaCl, and CsCl were weighed separately and quickly transferred into the conductivity cell. The ground joints carrying the conductivity electrodes and the sliding seals were then placed in position, as shown in Fig. 1. Prior to heating, the cell was evacuated and then argon was allowed in the system. Finally, the cell was heated under vacuum to a temperature below the melting point of the salt mixture and argon was again admitted.

After the salts had melted, they were thoroughly mixed by allowing argon gas to flow through the capillary tube by diverting the direction of gas flow. This also ensured removal of gas bubbles which adhere to capillary tubes and contribute to errors during measurements of conductivity by this technique. The sliding seals, shown in Fig. 1, allowed electrode height adjustment and electrode tip positioning as required.

During measurements, the gas flow was redirected to simply blanket the melt. A system of clamps and bypassing tubes were used for regulating the gas flow in or over the melt. Mixing was repeated until two successive resistance readings gave identical values. Resistance measurements were made for both increasing and decreasing temperatures. Temperature was measured using a Chromel-Alumel thermocouple in a fused quartz tube placed immediately alongside the cell. Temperatures were also measured at the bottom and the top of the capillary for every temperature to check for temperature gradients along the cell.

Occasionally at low temperatures, solid formation was evident by the rapid decrease in resistance with decreasing temperature. However, such salt freezing was only allowed for a short time and then the cell was reheated well into the all-liquid range and the molten salt was mixed by argon bubbling. The measurement of resistance made after reheating and mixing were in excellent agreement with any made before the freezing. The correction for lead wire resistance was usually of the order of 0.3 Ω .

Results

Using the variable frequency bridge the resistance was more frequency dependent at the lower frequencies studied. From 0.3 to 3 kHz the change was normally less than 0.2%. In the frequency range 1-5 kHz the frequency dependence was negligible. Frequencies higher than 5 kHz were sometimes examined, but sensitivity was poor. Because of the time required to balance the bridge, small variations in temperature would have effects similar in magnitude to the changes in resistance caused by frequency changes.

A single test of the calibration cell indicated that the frequency dependence was small; for example, the resistance at 0.3 and 3 kHz was 9659 and 9652 Ω , respectively. Thus, for the purposes of this work, resistance values obtained with the RC-18 model conductivity bridge at a frequency of 3 kHz were used both for calibration and molten salt electrical conductivity determinations.

Electrical conductivities have been represented in Table I for the 41 ternary compositions by quadratic expressions with respect to temperature as

$$\kappa = A + BT + CT^2$$

where T is in degrees Kelvin and A , B , and C are constants determined by a least squares computer technique.

Figure 2 shows the electrical conductivity as a function of y for five constant t values and at a temperature of 1075°K. In Fig. 2 there is a trend to lower elec-

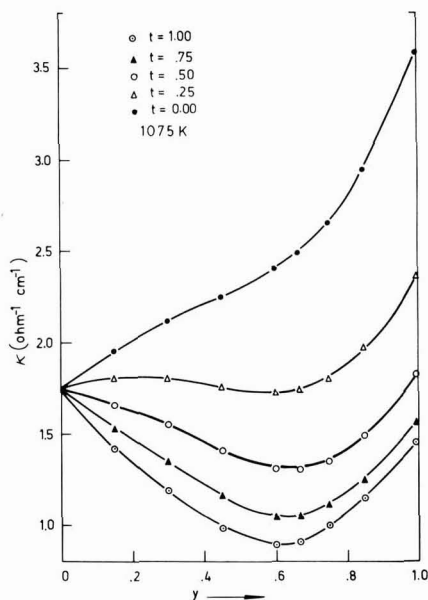


Fig. 2. Electrical conductivities in the ternary system NaCl-CsCl- MnCl_2 , as a function of y for constant t values, at 1075°K. $t = 0$ and $t = 1$ represent, respectively, the binary systems NaCl- MnCl_2 and CsCl- MnCl_2 .

trical conductivity as t increases, that is, as NaCl is replaced by CsCl. There is also a trend to a more pronounced minimum at about $X_{\text{MnCl}_2} = 0.33$ as t increases. Figure 3 shows the electrical conductivity as a function of t for eight constant y values at a temperature of 1075°K.

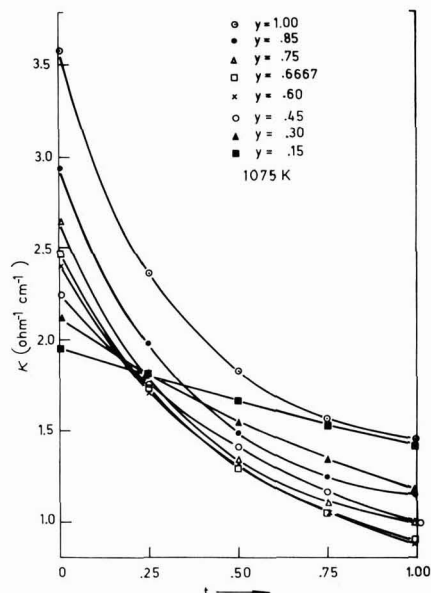


Fig. 3. Electrical conductivities in the ternary system NaCl-CsCl- MnCl_2 , as a function of t for constant y values, at 1075°K.

Table I. Least squares fit of electrical conductivity vs. temperature (°K) for various values of the composition parameters t and y for the MnCl₂-NaCl-CsCl ternary molten salt system

t	Temperature range (°C)	$\kappa = A + BT + CT^2$ ($\Omega^{-1} \text{ cm}^{-1}$)			(T is given in °K)		
		-A	$B \times 10^3$	$-C \times 10^6$	Standard error	Maximum deviation	Correlation coefficient
$y = 0.0000$ MnCl ₂	669-906	1.061475	3.3877	0.71957	0.0010	0.0022	0.99998
$y = 0.1500$							
0.0000	668-898	2.297217	5.9504	1.8586	0.0009	0.0019	0.99998
0.2500	649-903	2.348733	5.8511	1.8329	0.0010	0.0017	0.99999
0.5000	638-888	2.249338	5.4989	1.7317	0.0017	0.0028	0.99996
0.7500	676-906	2.276888	5.3733	1.7062	0.0013	0.0022	0.99997
1.0000	665-909	2.114909	4.9311	1.5279	0.0014	0.0025	0.99995
$y = 0.3000$							
0.0000	623-875	3.287108	8.1446	2.8968	0.0020	0.0026	0.99986
0.2500	613-904	2.843052	6.8946	2.3973	0.0024	0.0040	0.99994
0.5000	584-880	2.808208	5.6812	2.3520	0.0025	0.0041	0.99992
0.7500	575-890	2.483327	5.7543	2.0364	0.0018	0.0027	0.99995
1.0000	558-903	2.244086	5.1344	1.8120	0.0047	0.0086	0.99964
$y = 0.4500$							
0.0000	551-922	3.385402	8.5791	3.1059	0.0046	0.0097	0.99988
0.2500	539-891	3.174740	7.6979	2.8971	0.0018	0.0032	0.99997
0.5000	580-881	2.272072	5.5330	1.9632	0.0019	0.0027	0.99995
0.7500	579-893	1.693543	4.1326	1.3740	0.0013	0.0020	0.99997
1.0000	622-895	1.366115	3.3187	1.0588	0.0012	0.0021	0.99994
$y = 0.6000$							
0.0000	516-886	3.507201	9.0863	3.3382	0.0049	0.0084	0.99991
0.2500	510-877	2.439452	6.1523	2.1194	0.0025	0.0043	0.99996
0.5000	582-884	1.670298	4.1045	1.2458	0.0011	0.0017	0.99998
0.7500	599-876	1.323280	3.1107	0.84319	0.0009	0.0011	0.99998
1.0000	607-877	1.275368	2.6274	0.76103	0.0008	0.0018	0.99998
$y = 0.6667$							
0.0000	664-895	2.712518	7.6260	2.5985	0.0060	0.0119	0.99936
0.2500	638-891	2.088735	5.4126	1.7294	0.0012	0.0018	0.99997
0.5000	564-877	1.708030	4.0759	1.1890	0.0013	0.0021	0.99998
0.7500	563-889	1.519284	3.3873	0.93486	0.0005	0.0007	1.00000
1.0000	586-896	1.469415	3.1674	0.67821	0.0032	0.0076	0.99990
$y = 0.7500$							
0.0000	783-975	1.930467	6.5344	2.1124	0.0026	0.0051	0.99973
0.2500	700-905	2.236600	5.7115	1.8201	0.0017	0.0032	0.99991
0.5000	652-901	1.934476	4.4792	1.3300	0.0005	0.0008	1.00000
0.7500	590-899	1.718910	3.7808	1.0730	0.0006	0.0010	0.99999
1.0000	561-925	1.572225	3.3927	0.93926	0.0008	0.0015	0.99999
$y = 0.8500$							
0.0000	797-969	2.548333	7.9769	2.6699	0.0010	0.0018	0.99996
0.2500	717-899	2.818514	6.9354	2.3070	0.0016	0.0034	0.99992
0.5000	652-885	2.367649	5.4001	1.6888	0.0013	0.0025	0.99997
0.7500	605-901	2.115648	4.6295	1.3988	0.0015	0.0036	0.99997
1.0000	628-885	2.000014	4.3428	1.3183	0.0016	0.0021	0.99995
$y = 1.0000$							
0.0000	816-1054	3.477177	10.3525	3.5231	0.0022	0.0043	0.99980
0.2500	773-876	2.988353	7.6141	2.4554	0.0019	0.0037	0.99991
0.5000	697-999	2.977242	6.7904	2.1633	0.0009	0.0017	0.99999
0.7500	633-958	2.788570	6.1328	1.9382	0.0019	0.0037	0.99996
1.0000	694-850	3.322986	6.9990	2.3789	0.0039	0.0071	0.99954

The molten salt results were reproducible with increasing and decreasing temperatures. Separate "check" experiments gave good agreement with the main experiments. The uncertainty in calibration, salt composition, and temperature are the main sources of error. An estimate in the uncertainty in accuracy of the data is $\pm 2\%$.

The electrical conductivity data determined in this study may be compared with previously reported results for NaCl, CsCl, MnCl₂, and for certain compositions in the three binary systems. The data were compared over an overlapping range of temperature and absolute values of the maximum departure are given to the nearest 0.1%. Unless otherwise noted, the data for comparison was determined from fitted equations.

For NaCl, the departures are 0.6, 4.2, and 1.1% in comparison with the values of Kucharski and Flengas (6), van Artsdalen and Yaffe (13) as reported by Janz *et al.* (4), and Grjotheim *et al.* (14).

For CsCl, the departures are 1.0 and 11.0% in comparison with the data of Kucharski and Flengas (6) and by Yaffe and van Artsdalen (15) as reported by Janz *et al.* (4), respectively.

For MnCl₂, the departures are 0.5 and 1.1% in comparison with the data of Kucharski and Flengas (6) and by Murgulescu and Zuca (16) as reported by Janz *et al.* (4), respectively.

For approximate compositions $X_{\text{MnCl}_2} = 0.70$, $X_{\text{NaCl}} = 0.30$, and for $X_{\text{MnCl}_2} = 0.40$, $X_{\text{NaCl}} = 0.60$, the departures are 2.0 and 3.0%, respectively, in comparison with the values of Kucharski and Flengas (6).

For the compositions $X_{\text{MnCl}_2} = 0.70$, $X_{\text{CsCl}} = 0.30$, and for $X_{\text{MnCl}_2} = 0.40$, $X_{\text{CsCl}} = 0.60$, and for $X_{\text{MnCl}_2} = 0.25$, $X_{\text{CsCl}} = 0.75$, the departures are 0.8, 2.9, and 1.0%, respectively, in comparison with the data of Kucharski and Flengas (6).

For the compositions $X_{\text{NaCl}} = 0.75$, $X_{\text{CsCl}} = 0.25$, for $X_{\text{NaCl}} = 0.50$, $X_{\text{CsCl}} = 0.50$, and for $X_{\text{NaCl}} = 0.25$, $X_{\text{CsCl}} = 0.75$, the departures are 4.6, 0.7, and 1.6%, respectively, in comparison with the experimental unfitted data in binary systems by Zuca and Olteanu.

Kucharski and Flengas (6) assigned an accuracy of $\pm 2\%$ to their electrical conductivity data, and the values for NaCl and CsCl from Janz *et al.* (4) were given uncertainties of 0.8 and 5.0%, respectively. Thus, the agreement with Kucharski and Flengas is very good. The agreement of this work to the values in Janz *et al.* (4) for NaCl and CsCl is outside the combined error limits. But for NaCl and CsCl, a large difference in values has also been indicated at higher temperatures between the values in Janz *et al.* (4) and Zuca and Ionescu-Vasu (17) for NaCl and Zuca and Olteanu (18) for CsCl.

Discussion

Molar conductivity.—From the data on electrical conductivities, molar conductivities (Δ) were calculated using the standard expression

$$\kappa \Delta_M = V_M \quad [6]$$

where κ is the electrical conductivity and V is the molar volume of the solutions. Molar volumes measured at the same compositions in our previous work (10) were used in these calculations.

The molar conductivities have been calculated at 1075°K using Eq. [6]. Figure 4 shows the molar conductivity as a function of y at five constant t values. There is a trend to lower molar conductivities as t increases. For $t \geq 0.25$, the minimum molar conductivity occurs at about $y = 0.6$. The additivity of the molar conductivity $\Delta_{M(\text{add.})}$ is given as

$$\Delta_{M(\text{add.})} = X_{\text{MnCl}_2} \Delta_{\text{MnCl}_2}^\circ + X_{\text{NaCl}} \Delta_{\text{NaCl}}^\circ + X_{\text{CsCl}} \Delta_{\text{CsCl}}^\circ \quad [7]$$

where $\Delta_{\text{MnCl}_2}^\circ$, $\Delta_{\text{NaCl}}^\circ$, and $\Delta_{\text{CsCl}}^\circ$ are the molar conductivities of pure MnCl_2 , NaCl , and CsCl , respectively.

Let $\Delta \Delta_M$ represent the difference between the molar conductivity of the solution and the additive molar conductivity taken at the same temperature, then

$$\Delta \Delta_M = \Delta_{M(\text{system})} - \Delta_{M(\text{add.})} \quad [8]$$

Figure 5 shows the deviation from additivity, $\Delta \Delta_M$, as a function of y at five constant t values. The deviations are negative and tend to a minimum at y values between 0.6 and 0.67.

The nonzero intercepts at $y = 1.00$ for $t = 0.25$, $t = 0.50$, and $t = 0.75$ are due to the deviations from additivity in the NaCl - CsCl binary.

The dependence of $\Delta \Delta_M$ on composition changes in y shown may reflect the effect of complexing. The forming of a complex is expected to reduce the mobilities of the constituent ions of the complex relative to their states in the pure components, even though the com-

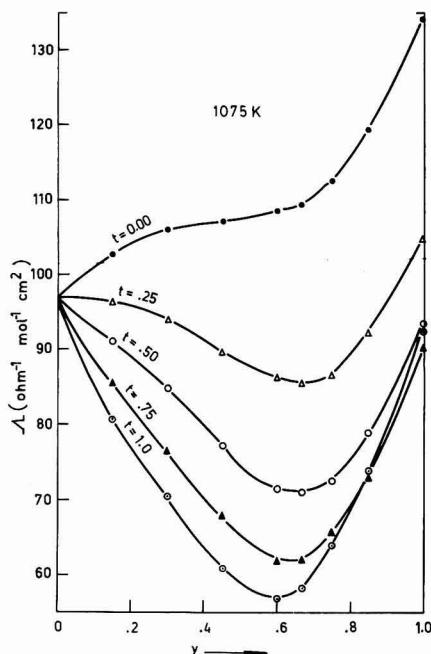


Fig. 4. Molar conductivities in the NaCl - CsCl - MnCl_2 ternary system, as a function of y for constant t values, at 1075°K.

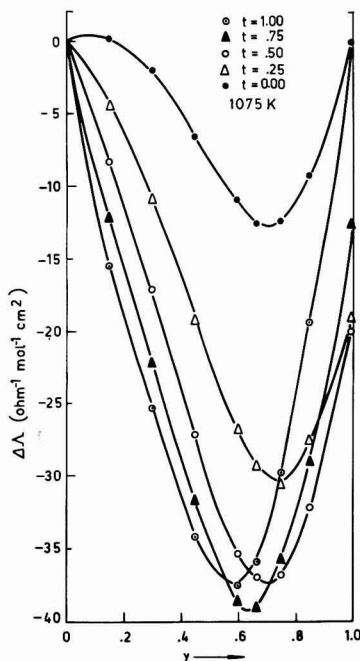


Fig. 5. Deviation from additivity of molar conductivity in the NaCl - CsCl - MnCl_2 ternary system, at 1075°K.

plex species need not be an independent carrier itself. Hence, as MnCl_2 is added to the NaCl - CsCl melt, complexing occurs and $\Delta \Delta_M$ is reduced. Since the excess molar conductivities shown in Fig. 5 indicate minimum values at about $X_{\text{MnCl}_2} = 0.33$, there is evidence for the complex to be of the form MnCl_4^{-2} , particularly in the CsCl -rich melts.

Figure 6 shows the molar conductivity as a function of t for the MnCl_2 - NaCl - CsCl ternary system for eight values of constant y .

Figure 6 indicates that the conductivities of the ternary solutions cannot be generally approximated by the t -fraction average relationship which was followed by the molar volumes in this system (10).

Figure 7 shows the effect of temperature on the molar conductivity in the NaCl - CsCl system. The temperature dependence of the molar conductivities is used to calculate the apparent activation energies for the conductivity at constant pressure, according to the expression

$$\Delta E_{M,p} = -R \left[\frac{\partial \ln \Delta_M}{\partial \frac{1}{T}} \right]_p \quad [9]$$

where Δ_M is given by Eq. [6]. For these calculations, molar volumes were available from our previous work (10).

Table II contains a compilation of the calculated apparent activation energies for molar conductivity for three different temperatures. For certain compositions, data valid in the liquid state had to be extended to temperatures below the liquidus.

In Table II, pure molten MnCl_2 is represented by $y = 0$ for all t values. Pure molten NaCl is given as $y = 1$, $t = 0$, and pure molten CsCl as $y = 0$, $t = 1$. The binary systems MnCl_2 - NaCl and MnCl_2 - CsCl are represented by $t = 0$ and $t = 1$, respectively. Finally, the binary system NaCl - CsCl is given as $y = 1$.

All apparent activation energies are temperature dependent and decrease with increasing temperature,

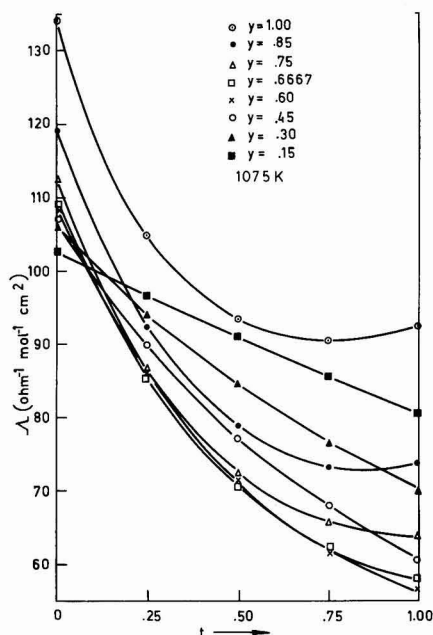


Fig. 6. Molar conductivities in the ternary system NaCl-CsCl-MnCl₂, as a function of t for constant y values, at 1075°K.

as expected. Figure 8 shows plots of the activation energy, $\Delta E_{M,p}$, as a function of the composition parameter t , at a temperature of 1075°K for y values varying between 0 and 1. The data indicate some interesting trends.

For compositions having y values up to 0.45, the activation energies increase as t increases from 0 to 1 and have values of the order of 3000 cal·mole⁻¹, which are close to that for pure molten MnCl₂ (2925 cal·mole⁻¹). In this composition range the solutions are expected to contain "unreacted" MnCl₂ in excess and its presence appears to dominate the activation process.

For compositions having y values between 0.667 and 1.00, the solutions are characterized by activation energies which are almost independent of y and show a more pronounced change with respect to t , as compared to compositions having low y values.

Accordingly, in Fig. 8 all compositions between $y = 0.667$ and $y = 1.00$ are represented by a single dotted line. This line is also followed by the results for the binary system NaCl-CsCl which are shown by $y = 1$. The similarity between the activation energy values for compositions between $y = 0.667$ and $y = 1$

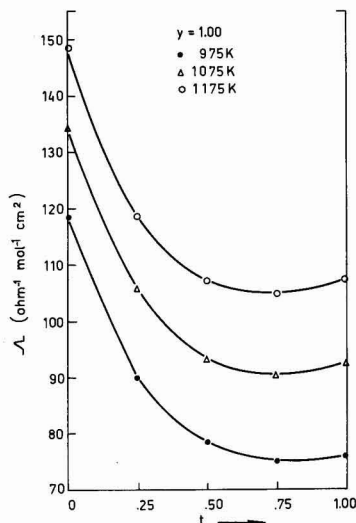


Fig. 7. Molar conductivities of the NaCl-CsCl binary system as a function of t , at three temperatures.

suggests that the alkali chlorides present dominate the over-all activation process.

According to the complex ion model, the solutions in this composition range are expected to contain "unreacted" alkali chloride and the amount of the free MnCl₂ should be at a minimum.

It may be concluded that the presence of complex species in these melts has very little effect on the activation processes which determine the temperature dependence of their electrical conductivity. On the contrary, the formation of complexes in a molten solution has the significant effect of decreasing its total electrical conductivity.

Acknowledgments

The authors would like to acknowledge the financial assistance of the International Nickel Company of Canada Limited and of the National Research Council of Canada.

Manuscript submitted Aug. 9, 1978; revised manuscript received Feb. 24, 1979.

Any discussion of this paper will appear in a Discussion Section to be published in the June 1980 JOURNAL. All discussions for the June 1980 Discussion Section should be submitted by Feb. 1, 1980.

Publication costs of this article were assisted by the University of Toronto.

Table II. Apparent molar activation energies at various temperatures and compositions (cal mole⁻¹)

y	$t = 0$			$t = 0.25$			$t = 0.50$			$t = 0.75$			$t = 1.0$		
	975°K	1075°K	1175°K	975°K	1075°K	1175°K	975°K	1075°K	1175°K	975°K	1075°K	1175°K	975°K	1075°K	1175°K
0	3050	2925	2820	3050	2925	2820	3050	2925	2820	3050	2925	2820	3050	2925	2820
0.15	3050	2930	2825	3175	3040	2900	3250	3100	2950	3425	3225	3050	3120	3350	3600
0.30	3050	2725	2490	3200	2950	2700	3330	3000	2650	3450	3100	2775	3550	3200	2850
0.45	2950	2675	2380	3175	2700	2250	3180	2825	2630	3300	3125	2850	3375	3250	3120
0.60	2825	2600	2290	3100	2810	2700	3360	3270	3200	3660	3620	3610	3950	3850	3820
0.667	—	—	—	3110	3025	2925	3530	3450	3400	3900	3800	3750	4200	4025	3925
0.75	2475	2475	2470	3100	3000	2875	3660	3525	3450	4000	3830	3760	4150	4000	3925
0.85	2530	2500	2425	3260	3100	2925	3725	3550	3380	4030	3825	3675	4100	3920	3750
1.00	2625	2550	2450	3210	3125	3025	3750	3550	3375	3980	3750	3560	4300	3875	3500

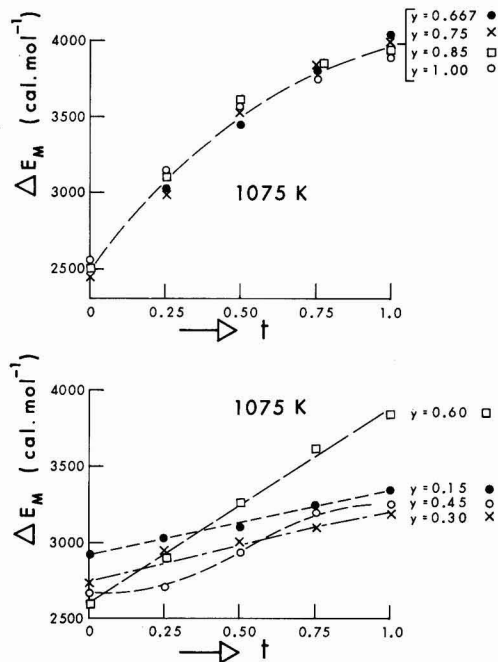


Fig. 8. Plots of the molar activation energies, ΔE_M , vs. t for y values varying between 0 and 1. Temperature is 1075°K. Single dotted line in upper diagram represents all four y compositions shown.

REFERENCES

1. J. W. Tomlinson, in "Physicochemical Measurements at High Temperatures," J. O'M. Bockris,

- J. L. White, and J. D. Mackenzie, Editors, pp. 247-275, Butterworths, London (1959).
2. G. J. Janz and R. D. Reeves, in "Advances in Electrochemistry and Electrochemical Engineering," Vol. 5, C. W. Tobias, Editor, pp. 137-204, Interscience Publishers, New York (1967).
3. C. Solomons, in "Physicochemical Measurements in Metals Research," Vol. 4, Part 2, R. A. Rapp, Editor, pp. 35-122, Interscience Publishers, Toronto (1970).
4. G. J. Janz, F. W. Dampier, G. R. Lakshminarayanan, P. K. Lorenz, and R. P. T. Tomkins, "Molten Salts, Vol. 1, Electrical Conductance, Density and Viscosity Data," (NSRDS-NBS15), National Bureau of Standards, Washington, D.C. (1968).
5. A. S. Kucharski and S. N. Flengas, *This Journal*, **119**, 1170 (1972).
6. A. S. Kucharski and S. N. Flengas, *ibid.*, **121**, 1298 (1974).
7. S. N. Flengas and A. S. Kucharski, *Can. J. Chem.*, **49**, 3971 (1971).
8. S. N. Flengas and J. M. Skeaff, *ibid.*, **50**, 1345 (1972).
9. D. R. Sadoway and S. N. Flengas, *This Journal*, **122**, 515 (1975).
10. N. R. Carmichael and S. N. Flengas, *ibid.*, **126**, 2098 (1979).
11. G. Jones and B. C. Bradshaw, *J. Am. Chem. Soc.*, **55**, 1780 (1933).
12. R. Colton and J. H. Canterford, "Halides of the First Row Transition Metals," p. 230, Wiley-Interscience, Toronto (1969).
13. E. R. van Artsdalen and I. S. Yaffe, *J. Phys. Chem.*, **59**, 118 (1955).
14. K. Grjotheim, R. Nikolic, and H. A. Øye, *Acta Chem. Scand.*, **24**, 489 (1970).
15. I. S. Yaffe and E. R. van Artsdalen, *J. Phys. Chem.*, **60**, 1125 (1956).
16. I. G. Murgulescu and S. Zuca, *Rev. Roum. Chim.*, **4**, 227 (1959).
17. S. Zuca and I. Ionescu-Vasu, *ibid.*, **12**, 1285 (1967).
18. S. Zuca and M. Olteanu, *ibid.*, **15**, 357 (1970).

Concentration Changes in Porous Zn Electrodes during Cycling

Drannan C. Hamby,* Nancy Jo Hoover, Jeffrey Wirkkala,¹ and Debbie Zahnle²

Linfield Research Institute, Linfield College, McMinnville, Oregon 97128

ABSTRACT

Concentration changes which occur in porous zinc secondary electrodes during cycling have been measured. Changes occurring within cycles are similar to those postulated in the convective flow theory of zinc secondary electrode shape change (1). The drastic cumulative changes in concentration as cycling progresses predicted by the theory were not observed in the cells studied. Overpotential measurements taken during cell operation have been compared with values of concentration overpotential calculated on the basis of the observed concentration changes. Failure of the experimental overpotentials to correlate with the calculated values is discussed.

The porous zinc electrode in a zinc-silver oxide secondary cell with "normal" convection has been modeled in the "y" direction (see Fig. 1) by Choi, Bennion, and Newman (1).³ The model was used to predict several observable properties associated with cell operation as functions of the y dimension and time, e.g., volume

average fluid flow rates, material distribution over the electrode, and cumulative concentration variations at the ends of cycles as cycling progresses. Also, cumulative changes in cell terminal potential difference at the ends of half-cycles due to resistive overpotential were predicted as a function of number of cycles.⁴ It was predicted that decreasing the membrane-pumped convective flows in these cells would decrease the rate of development of shape change of the zinc electrode.

* Electrochemical Society Active Member.

¹ Present address: Adtek Corporation, Newberg, Oregon.

² Graduate Student, Department of Chemistry, University of Oregon.

Key words: electrolyte, battery, convection, electroosmosis.

³ Normal convection: convection similar to that in commercial cells which use similar membrane separators:

⁴ The Choi, Bennion, and Newman predictions published in Ref. (1) are based on the properties of the RAI P2291 cation exchange membrane.

Several of these predictions have been tested experimentally and the results published (2, 3). In this paper the results of experiments designed to observe the predicted concentration variations in the y direction in the zinc compartment in zinc-silver oxide cells with normal convection are described. Certain features of the concentration variations during cycles as discussed in the original theoretical paper are confirmed; however, the drastic cumulative concentration effects predicted at the ends of cycles were not observed.

The cell used in these experiments incorporated several Hg-HgO reference electrodes which allowed observation of certain test electrode overpotentials during cell cycling. These overpotentials are described and discussed in terms of anticipated overpotentials based on observed concentration changes and apparent electrode current densities.

Equipment and Procedures

Test and counterelectrodes.—The zinc electrodes used were furnished by AFAPL (Air Force Aero Propulsion Laboratory, Wright-Patterson Air Force Base, Ohio). They came in the discharged state wrapped in Viskon (cellulose rayon) paper and consisted of pressed blended ZnO and HgO on expanded silver screen (3.23×10^{-2} g of Ag/cm²). They were prepared "in house," by Air Force employees according to the procedure described by Keralla (4, 5). They differed significantly from electrodes used in our previous work (2, 3) in that no inert nonconducting binder was included in the electrode mix. These electrodes evolved no measurable quantities of gas during normal cycling. They were approximately 10.2 cm long, 6.4 cm wide, and 0.2 cm thick. The quantity of ZnO present on each electrode was adequate to yield a theoretical capacity, at 100% utilization, in excess of 12 A-hr. The silver electrodes also came in the discharged state. They were of approximately the same apparent surface area, 66 cm², were 0.40 mm thick, and consisted of porous sintered silver (1% palladium) on expanded silver screen. They were prepared according to the procedure of Falk and Fleischer (6). Estimated theoretical capacity of these electrodes at 100% utilization was 6.5 A-hr.

Acrylic electrode holders.—The acrylic holder for the zinc electrode is shown in Fig. 1. It provides a rectangular chamber for the zinc electrode which is just large enough to contain the dry discharged electrode.

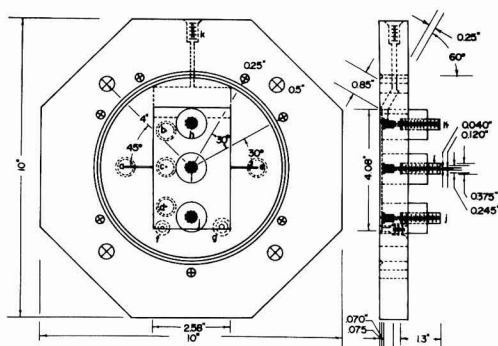


Fig. 1. Front and side schematic views of the acrylic holder for the test electrode. Positions of reference electrodes, a-e, are indicated. Sampling ports are designated h, i, j. The serum cap rubber material is indicated by cross-hatching. Electrode lead port, f; filling port, g. Opening k serves both as a filling port and as a lead through to the capillary for flow measurement during cycling. y axis parallels direction from k to j, z axis parallels a to e, x axis is perpendicular to the page, front view. The test electrode reservoir is immediately above the electrode chamber as shown but also includes volume above in the attached capillary and gas trap.

Five Hg-HgO reference electrodes, the design and preparations of which have been described previously (3), are designated by letters a through e. Electrodes b, c, and d are located behind the test electrode and are connected to the test electrode chamber through small, approximately 1 mm diam, holes in the acrylic walls as indicated in the figure. Electrodes a and e communicate with the fluid in the test electrode cavity between the electrode and the membrane by means of the shallow channels cut into the Lucite (approximately 0.005 in. deep) as shown. Ports g and k are used to evacuate and vacuum fill the cell. After filling is completed, port g is plugged. The sampling ports are designated by letters h, i, and j. An enlarged view of the sampling port design for the cell is shown in Fig. 2.

The acrylic holder for the silver electrode also provides a rectangular chamber just large enough to contain the electrode. Reference electrodes are provided as on the zinc side of the cell; however, no provision is made for sampling the silver compartment. Ports are provided for vacuum filling and for making electrical contact to the electrode as described previously (3).

Both zinc and silver electrode holders have reservoirs at one end as shown by the dotted line in Fig. 1. These communicate through ports similar to k, Fig. 1, with gas burettes and 0.20 cm diam horizontally positioned glass capillary tubes which are used to measure the average rate of gas evolution at each electrode and the volumetric fluid flow rates as described previously (2, 3). The cell is, therefore, almost identical in design to the experimental cell described by Choi (1, 2). It differs in the inclusion of the sampling ports, the reference electrodes, in the provision of larger volumes of reagents in the gas burettes above the reservoirs, and in membrane materials as described below. The cell differs from Choi's model in these same respects and also in that the real zinc electrodes are wrapped in Viskon paper which was not reflected in the model. The cell was operated with the electrodes positioned vertically and the reservoirs located above the electrodes. During cycling the electrode compartments and reservoirs were filled with fluid and the gas burettes and capillary tubes were partially filled; thus, both electrodes were operated flooded and with head space. As shown in Fig. 1 a large O ring, laid into a V groove surrounding the zinc electrode seals the cell when the zinc and silver electrode holders are bolted together with six 0.25 in. bolts. O rings are used for seals at reference, filling, and lead ports.

Sampling of cell fluid and analysis.—Sampling was done with a sharp beveled syringe which penetrated the serum cap (shown in Fig. 1 and 2) and the electrode to a controlled depth. The syringe sample was transferred to a small diameter (~0.1 cm diam) glass capillary tube; one end of the tube was plugged with modeling clay and the sample was spun in an ordinary laboratory centrifuge for 3 min. Immediately after centrifuging the visually clear sample fluid was released onto paraffin-covered paper then taken up in a 5.0 μ liter measuring pipette and transferred to a partially filled volumetric flask containing HCl and Cs⁺

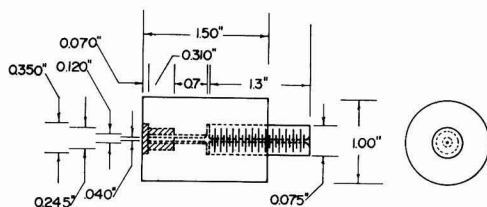


Fig. 2. Expanded view of the sampling port. The rubber serum cap is indicated by cross-hatching. The brass screw for path length adjustment is shown, but not the locking nut.

at 0.25N and 1000 ppm. After making to volume and shaking, the samples were determined by atomic absorption (AA) or atomic emission (AE) spectroscopy. Relative precision of the analysis as determined by repetitive analysis of solution used to fill the cell was $\pm 2\%$ for zinc and $\pm 1\%$ for potassium. Centrifuging methods were checked for effectiveness with standard solutions and no detectable difference could be found between 3, 5, and 15 min centrifuging times on the ordinary centrifuge nor were differences detected between samples centrifuged at the spin rate of the ordinary centrifuge and samples spun at 20,000 rpm on a high speed centrifuge.

Chemical analysis of used electrodes.—The distribution of zinc compounds over the zinc electrode surface after cycling was of interest. After removal from the cell the zinc electrode was sectioned with a sharp narrow scalpel blade and each section was labeled. Care was taken to record the position which the sample occupied on the electrode with respect to the electrode lead and the reference electrodes. Each section was treated with excess 6N HCl to dissolve the zinc, all solid zinc compounds, and materials in solution in the fluid trapped in the pores of the electrode. The resulting solutions were made to known volumes from which aliquots were taken, and Zn was determined by common EDTA titration. The results are reported in terms of ZnO (7). The silver screen from each section was dried and weighed.

Electrical equipment and measurements.—All cell-cycling experiments were carried out at constant current. Potential differences across the working cell terminals, i.e., between the zinc test and silver electrode, were recorded continuously (± 20 mV). A Flexopulse Hg 108A6,⁵ repeat-cycle timer, was used as a reversing switch which allowed continuous variation in cell charge and discharge times. The switch also allowed for brief intervals of a few minutes duration with no cell current between half-cycles. Potential differences between the various reference electrodes and the working electrodes were monitored periodically (± 2.0 mV) using a second channel of the high impedance recorder connected sequentially to different pairs of electrodes by an Eagle Signal Model MT-19 Step Switch⁵ controlled by another repeat-cycle timer. A small commercial Zn-HgO primary cell was used as a bucking potential in the reference electrode to zinc electrode circuit to allow the use of a more precise scale on the recorder.

Electrolytic solution.—The solution used for filling the cells was prepared from singly deionized distilled water and reagent grade chemicals. KOH was first dissolved in water to prepare a concentrated solution. This solution was diluted to a specific gravity of 1.40 at 20°C. Fine grained reagent grade ZnO was then added in excess of the amount required to saturate the solution, and magnetic stirring was continued for several days. The solution with excess crystalline ZnO was stored in tightly capped polyethylene bottles. Potassium and zinc concentrations in this solution were measured at $9.5 \pm 0.1F$ and $1.13 \pm 0.02F$, respectively, by AE and AA.

Cell filling.—The filling procedure in each case involved evacuation of the cell and rubber filling lines by mechanical pumping followed by slow simultaneous vacuum filling of the compartments with solution from a common reservoir. Following return of pressure in the filled cell to atmospheric, the cell was left to soak for at least 24 hr before the appropriate ports were plugged and cycling was begun.

Treatment of data.—Because it is difficult to measure the dimensions of the samples accurately and because of total weight differences between different elec-

trodes, the collector screen material is used to normalize the data. The normalization ratio used for each sample is

$$\frac{Q_{ZnO}}{Q_{ZnO^*}} = \left[W_{ZnO^1} / \left(W_{cs^1} 66.0 \text{ cm}^2 / \sum_i W_{cs^1} \right) \right] / \left[\sum W_{ZnO^1} / 66.0 \text{ cm}^2 \right]$$

where W_{ZnO^1} = weight of total zinc expressed as zinc oxide, sample i, and W_{cs^1} = weight of collector screen, sample i. The ratio, Q_{ZnO}/Q_{ZnO^*} , compares the ZnO per unit area at a particular position on the electrode with the average value for the electrode as a whole and serves as a measure of electrode uniformity.

Separator system, cell assembly, and precycling treatment.—The separator system in the cell consisted of one layer of 0.001 in. dynel between the silver electrode and the RAI membranes. Two layers of RAI P2291 40/30 were used as a dendritistic membrane and a layer of Viskon paper, 0.004 in. thick, separated the zinc electrode from the RAI membrane. Only the Viskon was wrapped around the zinc electrode, the other separator layers were simply in the form of flat sheets which overlapped the closing O ring.

After filling, the cell was charged to 2.4 A-hr at 0.10A followed by three 2.0 A-hr half-cycles at the same rate. After a brief evacuation and return to atmospheric pressure, the filling ports were sealed and the gas burettes and flow tubes attached.

Data-taking schedule.—Based on the predictions of Choi *et al.* (1) fluid samples were taken from each sampling port before cycling began at the 1.00A rate and at the ends of each of the first eight complete cycles. Volume average fluid flow rates were measured during cycle six and again during cycle sixteen for comparison with flow behavior previously reported in a similar cell (2).

After eight cycles and again after the sixteenth cycle, the cell was allowed to relax for over 16 hr and then cycling was resumed. Subsequently the cell was cycled until the 40th cycle after which it was opened, the zinc electrode removed, sectioned, and analyzed. Sampling of the zinc electrode compartment within the cycles was carried out during cycles 11, 16, 29, and 40.

Results

There was no measurable gas evolution detected during normal cycling of the cell. Average volumetric fluid flow rates measured during cycle 6 are shown in Fig. 3.

Zinc and potassium concentrations in the zinc compartment before cycling began at the 1.00A rate and at the ends of cycles one through eight are compared with Choi's predictions in Fig. 4 and 5. Zinc concen-

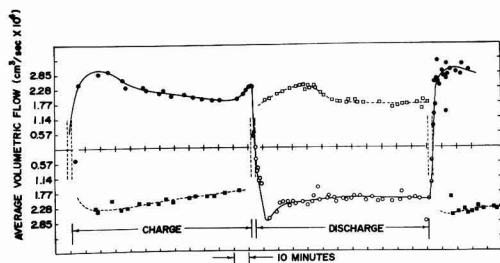


Fig. 3. Cycle 6, average volumetric flow rate data. Zn compartment: ●, charge; ○, discharge. Ag compartment: ■, charge; □, discharge. Positive flow indicates flow from the electrode into the electrode reservoir and capillary.

⁵ Eagle Signal, 736 Federal Street, Davenport, Iowa 52803.

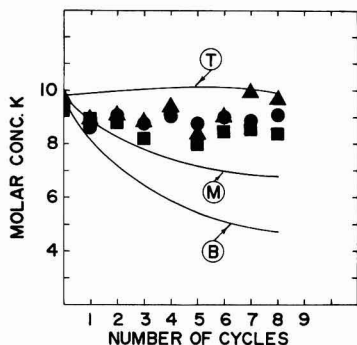


Fig. 4. Volume average molar concentration of potassium ion before cycling began and at the ends of cycles one through eight. The lines indicate the predicted concentrations [Choi *et al.* (1)] at top T, middle M, and bottom B of the cell at the ends of cycles. Experimental values at the top \circ , middle \blacksquare , and bottom \blacktriangle ports of the cell are shown.

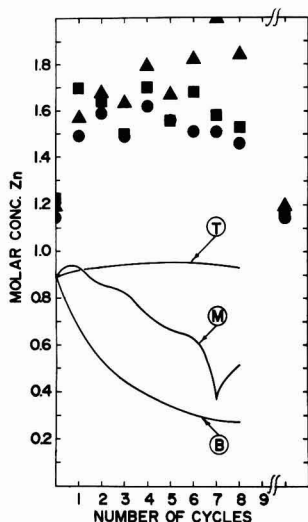


Fig. 5. Volume average molar concentrations of zinc before cycling began, after relaxation, and at the ends of cycles one through eight. The lines indicate the predicted concentrations [Choi *et al.* (1)] at the top T, middle M, and bottom B, of the cell at the ends of cycles. Experimental values at the top \circ , middle \blacksquare , and bottom \blacktriangle ports of the cell are shown.

trations after relaxation are shown for comparison with initial values.

Zinc and potassium concentrations measured within cycles are shown in Fig. 6 through 11.

ZnO distribution data for the zinc electrode is shown in Fig. 12 and 13. The electrode was cut into 30 sections with 10 cuts perpendicular to the y axis and 3 cuts parallel to the y axis. The distribution data shown in Fig. 12 have been summarized in Fig. 13 in order to compare it with the data of Choi *et al.* (2).

Summarized potential differences vs. time data are shown in Fig. 14 for cycle No. 11, three cycles after a 24 hr relaxation period. Concentration data were taken as indicated in the figure caption. Analysis of the potential vs. time data for all cycles indicated the characteristics listed below. Many of the listed characteristics are illustrated by the data in Fig. 14 and 15. The reader is cautioned that these two figures are un-

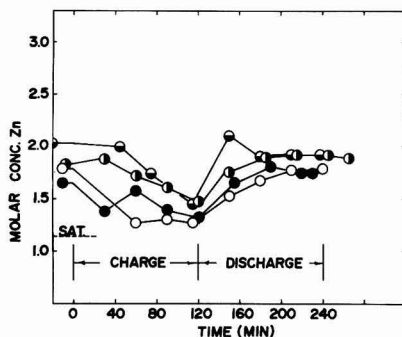


Fig. 6. Experimental values of volume average Zn concentrations at the top (h) sampling port during several cycles. Points \circ , \bullet , \ominus , and \odot refer to cycles 11, 16, 29, and 40 which were three, eight, thirteen, and twenty-three cycles since cell relaxation, respectively.

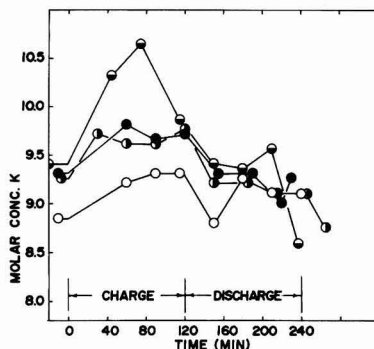


Fig. 7. Experimental values of volume average K ion concentrations at the top (h) sampling port during several cycles. Points \circ , \bullet , \ominus , and \odot refer to cycles 11, 16, 29, and 40 which were three, eight, thirteen, and twenty-three cycles since cell relaxation, respectively.

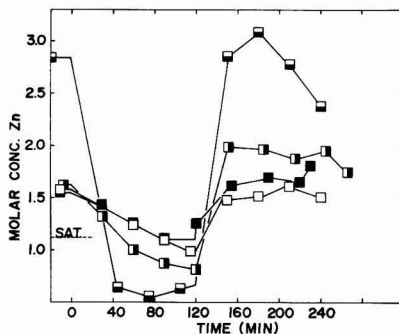


Fig. 8. Experimental values of volume average Zn concentrations at the middle (i) sampling port during several cycles. Points \square , \blacksquare , \boxminus , and \boxplus refer to cycles 11, 16, 29, and 40 which were three, eight, thirteen, and twenty-three cycles since cell relaxation, respectively.

usual in that time flows from right to left on the abscissas.

1. Overpotentials measured between the test electrode and references b, c, and d located behind the test electrode were remarkably uniform at about 10-15 mV during that portion of the charge half-cycle

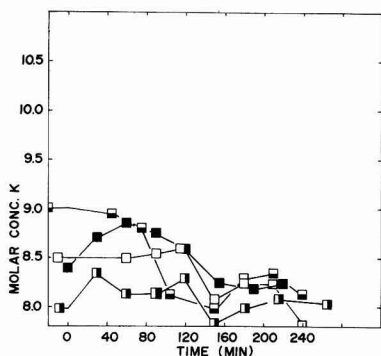


Fig. 9. Experimental values of volume average K ion concentrations at the middle (i) sampling port during several cycles. Points \square , \blacksquare , \square , and \blacksquare refer to cycles 11, 16, 29, and 40 which were three, eight, thirteen, and twenty-three cycles since cell relaxation, respectively.

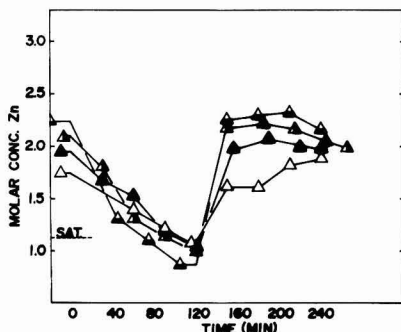


Fig. 10. Experimental values of volume average Zn concentrations at the bottom (j) sampling port during several cycles. Points \triangle , \blacktriangle , \triangle , and \blacktriangle refer to cycles 11, 16, 29, and 40 which were three, eight, thirteen, and twenty-three cycles since cell relaxation, respectively.

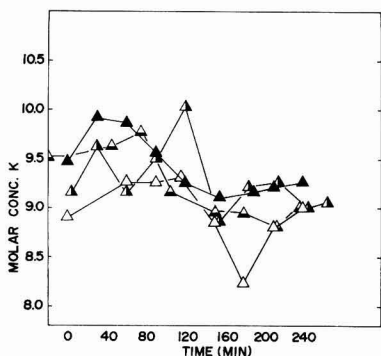


Fig. 11. Experimental values of volume average K ion concentrations at the bottom (j) sampling port during several cycles. Points \triangle , \blacktriangle , \triangle , and \blacktriangle refer to cycles 11, 16, 29, and 40 which were three, eight, thirteen, and twenty-three cycles since cell relaxation, respectively.

when divalent silver oxide was being formed. Inspection of data for later cycles in this region indicates a tendency for the overpotential indicated by electrode c, the one in the middle of the cell, to become smaller than those indicated by electrodes b and d. During

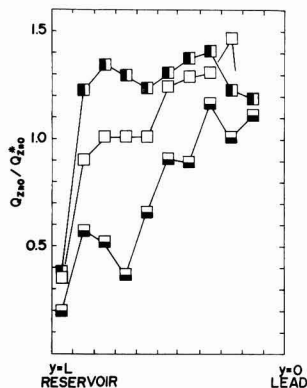


Fig. 12. Normalized ZnO distribution, cell with "normal" convection. Sections from middle of the electrode, \blacksquare ; and from the sides, \square . A uniform unused electrode corresponds to $Q_{ZnO}/Q_{ZnO^*} = 1.0$.

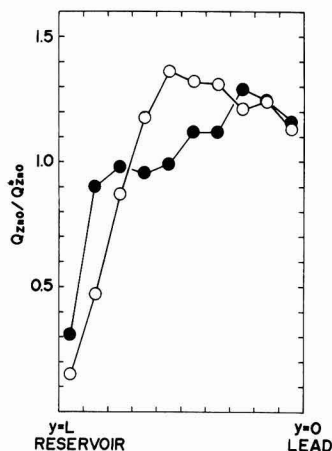


Fig. 13. Normalized ZnO distribution, cell with "normal" convection. This experiment, \bullet ; data of Choi *et al.* (2) \circ .

given half-cycles, this effect reached as great a value as 5 mV.

2. Up to about cycle 30, electrodes b and d consistently indicated test electrode overpotentials of 10-15 mV greater than electrode c during the initial part of the charge half-cycle while monovalent silver oxide was the predominant species being formed. From cycle 30 to 40, electrodes b, c, and d were in closer agreement but c still tended to indicate a smaller test electrode overpotential, ~ 5 mV, than b and d in the monovalent silver oxide formation region.

3. During most of the charge half-cycle, excluding that portion near the change-over from formation of monovalent to divalent silver oxide, electrodes a and e tended to indicate test electrode overpotentials 20-70 mV more negative than those indicated by electrodes b, c, and d; usually the difference was less, near 10 mV, during the early part of the formation of divalent silver oxide tending toward 30-40 mV difference toward the end of the half-cycle. Magnitudes of overpotential exhibited by the electrode pair a to test were generally slightly smaller (5-10 mV) than those exhibited by the pair e to test in this region.

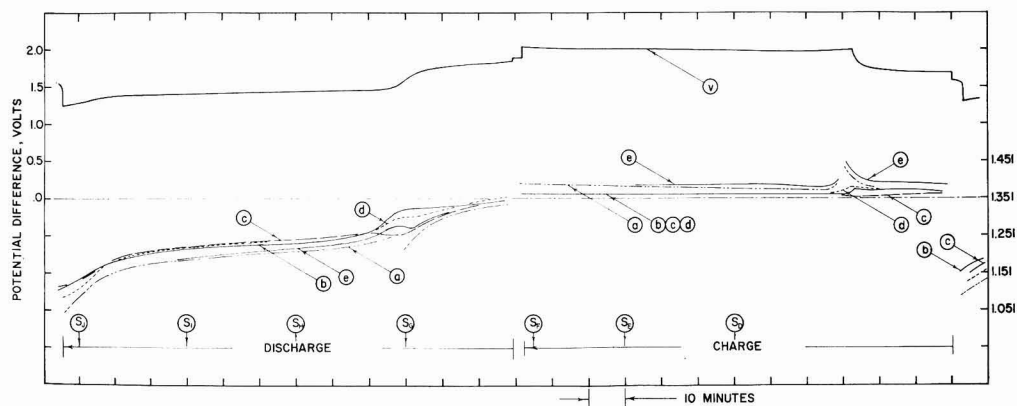


Fig. 14. Potential vs. time data for cycle 11. Time flows from right to left. *v* indicates potential difference between zinc test and silver counterelectrode; read from scale on left vertical axis. *a*, *b*, *c*, *d*, *e* indicate potentials measured between designated reference electrodes positioned as shown in Fig. 1 and the zinc test electrode. Read values from scale on right vertical axis. Related values of reference to test electrode potential differences were 1.347V. Letters *S_i* indicate points in time where fluid samples were taken from sampling ports.

4. In the silver oxide transition region where the zinc to silver electrode potential difference increases rapidly, commonly associated with the change-over to predominance of divalent silver oxide formation, the pairs *a* to test and *e* to test commonly indicated noticeably larger overpotentials, commonly 50 mV and at times 100 mV larger, than those indicated by *b*, *c*, and *d* (see Fig. 15).

5. Throughout the testing of the cell the test electrode overpotentials were generally larger in magnitude in the discharge region than in the charge region, i.e., commonly reaching over 100 mV and exhibiting greater changes than on charge; e.g., changing from near zero overpotential at the start of discharge to as much as 200 mV near the end of discharge. From cycles 1 to 20 the overpotential between electrode *c* and the test electrode was commonly 10 mV less near the end of discharge than electrodes *b* and *d*. After cycle 20 this trend reversed with *c* commonly indicating a higher overpotential, i.e., about 10 mV by the end of discharge.

6. During the discharge half-cycle difference between the behavior of *a* and *e* to test electrode potential differences and *b*, *c*, *d*, to test electrode potential differences were fairly regular, beginning at approximately 10-30 mV near the start of the half-cycle and increasing to 30 to over 50 mV near the end of the half-cycle.

7. At the transition from divalent to monovalent silver on discharge, the pair *a* to test commonly indicated, for a short time, a change to greater overpotential. To a lesser extent the pairs *c*, *d*, and *e* to test exhibited this same effect.

8. The data for early cycles and the data for late cycles are remarkably similar indicating that cycling of this cell could probably have been successfully continued.

Discussion

Our primary intent in this experiment was to test assumptions involved in the convective flow theory regarding concentration changes which occur within cycles and predictions made on the basis of the theory concerning cumulative concentration changes at the ends of cycles as cycling proceeds. Therefore, the physical design of the cell used in the experiment approximated, as closely as possible, that postulated in the theory and used in previous experiments (1,2).

Because of variability observed in the properties of membrane materials from batch to batch, it was believed important to establish close similarity of membrane materials used in this and earlier experiments. Volume average fluid flow rates under the same conditions of current density were chosen to provide the comparison.

Volume average fluid flow rates and features of the behavior of the flows at the ends and beginnings of half-cycles which may be compared with those of Choi *et al.* (2) are illustrated in Fig. 3. Both sets of data show the sharp changes in flow rates at ends and beginnings of half-cycles which have been interpreted as indicating the importance of electroosmotic driving forces. The magnitudes of the observed flows are very similar to those reported by Choi *et al.* (about 2×10^{-4} cm³/sec in the region of steady flow) at the same nominal current density of 15 mA/cm², leading us to conclude that membrane transport parameters were similar in the two cases. Experience with the flow measurements has led us to believe that the sharpness of the changes in flow rates at the ends and beginnings of half-cycles are typical of cells in which the electrodes are tightly packed so that membrane flexing is not extensive. Thus, the flow data also indicate that packing in the present cell was similar to that in the cells of Choi *et al.*

The concentration data in Fig. 4 and 5 indicate a discrepancy between predicted and observed cumulative concentration changes at the ends of cycles. As shown in Fig. 5 the solution was rapidly supersaturated with zincate on initiation of cycling and the supersaturation as measured at ends of cycles relaxed only after several hours with no cell current. Sample sizes taken from the cell were 10 μ liters, a size which would have essentially drained an electrode area of 0.1 cm² of solution. Thus, the measured quantities are recognized to be volume average quantities, as are the predicted values. These numbers are not offered as being typical of concentration values in individual pores.

Failure to observe the predicted large cumulative decreases in concentrations as cycling proceeded may be attributable to physical differences between the actual cell and the cell as modeled (1, 8). In particular, the larger reservoir volumes in the actual cell could be a factor since these volumes are coupled

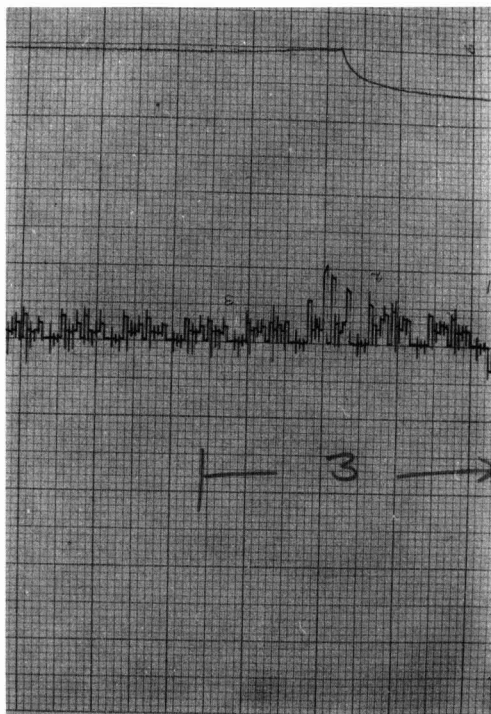


Fig. 15. Potential vs. time data for cycle 3 during the change from predominantly monovalent to predominantly divalent silver oxide at the positive. Time flows from right to left. The upper continuous line is the record of potential difference between the working electrodes. The broken line is the record of potential differences between the references and the test zinc electrode. Both pens are center zeroed. Chart scales for the two sets of data are different; for the continuous line, major chart divisions are 0.5V; for the broken line, major chart divisions are 100 mV. Due to inclusion of the bucking potential difference in the reference electrode measurements, the values should be read 1.351V plus the potential indicated by the recorder. Relaxed potential differences between reference electrodes and zinc electrodes are 1.347V. Reference sequence from right to left in the figure is a, b, c, d, e, open, a, b, c, d, e, open, open, open, open, open, repeat.

by the volumetric flows to the fluid in the Viskon paper next to the RA1 membrane. The possibility of channeling and enhanced mixing of fluid in this region should not be ignored.

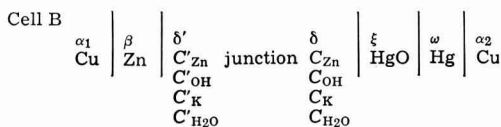
The data shown in Fig. 6-11, observed concentration changes during particular cycles, do reflect the kinds of trends within cycles postulated by the convective flow theory. The data also indicate a magnification of concentration effects as cycling proceeds with especially pronounced effects near the center and bottom of the electrode. Although Choi's computer codes did predict concentration changes within cycles, they have not been reported; therefore, within cycles, the data can only be compared with qualitative assumptions related to the theory.

A third comparison between the experiments reported here and the experimental and theoretical work of Choi *et al.* (1, 2) may be made with respect to material redistribution. Values of Q_{ZnO}/Q_{ZnO^*} in Fig. 12 indicate a substantial migration of active material from the reservoir end of the electrode toward the middle and lower end but also a movement from the sides toward the middle, i.e., the classic shape change pattern (the pattern was also reflected on the

silver counterelectrode). The data are averaged in Fig. 13 and compared with Choi's data. The migration of material away from the reservoir end of the electrode is in accord with predictions of the convective flow theory. Differences which do exist in the two sets of results may be related to the larger reservoir volume in the present case which would tend to moderate large fluctuations in electrolyte concentration at the reservoir end of the electrode. The movement of material from the sides toward the middle of the electrode was not predicted by the convective flow theory nor was it observed in the earlier work of Choi *et al.*, however this could be due to the different pattern of electrode sectioning. Finally, the initial physical uniformity of given electrodes is always questionable. Single electrodes from batches have been destructively tested for uniformity of material distribution but this does not guarantee the physical uniformity of a given test electrode.

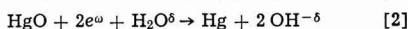
According to the convective flow theory, concentrations in the cell are a function of y dimension only and it would follow that concentration overpotential would be a function of y dimension only. In designing this cell, the reference electrodes were placed with the thought in mind that electrodes b, c, and d would give indications of concentration overpotential as a function of y dimension over the zinc electrode. It was assumed that activation overpotential would be only a few millivolts, at most, at the low nominal current densities used in these experiments (9). Because of cell geometry it was assumed that patterns of current distribution would be such that only negligible IR drops would be included in the measured b, c, or d to test electrode potential differences,⁶ and that overpotentials at b, c, and d would correspond to electrolytic solution samples taken from ports h, i, and j at approximately the same y dimension levels in the cell (see Fig. 1 for relative positions of sampling ports and reference electrodes).

Concentration overpotential or changes in concentration overpotential as indicated by potential differences between the various reference and test electrodes may be discussed in terms of the cells B and B'



Cell B' is the same as B except concentrations in the zinc compartment solution are different; the liquid phase in the zinc compartment is designated δ' and concentrations are C'_{Zn} , C'_{OH} , C'_K , and C'_{H_2O} , where C_{Zn} \equiv concentration of zincate, $Zn(OH)_4^{2-}$; C_{OH} \equiv concentration of hydroxide, OH^- ; C_K \equiv concentration of potassium, K^+ ; and C_{H_2O} \equiv concentration of water, H_2O .

The half-reactions are



The equilibrium between $Zn(OH)_4^{\delta'}$ and ZnO is not considered here because the data indicate (common existence of long-lived supersaturated zincate solutions) that these species are not equilibrated.

Designating the difference of electrical potential between phases α_1 and α_2 as U we may write

$$FU = \mu_a^{\alpha_1} - \mu_a^{\alpha_2} \quad [3]$$

where μ_a is the electrochemical potential of one mole of electrons in the phase designated by the superscript.

⁶ Recent experimental results have left little doubt that large IR drops are included in these measurements. These results will be reported in a following paper.

One can use Eq. [3] and appropriate conditions of local equilibrium to derive expressions for cell voltages U_B , or U'_B as functions of potassium, hydroxyl, zincate, and water concentrations and their activity coefficients. Differences, $U'_B - U_B$, yield expressions from which concentration overpotential or changes in concentration overpotential can be estimated for comparison with measured changes in total overpotential. Using the procedure outlined above, it can be shown that

$$U'_B - U_B = \frac{2RT}{F} \ln \left[\frac{C_{OH^{\delta'}} f_{KOH^{\delta'}}}{C_{OH^{\delta}} f_{KOH^{\delta}}} \right] - \frac{RT}{2F} \ln \left[\frac{C_{Zn^{\delta'}} f_{\pm}^{\pm} K_{2Zn(OH)_4}}{C_{Zn^{\delta}} f_{\pm}^{\pm} K_{2Zn(OH)_4}} \right] + \Delta\Phi_B - \Delta\Phi_B \quad [4]$$

where f^{\pm} mean ionic activity coefficient of the species. The expression given by Boden (10) has been used to calculate the mean ionic activity coefficients as functions of ionic strength in these solutions. The third and fourth terms in [4] have been neglected. Additional comments about these terms are offered below.

The results for cycle 11 are shown in Table I. In the calculations, concentrations at sampling time D, midway through the charge half-cycle, are taken to represent those in phase δ' .

For instance, consider sampling port h and the electrode pair consisting of reference electrode b and the test zinc electrode; the potential difference exhibited by the pair at sampling time D has been taken as a reference value characteristic of concentrations in phase δ' . At later sampling times, E, F, G, etc., concentrations of the zinc electrode have changed to values characteristic of phase δ'' and changes in the potential difference for the same pair have then been calculated on the basis of Eq. [4] and the measured concentration changes at sampling port h. These calculated changes are then compared with observed changes which are listed in the next column.

As shown in Table I, the predicted changes during charge are small as are the observed changes. The correlation between predicted and observed values is not good. In the region of cell discharge there is no agreement between the calculated and measured values leaving little doubt that concentration overpotential is not the dominant factor in this region.

The factors which have not been included in the above computations of concentration overpotential, i.e., the third and fourth factors in Eq. [4] can be estimated using the Henderson approximation (11). The estimated contributions of these additional terms are only a few millivolts, certainly not of the magnitude of the discrepancies between theory and observation on discharge which amount to hundreds of millivolts. Similarly, using electrode kinetic data as reported by Bockris and Nagy (13) one would predict activation overpotentials at these apparent current densities of only a few millivolts. An obvious explanation of the

observed discrepancies is that concentrations in the cell are not simply functions of the y dimension as postulated by the convective flow theory. Other related possibilities include nonuniform current densities over the electrode, i.e., higher current densities in active locations than that calculated by dividing total cell current by apparent electrode area. Reasons for nonuniform current distribution could be several, including channeling of fluid flows, nonuniform electrode construction, thin film passivation, pore plugging through product deposition, and loss of contact of active zinc from the current collector (12, 14-17).

It has been suggested (18) that closer study of the rate of decay of overpotential when cell current is terminated could shed light on the causes of the large overpotential on discharge. As illustrated in Fig. 14, at the termination of each half-cycle, a large fraction of the total cell overpotential decays within the response time of the recorder (time for full scale deflection, 0.5 sec) indicating a resistive effect. However, it is also clear that zinc electrode overpotential is not symmetrical between charge and discharge as would be expected for a simple resistive effect. The interpretation of transient overpotential data in porous electrode systems is not simple (19) and we are unable at this time to use the available data to attribute particular fractions of observed overpotentials to specific processes.

It was anticipated that comparisons of potential differences between reference electrodes a and e and the test electrode with those of the other three reference electrodes with respect to the test electrode would yield comparative data on overpotential at the front and back of the test electrode. Overpotentials as indicated by a and e were consistently larger than those indicated by b, c, and d and increased as time proceeded during both charge and discharge half-cycles. This observation is in accord with what one would expect on the basis of assumed conductivity decreases (increasing potassium hydroxide concentration) in the zinc compartment on charge; however, during discharge when conductivity should be increasing, the opposite effect was not observed. The data suggest that the larger overpotentials indicated by references a and e, at times, simply reflect higher current densities at the edges of the zinc electrode. This latter possibility would be more in accord with observations of the behavior of these electrodes in the time periods when the silver electrode is shifting from predominance of formation of one oxide to the other (Fig. 15). Electrodes a and e indicate strong shifts of current densities to the edges of the zinc electrode when the silver electrode is shifting from a potential characteristic of one oxide to the other. It appears that, on charge, the center of the silver electrode reacts first and, as formation of the monovalent oxide is completed, cell current is shifted to the electrode edges for completion of monoxide formation before the divalent oxide

Table I. Changes in overpotential during cycle 11,* mV

Time designation (see Fig. 14)	Sampling port h, reference electrode b to test		Sampling port i, reference electrode c to test		Sampling port j, reference electrode d to test	
	Calculated change in potential $U'_B - U_B$	Observed change in potential $U'_B - U_B$	Calculated change in potential $U'_B - U_B$	Observed change in potential $U'_B - U_B$	Calculated change in potential $U'_B - U_B$	Observed change in potential $U'_B - U_B$
D	—	Zero by definition	—	Zero by definition	—	Zero by definition
E	-1	+1	+5	-2	+6	0
F	0	+1	+9	-1	+11	+1
G	-8	..	-9	..	-7	..
H	-13	-127	-10	-121	-8	-121
I	-16	-149	-13	-141	-15	-145
J	-17	-219	-10	-228	-16	-248

* See Fig. 10 to relate sampling time designation to sampling times during the cycle.

.. Sampling time G coincided with the changeover from divalent to monovalent oxide, overpotentials show anomalously high values.

formation begins. Once divalent oxide formation begins, current density appears to shift back toward the middle of the electrode and current density again becomes more uniform. On discharge a similar set of events appears to happen in reverse, the current density on the zinc electrode being controlled by the availability of reactant at the silver electrode.

Acknowledgment

This work was performed with financial support from the Department of Energy, under Contract EY-76-S-06-2434. We also wish to thank Professor Douglas Bennion for his continuing interest, valuable discussions, and suggestions.

Manuscript submitted Dec. 27, 1978; revised manuscript received June 6, 1979.

Any discussion of this paper will appear in a Discussion Section to be published in the June 1980 JOURNAL. All discussions for the June 1980 Discussion Section should be submitted by Feb. 1, 1980.

Publication costs of this article were assisted by Linfield College.

REFERENCES

1. K. W. Choi, D. N. Bennion, and J. Newman, *This Journal*, **123**, 1616 (1976).
2. K. W. Choi, D. Hamby, and D. N. Bennion, *ibid.*, **123**, 1628 (1976).
3. D. Hamby and J. Wirkkala, *ibid.*, **125**, 1020 (1978).
4. J. A. Keralla, in "Zinc-Silver Oxide Batteries," A. Fleischer and J. J. Lander, Editors, pp. 183-198, John Wiley & Sons, Inc., New York (1971).
5. D. Pickett, Personal communication.
6. S. U. Falk and A. Fleischer, in "Zinc-Silver Oxide Batteries," A. Fleischer and J. J. Lander, Editors, pp. 199-208, John Wiley & Sons, Inc., New York (1971).
7. R. Giovanoli, H. R. Oswald, and W. Feitknecht, *Helv. Chem. Acta*, **49**, 1971 (1966).
8. K. Choi, Ph.D. Thesis, Department of Engineering, University of California, Los Angeles (1976).
9. J. O'M. Bockris and Z. Nagy, *This Journal*, **119**, 1131 (1972).
10. D. P. Boden, R. B. Wylie, and V. J. Spera, *ibid.*, **118**, 1298 (1971).
11. J. Newman, "Electrochemical Systems," p. 127, Prentice-Hall, Englewood Cliffs, N.J. (1973).
12. W. Sunu, Ph.D. Thesis, Department of Engineering, UCLA (1978).
13. Z. Nagy and J. O'M. Bockris, *This Journal*, **119**, 1129 (1972).
14. R. W. Powers and M. W. Breiter, *ibid.*, **116**, 719 (1969).
15. R. W. Powers, *ibid.*, **116**, 1652 (1969).
16. R. W. Powers, *ibid.*, **118**, 685 (1971).
17. T. Katan, J. R. Savory, and J. Perkins, Abstract 44, The Electrochemical Society, Fall Meeting, Atlanta, Georgia, Oct. 9-14, 1977.
18. F. Will, in "Battery Design and Optimization," S. Gross, Editor, The Electrochemical Society Softbound Proceedings Series, Princeton, N.J. (1979).
19. G. W. Heise and N. C. Cahoon, "The Primary Battery," p. 135, John Wiley & Sons, Inc., New York (1971).

Effect of Hydrogen Evolution on Current Distribution during Electrodeposition at Vertical Electrodes

Richard Alkire* and Po-Yen Lu*¹

Department of Chemical Engineering, University of Illinois, Urbana, Illinois 61801

ABSTRACT

Experiments were carried out at vertical sectioned electrodes on which copper was deposited in the presence of simultaneous hydrogen evolution. By measurement of copper deposited on each electrode section, it was possible to ascertain the local rate of each electrode reaction. The influence of hydrogen evolution on the rate of copper deposition supported the interpretation that two kinds of mass transfer effects occur simultaneously. In one, bubbles produced locally cause stirring on detachment while, in the other, bubbles produced below the point of interest rise upward and thereby cause stirring. A mathematical model was developed to predict the current distribution in cells having nonuniform potential fields. The model included ohmic resistance of electrolyte, Tafel kinetics for hydrogen evolution, mass transfer for copper deposition, and the particular cell geometry under study. Calculations agreed to within 20% of experimental data.

Industrial electrolytic processes often involve reactions which proceed with less than 100% current efficiency owing to gas evolution. Although gas evolution may seem disadvantageous from a current efficiency standpoint, the stirring provided by the gas-
ing may provide considerable enhancement of mass transfer processes near the electrode surface. In chlorate cells, for example, the anodic process is mass transport limited, and the mass transfer coefficient is determined by the rate of gas evolution. In the in-

vestigation reported here, the effect of gas evolution on the current density distribution was studied in order to develop an engineering model for scale-over between systems of different configuration.

The influence of gas evolution on mass transfer at a vertical electrode has been vigorously investigated during the past decade. In the more fundamental studies, gas evolution was carried out in the presence of a simultaneous redox reaction. The average mass transfer coefficient for the redox reaction was determined by measuring the change in concentration ratio of redox agents after a period of steady-state electrolysis. In this manner, studies by Venzel (1) and by Ibl et al. (2, 3) led to development of a penetration

* Electrochemical Society Active Member.

¹ Present address: Gould Laboratories, Rolling Meadows, Illinois 60008.

Key words: gas lift, current distribution, mathematical model, copper deposition, hydrogen evolution.

model for which the mass transfer coefficient for the redox reaction was proportional to the square root of the gas evolution rate. Their work supported the hypothesis that bubble detachment causes very localized flow of solution near the electrode which, in turn, is responsible for mass transfer enhancement. This concept was developed further by Roušar and Cezner (4) in a study of heat and mass transfer at gas-evolving electrodes. Along different lines, Janssen and Hoogland (5-7) proposed a hydrodynamic model by which mass transfer was controlled by upward flow of solution, caused by rising bubbles, as well as by local stirring owing to coalescence of rising bubbles.

While both of the aforementioned processes are evidently operative during gas evolution, the relative importance of each depends on electrolysis conditions in a way which is not yet agreed on. While investigating chlorate cell processes, T. R. Beck (8) found that the rate of hypochlorite oxidation was mass transfer limited and that the mass transfer coefficients resulting from gas bubble disengagement and from convective diffusion were additive, as had Rohsenow (9) for an analogous situation in heat transfer. Meanwhile, Kutateladze (10, 11) found that a different averaging rule gave an improved empirical fit of heat transfer data. Vogt (12) reexamined the early electrolytic data of Roald and W. Beck (13) and found agreement with the averaging rule of Kutateladze.

Mass transfer studies by Fouad and Sedahmed (14-17) have been carried out for various configurations. These authors have suggested that the stirring of electrolyte by gas evolution may be more economical than stirring by forced flow.

In the work reported below (18), copper deposition was carried out in the presence of hydrogen evolution in an electrolytic solution containing 0.01M CuSO_4 and 1.5M H_2SO_4 . The effect of electrolytic hydrogen evolution on the rate of copper deposition was studied by measuring the current distribution along a sectioned electrode. After electrolysis, the amount of copper deposited on each electrode section was determined by an electrochemical method. By this procedure, the current distributions for both copper and hydrogen reactions were found. Measurements were carried out in various cells having different configurations in order to ascertain whether a mathematical model could be developed for predicting gas evolution effects on the behavior of electrolysis cells. This study differed from previous investigations in that (i) direct measurement of local mass transfer rates were made possible by employing metal deposition onto a sectioned electrode, and (ii) mass transfer data were incorporated into a current distribution model to predict behavior of gas evolving cells.

Experimental Apparatus

Two classes of cell configurations, shown in Fig. 1, were investigated. In the cell of the left side, a Teflon cloth (C) permitted passage of current between electrodes but impeded flow circulation between anode and cathode compartments; in this cell, the current distribution along the electrodes was nearly uniform. The cell on the right side of Fig. 1 has an insulator (D) between electrodes so that current was forced to pass around the end of the insulator; in this geometry, the current distribution along the electrodes was highly nonuniform. The upper segment of the right-hand cell (G) extended above the surface of the electrolyte so that current flowed only around the lower end of the insulator (D).

Cells were immersed in a tank having dimensions $12.5 \times 20 \times 37.5$ cm. Various spacer shims (E, F) were used to establish the electrode-separator distance, ranging between 0.318 and 1.90 cm ($\frac{1}{8}$ to $\frac{3}{4}$ in.). Legs of various heights (H) were used to establish the relative position of the cell with respect to the upper and lower surfaces of the electrolyte.

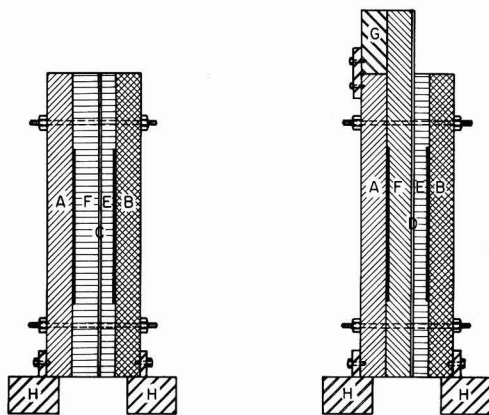


Fig. 1. Cell construction details. Left: A1 configuration for uniform current distribution. Right: A2 configuration for nonuniform current distribution.

The sectioned electrode (B) was prepared in eight sections, each 2×1.5 cm, cast in polystyrene and separated from each other by less than 0.1 cm. The unsectioned electrode (A) had the same over-all dimension, i.e., 2×12 cm. Both electrodes were fabricated by carefully rolling shiny platinum foil (0.010 cm thick) onto smooth copper slabs coated with conducting (silver) epoxy cement.

A constant current power supply (Lambda No. LK351-FMOV) was used for electrolysis. The current passing through each electrode section was found by measuring the voltage across calibrated resistors with a multipoint recorder (Leeds & Northrup Speedomax); the potential difference between electrode sections was less than 10 mV.

Following electrolysis, the amount of copper deposited on each electrode section was measured by anodic stripping chronopotentiometry. The potential/time trace was obtained with use of a constant current power supply (PAR 173) and X-Y time base recorder (Houston 2000). The anodic stripping method was calibrated by preparing platinum foils onto which known weights of copper had been previously deposited by electroplating. The anodic stripping measurements gave results which agreed to within 0.3% of the known weight of copper on the foils.

Experimental Procedure

Electrolytic solution was prepared with reagent grade chemicals and distilled water; the composition was 0.01M CuSO_4 and 1.5M H_2SO_4 . The copper concentration was determined by an ASTM method (19) in which copper is electrodeposited onto a Pt foil from a solution of known volume, and the foil is weighed.

After assembly and immersion of a cell, the electrodes were activated by applying alternately positive and negative potentials as described by Gileadi (20); this procedure was found necessary in order to obtain reproducible behavior. Electrolysis under gas-evolution conditions was usually carried out for a period of 60 sec and was immediately followed by anodic stripping chronopotentiometry of the copper deposit on each electrode section. Electrodes prepared in this manner exhibited reproducible behavior. For example, nine consecutive gas-evolution experiments were carried out at an applied current density of 30.5 mA/cm^2 ; it was found that the total amount of copper deposited varied by less than 0.2% from run to run. At 161 mA/cm^2 , the total amount of copper deposited in nine consecutive gas-evolution experiments varied by less than 0.4%.

Electrochemical behavior of the sectioned electrode was compared with that of the unsectioned electrode in order to observe whether the method of sectioning altered over-all performance. Gas-evolution experiments were thus carried out over a range of current densities between 0.41 and 406 mA/cm²; the amount of copper deposited on the sectioned electrode was found to agree to within 1.2% of the amount of copper deposited on the unsectioned electrode when operated under identical conditions. By direct visual observation, hydrogen evolution on the sectioned electrode appeared to be the same as hydrogen evolution from the unsectioned electrode. There was, for example, no evidence of preferential evolution at the electrode edges between sections.

Experimental Results and Discussion

Owing to the large number of cell configurations studied, it was convenient to adopt a shorthand notation, as in the example A1-2-3-S- $\frac{1}{8}$ - $\frac{1}{2}$. The symbol "A1" denotes that the electrode was assembled as shown on the left side of Fig. 1; the alternative assembly is denoted "A2." The second symbol gives the distance between the upper exit of the electrolyte slot and the solution level in the chamber, in this example 2 cm. The third symbol gives the clearance between the lower entrance of the electrolyte slot and the bottom of the tank, in this example 3 cm. The fourth symbol, S, means that the sectioned electrode was used as the working electrode (cathode); alternatively, we use "U" when the unsectioned electrode was cathodic. The fifth symbol gives the distance between the working electrode and separator, in this case $\frac{1}{8}$ in. The last symbol gives the spacing between counterelectrode and spacer, in this case $\frac{1}{2}$ in.

Effect of gas lift.—In cell A1-3-3-U- $\frac{1}{4}$ - $\frac{1}{4}$, there was 3 cm of electrolytic solution above and below the openings of the catholyte slot in which hydrogen evolution occurs. The gas bubbles thus streamed upward, out of the slot to the free surface where they dissipated. As a consequence of bubble motion, electrolyte was pumped upward through the cathode chamber. In Fig. 2, the total quantity of copper plated in the above cell "with pumping" is shown for two different current densities and for experiments of various duration ranging between 15 sec and 4 min. Under the conditions reported in Fig. 2, the current efficiency of the copper reaction was less than 10%. The quantity j_{H_2} denotes the current density for the hydrogen evolution reaction. These data indicate that the amount of copper plated was proportional to the plating time. Therefore, it may be concluded that steady-state conditions were rapidly established and that they remained unchanged during the periods of electrolysis used in this study. That is, copper did not become depleted from the electrolytic solution during the period of electrolysis. These results also illustrate that, even though deposited under limiting current conditions, the copper adheres to the surface. It was found that with substantially longer periods of electrolysis, the deposit was powdery and loosely adherent; such operating conditions were avoided in this study.

In cell A1-0-0-U- $\frac{1}{4}$ - $\frac{1}{4}$, there was no free electrolyte outside of the catholyte slot so that electrolyte circulation was possible only within the catholyte chamber; Fig. 2 provides results obtained in this cell "without pumping." These data indicate that recirculation of fresh electrolyte by gas lift through the catholyte compartment enhances mass transport of copper.

Effect of electrode inclination.—With cell A1-3-3-U- $\frac{1}{4}$ - $\frac{1}{4}$, studies were conducted at nine angles of inclination, ranging between +60° and -60° with respect to vertical, and at five current densities, ranging between 14 and 243 mA/cm². It was found that the average mass transfer coefficient for a vertical electrode was identical to "overhung" electrodes in which

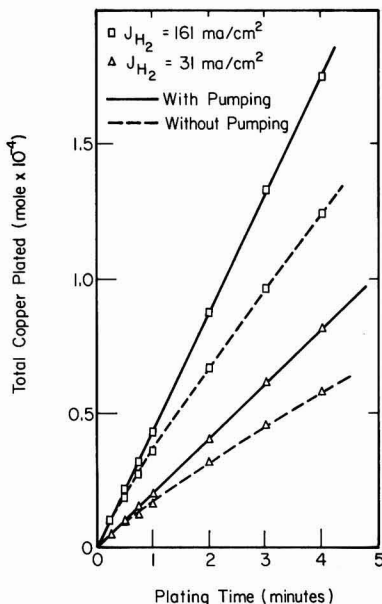


Fig. 2. Comparison of mass transfer rates for cells with and without pumping effect through catholyte compartment.

the gas bubbles continued to scour the electrode surface as they rose along it. For electrodes inclined in repose, the average mass transfer coefficient was 5-10% lower than for vertical electrodes. These results indicate that when the gas is evolved uniformly over the electrode surface (type A1 cells), mass transfer is controlled primarily by microconvection because of bubble detachment, not by macroconvection because of rising bubbles.

With cell A2-3-3-U- $\frac{1}{4}$ - $\frac{1}{4}$, studies were carried out at three angles of inclination between +15° and -15° with respect to vertical and at three current densities between 6.5 and 80 mA/cm². In this cell, gas evolution occurred primarily at the bottom edge of the cathode because of the nonuniform current distribution; the course of the bubble street was found highly dependent on angle of inclination. For overhung electrodes, the bubble street remained very close to the electrode surface during ascent. For electrodes in repose, the bubble street separated from the electrode and rose vertically until it encountered the opposite (insulating) wall of the catholyte chamber. At an inclination of +15° (overhang), the average mass transfer coefficient was about 15% greater than at vertical and about 30% greater than at an inclination of -15° (repose).

These two sets of experiments indicated that the average mass transfer coefficient for the copper reaction depends both on the local rate of gas evolution and on the path of the bubble street rising along the electrode. That is, the reaction rate distribution for the copper reaction can be expected, in general, to depend on the rate distribution of the hydrogen evolution reaction.

Effect of electrode-separator gap distance.—Experiments were conducted with two classes of cells: A1-3-3-U-x- $\frac{1}{4}$ and A2-3-3-U-x- $\frac{1}{4}$, where $x = 0.318, 0.476, 0.635, 0.952, 1.27, \text{ and } 1.90$ cm ($\frac{1}{8}, \frac{3}{16}, \frac{1}{4}, \frac{5}{8}, \frac{1}{2}$ and $\frac{3}{4}$ in.). For each cell, experiments at two current densities (30 and 161 mA/cm²) were carried out, each for 2 min. For both cells, it was found that the average mass transfer coefficient changed by less than 5% on variation of gap spacing.

Effect of electrode height.—Electrode heights of 1.5, 3, 6, and 12 cm were investigated with cell A1-3-3-S- $\frac{1}{2}$ - $\frac{1}{2}$ operated for periods of electrolysis equal to 1 min at nine different current densities. Experimental data are shown in Fig. 3, in which current densities are given for the partial hydrogen reaction (j_{H_2}). These data indicate that the average mass transfer coefficient depends not only on the local hydrogen evolution rate but also on electrode height.

The data in Fig. 3 support the view that there are two kinds of bubbles available for local stirring at any point along the electrode: (i) "Type 1 bubbles," produced locally, which lead to stirring on detachment, and (ii) "Type 2 bubbles," produced below the point of interest, which move past the point of interest at some distance from the surface. Owing to the linear nature of the lines in Fig. 3, we follow T. R. Beck (8) in proposing

$$k_m(y) = k_1(y) + k_2(y) \quad [1]$$

By extrapolation to zero length, the y intercepts in Fig. 3 are proportional to the mass transfer coefficient for type 1 stirring at various hydrogen evolution rates. For current densities above 0.080 A/cm² it was found that

$$k_1 = 0.0066j_{H_2}^{0.53} \text{ cm/sec} \quad [2]$$

where j_{H_2} is expressed in units of A/cm².

This result is in good agreement with the penetration model of Venczel and Ibl (1-3) for which an exponent of 0.5 is expected. Over the range $0.010 < j_{H_2} < 0.080$ A/cm², it was found that data fit the equation $k_1 = 0.0016 j_{H_2}^{0.15}$.

In Fig. 3 it may be seen that the amount of copper plated varied linearly with electrode height and that the slope of the data varied with gas evolution rate. Since the current distribution in Type A1 cells was essentially uniform, these data therefore support the interpretation that the mass transfer coefficient associated with Type 2 bubbles varies linearly with electrode height. By subtracting each y intercept from each data point in Fig. 3 and then plotting the difference vs. j_{H_2} , it was found

$$k_2 = 0.00070j_{H_2}y \text{ cm/sec} \quad [3]$$

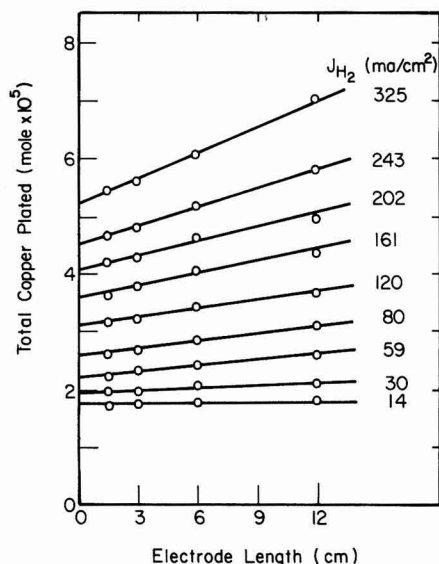


Fig. 3. Effect of electrode height on mass transfer rate for copper deposition in presence of hydrogen evolution. (Electrode area = 24 cm², duration of electrolysis = 60 sec.)

where j_{H_2} is expressed in A/cm² and y is the distance up from the bottom edge, expressed in cm.

The data in Fig. 3 have therefore shown that the over-all mass transfer coefficient for copper plating is

$$k_m = \begin{cases} 0.0066j_{H_2}^{0.53} + 0.00070j_{H_2}y & (\text{for } 0.080 < j_{H_2} < 0.330 \text{ A/cm}^2) \\ 0.0016j_{H_2}^{0.15} + 0.00070j_{H_2}y & (\text{for } 0.010 < j_{H_2} < 0.080 \text{ A/cm}^2) \end{cases} \quad [4]$$

In cases where the hydrogen evolution rate is not evenly distributed along the electrode, then it would be reasonable to modify Eq. [4] to obtain the local coefficient

$$k_m = \begin{cases} 0.0066j_{H_2}^{0.53} + 0.00070 \int_0^y j_{H_2}(y) dy & (\text{for } 0.080 < j_{H_2} < 0.330 \text{ A/cm}^2) \\ 0.0016j_{H_2}^{0.15} + 0.00070 \int_0^y j_{H_2}(y) dy & (\text{for } 0.010 < j_{H_2} < 0.080 \text{ A/cm}^2) \end{cases} \quad [5]$$

The form used in Eq. [5] was employed in the analysis of data taken in Type A2 cells described below for which the current distribution was highly nonuniform.

Effect of gas evolution on current efficiency.—Cells A1-3-3-U- $\frac{1}{2}$ - $\frac{1}{2}$ and A2-3-3-U- $\frac{1}{2}$ - $\frac{1}{2}$ were used to generate the dependence of the average mass transfer coefficient on the average gas evolution rate shown in the upper portion of Fig. 4. It is striking that the difference in mass transfer coefficient between these two cells is no more than 15% even though the current distributions within the cells were very different as shown below. The lower portion of Fig. 4 shows how the current efficiency for copper deposition depended on gas evolution rate for cell A1; these results were calculated from the data presented in the upper por-

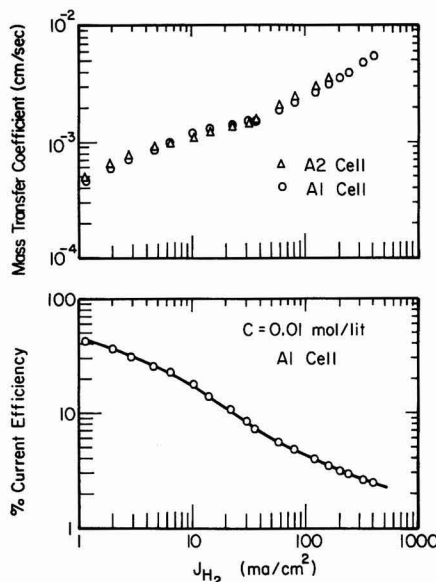


Fig. 4. Upper: Variation of average mass transfer coefficient with gas evolution rate. Lower: Variation of average current efficiency of metal deposition with gas evolution rate. (Electrode height is 12 cm.)

tion of Fig. 4. The foregoing data could be used, for example, in selecting the optimum gas evolution rate which would enhance mass transfer while maintaining reasonable current efficiency.

Measurement of local mass transfer rates.—By employing the sectioned electrode method, the local reaction rate was measured with cell A1-3-3-S- $\frac{1}{2}$ - $\frac{1}{2}$ during experiments of 1 min duration. It was found that the total current distribution (hydrogen plus copper reactions) was uniform to within 3% along the height of the electrode at each of the five current densities studied.

After electrolysis, the copper deposit on each section was stripped to determine the local mass transfer coefficient characteristic of each of the eight sections. Results are shown in Fig. 5. It is seen that the mass transfer coefficient was larger at the upper part of the electrode, where more type 2 bubbles were available for stirring.

The mass transfer flux of copper is defined by

$$Q(y) = k_m(y) [C^b(y) - C^s(y)] \quad [6]$$

Since the copper reaction occurred under limiting current conditions in this study, it is fair to assume that $C^s(y) = 0$. Also, the data in Fig. 2 indicated that depletion of reactants did not occur within the catholyte; therefore, $C^b(y)$ may be assumed to be constant along the electrode. Finally, the rate distribution of the hydrogen evolution reaction must have been very nearly uniform since the total current distribution was uniform and since the current efficiency for the copper deposition reaction was low (Fig. 4 shows between 1.5 and 15% over the range $0.014 < j_{H_2} < 0.243 \text{ A/cm}^2$). Therefore, substitution of Eq. [4] into Eq. [6] gives the quantity of copper to be expected on each electrode section. The solid lines in Fig. 5 show the calculated results for the three sets of data for which Eq. [4] is valid. The deviation between experimental data and the calculation is a

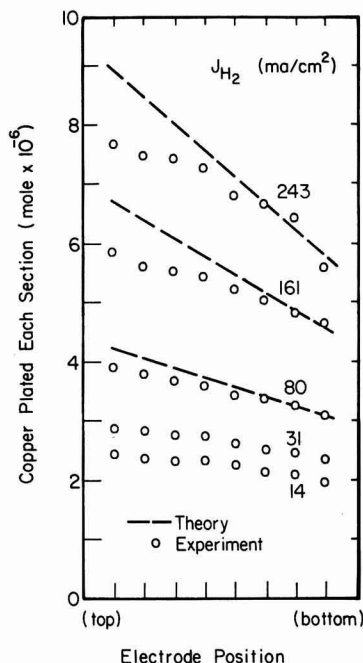


Fig. 5. Current distribution for copper deposition reaction at various hydrogen evolution rates (A1 configuration).

maximum of 16% at the upper portion of the electrode.

Sectioned electrode experiments were also carried out with cell A2-3-3-S- $\frac{1}{2}$ - $\frac{1}{2}$ in experiments of 1 min duration. In this cell, the current distribution was highly nonuniform; the distribution of plated copper after 1 min of electrolysis is shown in Fig. 6 for several values of applied current. The copper reaction rate was highest at the upper and lower edges of the cathode, where current entered the catholyte region. Comparison of Fig. 5 and 6 illustrates that changing the potential distribution influenced the mass transfer of copper because of the altered hydrogen evolution distribution. The hydrogen evolution rate was larger at the extremities of the cathode since, in cell A2, the current entered the cathode compartment at the upper and lower (open) ends of the catholyte region. It is also seen in Fig. 6 that the mass transfer coefficient for copper deposition was larger at the extremities of the cathode, since hydrogen evolution was most vigorous there.

Because both copper and hydrogen reaction rates were highly nonuniform in cell A2, it was necessary to develop a mathematical model for the current and potential distribution within the cell before further analysis of the data in Fig. 6.

Theoretical Model

The objective of the following theoretical study was to develop a mathematical model for predicting the current distribution in cells where electrolytic gas evolution influences the rate of a second simultaneous reaction. A detailed theoretical treatment was not possible since the basic transport processes were not yet agreed on. The foregoing experimental observations sufficed, however, for establishing a working model.

In the acid copper electrolyte investigated here, the copper concentration was sufficiently low that dilute solution transport theory can be used; also, the acid concentration was sufficiently high that migration effects do not influence copper ion transport. In the

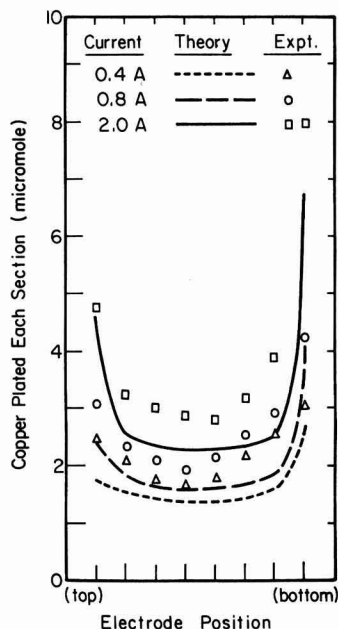


Fig. 6. Current distribution for copper deposition reaction in the presence of hydrogen evolution at various applied currents (A2 configuration).

electrochemical system studied here, only two electrode reactions occurred (copper deposition and hydrogen evolution), and there were no homogeneous reactions of importance. The foregoing experimental program provided evidence that the copper reaction rate was governed by mass transfer alone and that steady-state operation was rapidly achieved and maintained throughout the period of electrolysis. Also, the data in Fig. 2 indicated that depletion of copper from the catholyte was small during one pass through the cathode chamber; that is, depletion of copper occurred locally, near the cathode surface, but not extensively throughout the catholyte volume. Finally, visual observation during electrolysis indicated that the bubbles occupied a very small fraction of the catholyte volume, estimated to be less than 5%, so that the resistance of the electrolyte would not be expected to be altered appreciably because of the presence of the bubbles. The foregoing experimental observations were built into a quantitative model in order to provide a theoretical calculation of current distribution data reported in Fig. 6.

The geometry of the cathode in cell A2-3-3-S- $\frac{1}{2}$ - $\frac{1}{4}$ was 2 cm wide by 12 cm high; the catholyte layer was $\frac{1}{2}$ cm thick, and current entered from the ends of the catholyte slot. Since the ratio of height to thickness was very large ($12:\frac{1}{2}$), it was justifiable to assume that the potential varies in the vertical direction but not in the transverse direction. As a consequence, the potential distribution was modeled by a one-dimensional equation. Thus the flow of current in the catholyte solution obeys a one-dimensional form of Ohm's law

$$i = -\kappa \frac{d\phi(y)}{dy} \quad [7]$$

The current flowing in the catholyte varied with height along the electrode because of electrochemical reactions occurring on the cathode surface

$$\frac{di}{dy} = -\frac{1}{B} (j_{\text{Cu}+2} + j_{\text{H}+}) \quad [8]$$

According to Ref. (2), the rate of hydrogen reduction depended on potential according to the Tafel equation

$$j_{\text{H}+} = i_0 e^{-\frac{\alpha F}{RT} [\phi_m - \phi(y)]} \quad [9]$$

The rate of copper reduction was mass transfer limited

$$j_{\text{Cu}+2} = 2Fk_m(y)C_{\text{Cu}+2}^b \quad [10]$$

By combining Eq. [7] through [10] one finds

$$\frac{d^2\phi(y)}{dy^2} = \frac{1}{\kappa B} \left\{ 2Fk_m C_{\text{Cu}+2}^b + i_0 e^{-\frac{\alpha F}{RT} [\phi_m - \phi(y)]} \right\} \quad [11]$$

where $k_m(y)$ is to be found from Eq. [5] and [9]

$$k_m = a \left\{ i_0 e^{-\frac{\alpha F}{RT} [\phi_m - \phi(y)]} \right\}^d + b i_0 \int_0^y e^{-\frac{\alpha F}{RT} [\phi_m - \phi(y)]} dy \quad [12]$$

where $b = 0.00070$; $a = 0.00158$, and $d = 0.15$ when $0.010 < j_{\text{H}_2} < 0.080$ A/cm²; and $a = 0.0066$ and $d = 0.531$ when $0.080 < j_{\text{H}_2} < 0.330$ A/cm².

Equations [11] and [12] contain two unknowns, k_m and ϕ ; although the two equations could be reduced to a single equation by elimination of k_m , the resulting

single equation would be no easier to solve than the two simultaneous equations.

The second-order differential equation required that two boundary conditions be specified. In the electrolysis cell, current entered the catholyte slot at both ends. If " f " denotes the fraction of current entering the upper opening, then

$$\begin{aligned} \kappa \frac{d\phi}{dy} \Big|_{y=H} &= -fi_a \\ \kappa \frac{d\phi}{dy} \Big|_{y=0} &= (1-f)i_a \end{aligned} \quad [13]$$

where $y = 0$ represents the lower edge of the cathode, and $y = H$ represents the upper edge of the cathode.

Equations [11]–[13] were solved by an iterative scheme which involved finite difference methods implemented on a digital computer (18).

Comparison of Model with Experimental Data

Calculations were performed for comparison with data shown in Fig. 6 for an applied current of 2A. For applied currents less than 2A, the value of j_{H_2} in the center of the cathode was less than 10 mA/cm² so that the model would not be applicable (see constraints on validity of Eq. [5]).

The parameters used in the calculation included $i_0 = 10^{-6}$ mA/cm² (21), $\alpha = 0.5$ (21), $C^b = 10^{-5}$ gmole/cm³, and $\kappa = 0.5$ mho/cm (22). The value of f was chosen after examination of the total current distribution, which exhibited a minimum located halfway up the cathode. The total section currents for sections located beneath the minimum was three times the total current of the sections located above the minimum. Therefore the value of f was set at 0.25.

With use of the foregoing parameters, the results were found as given by the solid line in Fig. 6. It may be seen that agreement is good at the extremities of the cathode, where hydrogen evolution is most vigorous. Near the middle of the cathode, the theoretical results fall about 20% below the experimental data. Owing to the appearance of the integral term, it may be recognized that small errors in determination of j_{H_2} at the bottom of the cell (near $y = 0$) will beget errors in k_m over the remainder of the cathode surface. Since the maximum section current was encountered at the bottom of the cathode, it may be concluded that the discrepancy between theory and experiment arises from the uncertainty with which the local mass transfer coefficient may be predicted via Eq. [5].

Conclusions

By measuring local rates of metal deposition during simultaneous gas evolution, a mass transfer correlation was obtained (Eq. [5]) for predicting the effect of electrolytic hydrogen evolution on the rate of copper deposition from acidified sulfate solutions. The form of the correlation supported the interpretation that gas evolution influences metal deposition by two routes: Bubbles generated at the electrode surface stir the electrolyte within the diffusion layer, while bubbles moving upward past the electrode induce a convective flow which also enhances mass transfer.

It was found that the mass transfer coefficient attributed to bubble detachment varied with the square root of the gas evolution rate at rates above 80 mA/cm² in agreement with observations and theories by Ibl and co-workers (1-3). Below 80 mA/cm², the square root dependence was not followed. The abrupt change in exponent at 80 mA/cm² may be of fundamental interest and may therefore be worthy of further study.

Although the mass transfer coefficient represents a combination of the foregoing two influences of gas evolution, there remains some question over how the

mass transfer coefficient should be defined (12). The experimental technique developed in this study should be used to assist in the further resolution of the matter. The method of study used here could also be modified to study additional geometries, such as horizontal and inclined electrodes, as well as evolution of other gases and different ranges of solution pH.

The effect of nonuniform potential distribution was investigated in order to establish a mathematical model of the gas evolution process. The model included consideration of mass transport, reaction kinetics, ohmic resistance, and cell geometry. It was found that the current distribution predicted by the model agreed to within 20% of experimental data. The availability of a mathematical model makes possible a quantitative level for engineering scale-up and optimization which was previously unavailable. It would be useful to expand the model to include economic factors and thereby assess further the trade-off between pumping costs and stirring by gas evolution.

It seems important to develop strategies for the engineering of electrochemical systems in a quantitative manner even when the understanding of underlying fundamental principles is incomplete. The prediction of the current distribution is of central importance in the design of individual cells or cell components. However, during the past decade, current distribution models have tended to treat more complex physical situations with more complex mathematics. In contradistinction, the present investigation has sought simple strategies for modeling a complex process to within engineering tolerance but, at the same time, without recourse to empiricism.

Acknowledgment

This investigation was supported by the National Science Foundation (NSF ENG 72-04168 and 76-83379).

Manuscript submitted March 2, 1979; revised manuscript received June 11, 1979.

Any discussion of this paper will appear in a Discussion Section to be published in the June 1980 JOURNAL. All discussions for the June 1980 Discussion Section should be submitted by Feb. 1, 1980.

Publication costs of this article were assisted by the University of Illinois.

LIST OF SYMBOLS

B	spacing between cathode and separator, cm
C^b	local bulk concentration, mole/cm ³
C^s	local surface concentration, mole/cm ³
f	fraction of applied current entering top of cathode chamber, dimensionless
F	Faraday's constant, 96,500 C/equiv.
H	electrode height, cm

i	current density, A/cm ²
i₀	exchange current density, A/cm ²
i_a	total applied current density, A
j_{H2}	local reaction rate for gas bubbles, A/cm ²
k₁	local mass transfer coefficient (contributed by type 1 bubbles), cm/sec
k₂	local mass transfer coefficient (contributed by type 2 bubbles), cm/sec
k_m	local mass transfer coefficient, cm/sec
Q	local mass transfer rate, mole/cm ² -sec
R	universal gas constant, 8.3143 J/mole-°K
T	temperature, °K
y	distance from the bottom of the electrode, cm
α	cathodic transfer coefficient, dimensionless
φ	potential in the electrolyte, V
φ_m	potential in the metal phase, V
κ	conductivity, (Ω-cm) ⁻¹

REFERENCES

1. J. Venczel, *Electrochim. Acta*, **15**, 1909 (1970).
2. N. Ibl and J. Venczel, *Metalloberfläche*, **24**, 365 (1970).
3. N. Ibl, E. Adam, J. Venczel, and E. Schalch, *Chem. Ing. Techn.*, **43**, 202 (1971).
4. I. Roušar and V. Cezner, *Electrochim. Acta*, **20**, 289 (1975).
5. L. J. J. Janssen and J. G. Hoogland, *ibid.*, **15**, 1013 (1970).
6. L. J. J. Janssen and J. G. Hoogland, *ibid.*, **18**, 543 (1973).
7. L. J. J. Janssen, *ibid.*, **23**, 81 (1978).
8. T. R. Beck, *This Journal*, **116**, 1038 (1969).
9. W. M. Rohsenow, "Developments in Heat Transfer," M.I.T. Press, Cambridge, Mass. (1964).
10. S. S. Kutateladze, *Int. J. Heat Mass Transfer*, **4**, 31 (1961).
11. S. S. Kutateladze, "Fundamentals of Heat Transfer," Arnold, London (1963).
12. H. Vogt, *Electrochim. Acta*, **23**, 203 (1978).
13. B. Roald and W. Beck, *This Journal*, **98**, 277 (1951).
14. M. G. Fouad and G. H. Sedahmed, *Electrochim. Acta*, **17**, 665 (1972).
15. M. G. Fouad and G. H. Sedahmed, *ibid.*, **18**, 55 (1973).
16. M. G. Fouad, G. H. Sedahmed, and H. A. El-Abd, *ibid.*, **18**, 279 (1973).
17. M. G. Fouad and G. H. Sedahmed, *ibid.*, **20**, 615 (1975).
18. P.-Y. Lu, M.S. Thesis, Department of Chemical Engineering, University of Illinois, Urbana (1978).
19. "Annual Book of ASTM Standards," Part 12, ASTM, Philadelphia (1976).
20. E. Gileadi, I. Kirowa-Eisner, and J. Penciner, "Interfacial Electrochemistry," p. 311, Addison-Wesley Publishing Co., Inc., Reading, Mass. (1975).
21. K. J. Vetter, "Electrochemical Kinetics," p. 539, Academic Press, New York (1967).
22. J. S. Newman, "Electrochemical Systems," p. 365, Prentice-Hall, Englewood Cliffs, N.J. (1973).

Effect of Multiple Reactions on Metal Deposition in Flow-Through Porous Electrodes

Ronald M. Gould*¹ and Richard C. Alkire*

Department of Chemical Engineering, University of Illinois, Urbana, Illinois 61801

ABSTRACT

Two different reaction systems were investigated in a flow-through porous electrode: (i) FeSO_4 , $\text{Fe}_2(\text{SO}_4)_3$, and CuSO_4 in H_2SO_4 , and (ii) CuSO_4 and CoSO_4 in K_2SO_4 . The porous cathode was fabricated from Pt screens through which convection of electrolyte occurred parallel to the flow of electrical current in the solution phase. The local rate of each cathodic reaction was measured and compared to theoretical predictions. The mathematical model incorporated the effects of internal mass transport, ohmic resistance in the electrolyte, and multiple electrochemical reaction kinetics under conditions of steady plug flow of electrolyte. The use of literature values for system parameters yielded predictions of current distributions which agreed favorably with the experimental data over the range of flow rates, applied potentials, and reactor lengths investigated. Depending upon operating conditions, the calculated collection efficiencies agreed to within 0-9% of the corresponding experimental values.

One advantage of electrochemical processes is the high selectivity which may be obtained by accurate control of the electrode potential. Flow-through porous electrodes offer high volumetric reaction rates owing to the large internal surface area available for reaction. The attainment of both large production rates and high selectivity, however, requires optimization between the competing effects of reactant supply and ohmic resistance. Therefore, models of porous electrode behavior represent an important first step toward engineering scale-up and economic assessment of design trade-offs (1).

Reviews of porous electrode literature are available (2-4) and some aspects of industrial applications have been identified (5). However, treatment of multiple reaction systems has been limited to date. The first detailed theoretical treatment of multicomponent systems (6) evaluated several metal deposition and electroorganic sequences and is the basis for the present study. Other recent studies have considered the interaction of convection, axial diffusion, and ohmic resistance for two-step electron transfer reactions (7, 8). Theoretical models have been developed for two-component reaction systems where the parasitic secondary reaction occurs at a rate characterized by either its half-wave potential (9) or by a linear approximation to the polarization equation (10). The importance of feeder plate and counterelectrode placement in minimizing current efficiency loss by secondary reactions has also been studied (11). Various experimental studies are known and have been described previously (6). Continued interest in the removal of metal ions from multicomponent solutions has led recently to both fundamental (12) and applied studies (13, 14).

The purpose of the investigation reported here was to evaluate the effect of multiple reactions upon the recovery of metals in flow-through porous electrode cells within which electrolyte flow occurs parallel to the flow of electrical current in the solution phase. Two different electrochemical reaction systems were studied: metal deposition in the presence of a redox couple and codeposition of a mixture of metal ions. The electrode was designed in a manner which per-

mitted measurement of local rate for each reaction under conditions amenable to detailed comparison with the theoretical models.

Apparatus

The cylindrical electrolysis cell was fabricated from Plexiglas® as shown schematically in Fig. 1. The electrode was supported by a 1.5 mm ledge in the cell block wall. A saturated mercurous sulfate reference electrode was connected to a tap located 2 mm downstream from the support ledge. To withdraw solution samples, 24 gauge Teflon® tubing (Alpha Medical Supplies) was positioned 5 mm below the reference electrode tap in the center of the flow stream. Provisions for additional reference electrode and sample withdrawal taps were made in an adjoining area of the flow loop directly above the piston. A sintered glass

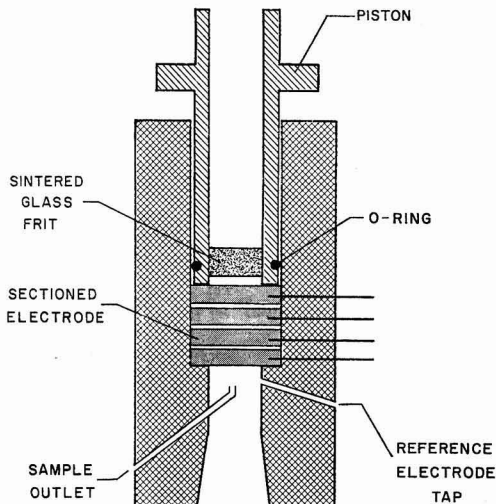


Fig. 1. Cross-sectional schematic diagram showing components of an assembled experimental flow-through cell.

* Electrochemical Society Active Member.

¹ Present address: Mobil Research and Development Corporation, Paulsboro, New Jersey 08066.

Key words: porous electrode, metal deposition, mathematical model, copper.

frit was sealed into a recessed area in the piston to ensure radial uniformity in the inlet electrolyte flow (15). Electrical connections to the electrode sections were made with 26 gauge platinum wire fed through small-diameter holes in the cell block which were fitted with compression gaskets.

The porous electrode was comprised of 1.3 cm-diam disks of 100 square mesh plain weave platinum screen (Unique Wire Weaving, Hillside, New Jersey) having a wire diameter of 0.003 in. Spacers of 1.4 cm-diam disks cut from 105 mesh Teflon® gauge (Cole-Parmer, No. 6630-72) were used to separate the electrode sections. The contact wires were sandwiched between adjacent metal disks in each section and the entire electrode was compressed between the edge of the piston and the electrode support ledge.

The 1 cm-thick platinum counterelectrode was constructed from stacked metal screen disks and was located in the flow stream approximately 6 cm downstream of the reference electrode tap. The cell assembly was connected to the remainder of the flow system with standard taper joints having seamless Teflon® sleeves. Electrolyte was stored under nitrogen in a glass reservoir and was gravity fed through the Teflon® and glass flow loop to the cell. Flow rates were controlled by the use of needle valves and were monitored by a series of precision rotameters (Gilmont, No. 2-5). When electrolysis was not in progress, the diffusion of oxygen into the system through the Teflon® tubing was counterbalanced by continuous sparging of nitrogen (Union Carbide, high purity dry grade) through the feed reservoir while circulating electrolyte through the recycle loop. A variable voltage controller and a magnetic drive "Met-Less" pump (March Manufacturing Company, Model MDX-MT-3) were used for this purpose.

The flow system was equipped with a bypass leg containing a small flow-through cell used for on-stream measurement of residual dissolved oxygen. An oxygen analyzer (Beckman No. 10081, sensor No. 93553) was used to monitor dissolved oxygen concentration at the inlet. An additional glass reservoir was used as a reactant-free feed source when reactor purging was required during the course of an experiment.

A potentiostatic power source (Wenking 68TS-3) was used to control the cathode potential with respect to the reference electrode nearest the counterelectrode. A multichannel, zero-resistance operational amplifier circuit (built in-house) was used to measure the individual section currents, which were displayed on a multipoint recorder (Leeds and Northrup Speedomax W). Total steady-state cell current was measured with an X-Y recorder (Houston Instruments 2000). A linear function generator (built in-house) was used to obtain polarization behavior or to implement programmed voltage changes at the cathode. A sweep rate of 1 mV/sec was used for all polarization curve traces; results were independent of sweep rate. The total cell current was integrated with a coulometer (Vari Tech VT-1176-B).

Procedure

Solutions were prepared from reagent grade chemicals and singly distilled, deionized water having a conductivity of less than $3 \times 10^{-6} (\Omega \text{ cm})^{-1}$. The solutions used in this study were: (i) 2 mmole FeSO_4 , 1 mmole $\text{Fe}_2(\text{SO}_4)_3$, and 2 mmole CuSO_4 in 1.5M H_2SO_4 and (ii) 2 mmole CuSO_4 and 2 mmole CoSO_4 in 0.1M K_2SO_4 . Copper and cobalt ion concentrations were measured by atomic absorption spectroscopy (Instrumentation Laboratory, Incorporated 251) following gravimetric dilution. Ferric and ferrous ion concentrations were determined spectrophotometrically (Beckman DU monochromator 2440, Gilford photomultiplier 222-A) using a 1,10-phenanthroline method (17). Solution conductivities were measured with a conductivity bridge (Leeds and Northrup 4959) in a cell calibrated with 0.1 demal KCl at 26°C. Solution densities were determined with an immersion hydrometer and electrolyte viscosities were measured with an Ostwald viscometer. Diffusion coefficients of reactive species were obtained from rotating disk polarization data. The parameters of the electrolyte solutions, reactant ions, and reduction reactions are listed in Tables I and II. The solution was placed in the feed reservoir and deoxygenated by sparging with nitrogen.

The dissolved oxygen concentration in the inlet stream was measured and, in the iron-copper system,

Table I. Properties of experimental systems

a) Iron redox/copper solution
0.002M FeSO_4 ,
0.001M $\text{Fe}_2(\text{SO}_4)_3$,
0.002M CuSO_4 ,
1.5M H_2SO_4

Properties of iron redox and copper solutions

Property	Value	Iron redox system	Reference	Copper system	Reference
κ	$(\Omega \text{ cm})^{-1}$	0.538*		0.538*	
μ	$\text{g}/(\text{cm sec})$	$1.307 \pm 0.005 \times 10^{-2*}$		$1.307 \pm 0.005 \times 10^{-2*}$	
ρ	g/cm^3	$1.085 \pm 0.0005^*$	(21)	$1.085 \pm 0.0005^*$	(21)
n	equiv./mole	1.0		2.0	
D	cm^2/sec	$4.22 \pm 0.21 \times 10^{-6*}$	(22)	$5.92 \pm 0.18 \times 10^{-6*}$	(25)
k	cm^2/sec	$(6.15 \times 10^{-3}) \text{ Re}^{0.384}$	(23)	$(6.98 \times 10^{-3}) \text{ Re}^{0.384}$	(23)
t_0	A/cm^2	9.7×10^{-4}	(24)	1.4×10^{-4}	(26)
α		0.5	(24)	1.09	(26)
β		-0.5	(24)	-0.38	(26)
ϕ_r	V	0.0		$0.540 \pm 0.025^*$	

b) Copper/cobalt solution
0.002M CuSO_4 ,
0.002M CoSO_4 ,
0.1M K_2SO_4

Property	Value	Copper system	Reference	Cobalt system	Reference
κ	$(\Omega \text{ cm})^{-1}$	$2.22 \times 10^{-2*}$		$2.22 \times 10^{-2*}$	
μ	$\text{g}/(\text{cm sec})$	$9.05 \pm 0.05 \times 10^{-3*}$	(27)	$9.05 \pm 0.05 \times 10^{-3*}$	(27)
ρ	g/cm^3	$1.012 \pm 0.0005^*$	(28)	$1.012 \pm 0.0005^*$	(28)
n	equiv./mole	2.0		2.0	
D	cm^2/sec	$6.42 \pm 0.19 \times 10^{-6*}$		$7.16 \pm 0.21 \times 10^{-6*}$	
k	cm^2/sec	$(7.34 \times 10^{-3}) \text{ Re}^{0.384}$	(23)	$(7.89 \times 10^{-3}) \text{ Re}^{0.384}$	(23)
t_0	A/cm^2	1.4×10^{-4}	(26)	1.4×10^{-4}	(29)
α		1.09	(26)	0.79	(29)
β		-0.38	(26)	-0.21	(29)
ϕ_r	V	0.0		$0.730 \pm 0.025^*$	

* Measured in this laboratory.

Table II. Electrode properties and experimental conditions

System	Cross-sectional area, cm ²	Electrode length, mm	No. of screens	No. of sections	Porosity	Estimated specific surface area, cm ² /cm ³	Flow rate, ml/min
Fe ³⁺ /Cu ²⁺	0.95	5.0 ^a	30	5	0.789	164 ^b	1.30-16.3
Cu ²⁺ /Co ³⁺	0.95	1.3	10	1	0.733	176	0.78-6.45
	0.95	2.6	20	1	0.733	176	0.83-6.64
	0.95	3.9	30	1	0.733	176	0.83-6.25

^a Includes separator material.^b Based on total length and Ref. (16).

saturated sodium sulfite was added to the feed reservoir to reduce the residual oxygen concentration in the flow circuit to less than 0.3 ppm. The addition of excess sulfite was carefully avoided since sulfite ion is electrolytically reactive in the range of electrode potentials employed in this study. Sulfite treatment was not required with the copper-cobalt system since the background current attributable to dissolved oxygen was less than 2% of the total cell current.

Electrolyte was pumped through the cell and recycle loop at a rate of 100 ml/min for 15 min. An inlet sample was extracted and the electrolyte flow was set by opening both the outlet sample port and the needle valves. The flow rate was determined by collecting measured volumes and was steady to within 2% of the mean value reported. Continuous electrolyte flow through the sample port enabled collection of an outlet sample without undue perturbation of the system. The flow through the port was less than 5% of the total flow. The desired potential was applied to the cell and, after a period of steady-state operation, an outlet sample was collected and the total cell current, section currents, potential drop across the electrode, total coulombs passed, and the time duration of the experiment were recorded. The cell was then purged with reactant-free electrolyte, while maintaining the applied potential to the cathode, until the total cell current had decreased to near zero.

The cell was removed from the flow system and the electrode separated into ten equal sections. The amount of metal deposited on each section was determined by nitric acid stripping and subsequent analysis by atomic absorption spectroscopy. Inlet and outlet reactant concentrations were determined by the aforementioned analytical procedures and gave mass balances which closed to within 4%.

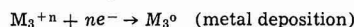
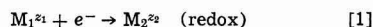
Theoretical Model

Since the theoretical models used in this work have been presented previously (6), the following paragraphs are intended only to review the underlying principles. Electrolyte flows in the direction of the y coordinate, the electrode is of thickness l , and the counterelectrode is located downstream of the porous electrode. Other details of cell construction are not considered in the development of the model equations. Electrolyte flows through the porous matrix, supplying reactants to the interior surface where electrochemical reaction occurs. The local reaction rate is a function of position since the potential and species concentration vary along the reactor length as the result of ohmic and transport limitations.

The model accounts for steady-state operations under isothermal conditions. The electrode phase is isopotential, is of uniform porosity, and has pore dimensions which are large with respect to the double layer thickness. The solid surface of the interior region, on which electrochemical charge transfer occurs, is of arbitrary configuration and is accounted for in the model by a specific area term. Conduction in the solution phase obeys Ohm's law; migration effects are neglected. Convection through the electrode occurs by plug flow. Mass transport of reactant species from

a well-mixed core region to the surface is assumed to occur across a mass transfer diffusion layer which occupies a negligible fraction of the pore volume. These constraints allow the model equations to be written in one-dimensional form in which the heterogeneous electrochemical reactions appear as pseudohomogeneous source terms.

For the case of metal deposition in the presence of a redox couple, the electrode reactions are



The reaction rate of the redox system will be characterized by

$$f_{\text{redox}} = i_{01} \left\{ \frac{c_2^s}{c_2^0} \exp \left[\frac{\alpha_1 n_1 F \phi}{RT} \right] - \frac{c_1^s}{c_1^0} \exp \left[\frac{-\beta_1 n_1 F \phi}{RT} \right] \right\} \quad [2]$$

Deposition of the metal is assumed to proceed independently of the redox reaction with the rate expression

$$f_{\text{metal}} = i_{02} \left\{ \exp \left[\frac{\alpha_2 n_2 F}{RT} (\phi + \phi_r) \right] - \frac{c_3^s}{c_3^0} \exp \left[\frac{-\beta_2 n_2 F}{RT} (\phi + \phi_r) \right] \right\} \quad [3]$$

In these equations, ϕ is the potential with respect to the rest potential of the redox couple, while ϕ_r is the thermodynamic rest potential of the redox couple with respect to the metal ion. The rest potential difference is computed by consideration of the ionic concentration of reactants as they enter the porous electrode.

By following the same derivation given in Ref. (6), the dimensionless model equations are

$$\begin{aligned} C_1'' - \xi_1 C_1' &= -x_1 F_1 \\ C_2'' - \xi_2 C_2' &= x_2 F_1 \\ C_3'' - \xi_3 C_3' &= -x_3 F_2 \\ \Phi'' &= \xi_1 F_1 + \xi_2 F_2 \end{aligned} \quad [4]$$

where

$$\begin{aligned} F_1 &= \frac{C_2 \exp[\alpha_1 \Phi] - C_1 \exp[-\beta_1 \Phi]}{1 + \frac{\xi_2}{\Gamma_2} \{ \exp[\alpha_1 \Phi] + \lambda_1 \exp[-\beta_1 \Phi] \}} \\ F_2 &= \frac{\exp[\alpha_2 n (\Phi + \Phi_r)] - C_3 \exp[-\beta_2 n (\Phi + \Phi_r)]}{1 + \frac{\xi_3}{\Gamma_3} \exp[-\beta_2 n (\Phi + \Phi_r)]} \end{aligned}$$

Symbols are defined in the List of Symbols section which follows the text. In Eq. [4], the single and double primes refer to first and second derivatives, respectively. The dimensionless boundary conditions for downstream counterelectrode placement are

$$\begin{aligned} \text{at } Y = 0 & \quad C_1 = 1 \quad \Phi' = 0 \\ \text{at } Y = 1 & \quad C_1' = 0 \quad \Phi = \Phi_0 \end{aligned} \quad [5]$$

Although a more rigorous expression for the boundary conditions might be specified (9), the contribution of a preelectrode diffusion layer to over-all cell behavior is negligible for the range of flow rates investigated here. Equations [4] and [5] constitute the dimensionless model for a redox-metal system and are solved by the procedure described at the end of this section.

For the case of multiple metal deposition, it is assumed that the deposition of each metal proceeds independently of the other so that the individual reaction rate expressions have the form given by Eq. [3]. By following the same algebraic procedures (6), the dimensionless equations of the model are

$$\begin{aligned} C_1' - \xi_1 C_1' &= -\kappa_1 F_1 \\ \Phi' &= \sum \xi_i F_i \end{aligned} \quad [6]$$

where

$$F_i = \frac{\exp[\alpha_i n_i (\Phi + \Phi_{ri})] - C_1 \exp[-\beta_i n_i (\Phi + \Phi_{ri})]}{1 + \frac{\xi_i}{\Gamma_i} \exp[-\beta_i n_i (\Phi + \Phi_{ri})]}$$

The appropriate boundary conditions are given by Eq. [5].

The model equations were first linearized about a trial solution, then recast into finite difference form by employing central difference operators. The resulting set of tri-diagonal matrices was inverted by a modified Gauss-Jordan elimination method (18) with the use of a CDC/CYBER-175 computer. Solution of the nonlinear coupled equations was obtained by successive approximation to within a convergence of 0.01%. The number of iterations required for convergence was dependent upon the system being modeled, but was usually less than ten. The choice of 101 mesh points gave results which were accurate to within the linewidth used in graphical representation of the results. At the limiting current, numerical calculations were found to give results which were identical to analytical calculations.

Comparison of Experiment and Theory

Values of the physical properties of the two chemical systems are listed in Table I. Electrode geometry properties are given in Table II along with the range of experimental conditions studied. While additional experimental studies could have been made, it was felt that the results shown in Fig. 2-11 were adequate to evaluate the accuracy of the theoretical model.

The effective electrolyte conductivity used in theoretical calculations was calculated with the Bruggemann (19) equation

$$\kappa_{eff} = \kappa \epsilon^{1.5} \quad [7]$$

Microscopic observation revealed that the wire surfaces of the screens were not smooth, as assumed correlations of specific surface area (16). Based on auxiliary limiting current data in a single reaction system (1), it was concluded that the value obtained by Ref. (16) should be increased by 15% to account for surface roughness effects. With this procedure, it was found that (i) the adjusted specific surface areas were essentially identical to those best values found by Gracon (15) using a different procedure, (ii) the total current for the single reaction system agreed to within 3% of model predictions, and (iii) current distribution data agreed well with model predictions as illustrated below.

It was found that numerical results obtained with the model were very sensitive to the value chosen for the applied potential, Φ_a . By estimating the IR correction external to the porous electrode, it was possible to measure the value of Φ_a to within an accuracy of 4%.

Within this experimental error limit, the value of Φ_a used in the model was chosen for achieving the best agreement between observed and predicted total cell current. Typically, this range of adjustment was less than 25 and 40 mV for the redox-metal and multiple metal systems, respectively. The calculated total cell current agreed to within 2% of the observed value.

Over-all electrode performance.—Table III contains data for the comparison of measured and predicted recovery effectiveness, defined by the relation

$$\theta_1 = 1 - \frac{C_1'}{C_1} \quad [8]$$

These data are illustrated in Fig. 2 and 3.

For the Cu/Co system, Fig. 2 shows that the recovery of the more noble metal (Cu) increases with electrode length for a given flow rate, indicating mass transfer control. At the highest flow rate studied, measured copper recovery is in good agreement with the model predictions while at lower flow rates, measured values are about 5% less than predicted values (see discussion of Fig. 3 below). The experimental data also indicate that cobalt recovery is independent of electrode length; model calculations are in good agreement and confirm that kinetic limitations control cobalt deposition under the experimental conditions studied.

Figure 3 depicts the flow dependence of metals recovery in the Fe redox/Cu system. The ferric reduction rate is mass transfer controlled and is in good agreement with the model predictions at high flow rates. At lower flow rates, ferric recovery deviates from the predicted value by up to 9%. The recovery of Cu is mass transfer controlled at low flow rates, where experimental deviations are at most 11% from the predicted values. At higher flow rates, copper deposition becomes limited more by reaction kinetics than by mass transfer. Good agreement exists between theory and experiment.

The data in Table III indicate that the differences observed between theoretical and experimental mass transfer controlled recovery data were most pronounced at low flow rates and long electrode lengths. A potential source of the discrepancies could be flow maldistribution of electrolyte within the porous electrode. To test the extent to which channeling occurred within the cell, copper deposition was conducted at the limiting current at a flow rate of 6.35 ml/min in an

Table III. Recovery effectiveness

(a)									
V , ml/min	$-I_{total}$, mA	Fe^{+3}	Cu^{+2}	Fe^{+3}	Cu^{+2}	$C.E., \%$	Cu^{+2}	Fe^{+3}	Cu^{+2}
1.30	11.85	0.97	0.90	1.00	0.97	35.4	60.2		
1.65	14.40	0.93	0.83	0.99	0.94	35.4	61.3		
2.89	24.42	0.87	0.75	0.96	0.81	35.8	56.0		
4.32	30.60	0.83	0.66	0.91	0.68	38.4	57.4		
6.08	35.50	0.80	0.51	0.85	0.55	46.0	50.0		
10.5	50.72	0.72	0.32	0.73	0.33	49.3	45.5		
16.3	56.80	0.60	0.13	0.59	0.13	57.2	39.7		

(b)									
l , mm	V , ml/min	$-I_{total}$, mA	Cu^{+2}	Co^{+3}	Cu^{+2}	Co^{+3}	$C.E., \%$	Cu^{+2}	Co^{+3}
1.3	0.78	11.03	0.94	0.94	0.97	0.97	41.8	44.1	
	1.26	16.15	0.91	0.88	0.95	0.88	45.9	44.5	
	1.72	18.37	0.87	0.70	0.92	0.75	50.5	42.8	
	2.47	22.05	0.83	0.51	0.87	0.54	59.1	36.7	
	3.95	25.98	0.77	0.21	0.77	0.21	73.9	25.3	
	6.45	32.40	0.63	0.06	0.63	0.05	79.4	7.3	
2.6	0.83	13.10	0.98	0.97	1.00	0.97	41.8	43.5	
	1.37	18.46	0.97	0.91	0.99	0.87	46.6	45.2	
	1.80	20.63	0.97	0.71	0.98	0.71	54.2	43.8	
	2.52	24.23	0.95	0.44	0.95	0.32	61.6	30.0	
	6.64	36.80	0.81	0.02	0.81	0.04	95.4	2.3	
3.9	0.83	13.00	0.99	0.99	1.00	0.97	42.7	43.0	
	1.40	19.50	0.99	0.83	1.00	0.86	48.0	41.4	
	2.61	25.43	0.95	0.37	0.99	0.50	63.1	27.8	
	6.25	38.84	0.88	0.04	0.87	0.05	88.4	6.7	

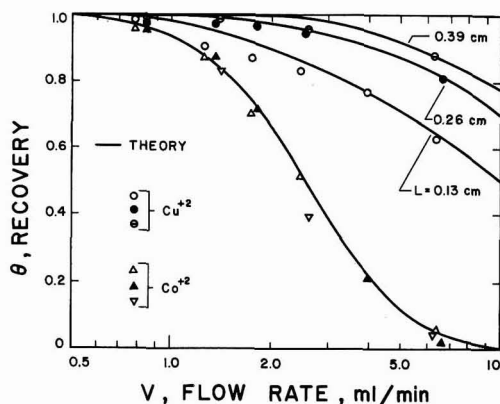


Fig. 2. Dependence of recovery efficiency upon flow rate and reactor length in the copper/cobalt systems. Solid lines give theoretical predictions.

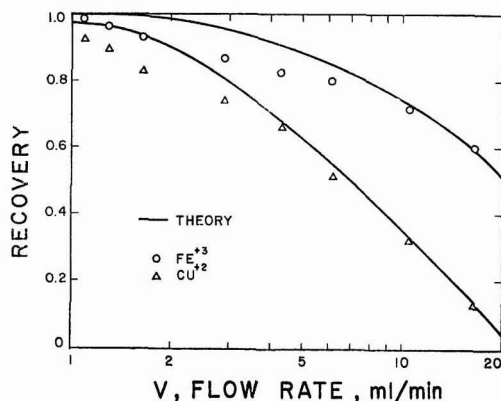


Fig. 3. Dependence of recovery efficiency upon flow rate in the iron/copper system with a reactor length of 5.0 mm. Solid lines give theoretical predictions.

electrode of thickness 0.39 cm. Postelectrolysis analysis of the radial distribution of copper indicated that 19% more copper per unit area was deposited on the 1 mm-wide periphery of the screens than upon the central region located in the mainstream of electrolyte flow. This corresponds to a situation where approximately 6% of the inlet flow is channeled along the wall of the cell block. This result is consistent with the recovery data reported in Table III as well as with the current distribution data presented in the following section.

These data indicate the high volumetric reaction rates which may be attained within small-scale, flow-through porous electrodes. The volumetric current densities reported in Table III range between 1.8×10^4 and 1.9×10^5 A/m³ or 500–5300 A/ft³.

Figure 4 illustrates the potential difference, $\Delta\phi$, measured between upstream and downstream electrode surfaces for various flow rates and electrode thicknesses. The values of $\Delta\phi$ given in Fig. 4 include correction for IR drop between the downstream reference electrode and downstream electrode surface. Correction for the liquid junction potentials was not made, but may be estimated to be on the order of 10 mV (1). These results illustrate that the model tracks measured behavior to within 20% and that the model

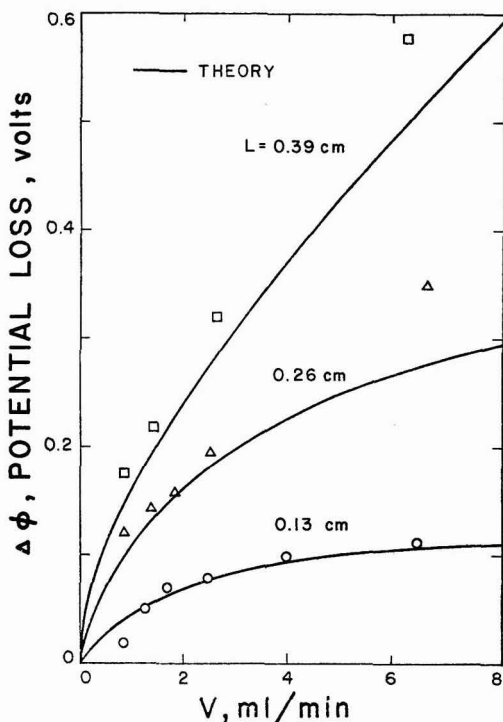


Fig. 4. Flow dependence of potential difference between upstream and downstream faces of cathodes of various lengths. Solid lines give theoretical predictions.

predicts values which are conservative with respect to the data.

Current distribution data.—In the absence of axial dispersion effects, the partial limiting current distribution for an electroactive species can be obtained (20) by integration of the expression for the local concentration over the entire electrode. The result, which is independent of counterelectrode placement, is

$$i = nFVc_l^0 \left[\exp\left(-\frac{aky}{v}\right) - \frac{c_l^1}{c_l^0} \right] \quad [9]$$

Figure 5 shows the partial current distribution of the more noble species in each system. The solid line corresponds to Eq. [9]. For high flow rates, the predictions are in good agreement with the data. The deviation of the experimental current distributions from the theoretical line is an inverse function of electrolyte flow rate; the exit concentration for the lowest flow rate is 6% larger than that predicted by the model. These observations provide additional support to the hypothesis of electrolyte channeling within the reactor.

The copper current distributions for the redox-metal system are shown in Fig. 6. The current distributions have been normalized so that the integral average is unity

$$\int_0^1 JdY = 1 \quad [10]$$

For a flow rate of 1.3 ml/min (not shown), copper deposition occurred at the mass transfer limited rate throughout the entire reactor as the result of the small potential gradient in the solution phase within the electrode. Consequently, electrode behavior resulting from the occurrence of parallel multiple reac-

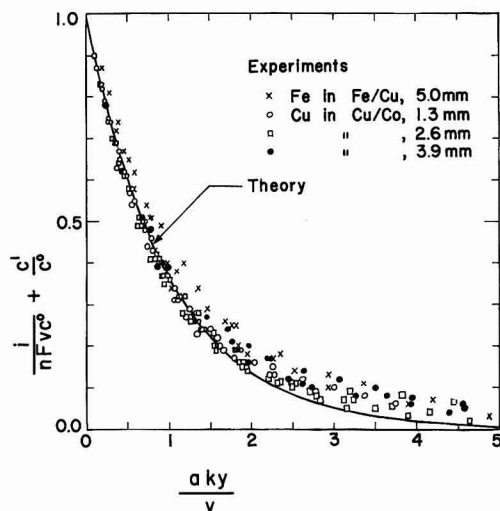


Fig. 5. Comparison of measured current distributions with theory (Eq. [9]) for the reacting species under mass transfer control: copper in Cu/Co systems, (0.78-6.64 ml/min), iron in Fe/Cu system (1.30-16.3 ml/min).

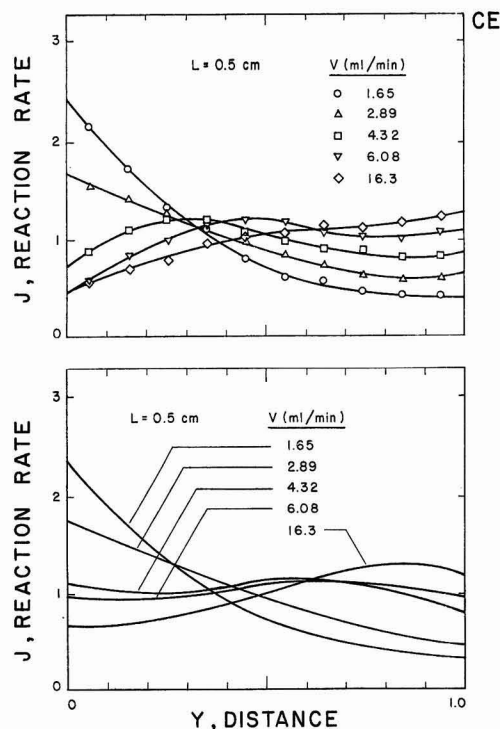


Fig. 6. Flow dependence of the rate distribution of copper reaction in the Fe/Cu system. Reactor length is 0.5 cm. Upper figure: experimental data. Lower figure: theoretical predictions.

tions can be predicted by a linear combination of the individual mass transfer controlled reaction rate distributions. At higher flow rates, however, electrode operation is more complex. For a flow rate of 1.65

ml/min, the convective supply rate is sufficiently low to allow removal of a significant percentage of the copper from solution in the upstream region of the electrode. Still larger flows yield increased nonuniformity in the potential distribution, precluding copper deposition at the mass transfer limited current in the upstream regions of the cathode. The local reaction rate exhibits a maximum owing to the interaction of ohmic and mass transport phenomena. Close to the counterelectrode, the local copper deposition rate decreases owing to depletion of copper ion in the electrolyte. The copper deposition rate rises slightly near the reactor outlet as the result of the wall channeling phenomenon discussed previously. Additional increases in the fluid flow rate cause a downstream shift in the maximum of the copper current distribution and eventually yield reaction rate distributions that are skewed towards the downstream regions of the electrode. Under these conditions, over-all electrode utilization is improved at the expense of lower reactant conversions.

Generally, the quantitative agreement between theoretical predictions and experimental data in Fig. 6 is good. The results indicate that, for a flow rate of 1.65 ml/min, the potential gradient within the electrode is sufficiently large that copper deposition is kinetically limited in approximately the upstream third of the reactor. The reaction is mass transfer limited in the downstream region (as indicated by a surface-to-bulk concentration ratio of less than 10^{-4}). Reaction kinetics exert a more pronounced influence on the copper current distribution at larger flow rates and eventually result in the local maxima observed experimentally. The model demonstrates qualitative accuracy by correctly predicting the range of operating conditions over which the maxima occur. The precise magnitudes of the maxima are underestimated slightly and are shifted into the downstream region. Alteration of the reaction kinetics for copper deposition resulting from the presence of the ferric-ferrous sulfate redox couple may contribute to the lack of agreement. Also, the decrease in interstitial electrolyte velocity as the result of wall channeling could account for some of the observed differences.

The current distributions for cobalt deposition in the presence of copper ion for three electrode lengths are depicted in Fig. 7-9. Qualitative reactor behavior was analogous to that observed for the iron redox-copper system. Local maxima in the cobalt current distribution were observed to occur as a consequence of the interaction of kinetic, ohmic, and mass transfer phenomena described above. The maxima appeared at significantly lower flow rates and for much shorter electrode lengths than in the iron-copper system because of the substantially lower electrolyte conductivity within the porous structure. The apparent sharpening and downstream shift of the cobalt distributions for the longer electrode lengths compared to Fig. 7 are an artificial consequence of the normalization procedure described by Eq. [10].

The agreement of the model with the experimental data is good, although the theory slightly underestimates the driving force for the cobalt reaction. The model accurately predicts the magnitude and location of the maxima and correctly indicates parameter ranges over which cobalt deposition in the upstream regions of the electrode is precluded owing to excessive ohmic losses in the solution phase.

Combination of Fig. 5 with Fig. 8 and 9 indicates the degree of separation of the two metal deposits which can be achieved within the porous electrode. This chromatographic-like behavior is a consequence of the opposing nature of the potential and concentration gradients existing within the electrode and is observed only when the counterelectrode is located in the downstream position. For an electrode length of 0.26 cm and a flow rate of 1.37 ml/min, 97 and 91%

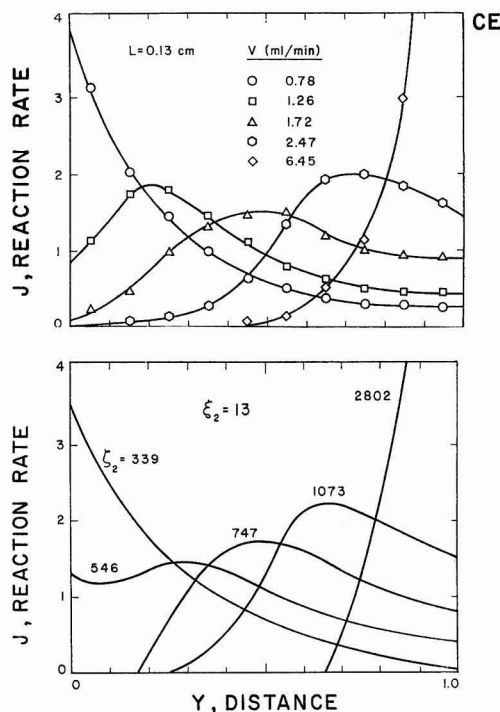


Fig. 7. Flow dependence of the rate distribution of the cobalt reaction in the Cu/Co system. Reactor length is 0.13 cm. Upper figure: experimental data. Lower figure: theoretical predictions.

of the inlet copper and cobalt, respectively, are reclaimed by the electrode. Whereas 90% of the recovered copper is removed from the feed stream and deposited in the upstream third of the reactor, less than 6% of the cobalt is found in this region. Increasing the flow rate to 1.80 ml/min reduces the degree of overlap in the two partial current distributions, yields a more uniform total current, and improves electrode utilization but reduces the fractional recovery of cobalt to 71%. Subsequent flow rate increases result in more uniform electrode behavior at the expense of lower recoveries of the secondary reactant.

In the data presented thus far, the overpotential at the downstream face of the cathode was maintained so that extensive evolution of hydrogen at the reactor outlet was avoided. The effect of the level of the applied potential on the reaction rate distributions of copper in the presence of the iron redox couple is shown in Fig. 10. All potentials are *vs.* the downstream saturated mercurous sulfate reference electrode (SMSE) and have been corrected for *IR* drop. The ferric ion current distributions for all runs were identical within experimental error and corresponded to mass transfer controlled behavior. For the lowest applied voltage, the driving force for reaction in the upstream region was so small that the copper deposition rate was only 10% of that nearest the counter-electrode. The relative rate of metal deposition in the upstream region increased as a function of the applied potential. Greater penetration of the potential into the electrode occurred in spite of the increased ohmic losses that result from the correspondingly higher volumetric reaction rates. The current distribution became more uniform as the potential increased to -648 mV *vs.* SMSE, where electrode operation is accompanied by the noticeable increase in the hydro-

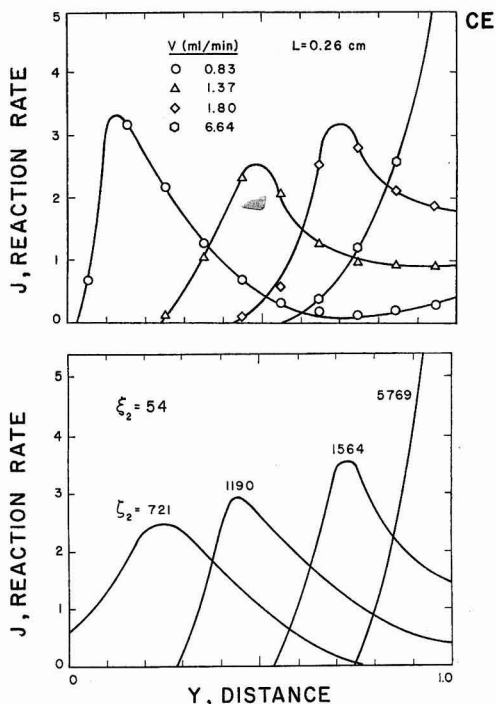


Fig. 8. Flow dependence of the rate distribution of the cobalt reaction in the Cu/Co system. Reactor length is 0.26 cm. Upper figure: experimental data. Lower figure: theoretical predictions.

gen evolution rate in the downstream regions. Further increases in the applied potential resulted in the evolution of undissolved hydrogen gas which collected at the exit face of the cathode.

The model predictions compare reasonably well with the experimental measurements from a qualitative viewpoint, but suffered from quantitative inaccuracy for intermediate values of the applied potential. In contradistinction to the disparity between the calculated and observed current distributions, the predicted copper recoveries agreed surprisingly well with the data. As Fig. 11 amply demonstrates, a significant improvement in the fractional recovery of copper was realized by affecting modest increases in the level of applied potential. For example, an increase in the metal recovery efficiency from 54 to 79% was gained by a 0.13V incremental increase in the cell potential. Further increases in ϕ_a beyond this point, however, yielded negligible improvements in the extent of copper removal due to radial mass transport limitations and increased hydrogen gas evolution in the downstream regions of the electrode.

Conclusions

This program was designed to investigate the fundamental aspects of porous electrode behavior. Large volumetric reaction rates were attained and desirable electrode operating regimes were identified for multi-component systems in simple, laboratory cells. The complex interaction among mass transport, ohmic, and kinetic phenomena affects reactor performance, which is very sensitive to operating conditions such as flow rate, applied potential, and electrode geometry. Experimental results obtained over the range of conditions studied indicate that existing theoretical models provide adequate predictions of electrode behavior. Consequently, the evaluation of practical porous elec-

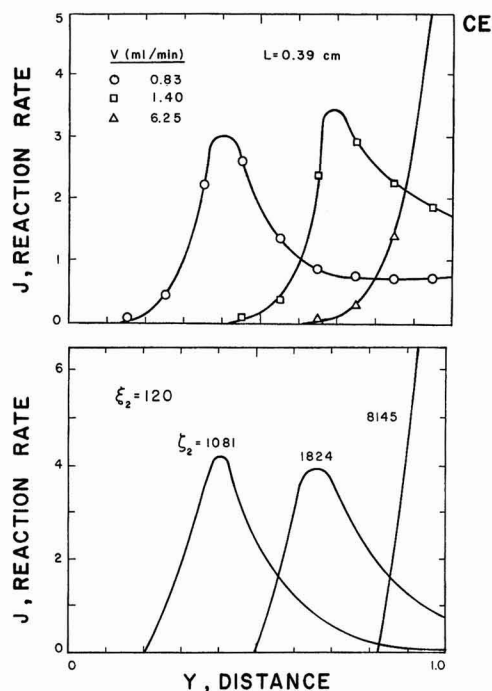


Fig. 9. Flow dependence of the rate distribution of the cobalt reaction in the Cu/Co system. Reactor length is 0.39 cm. Upper figure: experimental data. Lower figure: theoretical predictions.

trode applications would benefit from the incorporation of mathematical models in the conceptual stages of reactor design.

Models should be utilized with increased effectiveness to suggest optimum cell design, arrangement of cell clusters, and process control strategies for large scale equipment. This would circumvent the necessity of anticipating optimum operating conditions on the basis of intuition alone. The utility of highly sophisticated models, however, may be compromised if a large number of system parameters are unknown. Complications in scale-up are often encountered owing to occurrence of electrolyte channeling. Development of cell designs for which scale-up of flow effects is predictable would, therefore, be welcome.

Acknowledgments

Research costs were provided by NSF Grant 76-83379, and by fellowship support from E. I. du Pont de Nemours and Company, and the Exxon Education Foundation.

Manuscript submitted March 9, 1979; revised manuscript received June 12, 1979.

Any discussion of this paper will appear in a Discussion Section to be published in the June 1980 JOURNAL. All discussions for the June 1980 Discussion Section should be submitted by Feb. 1, 1980.

Publication costs of this article were assisted by the University of Illinois.

LIST OF SYMBOLS

English Characters

- a specific surface area, cm^2/cm^3 pore volume
 c concentration, gmole/cm^3
 C c/c° , concentration, dimensionless
 D axial diffusion coefficient, cm^2/sec
 d_p characteristic particle diameter, cm

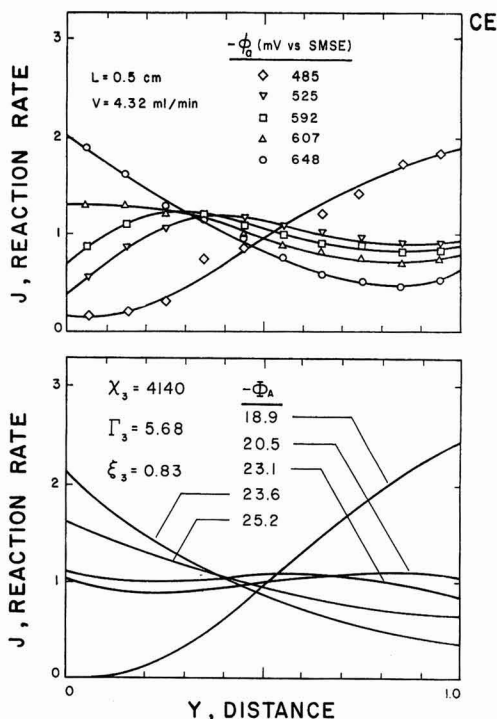


Fig. 10. Potential dependence of the rate distribution of the copper reaction in the Fe/Cu system. Reactor length is 0.5 cm. Upper figure: experimental data. Lower figure: theoretical predictions.

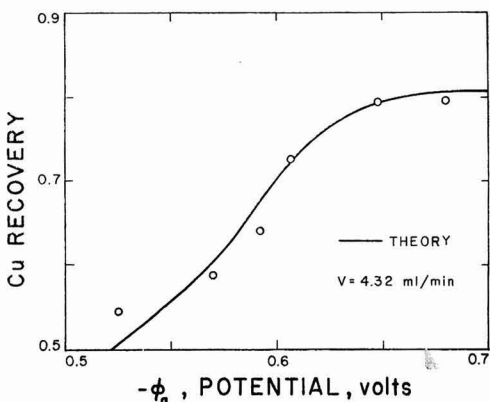


Fig. 11. Dependence of copper recovery upon applied potential in the Fe/Cu system and with a reactor length of 0.5 cm. Solid line gives theoretical prediction.

- e symbol of electronic charge
 f intrinsic reaction rate, A/cm^2
 F Faraday's constant, 96,500 C/g equiv.
 i current density, A/cm^2
 i_0 exchange current density, A/cm^2
 j electrochemical reaction rate, A/cm^2
 J reaction rate, dimensionless
 k mass transfer coefficient, cm/sec
 l electrode length, cm
 M_i symbol for species i participating in reaction
 n number of electrons in a reaction, g equiv./gmole

N	species flux, moles/cm ² -sec
R	gas constant, 8.314 J/gmole-deg
Re	$\rho v d_p / \mu$ Reynolds number, dimensionless
Sc	$\mu / \rho D$ Schmidt number, dimensionless
T	temperature, °K
v	mass average velocity, cm/sec
V	volumetric flow rate, cm ³ /min
y	distance along electrode, cm
Y	y/l distance along electrode, dimensionless
z_i	symbol of electronic charge of species i

Greek Characters

α	anodic transfer coefficient
β	cathodic transfer coefficient
ϵ	void fraction, cm ³ void space/cm ³ reactor volume
Γ	$aknF^2/2c_0/\kappa RT$, mass transfer coefficient, dimensionless
ζ	v_l/D , velocity, dimensionless
κ	electrolyte conductivity, (Ω -cm) ⁻¹
μ	viscosity, g/cm sec
λ	species concentration, dimensionless
ρ	density, g/cm ³
ξ	$i_0 a l^2 F / \kappa RT$, electrochemical reaction rate constant, dimensionless
ϕ	potential, V
Φ	potential, dimensionless
Φ_a	applied potential, dimensionless
x	$i_0 a l^2 / n F D c_0$, mass transfer resistance parameter, dimensionless

Superscripts

l	value at reactor outlet
o	value at reactor inlet
s	surface value

Subscripts

i	species i
r	reference value

REFERENCES

1. R. M. Gould, Ph.D. Dissertation, University of Illinois at Urbana-Champaign, Illinois (1979).
2. R. de Levie, *Adv. Electrochem. Electrochem. Eng.*, **6**, 329 (1967).
3. J. S. Newman and W. Tiedemann, *AIChE J.*, **21**, 25 (1975).
4. J. S. Newman and W. Tiedemann, *Adv. Electrochem. Electrochem. Eng.*, **11**, 353 (1978).
5. R. W. Houghton and A. T. Kuhn, *J. Appl. Electrochem.*, **4**, 173 (1974).
6. R. Alkire and R. Gould, *This Journal*, **123**, 1842 (1976).
7. B. G. Ateya, *J. Electroanal. Chem. Interfacial Electrochem.*, **76**, 315 (1977).
8. B. G. Ateya and L. G. Austin, *This Journal*, **124**, 1540 (1977).
9. J. A. Trainham and J. S. Newman, *ibid.*, **124**, 1528 (1977).
10. Y. Volkman, *J. Appl. Electrochem.*, **8**, 374 (1978).
11. J. A. Trainham and J. S. Newman, *This Journal*, **125**, 58 (1978).
12. R. Alkire and A. Mirarefi, *ibid.*, **124**, 1214 (1977).
13. G. M. Cook and C. Portal, Paper 28 presented at the Electrochemical Society Meeting, Las Vegas, Nevada, Oct. 17-22, 1976.
14. L. E. Vaaler, *This Journal*, **125**, 204 (1978).
15. R. Alkire and B. Gracon, *ibid.*, **122**, 1594 (1975).
16. J. C. Armour and J. N. Cannon, *AIChE J.*, **14**, 415 (1968).
17. A. E. Harvey, J. A. Smart, and E. S. Amis, *Anal. Chem.*, **27**, 26 (1955).
18. J. S. Newman, *Ind. Eng. Chem. Fundam.*, **7**, 514 (1968).
19. D. A. G. Bruggemann, *Ann. Phys. (N.Y.)*, **24**, 636 (1935).
20. D. N. Bennion and J. S. Newman, *J. Appl. Electrochem.*, **2**, 113 (1972).
21. G. W. Vinal and D. N. Craig, *Bur. Stand. J. Res.*, **10**, 781 (1933).
22. M. G. Fouad and G. H. Sedhamed, *Electrochim. Acta*, **20**, 615 (1975).
23. C. N. Satterfield and D. H. Cortez, *IEC Fundam.*, **9**, 613 (1970).
24. L. N. Klatt and W. J. Blaedel, *Anal. Chem.*, **39**, 1065 (1967).
25. A. J. Arvia and J. C. Bazan, *Electrochim. Acta*, **9**, 17 (1964); *ibid.*, **11**, 881 (1966).
26. R. Caban and T. W. Chapman, *This Journal*, **124**, 1371 (1977).
27. "Handbook of Chemistry," 10th ed., p. 1678, McGraw-Hill, New York (1967).
28. "Handbook of Chemistry," 10th ed., p. 1175, McGraw-Hill, New York (1967).
29. M. A. Zhamagortsyants, A. A. Yavich, and A. T. Vagramyan, *Elektrokhimiya*, **11** (1), 103 (1975).

Semiconductor Electrodes

XXII. Electrochromism and Photoelectrochemistry at WO₃ Layers

Prepared by Thermal and Anodic Oxidation of W

Benjamin Reichman and Allen J. Bard*

Department of Chemistry, The University of Texas at Austin, Austin, Texas 78712

ABSTRACT

Electrochromism was studied with WO₃ layers prepared by thermal oxidation of W, and compared to the electrochromic behavior of other WO₃ electrodes (anodic, amorphous, and annealed films). Although the WO₃ layers obtained by thermal oxidation of W are crystalline, the electrochromic performance with this electrode is comparable to that of the evaporated amorphous WO₃ electrode. The photoelectrochemical behavior of these electrodes, and in particular the effect of a pretreatment of repeated color-bleaching cycles, was also studied. Repeated color-bleaching cycles resulted in a significant improvement in the photoelectrolytic behavior of the WO₃ layers. The photocurrent increased and the spectral distribution of the photocurrent shifted to longer wavelengths. The repeated color-bleaching cycles also cause a great improvement in the electrochromic behavior of the WO₃ electrode as compared to that of the initially prepared electrode.

Electrochromism of WO₃ electrodes has been the subject of intensive investigation during the last few

years in connection with its use in display devices (1-5). A major problem with the WO₃ evaporated film which is commonly used as the display electrode, is the fact that it dissolves in the H₂SO₄-aqueous solution,

* Electrochemical Society Active Member.
Key words: electrode, electrolyte.

which is usually used as the electrolytic solution in the device (6-8). Several methods have been attempted to circumvent this problem [e.g., nonaqueous solvents with sulfuric acid or Li^+ as the electrolyte (6, 7, 9-11)]. In some solutions the WO_3 evaporated film electrode was found to be more stable than in aqueous solutions, but in these cases the response times for the color-bleach process were longer (6, 7). Display systems based on solid electrolytes have also been studied (12-14). Display devices based on dielectric materials which absorb water to replace the liquid electrolyte also failed to show satisfactory performance (15-18). As opposed to the amorphous WO_3 evaporated film (which is obtained by vacuum evaporation), polycrystalline WO_3 formed by heating the evaporated film to 400°C was found to be more stable in aqueous sulfuric acid solution; the electrochromic performance of such electrodes was very poor, however (1, 7, 13-21).

In this paper, we describe the electrochromic process with WO_3 electrodes obtained by thermal oxidation of tungsten metal. These WO_3 layers are crystalline, but as opposed to the crystalline WO_3 which is obtained by annealing the amorphous evaporated WO_3 films, they show good electrochromic behavior and with a performance similar to that of the amorphous WO_3 evaporated film. On the other hand, the stability of the WO_3 obtained by thermal oxidation of W is also high and therefore these WO_3 layers or modification of them seem to be promising materials for electrochromic display devices.

Because WO_3 is an n-type semiconductor, it has recently attracted attention in photoelectrochemical applications. Photooxidation of water was studied using WO_3 single crystals (22-23) and polycrystalline WO_3 prepared by several methods (24-28). In most of these electrodes, photoanodic current is generated only under irradiation with light of wavelength below 400-480 nm. Several methods have been tried to extend the response of wide bandgap semiconductor electrodes to longer wavelengths. We show here that treatment of the thermally oxidized WO_3 electrode by repetitive color-bleaching cycles leads to a marked extension of the photoelectrochemical response. This change in the spectral distribution of the photocurrent suggests that the repeated color-bleaching cycles cause the creation of new electronic states in the WO_3 lattice which are located at energies within the bandgap of the semiconductor.

Experimental

The thermally oxidized WO_3 electrodes were prepared by heating W disks in air in a furnace at about 750°C for 30 min. The WO_3 layers obtained were yellow in color with usual thicknesses of about $25\text{ }\mu\text{m}$ [as estimated by weighing before and after oxidation taking a WO_3 density of 7.16 g/cm^3 (1)]. Part of the WO_3 was scraped off and electrical contact to the underlying W was made with silver epoxy cement. The WO_3 anodic film was prepared as described earlier (7). The area of the electrodes was $\sim 1.3\text{ cm}^2$.

Electrochemical measurements were performed with a Princeton Applied Research (PAR) potentiostat (Model 173) which was supplied with voltage from a PAR Model 174 universal programmer. The reference electrode was $\text{Hg}/\text{Hg}_2\text{SO}_4/1\text{M H}_2\text{SO}_4$ ($+0.67\text{V vs. NHE}$) and the counter electrode was a Pt wire. The uncompensated IR, caused by solution and electrode resistance, was corrected with the positive feedback circuit of the potentiostat. An Oriol 450-W xenon lamp and Model 7240 grating monochromator were used to illuminate the electrodes. The radiant power was measured with Model 550-1 Radiometer/photometer (E.G.&G., Salem, Massachusetts). The semiconductor electrodes were irradiated through a flat Pyrex window. X-ray diffraction spectra were determined with a Philips Norelco x-ray diffractometer. IR spectra were taken with Beckman IR spectrophotometer IR5A. For these measurements, the WO_3 was scraped from the electrode and a pellet with KBr was made (0.5%).

Results

Electrochromic behavior.—Typical current-voltage curves, in the dark, of the $25\text{ }\mu\text{m}$ layer of WO_3 obtained by thermal oxidation of W in air are shown in Fig. 1(a). The cathodic current which starts at $\sim +0.55\text{V}$ is associated with coloration of the WO_3 . The potential where the coloration starts is similar to that for the evaporated and anodic WO_3 films (7, 32). The shape of the current-voltage wave, however, is more like that of the evaporated WO_3 film, i.e., the anodic (bleaching) current starts $\sim 200\text{ mV}$ after reversal of the potential scan. The variation of electrochromic current with scan rate, v , (Fig. 2) is close to $v^{1/2}$ dependence, as previously found for the evaporated WO_3 film (7, 32). As we discussed previously (7, 32), this dependence demonstrates that the electrochromic current is controlled by diffusion of hydrogen through the film, rather than by the nernstian (thin layer) response shown by the anodic film. This behavior has been reproduced by a digital simulation model and will be discussed elsewhere (38). The response time for the color-bleaching process is of the order of one second, as shown by potential-step experiments [Fig. 1(b)]. X-ray diffraction measurements made with these WO_3 layers show that they are crystalline. It has previously been reported that the crystalline WO_3 film obtained by annealing a WO_3 evaporated film at 400°C was not electrochromic (1, 7, 20-21). However, WO_3 crystalline layers formed by annealing the evaporated film have a monoclinic structure [Fig. 3(b)] (6, 20, 33) while the WO_3 layers obtained by thermal oxidation of W have a triclinic structure [Fig. 3(a)] (26, 33). The difference in the crystal structure of these two forms of WO_3 is clear from comparison of Fig. 3(a) and 3(b). The peak at $d = 3.84$, which is characteristic of triclinic structure (33), appears only in the x-ray pattern of the WO_3 obtained by thermal oxidation of W [Fig. 3(a)]. This peak never appears in the pattern of the monoclinic structure (33). Another distinct difference between the pattern of Fig. 3(a) and (b) is the pair of peaks at $d = 2.64$, and $d = 2.66$ which are characteristic of the triclinic structure (33) while in the monoclinic structure only the one in $d = 2.62$ appears. In both cases, there is some deviation from complete randomization of the crystallites and preference for some planes exists.

We previously studied an anodically formed WO_3 film (7, 32) which exhibited very good electrochromic behavior and was amorphous. Recently, an electrochromic WO_3 anodic film prepared under constant current conditions, which is crystalline was described (34). The crystal structure of these anodic films from the x-ray spectra shown in Ref. (34) also appears to be triclinic. Although the electrochromic behavior of the crystalline WO_3 obtained by thermal oxidation of W in the initially prepared form was poor, it improved on repeated cycling through a number of color-bleaching cycles. As shown in Fig. 4, the electrochromic current was low initially but increased gradually upon cycling. The current increased markedly during the first few scans, finally resulting in a steady-state i - E curve after about 20 hr of cycling at 100 mV/sec . Together with the observed increase in cathodic current, there was an increase in the depth of coloration. Although initially the coloration was weak, very good coloration was eventually attained by cycling. After this treatment, the i - E curves remained constant over a long period of time (i.e., for at least two months of continuous cycling in the aqueous sulfuric acid), implying good stability of the electrode. One can show that the higher stability of this electrode is not connected with the fact that the WO_3 layer here is thick compared to that usually used with the evaporated film electrode ($\sim 1\text{ }\mu\text{m}$). Neither is it connected with the fact that for the same amount of charge penetrating into the lattice, the concentration of charge in the thicker film is lower. As the digital simulation model clearly shows (38), in the time scale used in these experiments, the hydrogen does not

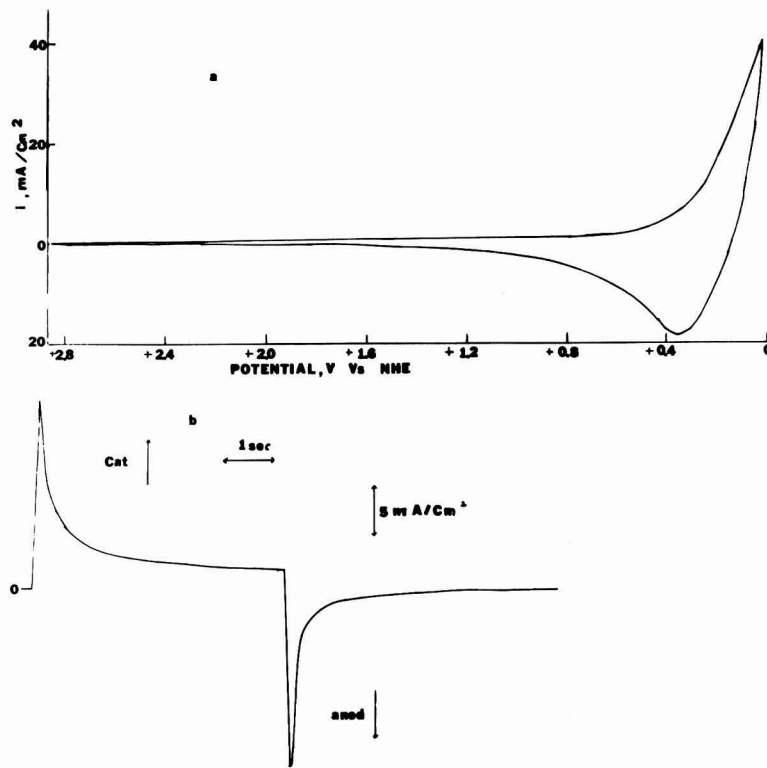


Fig. 1. (a) Current-voltage curve, in the dark, at $25 \mu\text{m}$ WO_3 layers obtained by thermal oxidation of W, recorded at scan rate of 100 mV/sec; (b) Current change at the WO_3 layers, recorded during potential steps in the coloration region between 0-0.9V. These curves were obtained with electrode after cycling in the color-bleach region for ~ 20 hr.

penetrate very deeply into the lattice and most of the charge at these times is concentrated in the first $1 \mu\text{m}$. Thicker films were used in these experiments simply to produce WO_3 layers which are yellow in color in the bleached form. The apparent stability of the electrode

can also not be attributed to further oxidation of the W substrate with continuous replenishment of oxide, as we have shown happened in the case of the WO_3 anodic film (7). The fact that we observe equal amounts of charge during the cathodic and the anodic

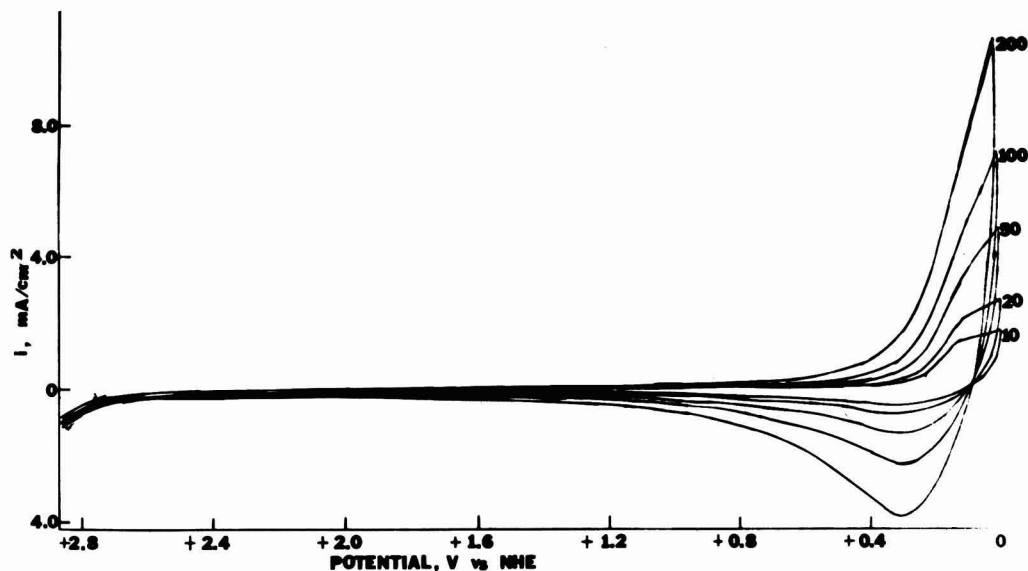


Fig. 2. Cyclic voltammograms recorded at different scan rates at WO_3 layers prepared as in Fig. 1. The numbers on the curves are scan rates in mV/sec.

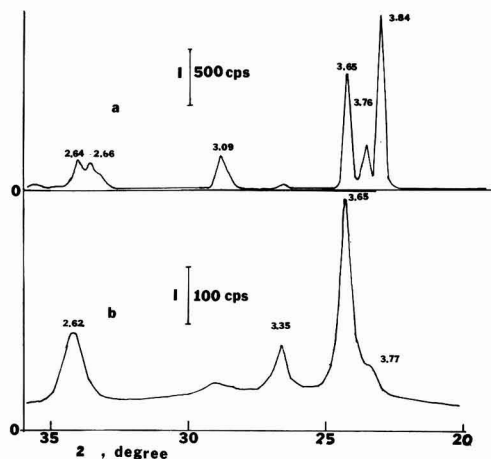


Fig. 3. X-ray diffraction pattern recorded for (a) WO_3 layers obtained by thermal oxidation of W; (b) WO_3 film obtained by annealing to 400°C , the evaporated film on glass. The d spacing associated with the different peaks is marked in the figures.

processes during cycling eliminates this possibility. Moreover, further oxidation of the W can probably not occur with such thick oxide films at the low positive polarizations ($\sim +2\text{V}$) used in these experiments; usually $\sim 100\text{V}$ is needed to grow $1\text{ }\mu\text{m}$ of WO_3 anodically (7). Thus, the stability of the WO_3 layers ob-

tained by thermal oxidation of W must be inherent in the material itself. During the repeated color-bleach cycling, no change in the degree of porosity of the film was found as can be judged from the scanning electron microscope pictures shown in Fig. 5(a, b). This is in contrast to the more porous WO_3 anodic film electrode (7) in which the degree of porosity increased during repeated color-bleach cycling [Fig. 5(c, d)]. Moreover, IR-spectroscopic measurements of pellets prepared with WO_3 scraped from the electrode show that the amount of water in the thermally oxidized film, which is initially small, does not increase during this color-bleaching process in contrast to the behavior of the anodic and evaporated film electrodes (7). In Fig. 6, IR spectra taken with (a) a typical anodic film electrode after cycling for several hours, (b) an evaporated film electrode, and (c) an electrode of WO_3 obtained by thermal oxidation are shown for comparison. The peaks at 1650 and 3500 cm^{-1} which are the characteristic IR peaks of water, are largest for the anodic film electrode which show that these films contain the highest amounts of water. They are smaller in the evaporated film electrode and are negligible for the WO_3 obtained by thermal oxidation, showing that these latter films are "dry." In the previous paper (7), we have shown that the amount of water in the anodic film and also in the evaporated film electrodes increases during continuous color-bleaching cycles and the rate of coloration is related to this amount of water. For the WO_3 layer obtained by thermal oxidation, the spectrum shown in (c) is typical for both a virgin layer or for a layer which was cycled many times in the color-bleach region. An IR spectrum similar to (c) was also obtained for evaporated films which were annealed at 400°C for 3 hr [x-ray pattern in Fig. 3(b)].

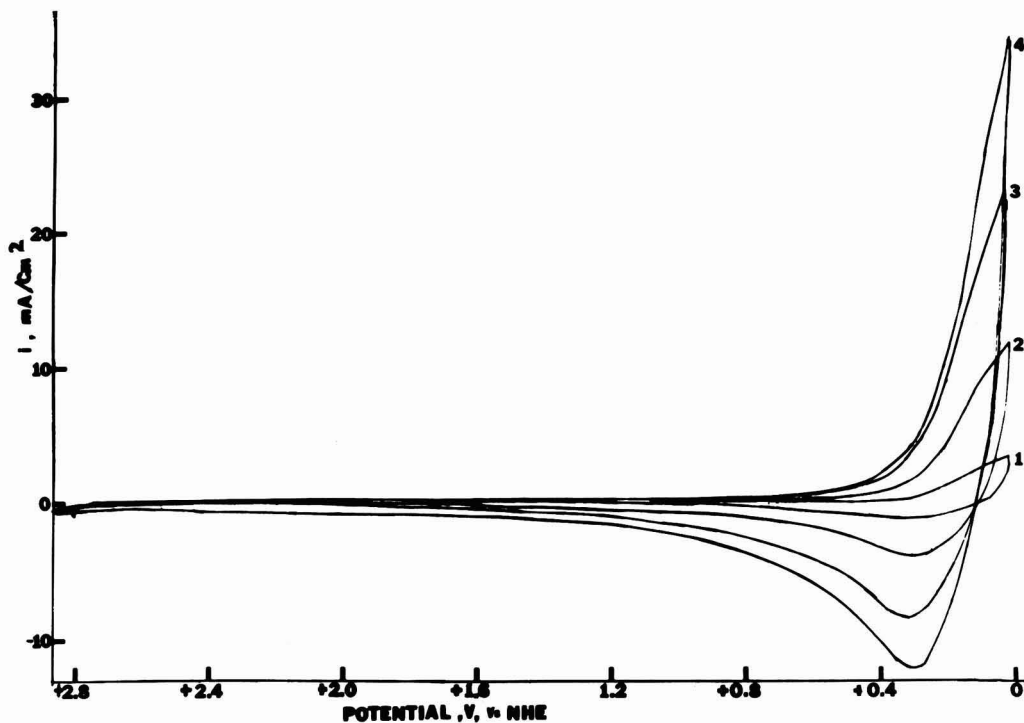


Fig. 4. Change of current during repeated color-bleach cycling at the WO_3 electrode prepared by thermal oxidation of W. The numbers in the figures represent voltammograms recorded at different times during the repeated color-bleaching process: curve 1, first cycle; curve 2, after 2 hr of color-bleaching steps between 0 and $+2.8\text{V}$ at 2 Hz frequency; curve 3, after additional 15 hr cycling at 100 mV/sec within the potential limits shown in Fig. 1; curve 4, after additional $3\frac{1}{2}$ hr color-bleaching steps as in No. 2.

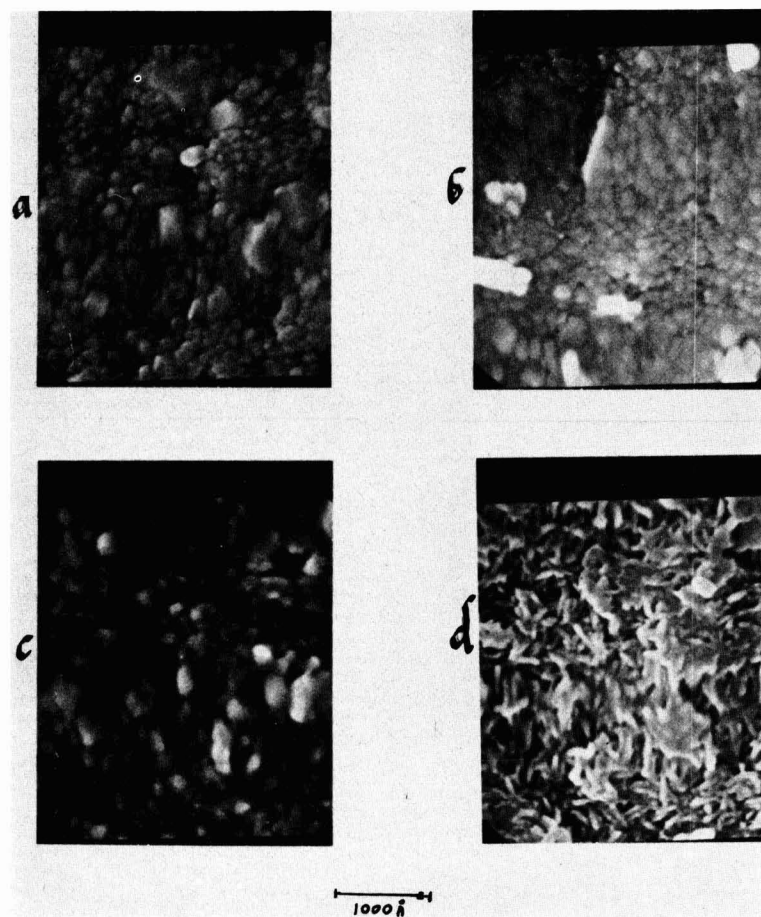


Fig. 5. Electron microscope picture of WO_3 obtained by thermal oxidation and anodic oxidation of W: (a) "as prepared" WO_3 thermally oxidized WO_3 ; (b) after cycling it in the color-bleaching region for about 20 hr; (c) "as prepared" anodic WO_3 film; (d) after cycling it in the color-bleaching region for about 20 hr.

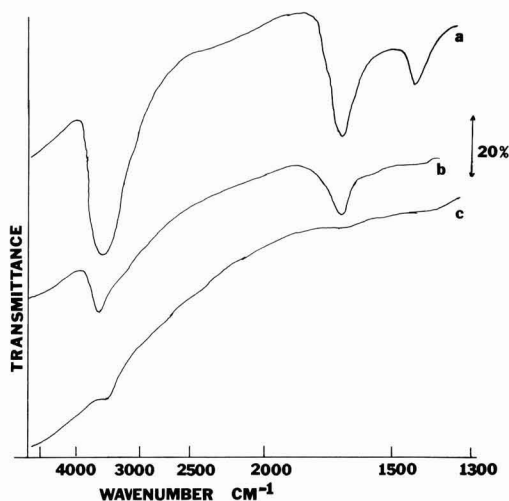


Fig. 6. IR spectra of (a) WO_3 anodic film electrode after cycling for 20 hr; (b) WO_3 evaporated film electrode after cycling for 7 hr; (c) WO_3 layer obtained by thermal oxidation of W metal, either fresh or after cycling.

Photoelectrochemical behavior of thermally oxidized WO_3 electrode and effect of cycling.—We also found, as described below, that these changes in the thermally oxidized WO_3 upon cycling also cause an improvement in the photoelectrochemical behavior of the electrode. The steady-state photocurrent-potential curves in 1M H_2SO_4 of the thermally oxidized WO_3 electrode after cycling through the color-bleach process for different times, with illumination of the electrode by the full power of 450-W xenon lamp is shown in Fig. 7. The photocurrent increased gradually as a result of the continuous cycling, paralleling the increase in the current for the electrochromic process. At the same time a small decrease in the dark current for the oxidation of water occurred. Continuous cycling finally resulted in the establishment of a maximum photocurrent; cycling beyond this point through the color-bleach process caused a small gradual decrease in the photocurrent. A similar phenomenon was also observed recently with TiO_2 (35). The increase in the photocurrent upon cycling is at least partially attributable to changes in the spectral distribution of the anodic photocurrent (Fig. 8). With the fresh electrode, the photocurrent started at about 400 nm. However, with continuous cycling through the color-bleach process the current response shifted to longer wavelengths with a peak in the photocurrent appearing at about 450 nm. This change in the spectral distribution of the photocurrent suggests that cycling causes the creation of new states

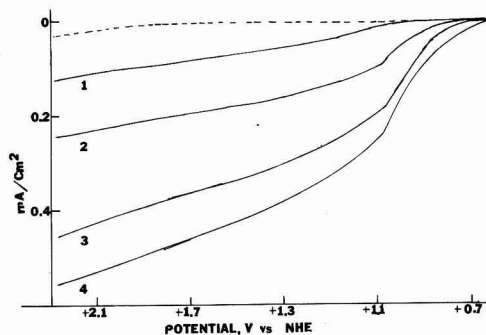


Fig. 7. Steady-state anodic photocurrent at the WO_3 electrode, obtained by thermal oxidation of W at different times during a continuous color-bleaching process in 1M H_2SO_4 solution. The numbers represent the times as in Fig. 4.

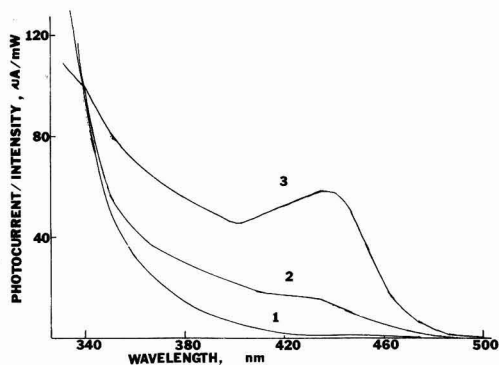


Fig. 8. Spectral distribution of the anodic current measured at +2.2V, at different times during the continuous color-bleaching process: curve 1, "as prepared"; curve 2, after 3 hr cycling in the color-bleaching region (100 mV/sec); curve 3, after 20 hr cycling. The spectra were corrected for the power spectra of the lamp.

in the WO_3 lattice, located at energies within the band-gap. The anodic photocurrent in such an activated electrode occurs, not only via the valence band-conduction band transitions, but also through transitions involving these new states. The photocurrent at this activated electrode was very stable for at least 3 hr under illumination. The space charge capacity of the electrode at different stages during the continuous color-bleach cycling could not be measured because a small dark current exists at potentials positive of the flatband potentials.

Photoelectrochemical behavior of anodic film WO_3 electrode and effect of cycling.—An anodic photocurrent could also be observed with the anodic film WO_3 electrode, prepared as previously described (7). The photocurrent observed with these amorphous WO_3 electrodes were 10-100 times smaller than those with the thermally oxidized WO_3 layers described above. The steady-state photocurrent-potential curves at different times after color-bleach cycling are shown in Fig. 9(a). The currents in the electrochromic region at the same times are shown in Fig. 9(b) for comparison. Note that as opposed to the case of the thermally oxidized WO_3 , the photocurrent with the anodic WO_3 film decreased as a result of the cycling, while at the same time the electrochromic current increased.

Discussion

We (7, 32) and others (20) have shown that the existence of water in the WO_3 amorphous film is im-

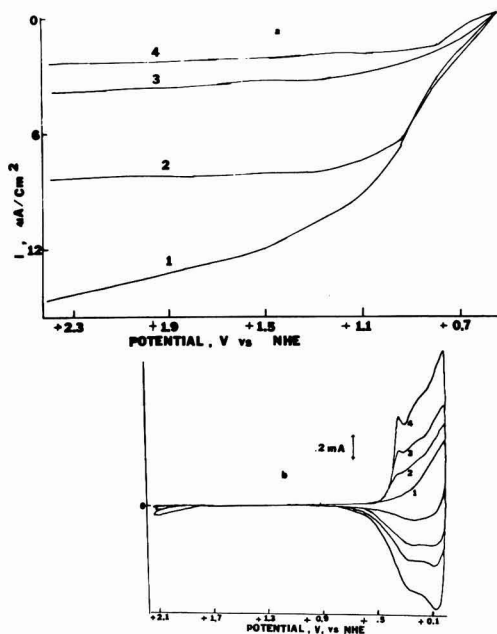


Fig. 9. (a) The anodic photocurrent, and (b) the electrochromic current recorded with WO_3 anodic film at different times during continuous color-bleaching cycles (100 mV/sec): curve 1, "as prepared" electrode; curve 2, after 1½ hr; curve 3, after 6 hr; curve 4, after 20 hr. The area of the electrode, 1.3 cm^2 .

portant for a good electrochromic performance with these films, and that "dry" WO_3 which was obtained by annealing the evaporated film to 400°C was a very poor electrochromic. In the present work, we see that the water in the film, high porosity, and low density are less important factors for good electrochromic behavior, if the WO_3 layer has the right crystal structure. The fact that the WO_3 obtained by thermal oxidation of W is electrochromic, while the WO_3 which is obtained by annealing the evaporated film to 400°C is not, although they are both polycrystalline, must be caused by the difference in the crystal structure of both films. The triclinic structure of the thermally oxidized WO_3 , must allow more rapid transfer of protons or hydrogen atoms within the crystal lattice to form the blue hydrogen tungsten bronze (H_xWO_3) as compared to the monoclinic structure of the annealed evaporated film. That the crystalline form of WO_3 shows electrochromic properties similar to those of the amorphous WO_3 is interesting from a practical point of view, because the crystalline form is much more stable as compared to the amorphous one in the aqueous sulfuric acid used as the electrolyte for display devices. The increase in the electrochromic current as well as the depth of coloration under repeated color-bleach cycling suggests further changes in the crystal lattice as a result of this continuous cycling process. As opposed to the behavior of WO_3 evaporated and anodic films described in a previous paper (7), the improvement in the electrochromic performance in the case of the thermally oxidized WO_3 layer is not associated with changes in the porosity or the amount of water in the film and does not result in qualitative changes in the shape of the current-voltage curves. For the thermally oxidized WO_3 films, the increase in the electrochromic current and the depth of coloration must be mainly due to an increase in the amount of hydrogen which can exist in the WO_3 lattice at equilibrium, rather than to an increase in the rates of reactions (38). The photocurrent measurements sug-

gest that on cycling new electronic levels are produced in the WO_3 which promote photooxidation of water. These new levels may involve defects which may also allow an increase in the amount of hydrogen which can penetrate the WO_3 lattice at equilibrium, and thus improving the electrochromic performance. It is interesting to compare this effect of continuous cycling on the photooxidation behavior with the effect of annealing of WO_3 electrodes obtained by sputtering, found by Gissler and Memming (27). These authors found that the current associated with the photooxidation of water increased upon annealing the sputtered WO_3 layer in an oxygen atmosphere; the longer was the annealing time, the higher was the photocurrent. The highest response was obtained with WO_3 formed by heating tungsten in an oxygen atmosphere to high temperatures ($760^\circ\text{--}780^\circ\text{C}$). These authors also found changes in the spectral distribution of the current on annealing similar to those found here and attributed these effects to the production of intraband bulk states. These findings suggest that the new states produced by Gissler and Memming by annealing the WO_3 samples in an O_2 atmosphere can also be created by continuous electrochemical cycling. Note that while the continuous cycling process causes an improvement in the photoelectrochemical properties for the thermally oxidized WO_3 film, it causes a degradation in the photocurrent for the anodic WO_3 films. This indicates that the nature of the change in the WO_3 lattice for these two films is different. In fact, we have previously shown (7, 32) that, as a result of the repeated color-bleach cycling with the anodic film, the amount of water in these films and its porosity increases. While these changes produce a large improvement in the electrochromic performance, they may well cause a deterioration in the photoelectrochemical behavior. On the other hand, the changes in the case of the thermally oxidized WO_3 layers on cycling, are not associated with changes in the water content or porosity of the film, but rather with the creation of states or defects in the film which lead to an improvement in both electrochromic and photoelectrochemical behavior.

Acknowledgment

The support of this research by Texas Instruments, Incorporated, is gratefully acknowledged.

Manuscript submitted April 23, 1979; revised manuscript received June 12, 1979.

Any discussion of this paper will appear in a Discussion Section to be published in the June 1980 JOURNAL. All discussions for the June 1980 Discussion Section should be submitted by Feb. 1, 1980.

Publication costs of this article were assisted by The University of Texas at Austin.

REFERENCES

1. S. K. Deb, *Philos. Mag.*, **27**, 801 (1973).
2. B. W. Faughnan, P. S. Crandall, and P. M. Heyman, *RCA Rev.*, **36**, 177 (1975).
3. H. N. Hersh, W. E. Kramer, and J. H. McGee, *Appl. Phys. Lett.*, **27**, 646 (1975).
4. I. F. Chang, B. L. Gilbert, and T. I. Sun, *This Journal*, **122**, 955 (1975).
5. R. S. Crandall and B. W. Faughnan, *Appl. Phys. Lett.*, **28**, 95 (1976).
6. J. P. Randin, *J. Electron. Mater.*, **7**, 47 (1978).
7. B. Reichman and A. J. Bard, *This Journal*, **126**, 583 (1979).
8. T. C. Arnolduseen, Abstract D-2 presented at The 20th Conference on Electronic Materials, University of California, Santa Barbara, California, June 1978.
9. T. B. Reddy and E. A. Battistelli, Abstract G-4 presented at The 19th Conference on Electronic Materials, Cornell University, Ithaca, New York, June 1977.
10. S. K. Mohapatra, *This Journal*, **125**, 284 (1978).
11. T. J. Knowles, H. N. Hersh, and W. Kramer, Abstract 1-3 presented at The 19th Conference on Electronic Materials, Cornell University, Ithaca, New York, June 1977.
12. M. Green and D. Richman, *This Solid Films*, **24**, 595 (1974).
13. W. C. Dautremont-Smith, M. Green, and K. S. Kang, *Electrochim. Acta*, **22**, 751 (1977).
14. G. Barna, *J. Electr. Mater.*, **8**, 153 (1979).
15. I. Shimizu, M. Shizukuishi, and E. Inoue, Private communication.
16. Y. Hajinota, M. Matsushima, and S. Ogura, Abstract B-3 presented at The 20th Conference on Electronic Materials, University of California, Santa Barbara, California, June 1978.
17. H. J. Stocker, S. Singa, L. G. VanUitert, and G. Zydrik, Abstract B-4, *ibid.*, 1978.
18. A. J. Hughes, P. Lloyd, and R. Hurditch, Abstract I-5 presented at The 19th Conference on Electronic Materials, Cornell University, Ithaca, New York, June 1977.
19. H. R. Zeller and H. U. Beyeler, *J. Appl. Phys.*, **13**, 231 (1977).
20. R. J. Hurditch, *Electron. Lett.*, **11**, 142 (1975).
21. B. W. Faughnan, R. S. Crandall, and M. A. Lampert, *Appl. Phys. Lett.*, **27**, 646 (1975).
22. M. A. Butler, R. D. Nasby, and R. K. Quinn, *Solid State Commun.*, **19**, 1011 (1976).
23. M. A. Butler, *J. Appl. Phys.*, **48**, 1914 (1977).
24. G. Hodes, D. Cahen, and J. Manassen, *Nature*, **260**, 312 (1976).
25. K. L. Hardee and A. J. Bard, *This Journal*, **124**, 215 (1977).
26. C. E. Derrington, W. S. Godek, C. A. Castro, and A. Wold, *Inorg. Chem.*, **17**, 977 (1978).
27. W. Gissler and R. Memming, *This Journal*, **124**, 1711 (1977).
28. W. A. Gerrard, *J. Electroanal. Chem.*, **86**, 421 (1978).
29. R. N. Noufi, P. A. Kohl, S. N. Frank, and A. J. Bard, *This Journal*, **125**, 246 (1978).
30. A. Fujishima, K. Honda, and S. Kikuchi, *J. Chem. Soc. Jpn.*, **72**, 108 (1969).
31. C. C. Dutoit, F. Cardon, F. V. Kerchove, and W. P. Gomes, *J. Appl. Electrochem.*, **8**, 247 (1978).
32. B. Reichman and A. J. Bard, Abstract B-9 presented at The 20th Conference on Electronic Materials, University of California, Santa Barbara, California, June 1978.
33. X-ray Powder Diffraction File, Search Manual, ASTM file No. 24-747, 20-1323, L. G. Berry, Editor, Philadelphia, Pa. (1975).
34. A. Di Paola, F. Di Quarto, and C. Sunseri, *This Journal*, **125**, 1344 (1978).
35. S. Gottesfeld, M. Yaniv, D. Laser, and S. Srinivasan, *J. Phys. Paris*, **38**, C5-154 (1977).
36. P. G. Dickens and M. S. Whittingham, *Q. Rev., Chem. Soc.*, **22**, 30 (1968).
37. A. B. Ellis, S. W. Kaiser, and M. S. Wrighton, *J. Am. Chem. Soc.*, **98**, 1635 (1976).
38. B. Reichman, D. Laser, and A. J. Bard, *This Journal*, In press.

The Influence of H_2SO_4 Concentration on Hydrogen and Oxygen Electrosorption at Platinum

R. O. Lezna, N. R. de Tacconi, and A. J. Arvia

*Instituto de Investigaciones Fisicoquímicas Teóricas y Aplicadas (INIFTA),
División Electroquímica, Sucursal 4, Casilla de Correo 16, 1900 La Plata, Argentina*

ABSTRACT

The potentiodynamic E/I displays covering the potential range of both the electrosorption of hydrogen and oxygen on platinum at 25°C , in H_2SO_4 solutions ($0.5\text{M} \leq C \leq 12.1\text{M}$) are presented. Through the changes of the profile with the acid concentration ($\text{HSO}_4^-/\text{SO}_4^{2-}$ ratio) different behaviors were observed in the hydrogen electrosorption and oxygen electrosorption potential regions. The electroreduction process of the oxygen-containing layer revealed a possible surface restructuring contribution which is comparable to that already described for the platinum/molten bisulfate interfaces. The different possibilities for anion interaction are qualitatively considered.

The electrosorption and electrodesorption of hydrogen and oxygen at platinum electrodes has been the subject of extensive research, both in dilute acid aqueous solutions (1-3), and in molten bisulfates (4-6). These processes are sensitive to the perturbation conditions at the interface, the ionic composition of the solution, the crystallographic structure of the metal, and the electrode history (7-12). Moreover, they are even more complex because surface restructuring also contributes to the over-all process, particularly in the oxygen electrosorption and electrodesorption potential range (13).

A relatively large amount of data on the influence of ionic adsorption has been published covering the whole potential range of water thermodynamic stability. The influence of the sulfuric acid concentration on the limiting oxygen coverage revealed that the Pt/O ratio changes from 0.5 to 1.0 as limiting values. When the acid concentration changes from 1M to 11M (7, 10, 14-20).

The relatively large amount of available data indicates that with sufficiently strong anion adsorption the potentiodynamic E/I profiles can be appreciably changed. The anion influence in the oxygen electrosorption potential range is explained in terms of both site blocking and electrostatic influence on the initial stage of the electrooxidation processes. In the hydrogen potential range, however, the anion influence seems to be more complex (9, 11, 21). The present investigation was undertaken to attempt to differentiate more comprehensively the anion influence in the oxygen-containing monolayer potential regions and to correlate the results with those previously obtained with the Pt/molten bisulfate interfaces (4-6).

The qualitative data obtained indicate that no single model for the interaction of the ions with the adsorbing electrode surface can be applied (11, 12) to explain the changes produced by the anions in the potential range of the hydrogen adatoms and in the potential range of the oxygen-containing monolayer.

Experimental

Conventional electrolysis cell and perturbation techniques were used to obtain the stabilized triangular potential sweep E/I displays at different potential sweep rates (v) ($0.01 \text{ V/sec} \leq v \leq 0.3 \text{ V/sec}$) as described in previous publications (4-6). The working electrode consisted of a smooth polycrystalline Pt wire (spectroscopically pure, Johnson-Matthey and Company) of 0.228 cm^2 apparent area. For each new experiment the working electrode was first polished with

alumina, washed in triply distilled water immersed in a 1:1 volume ratio $\text{H}_2\text{SO}_4\text{-HNO}_3$ (both Merck p.a.) for 30 min and then rinsed with triply distilled water. The potential of the working electrode was measured against a reversible hydrogen electrode in the same solutions, but all the potentials were referred to the normal hydrogen electrode. The equilibrium potentials of each Pt/ H_2SO_4 solution were independently measured against a saturated calomel electrode and later referred to the NHE scale. The estimated error due to the liquid junction potential in the concentration range covered by the present work is of the same magnitude as that of the proper potentiodynamic measurements.

Acid solutions of different concentrations ($0.5\text{M} \leq C \leq 12.1\text{M}$) were prepared with triply distilled water and 97% (Merck, p.a.) sulfuric acid which was treated with a.r. hydrogen peroxide (Riedel-de Haën) in the usual way (22). Before each run, the solutions were deoxygenated by bubbling purified nitrogen and the working electrode in the cell was first activated by repetitive triangular potential scans at either 0.05 or 0.1 V/sec from 0.03 to 1.5V (RHE) until a stable E/I profile was obtained. Runs were made at 25°C . The gas was continuously passed above the previously deoxygenated solutions in the cell during each run.

Results

Conventional stabilized E/I displays run with triangular potential sweeps at 0.05 V/sec between the $E_{\lambda,c}$ and $E_{\lambda,a}$ switching potentials comprised within the potential range corresponding to the thermodynamic stability of water, show that both the anodic and the cathodic E/I contours depend considerably on the electrolyte concentration (Fig. 1).

Although, in principle, the charge balance resulting from the present data confirms the findings of previous works (7, 10) further interesting details are observed. Thus, the charge balances of the stabilized E/I profiles show that Q_a , the over-all anodic charge ($Q_a = Q_{H,a} + Q_{O,a}$) to Q_c , the over-all cathodic charge ($Q_c = Q_{H,c} + Q_{O,c}$) ratios are close to one. $Q_{H,a}$, $Q_{H,c}$, $Q_{O,a}$, and $Q_{O,c}$ denote the anodic and cathodic charges associated to the potential region of the hydrogen and oxygen layer, respectively. The $Q_a/Q_c = 1$ ratio, however, is no longer obeyed when the hydrogen and oxygen monolayer regions are independently considered. Apparently only during the first potential sweep, in the hydrogen adatom region both the anodic and the cathodic charges are almost equal ($(Q_{H,a}/Q_{H,c})_{n=1} \approx 1$ while in the oxygen-containing monolayer region ($(Q_{O,a}/Q_{O,c})_{n=1} > 1$). Contrarily, when the stabilized E/I profile is considered, then $(Q_{H,a}/Q_{H,c})_{n=n} < 1$ and $(Q_{O,a}/Q_{O,c})_{n=n} > 1$. Nevertheless, when the $E_{\lambda,c}$ limit is con-

* Electrochemical Society Active Member.
Key words: hydrogen monolayer, oxygen monolayer, anion influence, anion adsorption, electrocatalysis.

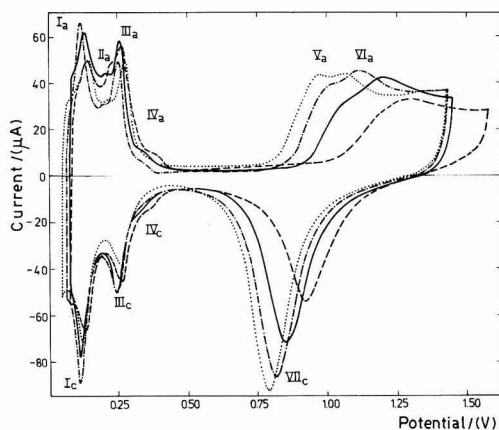


Fig. 1. Potentiodynamic E/I displays for different H_2SO_4 concentrations run at 50 mV/sec and 25°C . (.....) 0.50M; (---) 3.93M; (—) 7.42M; (-----) 12.1M.

fined to the potential region just preceding the oxygen monolayer electroformation, the charge ratio resulting from the stabilized E/I profile approaches the value of one. But this is not the case when the same charge analysis is extended to the hydrogen adatoms potential range. Then, the $Q_{\text{H,a}}/Q_{\text{H,c}}$ charge ratio only approaches one as v increases. The charge related to the electroformation of the oxygen-containing monolayer approaches a smooth sigmoid curve when plotted as a function of the potential. At a constant potential, the charge decreases quite appreciably as the H_2SO_4 concentration increases (Fig. 2).

The multiplicity of the hydrogen adatom E/I profile (Fig. 1) for sulfuric acid concentrations lower than ca. 7 to 8M involves at least three well-defined anodic current peaks (I_a , II_a , III_a), a hump at more anodic potentials (IV_a), two well-defined conjugate cathodic current peaks (I_c , III_c) and also the conjugate cathodic hump (IV_c). At the higher acid concentrations the contributions of current peak II_c and the humps IV_a and IV_c are appreciably magnified at the expense of current peaks I_a , I_c , III_a , and III_c when $E_{a,c}$ is more positive than 0.1V thereabouts (Fig. 1). Therefore, the

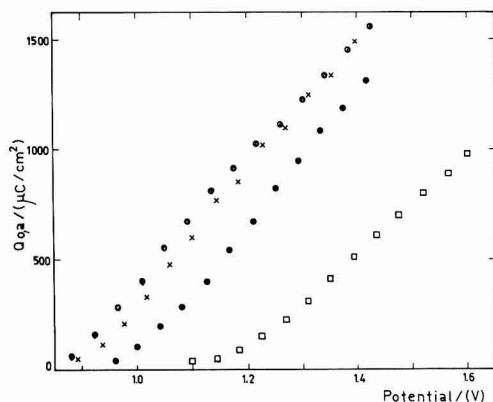


Fig. 2. Integral charge related to the oxygen-containing species read at different anodic potentials plotted as a function of the anodic potential. (○) 0.50M H_2SO_4 ; (×) 3.93M H_2SO_4 ; (●) 7.42M H_2SO_4 ; (□) 12.1M H_2SO_4 .

distribution of the hydrogen adatom current peaks depends on the sulfuric acid concentration. At a constant composition the current peak heights increase linearly with v . However, the shift of the hydrogen peaks, both in the anodic and in the cathodic sweep, towards more negative potentials with increasing acid concentration are not as large as reported (10) if the electrode potentials are referred to the NHE instead of the RHE. The reverse occurs in the potential range of the oxygen-containing layer. The resolution of the E/I displays, as far as the hydrogen adatom current peak is concerned, particularly current humps IV_a and IV_c is slightly improved when compared to previous data.

The electroadsorbed oxygen species in agreement with previous results (10, 14) start to form on the electrode at potentials which are more positive as the H_2SO_4 concentration increases (Fig. 1). The stabilized E/I displays in the potential range of the electroadsorption of the oxygen containing species show, with sulfuric acid concentrations lower than 12M, two anodic current peaks (V_a and VI_a) and a single wide cathodic current peak (VII_c). With higher sulfuric acid concentrations a wide anodic current peak is observed. As the potential sweep rate increases, the oxygen electroreduction current peak becomes wider and relatively more asymmetric due to the interference of the aging process during and after the electroformation of the oxygen-containing monolayer.

The potential difference between the hydrogen adatom potential region and the oxygen-containing monolayer potential region increases as the sulfuric acid concentration increases. But, although this suggests that the double layer region becomes more extended, the anodic current in this region is always smaller than the cathodic current. In principle, this reveals that during the negative going potential excursion there is a faradaic cathodic current contribution in the so-called double layer potential region.

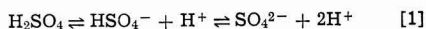
The heights of the current peaks (I_p) located in the oxygen electroadsorption potential range also fit linear I_p/v relationships but the cathodic current peak has to be referred to the unit anodic charge, since the latter, at a constant $E_{a,c}$ depends on v_a (Fig. 3). The influence of v both on the height and location of the current peaks associated with the oxygen-containing film is similar to those already known in other electrolytes under uncontrolled aging of the electroformed species. The situation is also similar for the hydrogen adatom current peaks, except that while the electrodesorption current peak potentials are independent of v , those of the electroadsorption process become slightly more negative as v increases.

The oxygen electroformation potential shifts linearly towards more positive potentials with the H_2SO_4 anion concentration ($\text{HSO}_4^- + \text{SO}_4^{2-}$) (Fig. 4). The same trend is observed for ΔE_p , the potential difference of the anodic and cathodic current peak potentials observed in the oxide region.

The electroreduction current peak VII_c under comparable perturbation conditions moves more slowly towards the positive potential side as the H_2SO_4 concentration increases. Simultaneously, the $I_{p,c}/\Delta I_{p,c,1/2}$ ratio also increases. $\Delta I_{p,c,1/2}$ denotes the cathodic current peak width at 0.5 $I_{p,c}$. These effects reveal that the increasing electrolyte concentration influences not only the charge but also the energetic distribution of the species anodically formed and hinders to a certain extent the rate of their chemical transformation into more stable species.

Discussion

The effects associated with changing H_2SO_4 concentration are, in part, derived from the change of the ionic composition of the electrolyte of the solution due to the ionization equilibria



The relative concentrations of the H_2SO_4 , HSO_4^- ,

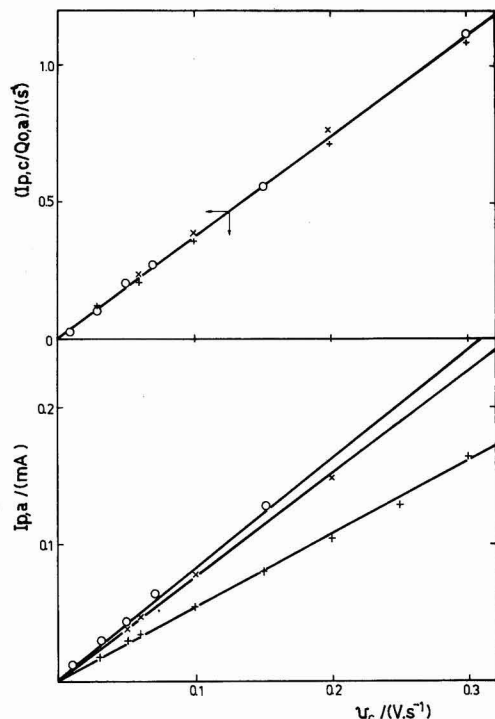


Fig. 3. $I_{p,c}/Q_{O,a}$ vs. v and $I_{p,a}$ vs. v plots. (○) 3.93M; (×) 7.42M; (+) 12.1M.

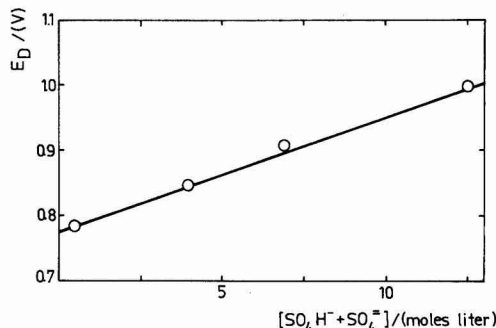


Fig. 4. E_D , the extrapolated potential related to the initiation of the oxygen containing film formation as a function of the H_2SO_4 anion concentration.

and SO_4^{2-} as a function of acid concentration covering the range employed in the present work are well established (15). On the other hand, the adsorption of HSO_4^- ions on platinum electrodes has been determined by using radio-tracer techniques (16, 18) and quantitatively studied (19) by means of the triangular potential sweep technique (17). It is concluded that adsorbed HSO_4^- occupies two oxygen adsorption sites (9). The adsorption equilibrium in 0.5M H_2SO_4 is attained after 100 sec and the maximum coverage (ca. 0.15) is reached at 0.8V (9), a potential which corresponds to that of the initiation of the oxygen-containing monolayer.

The increasing concentration of sulfuric acid anions affects in a different way the hydrogen and the oxy-

gen electrosorption regions. Thus, in the hydrogen adatom region, the distribution of both the anodic and cathodic current peaks are altered without a substantial trend in the shift of the corresponding peak potentials with the sulfuric acid concentration. Apparently under the present circumstances, the effect of increasing the anion concentration changes the relative heights of the hydrogen adatoms current peaks which can be explained as a simple selective blocking of the various hydrogen adsorption sites. This effect, in principle, coincides with that already described for the role of oxo-anions on the potentiodynamic displays with different acid electrolytes (11), but from the charge balances already described, the anion influence is complicated by the possible occurrence of different electrochemical processes in the potential range of the hydrogen adatoms electroformation. Thus, the values of the $Q_{H,a}/Q_{H,c}$ and $Q_{O,a}/Q_{O,c}$ ratios different from one indicate that a fraction of the oxygen-containing layer is electroreduced in the potential range of the hydrogen adatoms electroformation. The products which formed that fraction should be more stable than the product initially electroformed. Moreover, if the electroreduction of the oxygen-containing layer occurs irreversibly, then within a constant potential range the corresponding charge should decrease as the potential sweep rate increases. The existence of different surface species produced in the course of the anodic reaction are associated with the aging processes already described (1-6, 11). Therefore, the influence of anions in the hydrogen adatom potential range is actually more involved than was thought earlier. Other than the two possibilities already discussed (11, 15), namely either the prevalence of a simple blocking effect by the anions, or a significant disturbance of the adsorption energy for a particular type of site, a third possibility is that the electrode surface is simultaneously influenced both by the anion adsorption and by a residual layer of strongly bound oxygen-containing species. Thus, taking into account the location of the potential of zero charge for the Pt/ H_2SO_4 (aq) interface ($E_z \approx 0.3V$) (23, 24) in this potential range it is reasonable to expect either a relatively low electrostatic or rather unfavorable energetic conditions to the anion adsorption. There, the energetics of the surface is predominantly influenced by the remaining oxygen-containing species. This is particularly relevant when data from the stabilized E/I displays are considered. Then, the latter main contribution is the surface blocking. Therefore, unless the perturbation variables on the anion adsorption process are precisely adjusted, only a qualitative comparison of results is feasible.

The adsorption of H_2SO_4 anions on the platinum surface affects the oxygen electrosorption region in an entirely different manner, but very similar to that already described for other ions (9, 19). The change of the potential for the maximum oxygen coverage was attributed to an increasing strength of the Pt-O bond and/or to the greater extent of oxidation (25). The retardation effect was also assigned to the presence of HSO_4^- ions and/or undissociated H_2SO_4 molecules (14). The former ion is known to modify the oxygen chemisorption region on platinum (19). The electrosorption of the oxygen-containing species initiates at a more positive potential as the electrolyte concentration increases. The influence of the anions, in this case, as recently suggested (12) may act by blocking the surface sites and coupling the electrosorption of the oxygen-containing species and the anion desorption. This combined effect is produced by the strong anion adsorption, probably assisted by the electrostatic interaction between the positively charged electrode surface and the anion.

Finally, a third contribution of the anions is revealed through the electroreduction current peak of the oxygen-containing species. As already known, this current peak contour is a complex one and it involves

the electroreduction of different nonequilibrium species. The latter participates in chemical aging processes which quite likely involve a change in microstructure and distribution of lattice sites. Therefore, the changes revealed by the electroreduction current peak are associated with surface restructuring. In this manner the characteristics of the E/I profiles recorded with the highest H_2SO_4 concentration approaches those described in detail for the platinum/molten bisulfate interface (4-6), except that the hydrogen adatoms potential range and the oxygen monolayer potential ranges for the latter interface are closer together because of the effect of temperature. Furthermore, from the present results one explains at least qualitatively that the relatively slow aging rate of the oxygen monolayer on platinum in the molten bisulfates, at temperatures above 200°C thereabouts, as compared to aqueous solutions at room temperature, is probably due to adsorption of the HSO_4^- ion at the metal/electrolyte interface as the major contribution.

On the other hand, the strong interaction between HSO_4^-/SO_4^{2-} ions and platinum at high positive potentials assists the following electrochemical processes, namely, the platinum dissolution as Pt(II) and Pt(IV) (26, 27) in the aqueous electrolytes either at room or even higher temperatures, the $S_2O_8^{2-}$ electroformation in the same electrolytes at low temperatures, and the $S_2O_7^{2-}$ electroformation in the molten bisulfate electrolytes.

Acknowledgment

INIFTA is sponsored by the Consejo Nacional de Investigaciones Científicas y Técnicas, the Universidad Nacional de La Plata, and the Comisión de Investigaciones Científicas (Provincia de Buenos Aires). This work was partially supported by the Regional Program for the Scientific and Technological Development of the Organization of the American States.

Manuscript submitted Nov. 7, 1978; revised manuscript received May 15, 1979.

Any discussion of this paper will appear in a Discussion Section to be published in the June 1980 JOURNAL. All discussions for the June 1980 Discussion Section should be submitted by Feb. 1, 1980.

Publication costs of this article were assisted by the Instituto de Investigaciones Fisicoquímicas Teóricas y Aplicadas.

REFERENCES

1. S. Gilman, in "Electroanalytical Chemistry," Vol. 2, A. J. Bard, Editor, Marcel Dekker, Inc., New York (1969).
2. R. Woods, in "Advances in Electroanalytical Chemistry," Vol. 9, A. J. Bard, Editor, Chap. 1, Marcel Dekker, Inc., New York (1977).
3. G. Belanger and A. K. Vijh, in "Oxides and Oxide Films," Vol. 5, A. K. Vijh, Editor, Chap. 1, Marcel Dekker, Inc., New York (1977).
4. N. R. de Tacconi, A. J. Calandra, and A. J. Arvia, *J. Electroanal. Chem. Interfacial Electrochem.*, **51**, 25 (1974); **57**, 325 (1974).
5. R. O. Lezna, W. E. Triaca, and A. J. Arvia, *ibid.*, **57**, 113 (1974).
6. J. O. Zerbino, N. R. de Tacconi, A. J. Calandra, and A. J. Arvia, *This Journal*, **124**, 475 (1977).
7. T. Biegler and R. Woods, *J. Electroanal. Chem. Interfacial Electrochem.*, **20**, 73 (1969).
8. I. I. Labkovskaya, V. I. Luk'yanycheva, and V. S. Bagotskii, *Elektrokhimiya*, **5**, 580 (1969).
9. V. S. Bagotskii, Yu. B. Vassiliev, J. Weber, and J. N. Pirtskhalava, *J. Electroanal. Chem. Interfacial Electrochem.*, **27**, 31 (1970).
10. W. Vissoher and M. Blijlevens, *ibid.*, **47**, 363 (1973).
11. H. Angerstein-Kozłowska, W. B. A. Sharp, and B. E. Conway, in "Proceedings of the Symposium on Electrocatalysis," M. W. Breiter, Editor, p. 94, The Electrochemical Society Softbound Proceedings Series, Princeton, N.J. (1974).
12. J. C. Huang, W. E. O'Grady, and E. Yeager, *This Journal*, **124**, 1732 (1977).
13. M. E. Folger, J. O. Zerbino, N. R. de Tacconi, and A. J. Arvia, *ibid.*, **126**, 592 (1979).
14. M. R. Andrew, B. D. Mc Nicol, R. T. Short, and J. S. Drury, *J. Appl. Electrochem.*, **7**, 153 (1977).
15. T. F. Young, L. F. Maranville, and H. M. Smith, in "The Structure of the Electrolytic Solutions," W. J. Hamer, Editor, Chap. 4, p. 48, John Wiley and Sons, Inc., New York (1969).
16. V. E. Kazarinov and N. A. Balashova, *Dokl. Akad. Nauk SSSR*, **157**, 1174 (1964).
17. S. Gilman, *J. Phys. Chem.*, **68**, 2088 (1964); **68**, 2112 (1964); **71**, 2424 (1967).
18. M. A. Balashova and V. E. Kazarinov, *Collect. Czech. Chem. Commun.*, **30**, 4148 (1965).
19. I. I. Labkovskaya, V. I. Luk'yanycheva, and V. S. Bagotskii, *Elektrokhimiya*, **5**, 535 (1969).
20. J. Solt, G. Horanyi, and F. Nagy, *Acta Chim. Acad. Sci. Hung.*, **63**, 385 (1970).
21. A. Hubbard, R. Ishikawa, and J. Katekaru, *J. Electroanal. Chem. Interfacial Electrochem.*, **86**, 271 (1978).
22. W. Vissher and M. A. V. Devanathan, *ibid.*, **8**, 127 (1964).
23. J. C. Llopis and F. Colom, in "Encyclopedia of Electrochemistry of the Elements, Vol. IV, A. J. Bard, Editor, p. 169, Marcel Dekker, Inc., New York (1976).
24. N. Pangarov and G. Kolarov, *J. Electroanal. Chem. Interfacial Electrochem.*, **91**, 281 (1978).
25. P. Stonehart, H. A. Kozłowska, and B. E. Conway, *Proc. Roy. Soc. Ser. A*, **310**, 541 (1969).
26. L. A. Khanova, E. V. Kasatkin, and V. I. Veselovskii, *Elektrokhimiya*, **8**, 451 (1972).
27. K. Kinoshita, J. T. Lundquist, and P. Stonehart, *J. Electroanal. Chem. Interfacial Electrochem.*, **48**, 157 (1973).

Mixed Alkali Effect in Hydrate Melts

Cornelius T. Moynihan*

Vitreous State Laboratory, Catholic University of America, Washington, D.C. 20064

ABSTRACT

Electrical conductivities, densities, and glass transition temperatures have been measured as a function of composition in the hydrate melt systems $X\text{NaNO}_3 \cdot (0.2 - X) \text{MnO}_3 \cdot 0.8\text{Ca}(\text{NO}_3)_2 \cdot 4.09\text{H}_2\text{O}$ for $M = \text{K}$ and Tl . Unlike mixed monovalent cation fused salts and network oxide glasses and melts, in the experimental range of -5° to 70°C no minima were observed in the isotherms of equivalent conductance Δ for the Na/K hydrate melts and weak minima ($\sim 3\%$) only at the lowest temperature for the Na/Tl hydrate melts. A review of data and theories currently in the literature leads to the conclusion that a strong mixed alkali effect, i.e., minimum in the Δ isotherm, should be observed only if the time scale for rearrangement of the local liquid structure is very long compared to the time scale for local ionic transport. This condition is not met by the hydrate melts in the experimental temperature range. It should, however, be met at lower temperatures, and extrapolation of the data indicates that the hydrate melt Δ isotherms develop appreciable minima at such lower temperatures.

The "mixed alkali effect" refers to deviations from additivity in isotherms of various properties as a function of composition as one alkali is replaced for another in a glass or melt, e.g., the system $(1 - X)\text{Na}_2\text{O} \cdot X\text{K}_2\text{O} \cdot 3\text{SiO}_2$, where $0 \leq X \leq 1$ and the compositions refer to numbers of moles. The term "mixed alkali effect" should more properly be "mixed monovalent cation effect," since the phenomena of interest are also observed in systems containing noninert gas configuration monovalent cations such as Ag^+ or Tl^+ . However, in the present paper we defer to the more common usage and use the more restrictive term.

A number of comprehensive reviews of the mixed alkali effect in network oxide glasses and melts have been published in recent years (1-6). In general it is found that there is no mixed alkali effect for equilibrium thermodynamic properties; e.g., molar volumes, elastic moduli, heat capacities, etc., are either linear functions of composition in mixed alkali systems, or there are small deviations from additivity no larger than those encountered in typical nonmixed alkali systems. Also in mixed alkali glasses there are no changes with composition in infrared vibrational frequencies due to cation motions, and Raman vibrational frequencies due to network motions vary linearly with composition (6). On the other hand, a very pronounced mixed alkali effect is observed for properties related to ionic transport. This is illustrated in Fig. 1 by the very deep minima in isotherms of electrical conductivity σ_0 vs. composition for the system $(1 - X)\text{Na}_2\text{O} \cdot X\text{K}_2\text{O} \cdot 3\text{SiO}_2$ (7). There is some question as to whether a mixed alkali effect can be said to occur for properties related to the rearrangement of the over-all liquid structure, e.g., shear viscosity η and glass transition temperature T_g . Mixed network oxide glass viscosity and T_g isotherms generally show minima at intermediate compositions, but Shelby (4) has noted that these deviations from additivity are no larger than those typically observed in nonmixed alkali systems. In addition Moynihan and co-workers (8, 9) have noted that linear composition dependence of the parameters of the VTF equation for the temperature dependence of shear viscosities of liquids can lead to moderately nonlinear viscosity isotherms for systems which would ordinarily be expected to form fairly ideal solutions. Likewise Moynihan *et al.* (10) found that in mixed alkali glasses the parameters characterizing nonlinearity

and the distribution of relaxation times in structural relaxation are composition invariant.

In the present paper we present the results of an investigation to determine whether a mixed alkali effect could be detected in monovalent cation nitrate-calcium nitrate tetrahydrate melts. The properties measured were electrical conductivity, density, and glass transition temperature.

Experimental Procedure

The systems investigated were of molar composition $X\text{NaNO}_3 \cdot (0.2 - X) \text{MnO}_3 \cdot 0.8\text{Ca}(\text{NO}_3)_2 \cdot 4.09\text{H}_2\text{O}$ with $0 \leq X \leq 0.2$ and $M = \text{K}$ or Tl . Compositions studied corresponded to $X = 0.0, 0.1$, and 0.2 .

Reagent grade chemicals were used to prepare the melts. The exact $\text{H}_2\text{O}/\text{Ca}(\text{NO}_3)_2$ molar ratio in the calcium nitrate tetrahydrate was 4.090 ± 0.007 , as

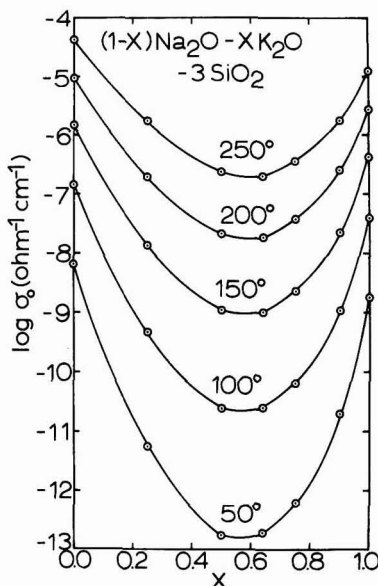


Fig. 1. Electrical conductivity isotherms for $(1 - X)\text{Na}_2\text{O} \cdot X\text{K}_2\text{O} \cdot 3\text{SiO}_2$ glass.

* Electrochemical Society Active Member.
Key words: conductivity, hydrate melt, mixed alkali, glass transition temperature, density.

determined by vacuum dehydration of three samples. The melts were prepared by weighing the components into a container, which was then tightly capped to prevent water loss, and heated to 50°C in a water bath to melt the calcium nitrate tetrahydrate. Agitation at 50°C with a magnetic stirrer caused the monovalent cation nitrates to dissolve in the molten calcium nitrate tetrahydrate.

During measurement of conductivity and density ρ the samples were thermostated in a water bath equipped with a refrigeration unit. Bath temperatures were determined to a precision of $\pm 0.02^\circ\text{C}$ using a calibrated Hg-in-glass thermometer for density measurements and a calibrated Pt resistance thermometer for conductivity measurements. Densities were determined to an accuracy of 0.1% over the range $0^\circ\text{--}70^\circ\text{C}$ with a dilatometer. Glass transition temperatures at a heating rate of $8^\circ\text{C}/\text{min}$ were measured by DTA to an accuracy of $\pm 0.5^\circ\text{C}$ using the procedure of Angell and Sare (11).

Electrical conductivities were measured over the range $-5^\circ\text{--}70^\circ\text{C}$ using a dipping cell with the electrodes separated by a length of glass capillary. The cell was calibrated with 0.1 demal KCl solution and had a cell constant of 51.28 cm^{-1} . Conductances were measured to an accuracy of 0.1% with a Wayne-Kerr B221 admittance bridge over the frequency range 0.35–5 kHz. Over this frequency range the measured conductances increased by about 0.5% at the highest temperatures and by only 0.1% at the lowest temperatures, showing that there were no substantial contributions to the measured conductances from electrode polarization. The conductivities reported below were calculated using the values measured at 1 kHz.

Results

Densities were linear functions of temperature within experimental error and are presented in Table I in the form of least squares fits to the equation

$$\rho(\text{g}/\text{cm}^3) = a - bT(^{\circ}\text{C}) \quad [1]$$

Also given in Table I are equivalent weights E and equivalent volumes V_e at 20°C . Within experimental error the equivalent volumes are linear functions of composition.

In Fig. 2 the temperature dependence of the electrical conductivity σ_0 for one of the melts is shown in the form of an Arrhenius plot. Arrhenius plots for the other melts were quite similar in appearance. The non-Arrhenius temperature dependence *i.e.*, curvature of the plot in Fig. 2, is typical for highly concentrated aqueous solutions in this temperature range. The isothermal dependence of the conductivity on melt composition is shown in Fig. 3. Our σ_0 values for the $0.2\text{KNO}_3\text{--}0.8\text{Ca}(\text{NO}_3)_2 \cdot 4.09\text{H}_2\text{O}$ melt are in good agreement with those interpolated from the results of Angell (12), taking into account the likelihood of small differences in the water contents of the melts in the two studies and the strong dependence of σ_0 on water content in this concentration range (13–15).

Equivalent conductances for the melts were calculated from the expression

$$\Lambda = \sigma_0 E / \rho \quad [2]$$

Table I. Parameters for density equation, equivalent weights, and equivalent volumes at 20°C for $\text{XNaNO}_3\text{--}(0.2 - \text{X})\text{MNO}_3\text{--}0.8\text{Ca}(\text{NO}_3)_2 \cdot 4.09\text{H}_2\text{O}$ melts

M	X	a	$10^4 b$	E (g/ equiv.)	V_e ($\text{cm}^3/\text{equiv.}$)
—	0.2	1.797	9.3	115.1	64.7
K	0.1	1.792	8.8	116.0	65.4
K	0.0	1.797	8.7	116.9	65.7
Tl	0.1	1.930	9.4	125.2	65.5
Tl	0.0	2.064	10.0	135.3	66.2

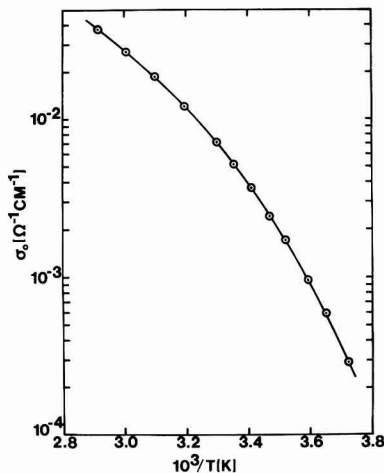


Fig. 2. Arrhenius plot of electrical conductivity of $0.2\text{KNO}_3\text{--}0.8\text{Ca}(\text{NO}_3)_2 \cdot 4.09\text{H}_2\text{O}$ melt.

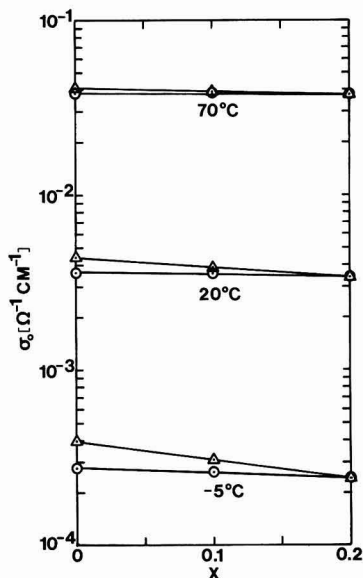


Fig. 3. Electrical conductivity isotherms for $\text{XNaNO}_3\text{--}(0.2 - \text{X})\text{MNO}_3\text{--}0.8\text{Ca}(\text{NO}_3)_2 \cdot 4.09\text{H}_2\text{O}$ melts, \circ , $M = \text{K}$, \triangle , $M = \text{Tl}$.

In the temperature range of this study the temperature dependence of Λ for hydrate melts can be well described by the so-called VTF equation (8, 12–16)

$$\ln \Lambda (\text{cm}^2/\Omega\text{equiv.}) = A - \frac{1}{2} \ln T(^{\circ}\text{K}) - B/(T(^{\circ}\text{K}) - T_0) \quad [3]$$

where A , B , and T_0 are adjustable parameters. The equivalent conductance data for the melts were fitted to Eq. [3] to the nearest 1°K in T_0 using a procedure described previously (16). The best fit parameters are given in Table II. In each case the VTF equation fits the data within a few tenths of a percent. The experimental glass transition temperatures are given in the last column of Table II.

Table II. Best fit VTF equation parameters and glass transition temperatures for $\text{XNaNO}_3 \cdot (0.2 - \text{X})\text{MnO}_3 \cdot 0.8\text{Ca}(\text{NO}_3)_2 \cdot 4.09\text{H}_2\text{O}$ melts

M	X	A	B	T_0	Std. dev. $\ln A$	T_g ($^{\circ}\text{K}$)
—	0.2	8.355	633.4	203	0.004	217.2
K	0.1	8.314	625.1	203	0.004	215.5
K	0.0	8.342	632.7	202	0.003	216.1
Tl	0.1	8.226	608.7	203	0.003	216.4
Tl	0.0	8.248	611.8	201	0.002	214.4

The B and T_0 values in Table II are about the same as those reported in previous studies (8, 12, 14-16) in this temperature range for melts containing substantial amounts of calcium nitrate tetrahydrate. The T_0 parameter may be interpreted theoretically as the temperature at which the free volume (17) or configurational entropy (18) of the melt vanishes. T_g is the temperature at which the shear viscosity reaches about 10^{11} P for concentrated aqueous solutions (19). The ratio T_g/T_0 for the systems studied here is constant within experimental error and equal to about 1.07. Roughly constant values of T_g/T_0 of about this magnitude have been observed for other ionic liquids in which T_0 has been extracted from data in a temperature range corresponding to the few orders of magnitude in shear viscosity above the highly fluid lower limit of around 10^{-2} P for liquids (8, 14, 20-24). This is the range in which free volume or configurational entropy theories of transport seem to give the best correlations with other liquid properties.

Comparing Fig. 1 and 3, it appears that the $\text{XNaNO}_3 \cdot (0.2 - \text{X})\text{MnO}_3 \cdot 0.8\text{Ca}(\text{NO}_3)_2 \cdot 4.09\text{H}_2\text{O}$ hydrate melts do not exhibit a mixed alkali effect in the temperature range studied here. That is, the logarithmic σ_0 isotherms in Fig. 3 do not show perceptible negative deviations from linearity.

A somewhat more sensitive indicator of the electrical mixed alkali effect is the deviation from additivity of the σ_0 or Λ isotherms on a linear scale. This may be characterized by the ratio r defined either as

$$r_{\sigma} = \sigma_{0,\text{add}}/\sigma_0 \quad [4a]$$

or as

$$r_{\Lambda} = \Lambda_{\text{add}}/\Lambda \quad [4b]$$

taken at the composition of maximum deviation from additivity, where $\sigma_{0,\text{add}}$ or Λ_{add} are the conductivity or equivalent conductance predicted on the basis of mole fraction weighted additivity of the σ_0 's or Λ 's of the two single alkali systems. (r_{σ} and r_{Λ} are generally not greatly different.)

In Table III are given values of r_{Λ} calculated from the parameters of Table II at the temperature extremes (-5°C and 70°C) of this study for the hydrate melts. In view of experimental uncertainties, the best accuracy that can be claimed for r_{Λ} is about ± 0.01 . Hence in terms of r_{Λ} only the Na/Tl hydrate melt at the lowest experimental temperature shows a mixed alkali effect ($r_{\Lambda} > 1$), and this barely outside experimental uncertainty.

The equivalent conductance activation enthalpy ΔH^* can be calculated from the VTF equation parameters of Table II

$$\Delta H^* = -R \ln \Lambda/d(1/T) = RBT^2/(T - T_0)^2 - RT/2 \quad [5]$$

where R is the ideal gas constant. In the experimental temperature range the ΔH^* values for the hydrate melts are all very similar at a given temperature and range from 6.9-7.2 kcal/mole at 70°C to 19.2-21.1 kcal/mole at -5°C . In the last column of Table III are tabulated the deviations of activation enthalpy from additivity as a function of composition

Table III. r_{Λ} and $\delta\Delta H^*$ as a function of temperature for $\text{XNaNO}_3 \cdot (0.2 - \text{X})\text{MnO}_3 \cdot 0.8\text{Ca}(\text{NO}_3)_2 \cdot 4.09\text{H}_2\text{O}$ melts. Entries in rows marked with an asterisk are extrapolated beyond the experimental temperature range.

M	T ($^{\circ}\text{C}$)	r_{Λ}	$\delta\Delta H^*$ (kcal/mole)
K	70	0.99	0.0
	-5	0.99	0.0
	-20*	1.01	0.2
Tl	-40*	1.18	1.4
	70	1.01	-0.1
	-5	1.03	0.1
	-20*	1.11	0.5
	-40*	1.88	2.7

$$\delta\Delta H^* = \Delta H^*_{0.5} - 0.5(\Delta H^*_{0.0} + \Delta H^*_{1.0}) \quad [6]$$

where the subscripts refer to the monovalent cation fraction, e.g., $M/(M + \text{Na})$, of one of the monovalent cations. In the experimental temperature range the ΔH^* values are additive functions of composition within experimental error.

Discussion

Experimental manifestations and theories of the mixed alkali effect.—To attempt to account for the lack of an appreciable mixed alkali effect in electrical conductivity of the hydrate melts, we begin with a more complete summary of experimental observations on mixed alkali system electrical transport properties and theories for this behavior. In this section references are given only for points which are not covered adequately in the general review papers (1-3, 5).

The following are the experimental characteristics of the electrical transport mixed alkali effect:

1. For vitreous substances the mixed alkali effect (i.e., $r > 1$) is observed both in glasses and liquids and in network oxide and fused salt systems. r can vary from very large values ($r_{\sigma} = 2.6 \times 10^4$ at 50°C in Fig. 1) to values close to unity [$r_{\Lambda} = 1.04$ for molten Na/KNO_3 at 350°C (25) and 1.14 for molten Na/TiNO_3 at 310°C (26)] to nearly unity within experimental error for the hydrate melts studied here.

2. ΔH^* , the conductivity activation enthalpy, exhibits positive deviations from additivity as a function of composition, i.e., $\delta\Delta H^* > 0$. This has the effect of making r increase with decreasing temperature (cf. Fig. 1 and 4). For the hydrate melts in the experimental temperature range $\delta\Delta H^* = 0$.

3. Other conditions being the same, r increases with an increase in difference in the alkali ion radii.

4. The source of the mixed alkali effect on electrical conductivity in terms of the individual monovalent ion mobilities is that the mobilities exhibit different composition dependences. Usually there is a crossover composition for the mobility isotherms, such that at the composition extremes the monovalent cation present in higher concentration possesses the higher mobility (27, 28).

5. For a given system the magnitude of the mixed alkali effect shows a complicated dependence on over-all monovalent cation concentration. At a given temperature there always seems to be a concentration below which the mixed alkali effect is absent (or at least undetectably small). This is shown in Fig. 4 in which isotherms of resistivity $\rho_0 (=1/\sigma_0)$ are plotted for three compositions for $\text{Y}(\text{Na}_2\text{O} + \text{K}_2\text{O}) \cdot (1 - \text{Y}) \text{B}_2\text{O}_3$ melts (29). At 1000°C no mixed alkali effect, i.e., no deviation from additivity in the ρ_0 isotherms, is observable for any of the compositions. By 850°C , however, the 20 and 28 mole percent (m/o) alkali melts exhibit a mixed alkali effect, i.e., a maximum in the ρ_0 isotherms, but no mixed alkali effect is yet discernible in the 12 m/o alkali melt. For the borate melts of Fig. 4 r_{σ} at a given temperature increases with increasing total alkali concentration. At high

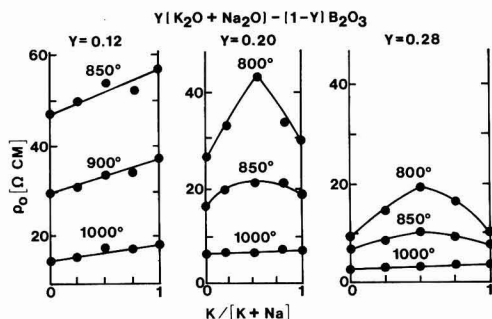


Fig. 4. Electrical resistivity isotherms for $Y(\text{Na}_2\text{O} + \text{K}_2\text{O}) - (1 - Y)\text{B}_2\text{O}_3$ melts.

alkali concentrations, however, this trend may be reversed. This is shown in Fig. 5 for $Y(\text{Na}_2\text{O} + \text{K}_2\text{O}) - (1 - Y)\text{SiO}_2$ melts (30) for which τ_σ decreases with increasing alkali content.

Numerous explanations have been proposed for the mixed alkali effect on electrical transport properties. Some of these have now been shown experimentally to be incorrect, e.g., the theory that the mixed alkali effect is due to phase separation. The remaining theories, all of which have at least some drawbacks, may be classified into two general categories: cationic interaction theories and structural/mechanistic theories.

The cationic interaction theories are typified by those proposed by Moynihan and Laity (27, 28), Mazurin (31), and Hendrickson and Bray (32). In general they suggest that partial replacement of one monovalent cation by a second leads to some sort of attractive interaction among the cations or, in the extreme, to the formation of associated cationic complexes. This in turn causes a relative reduction in the average ionic mobilities. While such interactions may account for moderate deviations from additivity in the σ_0 or Δ isotherms, they cannot explain the extreme sort of behavior typified by Fig. 1. In this case the initial replacement of a small amount of K_2O by Na_2O in the $\text{K}_2\text{O}-3\text{SiO}_2$ glass causes such a

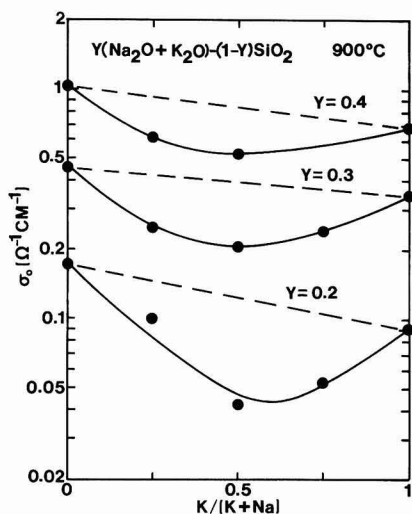


Fig. 5. Electrical conductivity isotherms at 900°C for $Y(\text{Na}_2\text{O} + \text{K}_2\text{O}) - (1 - Y)\text{SiO}_2$ melts.

rapid drop in σ_0 at 50°C that one would have to assume that each Na^+ ion complexed and completely immobilized some 40K^+ ions (33).

An example of a structural/mechanistic explanation of the mixed alkali effect is that of Stevels (34). He assumes that a variety of monovalent ion sites exist in a glass or liquid. When the glass or liquid contains a mixture of monovalent ions, each kind of ion preferentially occupies sites which are energetically most favorable for it. Presumably these most favored sites are different for different types of ions. Thus mixing of the monovalent ions leads to a net reduction in the number of ions loosely bonded to the network. If these are responsible for the measured electrical conductivity, then mixing of the monovalent ions leads to a relative reduction in σ_0 . Evidence in favor of this last point of view is to be found in the recent papers of Ravaine and Soquet (35) and of Tomozawa (36), who suggest that network oxide glasses are weak electrolytes and that electrical conductivity is due to the transport of a relatively small number of mobile, i.e., loosely bound, ions.

Whatever the correct explanation for the mixed alkali effect, it seems inevitable that it must predict that the effect will eventually decrease and disappear as the total concentration of monovalent cations decreases. As the average distance between cations increases, any intercationic interactions must become progressively weaker and any correlations among the interactions of the cations with the structure must vanish.

Importance of the relative rates of ionic transport and structural rearrangement.—A condition required by all of the structural/mechanistic theories for the mixed alkali effect, which is usually left unstated, is that the structure of the medium be fixed or, more precisely, that the time scale for rearrangement of the local structure be long compared to that required for the local diffusion of monovalent cations from site to site. If this condition is not met, to use Stevels' theory (34) as an example, the character of the sites occupied by the various ions will change constantly on the time scale of average occupancy, so that the notion of preferential occupancy of different types of sites by different ions becomes meaningless.

A good figure of merit for the relative time scales of local structural rearrangement and ion transport is the ratio (37)

$$\langle \tau_s \rangle / \langle \tau_\sigma \rangle = (\eta / G_\infty) / (\epsilon_0 \epsilon_\infty / \sigma_0) \quad [7]$$

$\langle \tau_s \rangle$ is the mean relaxation time at constant strain for disappearance of a shear stress via viscous flow and G_∞ the solid-like (i.e., limiting high frequency) shear modulus of the melt or glass. $\langle \tau_\sigma \rangle$ is the mean relaxation time at constant polarization for disappearance of an electric field within the material via the ionic transport process, $\epsilon_0 (= 8.854 \times 10^{-14} \text{ F/cm})$ the permittivity of free space, and ϵ_∞ the limiting high frequency dielectric constant. Typical values for ionic melts and glasses of G_∞ and ϵ_∞ are, respectively, $\sim 10^{11} \text{ dyne/cm}^2$ and ~ 6 , so that

$$\langle \tau_s \rangle / \langle \tau_\sigma \rangle \sim 20 \eta \sigma_0 \quad [8]$$

with η in P and σ_0 in $\Omega^{-1} \text{ cm}^{-1}$.

In Fig. 6 are shown logarithmic plots of $\langle \tau_s \rangle / \langle \tau_\sigma \rangle$ vs. η for a number of ionic melts. The data for $\text{LiCl} \cdot 5.77\text{H}_2\text{O}$ and $0.4\text{Ca}(\text{NO}_3)_2 \cdot 0.6\text{KNO}_3$ are from previous publications (19, 37). For $\text{Ca}(\text{NO}_3)_2 \cdot 8\text{H}_2\text{O}$ we have plotted the longitudinal stress to electric field relaxation time ratio $\langle \tau_L \rangle / \langle \tau_\sigma \rangle$ (38); this should differ very little from $\langle \tau_s \rangle / \langle \tau_\sigma \rangle$. The $\langle \tau_s \rangle / \langle \tau_\sigma \rangle$ ratios for the network oxide melts were calculated via Eq. [7] using measured values of η and σ_0 and estimated values of G_∞ and ϵ_∞ , taken all from the data compilations of Mazurin et al. (39), except for the σ_0 values at high η for $0.2\text{Na}_2\text{O}-0.8\text{SiO}_2$, which were

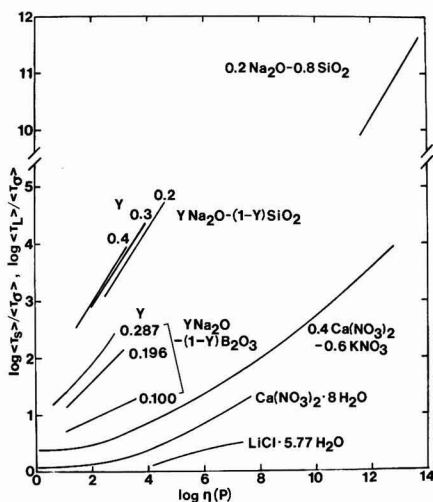


Fig. 6. Ratio of shear or longitudinal stress relaxation time to electric field relaxation time vs. shear viscosity for ionic liquids.

taken from the paper of Kaneko and Isard (40). The main uncertainties in Fig. 6 arise from the estimation of G_s and ϵ_s for the low viscosity melts; this may lead to errors of at most a factor of 2 in the $\langle\tau_s\rangle/\langle\tau_\sigma\rangle$ values.

The first thing to note about the plots of Fig. 6 is that at low viscosities and high temperatures the $\langle\tau_s\rangle/\langle\tau_\sigma\rangle$ ratios for all systems approach unity. This is in fact predicted from the approximate validity of the Stokes-Einstein equation (which relates η to ionic diffusion coefficient D) and the Nernst-Einstein equation (which relates σ_0 to D) for high temperature ionic melts (28). Combining these two expressions with Eq. [7] one gets

$$\langle\tau_s\rangle/\langle\tau_\sigma\rangle = N_A Z^2 e^2 C_M / 3\pi d \epsilon_0 \epsilon_s G_s \quad [9]$$

where N_A is Avogadro's number, Z the ionic charge in units of the electronic charge e , C_M the ionic concentration, and d the ionic diameter. Using typical values of $C_M = 20$ mole/liter for ionic melts (cf. Table IV), $Z = 1$, $d = 0.2$ nm, $\epsilon_s = 6$, and $G_s = 10^{11}$ dyne/cm², one obtains via Eq. [9] the value $\langle\tau_s\rangle/\langle\tau_\sigma\rangle = 0.3$, i.e., of the order of unity.

With decreasing temperature and increasing viscosity $\langle\tau_s\rangle/\langle\tau_\sigma\rangle$ increases and, in the case of the network oxide melts and the anhydrous fused salt, reaches extremely large values in the vicinity of the glass transition ($\eta \sim 10^{11}$ – 10^{13} P). This increase in $\langle\tau_s\rangle/\langle\tau_\sigma\rangle$ at high viscosities is due to the failure of the Stokes-Einstein equation, since it is known that the Nernst-Einstein equation is approximately valid for alkali ions in network oxide glasses in and below the glass transition region (41).

In view of all the foregoing, we suggest the following with regard to the causes and/or conditions for the mixed alkali effect on electrical transport properties. Monovalent cationic interactions may give rise to relatively small mixed alkali effects, i.e., τ values slightly larger than unity, such as those observed in fused salts at high fluidities where $\langle\tau_s\rangle/\langle\tau_\sigma\rangle \approx 1$. Such cationic interactions depend strongly on interionic distance and should decrease rapidly in magnitude, along with the magnitude of the mixed alkali effect, with decreasing monovalent cation concentration. For large mixed alkali effects of the magnitude of those in Fig. 1, 4, and 5 to be observed the condition must be met that $\langle\tau_s\rangle/\langle\tau_\sigma\rangle \gg 1$, i.e., that the melt structure remain fixed on the time scale of the

local diffusive steps of the monovalent cations. This condition allows structural/mechanistic effects to come into play. Probably structural/mechanistic effects do not depend as strongly on interionic distance as do the monovalent cation interactions.

In Table IV we have listed the viscosity ranges of the sodium ion melts of Fig. 6 corresponding to the temperature ranges of the conductivity data of Fig. 3-5. Correlations between the magnitude of the mixed alkali effect, i.e., of τ , and the value of $\langle\tau_s\rangle/\langle\tau_\sigma\rangle$ are immediately apparent. For the 12 m/o alkali borate melt of Fig. 4 $\langle\tau_s\rangle/\langle\tau_\sigma\rangle$ is small (between about 4 and 8) from 1000° to 850°C and no mixed alkali effect is observed in this temperature range. For the 20 and 28 m/o alkali borate melts $\langle\tau_s\rangle/\langle\tau_\sigma\rangle$ varies, respectively, from about 5 to 30 and from about 6 to 40 in the range 1000°–800°C. No mixed alkali effect is observed at the higher temperature where $\langle\tau_s\rangle/\langle\tau_\sigma\rangle$ is small. At the lower temperatures, where $\langle\tau_s\rangle/\langle\tau_\sigma\rangle$ becomes substantially larger, however, a pronounced mixed alkali effect is observed. For the alkali silicate melt data of Fig. 5 at 900°C $\langle\tau_s\rangle/\langle\tau_\sigma\rangle$ is about 5×10^4 , 2×10^4 , and 0.8×10^4 for the respective compositions 20, 30, and 40 m/o alkali; $\langle\tau_s\rangle/\langle\tau_\sigma\rangle$ decreases in the same order as the τ_σ values obtained from Fig. 5.

Mixed alkali effect in hydrate melts.—The absence or smallness of the mixed alkali effect in the $X\text{NaNO}_3 \cdot (0.2 - X)\text{MnO}_3 \cdot 0.8\text{Ca}(\text{NO}_3)_2 \cdot 4.09\text{H}_2\text{O}$ melts in the temperature range studied here is probably due to a number of reasons. First, the total alkali concentration C_M in the hydrate melts is considerably smaller than in the other systems discussed here, as shown in Table IV. This concentration is small enough probably to make any cationic interaction contributions to the mixed alkali effect negligible. Second, from the data for the two hydrate melts given in Fig. 6 and the estimated viscosity data for the present systems in Table IV, $\langle\tau_s\rangle/\langle\tau_\sigma\rangle$ is close to unity for this system in the experimental temperature range. Third, judging from reducible cation (Ag^+ , Tl^+ , and Cd^{2+}) diffusion coefficients in a $\text{Ca}(\text{NO}_3)_2 \cdot 4.09\text{H}_2\text{O}$ melt in the range 15°–60°C (42) the Ca^{2+} and alkali ions in this temperature range have comparable electrical mobility-charge products. This means that in the present experiments we are attempting to observe an effect on σ_0 due to the mixing of monovalent cations against a background due to the other ions which contributes at least 80% of the total σ_0 . Note that the second and third reasons are not unrelated. At lower temperatures $\langle\tau_s\rangle/\langle\tau_\sigma\rangle$ for these melts should gradually become considerably larger than unity. When this occurs some species in the system must become immobile relative to the monovalent cations. In silicate or borate systems the immobile part is the silicate or borate network. In the hydrate melts the immobile part would be presumably some sort of network formed at low temperature from the hydrated divalent cations and the anions.

We predict, consequently, that at temperatures somewhat below those investigated here these hydrate

Table IV. Temperature and viscosity ranges and alkali ion concentrations for sodium ion melts with conductivity data shown in Fig. 3-5

System	T (°C)	log η (P)	C_M (mole/liter)
0.2NaNO ₃ -0.8Ca(NO ₃) ₂ ·4.09H ₂ O	-5 to 70	-0.5 to 2.0	1.7
0.12Na ₂ O-0.88B ₂ O ₃	850 to 1000	0.5 to 1.3	6.3
0.20Na ₂ O-0.80B ₂ O ₃	800 to 1000	0.3 to 1.8	11.5
0.28Na ₂ O-0.72B ₂ O ₃	800 to 1000	-0.3 to 1.5	16.9
0.2Na ₂ O-0.8SiO ₂	900	4.6	15.1
0.3Na ₂ O-0.7SiO ₂	900	3.9	22.8
0.4Na ₂ O-0.6SiO ₂	900	3.2	30.4

melts should begin to show an appreciable mixed alkali effect. To provide a rough test of this prediction we have listed in Table III r_A and $\delta\Delta H^*$ at -20° and -40°C extrapolated from experimental data using Eq. [3] and [5] and the parameters of Table II. There is some danger in doing this, since it is known (15) that extrapolation of data to lower temperatures using the VTF equation invariably leads to underestimates of Λ and overestimates of ΔH^* . However since the errors in the extrapolated values of Λ and of ΔH^* for each of the hydrate melts should, respectively, all be of the same sign, the errors in r_A and $\delta\Delta H^*$, which measure properties of the melts relative to one another, should be considerably smaller than the errors in the Λ or ΔH^* values themselves.

The extrapolated $r_A (>1)$ and $\delta\Delta H^* (>0)$ values for the hydrate melts do indeed indicate that at lower temperatures these systems will exhibit appreciable mixed alkali effects. Confidence in this conclusion is enhanced by these observations: (i) The results show the expected trend of increase in r_A with decreasing T . (ii) That r_A is greater for the Na/Tl hydrate melt than for the Na/K hydrate melt in the extrapolated region agrees with the same trend in the experimental region, although the latter result is close to the limits of experimental uncertainty. (iii) In the anhydrous alkali nitrate melts r_A is also larger for the Na/Tl system than for the Na/K system (25, 26).

In the near future we intend to check experimentally whether these hydrate melts do exhibit appreciable mixed alkali effects at low temperatures and high viscosities. If indeed they do, mixed alkali nitrate-divalent cation nitrate systems, which are good glass formers over wide composition ranges in the form of both hydrate melts and anhydrous fused salts, may prove valuable low temperature model systems for unraveling the combined dependence of the mixed alkali effect on concentration and $\langle\tau_s\rangle/\langle\tau_\sigma\rangle$ ratio.

Acknowledgments

Experimental measurements were carried out in 1969 at Purdue University in the laboratory of Professor C. A. Angell, to whom the author is indebted for assistance at that time and for valuable discussions continuing up to the present. T_g measurements were done by Dr. E. J. Sare. The data interpretation and ideas relative to the mixed alkali effect were developed under support from Contract No. ER-78-S-05-5781 from the U.S. Department of Energy.

Manuscript submitted Jan. 22, 1979; revised manuscript received May 29, 1979. This was Paper 359 presented at the Pittsburgh, Pennsylvania, Meeting of the Society, Oct. 15-20, 1978.

Any discussion of this paper will appear in a Discussion Section to be published in the June 1980 JOURNAL. All discussions for the June 1980 Discussion Section should be submitted by Feb. 1, 1980.

Publication costs of this article were assisted by the U.S. Department of Energy.

REFERENCES

1. R. M. Hakim and D. R. Uhlmann, *Phys. Chem. Glasses*, **8**, 174 (1967).
2. J. O. Isard, *J. Non-Cryst. Solids*, **1**, 235 (1969).
3. R. Terai, *ibid.*, **6**, 121 (1971).
4. J. E. Shelby, *J. Appl. Phys.*, **46**, 193 (1975).
5. D. E. Day, *J. Non-Cryst. Solids*, **21**, 343 (1976).
6. G. B. Rouse, Jr., P. I. Miller, and W. M. Risen, Jr., *ibid.*, **28**, 193 (1978).
7. L. P. Boesch, Ph.D. Thesis, Catholic University of America (1975).
8. C. T. Moynihan, C. R. Smalley, C. A. Angell, and E. J. Sare, *J. Phys. Chem.*, **73**, 2287 (1969).
9. C. T. Moynihan, U. E. Schnaus, and D. Czaplak, *ibid.*, **82**, 1087 (1978).
10. C. T. Moynihan, A. J. Eastale, D. C. Tran, J. A. Wilder, and E. P. Donovan, *J. Am. Ceram. Soc.*, **59**, 137 (1976).
11. C. A. Angell and E. J. Sare, *J. Chem. Phys.*, **52**, 1058 (1970).
12. C. A. Angell, *This Journal*, **112**, 1224 (1965).
13. C. A. Angell, *J. Phys. Chem.*, **70**, 3988 (1966).
14. C. A. Angell and R. D. Bressel, *ibid.*, **76**, 3244 (1972).
15. J. H. Ambrus, C. T. Moynihan, and P. B. Macedo, *This Journal*, **119**, 192 (1972).
16. C. T. Moynihan, *J. Phys. Chem.*, **70**, 3399 (1966).
17. M. H. Cohen and D. Turnbull, *J. Chem. Phys.*, **31**, 1164 (1959).
18. G. Adam and J. H. Gibbs, *ibid.*, **43**, 139 (1965).
19. C. T. Moynihan, N. Balitactac, L. Boone, and T. A. Litovitz, *ibid.*, **55**, 3013 (1971).
20. C. A. Angell, E. J. Sare, and R. D. Bressel, *J. Phys. Chem.*, **71**, 2759 (1967).
21. A. J. Eastale and C. A. Angell, *ibid.*, **74**, 3987 (1970).
22. C. A. Angell and D. B. Helphrey, *ibid.*, **75**, 2306 (1971).
23. K. J. Rao, D. B. Helphrey, and C. A. Angell, *Phys. Chem. Glasses*, **14**, 26 (1973).
24. A. J. Eastale, E. J. Sare, C. T. Moynihan, and C. A. Angell, *J. Soln. Chem.*, **3**, 807 (1974).
25. L. A. King and F. R. Duke, *This Journal*, **111**, 712 (1964).
26. V. Wagner and S. Forcheri, *Z. Naturforsch., Teil A*, **22**, 891 (1967).
27. C. T. Moynihan and R. W. Laity, *J. Phys. Chem.*, **68**, 3312 (1964).
28. C. T. Moynihan, in "Ionic Interactions," Vol. 1, S. Petrucci, Editor, pp. 261-384, Academic Press, New York (1971).
29. K. A. Konstanyan, "The Structure of Glass," Vol. 2, pp. 234-236, Consultants Bureau, New York (1960).
30. R. E. Tickle, *Phys. Chem. Glasses*, **8**, 101 (1967).
31. O. V. Mazurin, "The Structure of Glass," Vol. 4, pp. 5-55, Consultants Bureau, New York (1965).
32. J. R. Hendrickson and R. J. Bray, *Phys. Chem. Glasses*, **13**, 107 (1972).
33. C. T. Moynihan, N. S. Saad, D. C. Tran, and A. V. Lesikar, *J. Am. Ceram. Soc.*, In press.
34. J. M. Stevels, "Handbuch der Physik," Vol. 20, S. Flugge, Editor, Springer-Verlag, Berlin (1957).
35. D. Ravaine and J. L. Soquet, *Phys. Chem. Glasses*, **18**, 27 (1977).
36. M. Tomozawa, in "Treatise on Materials Science and Technology," Vol. 12, M. Tomozawa and R. H. Doremus, Editors, pp. 283-345, Academic Press, New York (1977).
37. F. S. Howell, R. A. Bose, P. B. Macedo, and C. T. Moynihan, *J. Phys. Chem.*, **78**, 639 (1974).
38. J. H. Ambrus, H. Dardy, and C. T. Moynihan, *ibid.*, **76**, 3495 (1972).
39. O. V. Mazurin, M. V. Strel'tsina, and T. P. Shvaiko-Shvaikovskaya, "Properties of Glasses and Glass-Forming Melts Handbook," Vol. I and II, Nauka, Leningrad Otd., Leningrad, USSR (1973 and 1975).
40. H. Kaneko and J. O. Isard, *Phys. Chem. Glasses*, **9**, 84 (1968).
41. Y. Haven and B. Verkerk, *ibid.*, **6**, 38 (1965).
42. C. T. Moynihan and C. A. Angell, *J. Phys. Chem.*, **74**, 736 (1970).

A Model for the Anodic Dissolution of Iron in Sulfuric Acid

Clarence G. Law, Jr.* and John Newman**

Materials and Molecular Research Division, Lawrence Berkeley Laboratory and
Department of Chemical Engineering, University of California, Berkeley, California 94720

ABSTRACT

Potential and current distributions are calculated for a partially passivated rotating disk electrode. A discontinuous local polarization relation is used to reflect the change from the active to the passive state. Results of the model yield a z-shaped polarization curve similar to curves measured experimentally by Epelboin *et al.* The limiting cases of mass transfer control and ohmic control are treated. Comparison of previous experimental results with the model is in harmony with the conclusion that the electrode is mass transfer controlled in the transition region.

Passivation of iron in sulfuric acid has been noticed by investigators for some time. In his experiments Flade (1) observed a potential characteristic of the passive-active state transition. Somewhat later, Osterwald (2) considered the potentiostatic measurements of Franck (3). An explanation was presented which relates the oscillating current-potential behavior to an ohmic drop in the solution and the stability of an iron oxide film. In a series of papers, Hurlen (4-6) presented kinetic parameters important for the description of the iron electrode. In this paper a model is developed which corresponds to the experimental results obtained with an iron rotating disk electrode in sulfuric acid solution.

More recently, Epelboin *et al.* (7) showed the importance and validity of an electronic device for obtaining polarization curves. Briefly, they explained the hysteresis of the current-potential curve observed with potentiostatic control in terms of the operating characteristic of the potentiostat. They also introduced a negative impedance converter (NIC). This device was used to control the current-potential behavior of the iron electrode without hysteresis but with a continuous, reversible transition from the active to the passive state. Because of its shape, the curve is referred to as a z-shaped curve.

In this paper the portion of the polarization curve which descends from the limiting current plateau to a very small current is called the transition region. In the transition region, active and passive states exist on different portions of the disk electrode.

The polarization curves obtained by Epelboin *et al.* with a NIC are given in Fig. 1. The limiting current varies with the square root of rotation speed. The dotted region of the plateau is not a stable region; here the measured currents were reported to have large fluctuations.

In this paper Epelboin *et al.* suggest the applicability of a local polarization relation which decreases sharply to a low current density.

Model Development

A simple model is presented for the passivation of iron in 1 molar sulfuric acid which accounts for the kinetic resistance in the double layer and the nonuniform ohmic potential across the disk surface. The model does not consider mass transfer of chemical species explicitly. However, the effect of mass transfer limitations is included in the kinetic expression.

To characterize the over-all response of a disk electrode undergoing anodic polarization, a local polariza-

tion curve is needed. There are many kinetic expressions from which to choose; however, we have considered an expression which shows a discontinuous change from the active to the passive state. For example, in the active region a modified Butler-Volmer relationship is presumed to apply

$$i = nFk_a \exp \left[\frac{\alpha_a F}{RT} (V - \Phi_0) \right] - nFk_c c_{Fe^{++}} \exp \left[\frac{-\alpha_c F}{RT} (V - \Phi_0) \right] \quad [1]$$

At a characteristic value of the driving force, $V - \Phi_0 = (V - \Phi_0)^* = 0.28V$, a passive film is presumed to form; and the current density changes discontinuously to an extremely low value that remains constant with further increases in $V - \Phi_0$.

The electric driving force is the local potential difference $V - \Phi_0$, where V is the potential of the iron rotating disk electrode and Φ_0 is the potential measured by a saturated calomel electrode immediately adjacent to the surface but outside the double layer. The state of the electrode can be characterized by the value of $V - \Phi_0$. If $V - \Phi_0$ at the edge is equal to or less than $(V - \Phi_0)^* = 0.28V$, then the active state prevails. The passive state exists over the entire disk when $V - \Phi_0$ at the center of the disk is greater than $(V - \Phi_0)^*$. In the transition region which exists between these conditions, both states exist simultaneously on the disk. Figure 2 is a description of the local polarization relationship.

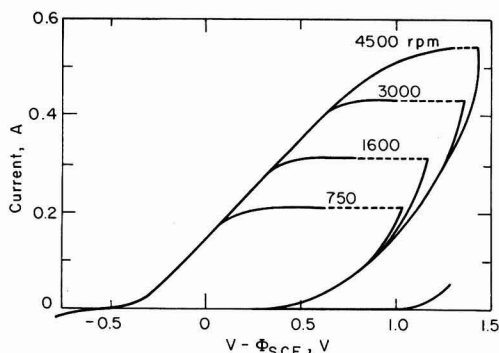


Fig. 1. Current-voltage behavior of a rotating disk electrode obtained by Epelboin *et al.*

* Electrochemical Society Student Member.

** Electrochemical Society Active Member.

Key words: corrosion, passivation, pitting and current, potential distribution.

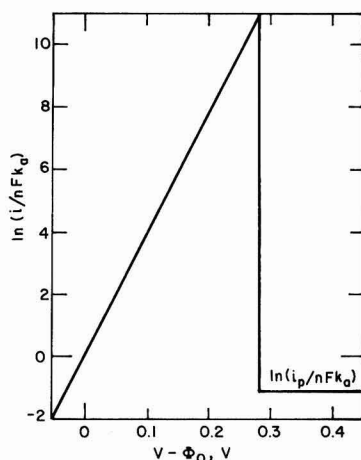


Fig. 2. Local polarization behavior for kinetic control

It is possible to include the effects of mass transfer limitations without explicitly calculating the mass transfer of chemical species. This is accomplished by including the concentration dependence of the limiting reactant in the kinetic expression. An applicable expression is

$$i = nFk_a \left(\frac{c_{R,0}}{c_{R,\infty}} \right)^p \exp \left[\frac{\alpha_a F}{RT} (V - \Phi_0) \right] - nFk_c c_{Fe^{++}} \exp \left[\frac{-\alpha_c F}{RT} (V - \Phi_0) \right] \quad [2]$$

The ratio $c_{R,0}/c_{R,\infty}$ is equivalent to $1 - i/i_{lim}$. The electrode is still presumed to passivate locally for values of $V - \Phi_0$ greater than $(V - \Phi_0)^*$. However, the shape of the local polarization curve is noticeably different. Figure 3 schematically illustrates the local polarization curve when the effect of a limiting species is included. Results will be presented which indicate the merits of the two polarization relations discussed here.

We must mention that the model presented here considers only one of the possible arrangements of the active and passive state. In addition to an active disk with a passive ring outside it, one could also consider a passive disk with an outer active ring, and

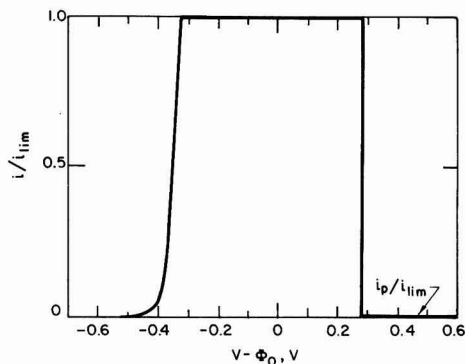


Fig. 3. Local polarization behavior when mass transfer limitations are considered. While this curve qualitatively represents the behavior for a range of parameters, the curve was actually drawn with $nFk_a = 1.0 \times 10^6 \text{ A/cm}^2$, $p = 0.01$, and $\Omega = 4500 \text{ rpm}$.

an active ring between an inner passive disk and an outer passive ring. All three possibilities were observed experimentally by Epelboin *et al.*

Analysis

Laplace's equation is solved for the region between the electrode surface and a counterelectrode well removed from the surface. The equations describing the problem are

$$\nabla^2 \Phi = 0 \quad [3]$$

$$r = 0 \quad \Phi \text{ is well behaved} \quad [4]$$

$$\left\{ \begin{array}{l} r < r_p \\ r = r_p \end{array} \right. \quad \left\{ \begin{array}{l} i = f(V - \Phi_0) \\ V - \Phi_0 = (V - \Phi_0)^* \end{array} \right. \quad [5] \quad [6]$$

$$z = 0 \quad \left\{ \begin{array}{l} r_0 \leq r < r_p \\ r > r_0 \end{array} \right. \quad \left\{ \begin{array}{l} i = i_p = 10^{-4} \text{ A/cm}^2 \\ \frac{\partial \Phi}{\partial z} = 0 \end{array} \right. \quad [7] \quad [8]$$

$$z \rightarrow \infty \quad \Phi \rightarrow 0 \quad [9]$$

where $i = f(V - \Phi_0)$ refers to Eq. [1] without mass transfer limitations and to Eq. [2] when mass transfer limitations are considered.

One does not hope to find a solution to Laplace's equation subject to these boundary conditions in the literature. A solution is obtained by superimposing solutions to Laplace's equation subject to boundary conditions which are algebraically equivalent to those given above. The three solutions are

$$\Phi = \Phi^I + \Phi^{II} + \Phi^{III} \quad [10]$$

where Φ^I , Φ^{II} , and Φ^{III} all satisfy Eq. [3], [4], [8], and [9]; while on the disk electrode at $z = 0$, they satisfy the following

$$r \leq r_p: \quad i^I = f(V - \Phi_0), \quad i^{II} = i_p, \quad i^{III} = i_p \quad [11]$$

$$r > r_p: \quad i^I = 0, \quad i^{II} = i_p, \quad i^{III} = 0 \quad [12]$$

A solution for Φ^I subject to the boundary conditions specified has been given in rotational elliptic coordinates by Newman (8) and takes the form

$$\Phi = \sum_{n=0}^{\infty} B_n P_{2n}(\eta) M_{2n}(\xi) \quad [13]$$

where

$$r = r_p \sqrt{(1 - \eta^2)(1 + \xi^2)}, \quad z = r_p \eta \xi$$

The current density at the working electrode is given by

$$i = -\kappa \frac{\partial \Phi}{\partial z} \bigg|_{z=0} \quad [14]$$

From the orthogonal properties of Legendre polynomials, the B_n coefficients can be expressed as

$$B_n = \frac{(4n+1)r_p}{M_{2n}'(0)\kappa} \int_0^1 i(\eta) \eta P_{2n}(\eta) d\eta \quad [15]$$

It is convenient to use the results of Nanis and Kesselman (9) for solutions to the second and third terms in Eq. [10]. The potential just outside the double layer is the potential of most concern and is given as

$$\Phi_0^{II} = \frac{2}{\pi} \left(\frac{i_p r_0}{\kappa} \right) E \left[\left(\frac{r}{r_0} \right)^2 \right] \quad r < r_0 \quad [16]$$

$$\Phi_0^{II} = \frac{2}{\pi} \left(\frac{i_p r_0}{\kappa} \right) \frac{r}{r_0} \left\{ E \left[\left(\frac{r_0}{r} \right)^2 \right] - \left[1 - \left(\frac{r_0}{r} \right)^2 \right] \left[K \left(\frac{r_0}{r} \right)^2 \right] \right\} \quad r > r_0 \quad [17]$$

where $K[(r_0/r)^2]$ and $E[(r_0/r)^2]$ are, respectively, the complete elliptic integrals of the first and second kind

as defined by Abramowitz and Stegun (10). [Newman (11) quoted the results of Nanis and Kesselman without realizing the difference in the definition of the elliptic integrals.] A similar expression applies for Φ^{III} but with τ_0 replaced by τ_p .

Solution Technique

The current and potential distributions on the active portion of the disk are determined from the B_n coefficients given by Eq. [15]. To calculate the B_n coefficients, the n -coupled equations are solved using a multidimensional Newton-Raphson iteration procedure.

To obtain a satisfactory initial guess for the most important B coefficient, B_0 , this coefficient was made equivalent to the ohmic potential given by the primary resistance relationship for a disk electrode (12). Thus we set $B_0 = \pi r_p i_{lim}/4k$.

In the transition from active to passive state, the point of passivation, r_p , is unknown. However, a constraint in addition to the n orthogonal constraints for B_n is obtained. The value of $V - \Phi_0$ is specified at the edge of the active region. Computationally it is convenient to replace the unknown r_p with V . Therefore the point of passivation is presumed to occur at a specified location, and the potential, V , of the working disk electrode is calculated. Now the $n + 1$ equations are calculated using the same Newton-Raphson technique.

In the completely passive region, no detailed calculations are needed as the current density is uniformly equal to i_p . The potential distribution is simply given by Eq. [16] and [17].

The Newton-Raphson method was found to be efficient, as convergence was obtained within a few iterations. For the transition region, calculations were also done using a method of successive approximations. Excellent agreement was obtained. However, convergence was very slow for this method, and it was necessary to damp the calculations strongly.

Results and Discussion

The principal value of the model and the analysis is an over-all description of the total current from the rotating iron electrode during anodic polarization. The kinetic parameters used to fit the model to the experimental results are included in Table I. The solution conductivity from the literature is also given (13). To obtain an adequate comparison of the experimental results and the model, it is necessary to decide exactly how the comparison should be made. For example, different results and different values of k_a are used if one decides to match the experimental and calculated currents at the point of passivation vs. a good comparison of the kinetically controlled regime.

Kinetic considerations.—Figure 4 presents a comparison of the experimental results of Epelboin *et al.* at a rotation speed of 4500 rpm and the model when the value of k_a is such that $I_{calc} = I_{expt}$ at the point where the disk begins to passivate. The highest rotation speed was chosen since mass transfer limitations were

Table I.

$\alpha_a = 1.0$	$\alpha_c = 1.0$	$n = 2.0$
$nFk_a = 1.00 \times 10^7 \text{ A/cm}^2$	$cr_{Fe^{++}} = 4.0 \text{ mole/liter}$	$cr_{Fe^{3+}} = 8.32 \times 10^{-16} \text{ A/cm}^2$
$(V - \Phi_0)_* = 0.28 \text{ V}$		
$i_p = 1.0 \times 10^{-4} \text{ A/cm}^2$		
$\kappa = 0.40 \text{ (}\Omega\text{-cm)}^{-1}$		
$cr_{Fe^{++}} = 4.0 \text{ mole/liter}$		
$\beta = 0.17496$	$\text{A} \cdot \text{sec}^{1/2}/\text{cm}^2$	

The reference electrode is positioned in the bulk solution.††

† This value of k_a corresponds to an exchange current density of $9.1 \times 10^{-6} \text{ A/cm}^2$ at $cr_{Fe^{++}} = 4.0 \text{ mole/liter}$.

†† Claude Gabrielli, Personal communication.

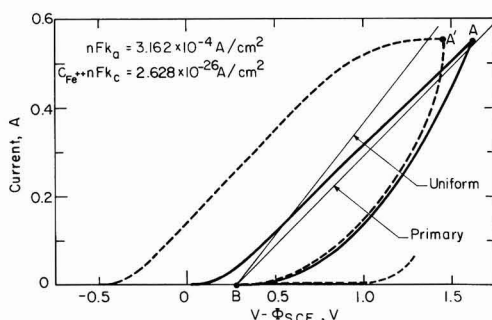


Fig. 4. Comparison of experimental results and calculations when kinetic factors control: (solid line) calculations, (dashed line) experimental results. The lines marked uniform and primary refer to the transition region behavior of a completely active disk which passivates at $(V - \Phi_0)_* = 0.28 \text{ V}$ at its edge for the respective current density distributions.

less than at the lower speeds. A good agreement in the transition region is obtained at the expense of poor agreement in the active kinetic region.

The transition region shown in Fig. 4 does not normally occur for an active electrode. Normally increases in $V - \Phi_{ref}$ result in further increases in I . However, from the viewpoint of the model, the transition region occurs as a result of boundary condition [6] and the ohmic potential drop. As one travels along the transition region from A to B, the size of the active portion decreases and the total disk current drops. To see how the electrode potential varies in this region it is helpful to recall the simple relationship for the primary resistance for a disk electrode given by Newman (12)

$$\frac{\Phi_0}{I} = \frac{1}{4\kappa r_0} \quad [18]$$

Since $V - \Phi_0$ is specified at $r = r_p$, the value of $V - \Phi_{ref}$ approaches 0.28 V as I and r_p approach zero. However, since r_0 should here be replaced by r_p in Eq. [18], the decreasing part of the transition is not linear but is bowed outward as shown in Fig. 4.

The shape of the transition can be seen in view of the current density specified at the edge and Eq. [18]. The measured driving force can be written as

$$V - \Phi_{ref} = V - \Phi_0(r = r_p) + (\Phi_0(r = r_p) - \Phi_{ref}) \quad [19]$$

or alternatively

$$V - \Phi_{ref} = 0.28 + \Phi_0(r = r_p) - \Phi_{ref} \quad [20]$$

It is convenient to express $\Phi_0(r = r_p)$ as

$$\Phi_0(r = r_p) = \frac{\epsilon I}{4\kappa r_p} \quad [21]$$

where ϵ is a number which varies from 1 for a primary distribution to $8/\pi^2 = 0.810569$ for a uniform distribution. Since r_p is unknown, let us replace it with the average current density i_{avg} according to

$$I = \pi r_p^2 i_{avg}$$

(with neglect of the small current on the passivated part of the disk). The electrode polarization in the transition region can now be expressed as

$$V - \Phi_{ref} = 0.28 + \frac{\epsilon \sqrt{\pi I i_{avg}}}{4\kappa} - \Phi_{ref} \quad [22]$$

In the experimental system, the reference electrode is in the bulk solution, and Φ_{ref} is essentially zero. Then, this relationship shows that the calculated transition

region curve should be a parabola if the average current density on the active portion and ϵ remain constant. The experimental curves have approximately this shape, and deviations can be explained in terms of variations in i_{avg} and ϵ .

Returning to Fig. 4, we observe that both the experimental and calculated curves deviate from a parabolic shape over the range of the transition. If point A' represents an entirely active electrode, then the difference between A and A' is attributable to different current distributions. Point A' has a more uniform distribution than that at the calculated point A.

Near point B the calculated results approach a disk of uniform current density, since the current density approaches that given by Eq. [6]. Using Eq. [22] we can determine that the current density at the bottom is greater than at the top of curve B-A. One can also conclude that the distortion from a parabola is caused by an increase in i_{avg} from A' to B in addition to changes in ϵ .

To show the calculated variation in current distribution that occurs over the course of the transition region, Fig. 5 is presented. Following Newman (14), we have normalized the ohmic potential with respect to the primary resistance for a disk of radius r_p . The uniform current density limit is provided for reference. One notices that as the active surface area decreases the current density on the active portion becomes more nearly uniform. For example, the ratio of the current density at the center to that at the edge varies from 0.07 when $r_p/r_o = 1.0$ to 1 when $r_p/r_o = 0$. The current distribution approaches the uniform limit as $r_p/r_o \rightarrow 0$ and the primary limit when $r_p = r_o$.

Mass transfer limitations.—If one considers mass transfer limitations, a local polarization relation given by Eq. [2] is valid. The results of the model using this equation are given in Fig. 6. Parameters are again given in Table I. β is determined from the data and the defining relation

$$i_{lim} = \beta \sqrt{\Omega} \quad [23]$$

It is also necessary to specify the reaction order, p ,

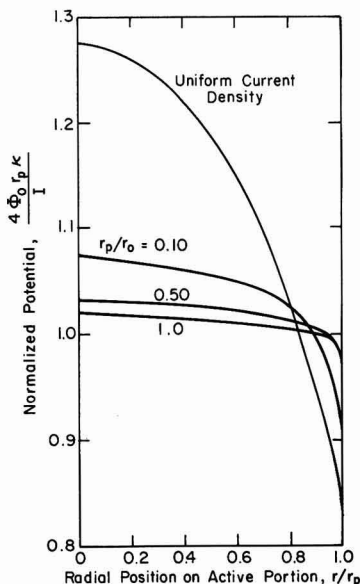


Fig. 5. Variation of the ohmic potential across the active portion of the disk.

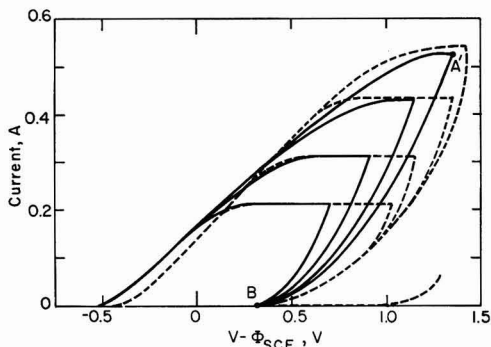


Fig. 6. Comparison of measured and calculated polarization curves: (solid line) calculations ($p = 0.01$), (dashed line) experimental results [Ref. (7)].

of the limiting reactant. Levich (15) has indicated the effect of the reaction order on the approach to a limiting current plateau; for smaller values of p the curve follows more closely the kinetic and limiting current limits. Figure 7 shows the effects of varying the reaction order p of the limiting reactant.

The calculated transition region shown in Fig. 6 and 7 is substantially mass transfer controlled. As one proceeds from the completely active to the completely passive state, the current density is uniform across the disk and given by Eq. [23]. The decrease in current is completely attributable to the decrease of the active area.

A discrepancy between the model and the experiments is revealed in Fig. 6. The model yields four distinct curves in the transition which are characteristic of the four rotation speeds. In the lower portion of the

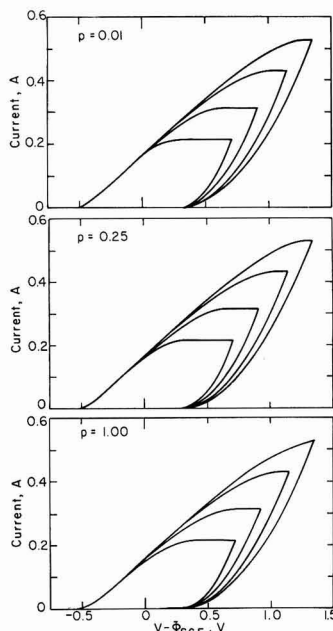


Fig. 7. Comparison of calculated polarization curves for different reaction orders of the limiting reactant. The four curves for any given value of p correspond to rotation speeds of 750, 1600, 3000, and 4500 rpm.

transition, the experimental curves overlap. The four distinct curves of the model indicate four different average or limiting current densities, although the superimposed experimental curves give evidence of the same uniform current density existing for all four rotation speeds. The experimental curves also reflect an increase in the average current density as one travels toward the passive state.

Epelboin *et al.* made measurements of the total current from the disk electrode and the dimensions of the active electrode. Figure 8 presents the results of these measurements and calculations from the model. However, it should be emphasized that some of the experimental results indicated that the current was restricted to a thin ring and no noticeable faradaic reaction occurred inside the inner radius or beyond the outer radius of the ring, whereas the model considers an active disk whose radius decreases as the passive state is approached. Therefore, comparison of the model with the experimental results for equivalent areas may compare the results of rings with those of a disk.

The upper curve on Fig. 8 refers to the situation where kinetic factors determine the current distribution on the disk (as was the case for the calculations shown in Fig. 4). Here the average current density on the disk in the transition region increases markedly as the size of the active disk approaches zero, although the increase is gradual for relatively large values of the active area.

The horizontal line on Fig. 8 is characteristic of a mass transfer controlled active-disk region (as was the case for calculations shown in Fig. 6 and 7). The experimental results of Epelboin *et al.* appear to resemble closely the behavior typical of a mass transfer region. In fact, their results look like two mass transfer regions coupled by a steep transition. Most of their experimental curve is for ring shapes. It is remarkable that a mass transfer controlled ring region would have a lower average current density than a disk region. One is also surprised that the experimental curve and the horizontal line do not meet when the disk is completely active as this shows an inconsistency between i_{avg} obtained from $\beta\sqrt{\Omega}$ and i_{avg} obtained from I and measurements of the active dimensions. An explanation could be given in terms of a region existing near A' (Fig. 6) where the disk remains active and a decrease in the current density occurs.

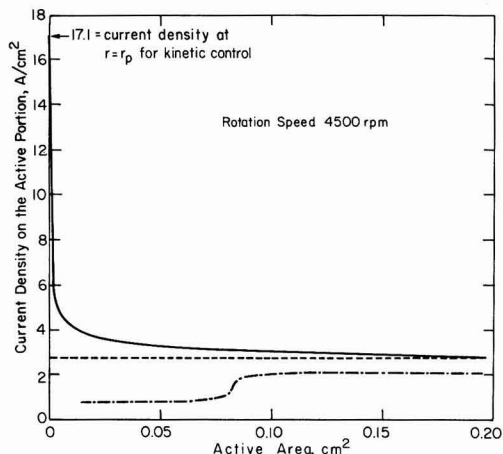


Fig. 8. Current density on the active portion of the disk electrode in the transition region: (—) experimental results of Epelboin *et al.*, (---) results of the model when mass transfer effects are included, (solid line) results of the kinetic model.

Of course, the model presented here cannot substantiate this.

Consideration of ring shapes.—Since a significant portion of the transition region is a ring and not a disk, one should consider whether a consideration of rings can account for the average current density decreasing as the passive state is approached (Fig. 8). A comparison of the measured potential and current with that calculated for rings may clarify this matter. Consider a normalized resistance function, $g(r/r_p)$, which contains the important measured parameters

$$g(r/r_p) = \frac{\kappa\Phi_0(r=r_p)}{\sqrt{i_{lim}}\sqrt{I}} \quad [24]$$

where

$$\Phi_0(r=r_p) = V - \Phi_{ref} - 0.28$$

Therefore with choice of a rotation speed, measured potential, and current, a value of $g(r/r_p)$ is defined. This measured value of g can be compared with functions defined for rings of various current distributions. Namely, consider g^0 defined by a ring of uniform current, $i_{avg} = \beta\sqrt{\Omega}$; g^* defined by a ring of average current density, $i_{avg} = \beta\sqrt{\Omega} f(r)$; g^+ defined by a ring of average current density, $i_{avg} = \beta\sqrt{\Omega} f(r)$ and the primary resistance of a ring given by Miksis and Newman (16). $f(r)$ is defined by Newman (17) as

$$\frac{\left[1 - \left(\frac{r_1}{r_p}\right)^3\right]^{2/3}}{\left[1 - \left(\frac{r_1}{r_p}\right)^2\right]}$$

$\Phi_0(r=r_p)$ for g^0 and g^* are calculated using the results of Nanis and Kesselman. g^* can be related to g^0 by

$$g^*(r/r_p) = g^0(r/r_p)\sqrt{f(r)} \quad [25]$$

Figure 9 illustrates the behavior of these functions. It is important to compare values of g obtained experimentally with g^0 , g^* , and g^+ . For example, if we consider a point where $\Omega = 4500$ rpm, $I = 0.54$ A, $i_{lim} = 2.80$ A/cm², $V - \Phi_{ref} = 1.42$ V, then $g(r/r_p)$ is calculated to be 0.37. This is the smallest value of g one can obtain from the data. For this example g intersects

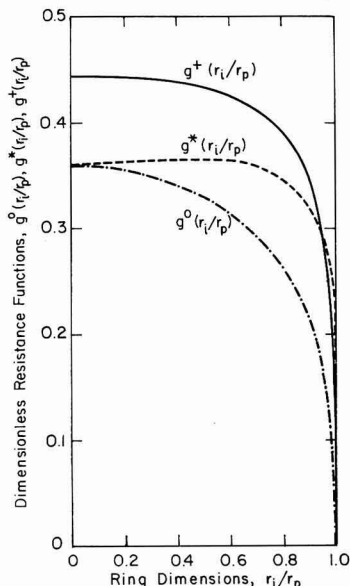


Fig. 9. Correlation of normalized resistance functions

the g^+ curve, $r_1/r_p = 0.85$, which corresponds to a thin ring near the periphery of the disk. However, it is inconsistent to have a g value obtained near the limiting current plateau equivalent to a calculated value of g , g^+ , which corresponds to the primary resistance of a thin ring. An increase in i_{lim} will lower the value of g and it will approach the more appropriate values of g^o and g^* . Also, as one travels down the transition region, the current distribution becomes more uniform and increases in i_{avg} must occur.

Summary and Conclusions

The simple model presented yields a z-shaped curve for the anodic polarization of iron in sulfuric acid very similar to that obtained experimentally by Epelboin *et al.* The model accounts for the kinetic resistance at the surface, the ohmic potential, and the effect of mass transfer limitations. In the transition region the model predicts the same general response of the disk electrode for the limit of mass transfer control and for the case of kinetic control. However, the calculated current density remains constant in the transition region when mass transfer limitations are included, whereas the current density increases in the transition region as the passive state is approached when strictly kinetic factors are considered. Epelboin *et al.* report current densities which decrease in the transition. Analysis presented here states that the experimentally obtained average current density must increase as the passive state is obtained. The analysis is valid for both disk and ring shapes.

Acknowledgment

This work was supported by the Division of Chemical Sciences, Office of Basic Energy Sciences, U.S. Department of Energy under Contract No. W-7405-Eng-48.

Manuscript submitted Jan. 26, 1979; revised manuscript received May 31, 1979.

Any discussion of this paper will appear in a Discussion Section to be published in the June 1980 JOURNAL. All discussions for the June 1980 Discussion Section should be submitted by Feb. 1, 1980.

Publication costs of this paper were assisted by the University of California.

LIST OF SYMBOLS

B_n	coefficient in the expansion for the potential, V
$C_{Fe^{2+}}$	concentration of ferrous ions at the electrode surface, mole/liter
$C_{R,0}$	concentration of the limiting reactant at the electrode surface, mole/liter
$C_{R,\infty}$	concentration of the limiting reactant in the bulk solution, mole/liter
E	complete elliptic integral of the second kind
F	Faraday's constant, 96,487 C/mole
f	dimensionless ratio defined in Ref. (17)
g	normalized resistance, defined by Eq. [24]
g^o	normalized resistance, Fig. 9
g^*	normalized resistance, Fig. 9

g^+	normalized resistance, Fig. 9
i	local current density, A/cm ²
i_{avg}	average current density, A/cm ²
i_{lim}	limiting current density, A/cm ²
i_p	current density on the passive portion of the disk, A/cm ²
I	total current on the disk, A
K	complete elliptic integral of the first kind
k_a	anodic rate constant, mole/sec cm ²
k_c	cathodic rate constant, cm/sec
M_{2n}	Legendre function of imaginary argument
n	number of electrons transferred
P_{2n}	Legendre polynomial of order $2n$
p	reaction order of limiting reactant
R	universal gas constant, 8.3143 J/mole-°K
r	radial coordinate, cm
r_i	inner radius of the ring, cm
r_o	electrode radius, cm
r_p	radius of the active portion, cm
T	absolute temperature, °K
V	potential of rotating disk electrode, V
$(V - \phi_o)$	passivation potential, 0.28V
z	axial coordinate, cm

Greek letters

α_a	anodic transfer coefficient
α_c	cathodic transfer coefficient
β	constant in equations, A-sec ^{1/2} /cm ² defined by Eq. [21]
ϵ	rotational elliptic coordinate
η	bulk solution conductivity, $\Omega^{-1}\text{-cm}^{-1}$
κ	rotational elliptic coordinate
$\Phi^I, \Phi^{II}, \Phi^{III}$	potential in the solution, V
ϕ_o	solution potential immediately adjacent to the electrode surface, V
Ω	rotation speed of the disk

REFERENCES

- Fr. Flade, *Z. Phys. Chem.*, **76**, 513 (1911).
- J. Osterwald, *Z. Elektrochem.*, **66**, 401 (1962), also UCRL-Trans-1544 (1977).
- U. F. Franck, *Z. Naturforsch., Teil A*, **4**, 378 (1949).
- T. Hurlen, *Acta Chem. Scand.*, **14**, 1533 (1960).
- T. Hurlen, *ibid.*, **14**, 1555 (1960).
- T. Hurlen, *ibid.*, **14**, 1564 (1960).
- I. Epelboin, C. Gabrielli, M. Keddam, J. C. Les-trade, and H. Takenouti, *This Journal*, **119**, 1632 (1972).
- J. Newman, *ibid.*, **113**, 1235 (1966).
- L. Nanis and W. Kesselman, *ibid.*, **118**, 454 (1971).
- M. Abramowitz and I. A. Stegun, Editors, "Handbook of Mathematical Functions," p. 590, National Bureau of Standards, Washington, D.C. (1965).
- J. Newman, in "Electroanalytical Chemistry," Vol. 6, Allen J. Bard, Editor, p. 328, Marcel Dekker, Inc., New York (1973).
- J. Newman, *This Journal*, **113**, 501 (1966).
- T. W. Chapman and J. Newman, UCRL-17767 (1968).
- J. S. Newman, "Electrochemical Systems," p. 350, Prentice-Hall, Inc., Englewood Cliffs, N.J. (1973).
- V. G. Levich, "Physicochemical Hydrodynamics," p. 76, Prentice-Hall, Inc., Englewood Cliffs, N.J. (1962).
- J. J. Miskis, Jr. and J. Newman, *This Journal*, **123**, 383 (1976).
- J. S. Newman, "Electrochemical Systems," p. 336, Prentice-Hall, Inc., Englewood Cliffs, N.J. (1973).



Evaluation of Sintered SiC as an Electrode and Container Material in Sodium/Sulfur Cells

R. R. Dubin*¹ and S. Prochazka

General Electric Corporate Research and Development, Schenectady, New York 12301

It has generally been found that the use of common metals and iron-based alloy steels as the cathode container material in a sodium/sulfur (Na/S) cell is unsatisfactory (1-4) unless protective coatings are employed. The molten sodium polysulfide (Na_2S_x) catholyte readily produces extensive physical degradation of such unprotected containers and forms metal sulfide corrosion products. The presence of corrosion products within the cathode structure has been linked to decline in general cell cycling performance and capacity (5). Physical degradation of the graphite current collector, increased internal cell resistance, and degradation of the beta (5) or beta" (6) solid electrolyte have also been associated with the presence of corrosion product impurities.

The preferred configuration for a Na/S battery seems to be one where the cathode container serves as both container and electrode. This further complicates the identification of acceptable cathode container materials since it requires the material to: (i) be a suitable electronic conductor, (ii) remain stable under both static conditions and under anodic and cathodic currents, (iii) remain impervious to molten catholyte and surrounding gaseous atmosphere, and (iv) be readily formable. Most metals fail to satisfy condition (ii) while most ceramics fail to satisfy conditions (i) and/or (ii). This work uses these criteria to evaluate an electrically conductive ceramic, sintered SiC, as a dual function cathode container/electrode in a sodium/sulfur cell. Our conclusion is that conditions (i-iv) can all be satisfactorily met with this material; however, it is clear that numerous additional conditions such as satisfactory mechanical strength, oxidation resistance, and cost must be met before a candidate material can be accepted as a practical solution to the Na/S battery container materials problem.

Several general physical properties of sintered SiC ceramic are given in Table I and can readily be seen as desirable in Na/S cell fabrication. In particular, the low density, high decomposition temperature, and high bend strength are particularly advantageous. Furthermore, the material can be readily formed into complex shapes by a variety of standard techniques such as injection molding, slip casting, and isostatic pressing.

Experimental

Sintered SiC test specimens were fabricated as both pressed disks and cast crucibles according to the method of Prochazka (7). Both types of specimens were made from submicron SiC powders having a specific surface area of about $8 \text{ m}^2/\text{g}$. The powders were obtained by pyrolysis of trichloromethylsilane and contained 1/2% of boron and 1% elemental car-

bon as sintering promoting additives. The disk specimens were fabricated using standard powder pressing techniques while the crucibles (OD = 2.54 cm) were prepared by slip casting (into plaster-of-Paris molds) an aqueous dispersion of SiC powder which was stabilized by tetramethylammonium hydroxide at pH 10.5 and an addition of 1/2% of ureaformaldehyde resol.¹ All specimens were sintered in 600 Torr nitrogen at 2180°C to a density of 3.05 g/cm^3 which corresponded to about 5% closed residual porosity. Nitrogen is introduced into SiC during sintering in N_2 resulting in electronic conductivity in the ceramic of about $30 \Omega^{-1} \text{ cm}^{-1}$ at room temperature as discussed in Ref. (7). The corrosion behavior of the various test specimens was evaluated in molten sulfur and sodium polysulfide under static (no applied potentials) and cycling conditions.

Chemical stability in molten sulfur and Na_2S_4 was evaluated under static conditions by reacting highly polished specimens of sintered SiC in each melt (350°C) for various time intervals (up to 14,540 hr) and then performing precision mass change measurements and optical and scanning electron microscopy on each specimen. Specimens were reacted with the appropriate melt contained within sealed, evacuated (10^{-5} Torr at 25°C), Pyrex ampuls. The Na_2S_4 was produced, according to reaction [1], by the reaction of dry powders of anhydrous Na_2S (99.9% Na_2S with H_2O less than 0.1%, Research Organic/Inorganic Corporation) and zone refined sulfur (99.9999% S, Atomergic Chemical Corporation)



The zone refined S was baked under vacuum and used as the reactant in stability experiments. Dry box and high vacuum bake-out techniques were rigorously employed to exclude water and water vapor from all chemical reactants during synthesis and storage.

Stability under cycling was evaluated in a laboratory cycling apparatus and in actual Na/S test cells. The laboratory cycling apparatus is shown in Fig. 1 and consisted of a glass (Corning 7052) outer tube into which a 1 cm diam sintered SiC rod was fitted. The exterior surface of the rod opposed a

¹ URAC 180, American Cyanamid Company.

Table I. Physical properties

Density:	3.2 g/cm ³
Percent theoretical density:	97.5%
Sintering temperature:	~2000°C
Peritectic decomposition temperature (does not melt):	~2700°C
Resistivity (minimum):	0.03 $\Omega \text{ cm}$ at 300°C
Bend strength:	>50K psi
Oxidation resistance:	Excellent

* Electrochemical Society Active Member.

¹ Present address: Mesurex Corporation, Cupertino, California 95014.

Key words: ceramics, battery, corrosion.

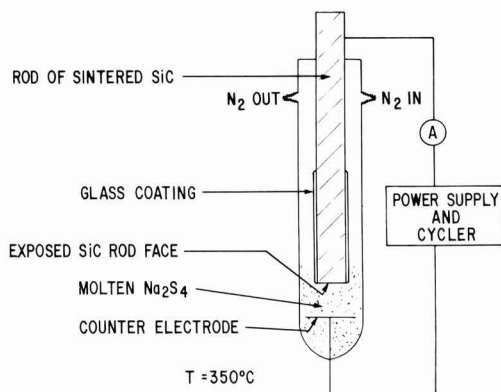


Fig. 1. Laboratory cycling apparatus

molybdenum disk counterelectrode and was coated with glass, leaving only an exposed face in electrical contact with the melt. The exposed test face was polished and three fiducial scratch marks were made on it. The physical features of the test face were observed under a microscope and photographed, after which time it was inserted into the molten Na_2S_4 and galvanostatically cycled (progressively) anodically and cathodically at current densities of 30, 80, and 125 mA/cm^2 for 675, 100, and 100 hr, respectively. The rod was removed from the apparatus periodically so that the physical features of the test face could be observed microscopically and photographed.

Cell cycling experiments were carried out using the slip cast sintered SiC cathode containers whose fabrication was described earlier. The sintered bodies were mass spectrometer helium leak tight and of nominal dimensions: OD = 2.54 cm, length = 7.4 cm, and wall thickness = 0.15 cm. Containers were fabricated with closed bottoms and flanged surfaces on the open end thus allowing the use of conventional metal O-ring mechanical seals and assembly techniques (5). A graphite felt current collector was friction fit into the container cavity as is common practice in conventional cells. Cell cycling was carried out at 300°C at approximately 20 mA/cm^2 average container wall current density for a total of 1100 hr using an automatic cycling apparatus. Precision mass determinations of the cathode container were made before and after cycling. Microscopic examination and analysis of electrical cycling data were all used to evaluate material performance. A photograph of an assembled cell with sintered SiC cathode container is shown in Fig. 2.

Results

The results of the chemical stability (static) experiments are summarized in Table II. No significant weight changes were noted except for the data point at 120 hr which is believed to reflect a measuring error. Specimen surfaces remained highly reflective and highly polished with no evidence of surface reaction, pitting, etching, or scale formation found in any

Table II. Chemical stability results

Environment	Exposure time (hr)	Sample	Thickness change (%)	Weight change (mg)	Percent wt change (%)
Sulfur	120	S-15	<0.5	+36.3	+6.7
Sulfur	360	S-13	<0.5	-0.08	-0.01
Sulfur	864	S-5	<0.5	-0.02	-0.03
Na_2S_4	1,360	NS-14	<0.3	-0.31	-0.1
Na_2S_4	14,540	NS-16	<0.3	+0.14	+0.05

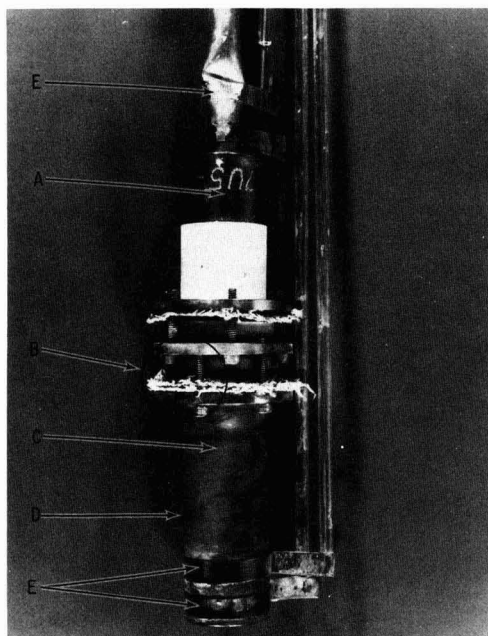


Fig. 2. Sodium-sulfur test cell with sintered SiC cathode container: (A) Sodium filled anode container, (B) mechanical O-ring cathode container clamp seal (see Ref. 5), (C) interior cell components (not shown, see Ref. 5) consisting of beta-alumina tube glass sealed to ceramic header and positioned along central axis of cathode container, graphite felt, catholyte, (D) sintered SiC cathode container, and (E) electrode contacts.

of the specimens, even after 14,540 hr exposure to molten Na_2S_4 .

Micrographs of the sintered SiC rod face are shown in Fig. 3 after cycling evaluation in the laboratory apparatus of Fig. 1. Figure 3(a) was taken prior to melt exposure while Fig. 3(b) and 3(c) were taken after cycling at a constant current density of 30 mA/cm^2 for 675 hr and 80 mA/cm^2 for 100 hr, respectively. Careful microscopic examination showed neither surface degradation nor detectable alteration of physical surface features. Note the consistency of the prominent features in the left portion of the micrographs.

Substantial surface degradation of the sintered SiC test face was caused by cycling at 125 mA/cm^2 for 100 hr as evidenced by Fig. 3(d). Significant roughening of the surface was evident; however, no reaction products were found on the test face or in the melt. This suggested that any reaction products formed were soluble in the melt. The average geometric cathode container wall current density found (8) in prototype Na/S cells is less than 70 mA/cm^2 which is significantly smaller than the 125 mA/cm^2 current density at which the sintered SiC decomposition occurred.

Figure 4 shows the first ten cycles of the capacity cycling diagram for the cell shown in Fig. 2. The cell passed 79 cycles and a total of 406 A-hr. The internal resistance was determined to be 0.33Ω from the initial cell polarization curve. This value corresponded to typical values obtained with conventional metal cell containers. The cathode chemical composition was calculated as a function of depth of discharge and is shown on the right-hand vertical axis of the capacity cycling diagram. Examination of the diagram shows that charge cycles consistently brought the cell into the two-phase region and that discharge compositions

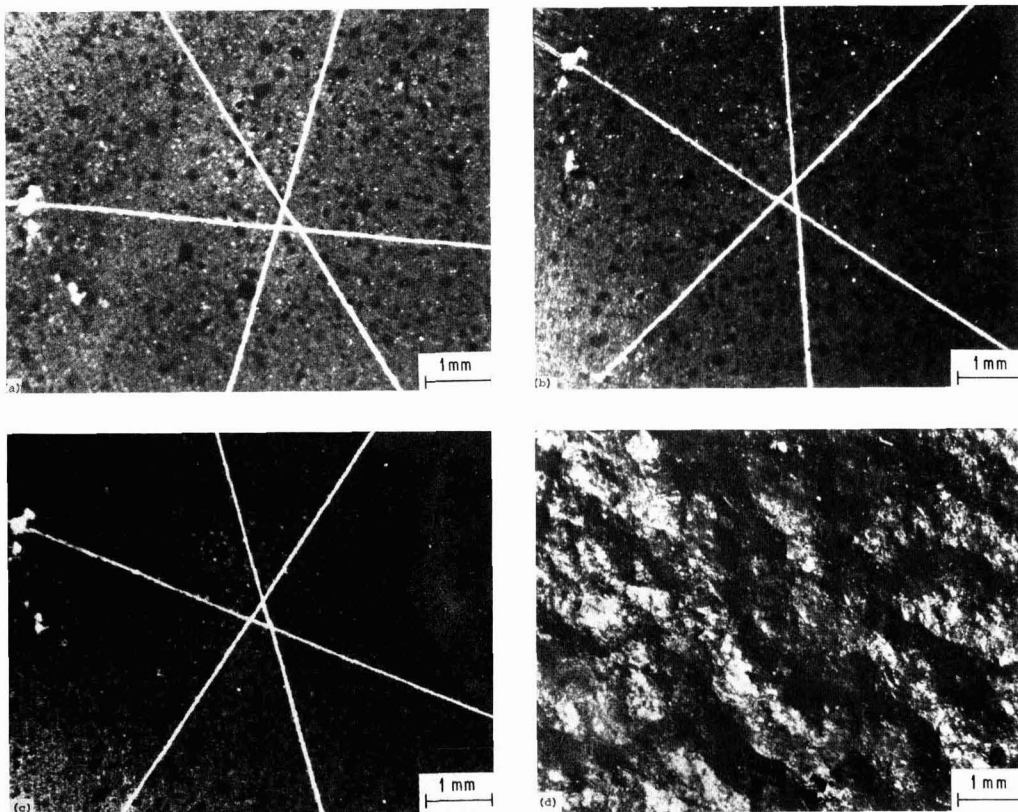


Fig. 3. Micrographs of sintered SiC rod test face after cycling in Na_2S_4 : (a) no cycling, (b) 675 hr cycling at 30 mA/cm^2 , (c) 100 hr cycling at 80 mA/cm^2 , and (d) 100 hr cycling at 125 mA/cm^2 .

were somewhat beyond the 100% depth of discharge composition given by Na_2S_3 .

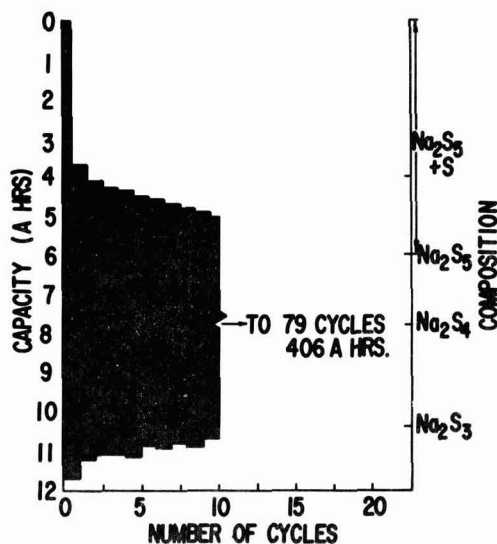


Fig. 4. Capacity cycling diagram for sintered SiC test cell

Microscopic observation of the sintered SiC cell body after cycling showed no evidence of corrosion at interior or exterior surfaces. Weight change results showed a 0.003% (1.05 mg) increase after 406 hr of cycling. This observed weight change was within the limits of experimental error.

Auger electron spectrometry was employed to evaluate the possibility of Si transport from the sintered SiC cell body to the beta-alumina solid electrolyte surface. The technique was applied to the surface of beta-alumina tubes employed in cells utilizing sintered SiC cathode containers. No conclusive evidence for Si transport was found.

Summary and Conclusions

The chemical inertness of sintered SiC has been demonstrated in anhydrous melts (350°C) of sulfur, and a range of sodium polysulfides (primarily Na_2S_4) under a variety of experimental conditions. These include: the application of anodic and cathodic currents for extended time periods, melt exposure with no applied potentials, and conditions of actual Na/S cell cycling. In addition, the ability to cycle such cells in the two-phase region was demonstrated. Lastly, the electrical and mechanical properties as well as the formability of this material were shown to be adequate for use in first generation prototype Na/S cells.

We conclude that sintered SiC can be used successfully as a noncorrodable structural material in Na/S cells. It may be used either as an electrically conducting or nonelectrically conducting cell component in contact with catholyte and/or oxidizing atmosphere.

Sintered SiC cathode containers may also be useful diagnostic tools in prototype Na/S cell development since their use should eliminate the presence of common metal sulfide corrosion products typically found in laboratory test cells employing conventional metal containers.

Although the use of sintered SiC in Na/S cells appears to offer many advantages compared to most unprotected metals, further evaluation is required (including cost) before this new material is proven practical for use in production line Na/S cells.

Manuscript submitted March 23, 1979; revised manuscript received May 21, 1979. This was Paper 18 presented at the Washington, D.C. Meeting of the Society, May 2-7, 1976.

Any discussion of this paper will appear in a Discussion Section to be published in the June 1980 JOURNAL. All discussions for the June 1980 Discussion Section should be submitted by Feb. 1, 1980.

Publication costs of this article were assisted by General Electric.

REFERENCES

1. M. Dell, J. L. Sudworth, and I. Wynn Jones, Paper presented at the Intersociety Energy Conversion Engineering Conference, Stateline, Nevada, September 1976.
2. Bones, Brook, Martin, *Power Sources*, 5, 539 1975.
3. R. R. Dubin, Abstract 11, p. 27, The Electrochemical Society Extended Abstracts, Toronto, Canada, May 11-16, 1975.
4. R. R. Dubin, Abstract 56, p. 154, The Electrochemical Society Extended Abstracts, Atlanta, Georgia, Oct. 9-14, 1977.
5. J. B. Bush, Jr., Interim Report to EPRI (Project RP128-2), May 1, 1974-April 30, 1975.
6. I. Yasui and R. H. Doremus, *This Journal*, 125, 1007 (1978).
7. S. Prochazka, C. A. Johnson, and R. A. Giddings, in "Proceedings Conf. on Factors in Sintering of Oxide and Nonoxide Ceramics," S. Somyia, Editor, Hakone Japan, October 1978, (In press); G. E. Report No. 78CRD192, October 1978.
8. S. P. Mitoff and D. Chatterji, Interim Report to EPRI (Project RP128-4), May 1978.

Trace Gas Flow Control Using Polymer Permeation

J. P. Franey

Bell Laboratories, Murray Hill, New Jersey 07974

In recent years the interest in and usage of gas-materials interaction experimentation has increased rapidly. This is primarily due to advanced semiconductor manufacture, and to increased environmental interest (1). Previous techniques of gas-materials testing generally have been qualitative (2, 3) due to difficulties in maintaining stable corrosive concentrations in laboratory test environments. The gas generation system described herein, however, can be used to provide very stable gas concentrations along with a wide dynamic range.

Assessment of Previous Techniques

The traditional procedures for making various concentrations of gases have been to use mechanical valves (4), gas syringes (5), or permeation tubes (6). For different reasons, each is less than satisfactory.

Difficulties encountered with mechanical valves are caused by variations during operation in orifice or needle sizes. The most severe concentration variations occur when blending a corrosive gas. Experience in this laboratory indicates that stainless steel needle valves are corroded in less than a week by H_2S . Such effects occur even with vacuum leak valves which use an optically flat sapphire for the sealing face and a nickel, chromium, and gold-plated copper gasket for the mating face. This is demonstrated in Fig. 1, where exposure for two days to pure H_2S is shown to have etched the mating face of the valve and formed copper sulfide particles.

In principle, syringe injection of a trace constituent into a carrier gas is capable of producing arbitrarily low concentrations. With typical experimental air-stream flows of <25 liters/min⁻¹, however, the minimum trace constituent level that can be achieved with commercially available syringes (2) is ≈ 100 ppm. Further, small syringes are often fabricated from stainless steel, which will corrode rapidly upon exposure to certain trace gases. Finally, syringes can only be used in a continuous system if the injectant is in liquid form. For most contaminants of interest, this requires cryogenic techniques. Syringe injection

is thus unsuitable for generation of controlled ppb/ppm concentration of gases in carrier flows.

A permeation tube method for gas concentrations is successful for short time periods. The corrosion-resistant permeation tubes operate at the vapor pressure of the gas being used. The diameter and wall thickness are limiting factors due to the high vapor pressures (e.g., H_2S at 23°C = 252 psi). Hence, only polymers of high strength can be used in this method (7) thus limiting its dynamic range. The tube is limited to a finite lifetime due to its limited gas supply (8); although refillable tubes (9) minimize this problem, the necessity for recalibration after refilling renders this method unsuitable for this application.

Laboratory Procedure

The technique presented in this paper uses a flat sheet of an appropriate polymer of arbitrary thickness and cross-sectional area which forms a seal between a gas source (H_2S was used in these tests, although the principal is a general one) and a chamber in which a low concentration is desired (Fig. 3).

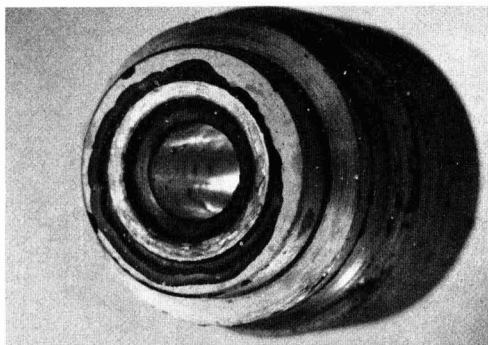


Fig. 1. Triple-plated gold allen screw seat for high-vacuum leak valve after two days of exposure to pure H_2S .

Key words: corrosion, gas, permeation, polymer, environment.

A glass joint with a polymer seal is shown in Fig. 2. The experimental apparatus (Fig. 3) was varying size disk holders of diameters 5-45 mm. The laboratory air supply is incorporated as a carrier gas after it is filtered through activated charcoal. The test chamber has an internal volume of 450 cm³ and the H₂S analyzer flow is 1180 cm³/min. H₂S is converted by a 99.9% efficient catalyst to SO₂. The detector measures SO₂ by pulsed fluorescence techniques. The sample polymer in its holder is subjected to the trace gas source via a pressure-regulated gas cylinder containing 60 pounds of > 99.5% pure H₂S which is used as a source. The chamber carrier flow is determined by the gas analyzer sample flow rate which is constant throughout the tests. The temperature variance of the polymer value is the same as the room ($\pm 2^\circ\text{C}$), which does not have a substantial effect on the system's stability. The regulated gas pressure is held con-

stant until the concentration level stabilizes which can be from 1 hr to 1 day depending on the polymer characteristics (diffusion rate + thickness). The concentrations of trace gases can be calculated using these formulas

$$\text{Concentration (ppb)} = \frac{PpA}{QT} [\text{Conversion Factor}]$$

where

$$P = \text{Permeation constant} \frac{(\text{cm}^3 \text{ of gas}) (\text{cm thickness})}{\text{cm}^2 \text{ area (cm Hg) sec}}$$

$$A = \text{Area of material (cm}^2\text{)}$$

$$Q = \text{Flow of diluent gas (cm}^3\text{/min)}$$

$$T = \text{Thickness of polymer (cm)}$$

$$p = \text{Pressure (cm Hg)}$$

$$(1 \text{ ppbv}) (6.02 \times 10^{23} \text{ molec of gas}) (60 \text{ sec})$$

$$\text{Conversion Factor} = \frac{(2.5 \times 10^{10} \text{ molec gas/cm}^3 \text{ } 25^\circ\text{C}) (2.24 \times 10^4 \text{ cm}^3 (1 \text{ min}) \text{ gas})}{(1 \text{ ppbv}) (6.02 \times 10^{23} \text{ molec of gas}) (60 \text{ sec})}$$

$$= 6.45 \times 10^{10}$$

Inserting the parameters of the test system into the equation above gives the calculated concentration

$$[\text{H}_2\text{S}] = \frac{(6.03 \times 10^{-9}) (1.28 \times 10^2) (2.27)}{(1180) (0.21)}$$

$$\times 6.45 \times 10^{10} = 456 \text{ ppbv}$$

The measured concentration was 560 ppb which was 18% higher than computed, but within the inherent error values of the measuring instruments. (The *Q* value has a maximum variation of 2% and the *p* value has a maximum variation of 20%.)

Results

A wide range of gas concentrations can be achieved. The minimum level achieved thus far (9 ± 1 ppb) has been maintained without intervention for periods exceeding 1 week. The maximum level achieved (3500 ± 70 ppb) is equally stable. Many polymer types, size configurations, and pressures were used to achieve the concentrations shown in Fig. 4.

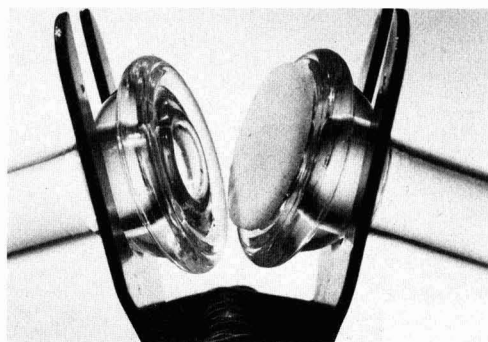


Fig. 2. Glass joint-polymer diffusion flow "valve" after two days of exposure to pure H₂S.

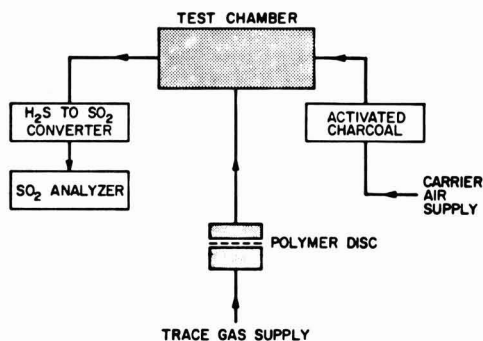


Fig. 3. Schematic diagram of experimental apparatus

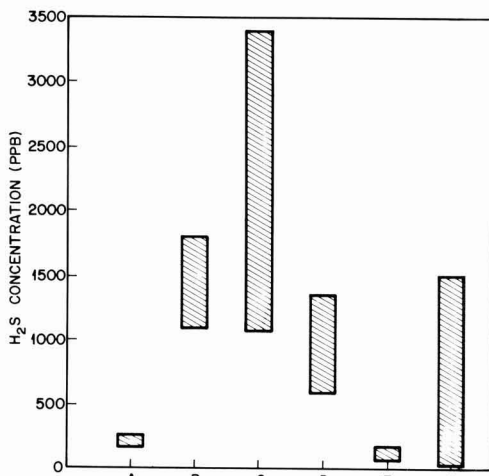


Fig. 4. Operating parameters of selected diffusant materials. (a) 17 mm diam PVC (84 mils thick); (b) 17 mm diam PVC (9.5 mils thick); (c) 9 mm PVC with filler (9.5 mils thick); (d) 7 mm PVC with filler (9.5 mils thick); (e) 45 mm poly(vinylidene) chloride (0.5 mils thick); (f) 45 mm cellulose acetate (10 mils thick).

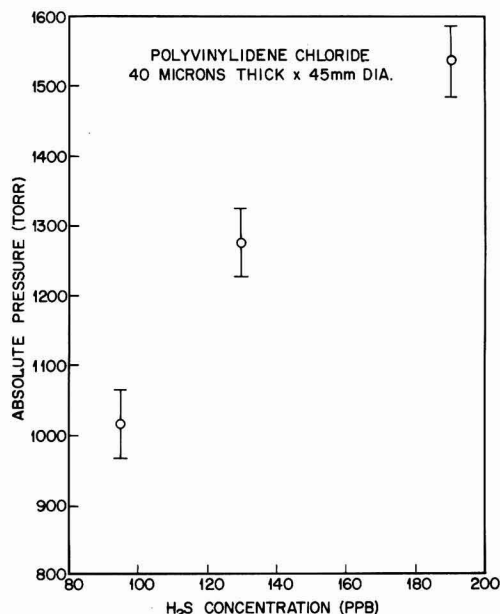


Fig. 5. H₂S concentration as a function of source pressure

Figure 5 shows changes in concentration with respect to pressure variation. The increases are linear within the tolerances of the error bars, as predicted by the concentrations equation previously given. Similar results have been derived for concentration changes as a function of cross-sectional areas of polymer exposed. All of the polymer films tested (Fig. 4) were exposed to pure H₂S for times in excess of a week.

Many polymeric materials have long been used in contact with gases without noticeable deterioration. The polymer films selected in these tests contain no materials that are expected to react with H₂S and thus no deterioration is anticipated. Exposures of as much as several weeks have not produced visual or permeation rate changes for any of the polymers, in contrast to that experienced with mechanical valve systems.

No visual degradation of any of the polymer corrosive gas handling devices have been apparent (Fig. 2), unlike the mechanical valve systems (Fig. 1).

It is of interest to determine the lifetime of an H₂S supply tank (60 lb H₂S) in a polymer permeation system with a concentration of 456 ppb and a flow of 1180 cm³/min. Calculations show that the supply would be depleted in 6×10^4 years. The number is so large it is conceivable that leaks in the system could pre-

dominate as a major source for depletion of the gas supply. Even a leak of many orders of magnitude above the permeation rate of the polymer would still not deplete the tank over a several year period. Given these facts, this type of gas generation can be considered a permanent source of trace gas at normal experimental flow rates.

Conclusions

A gas dilution system has been developed using polymers as "valves" to control the flow of corrosive H₂S gas in the ppm/ppb range. This technique can be applied to environmental trace gas testing (1) and gas blending, semiconductor manufacturing (10) or any process that requires metering of trace amounts of gas. In principle, the same technique should be satisfactory for all corrosive or noncorrosive gases. Using polymer characteristics, size, pressure, and temperature as variables, this system has an extremely wide dynamic range. Due to the inertness of selected polymers to H₂S gas, no degradation of the system is apparent even after several weeks of exposure.

Manuscript submitted Oct. 30, 1978; revised manuscript received April 30, 1979. This was Paper 245 presented at the Pittsburgh, Pennsylvania, Meeting of the Society, Oct. 15-20, 1978.

Any discussion of this paper will appear in a Discussion Section to be published in the June 1980 JOURNAL. All discussions for the June 1980 Discussion Section should be submitted by Feb. 1, 1980.

Publication costs of this article were assisted by Bell Laboratories.

REFERENCES

1. J. Potinecke, *Electrical Contacts/1975*, IIT Research Inst., Chicago, Illinois (1975); T. E. Graedel, J. P. Franey, and R. E. Schwab, *Electrical Contacts/1976*, Holm Seminar on Electrical Contacts, pp. 47-55, IIT Research Inst., Chicago, Illinois (1976); W. A. Crossland and E. Knight, in *Proc. Int. Symp. Electr. Contact Phenom.*, V. D. E. Verlag Gumbt Berlin, p. 324 (1970); T. Sydberger and R. Ericsson, "Laboratory Testing of the Atmospheric Corrosion of Steel," Chalmers Univ. of Tech. and University of Goteborg, Verlag Chemie, Gumbt D6940 Weinheim (1977).
2. G. O. Nelson, "Controlled Test Atmosphere," Ann Arbor Sci. Publ. Inc., Ann Arbor, Mich. (1971).
3. P. F. Preston, *Trans. Inst. Met. Finish.*, 50 (1972).
4. H. L. Kusnetz, B. E. Saltzman, and M. E. Lanier, *J. Am. Ind. Hyg. Assoc.*, 21, 361 (1960).
5. J. M. Rogoff, *J. Lab. Clin. Med.*, 25, 853 (1939).
6. S. B. Smith and R. J. Grant, Report No. NP-8-193, U.S. Public Health Service, Cincinnati, Ohio (1960).
7. H. D. Axelrod, J. B. Pate, W. R. Barchet, and J. P. Lodge, *Atmos. Environ.*, 4, 209 (1970).
8. Bulletin No. 20-68, Metronic Associates, Inc., Palo Alto, Calif.
9. A. Teckentrup and D. Klockow, *Anal. Chem.*, 50, 1728 (1978).
10. W. D. Johnston, Jr., TM76-1314-14, BTL Holmdel, Aug. 17, 1976.

Preparation of Pt-Fe Alloy Foils by Electrodeposition of Fe

A. D. Franklin* and J. Epp

National Bureau of Standards, Washington, D.C. 20234

Alloys of Fe in Pt are usually prepared from the melt. However, Bartholomew and Boudart (1) report preparing a 50% a/o Fe in Pt foil by electroplating Fe onto Pt foil from a room temperature aqueous electrolyte, followed by annealing in H_2 at elevated temperatures. We report here a somewhat similar technique. The electrolyte was an equimolar mixture of reagent grade KCl and $FeCl_2$, which was held in borosilicate glass at about 500°C, well above the liquidus temperature of about 400°C (2). A nitrogen atmosphere was provided, and a slug of Fe was kept in the bottom of the melt to keep the Fe in solution in the ferrous state. The glass, not far from its softening point, was a potential source of impurities. However, none of the oxides of which it was composed should be reducible by Fe at 500°C, and commercial laboratory glasses are otherwise quite pure. No impurities on a significant scale were expected. The anode was a piece of pure Fe and the cathode was the Pt foil to be converted to a Pt-Fe alloy.

The amount deposited was controlled by controlling the total number of coulombs passed. The weight loss of the Fe anode correlated well with the total charge passed if all of the Fe transported was assumed to

* Electrochemical Society Active Member.

Key words: fused salt electrodeposition, iron-platinum alloys, nonaqueous electrodeposition.

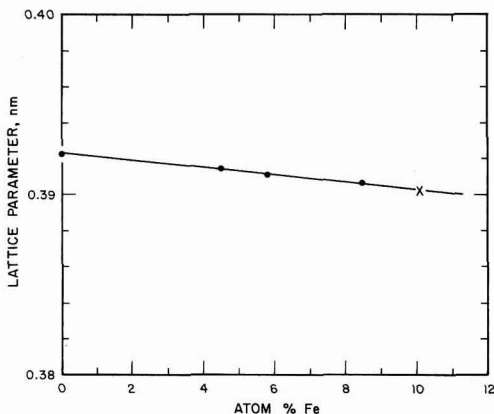


Fig. 1. Lattice parameters of Pt-Fe alloys prepared by electrodeposition. The point marked x is from Crangle and Shaw [Ref. (3)].

be in the ferrous state. The weight gained by the cathode was always somewhat less because of deposition on the lead wires. At current densities above approximately 60 mA/cm², the Fe deposited as long needles but below this current density the deposition appeared to be much more uniform.

X-ray diffraction powder patterns of the as-deposited surfaces showed either little diffraction or else showed complicated patterns indicating several ordered fcc or tetragonally-distorted fcc phases. No Fe patterns were observed for specimens prepared at low current densities. Evidently, even at this low temperature (500°C) the Fe alloys with the Pt, at least on the surface.

The foils were cleaned in dilute acetic acid and distilled water and annealed in a mixture of five percent H_2 in He at about 1200°C for 16 hr and then furnace cooled. After this treatment, the foils with Fe content up to about 10 a/o exhibited only a sharp disordered fcc x-ray pattern. Figure 1 displays the lattice parameter as a function of a/o Fe, obtained from the weight gain of the foil as measured after annealing. The data obey Vegard's law (linear dependence of lattice parameter on concentration), the points all falling on the same line as that reported by Crangle and Shaw (3) for a 10.1 a/o specimen prepared from the melt. It is quite apparent that these foils are homogeneous alloys in a well-annealed condition.

Acknowledgment

One of the authors was sponsored by the National Science Foundation/American University Program for High Ability High School Students and would like to thank the staff of that program for making her participation possible.

Manuscript submitted Feb. 20, 1979; revised manuscript received June 11, 1979.

Any discussion of this paper will appear in a Discussion Section to be published in the June 1980 JOURNAL. All discussions for the June 1980 Discussion Section should be submitted by Feb. 1, 1980.

Publication costs of this article were assisted by the National Bureau of Standards.

REFERENCES

1. C. H. Bartholomew and M. Boudart, *J. Catal.*, **29**, 278 (1973).
2. E. M. Levin, C. R. Robbins, and H. F. McMurdie, "Phase Diagrams for Ceramists," second edition, p. 377, American Ceramic Society (1964).
3. J. Crangle and J. A. Shaw, *Philos. Mag.*, **7**, 207 (1962).

Hydrogen in TiO_2 Photoanodes

D. S. Ginley* and M. L. Knotek*

Sandia Laboratories, Albuquerque, New Mexico 87185

Transition metal oxides show potential as photoanodes in photoelectrochemical cells for a variety of photocatalytic reactions of technological promise. A number of difficulties exist before their potential can come to fruition. Among these is a detailed understanding of the mechanisms of conduction and doping in most of the oxides. In addition, the chemistry of the surface is poorly understood. We have examined the effects of hydrogen in a number of titanium dioxide photoanodes with the goal of eventually understanding its role in these problems.

The precise nature of the defect is not obvious in this defect doped material. Simple oxygen vacancies or Ti^{3+} interstitials are not of themselves sufficient to explain the defect structure of rutile. Von Hippel (1), Hill (2), and others (3, 5), have suggested that the inclusion of hydrogen in the rutile lattice may have an important role in determining the properties of defects. Chester and Bradhurst (3) have shown that highly conductive surface layers may be formed by electrolytic doping with hydrogen. The layers are thin (20 nm) and the thickness is independent of dislocation density. Hydrogen is not unique in this respect and rutile may be electrochemically doped by other cations as well as has been recently shown by Haneman and Steenbeeke (4). Johnson (5) has also shown that TiO_2 may be interstitially doped with Li and that the characteristic blue color, as in the case of hydrogen reduction, results after Li diffusion. Van Ruyven and Chase (6) have also shown that hydrogen-free rutile exhibits no conductivity creep, while rutile with hydrogen shows creep. Bates and Perkins measured the IR absorption of incorporated OH^- , OD^- , and OT^- in TiO_2 and found a large shift from the free ion values (e.g., free OH^- at 3600 cm^{-1} vs. OH^- in TiO_2 at 3277 cm^{-1}). These observations suggest that understanding the nature of hydrogen in rutile is crucial to understanding the defect structure and its properties. Further, hydrogen is of crucial importance as an intermediate species in the water decomposition reaction on the rutile surface (8). Recent work by Wilson (9) and in this laboratory suggests that electrochemically generated intermediates on the TiO_2 surface greatly affect the measured flatband potential and thus the ability of the cell to operate without bias. Hydrogen probably plays an important part in this process.

In this paper, we show that hydrogen or deuterium can be incorporated into the rutile lattice both electrochemically and thermally. Measurements indicate that the hydrogen may be occupying two different sites, similar to what Jorgensen and Norton (10) have shown for SiO_2 . An activation energy has been obtained for the thermal diffusion process. Depth profiling electron-stimulated desorption (ESD) measurements have been obtained on these surfaces and show that in an electrochemically doped surface there is a high density of hydrogen in a shallow surface layer approximately 100 nm thick. In contrast to the work of Chester and Bradhurst, these surface layers appear highly resistive from both electrochemical measurements and ESD. It also appears that the activation energies for hydrogen diffusion, hydrogen reduction, and hydrogen scavenging by oxygen are vastly different as is reflected in the differing initiation temperatures for the processes. Preliminary electrochemical measurements on electrochemically doped rutile photoanodes will be presented. Large shifts in

both the flatband potential (V_{FB}) and the near-u.v. spectral response have been observed.

Experimental

All the samples employed were single crystal c-axis wafers of TiO_2 from N. L. Industries, Incorporated containing no Al_2O_3 or other stabilizer. Optical surfaces were obtained by polishing with diamond grit.

Deuterium-hydrogen exchange was accomplished in two ways: thermally and electrochemically. A complete or partial thermal exchange of hydroxyl hydrogens for deuterium in clear as grown TiO_2 (i.e., an $\text{OH} \rightarrow \text{OD}$ transformation) could be obtained in a platinum-lined autoclave of the standard configuration. Exchanges were performed from 250°C to 350°C by ensuring sufficient D_2O (Stohler isotope 99%+) or H_2O was present so that the sample remained immersed. This resulted in steam pressures from 1600-3000 psi above the liquid. Clear as grown TiO_2 samples with thermally exchanged OH and OD never exhibited any conductivity increases or blue color. The electrochemical doping of the TiO_2 anode and all electrochemical measurements were made with a PAR Model 173 potentiostat/galvanostat equipped with a PAR 179 digital coulometer and a PAR 175 universal programmer. All measurements were made using a standard three electrode setup with the TiO_2 anode, a smooth Pt cathode, and a Corning Model 476015 standard calomel reference electrode. The flatband potentials were determined from plots of the square of the photocurrent vs. potential (11). Extrapolation of the square of the photocurrent intercepts the potential axis at the flatband potential. Spectral response data were obtained using a 100W medium pressure xenon source through a Schoeffel grating monochromator. Intensities were measured with a HP-8330A radiant flux meter. Back contact to the TiO_2 was made with In/Ga eutectic and the electrolyte was composed of 1M LiOD in D_2O or 1M NaOH in H_2O for deuterium or hydrogen doping, respectively. Potentials were kept below 10V vs. SCE and currents less than 10 mA/cm^2 . Exchange was observed under both constant current (1 mA/cm^2) and constant voltage ($>2\text{V}$ cathodic) conditions.

TiO_2 wafers were reduced in vacuum (2×10^{-7} Torr) or hydrogen (1 atm) for between 5 min and 2 hr at 750°C depending on the conductivity desired ($\sim 10^2$ - $10^{-3}\text{ }\Omega\text{-cm}$). Samples reduced this way invariably were homogeneously blue in color, with the intensity of the blue color a function of the reduction time, while samples reduced in UHV (10^{-10} Torr) by electron beam bombardment were yellow but proceeded to turn blue on standing. We speculate that the defects created in UHV, Ti^{3+} interstitials, are hydrogen-free but pick up hydrogen as it diffuses in from the surface. The OH and OD infrared stretching modes and the blue color of reduced rutile could be removed by annealing in O_2 or air at between 500°C - 800°C . The blue, electrochemically introduced surface layers could be diffused evenly through the samples at 250°C in air.

Surface measurements were performed in a UHV system that was ion pumped with a base pressure of $<1 \times 10^{-10}$ Torr. Depth profiling was performed with a Physical Electronics Model 04-161 sputter ion gun using Ar^+ ions at 1 keV energy. Electron stimulated desorption (ESD) measurements were made using currents of approximately 150 nA ($\sim 0.5\text{ }\mu\text{A/cm}^2$) and an electron energy of 70 eV. The desorbed ions were accelerated through a CEC 440 quadrupole mass ana-

* Electrochemical Society Active Member.

Key words: catalysis, electrolysis, electrode, semiconductor.

lyzer and the ion current through the quadrupole was measured by counting techniques.

Results and Conclusions

The results of the bulk exchange experiments were monitored by the strength of the OH and OD IR stretching vibrations at 3276 and 2436 cm^{-1} , respectively (7). Figure 1 shows the IR absorption spectra for a sample before any treatment, showing the presence of OH, as well as two isothermal anneals at 250°C in D_2O which demonstrates that OD is replacing OH in the lattice. It was found that further treatment could completely exchange OD for OH so that no OH mode was observable. By a similar treatment, all OD could be reexchanged for OH.

We note that the condition of this exchange is much milder than others reported in the literature (i.e., 250°C vs. the 800°–900°C reported by Von Hippel *et al.*, and 450°–800°C by Hill).

Using Fick's law, the diffusion coefficient activation energy was estimated for D exchange. The total amount of exchanged D was taken as proportional to the strength of the OD IR absorption (12). The result obtained is $E_a \sim 0.45$ eV, which compares well with Hill's value for H migration (2).

One interesting point to note is that the level of OD after exchange is very near the "natural" OH level in the untreated virgin sample. If the OH is indeed associated with defects, then the fact that the OD level matches the initial OH level merely results from both being associated with the same defect density. We conclude from this that the OH's, being a nonneutral species are compensating some charged defects. We note that it is possible to remove totally both the OH and OD IR signals by annealing the sample in O_2 , 1 atm, at 500°C for 1 hr. This treatment either reacts the O_2 with the lattice H to form H_2O , or acts to remove the defects from the bulk, or both.

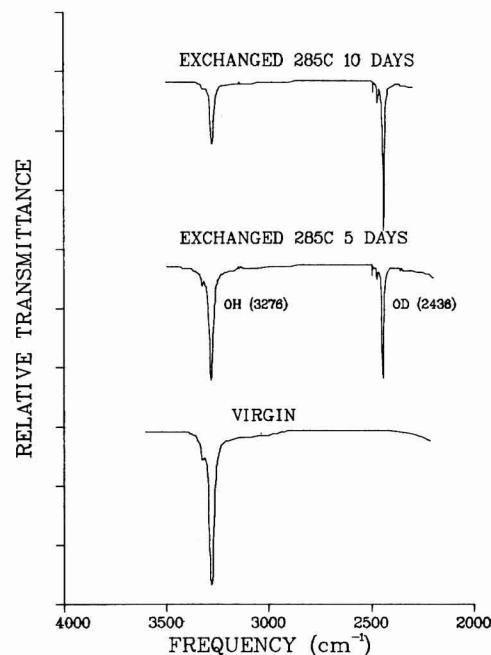


Fig. 1. Infrared absorption curves showing the OH and OD stretch exchange at 3275 and 2436 cm^{-1} , respectively, as a function of exchange time at 285°C. When driven to completion the OD level is equal to the OH level in the virgin sample.

Electrochemical doping.—Electrochemical exchange was carried out on samples which had been slightly vacuum or hydrogen annealed to increase their conductivity by defect introduction (10^{15} – 10^{17} donors/ cm^3). The samples were light blue in color before doping. The electrochemical doping was seen to exhibit a threshold at ~ -0.9 – 1.2 eV vs. SCE. After long periods of electrolysis (1–3 days, 100 μA –1 mA/cm^2), the current was seen to saturate and the cell impedance increased dramatically. The electrochemical exchange (D or H loading) produced a deep blue spot (Fig. 2a) which covered but was not uniform over the area exposed to the electrolyte. IR analysis showed that the OH level was changing in the spot and that OD was present, but high background absorptions limited precise measurement. It appears, however, that the bulk of the incorporated H or D cannot be accounted for in terms of incorporation as OD or OH. By loading at sufficiently high voltage, the sample could be made to shatter throughout the region exposed to the electrolyte, usually where cathodic currents were between 1 and 10 mA/cm^2 .

The blue spot was quite stable at room temperature in that there was no lateral (or other) diffusion of the blue color. Annealing at gradually increasing temperatures resulted in an abrupt diffusion of the blue spot to give a uniformly blue sample at a temperature of 250°C in the air. The samples were nominally c-axis normal to the surface and since the diffusion perpendicular to the c-axis is very small, it is reasonable to expect the small lateral diffusion. As we shall see below, however, the surface loading of D does not seem to be a straightforward process. There seems to be a surface layer with quite different properties than the bulk.

Electron stimulated desorption.—The blue spot on the electrochemically exchanged sample was examined by electron stimulated desorption to determine the density and makeup of surface species. An electron beam of 70 eV at 150 nA was impinged on the sample and the mass distribution of the desorbed positive ions was measured. The results are shown in Fig. 3. Masses 1, 2, 3, 4, 16, 17, and 18 are evident corresponding to H^+ , $(\text{D}^+, \text{H}_2^+)$, $(\text{H}-\text{D}^+)$, D_2^+ , O^+ , OH^+ , and OD^+ , respectively. No mass 7 corresponding to incorporated lithium was observed in runs with an LiOD electrolyte. It was possible to sample both on and off the blue spot and, as seen in the figure, there is a large difference in surface concentration between the blue spot and the virgin surface. The thermally exchanged samples were also examined in this way and surface levels very similar to the spot were found.

As the blue spot becomes more heavily loaded, it is found that the ESD electron beam caused charging, suggesting that the surface layer is insulating. The charging resulted in a large increase in the surface concentration of the H and D related species, indicating that considerable field induced migration was occurring. The levels before charging were still much higher on the blue spot than off it as noted above. This charging is similar to the effect seen in the exchange, namely, that an insulating layer seemed to have formed. These observations appear to be in conflict with those of Chester and Bradhurst. However, it may be that to a certain concentration level electrochemically introduced hydrogen compensates conductive defects and beyond that point acts as a donor. By this mechanism, it may be possible to get a very narrow inversion layer near the surface that is quite conductive.

The surface was depth profiled by argon ion sputtering using ESD as our probe. It was found that the layer of very high concentration of D was from 60 to 200 nm thick. The blue color, however, extended through a much thicker layer. We must wonder why such a shallow well-defined layer is formed, but note that similar layers with high H content are seen on other oxides as well by other techniques (13).

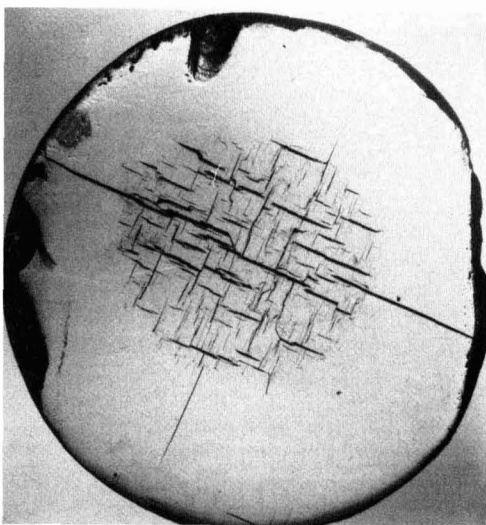
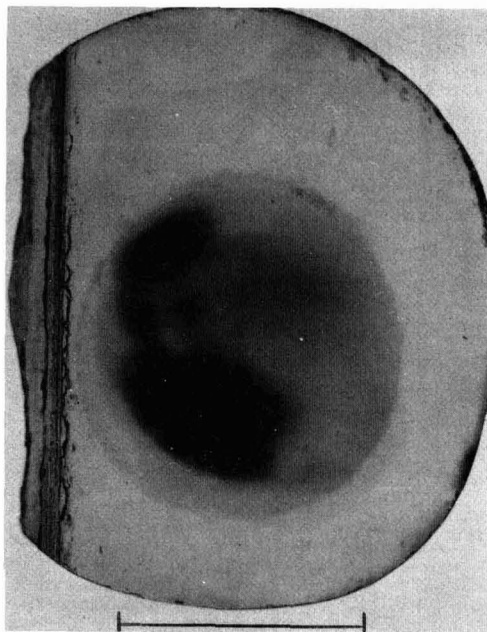


Fig. 2. (a, top) Photograph 5 \times magnification of an electrochemically deuterium-doped rutile wafer. Doping was accomplished by current controlled cathodic aging an undoped TiO₂ wafer in LiOD, D₂O for 48 hr at 100 μ A. The darkened circular region was exposed to the electrolyte and contains deuterium as determined by ESD, the remainder does not; (b, bottom) Identical to 2a except that the sample was aged at 10 mA for three days resulting in a shattering of the sample in the region exposed to the electrolyte.

As recently shown by Knotek and Feibelman (14), it is possible to extract considerable bonding information from ESD threshold data, since the thresholds reflect the core ionization potentials of the bonding site atom. Thus, under ideal conditions, it is possible to determine to which atom the bulk of the H is bonded, Ti as a hydride or O as a hydroxide. In this case, however, the charging of the surface made such

ESD MASS SCAN

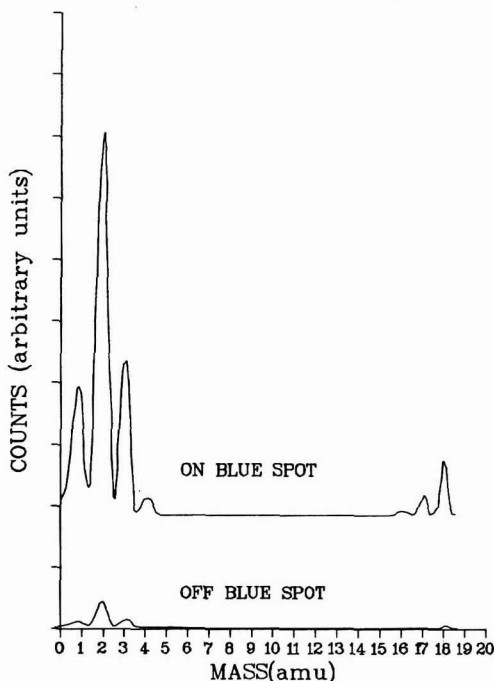


Fig. 3. Electron-stimulated desorption mass scans with the electron beam on and off the blue exchanged spot. Ar⁺ ion sputter depth profiling with ESD as the probe showed a layer of high D content was approximately 1000Å thick. The layer was highly resistive and caused charging effects in ESD.

a study impossible, but further work will include such an examination. Studies of surfaces prepared in UHV by exposure to H₂O show that there are both hydride type hydrogens bonded to Ti's and hydroxide-like hydrogens bonded to O's (15). This information comes from the threshold behavior of the ion yield vs. electron energy (14).

Electrochemical measurements.—To evaluate the importance of the incorporated hydrogen on photoelectrochemical properties of TiO₂ anode in a photoelectrolysis cell, a number of electrochemical experiments have been carried out on illuminated anodes. In general, these experiments entail aging lightly doped TiO₂ anodes in 1M NaOH in various potential and current regimes. Figure 4 and Table I enumerate the results of such an experiment on one rutile anode. Scan 1 is that for the virgin, lightly hydrogen reduced anode and its photoresponse is that expected, giving an effective gap of approximately 3.0 eV. Its measured flatband of -0.865 V vs. SCE is also normally found (16).

As the sample begins to age cathodically, one sees the gradual hydrogenation of the surface layer of the electrode. Current controlled aging was employed so as to avoid the incorporation of too much hydrogen and subsequent shattering of the sample, which occurs at current densities between 1-10 mA in 1-3 days. As the hydrogen doping proceeds, the flatband starts moving to positive values vs. SCE and then levels off. This shift is generated by three effects. Butler and Ginley have recently shown how the flatband potential of a photoanode can be predicted from the atomic electronegativity of the constituent atoms

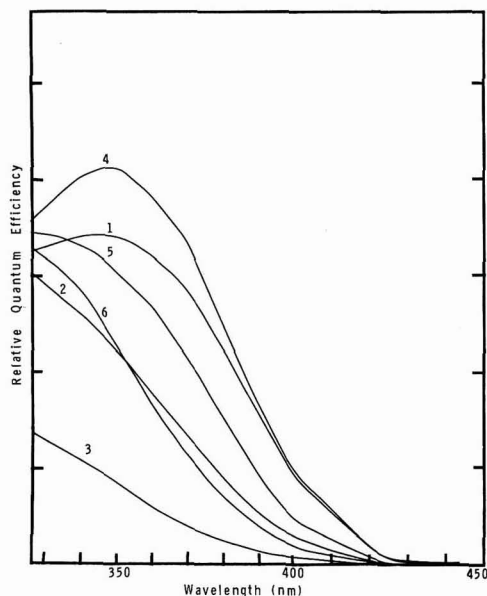


Fig. 4. Successive agings of a lightly hydrogen reduced rutile anode in 1M NaOH: curve 1, virgin sample, curve 2, 100 μ A 14 hr cathodic, curve 3, 100 μ A 20 hr cathodic, curve 4, 0.0V vs. SCE 20 hr, curve 5, +1.0V vs. SCE 23 hr, and curve 6, +5.0V vs. SCE 4 days.

of the semiconductor (17). In this case, the introduction of hydrogen into the lattice increases the bulk electronegativity of the oxide so as to move V_{FB} to more positive potentials. Rough calculations indicate that if one out of five TiO_2 moieties on the surface were hydrogenated, the appropriate shift in V_{FB} would result. However, two other factors must be evaluated; the change in the bandgap of the oxide which is small based upon photoresponse measurements, and the change in the point of zero zeta potential of the surface which may be significant if the relative pK_a of the surface is altered.

The relative lack of change in V_{FB} from scan two to scan three most likely results from the near saturation of the available surface sites with hydrogen. The substantial loss of quantum efficiency for the cathodically aged sample seems to indicate that the hydrogenated surface region acts as if it has many recombination centers or more likely that photoexcited states either radiatively or nonradiatively decay without giving rise to holes that can participate in photoelectrolysis. These hypotheses are currently under investigation.

Treatment four is the reverse aging of the sample under illumination at 0.0V vs. SCE. Most of the hydrogen is removed from the surface layer in this process, but the V_{FB} shows that perhaps 20-30% of the hydrogen remains. This is further substantiated by the continued presence of the blue spot. However, as the photoresponse curve number four shows, the quantum efficiency is totally restored. This indicates

that the remaining hydrogen is located on a lattice site that is normally not photoactive in the photoelectrolysis process.

Continued aging in the anodic direction at +1.0 and +0.5V vs. SCE, scans five and six respectively, result in the gradual diffusion of Ti^{3+} interstitials out of the surface layer as has recently been discussed by Butler (18). The removal of the electropositive Ti^{3+} results in a more positive V_{FB} and the reduced number of donors results in the observed decrease in Φ . The blue spot remains, indicating the continued presence of hydrogen in the surface.

Conclusion

Similar to the case for SiO_2 , more than one important lattice site for hydrogen is indicated for TiO_2 . Very high levels of hydrogen are found in the near surface region in exchanged samples and certainly the hydroxyl hydrogens represent only a portion of the incorporated hydrogen. We are now trying to determine the nature of the role of hydrogen in defects for both conduction and surface reactions. Further, large changes in V_{FB} and Φ result after hydrogenation, indicating the electromigration and the electrochemical doping of the surface layers in oxide photoanodes may be crucial in evaluating electrode stability and performance. The use of an appropriate electrochemical dopant may result in the advantageous modification of an electrodes properties.

Acknowledgments

This work was supported by the Materials Sciences Program, Division of Basic Energy Sciences, U.S. Department of Energy, under Contract DE-ACO4-76-DP00789.

Manuscript submitted Jan. 23, 1979; revised manuscript received April 30, 1979.

Any discussion of this paper will appear in a Discussion Section to be published in the June 1980 JOURNAL. All discussions for the June 1980 Discussion Section should be submitted by Feb. 1, 1980.

Publication costs of this article were assisted by Sandia Laboratories.

REFERENCES

1. A. Von Hippel, J. Kalnajs, and W. B. Westphal, *J. Phys. Chem. Solids*, **23**, 779 (1962).
2. G. J. Hill, *Br. J. Appl. Phys.*, **1**, 1151 (1968).
3. P. F. Chester and P. H. Bradhurst, *Nature*, **149**, 1056 (1963).
4. D. Haneman and F. Steenbeeke, *This Journal*, **124**, 861 (1977).
5. O. W. Johnson, *Phys. Rev. A*, **136**, 284 (1964).
6. L. J. Van Ruyven and J. D. Chase, *Appl. Phys. Lett.*, **12**, 214 (1968).
7. J. B. Bates and R. A. Perkins, *Phys. Rev. B*, **16**, 3713 (1977).
8. M. L. Knotek, Abstract 339, p. 869, The Electrochemical Society Extended Abstracts, Philadelphia, Pennsylvania, May 8-13, 1977.
9. R. H. Wilson, Abstract 415, p. 1038, The Electrochemical Society Extended Abstracts, Seattle, Washington, May 21-26, 1978.
10. P. J. Jorgensen and F. J. Norton, *Phys. Chem. Glasses*, **10**, 23 (1969).
11. M. A. Butler, *J. Appl. Phys.*, **48**, 1914 (1977).
12. O. W. Johnson, J. Deford, and J. W. Shaner, *ibid.*, **44**, 3008 (1973).
13. G. J. Clark, C. W. White, D. D. Allred, B. R. Appleton, F. B. Koch, and C. W. Mager, *Nucl. Instrum. Methods*, **149**, 9 (1978).
14. M. L. Knotek and P. J. Feibelman, *Phys. Rev. Lett.*, **40**, 964 (1978).
15. M. L. Knotek, To be published.
16. M. Wrighton, D. S. Ginley, P. T. Wolczanski, A. B. Ellis, D. L. Morse, and A. Linz, *Proc. Natl. Acad. Sci. U.S.A.*, **72**, 1518 (1975).
17. M. A. Butler and D. S. Ginley, *This Journal*, **125**, 228 (1978).
18. M. A. Butler, Paper 421 presented at The Electrochemical Society Meeting, Seattle, Washington, May 21-26, 1978.

Table I. Dependence of V_{FB} on aging conditions in 1M NaOH

Treatment	Conditions	Measured V_{FB} (vs. SCE)
1	Virgin	-0.865
2	Aged cathodically 100 μ A 14 hr	-0.735
3	Aged cathodically 100 μ A add. 20 hr	-0.750
4	Aged 0.0V vs. SCE 20 hr	-0.817
5	Aged anodically +1.0V vs. SCE 23 hr	-0.765
6	Aged anodically +5.0V vs. SCE 4 days	-0.705

DISCUSSION

SECTION



This Discussion Section includes discussion of papers appearing in the *Journal of The Electrochemical Society*, Vol. 126, No. 2, 3, 4, and 5, February, March, April, and May 1979.

The Electrochemistry of Electroless Deposition of Copper

S. M. El-Raghy and A. A. Abo-Salama (pp. 171-176, Vol. 126, No. 2)

Francis M. Donahue:¹ The subject paper purports to present a better method of studying electroless copper plating processes. This correspondent takes exception to this contention both in terms of their approach to the problem and, to some extent, the interpretation of their data.

The method of separating the partial processes and measuring the current flow was first used by Lukes² to demonstrate that hydrogen gas was not the reductant for cupric ion and as an aid in proposing a mechanism for formaldehyde oxidation, not to measure plating rates. The authors concede that the coupling current is less than the actual plating rate and that the working potentials for the anode and cathode are different from the actual mixed potential. The point of the experiments, therefore, is not clear. It cannot be to demonstrate that the separated processes operate; Lukes² did that. It cannot be to demonstrate that electrochemical reduction of cupric ion and electrochemical oxidation of formaldehyde are the partial processes; Paunovic³ did that.

The authors have apparently misunderstood our use of mixed potential analyses^{4,5}—see their concluding comments. The primary purpose of the mixed potential analysis is to establish rate laws for the partial processes. This is done by independently measuring the plating rate and the mixed potential for a series of plating baths. One of the consequences of these types of studies is the ability to determine interactions among the various reactant species.⁴ Since Schoenberg⁶ reported that formaldehyde was bonded with cupric ion in the plating bath, it was not surprising that Shippey's data^{5,7} showed that formaldehyde (the anodic partial process reactant) participates in the cathodic partial process. Experiments in separated compartments cannot reveal such interactions which occur under actual plating conditions. Incidentally, from the electroless plating data given in Fig. 10 and column 2 of Table I, this correspondent was able to estimate the reaction order for formaldehyde in the cathodic partial process; it was approximately equal to that of Shippey.⁵

Another interesting interaction which one may not be able to study using separated compartment experiments is the effect of gas evolution on mass transfer. It has been shown that hydrogen gas evolution (product of the anodic partial process) usually determines the mass transfer conditions in electroless copper plating baths and that cupric ion (reactant of the cathodic partial process) is the only species which is substantially affected.⁸ That the authors did not observe this effect (see Table I) has been ascribed to the low plating rates which they obtained.⁸

Finally, the authors' use of Evans diagrams is misleading. The authors have drawn more than eleven lines (Fig. 11 and 12) without benefit of essential information. In order to draw the lines, the exchange current densities and Tafel slopes for the partial processes must be known. On the basis of the data presented in the subject paper, it can be categorically stated that this information was not available. Therefore, there is no justification for the labelling of the lines with concentrations. Further, there is a clear implication from those lines that the respective Tafel slopes change with concentration, an unusual situation which cannot be substantiated.

The Composition of Anodically Formed Iron Oxide Films

M. Cohen, D. Mitchell, and K. Hashimoto
(pp. 442-444, Vol. 126, No. 3)

A. M. Olmedo:⁹ I agree with Cohen and co-workers that the temperature rise for RHEED is small and would be insufficient to cause any changes in the oxide or hydroxide. I have made some experiments with RHEED to characterize the oxide grown in an alkaline solution of 3M-NaOH and I found the presence of an hydrated iron oxide in the electrolyte used.

The specimens were prepared with a sheet of annealed spectroscopic grade polycrystalline iron. The slow cooling after the high temperature treatment led to sufficient grain growth in the polycrystalline sheet to allow diffraction patterns of iron to be obtained from single grains. Previous to each experiment the surface was prepared by electropolishing in butyl- α -cellosolve-perchloric acid mixture followed by abundant washing with methanol. The oxides were grown electrochemically in a conventional three electrode cell containing alkaline solution of 3M-NaOH using Hg/HgO/1M NaOH reference electrode. Solutions were deaerated with 4N N₂ prior to each experiment. All experiments were performed under potentiostatic conditions.

The phenomena of passivity of iron in alkaline solutions has been known for a long time.¹⁰ The oxides grown in this work have a thickness of a few tens of angstroms as it has been mentioned in a previous article¹¹ and from previous work it appeared that it was possible to prepare reproducible passivated surfaces in this media in the potential range -0.4 – 0.65 V vs. the reference electrode mentioned.^{11,12} The anodic limit corresponds to the onset of oxygen evolution reaction and the cathodic limit to the potential range where a slight partial reduction of the film starts. Two techniques were used: (i) the iron was passivated employing a single potential sweep from H₂ evolution to 0.3V and was cycled several times between these limits, (ii) the iron was passivated employing the step technique. Both responses may be found in the previous works mentioned,^{11,12} the plots are qualitatively similar for different concentrations of NaOH.

The electron diffraction pattern for the iron electrode cycled several times between H₂ evolution to 0.3V (vs. the reference electrode mentioned) is shown

¹ Department of Chemical Engineering, The University of Michigan, Ann Arbor, Michigan 48109.

² R. M. Lukes, *Plating*, 51, 1066 (1964).

³ M. Paunovic, *ibid.*, 55, 1161 (1968).

⁴ F. M. Donahue, *This Journal*, 119, 72 (1972).

⁵ F. M. Donahue and F. L. Shippey, *Plating*, 60, 135 (1973).

⁶ L. Schoenberg, *This Journal*, 118, 1571 (1971).

⁷ F. L. Shippey and F. M. Donahue, *Plating*, 60, 43 (1973).

⁸ F. M. Donahue, *This Journal*, accepted for publication.

⁹ Comisión Nacional de Energía Atómica, 1429 Buenos Aires, Argentina.

¹⁰ B. Kabanov, R. Burstein, and A. N. Frumkin, *Discuss. Faraday Soc.*, 1, 259 (1947).

¹¹ A. M. Olmedo, R. Pereiro, and D. J. Schiffrin, *J. Electroanal. Chem. Interfacial Electrochem.*, 74, 19 (1976).

¹² C. V. D'Alkaine, R. Pereiro, and D. J. Schiffrin, Paper No. 727 presented at the 25th I.S.E. Meeting, Brighton, England (1974).

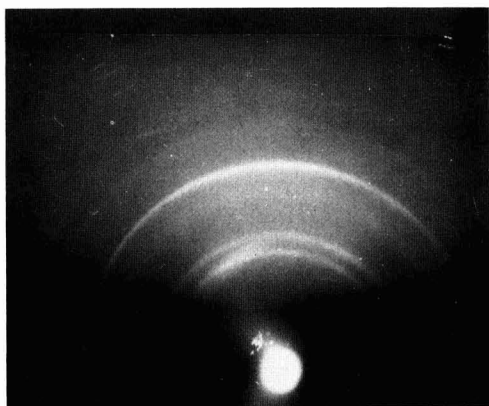


Fig. 1. Reflection electron diffraction pattern of iron passivated cyclically, 75 kV.

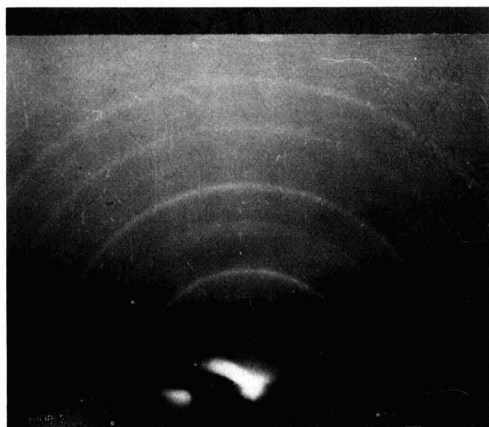


Fig. 2. Reflection electron diffraction pattern of iron passivated by potential step technique (passivated during two hours), 100 kV.

in Fig. 1. In Table I the d -values measured are presented. This diagram is perfectly consistent with a polycrystalline $\text{Fe}_2\text{O}_3 \cdot 1.2\text{H}_2\text{O}$ (ASTM card 22.1117). The pattern suggests that the oxide is composed of randomly oriented microcrystallites. The electron diffraction pattern for the film grown at 0.200V anodic (vs. the reference electrode mentioned) during 2 hr is shown in Fig. 2. The final current density observed at the end of the growth was approximately $0.4 \mu\text{A cm}^{-2}$. In Table II the d -values measured are presented. The inner ring, which is very faint and is masked by the shadow of the iron sheet, corresponds to a spacing of 2.52–2.53 Å which is present not only in the hydrated oxide mentioned before but also in Fe_3O_4 and $\gamma\text{-Fe}_2\text{O}_3$. The values of the two more intense rings are very close to those of α iron (ASTM card 6-0696). As the sample was rotated in the chamber the rings appeared fainter and in some cases showed up some points corresponding to the iron substrate.

The results presented here showed that the iron passivated in an alkaline solution of NaOH may form a hydrated film in accordance with some previous work mentioned in the paper of reference.

Morris Cohen:¹³ We were pleased to receive confirmation of a low temperature rise due to the use of RHEED. The observation of a hydrated oxide at high

¹³ National Research Council of Canada, Ottawa, Canada.

Table I

d (Å)
2.53
2.23
1.69
1.48
1.23
1.10
0.95
0.87
0.84

Table II

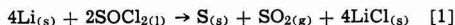
d (Å)
2.52
2.02
1.41
1.14
0.88
0.74
0.66
0.63
0.60
0.58

pH is not inconsistent with our observations of anhydrous oxide at near neutral pH's. In these highly alkaline solutions more iron may be going into solution which would then be anodically redeposited as hydrated oxide. The cycling used in the described experiments would increase the amount of iron in solution and hence also increase the thickness of the deposited film.

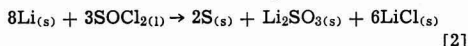
Discharge Reaction Mechanisms in Li/SOCl₂ Cells

C. R. Schlaikjer, F. Goebel, and N. Marincic
(pp. 513–522, Vol. 126, No. 4)

M. H. Miles:¹⁴ The abrupt change in the open-circuit potential of the Li/SOCl₂ cell below -20°C reported in the paper under discussion is interesting, however thermodynamic calculations do not support the postulate that this is due to the cell reaction changing from



or the related reaction involving (SO)_n to



at temperatures below -20°C . Calculations based upon available thermochemical data^{15–21} show only small differences in ΔH^0 for these two reactions unlike the large changes expected from the experimental results of Fig. 6 in the paper under discussion. For example, calculations based upon heats of formation give $\Delta H^0 = -86.1$ kcal/eq. for reaction [1] and a very similar value of -86.2 kcal/eq. for reaction [2] at standard conditions. However, using

$$\Delta H = -nFE + nFT(\partial E/\partial T)_P \quad [3]$$

and the results shown in Fig. 6 $\Delta H = -77$ kcal/eq. between $+72^\circ\text{C}$ and -20°C and changes abruptly to -66 kcal/eq. at temperatures below -20°C .

From basic thermodynamic relationships,²² it can be readily shown that

¹⁴ Chemistry Division, Naval Weapons Center, China Lake, California 93555.

¹⁵ Nat. Bur. Stand. Tech. Note, 270-3 (1968).

¹⁶ Nat. Bur. Stand. Circ., 500 (1952).

¹⁷ W. M. Latimer, "Oxidation Potentials," 2nd ed., pp. 72, 329, Prentice-Hall, New York (1952).

¹⁸ A. A. Shidlovskii and A. A. Voskresenskii, Zh. Fiz. Khim., 39, 3097 (1965); Chem. Abstr., 64, 8996a (1966).

¹⁹ D. E. Wilco and L. A. Bromle, Ind. Eng. Chem., 55(7), 32 (1963).

²⁰ E. Erdős, Collect. Czech. Chem. Comm., 27, 1428 (1962).

²¹ Ibid., 27, 2273 (1962).

²² F. Daniels and R. A. Alberty, "Physical Chemistry," 4th ed., pp. 31–33, 190–198, Wiley, New York (1975).

$$(\partial \Delta H / \partial T)_P = nFT (\partial^2 E / \partial T^2)_P = \Delta C_P \quad [4]$$

and

$$(\partial \Delta S / \partial T)_P = nF (\partial^2 E / \partial T^2)_P = \Delta C_P / T \quad [5]$$

where ΔC_P is the change in heat capacity for a reaction at constant pressure. Since ΔC_P is relatively small for most reactions, both ΔH and ΔS are usually fairly constant over moderate temperature ranges, hence E vs. T will generally show a linear relationship as observed for the Li/SOCl_2 cell reaction. From heat capacity data,^{15,16,21} ΔC_P^0 is only -4.2 cal/K for reaction [1] and -2.8 cal/K for reaction [2] per equivalent, hence ΔH^0 would change less than 0.5% over a 100°C temperature range for either reaction. Since $\ln K_{\text{eq.}} = -\Delta H^0/RT + \Delta S^0/R$, the constancy of ΔH^0 and ΔS^0 is also the basis of the linear relationship observed between $\ln K_{\text{eq.}}$ and $1/T$ for many reactions.²³

For the Li/SOCl_2 cell reaction below -20°C , another linear relationship between the open-circuit potential and the temperature is to be expected. Using $\Delta S = nF(\partial E / \partial T)_P$ and the data points at -40°C and -60°C in Fig. 6, it is found that $\Delta S = 58$ cal/K for a reaction involving one equivalent. At temperatures between $+72^\circ$ and -20°C , a quite different value of $\Delta S = 23.7$ cal/K is obtained. Any postulated changes in the cell reaction below -20°C should be consistent with abrupt changes in ΔH and ΔG to less negative values and with an abrupt increase in ΔS . Contrary to the statement by the authors (likely a misprint), ΔG is not constant over any temperature range for the Li/SOCl_2 reaction but varies directly with the cell potential according to $\Delta G = -nFE$.

Thermochemical calculations support the postulated formation of SO or $(\text{SO})_n$. If about half of the sulfur-containing products in reaction [1] were actually present as SO , then the calculated value of ΔH^0 would be close to the experimental value of -77 kcal/equiv. Differences reported between the experimental and standard state conditions would likely cause relatively small changes in the enthalpy for this cell reaction.

C. R. Schlaikjer:²⁴ The authors would like to thank Dr. Miles for submitting his comments.

For any electrochemical cell being discharged at vanishingly small current, the potential is determined by the free energy change associated with the electrochemical reactions occurring on the electrode surfaces. This potential is not affected by any chemical reactions involving products which may be present in the electrolyte subsequent to discharge, unless these products polarize one or both electrodes through direct chemical reaction. The enthalpy and entropy changes per equivalent for each of reactions [1] and [2], using the references cited by Dr. Miles, and those noted from the experimental data are as follows:

	ΔH^*	ΔS^{**}
reaction [1]	-86.1 kcal/equiv.	-5.62 cal/deq equiv.
reaction [2]	-86.2 kcal/equiv.	-9.78 cal/deq equiv.
found	-77 kcal/equiv.	$+23.7$ cal/deq equiv.

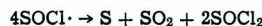
* Assuming SO_2 is formed as a condensed phase.

Apparently, neither reaction 1 nor 2 reflect the electrochemical reaction which occurs during the discharge of a $\text{Li}/\text{SOCl}_2/\text{C}$ cell at ambient temperature, even though the over-all reaction may be as indicated in Eq. [1].

These observations and the arguments presented in the paper indicate that one or more intermediates exist in the solution as the result of discharge, which decompose on standing to sulfur and sulfur dioxide. The abrupt change in slope of the open-circuit potential as a function of temperature below -20°C may indicate that another discharge reaction becomes significant, but does not necessarily mean that the

electrode reactions produce Li_2SO_3 and sulfur directly. Dr. Miles used the two points at -40° and -60°C to calculate ΔS for the electrochemical reaction in this region. The observed dependence may be affected by the kinetics of the electrode reactions below -20°C . We believe that the data presented in the paper are not sufficient to establish what the slope $\partial E / \partial T$ really is in this region.

Blomgren et al.²⁵ have reported that the initial or electrochemical step in the reduction of both thionyl chloride and sulfuryl chloride involved the transfer of only one equivalent per mole. Dey et al.²⁶ also reported that solutions of thionyl chloride when reduced in supporting electrolyte did not yield two equivalents per mole, but fell short of this value by the time the SOCl_2 had disappeared. On standing, the electrolyte was said to have regenerated thionyl chloride, which on further electrochemical reduction yielded a total value near two equivalents per mole. If these observations are correct, then SOCl could be an intermediate in the discharge of $\text{Li}/\text{SOCl}_2/\text{C}$ cells



Dr. Miles mentioned a misprint on page 517, first column, 5th line from the bottom: the entry ΔG should read ΔH .

Electrochemical Potential Spectroscopy: A New Electrochemical Measurement

A. H. Thompson (pp. 608-616, Vol. 126, No. 4)

T. Jacobsen, K. West, and S. Atlung:²⁷ In the paper by Thompson the incremental capacity, defined as $-\Delta x / \Delta V$ is determined for Li_xTiS_2 by a potential stepping technique. The $-\Delta x / \Delta V$ vs. x dependence (Fig. 2 and 3 of the paper) shows definite peaks at $x = 1/9$ and $x = 1/4$. It is argued that due to the coulombic interactions superlattices of intercalated Li^+ ions may be formed for $x = 1, 1/3, 1/4, 1/7, 1/9, \dots$ and the observed peaks are taken as a verification of the lattices $x = 1/9$ and $x = 1/4$.

Although we do agree with the author on the formation of regular structures during intercalation and his results are basically in agreement with our findings, we have some objections to his analysis of the capacity vs. composition dependence.

Consider the stage in the intercalation process, where a superlattice corresponding to $x = x_i$ has just been completed. On further intercalation this is gradually transformed into a new and denser lattice, which is completed at $x = x_{i+1}$. During this transformation all Li^+ ions are inserted at position with identical nearest neighbor distances and to a first approximation the interaction energy of these ions will not depend on the degree of transformation. Later on when the $i + 1$ lattice is completed the Li^+ ions now intercalated will have a shorter nearest neighbor distance and an increased interaction energy.

For $x_1 < x < x_{i+1}$ the Li_xTiS_2 electrode potential can be written as

$$V = V_{0i/i+1} + \frac{RT}{F} \ln \frac{1 - \theta_i}{\theta_i} + \Delta V_{\text{int}}(\theta_i) \quad [1]$$

where $V_{0i/i+1}$ is the standard potential of the $i/i + 1$ lattice transformation. θ_i is the degree of transformation defined as $(x - x_i) / (x_{i+1} - x_i)$ and $\Delta V_{\text{int}}(\theta_i)$ accounts for the minor change in interaction energy during the transformation.

Ignoring the interaction term $\Delta V_{\text{int}}(\theta_i)$ the normalized differential capacity, $-dx/dV$, can be derived from Eq. [1]

²⁵ G. E. Blomgren, V. Z. Leger, M. L. Kronenberg, T. Kalnoki-Kis, and R. J. Brodd, Paper No. 36, "Power Sources 7," J. Thompson, Editor, p. 583, Proceedings of the 11th International Symposium, Brighton, 1978. Academic Press, London (1979).

²⁶ A. N. Dey, W. Bowden, J. Miller, and P. Witalis, Report DELET-TR-78-558-1, April, 1979.

²⁷ Fysisk-Kemisk Institut, The Technical University of Denmark, DK 2800, Lyngby, Denmark.

²⁴ *ibid.*, pp. 170-173.

²⁵ GTE Laboratories, Waltham, Massachusetts 02154.

$$-\frac{dx}{dV} = \frac{-1}{x_{i+1} - x_i} \frac{d\theta_i}{dV} = \frac{F}{RT} \theta_i(1 - \theta_i) \quad [2]$$

As the term $\theta_i(1 - \theta_i)$ has a maximum for $\theta_i = 0.5$ this relation predicts capacity peaks to be present between the ordered structures. The differences in standard potential for the sequence of lattice transformations taking place during the complete discharge of Li_xTiS_2 is mainly determined by the decrease in nearest neighbor distance when denser structures are initiated. Therefore the capacity vs. composition relationship is expected to be a series of peaks, showing minimas where complete lattices are present. In case two (or more) lattice transformations have similar standard potentials the structure of intercalated Li^+ ions will be a mixture of the three (or more) lattices involved and the separating minimas may vanish.

Returning to Fig. 2 and 3 in Thompson's paper, it is seen that the capacity peaks at $x = 1/9$ and $x = 1/4$ are separated by a minimum for x close to $1/7$. Thus the first peak should preferably be attributed to the formation of the $1/7$ lattice. Although the expected minimum after the $x = 1/4$ peak is obscured by the superposition of denser structures, this peak is probably due to the transformation of the $1/7$ lattice into the $1/3$ lattice.

In a study of Li_xTiS_2 by means of slow linear potential sweeps we have obtained results very similar to the ones given by Thompson. At very slow scan rates, where the Li_xTiS_2 phase is close to equilibrium conditions, the observed current given by $i = Q_{\text{max}} dx/dV dV/dt$ is proportional to the differential normalized capacity $-dx/dV$. Figure 1 shows this quantity determined at a sweep rate of $28 \mu\text{V sec}^{-1}$ as a function of the electrode potential. To analyze this we have assumed a series of consecutive lattice transformations each having an emf expression of the form

$$V = V_{0/1+1} + \frac{RT}{F} \ln \frac{1 - \theta_i}{\theta_i} - f(\theta_i - 0.5) \quad [3]$$

where the interactions are accounted for by the term linear in θ_i . By differentiation it is easily seen that Eq. [3] predicts symmetrical peaks around $\theta_i = 0.5$

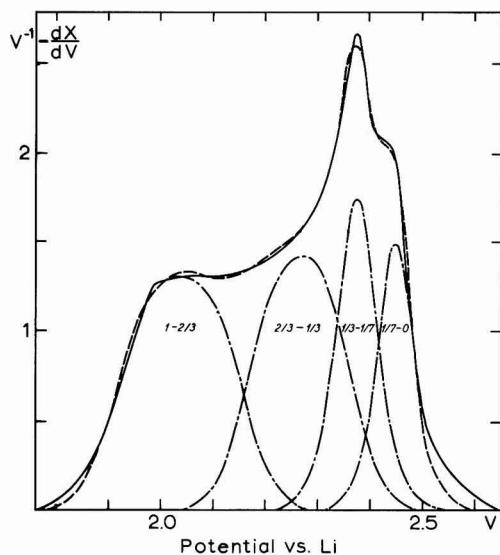


Fig. 1. Normalized differential capacity of Li_xTiS_2 vs. electrode potential determined by linear scan voltammetry (25°C , $28 \mu\text{V sec}^{-1}$): —, experimental; ----, calculated; - - - - -, contributions from the four lattice transformations considered.

Table I. Model parameters (Eq. [3])

Lattice	$V_{1/1+1}^0$ (V)	f (V)
0-1/7	2.455	-0.013
1/7-1/3	2.375	0.000
1/3-0.65	2.266	0.105
0.65-1	2.037	0.145

The peak width is determined by the interaction parameter f .

This model has been fitted to the experimental capacities by means of a nonlinear least squares computer program. The resulting calculated curve also given in Fig. 1 shows good agreement with the experimental one. As it is seen from the parameters in Table I the capacity behavior is described by the formation of a $1/7$ lattice, transformation of this into a $1/3$ lattice followed by a denser lattice at $x = 0.65$ before the complete close packed structure is formed. The value of $x = 0.65 \approx 2/3$ can be explained as a $1/3$ lattice of empty sites. The rather high values of the interaction parameter f for the dense states are not surprising as the Li^+-Li^+ distances in this region are small and interactions other than those between nearest neighbors may be of importance.

On the basis of these results the superlattice formation as suggested by Thompson appears a very suitable model for the intercalation of Li^+ into TiS_2 although more detailed studies are required to obtain a satisfactory description of the denser states.

A. H. Thompson:²⁸ The authors T. Jacobsen *et al.* raise some good points that were not fully discussed in my paper. I agree that the phase diagram for the Li_xTiS_2 system is still very much uncertain. The peaks in incremental capacity at the $x = 1/4$ and $1/9$ compositions seem to clearly suggest ordering effects. Also, the temperature dependent data clearly indicate that a probable ordering occurs at $x = 1/3$. But at present, there are not enough data to unambiguously specify the phase diagram. Additional electrochemical and particularly structural data are required. Nonetheless several specific replies need to be made to the Jacobsen discussion since I do not believe that the present data fully support the proposed model.

1. The model proposed by Jacobsen *et al.* assumes that all additional lithium ions intercalated between two ordered compositions enter identical sites. This would only be true if the ordered compositions are perfectly ordered and if the additional lithium do not interact with each other. The latter constraint would only be valid close to the x_1 composition. Also, the relatively high diffusivity of Li in Li_xTiS_2 suggests a highly defected structure involving both the octahedral and tetrahedral sites. Under these conditions, a highly defected or incipient model for the ordering is probably more appropriate.

2. The data of my paper do not support minima at $x = 1/7$ and $x = 1/3$. Close inspection of Fig. 3 shows that $x = 1/7$ lies on the falling edge of the $x = 1/9$ peak and that $x = 1/3$ lies on the falling edge of the $x = 1/4$ peak.

3. The qualitative differences between the electrochemical potential spectroscopy (ECPS) data and the linear potential sweep data may be explained by the rate differences. The ECPS data taken at $1-10 \mu\text{A/cm}^2$ correspond to continuous discharge rates of $10^{-2}-10^{-1} \mu\text{V/sec}$ compared to $\sim 30 \mu\text{V/sec}$ for the linear sweep data.

It should be further pointed out that minima in $-dx/dV$ would be expected when there is two phase formation. Recent studies on Li_xTaS_2 by the author^{29,30} describe ECPS results on two phase systems.

²⁸ Exxon Research and Engineering Company, Corporate Research Laboratories, Linden, New Jersey 07036.

²⁹ A. H. Thompson, To be published in the Conf. Proc., "Fast Ion Transport in Solids," Geneva, Wisconsin, May 1979.

³⁰ A. H. Thompson, *Physica*, To be published.

In these cases there are sharp minima in $-dx/dV$ at the unique compositions and broad maxima between the phase boundaries similar to the model discussed by Jacobsen *et al.* Such behavior may also be seen in Li_2TiS_2 at lower temperatures.

In conclusion, the comment by Jacobsen *et al.* presents some new, independent data supporting the electrochemical evidence that lithium ions form ordered arrays in Li_2TiS_2 . The details of the phase diagram remain uncertain but it is now clear that such ordering effects are common among the alkali metal intercalates of layered compounds. The model proposed in the comment would not appear to fit the LiTiS_2 results in detail but may be appropriate at lower temperatures.

Electrochromism in Anodic Iridium Oxide Films: II. pH Effects on Corrosion Stability and the Mechanism of Coloration and Bleaching

S. Gottesfeld and J. D. E. McIntyre (pp. 742-750, Vol. 126, No. 5)

D. N. Buckley³¹ and L. D. Burke³² Arising from the article of Gottesfeld and McIntyre, we would like to comment on a few aspects of anodic oxide films formed by potential cycling.

When we first reported³³ in 1975 that visible color changes could be reversibly induced in iridium oxide films by changing their potential, this behavior was thought to be unique among the noble metals. Indeed the growth of such thick films by potential cycling reported a few years earlier^{34,35} was also considered unique to iridium. More recent work³⁶ has shown, however, that similar films on rhodium also clearly exhibit visible color changes under the influence of potential. These films can be grown on rhodium in NaOH solutions under potential cycling conditions (0.01-1.55V (HE), 5 Hz, 25°-80°C). At suitable thicknesses, their color changes reversibly from pale yellow at lower potentials to dark green at higher potentials. A disadvantage of rhodium is the relatively high potential required for coloration, leading to some simultaneous oxygen evolution. However, although it is only slightly less expensive than iridium on a weight basis, films of rhodium require a smaller mass of metal than similar films of iridium because of its considerably lower density (55% that of iridium). Thus possible applications in electro-optical devices of the originally discovered iridium system suggest similar applications for the more recently reported rhodium system.

The paper under discussion strongly supports the originally suggested proton migration mechanism^{33,37,38} for color changes in iridium oxide films. There have been recent suggestions³⁹ that these changes involve not proton migration but electron transfer across the oxide-electrolyte interface. The species in the electrolyte which would be oxidized and reduced under such a mechanism have not been identified by the proponents of this theory and it is difficult to see how such oxidation/reduction could occur in the electrolytes in question. In any case the observations reported in the paper under discussion, in particular the kinetic effects of stirring and of buffering the electrolyte together with the observations in aprotic solvents, clearly demonstrate the involvement of protons and should effectively end this controversy.

We agree that, in practical applications, activation (i.e., film growth) would probably be most conveniently achieved by means of square waveforms. However, the reported rate of activation by 0.5 Hz square waves ($4.8 \times 10^{-2} \text{ mC cm}^{-2} \text{ sec}^{-1}$) is, in fact, slower than the rate observed by us³³ using 10 Hz triangular waves ($18 \times 10^{-2} \text{ mC cm}^{-2} \text{ sec}^{-1}$). It would be interesting therefore to observe the rate of activation by square waves of frequency higher than 0.5 Hz. In this connection it should be noted that at the current densities encountered at higher frequencies (as high as 1 A cm^{-2} for 10 Hz triangular waves and typical iridium oxide films) the relatively small (typically $\sim 0.1\text{-}0.5 \Omega$ for a 1 cm^2 electrode in $0.5M \text{ H}_2\text{SO}_4$) resistance between the working and reference electrodes can cause appreciable error in electrode potential. Thus, in the absence of automatic IR compensation, increasing frequency will cause the actual potential experienced by the electrode to become increasingly distorted from the nominal waveform so that results obtained with triangular and square waves are expected to become similar.

Finally, the effect³⁷ on the activation rate, of the maximum and minimum potentials of the waveform, confirmed in the paper under discussion, raises the question of the mechanism of film growth. Similar results have been obtained for rhodium.³⁶ This could be regarded as being in accord with classical passivation behavior so that periodic breakdown at lower potentials of a passive inner film is necessary for continued growth of the over-all film. A dissolution-precipitation mechanism suggests itself but we have so far found no evidence for this in the case of rhodium. Thus, details of the mechanism of film growth are not clear at this stage.

J. D. E. McIntyre⁴⁰ *Electrochromism.*—The phenomenon of electrochromism (EC) in hydrous Group VIII metal oxides has proven to be widespread.⁴¹ For example, thick oxide films of iridium, rhodium, and nickel can be grown by potential cycling and/or electrochemical or chemical precipitation. In contrast to WO_3 , these oxides are all colored by anodic transfer of an electron into the metal substrate coupled with cation ejection into, or anion injection from, the electrolyte in order to preserve electroneutrality. Following the report of EC in anodic rhodium oxide by Burke and O'Sullivan,⁴² Gottesfeld⁴³ investigated its characteristics for optical displays. Color changes from yellow to dark green or purple-brown were observed, depending on the amplitude of the cathodic pulse limit employed. McIntyre *et al.*^{44,45} have investigated the formation and electrochromic properties of nickel oxide.

Continuing studies of these hydrous Group VIII metal oxides have further extended our understanding of their complex electrochromic behavior. The experimental results⁴⁶ of Gottesfeld and McIntyre (GM) showed that coloration of anodic iridium oxide proceeds by a mechanism involving transfer of electrons into the metal substrate and transport of ions across the oxide-electrolyte interface. The excess positive charge generated in the lattice by oxidation of Ir^{3+} ions to Ir^{4+} could be compensated either by ejection of mobile cations or injection of mobile anions, just as for the electrolyte contained within the film pores.⁴⁶ No evidence was found in either aqueous or nonaqueous electrolytes for an electroneutralization mechanism proposed by Beni and Shay,^{47,48} which involved

³¹ Department of Materials Science and Engineering, University of Pennsylvania, Philadelphia, Pennsylvania 19104.

³² Department of Chemistry, University College, Cork, Ireland.

³³ D. N. Buckley and L. D. Burke, *J. Chem. Soc. Faraday Trans. I*, **71**, 1447 (1975).

³⁴ A. Capon and R. Parsons, *J. Electroanal. Chem. Interfacial Electrochem.*, **39**, 275 (1972).

³⁵ D. A. J. Rand and R. Woods, *ibid.*, **55**, 375 (1974).

³⁶ L. D. Burke and E. J. M. O'Sullivan, *ibid.*, **93**, 11 (1978).

³⁷ D. N. Buckley, L. D. Burke, and J. K. Mulcahy, *J. Chem. Soc. Faraday Trans. I*, **72**, 1896 (1976).

³⁸ S. Gottesfeld, J. D. E. McIntyre, G. Beni, and J. L. Shay, *Appl. Phys. Lett.*, **33**, 208 (1978).

³⁹ G. Beni and J. L. Shay, *ibid.*, **33**, 567 (1978).

⁴⁰ Bell Laboratories, Murray Hill, New Jersey 07974.

⁴¹ J. D. E. McIntyre, Paper 301 presented at The Electrochemical Society Meeting, Los Angeles, California, October 14-19, 1979.

⁴² L. D. Burke and E. J. M. O'Sullivan, *J. Electroanal. Chem. Interfacial Electrochem.*, **93**, 11 (1978).

⁴³ S. Gottesfeld, *This Journal*, in press.

⁴⁴ J. D. E. McIntyre, W. F. Peck, Jr., and G. P. Schwartz, Abstract D-4 presented at the Electronic Materials Conference, Boulder, Colorado, June, 1979.

⁴⁵ J. D. E. McIntyre and W. F. Peck, Jr., To be published.

⁴⁶ S. Gottesfeld and J. D. E. McIntyre, *This Journal*, **126**, 742 (1979).

transfer of electrons across the oxide-electrolyte interface from or to unknown donor or acceptor species in solution. In the acidic aqueous solutions investigated by GM, it was concluded⁴⁶ that the mobile ions responsible for electroneutralization were protons and that these species may migrate through the hydrous oxide by a Grotthus-type chain mechanism involving chemically bound or occluded water, possibly assisted by proton tunneling. Ejection of a proton from the lattice by such a mechanism is formally equivalent to OH⁻ injection, but the actual species transferred is, of course, H⁺.

The presence of bound water appears to be essential for fast coloration and bleaching of these films. Iridium and nickel oxide films formed by thermal oxidation of the metals are electrochemically inactive, as are thermally dehydrated anodic iridium oxide films. The latter films can also be deactivated by immersion in nonaqueous electrolytes containing dissolved hygroscopic ions (e.g., Li⁺), or solvent molecules (e.g., DMSO) which can strongly coordinate iridium metal ions (and also protons), replacing bound H₂O in the film.⁴¹ The porous anodic films can be rehydrated by cycling in aqueous electrolyte.⁴⁶ The mechanism of the electrochromic effect in anodic iridium oxide films thus differs significantly from that in WO₃, since "dry" evaporated films of this material are electrochemically active and electrochromic. Protons are apparently able to migrate into an amorphous WO₃ film without large amounts of water being present, possibly owing to the more open channel structure of this oxide. The latter is evidenced by the ability of WO₃ to accommodate the large cations K⁺, Rb⁺, Cs⁺, Tl⁺, and NH₄⁺.⁴⁹ However, the kinetics of the electrochromic reaction are improved by two to three orders of magnitude in anodic WO₃ films containing water.⁵⁰ Multicrystalline IrO₂ electrodes grown by a high temperature vapor-transport method also exhibit electrochemical redox behavior,⁵¹ the large currents observed probably indicating ion penetration into the solid. The latter material was not reported to be electrochromic, however.

It was also noted by GM,⁴⁶ that the channeled rutile-type structure of IrO₂ could facilitate injection of small foreign ions into its lattice. According to a rigid sphere model, the maximum radius of an ion which can be inserted into this structure is only ~0.65 Å. The only monovalent ions which satisfy this criterion are H⁺ and Li⁺ and these would require desolvation before injection. Anions such as F⁻ ($r = 1.36$ Å) and CN⁻ ($r \approx 1.9$ Å) are too large to be inserted into this type of lattice. Rice,⁵² however, has recently reported that electrochromism can be generated in anodic iridium oxide films by injection of these anions from nonaqueous electrolytes. This implies that the structure of the grains in these porous amorphous films is not rutile-like, unless only surface iridium ions are oxidized and reduced in nonaqueous electrolytes. Recent studies by McIntyre and Peck⁵³ have shown that in aqueous acid solutions all iridium ions in this oxide, whether surface or bulk, can undergo the electrochromic redox reaction, changing oxidation state from III to IV. Analysis of a deuterated oxide film in both colored and bleached states, utilizing the nuclear reaction ³He(d,p)⁴He to measure the total D content in each, revealed conclusively that D⁺ ions were ejected during coloration.⁵⁴ Simultaneous Rutherford backscattering measurements showed that the O

content remained virtually unchanged. These results appear to prove that an OD⁻ anion injection mechanism (non-Grotthus) was not operative in this case.

According to currently available evidence the coloration reaction in hydrous iridium oxide films can proceed by anodic removal of an electron coupled with charge neutralization by either cation ejection or anion injection. The mechanism that predominates will be determined by which ions have the highest mobility in the oxide lattice and/or which have the lowest desolvation energy. Further work is required to clarify the roles of the electrolyte and oxide structure, composition and solvation in the electrochromic reaction.

Film Growth.—In the experimental studies of anodic iridium oxide film growth by GM,^{55,46} no attempt was made to maximize the film growth rate. Square-wave potential cycles were employed to maximize the time spent by the electrode at the anodic and cathodic extremes and to grow the film at a convenient rate. Since the initial large current pulse in each half-cycle decays rapidly, it is probable that modulating frequencies higher than 0.5 Hz could be well employed. With large area electrodes, trapezoidal or sinusoidal potential waves can be used to avoid current-limiting or uncompensated resistance effects.

Electron microscopy studies⁵⁶ reveal clearly that the anodic iridium oxide film grows by a dissolution-precipitation mechanism to form a highly porous structure which has an average grain size of 0.05–0.1 μm and which, in addition to macrovoids, contains large numbers of microvoids ~25 Å in diam. Growth of the anodic oxide at higher cycling frequencies might produce a smaller grained film with faster coloration and bleaching times. However, corrosion and stability tests would be required to assess the suitability of such films for device applications.

In this connection, it should be noted that the stability data for anodic iridium oxide films formed by rapid square-wave cycling (0.5 Hz) in 0.5M H₂SO₄ and those grown by slow (100 mV sec⁻¹) linear potential sweeps may not be directly comparable. In the experimental studies of GM⁴⁶ the 0.5 Hz cycling frequency used in the stability tests caused the films to be exposed to 0.5M Na₂SO₄ (pH 3.5) electrolyte under dynamic corrosion conditions for >0.5 × 10⁶ cycles, a time ~20× longer than in the studies of Beni and Shay.^{47,48} The latter workers employed 0.5M H₂SO₄ electrolyte and a modulating frequency of 10 Hz for a similar number of cycles. The lengths of time spent by the electrode at the anodic and cathodic potential limits in each c-b cycle well may have a significant effect on the film corrosion rate and the degradation of bleaching times.

Care must also be exercised in interpreting the results of optical measurements alone in such tests. For normally incident light, interference effects cause the reflection contrast ratio, $CR = R_{\text{bleached}}/R_{\text{colored}}$, to saturate over the film thickness range 125–230 nm,⁵⁷ which is in the range of interest for electro-optic device applications. Such measurements must be combined with coulometry to show that improved color-bleach times resulting from chemical or heat-treatments are not simply due to film dissolution. By employing light incident at 45° to the surface and polarized parallel to the plane of incidence, this anomalous saturation effect can be avoided. At $\lambda = 546$ nm, the incident angle of 45° is very close to the Brewster angle of the hydrous oxide-electrolyte interface. Interference effects are therefore suppressed and under these conditions log CR is linearly proportional to both film thickness and absorption coefficient, i.e., the Beer-Lambert law is obeyed.

⁵⁵ S. Gottesfeld, J. D. E. McIntyre, G. Beni, and J. L. Shay, *Appl. Phys. Lett.*, **33**, 208 (1978).

⁵⁶ J. D. E. McIntyre, S. Nakahara, and W. F. Peck, Jr., To be published.

⁵⁷ J. D. E. McIntyre and W. F. Peck, Jr., Paper 302 presented at The Electrochemical Society Meeting, Los Angeles, California, October 14–19, 1979.

⁴⁷ G. Beni and J. L. Shay, *Appl. Phys. Lett.*, **33**, 567 (1978).

⁴⁸ J. L. Shay and G. Beni, Conference Report of 1978 Biennial Display Conference, Cherry Hill, New Jersey, October, 1978.

⁴⁹ P. G. Dickens, in "Solid State Chemistry of Energy Conversion and Storage," J. B. Goodenough and M. S. Whittingham, Editors, *Advances in Chemistry Series No. 163*, p. 165, American Chemical Society, Washington, D. C. (1977).

⁵⁰ B. Reichman and A. J. Bard, *This Journal*, **126**, 583 (1979).

⁵¹ J. Horkans and M. W. Shafer, *ibid.*, **124**, 1202 (1977).

⁵² C. E. Rice, Proceedings International Conference on Fast Ion Transport in Solids, Lake Geneva, Wisconsin, May, 1979.

⁵³ J. D. E. McIntyre and W. F. Peck, Jr., To be published.

⁵⁴ W. L. Brown, T. M. Buck, J. D. E. McIntyre, and W. F. Peck, Jr., To be published.



The Effect of Carbon, Zirconium, Niobium, and Titanium on the Oxidation Resistance of Chromium Stainless Steel

Taishi Moroishi, Hisao Fujikawa, and Hirobumi Makiura

Sumitomo Metal Industries, Limited, Central Research Laboratories, Amagasaki, Japan

ABSTRACT

The effects of C, Zr, Ti, and Nb on the oxidation resistance of 17% Cr steels have been investigated by means of isothermal heating and cyclic heating at temperatures up to 1000°C. It has been found that C has a detrimental effect on the oxidation resistance of 17% Cr steels. The oxidation behavior of steels containing Zr is different from that of steels containing Ti and Nb. Zr improves the oxidation resistance of 17% Cr steels to a great extent. Particularly, alloys containing Zr at a concentration which exceeds the stoichiometric equivalent of the total amount of C and N show excellent oxidation resistance up to 1000°C. Electron probe microanalysis shows the presence of a protective oxide layer consisting of Si-rich oxide at the metal-oxide interface, and no Zr is detected in the scales. With steels containing Ti and Nb, on the other hand, there is no protective Si-rich oxide, but Ti and Nb are detected in the scales. These scales are not protective. As the effective factors of excellent oxidation resistance of Cr steels containing Zr, the behavior of carbide, grain growth, and phase transformation have been investigated.

Many investigators have been concerned with the high temperature oxidation behavior and kinetics of Fe-Cr alloys (1). Seybolt found that Cr_2O_3 is formed in the scale by oxidizing Fe alloys containing more than 13% chromium (2). Coplan and Cohen and others have reported that Fe alloys containing more than 16-20% chromium show excellent oxidation resistance (3).

The allowable oxidation temperature of commercial 17% chromium steel (AISI 430 steel) is about 800°C. It is well known that increasing the chromium content and adding elements such as silicon, aluminum, and rare earth metals will greatly improve the oxidation resistance of 17% chromium steel (4-7). However, these methods involve addition of a large amount of the effective elements. Moreover these alloys have many problems in production, formability, weldability, etc., so they are scarcely used.

It is inevitable that 17% chromium steels contain various added elements and impurities. It is important to study the effects of these elements. The effect of carbon has been reported for carbon steels, low alloy steels, Fe-Al alloys, and Ni-Cr austenitic steels (1, 8). It has been reported that carbon in steels changes into CO and breaks the oxide film. It is surprising that there are so few reports about the effect of carbon on the oxidation resistance of commercial 17% chromium steels. 17% chromium steels partially transform the austenitic structure by increasing carbon content above 800°C (9). Therefore, it is important to study how structure affects high temperature oxidation.

First, the present authors have investigated the effect of carbon on the oxidation resistance of 17%

chromium steels. In the results, it was found that carbon is extremely detrimental to high temperature oxidation. For improving the oxidation resistance of 17% chromium steels, it would seem necessary to remove the detrimental effect of carbon.

Chromium steels with extra low carbon contents have no practical use, because their toughness is lowered due to the increasing coarseness of grain which occurs at temperatures above 800°C. Therefore, the effect of the addition of zirconium, titanium, and niobium which have a strong affinity for carbon and nitrogen, and also form carbide and nitride, have been investigated. Wright and others had studied the oxidation resistance of 16% Cr-Fe alloy containing 0.05% zirconium at 1100° and 1200°C and reported only a slight effect of zirconium (6). The present authors have systematically investigated the oxidation resistance of 17% chromium steels containing up to 1% zirconium, and it was found that at this concentration zirconium is an extremely beneficial element (10).

Comstock studied the effect of titanium to see whether this element could be used to prevent break-away behavior during oxidation of chromium steels (11).

In the present paper, the effect of zirconium is compared with that of titanium and niobium. Zirconium, found to be the most beneficial element, was investigated thoroughly in relation to carbon and nitrogen. Also, the long-term high temperature oxidation resistance of chromium steels containing zirconium was studied.

It was found that chromium steels containing zirconium are superior to AISI 430 and 304 steels in

Key words: oxide scale, grain size, ferrite, nitride, carbide.

oxidation resistance. Chromium steels containing zirconium have already been used commercially.

Specimen Preparation

Thirty-five test alloys were produced by melting electrolytic iron and the required amounts of additives in a 17 kg vacuum induction furnace and a 50 kg air induction furnace. These ingots were made of 3.2 mm thick plates by forging and hot-rolling. After sheets of 1.2 mm in thickness were made by cold-rolling, the sheets were heat-treated and pickled in acid. Various kinds of samples were produced from these sheets. They were used in various tests after polishing with emery paper No. 320, degreasing, and washing in acetone-alcohol.

The chemical compositions of alloys are shown in Table I. Commercially produced materials were used in the case of 430 Zr, AISI 430, and 304 steels.

Experiment

The samples of 20 mm in width, 25 mm in length, and 1.2 mm in thickness were used in isothermal oxidation tests at 825°-1000°C for 100 and 250 hr. The degree of oxidation resistance was measured by the weight gain. Oxide scales were collected in an Al_2O_3 crucible covered with a lid to prevent the scattering of scales while cooling.

In the case of long-term oxidation tests at 800° to 900°C for 1000 hr it was usually impossible to collect oxide scales and only weight change was measured. However, for AISI 304 and 430 steels, oxide scales could be collected. Alloys of the types considered are often used for automobile exhausts.

Because the automobile exhaust is usually heated cyclically, cyclic heating tests were done on our alloys by 30 min heating-cooling cycles. These experiments were done at 1000°C for 500 cycles and at 800°-900°C for 1000 or 2000 cycles. Because it is impossible to gather oxide scales in cyclic heating tests, the results were shown by the amount of weight change. We found the amount of scaling off of ferritic stainless steels to be slight and the amount of weight change to be nearly equal to the amount of weight gain.

Table I. Chemical composition of alloys (w/o)

Alloy	C	Si	Mn	Cr	Zr	N	Zr/ (C + N)
1	0.004	0.56	0.53	18.88	—	0.003	0
2	0.004	0.59	0.53	18.72	0.14	0.011	9.33
3	0.002	0.56	0.53	18.71	0.13	0.003	26.0
4	0.005	0.55	0.53	18.89	0.32	0.003	40.0
5	0.005	0.54	0.53	18.51	0.91	0.003	113.75
6	0.010	0.56	0.54	18.61	—	0.005	0
7	0.009	0.61	0.54	18.64	0.13	0.004	10.0
8	0.011	0.56	0.54	18.82	0.29	0.004	19.33
9	0.006	0.55	0.53	18.62	0.49	0.003	54.44
10	0.011	0.57	0.53	18.75	0.90	0.004	60.0
11	0.011	0.46	0.49	16.71	—	0.014	0
12	0.016	0.49	0.46	17.01	0.10	0.018	2.94
13	0.013	0.47	0.45	16.81	0.21	0.016	7.24
14	0.011	0.49	0.46	17.07	0.32	0.011	14.55
15	0.010	0.48	0.45	16.38	0.54	0.012	24.55
16	0.029	0.56	0.52	17.06	—	0.028	0
17	0.033	0.51	0.47	16.50	0.24	0.027	4.0
18	0.032	0.49	0.50	16.89	0.28	0.020	5.38
19	0.031	0.54	0.51	16.61	0.39	0.017	8.03
20	0.030	0.54	0.52	16.80	0.62	0.016	13.48
21	0.033	0.47	0.48	16.21	0.96	0.008	23.41
22	0.047	0.48	0.48	16.97	—	0.068	0
23	0.043	0.50	0.48	17.49	0.08	0.076	0.67
24	0.051	0.47	0.45	16.89	0.33	0.012	5.24
25	0.056	0.46	0.45	16.63	0.53	0.010	8.03
26	0.043	0.51	0.47	16.61	0.73	0.014	12.81
27	0.019	0.53	0.46	17.57	0.21*	0.008	7.78
28	0.025	0.53	0.46	17.54	0.43*	0.006	13.87
29	0.025	0.53	0.45	17.38	0.64*	0.005	21.33
30	0.037	0.46	0.46	17.12	0.23†	0.008	5.11
31	0.037	0.45	0.45	16.97	0.47	0.007	10.68
32	0.034	0.42	0.43	17.02	0.67	0.006	16.75
AISI 430	0.055	0.61	0.53	16.43	—	0.019	—
AISI 304	0.031	0.83	0.59	19.08	10.40‡	—	—
430 Zr	0.018	0.41	0.51	16.58	0.38	0.010	13.57

* Ti,
† Nb,
‡ Nd.

The oxidation behavior of steels containing Zr, Ti, and Nb at 1000°C for 24 hr was determined with the differential thermobalance.

The structures of oxide scale were shown with the optical microscope, x-ray diffraction, and electron probe microanalysis.

Grain sizes and amount of carbonitride precipitates of test alloys were determined.

Experimental Results

Effect of carbon.—First, the effect of C on oxidation resistance has been studied in detail.

Figure 1 shows the weight increase in isothermal oxidation of Cr steels containing 0.01-0.05% C at 825°-1000°C after 250 hr. In all steels, the weight gain abruptly increases above 900°C. Increasing C content increases the weight gain. However, it is difficult to recognize differences in weight gain due to different C contents at less than 875°C because here the weight gain is small.

Figure 2 shows the effect of C on cyclic oxidation at 1000°C for 500 cycles. Increasing the C content in steels linearly increases the weight gain.

It is clear that C has a detrimental effect on the oxidation resistance of 17% Cr steels. In the case of Cr steels containing more than 0.03% C, the amount of weight gain greatly increases, and also the samples expand and transform.

It has been suggested that C may gasify and break the scale in carbon steels. In 17% Cr steels, Cr_2O_3 is formed on the alloy surface. Because CO cannot be produced at partial pressure of oxygen at the metal-oxide interface, it is difficult to accept the above theory. Therefore, it may be more valid to rely on structure changes to determine the oxidation resistance.

Figure 3 shows phase boundary α , $\alpha + \gamma$ in the Fe-Cr (9). The amount of the austenitic phase (γ) increases with the amount of C and N. In the austenitic structure, the diffusion rates of elements are much lower and the thermal expansion coefficient is larger than in the ferritic (α) structure. By increasing the fraction present in the austenitic structure, the diffusion rates of Cr and Si toward the alloy surface become slower (12-14). The diffusion of these effective

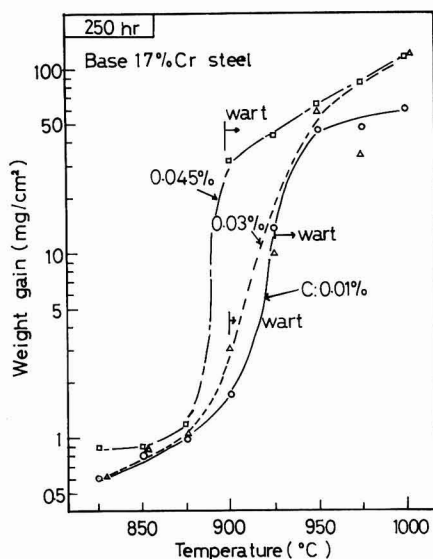


Fig. 1. Weight gain of 17Cr steels with various amounts of carbon after 250 hr at 850°-1000°C. (Wart: abnormal oxidation.)

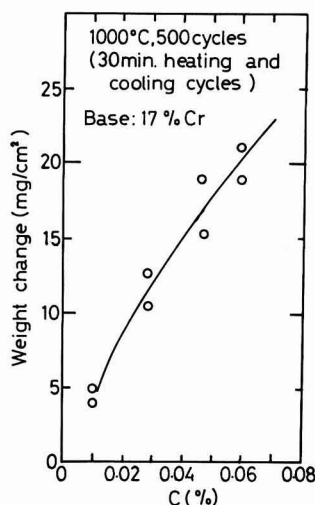


Fig. 2. Effect of C content on oxidation resistance of 17Cr steels at 1000°C for 500 thermal cycles.

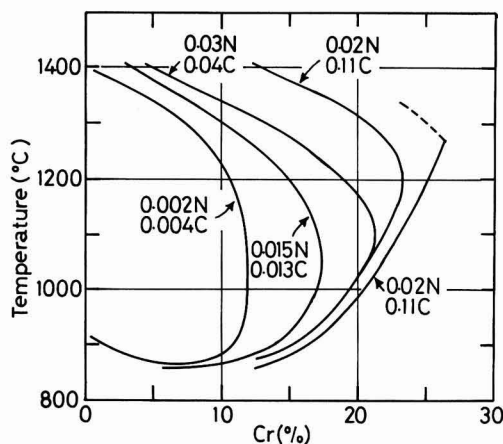


Fig. 3. Effect of C and N content on the $\alpha/(\alpha + \gamma)$ boundary in the Fe-Cr system.

elements toward the surface becomes insufficient, thermal strain arising from the different thermal expansion breaks (15) the oxide scale, and then the diffusion of Fe is accelerated. The above results are explained in detail later.

It is found from Fig. 2 that steels containing extra low C and N are resistant to oxidation to a certain degree. If these steels are used as heat-resistant materials, the deterioration of the toughness due to the coarseness of grain at more than 800°C causes problems which make it difficult to use these steels. Therefore, it may be preferable to fix C and N with Zr, Ti, or Nb.

Effect of zirconium.—Figure 4 shows the effects of Zr, Ti, and Nb on the isothermal heating resistance at 1000°C for 100 hr. We already reported that the oxidation resistance of 17% Cr steels is improved by increasing the Zr content. The behavior in Fig. 4 is in accordance with the oxidation behavior which was examined with the thermobalance at 1000°C, as shown in Fig. 5. All alloys used contain about 0.03% C. Steel

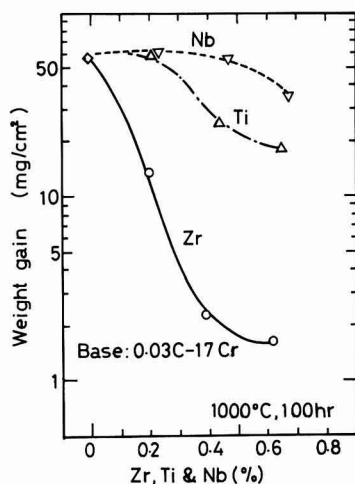


Fig. 4. Effect of Zr, Ti, and Nb content on weight gain of 17Cr steels at 1000°C after 100 hr.

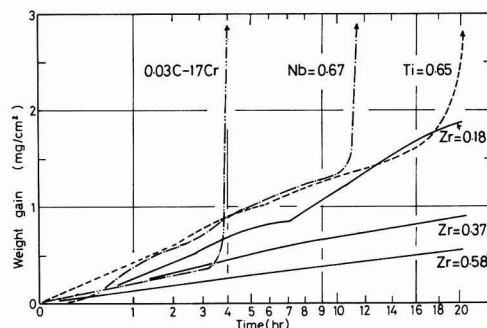


Fig. 5. Weight gain as function of time for 17Cr steels with different amount of Zr, Ti, and Nb at 1000°C in air.

containing no Zr shows abnormal oxidation within a short period, abruptly increasing weight gain. Alloying Zr eliminates the abnormal oxidation and improves the oxidation resistance of 17% Cr steels to a great extent. The oxidation behavior of 17% Cr steels containing Zr obeys one parabolic law up to 1000°C.

Figure 6 shows changes of the allowable oxidation temperature of 17% Cr steels with Zr/(C+N) ratio, resulting from the fact that Zr has a strong affinity for C and N. The steel containing no Zr, causes abnormal oxidation and greatly increases its weight at temperature above 900°C. The alloys in which Zr/(C+N) ratios are 4.5 and 5.5 show a strong increase of weight gain in the temperature range 925°–950°C. The alloys containing Zr, in a concentration which exceeds the stoichiometric equivalent of the total amount of C and N in the steels (i.e., alloys in which Zr/(C+N) ratio is more than 8.1), show excellent oxidation resistance up to 1000°C and are covered with a fine protective oxide scale. The above facts suggest that fixing C and N with Zr is very effective for oxidation resistance.

Figure 7 shows the effect of the Zr/(C+N) ratio on the cyclic oxidation of steels containing 0.01, 0.03, and 0.05% C at 1000°C, the same effect of Zr is expected in cyclic heating. Figure 7 and Fig. 6 show that all C contents increasing Zr/(C+N) ratio in

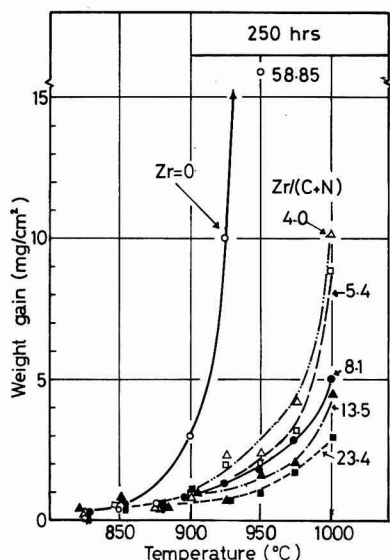


Fig. 6. Weight gain as $F(t)$ for 17Cr steels with different $Zr/(C+N)$ ratios.

steels is very effective for increasing resistance to oxidation after cyclic heating.

Therefore, an excellent oxidation resistant steel is obtained by incorporation of Zr, at a concentration which exceeds the stoichiometric equivalent of the total amount of C and N.

The effect of Zr is greater in steels containing a large amount of C. Alloying Zr at a concentration exceeding its stoichiometric equivalent gives the same degree of oxidation resistance in steels at all levels of C to prevent abnormal oxidation. The excellent oxidation resistance is due to coverage of the alloy surface with a fine protective oxide scale.

Effect of titanium.—As shown in Fig. 4, if 17% Cr steel contains a small amount of Ti (less than 0.3%), the oxidation resistance of the steel is slightly lowered, while steel containing a large amount of Ti (more than 0.5%) has good oxidation resistance. However, the effect of Ti is smaller than that of Zr. The oxidation behavior of steel containing 0.64% Ti studied through weight gain determined with a thermobalance is shown in Fig. 5. Incorporation of 0.64% Ti delays the occurrence of abnormal oxidation, but abnormal oxidation is not completely suppressed and oxidation of this alloy does not obey a parabolic law.

Ti, as well as Zr, fixes C and N, but the affinity of Ti with C and N is slightly weaker than that of Zr. Therefore, the effect of Ti on oxidation resistance at 1000°C is weaker than that of Zr. Also Ti is more mobile in steel than Zr, because the atomic size of Ti is smaller than that of Zr. The size difference also makes us expect that Ti affects the structure of the oxide scale. The results of observations of the oxide scale are explained later.

Effect of niobium.—It might be expected that Nb has a similar effect as Ti or Zr, because of fixing C and N. However, the effect of Nb on oxidation resistance at 1000°C is much weaker than that of Zr and Ti, as shown in Fig. 4. The oxidation behavior of steels containing Nb is clearly different from that of steels containing Zr and resembles that of steels containing Ti. Alloying a small amount of Nb in the steels (less than 0.5%) causes a lowering of the oxidation resistance. If a large amount of Nb (more than

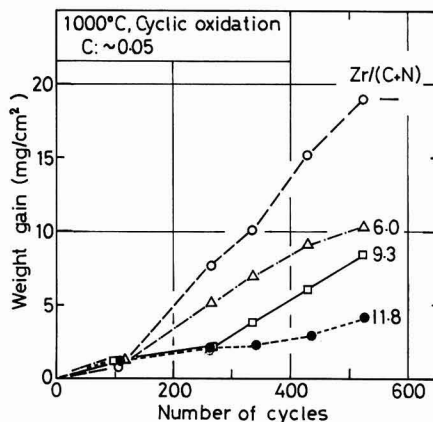
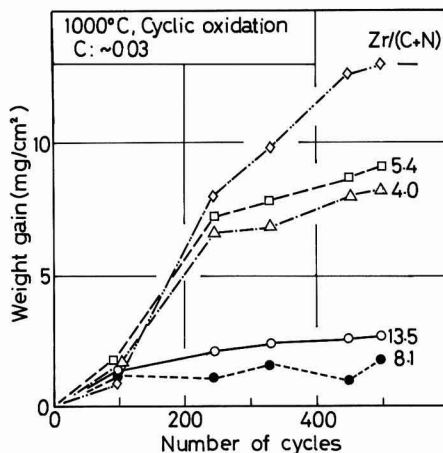
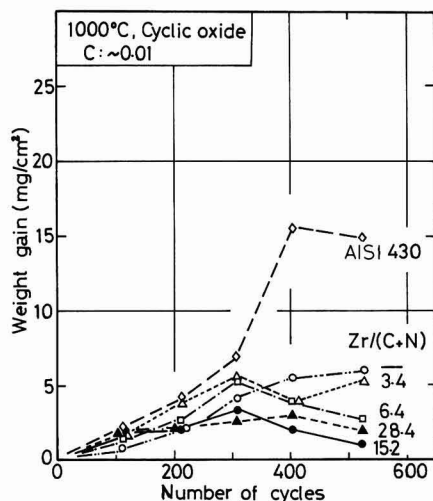


Fig. 7. Effect of $Zr/(C+N)$ ratio on cyclic oxidation resistance of 17Cr steels containing various amounts of carbon. a (top) = $\sim 0.01\%$, b (center) = $\sim 0.03\%$, c (bottom) = $\sim 0.05\%$.

0.6%) is alloyed, the oxidation resistance is slightly improved. Steel containing 0.67% Nb causes abnormal oxidation sooner than steel containing 0.64% Ti (Fig. 5), and its oxidation behavior does not obey a parabolic law.

The long-term oxidation resistance of Cr steel which contains Zr.—In order to investigate whether the oxidation resistance of steel containing Zr is lowered by heating at high temperatures for a long period, the alloys used were isothermally heated at 800°–900°C for 1000 hr, as shown in Fig. 8.

In all oxidation tests, steel containing Zr is uniformly covered with thin oxide scale and shows excellent oxidation resistance. On the other hand, AISI 430 steel shows abnormal oxidation and large weight gains in severe oxidation tests at more than 850°C for 1000 hr; steel containing Ti shows abnormal oxidation at 900°C for 1000 hr, AISI 304 steel has poor oxidation resistance in all oxidation tests, because the oxide scale peels off.

Figure 9 shows the results of cyclic heating tests at 800°–900°C for 1000 or 2000 cycles and at 1000°C for 500 cycles. Steel containing Zr shows the best oxidation resistance of all steels used. AISI 430 steel shows a large weight increase at $T > 900^\circ\text{C}$, and AISI 304 steel shows a very high rate of peeling off of the scale at $T > 800^\circ\text{C}$. These results also agree with Fig. 10.

The oxide scale structure.—The structure of oxide scale formed in several oxidation tests was studied by observation with the optical microscope, by x-ray diffraction, and by analysis with the EPMA. Figure 11 shows the cross section of the oxide scale formed on steel containing Zr. The oxide scale adheres uniformly and tightly. No inner oxidation occurs on this steel. Oxides in steel containing Ti or Nb have an extremely high rate of peeling off and are covered with a porous, thick oxide scale.

Second, the oxide scale was analyzed with the x-ray diffraction technique, as shown in Table II. It was

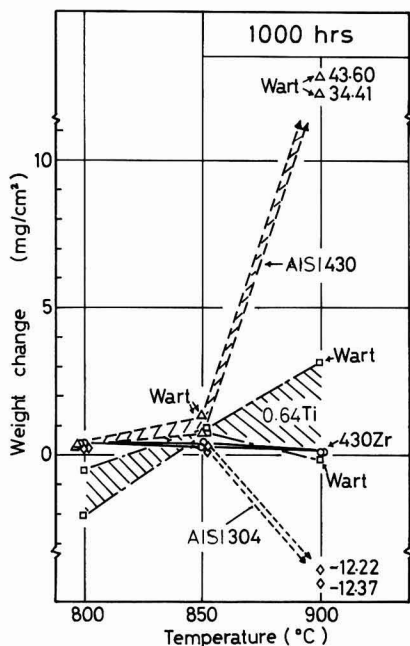


Fig. 8. Long-term oxidation resistance of 430 Zr steel at 800°–900°C.

observed that all steels involved form both the corundum type and the spinel type of oxides when heated to the oxidation condition as in the above test. On steel containing Ti, TiO_2 is formed, besides the corundum-type and the spinel-type oxides. However, Zr oxide is not detected in the oxide scale formed on the steel containing Zr. It seems obvious that the difference in oxidation resistance is directly related to the difference in structure of formed oxides.

Figure 12 shows the EPMA image analysis of the oxide scales of the various steels. In the steel containing Zr, the outer oxide layer consists of the oxides of Mn and Cr. Mn is found particularly in the outermost layer. Si concentrates uniformly at the metal-oxide interface; Fe is scarcely detected in any oxide of the layers. Excess Zr is observed as Zr oxide particles beneath the alloy surface. This phenomenon is notably found at 1000°C but the oxide structure at 1000°C is essentially similar to that at 900°C. These results agree fairly well with those of the micro-analyzer line analysis in Fig. 13.

The latter shows that the oxide scale has three layers. The outermost layer is rich in Mn and Cr and contains a slight amount of Fe. The second layer is rich in Cr and contains Si. The innermost layer consists of Si-rich oxide which contains Cr. Furthermore, Zr oxide particles are found at a small distance from the metal-oxide interface.

In the steel containing Ti, a large amount of Ti is found in the oxide scale, probably because it diffuses rapidly in the steel. In steel containing Ti, the oxide scale has four layers. The outermost layer is rich in Fe, Ti, and Mn. The second layer is rich in Cr. The third layer is rich in Cr, Si, and Ti and in the innermost layer Ti can be detected. Ti oxide particles are detected just beneath the metal-oxide interface. Unlike Zr, Ti is present in oxide scale and the amount of Si in the oxide scale is very small. Also, the outermost oxide scale is thick and porous, causing it to easily peel off.

Ti has a stronger affinity for oxygen than Si, and therefore the scale in steel containing Ti has hardly any Si oxide in the inner layer. The steel has to contain a large amount of Ti to keep good oxidation resistance. It is likely that abnormal oxidation observed in the experiments resulted from the fact that the steels contained only a small amount of Ti (less than 0.64%).

Nb diffuses more slowly in steel and has a weaker affinity for oxygen than Ti. Nb is found in diluted form in the oxide scale. Therefore, the oxide scale of steel containing Nb is similar to that of AISI 430 steel, except for the fact that steel containing Nb produces Nb oxide.

In steel containing Nb, as well as in steel containing Ti, the oxide scale is thick and porous, peeling off easily. The oxide scale has three layers. The outermost layer is rich in Fe, Mn, and Nb. The second layer is rich in Cr and in the innermost layer Cr and Si are detected. Also, Nb oxide particles, as well as Zr oxide particles, are detected a small distance from the metal-oxide interface.

The oxide scale on AISI 430 steel has four layers. The outermost layer is rich in Fe and Mn. The second layer is rich in Fe, Mn, Cr, and Si. The third layer is rich in Cr, Mn, Si, and Fe, and in the innermost layer Cr, Si, Mn, and Fe are detected.

Changes of carbonitrides and hardness by heating.—In the case of alloying Zr which is the most effective element for increasing oxidation resistance, the change in the amount of carbides and nitrides and the change in the hardness of the steels were investigated by heating at high temperatures for 15 min. The results are shown in Fig. 14. X-ray diffraction shows that precipitates present in steel containing Zr are Zr(C, N) and in AISI 430 steel are M_{23}C_6 . In steel containing

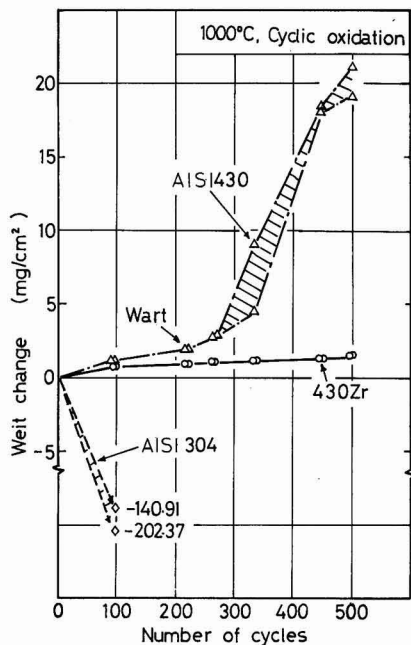
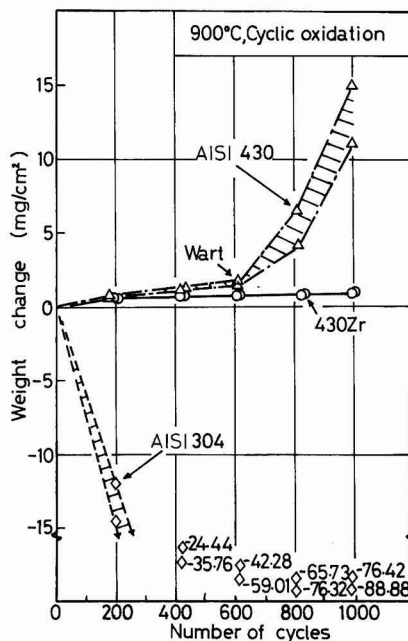
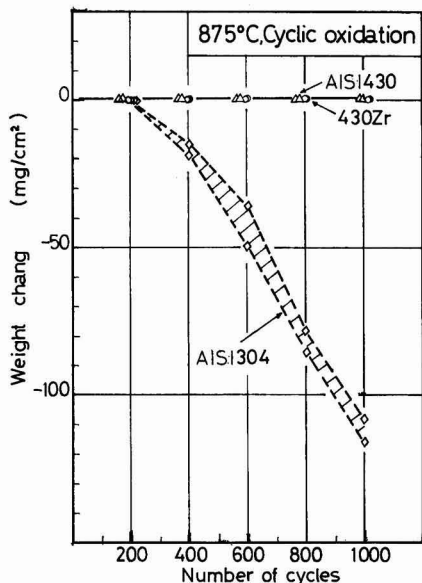
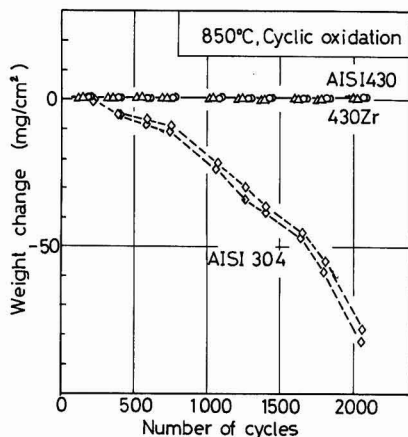
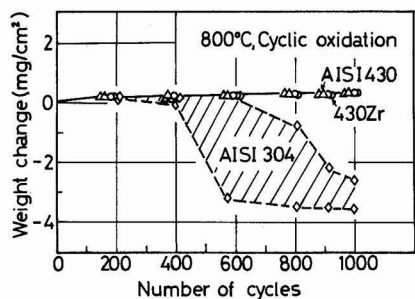


Fig. 9. a (top left) Cyclic oxidation resistance of 430 Zr steel at various temperatures. a (top left) = 800°C, b (top right) = 850°C, c (center left) = 875°C, d (lower right) = 900°C, e (bottom left) = 1000°C.










800°C 1000 cycles	 430Zr	 AISI 430	 AISI 304
900°C 1000 cycles	 430Zr	 AISI 430	 AISI 304
1000°C 500 cycles	 430Zr	 AISI 430	 AISI 304

Fig. 10. Appearance of 430 Zr steels after cyclic oxidation

Zr, the amount of precipitates is in agreement with the amount of the carbonitrides expected from the amount of C and N. Apparently Zr fixes C and N completely. In AISI 430 steel, $M_{23}C_6$ dissolves above 900°C.

From the results of hardness measurements, steel containing Zr shows single structure, but AISI 430 steel shows the precipitation of martensite due to a partially austenitic transformation.

Furthermore, the stable Zr precipitates prevent grain growth in the steel when it is heated up to 1000°C (Fig. 15).

Discussion

The above results clearly demonstrate the effects of C, Zr, Ti, and Nb. Evidently C is very harmful to oxidation resistance, and the oxidation resistance

caused by Zr, Ti, and Nb, respectively, decreases in the sequence

$$\text{Zr} \gg \text{Ti} > \text{Nb}$$

It is explained below how these elements behave during heating at high temperature.

As seen in Fig. 5, the oxidation behavior of alloys used is similar until abnormal oxidation occurs, therefore it can be suggested that the oxides formed in the early stage are almost the same. However, the steels containing no Zr show abnormal oxidation in the next stage, while steels containing Zr show no abnormal oxidation. It is recognized that one of the most important factors that cause the above difference is the behavior of C during heating at high temperatures. On steel containing Zr, C couples with Zr. In the absence of Zr, C is dissolved or almost dissolved by heating at high temperatures. Therefore, the steels containing no Zr transform ($\alpha + \gamma$) two-phase structures at 1000°C, while the steel containing Zr consists of a single phase α structure, because Zr fixes C and N. The diffusion rate of Cr in the austenitic structure is very much slower than in the ferritic structure (Table III) (12-14). Therefore, the Cr concentration of the surface is lower in the austenitic phase.

From the observations of the oxide scale, it is evident that there is a large difference between the high temperature behavior of Zr, Ti, and Nb. Figure 16 shows schematically the oxide scale formed on steels containing Zr, Ti, and Nb and AISI 430 steel. On the presence of Zr, Zr carbides and nitrides are formed which are stable in the steel up to 1000°C, also, oxygen which diffuses into the steel is fixed by the excess Zr content. So the diffusion of Cr and Si toward the surface is accelerated and a protective oxide scale composed of these elements is formed on the surface.

At high temperatures, Ti or Nb carbides are almost dissolved near the metal surface. Ti can diffuse rapidly toward the surface of the steel, and it is found in the oxide scale. Furthermore, Ti has a stronger affinity for oxygen than Si, so it is difficult for Si

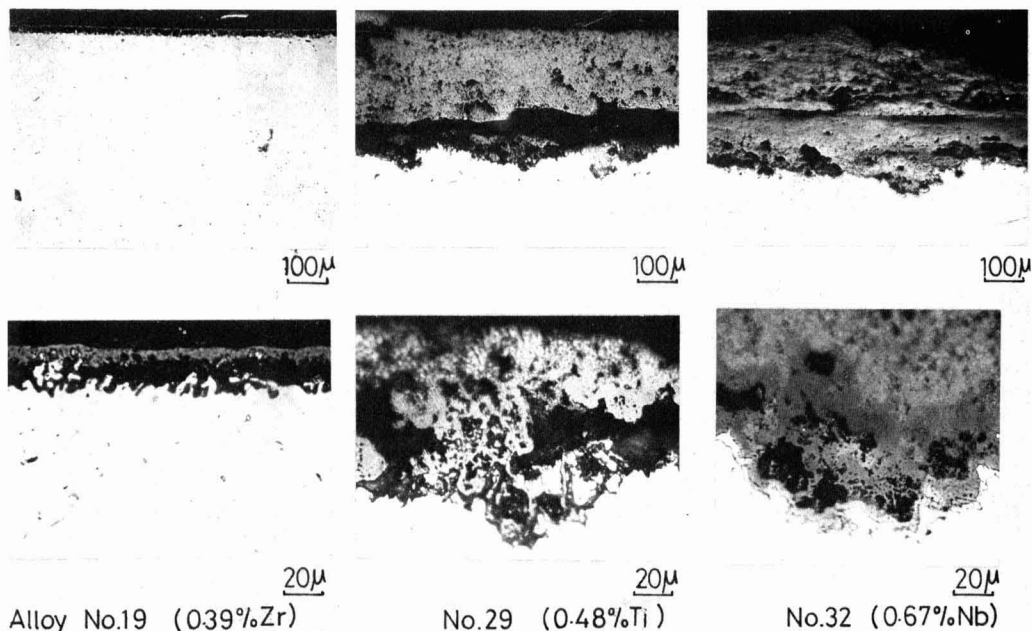
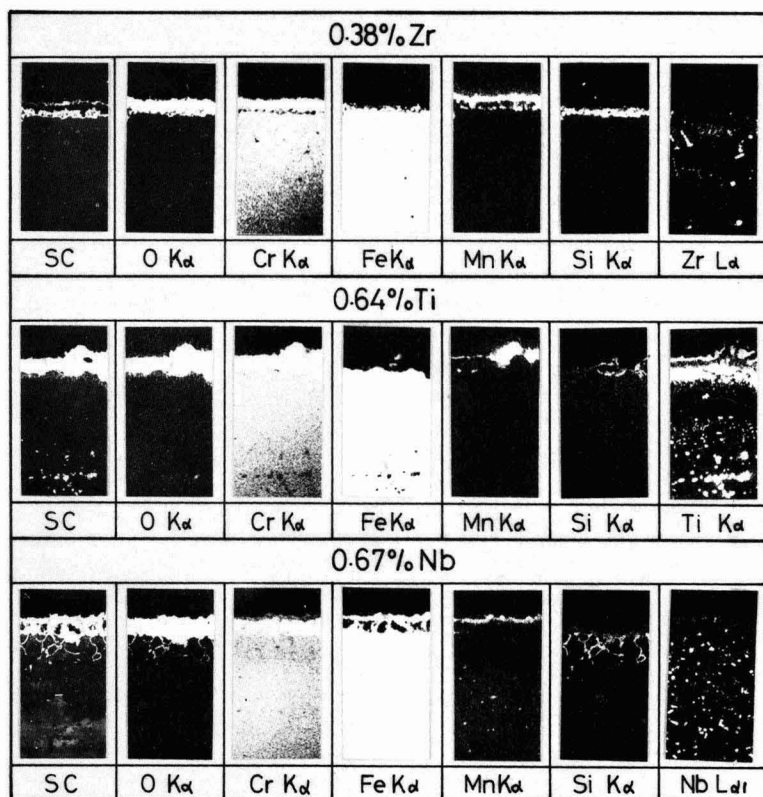


Fig. 11. Cross sections of oxide scales of 17Cr steels containing Zr, Ti, and Nb at 1000°C for 250 hr.

Fig. 12a. EPMA image analysis of oxide scale formed on 17Cr steels containing Zr, Ti, and Nb heated at 1000°C for 250 hr.



oxide to be formed. However, in order to get the oxidation resistant steel by alloying Ti, a large amount of Ti (perhaps, about 1%) must be added to the steel. This steel would have no practical use.

Nb is similar in behavior to Ti, but the effect of Nb on oxidation resistance is lower than that of Ti, the diffusion rate of Nb being slow, because of its large atomic size. Therefore, Nb has a poorer effect than Ti.

Therefore, Zr-containing steel causes no abnormal oxidation at 1000°C during a long period, while the oxide scale on steel containing Ti or Nb or AISI 430 steel is broken due to the precipitation of austenitic structure and then causes abnormal oxidation after an incubation period. Once abnormal oxidation occurs, the protective resistance of the scale is lost and abnormal oxidation is at an accelerated rate.

Ti and Nb, as well as Zr, are ferrite formers. Alloying a large amount of Ti and Nb controls the precipitation of austenitic structure. Also, the volume

ratio in which the carbides are stable becomes very large. If the steels contain a large amount of Ti or Nb, the decomposition of the carbides is to a certain degree controlled. These steels are resistant to oxidation, but they are not used in practice.

Conclusion

C has a harmful effect on the oxidation resistance of 17% Cr steels, and it was investigated whether this harmful effect could be eliminated by alloying with Zr, Ti, and Nb which may be expected to fix C and N by compound formation. This proved indeed the case, the effect of Zr being more beneficial than that of Ti and Nb. The difference in those effects results from the stability of carbonitrides at the high temperature and depend on whether the steels have a single structure (α) or a two-phase ($\alpha + \gamma$) structure. Zr-containing steel forms uniformly a protective Si-rich oxide in the inner, and Cr-rich oxide in the outer oxide layer. These oxides prevent the oxida-

Table II. X-ray diffraction analysis of oxide scales

Alloys	0.38% Zr				0.64% Ti				0.67% Nb				AISI 430			
	900 Time, hr		1000 100		900 1000		1000 100		900 1000		1000 100		900 1000		1000 50	
Scale layer	O*	I**	O	I	O	I	O	I	O	I	O	I	O	I	O	I
Spinel type†	ss	w	s	s	s	—	s	w	—	—	w	—	w	w	—	ss
Corundum type	ms	—	ms	—	m	—	m	w	—	—	ss	—	s	s	s	mw
TiO ₂	—	—	—	—	—	w	—	—	—	—	—	—	—	—	—	—
α -Fe	ss	ss	s	ss	—	ss	—	s	—	—	—	—	—	—	—	—

* O, outer layer.

** I, inner layer.

† ss > s > ms > m > w > mw > ww.

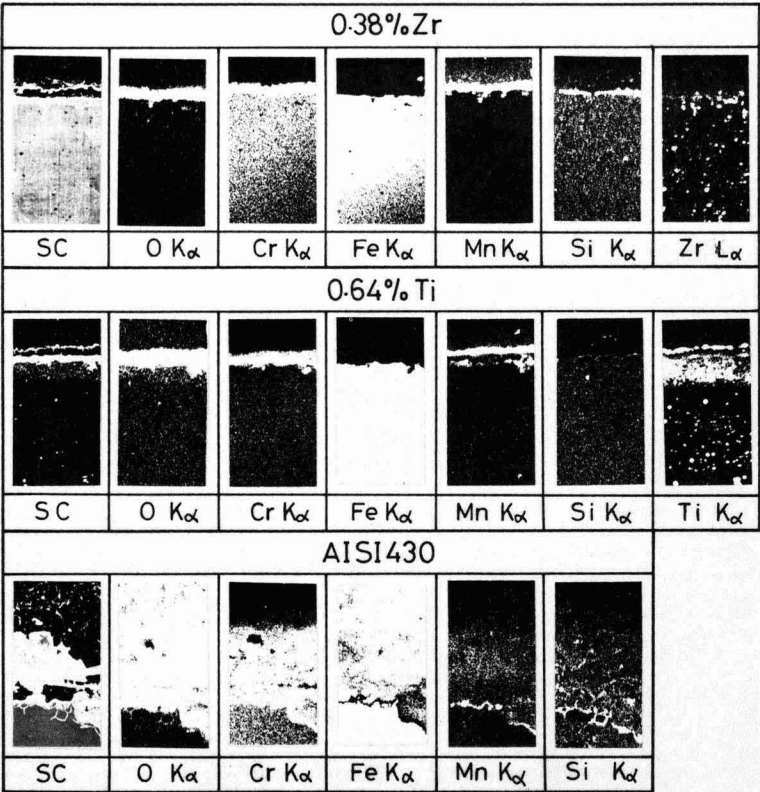


Fig. 12b. EPMA image analysis of oxide scales formed on 17Cr steel containing Zr, Ti, and AISI 430 steel heated at 900°C for 1000 hr.

tion of Fe. Therefore, this alloy shows excellent oxidation resistance up to 1000°C.

The carbides are unstable in Ti- or Nb-containing steels and Ti or Nb are found in the oxide scale.

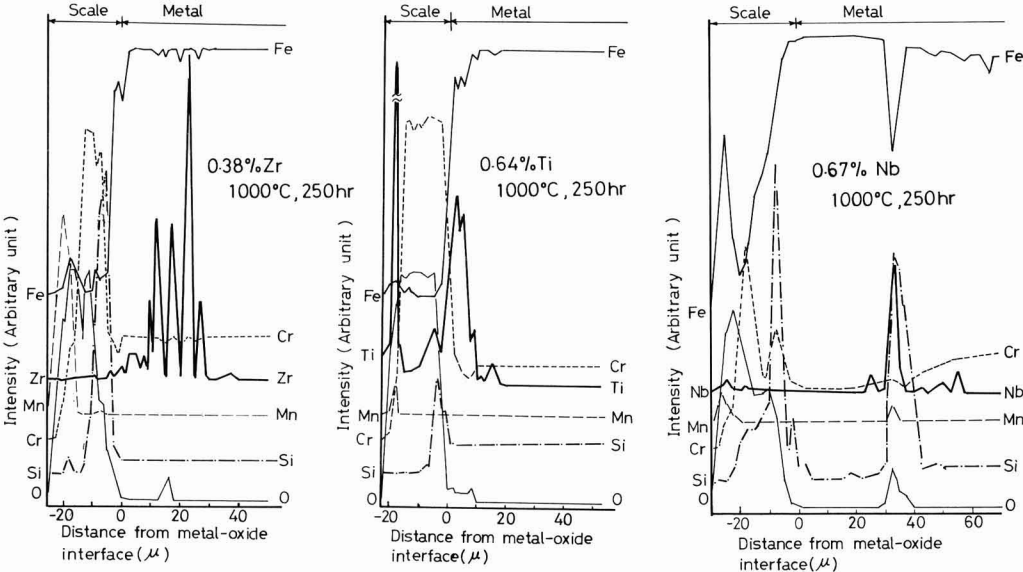


Fig. 13. EPMA line analysis of oxide scale formed on 17Cr steels containing Zr, Ti, and Nb heated at 1000°C for 250 hr.

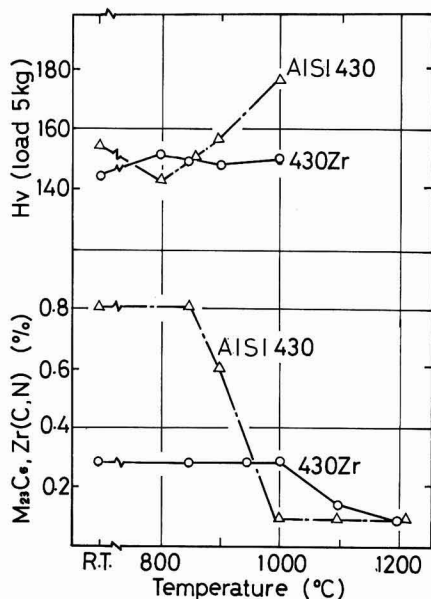


Fig. 14. Changes of the amount of carbides and nitrides and hardness of the steels by heating for 15 min at various temperatures.

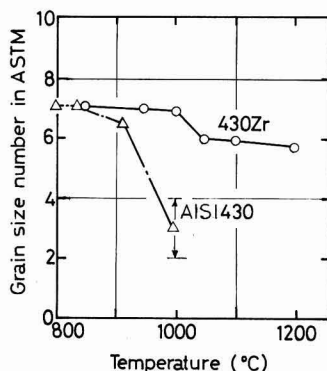


Fig. 15. Grain size changes by heating for 15 min

Particularly steel containing Ti has a large amount of Ti oxide in the scale. Steel containing Zr has no Zr in the oxide scale.

Table III. Self-diffusion rates in ferritic Fe-Cr and austenitic Fe-Cr-Ni alloys

Alloy	Structure	Element diffusing	D at 1000°C (cm ² · sec ⁻¹)	Reference
Fe-25Cr	α	Cr	8.67×10^{-10}	(12)
Fe-49Cr	α	Cr	4.60×10^{-11}	(12)
Fe-18Cr-8Ni	γ	Cr	8.42×10^{-12}	(13)
Fe-17Cr-12Ni	γ	Cr	2.25×10^{-12}	(14)

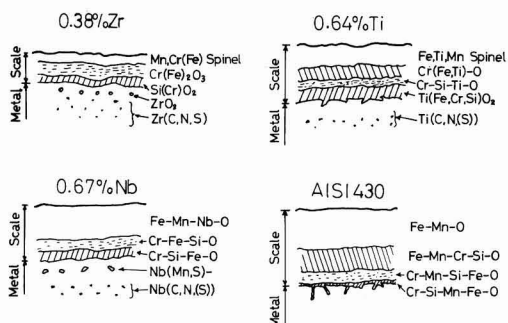


Fig. 16. Schematic models of oxide scale formed on 17Cr steels containing Zr, Ti, Nb, and AISI 430 steels heated at 1000°C.

The alloy containing Zr, at a concentration which exceeds the stoichiometric equivalent of the total C and N in the steel, shows excellent oxidation resistance up to 1000°C. Because Zr carbonitrides are stable in the steel at 1000°C, Zr carbonitrides prevent the grain growth and keep the single phase (α) structure. Therefore, preservation of the protective oxide scale structure contributes to the improvement of oxidation resistance.

Manuscript submitted Oct. 10, 1978; revised manuscript received May 21, 1979. This was Paper 13 presented at the Seattle, Washington, Meeting of the Society, May 21-26, 1978.

Any discussion of this paper will appear in a Discussion Section to be published in the June 1980 JOURNAL. All discussions for the June 1980 Discussion Section should be submitted by Feb. 1, 1980.

Publication costs of this article were assisted by Sumitomo Metal Industries, Limited.

REFERENCES

- O. Kubaschewski, *Oxidation of Metals and Alloys*.
- A. V. Seybolt, *This Journal*, **107**, 147 (1960).
- D. Coplan and M. Cohen, *Trans. AIME*, **160**, 1057 (1952).
- H. J. Yearian, E. C. Randell, and T. A. Longs, *Corrosion*, **12**, 515t (1956).
- D. Mortimer, W. B. A. Sharp, and D. R. Holmes, in *Proceedings of the 3rd International Congress on Metallic Corrosion*, Moscow, **4**, 382 (1969).
- I. G. Wright and B. A. Wilcox, *Oxid. Met.*, **8**, 283 (1974).
- E. J. Felten, *This Journal*, **108**, 490 (1961).
- W. E. Boggs, *ibid.*, **118**, 906 (1971).
- E. Baerlecken et al., *Stahl Eisen*, **81**, 768 (1961).
- T. Moroiishi, H. Fujikawa, and H. Makiura, *JISI Jpn.*, **63**, 114 (1977).
- G. F. Comstock and G. L. Clark, *Metals and Alloys*, **8**, 142 (1937).
- H. W. Paxton and T. Kunitake, *Trans. AIME*, **218**, 1008 (1960).
- C. Strawstrom and M. Hillert, *J. Iron Steel Inst.*, **207**, 77 (1969).
- R. A. Parkins, R. A. Padgett, Jr., and N. K. Tunali, *Met. Trans.*, **4**, 2535 (1973).
- ASTM STP-296 (Data Series 22) (1961).

Electrochemical Characterization of the Point Defects Associated with Copper Dissolved in Stabilized Zirconia

P. Fabry and M. Kleitz*

Laboratoire d'Energétique Electrochimique (L.A. 265) E.N.S.E.E.G., B.P. 44, 38401 Saint Martin d'Heres, France

ABSTRACT

As an exploratory experiment, the sweep voltammetry technique along with the "point electrode" technique were applied to a single crystal of stabilized zirconia doped with copper. Both techniques clearly showed the existence of a well-defined change in the oxidation state of the copper. The sweep voltammetry equations were fairly well obeyed and gave an activation energy for the diffusion coefficient of the active species of about 1.6 eV. The close similarities observed between the oxidation and reduction processes favor an explanation in terms of a prevalent diffusion of electronic carriers toward fixed copper centers.

The change in the oxidation state of species dissolved in solid electrolytes can have a profound influence on the behavior of electrochemical systems based on these materials. It has been suggested (1) that impurities with variable valencies might induce significant modifications in the electronic conductivity of solid-oxide electrolytes and therefore alter the performances of oxygen gauges. If such a suggestion is confirmed it is probable that impurities might also markedly influence the shelf life of batteries. On the other hand, such redox reactions can be put to use in electrical energy storage systems, for example in single phase batteries as has been recently proposed (2,5). From a more academic view a key point is the extent to which a redox electrochemical reaction occurring in a solid electrolyte can be compared to a regular electrode reaction. Can we define and measure a relevant redox potential? Some exploratory experiments (3) performed on iron and cerium-doped stabilized zirconia indicated rather smeared-out phenomena. Other data obtained with the point electrode technique (4) showed the existence of rather well-defined redox potentials. The lower limit in the concentration which might result in the formation of an impurity band might also be crucial for some applications. More generally, redox reactions are obviously correlated to electrochemical coloration (5).

Very few electrochemical studies have been devoted to redox reactions in solid electrolytes. A series of investigations by Hladik (6) dealt with reduction to the metallic state of mercury, cadmium, and cobalt ions dissolved in a LiCl-KCl eutectic. A recent review paper (5) summarizes research done in this field and proposes a specific description of this type of redox reaction.

The goal of the work reported here is to estimate the capability of linear sweep voltammetry in characterizing a change in valency of a dissolved ion. Copper dissolved in stabilized zirconia was selected as it is likely to change its valency within the redox stability interval of the electrolyte.

According to the arguments developed in the review paper quoted above (5), a valence change of a point defect is compensated by a variation in the stoichiometric ratio. In stabilized zirconia it corresponds to a change in the oxide vacancy concentration. However, if the concentration of this point defect is small, as compared to the main dopant concentration, the va-

cancy concentration can be viewed as constant to within a good approximation and the redox process will not result in any significant variation of the ionic conductivity. The electronic conductivity will also remain small compared to the ionic conductivity if the energy levels associated with the investigated point defects are distant from the bandedges and if their concentration is small enough to prevent the formation of an impurity band. Under these circumstances, the inner electrostatic potential is constant within the bulk of the material under open-circuit conditions (7,3). The space charge, which may have resulted from the entrapping of electrons or electron holes, remains negligible due to an effective ionic compensation. The situation is thus similar to that prevailing in conventional aqueous electrolytes.

Regarding the redox reactions proper, one specific question remains: Can the oxidized and reduced states of the investigated point defect be treated as true chemical species? Is diffusion of electroactive species more likely to occur than a simple transfer of electrons between the relevant electronic states?

Experimental Technique

The theory of linear sweep voltammetry was developed by Delahay (8) in aqueous electrochemistry. This technique simply consists of applying a potential varying linearly with time to an appropriate electrode and recording the resulting current.

When the electrode reaction is sufficiently rapid and when a diffusion process is primarily involved, the current plot $I = f(t)$ or $I = f(E)$ exhibits a peak. In the case of linear diffusion within a semi-infinite matrix, the value of the peak current, I_p , obeys the equation

$$I_p = A \left(\frac{D_0}{T} \right)^{1/2} C_0 v^{1/2} \quad [I]$$

where A is a constant which depends on the electrode area and on the nature of the electrode, in the case of a reduction process, D_0 is the diffusion coefficient of the oxidized species, C_0 its initial concentration, T the absolute temperature, and v the sweep rate.

This equation is applicable with either soluble or insoluble species produced in the reaction.

In the case of a very rapid electrode reaction, the peak potential E_p on the current plot $I = f(E)$ is independent of the sweep rate. On the other hand, with slow electrode reactions it varies as the logarithm of v .

* Electrochemical Society Active Member.

Key words: voltammetry, copper, zirconia, point defect, diffusion.

Experimental

The measurements were made on a zirconia single crystal (about $5 \times 3 \times 2$ mm) stabilized with 9 mole percent (m/o) of Y_2O_3 . A single crystal was selected in order to eliminate possible precipitation and diffusion of dissolved species at grain boundaries (9). This single crystal was prepared in our laboratory by Giroud and Vitter (10) by a combination of the zone melting and the self-crucible techniques.

The dissolution of copper was obtained by chemical diffusion. The crystal was immersed in powdered CuO for 3 days at 1000°C . The diffusion coefficient of copper in stabilized zirconia is certainly very low, as discussed in the conclusion. To improve the homogeneity of copper concentration, it was necessary to heat the crystal, without CuO, for a long time before the measurements. In our experiment, it was kept at 1000°C in air for a week. The surface was polished to eliminate all traces of the CuO powder.

An analysis performed after the experiments yielded $15 \text{ ppm} \pm 2$ of copper. This concentration is greater by a factor of approximately 5 than the concentration usually observed.

To perform the experiments under adequate conditions and especially to prevent any parallel oxygen electrode reaction, it was necessary to maintain a very low oxygen pressure over the measuring electrode. For this purpose we used an experimental setup previously described (11) in which a stabilized zirconia pellet is pressed between two alumina tubes with gold O-rings inserted between the tubes and the pellet to insure gas tightness. In this investigation, the pellet had the same yttria content as the single crystal and the crystal was simply placed in contact with it as shown in Fig. 1.

A recent study (12) of the electrical characteristics of the contact between two stabilized zirconia samples of identical composition has shown it to be purely ohmic. No overpotential appears at such a contact in particular under the conditions prevailing in the cyclic voltammetry experiments (current of a few μA , under pure argon.)

The counterelectrode was formed by a porous layer of platinum coated on the lower base of the pellet (Fig. 1). It was surrounded by air.

The working electrode was a platinum foil pressed in contact with the single crystal. Obviously this foil did not ensure an intimate contact with the crystal surface and the actual area of the electrode was considered unknown.

With this geometry, the current lines were probably not rigorously parallel; however, to a first approximation, a linear diffusion of the electroactive species was assumed.

Another characteristic of this electrochemical cell is its rather high ohmic resistance.

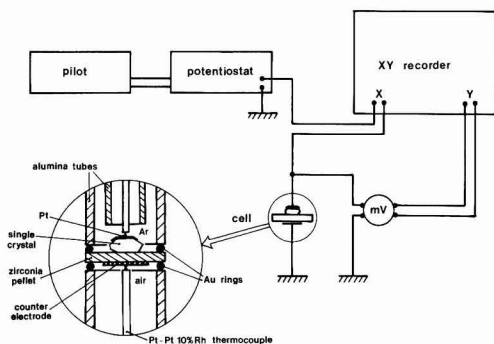


Fig. 1. Circuit diagram of the sweep voltammetry experiments

The electric circuit is depicted in Fig. 1. The X-Y recorder shown in this figure gave the $I = f(U)$ plot from which the values of I_p and E_p could be directly extracted. The parameter U is the cell voltage. It includes the electrode potential E and the IR drop.

Figure 2 shows an example of a $U(I)$ plot obtained at 1232°K at a sweep rate of 36 mV sec^{-1} . A peak is observed both on forward and reverse sweeps.

Figure 3 shows the influence of the sweep rate on the position and magnitude of the experimental peaks at 1000°K .

These curves are not perfectly consistent with expected shapes either in the case of two soluble species or in the case of an electrochemical deposition. One reason is the important ohmic drop; another is the existence of a small parallel reaction involving traces of oxidized species (O_2 , CO_2 , H_2O). It cannot be completely eliminated as demonstrated by the previous oxygen electrode reaction studies (13).

To take into account the latter phenomena, the peak current was measured as indicated in Fig. 2 (the additional current to be corrected for was assumed to vary linearly in the range of interest).

Forward Sweep

According to the usual treatment, the peak current measured on the forward sweep curve was plotted as a function of the square root of the sweep-rate. Figure 4 shows an example of plots so obtained for the corrected current and the crude experimental values (cf. Fig. 2). Both obey the conventional square-root law.

From the expression of the peak current (I) the proportionality coefficient γ , can be written as

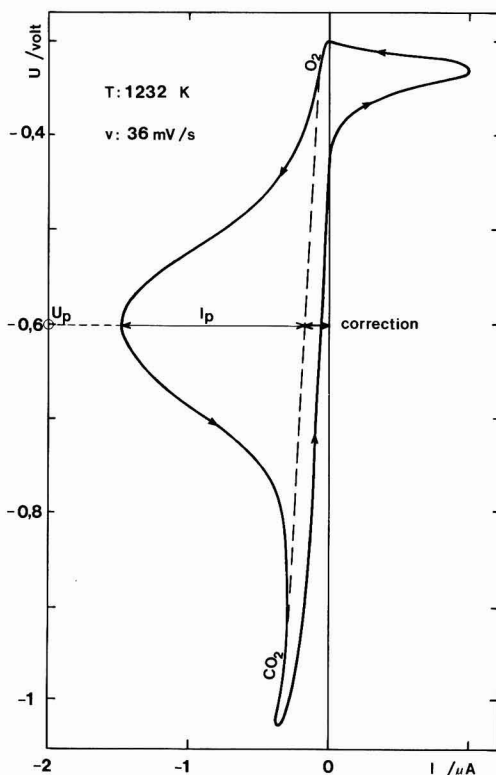


Fig. 2. Voltammogram of the electrode $\text{Pt/ZrO}_2\text{-Y}_2\text{O}_3\text{-Cu}_2\text{O}$

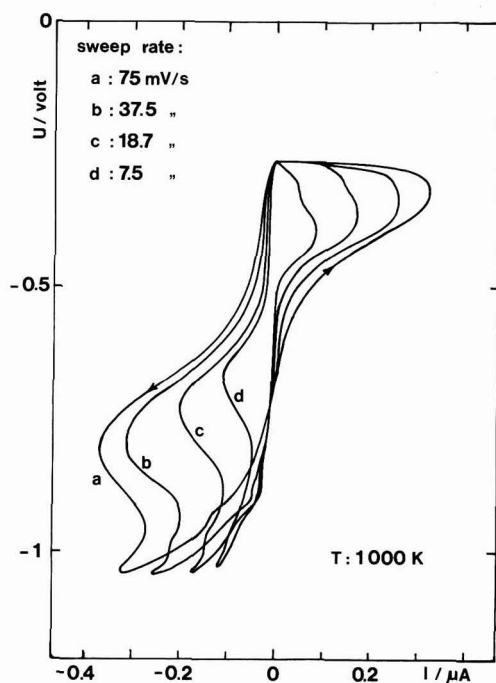
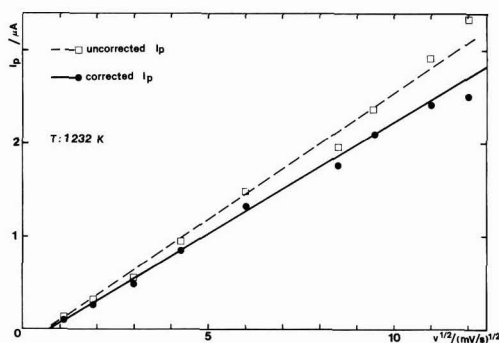


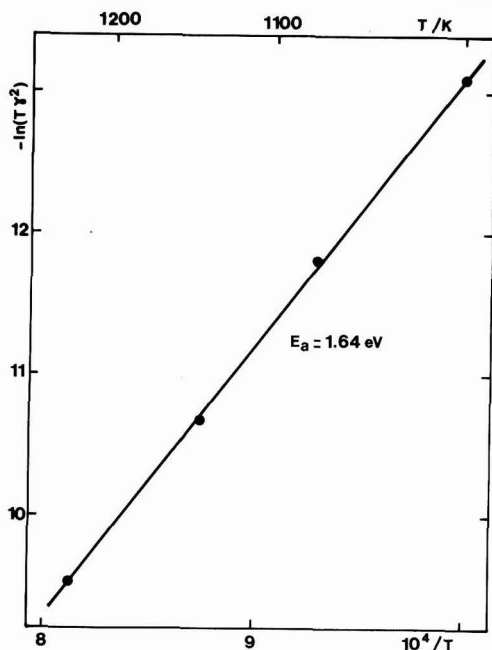
Fig. 3. Influence of the sweep rate on the voltammogram

Fig. 4. Peak current I_p vs. the sweep rate

$$\gamma = K \left(\frac{D_0}{T} \right)^{1/2} \quad \text{[II]}$$

where K is a constant including the electrode area and C_0 which is assumed to be a constant. Since its actual value is unknown, it is not possible to calculate D_0 from the experimental value of γ . Nevertheless it is reasonable to assume that K does not vary markedly with temperature (14) and therefore that $T\gamma^2$ has the same activation energy as D_0 . Figure 5 shows the measured variations of $T\gamma^2$ vs. reciprocal temperature. The activation energy E_a , obtained for D_0 in this way, is equal to 1.64 eV.

The activation energy derived similarly from the values of I_p without correction (cf. Fig. 2) is 1.55 eV. The small difference between these values indicates that the uncertainty of the experimental results does not induce a broad scatter in the determination of E_a (it probably has a major effect on the preexponential factor of D_0). This method thus seems appropriate for

Fig. 5. Variations of the $T\gamma^2$ coefficient vs. temperature

the determination of the activation energy of the electroactive diffusion coefficient.

It should be noted that the sweep rate was considered to be equal to the variation in the voltage, U , applied to the cell and not to the variation of the electrode potential E , as it should be. The variation of the latter is not perfectly linear because of the ohmic drop. The calculation of the correction for this, according to the formulas of Delahay (8), indicates that here also the resulting error is small, of the order of 3% in the values of γ .

Following the usual procedure for this type of investigation, we have also plotted the peak electrode-potential variations vs. the sweep rate. The peak potential was calculated from the experimental peak voltage, U_p , according to

$$E_p = U_p - I_p R \quad \text{[III]}$$

The ohmic drop $I_p R$ was measured by the switch technique. It is approximate, but in this case the possible induced error is significant only for sweep rates higher than 50 mV sec⁻¹. A typical example is shown in Fig. 6. It was found that E_p is independent of the sweep rate.

Reverse Sweep

The characteristics of the reverse sweep are relevant to the reoxidation of the point defects reduced during the forward sweep. The conditions prevailing were not identical to those of the forward process; in fact, the reverse sweeps started before all of the investigated point defects were in the reduced state in the bulk of the material. In principle the conventional sweep voltammetry equations cannot be applied to this situation and the characteristic parameters deduced from the reverse sweep plots, and presented below, must be considered with some circumspection.

As for the forward sweep, we observed that: (i) the peak current is a linear function of the square root of the sweep rate. The Arrhenius plot of the $T\gamma^2$ coefficient is also a straight line. The activation energy E_a'

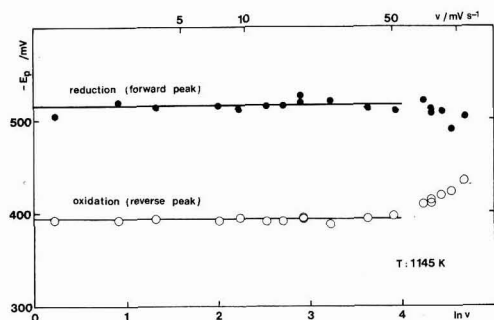


Fig. 6. Variations of the peak potential $E_p = U_p - RI_p$ vs. the sweep rate.

obtained from it for the diffusion coefficient of the reduced electroactive species is equal to 1.5 eV, and (ii) the peak potential is independent of the sweep rate (Fig. 6).

Theoretically, according to Delahay (8), when both electroactive species are soluble this peak potential obeys the following equations, for the negative sweep

$$E_p = E_{1/2} - 1.1 \frac{RT}{nF} \quad [\text{IV}]$$

For the positive sweep it is

$$E_p' = E_{1/2} + 1.1 \frac{RT}{nF} \quad [\text{V}]$$

The parameter n is the number of electrons exchanged in the redox reaction. The half-wave polarographic $E_{1/2}$ is equal to

$$E_{1/2} = E^\circ - \frac{RT}{nF} \ln \frac{f_o}{f_r} \left(\frac{D_o}{D_r} \right)^{1/2} \quad [\text{VI}]$$

and f_o and f_r are the chemical activity coefficients of the oxidized and reduced electroactive species, respectively.

The difference between the reverse and forward peak potentials is equal to

$$\Delta E_p = 2.2 \frac{RT}{nF} \quad [\text{VII}]$$

In principle the calculation of this difference provides a direct determination of n . Experimentally the scatter observed in this determination was rather broad; the values of n so calculated lie between 1 and 2 without any noticeable trend.

$E_{1/2}$ may also be obtained from the above formulas; its variation as a function of temperature is shown in Fig. 8.

Direct Determination of E°

A simple method called the "point electrode technique" for direct determination of redox potentials in solid electrolytes was proposed some years ago (4) and has been successfully applied to various oxides (3). It consists, first, in electrochemically reducing a small amount of the investigated material around a point electrode simply by passing an appropriate current. Then, under open-circuit conditions, the potential, E , of this electrode is recorded during the slow reoxidation of the material in a constant low oxygen pressure. In the case of a single phase system, the plot of E vs. time exhibits a wave. The calculation (3) showed that the potential at the inflection point is E° .

This technique was applied to the sample. A typical plot is shown in Fig. 7. In the entire investigated temperature range ($900^\circ < T < 1300^\circ\text{K}$) a marked wave with an inflection potential around -450 mV/air was observed. Another small wave could be distinguished at about -750 mV/air. The latter completely

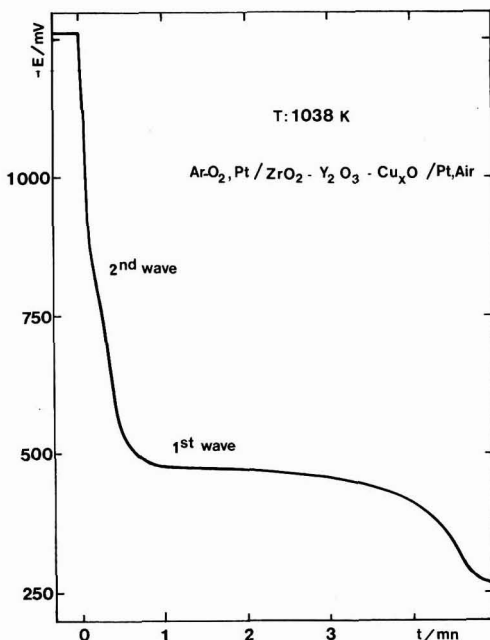


Fig. 7. Depolarization curve obtained by the "point electrode" technique with the electrode Pt/ZrO₂-Y₂O₃-Cu₂O.

vanished at temperature below 1000°K . Both waves are not observed on stabilized zirconia without copper doping. The redox potentials which were deduced from these waves are shown in Fig. 8 as functions of temperature.

The fact that the waves were not horizontal plateaus, as generally observed with multiphase systems (11),

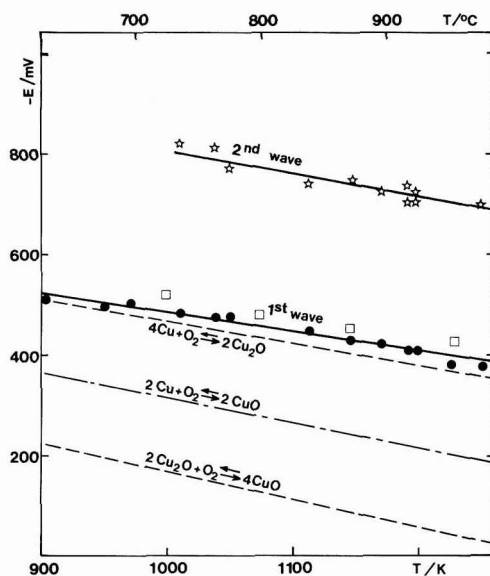


Fig. 8. Redox potentials: dashed lines: thermodynamical coexistence electrode potentials (16); \square : derived from the voltammograms ($E_{1/2}$); \star : derived from the depolarization curves (E°).

indicates that copper is indeed dissolved in the electrolyte. To further confirm this point, a selective electrolysis (3) of the sample was carried out. An appropriate voltage corresponding to a reduction stage intermediate between the two waves was applied during one day so that almost all of the crystal was reduced. The voltage was maintained during the cooling of the sample. It was observed that at room temperature the crystal was transparent and clear before doping; after doping it was slightly reddish and after electrolysis it had a milky appearance. No traces of copper were detected on the platinum electrode after electrolysis.

Discussion and Conclusion

Despite the reserves made regarding the experimental conditions, it seems reasonable to conclude that the investigated electrode reaction is rapid. This is well substantiated by the absence of any variation in the peak voltage with the sweep rate.

The diffusion coefficients of active species cannot be evaluated from Eq. [I] or [II] since the surface area of the electrode is absolutely unknown. Nevertheless, it can be observed that the calculated activation energies for diffusion of active species are similar and the potentials E^* and $E_{1/2}$ do not differ by more than 20–30 mV (cf. Fig. 8). This implies that the term $f_0/f_R (D_0/D_R)^{1/2}$ is certainly less than 10. The radii of Cu, Cu^+ , and Cu^{++} are very different (1.28, 0.96, and 0.69 Å, respectively) and their activation energies for diffusion certainly differ by more than observed (1.6 and 1.5 eV). On the other hand, the activation energies of cationic diffusion in zirconia are generally much higher than these values (15): about 4.4 eV for Ca^{++} (ionic radii of Ca^{++} : 0.99 Å) and between 2.7 and 4 eV for Zr^{4+} (ionic radii of Zr^{4+} : 0.8 Å). The activation energy for hole diffusion in stabilized zirconia can be estimated to 1.2–2.3 eV (17, 18).

A reasonable explanation would be that the redox process is delocalized and due to diffusion of electronic carriers towards the copper centers instead of copper particles diffusion. Within this model the same species would be involved in both reduction and oxidation processes. This would be consistent with the arguments developed in the introduction if it is assumed that copper diffuses extremely slowly in stabilized zirconia. All the data on cation diffusion in this material (15) show that indeed the diffusion of this type of ion is very slow.

Such a description of the redox process in terms of a prevalent displacement of electronic carriers is obviously consistent with the previous conclusion regarding the rapidity of the electrode reaction.

However, this raises a question: Is it correct to refer to the sweep voltammetry equations if electronic carrier motion dominates? Following the reasoning developed in a previous paper (5) it can be assumed that under our experimental conditions the displacement of the electronic carriers was mostly due to a chemical diffusion. But even under these circumstances, the basic equations describing the process are different from those of the usual electrochemical reaction (3, 5).

As a first remark it must be mentioned that the measured activation energy would then characterize the product C^2D ; the electronic carrier concentration C would not be constant conversely to the previous situation where ions were supposed to be mobile.

If this explanation in terms of electronic carrier diffusion is confirmed and appropriate equations derived, sweep voltammetry will appear to be a convenient and accurate technique to characterize the chemical diffusion of these species.

A third point concerns the identification of the point defects which undergo the oxidation state change. In Fig. 8 the measured redox potentials are compared to the coexistence electrode potentials observed with the corresponding mixtures of copper metal and copper oxides.

One possible explanation is to ascribe the wave at -450 mV/air to the reduction $\text{Cu}^+ \rightarrow \text{Cu}^0$. This would suppose that copper dissolved in stabilized zirconia in air at high temperature is in the $+1$ oxidation state. The second wave could be interpreted in terms of a reduction of an associated defect, for instance (Cu_2O , V_O).

The other explanation is that the first wave corresponds to the reduction $\text{Cu}^{++} \rightarrow \text{Cu}^+$ and the second to a further reduction into Cu^0 . If such is the case the redox potentials would show shifts of about 300 mV with respect to the coexistence electrode potentials. Similar exploratory experiments performed on ions of iron (0.45 m/o) and cerium (1 m/o) dissolved in stabilized zirconia indicated the same trend. The potentials where redox processes were observed were higher than the corresponding coexistence electrode potentials (around 1.1 V/air with iron for instance). But in these cases the redox potentials were far from being as well-defined as with copper. In fact with these ions, the voltammograms did not exhibit marked peaks but oscillations instead. Their periods were of the order of second with iron and 5 sec with cerium.

Acknowledgment

The authors thank J. Bouteillon and J. de Lepinay for fruitful discussions and G. Giroud and G. Vitter for preparing the single crystal of stabilized zirconia.

Manuscript submitted Dec. 4, 1978; revised manuscript received May 2, 1979.

Any discussion of this paper will appear in a Discussion Section to be published in the June 1980 JOURNAL. All discussions for the June 1980 Discussion Section should be submitted by Feb. 1, 1980.

Publication costs of this article were assisted by the Laboratoire d'Énergie Electrochimique.

REFERENCES

1. B. C. H. Steele, in "Mass Transport in Oxides," J. B. Wachtman, Jr. and A. D. Franklin, Editors, p. 165, Nat. Bur. Stand. Special Publ. (1968).
2. M. Kleitz, P. Fabry, and J. Fouletier, Paper 78 presented at The Electrochemical Society Meeting, Washington, D.C., May 2–7, 1976.
3. P. Fabry, Thesis, Grenoble, France (1976).
4. P. Fabry, M. Kleitz, and C. Deportes, *J. Solid State Chem.*, **6**, 230 (1973).
5. P. Fabry and M. Kleitz, in "Electrode Processes in Solid State Ionics," M. Kleitz and J. Dupuy, Editors, p. 331, D. Reidel Publishing Co., Dordrecht, Holland (1976).
6. J. Hladik, in "Physics of Electrolyte," Vol. 2, J. Hladik, Editor, p. 867, Academic Press, London (1972).
7. M. Kleitz, P. Fabry, and E. Schouler, in "Fast Ion Transport in Solids-Solid State Batteries and Devices," W. Van Gool, Editor, p. 439, North Holland Publishing Co., Amsterdam (1973).
8. P. Delahay, "New Instrumental Methods in Electrochemistry," Interscience Publishers, Inc., New York (1954).
9. N. M. Beekmans and L. Heyne, *Electrochim. Acta*, **21**, 303 (1976).
10. G. Giroud, G. Vitter, and C. Deportes, *Rev. Int. Hautes Temp. Refract.*, **11**, 25 (1974).
11. P. Fabry, Thesis of speciality, Grenoble, France (1970).
12. P. Fabry, E. Schouler, and M. Kleitz, *Electrochim. Acta*, **23**, 539 (1978).
13. M. Kleitz, J. Besson, and C. Deportes, *Proc. SERAI-COMASI*, p. 354, Bruxelles (1967).
14. P. Fabry and M. Kleitz, *Electroanal. Chem. Interfacial Electrochem.*, **57**, 165 (1974).
15. T. H. Etsell and S. N. Flengas, *Chem. Rev.*, **70**, 339 (1970).
16. J. F. Elliott and M. Gleiser, "Thermochemistry for Steelmaking," Vol. 1, Addison Wesley Publishing Co., London (1960).
17. L. Heyne and N. M. Beekmans, *Proc. Br. Ceram. Soc.*, No. 19, 229 (1971).
18. K. Kitazawa and R. L. Coble, *J. Am. Ceram. Soc.*, **57**, 360 (1974).

High Field Intrinsic Ionic Conduction in Solids

Michael J. Dignam*

Department of Chemistry, University of Toronto, Toronto, Ontario, Canada M5S 1A1

ABSTRACT

The high field intrinsic ionic conduction model, proposed originally by Bean, Fisher, and Vermilyea in connection with the kinetics of growth of anodic oxide films on Ta, is extended to include motion of both defects generated by the field, and in addition the role of the interfaces is examined. It is found that for thin films ($\sim 10^4 \text{ \AA}$), one of two situations can be expected: (i) The rate-controlling step is injection of one of the defects at the appropriate interface, leading to Mott-Cabrera kinetics, or (ii) Defects are generated homogeneously in pairs and migrate to opposite interfaces with negligible recombination and negligible space charge. The two cases lead to steady-state ionic conduction proportional to $\exp(-W(\bar{E})/kT)$ and $X \exp(-W(\bar{E})/kT)$, respectively, where $W(\bar{E})$ is the net activation energy and is a function of the mean field strength \bar{E} , and X is the film thickness. In the author's opinion, data currently available do not allow a decisive choice to be made between these two forms for the steady-state anodic oxidation of valve metals, at least for film thicknesses up to several thousand angstroms.

The kinetics of growth of thin films on metals and semiconductors have for a very long time been interpreted in terms of the so-called high field ionic conduction equation

$$J = A \exp \beta E \quad [1]$$

where J is the flux density of an ionic species in the product film, E the electric field strength in the film, and A and β temperature-dependent constants. In particular, the kinetics of growth of anodic oxide films on the "valve metals" (principally Ta, Nb, and Al) have been interpreted using an equation either of the form of [1] or close to it (1-9). Likewise, the Mott-Cabrera (10) model for the growth of thin tarnish films is based on an equation of the same form.

Almost any model for ionic conduction based on the field-assisted transport of ionic species across one or more activation barriers can under certain circumstances lead to an equation of this form. Thus if a model is chosen in which ionic species of charge q surmount a succession of identical and symmetrical potential barriers of height U and spacing $2a$, with only motion with and against the field considered, the following transport equation can be deduced (11, 12)

$$J = - \frac{Dn}{kT} \frac{\partial \bar{\mu}}{\partial x} \frac{\sin h(qaE/kT)}{(qaE/kT)} \quad [2]$$

where D is the diffusion coefficient for the model, and $\bar{\mu}$ the electrochemical potential for the mobile ionic defects, given, respectively, by

$$D = 4a^2\nu \exp(-U/kT) \quad [3]$$

$$\bar{\mu} = \mu^0 + kT \ln n + q\psi \quad [4]$$

and ν is the frequency at which the ionic species attempt the barrier crossing, μ^0 the standard electrochemical potential, n the concentration of the ionic species, ψ the electrostatic potential, and x the position coordinate.

The conditions on [2] in order that it accurately represent the model are: (i) The space charge concentration must not exceed about 10^{20} e/cm^3 . (ii) The mobile ionic defect concentration must be small compared with the lattice ion concentration (a condition applying to [4] as well). (iii) Transport conditions must not depart radically from steady-state conditions. (iv) The field strength must not be too large, specifically $|qaE| \ll U$.

* Electrochemical Society Active Member.

Key words: films, anode, current density, transport.

For sufficiently high field strengths, and on substituting for D and $\bar{\mu}$ from Eq. [3] and [4], Eq. [2] reduces to (11)

$$J = 2a\nu n \exp[-W(E)/kT] \quad [5]$$

where $W(E)$ is the net activation energy, given by

$$W(E) = U - qaE \quad [6]$$

If we wish to extend the realm of validity of Eq. [5] to very high field strengths, where $|qaE|$ is not small compared to U , then higher order field terms must be added to Eq. [6] (7) in the manner first demonstrated experimentally by Young for the anodic oxidation of Ta (13)

$$W(E) = U \left[1 - \frac{qaE}{U} + d_2 \left(\frac{qaE}{U} \right)^2 \dots \right] \quad [7]$$

Equation [5] is written in the form appropriate for J positive, and is Verwey's (14) equation for interpreting the kinetics of anodic oxidation of the valve metals. As it stands, however, the model upon which Eq. [5] is based is incomplete as it takes no account of either space charge effects or boundary processes. Equation [5] simply relates the flux density, J , to the local field strength and defect concentration.

Mott and Cabrera (10) supposed that for thin films and high field strength, ion transport would be controlled by the rate at which they were generated at the appropriate boundary. They assumed that, once formed, the defects would move very rapidly through the film and hence would contribute a negligible space charge. In that case, the field at the interface would equal the mean field strength in the film. Their equation can be written

$$J = \nu_0 M_0 \exp[-W_0(E_0)/kT] \quad [8]$$

where ν_0 and $W_0(E_0)$ are analogous to ν and $W(E)$ but apply to the interfacial process and barrier, M_0 is the concentration per unit area of species in a position to enter the film as ionic current carriers, and E_0 the field at the interface, equal to the mean field, \bar{E} , according to Mott and Cabrera (10).

Dewald (15) was the first to treat the problem, allowing for an entrance barrier, diffusion barriers, and space charge due to the mobile ionic species. Young (16) subsequently extended Dewald's treatment to include a uniform background space charge of sign opposite to that of the mobile species. Here, only the results obtained in the various limiting cases are presented.

Defining $-n_a q$ as the background space charge concentration, X as the film thickness, and α according to

$$\alpha = (4\pi q^2 a / K k T) \quad [9]$$

where K is the dielectric constant of the film (un-rationalized electrostatic units) the limiting cases are as follows (7): (i) For $\alpha n_a - n_a X \ll 1$, Eq. [8] with $E_0 = \bar{E}$, or the Mott-Cabrera equation results. (ii) For $\alpha n_a X \gg 1$, Eq. [5] with $n = n_a$ and $E = \bar{E}$ results, which is essentially Verwey's equation. (iii) Finally for $\alpha n_a X \gg 1$ and $\alpha n_a X \ll 1$ the following result is obtained

$$J = X^{-1} (K k T / 2 \pi q^2) \exp[-\tilde{W}(E) / k T] \quad [10]$$

where \tilde{W} is the differential field strength defined as $-(\partial V / \partial X)_{J,T}$ with V the anodic overpotential.

This section is completed by summarizing the conduction model proposed by Bean, Fisher, and Vermilyea (17). The model may be described as an intrinsic one as it involves the homogeneous generation of defect pairs, with no impurities, or background space charge. It is essentially an extension of the Frenkel defect model for linear ionic conduction in crystals to high field strengths where dissociation of lattice cations to produce interstitial cations and vacancies (Frenkel defects) and their recombination are strongly influenced by the applied electric field. The result obtained by Bean *et al.* on making the following assumptions (some implicitly) is given below: (i) Only the interstitial cations are mobile, i.e., the vacancies are immobile. (ii) The concentration of defect pairs is low compared to the lattice ion concentration. (iii) The concentrations of cation vacancies and interstitials are everywhere essentially equal, hence space charge is negligible. (iv) Under steady-state transport conditions, the net rate of formation of defect pairs is everywhere zero. (v) The interfacial processes do not need to be considered

$$J = \left(\frac{2 a_h N_{VT} v_h}{\sigma} \right)^{1/2} \exp \left(\frac{W_f(E) + W_h(E)}{2 k T} \right) \quad [11]$$

where N is the concentration of cation lattice sites, a_h the diffusion activation distance, a , for the mobile defect, v_h and v_f the kinetic frequency terms for defect migration and lattice dissociation, respectively, and $W_h(E)$ and $W_f(E)$ are the net activation energies for defect migration and lattice dissociation, respectively, and are of the form given in Eq. [6] or [7].

As was the case for Verwey's equation, the model on which Eq. [11] is based is incomplete, and for the same reason, so it cannot be used with any confidence to describe film growth without further clarification. This clarification has been provided by Dignam and Ryan (18, 7) for the Bean-Fisher-Vermilyea equation, in precisely the same way as it was provided by Dewald for Verwey's equation, i.e., by introducing explicitly space charge and interfacial kinetics, the latter being associated with injection of interstitial cations at the metal-oxide interface. The treatment leads to a characteristic space charge length, X_c , given by

$$X_c = \left(\frac{2 \sigma v_h a_h}{N_{VT}} \right)^{1/2} \left(\frac{k T K}{4 \pi q^2 (a_h + a_f)} \right) \times \exp \left(\frac{W_f(E) - W_h(E)}{2 k T} \right) \quad [12]$$

For $X \ll X_c$, the result is adherence to the Mott-Cabrera equation (i.e., interfacial control) while for $X \gg X_c$ to the Bean-Fisher-Vermilyea equation.

This completes the summary of the models for high field ion conduction which have been proposed to date, with two possible exceptions, which are now men-

tioned only briefly as they do not bear directly on the content of this paper. The first concerns whether or not the proper field to insert in the expressions for the net activation energies, $W(E)$, should be the Maxwell field, rather than some other field, such as the Lorentz field. While this question is of considerable importance in connection with transient ionic conduction phenomena, and certain other phenomena (2, 7), it introduces nothing new in the case of steady-state transport within an idealized, periodic, transport medium, the subject of this paper.

The second concerns equations proposed by Young (19, 20) to account for transient ionic conduction according to which conducting species are generated at a rate proportional to $J n E$. As this equation has no precedence, and there is no well-defined microscopic model underlying either it, or the process which prevents n increasing indefinitely, a quantitative analysis of ion transport based on these equations is not possible at present.

The purpose of this paper is to examine the very restrictive conditions which Bean *et al.* imposed in deriving their equation for high field intrinsic ionic conduction and to investigate the results of relaxing some of these.

Qualitative Analysis of High Field Ionic Conduction Through Thin Films

Before beginning a detailed analysis, a qualitative discussion of high field ionic conduction through thin films is presented. The various possible consequences of slowly increasing the potential drop across a thin film specimen which is in contact at both interfaces with good conducting media, one of which is a source of cations, the other a source of anions, is considered.

The film will be treated as uniform in thickness and initially free of ionic current carriers for all practical purposes. As the field in the film and at its interfaces increases, ionic defects will first be generated at appreciable rates at the weakest points for the system. Only three possible processes (or conceivably a combination of them) exist: (i) generation of cationic defects at the appropriate interface; (ii) generation of anionic defects at the appropriate interface; (iii) generation of Frenkel (or conceivably Schottky) defect pairs within the film, by lattice dissociation (or at dislocations and grain boundaries). The assumption is made that for present purposes the cationic defects can be regarded as interstitial cations, the anionic defects as cation vacancies, and only Frenkel defect pair generation need be considered. Since many oxide films appear to have a vitreous structure, the true nature of the defects may be quite different from these. Apart from the possible introduction of a distribution of kinetic parameters, the essential picture should not be altered if other defect pairs are considered.

Suppose that the first process to take place is defect injection at one of the interfaces. If the resulting defects were to move with an appreciable velocity at the fields required for their generation, the onset of ionic conduction would correspond to the onset of defect injection, and Dewald's model would result. For sufficiently high velocity and thin enough films, space charge would be negligible and the Mott-Cabrera limit of Dewald's model would apply. In the other limit a space charge would be established throughout the film, but concentrated near the entrance interface, and would act to isolate the interfacial and transport processes, leading to adherence to Eq. [10] for sufficiently thick films.

It is possible, though not very likely, that under conditions of significant rate of production of defects at one interface (cation vacancies, say), their velocity of migration would be negligible. The result, as the voltage is slowly increased, would be the establishment of a negative space charge concentrated at the

generating interface, the effect of which would be to increase the magnitude of the field in the interior of the film and at the far interface, relative to that at the generating interface. This could again reduce to Dewald's model, but it is also conceivable that before the cation vacancies achieve a significant velocity (as the voltage is increased) a significant rate of generation of interstitial cations could be achieved, either by lattice dissociation within the film, or by injection at the other interface. If the former took place, the interstitial cations so produced would migrate with an appreciable velocity, since the net activation energy for formation of a defect pair (Frenkel defect) must surely be greater than the lesser of the net activation energies for migration of the defects generated. This alone, however, would not allow a steady current to be established. For that to happen, either significant mobility for the cation vacancies or significant rate of injection of interstitial cations at the other interface must be achieved as the voltage is increased. In both cases, the modified Bean-Fisher-Vermilyea model (i.e., the model as modified by Dignam and Ryan (18, 7)) results. In the latter case, however, there is the additional complication of a space charge zone next to the interface toward which the mobile defects (interstitial cations) move. This possibility will not be considered since no new type of behavior is expected to result from it. The possibility also seems rather remote.

We turn now to consider what would happen in the event that the first process to take place, on increasing the voltage, is the homogeneous generation of defect pairs (Frenkel defects, say). As for the case in which boundary defect injection is the "primary" process, there are several possibilities which are now explored.

As noted before, at least one of the defects must have an appreciable drift velocity under condition of appreciable rate of formation of the Frenkel defects. Let us suppose it is the interstitial cation. Again, in order for a steady current to be established, either significant mobility for the cation vacancy or significant rate of production of interstitial cations at the appropriate interface must be achieved as the voltage is increased. While the latter situation leads once more to the modified Bean-Fisher-Vermilyea model, the former represents a possibility not previously considered, and a possibility that is by no means improbable. It is this situation that is now examined analytically.

High Field Intrinsic Ionic Conduction with Both Defects Mobile and Negligible Defect Injection at the Boundaries

From elementary rate theory, the rate of formation of Frenkel defects per unit volume, R_f , is given by

$$R_f = (N - n_-) \nu_f \exp[-W_f(E)/kT] \\ = N \nu_f \exp[-W_f(E)/kT] \quad \text{for } n_- \ll N \quad [13]$$

where n_- is the concentration of cation vacancies. The symbols f , $+$, and $-$ are used as subscripts to distinguish kinetic parameters associated with: defect pair formation (f), cation migration ($+$), and anion migration ($-$). The net activation energy for the process is given by an expression of the form of [6] or [7]. In the interest of simplicity, we set

$$W_f(E) = U_f - qa_f E \quad [14]$$

where q is the charge on the interstitial cation and its direction of migration is taken as the positive x direction, so that E is positive. With this same convention, the flux densities of the ionic defects are given by

$$J_{\pm} = \pm n_{\pm} v_{\pm} \quad [15]$$

where v is the speed of the defect in question and

from Eq. [15] and [5] is given by

$$v_{\pm} = 2a_{\pm} \nu_{\pm} \exp[-W_{\pm}(E)/kT] \quad [16]$$

with $W_{\pm}(E)$ in turn given by

$$W_{\pm}(E) = U_{\pm} - qa_{\pm} E \quad [17]$$

Defining σ as the capture cross section of a cation vacancy for an interstitial cation, the rate of recombination of defect pairs per unit volume, R_r , takes the form

$$R_r = \sigma n_+ n_- (v_+ + v_-) \quad [18]$$

The continuity condition must be separately satisfied for each of the defect fluxes, so that

$$\frac{\partial J_{\pm}}{\partial x} + \frac{\partial n_{\pm}}{\partial t} = R_f - R_r \quad [19]$$

where $R_f - R_r$ is the net rate of generation of defect pairs per unit volume. For steady-state transport conditions, $\partial n_{\pm}/\partial t = 0 = \partial E/\partial t$ and these equations will be very nearly satisfied for conditions which do not depart radically from those for steady state (21). Thus on setting $\partial n/\partial t = 0 = \partial E/\partial t$ and substituting for J and R_r using Eq. [15] and [18], Eq. [19] becomes

$$\frac{d(n_+ v_+)}{dx} = - \frac{d(n_- v_-)}{dx} = R_f - \sigma n_+ n_- (v_+ + v_-) \quad [20]$$

Finally, the variation of E with position is given by Poisson's equation which, for unrationalized electrostatic units, takes the form

$$\frac{dE}{dx} = (4\pi q/K) (n_+ - n_-) \quad [21]$$

The problem now reduces to solving simultaneously Eq. [20] and [21], subject to the following boundary conditions imposed by our restriction that no defect injection occur at either of the film interfaces

At $x = 0$

$$n_+ = 0, \quad n_- = n_-, \quad J_+ = 0, \quad J_- = -J$$

At $x = X$

$$n_+ = n_+, \quad n_- = 0, \quad J_+ = J, \quad J_- = 0 \quad [22]$$

where $J = J_+ - J_-$ and is the total metal ion flux carried by the interstitials and vacancies, and the positions $x = 0$ and $x = X$ corresponding to the film interfaces. As this problem cannot be solved analytically, we turn first to the simpler problem which arises when space charge can be neglected so that $dE/dx = 0$ and v_{\pm} can be treated as constants independent of position.

Negligible space charge.—For $dE/dx = 0 = dv_{\pm}/dx$, the first part of Eq. [20] integrates directly to give, on using the boundary conditions, [22]

$$n_+ v_+ + n_- v_- = n_+^0 v_+ \quad [23]$$

Elimination of n_- between Eq. [20] and [23] gives an equation which can be written in the form

$$\frac{dc}{ds} = 1 - 4c(C - c) \quad [24]$$

where c and s are dimensionless variables representing the interstitial cation concentration and position in the film, respectively, and are defined according to

$$c = \frac{1}{2} [\sigma (v_+^{-1} + v_-^{-1}) / R_f]^{1/2} v_+ n_+ \quad [25]$$

$$s = \frac{1}{2} [\sigma (v_+^{-1} + v_-^{-1}) R_f]^{1/2} x = x/X_r \quad [26]$$

and C is the value of c at $x = X$ (or $s = S$). Equation [24] has a physically meaningful solution only if $C < 1$. This solution is

$$\frac{1}{2(1-C^2)^{1/2}} \arctan \frac{2c-C}{(1-C^2)^{1/2}} \\ = s + \frac{1}{2(1-C^2)^{1/2}} \arctan \frac{-C}{(1-C^2)^{1/2}} \quad [27]$$

where the final term is the integration constant evaluated from $c = 0$ at $s = 0$ (see [22]). On substituting for c and s according to $c = C$ at $s = S$, multiplying by $2(1-C^2)^{1/2}$ and taking the tangent, Eq. [27] becomes

$$C(1-C^2)^{-1/2} = \tan[S(1-C^2)^{1/2}] \quad [28]$$

Since this equation leads to a rather complicated dependence of C on S (or n_+^X on X), as discussed at the beginning of this paper, only the limiting cases, corresponding to the thin and thick film limits, respectively, will be examined. We anticipate that for sufficiently thin films, defect recombination will be negligible so that the flux density will be given simply by the rate of formation of defect pairs per unit area, i.e., by XR_f . For sufficiently thick films, however, defect recombination (and possibly space charge as well) will play an important part in the over-all transport rate.

Thin film limit.—For $S \ll 1$ (or $x \ll X_r$) the tangent in Eq. [28] may be replaced by its argument, giving

$$C \simeq S(1-C^2) \simeq S, \quad S \ll 1 \quad [29]$$

Expressions for C and S can be obtained from Eq. [25] and [26], respectively, on replacing n_+ and x by n_+^X and X . Substituting the results into Eq. [29] gives

$$n_+^X = XR_f/v_+ \quad [30]$$

However, from [22], at $x = X$, $J = J_+$ which in turn equals $n_+^X v_+$ from Eq. [15], so that

$$J = n_+^X v_+ = XR_f \quad [31]$$

where the final equality follows from Eq. [30]. This is the result anticipated. Substituting for R_f from Eq. [13], Eq. [31] takes the form

$$J = XN_{VF} \exp[-W_f(E)/kT], \quad X \ll X_r \quad [32]$$

where E is independent of position and hence equal to the mean field. Equation [32] remains valid when $W_{\pm}(E)$ and $W_f(E)$ are represented by nonlinear functions of E .

Thick film limit.—For $S \gg 1$, Eq. [28] reduces to

$$C \simeq 1 \quad [33]$$

since $S(1-C^2)^{1/2}$ can never be as large as $\pi/2$ and C is inherently positive. Substituting for C from Eq. [25] with n_+ replaced by n_+^X , Eq. [33] can be written in the form

$$n_+^X = (2/v_+) [\sigma(v_+^{-1} + v_-^{-1})/R_f]^{-1/2} \quad [34]$$

Substituting for R_f and v_{\pm} from Eq. [13] and [16], and making the simplifying assumption that v_+ and v_- differ in magnitude by approximately two powers of ten or more, Eq. [34] becomes

$$J = 2 \left(\frac{2a_1 N_{VF}}{\sigma} \right)^{1/2} \exp \left[- \frac{W_f(E) + W_i(E)}{2kT} \right] \quad [35]$$

where a_1 , v_1 , and $W_1(E)$ belong to the defect having the lower speed, v . Again, this equation remains valid when $W_f(E)$ and $W_{\pm}(E)$ are represented by nonlinear functions of E .

The similarity between Eq. [35] and the Bean-Fisher-Vermilyea equation, [11], is striking; formally they differ simply by a factor of 2. The mechanisms are, however, quite different, as can be seen from the fact that while in Eq. [35], a_1 , v_1 , and $W_1(E)$ be-

long to the defect having the lower speed, in Eq. [11] the corresponding quantities belong to the defect having the higher speed.

It is clear from the foregoing analysis that X_r plays the role of a characteristic recombination length in the sense that for $X \ll X_r$, recombination is negligible, while for $X \gg X_r$, it plays an important part in the transport kinetics. From Eq. [26], [13], and [16], and again making the simplifying assumption that v_+ and v_- differ greatly in magnitude, the following expression for X_r is obtained

$$X_r = 2 \left(\frac{2a_1 v_1}{N_{VF} \sigma} \right)^{1/2} \exp \left(\frac{W_f(E) - W_i(E)}{2kT} \right) \quad [36]$$

Although we can safely assume that for thin enough films, Eq. [32] represents the correct solution for the model being analyzed, we cannot say with any certainty that Eq. [35] will ever represent the model, since we have excluded space charge from the analysis. The consequences of including space charge is examined next, first for conditions in which defect recombination may be neglected, then for conditions in which it plays an important part.

Space charge effects for $R_f \gg R_r$ or $X \ll X_r$.—Under conditions in which both space charge and defect recombination may be neglected ($dE/dx \simeq 0$, $R_f \gg R_r$) the model leads to transport equation, [32]. The form of J for steady-state transport with $R_r = 0$ but $dE/dx \neq 0$ is now determined. For these conditions, Eq. [20] can be written

$$\frac{d(n_{\pm} e^{\beta E})}{dx} = \pm e^{\beta E} F/A_{\pm} \quad [37]$$

where we have substituted for R_f using Eq. [13] and [14], and for v_{\pm} using Eq. [16] and [17], and have introduced the following new parameters

$$\beta_{\pm} = qa_{\pm}/kT, \quad \beta_f = qa_f/kT \quad [38]$$

$$A_{\pm} = (2a_{\pm} v_{\pm}/N_{VF}) \exp[(U_f - U_{\pm})/kT] \quad [39]$$

Since ultimately we will assume that A_+ and A_- differ in magnitude by at least 2 powers of ten, the algebra is simplified at this stage by setting $\beta_+ = \beta_- = \beta$. (Note that for these conditions, $A_+/A_- = v_+/v_-$.)

On multiplying Poisson's equation, [21], by $e^{\beta E}$ it can be written

$$dz/dx = (4\pi q\beta/K) (n_+ e^{\beta E} - n_- e^{\beta E}) \quad [40]$$

where

$$z = \exp(\beta E) \quad [41]$$

Differentiating Eq. [40] by x and substituting for $d(n_{\pm} e^{\beta E})/dx$ from Eq. [37] then gives

$$d^2 z/ds^2 = [(\gamma + 1)/2] z^{\gamma} \quad [42]$$

where s is a new dimensionless distance, defined according to

$$s = [(A_+^{-1} + A_-^{-1}) 8\pi q\beta/K(1 + \gamma)]^{1/2} x = x/X_c, \quad [43]$$

and

$$\gamma = \beta_f/\beta = a_f/a \quad [44]$$

Integration of Eq. [42] leads to

$$dz/ds = \pm (z^{\gamma+1} - z_n^{\gamma+1})^{1/2} \quad [45]$$

where z_n is the value of z for $n_+ = n_-$ or for $dE/dx = 0 = dz/ds$. From Eq. [40] and the fact that $n_+ = 0$ at $x = 0 = s$ (Eq. [22]) it follows that in Eq. [45], the negative sign applies for $s < s_n$, the positive sign for $s > s_n$, where $n_+ = n_-$ at $s = s_n$.

An analytical solution to Eq. [45] does not exist for arbitrary γ . Furthermore, since the main objective of the present analysis is to show that X_c (Eq. [43]) acts as the characteristic space charge length for this

model we present here only the final results, with the details given in the Appendix.

For the particular case $\gamma = 1$ (i.e., $a = a_f$) we obtain for $X \ll X_c$, Eq. [32] (derived for no space charge and negligible recombination rate), while for $X \gg X_c$, and $v_h/v_l \gg e^{X/X_c}$, the following result is obtained

$$J = \left(\frac{N_{tr} v_h K k T}{2 n q^2} \right)^{1/2} \exp \left(- \frac{W_f(\bar{E}) + W_h(\bar{E})}{2 k T} \right) \quad [46]$$

Equation [46] is an interesting result as it is of a form that might suggest there are no space charge effects, since for constant temperature J is predicted to be a function of \bar{E} only, and independent of film thickness. Yet space charge effects are definitely present, since E varies with position in the film (see Appendix, Eq. [A-10]). Apparently for the particular conditions chosen in deriving Eq. [46] (i.e., $a_{\pm} = a_f$ and $v_h/v_l \gg e^{X/X_c}$) the increase in J with increasing X resulting from homogeneous generation of defect pairs (see Eq. [32]) is just compensated by the inhibiting effect of space charge buildup with increasing X (see Eq. [10]). For the more general case (i.e., for $a \neq a_f$ and no restriction on v_h/v_l) this compensation would almost certainly be incomplete, but present nevertheless.

An expression for the characteristic space charge length, X_c , for this model is obtained from Eq. [39] and [43], again neglecting the magnitude of one of A_{\pm} relative to the other, to give

$$X_c = \left[\frac{K(1 + \gamma) k T v_l}{4 \pi N q^2 v_f} \right]^{1/2} \exp \left[\frac{W_f(\bar{E}) - W_l(\bar{E})}{2 k T} \right] \quad [47]$$

Note that while it is the parameters for the defect having the higher speed that enter the expression for the flux density, it is those of the defect of lower speed that enter the expression for the characteristic space charge length.

Space charge effects for $X \gg X_c$ and X_r .—A complete analytical approach to the situation in which both space charge and defect recombination are important will not be attempted, as it can only be treated by numerical methods. However, it is clear that for sufficiently thick films, through most of the film, both the net rate of formation of defect pairs and the space charge concentration will be essentially zero. That this does indeed represent a possible condition can be seen by making the substitutions

$$R_t - \sigma n - n - (v_+ + v_-) = 0 \quad [48]$$

$$n_+ = n_- = n \quad [49]$$

into Eq. [20] and [21]. The net result is simply the Bean-Fisher-Vermilyea equation, [11], if one of the defects has a much higher speed than the other.

Equations [48] and [49] cannot be applied at or near the two interfaces, however, as they are contrary to the boundary conditions, [22], for those regions. Near the interface $x = 0$ there will be a negative space charge ($n_- > n_+$, see [22]) and a net positive rate of generation of defect pairs. Similarly, near the interface $x = X$ there will be a positive space charge zone and again a net positive rate of formation of defect pairs. From Poisson's equation, [21], the field therefore increases on approaching either of the interfaces from the space charge free region (neutral region) of the film. Since there is no net formation of defects in the neutral region of the film, cationic defects migrating through the neutral region can in a sense be considered as having been formed in the space charge zone near $x = 0$. Similarly the anionic defects traversing the neutral region can be considered as having been formed in the other space charge

zone. If the anionic defects are very much less mobile than the cationic defects, then virtually all of the net defect formation, both anionic and cationic, must take place in the space charge zone near $x = 0$, with the lower mobility of the anionic species being compensated by the shorter path they must travel before reaching the appropriate interface. The net result in that case is qualitatively the same as for the modified Bean-Fisher-Vermilyea model. The detailed form of the space charge zone in the two cases is, however, different.

Summary and Conclusions

In the preceding sections, three different characteristic lengths have been introduced for models involving homogeneous generation of defect pairs. These act to define regions of transition from one form of kinetic behavior to another. All three may be expressed as follows

$$X_t = X_t^0 \exp \left(\frac{W_f(E) - W(E)}{2 k T} \right) \quad [50]$$

where $t = c$ (Eq. [12]), r (Eq. [36]), or c' (Eq. [47]); $W(E) = W_h(E)$ for $t = c$, otherwise $W_l(E)$; and X_t^0 , $t = c, r$, or c' are constants essentially independent of temperature. On setting $K \sim 10$, $a \sim 10^{-8}$ cm, $q \sim 1e$, $T \sim 300^\circ K$, $v \sim v_f$, $\sigma \sim 10^{-14}$ cm², and $N \sim 10^{22}$ cm⁻³, the result $X_t^0 \sim 1A$ is obtained in all three cases.

One consequence of the above is that $X_r \sim X_c$, so that for the situation in which negligible defect injection occurs at the interfaces, there are in fact only two kinetic regimes, according to $X \ll X_r, X_c$, and $X \gg X_r, X_c$, respectively, and a complicated transition regime for $X \sim X_r, X_c$. The high field intrinsic ionic conduction model leads therefore to only three forms of limiting kinetic behavior: for thin films, either Mott-Cabrera kinetics (Eq. [2]) or kinetics according to Eq. [32], and for thick films, Bean-Fisher-Vermilyea kinetics. We next estimate the ranges of film thickness required to satisfy the conditions on each of the limiting kinetic equations.

On using the Frenkel defect model for the defect pairs, since U_f is typically of the order of several electron volts, it is expected that $W_f(E) - W(E) > 0.5$ eV and hence that $X_t \gg 10^4 A$. Thus thin film behavior is expected for $X \lesssim 10^4 A$ and possibly for much thicker films. On the other hand, it is certain that for some forms of extended defects (e.g., in vitreous or amorphous media), $W_l(E)$ can be substantially greater than $W_f(E)$. For such a situation, one that is realized for Na^+ ion migration through sodium borosilicate glasses, and for the migration of ions through ion exchange polymers, boundary injection of the high mobility defect is expected to take place more readily than migration of the low mobility defect. This leads again to Mott-Cabrera kinetics for $X \gtrsim 10^4 A$, since the condition $W_f(E) - W_h(E) > 0.5$ eV is still expected to be satisfied. (If small activation energies are involved, linear, not high field, transport conditions are expected, and such behavior lies outside the bounds of the present analysis.)

It is just conceivable, however, that a situation might arise in which $W_l(E) \sim W_f(E)$ and at the same time $W_0(E_0) > W_l(E), W_f(E)$, where $W_0(E_0)$ is the net activation energy for boundary injection of the high mobility defects. In that case, the Bean-Fisher-Vermilyea equation would be satisfied for all films thicker than about one or two molecular layers. This situation is highly improbable, however, since defect pair formation at the appropriate boundary constitutes in effect boundary injection of the more mobile defect, leading to $W_0(E) \sim W_f(E)$ and hence $W_0(E_0) \ll W_f(E)$, since E_0 is greater than E (see discussion following Eq. [49]).

In summary, therefore, for films $\gtrsim 10^4 A$, one of two situations can be expected: kinetics in accord either

with Eq. [8] (Mott-Cabrera) or Eq. [32]. Although Eq. [32] predicts a dependence of E on X for fixed J , the dependence is difficult to detect for β large. Thus Eq. [32] predicts the same dependence of E on X for fixed J as of E on J for fixed X . For high field anodic film formation, the latter is typically a few percent per decade change in J so that the dependence of E on X can only be observed if measurements covering a range in X are characterized by a large ratio of the largest to smallest X . Even then difficulties are introduced by changes in electrode area during anodization. Thus in the very thin film region, ($X < 100\text{\AA}$) some reduction in electrode area with increasing X is expected due to a reduction in electrode roughness as film growth proceeds. This effect will tend to offset the thickness dependence of J predicted by Eq. [32]. For thicker films, on the other hand, it is difficult to eliminate the creeping of electrolyte up the electrode tab, producing an effect in the same sense as that predicted by Eq. [32], and hence serving as a plausible explanation for it.

In the author's opinion, there are to date no results for the anodic oxidation of the valve metals that rule out the possibility that for thin films the correct steady-state conduction equation is of the form of Eq. [32]. To lend credibility to this statement, three sets of data that relate to the thickness dependence of the field for galvanostatic conditions are examined in turn.

In 1955 Vermilyea (22) published data for the anodic oxidation of Ta in order to show that Dewald's model (15) (see beginning of this paper) was not in agreement with the experiment. This he did by showing that a graph of film thickness, X , (obtained by capacitance measurements) vs. anodizing potential, V , was much better represented by a straight line than it was by a concave downward curve of the form predicted by Dewald's equation. This data covered a range of thickness from about 100 to 5000Å. For these conditions, Dewald's equation (Eq. [10]) predicts that on increasing the film thickness from 100 to 5000Å (a factor of 50 increase in X) under galvanostatic conditions, an increase in the differential field strength will be required equal to that required to produce a 50-fold increase in current density at constant X , which is about a 12% increase (2). This should have been reflected as a 12% decrease in the slope of X vs. V (i.e., $dX/dV = 1/\bar{E}$).

Interpreting Vermilyea's result in terms of Eq. [32], or more accurately, in terms of the model leading to Eq. [32], we first inquire as to what is expected on the basis of this model. For sufficiently thin films, Eq. [32] would be a valid approximation and would predict the graph of X vs. V to be concave upward, with the slope increasing at the rate of about 7% per 10-fold increases in the film thickness. As the thickness approaches the value corresponding to the characteristic recombination length, X_r , and/or the characteristic space charge length, X_c , the ever increasing effect of defect recombination and space charge will cause the slope of X vs. V to fall below that predicted by Eq. [32], ultimately leading to a concave downward shape to the graph. Thus we expect the curve to be initially concave upward, going through an inflection point for $X \sim X_r, X_c$ (i.e., for $X \lesssim 10^4\text{\AA}$), then becoming concave downward, and finally becoming linear for $X \gg X_r, X_c$, in accordance with the Bean-Fisher-Vermilyea equation (Eq. [11]). Thus for the range of thickness studied by Vermilyea, the model predicts either that the curve be concave upward over its entire length, with a ratio of final to initial slope of 1.12, or else sigmoidal in shape, with the slope a maximum at the inflection point. An examination of Vermilyea's published graph led the author to the conclusion that the data are entirely consistent with this latter prediction, with the slope at the inflection

point (at about 3000Å) being several percent higher than that at the ends of the curve. The fact is the data are not sufficiently precise to settle the issue. Other data of this nature are equally ambiguous in this connection.

Young has made a more direct evaluation of the variation of field with film thickness for the growth of Ta_2O_5 films (23). These data are reproduced in Fig. 1. Films were formed at a current density of 10 mA/cm² with the charge, ΔQ_V , required to form the film from an overpotential of 10.1V to V noted. In addition the electrode capacitance at 10.1V and V were measured. Measurements were made covering a range of V from about 15 to 140V with a separate electrode used for each determination. From the data, the incremental field, $E_{\text{inc}} \propto (V - 10.1)/\Delta Q_V$, was calculated and graphed as a function of $(V - 10.1)$ (upper curve Fig. (1)). For the middle curve, E_{inc} was calculated by Young using the quantity $[\Delta Q \cdot \Delta(1/c)]^{1/2}$ as a measure of the increment in film thickness, where $\Delta(1/c)$ is the change in the reciprocal capacitance on forming the film from 10.1V to V . Since ΔQ should be proportional to electrode area, while $\Delta(1/c)$ is inversely proportional to it, it would appear that $[\Delta Q \cdot \Delta(1/c)]^{1/2}$ should be a measure of ΔX which is independent of electrode area. This will only be true if neither the electrode area nor the effective dielectric constant change on forming from 10.1V to V . The compensation for surface area should be good, however, provided it changes by no more than a few percent.

Superimposed on the data are horizontal lines, drawn by Young on the assumption that E_{inc} is independent

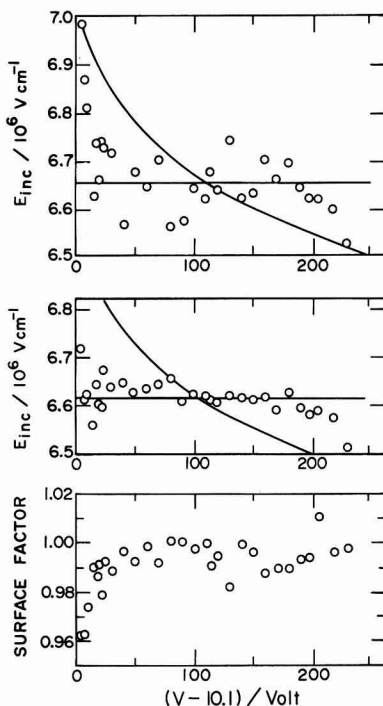


Fig. 1. Incremental field, E_{inc} , as a function of formation overpotential less 10.1V, for the anodic oxidation of Ta at 10 mA/cm² and 25°C. For the upper set of data, increments in film thickness were determined from measurement of the charge passed; for the middle by a combination of charge passed and capacitance; and in the lower curve the ratio of "true" to apparent electrode area is graphed. The data are according to Young (23).

of V , and curved lines, calculated from Eq. [32], on the basis that a factor of 10 increase in X produces a 7% decrease in E at fixed current density [i.e., a factor of 10 increase in current density at fixed X produces a 7% increase in $E(2)$]. The curved line represents the upper set of data about as well as does the horizontal line (better up to about 3000 Å), while it definitely is a poorer representation of the middle set. For the upper and middle sets of data to be compatible, the ratio of the "true" to apparent electrode area must vary with V according to the bottom set of data (23). The fact that this ratio falls well below 1 for small values of V means that there is some effect missing from the analysis (e.g., a variation of effective dielectric constant or porosity with thickness) so there is no basis for preferring the middle to the upper set of data. To account for the apparent curvature in the upper set of data by area and current efficiency effects alone would require one to postulate that the electrode area increased with increasing film thickness, or the current efficiency decreased with increasing film thickness. The former is contrary to expectation, film forming should exert a polishing action on the metal surface reducing its area. The latter effect is limited to 1% or less (and hence cannot account for the curvature) since the current efficiency is known to be high up to $V \sim 200V$ (2).

Recalling that as the voltage is increased, the curve predicted by Eq. [32] will ultimately yield values for E_{inc} which are too low, and noting the uncertainties introduced by possible variations in electrode area and effective dielectric constant with film thickness, one cannot with justification reject the model leading to Eq. [32] on the basis of these data either.

The final set of data to be examined were obtained by Dignam and Ryan (24). The data in Fig. 2 are for Al anodically oxidized at constant current, i , in a glycol-borate electrolyte (25) with the time derivative of the anodic overpotential, $(\partial V/\partial t)_i$, determined by electronic differentiation. Data were obtained for a range of current densities, with the fractional change in $(\partial V/\partial t)_i$ with increasing film thickness being essentially independent of current density beyond the smooth maximum [at $\Delta Q \sim 3$ mC/cm² in Fig. 2]. $\Delta Q = 0$ corresponds to the film left after electropolishing, which is about 25 Å thick (26). Since 1 mC/cm² corresponds to about 5.5 Å, the ratio of the film thickness at $\Delta Q = 18$ mC/cm² to that at $\Delta Q = 3$ is about 2.4. Analysis of all of the data presented in Ref. (24) leads to the results summarized in Table I.

It is readily shown that for electrode area and current efficiency constant, Eq. [32] leads to the result

$$\left(\frac{\partial V}{\partial t}\right)_i = \left(\frac{\Omega i}{\beta_i F}\right) [\beta_i E_X - 1] \approx \left(\frac{\Omega}{F}\right) i E_X \quad [51]$$

where Ω is the volume of oxide per faraday of charge passed, F the faraday, i the current density, and E_X the field strength for thickness X .

From the data of Bernard and Cook (25), a three-fold increase in i at constant X results in a 3% in-

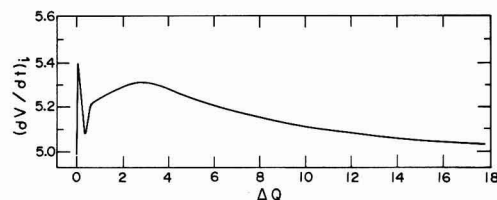


Fig. 2. Time derivative of the formation overpotential as a function of charge passed for the anodic oxidation of Al at 1.98×10^{-2} mA/cm² and 25°C. The units for $(\partial V/\partial t)_i$ are arbitrary, those for ΔQ , mC/cm². Data according to Dignam and Ryan (24).

Table I. Fractional decrease in field for about a three-fold increase in film thickness (~ 45 -135 Å) for the anodic oxidation of Al at constant current. The data are taken from Fig. 3 of Ref. (24).

Current density (mA/cm ²)	Final over initial film thickness	% decrease in $(\partial V/\partial t)_i$	% decrease adjusted to a 3-fold increase
9.51×10^{-3}	3.04	4.7	4.6
1.98×10^{-2}	3.17	5.8	5.5
4.86×10^{-2}	2.63	3.7	4.2
2.20×10^{-1}	3.17	3.0	2.9
Average, 4.3 ± 1.1			

crease in E , so that a three-fold increase in X at constant i would require a 3% decrease in E and hence in $(\partial V/\partial t)_i$. The observed decrease of $(4.3 \pm 1.1\%)$ is in satisfactory agreement with this value. The shape of the curve of $(\partial V/\partial t)_i$ vs. ΔQ is certainly qualitatively correct [$E_X = \text{const} - \beta_i^{-1} \ln(X/i)$].

Other explanations for these data can, of course, be offered, and in fact the author has on two occasions (25, 7) offered different explanations for these data both differing from the present one. Clearly, however, one cannot rule out the model leading to Eq. [32] on the basis of these data. The question remains, therefore, an open one.

Manuscript submitted Nov. 9, 1978; revised manuscript received May 11, 1979.

Any discussion of this paper will appear in a Discussion Section to be published in the June 1980 JOURNAL. All discussions for the June 1980 Discussion Section should be submitted by Feb. 1, 1980.

Publication costs of this article were assisted by the University of Toronto.

APPENDIX

Solution of Eq. [45] for the Particular Case $\gamma = 1$

As an analytical solution to Eq. [45] does not exist for arbitrary γ , the particular case $\gamma = 1$ (i.e., $a = a_f$) will be considered. For such a case, the solution is

$$z = z_n \cosh(s - s_n) \quad [A-1]$$

Using this result, with Eq. [37] and [41] (setting $\beta_+ = \beta_- = \beta_f = \beta$), we can write

$$d(n+z)/ds = \pm (z_n X_c/A_{\pm}) \cosh(s - s_n) \quad [A-2]$$

Using the boundary conditions $n_+ = 0$ at $s = 0$, $n_- = 0$ at $s = S$, Eq. [47] integrates to give

$$n+z = (z_n X_c/A_+) [\sinh(s - s_n) + \sinh s_n] \quad [A-3]$$

$$n-z = (z_n X_c/A_-) [\sinh(S - s_n) - \sinh(s - s_n)] \quad [A-4]$$

At $s = s_n$, $n_+ = n_- = n_n$ and $z = z_n$, which with Eq. [A-3] and [A-4] gives

$$n_n = (X_c/A_+) \sinh s_n = (X_c/A_-) \sinh(S - s_n) \quad [A-5]$$

Since X_c , A_+ , A_- , and S are all finite and positive, it follows from Eq. [A-5] that

$$S > s_n > 0 \text{ and } n_n > 0 \quad [A-6]$$

Evaluating $J = J_+(x = x_n) - J_- (x = x_n)$ using Eq. [15], [16], [39], and [41] gives

$$J = n_f [\exp(-U_f/kT)] (A_+ + A_-) n_n z_n \quad [A-7]$$

Once again, an explicit analytical expression for J cannot be obtained, so we examine the two limits $S \ll 1$ and $S \gg 1$.

For $S \ll 1$ (i.e., for low space charge conditions), Eq. [A-5] with [A-6] leads to

$$n_n = X_c s_n/A_+ = X_c (S - s_n)/A_- \quad [A-8]$$

which on eliminating s_n and rearranging gives

$$(A_+ + A_-) n_n = S X_c = X \quad [A-9]$$

where the final equality follows from Eq. [43]. Furthermore, from Eq. [A-1] and [A-6], z is independent of position for $S \ll 1$. Making use of this result and Eq. [A-9], Eq. [A-7] reduces to Eq. [32], as of course it must if the analysis has been carried out correctly, since Eq. [32] was derived for conditions of no space charge and negligible recombination rate.

For high space charge conditions, given by $S \gg 1$, we may replace Eq. [A-1] by the following approximate one

$$z = (z_n/2) \exp[s - s_n] \quad [\text{A-10}]$$

On taking the logarithms and replacing z by $e^{\beta E}$, and E by $-(d\psi/ds)/X_c$, Eq. [A-10] becomes

$$-\frac{\beta}{X_c} \frac{d\psi}{ds} = \ln(z_n/2) \mp (s - s_n) \quad [\text{A-11}]$$

where the negative sign applies for $s < s_n$, the positive sign for $s > s_n$. Integration of Eq. [A-11] from $s = 0$ to $s = s_n$, and from $s = s_n$ to $s = S$ and adding gives on solving for $\ln z_n$ and taking the antilog

$$z_n = 2[\exp(\beta \bar{E})] \exp \left[-\frac{(S - s_n)^2 + s_n^2}{2S} \right] \quad [\text{A-12}]$$

where $\bar{E} = [\psi(s=0) - \psi(s=S)]/SX_c$, and is the mean field strength in the film.

To complete the analysis we solve Eq. [A-5] for n_n making the same approximation as was used in writing down Eq. [A-10], to give

$$n_n = \frac{1}{2} X_c (A_+ A_-)^{-1/2} \exp(S/2) \quad [\text{A-13}]$$

which with Eq. [A-12] leads to

$$n_n z_n = \frac{X_c \exp(\beta \bar{E})}{(A_+ A_-)^{1/2}} \exp \left[\frac{s_n(S - s_n)}{S} \right] \quad [\text{A-14}]$$

From Eq. [A-5] we deduce that for $(A_+/A_-) \ll e^{-S}$, $s_n \ll 1$, whereas for $(A_-/A_+) \ll e^{-S}$, $(S - s_n) \ll 1$. For either case, the final exponential factor in Eq. [A-14] reduces approximately to unity. Thus if one of the defects moves with a speed much larger than the other, Eq. [A-7] and [A-14] lead to

$$J = \nu_f \frac{(A_+ + A_-)}{(A_+ A_-)^{1/2}} X_c [\exp(-U_f/kT)] [\exp(\beta \bar{E})] \quad [\text{A-15}]$$

On substituting for X_c from Eq. [43], for A_{\pm} from Eq. [39], for β from Eq. [38], and neglecting one of A_{\pm} relative to the other, Eq. [A-15] can be written

$$J = \left(\frac{N_{\nu_f} \nu_h K k T}{2\pi q^2} \right)^{1/2} \exp \left[-\frac{W_f(\bar{E}) + W_h(\bar{E})}{2kT} \right] \quad [\text{A-16}]$$

where ν_h and $W_h(\bar{E})$ belong to the defect having the higher speed, in contrast to Eq. [35] obtained by

including defect recombination but excluding space charge.

Equation [A-16] is presented in the body of the paper as Eq. [46].

REFERENCES

1. T. P. Hoar, in "Modern Aspects of Electrochemistry," Vol. 2, J. O'M. Bockris, Editor, Academic Press, New York (1959).
2. L. Young, "Anodic Oxide Films," Academic Press, New York (1961).
3. D. A. Vermilyea, in "Advances in Electrochemistry and Electrochemical Engineering," Vol. 3, P. Delahay and C. W. Tobias, Editors, Interscience, New York (1963).
4. L. Young, W. S. Goruk, and F. G. R. Zobel, in "Modern Aspects of Electrochemistry," Vol. 4, J. O'M. Bockris, Editor, Butterworths, London (1966).
5. J. W. Diggle, T. C. Downie, and C. W. Goulding, *Chem. Rev.*, **69**, 365 (1969).
6. C. J. Dell'Oca, D. J. Pulfrey, and L. Young, in "Physics of Thin Films," Vol. 6, M. H. Francomb and R. W. Hoffman, Editors, Academic Press, London and New York (1971).
7. M. J. Dignam, in "Oxides and Oxide Films," Vol. 1, J. W. Diggle, Editor, Dekker, New York (1973).
8. A. K. Vijh, "Electrochemistry of Metals and Semiconductors," Dekker, New York (1973).
9. A. T. Fromhold, Jr., in "Oxides and Oxide Films," Vol. 3, J. W. Diggle and A. K. Vijh, Editors, Dekker, New York (1976).
10. N. Cabrera and N. F. Mott, *Rep. Prog. Phys.*, **12**, 163 (1948).
11. M. J. Dignam, D. J. Young, and D. G. W. Goad, *J. Phys. Chem. Solids*, **34**, 1227 (1973).
12. M. J. Dignam, *Can. J. Chem.*, in press.
13. L. Young, *Proc. R. Soc. London, Ser. A*, **258**, 496 (1960).
14. E. J. W. Verwey, *Physica*, **2**, 1059 (1935).
15. J. F. Dewald, *This Journal*, **102**, 1 (1955).
16. L. Young, *Can. J. Chem.*, **37**, 276 (1959).
17. C. P. Bean, J. C. Fisher, and D. A. Vermilyea, *Phys. Rev.*, **101**, 551 (1956).
18. M. J. Dignam and P. J. Ryan, *Can. J. Chem.*, **41**, 3108 (1963).
19. L. Young, *Proc. R. Soc. London, Ser. A*, **263**, 395 (1961).
20. L. Young, *Can. J. Chem.*, **50**, 574 (1972).
21. A. T. Fromhold, Jr., *J. Phys. Chem. Solids*, **24**, 1081 (1963).
22. D. A. Vermilyea, *Acta Met.*, **3**, 106 (1955).
23. L. Young, *Proc. R. Soc. London, Ser. A*, **244**, 41 (1958).
24. M. J. Dignam and P. J. Ryan, *Can. J. Chem.*, **41**, 3108 (1963).
25. W. J. Bernard and J. W. Cook, *This Journal*, **106**, 643 (1959).
26. M. J. Dignam, W. R. Fawcett, and H. Bohne, *ibid.*, **113**, 656 (1966).

Glow Discharge Tube Glass Electrodes

William Primak and Emmet Monahan

Argonne National Laboratory, Argonne, Illinois 60439

ABSTRACT

When glass plates are used as electrodes at several hundred °C in a glow tube, the alkali and light alkaline earth ions migrate, and a depleted surface layer forms. The surfaces may collapse and fracturing may occur. On the opposite face of a cathode plate, the alkali may segregate, in part within the glass, causing blistering. On the opposite face of an anode plate, segregation of gas may occur, but this is uncertain as the effects are less obvious. The depleted zone appears to have quite a sharp boundary as the volume of glass possessing reduced refractive index corresponds to the volume containing the number of ions equivalent to the charge transported for several of the glasses. For Pyrex glass the equivalency corresponds to about 20% of the sodium ions being tied up by aluminum. Deterioration of cathode plates is greater than that of anode plates. The most severe effects are found at blocking interfaces. The glasses studied were Pyrex, an optical crown glass, a soda-lime glass, a borosilicate glass containing zinc oxide and titania in addition to alkali, and a barium crown glass.

The behavior of a glow tube with heated glass electrodes was described by Wolf (1) many years ago. He used a large area heated soda-lime glass electrode separated from an iron electrode, apparently by a few inches, and the assembly was located under a glass bell jar. He was concerned mainly with the form of the discharge and its characteristics. He took special note of the manner in which the discharge broke up into rosette type figures.

Our own interest in the behavior of glass electrodes in a glow tube stemmed from trying to understand the behavior of glass in ion bombardment where we found the charge had been conducted ionically causing ion depletion in a surface layer of the glass (2). The glow discharge experiments were begun to study the effects of ionic conduction in the absence of (i) the high energy transfers and (ii) penetration depths of the ions comparable, in some cases, to the thicknesses of the layers being depleted.

The present paper deals with the destructive effects which are observed in the glass electrodes. Similar destructive effects have been seen in attempts to use ceramic electrodes in other cases, notably as electrodes in open cycle MHD generators. The glow tube offers a more controlled means for studying some of the effects of ionic conductivity on electrodes; and the use of glass, which is transparent, offers the opportunity to make observations and measurements which would be more difficult or impossible on ceramic bodies.

Methods

The glow tube.—The problem in designing the glow tube was to confine the discharge to the glass electrode since it was desired to measure the current flowing through the glass. Since the electrical instrumentation was to be connected to it, this electrode had to be near ground potential. Because of the behavior of the discharge as a function of pressure in the glow tube (the Paschen curve) which has a minimum, two modes of operation are possible: on the low pressure side, the pumping tube (which is an alternate ground) must be short compared to the glow tube; while on the high pressure side of the minimum, the pumping tube must be long. The advantage of working on the low pressure side is that the curve is very steep on this side, whereas on the high pressure side the slope is small. The latter condition requires a very large ratio of the length of the pumping tube compared to the discharge path, hence the former arrangement was tried first. However, it was found to be unsatisfactory because the currents

attainable at the low pressure were too small. In the present arrangement the pumping tube is about 3.5 m long, and the discharge length is about 50 cm. It is possible to have a potential drop across the glow tube and glass electrode of 3–3.5 kV before breakdown to the pump occurs.

The glow tube is mounted vertically. The high voltage electrode, an aluminum disk on a tungsten lead-in, is located at the upper end. The pumping tube is attached at this end. Both the glow tube and the pumping tube are made of 25 mm Pyrex glass tubing. The glass electrode assembly is inserted at the lower end through a conical joint and extends 35 cm into the glow tube. This region of the glow tube is surrounded with a pot furnace about 6 in. long. The thermocouple to read the temperature is located in the pot furnace, and it is presumed to be but a few degrees different from the electrode temperature. The thermocouple and McLeod gauges to read the pressure are mounted near the end of the pumping tube. A grounded electrode is located in this vicinity to protect the pump and instrumentation.

The glass electrode plate to be studied sits on a stainless steel cylinder 3/8 in. diam and about as long (graphite was used also, see below), the contact surface of which is finished flat to about a fringe or less over a goodly portion of its surface as determined by placing the optically finished glass disk upon it and examining the Fizeau fringes. The metal surface was refinished for each run by means of a suitably finished set of hones used with ethanol as a lubricant. The stainless steel cylinder was supported on an aluminum rod about 1/8 in. diam within a closely fitting vitreous silica tube which had been fire polished on the end until it had become constricted slightly, enough to prevent the glass electrode plate from passing through. As described above, this silica tube assembly was 35 cm long. It rested on the tungsten lead-in in a short conical joint. Electrical contact and mechanical stability were obtained by placing a short aluminum cylinder 3/8 in. diam between the tungsten lead-in and the aluminum rod. A tabulation through which gas could be leaked to maintain the desired pressure was attached to the side of the conical joint.

Operating procedure.—After assembly, the tube was pumped down with a rotary oil pump while helium was leaked in to maintain pressure at about 0.1 mm Hg. The furnace was raised to the desired temperature. Then the tube was pumped down to the minimum pressure reached with the leak turned off, 0.03–0.04 mm Hg, backfilled with helium to a pressure over 0.1 mm Hg,

Key words: glass, electrode, tubes.

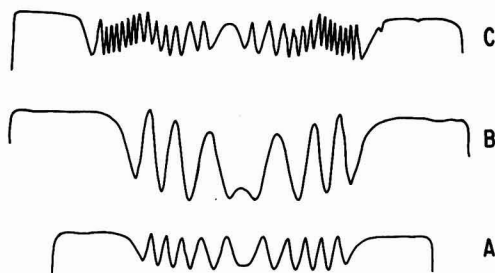


Fig. 1. Monochromatic fringes observed on scanning C-1 glass cathodes; curve A, after 19 mC at 0.55μ ; curve B, after 9.7 mC at 0.545μ ; and curve C, after 46 mC at 0.447μ .

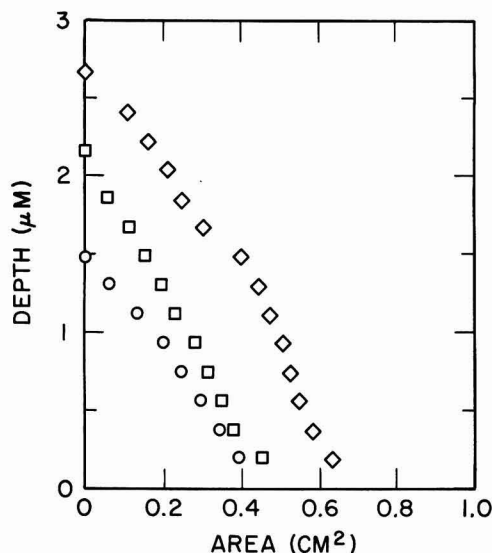


Fig. 2. Profiles of depleted zones (plotted against $\pi \times (\text{radius})^2$ to permit a determination of the volume by integration) of Pyrex glass cathodes after 8.1 (circles), 13.1 (squares), and 25.8 mC (diamonds).

and this was repeated several times. Then the main pumping valve was turned off, the system pumped through a leak which bypassed the valve, and the helium leak was adjusted until the system remained at a steady pressure of 1-1.2 mm Hg. Conical joints in the vicinity of the glow tube were lubricated with Apiezon "T"; all other joints were lubricated with Apiezon "N". The helium leak was a micrometer leak valve terminating in a copper tube which was sealed into the system with Apiezon "W". The pumping leak was a bellows sealed semineedle valve connected in parallel with the main stopcock with rubber tubing.

The power supply was connected to the glow tube with a protecting resistor chain in series to limit the current. A number of runs were made with a power supply whose voltage was adjusted with step switches, but problems with the discharge arose when the voltage had to be adjusted to control the current as the run progressed. This power supply was replaced with a Plastic Capacitor, Incorporated power pack (5000V with 110V a-c input) which was continuously adjustable with a small variable autotransformer in the input line. Most of the results reported here were obtained with this power supply.

For most of the runs the current was recorded with a General Electric photoelectric recording potentiom-

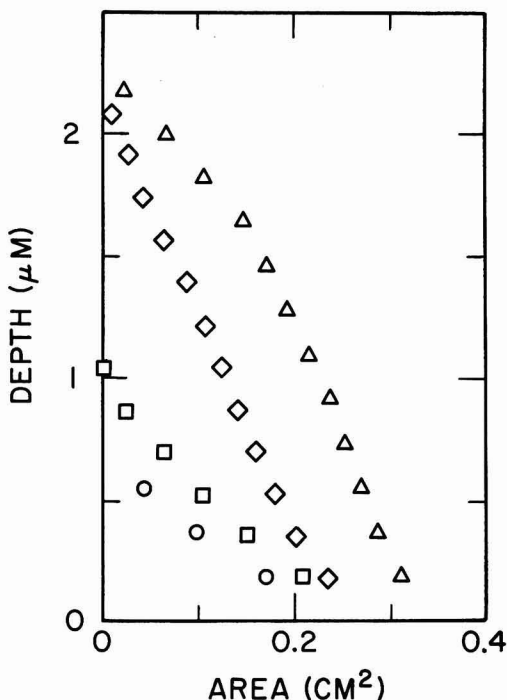


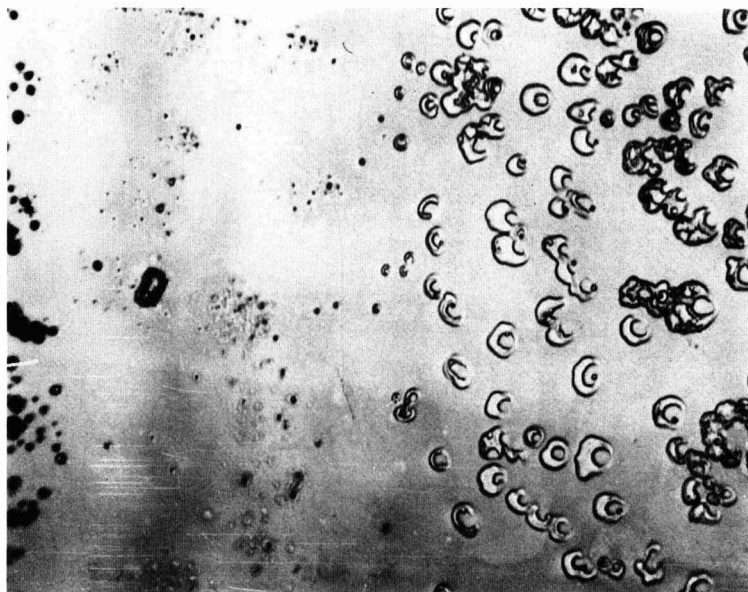
Fig. 3. Profiles of depleted zones of a C-1 glass cathode after 9.7 (circles), 18.7 (squares), 46.3 (diamonds), and 76.7 mC (triangles).

eter placed across a 10 Ω resistor between the glow tube and ground. The charge was determined by integrating the charts. The voltage across the glow tube was determined with a high voltage probe designed for and attached to a Simpson digital volt-ohm meter. Currently, the current is determined by a second Simpson digital volt-ohm meter, and both the current and the voltage are recorded on a dual-trace recorder connected to the analogue outputs from these meters. The analogue output of the current measuring meter is also connected to an integrator based on a frequency counter with automatic cutoff when the desired charge is reached. All of the anode plate data and a few of the cathode plate data were obtained with this equipment. For the higher charge runs, currents of about 195 μ A were maintained. This was reduced to make the lower charge runs of convenient length.

When the runs are started, the voltage across the glow tube may drop, sometimes precipitously, as contact with the supporting conducting cylinder is developed. Then it may remain relatively constant for a long time until a considerable depletion occurs, when the voltage rises until, if the run is long enough, discharge to the pump or around the protecting vitreous silica tube occurs. The well-known peculiar characteristics of the glow tube, which has led to its application for voltage regulation, are such that large changes in voltage applied across the resistor chain and glow tube cause much smaller changes in voltage drop across the tube.

Optical and other examination of the glass plates.—Both sides of the plates were examined under the binocular microscope with reflected light, as was also the block on which it sat. The plate was then examined under vertical illumination with monochromatic light in a metallurgical microscope. When fringe patterns were observed, they were recorded by illuminating a very small area, measuring the reflected light with a

Fig. 4. Photomicrograph of a portion of the lower surface (in contact with stainless steel) showing the central "C"-shaped blisters on the right and the outer ring blisters on the left. The vertical dimension of the figure is 3/4 mm of the plate.



photomultiplier tube, and recording the light intensity as the plate was translated on the microscope stage (fringe profiles). To further understand the fringe systems, the fringe profiles were obtained at several wavelengths, and the chromatic fringe system observed at particular points on the plate were obtained by recording the light intensity as the wavelength was altered. These procedures were employed for fringe systems which covered the whole plate. Where local effects were seen, the fringe systems were photographed. In order to prevent confusion from reflection from the face opposite that being studied, the plate was set with an oil of matching refractive index on a glass plate whose back side was blackened. In particular cases, the chromatic fringe system over a larger wavelength range was obtained in a reflectivity unit for a DK-2A spectrophotometer in which an area about 1.2 mm across was illuminated. The contours of the plate surfaces were studied in a Twyman-Green interferometer, and defects which formed were examined in a Zeiss interference microscope.

The depth profiles of the depleted zones were determined from the scanning microscope recordings with monochromatic light (fringe profiles). The recorder tracings showed fringe maxima and minima whose positions were digitized and fed into a computer along with the assumed refractive index, the measured wavelength, the fringe order, and the plate dimensions. Then the computer performed the necessary computations and plotted the depth profile. Occasionally the fringes were irregular or confused and sometimes it was not certain that the first fringe at the edge of the plate was the first order. In these cases the fringe order at particular points on the plate were identified from the chromatic fringes. Their recorder tracings were digitized, and in the computer the data were converted to fringe location as a function of wave number, which is a linear function. A least squares fit was made and the thickness at this point was calculated from the slope of the regression. This thickness and the wavelength of the monochromatic fringes could be used to calculate the fringe order at this point.

If the boundary of the depleted zone is sharp, the amplitude of the chromatic fringes can be used to estimate the refractive index in the depleted zone from the

well-established formulas for the reflectivity of a layer on a substrate.

The weight loss of the plate (50-75 μg for the longer runs) as determined on a microbalance was sufficiently precise to calculate which constituents were depleted.

Materials.—Extensive results are reported here for Pyrex glass, an optical crown glass C-1 obtained from Hayward Scientific Glass Corporation whose composition is unknown (with refractive index 1.521 and density 2.57 g/cm^3), and a soda-lime glass whose typical pot composition was furnished to us as 13.86% Na_2O , 8.63% CaO , 3.82% MgO . One run was made on a

Table I. Ion equivalent of the measured charge (charges) and the original ion content of the depleted volume (DVC)

Sample No.	Charge (mC)	Depleted volume (10^{-6} cm^3)	Charges (10^{16})	DVC (10^{16})
C-1 glass cathodes ^a				
1	18.7	1.16	11.7	11.8
2	9.7	0.79	6.1	8.0
3	76.7	4.53	48.2	46.0
4	46.3	2.65	29.1	26.9
C-1 glass anode ^a				
19	226	14.3	142	146
Pyrex glass cathodes ^b				
14	8.1	3.36	5.09	5.95
15	13.1	5.3	8.25	9.39
16	25.8	10.1	16.2	17.9
17	51.3	20.4	32.2	36.1
Soda-lime glass ^c				
3907-1	34.6	2.72	21.9	21.7
3907-2	91.1	6.75	57.7	53.8
3907-3	75.7	6.25	48.0	49.8
Frit glass (borosilicate with titania) ^d				
3908-1	61.6	7.56	39.0	40.6

^a Assuming composition in text, no collapse correction, density 2.57 g/cm^3 , 1.02×10^{22} conducting charges/ cm^3 .

^b No correction for collapse.

^c Corrected for collapse.

^d Assuming zinc does not migrate, titanium changes valency by one, and sodium and calcium do migrate.

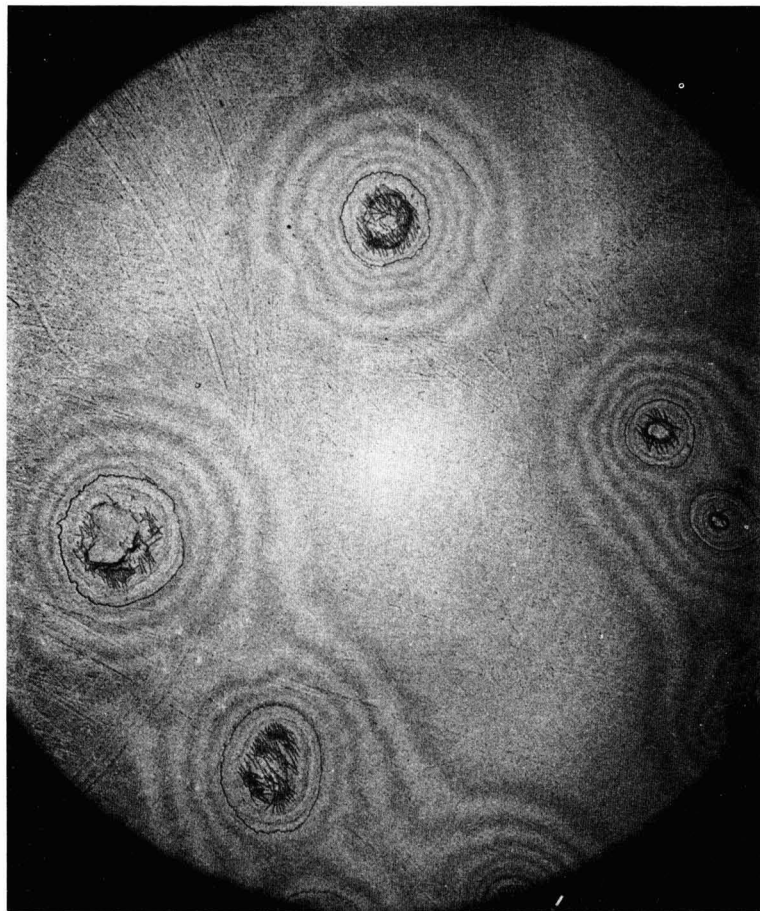


Fig. 5. Photomicrograph of some of the blisters in the central area seen in monochromatic light. The area covered is 1.8 mm across on the plate.

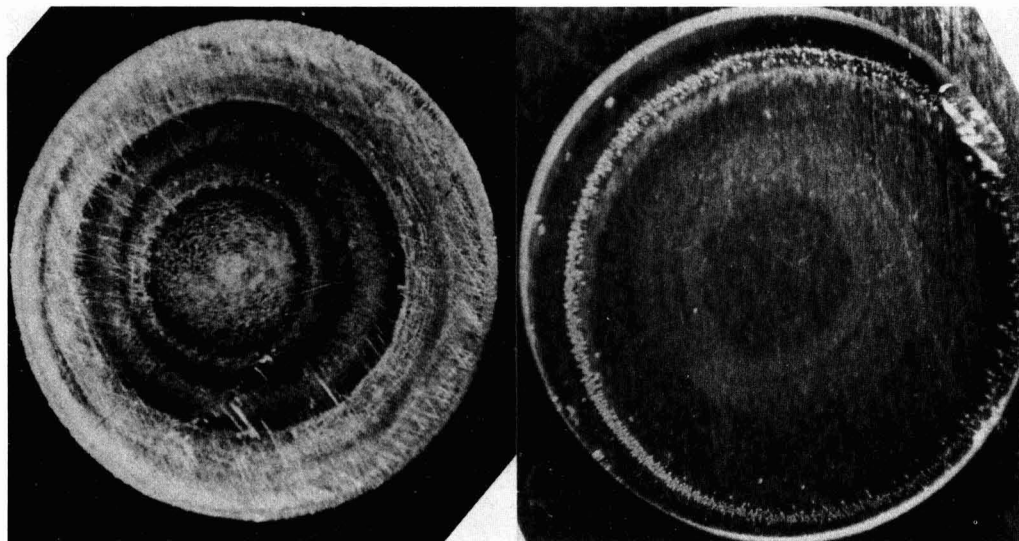


Fig. 6. Left, microphotograph of the stainless steel block; right, of the plate in contact with it. Note that the ring patterns of the blisters match.

Fig. 7. Interferogram of C-1 glass cathode after 135 mC. This is the face toward the discharge.



borosilicate glass containing 11.2% soda, 3% calcia, 7.45% zinc oxide, and 4.45% titania. All of the plates were about 1 cm diam.

Results

Most of the results were for the glass as the cathode. These were interpreted more easily because of the uniformity of the effects obtained. When the glass is the cathode, sodium migrates to the supporting plate and provides a more uniform electrical contact. When the glass is the anode, every irregularity and scratch in the supporting cylinder becomes visible on the contacting face of the glass, making the optical effects very irregular.

The Pyrex glass was found to conduct by 370°C, but the resistance was too high to conduct sufficient current until over 400°C. The results reported here are for 425°–430°C. The C-1 glass showed sufficient conduction by 219°C to permit a low current experiment. Most of the runs were at temperatures between 275° and 430°C. The soda-lime glass behaved in the same manner.

Cathodes.—The glass cathodes showed a well-defined depletion zone on the surface facing the discharge. This

could be examined and measured by the techniques described above. The shape of this zone depended somewhat on the conformity of the lower face with the stainless steel plate with which it was in contact and on the temperature. Typical scans of such plates taken with small aperture monochromatic illumination are shown in Fig. 1. Typical profiles of the depleted zones are shown in Fig. 2 and 3.

From the calculated volume of the depleted zones and the composition, the ionic content could be calculated, and this could be compared with the ion equivalent of the measured charge. In the case of the Pyrex glass, the ion equivalent of the measured charge was typically about 14% lower than the ionic content calculated from the volume of the depletion zone and the composition, corresponding to about 20% of the sodium being tied down by the aluminum (assuming a sharp boundary for depleted zone). For the soda-lime glasses whose composition was known, the ionic content matched the measured charge provided it was assumed that the calcium was also depleted and, in the glass containing titanium, that it changed in valence by

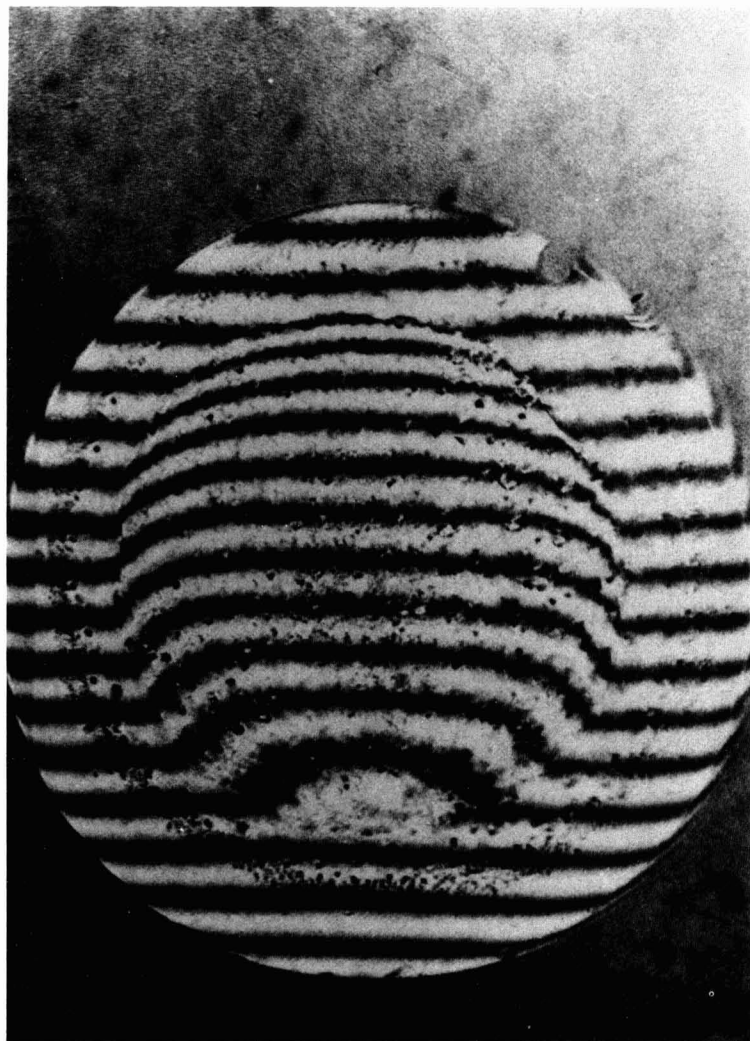


Fig. 8. Same as Fig. 7 but the face on the stainless steel plate.

1. The composition of the C-1 glass was not known, but if it is assumed to have a typical optical crown glass composition, 6.1% soda, 10.1% potassia, and 11.4% calcia, depletion of these ions would account, closely, for the observed depletion volumes. Results are given in Table I.

When the glass plate was removed from the stainless steel, droplets could be seen to condense on the contacting glass surface; and from the droplets, under the binocular microscope, little gas bubbles could be seen arising, evidently alkali reacting with water to evolve hydrogen. When the surface was washed off with water and dried, peculiar blisters were seen. In the center of the plate, which conformed more closely to the stainless steel, the blisters were larger and possessed a "C"—or donut shape. Farther out, toward the periphery, was a ring of smaller blisters, and this is presumed to be the edge of close electrical contact. The diameter of the peripheral ring varied, depending on the flatness which had been achieved in working the stainless steel. Photographs of the blisters are shown in Fig. 4 and 5. These figures should be compared with Fig. 8, shown above for another purpose, where the

whole surface can be seen, the outer row of blisters near the edge of the contact area and the collapsed central area where the "C"-shaped blisters occur. The stainless steel became stained with a pattern which matched the pattern of the blistering, as can be seen in Fig. 6. As is evident from the fringe pattern in Fig. 5, there are changes in refractive index, presumably associated with changes in composition, over a much larger volume than the volume of the blisters. Each of the blisters is fractured in the center, presumably where the sodium exuded and made contact with the stainless steel.

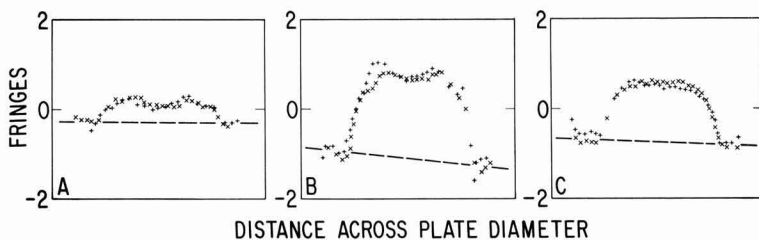
Pyrex glass has the refractive index 1.472 and a layer of vitreous silica (refractive index 1.458) will give chromatic fringes 9.4% of the reflectivity of the Pyrex glass. The amplitude of the chromatic fringes on the depleted layer was 6.7% corresponding to a refractive index 1.462. The same calculation made for the C-1 glass gave a value 1.483-1.487 for the refractive index of the depleted layer compared to 1.52 for the original glass.

The depleted layers on the Pyrex glass showed little collapse. The collapse observed with the C-1 glass

Fig. 9. Same as Fig. 8, but viewed through the thickness of the glass plate.



Fig. 10. The contours calculated A, from interferogram shown in Fig. 7; B, from Fig. 9; and C, from Fig. 8 are plotted as crosses. Also plotted, as x's are the contours from another set of interferograms of the same surfaces in which the fringes are vertical. The former gives the plate contour along the vertical diameter, the latter along the horizontal diameter.



varied but was particularly noticeable for the longer runs at the higher temperatures. Sample 12, run for 135 mC at 325°C was studied in detail because a central area had collapsed leaving an uncollapsed rim. Collapse occurred on both the depleted side and the side in contact with the stainless steel. The following interference patterns observed in the Twyman-Green interferometer were photographed: the reflection from each face; and the reflection from the back face, the

light passing through the sample. These were separated easily because the interferometer was illuminated with white light passing through an interference filter, and the visibility curve consisted of only about 50 fringes. Since the reflections from each face depend only on the distance and the reflection for light passing through the plate depends also on $(N-1)$ where N is the refractive index, the contour data could be used to calculate the refractive index of the collapsed region. The front face



Fig. 11. Photomicrograph of a C-1 glass anode, side in contact with stainless steel. A fracture traverses from the upper right to the left lower edge. The smaller dimension of the figure is 1 mm of the plate.

showed chromatic fringes corresponding to a 20.4 fringe thickness at wavelength 0.5461μ . The rear face also showed chromatic fringes which, in this case, corresponded to an increase in refractive index which was estimated as 0.036 and to a thickness corresponding to 2.22 fringes at wavelength 0.5461μ ; a small correction. The Twyman-Green interferograms were read by techniques which have been described (3), and the surface contours were calculated. The interferograms are shown in Fig. 7, 8, and 9 and the calculated contours in Fig. 10. It is seen that the front face collapsed 0.33 fringes, the back face 1.27 fringes, and fringe change in the interferogram of the reflection through the plate corresponded to 1.79 fringes. This last corresponds to

$$1.79 = (N - 1)D_2 + ND_1 + \Delta N_1[n_1/(N - \Delta N_1)] - \Delta N_2[n_2/(N + \Delta N_2)]$$

where N is the refractive index of the unaltered plate, 1.521, n is the fringe order, the subscript 1 refers to the

front face, and 2 refers to the back face. When the data are inserted, the equation becomes

$$1.79 = 0.521 \times 0.127 + 1.521 \times 0.33 + \Delta N_1[20.45/(1.521 - \Delta N_1)] - 0.036(2.22/1.557)$$

which gives 0.0488 for ΔN the change in index of refraction of the depleted zone, hence refractive index 1.4722. This is nearly the refractive index of vitreous silica. It indicates that both the alkali and the alkaline earths have migrated out of the depleted zone in this plate.

During a 212 mC run with the C-1 glass a $75 \mu\text{g}$ ($\pm 4 \mu\text{g}$) weight loss was found. If the C-1 glass is a typical optical crown glass, the soda-calcia/potassia ratio would be about 3/2, hence the electrochemical equivalent weight loss for the alkali, alkaline earth, and accompanying oxygen would account for the weight loss observed.

The occurrence of "C"-shaped blisters was typical for the back faces of the glass cathodes supported on stainless steel. For several runs, a graphite cylinder

was polished flat by rubbing on a flat lapped glass plate, and this was used as the supporting cylinder. For a 135 mC run with C-1 glass at a temperature of 330°C, the face in contact with the graphite showed a fairly uniform distribution of ordinary protuberances. The graphite, originally flat to a fringe, became convex about 6 fringes and was altered in color to a blue violet with gray spots. It is presumed that the reason for the glass behaving differently on the graphite is that the graphite absorbs and combines with the alkali.

Anodes.—Our initial attempts to utilize the glass plates as anodes were unsuccessful; the runs were interrupted by discharges and breakdown around the glass plate. However, when the technique of flattening the supporting cylinder was developed and the continuously adjustable voltage power supply was secured, the glass was operated successfully as the anode at the higher temperatures used with these glasses. If the runs were of any length, and particularly with the Pyrex glass, the glass plates were held with considerable force to the stainless steel when the electrode assembly was removed from the glow tube. It is presumed that this force was an electrostatic potential across the depleted layer. The pattern of scratches on the stainless steel cylinder was reproduced on the glass plate, in reverse; i.e., the scratches on the metal were matched with elevated lines on the glass. Typically, on cooling or after standing for some time, many of the plates developed curved fractures on the depleted side, having radii of a considerable fraction of the plate radius. Some of these fractures were close to the edge of the depleted region, others well within it. The fractures could be seen by tipping the plate under the binocular microscope to catch a reflection by side illumination, and they appeared to be much deeper than the depleted layer. There appeared to be a metallic deposit (possibly sputtered material) on the surface which was not easily removed. It was dissolved with boiling aqua regia. The scratch pattern then appeared to be fainter, but it was not removed. The above observations about its depth were made after removal of deposit. Between the lines of the scratch pattern there could be seen under the microscope in monochromatic light a patchy appearance which showed chromatic effects (relative intensity change with wavelength) indicating it may have been caused by small bubbles. This may be oxygen segregating when the zone is depleted. A photomicrograph is shown in Fig. 11.

It was not possible to study the depleted layer of these plates by scanning them under the microscope with monochromatic light because of the scratch pattern (or for the plates depleted on graphite, of the porosity pattern). However, it was possible to obtain the depth at a number of points along the radius by recording the chromatic fringes observed under the microscope with a small aperture. About the same volume relationships were found as for the depleted layers on the cathodes. Thus, it appears there is a fairly sharp boundary for the depleted layer under these conditions. The depleted layers of the anodes appear to have a rectangular profile compared to the "hat" shape of the cathodes. An example is shown in Fig. 12.

After standing for some time, the face in contact with the plasma developed a pattern which, under the microscope, appeared to consist of lighter patches and smaller circular darker areas. They did not show chromatic effects. In the interference microscope, the light patches were found to be areas which had spalled off; they were depressed to various depths from about 0.015 to 0.07 μ . A photomicrograph is shown in Fig. 13. At high magnification the interference pattern showed small concave areas in contact with each other, a scalloped surface, and in the midst of these concave areas sat the areas which had spalled off. The dark patches may have been an optical effect associated with

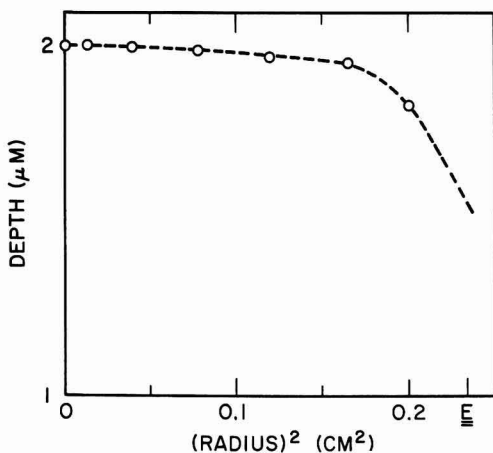


Fig. 12. Profile of the depleted zone of a C-1 glass anode plotted against the radius squared after 226 mC. E is the edge of the depleted zone.

the scalloping rather than the image of objects on the surface.

Discussion

When the glasses which have been studied (Pyrex, crown, soda-lime, and others) are used as electrodes in a glow tube, the alkali and light alkaline earth ions are transported leaving a depleted layer. Light alkaline earths are specified because chromatic fringes seen when a barium crown glass was employed were of small amplitude, indicating the barium had not been transported. Little evidence of the oxygen was seen, and it is presumed that, mostly, it diffuses out of the surface. However, there may have been some segregated within the glass when the depleted zone rested on a metal plate. When the anode is the free surface it is relatively undamaged, although secondary destruction may occur later (spallation of very thin layers). When the anode face of the plate is in contact with the metal (glass cathode) some of the segregation of metal occurs within the glass plate (much as growths may occur on electrodes in aqueous solutions) causing blistering and similar destruction. Similar but less severe destructive effects may be occurring with oxygen segregation in the cathode surfaces of the glass anodes, but the effects are less evident. However, because of the absence of the electrical contacting agent present in the other case (the deposited alkali metal) the experiments could not be carried as far.

Attempts have been made to utilize ceramic electrodes in open cycle MHD devices, and very destructive effects and short lifetimes have been encountered. As found here, the effects observed on cathodes have been much more severe than on anodes, suggesting the kinds of effects observed here make a significant contribution to the deterioration. These may be described briefly as caused by ionic transport to and segregation at interfaces, and by volume changes and associated stresses associated with the depletion and the "piling-up" of ionic constituents.

Acknowledgment

This work was supported by the U.S. Department of Energy.

Manuscript submitted Feb 28, 1979; revised manuscript received May 14, 1979.

Any discussion of this paper will appear in a Discussion Section to be published in the June 1980 JOURNAL. All discussions for the June 1980 Discussion Section should be submitted by Feb. 1, 1980.

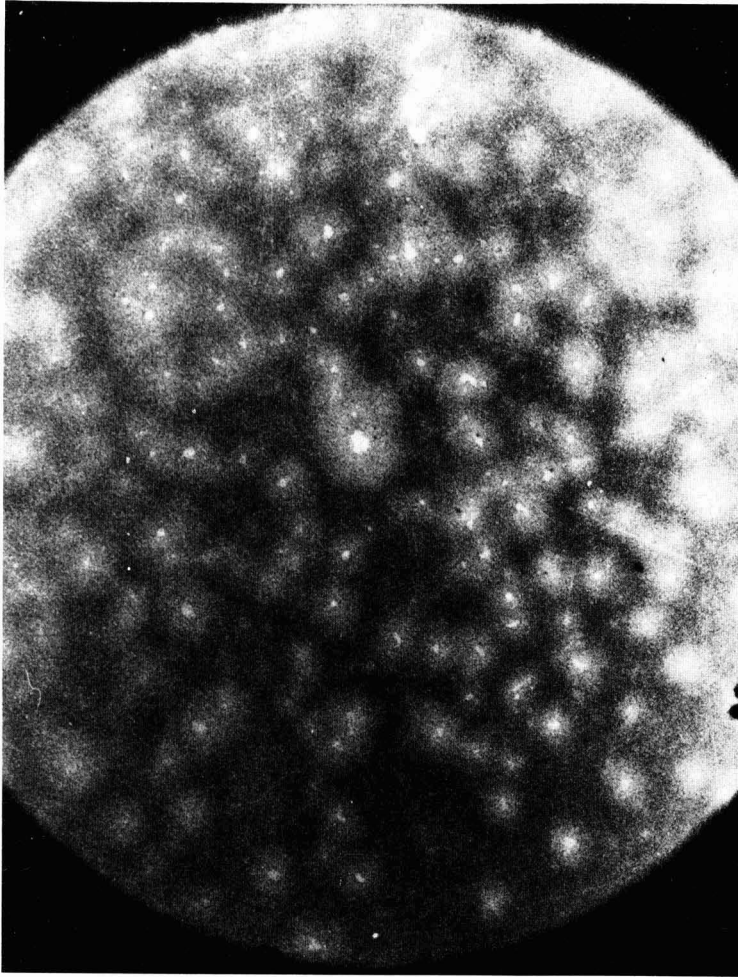


Fig. 13. Photomicrograph of a C-1 glass anode, side facing discharge, in interference contrast; the shading indicates different elevations, dark high. The diameter is 0.72 mm on the plate.

Publication costs of this article were assisted by Argonne National Laboratory.

REFERENCES

1. K. Wolf, *Z. Phys.*, **112**, 96 (1939).
2. W. Primak and E. Monahan, *This Journal*, **124**, 1816 (1977).
3. W. Primak, *Appl. Opt.*, **12**, 2894 (1976); *J. Nucl. Mater.*, **74**, 88 (1978).

Luminescence of Terbium-Activated Alkali Rare Earth Metaphosphate Glasses

T. Takahashi and O. Yamada

RCA Research Laboratories, Incorporated, Machida City, Tokyo, Japan

ABSTRACT

Excitation and emission spectra of Tb^{3+} were measured in alkali yttrium terbium metaphosphate glasses having the general composition $n(M_2O \cdot P_2O_5) [(1-x)Y_2O_3 \cdot xTb_2O_3 \cdot 3P_2O_5]$. The effects of Tb concentration, Ce codoping, and alkali and its concentration on the intensities of Tb^{3+} emission at the 4f–5d transition bands were investigated. The Tb^{3+} emission was anomalously enhanced at a Tb concentration where the population of Tb^{3+} – Tb^{3+} pairs becomes maximum. Sensitization of Tb^{3+} emission at the f–d bands was found to take place at a very low Ce concentration (<100 ppm), whereas the sensitization via the direct energy transfer from the Ce^{3+} absorption band occurred at higher Ce concentrations. The intensities of Tb^{3+} emission was found to increase in the order of Li, Na, K, when n is fixed, and with increasing alkali, when M is fixed.

Investigations on absorption and fluorescence spectra of rare earths in inorganic glasses such as borate, silicate, and phosphate glasses were extensively made in the past (1–3). However, the practical use of the glassy phosphor was seldom reported. The use of Nd or other rare earth-doped glasses in laser applications is perhaps the only exception (4). This is probably due to its weak fluorescence as compared with its crystalline counterpart. Recently, several crystalline rare earth metaphosphate compounds such as RP_3O_9 (5) and MRP_4O_{12} (6–8) have been investigated as laser materials or vacuum ultraviolet phosphors. In these stoichiometric compounds, the concentration quenching of fluorescence from the activator rare earth such as Nd, Eu, and Tb is suppressed due to the reduced interactions of these rare earths in the continuous PO_4 tetrahedra network. More recently, it was found that the metaphosphate glass having a composition identical to or related to these metaphosphate compounds could be made easily (9). A series of glasses having a composition $n(M_2O \cdot P_2O_5) (R_2O_3 \cdot 3P_2O_5)$, where $n \geq 0$, M = alkali, and R = yttrium or rare earth was prepared. Moreover, these glasses were found to fluoresce strongly when a suitable activator was incorporated. Indeed, the intensity of green emission of the Tb-activated glass was comparable to that of a good green emitting crystalline phosphor, $Zn_2SiO_4:Mn$ under 254 nm u.v. excitation. Therefore, it was thought that the fundamental fluorescent properties of these glasses should be understood in order to develop better glassy phosphors of practical importance. In this report, alkali yttrium terbium and alkali terbium glasses having the general composition $n(M_2O \cdot P_2O_5) [(1-x)Y_2O_3 \cdot xTb_2O_3 \cdot 3P_2O_5]$ were chosen to study the effects of various parameters such as Tb concentration, Ce coactivation, and alkali and its concentration on the fluorescent properties of Tb^{3+} ions. In the following text, the composition $n(M_2O \cdot P_2O_5) [(1-x)Y_2O_3 \cdot xTb_2O_3 \cdot 3P_2O_5]$ is abbreviated to $M_nY_{1-x}Tb_xP$ with M = L, N, or K, where L stands for Li and N stands for Na, respectively.

Experimental Procedure

Glass samples were prepared by casting the glassy melts of stoichiometric mixtures of M_2HPO_4 or M_2CO_3 , $(NH_4)_2HPO_4$, Y_2O_3 , and Tb_4O_7 into a cylindrical graphite die of 20 mm in diameter. They were then annealed in an electric furnace to remove thermal stresses. The purity of M_2HPO_4 , M_2CO_3 , and $(NH_4)_2HPO_4$ was of reagent grade. Y_2O_3 was 99.9%

grade. As Tb_4O_7 , five different reagents, three of which are of 99.9% grade and the other two of 99.999% grade, from four different suppliers were used. For Ce-doped samples, Ce-doped Tb_4O_7 was prepared by firing, at 1100°C, respective oxalates precipitated from the stoichiometric acidic solution. A polished glass plate of a few millimeters thick was used for various measurements.

Excitation, emission, and transmission spectra were measured with a Hitachi MPF-4 fluorescence spectrophotometer equipped with two gratings blazed at 300 nm and an on-line data processor that processes the measured data with an interval of 1 nm. The excitation spectra were corrected for the spectral sensitivity of the instrument with the on-line data processor, assuming a constant quantum efficiency of rhodamine B solution. No such correction was made for the emission spectra used for half-bandwidth measurements. Unless otherwise noted, all the excitation spectra of Tb^{3+} emission were measured on the Tb^{3+} emission due to the $^5D_4 \rightarrow ^7F_5$ transition at 543 nm with slit width of 5 nm.

Results and Discussion

Emission and transmission spectra.—Figure 1 shows an emission spectrum for a N_2TP glass under 250 nm excitation. The emission spectrum consists of emission lines due to $^5D_4 \rightarrow ^7F_k$ transitions of Tb^{3+} only. However, in glasses with low Tb content weak emission lines due to $^5D_3 \rightarrow ^7F_k$ transitions also appeared. The general features of the emission spectrum, i.e., peak position, peak shape, and relative intensity ratio of the observed emission lines changed very little with Tb or alkali atom concentration. Detailed descriptions of half-bandwidth variations with these parameters are to be discussed later.

Figure 2 shows a transmission spectrum for the same N_2TP glass. The glass has several absorption bands due to 4f–4f transitions of Tb^{3+} in the near u.v. region but it is fairly transparent from 400 to 700 nm except for an absorption band at ~480 nm. The intensities of these absorptions were proportional to the Tb concentration, as expected.

Effect of Tb concentration.—Excitation spectra of the $N_2Y_{1-x}Tb_xP$ system were measured to investigate the effect of Tb concentration on the intensity of Tb^{3+} emission. The Tb_4O_7 used in this experiment (designated $Tb_4O_7(A)$ in Table I) contained the least amount of Ce as an impurity so that the effect of Ce sensitization was very small (see next section). In Fig. 3, excitation spectra of three different glasses, i.e., $N_2Y_{1-x}Tb_xP$ glasses with $x = 0.1, 0.3$, and 1.0 are shown.

Key words: glassy phosphors, concentration dependence, Ce co-activation, energy transfer, inhomogeneous broadening.

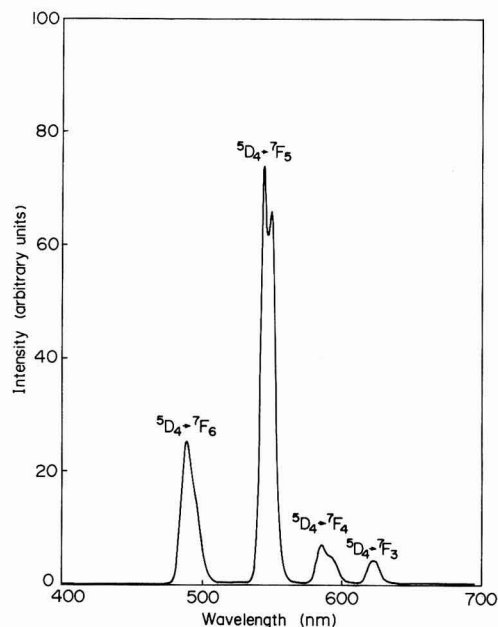


Fig. 1. Emission spectrum of $2(\text{Na}_2\text{O} \cdot \text{P}_2\text{O}_5)$ ($\text{Tb}_2\text{O}_3 \cdot 3\text{P}_2\text{O}_5$) glass under 250 nm excitation.

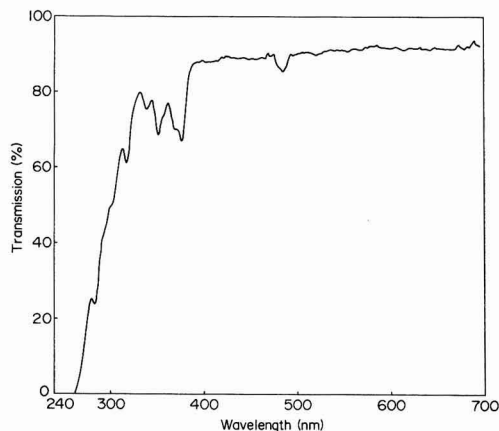


Fig. 2. Transmission spectrum of $2(\text{Na}_2\text{O} \cdot \text{P}_2\text{O}_5)$ ($\text{Tb}_2\text{O}_3 \cdot 3\text{P}_2\text{O}_5$) glass. Sample thickness = 1.5 mm.

It is seen that there exist two major bands in the excitation spectra, one at 220 ± 1 nm and another at 250 ± 1 nm. These two bands are known to be due to the $4f^8 \rightarrow 4f^75d$ transitions of Tb^{3+} . The transition $7F \rightarrow 7D$ is responsible for the stronger band at 220 nm, while the spin-forbidden transition $7F \rightarrow 9D$ is responsible for the weaker band at 250 nm (10, 11). The peak positions of these $f-d$ bands ($45.4 \times 10^3 \text{ cm}^{-1}$ and $40.0 \times 10^3 \text{ cm}^{-1}$) are in a fair agreement with those in Tb -doped YPO_4 crystal ($44.7 \times 10^3 \text{ cm}^{-1}$ and $37.3 \times 10^3 \text{ cm}^{-1}$) (12). Much weaker bands at longer wavelengths ($\lambda \geq 280$ nm) are due to $4f-4f$ transitions, as was pointed out previously. In Fig. 4, the peak intensities of Tb^{3+} emission at the two $f-d$ bands, $I(7F \rightarrow 7D)$ and $I(7F \rightarrow 9D)$, in the $\text{N}_2\text{Y}_{1-x}\text{Tb}_x\text{P}$ system are plotted against x . It is seen from Fig. 3

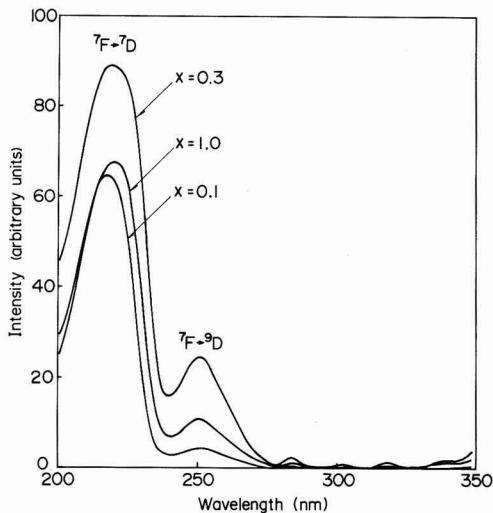


Fig. 3. Excitation spectra of Tb^{3+} emission in $2(\text{Na}_2\text{O} \cdot \text{P}_2\text{O}_5)$ $[(1-x)\text{Y}_2\text{O}_3 \cdot x\text{Tb}_2\text{O}_3 \cdot 3\text{P}_2\text{O}_5]$ glasses, $x = 0.1, 0.3$, and 1.0 .

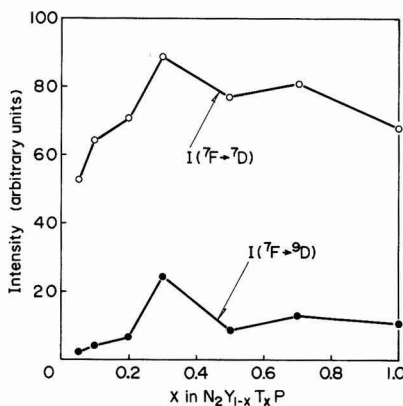


Fig. 4. Peak intensities of Tb^{3+} emission at $4f-5d$ transition bands vs. Tb concentration x in $2(\text{Na}_2\text{O} \cdot \text{P}_2\text{O}_5)$ $[(1-x)\text{Y}_2\text{O}_3 \cdot x\text{Tb}_2\text{O}_3 \cdot 3\text{P}_2\text{O}_5]$ glasses.

and 4 that the anomalous enhancement of the peak intensities, particularly of $I(7F \rightarrow 9D)$, took place at $x = 0.3$. The density of the $\text{N}_2\text{Y}_{1-x}\text{Tb}_x\text{P}$ glass, on the other hand, increased linearly with increasing Tb concentration from 2.82 g/cm^3 at $x = 0.05$ to 3.18 g/cm^3 at $x = 1.0$. No anomaly existed at $x = 0.3$ in the density data. This should mean that the enhancement of Tb^{3+} emission in the $\text{N}_2\text{Y}_{0.7}\text{Tb}_{0.3}\text{P}$ glass could not be caused by changes in structure or by phase segregation in it. Therefore, the enhancement effect must be accounted for by the $\text{Tb}-\text{Tb}$ interaction that was characteristic of this particular composition.

As in the case of YbP_3O_9 crystal (5), Tb^{3+} ions are most likely in truncated octahedra formed by six oxygens at the corners in the metaphosphate glass. Since the $\text{Na}-\text{O}$ bonds are weaker than $\text{Y}-\text{O}$ or $\text{Tb}-\text{O}$ bonds, sodium ions are distributed in interstitial sites in the YbP_3O_9 like structure. Each Tb^{3+} ion is then surrounded by six other Y^{3+} or Tb^{3+} ions as its nearest neighbors. When n out of Z nearest neighbor positions are occupied by Tb^{3+} ions, a molecule of $(n+1)$ activators results. The general relationship

for the activator concentration x_{n+1} at which the concentration of $(n+1)$ activator molecules becomes maximum is given by (13)

$$x_{n+1} = n + 1/1 + Z$$

The concentration for the maximum Tb^{3+} - Tb^{3+} pair population is then given by substituting $n = 1$ and $Z = 6$, i.e.

$$x_2 = 2/7 \sim 0.289 \sim 0.3$$

Accordingly, the population of Tb^{3+} - Tb^{3+} pairs should become maximum at $x \sim 0.3$ in the $N_2Y_{1-x}T_xP$ system. Recently, Danielmeyer (14) suggested that when active ions are arranged in pairs in an insulating medium, enhanced fluorescence could result due to crystal field overlap mixing of 4f and 5d states of pairing rare earth ions. The present observation could indeed be a typical example of such an enhancement effect.

On the other hand, the half-bandwidths of Tb^{3+} emission lines due to $^5D_4 \rightarrow ^7F_k$ transitions ($k = 3-6$) decreased with increasing Tb concentration. For example, the half-bandwidths of $^5D_4 \rightarrow ^7F_6$ emission band was 578 cm^{-1} for $x = 0.05$, and 525 cm^{-1} for $x = 1.0$, respectively. Again, there existed no anomaly at $x = 0.3$. The results indicate that the degree of inhomogeneity in crystalline symmetry around Tb^{3+} ions becomes large when the active ions are diluted.

Sensitization of Tb^{3+} emission by Ce^{3+} doping.—During the course of our above-mentioned experiments, it was noticed that the peak intensities of Tb^{3+} emissions at the f-d bands, especially $I(^7F \rightarrow ^9D)$ at $\sim 250\text{ nm}$, changed considerably when Tb_4O_7 raw materials from other suppliers were used. A careful examination of the emission spectra of these glasses revealed the presence of a weak emission band peaking at about 320 nm that was confirmed to be due to Ce impurity contained in the Tb_4O_7 raw materials. It was also found that the degree of enhancement of $I(^7F \rightarrow ^9D)$ was roughly proportional to the intensity of Ce^{3+} emission, i.e., to the Ce^{3+} concentrations. Table I shows the ratio of peak intensities of Tb^{3+} emissions, $I(^7F \rightarrow ^9D)/I(^7F \rightarrow ^7D)$ as well as the intensity of Ce^{3+} emission at 314 nm in the N_2TP glasses prepared from five different Tb_4O_7 raw materials. To find the approximate concentration of the impurity Ce in respective Tb_4O_7 , a series of Ce-doped N_2TP glasses were prepared by using Tb_4O_7 containing 200 to 5000 ppm Ce (with respect to Tb). The intensity of the Ce^{3+} emission peak at 314 nm in these glasses were measured. The Ce concentration in respective Tb_4O_7 was then estimated by extrapolating the log-log plot of Ce concentration vs. Ce emission intensity for the Ce-doped N_2TP glasses. Such numbers are listed in the last column of Table I. The error of this estimate could be as much as 40%. It should be noted that the claimed purity of Tb_4O_7 has little to do with the actual Ce contamination level. Figure 5 shows the excitation spectra of Tb^{3+} emission in 0.2 and 0.5% Ce-doped N_2TP glasses. It is seen that there appears a new band at 295 nm at this high Ce doping level. The in-

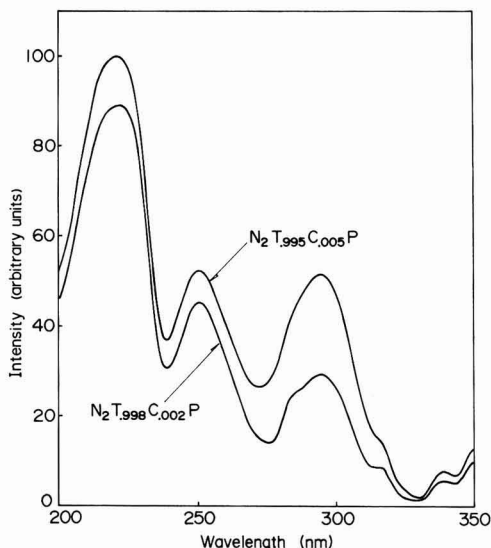


Fig. 5. Excitation spectra of Tb^{3+} emission in $2(Na_2O \cdot P_2O_5)$ $[(1 - \gamma)Tb_2O_3 \cdot \gamma Ce_2O_3 \cdot 3P_2O_5]$ glasses, $\gamma = 0.002$ and 0.005 .

tensities of Tb^{3+} emission at the f-d bands as well as that at 295 nm in the N_2TP glasses, both Ce-doped and undoped, are plotted against Ce concentration in Fig. 6. It is clearly seen that there exist two different sensitization mechanisms which are operative at different concentration ranges of Ce. First, the sensitization of Tb^{3+} emission at the f-d bands, particularly that of $I(^7F \rightarrow ^9D)$, is probably due to the nonradiative energy transfer from the 5d levels of Ce^{3+} to the 5d levels of Tb^{3+} , and starts to take place at a very low Ce concentration ($\geq 10\text{ ppm}$). Saturation seems to occur at about 100 ppm . In Fig. 7, the excitation spectra of Ce^{3+} emission at 314 nm in $N_2Y_{0.8}C_{0.2}P$ and $N_2T_{0.995}C_{0.005}P$ glasses (C stands for Ce) are shown. It can be seen that quenching of Ce^{3+} emission takes place approximately at the positions of f-d bands of Tb^{3+} in $N_2T_{0.995}C_{0.005}P$ glass. This may be taken as an evidence for the energy transfer from the 5d levels of Ce^{3+} to those of Tb^{3+} .

At a Ce concentration of 100 ppm or higher, the sensitization of Tb^{3+} emission via the energy transfer from the Ce absorption band at 295 nm to the 4f levels of Tb^{3+} becomes appreciable. Similar sensitization of Tb^{3+} emission by Ce^{3+} ions was reported in

Table I. Intensity ratio of Tb^{3+} emissions at f-d bands, intensity of Ce^{3+} emission at $\lambda = 314\text{ nm}$, and estimated Ce concentration in $2(Na_2O \cdot P_2O_5)$ $(Tb_2O_3 \cdot 3P_2O_5)$ glasses prepared from five different Tb_4O_7 raw materials

Tb_4O_7	Purity (%)	$I(^7F \rightarrow ^9D)/I(^7F \rightarrow ^7D)$	Intensity of Ce^{3+} emission (arbitrary units)	Ce concentration (ppm Ce/Tb)
A	99.9	0.143	10	4
B	99.9	0.405	24	10
C	99.9	0.487	733	130
D	99.999	0.509	160	35
E	99.999	0.484	40	15

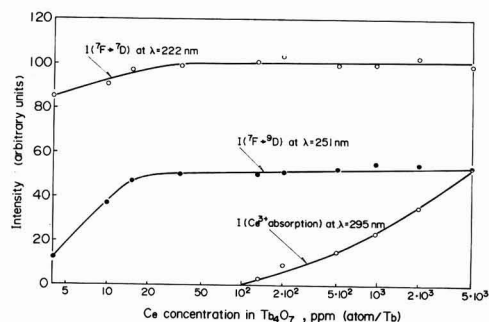


Fig. 6. Peak intensities of Tb^{3+} emission at 4f-5d transition bands, and at Ce absorption band, vs. Ce concentration in $2(Na_2O \cdot P_2O_5)$ $[(1 - \gamma)Tb_2O_3 \cdot \gamma Ce_2O_3 \cdot 3P_2O_5]$ glasses.

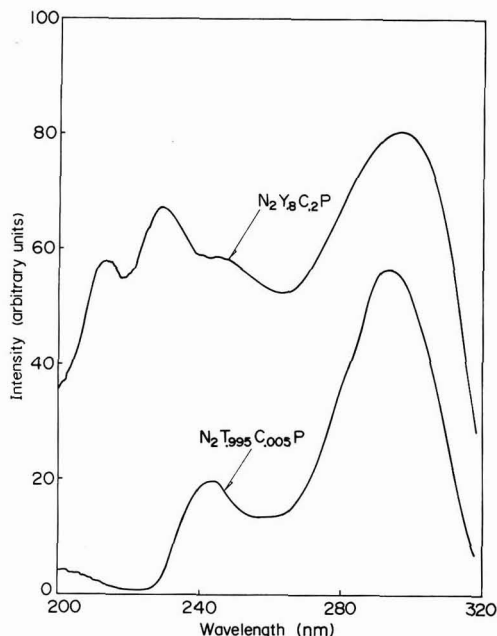


Fig. 7. Excitation spectra of Ce^{3+} emission in $2(\text{Na}_2\text{O} \cdot \text{P}_2\text{O}_5) (0.8\text{Y}_2\text{O}_3 \cdot 0.2\text{Ce}_2\text{O}_3 \cdot 3\text{P}_2\text{O}_5)$ and $2(\text{Na}_2\text{O} \cdot \text{P}_2\text{O}_5) (0.995\text{Tb}_2\text{O}_3 \cdot 0.005\text{Ce}_2\text{O}_3 \cdot 3\text{P}_2\text{O}_5)$ glasses.

$\text{Ca}(\text{PO}_3)_2$ glasses (15), in $\text{LiTb}_{1-x}\text{Ce}_x\text{P}_4\text{O}_{12}$, and in $\text{Tb}_{1-x}\text{Ce}_x\text{P}_3\text{O}_9$ crystalline phosphors (8).

In summary, we have observed the sensitization of Tb^{3+} emission at the f-d bands by Ce^{3+} ions. Since this sensitization seems to be operative only at a very low Ce concentration, interesting phenomena such as the pair enhancement described in the preceding section could well be masked unless the concentration of the Ce impurity in Tb_4O_7 is checked carefully.

Effects of alkali and its concentration.—As mentioned previously, the emission spectrum of $\text{M}_n\text{Y}_{1-x}\text{I}_x\text{P}$ glasses changes very little with M, n and x. However, the intensity of Tb^{3+} emission at the f-d bands, as well as the half-bandwidth of Tb^{3+} emission lines, change considerably with these parameters. The effect of Tb concentration has already been discussed. To investigate the effect of alkali M and its concentration n on Tb^{3+} emission, a nonalkali-containing TbP_3O_9 glass and a series of alkali terbium glasses M_nTP , with M = Li, Na, or K, and n = 2, 4, or 6, were prepared. The Tb_4O_7 raw material, Tb_4O_7 (B) of Table I, was used throughout. In Fig. 8, the intensities of Tb^{3+}

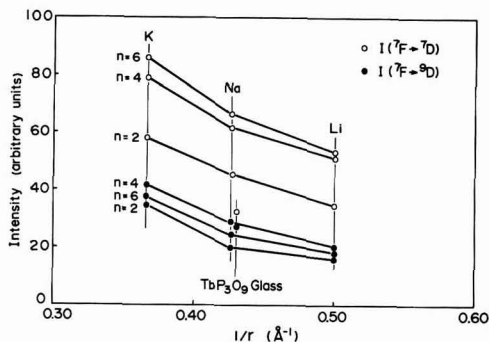


Fig. 8. Peak intensities of Tb^{3+} emission at 4f-5d transition bands vs. $1/r$ in TbP_3O_9 and $n(\text{M}_2\text{O} \cdot \text{P}_2\text{O}_5) (\text{Tb}_2\text{O}_3 \cdot 3\text{P}_2\text{O}_5)$ glasses. The quantity r is the radius of Tb^{3+} or M^+ ion plus that of oxygen (1.40 Å).

emission at the f-d bands for these glasses are plotted against $1/r$, where r is the radius of Tb^{3+} or M^+ ion plus the radius of the oxygen ion (1.40 Å). The peak positions of the f-d bands of these glasses are listed in Table II. In Table III, the half-bandwidth data of Tb^{3+} emission lines due to $^5\text{D}_4 \rightarrow ^7\text{F}_k$ transitions ($k = 3-6$) are summarized. First, it is seen that both $I(^7\text{F} \rightarrow ^7\text{D})$ and $I(^7\text{F} \rightarrow ^9\text{D})$ decrease linearly with increasing $1/r$, or increase with increasing r , when n is fixed. At the same time, the peak positions of the f-d bands shift slightly toward longer wavelengths, and the half-bandwidth increases in the order of Li, Na, and K, respectively. According to Reisfeld (1), the shift of the f-d absorption of Ce^{3+} or Tb^{3+} toward longer wavelengths, a so-called nephelauxetic effect, can be brought about when active ion-oxygen ion bonds become more covalent. On the other hand, the half-bandwidth is considered a measure of inhomogeneity in microcrystalline symmetry around active ions. The wider the half-bandwidth, the more inhomogeneous the microcrystalline symmetry. The peak intensity of emission from active ions is generally expected to decrease with increasing inhomogeneity in microcrystalline symmetry. Accordingly, the observed intensity change with alkali must be explained by the change in nature of Tb-O bonding. As was mentioned, the presence of an increasing nephelauxetic effect in the order of Li, Na, and K means that the covalency of Tb-O bonding increases in this order. This can be expected because the electrons of oxygen ions are shifted more toward Tb^{3+} ions as M-O bonds become increasingly ionic with increasing electronegativity difference between M and O. Therefore, the increasing covalency of Tb-O bonding seems to explain the observed intensity increase with increasing ionic radius of alkali. The same rea-

Table II. Peak positions of f-d transition bands in TbP_3O_9 and $n(\text{M}_2\text{O} \cdot \text{P}_2\text{O}_5) (\text{Tb}_2\text{O}_3 \cdot 3\text{P}_2\text{O}_5)$ glasses (wavelength in nm)

	TbP_3O_9	L/TP	L/TP	L/TP	N/TP	N/TP	N/TP	K/TP	K/TP	K/TP
$^7\text{F} \rightarrow ^7\text{D}$	224	221	220	220	221	221	222	221	225	224
$^7\text{F} \rightarrow ^9\text{D}$	246	248	248	249	250	252	252	252	253	254

Table III. Half-bandwidths of $^5\text{D}_4 \rightarrow ^7\text{F}_k$ Tb^{3+} emission bands in $n(\text{M}_2\text{O} \cdot \text{P}_2\text{O}_5) (\text{Tb}_2\text{O}_3 \cdot 3\text{P}_2\text{O}_5)$ glasses (wave numbers in cm^{-1}).

	TbP_3O_9	L/TP	L/TP	L/TP	N/TP	N/TP	N/TP	K/TP	K/TP	K/TP
$^5\text{D}_4 \rightarrow ^7\text{F}_6$	611	519	498	481	525	501	505	539	497	513
$^5\text{D}_4 \rightarrow ^7\text{F}_5$	378	352	330	337	357	341	361	374	344	361
$^5\text{D}_4 \rightarrow ^7\text{F}_4$	487	410	397	405	410	400	402	427	391	410
$^5\text{D}_4 \rightarrow ^7\text{F}_3$	301	263	242	252	260	262	258	276	260	268

soning may also be applied to explain the anomalously weak $I(^7F \rightarrow ^7D)$ of TbP_3O_9 glass, since its $Tb-O$ bonding is expected to be more ionic than that in any of M_nTP glasses. However, it cannot explain the disproportionately strong $I(^7F \rightarrow ^9D)$ of the same glass.

When alkali M is fixed, on the other hand, $I(^7F \rightarrow ^7D)$ increases with increasing n , but $I(^7F \rightarrow ^9D)$ becomes maximum at $n = 4$. No nephelauxetic effect seems to exist when the alkali content is changed. The half-bandwidth decreases markedly when alkali is added compared to the case of TbP_3O_9 glass. It becomes minimum at $n = 4$, coinciding with the occurrence of a maximum $I(^7F \rightarrow ^9D)$ at the same n . These results seem to indicate that as more alkali is added certain atomic arrangements are stabilized more frequently than others so that inhomogeneity in microcrystalline symmetry around Tb^{3+} ions is decreased. Therefore, the intensity increase with increasing alkali can be explained well by the improved or more homogeneous microcrystalline symmetry around Tb^{3+} ions.

Summary

The effects of Tb concentration, Ce coactivation, and alkali and its content on Tb^{3+} emission intensities at the $f-d$ bands were investigated in $M_nY_{1-x}T_xP$ glasses. In the $N_2Y_{1-x}T_xP$ system, the enhancement of Tb^{3+} emission was found to occur at the Tb concentration where the $Tb^{3+}-Tb^{3+}$ pair concentration becomes maximum. This pair enhancement might be explained by a crystal field overlapping model. In the $N_2T_{1-y}C_yP$ system, the sensitization of Tb^{3+} emission at the $f-d$ bands, via a probable energy transfer from 5d levels of Ce^{3+} to those of Tb^{3+} , was found to take place at very low Ce concentrations. At higher Ce concentrations (>100 ppm), the sensitization via an ordinary energy transfer from the Ce^{3+} absorption band took place. In the M_nTP system, the intensity of Tb^{3+} emission increased with increasing ionic radius of alkali, when n is fixed, and with increasing n , when M is fixed. The former observation was explained by the change in the bonding nature of $Tb-O$ bonds, whereas the latter was interpreted by the change in microcrystalline symmetry around Tb^{3+} ions.

Acknowledgments

The authors wish to thank E. O. Johnson and F. Okamoto for their continuous encouragement during the course of this work. They also wish to thank H. Fujita for his technical cooperation at the early stage of this work.

Manuscript submitted April 23, 1979; revised manuscript received May 14, 1979. This was Paper 223 presented at the Boston, Massachusetts, Meeting of the Society, May 6-11, 1979.

Any discussion of this paper will appear in a Discussion Section to be published in the June 1980 JOURNAL. All discussions for the June 1980 Discussion Section should be submitted by Feb. 1, 1980.

Publication costs of this article were assisted by RCA Research Laboratories.

REFERENCES

1. R. Reisfeld, *Struct. Bonding*, **13**, 53 (1973).
2. T. Komiya and T. Ueno, *Yogyo Kyokai Shi*, **80**, 227 (1972).
3. T. Komiya, *ibid.*, **83**, 32 (1975).
4. E. Snitzer, *Ceramic Bull.*, **52**, 516 (1973).
5. H. Y-P. Hong, *Acta Crystallogr., Sect. B*, **30**, 1857 (1974).
6. T. Yamada, K. Otsuka, and J. Nakano, *J. Appl. Phys.*, **45**, 5096 (1974).
7. H. Y-P. Hong, *Mater. Res. Bull.*, **10**, 1105 (1975).
8. T. Tsujimoto, Y. Fukuda, and M. Fukai, *This Journal*, **124**, 553 (1977).
9. T. Takahashi, O. Yamada, and H. Fujita, in *Proceedings of 38th meeting, Japan Soc. Appl. Phys.*, p. 200 (1977).
10. J. L. Ryan and C. K. Jørgensen, *J. Phys. Chem.*, **70**, 2845 (1966).
11. T. Hoshina, *J. Chem. Phys.*, **50**, 5158 (1969).
12. T. Hoshina and S. Kuboniwa, *J. Phys. Soc. Jpn.*, **31**, 838 (1971).
13. L. G. Van Uitert and L. F. Johnson, *J. Chem. Phys.*, **44**, 3514 (1966).
14. H. G. Danielmeyer, *J. Luminescence*, **12/13**, 179 (1976).
15. S. Shionoya and E. Nakazawa, *Appl. Phys. Lett.*, **6**, 118 (1965).

Optical and Electrical Characterization of Electrophoretic Displays

V. Novotny and M. A. Hopper*

Xerox Research Centre of Canada, Mississauga, Ontario, L5L 1J9 Canada

ABSTRACT

The operational optical and electrical characteristics of an electrophoretic display based on anatase TiO_2 suspended in a dyed dielectric fluid are described. Optical response times as low as 10 msec were obtained with this system. The optical response of the device is related to the TiO_2 particle mobility and to the dynamics of removal of a charged particle from a conducting electrode. The electric field threshold was found to be controlled by the particle-electrode interaction forces which are in the 10^{-10}N range. The electrical conductivity of the system results mainly from charge control agent (which dissociates into ions) remaining in solution. Despite this ionic conduction, electrical resistivities of the order of $10^{10}\ \Omega\text{cm}$ and switching energy densities of $3\ \mu\text{J}/\text{cm}^2$ were obtained. The optimal performance of this type of display device is predicted. The response time, electric field threshold, and electrical conductivity limitations of the electrophoretic display are outlined. Possible improvements in the materials package and cell fabrication techniques to overcome some of these drawbacks are suggested.

The electrophoretic display (EPD) is a passive device utilizing electric field induced migration of charged pigment particles in a fluid suspension containing a contrasting dye. The "on" and "off" optical states are produced by moving the particles toward or away from a viewing transparent electrode. With the development of a suitable materials package this concept has the potential of providing a low profile display device that would operate at reasonably low voltages with low power consumption. In addition, it can provide high optical contrast under ambient lighting conditions.

In the years following the invention of the EPD (1) various groups (2-4) have studied the behavior of different versions of these devices. This work has confirmed that the EPD has many of the features desired for passive display application. However, the device has certain limitations mainly associated with the complexities of formulating a suitable materials package and the influence of the properties of the suspension on the characteristics of the system.

In this publication we present the results obtained in a study of a tightly controlled EPD materials package. Simultaneous measurement of the optical and electrical characteristics of an EPD cell were made as a function of variations in the formulation of the suspension. We also examined some basic properties of these charged particles in dielectric media and attempted to relate the operating characteristics of the device to the particle mobility, charge, and the force of interaction between a charged particle and a conducting electrode. In this way we are able to define which materials formulation parameters have to be modified to produce a display with optimal characteristics and to examine the fundamental limitations of the process.

Materials: Selection

The choice of a materials package for the EPD depends, to some extent, on the features desired in the particular display application under consideration. We started from the premise that a passive device should closely resemble the optical properties of a printed page. This application requires investigation of a system which alternates between white and a dark contrasting color. The choice of available materials is thus somewhat reduced and we considered a suspension of

charged "white" particles in a dielectric fluid containing molecularly dissolved dye.

The particles that provide the best "white" image are those exhibiting a large scattering power. Of all the readily available pigments titanium dioxide has the greatest refractive index and is the obvious choice for the "white" particles. We chose to use the anatase form of this pigment rather than rutile even though it has a lower refractive index. Anatase is less dense and has a smaller static dielectric constant than rutile. These factors compensate, to some degree, for the decreased optical reflectivity by reducing gravitational settling and dielectrophoretic phenomena.

As TiO_2 particles are not readily dispersed in an insulating fluid a dispersant must be used to facilitate dispersion. In addition, a charge control agent (CCA) is required to impart a permanent charge to the pigment particles. We used an ionic surfactant in a dual role of dispersant and CCA for xylene suspensions of TiO_2 . This surfactant may not provide optimal stability or particle charge but appears to impart a stable charge to the TiO_2 particles. Preliminary experiments indicated that the conductivity of a suspension of TiO_2 in xylene with added CCA was dominated by surfactant remaining in solution, particularly when the materials were not maintained in a moisture-free environment. The adsorption isotherm for the CCA on TiO_2 was determined using atomic absorption and infrared spectroscopy and electrical conductivity measurements. At monolayer coverage of the surfactant on the TiO_2 the dispersion has maximum stability.

Optical contrast with the "white" TiO_2 particles is developed by adding a dye to the dielectric suspending fluid. To provide good hiding power the dye solution should be as absorbing as possible in the visible spectral region. The dye should be reasonably pure and free of ions as it is used at high concentration. In many applications the electrical conductivity of the system has to meet rather severe criteria. Moreover, the dye should preferably be a passive component of the system. Interactions between the particles and the dye should be minimal to maintain the optical contrast and particle charge. Two dyes which appear to satisfy the conductivity requirements, but interact somewhat with the particles are Oil Blue A and Sudan Black B.

A suspension was prepared by adding an appropriate amount of dried CCA and TiO_2 to the suspending fluid (xylene). This mixture was dispersed using ultrasonic agitation and the dye was then added to the solution.

* Electrochemical Society Active Member.

Key words: display, electrophoresis, titanium dioxide, conductivity, particle-electrode interactions.

This suspension was then transferred to the measuring cell.

Methods of Characterization

The performance of any display device is characterized by its optical and electrical behavior. Important parameters include response times, electrical field thresholds, memory, contrast ratio, electrical current densities, and over-all power consumption. In this work we set out to examine both the performance of the EPD and to estimate some fundamental properties of the electrophoretic dispersion system, such as particle size, mobility, charge, particle-substrate interaction forces, and relevant ionic mobilities. For this task we refined the technique of simultaneous optical and electrical transient measurements. In this procedure a voltage waveform is applied to the particle dispersion contained in a suitable cell and its optical and electrical response is monitored. The technique is schematically illustrated in Fig. 1. The dispersion containing the particles and the dyed suspending fluid is placed in a planar capacitor cell. The cell thickness is defined by an inert polymeric spacer which is clamped mechanically between two glass plates coated with transparent tin or indium oxide electrodes. Monochromatic light is directed onto the cell at an angle of incidence of 45° and the light scattered from the particles is detected by a photomultiplier positioned normal to the cell surface. Measurements with a white light source would, in certain cases, provide more appropriate device characteristics but as we are interested in understanding the fundamental aspects of the device, use of monochromatic light allows for a simplified interpretation of the data. The scattered light intensity reflects changes in the spatial distribution of particles in the cell which in turn can be related to the response times, memory, and under some conditions, to particle velocities. The photomultiplier signal is amplified and fed into one channel of a multichannel analyzer. The driving voltage waveforms were produced either by a wave generator or by a digital-to-analog converter operating under microprocessor control. These waveforms were amplified by power supplies capable of delivering high voltages and currents allowing cell charging to occur on a time scale ($<10 \mu\text{sec}$ to 99% of the final voltage) that is short when compared to the observed optical or electrical transients.

The electrical currents are followed by measuring the voltage developed across a resistor in series with the cell. This voltage is amplified and fed into a second channel of the multichannel analyzer. The charge flowing through the electrophoretic cell was evaluated by numerical integration of the current. The analyzer is interfaced to a minicomputer which is used for data analysis and graphical recording.

Details of the methods used to study the fundamental properties of suspensions of charged particles in a fluid are described in another publication (5), where the

analysis of the optical transients is discussed and additional experimental details are given.

In the remainder of this section we define the relevant device parameters. The on-time t_{on} and off-time, t_{off} , are defined, in this paper, as the elapsed time for the intensity of the scattered light to change by $\Delta I(1 - z)$. ΔI is the difference between the saturated scattered light intensities in the on and off states, i.e., $\Delta I = I_{\text{on}} - I_{\text{off}}$. The selection of a particular value of z is somewhat arbitrary but for an approximately exponential process the choice of $z = 1/e$ is appropriate. Alternative values such as $z = 0.1$ could also be employed. The memory time may be defined in a similar manner. For a square wave driving voltage reproducible response is observed if the voltage is applied for a time about three times longer than the response time. Measurements are made after about 100 cycles of the applied voltage have elapsed. The definitions of voltage or electric field thresholds required for switching this display device are somewhat arbitrary as the number of particles removed from the electrodes depends on the previous applied voltage history. We measure the intensity of scattered light, I , as a function of the applied square wave field, E , with monotonically increasing or decreasing field and define threshold as equivalent to dI/dE . Finally, the energy required to switch the device is equal to the integral of the product of applied voltage and device current over the longer response time (t_{on} or t_{off}).

Results and Discussion

Optical properties.—The optical response of a typical EPD cell to a square wave driving voltage is shown in Fig. 2. This particular cell was fabricated using a $64 \mu\text{m}$ spacer and encloses a suspension containing sufficient TiO_2 particles to give an electrode coverage of approximately three and one-half particle layers when fully imaged on the electrode. For the concentration of dye used in this experiment the extinction distance was $20 \mu\text{m}^{-1}$ at 632.8 nm . The amplitude of the applied 8 Hz square wave driving voltage was 100V. The inserts in Fig. 2 show, on expanded time scales, the details of the optical changes that occur in the period immediately following the reversal of the applied driving field.

The optical response of the device is naturally field dependent. Figure 3 shows the observed field dependence of both the on-time, t_{on} , and the off-time, t_{off} , for four different cells. These results show the reasonable consistency between cells of varying spacing containing different concentrations of particles and of added charge control agent. As outlined in the previous section the response times are measured at the $1/e$ points in the optical response characteristic and this is depicted in the inserts in Fig. 3. The scatter in the points shown in Fig. 3 is not due to inaccuracies in the measurements but reflects the dependence of the response times on waveform frequency. The lines drawn in the figure indicate a linear time vs. $1/E$ dependence.

To understand the relation between the measured optical response of the EPD cell and the fundamental properties of the materials, optical and electrical transient experiments were also performed on a system containing very few particles. These sub-monolayer studies are described in detail elsewhere (5) and only observations relevant to the EPD will be reported here. At low pigment concentration particle-particle interactions are minimized and the transient optical response can be used to estimate the mobility of the particles. This allows an estimate of the particle charge using the usual treatment of the electrostatic driving force being balanced by viscous drag giving rise to a condition of constant velocity. The size of the particles was determined by *in situ* quasi-elastic light scattering and the average diameter found to be $1.2 \mu\text{m}$ even though the primary particle size is $\sim 0.2 \mu\text{m}$.

The sub-monolayer studies showed that the mobilities of the particles were strongly dependent on the concentration of excess CCA in the fluid. The adsorp-

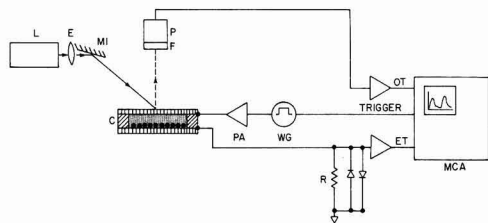


Fig. 1. Experimental arrangement for optical and electrical characterization of electrophoretic displays. C is the electrophoretic cell containing the suspending fluid with dissolved dye, charge control agent, and particles; L is a laser; E is a beam expander; M a mirror; F a filter; P a photomultiplier; WG a wave generator; PA a power amplifier, and MCA a multichannel analyzer.

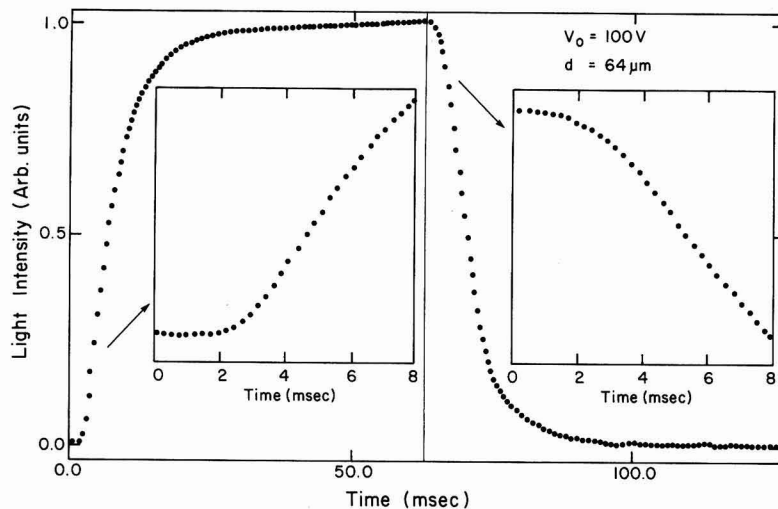


Fig. 2. The optical response of an EPD containing approximately 3.5 layers of TiO_2 particles for an applied voltage of 100V with a $64 \mu\text{m}$ cell. The inserts show, on an expanded scale, details of the response at times shortly after the polarity of the square wave driving field was reversed.

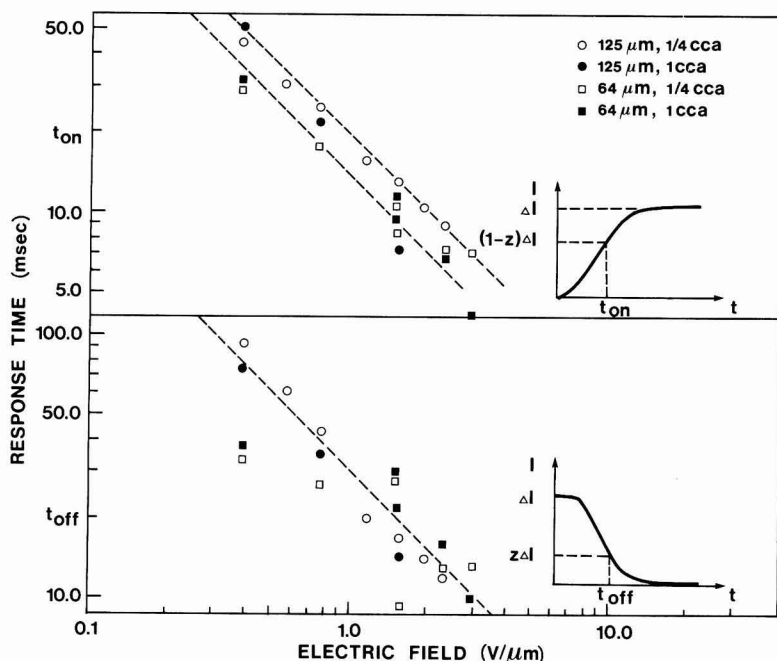


Fig. 3. Field dependence of the response times, t_{on} and t_{off} for four EPD cells. The $64 \mu\text{m}$ cell contained approximately 3.5 layers of particles and the two formulations shown differed in the charge control agent content (by factor of four). The same EPD mixtures were used for the $125 \mu\text{m}$ cell resulting in a doubling in the number of particle layers. Schematic diagrams illustrating the definitions of the response times are included.

tion of this CCA on the particle is partially reversible, i.e., it appears impossible to completely remove the "free" CCA from the fluid volume. Minimizing the amount of CCA in solution leads to an optimal particle mobility. Experiments were made on systems with and without the addition of the contrasting dye. The results of these experiments show that addition of the dye decreases the particle mobility. Adsorption of dye on the TiO_2 surface was also detected. These results suggest that adsorbed dye interferes with the charging process at the TiO_2 /fluid interface. Furthermore, it was observed that the apparent particle mobility increases with increasing electric field. At typical imaging fields and CCA concentrations used in EPD the mean particle mobilities were $5 \times 10^{-5} \text{ cm}^2/\text{Vsec}$ in the presence of the dyes. These mobilities correspond to a particle charge $Q = 4.5 \times 10^{-17} \text{ C}$ or 300 positive unit charges.

If the "on" response times were limited only by particle transit through the cell, then the on-time would be 5.0 msec for a $50 \mu\text{m}$ cell at a driving voltage of 100V. At CCA concentrations lower than those required in our EPD mobilities up to $8 \times 10^{-4} \text{ cm}^2/\text{Vsec}$ were observed.

At low particle concentration, corresponding to far less than a layer of particles on the electrodes after imaging, reversal of the field applied to an imaged cell did not result in an instantaneous removal of particles from the electrode. A certain delay time before any particles migrate was observed. This delay time in the removal of particles from an electrode was field dependent, decreasing with increasing field. Under certain conditions, generally at the lower cell thicknesses, it was observed that the removal time in the sub-monolayer case was comparable to, or greater than

the transit time of the particles through the cell. Removal times, defined as that time where a maximum number of particles leaves the electrode per unit time, were measured directly and found to be around 6.0 msec at imaging fields of $1.6 \text{ V}/\mu\text{m}$.

In the EPD cell sufficient particles have to be present to provide an acceptable optical contrast. For our anatase particles in the dyed fluid this requires that at least three to four layers of TiO_2 particles must be present to give a reasonable "white" image. In the simplest description of the processes involved in removing these particles from an electrode we might consider that the second, or any subsequent layer, is less strongly attached to the electrode than the layer directly in contact with the electrode. This will lead to instantaneous removal of the outer layers or removal with a shorter delay time than that for a sub-monolayer from the electrode. The delay time for the monolayer in contact with the electrode will reflect the removal times of all other layers and its own removal time.

In the optical response of the EPD the amplitude of the reflected signal is controlled mainly by the presence of the first most strongly held layer of particles. This layer was estimated to contribute about $(1 - 1/e)$ of the maximum signal attainable with the anatase/dye system. This means that the time taken to convert the image from "black" to "white," t_{on} , mainly reflects the arrival of the first layer of particles at the viewing electrode. These particles are those originating in the more weakly bound layers at the opposite electrode or those particles redistributed spatially through the cell. Comparison of the on-time with our earlier studies on the mobility of these particles at low concentration indicates that t_{on} is partially controlled by the particle transit time. The times plotted in Fig. 4 show that t_{on} is not completely proportional to cell thickness. However, the thicker cells contained more layers of particles and some spatial distribution of particles through the cell leads to a shortening of the on-times.

The off-time, t_{off} , is governed by the removal of the most strongly bound particles. The results summarized in Fig. 4 show that at any particular field t_{off} is greater than t_{on} and this is further evidence that particle removal from the electrodes controls the off-time. A quantitative description of the above concept has been developed to model the optical response of the EPD device and details were presented in another publication (6).

Electrical properties.—The transient electrical response accompanying the optical changes for the EPD device depicted in Fig. 2 is given in Fig. 4. The electrical transient behavior arises from many different contributions and this is discussed in more detail below.

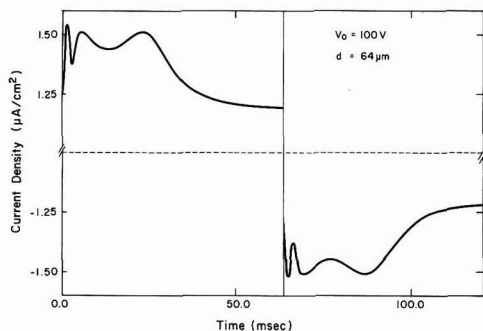


Fig. 4. The electrical current transient of an EPD observed simultaneously with the optical transient shown in Fig. 2. Note that the major portion of the steady-state current density has been removed in plotting the current.

The complex electrical transient behavior accompanying the imaging process is the result of many different interactions in the materials package. To assess the relative importance of the various contributions, the electrical transient accompanying application of a square wave driving voltage to a cell containing various sub-sets of the materials package was determined. Figure 5 shows the relative current densities observed as the various components are added to the suspension fluid. Xylene alone exhibits transient current densities of $\sim 1.0 \text{ nA}/\text{cm}^2$ for $100 \mu\text{m}$ cell at a field of $1 \text{ V}/\mu\text{m}$ and the addition of the dye, at EPD concentration, leads to an order of magnitude increase in the transient current and the appearance of a defined current peak. Addition of the charge control agent to the xylene produces a much larger "steady" current as this compound ionizes, to some degree, in the fluid. A current peak characteristic of the solute is observed on reversing the applied field. The transient electrical behavior of this system was studied in considerable detail and the results have been reported elsewhere (7). A solution containing both the charge control agent and the dye shows transient currents greater than the sum of the currents of solutions of these species alone. This indicates an interaction between these solutes producing a greater concentration of ionic species. It should be noted that moisture present in any of these materials can produce even greater changes than those shown in Fig. 5 and at every stage we attempted to keep the water content of all materials at the lowest practical level. It is obvious from Fig. 5 that addition of anatase particles to the system also results in a dramatic increase in the transient conductivity. The first current peak, in Fig. 4 and 5, may be ascribed to the positive ion of the charge control agent as its position corresponds exactly to that observed for the CCA in xylene (7). This current peak time varies with applied field and cell thickness in exactly the same manner as was found for the surfactant in the solvent. The large increase in current observed on adding the particles to the fluid system shows that further interactions need to be considered. The particles appear to interact with both the charge control agent and the dye and it is possible that the fluid may remove ionizable species from the surface of the TiO_2 . The result is an increased ionic content in the suspension.

The transient current behavior of the device is important as the power consumed by a display is an important selection criterion. The EPD has inherent memory and to form an image or erase an area of the display requires only the application of voltage for sufficient time to achieve the required optical contrast. As t_{off} is greater than t_{on} the erase charge may be

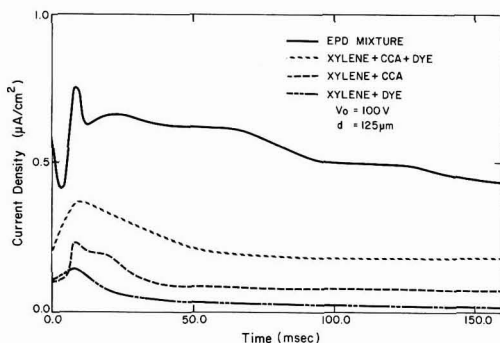


Fig. 5. The observed current density for the different components of the EPD. The measurements were performed on a $125 \mu\text{m}$ cell with a driving voltage of 100 V . The current density scale for the xylene + dye system has been expanded ten times.

larger than the imaging charge and we chose to use the erase energy as a measure of the energy required to switch the device. At an applied field of $1 \text{ V}/\mu\text{m}$ the switching energy density is $\sim 3 \mu\text{J}/\text{cm}^2$ for the cell whose characteristics are shown in Fig. 2 and 3.

"Steady-state" currents measured at times corresponding to five optical response times were found to increase linearly with field at lower fields, tending to saturate at higher fields. The "steady-state" currents increase approximately as the square root of the concentration of added charge control agent. These currents are generated by dissociation of neutral molecules in the bulk of the cell. The peak currents (defined as the currents in excess of the "steady-state" current) increase, roughly linearly, with electric field. The average resistivities of the EPD materials at operating fields of $1\text{--}2 \text{ V}/\mu\text{m}$ are about $10^{10} \Omega\text{cm}$.

The excess currents when integrated over several optical response times are approximately independent of the applied field. Total currents integrated over several response times typically exceed the C-V product of the cell by a factor of five. Again bulk generation of ions is responsible for this effect. Most of these observations parallel the behavior of the charge control agent alone in dielectric media. A theoretical investigation of the transient conductivity in this system indicates that space charge perturbations of the electric field do not appear to be important at EPD operating conditions if ionic charge neutralization takes place at the electrodes, but have to be taken into account at low fields. It is also interesting to note that the observed excess charge density of $\sim 8 \text{ nC}/\text{cm}^2$ is in rough agreement with the estimated total charge of the TiO_2 particles.

Threshold and memory.—The interaction between the charged particles and the electrodes governs the threshold behavior of the device. Figure 6 shows the total number of particles, N , removed from the electrode as a function of the magnitude of the applied square wave driving field. This plot was determined from the saturated optical response of the cell as the applied field was decreased in definite steps. The optical response was found to show large and slowly varying hysteresis effects dependent on both the magnitude and frequency of the voltage that had been applied to the device.

The relative number of particles that migrate per unit change in field, dN/dE , is also plotted against field in Fig. 6. This characteristic of the EPD is contrasted with the threshold behavior of a submonolayer of particles. For the latter, a reasonably well-defined threshold field was observed but at the high EPD particle concentration such a threshold is absent. It is also of interest to note that if insufficient charge con-

trol agent is added to the system then a considerable fraction of the particles swept to an electrode on the first application of a field cannot be removed at any applied voltage. In this case it appears that the particles lose their charge on contacting the electrode and the adhesive (van der Waals) force is sufficient to hold the particle on the surface.

We attempted to compare the calculated particle-electrode interaction forces with the observed thresholds. The interaction force between a charged dielectric particle and the conducting substrate in an external field includes a removal force proportional to QE which is opposed by attractive forces. These are the image force, proportional to Q^2 , the induced dipole-image force (8), proportional to E^2 , and the adhesive force. Neglecting the adhesive force and approximating the dielectric constant of the TiO_2 agglomerates by $\epsilon = 30$ we obtain a range of electric field extending from 0.1 to $0.45 \text{ V}/\mu\text{m}$ for which spherical particles should be removed from the electrodes. Experimental values are around $0.7 \text{ V}/\mu\text{m}$ indicating a contribution from the adhesive forces. The average particle-electrode interaction forces based on experimental values of the removal field and particle charge are about $0.9 \times 10^{-10} \text{ N}$. The removal force for a second layer of particles was estimated by considering the first layer as a dielectric, uncharged barrier. We found that the average removal force for the second layer is $\sim 0.5 \times 10^{-10} \text{ N}$ showing that the removal forces have a wide distribution in a multilayer system resulting in a poorly defined threshold.

The particle-electrode interaction which is a combined effect of adhesive and electrostatic forces gives the EPD an inherent memory. Once imaged on a surface the particles are only slowly removed in the absence of an applied field. This property of the device allows for considerable savings in device power consumption and requirements on addressing circuitry by reducing the need for frequent refreshing. The typical memory times of our devices were several hours.

Finally, it should be emphasized that electrophoretic displays exhibit noticeable history effects. The response times depend, for example, on the time the cell is kept at open circuit between the erasure and writing cycles. In square wave simulations of the optical responses, the response times increase as the driving frequency decreases presumably because of changes in packing of the particles on the electrodes. As pointed out above, the electric field thresholds are also strong functions of the previous voltages applied to the cell.

Summary

Optical and electrical characteristics of EPD devices were investigated together with a study of fundamental properties of TiO_2 dispersions in nonaqueous media. This permitted us to examine the inherent limitations of EPD's and also to assess the possibility of device improvement.

The EPD has certain attractive features which distinguish it from other passive display devices. EPD's can be made to provide high optical contrast coupled with wide angle viewability. This is possible despite the lowered contrast resulting from the presence of dye in the fluid between the particles and particle-dye interactions. In a thin film sandwich structure the cell may be operated at reasonably low voltage without consuming excessive power. The inherent memory of the device is a great advantage as this can be the most significant factor in reducing the over-all energy consumed in operating the device.

The response times of our EPD mixture are as low as 10 msec . In this system the off-times are governed by the dynamics of removing particles from an electrode. The on-times appear to be partially controlled by the transit of particles through the cell. However, in cells with high particle concentration complete

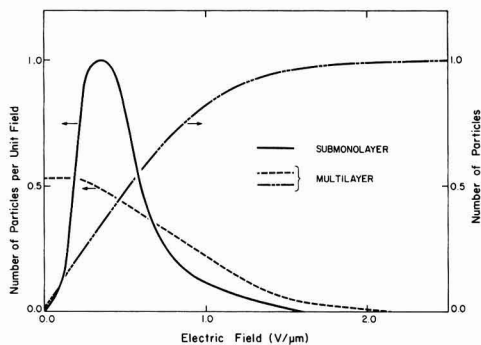


Fig. 6. The electric field threshold dN/dE for systems containing both a sub-monolayer and multilayers of particles. The total number of particles, N , moving at a given field, E , is also shown for the multilayer case.

sweepout of particles onto the electrode does not occur and some particles may remain spatially distributed through the cell. These particles can control the on-times. Some improvement of the response time can be achieved by altering the removal of particles from the electrodes. This might be achieved by modifying the particle-substrate forces either by employing blocking layers on the electrodes or overcoating the particles with a polymer. However, these changes will likely effect the threshold characteristics and memory.

More substantial improvements in the electrical characteristics of the EPD should be possible if charge control agents which do not leave excess neutral molecules and ions in solution can be identified. With such a material the steady-state currents would be significantly decreased and the excess currents would be associated only with the motion of charged particles and counterions.

The nature of the particle-electrode and particle-particle interactions lead to a system having a poorly defined threshold field for multilayers of particles. This characteristic limits the choice of an addressing scheme for any graphic display system using this technology and some details of the procedures available to fabricate an addressed display will be detailed in a subsequent publication.

Manuscript submitted Oct. 24, 1978; revised manuscript received June 22, 1979.

Any discussion of this paper will appear in a Discussion Section to be published in the June 1980 JOURNAL. All discussions for the June 1980 Discussion Section should be submitted by Feb. 1, 1980.

Publication costs of this article were assisted by Xerox Research Centre of Canada.

REFERENCES

1. P. R. Evans, H. D. Lees, M. S. Maltz, and J. L. Dailey, U.S. Pat. 3,612,758 (1971).
2. I. Ota, *Proc. IEEE*, **61**, 832 (1973).
3. A. L. Dalisa and R. J. Seymour, *ibid.*, **61**, 981 (1973); A. L. Dalisa, *Proc. SID*, **18**, 43 (1977).
4. J. C. Lewis, in "Nonemissive Electrophoretic Displays," A. R. Kmetz and F. K. von Willisen, Editors, p. 223, Plenum Press, New York and London (1976).
5. V. Novotny, *J. Appl. Phys.*, **50**, 324 (1979).
6. M. A. Hopper and V. Novotny, *IEEE Trans. Electron Devices*, **ED-26**, 1148 (1979).
7. V. Novotny and M. Hopper, *This Journal*, **126**, 925 (1979).
8. G. C. Hartmann, L. M. Marks, and C. C. Yang, *J. Appl. Phys.*, **47**, 5409 (1976).

Debris-Induced Effects from Spin-on Diffusion Sources

T. C. Chandler, Jr.,* J. W. Faust, Jr.,* and R. B. Hilborn

College of Engineering, University of South Carolina, Columbia, South Carolina 29208

ABSTRACT

This paper explores the problems associated with some commonly occurring disturbances in spin-on silica film thickness. Among the problems encountered with these films are "potholes" and "comet-like" variations in the film thickness induced by debris and airborne particles. Data are presented which reveal the degree to which such disturbances degrade the uniformity of the diffused region.

It has been established that silica film diffusion sources can be successfully applied to a variety of problems in electronics device fabrication. Becker (1) has shown that commercially available silica films can be utilized successfully in integrated circuit fabrication and, in fact, provide some advantages over the more common gaseous diffusion sources. Chandler *et al.* (2) have demonstrated that high quality solar cells can be manufactured using silica film diffusion sources when proper care is taken to insure a uniform deposition of the source film. Studies such as these have confirmed that silica film diffusion sources display advantages such as high purity, low temperature deposition, and better flexibility in process control. In addition it has been observed (1-4) that the various forms of doped SiO₂ diffusion sources provide approximate time and temperature independent surface concentrations, minimal surface damage, and the advantage of ambient controlled diffusion limiting (3).

Despite the routine use of silica films by some manufacturers, little guidance for their usage is provided in detail in the open literature. This lack of information can pose problems for the nonroutine user such as the small production operation. Part of the problems

with utilizing the spin-on silica film is the occasional occurrence of macroscopic disturbances in the film thickness appearing as round "potholes" or "comet" shaped nonuniformities. These disturbances can be quite large (greater than 200 μ m across) resulting in a nonuniform diffusion in the affected area.

It is the purpose of this paper to show the causes for these larger disturbances and to establish a simple basis for the identification of debris-induced disturbances. In addition, experimental results are given which yield a quantitative view of diffused layer nonuniformities that result from the gross disturbances typically encountered.

Theory

The theoretical aspects of this phenomenon are quite straight forward. It has been verified in previous studies (4-6) that silica films act as nearly constant diffusion sources under certain conditions. In most cases silica films (including anodized, sputtered, spin-on, and paint-on films) maintain their constant source characteristics for temperatures above 900°C in a suitable ambient. Another factor, the importance of which is less obvious, is the final thickness of the deposited film. The thickness of the silica film is an important factor because it is a principal variable which governs the behavior of the dopant concentration in the film. A simple model exists (5,6) which

* Electrochemical Society Active Member.

Present address: U.S. Air Force Materials Laboratory, Electro-magnetic Materials Division (LPO), WPAFB, Ohio.

Key words: diffusion, contamination, uniformity, silica film.

for the first-order case is an accurate representation of the oxide silicon diffusion system

$$C_{sl}(X, t) = C_s \operatorname{erfc} \left(\frac{X}{2\sqrt{D_{sl}t}} \right) \quad [1]$$

where C_s , the surface concentration of impurities, is dependent on the concentration of dopant in the silica layer. More correctly, the value of C_s is a constant which is some fraction of dopant concentration, C_o , in the oxide film

$$C_s = C_o \left(\frac{M}{1 + \sqrt{D_{sl}/D_{ox}}} \right) \quad [2]$$

where M is the segregation coefficient and D_{sl} and D_{ox} are the diffusion coefficient for the dopant in the two media. Barry (5, 6) has also shown that for well-controlled depositions Eq. [2] is valid when

$$b \geq 2\sqrt{D_{ox}t} = L_{ox} \quad [3]$$

where b is the silica film thickness and the quantity L_{ox} is the diffusion length of an impurity atom in the oxide layer. Radiotracer studies (7) have also confirmed the relationship between C_s , C_o , and b , but it must be understood that for this simple model Eq. [2] is only valid when $b \geq L_{ox}$.

When inequality [3] is maintained the silica film can easily yield a value of C_s equal to 99.7% of the given C_o value. Observations in previous studies (2, 3) revealed that when b was less than $2\sqrt{D_{ox}t}$ no significant diffusion of impurities across the oxide-silicon interface occurred.

The simple model represented by Eq. [1] and inequality [3] has some serious implications. It is obvious that nonuniform diffusions from chemically homogeneous silica films are quite possible and it would appear that any disturbance or effect which alters the film thickness can produce these variations.

Theoretical limitations.—It should be noted that silica films of all types are referred to as constant diffusion sources, but as pointed out above this is not entirely true. The value of C_o in any silica film is constantly changing during the diffusion cycle. When the requirements of inequality [3] are maintained very good approximations to constant source conditions are possible. It has been found that silica films provide good constant source conditions for limited periods of time, usually less than 60 min. Most simple diffusion models cannot account for this behavior because these models do not consider the loss of dopant from the oxide to the ambient. In reality these losses are considerable. During a normal diffusion cycle the oxide layer is quickly depleted of its dopant at the oxide-silicon interface and at the oxide-ambient interface. As the cycle progresses the diffusion flux at the oxide-silicon interface will become sufficiently limited as to yield a gaussian distribution of impurities in the substrate as opposed to the erfc of Eq. [1].

Experimental

It has been found that when using the common spin-on or paint-on diffusion sources two distinct classes of nonuniformity may result. The first group includes striations, bubble-induced pinholes, and microcracks. All three of these disturbances result from improper deposition procedures and can occur under the cleanest of conditions. The second class of disturbance is more severe and includes the "pot-holes" and "comets" mentioned previously. These disturbances, unlike those of class I, vary radically in size and shape (no two are alike) and, if adjacent to each other on the wafer, these disturbances can combine to produce areas of poor coverage many millimeters wide.

The procedures are outlined here for the characterization of the class II disturbances and the deter-

mination of the role that dust and debris play in the formation of these disturbances. Ten p-type wafers, with (111) orientation, having a background boron concentration from 1×10^{16} to 6×10^{16} atoms/cm³, were etched in a buffered HF solution for 10 min to remove all residual oxides and then treated 1 min in aqua regia to eliminate any metallic ions adhering to the surfaces. The wafers were rinsed four times in deionized water. This procedure was repeated four times and the wafers were stored separately in high purity methanol until needed.

Five of these wafers were used to establish the existence of the various disturbances described above. The diffusion source used was a boron-doped spin-on silica film. No care was taken to insure film uniformity, but all spin procedures and precautions (given by the source film manufacturer) were observed. The disturbances in the silica film did not always occur, and on the initial run only two out of five samples displayed any appreciable variations in the film integrity. The flawed samples were saved for further examination. The remaining wafers were cleaned and the deposition repeated until five flawed samples were obtained. The various disturbances were photographed while the film was wet and photographed after the bake-out cycle. The bake-out cycle, which drives off the carrier fluids, was accomplished by baking the wafers in dry nitrogen at approximately 90°C for 1 hr and then increasing the temperature to a maximum of 200°C over an additional 3 hr period. [This is a refinement of the procedure of Ref. (3).]

The five samples, two of them displaying representative flaws, were fired at 1000°C in a nitrogen ambient for 10 min. This allowed the film to form a rigid layer suitable for profilometer scanning. The profilometer, sensitive to 30Å, was employed to profile the larger disturbances. Because it was suspected that these larger disturbances were due, at least in part, to dust and residual debris, the remaining five cleaned wafers were prepared with great care to insure a uniform silica film thickness. Before the carrier fluids were baked out, the wafers were exposed to alumina grit of various particle sizes to see what effect these particles would have on the film uniformity. These samples were then photographed, heat-treated, and profiled as described above. In addition, a particle density count was taken for correlation with the total area of poor coverage on each wafer.

To evaluate the uniformity of the diffusion in the regions of poor coverage, the diffusion source layer was etched away and a profile of the resistivity was constructed using the well-known four-point probe method (8). Each wafer chosen for the four-point probe profiling was eventually stain etched using the commonly employed HF-HNO₃ formulation (9). The silica film employed in this study yields, under perfect conditions, a surface concentration, C_s , of 1×10^{20} atoms/cm³; the stain will blacken any area of concentration greater than or equal to 1×10^{18} atoms/cm³ (10). Those areas which are left unetched represent regions of poor diffusion. The total area of poor diffusion was approximated and correlated with the particle count data.

Results

In doing repeated spins using the first five wafers, it was confirmed that the more common nonuniformities in silica film thickness could be eliminated using simple procedures. The striation problem and bubble damage can be eliminated by adjusting the spin-speed and temperature of the spin-on source liquid. The nonuniformities resulting from cracking of the drying film can be avoided by employing lower temperatures and longer cycle times during bake-out. In general these three film disturbances are rare when one truly adheres to recommended deposition procedures. The second class of disturbance, the gross variations in the film integrity, appear not to be related to either the striation phenomenon or the micro-

cracking. These very large "potholes" are due to bubble formation interacting with debris to form large areas of disturbed silica film. Consider Fig. 1A. This figure represents a typical formation induced by the impact of a particle with the wet film. Bubble formation is found to be especially prevalent in such situations. The evolution of this disturbance can be observed in progress under an optical microscope. The disturbance is formed in two stages. First the impact; bubbles and ripples form quite rapidly, in fact, the nucleation of bubbles appears to be more easily achieved in the presence of debris. The result of this rapid bubble generation is an enhancement of the disturbing effect of the impact. This situation is very similar to Fig. 2 which represents such a formation prior to the bursting of the bubbles. The second stage of the evolving disturbance is its equilibrium condition which can take one of two forms. Figure 1B shows a small light weight particle floating in the fluid. The meniscus around the particle appears to be concave and thickness variations near the particle are quite small. This type of equilibrium configuration does not greatly degrade film integrity. In support of this conclusion, a comparison between the particle counts and the total area of poor diffusion, Fig. 3, reveals that most submicron particles have little effect on the final diffused region uniformity. A possible explanation is that the surface tension of the spin-on silica solution is sufficient to prevent the situation of Fig. 1C from occurring.

The second common way that this equilibrium condition manifests itself is illustrated in Fig. 1C where the particle adheres to the silicon surface. This situation is also accompanied by thickness variations, but their effect is only a secondary hazard. Here one can see the danger of localized contamination of the silicon from the particle or in some cases diffusion flux limiting due to the barrier the particle presents. Either case is unacceptable. In some cases submersed particles can produce the disturbance illustrated in Fig. 4. When a particle adheres to the silicon prior to or during the spinning the comet-like formation is produced. This disturbance resembles most others except for the tail which is a region of excessively thin silica film.

Unfortunately another situation arises in initially bubble-free liquids, see Fig. 5. Figure 5 illustrates a single, extremely large bubble containing a particle of unknown origin. The bubble is generated at some

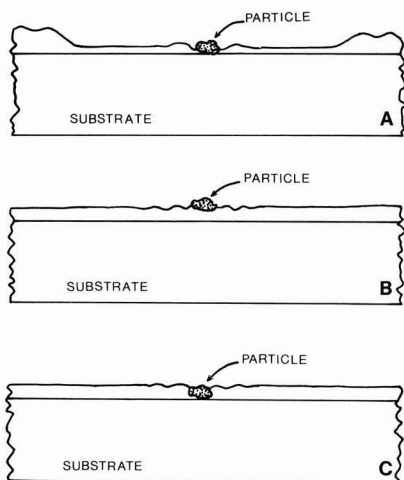


Fig. 1. The three stages in the evolution of a debris-induced disturbance. (A) Impact or simple contact; (B) and (C), two equilibrium conditions possible, seen via microscope examination.

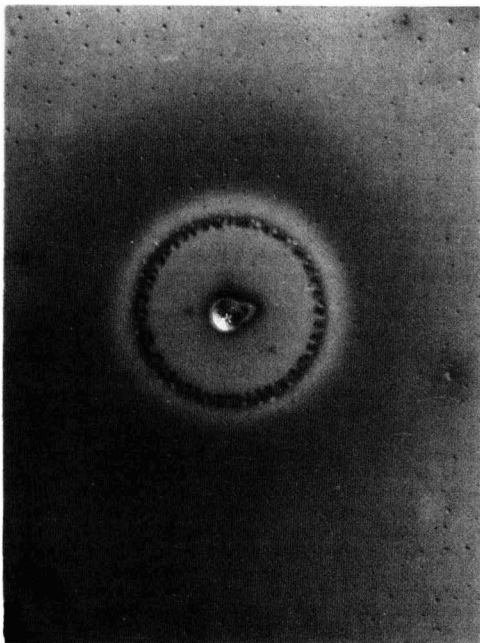


Fig. 2. A disturbed region induced by a particle impact. The bubbles have not burst, tending to enhance the ill effects of the impact.

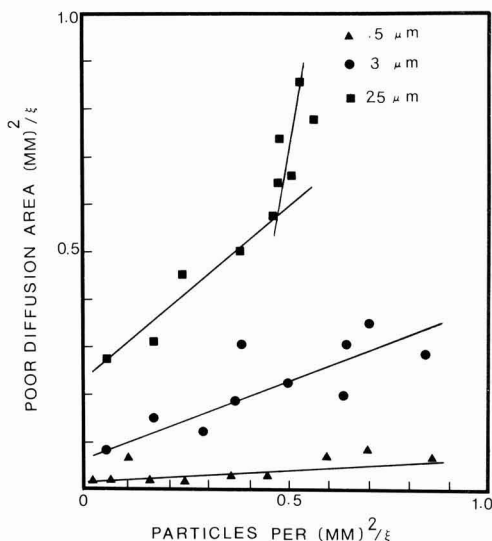


Fig. 3. Normalized graph of particle count vs. the region of poor diffusion. The quantity ξ represents the maximum data point for each scale. This graph yields a qualitative view of debris-induced effects, but note that the trend is toward decreased quality with increased particle size.

point during the particle impact, producing a total disturbed region much larger than the particle. The bubble aids in maintaining the thin region around the particle. When these bubbles burst, as they were observed to do, the displaced film will creep toward

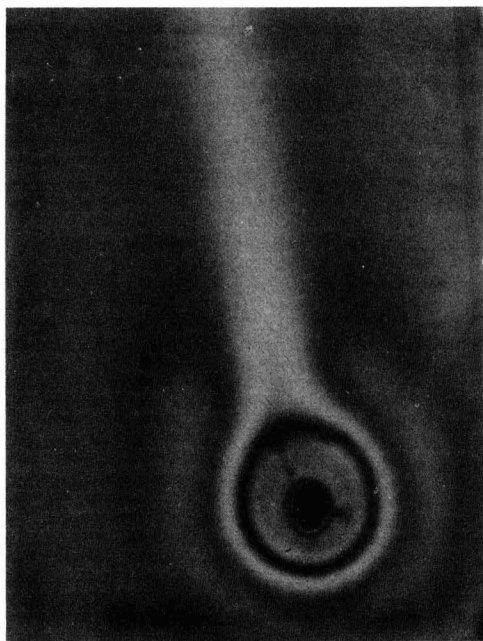


Fig. 4. A comet-like formation produced by a particle which has adhered to the substrate during spinning. Notice the long tale of thin silica film.

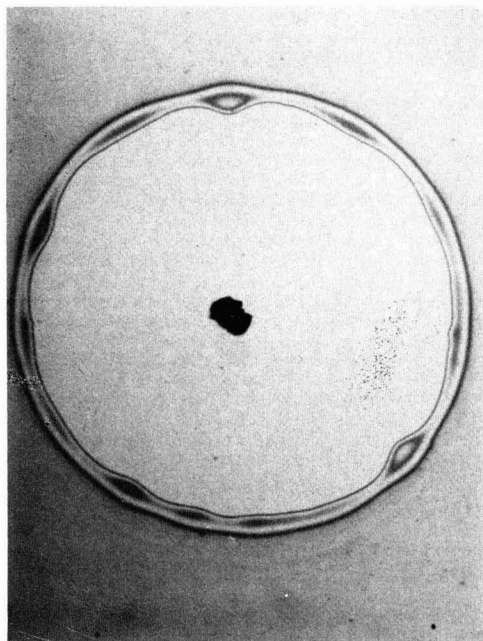


Fig. 5. A large pothole generated by a particle enclosed by a bubble. The thickness of the silica inside the bubble is too small to measure.

the particle, but the carrier liquid will evaporate long before the region of poor coverage can be restored.

It would appear that the simplest solution to the problem of these gross disturbances is to guard against the generation of bubbles in the silica film during deposition. Bubble formation is the only observable trait class I and class II disturbances have in common, thus their elimination may insure significant decreases in both types of disturbance. As described in Ref. (3) this bubble formation is a complex process and a detailed discussion is beyond the scope of this paper, but in brief, bubbles originate during the rapid evaporation of the source solution. The solvents utilized in many common formulations are quite volatile and thus are sensitive to ambient pressures and temperatures. Even so, it has been found (2) that adherence to recommended deposition procedures prevent bubbles from forming.

Diffused region.—Evaluation of the diffused regions of selected samples confirm that the surface concentration, C_s , is not uniform for samples displaying variations in the silica film. Stain etching of some samples reveal spots where essentially no diffusion took place. To gain a better comparative review of these effects, a typical sample was profiled by the four-point probe technique. The results were seen in Fig. 6A; notice that there is no region on which a device could be reproducibly fabricated. The range of resistivities observed are 1.0–0.001 Ω -cm, the latter value being characteristic of a normal diffusion from this source. The high resistivity regions indicate that the flux of impurity atoms was greatly restricted in these regions. Figure 6B is a plot of the profilometer data for the region also shown in Fig. 6A. Notice the one-to-one relationship between this disturbance and the resistivity data.

Conclusions

This study provides evidence to support the claims of the foregoing discussion that nonuniform diffusions from chemically homogeneous spin-on source solu-

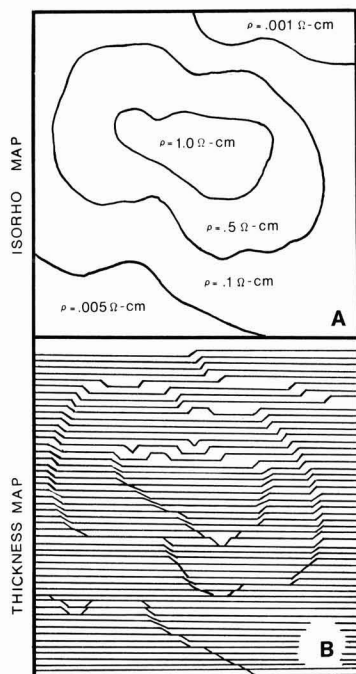


Fig. 6. Plots of data gathered on the diffused region below a very large disturbance. (A) Isorho (constant resistivity) map. (B) Film thickness map.

tions are possible. The silica film thickness acts as a controlling factor such that normal diffusion will occur only when the thickness is greater than or equal to L_{ox} as stated in inequality [3]. Films which do not meet this condition will act as a limited source. The results of this study indicate that many (if not most) gross variations in diffused layers are the result of debris-induced variations in the silica film thickness. It has been established that many kinds of disturbances can occur when using spin-on films, but all of them can be eliminated. Debris-induced damage is the easiest to eliminate because the problem is centered around contamination due to residual particles from etchants, sample preparation, and airborne dust. In the final analysis it would appear that the obvious answer is to maintain the optimum conditions of cleanliness and process control.

Because debris-induced damage and bubble damage are induced by similar mechanisms, the equilibrium state of both types of disturbance resemble each other. It was found that when debris was involved this fact could be easily established by microscope examination. Bubble damage appears as pinholes, usually quite small ($<1 \mu\text{m}$ wide). Under extreme magnification these pinholes are circular with a "halo" of thin silica around them. One should consult the photomicrographs of Ref. (3). In the case of debris-induced disturbances any particle sufficiently massive to induce macroscopic thickness variations are quite conspicuous under the microscope. If no particle similar to those in Fig. 2 and 5 can be found, then, most probably, it is simple bubble damage. In the case of the comet-like formations, Fig. 4, these can form only when a particle is present. The basic problem with controlling debris-induced damage is not that adequate clean factors are impossible to maintain. On the contrary, it was observed in this research that excellent results could be achieved maintaining moderate

precautions. There are some misconceptions about silica films, one of which is that because the film covers the surface it will invariably have a uniform diffusion and the film will protect the substrate from impurity contamination. This and previous studies together reveal this not to be the case. Uniform diffusions require uniformly thick films and although a film may prevent contamination from a particle, the mere presence of the particle may destroy the uniformity of the diffused layer.

Manuscript submitted Dec. 16, 1978; revised manuscript received May 29, 1979.

Any discussion of this paper will appear in a Discussion Section to be published in the June 1980 JOURNAL. All discussions for the June 1980 Discussion Section should be submitted by Feb. 1, 1980.

Publication costs of this article were assisted by the University of South Carolina.

REFERENCES

1. J. A. Becker, *Solid State Electron.*, **17**, 87 (1974).
2. T. C. Chandler, R. B. Hilborn, and J. W. Faust, in *Proceeding of the IEEE 12th Photovoltaic Specialists Conference*, p. 282 (1976).
3. T. C. Chandler, R. B. Hilborn, and J. W. Faust, *This Journal*, **124**, 1409 (1977).
4. U. K. Chakrabarti, *Solid State Electron.*, **20**, 111 (1977).
5. M. L. Barry and P. Olofsen, *This Journal*, **116**, 854 (1969).
6. M. L. Barry, *ibid.*, **117**, 1405 (1970).
7. I. Franz and W. Laagheirich, *Solid State Electron.*, **18**, 209 (1975).
8. D. S. Perloff, F. E. Wahl, and J. Conragan, *This Journal*, **124**, 582 (1977).
9. C. S. Fuller and J. A. Ditzenger, *J. Appl. Phys.*, **27**, 544 (1956).
10. R. J. Archer, *J. Phys. Chem. Solids*, **14**, 104 (1960).

Relaxation Spectrum Analysis of Semiconductor-Electrolyte Interface-TiO₂

M. Tomkiewicz^{*1}

Union Carbide Corporation, Tarrytown Technical Center, Tarrytown, New York 10591

ABSTRACT

A new technique to evaluate the equivalent circuit elements of a semiconductor-electrolyte interface is presented. The technique is based on impedance measurements over a wide frequency range. We present results on n-type TiO₂-aqueous electrolyte interfaces, which we can represent in terms of an equivalent circuit of passive elements. The equivalent circuit was interpreted in terms of two space charge layers with two different doping levels. The effect of surface treatment on the relative areas and on the lateral distribution of the two regions is also presented.

Over the last twenty-five years, many attempts have been made to determine the electrical properties of semiconductor-electrolyte interfaces from impedance measurements (1-12).

The basic physical phenomena which are associated with distribution of charges on the electrolyte-semiconductor interface and their importance in photoelectrochemistry are fairly well understood and can be represented in terms of generalized equivalent circuits (13) but their actual measurement and identification in terms of an equivalent circuit for a particular system has rarely been attempted. It is par-

ticularly desirable to be able to represent the semiconductor-electrolyte interface in terms of passive elements, the physical significance of which can be ascertained by variations of the electrode potential, pH, and other external parameters. It is also important to assign the passive elements to a spatial configuration of the various charge accumulation modes.

We present here an experimental method (14) which meets these requirements, and we demonstrate the method with a study of the TiO₂-aqueous electrolyte interface.

Experimental

The experimental arrangement is shown in Fig. 1. Terminals A and B are connected to a gain-phase meter, which is part of a Hewlett-Packard 3043A net-

* Electrochemical Society Active Member.

¹ Present address: Department of Physics, Brooklyn College, Brooklyn, New York 11210.

Key words: semiconductor, electrolyte, interface, impedance.

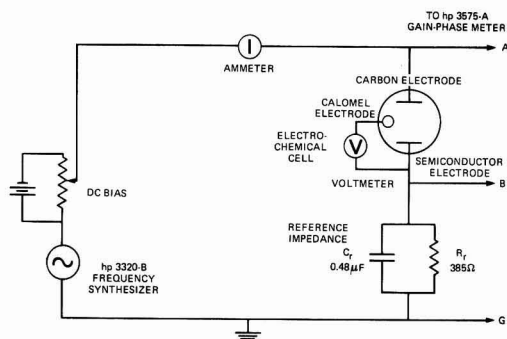


Fig. 1. Schematic diagram of the experimental apparatus. (For more details, see text.)

work analyzer. The gain-phase meter measures the relative magnitude, M , and the phase difference, θ , of the two input signals. This information is equivalent to the complex voltage ratio

$$E_B/E_A = Z_r/(Z + Z_r) \quad [1]$$

where Z_r is the impedance of the reference circuit and Z is the impedance of the electrochemical cell.

The real and the imaginary parts of the impedance of the cell can be deduced from Eq. [1] by using the following relations

$$Z = R + jX \quad [2]$$

$$R = \frac{R_r}{1 + (\omega\tau_r)^2} \left[\frac{\cos \theta}{M} - \frac{\omega\tau_r \sin \theta}{M} - 1 \right]$$

$$X = \frac{R_r}{1 + (\omega\tau_r)^2} \left[\omega\tau_r - \frac{\sin \theta}{M} - \frac{\omega\tau_r \cos \theta}{M} \right] \quad [3]$$

where ω is the angular frequency, θ is the phase angle, M is the magnitude, and $\tau_r = C_r R_r$ is the relaxation time of the reference circuit.

TiO₂ single crystals were purchased from Atomergic, sawed and measured perpendicular to the C axis. The resulting wafers (~1 mm thick) were mechanically polished, etched in NaOH at 500°C for 1 hr, rinsed in running distilled water, rinsed for 2 hr in boiling HCl, and washed again with running distilled water. The wafers were doped with H₂/Ar mixture at 850°C for 20 min. The counterelectrode was Pt or carbon rod with surface area at least an order of magnitude larger than the working electrode. The reference electrode was standard calomel electrode. Ohmic contact was made by rubbing In-Ga alloy. In each case the contact was checked with a curve tracer. Measurements were made in a standard 3-electrode single compartment electrochemical cell made out of Teflon, under N₂ atmosphere. The electrodes were mounted in the cell by pressure fit between two silicon rubber gaskets, which also determined the electrode area which was exposed to the electrolyte. Electrolytes were made with off-the-shelf analytical grade chemicals and 18 MΩ resistivity distilled water. Measurements were made at "zero" current (< 10 μA/cm²).

Results

The equivalent circuit.—A general equivalent circuit which represents the semiconductor-electrolyte interface is shown in Fig. 2A (13). The impedance, Z_1 , is given by an unknown number of R-C elements in parallel, shown in Fig. 2B. As far as the frequency response is considered, Fig. 2A can be represented by the simpler equivalent circuit given in Fig. 2C (2).

The voltage dependence should tell us if C_H can be neglected and if C_{SC} is equal to C'_{SC} or a correction for the capacitance of the Helmholtz layer should be made (15).

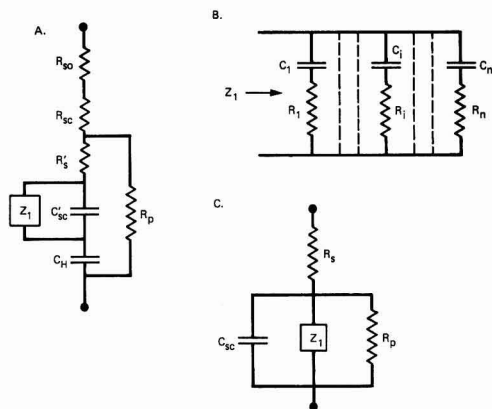


Fig. 2. Equivalent circuit of the semiconductor-electrolyte interface. (A) R_s is the resistance associated with the faradic current flow. R_{so} , R_{sc} , and R_s' are the resistances of the solution, semiconductor, and space charge layer. C_H and C'_{SC} are the capacitances associated with the Helmholtz layer and the space charge layer. Z_1 is the impedance associated with any charge accumulation parallel to the space charge layer with a different time constant. (B) Detailed description of Z_1 . (C) Reduced equivalent circuit:

$$C_{SC} = C'_{SC} \text{ if } C_H \gg C'_{SC}$$

$$R_s = R_{so} + R_{sc} \text{ if } R_s' \ll R_{sc}$$

Assuming that $\tau_s = R_s C_{SC}$ is the smallest time constant in the equivalent circuit, then at very high frequency the system will behave as a single capacitor and resistor connected in series. In this frequency range, the impedance is given by

$$Z_{HF} = R_s - \frac{j}{\omega C_{SC}} \quad [4]$$

We can subtract the series resistance from Z and get

$$Z' = Z - R_s = R - R_s + jX = R' + jX \quad [5]$$

The admittance of this circuit is given by

$$Y' = \frac{1}{R' + jX} = \frac{R' - jX}{(R')^2 + X^2} = G + jB \quad [6]$$

and in terms of the equivalent circuit in Fig. 2C we get

$$G = \frac{1}{R_p} + \sum_{i=1}^n \frac{\omega^2 C_i \tau_i}{1 + (\omega\tau_i)^2} \quad [7]$$

$$B = \omega C_{SC} + \sum_{i=1}^n \frac{\omega C_i}{1 + (\omega\tau_i)^2} \quad [8]$$

From the high frequency portion of the response curve we can obtain C_{SC} and subtract ωC_{SC} from B to get

$$B_{SS} = \sum_{i=1}^n \frac{\omega C_i}{1 + (\omega\tau_i)^2} \quad [9]$$

The last expression is a superposition of curves with Lorentzian line shape. If the overlap is small enough, we should get a series of maxima which completely characterize each R-C element. The position of the maximum will give us the inverse relaxation time while the ratio of the amplitude to the position will give us the capacitance.

Figure 3 illustrates the procedure and shows the accuracy and resolution that can be obtained with this technique. An analog test circuit, consisting of resistors and capacitors with the values shown in parentheses, was measured with the network analyzer. Curve

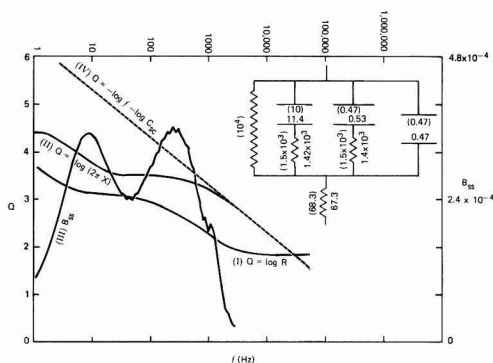


Fig. 3. Response curves for model circuit shown at the right-hand corner. In parentheses are shown the values of the various elements taken at their stated values. Below them are the values measured from the response curves.

(I) is a plot of $\log R$ vs. $\log f$. At high frequencies this curve becomes independent of frequency and gives the value of R_S according to Eq. [4]. Curve (II) is a plot of $\log (2\pi X)$ vs. $\log f$. If the high frequency part of the curve can be represented as a single resistor and a capacitor connected in series, then according to Eq. [4]

$$\log (2\pi X) = -\log f - \log C_{SC} \quad [10]$$

and in the high frequency range curve (II) should have a slope of 1 and C_{SC} can be evaluated from the intercept. The parameters R_S and C_{SC} are used to calculate curve (III) which is a plot of B_{SS} vs. $\log f$. The positions and amplitudes of the maxima in curve (III) are used to calculate the capacitive and resistive elements in Z_1 . In Fig. 3, these calculated values are listed on the circuit diagram. We can see from the comparison of the actual values to the measured ones that the accuracy is adequate. Figure 4 illustrates the procedure on an electrochemical cell with n-type TiO_2 as the anode and Pt as the cathode. The concentration of the electrolyte is such that the imaginary part of the impedance originates entirely from the TiO_2 -electrolyte interface. The equivalent circuit Z_1 is found to consist of a single resistor R_A in series with a single capacitor C_A .

The equivalent circuit of the TiO_2 -electrolyte interface remains the same under various pH conditions,

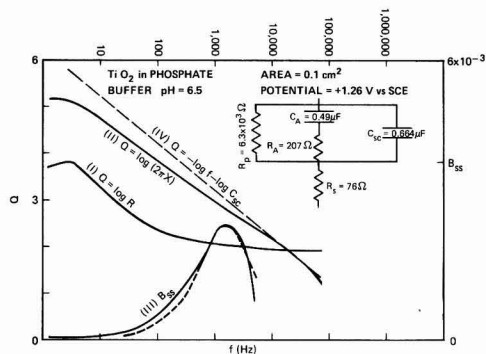


Fig. 4. Response curves for n-type TiO_2 in 0.33M phosphate buffer. On the right-hand corner is the equivalent circuit constructed from the curves in the manner explained in the text. Capacitances are in μF and resistances in ohms. The dashed curve under B_{SS} is the theoretical fit to a single Lorentzian according to Eq. [9].

potentials, doping levels, etchants, etc. The only deviation from this equivalent circuit, as manifested by the fit of B_{SS} to a single Lorentzian line, was observed when we approach the flatband potential. Figure 5 shows that potential dependence of the capacitive elements in the equivalent circuit of TiO_2 , polished to 0.3μ finish but unetched. It is obvious that both C_{SC} and C_A obey the Mott-Schottky relation (16, 17)

$$\frac{1}{C_{SC}^2} = \frac{2}{\epsilon e N_D A^2} \left(U - U_{fb} - \frac{kT}{e} \right) \quad [11]$$

where ϵ is the dielectric constant, A is the area, e the electronic charge, N_D the effective doping level, U the electrode potential, U_{fb} the flatband potential, and T the temperature, indicating that the capacitive elements originate from the space charge layer. R_S is independent of potential, as shown in Fig. 6, and results from the electrolyte resistivities. The ratio of R_S between electrolytes under different ionic strength conditions is the same as that found by an independent measurement of the conductivity of the various electrolytes. R_A is dependent on potential being high at anodic potentials and lower when we approach the flatband conditions. This qualitative behavior of R_A and R_S as a function of potential is also highly reproducible and independent of electrolyte, doping, etching, equilibrium time, etc. The quantitative behavior of R_A is not as reproducible as evident from the scatter of the points in Fig. 6.

When the polished TiO_2 crystals are etched for 1 hr in NaOH at 500°C , two distinct topographies are apparent and their SEM pictures are shown in Fig. 7. We were able to measure the impedance characteristics of the two regions on the same wafer, by moving the area which was exposed to the electrolyte from one region to the next. The equivalent circuit was the same at both surfaces and identical to the

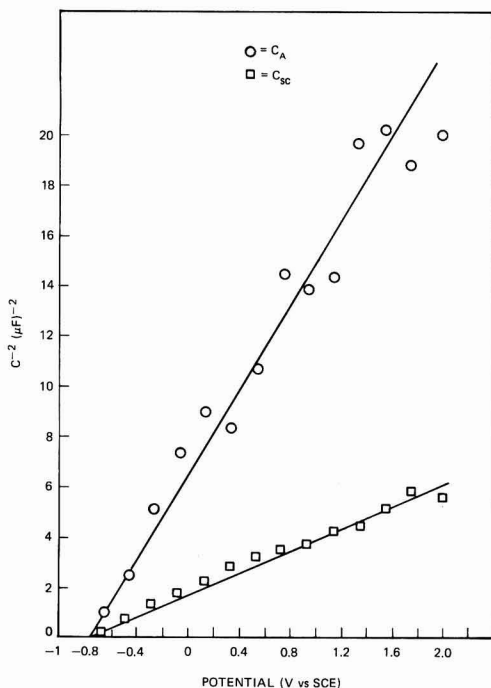


Fig. 5. Mott-Schottky plots of C_{SC} and C_A for 0.1 cm^2 n-type TiO_2 , polished but unetched in 0.33M phosphate buffer, pH = 6.5.

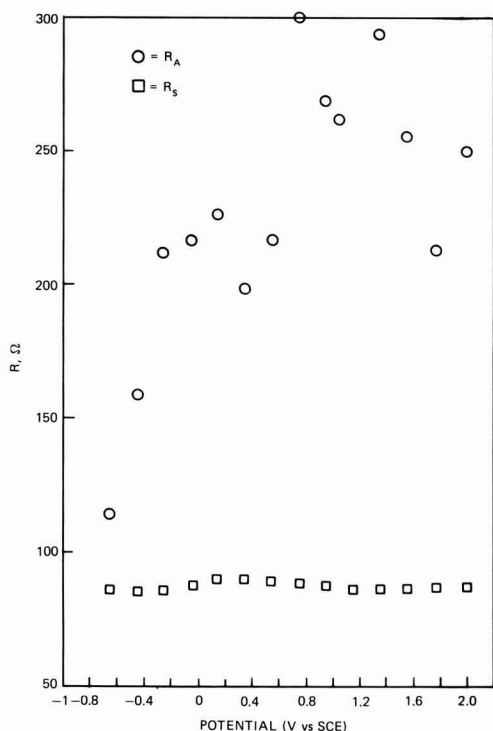


Fig. 6. Potential dependence of R_S and R_A . The same conditions as in Fig. 5.

one shown before. The potential dependence of the resistive elements was also the same. Figure 8 shows the Mott-Schottky plot of the two capacitors on the matte surface and both behave in a linear way. Figure 9 shows the Mott-Schottky plots of the two capacitors on the smooth surface and both are highly nonlinear. But when we add the two capacitors and plot the Mott-Schottky plot of the sum, the behavior is linear as shown in the same figure.

Discussion

The experimental finding that lies in the heart of this work is the establishment of the equivalent circuit of the TiO_2 -electrolyte interface. In depletion and weak inversion modes the TiO_2 -electrolyte interface is characterized by two R-C elements connected in parallel. Under most experimental conditions, both capacitive elements seem to result from charge distributions that obey the Poisson equation as manifested here by the linear Mott-Schottky plots. With the NaOH-etched smooth surface the individual capacitive elements do not obey the Mott-Schottky relation but their sum does. Both C_A and C_{SC} show approximately the same flatband potential which varies with the expected Nernstian dependence of pH (18). This indicates that both capacitance elements result from charge accumulation at the semiconductor space charge layer and not from surface states.

The linear behavior of the Mott-Schottky plots also indicates a constant distribution of dopant normal to the TiO_2 -electrolyte interface. The resistivity of the TiO_2 is of the order of $0.1 \Omega\text{-cm}$ so its contribution to R_S is negligible and R_S is determined exclusively by the conductivity of the electrolyte. This accounts for the fast relaxation time, $\tau_{SC} = R_S C_{SC}$, and leaves us to explain the origin of the slower relaxation time, $\tau_A = (R_S + R_A)C_A$. There are several alternative explanations for the existence of the two distinct relaxation times. Most of them originate from explanation of a similar equivalent circuit which has been found in MOS devices (19-21). They range from lateral heterogeneity in a-c current flow (19, 20) to contributions from minority carriers to charge accumulation at the interface (21, 22). Although none of these explanations can be excluded, the simplest explanation to account for our observations is to assume that we are dealing with a heterogeneous crystal with two different regions having two different doping levels that extend uniformly at least to depths larger than the thickness of the space charge layer. Assuming the same flatband potential in both regions, from Eq. [11] we get

$$\frac{C_A}{C_{SC}} = \frac{A_A}{A_{SC}} \sqrt{\frac{N_D^A}{N_D^{SC}}} \quad [12]$$

where A is the area and N_D is the doping level of the two regions. This ratio should be independent of potential. The faster relaxation time measured is determined by the resistance of the electrolyte

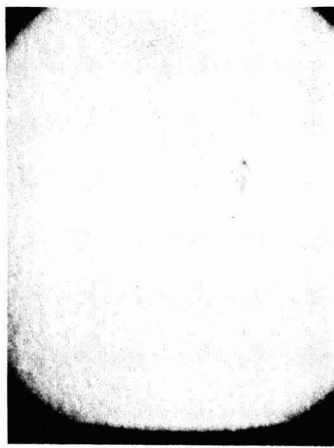
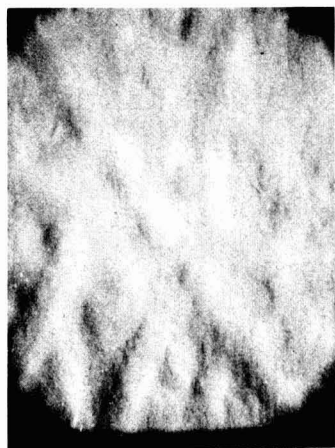


Fig. 7. SEM pictures of the matte and smooth surfaces obtained from n-type TiO_2 polished and etched with NaOH.

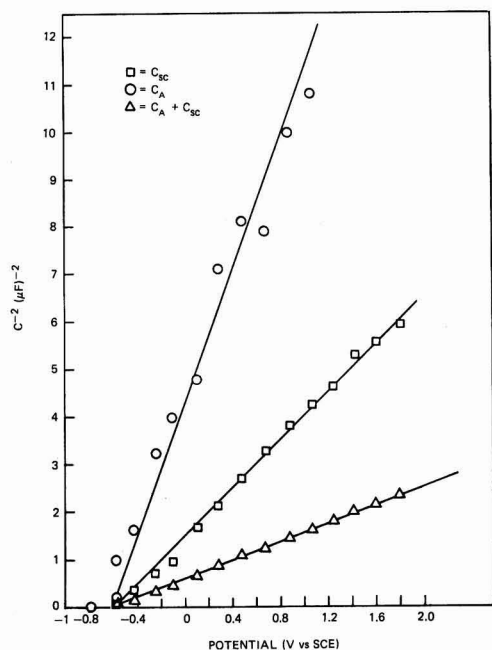


Fig. 8. Mott-Schottky plots of C_{SC} , C_A , and $C_A + C_{SC}$ for the matte area of 0.1 cm^2 n-type TiO_2 , polished and etched with NaOH , in 0.33M phosphate buffer, $\text{pH} = 6.5$.

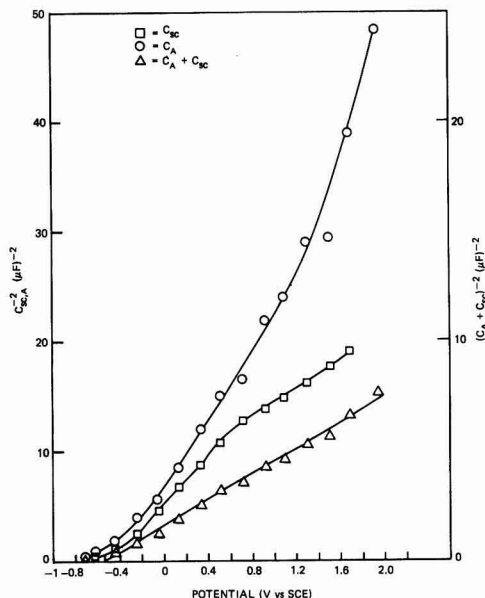


Fig. 9. Mott-Schottky plots of C_{SC} , C_A , and $C_A + C_{SC}$ for the smooth area of the same wafer as in Fig. 8.

$$\tau_{SC} = R_S^0 C_{SC}^0 = R_S C_{SC} \quad [13]$$

where C_{SC}^0 is the capacitance of the SC region per unit area of this region and R_S^0 is the resistance of the electrolyte per unit area of the SC region. The resistive element in the slower relaxation time might

have a contribution from the bulk of the semiconductor

$$\tau_A = (R_S^0 + \rho^A l_{SC}) C_A^0 = (R_S + R_A) C_A \quad [14]$$

where ρ^A is the resistivity of region A and l_{SC} is the thickness of the semiconductor. This implies that

$$\frac{\tau_A}{\tau_{SC}} = \left[1 + \frac{\rho^A l_{SC}}{R_S^0} \right] \frac{C_A^0}{C_{SC}^0} \quad [15]$$

If both regions have the same flatband potential then we can apply Eq. [11] and get

$$\frac{\tau_A}{\tau_{SC}} = \left[1 + \frac{\rho^A l_{SC}}{R_S^0} \right] \sqrt{\frac{N_D^A}{N_D^{SC}}} \quad [16]$$

If $\rho^A l_{SC} \ll R_S^0$, then

$$\frac{\tau_A}{\tau_{SC}} = \sqrt{\frac{N_D^A}{N_D^{SC}}} \quad [17]$$

From Eq. [12] and [17] we can evaluate the absolute areas and the ratio of the doping levels. Knowing the areas, we can evaluate the doping levels in the individual regions from their prospective Mott-Schottky plots. This was done for the unetched sample in Fig. 5 and the results are shown in Fig. 10 and 11.

A critical test that will determine the self-consistency of the model is that the areas of the two regions and the series resistance are independent of the electrode potential. From Fig. 11 we can see that A^{SC} is independent of potential over the entire potential range and occupies 80% of the available surface. From Fig. 10 we can see that R_S^0 is also very closely potential independent, being $7 \pm 1 \Omega\text{-cm}^2$ over the en-

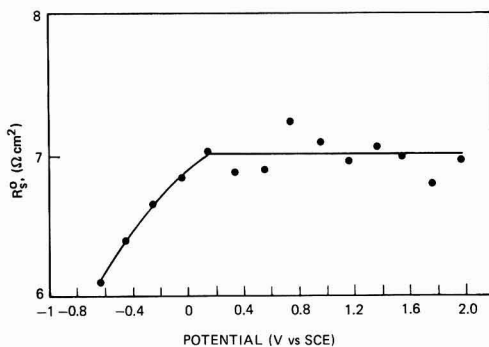


Fig. 10. Potential dependence of the electrolyte resistance for 1 cm^2 TiO_2 wafer that was described in Fig. 5.

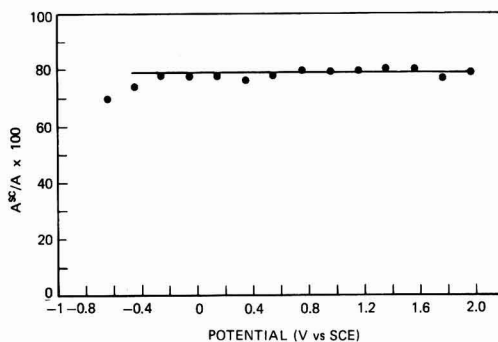


Fig. 11. Fraction of the area $A^{SC}/(A^{SC} + A^A)$ of the TiO_2 wafer with the lower doping level.

tire potential range. When we approach the flatband potential, R_S^0 starts to fall, but this can easily be due to the fact that close to the flatband potential we start to get some deviations from the equivalent circuit with two relaxation times. After knowing the relative areas, we can return to Fig. 5 and determine the doping levels of the two regions and we find that

$$N_D^{SC} = 5.9 \times 10^{19}/\text{cm}^3 \quad N_D^A = 2.5 \times 10^{20}/\text{cm}^3 \quad [18]$$

With such doping levels ρ_{AL}^{SC} must be $\ll R_S^0$ as assumed, because the conductivity of the semiconductor scales linearly with the doping level. We can summarize the equivalent circuit of TiO_2 -electrolyte interface as shown in Fig. 4 as being due to two regions with different doping levels. The regions must extend at distances greater than the thickness of the space charge layer, the dominant area being the area with the lower doping level. The roughness did not enter into the calculation of the doping level here, and a roughness factor of at least 2 is needed to explain the lack of observable shift of the flatband potential of the more highly doped region, from the expected contribution of the capacitance of the Helmholtz layer (15). The two capacitive elements, C_{SC} and C_A , result from two space charge layers of two regions on the crystal with two different doping levels. The relevant independent parameters in Fig. 4 are not R_S and R_A but, rather, R_S and the relative geometric area of the two regions. Any potential dependence of R_S will be amplified in R_A by the factor $A_{SC}/A_A - 1$. The observations that the areas of the two regions are independent of potential, as shown in Fig. 11, and that the series resistance of the two regions is the same after normalization to the same area and is also independent of potential, as shown in Fig. 10, constitute a strong self-consistent support for the interpretation of the impedance measurements.

The presence of two regions with two different doping levels can also account for the results on the etched samples which are shown in Fig. 7, 8, and 9. The results here tell us about the spatial distribution of the two regions as well. On the smooth surface, the two regions are mixed in patches which are smaller in size than the thickness of the space charge layer and, as a result, the individual Mott-Schottky plots are not linear while the sum of the capacitances measures the "average" doping level and is linear. In this case, it is impossible to measure the relative areas and the individual doping levels of the two regions. On the other hand, in the matte area, the individual regions are larger than the thickness of the space charge layer. The individual areas show good Mott-Schottky behavior as is evident in Fig. 8. The relative areas and the individual doping levels can be evaluated and they come out to be

$$\begin{aligned} A_{SC} &= 82\% & A_A &= 18\% \\ N_D^{SC} &= 4.8 \times 10^{19}/\text{cm}^3 & N_D^A &= 1.3 \times 10^{21}/\text{cm}^3 \quad [19] \end{aligned}$$

Conclusions

The results that were presented here fully describe the equivalent circuit of the interface between a TiO_2 single crystal and an aqueous electrolyte in terms of completely passive elements. We have thus, for the first time, eliminated the difficulties previously encountered (23) in determination of such important parameters as flatband potential and doping level.

The equivalent circuit is shown in Fig. 4. The equivalent circuit was interpreted in the following way: the two capacitive elements result from space charge layers of two regions on the crystal, one which occupies $\sim 80\%$ of the area and has lower doping level, while the other occupies $\sim 20\%$ of the area and has higher doping level. The resistive elements in both regions are due to the electrolyte. We did not find any significant difference in the flatband potential. The

subject of the flatband potential of TiO_2 as a function of pH and doping level will be discussed in a subsequent paper. Although the explanation of the equivalent circuit in terms of two regions with different doping levels is self-consistent, an independent evaluation of the surface heterogeneity will be required to determine the uniqueness of this interpretation.

The results here are representative of experimental results from many wafers which were taken from two single crystals which were obtained from the same source over a period of 15 months and doped under a variety of conditions, but it is obvious that the results should be a function of the method under which the crystal is grown and doped. In this respect, the results should be regarded as a demonstration of the utility of a technique rather than a demonstration of inherent properties of the TiO_2 -electrolyte interface.

Acknowledgments

The author gratefully acknowledges Mr. R. J. Serino of Union Carbide for his valuable technical assistance, Prof. M. H. Cohen from the University of Chicago, and Dr. H. Fay of Union Carbide for enlightening and helpful discussions and critical comments.

Manuscript submitted Oct. 11, 1978; revised manuscript received April 25, 1979.

Any discussion of this paper will appear in a Discussion Section to be published in the June 1980 JOURNAL. All discussions for the June 1980 Discussion Section should be submitted by Feb. 1, 1980.

Publication costs of this article were assisted by Union Carbide Corporation.

REFERENCES

1. J. F. Dewald, *Bell Syst. Tech. J.*, **39**, 615 (1960).
2. R. Memming, *Philips Res. Rep.*, **19**, 323 (1964).
3. R. D. Levin and L. Pospisil, *J. Electroanal. Chem. Interfacial Electrochem.*, **22**, 277 (1969).
4. D. M. Tench and E. Yeager, *This Journal*, **120**, 164 (1973).
5. J. R. Macdonald, *J. Electroanal. Chem. Interfacial Electrochem.*, **53**, 1 (1974).
6. E. C. Dutoit, R. L. Van Meirhaeghe, F. Cardon, and W. P. Gomes, *Ber. Bun. Gesell.*, **79**, 1206 (1975).
7. W. H. Lafere, R. L. van Meirhaeghe, F. Cardon, and W. P. Gomes, *Surf. Sci.*, **59**, 401 (1976).
8. E. Schouler, A. Hammou, and M. Kleitz, *Mater. Res. Bull.*, **11**, 1137 (1976).
9. J. R. Macdonald and J. A. Garber, *This Journal*, **124**, 1022 (1977).
10. M. J. Madou, F. Cardon, and W. P. Gomes, *ibid.*, **124**, 1623 (1977).
11. J. R. Macdonald and D. R. Franceschetti, *J. Chem. Phys.*, **68**, 1614 (1978).
12. G. Horowitz, *J. Appl. Phys.*, **49**, 3571 (1978).
13. P. J. Boddy, *J. Electroanal. Chem. Interfacial Electrochem.*, **10**, 199 (1965).
14. M. Tomkiewicz, in "Semiconductor Liquid-Junction Solar Cells," A. Heller, Editor, p. 92, The Electrochemical Society Softbound Proceedings Series, Princeton, N.J. (1977).
15. R. DeGryse, W. G. Gomes, F. Cardon, and J. Vennik, *This Journal*, **122**, 711 (1975).
16. W. Schottky, *Z. Phys.*, **113**, 367 (1939); **118**, 539 (1942).
17. N. F. Mott, *Proc. R. Soc. London, Ser. A*, **171**, 27 (1939).
18. H. Gerischer, in "Physical Chemistry An Advanced Treatise," Vol. IXA, H. Eyring, Editor, Chap. 5, Academic Press, New York (1970).
19. E. H. Nicollian and A. Goetzberger, *IEEE Trans. Electron Devices*, **ed-12**, 108 (1965).
20. S. R. Hofstein, K. H. Zaininger, and G. Warfield, *Proc. IEEE*, **52**, 971 (1964).
21. K. Lehovec and A. Slobodskoy, *Solid-State Electron.*, **7**, 59 (1964).
22. A. S. Grove, E. H. Snow, B. E. Deal, and C. T. Sah, *J. Appl. Phys.*, **35**, 2458 (1964).
23. E. C. Dutoit, F. Cardon, and W. P. Gomes, *Ber. Bun. Gesell.*, **80**, 475 (1976).

Effect of Excess Component Element during LPE on Electrical Properties of CdTe

J. Saraie,* M. Kitagawa, and T. Tanaka

Department of Electronics, Kyoto University, Kyoto 606, Japan

ABSTRACT

Epitaxial layers of CdTe from CdCl₂ solution show n-type conduction and their carrier concentration increases with the increase in the amount of excess Cd added to the solution during growth. The maximum available value is $4.8 \times 10^{17}/\text{cm}^3$. Carrier concentrations of p-type substrates change after growth from that of before growth and they decrease with the increase in the amount of excess Cd. High temperature defect equilibria have been calculated in which cadmium vacancy, interstitial cadmium, and vacancy-chlorine associates are taken into account. Equilibrium constants of formation of those associates have been determined. The carrier concentrations at room temperature have been explained by assuming the precipitation of some fraction of the native defects into neutral clusters during quenching.

The II-VI compounds have a strong tendency of self-compensation due to the ionic properties of bonding and it is well known that electrical properties of these materials are severely affected by the vapor pressure of a component element. It is desirable that the crystal growth is carried out under a well-defined pressure of component element in order to control the material properties. It has been reported as for CdTe that the electrical properties of bulk crystals grown under different Cd vapor pressures are very different (1, 2).

Recently we have reported the experimental results of LPE of n-CdTe in the CdTe-CdCl₂ system (3). The method employed in that paper is adequate for the growth of highly doped low resistivity material since chlorine is automatically doped and it is a shallow donor in CdTe. The growth is carried out in a sealed quartz ampul and a well-defined vapor pressure is maintained during growth. The addition of small amount of excess component element to the nutrient charge can change the vapor pressure inside the ampul during growth and hence the electrical properties of grown layers and substrates. In this paper we report the experimental results on the electrical properties of the epitaxially grown CdTe layers and those of the substrate as a function of growth temperature and an amount of excess component element (Cd or Te).

Theoretical calculation of defect equilibria of CdTe was performed first by de Nobel (4, 5) and many works have been published later (6-16). de Nobel has proposed the defect model in which cadmium vacancy (V_{Cd}) is a doubly ionizable native acceptor and interstitial cadmium (Cd_i) is a singly ionizable native donor. But it has been proved later that Cd_i is doubly ionizable from the experimental results of high temperature conductivity (7, 9, 11) and high temperature carrier concentration (10). Cd_i and V_{Te} , or V_{Cd} and Te_i cannot be distinguished by the sign of the electric charge and Chern *et al.* (13, 14) and Selim *et al.* (16) have considered those four native defects. V_{Cd} can make single and double associates with donors. The single associate is an acceptor and the double associate is a neutral one. As for halogen donor Canali *et al.* (17) have deduced the enthalpy of formation of single and double associate and Stuck *et al.* (15) have calculated the defect equilibria of halogen-doped semi-insulating CdTe using these values. As for indium donor Chern *et al.* (13) have determined the equilibrium constant of formation of the single associate. In

the calculation of the defect equilibria of heavily chlorine-doped CdTe in this paper, V_{Cd} and Cd_i (both are doubly ionizable) are considered as the native defects, and the single and double associates are taken into account. The experimental results are compared with the calculated results.

Experimental

CdTe layers were epitaxially grown using CdCl₂ as a solvent on (111) oriented substrates of p-type CdTe doped with phosphorus. The detailed technique was previously reported (3). A sealed quartz ampul containing the growth boat is shown in Fig. 1. The growth temperatures (T_G) were 550°-650°C, the cooling rate (R_c) was 0.55°C/min, and the temperature range in cooling (ΔT) was 20°C. The excess amounts of the component element added to the charge were 6, 4, 2, 1, 0.4 atomic percent (a/o) of Cd and 1 a/o of Te. These atomic fractions are referred to the amount of CdTe in the charge. The experiments without the excess element were also performed and we refer to them as the growth from the "stoichiometric solution" in the following part. After growth the solution was decanted and the ampul was pulled out from the furnace and air-quenched in order to freeze out the equilibrium state at a growth temperature.

Small indium electrodes were alloyed on the grown layer and the electrical properties were measured by the van der Pauw method between room and liquid nitrogen temperature. Electroless plated gold was used as the electrodes for the measurement of the p-type substrates.

Experimental Results

The grown layers were flat and mirror-smooth and the thickness was 30-60 μm . All the samples showed n-type conduction. Some papers on III-V compounds (18-21) have reported that the grown layers on (111)_A and (111)_B substrates show rather different properties. In our case the differences of the electrical properties between the layers on (111)_{Cd} and (111)_{Te} were small and we discuss the averaged data.

Figure 2 shows the electrical properties of the grown layers at room temperature as a function of the growth

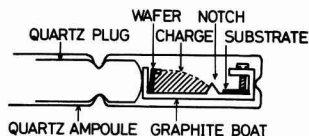


Fig. 1. Schematic drawing of the growth ampul

* Electrochemical Society Active Member.

Key words: CdCl₂ solvent, epitaxial growth, carrier concentration, component vapor pressure, defect equilibria.

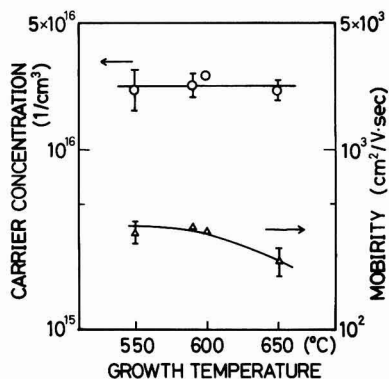


Fig. 2. Electrical properties of grown layers at room temperature as a function of growth temperature. These samples were grown from stoichiometric solution.

temperature T_G in the case of the stoichiometric solution. The carrier concentrations are $2 \times 10^{16}/\text{cm}^3$ and do not depend on T_G . The mobility is $300\text{--}400\text{ cm}^2/\text{V}\cdot\text{sec}$ and decreases slightly with the increase in T_G . The resistivity is as low as $1\ \Omega\cdot\text{cm}$. Figure 3 shows the dependence of the electrical properties on the excess amount of Cd or Te. In this case the growth temperature is 550°C . The carrier concentration increases with the increase of excess amount of Cd. The mobility curve has a maximum at about 2 a/o excess of Cd. In Fig. 4 examples of the temperature dependence of the carrier concentration and the mobility are shown. The mobility of all the samples decreases with decreasing temperature. Figure 5 shows the electrical properties of the p-type substrate after growth. The carrier concentration of the substrate is about $1.3 \times 10^{17}/\text{cm}^3$ before growth and it does not change after the growth from the stoichiometric solution, while it decreases with the increase of excess amount of Cd.

Discussion

Donors which are the origin of n-type conductivity are considered to be chlorine introduced from the

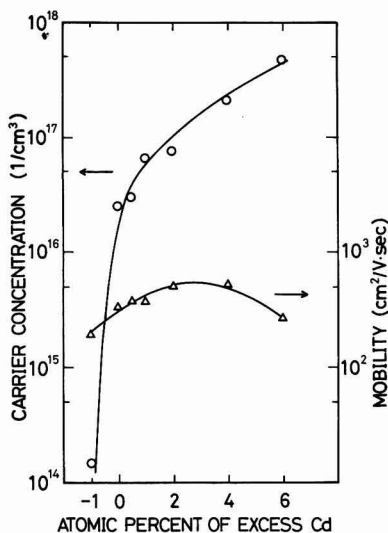


Fig. 3. Electrical properties of epitaxial layers grown under cadmium or tellurium excess conditions.

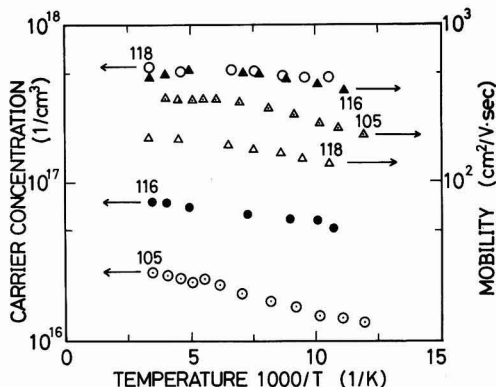


Fig. 4. Temperature dependence of electrical properties of grown layers. Sample 105 was grown from stoichiometric solution, sample 116 was grown under 2% Cd excess condition and sample 118 under 6% Cd excess condition.

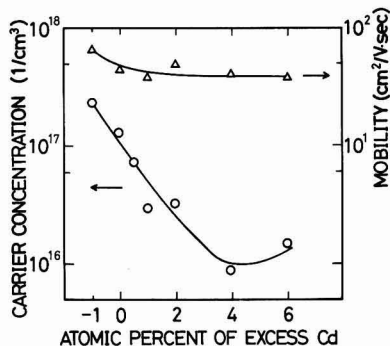


Fig. 5. Electrical properties of p-type substrate after growth under cadmium or tellurium excess conditions.

CdCl_2 solution. Chlorine would be contained up to the solubility limit and the grown layers are highly doped. It is the reason why all the samples show the tendency of ionized impurity scattering in Fig. 4. The maximum carrier concentration, $4.8 \times 10^{17}/\text{cm}^3$, is higher by a factor of 10^2 than that of the indium-doped epitaxial layer from Bi solvent (22, 23) and CdCl_2 seems to be an adequate solvent for the growth of low resistivity material.

The dependence of carrier concentration on excess Cd or Te is due to the change in the vapor pressure of Cd during growth. The crystal growth will be performed maintaining equilibrium between solid and vapor phase through the solution. The carrier concentration at room temperature can be estimated by calculating the defect equilibria at the growth temperature and assuming the rate of precipitation of native defects during quenching.

Defect formations and their ionization are described by the following relations and equilibrium constants for chlorine-doped grown layers

$$\text{Cd}_{\text{Cd}} = V'_{\text{Cd}} + \text{Cd}_i \quad K'_F = [V'_{\text{Cd}}][\text{Cd}_i] \quad [1]$$

$$0 = e^- + e' \quad K_i = n_i^2 = np \quad [2]$$

$$\text{Cd}(\text{g}) + V_i = \text{Cd}_i + e' \quad K_R = [\text{Cd}_i]n/p_{\text{Cd}} \quad [3]$$

$$V''_{\text{Cd}} + \text{Cl}'_{\text{Te}} = (V''_{\text{Cd}}\text{Cl}'_{\text{Te}})'$$

$$K_P = [(V''_{\text{Cd}}\text{Cl}'_{\text{Te}})']/[V''_{\text{Cd}}][\text{Cl}'_{\text{Te}}] \quad [4]$$

$$(V_{\text{Cd}}\text{Cl}_{\text{Te}})' + \text{Cl}'_{\text{Te}} = (V_{\text{Cd}}2\text{Cl}_{\text{Te}}) \times$$

$$K_{DP} = [(V_{Cd}2Cl_{Te})^*] / [(V_{Cd}Cl_{Te})'] [Cl_{Te}] \quad [5]$$

$$Cd^{\times}_1 = Cd_1 + e' \quad K_1 = 2n_0 \exp(-\Delta E_1/kT) \quad [6]$$

$$Cd'_1 = Cd_1 + e' \quad K_2 = 0.5n_0 \exp(-\Delta E_2/kT) \quad [7]$$

$$V^{\times}_{Cd} = V'_{Cd} + e' \quad K_3 = 2p_0 \exp(-\Delta E_3/kT) \quad [8]$$

$$V'_{Cd} + e' = V''_{Cd} \quad K'_4 = 0.5/n_0 \exp(\Delta E_4/kT) \quad [9]$$

$$(V_{Cd}Cl_{Te})^{\times} = (V_{Cd}Cl_{Te})' + e'$$

$$K_5 = 0.5p_0 \exp(-\Delta E_5/kT) \quad [10]$$

$$Cl^{\times}_{Te} = Cl_{Te} + e' \quad K_6 = 0.5n_0 \exp(-\Delta E_6/kT) \quad [11]$$

where $n_0 = 2(2\pi m^*_{\text{n}} kT/h^2)^{3/2}$, $m^*_{\text{n}} = 0.11 m_0$; $p_0 = 2(2\pi m^*_{\text{p}} kT/h^2)^{3/2}$, $m^*_{\text{p}} = 0.40 m_0$; ΔE_1 = ionization energy.

Charge neutrality equation

$$n + [V'_{Cd}] + 2[V''_{Cd}] + [(V_{Cd}Cl_{Te})'] = p + [Cd'_1] + 2[Cd''_1] + [Cl_{Te}] \quad [12]$$

Total concentration of chlorine

$$[(Cl)_{\text{total}}] = [Cl^{\times}_{Te}] + [Cl_{Te}] + [(V_{Cd}Cl_{Te})^{\times}] + [(V_{Cd}Cl_{Te})'] + 2[(V_{Cd}2Cl_{Te})^{\times}] \quad [13]$$

The symbols used are usual ones.

The set of equations, [1]-[13], was solved with a computer as a function of cadmium vapor pressure (p_{Cd}) using $[(Cl)_{\text{total}}]$ as a parameter. The energy level diagram in Fig. 6 shows the most probable position of energy levels of defects in CdTe deduced from the literature. Table I lists the value of equilibrium constants used in the calculation.

Calculated isotherms of CdTe:Cl at 550°C are shown in Fig. 7 and Fig. 8. Figure 7 is a result using the value of equilibrium constants in Table I. Figure 8 is a result using the value of $4/1.55 \times 10^{22}$ as the pre-exponential factor of K_P and assuming $K_P = K_{DP}$ as Canali *et al.* (17) have proposed. In Fig. 8 the concentration of the $(V_{Cd}Cl_{Te})^{\times}$ acceptors is larger than that of the Cl_{Te} donors. It means that the grown layers are essentially p type. This situation is the same in the above range of p_{Cd} and the range of $[(Cl)_{\text{total}}]$ between 1×10^{17} and $5 \times 10^{19} \text{ cm}^{-3}$. It contradicts the experimental results and it is why we adopt the value of $0.04/1.55 \times 10^{22}$ as the pre-exponential factor of K_P .

The carrier concentrations at room temperature can be deduced from the isotherms in Fig. 7. In the case of the stoichiometric solution p_{Cd} inside the ampul during growth is determined by the dissociation of $CdCl_2$ and CdTe if we neglect the interaction of $CdCl_2$ and CdTe. The vapor pressure of $CdCl_2$ is rather high and about 10^{-3} atm at 550°C. But p_{Cd} resulting from dissociation of $CdCl_2$ is very low and is calculated to be 1.4×10^{-6} atm at 550°C from the

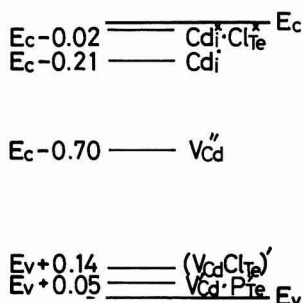


Fig. 6. Energy level in CdTe introduced by disorders

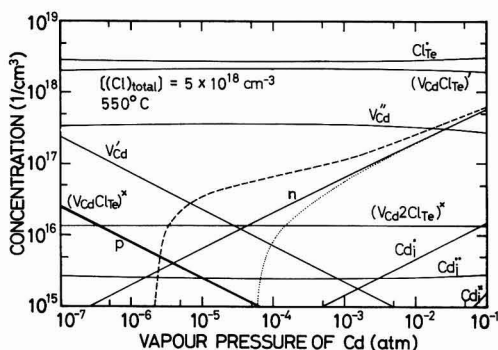


Fig. 7. Defect concentration isotherms at 550°C for chlorine-doped grown layers. $[(Cl)_{\text{total}}]$ is taken to be $5 \times 10^{18} \text{ cm}^{-3}$. The dotted curve shows the electron concentration at room temperature when all V_{Cd} are frozen during quenching. The broken curve shows the one when 8.4% of V_{Cd} precipitate into neutral clusters.

thermodynamic data (36). It is about 1/3 of the minimum pressure of CdTe at 550°C, 4.5×10^{-6} atm (4). It means that the dissociation of $CdCl_2$ is suppressed by that of CdTe. p_{Cd} in the ampul is considered to be 4.5×10^{-6} atm at 550°C. Then we can also neglect the contributions of $CdCl_2$ dissociation to p_{Cd} in the case of the Cd excess condition. It is assumed in the following that the grown layers at 550°C from the stoichiometric solution are equilibrated with p_{Cd} of 4.5×10^{-6} atm due to the dissociation of CdTe.

In order to calculate the room temperature carrier concentrations we must assume the condition of the redistribution of atomic disorders and free carriers

Table I. Equilibrium constants, $K = K_0 \exp(-H/kT)$ or $K_0 \exp(-\Delta E/kT)$. Concentrations are expressed in cm^{-3}

	K_0	H or ΔE (eV)	References	Remarks
K_F'	7.6×10^{30}	1.04	(6)	
K_1	$1.03 \times 10^{30} T^3$	1.73		
K_R	1.0×10^{30}	-0.81	(5)	Adjusted from Smith (10) by increasing the activation energy leaving the absolute values at 550°C unchanged.
K_P	$0.04/1.55 \times 10^{22}$	-0.96		Reduced pre-exponential factor from Canali <i>et al.</i> (17)
K_{DP}	$0.04/1.55 \times 10^{22}$	-0.48		
K_1	$2n_0^*$	0.02	(4)	
K_2	$0.5n_0$	0.21	(7, 11, 24)	
K_3	$2p_0^*$	0.05	(24-28)	
K_4'	$0.5/n_0$	-0.70	(4, 25-30)	
K_5	$0.5p_0$	0.14	(31, 32)	
K_6	$0.5n_0$	0.02	(4, 6, 33, 34)	
K_7	$0.5p_0$	0.05	(35)	

* $n_0 = 1.75 \times 10^{14} T^{3/2}$; $p_0 = 1.22 \times 10^{12} T^{3/2}$.

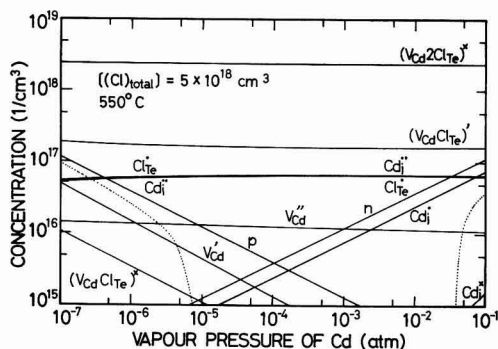


Fig. 8. Defect concentration isotherms at 550°C for chlorine-doped grown layers. The pre-exponential factor of K_P and K_{DP} is taken to be $4/1.55 \times 10^{22}$ and K_{DP} is taken to be equal to K_P . The dotted curve shows the one as in Fig. 7 (left, hole concentration; right, electron concentration).

during quenching. If it is assumed that all the atomic disorders are frozen and only the free carriers redistribute, the grown layers from stoichiometric solution must be semi-insulating as shown in Fig. 7 by the dotted curve. The speed of quenching is not sufficiently rapid because the samples are quenched together with the graphite boat with rather large heat capacity and in these cases it is necessary to consider the precipitation of atomic disorders. Such effects have been reported by de Nobel (4, 5), and Chern *et al.* (13) have taken account of the precipitation of Cd_i and V_{Cd} for indium-doped CdTe. There are many V_{Cd} 's at high temperature as shown in Fig. 7. If some fraction of them precipitate into neutral clusters, the same number of electrons as that of total charges of precipitating V_{Cd} must be created in order to maintain electrical neutrality. Those electrons can make the sample conductive n-type which otherwise is semi-insulating. We have adjusted the rate of precipitation to satisfy the condition that the carrier concentration at room temperature is $2 \times 10^{16} \text{ cm}^{-3}$ at the p_{Cd} of $4.5 \times 10^{-6} \text{ atm}$ as for the grown layers from the stoichiometric solution. The value has been determined to be 0.084. The broken line in Fig. 7 shows the carrier concentrations at room temperature assuming that the rate of precipitation of V_{Cd} is constant in the shown range of p_{Cd} . The rate of precipitation of Cd_i is assumed to be unity in the above calculation, it does not affect the result, however, because the concentration of Cd_i is small in the n-type material. The minimum value of $[(Cl)_{total}]$ is adopted in Fig. 7 which gives our maximum carrier concentration of $4.8 \times 10^{17} \text{ cm}^{-3}$ at smaller p_{Cd} than the saturation pressure of pure Cd at 550°C. Even if we assume the larger $[(Cl)_{total}]$, the calculated curves of carrier concentrations at room temperature differ only slightly with each other so far as we adjust the rate of precipitation of V_{Cd} as above. But the concentration of the double associates increases with the increase in $[(Cl)_{total}]$ and as discussed in the following, $[(Cl)_{total}]$ cannot exceed $2.4 \times 10^{19} \text{ cm}^{-3}$ in order to describe the experimental value of mobility.

If we use the value of $0.04/1.55 \times 10^{22}$ for the pre-exponential factor of K_P and assume that $K_{DP} = K_P$, the value of $[(Cl)_{total}]$ and the rate of precipitation of V_{Cd} can be adjusted so as to satisfy the above condition. It is necessary to know the number of double associates to determine the value of K_{DP} . We can estimate the maximum number of the double associates from the value of mobility. The double associates can scatter electrons as neutral centers. The mobility of electrons in CdTe due to neutral impurity scatter-

ing is expressed as follows

$$\mu_N = 1.52 \times 10^{20}/N_n \quad \text{cm}^2/\text{V} \cdot \text{sec} \quad [14]$$

where N_n is the concentration of the neutral centers. It reveals that the value of N_n cannot exceed $3.0 \times 10^{17} \text{ cm}^{-3}$ by roughly assuming that the value of the room temperatures mobility of 500 $\text{cm}^2/\text{V} \cdot \text{sec}$ is determined only by neutral impurity scattering. This condition is satisfied if $K_{DP} \leq K_P/100$. We estimate $H_{DP} = H_P/2$ in Table I because H_P is pairing enthalpy between divalent and monovalent centers and H_{DP} is that between monovalent centers. In our case $K_{DP} \approx K_P/1000$ at the temperatures of 550°-650°C.

Figure 9 shows the carrier concentrations at room temperature of the layers grown at 550°, 600°, and 650°C. The total chlorine concentration and the rate of precipitation of V_{Cd} are roughly assumed to be the same at 600° and 650°C as those at 550°C. The experimental data are plotted at the minimum pressure of CdTe and are rather well described by the calculated curves.

The effective p_{Cd} during growth has been deduced from Fig. 3 and 7. They are shown in Fig. 10. It seems

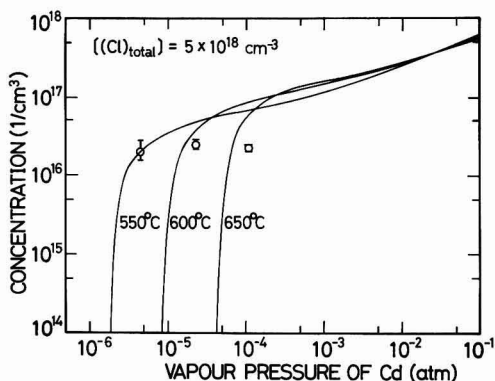


Fig. 9. Calculated electron concentration at room temperature of the layers grown at 550°, 600°, and 650°C. The value of $[(Cl)_{total}]$ and the rate of precipitation of V_{Cd} during quenching are assumed to be the same for all temperatures. Open circles are the experimental results for the grown layers from stoichiometric solution.

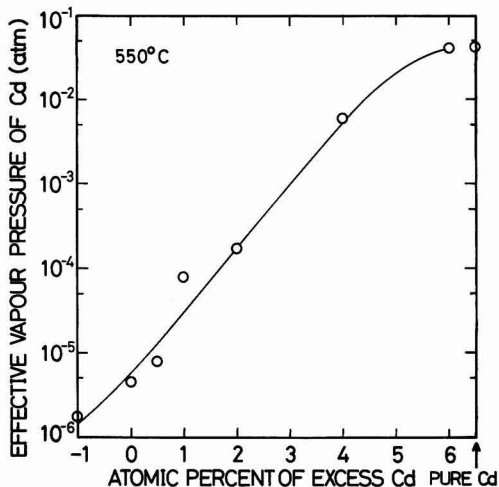


Fig. 10. Effective vapor pressure of cadmium inside the ampul vs. excess amount of cadmium added to the charge.

that they change nearly exponentially with excess Cd content in the solution.

The change of the properties of the substrates is described under the same calculation. Phosphorus is considered to be a shallow acceptor substituting Te site. As the reaction of defect formation and ionization, the aforementioned formulas [1]-[3], [6]-[9], and the following are considered

$$P^{\times}Te = P'Te + e^{-} \quad K_7 = 0.5p_0 \exp(-\Delta E_7/kT) \quad [15]$$

Charge neutrality equation

$$n + [V'_{Cd}] + 2[V''_{Cd}] + [P'Te] \\ = p + [Cd_i] + 2[Cd\cdot i] \quad [16]$$

Total concentration of phosphorus

$$[(P)_{total}] = [P^{\times}Te] + [P'Te] \quad [17]$$

The value of K_7 is listed in Table I. The equilibrium reactions of phosphorus itself with vapor phase are neglected. The set of those equations can be solved by Brouwer's plot but we have solved it with a computer.

Figure 11 shows the isotherms at 550°C in the case of total phosphorus concentration of $5 \times 10^{18} \text{ cm}^{-3}$. This value of $[(P)_{total}]$ is close to that obtained by Hall *et al.* at 900° and 950°C (39). The experimental results are plotted simultaneously in Fig. 11 at p_{Cd} shown in Fig. 10. Those experimental results seem to be near the calculated curve of the hole concentration at high temperature except two points at high p_{Cd} . If we adjust the rate of precipitation of Cd_i by making the hole concentration at room temperature to be $1.3 \times 10^{17} \text{ cm}^{-3}$ at p_{Cd} of $4.5 \times 10^{-6} \text{ atm}$, the value has been determined to be small and to be 0.0046. This small value means that Cd_i is stabilized by the existence of acceptors as in the case of CdTe: Au (37, 38). The broken curve in Fig. 11 is the calculated hole concentration at room temperature. (The dotted curve is the one when we assume complete freeze of Cd_i .) The rate of precipitation of V_{Cd} is arbitrarily chosen to be the same as that estimated above for the grown layers, but it does not affect the results essentially since the concentration of V_{Cd} is small in p-type substrates. The broken curve in Fig. 11 explains well the experimental data under p_{Cd} of $2 \times 10^{-4} \text{ atm}$, but above $3 \times 10^{-4} \text{ atm}$ the sample should be semi-insulating and the calculated results do not explain the experimental data. We cannot fit all the experimental data by changing the value of $[(P)_{total}]$ and the rate of precipitation of Cd_i so far as we adjust the carrier

concentration at $4.5 \times 10^{-6} \text{ atm}$. This deviation seems to be easily described by the increase in $[(P)_{total}]$ (39) and/or the rate of precipitation at high p_{Cd} .

In all the above discussion we have adjusted the value of the rate of precipitation of native defects so as to explain the experimental results. Chern *et al.* (13) have considered two kinds of native donors (Cd_i and V_{Te}) and two kinds of native acceptors (V_{Cd} and Te_i). They have proposed the model in which only Cd_i and V_{Cd} easily precipitate into neutral clusters and others are stable during quenching. It may be possible to correspond our values of the rate of precipitation to the roughly estimated values of the rate of the concentration of easily precipitating defects in their model. As for phosphorus-doped CdTe Selim *et al.* (16) have proposed the complex defect model including P_{Te} , P_i , P_{Cd} , their associates and four kind of native defects. They have reported the calculated results at 700°C in which the hole concentrations have a maximum at high p_{Cd} . It may be possible to explain the experimental data not by adjusting the rate of precipitation but by adopting different defect models from ours but the further discussion of detailed defect model is beyond the scope of this paper.

Summary

Epitaxially grown CdTe layers in the CdTe-CdCl₂ system show n-type conduction. The electron concentrations at room temperature change by many orders by the addition of Cd or Te to the charge during LPE, and maximum value available is $4.8 \times 10^{17} \text{ cm}^{-3}$. The properties of the p-type substrates also change after growth from that before growth and the hole concentrations decrease with the increase in the amount of excess Cd. It reveals that the addition of excess component element to the charge is a useful and simple method to control the component vapor pressure inside the ampul and hence to control the electrical properties of grown layers.

We have calculated the defect equilibria at the growth temperature, considering the doubly ionizable native defects, V_{Cd} and Cd_i and taking into account the single and double associates between V_{Cd} and Cl_{Te} . The probable values of the equilibrium constants of the formation of those associates have been determined. The experimental results of the electron concentration of the grown layers are explained, assuming the values of $[(Cl)_{total}]$ and the rate of precipitation of V_{Cd} . The effective vapor pressure of cadmium inside the ampul has been determined with which the grown layers were equilibrated during growth. The calculation in which simple phosphorus acceptor, P_{Te} , is considered shows that the experimental results of the hole concentration of the substrates are well explained at $p_{Cd} < 2 \times 10^{-4} \text{ atm}$ but they cannot be explained at $p_{Cd} > 3 \times 10^{-4} \text{ atm}$ so far as the same values of $[(P)_{total}]$ and the rate of precipitation of Cd_i as those at the low p_{Cd} are used. The possible origin of the deviation was discussed.

Acknowledgment

The authors would like to thank Mr. K. Nishimoto for his assistance in this work.

Manuscript submitted June 22, 1978; revised manuscript received June 11, 1979.

Any discussion of this paper will appear in a Discussion Section to be published in the June 1980 JOURNAL. All discussions for the June 1980 Discussion Section should be submitted by Feb. 1, 1980.

REFERENCES

1. N. R. Kyle, *This Journal*, **118**, 1790 (1971).
2. T. Taguchi, J. Shirafuji, and Y. Inuishi, *Rev. Phys. Appl.*, **12**, 1 (1977).
3. J. Sraia, M. Kitagawa, M. Ishida, and T. Tanaka, *J. Cryst. Growth*, **43**, 13 (1978).
4. de Nobel, *Philips Res. Rep.*, **14**, 361 (1959).
5. de Nobel, *ibid.*, **14**, 430 (1959).

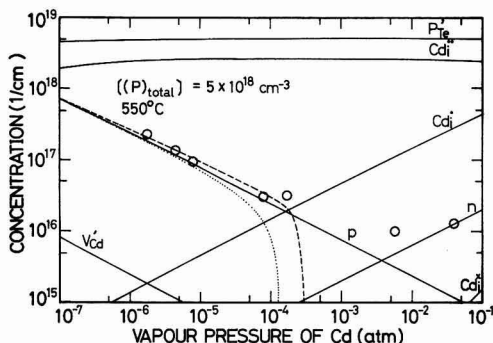


Fig. 11. Defect concentration isotherms at 550°C for the phosphorus-doped substrates. $[(P)_{total}]$ is taken to be $5 \times 10^{18} \text{ cm}^{-3}$. The dotted curve shows the hole concentration at room temperature when all Cd_i are frozen during quenching. The broken curve shows the one when 0.46% of Cd_i precipitates into neutral clusters. Open circles are the experimental results.

6. F. A. Kröger, *J. Phys. Chem. Solids*, **26**, 1717 (1965).
7. R. C. Whelan and D. Shaw, *Phys. Status Solidi*, **29**, 145 (1968).
8. O. A. Matveev, Yu. V. Rud', and K. V. Sanin, *Sov. Phys. Semicond.*, **3**, 779 (1969).
9. K. R. Zanio, *Appl. Phys. Lett.*, **15**, 260 (1969).
10. F. T. J. Smith, *Metal. Trans.*, **1**, 617 (1970).
11. Yu. V. Rud' and K. V. Sanin, *Sov. Phys. Semicond.*, **5**, 244 (1971).
12. F. A. Selim, V. Swaminathan, and F. A. Kröger, *Phys. Status Solidi*, **A**, **29**, 465 (1975).
13. S. S. Chern, H. R. Vidyantath, and F. A. Kröger, *J. Solid State Chem.*, **14**, 33 (1975).
14. S. S. Chern and F. A. Kröger, *ibid.*, **14**, 44 (1975).
15. R. Stuck, A. Cornet, C. Scharager, and P. Siffert, *J. Phys. Chem. Solids*, **37**, 989 (1976).
16. F. A. Selim and F. A. Kröger, *This Journal*, **124**, 401 (1977).
17. C. Canali, G. Ottaviani, R. O. Bell, and F. V. Wald, *J. Phys. Chem. Solids*, **35**, 1405 (1974).
18. H. Kressel and H. Nelson, *J. Appl. Phys.*, **40**, 3720 (1969).
19. H. Benking and W. Vits, in Proceedings of International Symposium on Gallium Arsenide, 2nd (1968), Inst. Phys. Soc. Conf. Ser. No. 7, p. 96 (1969).
20. C. S. Kang and P. D. Greene, *ibid.*, p. 18.
21. B. H. Ahn, R. R. Shurtz, and L. W. Trussell, *J. Appl. Phys.*, **42**, 4512 (1971).
22. H. Ishida and K. Tanaka, in Proceedings of 3rd Conference on Solid State Devices, Tokyo, 1971, *Oyo Buturi (J. Jpn. Soc. Appl. Phys.)*, **41**, Suppl. p. 117 (1972).
23. S. Fujita, Ph.D. Thesis, Kyoto University (1975).
24. V. S. Ivanov, V. B. Stopachinskii, and V. A. Chapin, *Sov. Phys. Semicond.*, **5**, 83 (1971).
25. M. R. Lorentz and B. Segall, *Phys. Lett.*, **7**, 18 (1963).
26. M. R. Lorentz and B. Segall, *Phys. Rev.*, **134**, 751 (1963).
27. B. M. Vul, V. S. Vavilov, V. S. Ivanov, V. B. Stopachinskii, and V. A. Chapin, *Sov. Phys. Semicond.*, **4**, 52 (1970).
28. B. M. Vul, V. S. Vavilov, V. S. Ivanov, V. B. Stopachinskii, and V. A. Chapin, *ibid.*, **6**, 1255 (1973).
29. N. V. Agrinskaya, E. N. Arkad'eva, and O. A. Matveev, *ibid.*, **4**, 306 (1970).
30. K. Zanio, W. M. Akutagawa, and R. Kikuchi, *J. Appl. Phys.*, **39**, 2818 (1968).
31. A. A. Abramov, V. S. Vavilov, and L. K. Vodop'yanov, *Sov. Phys. Semicond.*, **4**, 219 (1970).
32. B. Furgolle, M. Hoclet, M. Vandevyver, Y. Marfaing, and T. Triboulet, *Solid State Commun.*, **14**, 1237 (1974).
33. F. V. Wald and R. O. Bell, *Nature*, **237**, 13 (1972).
34. N. V. Agrinskaya, E. N. Arkad'eva, and O. A. Matveev, *Sov. Phys. Semicond.*, **5**, 762 (1971).
35. E. N. Arkad'eva, O. A. Matveev, and Yu. V. Rud', *Sov. Phys. Solid State*, **8**, 2260 (1967).
36. O. Kubashevski, E. L. Evans, and C. B. Alcock, in "Metallurgical Thermochemistry," 4th ed., Pergamon Press (1967).
37. W. Akutagawa, D. Turnbull, W. K. Chu, and J. W. Mayer, *Solid State Commun.*, **15**, 1919 (1974).
38. W. Akutagawa, D. Turnbull, W. K. Chu, and J. W. Mayer, *J. Phys. Chem. Solids*, **36**, 521 (1975).
39. R. B. Hall and H. H. Woodbury, *J. Appl. Phys.*, **39**, 5361 (1958).

Outdiffusion of Recombination Centers from the Substrate into LPE Layers; GaAs

L. Jastrzebski,¹ J. Lagowski, and H. C. Gatos*

Department of Materials Science and Engineering,
Massachusetts Institute of Technology, Cambridge, Massachusetts 02139

ABSTRACT

Experimental results are presented showing that outdiffusion of recombination centers from the GaAs substrate into the epitaxial layer takes place during growth. Such outdiffusion decreases the carrier lifetime in the epitaxial layer to much lower values than the radiative recombination limit. Furthermore, it introduces a lifetime gradient across the epitaxial layer which depends critically on the growth velocity and thermal treatment. High rates of growth (such as those attainable in electroepitaxy) and high cooling rates can minimize the adverse effects of normally available substrates on the epitaxial layers; however, good quality substrates are essential for the consistent growth of device quality layers.

It has been established that the performance of many compound semiconductor devices is adversely affected by nonradiative recombination centers. Their presence in the device active region leads to a decrease in the device efficiency [as in the case of solar cells (1)]. Furthermore, the recombination-enhanced diffusion of such centers (2) causes a slow degradation of the device performance [as in the case of semiconductor lasers (3)].

The nonradiative recombination centers in GaAs are usually associated with residual impurities such as oxygen (4), transition metals (5), and nonstoichiometric point defects (6). The origin of nonstoichiometric defects is not fully understood, although in GaAs it has been attributed to the solidus of the phase

diagram (7) and/or to As depletion of the substrate during the heating cycle prior to epitaxial growth (8). Growth at low temperatures and backmelting of the substrate prior to growth (9) tend to reduce the concentration of nonstoichiometric defects and improve the quality of the grown epitaxial layer.

Poor quality GaAs substrate material is a source of defects which can diffuse into the epitaxial layer during the growth process. The available melt-grown GaAs substrates are in most instances highly compensated (10), exhibit large carrier concentration inhomogeneities (11), and contain high concentration of nonradiative recombination centers (12, 13).

The present work is concerned with the outdiffusion of recombination centers from GaAs substrates into GaAs LPE layers. Minority carrier diffusion length and lifetime profiles obtained with EBIC-mode (SEM) measurements are employed for the study of such outdiffusion. Growth conditions required to minimize

* Electrochemical Society Active Member.

¹ Present address: RCA Research Laboratories, David Sarnoff Research Center, Princeton, New Jersey 08540.

Key words: growth, semiconductor, lasers.

the outdiffusion of recombination centers are pointed out.

Experimental

Epitaxial growth and sample preparation.—LPE growth of GaAs was carried out employing classical thermal coating techniques and electromigration-controlled electroepitaxy (14, 15). Cd-doped ($p \approx 2 \times 10^{17} \text{ cm}^{-3}$) 300 μm thick (100) substrates were used. Epitaxial growth was performed in a two-well graphite boat. In one of the wells the substrates were backmelted (about 25 μm) with an under-saturated solution to remove the As depleted layer formed during the heating cycle. After backmelting the substrate was positioned in the second well containing 2.5g of an undoped Ga-As solution with a GaAs source on top. In the electroepitaxy experiments layers ranging in thickness from 10 to 100 μm were grown at 900°C on an area of 0.5 cm^2 at a rate of about 6 $\mu\text{m}/\text{min}$ by passing an electric current of 60 A/ cm^2 for a period of 2–20 min. Growth was terminated by turning the current off. In the thermal growth experiments the growth was performed from equilibrated solutions by cooling from 910° to 900°C at a rate of 1°C/min.

In both procedures, after growth was completed, the system was kept at the growth temperature for time periods ranging from 1 min to 3 hr with the grown layer in contact with the solution. The experiment was terminated by quenching the system to room temperature with an initial cooling rate (from 900° to 700°C) of about 70°C/min. The solution was left over the epitaxial layer or wiped by the moving slider prior to cooling.

After cooling, if the excess Ga-GaAs mixture was not wiped, it was removed from the epitaxial layer surface by boiling in HCl; the epilayer was cleaved and etched in AB etchant for about 30 sec. Interference contrast microscopy was employed to determine the thickness of the epitaxial layers. Whenever necessary, the part of the epitaxial layer grown during cooling to room temperature (about 5–10 μm in thickness) was etched away in 5 parts $\text{H}_2\text{SO}_4 + 1 \text{ H}_2\text{O} + 1 \text{ H}_2\text{O}_2$. Ohmic contacts were soldered on the substrate and the epilayer employing Sn and In in an H_2 atmosphere.

The epitaxial layers were n-type with a carrier concentration of about $5 \times 10^{16} \text{ cm}^{-3}$. Schottky barriers required for EBIC-mode measurements were made by evaporating aluminum or gold on the surfaces of the epitaxial layer.

Minority carrier diffusion length and lifetime.—Measurements of the minority carrier diffusion length were performed utilizing electron beam excitation as shown schematically in Fig. 1. The diffusion length was obtained from the dependence of the electron beam-induced current (EBIC) on the distance between the generation position and the collecting Schottky barrier or the p-n junction (16). Reabsorption of photons resulting from radiative recombination in general intro-

duces uncertainties in the determination of the minority carrier diffusion length. However, in the present case, such uncertainties are of no consequence, since the lifetime of the minority carriers was significantly lower (up to two orders of magnitude) than the radiative recombination limit. A 35 keV electron beam energy was used in all experiments to minimize the effect of surface recombination on the measured diffusion length (17).

The configuration shown in Fig. 1 made possible the determination of the diffusion length, L_p , of the minority carriers in the epitaxial layer near the epilayer surface (with the electron beam at position 1 and with current circuit I), and near the substrate (with the electron beam in position 2 and with current circuit II); the minority carrier diffusion length was also determined in the p-type substrates (with the electron beam in position 3 and with current circuit II).

Values of lifetime, τ , were estimated from the standard relationship, $L = \left(\frac{kT}{e} \mu \tau \right)^{1/2}$, where μ is the

minority carrier mobility and kT/e equals 0.026V at 300°K. In p-type GaAs (substrates in the present case) the electron mobility can be noticeably smaller than the mobility of electrons in n-type material of similar free carrier concentration (18). Accordingly, in evaluating the electron lifetime in the substrates recently calculated theoretical values of electron mobility in p-type GaAs were used (18). In these calculations the contribution of electron scattering by heavy holes and the difference in screening energies between holes and electrons have been taken into account. In the case of holes their mobility as majority or minority carriers is expected to be similar at room temperature and for free carrier concentrations below 10^{17} cm^{-3} (since screening effects and carrier-carrier scattering are not significant). Accordingly, in evaluating the hole lifetime in epitaxial layers, the hole mobility value of $\mu_p \approx 300 \text{ cm}^2/\text{V-sec}$ was used, i.e., the hole mobility in p-type GaAs with hole concentration of $5 \times 10^{16} \text{ cm}^{-3}$ (19), which is similar to the electron concentration in the epitaxial layers.

Results and Discussion

Substrate.—The minority carrier lifetime in the substrate material was found to be about 10^{-10} sec , i.e., two orders of magnitude smaller than the lifetime value expected from band-to-band radiative recombination (20). It was also determined that the substrate material is highly inhomogeneous with local lifetime fluctuations exceeding a factor of 4. These findings clearly indicate that the lifetime in the substrates is controlled entirely by nonradiative recombination and thus the substrate must contain a high, nonuniform, concentration of recombination centers.

Outdiffusion of recombination centers from the substrate.—The lifetime in the epitaxial layers was measured as a function of position on a given plane parallel to the surface, as a function of distance from the substrate-epitaxial layer interface, and as a function of time the layer was kept at the growth temperature.

Typical results of the lifetime measurements as a function of position on a plane parallel to the surface of the epitaxial layer are given in Fig. 2. The upper curve corresponds to positions near the surface of the epitaxial layer. The layer was 40 μm thick; it was grown electroepitaxially and was kept 20 min at the growth temperature (from the beginning of growth to the beginning of cooling). It is evident from Fig. 2 that lifetime inhomogeneities of a similar nature are present near the substrate-epitaxial interface and near the surface of the layer; however, near the surface the lifetime values are significantly higher. It should be noted that even the highest values of lifetime are well below the values (of the order of 10^{-7} sec) expected from radiative band-to-band recombination (20).

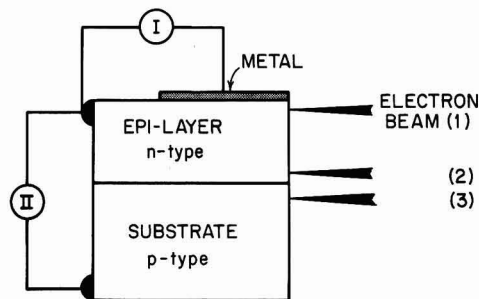


Fig. 1. Schematic representation of the experimental configuration for the determination of the minority carrier diffusion length by the EBIC method; see text.

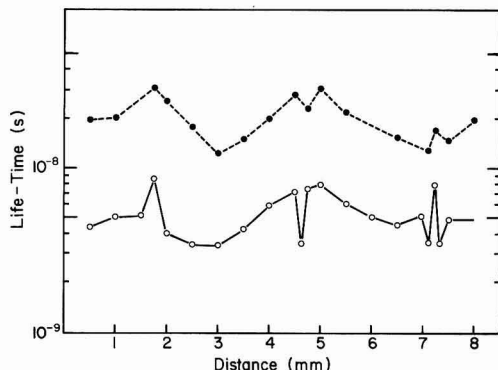


Fig. 2. Minority carrier lifetime profiles along two planes parallel to the growth interface; \circ —near the original growth interface (position 2 in Fig. 1); \bullet —near surface of epitaxial layer (position 1 in Fig. 1).

The above behavior of the minority carrier lifetime can be understood if one considers that the substrate represents a source of recombination centers which diffuse into the epitaxial layer during the growth process and thermal treatment. On this basis, the difference between the lifetime near the epitaxial layer surface and the lifetime near the epitaxial layer-substrate interface should decrease with increasing exposure time of the system to the growth temperature. Similarly, the lifetime in the epitaxial layer should decrease with increasing exposure time to the growth temperature. As is seen from Fig. 3, such behavior is indeed found in electroepitaxially and in thermally grown layers. The lifetime in both electroepitaxially and thermally grown layers behaves similarly upon exposure to high temperature after growth, as it is dominated by recombination at outdiffused centers.

The fact that recombination centers outdiffuse from the substrate into the epitaxial layers is further sup-

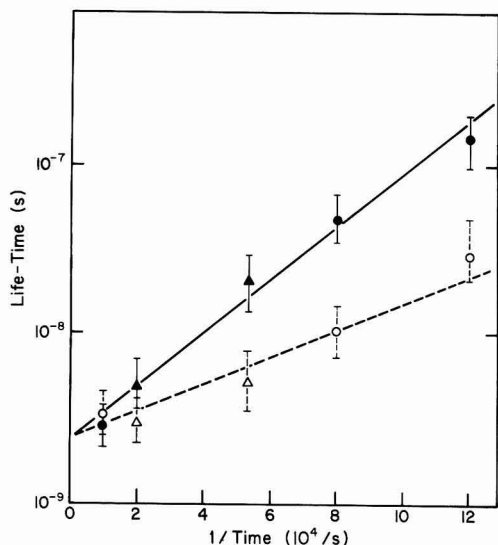


Fig. 3. Minority carrier lifetime as a function of time at the growth temperature (900°C); Δ , \circ near the original growth interface; \blacktriangle , \bullet —near the surface of the epitaxial layer; circles correspond to layers grown by electroepitaxy and triangles to thermally grown layers; all layers were 40 μ m thick.

ported by the results shown in Fig. 4. Here the lifetime measured near the epitaxial layer surface is plotted as a function of thickness of the epitaxial layers, all of which have been exposed to a high temperature (growth temperature) for the same period of time (20 min). The layers were grown by electroepitaxy and at the same growth rate of about 6 μ m/min. It is seen that the lifetime increases by about two orders of magnitude (near the surface) as the distance from the substrate (thickness of the layer) increases from 5 to 90 μ m.

If the simplified assumption is made that the lifetime is inversely proportional to the concentration of the recombination centers, the data of Fig. 3 and 4 can be used to estimate the diffusion constant of the recombination centers. Thus, treating the substrate-epitaxial layer interface as a limited diffusion source (21) the lifetime becomes

$$\frac{1}{\tau} \sim \frac{1}{\sqrt{Dt}} \exp\left(-\frac{x^2}{4Dt}\right) \quad [1]$$

where x is the distance from the substrate-epitaxial layer interface, t is the time, and D is the diffusion constant of recombination centers. From this expression the solid line in Fig. 3 is obtained by taking $x = \text{constant}$ and the solid line in Fig. 4 by taking $t = \text{constant}$. From these plots a value for the diffusion constant of the recombination centers of approximately 5×10^{-9} cm²/sec is obtained (900°C). The same value of 5×10^{-9} cm²/sec has been reported for point defect diffusion in GaAs (gallium vacancies) at 1000°C (22).

It is important to note that the observed lifetime behavior which is consistent with the above diffusion model, cannot be explained on the basis of impurity segregation effects. A recent experimental and theoretical analysis of impurity segregation in GaAs during electroepitaxy (23) has shown that the maximum changes of the dopant segregation coefficients do not exceed 40%, i.e., they are two orders of magnitude smaller than the changes required to account for the presently reported lifetime behavior.

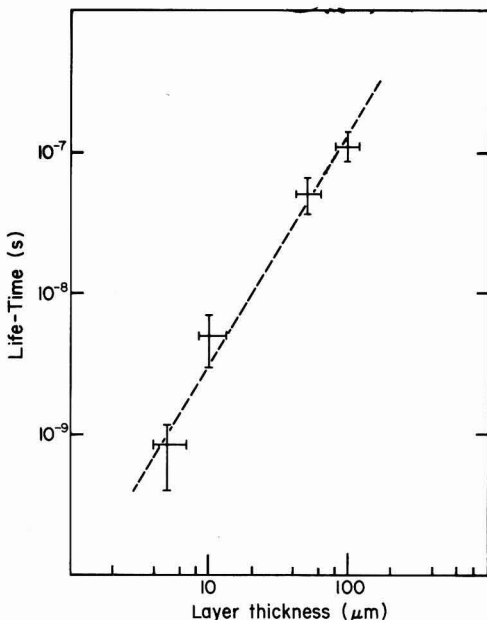


Fig. 4. Minority carrier lifetime near the surface of the layers as a function of the layer thickness.

Growth velocity and the effects of outdiffusion.—The diffusion constant of impurities and point defects decreases exponentially with decreasing temperature, and thus lowering the growth temperature should drastically reduce the effects of outdiffusion from the substrate. However, there are limitations to the lowering of the growth temperature as the attainable growth rate decreases significantly and single crystal growth becomes problematic.

On the other hand, it is evident that the effects of outdiffusion can be reduced if the growth velocity, R , is much greater than the velocity of the diffusion front propagation v_D . In a diffusion process a constant concentration profile can be approximated as $x^2/4Dt = \text{const.}$; consequently, $v_D = dx/dt = \text{const.} \sqrt{D/t}$. Thus, the condition $R \gg v_D$ can be expressed as

$$R \gg \left(\frac{D}{t} \right)^{1/2} \quad [2a]$$

or

$$R \gg \frac{D}{t} \quad [2b]$$

Equation [2a] represents the case where growth is performed for certain time t and Eq. [2b] represents the case where the growth of a layer of a thickness d is required.

In the present case the outdiffusion constant of recombination centers was found to be $5 \times 10^{-9} \text{ cm}^2/\text{sec}$. Thus, according to Eq. [2b], for a layer $40 \mu\text{m}$ thick the growth rate required to reduce significantly the effect of outdiffusion is $R \gg 0.75 \mu\text{m}/\text{min}$. In the present experiments the electroepitaxial growth velocity was about $6 \mu\text{m}/\text{min}$, which is high enough to satisfy the above condition for reducing significantly the effects of outdiffusion of recombination centers. Accordingly, it is not surprising that, without a postgrowth heat-treatment epitaxial layers $40 \mu\text{m}$ thick were consistently grown with a lifetime of about 10^{-7} sec .

The growth velocity in thermal LPE is limited by the slow solute transport to the growth interface and by the fact that the relatively small supercooling must be used to prevent spurious nucleation in the solution (24). These limitations are overcome in electroepitaxy (15).

Summary and Conclusions

It was found that outdiffusion of recombination centers from a substrate to the epitaxial layer takes place during liquid phase epitaxial growth. From the study of the time dependence of the diffusion process a diffusion constant of $5 \times 10^{-9} \text{ cm}^2/\text{sec}$ at 900°C was obtained for the outdiffusion of recombination centers. This value is the same as that reported for the diffusion constant of Ga vacancies in GaAs at 1000°C . It should be noted that outdiffusion of point defects from the substrate has recently been suggested (25) on the basis of measurements on the distribution of residual deep levels in LPE GaAs crystals employing photocapacitance in conjunction with step-etching.

According to the present results, the recombination of minority carriers at the outdiffused defects constitutes the limiting factor for the minority carrier lifetime in the epitaxial layers. It has also been shown that the substrate-epitaxial layer interaction during the growth process can be reduced by increasing the growth velocity. Thus utilizing high growth velocities attainable in electroepitaxy, an improvement of as much as two orders of magnitude in the minority carrier lifetime was observed. The present results could account for the improved characteristics of GaAs lasers grown under high growth velocities (26).

Thus, the recombination characteristics of excited carriers in epitaxial layers are significantly influenced by compositional and structural defects in the sub-

strate. Since it is generally accepted that the quality of melt-grown GaAs substrates is poor (in terms of defects, residual impurities, and compositional inhomogeneities) (13) improved GaAs substrates are essential for the consistent growth of device quality GaAs LPE layers.

Acknowledgment

The authors are grateful to the National Science Foundation and the National Aeronautics and Space Administration for financial support.

Manuscript submitted March 26, 1979; revised manuscript received June 11, 1979.

Any discussion of this paper will appear in a Discussion Section to be published in the June 1980 JOURNAL. All discussions for the June 1980 Discussion Section should be submitted by Feb. 1, 1980.

Publication costs of this article were assisted by Massachusetts Institute of Technology.

REFERENCES

1. See, for example, J. H. Reynolds and A. Meulenberg, Jr., *J. Appl. Phys.*, **45**, 2582 (1974).
2. D. V. Lang and L. C. Kimerling, *Phys. Rev. Lett.*, **33**, 489 (1974).
3. P. Petroff, W. D. Johnston, Jr., and R. L. Hartman, *Appl. Phys. Lett.*, **25**, 226 (1974), and H. Kressel and H. F. Lockwood, *J. Phys.*, **35**, 223 (1974).
4. M. Ishii, H. Kan, and W. Susaki, *Appl. Phys. Lett.*, **29**, 375 (1976).
5. A. G. Milnes, Private communication.
6. J. A. Van Vechten, *J. Electron. Mater.*, **4**, 1159 (1975).
7. G. M. Bloom, *J. Cryst. Growth*, **36**, 125 (1976).
8. See, for example, R. Zucca, in "Proceedings 6th International Symposium on GaAs and Related Compounds, St. Louis, 1976, p. 228, Inst. of Physics, London (1977).
9. L. Jastrzebski and H. C. Gatos, *J. Cryst. Growth*, **42**, 309 (1977).
10. W. Walukiewicz, J. Lagowski, L. Jastrzebski, M. Lichtensteiger, and H. C. Gatos, *J. Appl. Phys.*, **50**, 899 (1979).
11. L. Jastrzebski, J. Lagowski, W. Walukiewicz and H. C. Gatos, submitted to *J. Appl. Phys.*
12. A. M. Sekela, D. L. Feucht, and A. G. Milnes, in "Proceedings of the Symposium on GaAs and Related Compounds, Deauville, France, 1974" Conf. Ser. **24**, p. 245, Inst. of Physics, London and Bristol (1974).
13. H. C. Gatos, J. Lagowski, and L. Jastrzebski, "Present Status of GaAs," NASA Report 3093, January 1979.
14. L. Jastrzebski, Y. Imamura, and H. C. Gatos, *This Journal*, **125**, 1140 (1978).
15. L. Jastrzebski, J. Lagowski, H. C. Gatos, and A. F. Witt, *J. Appl. Phys.*, **49**, 5909 (1978).
16. D. B. Wittry and D. F. Kyser, *ibid.*, **36**, 1387 (1965).
17. L. Jastrzebski, J. Lagowski, and H. C. Gatos, *Appl. Phys. Lett.*, **27**, 537 (1975).
18. W. Walukiewicz, J. Lagowski, L. Jastrzebski, and H. C. Gatos, *J. Appl. Phys.*, in press.
19. J. D. Wiley, in "Semiconductors and Semimetals," Vol. 10, R. K. Willardson and A. C. Beer, Editors, Chap. 2, Academic Press, New York (1975).
20. See, for example, "Gallium Arsenide, Growth, Properties and Applications," F. P. Kesamanly and D. N. Nasledova, Editors, Chap. 5, Izdatel'stvo Nauka, Moscow (1973) in Russian.
21. S. M. Sze, "Physics of Semiconductor Devices," p. 82, Wiley-Interscience, New York (1969).
22. J. Blanc, *J. Appl. Phys.*, **45**, 1948 (1974).
23. J. Lagowski, L. Jastrzebski, and H. C. Gatos, Submitted to *J. Appl. Phys.*
24. A. Ju. Malinin and O. B. Nevsky, *J. Electronic Mater.*, **7**, 757 (1978).
25. T. Okumura and T. Ikoma, *J. Cryst. Growth*, **45**, 459 (1978).
26. M. Ettenberg and H. Kressel, *Appl. Phys. Lett.*, **26**, 478 (1975).

Etching Uniformities of Silicon in $\text{CF}_4 + 4\% \text{O}_2$ Plasma

Masanobu Doken and Isao Miyata

Nippon Telegraph and Telephone Public Corporation,
Musashino Electrical Communication Laboratory, Tokyo 180, Japan

ABSTRACT

The etch rate uniformity of silicon and polysilicon in a $\text{CF}_4 + 4\% \text{O}_2$ plasma was investigated using a volume-loading apparatus. The results of experimental and theoretical studies show that the etching process of silicon and polysilicon in $\text{CF}_4 + 4\% \text{O}_2$ plasma is a diffusion limited one. Therefore the etch rate can be made uniform across a wafer by using rings which control the diffusion of free radicals from the direction normal to the surface of wafer.

Silicon-gate technology provides higher packing density and higher switching speed for MOS LSI (1, 2). Patterning of the polysilicon gate electrode requires an etching technology that is capable of providing precise and uniform etching across the wafer. Plasma etching is one of the promising processes out of many etching techniques that have been tried because it results in a closer etching tolerance.

As plasma etching is a chemical process, some undercutting can occur. So a uniform etch rate is necessary to obtain uniform pattern generation.

For slow etch rate materials such as silicon dioxide, etch rate uniformity of $\pm 3\%$ can be readily achieved with a perforated metal tunnel (etch tunnel) (3-6).

For fast etch rate materials such as silicon or polysilicon, however, etch rate uniformity becomes 20-30%, and is degraded as the wafer spacing is decreased. The etch rate is also nearly inversely proportional to the load size (area to be etched) in a volume-loading apparatus (7).

In this paper we report that a sufficiently uniform etch rate can be achieved by using simple aluminum rings mounted in the apparatus. The rings are thought to control the diffusion of free radicals from the direction normal to the surface of wafer and make the density of free radicals uniform at the surface of wafer.

Theoretical calculation of the etch rate uniformity is performed based on a diffusion limited model and the results show good agreement with the experimental data.

Experimental Procedures and Results

Plasma etching was carried out in the IPC 2005-1813 SC plasma etcher which has a quartz reaction chamber of 8 in. in diameter and 13 in. in length. The etch tunnel was also used. The etching gas used was $\text{CF}_4 + 4\% \text{O}_2$. The pressure and the flow rate of the gas in the reaction chamber were maintained constant through the experiments at 0.55 ± 0.05 Torr (about 73 Pa) and $22 \pm 2 \text{ cm}^3/\text{min}$, respectively.

The rf power (at 13.56 MHz) was coupled into the external electrodes of the reaction chamber with an automatic impedance matching network.

Figure 1 shows a schematic representation of the plasma etcher. The wafers to be etched were loaded onto an aluminum boat perpendicular to the cylindrical axis of the reaction chamber.

Polished single crystal silicon wafers of 5 $\Omega\text{-cm}$, n-type conductivity and oriented in $\langle 100 \rangle$ direction were mainly used in the experiments. The wafer size was 3 in. in diameter. In the experiment on undercutting, wafers on which an oxide thickness of 1000 Å was thermally grown and then 5000 Å of phosphorus-doped polysilicon was deposited were used. Shipley Chemical Company's AZ1350J photoresist was used as the etching mask and the etching depth was measured with Talystep.

Key words: diffusion, gas plasma, etch rate, patterning, reactor.

Figure 2 shows the variation of the etch rate of single crystal silicon wafers vs. the number of wafers loaded in the reaction chamber. The value of the etch rate was measured at the center of wafer. The wafer spacing was 9.5 mm, the area exposed to free

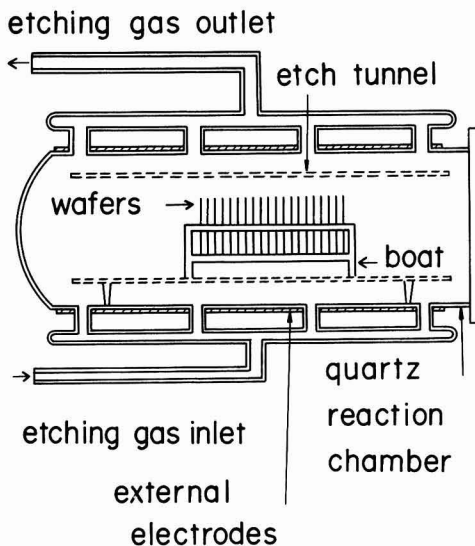


Fig. 1. Schematic representation of plasma etcher

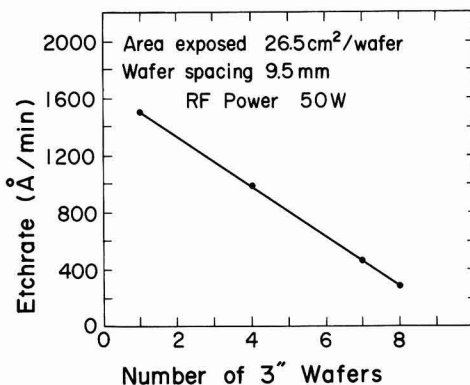


Fig. 2. Silicon etch rate variation with wafer load

radicals was 26.5 cm^2 per wafer, and the rf power was set at 50W.

In this experiment, quartz dummy wafers which were the same size as the silicon wafers were used to keep the gas flow constant. Therefore, the total number of the silicon and quartz wafers was 8 throughout this experiment. The etch rate of the silicon wafer decreased at the rate of 10% per silicon wafer. This loading effect is thought to arise from the competition among the wafers to acquire the available etching radicals (4, 8, 10).

Figure 3 shows the etched depth and the wafer temperature *vs.* etch time. The rf power was 200W and the area exposed was 90 cm^2 . The wafer temperature was measured with Hermet which was a heat sensitive label and had hermetically sealed temperature indicators. The wafer temperature was nearly uniform over the wafer, for the temperature difference between the center and the periphery was less than 3°C .

The etching depth increased almost linearly with etching time. In order to investigate the temperature dependence of the etch rate in detail, the etching behavior in the initial few minutes was analyzed.

In general the etch rate A can be expressed as

$$A = B \exp(-E/kT) \quad [1]$$

where T is absolute temperature, k is Boltzmann constant, E is activation energy, and B is a proportional constant.

E can be obtained from the slope of the $\log A$ *vs.* $1/T$ plot as shown in Fig. 4. The value of E is $0.02\text{--}0.04 \text{ eV}$. Almost the same activation energy has been reported by Horike and Shibagaki, and Mogab from different experiments (9, 10).

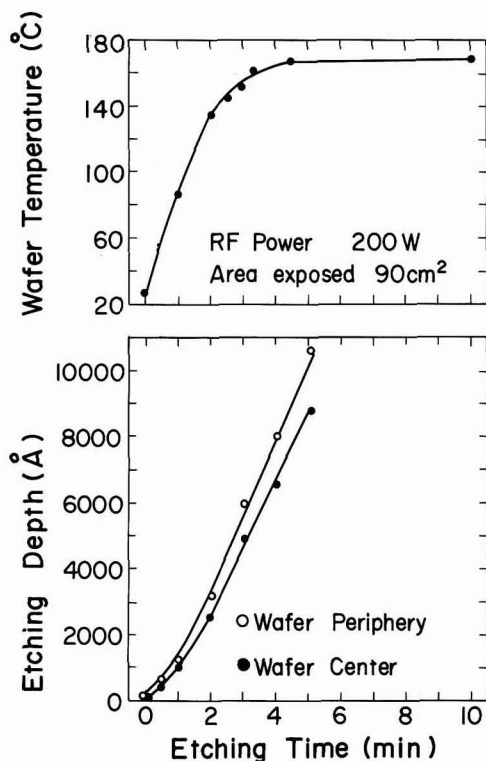


Fig. 3. Wafer temperature and etching depth *vs.* etching time

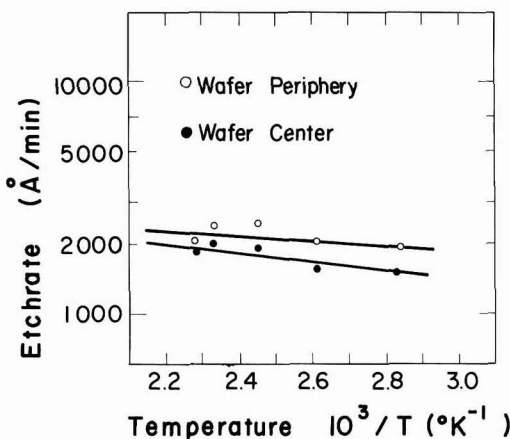


Fig. 4. Temperature dependency of etch rate

Figure 5 shows the etch rate uniformity across a wafer *vs.* the wafer spacing L . Two silicon wafers were set back to back between two aluminum dummy wafers as shown in Fig. 5(b). $L = \infty$ means to remove the aluminum dummy wafers in Fig. 5(a).

Only the etch rate at the wafer center was slower than that of the wafer periphery and the etch rate uniformity was degraded as the wafer spacing decreased. Then the average etch rate per wafer decreased as the wafer spacing decreased (11).

The following results were obtained from the above experiments about the etch rate of silicon in $\text{CF}_4 + 4\% \text{ O}_2$ plasma: (i) considerable loading effect; (ii) small temperature dependence; and (iii) large wafer spacing dependence. These experimental results suggest that the etching process of silicon in $\text{CF}_4 + 4\% \text{ O}_2$ plasma is a diffusion limited one.

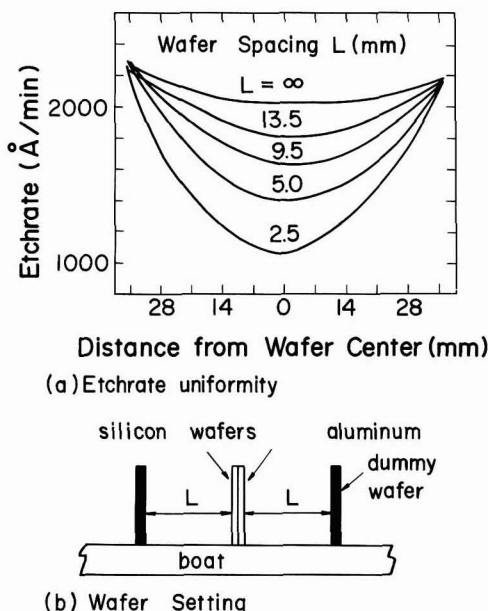


Fig. 5. Radial etch rate uniformity across wafer with wafer spacing.

Theoretical Calculation

The etch rate uniformity was calculated based on a diffusion limited model under the following assumptions.

(i) The lifetime of free radicals contributing to the etching process is sufficiently long that all arrive at the wafer surface (9). So, the etch rate is simply proportional to the density of the free radicals at the diffusion layer surface.

(ii) The free radicals are generated within the space between the reaction chamber and the etch tunnel. Since this space is cylindrically symmetrical about the tube axis and narrow compared with tube diameter, the generation rate G can be treated as constant with location.

(iii) The thickness of the diffusion layer h , the diffusion coefficient D in the reaction chamber, and the diffusion coefficient d in the diffusion layer of the free radicals are independent of the density and location of the free radicals.

(iv) The thickness of diffusion layer is negligible compared to thickness of wafer and the wafer spacing.

(v) The diffusion velocity of the free radicals is faster than the drift velocity. With this assumption, the density of the free radicals can be considered to have cylindrical symmetry about the axis of the reaction chamber.

As the volume of the reaction chamber is about 10 liters and the gas flow rate is 22 cm³/min at 1 kg/cm², the drift velocity is estimated to be about 0.85 cm/sec. From kinetic theory of molecule, the diffusion coefficient is expressed as

$$D = cf/3 \quad [2]$$

where f is mean free path of free radicals and c is the mean square velocity.

If the free radicals are all fluorine and the density of carbontetrafluoride is higher than that of fluorine free radicals (7), f and c are 8×10^{-3} cm and 6×10^4 cm/sec at 25°C and 0.5 Torr, respectively. Then D is calculated as 160 cm²/sec. Therefore the assumption (5) may be reasonable.

The diffusion equation is expressed as follows using cylindrical coordinates (r, ϕ, z) as shown in Fig. 6

$$D \left(\frac{\partial^2 N}{\partial r^2} + \frac{1}{r} \frac{\partial N}{\partial r} + \frac{\partial^2 N}{\partial z^2} \right) + G = 0 \quad [3]$$

where $N = N(r, z)$ is the density of the free radicals. Variable ϕ is eliminated by the symmetry, and the diffusion equation becomes a two dimensional equation.

The boundary conditions are as follows

$$\frac{\partial N}{\partial n} = 0 \quad \text{at all surfaces} \quad [4]$$

Here, ∂n implies the differential to normal direction against the reaction chamber walls and dummy wafer

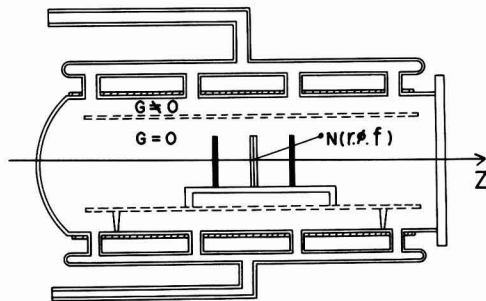


Fig. 6. Calculation model

surfaces.

$$G = 0 \quad \text{inside tunnel} \quad [5]$$

This condition is used within the etch tunnel and means that generation and recombination of the free radicals do not occur.

$$D \frac{\partial N(r, z)}{\partial z} = d \frac{N(r, z)}{h} \quad \text{at the diffusion layer surface} \quad [6]$$

This condition is used at the diffusion layer surface and means that the flow of free radicals is continuous.

The values of D , d , and h are unknown but only the ratio of $d/Dh = K$ is sufficient to solve the diffusion Eq. [3]. So K is treated as a parameter in calculation of N . As N is proportional to G/D , ND/G was calculated and G/D can be selected arbitrarily in this calculation. The calculation was carried out by numerical method about the case shown in Fig. 5. The procedure of calculation is shown in the Appendix.

The calculated etch rate uniformity across a wafer and the experimental results are shown in Fig. 7. The uniformities are normalized by the etch rate at the wafer center in the case of $L = \infty$. The calculated results are shown only in the case of $K = 0.088 \text{ cm}^{-1}$. The experimental values are the same used in Fig. 5.

The calculation shows that the etch rate uniformity is degraded as the wafer spacing decreases and K increases. Free radicals are generated only in the annular volume between the etch tunnel and the reactor wall, so there is a density gradient of free radicals across the wafer surface. The calculated results show that this gradient decreases as the wafer spacing increases and K decreases.

Coincidence between the experimentally and theoretically calculated etch rate uniformity becomes quite good when the value of K is set at 0.088 cm^{-1} as shown in Fig. 7. The change in etch rate at the center of the wafer with wafer spacing also shows good agreement with experiments as shown in Fig. 8.

Radical Diffusion Control

From the studies mentioned above, the etch rate uniformity of silicon wafers can be explained by a diffusion limited model. Therefore, to improve the etch rate uniformity, it can be thought effective to control the diffusion of free radicals.

For this purpose we have tried to use simple aluminum rings as shown in Fig. 9. These rings are set in parallel with the wafers in the apparatus. The rings restrict the diffusion of free radicals from the direc-

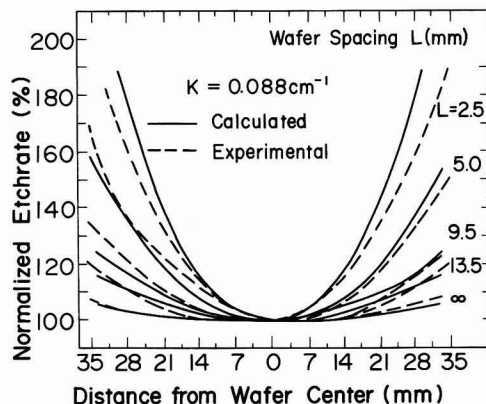


Fig. 7. Calculated radial etch rate uniformity across wafer with wafer spacing. K is set at 0.088 cm^{-1} in calculation.

tion normal to the wafer surface at the wafer periphery to slow down the etch rate there.

One of the experiments using these rings is shown schematically in Fig. 10. The wafers covered with phosphorus-doped polysilicon were used to investigate the undercutting in this experiment and were placed as shown in Fig. 10(b). The wafer spacing was 13.8 mm, the rf power was 50W, and the area of polysilicon exposed to free radicals was 26.5 cm².

The etch rate uniformity improved from a value of 10% without the rings to a value less than 5% with the rings. The improvement in the etch rate uniformity is especially pronounced in the center of the wafer. With this effect the uniformity of the undercutting over the wafer was also greatly improved.

Figure 11 shows the uniformity of the undercutting on the wafer with the etching time and the width of the mask pattern as parameters. As can be seen from this experiment, aluminum rings offer a quite uniform etch rate over the wafer which causes a uniform pattern generation on the wafers as shown in Fig. 11(b).

Conclusions

The main conclusions of the present investigation are the following: (i) The etching process of silicon and polysilicon in a CF₄ + 4% O₂ plasma is diffusion limited; and (ii) The variation in etch rate across a wafer can be reduced by the addition of rings which control the diffusion of free radicals. Uniform etch rate offers

$$N_{i,j} = \frac{\left(\frac{m}{n}\right)^2 \left(n^2 \frac{G}{D} + \left(1 + \frac{1}{2(i-1)}\right) N_{i+1,j} + \left(1 - \frac{1}{2(i-1)}\right) N_{i-1,j} \right)}{2 \left(1 + \left(\frac{m}{n}\right)^2\right)} + \frac{N_{i,j+1} + N_{i,j-1}}{2 \left(1 + \left(\frac{m}{n}\right)^2\right)} \quad [\text{A-1}]$$

uniform pattern generation because plasma etching is an isotropic etching process.

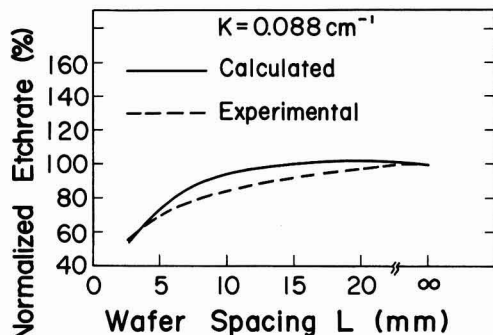


Fig. 8. Etch rate at wafer center vs. wafer spacing. K is set at 0.088 cm^{-1} in calculation.

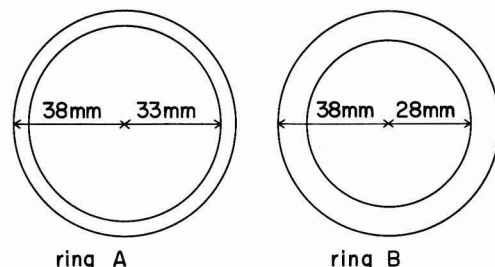


Fig. 9. Example of aluminum rings for uniform etching. Thickness of aluminum is 0.4 mm.

Acknowledgment

The authors wish to thank Mr. Ariyoshi, Chief of Electronic Circuit Section in Musashino Electrical Communication Laboratory, for direction and encouragement.

Manuscript submitted Nov. 27, 1978; revised manuscript received May 18, 1979.

Any discussion of this paper will appear in a Discussion Section to be published in the June 1980 JOURNAL. All discussions for the June 1980 Discussion Section should be submitted by Feb. 1, 1980.

Publication costs of this article were assisted by Nippon Telegraph and Telephone Public Corporation.

APPENDIX

Equation [3] was solved by the difference method. We divide z and r into thin layers of thickness m and n , respectively, and consider only the region as shown in Fig. 12, because of the cylindrical and plane ($z = 0$) symmetry. Derivatives were approximated by difference quotients. From Eq. [3]

$$\frac{N_{i+1,j} - 2N_{i,j} + N_{i-1,j}}{n^2} + \frac{1}{(i-1)n} \frac{N_{i+1,j} - N_{i-1,j}}{2n} + \frac{N_{i,j+1} - 2N_{i,j} + N_{i,j-1}}{m^2} + \frac{G}{D} = 0$$

where i and j are integers and $N_{i,j} = N((i-1)n, (j-1)m) = N(r, z)$. From this difference equation

The chamber wall, Al dummy wafer surface, and the surface of the diffusion layer are represented by $i = I$ or $j = J$, $j = J1$ and $j = J2$, and $j = 2$, respectively, as shown in Fig. 12. Then the boundary conditions are as follows.

From Eq. [4]

$$N_{I,j} = N_{I-1,j}; \quad N_{i,J} = N_{i,J-1} \quad \text{at the chamber wall} \quad [\text{A-2}]$$

$$N_{i,J2} = N_{i,J2+1}; \quad N_{i,J1} = N_{i,J1-1} \quad \text{at Al dummy wafer surface} \quad [\text{A-3}]$$

From Eq. [5]

$$G = 0 \quad \text{inside etch tunnel} \quad [\text{A-4}]$$

From Eq. [6]

$$\frac{D}{m} \frac{N_{i,2} - N_{i,1}}{m} = \frac{dN_{i,2}}{h}$$

Namely

$$N_{i,2} = \frac{1}{1 + \frac{dm}{hD}} N_{i,1} \quad \text{at the diffusion layer surface} \quad [\text{A-5}]$$

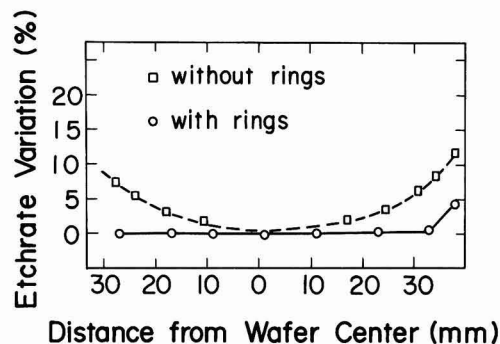
And from the symmetry

$$N_{1,j} = N_{2,j}; \quad N_{I,1} = N_{I,2} \quad \text{without wafer surface} \quad [\text{A-6}]$$

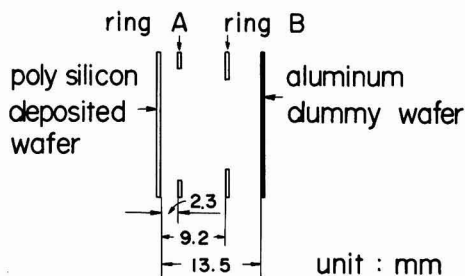
$N_{i,j}$ was calculated by the iterative method using Eq. [7] under the boundary conditions of Eq. [A-2]–[A-6]. In calculation, m and n were chosen at $1/32$ and $1/16$ in., respectively.

As N is proportional to G/D , G/D can be selected arbitrarily in this calculation. The boundary condition of Eq. [A-5] contains $d/hD = K$. So N was calculated for various values of K .

Since etch rate is proportional to N at the surface of the diffusion layer, theoretically calculated etch rate uniformity can be obtained and compared to the experimental etch rate uniformity. K was selected at the value of 0.088 cm^{-1} that gave good coincidence between calculation and experiment.

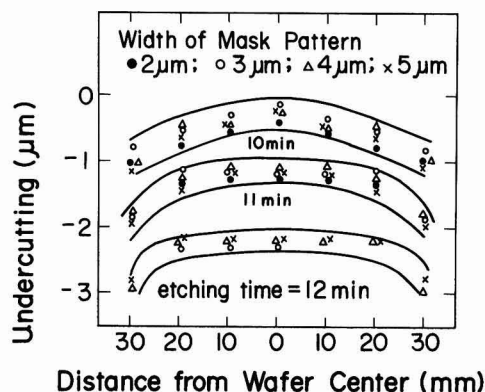


(a) Radial etchrate variation

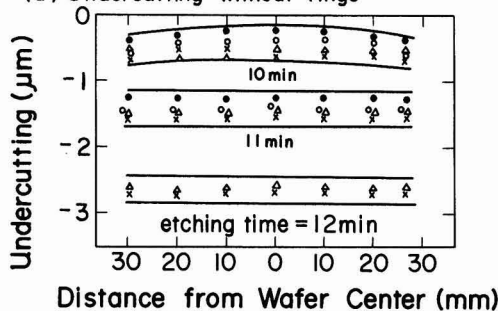


(b) Wafers and rings setting

Fig. 10. Example of etch rate uniformity with rings



(a) Undercutting without rings



(b) Undercutting with rings

Fig. 11. Undercutting variation

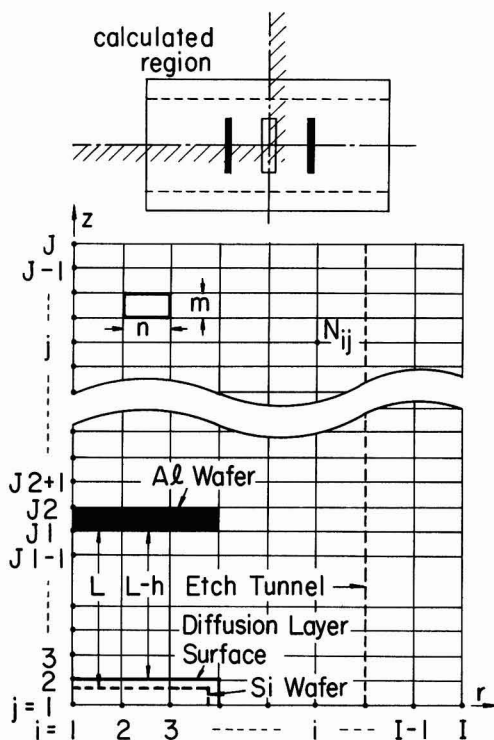


Fig. 12. Mesh for numerical calculation

REFERENCES

1. J. C. Sarace, R. E. Kerwin, D. L. Klein, and R. Edwards, *Solid-State Electron.*, **11**, 653 (1968).
2. F. Faggin and T. Klein, *ibid.*, **13**, 1125 (1970).
3. A. Jacob, *Solid State Technol.*, **20**, 31 (June, 1977).
4. R. G. Poulsen, *J. Vac. Sci. Technol.*, **14**, 266 (1977).
5. R. Bersin and M. Singleton, US Pat. 3,879,597.
6. New Products-LFE Corp., *Electronics*, **45**, 175 (1975).
7. R. L. Bersin, *Solid State Technol.*, **19**, 31 (May, 1976).
8. R. Kumar, C. Ladas, and G. Hudson, *ibid.*, **19**, 54 (October, 1976).
9. Y. Horiike and M. Shibagaki, *Jpn. J. Appl. Phys. Suppl.*, **15**, 13 (1976).
10. C. J. Mogab, *This Journal*, **124**, 1262 (1977).
11. S. Chung, *Solid State Technol.*, **15**, 114 (April, 1978).

Effect of Microscopic Growth Rate on Oxygen Microsegregation and Swirl Defect Distribution in Czochralski-Grown Silicon

A. Murgai* and H. C. Gatos*

Department of Materials Science and Engineering
Massachusetts Institute of Technology, Cambridge, Massachusetts 02139

and W. A. Westdorp

IBM System Product Division, East Fishkill Facility, Hopewell Junction, New York 12533

ABSTRACT

Oxygen microsegregation and swirl defect formation in Czochralski-grown silicon were studied by employing interface demarcation, spreading resistance measurements, infrared absorption, high resolution etching, and x-ray topography. It was found that for forced convection conditions of growth, oxygen segregation is microscopic growth rate-controlled. Maxima in oxygen concentration occurred at minima in the microscopic rates indicating that the segregation coefficient of oxygen is greater than 1. The distribution of swirl defects was found to be critically dependent on the amplitude of the microscopic growth rate fluctuations; this dependence made it possible to show that the critical impurity nuclei are not related to oxygen but to some impurity, most likely carbon, having a segregation coefficient less than 1.

Unlike float-zone grown silicon, the study of swirl defects in Czochralski (1-4) grown silicon has thus far received little attention. The presence of a high concentration of impurities, particularly oxygen (5, 6) and carbon (7, 8) constitutes an interference in the study of swirls in Czochralski silicon. Thus, the possibility of impurity precipitation (9-13) during crystal cool-down and subsequent heat-treatments has prevented the unambiguous identification of the nuclear mechanisms (14) of swirls. In fact, the presence of oxygen precipitates (SiO_2) in a swirl-like pattern in Czochralski-grown silicon are often referred to as swirls while no SiO_2 precipitation is observed for float-zone silicon. This leads to the question as to whether or not swirls in Czochralski silicon act as nucleation centers for SiO_2 precipitates.

Since oxygen is the most predominant impurity in Czochralski-grown silicon and has been found to affect various stages of thermal device processing (15-17), oxygen microsegregation was studied in the present investigation; the study was correlated with a study of swirl defect formation. Interface demarcation (18) (for the determination of the microscopic growth rates) was employed in conjunction with spreading resistance measurements, x-ray topography, infrared absorption, and high resolution etching.

Experimental

Crystal growth.—Silicon crystals were grown in the $\langle 100 \rangle$ direction at constant pulling rates and doped with boron or antimony to concentration levels of $\sim 10^{15}/\text{cm}^3$ and $10^{18}/\text{cm}^3$. The crystals were pulled either from 75g melts or 10 kg melts. The crystal pull rates, crystal and crucible rotation rates, crystal diameters, and crucible aspect ratios (d/h) employed were:

Rotation rate					
	Pull-rate	Crystal	Crucible	Diameter	Aspect ratio
75g melts:	40 mm/hr	0-20 rpm	0-20 rpm	~ 20 mm	(2.2.5)
10 kg melts:	75 mm/hr	0-40 rpm	0-20 rpm	~ 75 mm	(1.7-2.2)

* Electrochemical Society Active Member.

Key words: defects, infrared, x-ray.

Interface demarcation was applied during growth from 75g melts by employing current pulses of 18A and 50 msec duration with a repetition rate of 0.5 sec. The details of the technique and the mathematical analyses for the determination of microscopic rates of growth are similar to those employed elsewhere (18).

Measurements.—From IR absorption measurements (19) (using a Fourier spectrometer) the variation in mean oxygen concentration from seed to tail end was determined to be 2×10^{18} – $5 \times 10^{17}/\text{cm}^3$ for crystals pulled from 10 kg melts and 1×10^{18} – $7.5 \times 10^{17}/\text{cm}^3$ for crystals pulled from 75g melts. Carbon concentrations were also determined from IR absorption measurements (20), and typically were found to be about $10^{16}/\text{cm}^3$.

All microscopic measurements were carried out on longitudinal (100) slices (1 ~ 2 mm thick), cut along the $\langle 100 \rangle$ direction. Fluctuations in dopant concentration were determined from single probe spreading resistance measurements at 5 μm intervals on slices heat-treated at 800°C for 1 hr (to eliminate oxygen donors) and lapped, etched, and Syton polished. For the determination of fluctuations in oxygen concentration, the slices were heat-treated at 450°C (21-24) for 50 hr, lapped again to remove about 50 μm of the surface layer, reetched, and Syton polished; spreading resistance measurements were carried out again on the identical locations used prior to heat-treatment; reference marks were employed for identifying these locations. The difference in carrier concentrations, determined from the successive spreading resistance measurements was taken equal to the thermally activated oxygen donor concentration. The latter was converted to oxygen concentration through silicon samples from the same crystal, for which the thermal donor concentration was determined as above and the oxygen concentration from IR absorption measurements. The mean thermal donor concentrations and the corresponding oxygen concentration values for two silicon samples employed in the present analysis are shown in Table I.

Interface demarcation lines and dopant striation (in crystals doped to concentration levels of $\sim 10^{18}$ atoms/ cm^3) were revealed by employing the Sirtl etchant following Syton polishings; the details of the etching procedure are discussed elsewhere (18).

The swirl defect distribution was revealed through copper decoration (at 1000°C for 45 min). The slices were subsequently lapped, polished, and preferentially etched with the Sirtl or Wright etchant (25). The swirl defect distribution and dopant striations, as revealed by etching, were recorded using interference contrast microscopy. In some instances the swirl distribution was obtained with x-ray transmission topography.

Results and Discussion

The present investigation is based on experimental correlations between variations in dopant concentration, oxygen concentration, microscopic growth rate, and distribution of swirl defects.

Dopant concentration variations and microscopic growth rate.—A segregation analysis was carried out (dopant concentration distribution as a function of microscopic growth rate) for Sb-doped crystals ($10^{18}/\text{cm}^3$) pulled from 75g melts (about 20 mm in diam) under seed rotation (5 rpm) and under crucible rotation (7.4 rpm). Measurements were carried out on longitudinal (100) slices, 0.5 mm from the periphery; the results are shown in Fig. 1 and 2, respectively. In both figures the photomicrographs exhibit periodic dopant striations (broad lines), interface demarcation lines (fine lines), and spreading resistance probe impact traces. The microscopic growth rates (obtained from the space of the demarcation line and the frequency of the current pulses) and the dopant concentration (obtained from the spreading resistance measurements) along the region depicted by the photomicrographs are also shown in the two figures.

The period of the dopant striations coincides with the period of seed rotation in Fig. 1 and that of crucible rotation in Fig. 2. Thus, the striations in Fig. 1 are 135 μm apart; since the average pulling rate was 11 $\mu\text{m}/\text{sec}$, the period of the striations is 12.2 sec in good agreement with the period of rotation of 12 sec (5 rpm). In Fig. 2 the striations are 105 μm apart; since the average pulling rate was 13 $\mu\text{m}/\text{sec}$, the period of striations is 7.7 sec, in good agreement with the period of crucible rotation of 8.1 sec.¹ The coincidence of the period of dopant striations with the period of seed and crucible rotation indicates that growth in

¹ Although under the present experimental conditions the striations exhibited the same period as that of the crucible rotation, in general significant differences between these may be observed.

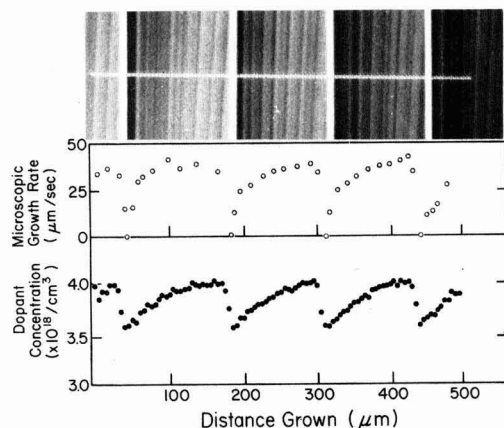


Fig. 1. Microsegregation analysis in Si: microscopic growth rates and dopant concentration variation for longitudinal segment of a (20 mm diam) crystal pulled under seed rotation (5 rpm) pulling-rate: 40 mm/hr. Dopant remelt-striations (dark lines), interface demarcation (faint lines), and the impact traces of spreading resistance measurements are visible.

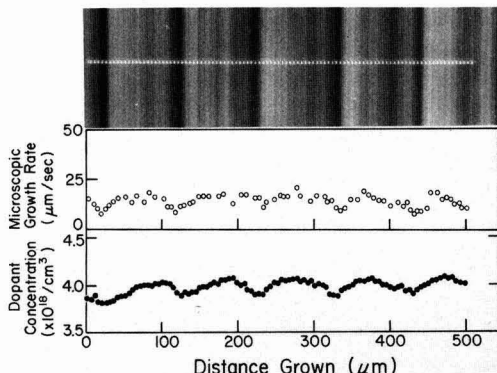


Fig. 2. Microsegregation analysis in Si: growth rate and dopant concentration variation for longitudinal segment of a crystal (20 mm in diam) pulled under crucible rotation (7.4 rpm); pulling-rate: 40 mm/hr. Dopant striations (dark lines), interface demarcation (faint lines) and impact traces of the spreading resistance measurements are again visible in the photomicrograph. No backmelting is associated with striations under crucible rotation. The amplitudes of microscopic growth rate and dopant concentration variation under crucible rotation are significantly smaller than under seed rotation (see Fig. 1).

both cases took place under forced convection conditions (18, 26, 27).

As seen in Fig. 1 and 2, the dopant concentration maxima and minima coincide with the microscopic growth rate maxima and minima, respectively. Accordingly, segregation in the present case is microscopic growth rate-controlled (the distribution coefficient of Sb in Si is less than one).

In the case of seed rotation, there are about nine interface demarcation lines between successive rotation striations, as seen in Fig. 1. The demarcation lines were introduced at 0.5 sec intervals; thus, between successive rotational striations 4.5 sec of growth elapsed while the seed rotation period was 12 sec. Accordingly, in the seed rotation case, there is significant backmelting within each rotational cycle. As is typical for growth with backmelting, between two successive rotational striations the microscopic rate increases to a maximum and then subsequently decreases abruptly; the microscopic growth rate varies from zero to 45 $\mu\text{m}/\text{sec}$.

In the case of crucible rotation (Fig. 2) there are about 15 demarcation lines between two successive striations, i.e., the elapsed growth time is 7.5 sec or approximately equal to the crucible rotational period (8.1 sec). Thus, under crucible rotation there is no backmelting and the amplitude of variations in microscopic growth rate and dopant concentration are a fraction of those observed under seed rotation although the thermal configuration of the growth apparatus was the same in both cases.

Oxygen concentration variations and microscopic growth rate.—The oxygen concentration distribution in Si can be determined by spreading resistance measurements after the oxygen in the crystal is activated to oxygen donor levels by heat-treatment at 450°C (for 50 hr in the present case). Accordingly, the boron dopant concentration should not exceed the activated oxygen donor concentration which for Czochralski-grown crystals has a maximum value of about $10^{16}/\text{cm}^3$. At these boron concentrations it is not possible to relate directly the carrier concentration variations to the microscopic growth rate because interface demarcation lines cannot be revealed by chemical etching. It will be assumed, however, that the dependence of dopant concentration variations on the microscopic growth rate found in crys-

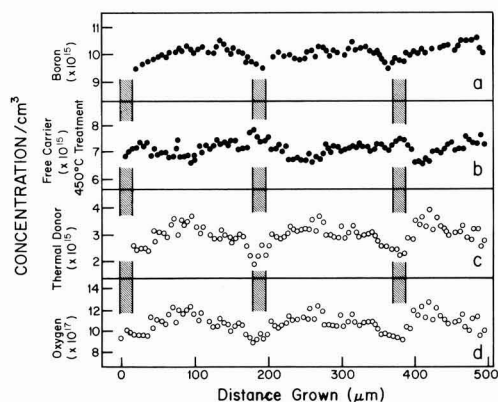


Fig. 3. Oxygen microsegregation analysis for a crystal pulled under seed rotation (4 rpm); crystal diameter: 20 mm; pull rate: 12 $\mu\text{m}/\text{sec}$; mean B-dopant concentration: $1.03 \times 10^{16}/\text{cm}^3$. (a) Dopant concentration variation determined from longitudinal spreading resistance measurements after a heat-treatment at 800°C for 1 hr; (b) net free carrier concentration determined from spreading resistance measurements in the same region as (a), measurements were made after a subsequent heat-treatment at 450°C for 50 hr; (c) thermal donor concentration obtained from the difference of measurements, between (a) and (b), point by point; (d) oxygen concentration variation computed from thermal donor concentration values in (c) and calibration values in Table I.

tals with high dopant concentrations (Fig. 1 and 2) is the same for crystals with low boron concentrations grown under identical conditions.

Typical boron concentration variations along the growth direction (0.5 mm from the periphery) in a Si crystal pulled from a 75g melt (at a rate of 12 $\mu\text{m}/\text{sec}$) with seed rotation (4 rpm) are shown in Fig. 3a. Spreading resistance measurements were carried out after the crystal was heat-treated at 800°C, as in the crystal analyzed in Fig. 1. The periodic variation in concentration is associated with rotational striations as in the case of Fig. 1 and thus the concentration maxima must correspond to microscopic growth rate maxima. The variation of carrier concentration after heat-treatment at 450°C (see above) is shown in Fig. 3b; the values represent the difference between the acceptor (boron) concentration and the activated oxygen donor concentration. Subtracting the values in Fig. 3b from the values in Fig. 3a (point by point) one obtains Fig. 3c, and converting the activated oxygen donor concentration to oxygen concentration through calibration data (Table I) one obtains Fig. 3d.

It is seen in Fig. 3d that the variation in oxygen concentration is periodic and exhibits the same period as the boron concentration variations; thus, oxygen segregation is microscopic growth rate-controlled. Furthermore, since the maximum change in carrier concentration following the 450°C heat-treatment (Fig. 2b) occurs near boron concentration minima, the oxygen concentration maxima occur near microscopic growth rate minima (see Fig. 1). It is thus concluded that the segregation coefficient of oxygen in Si is greater than 1, consistent with earlier reports (28).

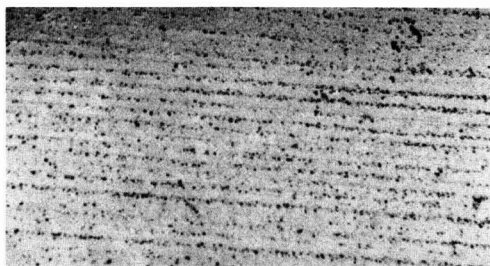


Fig. 4. Swirl defect distribution on a (100) longitudinal slice of a crystal pulled under 5 rpm seed rotation; crystal diameter: 75 mm; pull-rate: 75 mm/hr; boron dopant concentration: $10^{15}/\text{cm}^3$. Slice was Cu-decorated for 45 min at 1000°C and Sirtl-etched. Swirls are striated with the period of seed rotation. $7\times$.

Although the segregation of both boron and oxygen is microscopic growth rate-controlled, the variations in oxygen concentration are appreciably greater than the variations in boron concentration. On the basis of steady-state segregation (29), the variation in concentration, $\Delta C/C$ (C is the average concentration) can be related to the distribution coefficient (k_0), the boundary layer thickness (δ), and the diffusion coefficient (D) according to: $\Delta C/C \approx (1 - k_0) \Delta V \delta / D$ where ΔV is the amplitude of the rate variation, since in the present case the absolute value of $|1 - k_0| \approx 0.2$ for oxygen (28) and for boron (30), the observed larger variation in oxygen concentration must be due to larger values of δ/D in the case of oxygen.

Swirl defect and dopant striations.—Swirl defects and their distribution were investigated in Si crystals (75 mm in diam) grown by the Czochralski method from 10 kg melts in the $\langle 100 \rangle$ direction and B-doped to a level of $\sim 10^{15}/\text{cm}^3$. Longitudinal segments near the periphery of the crystals, grown under forced convection (31), were employed in this study. To reveal swirl defects the crystals were Cu-decorated at 1000°C; the time of heat-treatment was kept to 45 min to minimize oxygen clustering (9).

Typical results for a crystal pulled with seed rotation (5 rpm) are shown in Fig. 4 and at a higher magnification in Fig. 5a. It is seen that the microdefects are striated with a period corresponding to that of the seed rotation (see below). A (400) MoK α x-ray transmission topograph obtained from the identical region of Fig. 5a is shown in Fig. 5b. The distribution of microdefects in both instances is identical. The microdefects are thus believed to correspond to A-type swirl defects found in float-zone Si. Consistent with the prevailing view that swirl defects in Si are clusters of thermally generated point defects (1), they are not observed when a high density of dislocations is present, since dislocations serve as sinks for point defects. A typical x-ray transmission topograph of a Cu-decorated Czochralski-grown Si crystal (doped with B to $10^{15}/\text{cm}^3$) with a high density of dislocations is shown in Fig. 6; tangles of dislocations are seen but swirl microdefects are absent. If, however, dislocations are introduced after growth in a dislocation-free crystal, swirl microdefects are not annihilated; as seen in the photomicrograph of Fig. 7, swirl defects

Table I. Dependence of thermal donor concentration on oxygen concentration after heat-treatment at 450° for 50 hr

No.	Initial hole concentration, cm^{-3}	Hole concentration after heat-treatment, cm^{-3}	Oxygen thermal donor concentration, cm^{-3}	Oxygen concentration, cm^{-3}
1	9.72×10^{15}	8.40×10^{15}	1.32×10^{15}	7.76×10^{17}
2	13.08×10^{15}	10.54×10^{15}	2.44×10^{15}	9.64×10^{17}

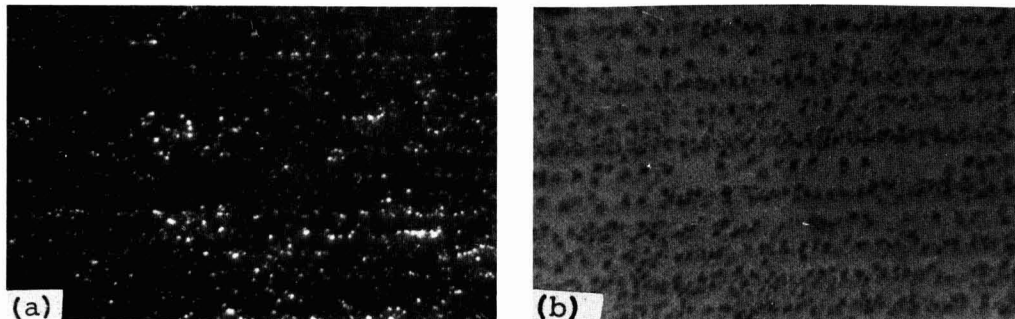


Fig. 5. Swirl defect distribution on a portion of the slice in Fig. 4, revealed through Sirtl etching, is shown in Fig. 5(a). A (400) Lang transmission topograph from the identical region shown in Fig. 5(a) is seen in Fig. 5(b). The distribution of swirl defects in both Fig. 5(a) and 5(b) is identical. $12\times$.

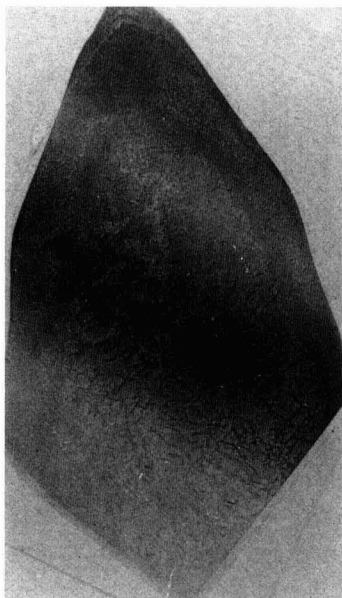


Fig. 6. A (220) Lang transmission topograph of a (100) longitudinal slice from a crystal having a high density of dislocations; boron dopant concentration: $10^{15}/\text{cm}^3$. Tangles of dislocations are seen but striated distribution of swirl defects is absent (see Fig. 5). Dark bands are due to variations in slice thickness. $1.1\times$.

are formed during crystal growth rather than during postgrowth heat-treatments.

Unlike the swirl defects in float-zone Si, those in as-grown Si by the Czochralski method cannot be reproducibly revealed by chemical etching. This fact need not be surprising since the high impurity concentration, particularly carbon and oxygen, present in Czochralski-grown Si (orders of magnitude higher than in float-zone grown Si) may attenuate the difference in etching behavior between the matrix material and the swirl defects. Actually, when hydrogen is introduced into Si during growth by the float-zone method, swirl defects cannot be revealed by chemical etching (32).

The effect of the microscopic growth rate on swirl defect distribution is seen in Fig. 8; the period of the swirl defect striations is the same as the period of

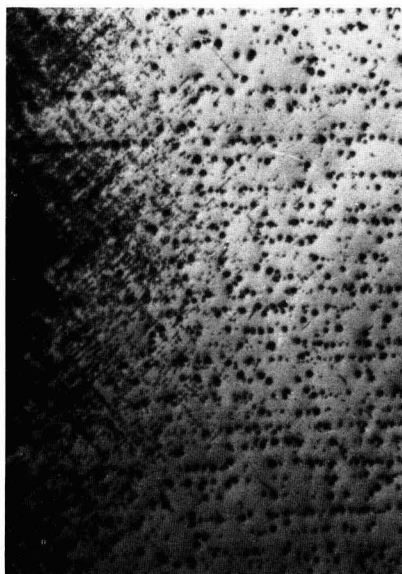


Fig. 7. Presence of swirl defects in region of crystal (left-hand side) where thermal slip was introduced during Cu decoration. Slice was Sirtl-etched for revealing swirl defects.

seed rotation (the crystal was grown under forced convection conditions with 20 rpm seed rotation and a pulling rate of $21 \mu\text{m}/\text{sec}$). This striated distribution of defects cannot be attributed to mechanisms proposed in the literature, i.e., neither to growth rate-controlled incorporation of excess point defects from the crystal-melt interface (33) nor to the extent of supersaturation of equilibrium point defects during crystal cool-down (34); on the basis of their diffusion coefficient near the melting temperature of Si ($\sim 10^{-5} \text{ cm}^2/\text{sec}$ (1)), thermal point defects can diffuse over distances well in excess of the $68 \mu\text{m}$ periodic spacing of swirl defects (Fig. 8) in one rotational cycle (3 sec) which from the above models should result in a uniform, nonstriated distribution of swirl defects. On the other hand, since rotational striations are microscopic growth rate-controlled, it must be concluded that the observed striated distribution of swirls, having the periodicity of rotational striations, is also microscopic growth rate-controlled; the microscopic

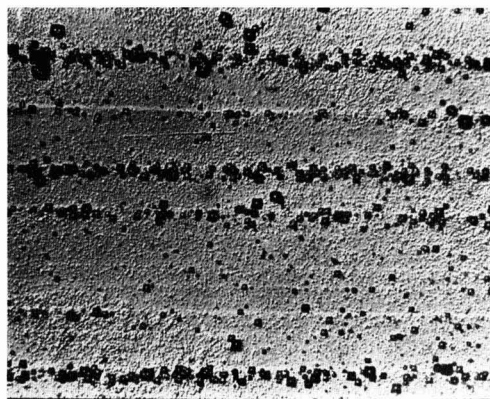


Fig. 8. Swirl defect striations on a (100) longitudinal slice of a crystal pulled under a seed rotation of 20 rpm (no crucible rotation); pulling-rate: 21 $\mu\text{m}/\text{sec}$; crystal diameter: 75 mm. Slice was Cu-decorated and preferentially etched. Region shown corresponds to forced convection conditions of growth. The period of swirl striations is microscopic growth rate-controlled (see text). 150 \times .

growth rate, through its variations, determines the location of critical impurity nuclei needed for swirl defect formation.

A closer examination of the swirl defect distribution shows that the swirl defect striations do not coincide with the dopant striations; instead the swirl microdefects are located at the seed side of the dopant striations (Fig. 8) and thus, near microscopic growth rate maxima (see Fig. 3 and 9). As pointed out above, however, the oxygen concentration maxima are found near microscopic growth rate minima. Thus, swirl defect formation does not take place at oxygen concentration maxima. Accordingly, the critical nuclei for swirl defect formation are not related to oxygen but to an impurity whose concentration maxima are near microscopic growth rate maxima, i.e., to an impurity with a distribution coefficient less than one. Carbon is present in moderately high concentrations (about $10^{18}/\text{cm}^3$) and its distribution coefficient is 0.07 (13); thus, the critical nuclei for swirl defect formation must be related to carbon.

The striated nature of swirl defects in Fig. 8 is consistent with this conclusion since the variations in carbon concentration should be significant under the growth conditions of this crystal; thus, from the carbon segregation coefficient, the amplitude of the microscopic growth rate variations (45 $\mu\text{m}/\text{sec}$) and assuming a diffusion boundary layer thickness of about 350 μm it is calculated (27) that the $\Delta C/C_{\text{average}} \approx 58\%$. When fluctuations of the concentration of car-

bon are not pronounced, the distribution of swirl defects is not striated but random as shown in Fig. 10. In this case the crystal was grown under the same conditions as the crystal shown in Fig. 8 except with crucible rotation (20 rpm) rather than seed rotation. As pointed out above, with crucible rotation the microscopic growth rate fluctuations are far less pronounced than with seed rotation. In the present case, the rate fluctuations are about 10 $\mu\text{m}/\text{sec}$ leading to $\Delta C/C_{\text{average}}$ values of about 14%, assuming the same values for the carbon segregation coefficient and diffusion boundary layer thickness assumed for the case of seed rotation.

Summary

On the basis of a microscopic growth rate analysis carried out through interface demarcation, it was shown that, in the presence of forced convection conditions of growth, the amplitude of fluctuations in the microscopic growth rate is far greater (i.e., by a factor of 4-5) under crystal rotation than under comparable rates of crucible rotation. Under the forced convection conditions, oxygen segregation was shown to be microscopic growth rate-controlled, with maxima in oxygen concentration corresponding to minima in microscopic rates of growth. Thus, the segregation coefficient of oxygen was shown to be greater than 1.

Microdefects in dislocation-free Czochralski-grown silicon were found to be similar to swirl microdefects (A clusters) in float-zone silicon. The distribution of these swirl microdefects was found to be critically dependent on the amplitude of fluctuations in the microscopic growth rate. For large variations in the microscopic growth rate the distribution of swirls was found to be striated; for relatively small rate variations, however, a fairly uniform swirl distribution was found. Thus, depending on the growth conditions, swirls (microdefects) may not necessarily be distributed in a swirl-like pattern in Czochralski silicon.

The distribution of swirls was related to a corresponding distribution of critical impurity nuclei responsible for swirl formation. Since the striated distribution of swirls was found displaced from oxygen concentration maxima [where oxygen precipitation normally occurs (35)] it was concluded that the critical nuclei are not related to oxygen. Thus, the exact microscopic locations of swirls and swirl-like patterns of SiO_2 precipitates are not expected to coincide under conditions of microscopic growth rate-controlled segregation. Under conditions of nonsteady-state segregation, however, it is possible for the lo-

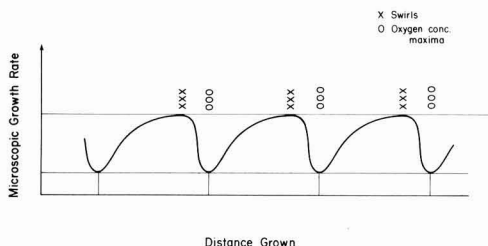


Fig. 9. Schematic representation of the relative location of swirl striations, oxygen concentration maxima, and microscopic growth rate fluctuations in Si grown under seed rotation. Swirl striations are located near the growth rate maxima, whereas oxygen concentration maxima are found near growth rate minima.

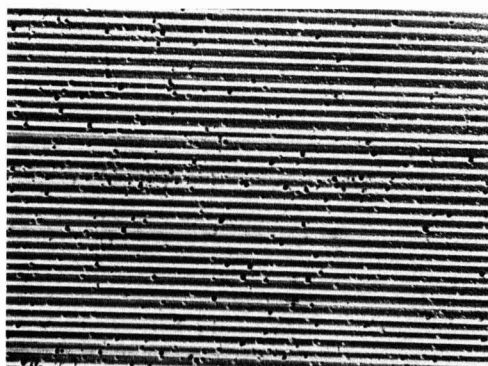


Fig. 10. Swirl defect striations in a (100) longitudinal slice of a crystal pulled under a crucible rotation of 20 rpm (no seed rotation); pulling-rate: 21 $\mu\text{m}/\text{sec}$; crystal diameter: 75 mm. Slice was Cu-decorated and preferentially etched. Region shown corresponds to forced convection conditions of growth. The relatively small microscopic growth-rate fluctuations result in random swirl distribution (see Fig. 7 and text). 150 \times .

cation of swirl microdefects and SiO_2 precipitates to coincide.

Since swirl formation was found to take place near microscopic growth rate maxima, the critical nuclei must be related to an impurity with a segregation coefficient less than 1, as the concentration of such an impurity does exhibit concentration maxima at microscopic growth rate maxima. Because carbon has a segregation coefficient less than one and is present in fairly high concentrations in Czochralski-grown silicon, it is believed that the critical nuclei for swirl microdefect formation are related to carbon. In fact, the average carbon concentration in the present investigation was within the range for which swirls are found in float-zone silicon; the swirl distributions in these cases were striated.

Manuscript submitted Dec. 1, 1978; revised manuscript received April 23, 1979.

Any discussion of this paper will appear in a Discussion Section to be published in the June 1980 JOURNAL. All discussions for the June 1980 Discussion Section should be submitted by Feb. 1, 1980.

Publication costs of this article were assisted by the Massachusetts Institute of Technology.

REFERENCES

1. A. J. R. de Kock, in "Semiconductor Silicon 1977," H. R. Huff and E. Sirtl, Editors, p. 508, The Electrochemical Society Softbound Proceedings Series, Princeton, N.J. (1977).
2. T. F. Cizek, in "Semiconductor Silicon 1973," H. R. Huff and R. R. Burgess, Editors, p. 150, The Electrochemical Society Softbound Proceedings Series, Princeton, N.J. (1973).
3. K. V. Ravi and C. J. Varker, *J. Appl. Phys.*, **45**, 263 (1974).
4. W. C. Dash, *ibid.*, **30**, 459 (1959).
5. W. Kaiser, P. H. Keck, and C. F. Lange, *Phys. Rev.*, **101**, 1264 (1956).
6. W. Kaiser and P. H. Keck, *J. Appl. Phys.*, **28**, 882 (1957).
7. A. R. Bean and R. C. Newman, *J. Phys. Chem. Solids*, **32**, 1211 (1971).
8. T. Nozaki, T. Y. Yatsurugi, and N. Akiyama, *This Journal*, **117**, 1566 (1971).
9. J. R. Patel and B. W. Batterman, *J. Appl. Phys.*, **34**, 2716 (1963).
10. W. Kaiser, *Phys. Rev.*, **105**, 1751 (1957).
11. D. M. Maher, A. Staudinger, and J. R. Patel, *J. Appl. Phys.*, **47**, 3813 (1976).
12. T. Y. Tan and W. K. Tice, *Philos. Mag.*, **34**, 615 (1976).
13. F. W. Voltmer and F. A. Padovani, in "Semiconductor Silicon 1973," H. R. Huff and R. R. Burgess, Editors, p. 75, The Electrochemical Society Softbound Proceedings Series, Princeton, N.J. (1973).
14. G. A. Rozgonyi, S. Mahajan, M. H. Read, and D. Brasen, *Appl. Phys. Lett.*, **29**, 531 (1976).
15. K. Graff, J. Hilgarth, and H. Neubrand, in "Semiconductor Silicon 1977," H. R. Huff and E. Sirtl, Editors, p. 575, The Electrochemical Society Softbound Proceedings Series, Princeton, N.J. (1977).
16. K. Tempelhoff, F. Speigelberg, and R. Gleichmann, *ibid.*, p. 585.
17. J. T. Yue and H. J. Ruiz, *ibid.*, p. 596.
18. A. Murgai, H. C. Gatos, and A. F. Witt, *This Journal*, **123**, 244 (1976).
19. K. Graff, E. Grallath, S. Ades, G. Goldbach, and G. Tolg, *Solid-State Electron.*, **16**, 887 (1973).
20. J. A. Baker and T. N. Tucker, *J. Appl. Phys.*, **39**, 4365 (1968).
21. C. S. Fuller, J. A. Ditzenger, N. B. Hannay, and E. Buehler, *Phys. Rev.*, **96**, 833 (1954) and *Acta Metall.*, **3**, 97 (1955).
22. W. Kaiser, H. L. Frisch, and H. Reiss, *Phys. Rev.*, **112**, 1546 (1958).
23. V. N. Mordkovich, *Sov. Phys. Solid State*, **6**, 654 (1964).
24. K. Graff and H. Pieper, *J. Electron. Mater.*, **4**, 281 (1975).
25. M. W. Jenkins, *This Journal*, **124**, 757 (1977).
26. A. Murgai, A. F. Witt, and H. C. Gatos, *ibid.*, **122**, 1276 (1975).
27. A. Murgai, H. C. Gatos, and A. F. Witt, in "Semiconductor Silicon 1977," H. R. Huff and E. Sirtl, Editors, p. 72, The Electrochemical Society Softbound Proceedings Series, Princeton, N.J. (1977).
28. Y. Yatsurugi, N. Akiyama, Y. Endo, and T. Nozaki, *This Journal*, **120**, 975 (1973).
29. J. A. Burton, R. C. Prim, and W. P. Slichter, *J. Chem. Phys.*, **21**, 1987 (1953).
30. W. R. Runyan, in "Silicon Semiconductor Technology," p. 108, McGraw-Hill Book Company, New York (1965).
31. A. Murgai and W. A. Westdorp, Paper presented at ICCG-5, Boston, July 1977.
32. A. J. R. de Kock, *This Journal*, **118**, 1851 (1971).
33. A. J. R. de Kock, P. J. Roksnoer, and P. G. T. Boonen, *J. Cryst. Growth*, **22**, 311 (1974).
34. F. G. Vieweg-Gutberlet, in "Semiconductor Silicon 1973," H. R. Huff and R. R. Burgess, Editors, p. 119, The Electrochemical Society Softbound Proceedings Series, Princeton, N.J. (1973).
35. A. Murgai, J. Y. Chi, and H. C. Gatos, submitted to *This Journal*.

Radiation Levels Associated with Advanced Lithographic Techniques

K. F. Galloway,* S. Mayo,* and P. Roitman

National Bureau of Standards, Electron Devices Division, Washington, D.C. 20234

ABSTRACT

Estimates of the radiation absorbed dose in critical device oxide layers due to x-ray and direct-write electron beam lithography are developed. Layered structures of photoresist, aluminum, silicon dioxide, and silicon are used for explicit calculations. It is shown that radiation levels in the Megarad (SiO_2) range can be expected for both of these advanced lithographic techniques. The consequences of this process-induced radiation damage are briefly considered.

X-ray and direct-writing electron beam lithography techniques for integrated circuits are expected to be

significant for very large scale integration (VLSI). These lithographic technologies have demonstrated linewidth resolution capability below 1 μm . Significant radiation damage to device structures may occur

* Electrochemical Society Active Member.
Key words: x-rays, electrons, films.

during the use of these technologies and is a potential problem. If the x-rays and electrons have sufficient energy to penetrate to critical dielectric layers such as silicon dioxide, the radiation damage phenomena observed in dielectric films exposed to ionizing radiation will result (1, 2). Process sequences must be designed to take this damage into account so that its effects can be minimized. Comparisons of the radiation damage associated with various lithographic processes and between these and other radiation exposures can be made from estimates of the associated radiation dose levels. Estimates of the radiation absorbed dose in critical device structures are developed in this paper. The consequences of this process-induced radiation damage are briefly considered.

X-Ray Lithography

In order to estimate the radiation absorbed dose due to x-ray lithography, consider the typical metal oxide semiconductor (MOS) device structure schematically represented in Fig. 1. The silicon substrate is covered by a film of silicon dioxide which is covered by a film of aluminum metallization which is in turn covered with a film of photoresist to be patterned with x-ray lithography. The x-rays are assumed to impinge on this assemblage in a narrow parallel beam. The x-ray intensity is exponentially attenuated as it passes through the films (3). The intensity loss per unit area ΔI in an incremental thickness t_0 of silicon dioxide is (4)

$$\Delta I = I_X [\exp(-\mu_R t_R - \mu_{Al} t_A)] \cdot [1 - \exp(-\mu_{SiO_2} t_0)] \quad [1]$$

where I_X = incident x-ray intensity, in photons/cm²; μ_i = absorption coefficients for the resist (R), aluminum (A), or silicon dioxide (O), in cm²/g; and t_i = thickness of resist, aluminum, or silicon dioxide, in g/cm². Effects such as photon backscattering have been neglected. The x-ray absorption coefficients can be obtained from data compiled by Henke and Ebsu (5). The absorption coefficients used for silicon dioxide and the resists were calculated as a weighted average of the coefficients of the constituents of these films. Table I summarizes the absorption coefficients used in the calculations in this paper. Values are given for three different x-ray energies representing the characteristic x-rays of copper, aluminum, and rhodium. The choice of an optimum x-ray energy has been discussed by Sullivan and McCoy (6). The resist formulation used for calculating the coefficients in Table I was (C₅H₈O₂)_n better known as PMMA. The actual coefficients for other resists considered in this paper will not vary significantly from these values. The calculations summarized in this paper are for aluminum gate structures, however the results would be the same for silicon gate structures since the absorption coefficients for

Table I. X-ray absorption coefficients and x-ray characteristics

	Cu K α	Al K α	Rh L α
Energy (keV)	0.930	1.487	2.697
Wavelength (Å)	13.336	8.339	4.597
Resist	3350	970	170
Aluminum	1453	404	1100
SiO ₂	3150	1100	780

silicon and aluminum are essentially the same in the x-ray energy range 0-3 keV considered here.

The effect of varying the x-ray energy was first explored. As an example, an explicit calculation was made for a structure of 50 nm of silicon dioxide beneath 0.7 μ m of aluminum beneath 0.5 μ m of resist (see Fig. 1). The energy loss per unit mass (dose) in the incremental oxide thickness or the radiation absorbed dose in the oxide was obtained by multiplying the intensity loss in the oxide from Eq. [1] by the x-ray energy and dividing by the mass of the oxide film (4) and expressed in Megarad (SiO₂) (1 rad¹ corresponds to 100 erg/g of energy absorbed in the material of interest). The oxide dose normalized to an x-ray energy deposition density of 1 J/cm³ absorbed in the resist film was calculated as a function of x-ray energy. For the aluminum K α x-ray, for example, an intensity of 3.6×10^{12} photons/cm² is required for an x-ray deposition density of 1 J/cm³ in the 0.5 μ m resist film. Figure 2 illustrates the variation of the oxide dose as a function of x-ray energy under the conditions specified. The energies of copper, aluminum, and rhodium characteristic x-rays are indicated. The dip in absorbed dose near 1.6 keV is due to x-ray absorption edges.

The effect of varying either the resist thickness or the gate conductor (aluminum) thickness on the

¹ The SI unit for absorbed dose is the gray (Gy) in units of J/kg. One rad equals 1×10^{-2} Gy.

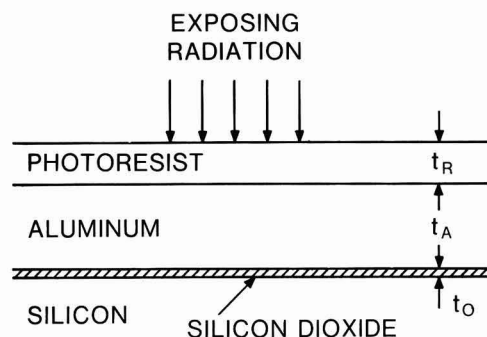


Fig. 1. Schematic diagram of typical device structure

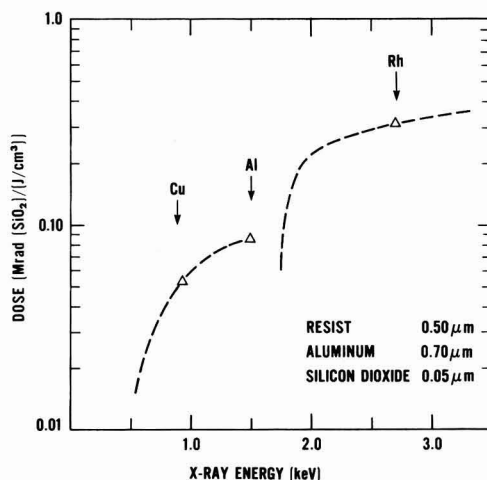


Fig. 2. Radiation absorbed dose in the oxide layer due to x-ray exposure of the typical structure specified in the text. The energies of copper, aluminum, and rhodium characteristic x-rays are indicated. Dose is normalized to an x-ray energy deposition density of 1 J/cm³ absorbed in the resist film.

radiation absorbed dose in the oxide was also examined. The oxide thickness was assumed constant at 50 nm. Figure 3 shows the variation in oxide dose (normalized as before) with aluminum thickness for aluminum and copper characteristic x-rays. The upper bound of the band on this figure represents the result for a 0.5 μm resist film, while the corresponding lower bound represents a 1.0 μm resist film. It is obvious from this figure that the dose in the oxide varies only slowly with either resist or metallization thickness.

Figure 4 illustrates the variation in radiation absorbed dose in the oxide as a function of x-ray energy deposition density or resist absorbed dose required for resist exposure. The calculations represented in

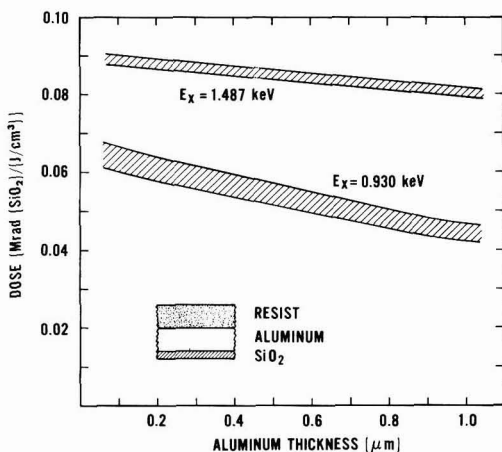


Fig. 3. Radiation absorbed dose in the oxide layer vs. aluminum thickness for x-ray exposure. Bands for aluminum and copper characteristic x-rays are shown. The bandwidth indicates a variation of 0.5–1.0 μm in resist thickness. Dose is normalized to an x-ray energy deposition density of 1 J/cm^2 absorbed in the resist film.

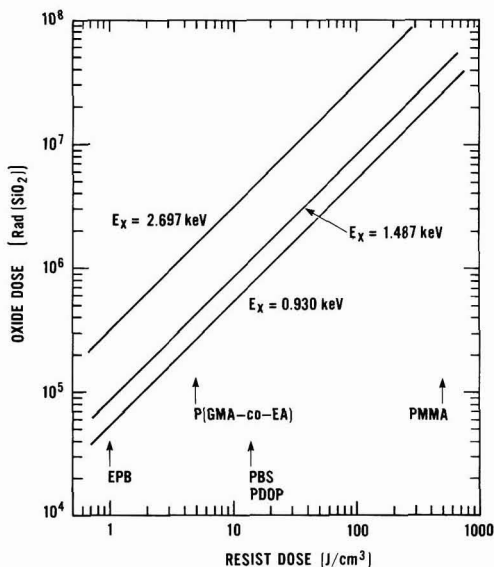


Fig. 4. Radiation absorbed dose in the oxide as a function of x-ray energy deposition density in the photoresist. Device structure is specified in text.

this figure have been made for a typical device structure (0.5 μm resist, 0.7 μm aluminum, 50 nm oxide) and for three x-ray energies. The energy deposition densities required for the exposure of several commonly used x-ray resists are indicated on this figure (7,8). Thus, for typical x-ray resists, device structures, and x-ray sources, the expected dose in the oxide of the device will range from about 0.1 Mrad (SiO_2) to tens of Mrad (SiO_2).

Direct-Write Electron Beam Lithography

For direct-write electron beam lithography, the radiation absorbed dose in the oxide layer (see Fig. 1) can be determined by applying an expression which relates electron energy deposition with penetration depth such as the one given by Everhart and Hoff (10). Figure 5 gives energy deposition vs. penetration depth for 15 and 25 keV electrons based on the work by Everhart and Hoff. The energy deposited in the oxide and the resultant absorbed dose can be calculated by integrating the energy deposition curves of Fig. 5 over the portion of the curve subtended by the oxide.

The variation in oxide absorbed dose with aluminum thickness for 15 and 25 keV incident electrons is shown in Fig. 6. The oxide thickness was 50 nm and the resist thickness 0.5 μm for the curves shown here. Varying the resist thickness between 0.5 and 1.0 μm resulted in negligible differences. The oxide dose ex-

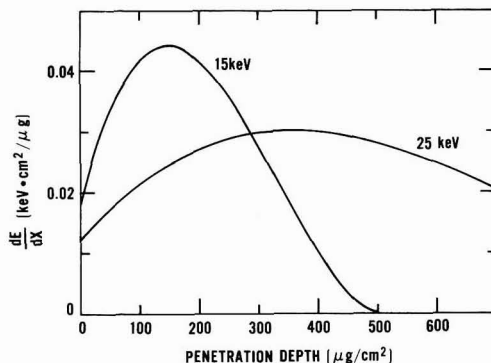


Fig. 5. Energy deposition per unit path length vs. penetration depth for 15 and 25 keV electrons. The measure of penetration depth used here is mass thickness—the product of material density and thickness.

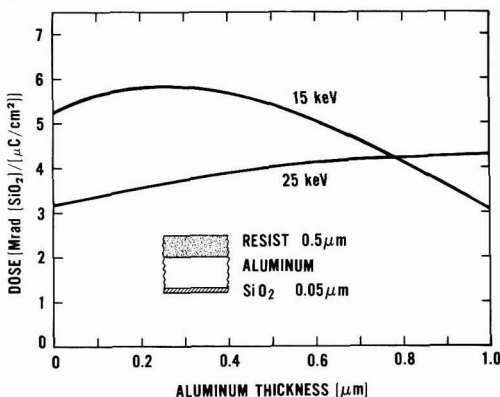


Fig. 6. Radiation absorbed dose in the oxide layer vs. aluminum thickness for 15 and 25 keV electrons. Device structure is specified in text. Dose is normalized to an incident electron fluence of 1 $\mu\text{C}/\text{cm}^2$.

pressed in Megarad (SiO_2) is normalized to an electron beam exposure flux of $1 \mu\text{C}/\text{cm}^2$ incident on the resist film.

Figure 7 illustrates the variation in radiation absorbed dose in the oxide as a function of electron beam flux required for resist exposure. The calculations represented in this figure have been made for a typical device structure ($0.5 \mu\text{m}$ resist, $0.7 \mu\text{m}$ aluminum, 50 nm oxide) and for two electron beam energies. The electron beam fluence required for the exposure of several commonly used electron beam resists (8,9,11) are indicated on this figure. The electron fluence required for resist exposure varies from approximately $0.05 \mu\text{C}/\text{cm}^2$ for EPB to as much as $50 \mu\text{C}/\text{cm}^2$ for PMMA. This, in turn, results in an oxide dose in a typical device structure in the Megarad (SiO_2) range when direct-write electron beam lithography is used.

Discussion

The estimates given in previous sections illustrate that the radiation absorbed dose incurred in critical device oxide layers while using these techniques is as large as that which has been observed to cause severe device degradation (1, 2, 12). The calculations have assumed the use of positive resist. The use of negative resist would reduce the problem since critical device areas would not be directly exposed to the radiation used for exposing the resist. However, laterally scattered radiation and background radiation associated with the exposure apparatus will yield exposure levels of 10-50% of the primary exposure within approximately $0.5 \mu\text{m}$ of the directly exposed areas.

It has been generally assumed that the oxide damage incurred by ionizing radiation, such as is present with the advanced lithographic techniques, can be removed by thermal treatment at moderate temperatures ($<400^\circ\text{C}$). However, this annealing which restores the preirradiation electrical characteristics may not be sufficient to remove trapping centers.

It has been shown that ionizing radiation, both low energy x-ray and electron beams, generates neutral electron traps in silicon dioxide layers (13-16). These traps are distributed throughout the oxide layer. Moderate temperature thermal anneals depopulate these traps, but do not eliminate them. Since these traps are neutral until they are filled with electrons, they are

not detected by capacitance-voltage measurements alone. Annealing at temperatures in excess of 550°C has been found necessary to remove these traps (13, 16).

If not removed, these neutral electron traps can contribute to device instability or to reliability problems by trapping hot electrons (17). The thinner oxides required for VLSI will lead to higher electric fields in the devices. Device operation under these high field conditions will result in energetic carriers which can be injected into the oxide. These carriers can charge the neutral trapping centers and thereby modify the device characteristics. In particular, a combination of transconductance degradation and threshold voltage shift might be expected for MOS transistors.

These problems will certainly be overcome by the ingenuity of process designers as the thrust toward VLSI accelerates. However, these considerations suggest that the limits of optical lithography, resist sensitivity, and the understanding of removing ionizing radiation damage by annealing are concerns relevant to the development of reliable VLSI circuits.

Acknowledgment

This work was conducted as part of the Semiconductor Technology Program at the National Bureau of Standards. This program is supported in part by the Defense Advanced Research Projects Agency (Order 2397) and the National Bureau of Standards.

Manuscript submitted Jan. 8, 1979; revised manuscript received June 6, 1979. This was Paper 178 presented at the Pittsburgh, Pennsylvania, Meeting of the Society, Oct. 15-20, 1978.

Any discussion of this paper will appear in a Discussion Section to be published in the June 1980 JOURNAL. All discussions for the June 1980 Discussion Section should be submitted by Feb. 1, 1980.

Publication costs of this article were assisted by the National Bureau of Standards.

REFERENCES

1. C. W. Gwyn, Sandia Development Report, SLA-73-0013 (1973).
2. W. C. Johnson, *IEEE Trans. Nucl. Sci.*, **ns-22**, 2144 (1975).
3. G. L. Clark, Editor, "The Encyclopedia of X-rays and Gamma Rays," Reinhold Publishing Corp., New York (1963).
4. S. Mayo, K. F. Galloway, and T. F. Leedy, *IEEE Trans. Nucl. Sci.*, **ns-23**, 1875 (1976).
5. B. L. Henke and E. S. Ebusu, *Adv. X-Ray Anal.*, **17**, 150 (1974).
6. P. A. Sullivan and J. H. McCoy, *IEEE Trans. Electron Devices*, **ED-23**, 412 (1976).
7. P. V. Lenzo and E. G. Spencer, *Appl. Phys. Lett.*, **24**, 289 (1974).
8. L. F. Thompson, E. D. Feit, M. J. Bowden, P. V. Lenzo, and E. G. Spencer, *This Journal*, **121**, 1500 (1974).
9. L. F. Thompson and R. E. Kerwin, in "Annual Review of Materials Science," Vol. 6, pp. 267-301, Annual Reviews, Inc., Palo Alto, California, (1976).
10. T. E. Everhart and P. H. Hoff, *J. Appl. Phys.*, **42**, 5837 (1971).
11. T. H. P. Chang, M. Hatzakis, A. D. Wilson, and A. N. Broers, *Electronics*, **50**, No. 10, 89 (1977).
12. B. L. Gregory and C. W. Gwyn, *Proc. IEEE*, **62**, 1264 (1974).
13. J. M. Aitken, D. R. Young, and K. Pan, *J. Appl. Phys.*, **49**, 3386 (1978).
14. J. M. Aitken and D. R. Young, *J. Appl. Phys.*, **47**, 1196 (1976).
15. J. M. Aitken, Abstract L-3, 20th Annual Electronic Materials Conference, Santa Barbara, California, June 28-30, 1978.
16. T. H. Ning, *J. Appl. Phys.*, **49**, 4077 (1978).
17. T. H. Ning, C. M. Osburn, and H. N. Yu, *J. Electron. Mater.*, **6** (1977).

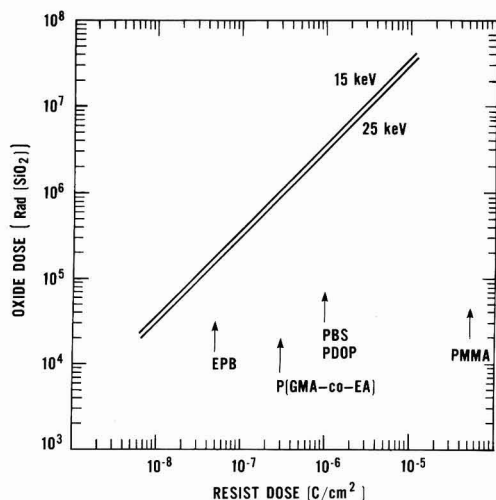


Fig. 7. Radiation absorbed dose in the oxide layer as a function of the electron fluence incident on the resist. Device structure is specified in text.

Kinetics and Oxide Properties of Silicon Oxidation in O_2 - H_2 -HCl Mixtures

K. Ehara, K. Sakuma, and K. Ohwada

Nippon Telegraph and Telephone Public Corporation,

Musashino Electrical Communication Laboratory, Musashino-shi, Tokyo 180, Japan

ABSTRACT

The thermal oxidation kinetics of silicon in O_2 - H_2 -HCl mixtures and the electrical properties of the silicon dioxide films grown in the mixtures have been studied in order to characterize the effect of H_2O and Cl_2 on silicon oxidation. Oxidations were carried out at $1100^\circ C$ over a wide range of H_2 and HCl flow rates at a constant O_2 flow rate. The partial pressures of O_2 , H_2 , H_2O , HCl, and Cl_2 were calculated from equilibrium chemical thermodynamics. Parabolic rate constants were calculated from the O_2 and H_2O partial pressures and the values were in quite good agreement with the experimental data. But the experimental data showed that linear rate constants were greatly dependent on Cl_2 partial pressure. The effective mobile ion density depended only on the Cl_2 partial pressure (p_{Cl_2}) and was independent of the H_2O partial pressure. The effective mobile ion density was rapidly decreased with increasing p_{Cl_2} before it approached a minimum constant value. The fixed charge density also depended only on p_{Cl_2} , but the decreasing rate with increasing p_{Cl_2} was small.

Many investigations have been reported concerning the thermal oxidation of silicon in O_2 -HCl mixtures. The oxidation results in a bias-temperature stability, a lower interface state density, and a larger minority carrier lifetime (1-6). On the other hand, the oxidation kinetics and the dependence of the resulting oxide properties on H_2O and Cl_2 have not been studied sufficiently. The oxidation relationships have been investigated using the mixed oxidant O_2 and H_2O produced by the reaction of O_2 and HCl (7-9). However, the oxidation rates have not been explained quantitatively as yet because of insufficient consideration of the partial pressures of the gases actually present. For that purpose, partial pressures must be calculated from thermodynamic considerations of the chemical reaction involved (10, 11). For the silicon oxidation in O_2 -HCl mixtures, it is very difficult to identify the separate effects of H_2O and Cl_2 on the oxidation rates and the oxide properties since the ratio of H_2O to Cl_2 partial pressures is always constant. In order to evaluate the effects of H_2O and Cl_2 independently, it is necessary to vary the partial pressures of H_2O and Cl_2 by means of the additions of H_2O , Cl_2 , or H_2 to the O_2 -HCl mixtures.

This work studies the thermal oxidation kinetics of silicon in O_2 - H_2 -HCl mixtures in order to characterize the effect of H_2O and Cl_2 on silicon oxidations. This work also discusses the dependence of the oxide properties on the partial pressures. Oxidations were carried out at $1100^\circ C$ over wide ranges of H_2 and HCl flow rates at a constant O_2 flow rate. The partial pressures of H_2O and Cl_2 produced by the high temperature reaction of O_2 , H_2 , and HCl were calculated on the basis of chemical equilibrium theory. Values of parabolic and linear rate constants in the silicon oxidation relationship for O_2 - H_2O mixtures were determined using these partial pressures for comparison with the experimental values. The effects due to the H_2O and Cl_2 partial pressures on the fixed charge density and the effective mobile ion density are discussed.

Experimental

The silicon wafers were (100) oriented, 4-6 Ωcm , and n-type. All the wafers were cleaned using boiling

Key words: silicon oxidation kinetics, silicon dioxide, hydrogen chloride.

trichlorethylene, then boiling acetone, a deionized-water rinse, boiling nitric acid, a 2.5% hydrofluoric acid dip, and a deionized water rinse. They were oxidized at $1100^\circ C$ in various mixtures of O_2 , H_2 , and HCl immediately after cleaning. Flow rates of the gases were 1.5 liters/min for O_2 , 0-3.0 liters/min for H_2 , and 0-0.72 liter/min for HCl. The HCl was of 99.99% purity and was used as obtained from the manufacturer. In order to prevent silicon corrosion by the HCl added to the oxidation gas, the HCl flow was started after a 1 min oxidation was carried out in pure O_2 for the O_2 -HCl oxidations, or in a O_2 - H_2 mixtures for the O_2 - H_2 -HCl oxidations.

MOS capacitor structures were fabricated in the following manner. The silicon dioxide layers were 1 μm in thickness in consideration of field oxide application. Aluminum of 7000Å thickness was evaporated using an electron beam. The wafers were then annealed for 30 min in H_2 at $400^\circ C$, and the electrode patterns were formed by photoresist operations.

The oxide thickness was measured with a Taylor-Hobson Talysurf 4. The MOS capacitors were evaluated using the capacitance-voltage (C-V) technique at a frequency of 1 MHz. The C-V characteristics measured were enough to obtain the flatband voltage (V_{FB}). The values of the fixed charge density were determined from V_{FB} of the C-V characteristics after a 60 min bias-temperature (BT) stress at $200^\circ C$ under the short circuit for the initial MOS capacitors. The effective mobile ion density was determined from the V_{FB} shift of the C-V characteristics after a 60 min BT stress at $200^\circ C$ with an applied voltage of -200 to $200V$.

Results and Discussion

Kinetics and oxide growth.—The plots of oxide thickness vs. oxidation time with H_2 flow rates of 0, 0.6, 1.8, and 3.0 liters/min are shown in Fig. 1. The dependence of oxidation rates on HCl flow rates changes with H_2 flow rates. Oxidation rates increase with increasing HCl flow rates for an H_2 flow rate of 0 liter/min. However, they decrease for H_2 flow rates of 0.6 and 1.8 liters/min.

The oxide thickness vs. oxidation time data presented in Fig. 1 were evaluated using the linear parabolic oxidation model (12). The general relationship in the model can be rewritten as

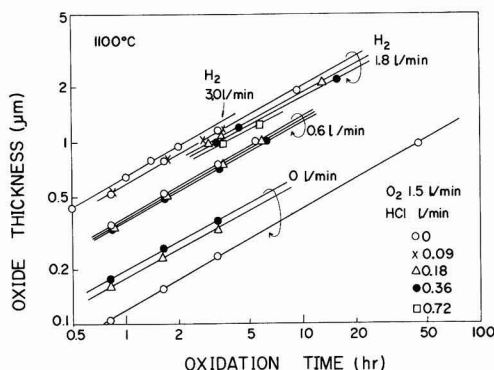
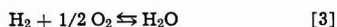
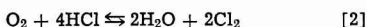


Fig. 1. Oxide thickness vs. oxidation time for silicon oxidation in O_2 - H_2 -HCl mixtures.

$$(x_0 + x_1) = B \left(\frac{t}{x_0 - x_1} \right) - A \quad [1]$$

where t is oxidation time, x_0 is oxide thickness, x_1 is the thickness of an initial layer of oxide, and B and B/A are the parabolic and linear rate constants, respectively. We made an assumption that the values of x_1 of O_2 -HCl oxidation and O_2 - H_2 -HCl oxidation were the same as O_2 oxidation and H_2O oxidation, respectively, so the values of x_1 were settled as $x_1 = 230\text{\AA}$ and $x_1 = 0\text{\AA}$ for each case. The experiments were carried out to assure the condition of $x_0 \gg x_1$ in which condition the error in x_1 had little effect on the experimental value of B and B/A in Eq. [1]. The value of oxide thickness x_0 was given experimentally as the function of oxidation time as shown in Fig. 1. Using these values we can plot $(x_0 + x_1)$ vs. $t/(x_0 - x_1)$, whose slope means B and the intercept means $-A$, respectively. The experimental data of B and B/A for O_2 - H_2 -HCl oxidations with various H_2 and HCl flow rates including zero H_2 flow rate are shown in Table I.

These rate constants, B and B/A , were also calculated under the following model. It was assumed that the gas phase equilibria were established rapidly as



The partial pressures of the gaseous species were obtained from Eq. [2] and [3]. The calculation processes are shown in detail in the Appendix. We assumed that O_2 and H_2O were the only oxidants, so the oxidation rate constants only depended on the partial pres-

ures of O_2 and H_2O . With this assumption, we used the general relationship for O_2 - H_2O silicon oxidation (7, 8) with the partial pressures of O_2 and H_2O calculated from Eq. [2] and [3]. The general relationship became the same form as Eq. [1], at 1100°C oxidation, in which B and B/A are (7, 8)

$$B = B_1 + B_2 \quad [4]$$

$$B_1 = p_1 B_3 \quad [5]$$

$$B_2 = p_2 B_4 \quad [6]$$

$$B/A = (B_1 + B_2)^2 / (A_1 B_1 + A_2 B_2) \quad [7]$$

where the subscript 1 refers to oxidation by O_2 and subscript 2 to oxidation by H_2O . The values of B_1 and B_2 are proportional to the partial pressures of the oxidants, while A_1 and A_2 are independent of the partial pressures. B_3 and B_4 are parabolic rate constants at atmospheric pressures of O_2 and H_2O , respectively. The values of p_1 and p_2 are the partial pressures of the oxidants, which are shown in Fig. 2. The constant B was calculated from Eq. [4], [5], and [6]. Where B_3 and B_4 were substituted with the value shown in Table I, the values of p_1 and p_2 were taken from Fig. 2. The constant B/A was calculated from Eq. [7] using the values of B_1 and B_2 calculated from Eq. [5] and [6], and A_1 and A_2 were substituted with the values from Table I. The calculated values of B and B/A are tabulated in Table II. Experimental and calculated values of B and B/A are plotted against HCl flow rate in Fig. 3 and 4, respectively.

As shown in Fig. 3, the agreement between the calculated and experimental values of the parabolic rate constant was satisfactory. The results suggest that the assumptions for the gas phase equilibria and the calculations of the partial pressures are adequate and that the parabolic rate constant is independent of p_{Cl_2} . On the other hand, Fig. 4 shows that the calculated and experimental values of linear rate constants were mismatched. The present model, which assumes that the oxidation rate constants are independent of p_{Cl_2} , cannot explain the experimental values of the linear rate constant. Minkowski *et al.* (13) have reported an additional phase formed at the oxide-silicon interface for O_2 -HCl oxidation. Therefore, the interfacial reaction for O_2 - H_2 -HCl oxidation is considered to also be influenced by HCl similar to O_2 -HCl oxidation. The linear rate constant involves the reaction rate constant at the oxide-silicon interface, so that it is considered that the linear rate constant for O_2 - H_2 -HCl oxidation is dependent on p_{Cl_2} .

Fixed charge density and effective mobile ion density.—The values of V_{FB} is given by (14)

$$V_{FB} = \Phi_{MS} - \frac{Q_{ss}}{C_o} - \frac{Q_o}{C_o} \quad [8]$$

Table I. Experimental values of rate constants for silicon oxidation in O_2 - H_2 -HCl mixtures at 1100°C [N-type, 4-6 Ωcm , (100) oriented silicon]

O_2 (liters/min)	H_2 (liters/min)	HCl (liters/min)	B ($\mu\text{m}^2/\text{hr}$)	A (μm)	B/A ($\mu\text{m}/\text{hr}$)
1.5	0	0 (O_2 oxidation)	0.024 (= B_3)	0.14 (= A_1)	0.17
		0.18	0.038	0.07	0.54
		0.36	0.049	0.07	0.70
	0.6	0	0.22	0.20	1.1
		0.18	0.18	0.08	2.3
		0.36	0.18	0.12	1.5
	1.8	0	0.46	0.20	2.3
		0.09	0.46	0.20	2.3
		0.18	0.37	0.08	4.7
		0.36	0.34	0.06	5.6
		0.72	0.32	0.13	2.4
	3.0	0 (H_2O oxidation)	0.54 (= B_4)	0.19 (= A_2)	2.8

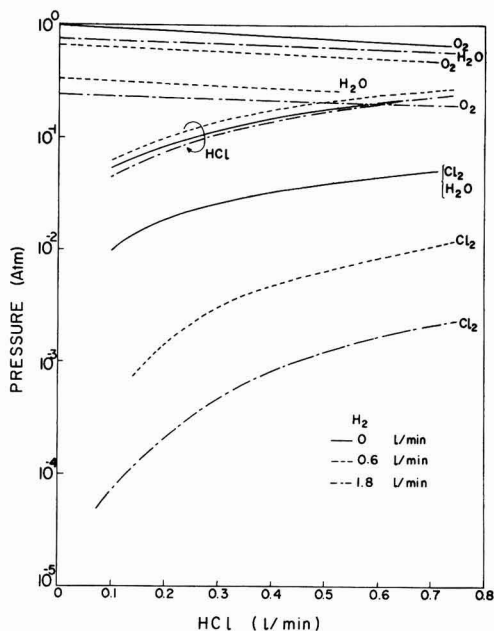


Fig. 2. Equilibrium partial pressures in O₂-H₂-HCl mixtures at 1100°C vs. the HCl flow rate. The O₂ flow rate is 1.5 liters/min. The total pressure is 1 atm.

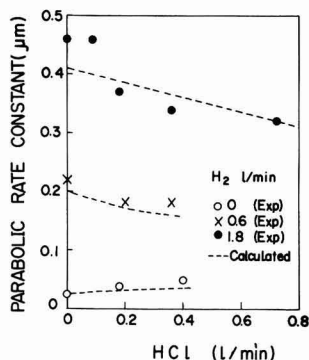


Fig. 3. Comparison of experimental and calculated values of the parabolic rate constant vs. the HCl flow rate in O₂-H₂-HCl mixtures.

where Φ_{MS} is the metal-semiconductor work function difference, Q_{ss} the fixed charge at the oxide-semiconductor interface, C_o the oxide capacitance, and Q_o the excess charge induced in the silicon by the mobile ion in the oxide. The V_{FB} shift, ΔV_{FB} , which can be obtained from the difference between the V_{FB} after BT stress with any applied voltage and the V_{FB} after BT stress under the short circuit, is equal to $-\Delta Q_o/C_o$. A plot of the fixed charge density (Q_{ss}/q) vs. HCl flow rate is shown in Fig. 5. It can be observed from Fig. 5 that Q_{ss}/q tends to decrease with increasing HCl flow rate, the decrease being greater the smaller the H₂ flow rate. Plots of $\Delta Q_o/q$ vs. the applied voltage (V_A) are presented in Fig. 6-8. For the case of 0 liter/min H₂, $\Delta Q_o/q$ increases with increasing V_A for 0 liter/min HCl, while it is almost constant for 0.18 and 0.36 liter/min HCl. For the case of 0.6 liter/min

Table II. Calculated values of rate constants for silicon oxidation in O₂-H₂-HCl mixtures at 1100°C [n-type, 4-6 Ωcm, (100) oriented silicon]

O ₂ (liters/ min)	H ₂ (liters/ min)	HCl (liters/ min)	B (μm ² / hr)	A (μm)	B/A (μm/ hr)
1.5	0	0	0.024	0.14	0.17
		0.18	0.031	0.16	0.19
		0.36	0.035	0.16	0.22
	0.6	0	0.20	0.19	1.1
		0.18	0.17	0.19	0.89
		0.36	0.16	0.19	0.84
3.0	1.8	0	0.41	0.19	2.2
		0.09	0.40	0.19	2.1
		0.18	0.39	0.19	2.1
		0.36	0.36	0.19	1.9
	3.0	0	0.52	0.19	1.7
		0	0.54	0.19	2.8

H₂, $\Delta Q_o/q$ diminishes with increasing HCl flow rate (Fig. 7). For the case of 1.8 liters/min H₂, $\Delta Q_o/q$ is almost independent of HCl flow rate (Fig. 8). From these results, $\Delta Q_o/q$ tends to decrease with increasing HCl flow rate, and this tendency is greater for a small H₂ flow rate. The increase of $\Delta Q_o/q$ tends to level off at about 100V of an applied voltage.

The effective mobile ion density (N_{ion}), which is the number of unneutralized N_a^+ ions after BT stress (1, 2, 4-6), was calculated from the $C_o \Delta V_{FB}(+) - \Delta V_{FB}(-)/q$ (1). Here, $\Delta V_{FB}(+)$ is the V_{FB} shift

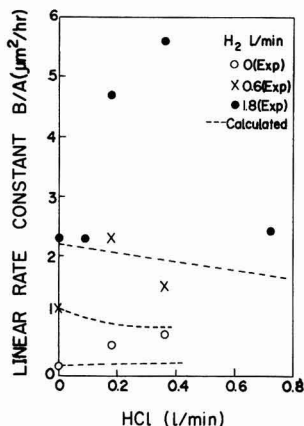


Fig. 4. Comparison of experimental and calculated values of the linear rate constant vs. HCl flow rate in O₂-H₂-HCl mixtures.

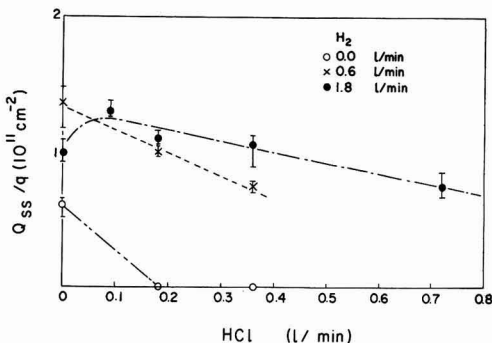


Fig. 5. Dependence of fixed charge density on HCl flow rate added to O₂-H₂ ambient during oxidation.

after a positive BT stress, and $\Delta V_{FB}(-)$ the V_{FB} shift after a negative BT stress. Plots of N_{ion} calculated from the data in Fig. 6-8, are presented as a function of HCl flow rate in Fig. 9. The dependence of Q_{ss}/q on p_{Cl_2} was determined from Fig. 2 and 5. It can be observed in Fig. 10 that Q_{ss}/q is gradually decreased with increasing p_{Cl_2} , and it little depends on H_2 flow rate, i.e., the H_2O partial pressure. Some authors state that Q_{ss}/q is independent of p_{Cl_2} (4). Figure 11 shows N_{ion} as a function of p_{Cl_2} . N_{ion} rapidly decreases with increasing p_{Cl_2} and falls to the minimum value at a critical Cl_2 partial pressure of $5 \times$

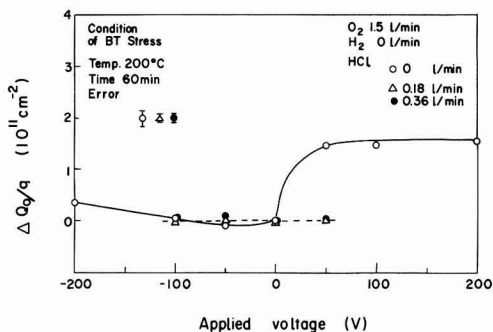


Fig. 6. Change of the shift $\Delta Q_0/q$ after BT stress with applied voltage under BT stress in silicon dioxide grown in O_2 -HCl mixtures.

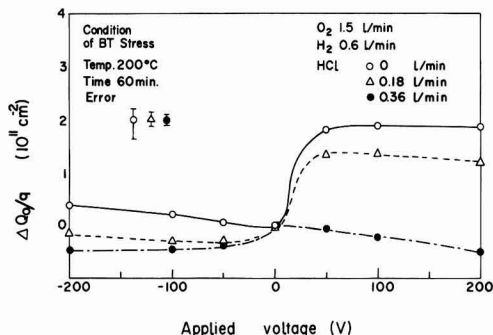


Fig. 7. Change of the shift $\Delta Q_0/q$ after BT stress with applied voltage under BT stress in silicon dioxide grown in O_2 - H_2 -HCl mixtures with the H_2 flow rate of 0.6 liter/min.

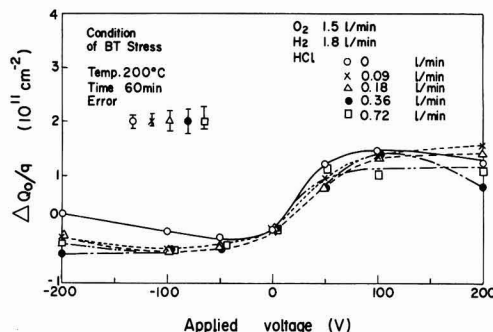


Fig. 8. Change of the shift $\Delta Q_0/q$ after BT stress with applied voltage under BT stress in silicon dioxide grown in O_2 - H_2 -HCl mixtures with the H_2 flow rate of 1.8 liters/min.

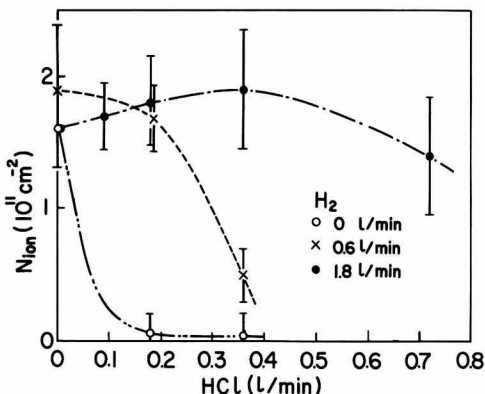


Fig. 9. Dependence of effective mobile ion density on HCl flow rate for the thermal oxidation of silicon in O_2 - H_2 -HCl mixtures.

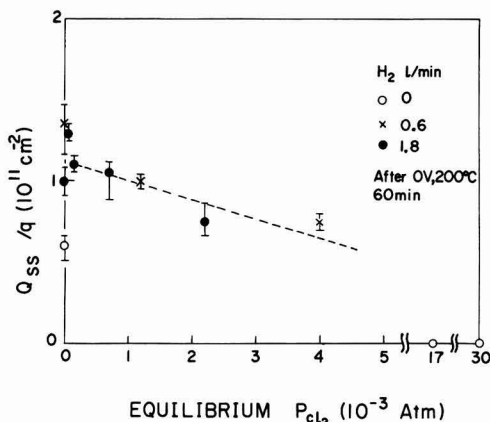


Fig. 10. Dependence of fixed charge density Q_{ss}/q on Cl_2 partial pressure p_{Cl_2} for the thermal oxidation of silicon in O_2 - H_2 -HCl mixtures.

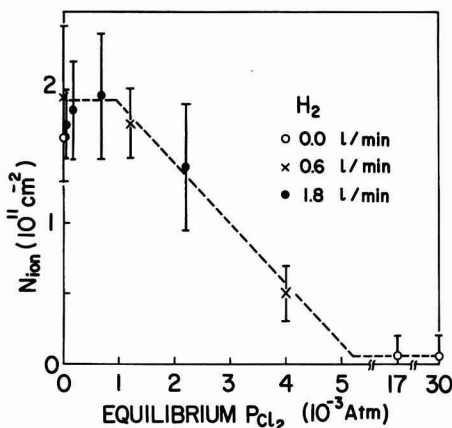


Fig. 11. Dependence of effective mobile ion density N_{ion} on Cl_2 partial pressure p_{Cl_2} for the thermal oxidation of silicon in O_2 - H_2 -HCl mixtures.

10^{-3} atm. Furthermore, it depends only on p_{Cl_2} and is independent of the H_2 flow rate, i.e., actually the H_2O partial pressure.

Rohatgi *et al.* (5, 6) have analyzed the passivation mechanism in O_2 -HCl oxides. They established relations wherein passivation P , expressed as $(N - N_{ion})/N$, was proportional to n_{Cl} , the Cl content of the oxide film, where N is the mobile ion density. The dependence of N_{ion} on p_{Cl_2} for zero H_2 flow rate, shown in Fig. 11, can be explained from the experimental data of the plot of P vs. p_{HCl} by Rohatgi (6). Therefore, the Cl content of the oxide film is suggested to be the dominant factor in the passivation mechanism for O_2 -H₂-HCl oxides similar to O_2 -HCl oxides. Tressler *et al.* (10) have analyzed the experimental data of O_2 -HCl oxidation obtained by Kriegler *et al.* (1) and reported that N_{ion} in the oxide film achieves the minimum value at Cl_2 partial pressure higher than 7×10^{-3} atm. This value is approximately the same as the experimental value in this work. Therefore, it is considered that N_{ion} is independent of the H_2O partial pressure and depends only on p_{Cl_2} . It was reported by Kriegler *et al.* (15) that the passivating effect of HCl on the oxidation was not observed when H_2O was mixed in the O_2 -HCl mixtures. From the above discussion, it is clear that the decrease of the Cl_2 partial pressure that occurs by introducing H_2O causes N_{ion} to increase, and H_2O itself is not a dominant factor in controlling N_{ion} . Therefore, even if H_2O is mixed in the oxidation gases, the passivation due to HCl gas can be retained by introducing HCl gas which provides the Cl_2 partial pressure required to decrease N_{ion} .

Summary

The O_2 -H₂-HCl oxidation processes were studied in order to clarify the effect of the thermal oxidation kinetics of silicon on the electrical properties of silicon dioxide. The oxidation kinetics were related to the partial pressures of the gases in the equilibrium mixtures. Values of the parabolic rate constant for the oxidation calculated from a treatment that uses the equilibrium partial pressures of O_2 and H_2O agreed approximately with the experimental values. The dominant factors in the oxidation rate are the partial pressures of O_2 and H_2O .

The fixed charge density and the effective mobile ion density in the oxide films were measured and the effects due to the partial pressures of the reacting gases on these properties were investigated. The effective mobile ion density depends only on the Cl_2 partial pressure in the oxidation gases and decreases with increasing the Cl_2 partial pressure. The effective mobile ion density achieves the minimum value at Cl_2 partial pressure higher than a certain value. It can also be shown that the fixed charge density is gradually decreased with increasing Cl_2 partial pressure, while most authors have said that the fixed charge density is independent of p_{Cl_2} .

Acknowledgment

The authors wish to thank Mr. H. Ariyoshi for helpful discussions and encouragement during the course of this work.

Manuscript submitted July 14, 1978; revised manuscript received June 8, 1979.

Any discussion of this paper will appear in a Discussion Section to be published in the June 1980 JOURNAL. All discussions for the June 1980 Discussion Section should be submitted by Feb. 1, 1980.

Publication costs of this article were assisted by Nippon Telegraph and Telephone Public Corporation.

APPENDIX

Calculations of the equilibrium partial pressures are made from the following equations. The equilibrium constants of reaction [2] and [3] are (11)

$$K_a = \frac{p_{H_2O} p_{Cl_2}}{p_{O_2}^{1/2} p_{HCl}^2} \quad [A-1]$$

$$K_b = \frac{p_{H_2O}}{p_{H_2} p_{O_2}^{1/2}} \quad [A-2]$$

where, K_a and K_b denote the equilibrium constants of reactions [2] and [3], respectively, and the p 's are the equilibrium partial pressures. The used units of K_a and K_b are $\text{atm}^{-1/2}$, and the used units of the p 's are atm. Values of the p 's are

$$p_{H_2} = (n_{H_2}/N)P \quad [A-3]$$

$$p_{HCl} = (n_{HCl}/N)P \quad [A-4]$$

$$p_{O_2} = (n_{O_2}/N)P \quad [A-5]$$

$$p_{H_2O} = (n_{H_2O}/N)P \quad [A-6]$$

$$p_{Cl_2} = (n_{Cl_2}/N)P \quad [A-7]$$

$$N = n_{H_2} + n_{HCl} + n_{O_2} + n_{H_2O} + n_{Cl_2} \quad [A-8]$$

where the n 's are the numbers of moles, N is the total numbers of moles, and P the total pressure which is 1 atm in this study. Values of the n 's are

$$n_{H_2} = X - a \quad [A-9]$$

$$n_{HCl} = Z - b \quad [A-10]$$

$$n_{O_2} = Y - a/2 - b/4 \quad [A-11]$$

$$n_{H_2O} = a + b/2 \quad [A-12]$$

$$n_{Cl_2} = b/2 \quad [A-13]$$

where X , Y , and Z are the numbers of moles for H_2 , O_2 , and HCl before reaction, respectively. Values of a are the numbers of moles for H_2 converted into H_2O , and b the numbers of moles for HCl converted into H_2O and Cl_2 . Values of the equilibrium constants at 1100°C used for these calculations were taken from the previous work (11). Values of K_a and K_b are 5.623×10^{-2} and $5.623 \times 10^9 \text{ atm}^{-1/2}$, respectively. Values of X , Y , and Z were the ratio of each reaction gas flow rate to the total gas flow rate. Equations [A-1]-[A-13] give a unique set of a and b for a given set of K_a , K_b , X , Y , and Z . Values of the partial pressures can be obtained from Eq. [A-3]-[A-7].

LIST OF SYMBOLS

B	parabolic rate constant for O_2 -H ₂ -HCl oxidation, $\mu\text{m}^2/\text{hr}$
B_1	parabolic rate constant for O_2 oxidation, $\mu\text{m}^2/\text{hr}$
B_2	parabolic rate constant for H_2O oxidation, $\mu\text{m}^2/\text{hr}$
B/A	linear rate constant for O_2 -H ₂ -HCl oxidation, $\mu\text{m}/\text{hr}$
B_1/A_1	linear rate constant for O_2 oxidation, $\mu\text{m}/\text{hr}$
B_2/A_2	linear rate constant for H_2O oxidation, $\mu\text{m}/\text{hr}$
B_3	value of B_1 for the case of $p_1 = 1$, $\mu\text{m}^2/\text{hr}$
B_4	value of B_2 for the case of $p_2 = 1$, $\mu\text{m}^2/\text{hr}$
C_0	capacitance per unit area of the oxide, farad/cm ²
K_a, K_b	equilibrium constant, $\text{atm}^{-1/2}$
n_{H_2}, n_{HCl}, \dots	numbers of moles of H_2 , HCl, ...
N_{ion}	effective mobile ion density, cm^{-2}
p_1	partial pressure of oxidant, atm
p_{H_2}, p_{HCl}, \dots	partial pressure of H_2 , HCl, ... atm
Φ_{MS}	metal-semiconductor work function difference, V
Q_{ss}/q	fixed charge density, cm^{-2}
Q_o/q	excess charge induced in the silicon by the mobile ion in the oxide, cm^{-2}
t	oxidation time, hr
V_A	applied voltage, V
x_o	oxide film thickness, μm
x_i	thickness of an initial layer of oxide, μm

REFERENCES

1. R. J. Kriegler, Y. C. Cheng, and D. R. Colton, *This Journal*, **119**, 388 (1972).
2. R. J. Kriegler, *Appl. Phys. Lett.*, **20**, 449 (1972).
3. D. R. Young and C. M. Osburn, *This Journal*, **120**, 1578 (1973).

4. B. R. Singh and P. B. Balk, *ibid.*, **125**, 453 (1978).
5. A. Rohatgi, S. R. Butler, F. J. Feigl, H. W. Kraner, and K. W. Jones, *Appl. Phys. Lett.*, **30**, 104 (1977); A. Rohatgi, S. R. Butler, F. J. Feigl, H. W. Kraner, and K. W. Jones, *This Journal*, **126**, 143 (1979).
6. A. Rohatgi, S. R. Butler, and F. J. Feigl, *This Journal*, **126**, 149 (1979).
7. K. Hirabayashi and J. Iwamura, *ibid.*, **120**, 1595 (1973).
8. B. E. Deal, D. W. Hess, J. D. Plummer, and C. P. Ho, *ibid.*, **125**, 339 (1978).
9. B. E. Deal, *ibid.*, **125**, 576 (1978).
10. R. E. Tressler, J. Stach, and D. M. Metz, *ibid.*, **124**, 607 (1977).
11. Y. J. van der Meulen and J. G. Cahill, *J. Electron Mater.*, **3**, 371 (1974).
12. B. E. Deal and A. S. Grove, *J. Appl. Phys.*, **36**, 3770 (1965).
13. J. Minkowski, R. E. Tressler, and J. Stach, *This Journal*, **125**, 1867 (1978).
14. E. H. Snow, A. S. Grove, B. E. Deal, and C. T. Sah, *J. Appl. Phys.*, **36**, 1664 (1965).
15. R. J. Kriegler, *Denki Kagaku*, **41**, 466 (1973).

Fe-Cr-Al Alloy, High Temperature Corrosion in Sulfur Vapor

E. M. Jallouli, J. P. Larpin, M. Lambertin, and J. C. Colson

*Laboratoire de Recherches sur la Réactivité des Solides,
Faculté de Sciences Mirande, B.P. 138—21004 Dijon Cedex, France*

ABSTRACT

The corrosion of Fe-17Cr-xAl [$x = 4$ or 6 weight percent (w/o)] steels is studied at high temperature (750°–950°C) under a low sulfur vapor pressure (6.2×10^{-2} Torr). Observation and analysis of the kinetic curves obtained allowed several successive corrosion steps to be clarified. The study of the morphology and the composition of the corrosion scales show their transformation during the different steps of the sulfidation process. All the results obtained allow a mechanism of corrosion, closely dependent on the mechanical stresses developed in the scales during the reaction, to be proposed.

The efficiency of adding aluminum to steels in order to improve their resistance against oxidation has been known for several years now (1–3). This element addition also seems beneficial for alloys intended to be used at high temperature in S_2 , H_2S , and SO_2 atmospheres (4–9).

However, if the corrosion mechanisms of Fe-Cr-Al alloys by oxygen are relatively well-known and have led to much work it is not so for corrosion mechanisms by sulfur.

Most authors who have dealt with those questions have examined the behavior of this type of alloys in H_2S/H_2 mixtures of various compositions (10–12). Mrowec studied the corrosion of alloys with various chromium (18–25%) and aluminum (1–5%) contents (13) or with constant chromium (20%) and various aluminum (1–20%) contents (14) in sulfur vapor at atmospheric pressure. In similar conditions, Nishida effected the sulfidation of cast irons (2% C) containing up to 25% Al (8). He also tried to determine the composition and structure of the various mixed sulfides (Fe-Cr-Al)₂S likely to occur during sulfidation on Fe-Cr-Al alloys (15).

There is a basic difference between the oxidation and sulfidation of alloys containing aluminum. Indeed, if it is easy to obtain a compact and protective layer of alumina on the metal as soon as the aluminum concentration reaches about 4–5%, alternatively, it is much more difficult to observe the formation of a sulfide layer (13). This is probably due, on the one hand to far larger diffusion rates in the sulfide than in the oxide (16, 17) and, on the other, to the rather slight differences between the values of free energy of formation of aluminum sulfide and the sulfides of the other elements (18). The present paper is devoted to studying corrosion by sulfur vapor, at high temperature, of Fe-17 Cr-xAl alloys containing 4 and 6% aluminum, respectively, in order to compare their be-

havior with that of Fe-17 Cr alloys previously investigated, in the same conditions (19).

Experimental

The kinetic study was achieved in thermogravimetry with a silica spring thermobalance specially adapted to operate under sulfur vapor pressure (20). That later is established following the "cold point principle" and fixed by the temperature of liquid sulfur. The whole apparatus was heated at a higher temperature (200°C) in order to avoid sulfur condensation. The accuracy of the thermobalance is better than 0.2 mg. The other techniques used were optical and scanning electron microscopy, x-ray wavelength dispersive analysis, and x-ray diffraction.

Both alloys investigated were prepared in a vacuum induction furnace. The ingot obtained was hot-rolled, then annealed for 30 min at 800°C in a N_2 -10% H_2 atmosphere and finally quenched in the air.

Small bored platelets about $10 \times 10 \times 2.5$ mm were used. Before use, the samples were carefully polished with grit paper through 800 grade, and then washed successively in water and alcohol.

Account taken of their composition (listed in Table I) both alloys investigated show a ferritic structure at high temperature. Their approximate grain size is ASTM 2.

The sulfidation study was conducted under a pressure of 6.2×10^{-2} Torr in the temperature range 750°–950°C; the reaction time was up to 100 hr.

Table I. Composition of the investigated alloys

Alloy No.	Alloy composition				
	w/o Fe	w/o C	w/o Cr	w/o Al	w/o O ₂
I	bal.	0.004	16.14	4.05	0.0024
II	bal.	0.005	16.55	6.05	0.0012

Key words: Fe-Cr-Al alloys, sulfidation kinetics, morphological study, corrosion model.

Table II. Parabolic rate constants determined in the two parabolic parts of the reaction

Alloy No.	First parabolic part $K_p (g^2 \cdot cm^{-4} \cdot min^{-1}) (\times 10^{-6})$					Second parabolic part $K_p (g^2 \cdot cm^{-4} \cdot min^{-1}) (\times 10^{-6})$				
	750	800	850	900	950	750	800	850	900	950
I	0.021	0.078	0.12	0.22	0.62	0.12	0.54	0.90	2.19	3.96
II	0.012	0.026	0.074	0.19	0.33	0.10	0.22	0.58	2.51	2.81

Results

In the above conditions, the kinetic curves $\Delta W/A = f(t)$ (ΔW = weight gain; A = sample surface; t = time) all show the same profile (Fig. 1); first a parabolic part, followed by a second where the rate increases, then a third one again parabolic. The $(\Delta W/A)^2 = f(t)$ curves (Fig. 2) show that the rate constants corresponding to the second parabolic part are, in all cases, higher than those of the first parabolic part (Table II).

For each alloy, the activation energies were determined for the two parabolic parts; they are listed in Table III. For a same alloy the values obtained are identical.

Account taken of the $(\Delta W/A) = f(t)$ curve profiles the morphological observations were achieved systematically in the three parts.

At the beginning of the reaction, three distinct layers can be observed (Fig. 3). The microcrystallized outer layer is made of pyrrhotite $Fe_{1-x}S$. The intermediate layer is composed of an iron, chromium, and aluminum sulfide whose x-ray analysis shows that it is similar to daubreelite $FeCr_2S_4$. Nishida (15) showed that in fact there is a whole series of sulfides of this type $FeCr_xAl_{2-x}S_4$ with neighboring parameters. Mrowec (13, 14) considers that a fraction of trivalent chromium ions in the sulfospinel $FeCr_2S_4$ can be substituted by

Table III. Activation energy values determined in the two parabolic parts of the reaction

Alloy No.	E (kcal · mole ⁻¹)	
	First parabolic part	Second parabolic part
I	37	37
II	45	45

trivalent ions of iron and aluminum. The stoichiometric formula of this phase can be written as $Fe(Fe_xAl_yCr_{2-x-y})S_4$. Let us term it $Fe(Fe, Cr, Al)_2S_4$. Finally, the inner porous layer is composed of a $Fe_{1-x}S$ and sulfospinel mixture. This morphology corresponds to the first parabolic part of the curves and can be observed on both alloys.

As sulfidation proceeds cracks occur in the intermediate compact $Fe(Fe, Cr, Al)_2S_4$ layer (Fig. 4). The thickness of the porous inner layer, then, increases abnormally. Meanwhile, under the larger cracks, nodules of a new compact layer of $Fe(Fe, Cr, Al)_2S_4$ can be observed on the metallic core. This morphology corresponds to the period when the reaction rate increases and this for both alloys under examination.

Finally, after an even longer time, corresponding to the second parabolic part of the curves a complex morphology occurs. Six distinct layers can be observed

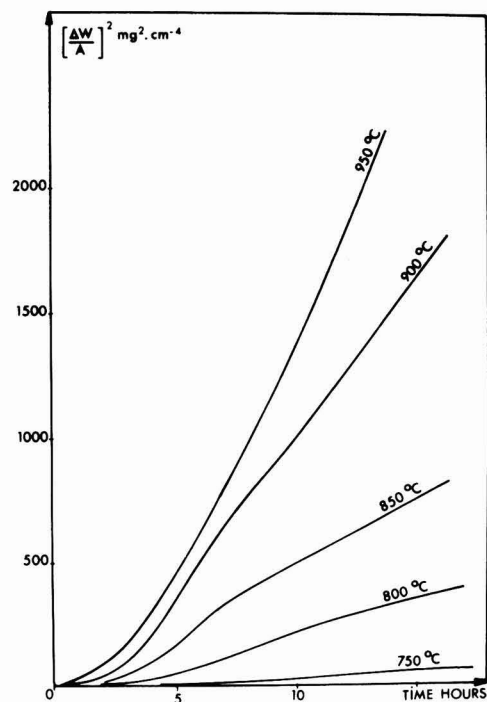


Fig. 1. Sulfidation kinetics of the alloy I in sulfur at 6.2×10^{-2} Torr.

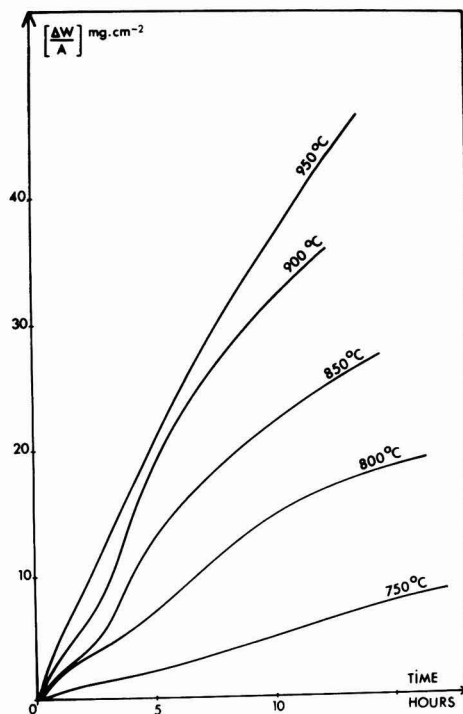


Fig. 2. Sulfidation kinetics plotted in parabolic form of the alloy I in sulfur at 6.2×10^{-2} Torr.



Fig. 3. Cross section of an alloy I specimen sulfidized at 850°C in 6.2×10^{-2} Torr sulfur for 4 hr ($\times 1000$).

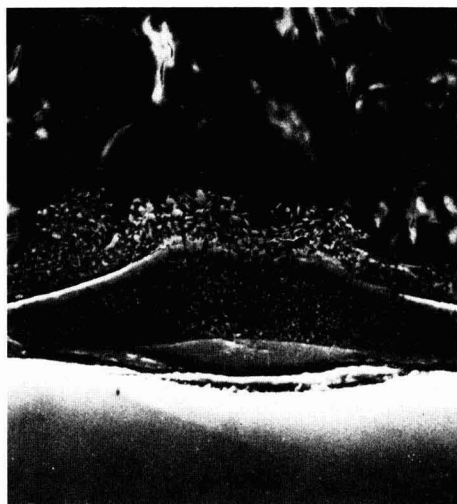


Fig. 4. Cross section of an alloy I specimen sulfidized at 850°C in 6.2×10^{-2} Torr sulfur for 7 hr ($\times 200$).

on alloy (I). From the outer sulfide-gas interface to the inner metal-sulfide interface we can observe successively (Fig. 5) (i) a porous layer of pyrrhotite Fe_{1-x}S ; (ii) a cracked, compact layer of mixed sulfide $\text{Fe}(\text{Fe}, \text{Cr}, \text{Al})_2\text{S}_4$; (iii) a porous layer formed of a mixture $\text{Fe}_{1-x}\text{S}-\text{Fe}(\text{Fe}, \text{Cr}, \text{Al})_2\text{S}_4$; (iv) a compact layer of Fe_{1-x}S ; (v) a compact layer of $\text{Fe}(\text{Fe}, \text{Cr}, \text{Al})_2\text{S}_4$; and (vi) a porous layer of mixture $\text{Fe}_{1-x}\text{S}-\text{Fe}(\text{Fe}, \text{Cr}, \text{Al})_2\text{S}_4$.

For alloy (II) the intermediate compact layer of pyrrhotite [layer (iv)] could never be observed.

It should be noticed that the presence of sulfides Cr_2S_3 and Al_2S_3 could never be detected, as done by Mrowec (13, 14), either in the inner or intermediate layer even at room temperature.

Discussion

Both the kinetic and morphological results obtained show that the sulfidation of Fe-17 Cr- x Al alloys oc-

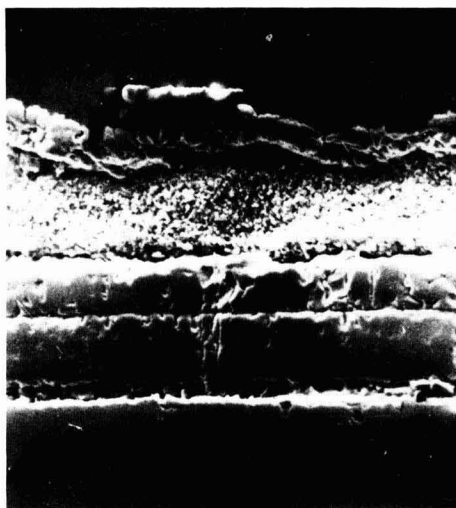


Fig. 5. Cross section of alloy I specimen sulfidized at 850°C in 6.2×10^{-2} Torr sulfur for 50 hr ($\times 200$). The external FeS layer is very brittle and disappeared during polishing.

curs in several successive steps, the corrosion layer morphology being a function of the reaction progress.

During the first parabolic period it could be shown that, whatever the composition of the alloys, three layers developed: a Fe_{1-x}S outer layer, a sulfospinel intermediate layer, and an inner layer consisting of a mixture of both previous sulfides. However, contrary to what has been shown by Mrowec (13, 14) the pyrrhotite outer layer is not compact but porous. Although our experimental conditions are different ($P_{\text{S}_2} = 6.2 \times 10^{-2}$ Torr instead of 1 atm) this probably does not justify this particular morphology of sulfide Fe_{1-x}S and the explanation is to be looked for in the growth process of the corrosion layer. It may be thought that, at the very beginning of the reaction, two compact layers form on the alloy: an inner layer of sulfospinel and an outer layer of pyrrhotite [Fig. 6 (I)]. Then the three constituents of the alloy (Fe , Cr , Al) diffuse throughout the inner compact layer [Fig. 6 (II)] to form at the interface of both layers, a new building element of $\text{Fe}(\text{Fe}, \text{Cr}, \text{Al})_2\text{S}_4$, destroying the compactness of the outer layer [Fig. 6 (III)]. The excess of iron sulfidizes in its turn. As for the porous inner layer which grows subsequently, it is certainly formed through a well-known, internal dissociation-resulfidation process (18). The progress curves $\Delta W/A = f(t)$ being parabolic, the over-all rate of corrosion is certainly governed by a cationic diffusion step through the compact layer of mixed sulfide. Unfortunately the results available do not allow us to stage the diffusion of whichever element (Fe , Cr , or Al) is prevailing to determine the rate.

As the reaction proceeds cracks occur in the compact layer, probably related to the internal dissociation process and to mechanical stresses. Sulfur can then penetrate through gas diffusion and bring about an abnormal thickening of the inner porous layer. Straight below the layer cracks, nodules of mixed sulfide $\text{Fe}(\text{Fe}, \text{Cr}, \text{Al})_2\text{S}_4$ develop on the alloy. This evolution of the layer results in the acceleration observed on the kinetic curves.

The nodules then develop and join to give a new inner compact layer of mixed sulfide. Finally (for alloy I only) an intermediate layer of iron sulfide occurs. The innermost, porous layer probably forms by internal dissociation-resulfidation, as in the first part

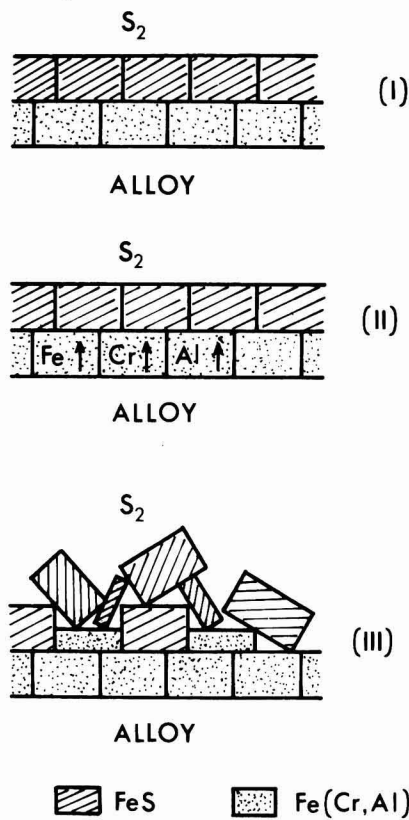


Fig. 6. Mechanism of formation of the different corrosion layers at the beginning of the sulfidation.

of the reaction. The progress curves being identical for each alloy, the rate is probably still governed by the diffusion of one of the three constituting elements of the alloy (Fe, Cr, or Al) through the innermost, compact layer of mixed sulfide.

Summary

This work shows that high temperature sulfidation of Fe-17 Cr- x Al alloys does not occur uniformly but that several successive steps are involved resulting in composition change of the corrosion layers which form and changes in the profile of the kinetic curves. The morphology of these layers is closely dependent on the mechanical stresses which develop and their composition is determined by the initial alloy.

Despite the complexity of this question, all our results enable us to put forward a mechanism which allows the corrosion layer growth to be explained.

Several questions, however have still no answer. First, we do not understand why, at the beginning of the reaction, we do not observe the formation of two compact layers as, for example, in the case of Ni/Cr alloys (21, 22) whose growth would be governed by

a mechanism similar to that described by Smeltzer (23).

Then it is difficult to explain why the sulfidation rates are different in the two parabolic parts of the curves as everything tends to show that the processes fixing these rates are identical.

Finally, it is difficult to understand in which way the composition difference of the alloys justifies the formation of different corrosion layers over the second parabolic part of the transformation.

Acknowledgments

This work forms a part of the thesis submitted by E. M. Jallouli in partial fulfillment of the requirements for award of the "3eme Cycle" degree at the University of Dijon under auspices of the Délégation Générale à la Recherche Scientifique et Technique. He wishes to acknowledge the award of a D.G.R.S.T. fellowship.

Manuscript submitted Dec. 4, 1978; revised manuscript received May 31, 1979.

Any discussion of this paper will appear in a Discussion Section to be published in the June 1980 JOURNAL. All discussions for the June 1980 Discussion Section should be submitted by Feb. 1, 1980.

Publication costs of this article were assisted by the Faculté des Sciences Mirande.

REFERENCES

1. E. Scheil and K. Kiwit, *Arch. Eisenhuettenwes.*, **6**, 155 (1933).
2. A. Portevin, E. Pretet, and H. Jolivet, *Rev. Metall. (Paris)*, **101**, 186 (1934).
3. E. Felten, *This Journal*, **108**, 490 (1961).
4. F. A. Golightly, F. H. Stott, and G. C. Wood, *Oxid. Met.*, **10**, 163 (1976).
5. I. Kvernes, M. Oliveira, and P. Kofstad, *Corros. Sci.*, **17**, 237 (1977).
6. K. N. Strafford and R. Manifold, *ibid.*, **9**, 489 (1969).
7. K. N. Strafford and R. Manifold, *Oxid. Met.*, **5**, 85 (1972).
8. K. Nishida and T. Narita, *Trans. ISIJ*, **12**, 422 (1972).
9. H. Morrow, D. L. Sponseller, and E. Kalns, *Metall. Trans.*, **5**, 673 (1975).
10. E. B. Backensto, R. E. Drew, J. E. Prior, and J. W. Sjöberg, *Corrosion (Houston)*, **14**, 27 (1958).
11. E. Malinowski, R. Bigot, and E. Herzog, *Métallurgie*, **94**, 321 (1962).
12. P. D. Zelanko and G. Simkovich, *Oxid. Met.*, **8**, 343 (1974).
13. S. Mrowec, S. Tochowicz, T. Werber, and J. Podhorodecki, *Corros. Sci.*, **7**, 697 (1967).
14. S. Mrowec and M. Wedrychowska, *Bull. Acad. Pol. Sci. Ser. Sci. Chim.*, **25**, 877 (1977).
15. K. Nishida and T. Aoki, *Met. Res. Inst.*, **48**, 121 (1968).
16. S. Mrowec, T. Werber, and M. Zastawnik, *Corros. Sci.*, **6**, 47 (1966).
17. H. Krainer, L. Wettechnik, and C. Carius, *Arch. Eisenhuettenwes.*, **22**, 103 (1951).
18. A. Brückmann and S. Mrowec, *Werkst. Korros.*, **25**, 502 (1974).
19. E. M. Jallouli, Thesis, Dijon (1978).
20. M. Lambertin and J. C. Colson, *Bull. Soc. Chim. Fr.*, **2**, 561 (1971).
21. J. F. Nowak, Thesis, Dijon (1975).
22. J. F. Nowak, M. Lambertin, and J. C. Colson, *Corros. Sci.*, **18**, 971 (1978).
23. G. Romeo, W. W. Smeltzer, and J. S. Kirkaldy, *This Journal*, **118**, 740 (1971).

Thermodynamic and Mass Transport Properties of "LiAl"

C. John Wen,* B. A. Boukamp,* and R. A. Huggins*

Department of Materials Science and Engineering, Stanford University, Stanford, California 94305

and W. Weppner

Max-Planck-Institut für Festkörperforschung, 7000 Stuttgart 80, Germany

ABSTRACT

The compositional variations of the thermodynamic and mass transport properties of the β phase "LiAl" in the lithium-aluminum system have been investigated over the temperature range from 415° to 600°C. At 415°C, the emf of the single phase "LiAl" lies between 300 and 70 mV relative to pure Li and this corresponds to a Li activity increasing from 0.0063 to 0.31 over the phase stability range from 46.8 to 55.0 atomic percent Li. At the ideal stoichiometry, the standard Gibbs free energy of formation of "LiAl" is -29.2 kJ/mole at 415°C and the corresponding enthalpy and entropy are -43.3 kJ/mole and -20.6 J/mole °K, respectively. Two different electrochemical transient techniques have been used to measure the chemical diffusion coefficient in "LiAl" as a function of the stoichiometry; the experimental results obtained are in good agreement. On the lithium deficit side of the ideal stoichiometry, the chemical diffusion coefficient increases with decreasing Li concentration, becoming about 10^{-4} cm²/sec near the phase boundary. On the other hand, it is composition independent on the Li excess side of "LiAl," varying with temperature from 2.4×10^{-6} cm²/sec at 415°C to 1.8×10^{-5} cm²/sec at 600°C.

Lithium, being the most electronegative and one of the lightest elements, is presently being considered for use as an anode material in both ambient and elevated temperature batteries being developed for load leveling and for use as power sources for electric vehicles. However, lithium is highly corrosive and presents difficulties in materials selection and cell design. Also, lithium dissolves appreciably in the chloride salts typically used in high temperature cells, causing self-discharge due to the corresponding increased electronic conduction in the molten salt electrolyte. Furthermore, if potassium is allowed to evaporate, it will tend to be displaced by lithium at high activity, and it is difficult to retain liquid lithium in a porous metallic matrix for a prolonged period of time during repeated charge-discharge cycles. These problems may be reduced or avoided by the use of certain solid lithium alloys as anode materials.

One such candidate material is a two-phase lithium-aluminum alloy. During charge-discharge cycles, the over-all electrode composition traverses a two-phase region bounded by the saturated solid solution of lithium in aluminum, the α phase, and the aluminum-rich side of the vario-stoichiometric intermetallic compound whose nominal composition is "LiAl," the β phase. In this two-phase region the lithium activity is composition independent. The open-circuit voltage *vs.* pure lithium, measured using a lithium-conducting electrolyte, has been determined over an appreciable range of temperature (1-3). There have also been a few measurements of the potential in the more lithium-rich portion of the lithium-aluminum system (4). However, such data are not consistent, and little is known about the variation of the lithium activity with respect to composition in the α and β single phase regions.

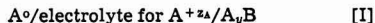
On charging and discharging of a lithium-aluminum electrode, lithium is transported through the bulk solid electrode due to the presence of concentration gradients. The values of the chemical diffusion coefficient in these alloys are, therefore, of interest from both practical and theoretical points of view. James (5) carried out a study of the charge-discharge char-

acteristics of lithium-aluminum electrodes and inferred that the chemical diffusion coefficient in "LiAl" is 5×10^{-5} cm²/sec at 430°C. Using a galvanostatic method, L'vov and co-workers (6) reported that the chemical diffusion coefficient in "LiAl" with a composition of 48 atomic percent (a/o) Li increases from 2×10^{-7} to 6.9×10^{-8} cm²/sec over the temperature range from 380° to 500°C, with an apparent activation energy of 30 kcal/mole. From galvanostatic transient measurements, Melendres (7) estimated that the chemical diffusion coefficient in "LiAl" is of the order of 10^{-8} cm²/sec at 450°C. There is a considerable amount of disparity among these results and no information about the composition dependence of this phenomenon within the "LiAl" phase.

To provide a better fundamental understanding of the electrochemical behavior of this practically important solid alloy electrode, the thermodynamic properties and chemical diffusion coefficient have been determined within the vario-stoichiometric β phase "LiAl." Similar data have also been obtained within the α phase and will be reported elsewhere.

Theoretical Considerations

Determination of thermodynamic properties from emf measurements.—For the purpose of illustration, consider that one has the following galvanic cell



where A_yB is a general formula which can denote the one-phase or two-phase solid electrode in question, y is the A/B ratio, and A° serves as a source or sink of the electroactive species A and also provides a reference activity for component A. With the help of such a galvanic cell, the activity can be determined as a function of composition for the binary system A_yB by using the coulometric titration technique as briefly described below. This method was first demonstrated by Wagner (8) in an investigation of the dependence of the activity of Ag on the Ag/S ratio in "Ag₂S."

It is assumed that both A_yB and A° are electronic conductors and that the electrolyte is a purely ionic conductor. Under equilibrium conditions, the open-circuit voltage of the above cell, E , provides a mea-

* Electrochemical Society Active Member.

Key words: LiAl, chemical diffusion, electrochemical cell method, Gibbs free energy of formation, coulometric titration.

sure of the activity of A, a_A , in the electrode A_yB , since

$$-z_A F E = RT \ln a_A \quad [1]$$

where z_A , F , R , and T are the charge number of the electroactive species A in the electrolyte phase, the Faraday constant, the gas constant, and the absolute temperature, respectively. In the above expression, the reference electrode A° is assumed to be pure A at its standard state with unit activity, i.e., $a_A^\circ = 1$, for simplicity. Of course, an electrode containing A with a fixed activity other than unity may also be used as a reference electrode. In such a case, an additional term, $-RT \ln a_A^\circ$, must be added to the right-hand side of Eq. [1].

The composition of the binary solid A_yB can be systematically changed by passing current through the cell. In so doing, a definite amount of A will be transported across the cell via ionic conduction in the electrolyte and electronic transport in the external circuit. Depending on the direction of the applied current, the species A can thus be added to or removed from the solid electrode A_yB electrochemically. Assuming the electrolyte is a purely ionic conductor, the change in the over-all composition, Δy , from Faraday's law, is

$$\Delta y = \int_0^t I dt / z_A F n_B \quad [2]$$

where n_B is the number of gram atoms of component B in A_yB . The activity of A in the new composition may be evaluated from the cell emf after waiting a sufficiently long time to allow the composition to achieve equilibrium throughout A_yB , as evidenced by the achievement of a steady-state open-circuit voltage. If chemical diffusion within the A_yB is rapid, it is possible, within certain restrictions, to obtain activity-composition data (coulometric titration curves) over appreciable ranges of composition and temperature by this method.

Since the left-hand electrode of cell [I] is used to supply or remove component A from A_yB , it is generally desirable to use a third separate reference electrode, as has been done in coulometric titration experiments on several other materials (3, 9-11).

In such experiments, one generally has to know the composition of A_yB at one point in the concentration range studied in order to convert the precisely measurable compositional changes produced by this method to exact compositions according to Eq. [2]. Thus even though one can achieve unusually precise resolution in compositional changes, the accuracy of the actual values may be limited by the techniques used for sample preparation or composition analysis. This problem may become more difficult if one wants to study a single phase material with a narrow range of phase stability. In appropriate cases, this difficulty may be overcome by starting the coulometric titration from pure B. If the electrolyte is an essentially ionic conductor and there is no loss of either A or B from the A_yB by evaporation, dissolution in the electrolyte, or diffusion into the electronic contact material, the composition can be easily evaluated and controlled to within about 10^{-10} moles, for example, by passing a constant current of $1 \mu A$ for 10 sec. This precision is well above that which can be obtained by using conventional materials preparation or analytical techniques. The success of this coulometric titration technique also requires that the rate of homogenization, which is determined by diffusion processes within the A_yB , be relatively fast.

If the coulometric titration curve is determined by starting with pure B the standard Gibbs free energy of formation for A_yB , $\Delta G_f^\circ(A_yB)$, can be evaluated as a function of composition by integration of the titration curve according to the following expression (3)

$$\Delta G_f^\circ(A_yB) = -z_A F \int_0^y E dy \quad [3]$$

The variation of the corresponding enthalpy, $\Delta H_f^\circ(A_yB)$, and entropy, $\Delta S_f^\circ(A_yB)$, with composition can also be determined from the temperature dependence of these data, using well-known thermodynamic relations (3).

Determination of chemical diffusion coefficients using electrochemical methods.—The use of various electrochemical techniques for the study of transport properties within solids was recently reviewed in detail by Weppner and Huggins (12). Two different transient electrochemical techniques were employed in this study to determine the chemical diffusion coefficient within the "LiAl" phase. The basic principles and the resulting equations are briefly summarized in this section. Such techniques generally involve the displacement of the composition of an electrode system from equilibrium or steady state by the imposition of a step in either potential or current, and the measurements of the other (dependent) variable as a function of time.

For the sake of simplicity, the variation of the volume with composition is neglected. It is also assumed that diffusion in the solid electrode is the rate-determining process and that the system is isothermal and isobaric. The composition of the electrode is expressed as $A_{y+\delta}B$, where δ represents a small deviation from the stoichiometric ratio y .

Potentiostatic method.—One technique involved the imposition of a sudden step in the potential across the cell [I], which we shall call the potentiostatic intermittent titration technique (PITT), for convenience. In such experiments, it is assumed that a planar electrode initially has a uniform concentration of the mobile species A, C_0 , corresponding to an equilibrium voltage E_0 with respect to a suitable reference electrode. At $t = 0$ a new activity (and therefore concentration) of A is imposed on the electrode surface of the $A_{y+\delta}B$ by applying a voltage step, ΔE , between the sample and the reference electrode. The new concentration in the $A_{y+\delta}B$ at the electrode-electrolyte interface ($x = 0$) is C_s . Chemical diffusion will occur due to the concentration gradient imposed within the $A_{y+\delta}B$. As a result, the electroactive species must be continuously supplied by transport through the electrolyte phase in order to keep the surface concentration constant at the imposed value C_s , until the electrode reaches the composition C_s everywhere. The magnitude of this transient current I provides a measure of the chemical diffusion flux as a function of time t . Assuming one-dimensional transport, the chemical diffusion process in the solid is described by Fick's second law

$$\frac{\partial C_A}{\partial t} = D \frac{\partial^2 C_A}{\partial x^2} \quad [4]$$

where x is distance into the solid from the electrolyte/electrode interface, C_A the local concentration, and \tilde{D} the chemical diffusion coefficient. The latter is assumed to be approximately concentration independent in the molar concentration range from C_0 to C_s . The appropriate initial and boundary conditions for such potentiostatic experiments are

$$C_A = C_0 \quad 0 \leq x \leq L, \quad t = 0 \quad [5]$$

$$C_A = C_s \quad x = 0, \quad t > 0 \quad [6]$$

$$\frac{\partial C_A}{\partial x} = 0 \quad x = L, \quad t \geq 0 \quad [7]$$

Equation [7] expresses the condition that the electroactive species A, enters the solid only at $x = 0$, and the phase boundary at $x = L$ is impermeable. This

same condition holds if the electrolyte is in contact with both sides of a planar electrode and there is no diffusion across the centerline.

The solution of Eq. [4]-[7] giving the composition in terms of position and time has one of two standard forms. Either it is comprised of a series of error function or related integrals, in which it is most suitable for numerical evaluation at small times, or it is in the form of a trigonometrical series which converges most satisfactorily for large values of time (13). These can be written for the present case as

$$\frac{C_A(x, t) - C_0}{C_s - C_0} = \sum_{n=0}^{\infty} \left[(-1)^n \left(\operatorname{erfc} \frac{(n+1)L - x}{\sqrt{Dt}} + \operatorname{erfc} \frac{nL + x}{\sqrt{Dt}} \right) \right] \quad [8]$$

and

$$\frac{C_A(x, t) - C_s}{C_s - C_0} = -\frac{4}{\pi} \sum_{n=0}^{\infty} \left[\frac{1}{2n+1} \sin \frac{(2n+1)\pi x}{2L} \exp \left(-\frac{(2n+1)^2 \pi^2 \tilde{D} t}{4L^2} \right) \right] \quad [9]$$

The time-dependent electric current $I(t)$ is related to the concentration gradient at the electrode-electrolyte interface by

$$I(t) = -z_A F S \tilde{D} \left(\frac{\partial C_A}{\partial x} \right)_{x=0} \quad [10]$$

where S is the cross-sectional area common to both the electrolyte and the sample electrode. Neglecting the higher order terms in Eq. [8] and [9], the expressions for the current as a function of time are found to be

$$I(t) = z_A F S (C_s - C_0) (\tilde{D}/\pi t)^{1/2} \quad \text{if } t \ll L^2/\tilde{D} \quad [11]$$

and

$$I(t) = \frac{2z_A F S (C_s - C_0) \tilde{D}}{L} \exp -\frac{\pi^2 \tilde{D} t}{4L^2} \quad \text{if } t \gg L^2/\tilde{D} \quad [12]$$

Therefore, in the short time approximation, i.e., in the initial stage of diffusion, when $t \ll L^2/\tilde{D}$, the

chemical diffusion coefficient \tilde{D} can be determined from the slope of the linear plot of I vs. $1/\sqrt{t}$, provided that the concentration difference $(C_s - C_0)$ is known. The expression of Eq. [11] is sometimes known as the Cottrell equation (14). In the long time

approximation, i.e., $t \gg L^2/\tilde{D}$, the chemical diffusion coefficient \tilde{D} can be evaluated from either the slope of a linear plot of $\ln I$ vs. t without a knowledge of $(C_s - C_0)$, or from the intercept on the $\ln I$ axis at $t = 0$ on the same plot, if $(C_s - C_0)$ is known. Because of this, one can therefore also use these conditions to obtain a value for the quantity $(C_s - C_0)$.

After equilibration following each voltage step, the change of stoichiometry, $\Delta\delta$, is directly related to the concentration difference $(C_s - C_0)$ by the following expression

$$\Delta\delta = V_M (C_s - C_0) = Q/z_A F n_B \quad [13]$$

with

$$Q = \int_0^\infty I(t) dt \quad [14]$$

where V_M is the molar volume of the electrode sample. Q represents the total charge transferred during the titration corresponding to the voltage step ΔE , and n_B is the number of moles of the static component B.

Knowing the fact that $V_M n_B/S = L$, one may rewrite the current-time expressions in terms of charge Q and the thickness of electrode by substituting Eq. [13] into Eq. [11] and [12] as follows

$$I(t) = \frac{Q \tilde{D}^{1/2}}{L \pi^{1/2}} \frac{1}{\sqrt{t}} \quad \text{if } t \ll L^2/\tilde{D} \quad [15]$$

$$I(t) = \frac{2Q \tilde{D}}{L^2} \exp \left(-\frac{\pi^2 \tilde{D} t}{4L^2} \right) \quad \text{if } t \gg L^2/\tilde{D} \quad [16]$$

After each voltage step, the charge Q can be determined either by graphically evaluating the area under the I - t curve or by using a coulometer in the external circuit.

An advantage of using the PITT method is that side reactions such as the nucleation of new phases can be avoided if the voltages are controlled within the stability range of the single phase. A disadvantage is that the ohmic voltage drop in the bulk electrolyte, which varies with time, cannot be readily eliminated from the imposed voltage difference. In addition, there is typically a small initial current transient related to the accumulation of charge at the electrolyte-electrode interface.

Galvanostatic method.—A new method known as the galvanostatic intermittent titration technique (GITT) was recently introduced by Weppner and Huggins (9, 15) which does not have the shortcomings mentioned above. It involves the imposition of a constant current I through the cell for a time interval τ . The voltage between the working electrode and the reference electrode, E , is measured as a function of time during the current pulse. This causes the passage of a constant flux of the mobile species A across the electrode-electrolyte interface. The diffusion process within the sample is assumed to obey Fick's second law of diffusion, i.e., Eq. [4]. Under galvanostatic conditions, the initial and boundary conditions are

$$C_A = C_0 \quad 0 \leq x \leq L, \quad t = 0 \quad [17]$$

$$-\tilde{D} \frac{\partial C_A}{\partial x} = I/z_A F S \quad x = 0, \quad t > 0 \quad [18]$$

$$\frac{\partial C_A}{\partial x} = 0 \quad x = L, \quad t \geq 0 \quad [19]$$

The solutions of Eq. [4] with Eq. [17]-[19] are given elsewhere (16)

$$C_A(x, t) - C_0 = \frac{2It^{1/2}}{z_A F S \tilde{D}^{1/2}} \sum_{n=0}^{\infty} \left[\operatorname{ierfc} \frac{2(n+1)L - x}{2(\tilde{D}t)^{1/2}} + \operatorname{ierfc} \frac{2nL + x}{2(\tilde{D}t)^{1/2}} \right] \quad [20]$$

and

$$C_A(x, t) - C_0 = \frac{It}{z_A F S L} + \frac{IL}{z_A F S \tilde{D}} \left[\frac{3(L-x)^2 - L^2}{6L^2} - \frac{2}{\pi^2} \sum_{n=1}^{\infty} \frac{(-1)^n}{n^2} \exp \left(-\frac{n^2 \pi^2 \tilde{D} t}{L^2} \right) \cos \frac{n\pi(L-x)}{L} \right] \quad [21]$$

For small values of time, i.e., $t \ll L^2/\tilde{D}$, the time variation of the concentration of the electroactive species at the electrolyte-electrode interface ($x = 0$) can be approximated by the first term in the infinite series of Eq. [20]. The resulting expression, known to electrochemists as the Sand equation [17], is

$$C_s(t) - C_0 = 2It^{1/2}/z_A F S (\tilde{D}\pi)^{1/2} \quad \text{if } t \ll L^2/\tilde{D} \quad [22]$$

In principle, Eq. [22] may be employed to evaluate the chemical diffusion coefficient \tilde{D} if the time variation of the surface concentration $C_s(t)$ is known. Unfortunately, the instantaneous value of the concentration at the electrolyte-electrode interface is usually not directly measurable. This difficulty can be avoided for the short time case, for example, differentiating Eq. [22] with respect to the square root of time and then expanding it by dE as follows

$$\frac{dE}{d\sqrt{t}} = \frac{2IV_M}{z_A F S \sqrt{D\pi}} \frac{dE}{d\delta} \quad (t \ll L^2/\tilde{D}) \quad [23]$$

in which the surface concentration C_s is replaced by the stoichiometric parameter δ through the relationship $C_A = (y + \delta)/V_M$ for a solid binary compound $A_y + \delta B$. Rearrangement of this expression yields

$$\tilde{D} = \frac{4}{\pi} \left(\frac{IV_M}{z_A F S} \right)^2 \left[\left(\frac{dE}{d\delta} \right) / \left(\frac{dE}{d\sqrt{t}} \right) \right]^2 \quad (t \ll L^2/\tilde{D}) \quad [24]$$

The chemical diffusion coefficient, \tilde{D} , can be determined from Eq. [24] because all the quantities are either known or experimentally measurable. The quantity $dE/d\sqrt{t}$ is directly obtained from the measurement of the voltage as a function time during the constant current pulse. The value of $dE/d\delta$ in the above expression is determined from the slope of coulometric titration curve, which is obtained by plotting the steady-state equilibrium voltage of the electrode against the composition or the stoichiometric parameter after each galvanostatic titration step.

If sufficiently small currents and short time intervals are employed so that the transient response of the voltage E is a linear function of the square root of time, i.e., $dE/d\sqrt{t} = \Delta E_t/\sqrt{t}$, and the coulometric titration curve is reasonably linear over the composition range involved in that step, i.e., $dE/d\delta = \Delta E_s/\Delta\delta$, Eq. [24] can be put into the simplified form (15)

$$\tilde{D} = \frac{4L^2}{\pi} \left(\frac{\Delta E_s}{\Delta E_t} \right)^2 \quad (t \ll L^2/\tilde{D}) \quad [25]$$

Here ΔE_s represents the change in the steady-state voltage as a result of the current pulse, and ΔE_t is the total change of voltage during the passage of the constant current, eliminating the IR_b drop.

In this method the ohmic voltage drop in the bulk electrolyte between the working electrode and the reference electrode, which is present as an added time-independent constant, can be easily eliminated by subtraction through the extrapolation of E vs. \sqrt{t} data to zero time (15).

At larger times, i.e., when $t > L^2/\tilde{D}$, the concentration at the electrode surface can be approximated by the first two terms on the right-hand side of Eq. [21], giving

$$C_s(t) - C_0 = It/z_A FSL + \frac{IL}{3z_A F S \tilde{D}} \quad \text{if } t > L^2/\tilde{D} \quad [26]$$

Thus at longer times the concentration change, as well as the potential change, at the surface will approach a linear relationship. It can be seen from Eq. [26] that the slope is independent of the chemical diffusion coefficient. This is not true, however, for the extrapolated intercept at $t = 0$, for

$$(E(t) - E(t=0))_{t=0} = \frac{ILV_M}{3z_A F S \tilde{D}} \left(\frac{dE}{d\delta} \right) \quad \text{if } t > L^2/\tilde{D} \quad [27]$$

which permits the evaluation of \tilde{D} in this manner as

well, provided, as before, that the coulometric titration curve can be assumed to be linear over the range of composition involved in the current pulse. That is

$$E(t) - E(t=0) = (C_s(t) - C_0)V_M \frac{dE}{d\delta} \quad [28]$$

Experimental Considerations

Experiments were performed using an electrochemical cell consisting of three electrodes, namely, working (sample) electrode, counterelectrode, and reference electrode immersed in a molten chloride electrolyte, similar to that reported in earlier studies (3, 10, 15). In order to avoid contamination, both sample preparation and experiments were carried out in a helium glove box from which the oxygen, nitrogen, and moisture were continuously removed. Both the reference and counter (lithium reservoir) electrodes were electrochemically prepared by coulometric titration of Li into a spiral of pure (99.9999%) aluminum with a diameter of 0.2 cm to a composition of 40 a/o of Li. The two-phase Al, "LiAl" electrode had a stable voltage of about +300 mV relative to pure lithium. An important advantage of using these lower lithium activity two-phase electrodes is to reduce the solution of Li in the molten LiCl-KCl(e) electrolyte (18), and thereby minimize the electronic leakage current (19).

The LiCl-KCl eutectic electrolyte was purchased from Lithcoa (Lithium Corporation of America, Bessemer City, North Carolina). It was ground to powder in a mortar and pestle and then heated in an alumina crucible at about 420°C for 12 hr in the glove box. These molten salt electrolytes were clear and colorless without any further purification. Alumina crucibles have been found to be suitable for use as containers for such molten salt electrolytes (9, 10, 11, 15).

The "LiAl" electrode was made by melting the high purity Al wire and Li ribbon (99.9%) in a molybdenum crucible at a temperature about 15°-20°C above the melting point of "LiAl" (718°C). This was followed by annealing at 450°C for 15 hr for homogenization. The single phase "LiAl" was hard and brittle and had an initial composition of 50 a/o of Li. Dense electrodes were made by carefully grinding the cast and annealed alloy into the form of a thin pellet. Other samples of the "LiAl" compounds were ground to fine powder in a porcelain mortar and pestle, sieved to 150 mesh, and then cold pressed into pellets using a stainless steel die with a plunger at a pressure about 1.2×10^5 psi under helium atmosphere. The resulting pressed pellets generally had densities near 90% of the theoretical value (1.739 g/cm³). The sample electrodes were held in a cage made of 0.02 cm diam Mo wire, which was also used as the electrical lead.

Electrical measurements were made at temperatures from 415° to 600°C using a potentiostat/galvanostat (PAR Model 173) with a plug-in digital coulometer (PAR Model 179). The voltage-time or current-time behavior was directly measured by use of a Hewlett-Packard 34702 multimeter, which was connected to the output of the PAR potentiostat/galvanostat, and a digital timer. Simultaneously, the transient behavior of voltage or current was also displayed on a chart recorder. The cell temperature was determined by means of two Chromel-Alumel thermocouples.

Results and Discussion

Thermodynamic properties.—All the experimental data reported in this paper were measured with respect to the solid two-phase Al, "LiAl" reference electrode with a composition of 40 a/o Li, but are plotted with reference to pure Li, using the following expression for the potential difference between Li and Al, "LiAl" electrodes as a function of temperature.

$$E_{\text{Al, "LiAl"}} - E_{\text{Li}} = 451 - 0.220T(^{\circ}\text{K})\text{mV} \quad [29]$$

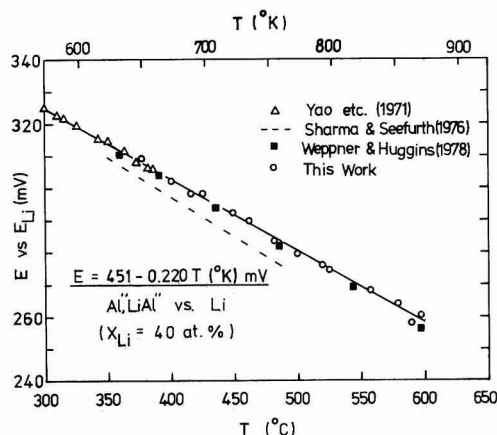


Fig. 1. Temperature dependence of emf for two-phase Al, "LiAl" reference electrode.

This relation was determined from measurements at temperatures from 375° to 600°C as shown in Fig. 1. Experimental results reported in the literature are also included for comparison. The new data are in excellent agreement with those determined by Yao *et al.* (1), and Weppner and Huggins (3). However, the emf values reported by Sharma and Seefurth (2) are lower by about 5 mV than those represented by Eq. [29]. Equation [29] is the same expression as that reported by Yao *et al.* (1) from emf measurements of electrochemically prepared lithium-aluminum alloys at lower temperatures, from 280° to 380°C. Using pure Al as the starting material, the coulometric titration curve, *i.e.*, the steady-state open-circuit voltage of the lithium-aluminum electrode over a wide range of composition, at 423°C is shown in Fig. 2. It clearly shows that three single phases, *i.e.*, α , β , and γ , exist at 423°C. The solid solubility of Li in Al is 9.2 a/o Li, and the β phase of "LiAl" extends from 46.8 to 56 a/o Li at that temperature.

The γ phase was found to exist between 60.3 and 61.7 a/o Li. Thus this intermediate phase has a nominal composition Li_3Al_2 , rather than Li_2Al , as reported in the standard compilations of phase diagrams for binary systems (20). Phases with compositions of Li_3Al_4 and Li_3Al_2 have been reported at room temperature by several investigators (21, 22). The most

recent DTA investigation of the Li-Al systems by Myles *et al.* (23) indicates that the solid compound Li_3Al_2 exists, but that neither Li_2Al nor Li_3Al_4 are present at 423°C. They found that the compound Li_3Al_2 decomposes peritectically at 520°C, while the compound Li_3Al_4 undergoes a peritectic decomposition at 335°C. At 423°C the stable phases are Li_3Al_2 and liquid lithium saturated with aluminum for Li concentrations in excess of 60 a/o. No attempts were made to establish the liquidus compositions because of voltage drift at high Li activities. The emf data of lithium-rich lithium-aluminum alloys reported by Selman and co-workers (4) indicate that the Li-rich liquidus composition is 82.8 a/o Li at 427°C (700°K).

It is well known that the coulometric titration curve may be used to map out the phase diagram. In binary systems, the composition range of constant activity or chemical potential at fixed temperature and pressure corresponds to two-phase mixtures, according to the Gibbs phase rule. As shown in Fig. 2, three single phase regions separated by constant-voltage regions of two-phase mixtures can be clearly identified. Thus, the temperature variation of the phase boundaries can be determined from measurements of emf as a function of composition at various temperatures.

Figure 3 shows coulometric titration curves in the β phase region at three different temperatures. Over the temperature range investigated, the titration curves all exhibit a similar composition dependence. As can be seen, the potential rises rapidly on the lithium deficit side of the β phase "LiAl" as the Li concentration decreases. In the region of positive deviation from the ideal stoichiometry, *i.e.*, $\delta > 0$, the emf however varies almost linearly with the stoichiometric parameter δ .

In the temperature range of 415°–505°C, the stability range of the β phase was found to be nearly independent of temperature. The minimum composition on the lithium deficit side of "LiAl" is 46.8 ± 0.3 a/o Li and that at the lithium excess boundary 55.5 ± 0.5 a/o Li. The earlier emf measurements of electrochemically prepared lithium-aluminum alloys by Yao *et al.* (1) indicated that the phase boundary on the lithium deficit side is about 47 a/o Li in the temperature range of 300°–380°C. Using two independent techniques, quantitative metallography and lattice parameter measurements, Levine and Rappaport (24) reported that this phase boundary composition is 45.8 a/o over the temperature range 150°–550°C.

Thus, although differing in the value of its composition, experimental data obtained by various investigators using different techniques indicate that the lithium deficit boundary of "LiAl" is nearly temperature independent over a wide temperature range. However, at temperatures higher than 500°C, the

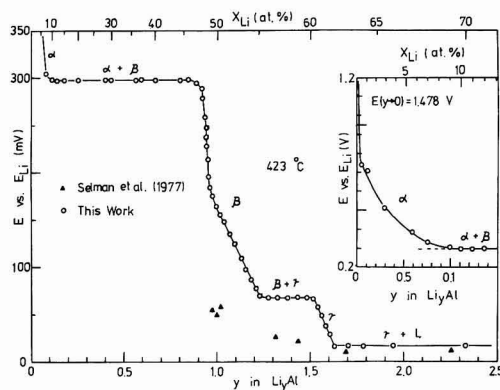


Fig. 2. Coulometric titration curve for lithium-aluminum system at 423°C.

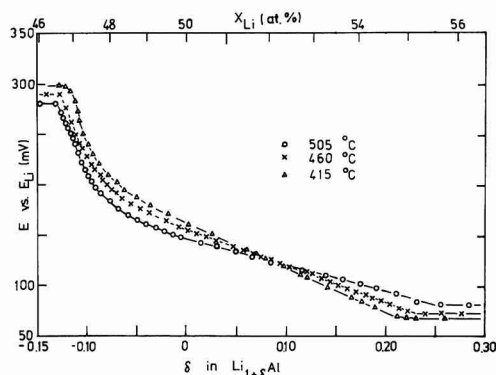


Fig. 3. Coulometric titration curves for "LiAl" at different temperatures.

locations of the phase boundaries were difficult to determine with confidence owing to a high self-discharge rate as evidenced by a slow voltage drift with time.

The coulometric titration curve data determined by means of GITT coincide well with those measured with PITT, as illustrated in Fig. 4. The emf of "LiAl" lies between 300 and 70 mV relative to pure Li at 415°C. This corresponds to a lithium activity which increases from 0.0063 to 0.31 over the composition range of the phase at this temperature. These data are rather close to those obtained by extrapolation of the emf measurements by Yao *et al.* (1) but substantially different from those recently reported by Selman *et al.* (4). The enhancement factor, $d \ln a_{Li} / d \ln C_{Li}$, which relates the chemical diffusion coefficient to the component diffusion, may be determined from the slope of the titration curve (15) according to the expression

$$\frac{d \ln a_{Li}}{d \ln C_{Li}} = \frac{F}{RT} (1 + \delta) \frac{dE}{d\delta} \quad [30]$$

This quantity varies as a function of composition, as shown in Fig. 5. As it may be seen, it is large and strongly dependent on the composition on the lithium deficit side of "LiAl," but remains nearly composition independent on the lithium excess side.

Figure 6 shows the standard Gibbs free energy of formation of "LiAl" as a function of the stoichiometry at 415°C, evaluated by integration of the coulometric titration curve according to Eq. [3]. At the ideal stoichiometry, i.e., $\delta = 0$, the standard Gibbs free energy of formation is -29.2 kJ/mole. The largest negative value was found to occur at about 50.6 a/o Li, or $\delta = 0.025$.

In the temperature range from 375° to 500°C, the temperature dependence of the emf was found to be linear for all compositions within "LiAl." The partial molar entropy of Li, $\Delta \bar{S}_{Li}$, at each composition was determined by

$$\Delta \bar{S}_{Li} = - \left(\frac{\partial \Delta \bar{G}_{Li}}{\partial T} \right)_P = F \left(\frac{\partial E}{\partial T} \right) \quad [31]$$

The experimental results are given in Fig. 7. Other

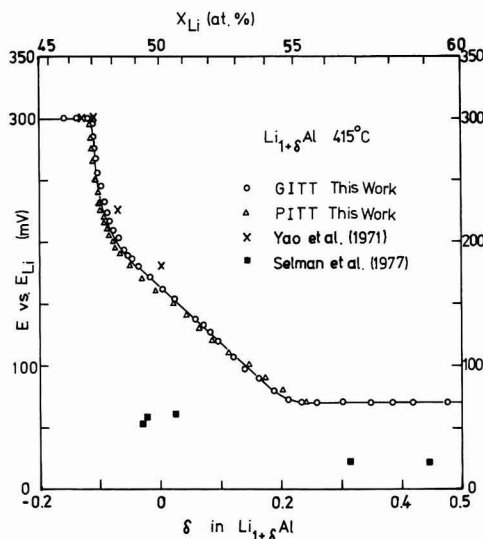


Fig. 4. Coulometric titration curve of "LiAl," comparison of results from PITT and GITT.

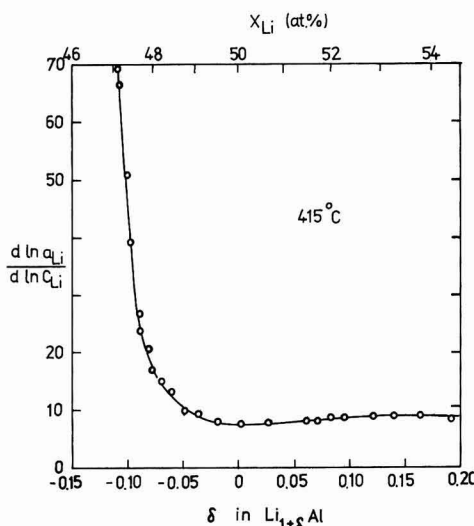


Fig. 5. Compositional variation of the enhancement factor within "LiAl" at 415°C.

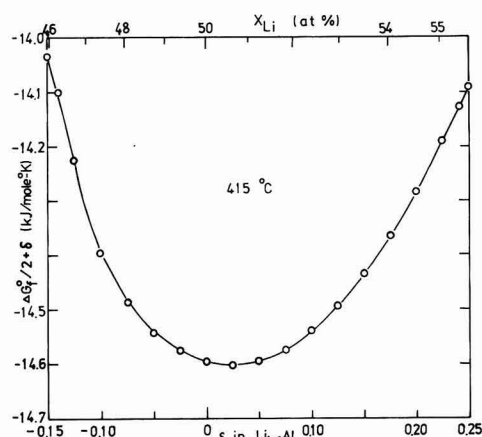


Fig. 6. Standard Gibbs free energy of formation of "LiAl" as a function of composition at 415°C.

data reported in the literature are also included for comparison. Again the values of $\Delta \bar{S}_{Li}$ determined in this work are in good agreement with those extrapolated from the results reported by Yao *et al.* (1), but are quite different from those reported by Selman *et al.* (4). The partial molar entropy of Li in "LiAl" shows a minimum near 47.4 a/o Li ($\delta = -0.10$). In addition, $\Delta \bar{S}_{Li}$ is negative for compositions less than about 51.9 a/o Li and positive for lithium excess compositions, where it increases linearly with stoichiometric parameter δ .

The standard entropy of formation of $Li_{1+\delta}Al$, ΔS°_f , is also shown as a function of composition in Fig. 7. It was determined by using the expression

$$\Delta S^\circ_f = F \int_0^{1+\delta} \left(\frac{\partial E}{\partial T} \right) d(1 + \delta) \quad [32]$$

The minimum value of $\Delta S^\circ_f/2 + \delta$ is at $\delta = 0.025$. At $\delta = 0$, the value of ΔS°_f is -20.6 J/mole °K.

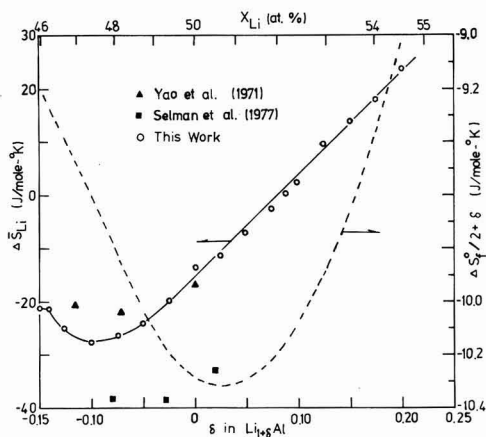


Fig. 7. Partial molar entropy of Li and standard entropy of formation of "LiAl" vs. composition.

The standard enthalpy of formation, ΔH_f^0 , was calculated as a function of the stoichiometry according to the definitional expression

$$\Delta H_f^0 = \Delta G_f^0 + T\Delta S_f^0 \quad [33]$$

The results at 415°C are shown in Fig. 8. The standard enthalpy of formation at $\delta = 0$ is -43.3 kJ/mole. $\Delta H_f^0/2 + \delta$ has a minimum value at $\delta = 0.025$ and its compositional dependence is similar to that of $\Delta G_f^0/2 + \delta$.

Mass transport.—Typical current-time measurements using PITT are presented in Fig. 9, in which the current is plotted as a function of $1/t^{1/2}$. According to Eq. [15], a straight line passing through the origin is expected for small times in such a plot. Indeed, a linear relationship can be seen for times between 80 and 800 sec.

At very short times after a voltage step, deviations from this linear relationship were found, being more pronounced when using larger voltage steps. According to Eq. [15] the current should be infinite at the moment when the chemical diffusion process starts. This theoretical situation is not experimentally possible, however, as the applied voltage step ΔE is given

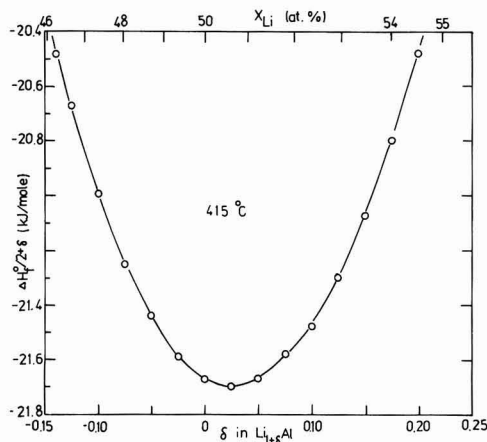


Fig. 8. Standard enthalpy of formation of "LiAl" as a function of composition at 415°C.

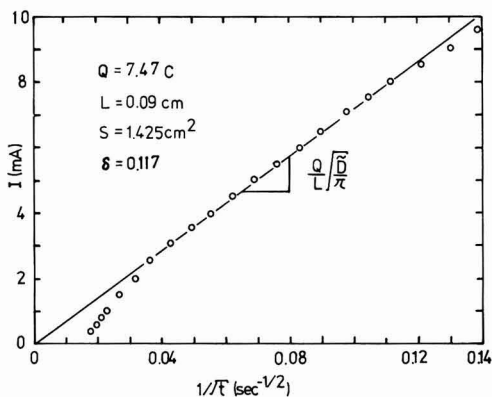


Fig. 9. Current vs. $1/t^{1/2}$; short time PITT approximation

by the expression

$$\Delta E = \frac{RT}{F} \ln \frac{a_{Li}}{a_{Li}^0} + IR_b \quad [34]$$

where a_{Li} is the Li activity in the surface of the sample, a_{Li}^0 is the fixed lithium activity of the reference electrode, and IR_b represents the ohmic voltage drop in the bulk electrolyte phase between the sample and the reference electrode. This ohmic voltage drop in the electrolyte varies with the current and thus cannot be completely eliminated using the PITT approach. Therefore, the boundary condition of instantaneous change in the surface concentration is not fulfilled at very small values of time. This problem may be minimized by placing the reference electrode very close to the working electrode and using small voltage steps, e.g., 5 to 10 mV.

Figure 9 also shows a nonlinear relation at large times, when the short time approximation is no longer valid. Figure 10 shows the same experimental results in a semilogarithmic plot. A straight line can be seen

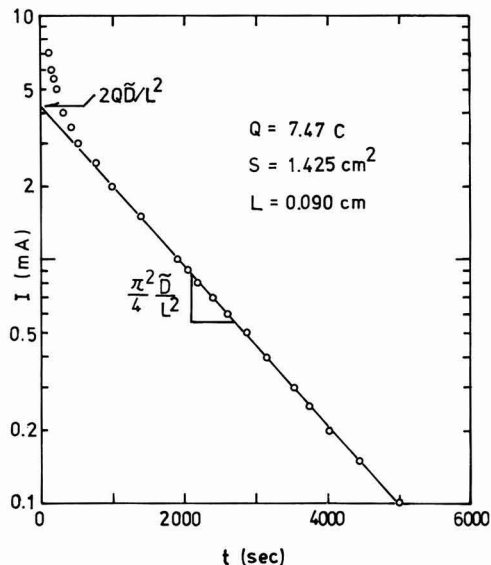


Fig. 10. Exponential dependence of current on time; long time PITT approximation.

except at short times, in agreement with the theoretical prediction of Eq. [16].

The chemical diffusion coefficient, \tilde{D} , calculated from the linear portion of the short time data shown in Fig. 9 is 3.06×10^{-6} cm²/sec. Values evaluated from the slope and the intercept at $t = 0$ in the plot given in Fig. 10 are 2.46×10^{-6} and 2.62×10^{-6} cm²/sec, respectively. These three values correspond quite well, as expected from the theory.

Figure 11 shows the typical transient voltage response obtained by means of GITT. At small times, the voltage varies linearly with the square root of time as expected from Eq. [23]. According to Eq. [24]

the chemical diffusion coefficient \tilde{D} can be determined from the slope $dE/dt^{1/2}$ and the factor $dE/d\delta$, which is assumed to be constant during each small current pulse. These two quantities are not affected by the voltage drop, IR_b , in the bulk electrolyte between the sample and reference electrode. Therefore, ohmic effects in the electrolyte and interface are totally eliminated when using the GITT method.

Using both GITT and PITT the compositional variation of the chemical diffusion coefficient was determined in "LiAl." These data are plotted in Fig. 12. Although there is some scatter in the values of the chemical diffusion coefficient, this parameter is quite composition dependent on the lithium-deficient side of the ideal stoichiometry, approaching an extremely high value in the order of 10^{-4} cm²/sec near the $(\alpha + \beta)$ - β phase boundary. It may be regarded as virtually composition independent with an average value of 2.4×10^{-6} cm²/sec at 415°C for the lithium-rich side.

It can be seen from Fig. 12 that the chemical diffusion coefficient data obtained by means of the PITT and GITT methods are in good agreement. Also, data obtained using dense pellets are not significantly different from those measured by employing electrodes made of cold-pressed pellets. Furthermore, the chemical diffusion coefficients given in Fig. 12 show no observable difference between charging and discharging. This result is in contradiction with the contention of other investigators (7) that there is considerable difference in diffusion mechanism between charge and discharge.

For the purpose of comparison, the chemical diffusion coefficient interpolated from the data reported by L'vov and co-workers (6) is also given in Fig. 12. The results presented by James (5×10^{-5} cm²/sec at 430°C) (5) and Melendres (10^{-8} cm²/sec) (7) are not included because the composition was unspecified.

An attractive feature of electrochemical transient techniques for the study of transport properties within solids is that a number of kinetic parameters may be obtained in a single experiment under specific condi-

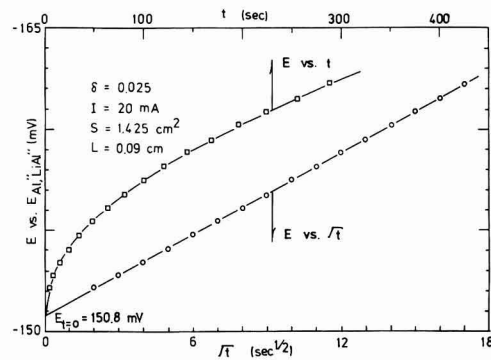


Fig. 11. Time dependence of voltage using GITT

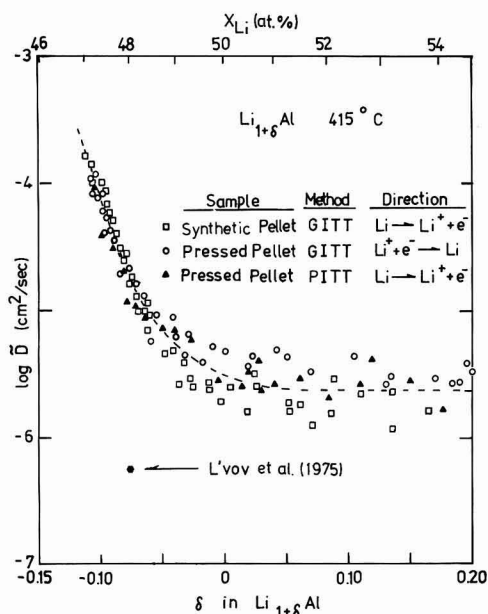


Fig. 12. Chemical diffusion coefficient in "LiAl" as a function of composition at 415°C.

tions. One quantity of particular interest is the diffusivity, also sometimes called the component diffusion coefficient or self-diffusion coefficient. The diffusivity D_{Li} is different from the chemical diffusion coefficient, \tilde{D} , as defined by Fick's first law of diffusion in the presence of an activity gradient, but they are related to each other through an enhancement factor (15) according to the equation

$$\tilde{D} = D_{Li} \frac{d \ln a_{Li}}{d \ln C_{Li}} \quad [35]$$

This relation is valid only when the lithium atoms or ions dominate the mass transport process, i.e., the aluminum atoms or ions are virtually immobile. In fact, NMR studies on "LiAl" (25, 26) support this assumption.

The diffusivity of Li in "LiAl" as a function of stoichiometry at 415°C is shown in Fig. 13. The enhancement factor and the chemical diffusion coefficients were taken from Fig. 5 and 12, respectively. At this temperature, the diffusivity is seen to gradually decrease by almost an order of magnitude from 1.6×10^{-8} cm²/sec at $\delta = -0.1$ to 3.0×10^{-7} cm²/sec at $\delta = -0.17$. The self-diffusion coefficient of Li⁷ in "LiAl," measured by Willhite and co-workers (26) using NMR techniques, is also shown in Fig. 13 for comparison. Thus, the experimental results determined by various investigators using completely different techniques are in close agreement.

The composition dependence of the chemical diffusion coefficient at five different temperatures from 415° to 600°C is shown in Fig. 14. The influence of composition is seen to be similar at all temperatures investigated. The chemical diffusion coefficient is nearly constant on the Li excess side, but increases with decreasing Li concentration on the Li deficit side.

The temperature dependence of the experimental data at fixed compositions could be fit to an expression of the form

$$\tilde{D} = \tilde{D}_0 \exp(-\Delta \tilde{H}/RT) \quad [36]$$

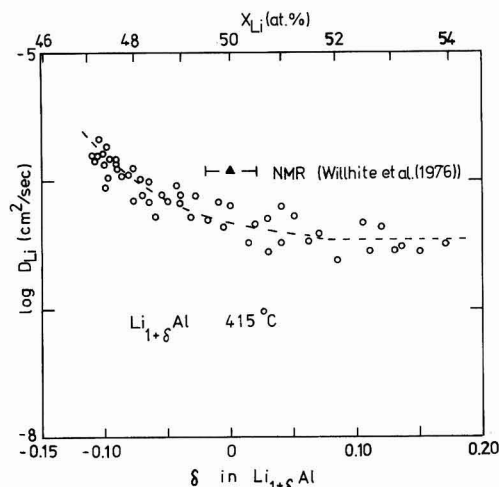


Fig. 13. Variation of diffusivity of Li in "LiAl" with composition at 415°C.

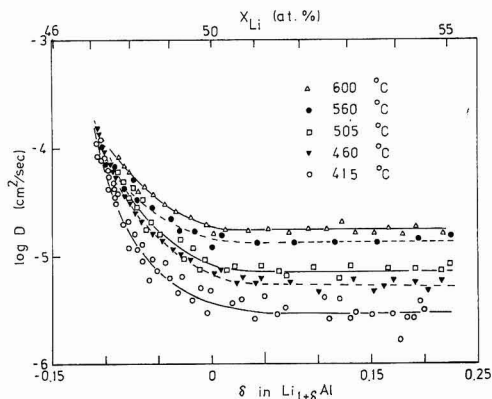


Fig. 14. Compositional variation of chemical diffusion coefficient within "LiAl" at different temperatures.

The apparent activation energy $\tilde{\Delta H}$ was found to be essentially independent of lithium concentration for lithium-rich compositions, with a value of 47.7 kJ/mole (11.4 kcal/mole). On the Li-deficit side, however, $\tilde{\Delta H}$ was observed to linearly decrease with decreasing lithium concentration, reaching 7.5 kJ/mole (1.8 kcal/mole) near the phase boundary.

The dependence of the apparent activation energy on the composition in this phase is not understood at this time. Equation [36] indicates that the temperature dependence of the chemical diffusion coefficient \tilde{D} depends on the influence of temperature on both the diffusivity D_{Li} and the enhancement factor d in a_{Li}/d in C_{Li} . Unless the enhancement factor is temperature-

independent, or they both exhibit Arrhenius behavior, the chemical diffusion coefficients should not have a temperature dependence of the simple Arrhenius form.

Acknowledgment

This work received support from the U.S. Department of Energy under Contract No. EC-77-S-02-4506.

Manuscript submitted Feb. 12, 1979; revised manuscript received May 3, 1979.

Any discussion of this paper will appear in a Discussion Section to be published in the June 1980 JOURNAL. All discussions for the June 1980 Discussion Section should be submitted by Feb. 1, 1980.

Publication costs of this article were assisted by Stanford University.

REFERENCES

1. N. P. Yao, L. A. Heredy, and R. C. Saunders, *This Journal*, **118**, 1039 (1971).
2. R. A. Sharma and R. N. Seefurth, *ibid.*, **123**, 1763 (1976).
3. W. Weppner and R. A. Huggins, *ibid.*, **125**, 7 (1978).
4. J. R. Selman, D. K. DeNuccio, C. J. Sy, and R. K. Steunenberg, *ibid.*, **124**, 1160 (1977).
5. S. D. James, *Electrochim. Acta*, **21**, 157 (1976).
6. A. L. L'vov, A. A. Gnilomedov, A. P. Selemenev, and E. N. Protasov, *Elektrokhimiya*, **11**, 1322 (1975).
7. C. A. Melendres, *This Journal*, **124**, 650 (1977).
8. C. Wagner, *J. Chem. Phys.*, **21**, 1819 (1953).
9. W. Weppner and R. A. Huggins, *J. Solid State Chem.*, **22**, 297 (1977).
10. B. E. Liebert, W. Weppner, and R. A. Huggins, in "Electrode Materials and Processes for Energy Conversion and Storage," J. D. E. McIntyre, S. Srinivasan, and F. G. Will, Editors, p. 821, The Electrochemical Society, Inc. Softbound Proceedings Series, Princeton, N.J. (1977).
11. B. E. Liebert, Ph.D. Dissertation, Stanford University (1977).
12. W. Weppner and R. A. Huggins, *Ann. Rev. Mat. Sci.*, **8**, 269 (1978).
13. J. Crank, "The Mathematics of Diffusion," p. 17, 45, Oxford University Press, London (1967).
14. F. G. Cottrell, *J. Phys. Chem.*, **A42**, 385 (1902).
15. W. Weppner and R. A. Huggins, *This Journal*, **124**, 1569 (1977).
16. H. S. Carslaw and J. C. Jaeger, "Conduction of Heat in Solids," p. 112, Oxford University Press, London (1959).
17. H. J. S. Sand, *Phil. Mag. J. Sci.*, **1**, 45 (1901).
18. R. N. Seefurth and R. A. Sharma, *This Journal*, **122**, 1049 (1975).
19. R. J. Heus and J. J. Egan, *J. Phys. Chem.*, **77**, 1989 (1973).
20. M. Hansen and K. Anderko, "Constitution of Binary Alloys," McGraw-Hill Book Co., Inc., New York (1958).
21. D. A. Hansen and J. F. Smith, *Acta Crystallogr.*, **24**, 913 (1968).
22. K. F. Tebbe, H. F. v. Schnering, B. Ruter, and G. Rabenack, *Z. Naturforsch., Teil B*, **28**, 600 (1973).
23. K. M. Myles, F. C. Mrazek, J. A. Smaga, and J. L. Settle, in Proceedings of Symposium and Workshop on Advanced Battery R & D, March 1976, U.S. ERDA Report No. ANL-76-8, p. B-50.
24. E. D. Levine and E. J. Rappaport, *Trans. Met. Soc. AIME*, **227**, 1204 (1963).
25. H. E. Schone and W. D. Knight, *Acta Metall.*, **11**, 179 (1963).
26. J. R. Willhite, N. Karnezos, P. Cristea, and J. O. Britain, *J. Phys. Chem. Solids*, **37**, 1073 (1976).



Optical Evaluation of Polycrystalline Silicon Surface Roughness

K. L. Chiang, C. J. Dell'Oca,* and F. N. Schwettmann*

Hewlett Packard Laboratories, Palo Alto, California 94304

The surface roughness of polysilicon films is becoming increasingly important in the fabrication of integrated circuits. Surface roughness can interfere with photolithographic processes required to achieve ever decreasing polysilicon geometries. The operation limits of devices formed on polysilicon (e.g., capacitors) are also surface roughness dependent. In many cases, processes and devices can be tailored such that the reproducibility rather than the absolute surface roughness becomes most important. This note describes the nondestructive, optical evaluation of polysilicon film roughness.

The reflectance, R , of a rough surface is related to the reflectance of an ideally smooth surface R_0 by the equation (1-3)

$$R/R_0 = \exp - (4\pi \cos \phi_0 \sigma_0 / \lambda)^2 + 32\pi^3 \cos^3 \phi_0 \Delta\omega (\sigma_0 / \lambda)^4 / m_0^2$$

where λ , ϕ_0 , and $\Delta\omega$ represent, respectively, the wavelength, the angle, and the solid angle of observance. The surface roughness is characterized by an rms height, σ_0 , and an rms slope, m_0 . If the wavelength is much larger than the rms roughness, then the diffuse reflectance term can be neglected and the result is specular reflectance from a surface with an "effective" refractive index. The equation then reduces to

$$R/R_0 = \exp - (4\pi \cos \phi_0 \sigma_0 / \lambda)^2$$

This analysis holds as long as the material is infinitely thick, that is, there are no returning waves from reflection at the back interface of the material.¹

The polysilicon films were grown on a previously formed oxide film on silicon. In the ultraviolet, polysilicon (like silicon) is highly absorbing and films on the order of 2000 Å thick appear optically infinite.

The surface roughness was measured using a Beckman Model 25 double beam spectrophotometer modified to accommodate two 3-in. wafers. The reference was a single crystal silicon wafer which had the standard chemical-mechanical polish and a mirror-like surface. The angle of incidence was 10 deg and measurements were made in the u.v. region, 200 to 350 nm wavelengths. This spectrophotometer measures in absorbance units, A , where

$$R/R_0 = 10^{-A}$$

or, using the previous equations

$$A = (4\pi \cos \phi_0 \sigma_0 / \lambda)^2 / 2.3$$

Thus, A is linearly dependent on λ^{-2} with a slope of $(4\pi \cos \phi_0 \sigma_0)^2 / 2.3$ and a zero intercept.

Since roughness is mostly governed by deposition temperature, polysilicon films were prepared at 980°,

930°, and 880°C and the surface of these films was analyzed optically. As expected, the absorbance in the ultraviolet wavelength range is higher for the higher deposition temperatures (Fig. 1). That is, the reflectance is decreasing or the film surface roughness is increasing with deposition temperatures. If the optical model is correct, the rms surface roughness can be obtained from the dependence of A on the reciprocal of the wavelength squared. This is depicted in Fig. 2 where, to a good approximation, the linear dependence of A on $1/\lambda^2$ is verified as well as the intercept at zero. The surface rms roughness obtained from the slope of these lines is given in Table I. Note that it increases with deposition temperature and, further, that $\sigma_0 < \lambda$ as is required by the approximations made in the model.

Verification of results was qualitatively made with a scanning electron microscope (Fig. 3) and a mechanical profilometer (Fig. 4). In each case, the roughness is larger for the 980°C deposition. The peak to peak value obtained with the surface profilometer

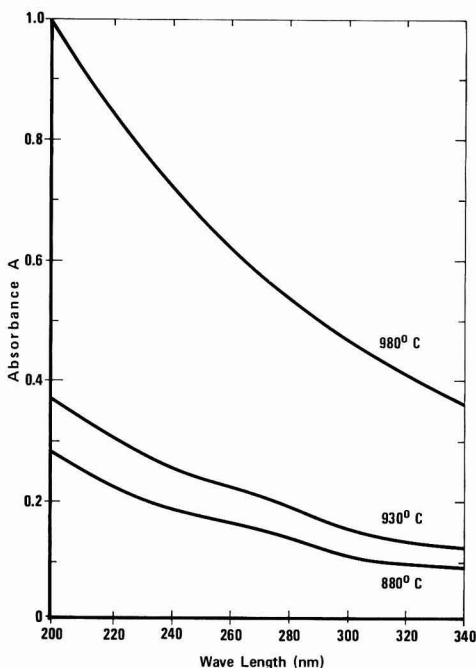


Fig. 1. Ultraviolet absorbance of polysilicon films grown at the indicated temperatures.

* Electrochemical Society Active Member.

Key words: polysilicon, roughness, reflectance.

¹ The theory was originally based on the analysis of radar wave reflection from a highly conducting surface.

Table I. Polysilicon film properties

Deposition temperature (°C)	Film thickness (Å)	Deposition rate (Å/min)	Calculated σ_0 (Å)
980	4967	856	240
930	4865	839	147
880	4527	780	122

for the 980°C deposition is between 100-300Å, which is in the same range as the optically measured value. However, the profilometer tip covers a large area and tends to underestimate the roughness.

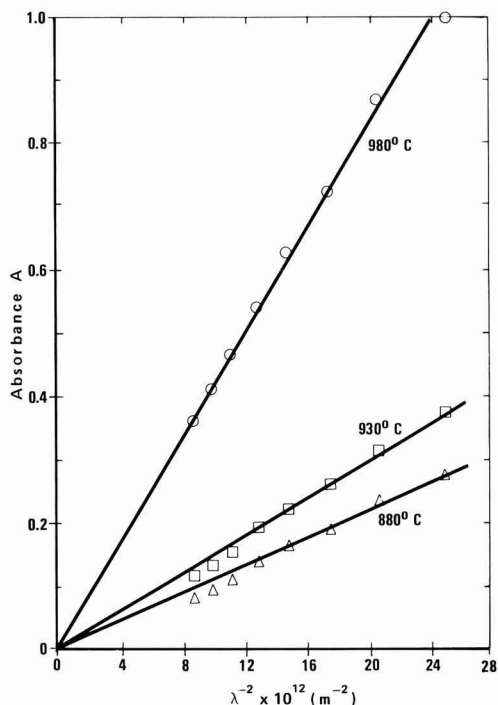


Fig. 2. The dependence of absorbance on the reciprocal of wavelength squared (λ^{-2}) for the films in Fig. 1.

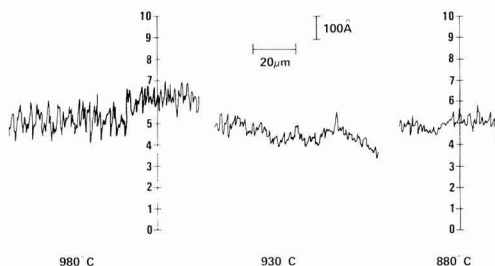


Fig. 4. Representative profile measurements of surface roughness for polysilicon deposited at the indicated temperatures.

The possibility that the observed effects are to some extent due to the result of using a polished single crystal reference surface was checked. Thick polysilicon layers ($\sim 7 \mu\text{m}$) on oxidized silicon were polished with the same process used for single crystal wafers. Then, the polished polysilicon surface was compared to that of the single crystal. Over the u.v. range of interest, the difference between the two surfaces is 0.008 absorbance units, which is about the accuracy of the instrument. Thus, single crystal silicon can be used as the reference for convenience.

For thin polysilicon films ($< 2000 \text{ Å}$), it may be possible to do the measurement at one wavelength since the refractive index of polysilicon is approximately the same as that of single crystal silicon. Near total destructive interference can be realized at the silicon oxide-polysilicon interface.² This approach is feasible by choosing the thickness of the oxide between silicon and polysilicon such that destructive interference occurs within this layer at the particular wavelength.

In conclusion, the surface roughness of polysilicon can be easily evaluated by a spectrophotometer measurement of reflectance in the ultraviolet. A single reading at one wavelength can be sufficient for this characterization. Convenient wavelengths are 2039 and 3262 Å where σ_0 is given by $250/\sqrt{A}$ and $400/\sqrt{A}$ Å, respectively.

Acknowledgments

Thanks to Silicon Material, Incorporated, for polishing the various groups of wafers and to Frank Perlaki for all the SEM micrographs.

² The result follows directly from the optical formula for reflection from two layers on an infinite substrate. See, e.g., T. I. Kamins and C. J. Dell'Oca, *This Journal*, 119, 112 (1972).

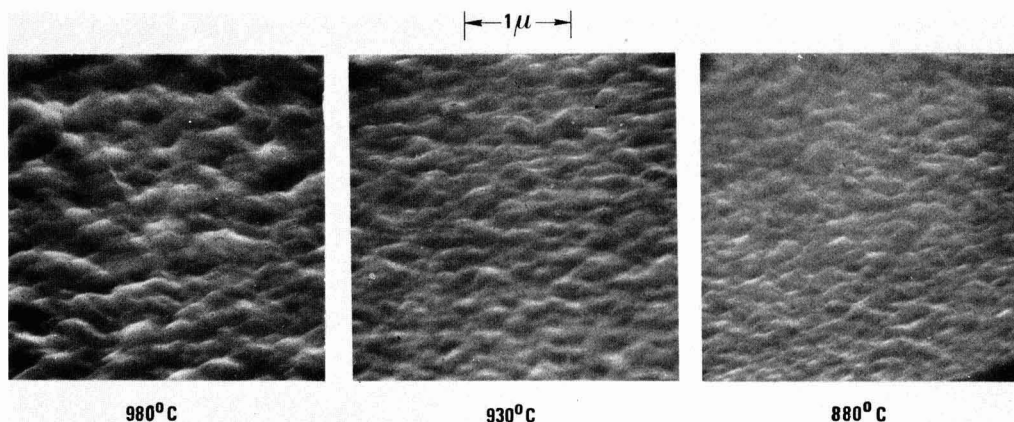


Fig. 3. Representative SEM micrographs of polysilicon surface roughness for various deposition temperatures

Manuscript submitted Jan. 22, 1979; revised manuscript received June 29, 1979.

Any discussion of this paper will appear in a Discussion Section to be published in the June 1980 JOURNAL. All discussions for the June 1980 Discussion Section should be submitted by Feb. 1, 1980.

Publication costs of this article were assisted by Hewlett Packard Laboratories.

REFERENCES

1. A. Abdulkadir and R. C. Birkebak, *Rev. Sci. Instrum.*, **45**, 1356 (1974).
2. H. Davies, *Proc. IEEE*, **101**, 209 (1954).
3. H. E. Bennett and J. M. Bennett, in "Physics of Thin Film," Vol. 4, pp. 1-96, Academic Press, New York (1967).

Chemical Etching of InP by $\text{H}_2\text{O}_2\text{-H}_2\text{SO}_4\text{-H}_2\text{O}$ Solution

Yorimitsu Nishitani and Tsuyoshi Kotani

Fujitsu Laboratories, Limited, Nakahara-ku, Kawasaki, Japan

InGaAsP/InP has been considered a useful semiconductor material for microwave and optoelectronics devices. Liquid phase epitaxy (LPE) and vapor phase epitaxy (VPE) have been used for growing InGaAsP or InP layers on InP substrate. A surface treatment of InP substrate before the growth is important to obtain high quality epitaxial layers. Usually, InP substrate is etched by $\text{Br}_2\text{-CH}_3\text{OH}$ solution (1, 2). $\text{Br}_2\text{-CH}_3\text{OH}$ solution is suitable for etching of InP substrate before growth, because the etch rate is high enough to eliminate the mechanically damaged layer. However, it is difficult to obtain a reproducible smooth surface because a large number of small pits and scratches appear on the etched surface.

This note describes the characteristics of InP etching by $\text{H}_2\text{O}_2\text{-H}_2\text{SO}_4\text{-H}_2\text{O}$ solution and a technique for etching InP substrates which provides a smooth surface by preetching in the $\text{H}_2\text{O}_2\text{-H}_2\text{SO}_4\text{-H}_2\text{O}$ solution, before a $\text{Br}_2\text{-CH}_3\text{OH}$ solution etch. $\text{H}_2\text{O}_2\text{-H}_2\text{SO}_4\text{-H}_2\text{O}$ solution has been used for selective etching of InGaAsP (3, 4) but the details of etching InP have not been reported.

InP(100) doped with Sn and InP(111)B doped with Sn and Cr were used for the experiments. Specimens were mirror-polished mechanically on one side. They were approximately 400 μm in thickness and $5 \times 5 \text{ mm}^2$ in area. The etching was carried out in a 30/cm³ solution in a Teflon vessel. The specimens were cleaned in trichloroethylene, acetone, and alcohol, and etched by the solution with stirring at room temperature. Etched depth of each sample was measured by an interference technique. Surface conditions were evaluated by an optical microphotograph. A conventional horizontal LPE growth system was used for the growth of InP. The starting growth temperature was 650°C.

Figure 1 shows the dependence of etching time for the etched depth of specimens etched by 0.92 $\text{H}_2\text{O}_2\text{-100 H}_2\text{SO}_4\text{-5H}_2\text{O}$ solution. The etch rate for each plane was constant. It was as small as 0.06 $\mu\text{m}/\text{min}$ for InP(111)B and 0.02 $\mu\text{m}/\text{min}$ for InP(100). There were no noticeable differences between dopants Sn or Cr on the etch rate. Surfaces etched by this solution were smooth. Figure 2 shows the H_2O_2 content dependence of etch rate. The etch rate increases linearly with increasing H_2O_2 content. The etch rate for InP(111)B was three times larger than that for InP(100) and is independent of dopants in the case of InP(111)B. Moreover, the etch rate seems to be independent of the ratio of H_2SO_4 and H_2O content. However, for the H_2O_2 content of more than 30 volume percent (v/o) (etch rate = 0.68 $\mu\text{m}/\text{min}$ for InP(111)B), the etched surface was not smooth. Figure 3a shows an example of the etched surface of InP(111)B doped with Sn etched in $\text{Br}_2\text{-CH}_3\text{OH}$ solution of 0.3 v/o Br_2 for 3 min and etched off 6 μm after cleaning in trichloroethylene, acetone, and alcohol. A number of small pits and scratches were ob-

served on the surface due to the selective etching at the damaged areas remaining on the polished surface. Such extreme defective surfaces are sometimes obtained independently of Br_2 content in the solution when InP substrate was etched in the $\text{Br}_2\text{-CH}_3\text{OH}$ solution Figure 3(b) shows a surface of InP epitaxial layer grown on the InP(111)B substrate shown in Fig. 3(a).

A number of defects were observed on the surface. The defect pattern is the same as that of the substrate shown in Fig. 3(a). Therefore, it is clear that almost all of these surface defects propagate from the substrate. Figure 3(c) shows a surface of InP(111)B doped with Sn etch by $\text{Br}_2\text{-CH}_3\text{OH}$ solution of 0.3 v/o for 3 min after etching by $\text{H}_2\text{O}_2\text{-H}_2\text{SO}_4\text{-H}_2\text{O}$ solution of 14 v/o H_2O_2 (etch rate = 0.36 $\mu\text{m}/\text{min}$ for InP(111)B) for 1 min. Such defects as shown in Fig. 3(a) were not ob-

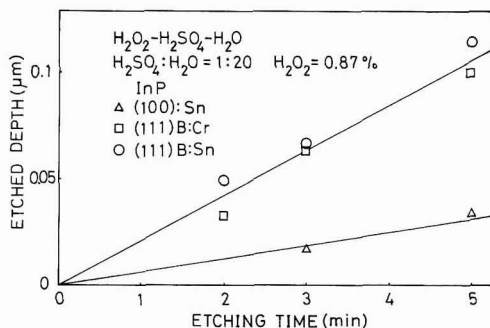


Fig. 1. Etching time dependence for etched depth of InP etched by $\text{H}_2\text{O}_2\text{-H}_2\text{SO}_4\text{-H}_2\text{O}$ solution.

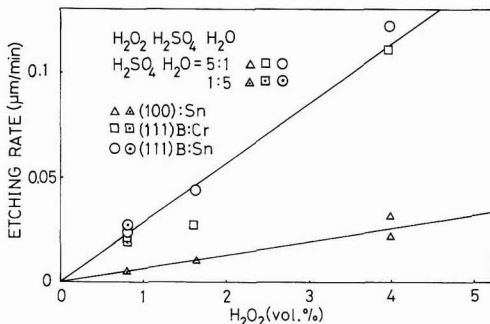


Fig. 2. H_2O_2 content dependence for etching rate of InP etched by $\text{H}_2\text{O}_2\text{-H}_2\text{SO}_4\text{-H}_2\text{O}$ solution.

Key words: liquid phase epitaxy, InP, etching, surface defects.

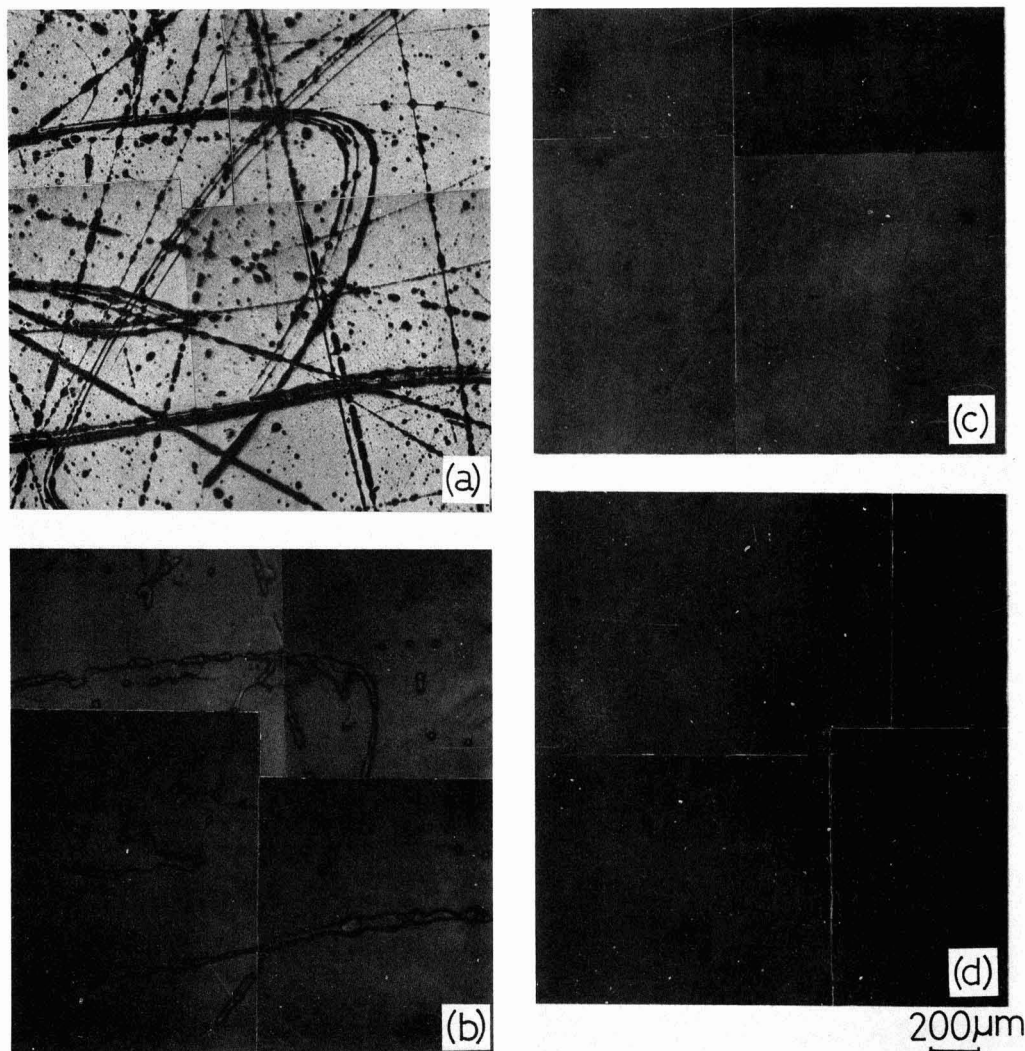


Fig. 3. (a) Surface of InP substrate etched by $\text{Br}_2\text{-CH}_3\text{OH}$ solution for 3 min without preetching, (b) Surface of InP epitaxial layer grown on the same substrate as shown in (a), (c) Surface of InP substrate etched by $\text{Br}_2\text{-CH}_3\text{OH}$ solution with preetching by $\text{H}_2\text{O}_2\text{-H}_2\text{SO}_4\text{-H}_2\text{O}$ solution for 1 min, (d) Surface of InP epitaxial layer grown on the same substrate as shown in (c).

served and reproducible smooth surfaces were obtained. Figure 3(d) shows a surface of the InP epitaxial layer grown on the InP(111)B substrate shown in Fig. 3(c). The surface was smooth relative to the former case. The same results were obtained for InP(111)B doped with Cr and InP(100) doped with Sn.

HNO_3 , H_2SO_4 , HCl , and HF were examined for the preetching solution before etching by $\text{Br}_2\text{-CH}_3\text{OH}$ solution. HNO_3 and H_2SO_4 were slightly effective in decreasing those defects generated on the surface after subsequent $\text{Br}_2\text{-CH}_3\text{OH}$ etch, especially scratches, because InP can be etched by HNO_3 or H_2SO_4 only a very little, but they were not effective for small pits. HCl made the surface of InP rough (5) and HF was not effective in obtaining a smooth surface. Therefore, for obtaining a smooth surface, it is necessary to clean the polished surface chemically by preetching and then

eliminate the damaged layer by $\text{Br}_2\text{-CH}_3\text{OH}$ solution which has a high etching rate.

In summary, it is shown that the smooth etched surface of InP is obtained with good reproducibility by using an $\text{H}_2\text{O}_2\text{-H}_2\text{SO}_4\text{-H}_2\text{O}$ solution in which the H_2O_2 content is less than 30 v/o. We have also described an etching technique by which a smooth and damage-free surface can be obtained for the preparation of InP substrate before growth, by using an $\text{H}_2\text{O}_2\text{-H}_2\text{SO}_4\text{-H}_2\text{O}$ solution.

Acknowledgments

The authors wish to thank O. Ryuzan, T. Yamaoka, and K. Akita for helpful discussions. They also wish to thank S. Nakai for technical assistance.

Manuscript submitted Feb. 12, 1979; revised manuscript received May 1, 1979.

Any discussion of this paper will appear in a Discussion Section to be published in the June 1980 JOURNAL. All discussions for the June 1980 Discussion Section should be submitted by Feb. 1, 1980.

Publication costs of this article were assisted by Fujitsu Laboratories, Limited.

REFERENCES

1. K. Pak, T. Nishinaga, and S. Uchiyama, *J. Appl. Phys.*, **14**, 1613 (1975).
2. R. Sankaran, R. L. Moon, and G. A. Antypas, *J. Cryst. Growth*, **33**, 271 (1976).
3. J. J. Hsieh and C. C. Shen, *Appl. Phys. Lett.*, **30**, 429 (1977).
4. T. P. Pearsall and M. Papuchon, *ibid.*, **33**, 640 (1978).
5. B. Tuck and A. J. Baker, *J. Mater. Sci.*, **8**, 1559 (1973).

Ge-Doped Si₃N₄ Film

Y. Tamaki, S. Isomae, A. Shintani,* and M. Maki

Hitachi Limited, Central Research Laboratory, Kokubunji Tokyo 185, Japan

Si₃N₄ films have been extensively used in silicon semiconductor device fabrication as an oxidation mask, a diffusion mask, or a passivating film because of its chemical stability. However, chemical vapor deposited (CVD) Si₃N₄ films on Si substrates often cause dislocations in the substrate. This is because the intrinsic stress in Si₃N₄ films is large (1-3). It is difficult to reduce this stress effectively by varying deposition conditions, although stress in the film does depend somewhat on deposition conditions.

In order to avoid the stress effect, silicon oxynitride (Si_xO_yN_z) films have been studied (4-6). It is known that the properties of Si_xO_yN_z films depend on film composition. Although the stress in Si_xO_yN_z films, with a composition near SiO₂, is fairly small, resistance to oxidation is low. Therefore, the development of a new oxidation-resistant film with low intrinsic stress has been desirable. In line with this, recent investigations revealed that the stress in Si₃N₄ films is lowered by Ge doping during deposition.

In this paper, the deposition conditions and film properties of Ge-doped Si₃N₄ films (for simplicity, Ge-SiN films) are described. It is shown that Ge-SiN films deposited at temperatures about 700°C with suitable gas flow rates have low stress levels ($\sim 1.5 \times 10^8$ N/m²) and relatively low oxidation rates (~ 0.1 nm/min).

The furnace used for CVD was a horizontal, infrared, lamp-heated reactor. The temperature of the susceptor, on which Si substrates were placed, was measured using a thermocouple, and temperature fluctuations were controlled to within $\pm 1^\circ\text{C}$. SiH₄ (4% in Ar), NH₃, and GeH₄ (0.1% in N₂) were used as the reacting gases and N₂ as the carrier gas.

During experiments, the following gas flow rates were kept constant: N₂: 24 liter/min, SiH₄: 16 ml/min, and NH₃: 1.5 l/min. The GeH₄ flow rate was varied from 0.08 to 1.28 ml/min to control the Ge content in the film. Deposition time ranged from 6 to 15 min and film thickness was about 200 nm. The substrates used were dislocation free, (100) oriented, n-type, 0.01 Ωm , 40 mm in diameter, and 250 μm thick.

Thickness, Ge content, stress, and oxidation rate were measured in order to evaluate the properties of Ge-SiN films. The thickness of the films were mechanically measured using a Dektak. Variations in the film thickness within a wafer were less than 10%. To investigate the Ge content in the film, the ratio of Ge to Si was estimated using an ion microanalyzer (IMA). The stresses in the films were measured by means of x-ray diffraction (7). Ge-SiN film stresses were found to be tensile as in Si₃N₄ films. To estimate the oxidation rate, the oxide layer formed on Ge-SiN film by oxidation was etched off with diluted hydrofluoric acid, and the resultant film thickness was compared with that of as-deposited film.

The Ge content in Ge-SiN films depended on deposition temperatures and GeH₄ flow rates. The Ge content increased with GeH₄ flow rates (GeH₄/SiH₄ ratio) but decreased with increasing deposition temperature. No Ge atoms were detected by IMA in films deposited at temperatures above 850°C. The deposition rate decreased with deposition temperature and became quite low (< 1 nm/min) at temperatures below 650°C. To obtain both the desired composition and suitable deposition rate, it is necessary to deposit Ge-SiN films in the temperature range between 700°-800°C.

The properties of Ge-SiN films deposited at temperatures around 700°C were studied in detail. The deposition rate for Ge-SiN films is shown in Fig. 1. The deposition rate increases with increasing GeH₄/SiH₄ ratios. A steep increase in the deposition rate is found at the ratio of 0.01-0.02, and a gradual increase is observed when the ratio is larger than 0.02. However, the film surface tended to be rough or milky with increasing GeH₄/SiH₄ ratios. In particular, if the ratio exceeded 0.04, surface smoothness became unacceptable for practical use.

IMA analysis revealed that almost uniform Ge doping is realized throughout the film. In addition, the

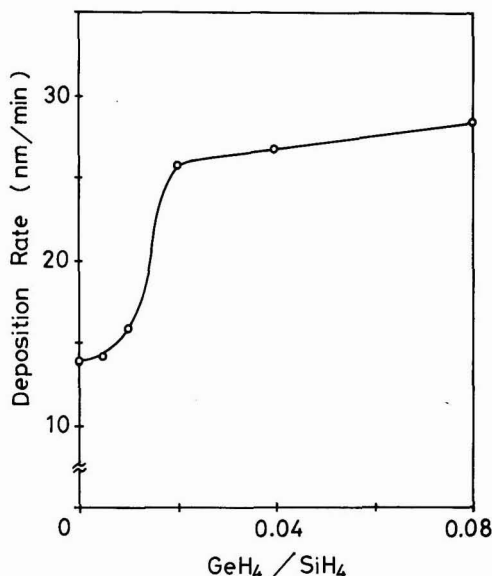


Fig. 1. Deposition rate of Ge-SiN films as a function of GeH₄/SiH₄ ratio.

* Electrochemical Society Active Member.

Key words: chemical vapor deposition, stress, oxidation mask.

Ge/Si ratio in the films deposited at 720°C, where the ratio of $\text{GeH}_4/\text{SiH}_4 = 0.01 \sim 0.08$, was measured. The Ge/Si ratio in Ge-SiN films is shown in Fig. 2. The Ge content in the film is nearly proportional to the $\text{GeH}_4/\text{SiH}_4$ ratio.

The stress in Ge-SiN films is shown in Fig. 3. Stress decreases considerably when the Ge/Si ratio is larger than 0.01. This tendency is similar to that of the deposition rate. Minimum stress is found at a ratio of 0.015, and this minimum value is approximately 1/5 of that of undoped Si_3N_4 .

Next, the resistance of Ge-SiN films to oxidation was evaluated. The oxidation rates for Ge-SiN film at 1000°C in wet oxygen are shown in Fig. 4. Although the oxidation rate grew rapidly with increasing Ge/Si ratios, the rate of Ge-SiN film oxidation for Ge/Si ratios of less than 0.02 is, at most, twice as fast as in

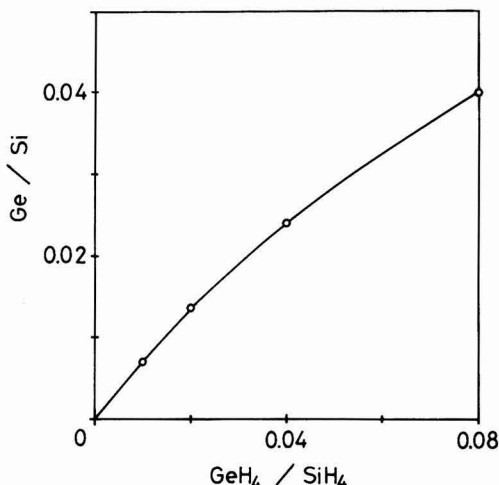


Fig. 2. Ge/Si ratio in Ge-SiN films as a function of $\text{GeH}_4/\text{SiH}_4$ ratio.

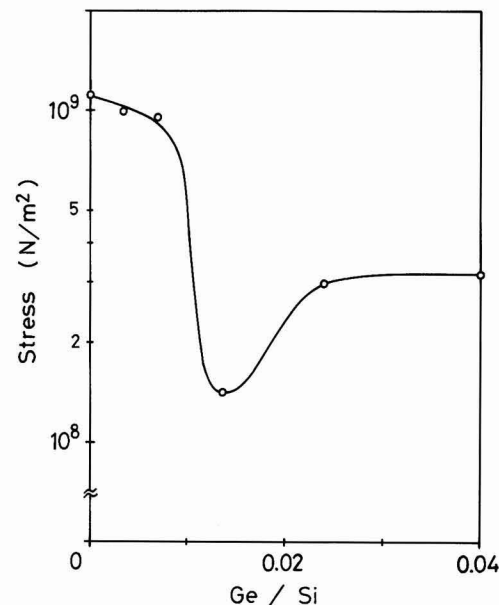


Fig. 3. Stress in Ge-SiN films as a function of Ge/Si ratio.

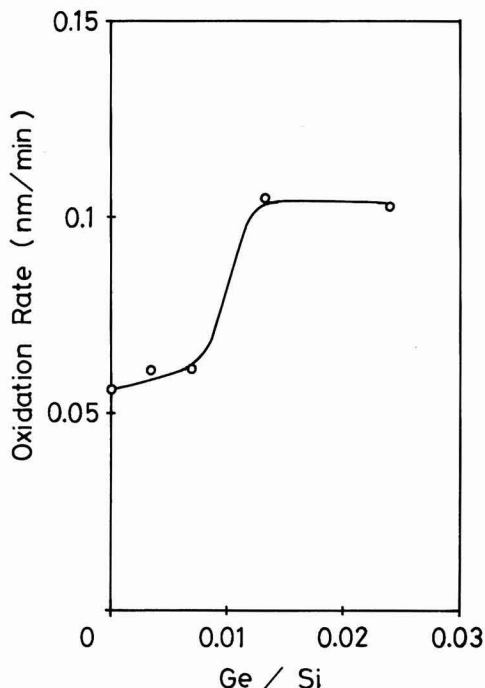


Fig. 4. Oxidation rate of Ge-SiN films as a function of Ge/Si ratio.

Si_3N_4 films. The Ge-SiN film oxidation rate for Ge/Si ratios greater than 0.04 could not be measured because of surface roughness.

These four figures indicate that the deposition rate, stress, and oxidation rate of Ge-SiN films are closely related to the Ge/Si ratio. In addition, drastic changes in these three curves are found at Ge/Si ratios around 0.01. It is considered that some structural changes occur at around the 0.01 ratio.

From the present results, the best conditions were deposition temperatures of about 700°C and $\text{GeH}_4/\text{SiH}_4$ ratios of about 0.02. For example, a 100 nm thick Ge-SiN film deposited at 700°C and $\text{GeH}_4/\text{SiH}_4 = 0.02$ (stress was about 1/5 that of Si_3N_4 films) successfully resisted oxidation for 10 hr at 1000°C in wet oxygen. A 1.4 μm thick SiO_2 film is normally grown on bare Si under these oxidation conditions. Therefore, the Ge-SiN film can be used as a mask for selective oxidation. On the contrary, a 100 nm thick $\text{Si}_2\text{O}_5\text{N}_2$ film with an equivalent Si_3N_4 mole fraction of 0.3 (stress was about 1/2 that of Si_3N_4 films) has been completely converted to SiO_2 under the same oxidation conditions (6).

The new Ge-SiN films have made it possible to realize considerable reductions in intrinsic stress with gradual increases in the oxidation rate. However, some related problems still remain unresolved. These will be the subjects of future studies to improve surface smoothness and to investigate the structure of Ge-SiN films. It is considered that Ge-SiN films will find practical applications as thin films in the fabrication of semiconductor devices, particularly because they have much less stress than the Si_3N_4 films presently used.

Acknowledgments

The authors wish to thank Drs. K. Sugawara and M. Ogirima for useful discussions.

Manuscript submitted Jan. 29, 1979; revised manuscript received May 15, 1979.

Any discussion of this paper will appear in a Discussion Section to be published in the June 1980 JOURNAL. All discussions for the June 1980 Discussion Section should be submitted by Feb. 1, 1980.

Publication costs of this article were assisted by Hitachi Limited.

REFERENCES

1. W. A. Westdorp and G. H. Schwuttke, in "Thin Film Dielectrics," F. Vratny, Editor, p. 546, The Electrochemical Society Softbound Proceedings

- Series, New York (1969).
2. M. Tamura and H. Sunami, *Jpn. J. Appl. Phys.*, **11**, 1097 (1972).
3. E. A. Irene, *J. Electron. Mater.*, **5**, 287 (1976).
4. D. M. Brown, P. V. Gray, F. K. Heumann, H. R. Philipp, and E. A. Taft, *This Journal*, **115**, 311 (1968).
5. M. J. Rand and J. F. Roberts, *ibid.*, **120**, 446 (1973).
6. A. K. Gai and E. W. Hearn, *ibid.*, **125**, 139 (1978).
7. T. Tokuyama, Y. Fujii, Y. Sugita, and S. Kishino, *Jpn. J. Appl. Phys.*, **6**, 1252 (1967).

DISCUSSION SECTION



This Discussion Section includes discussion of papers appearing in the *Journal of The Electrochemical Society*, Vol. 126, No. 4 and 6, April and June 1979.

Editor's Note:

The article to which this refers perhaps should have been a discussion and not a stand-alone communication. This note is to make amends for that.

Refers to A. G. Revesz (pp. 502-503, Vol. 126, No. 3) and E. A. Irene (pp. 1708-1714, Vol. 125, No. 10)

Dear Dr. Hackerman:

It was with astonishment that I read A. G. Revesz's attempted denigration¹ of my recent paper² in *J. Electrochem Soc.* My surprise does not stem from a belief that my work is sacrosanct but rather that you authorized the publication of a clear and direct criticism (as opposed to new data or theory) of a reviewed paper as an "accelerated brief communication" rather than as a "discussion" which, I presume, would have afforded me a simultaneous reply to the attack.

I consider this action as an affront to my integrity and to prospective authors. I, therefore, request that you also publish this letter which contains below my answer to Revesz's objections.

The goals of my paper² were firstly to present several interesting experimental results on very thin SiO_2 films (oxidation kinetics, dielectric breakdown, and TEM) which show differences between dry O_2 and H_2O grown films, and secondly to suggest a unifying idea which seems to correlate the results and may lead to further research.

Pertaining to the oxidation kinetics, I make no attempt to describe the initial oxidation regime by an analytical function. Rather, I compare the linearity (or curvature) of the dry O_2 and H_2O oxidation data. In this context I believe that my analysis is valid. Based on this analysis and the physical idea underlying the linear parabolic model,³ I postulate that the H_2O grown thin SiO_2 films are more protective than dry O_2 films since the kinetics of oxidation for the H_2O grown films is more diffusion limited. This simple idea is borne out by the dielectric breakdown measurements.

The TEM results show that the films have very small (<20 Å) inhomogeneities. If the inhomogeneities are micropores and if the dry O_2 grown films have more or larger micropores, then micropores explain the data. Revesz⁴ had argued that SiO_2 films contained microchannels which are characterized by $\pi\text{-}\sigma$ bonding of Si to O. It is my understanding that such bonding results in greater electron densities and shorter bond

lengths hence a positive density fluctuation in regions with more $\pi\text{-}\sigma$ bonding. Such higher density regions in the oxide as an explanation of my results are not excluded by the TEM results but they are excluded by the kinetics and conductivity results. The existence of micropores is common in ceramic materials and we are presently trying to image micropores in SiO_2 films.

Sincerely,

Eugene A. Irene

IBM Thomas J. Watson Research Center
Yorktown Heights, New York 10598

The Dissolution of SiC and Other Materials in Molten Si

W. P. Minnear (pp. 634-636, Vol. 126, No. 4)

Werner Kürzinger:⁵ Results of growth velocity of my own experiments in liquid phase epitaxy of SiC from a C-saturated Si-solution on SiC substrate-crystals confirm your results in calculating boundary layer thickness. Assuming the same diffusion constant, growth velocity was calculated from temperature dependent solubility of C in Si and temperature gradient in the melting volume.

But the summary conclusion that the only practical limits of dissolution rate are the boundary layer and solute concentration can only be valid for a very small material quantity like filaments. For greater quantities, such as bigger crystals, and more complicated geometries the melting heat and heat conductions must be taken into consideration. What is the influence of the melting heat?

W. P. Minnear:⁶ My paper basically establishes that Fick's law, Eq. [1]

$$J = -D \text{ grad}(C) \quad [1]$$

describes the rate of disappearance of SiC, Si_3N_4 , SiO_2 , and carbon in molten Si. Since the diffusion constant, D , is not independently variable, the concentration gradient is what for practical purposes establishes the flux of solute, J , to the solvent. Two terms constitute $\text{grad}(C)$: (i) the difference in solute concentration, ΔC , between the surface of the dissolving body, C_s , and the bulk of the solvent, C , and (ii) the effective boundary layer thickness, δ . The value of C_s should nearly always be approximately the saturation value for the conditions which prevail at the surface of the body. The only remaining variables affecting J are C and δ . For the experimental configuration discussed in the

¹ A. G. Revesz, *This Journal*, **126**, 502 (1979).

² E. A. Irene, *ibid.*, **125**, 1708 (1978).

³ B. E. Deal and A. S. Grove, *J. Appl. Phys.*, **36**, 3770 (1965).

⁴ A. G. Revesz, *J. Non-Cryst. Solids*, **4**, 347 (1970).

⁵ D-3200 Hildesheim, West Germany.

⁶ General Electric Company, Corporate Research and Development, Schenectady, New York 12301.

original paper, these terms can be treated macroscopically as scalar quantities due to radial symmetry. In other practical situations such as the growth of single crystals, large with respect to δ , $\text{grad}(C)$ may vary spatially and may not be everywhere characterizable by a single value for the ratio $\Delta C/\delta$. However, the flux defining parameters at any point still remain C and δ .

It is true that a heat of reaction, ΔH , associated with the solute/solvent interface can affect the dissolution rate. The driving force for free convection is the difference in density of the solvent, $\Delta\rho$, across the mass boundary layer. Density differences are directly related to temperature differences through the coefficient of thermal expansion. Therefore, a ΔH which affects the temperature at the solid/liquid interface affects δ through $\Delta\rho$. Alternatively

$$\delta = f(\Delta\rho) \quad [2]$$

$$\Delta\rho = g(\Delta T) \quad [3]$$

$$\Delta T = h(\Delta H) \quad [4]$$

Furthermore, Eq. [2] and [4] are geometry sensitive. The actual temperature rise at the solid/liquid interface does indeed depend on the heat transfer and dissipation at the interface, but ultimately the total effect can be represented by some effective boundary layer thickness.

The original conclusions are correct. It must be recognized however that except for idealized geometries δ may vary from point-to-point near a dissolving body.

Enhancement of Lateral P-N-P Current Gain by Gettering

R. Kesavan, P. N. Andhare, K. L. Bhola, and D. V. Singh
(pp. 642-644, Vol. 126, No. 4)

James A. Topich:⁷ In the paper Kesavan *et al.* make the statements, "If the lateral p-n-p current gain is increased by an order because of improved lifetime, one would expect the beta of n-p-n also to increase by similar order. The fact that this does not happen shows an interesting interaction of surface and bulk lifetime. In n-p-n transistor the lifetime is governed by the surface lifetime whereas in the lateral p-n-p significant contribution comes from the bulk lifetime." I do not dispute their claims that changes in the fabrication procedure produced improved devices due to a gettering effect but I feel that their suggested reasons are in error.

The authors seem to have overlooked some of the factors which govern the current gain of a bipolar transistor. In the standard textbook analysis⁸ there are three terms which make up the common base current gain, alpha, from which beta is easily calculated. These terms are (i) the emitter injection efficiency, (ii) the base transport factor, and (iii) the collector collection efficiency. For the paper under consideration only the first two terms need to be looked at.

If we consider the base transport factor first, we see that it is equal to $(\cosh(W_B/L_{PB}))^{-1}$ where W_B is the basewidth and L_{PB} is the minority carrier diffusion length in the base. As the lifetime in the material increases L_{PB} will also increase. For $W_B \ll L_{PB}$, $\cosh(W_B/L_{PB})$ is very nearly one and the current gain is determined primarily by the emitter injection efficiency. For a shallow emitter device the emitter injection efficiency is given by $(1 + (\sigma_B W_B / \sigma_E W_E))^{-1}$ where σ_B and σ_E are the conductivities of the base and emitter and W_B and W_E are the basewidth and the emitter depth. It should be noted that this term is independent of the minority lifetime in the base.

For the case of the lateral transistor described in the paper the basewidth was not "much less" than the

minority carrier diffusion length. Thus the base transport factor should have had a substantial effect on the current gain and any improvement in the bulk lifetime would be reflected in an improvement in beta. For a vertical transistor however the improvement in lifetime will not have as dramatic an effect since the base transport factor would have already been close to unity because of the narrow basewidth.

One further comment concerns the surface lifetime. One would expect that any surface effects on lifetime would contribute to the degradation of lateral transistor beta since one side of the active base region would be bounded by the oxide-silicon interface.

Thus it would seem that an improvement in bulk lifetime can easily explain the large improvement in lateral transistor beta with a significantly smaller improvement for the vertical transistors.

R. Kesavan, P. N. Andhare, K. L. Bhola, and D. V. Singh:⁹ The author has commented that "For a vertical n-p-n transistor the improvement in lifetime will not have as dramatic an effect since the base transport factor would have already been close to unity because of the narrow basewidth." Accepting the fact that the basewidth in the vertical n-p-n transistor is about five times less than the basewidth in the lateral p-n-p transistor, the minority carrier lifetime in the base of the vertical n-p-n will have to be of the order of microseconds to make the ratio $W_B/L_{NB} \approx 0.1$ and $[\cosh(W_B/L_{NB})]^{-1}$ close to unity. In our transistor it is of the order of nanoseconds. It can be seen that $[\cosh(W_B/L_{NB})]^{-1}$ will be much less than 1 for lifetime of this order. For example, even for a diffusion length of the order of $1\ \mu\text{m}$ (approximately corresponding to the lifetime of the order of 10 nsec) the factor $[\cosh(W_B/L_{NB})]^{-1}$ would be of the order of 0.65 only.¹⁰ For our n-p-n transistors the lifetime being only a fraction of a nanosecond the base transport factor will be far away from unity. Hence it is justified in expecting the transport factor to improve if the process employed by us can improve the bulk lifetime. So the contention of the author will be true only in special cases where the lifetime is of the order of microseconds.

Thus it can be seen that there is scope for improvement in the transport factor of the vertical n-p-n transistor. Yet no significant improvement in the beta of n-p-n has taken place. One has, therefore, to look up the expression for base transport factor given in Eq. [9]-[14] in footnote 10 wherein the effective lifetime in the base region of the vertical n-p-n is given as a parallel combination of the bulk and surface lifetime. Combining this with the fact that the beta in lateral p-n-p is governed by bulk lifetime rather than surface lifetime,¹¹ one can say that the improvement in beta of vertical n-p-n is not of the same order though bulk lifetime is improved by gettering only because the surface lifetime is masking the effective lifetime of the n-p-n transistor. Hence the improvement in beta of the n-p-n is not very significant in spite of improved bulk lifetime.

Now regarding the comment concerning the surface lifetime. One would expect that any surface effects on lifetime would contribute to the degradation of lateral transistor beta provided the surface lifetime in the lateral p-n-p and that in the vertical n-p-n are of the same order. Further the fact that the lateral p-n-p is insensitive to the surface lifetime whereas the vertical n-p-n is more sensitive to the surface lifetime shows that the absolute values of surface lifetime in the two cases are of different order. This could presumably be due to the fact that the base region of the lateral p-n-p is formed by epitaxy and the base of the

⁹ Solid State Physics Laboratory, Delhi, India 110007.

¹⁰ Alvin B. Phillips, "Transistor Engineering," p. 184, McGraw Hill Book Company, New York.

¹¹ J. Lindmayer and W. Schneider, *Solid-State Electron.*, **10**, 229 (1967).

⁷ Tektronix, Inc., Beaverton, Oregon 97077.

⁸ S. K. Ghandi, "The Theory and Practice of Microelectronics," John Wiley and Sons, Inc., New York (1968).

vertical n-p-n is formed by diffusion. These regions also differ in type and concentration.

The Relationship Between Oxide Grain Morphology and Growth Mechanisms for Fe-Cr-Al and Fe-Cr-Al-Y Alloys

F. A. Golightly, F. H. Stott, and G. C. Wood
(pp. 1035-1042, Vol. 126, No. 6)

James L. Smialek:¹² In the above recent paper the relationship of growth stress and Al_2O_3 scale adherence on FeCrAl alloys was reemphasized. The authors have argued that a coupling of inward oxygen diffusion and outward aluminum diffusion causes lateral growth within the scale. The growth stress is a direct result of the lateral oxide growth subject to the constraints of the underlying metal substrate. The existence of the growth stress has been impressively documented by micrographs of the severely convoluted scale on pure FeCrAl alloys. The absence of growth stress and lateral growth in Al_2O_3 scales formed on Y-doped alloys has been attributed to blocking the outward diffusion of aluminum.^{13,14}

Golightly *et al.* have also reviewed convincing evidence that the primary transport mechanism is by inward grain boundary diffusion of oxygen. The secondary mechanism of aluminum outward diffusion was proposed to be via a limited number of short-circuit paths. Thus, only a small amount of Y would be required to segregate to these paths and block or retard aluminum diffusion in the scale. The nature of the short-circuit paths for aluminum diffusion remains somewhat speculative. Grain boundary diffusion has been discounted in light of diffusion studies of bulk Al_2O_3 ;¹⁵ dislocation pipe diffusion was favored instead. The purpose of the present note is to call attention to the possibility of oxide grain boundaries as short-circuit paths for aluminum in Al_2O_3 materials.

The commonly cited paper minimizing grain boundary diffusion of aluminum in bulk Al_2O_3 is that by Paladino and Kingery.¹⁵ There are a number of factors which limit the applicability of this work: (i) No comparison was made between single crystal and polycrystalline specimens. Only polycrystalline samples were studied. (ii) The grain size of the polycrystals studied was 130 and 200 μm , nearly two orders of magnitude greater than normally observed in Al_2O_3 scales formed at 1200°C. (iii) The absence of grain boundary diffusion of aluminum was concluded only from the shape of the diffusion profiles and from the equivalent results obtained for both grain sizes. (iv) The lowest temperature studied was 1670°C, nearly 500°C higher than the range of interest for MCrAl oxidation.

The possibility of observing grain boundary diffusion of aluminum in the work by Paladino and Kingery can be discussed directly by invoking the usual concept of effective diffusion coefficients

$$D_{\text{eff}} = (1 - f)D_1 + f(D_{\text{gb}}) \quad [1]$$

where D_{eff} = effective (measured) coefficient; D_1 = lattice coefficient; D_{gb} = grain boundary coefficient; and f = volume fraction of grain boundaries.

For a model grain shape [tetrakaidecahedron (Footnote 16)]

$$f = \frac{3.3\delta}{\text{GS}} \quad [2]$$

where δ = grain boundary width [$\sim 100\text{\AA}$ for Al_2O_3 (Footnote 16)].

Thus for 130 and 200 μm grain sizes

$$D_{\text{eff},130} = D_1 + 2.5 \times 10^{-4}D_{\text{gb}} \quad [3]$$

¹² NASA-Lewis Research Center, Cleveland, Ohio 44135.
¹³ F. A. Golightly, F. H. Stott, and G. C. Wood, *This Journal*, **126**, 1035 (1979).

¹⁴ F. A. Golightly, F. H. Stott, and G. C. Wood, *Oxid. Met.*, **10**, 163 (1976).

¹⁵ A. E. Paladino and W. D. Kingery, *J. Chem. Phys.*, **37**, 957 (1962).

$$D_{\text{eff},200} = D_1 + 1.7 \times 10^{-4}D_{\text{gb}} \quad [4]$$

Clearly, in order to produce a measurable change in D_{eff} , we must have $D_{\text{gb}} \geq 10^4 D_1$. At 1670°C, $D_{\text{gb}}^0 \approx 10^4 D_1^{0,16,17}$ and indeed oxygen diffusion is noticeably greater in polycrystalline materials than in single crystals. If grain boundary diffusion of aluminum was significant (e.g., $10^2 D_1^{\text{Al}}$), although not as high as $10^4 D_1^{\text{Al}}$, the grain boundary effect of aluminum would not have been observed in 130 μm grain size samples. It is therefore strongly urged that the role of grain boundary diffusion of aluminum be reconsidered in transport controlled processes in Al_2O_3 .

There is evidence that some outward diffusion of aluminum occurs at Al_2O_3 grain boundaries in scales formed on NiAl¹⁸ and PtAl.¹⁹ Often the oxide grain boundaries exhibit distinct ridges at the gas-oxide interface. It thus appears that preferential aluminum transport up grain boundaries has occurred and that new oxide has formed at the gas-oxide interface (lacey structure). This may be an accentuated form of the dimpled oxide structure normally observed on MCrAl alloys.

The effect of Y on transport in bulk Al_2O_3 materials has not been studied extensively. In the sintering study of Y-doped Al_2O_3 ,²⁰ originally cited by Golightly *et al.*, it was found that Y indeed segregated to grain boundaries, allowed pores to become situated on slow-moving grain boundaries, and reduced the rate of pore removal (although full density was eventually achieved). These phenomena were discussed as the results of a two-fold reduction in the grain boundary interdiffusion coefficient (at 1250°C). The amount of segregant required to cause this effect was estimated to be less than 0.2 monolayers of yttria at the grain boundaries. (This is in accord with the small levels of Y alloy additions required to eliminate buckling of the Al_2O_3 scales.) It could not be determined from the sintering study whether the reduction in grain boundary diffusion coefficient was primarily due to oxygen or aluminum effects.

Transmission electron microscopy of Al_2O_3 scales formed on Y-doped NiCrAl have indeed shown large areas where grain boundary porosity was widespread.²¹ By analogy to the sintered Al_2O_3 morphology, Y has probably segregated to oxide grain boundaries. By reducing grain boundary diffusion in the scales, the grain boundary porosity is allowed to persist. Conversely, in the scales on pure NiCrAl, very few grain boundary pores were observed, while entrapped intergranular pores were common.

Reductions in oxidation rates of Y-doped FeCrAl,¹⁴ Y and Hf-doped CoCrAl,²² and Zr-doped NiCrAl²³ have been measured. From the 100 hr weight change data for CoCrAl, it is estimated that k_p was reduced by a factor of 1.5-2.2 (1100° and 1200°C) with the addition of ≤ 0.3 w/o Y or Hf. Similarly, the addition of ≤ 0.07 w/o Zr to NiCrAl reduced k_p by a factor of 4 at 1150° and 1200°C. Thus, these kinetic oxidation studies suggest that the additions of limited amounts of oxygen-active metals such as Hf or Zr, as well as Y, are effective in retarding diffusional transport in Al_2O_3 . It also becomes particularly compelling to suggest that these adherence additives reduce grain boundary diffusion of aluminum and prevent growth stress as a consequence.

Recent O¹⁸ tracer studies of Al_2O_3 scales formed on FeCrAl alloys have indeed shown that Y additions

¹⁶ R. E. Mistler and R. L. Coble, *J. Appl. Phys.*, **45**, 1507 (1974).

¹⁷ Y. Oishi and W. D. Kingery, *J. Chem. Phys.*, **33**, 480 (1960).

¹⁸ J. L. Smialek, *Mater. Trans.*, **9A**, 309 (1978).

¹⁹ E. J. Felten and F. S. Pettit, *Oxid. Met.*, **10**, 189 (1976).

²⁰ P. Nanni, C. Stoddart, and E. D. Hondros, *Mater. Chem.*, **1**, 297 (1976).

²¹ J. L. Smialek and R. Gibala, NASA TM 79259, July, 1979.

²² I. M. Allam, D. P. Whittle, and J. Stringer, *Oxid. Met.*, **12**, 35 (1978).

²³ A. S. Khan, C. E. Lowell, and C. A. Barrett, Accepted for publication, *This Journal*.

do suppress aluminum outward diffusion.²⁴ Similar studies have shown only primary inward oxygen diffusion for both pure and Zr-doped NiCrAl scales.²⁵ Differences in oxidation time and temperature may account for the apparent discrepancy in the relative amounts of outward aluminum diffusion.

In summary, the kinetic oxidation studies do show some reduction in oxidation rates with the addition of Y, Hf, or Zr. Since grain boundary diffusion has been identified as a major transport mechanism for Al_2O_3 scale growth, it is likely that this rate reduction was caused by a reduction in grain boundary diffusion. This is consistent with reduced grain boundary diffusion found in sintering studies of Y-doped Al_2O_3 . The intergranular porosity in the sintered Y-doped Al_2O_3 and in the Al_2O_3 scale on Y-doped NiCrAl also suggests that similar grain boundary diffusion effects may be operating. The extent to which this grain boundary effect reflects a reduction in aluminum diffusion rather than oxygen diffusion cannot be assessed. Grain boundary ridges at the gas surface suggest the occurrence of some aluminum grain boundary diffusion.

The original work on aluminum diffusion in bulk Al_2O_3 does not preclude at least some degree of enhanced grain boundary diffusion of aluminum, although it purports to do so. The significance of aluminum grain boundary diffusion in fine grained Al_2O_3 is suggested, at least as a secondary or tertiary transport mechanism. Its occurrence is believed to support the growth stress model of Golightly *et al.* for Al_2O_3 scales.

F. A. Golightly, F. H. Stott, and G. C. Wood:²⁶ It is pleasing to read Dr. Smialek's interesting discussion of the mechanism of growth of $\alpha\text{-Al}_2\text{O}_3$ scales at high temperature. His own transmission electron microscopical studies of such oxides have provided valuable information and this contribution is most welcome. It is apparent that he agrees essentially with the model proposed in our papers, although there are some significant differences in the precise detail. We should like to respond to some of his comments and hope that this will encourage further research in this area.

As indicated in our earlier publication¹⁴ and emphasized by Dr. Smialek, the results of Paladino and Kingery have only limited applicability to the present work and conclusions about transport in thermally grown $\alpha\text{-Al}_2\text{O}_3$ can only be speculative. It is not possible to be dogmatic about the relative fluxes of alu-

minum or oxygen in the scale or about their diffusion paths. The suggestion that oxide grain boundaries provide short-circuit paths for both aluminum and oxygen is interesting but there is no real evidence that aluminum diffuses faster along such boundaries than along other short-circuit paths in the oxide. The concept of counter current flow of Al^{3+} and O^{2-} (or OH^-) ions is quite widely accepted in the growth of thin anodic films under high fields when produced by anodizing in electrolytes. However, it must be remembered that this is a low temperature process through glassy, amorphous, or very fine grained $\gamma\text{-Al}_2\text{O}_3$. Growth by diffusion at high temperature in polycrystalline $\alpha\text{-Al}_2\text{O}_3$ is by no means necessarily the same process. It is difficult to envisage Al^{3+} ions being able to diffuse along oxide grain boundaries when a counter flux of oxygen predominates. We remain to be convinced that Al^{3+} and O^{2-} ions can pass each other in the boundaries.

The discussion paper cites the fact that the oxide grain boundaries exhibit distinct ridges at the gas-oxide interface as evidence for outward diffusion of aluminum along the boundaries. However, in the original paper,¹³ it was indicated that such features could be accounted for by formation of oxide within the vicinity of the oxide grain boundaries. It is not necessary to invoke grain boundary diffusion of aluminum. Dr. Smialek quotes several references which indicate that yttrium and similar additions reduce the oxidation rate of $\alpha\text{-Al}_2\text{O}_3$ -forming alloys and thus are effective in reducing diffusional transport in the oxide. However, although the observed weight gains during oxidation of the yttrium-containing alloys were indeed less (although not considerably so) than those for the yttrium-free alloys in our own research, it is difficult to make precise correlations between the complex oxidation kinetics and diffusion processes in the scale. The rates of weight gain during oxidation are determined not only by the $\alpha\text{-Al}_2\text{O}_3$ scale thickness, but also by the extent of oxide convolutions and by oxidation of the reactive element additions.

Finally, in considering growth of $\alpha\text{-Al}_2\text{O}_3$, it is not really sufficient to consider the oxide alone. From results quoted in the literature, it is apparent that the oxide-alloy substrate system should be taken as a whole. The morphology of $\alpha\text{-Al}_2\text{O}_3$ developed on one particular alloy is often quite different from that developed on another. The alloy substrate and the oxide/alloy interface as well as the oxide are important. For instance, deformation and plastic flow of the alloy surface, which we believe to be quite significant during development of $\alpha\text{-Al}_2\text{O}_3$ on the relatively weak Fe-Cr-Al alloys, may occur considerably less easily on stronger materials. This will affect the scale morphology and configuration and, possibly, the over-all oxidation behavior.

²⁴ D. G. Lees and J. M. Calvert, University of Manchester, Unpublished research.

²⁵ K. P. R. Reddy, and J. L. Smialek, and A. R. Cooper, Case Western Reserve University, Unpublished research.

²⁶ Corrosion and Protection Centre, University of Manchester Institute of Science and Technology, Manchester, England.



Amorphous Molybdenum Disulfide Cathodes

A. J. Jacobson, R. R. Chianelli, and M. S. Whittingham*

Exxon Research and Engineering Company, Linden, New Jersey 07036

Interest in secondary lithium batteries has recently centered around crystalline layered compounds such as titanium disulfide (1). Although the group IVB and VB dichalcogenides were found to be electrochemically active, those of group VIB were much less active. Thus crystalline compounds such as MoS_2 react in electrochemical cells with only about 0.1 Li/Mo (1, 2). In contrast, when a chemical lithiating agent such as *n*-butyl lithium is used, around 1.5 Li/Mo are consumed (3). However, x-ray powder diffraction data suggests that this additional reaction is a result of the formation of lithium sulfide and not of a highly intercalated MoS_2 (4). This decomposition behavior can be explained on thermodynamic grounds (1).

Here we report electrochemical data on amorphous MoS_2 prepared at ambient temperatures by the reaction of lithium sulfide with molybdenum chloride (5). This synthetic technique gives materials with properties radically different from those commonly produced at higher temperatures, and in some cases such as VS_2 compounds that cannot be made at elevated temperatures. X-ray diffraction studies indicated that amorphous molybdenum disulfide is formed in this reaction, and that crystallization although initiated on heating at around 200–300°C is not complete until 800°C. A very large increase in the surface area, found on heating the material to 200–300°C, is suggestive of a radical reorganization of the crystalline structure. Table 1 shows these surface areas, measured by standard BET techniques, and the capacities of the sulfides in lithium cells to a 1.4** volt

TABLE 1. PROPERTIES OF MoS_2

TEMP °C	SURFACE AREA m^2/gm	CAPACITY Li/Mo
150	5	0.83
275	50	1.12
400	63	0.37
600	44	0.11
Crystalline	<5	0.03

cut-off at 0.5 ma/cm^2 ($\text{LiClO}_4/\text{dioxolane}$ electrolyte). Very clearly the low temperature MoS_2 structure has a substantially larger capacity for electrochemical reaction with lithium than the common crystalline MoS_2 (>800°C sample). The discharge behavior is shown in Fig. 1. Whereas the two lowest temperature samples show a smoothly varying voltage/composition profile, the break in the curve of the 400°C sample is suggestive of the presence of two phases. At higher temperatures, the capacity falls off rapidly just as reported earlier (1,2) for crystalline MoS_2 .

Equally surprising, we found that this low temperature molybdenum sulfide phase is highly reversible; even after 244 discharge/charge cycles the electrochemical capacity exceeded 50% of that of the 2nd discharge. This data is shown in Fig. 2. The 400°C sample also showed high reversibility, but at a much lower capacity, ~0.2 Li/Mo on the second discharge dropping to ~0.1 after 500 cycles.

The sloping discharge/charge data of Fig. 2 bears similarity to that of the Li/TiS_2 reaction, which may suggest that a similar non-stoichiometric reaction may also be taking place between lithium and this amorphous molybdenum sulfide phase. If high *x*-value phases of the formula Li_xMoS_2 are formed then the amorphous

*Electrochemical Society Active Member
Key words: battery, cathode, molybdenum disulfide, amorphous material.

**1.6 volts for 275°C sample.

MoS₂ phase is at least kinetically more stable than the crystalline MoS₂ phase, with respect to the reaction (1,2,4) $x > 0.1$



Whether this apparent stability reflects differences in the electronic (i.e. long range) structure or in the local bonding environment is unknown. We are presently making a study of the bonding within this general class of amorphous sulfides using EXAFS and other x-ray techniques. This structural study combined with electrochemical examination of other amorphous sulfides (6) should help determine the chemistry occurring, and whether materials of this type have improved long term cathode capabilities over the more conventional intercalation compounds.

REFERENCES

1. M.S. Whittingham, *Progress in Solid State Chem.*, **12**, 41 (1978).
2. J.O. Besenhard, H. Meyer and R. Schöllhorn, *Naturforsch.*, **316**, 907 (1976).
3. M.B. Dines, *Mat. Res. Bull.*, **10**, 287 (1975).
4. M.S. Whittingham and F.R. Gamble, *Mat. Res. Bull.*, **10**, 363 (1975).
5. R.R. Chianelli and M.B. Dines, *Inorg. Chem.*, **17**, 2758 (1978).
6. A.J. Jacobson, R.R. Chianelli and M.S. Whittingham, *U.S. Pats.*, 4,144,384 and 4,166,160.

Manuscript received Sept. 7, 1979.

Publication costs of this article were assisted by Exxon Research and Engineering Company.

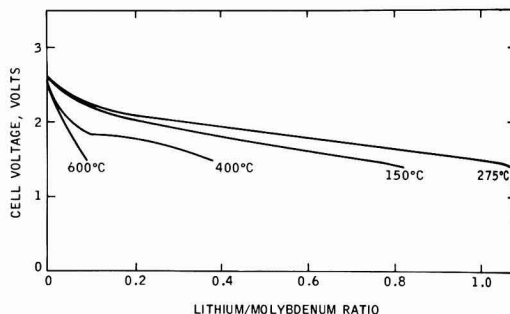


FIG 1 Effect of heat treatment on MoS₂ in lithium cells

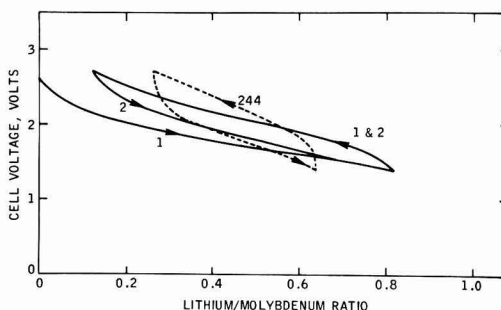


FIG 2 Cycling behavior of 150°C dried MoS₂ in lithium cell

Arsenic Diffusion Through Thin Oxides

Sunil N. Shabde and Kim Helliwell¹

American Microsystems, Incorporated, Santa Clara, California 95051

In the high density NMOS and VMOS processes Arsenic diffusion is normally used to form source and drain junctions. One parameter of practical interest is the minimum oxide thickness that will mask the As diffusion at a given temperature. The masking oxide thickness can be predicted if the As diffusivity in SiO_2 is known. In this investigation we report the experimental determination of the masking oxide thickness and the diffusivity of As in SiO_2 at 1000°C for sealed capsule diffusion. The results of our work are compared with the previously published diffusivity values. It was also found during the investigation that the etch rate of oxide abruptly slowed down for oxide thickness less than 120\AA . Another anomaly discovered is that for thicknesses less than 25\AA the diffusivity of As in the oxide becomes very large approaching that in pure silicon.

EXPERIMENTAL PROCEDURE

The experimental approach used was to diffuse arsenic at 1000°C in a number of silicon samples with varying thicknesses of thermally grown SiO_2 . The oxide was then stripped and the sheet resistivity of the arsenic diffusion was measured. A plot of V/I vs. oxide thickness gives an estimate of the masking oxide thickness. By matching a theoretically calculated plot of V/I vs. oxide thickness with the experimental plot, a value for the diffusion coefficient of arsenic in SiO_2 was obtained.

The samples were prepared by etching down oxidized wafers to given thicknesses using a known etch rate solution of 20:1 HF. To measure the etch rate accurately, four wafers of $14\text{--}23\ \Omega\text{cm}$ p-type 1-0-0 silicon with known beginning thicknesses were etched simultaneously for carefully timed intervals. The

measurements of the oxide thickness were taken after each etch step, at 5 positions on each wafer using an IBM 7840 film thickness analyzer (FTA).

EXPERIMENTAL RESULTS

Plots of the measured oxide thicknesses for one wafer as a function of cumulative etch time is given in Figure 1. The slope is fairly constant, as expected, down to about 120\AA , where there is an abrupt change in the slope. This change occurred to the same degree for all four wafers. Also, the "dewet" times for these wafers were consistent with the slowed etch rate below 120\AA . The maximum error in measuring the dewet time was estimated to be 5 sec. From the available measurements a normal etch rate

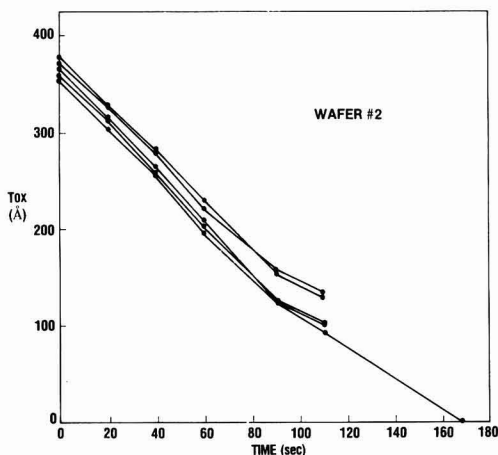


Fig. 1. Etch time in 20:1 HF vs. oxide thickness

Keywords: Arsenic, Sealed-capsule, diffusivity, SiO_2

of $2.20 \pm 0.4^\circ$ per sec and the transition oxide thickness of $122 \pm 18\text{\AA}$ were determined. The error limits given are 1σ limits. The slow etch rate determined from the dewet times was $1.22 \pm 0.5\text{\AA}$. Combining all the uncertainties in the measurement statistically, we find that the standard deviation for the final oxide thickness is 12\AA .

After being etched, the wafers were diffused with As at 1000°C for 1 hour in a sealed capsule, and then stripped of oxide. The V/I was measured at roughly the same points on each wafer where the oxide thicknesses were previously measured. The resulting relation between V/I and oxide thickness is plotted in Figure 2. The point at which arsenic appears to begin penetrating is 40\AA .

THE MODEL

Sah, et al. (1) have given an expression for the concentration profile of a dopant which is partially masked. The expression is:

$$C = m(1 - \alpha) C_0 \sum_{n=0}^{\infty} \alpha^n \operatorname{erfc} \frac{(2n+1)x_0 + rx}{2\sqrt{Dt}}$$

where m is the coefficient of segregation of the dopant between the SiO_2 and Si; $\alpha = (m-r)/(m+r)$; $r = \sqrt{D_0/D}$; D_0 and D are the diffusion coefficients of the arsenic in oxide and silicon, respectively, and x_0 is the oxide thickness. The variable x represents the depth in the silicon with $x = 0$ corresponding to the interface.

Using this expression, V/I can be determined theoretically for a given oxide thickness and oxide diffusion coefficient. The silicon diffusion coefficient is taken as $4.6 \times$

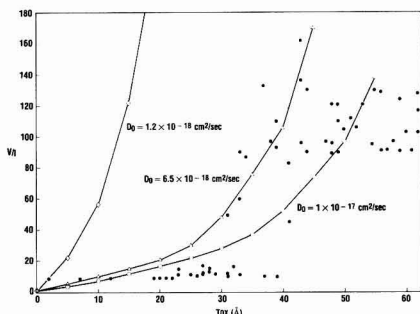


Fig. 2 V/I Variation with the oxide thickness. Solid circles represent experimental data.

$10^{-15} \text{ cm}^2/\text{sec}$ which is consistent with the junction depth of 0.3μ measured in diffused bare wafers. Our procedure was to fit the theoretical curve to the experimental points by adjusting D_0 until V/I at 40\AA was consistent with the experimental result of roughly 110. In this way D_0 is found to be $6.5 \times 10^{-18} \text{ cm}^2/\text{sec}$. The curve corresponding to this value of D_0 is plotted in the figure, together with curves for $D_0 = 1.2 \times 10^{-18} \text{ cm}^2/\text{sec}$, and $D_0 = 1 \times 10^{-17} \text{ cm}^2/\text{sec}$, to show the sensitivity of D_0 to the position of the theoretical curve. A comparison of our results with previously published data is given in Table I.

Table I. As Diffusivity in SiO_2

	Diffusivity in SiO_2 (cm^2/sec)	Temp/ Ambient	Diffusion Source
Our Work	6.5×10^{-18}	1000°C sealed capsule	Sealed capsule
Ghezzi and Brown (2)	3.5×10^{-15} 1.5×10^{-16}	1100°C Argon 1100°C O_2	Arsenic glass Arsenic glass
Tsukamoto (3)	1×10^{-17}	1200°C N_2	Arsenic implant

CONCLUSIONS

The following conclusions are drawn from the above work:

1. The masking oxide thickness for As diffusion in silicon at 1000°C for 1 Hr in sealed capsule ambient is $40\text{\AA} \pm 12\text{\AA}$.
2. The As diffusivity in the thermally grown oxide at 1000°C in the inert ambient of sealed capsule is determined to be $6.5 \times 10^{-18} \text{ cm}^2/\text{sec}$.
3. As a side result it was found that the etch-rate of SiO_2 in 20:1 HF slows down abruptly below 120\AA . The slow down could be a result of boron oxide near the Si- SiO_2 interface or the excessive unoxidized Si atoms within SiO_2 near the interface.

4. The flatness of the V/I vs. oxide thickness plot below 20Å does not match well with the theoretical plot. A possible reason for this is that below 20Å the oxide becomes more or less transparent to As diffusion, i.e. the diffusion coefficient approaches that of Si. This may happen either due to excessive pinholes in the thin oxide or due to the oxide being silicon rich or both of these reasons.

REFERENCES

1. C.T. Sah, H. Sello, and D.A. Tremere, J. Phys. Chem. Solids, 11, 288 (1959).
2. M. Ghezzi and D.M. Brown, J. Electrochem Soc, 120, 110 (1973).
3. K. Tsukamoto, Y. Akasika, and K. Horie, Appl. Phys. Lett., 32, 117 (1978).

¹ Present address: Lockheed Research Lab,
Palo Alto, California 94304

Manuscript submitted July 9, 1979;
revised manuscript received Sept. 12,
1979.

Publication costs of this article were
assisted by American Microsystems,
Incorporated.

Determination of Electroless Copper Deposition Rate from Polarization Data in the Vicinity of the Mixed Potential

M. Paunovic* and D. Vitkavage

Kollmorgen Corporation, PCK Technology Division, Glen Cove, New York 11542

There are basically two electrochemical methods for determination of the rate of an electrochemical reaction at the mixed potential. In the first method (the intercept method) the rate is determined as the current coordinate of the intersection of the high overvoltage polarization curves for the partial cathodic and anodic process, measured from the rest potential. In the second method (the low overvoltage method) the rate is determined from the low overvoltage polarization data for the partial cathodic and anodic process, measured from the mixed potential.

Both methods have been extensively used for the determination of the rate of corrosion of metals (1-6). Considerably less has been published so far on the determination of rate of electroless deposition of metals, on the basis of these methods (7,8).

The subject of this communication is the evaluation of applicability of various forms of the low overvoltage method to the determination of the rate of the electroless copper deposition.

EXPERIMENTAL

The solutions were prepared with analytical grade reagents and deionized water. The electroless copper bath used for these studies contained: 0.05 M $\text{CuSO}_4 \cdot 5\text{H}_2\text{O}$, 0.15 M EDTA, 0.072 M CH_2O ,

NaOH to pH 12.5. Formaldehyde was 37% solution "Baker Analyzed" Reagent. Oxygen was removed by bubbling nitrogen. Temperature was 25°C.

An all-glass three compartment cell with three electrodes was used. The test electrode was a platinum wire (0.397 cm^2 in area) and the auxiliary electrode a platinum sheet (2 cm^2 in area) electroplated with copper. Plating was done in an acid copper solution ($\text{CuSO}_4 \cdot 5\text{H}_2\text{O}$ - 188 g/l, H_2SO_4 - 74 g/l) at 10 mA/cm^2 for 5 min. A saturated calomel electrode (SCE) was used as a reference electrode.

The current-potential curves were obtained with a PAR (Princeton Applied Research, Princeton, N.J.) Model 174A Polarographic Analyzer. The potential sweep in these measurements was 1 mV/sec.

RESULTS AND DISCUSSION

Typical current-potential curves in the vicinity of the mixed potential for the electroless copper deposition (average of six trials) are shown in Fig. 1. Calculation of the rate of deposition from these curves requires knowledge of the anodic and cathodic Tafel slopes, b_a and b_c , respectively.

Tafel slopes were determined using Mansfeld's curve fitting procedure (3,4) and the direct curve fitting procedure to the Stern-Geary equation

$$i_j = i_{\text{dep}} E_j$$
$$E_j = 10^{-\eta_j/b_a} - 10^{-\eta_j/b_c} \quad [1]$$

*Electrochemical Society Active Member

Key words: deposition, metals, overvoltage, polarization

where i_j is the current density, η_j the overvoltage (polarization), and i_{dep} the deposition current at the mixed potential (2). Equation [1] represents the Stern-Geary equation applied to the electroless metal deposition (i_{dep} replaced for i_{corr} in the original equation). We obtained that $b_a = 940$ and $b_c = 310$ mV. The Mansfeld's method was used for the anodic region only.

The rate of deposition, i_{dep} , was calculated from (a) the equation [1], (b) the Stern-Geary equation with the polarization resistance, R_p

$$i_{dep} = B/R_p \quad [2]$$

$$B = (b_a b_c) / 2.303 (b_a + b_c)$$

and (c) the Le Roy equation (5,6)

$$i_{dep} = \frac{\sum_{j=1}^n [i_j E_j]}{\sum_{j=1}^n [(E_j)^2]} \quad [3]$$

The rate of electroless copper deposition determined gravimetrically, for the used bath, was 1.59 mg/hr/cm^2 , or i_{dep} was 1.35 mA/cm^2 with the mixed potential $E_{mp} = -680 \text{ mV vs. SCE}$.

Equation [1] was used to calculate the rate i_{dep} from a pair of i_j - η_j values. The polarization resistance R_p , for equation [2], was calculated as the slope of the straight line obtained from the least squares fitting of data. R_p values for curves 1, 2c and 2a (Fig. 1) are 62.5, 57.3 and 81.9Ω respectively. The computer was used to calculate the rate from equation [3].

Rates of deposition calculated from equations [1-3] are shown in Table I.

The comparison of these, and other results, shows that the best results are obtained with the Le Roy equation applied to the polarization data in the anodic range.

Table I. Rate of deposition calculated from polarization data; (i_{dep}) grav. = 1.35 mA/cm^2

Eq.	i_{dep} , mA/cm ²		
	Fig. 1, Curve		
	1	2c	2a
[1]	1.38	1.60	1.40
[2]	1.62	1.76	1.24
[3]	1.63	1.62	1.38

For equation [1] rate was calculated from $\eta_j = 20 \text{ mV}$ for curves 1 and 2a and $\eta_j = -20 \text{ mV}$ for curve 2c.

It is interesting to note that here, in the metal deposition, as in the corrosion (9) the partial reaction which does not involve destruction or building of a crystal lattice of a metal gives better results.

CONCLUSIONS

Described experimental results show that the rate of electroless copper deposition can be determined from the polarization data in the vicinity of the mixed potential. The best results were obtained using Le Roy equation.

A subsequent paper will report more complete data and take into account other factors that determine the current-potential relationship, e.g. diffusion, multiple barrier (10), and others.

ACKNOWLEDGEMENTS

The authors would like to thank Dr. Karl Egerer, President of Kollmorgen Technologies and John McCormack, Director of Research PCK Technology Division for permission to publish this paper.

REFERENCES

1. C. Wagner and W. Traud Z. Elektrochem., 44, 391 (1938).
2. M. Stern and A. L. Geary, This Journal, 104, 56 (1957)
3. F. Mansfeld, *ibid*, 120, 515 (1973)
4. F. Mansfeld, Corrosion, 29, 397 (1973)
5. R. L. Le Roy, *ibid*, 31, 173 (1975)
6. R. L. Le Roy, This Journal, 124, 1006 (1977)
7. M. Paunovic, Plating, 55, 1161 (1968)
8. M. Paunovic, This Journal, in press
9. E. McCafferty and A. C. Zettlemoyer, J. Phys. Chem, 71, 2444 (1967)
10. B. Conway, Proc. Roy. Soc., 269 419 (1962)

Manuscript received Sept. 27, 1979.

Publication costs of this article were assisted by the Kollmorgen Corporation.

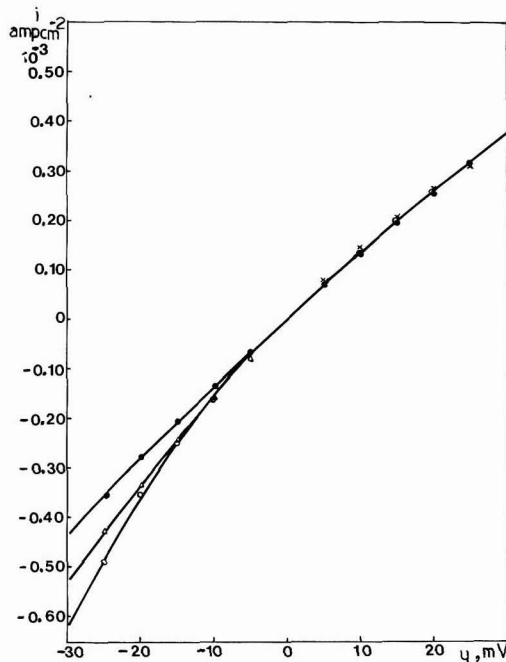


Fig. 1. Polarization data for electroless copper deposition.

- o Curve 1, initial potential $E_{mp} - 30$ mV
- x Curve 2a, initial potential E_{mp} , anodic sweep
- Δ Curve 2c, initial potential E_{mp} , cathodic sweep
- Curve drawn from Eq. [1] for $b_a = 940$ mV, $b_c = 310$ mV, and $i_{dep} = 1.35$ mA/cm²

The Calculation of Polarization Curves in the Vicinity of the Limiting Current

J. M. Bailey and I. M. Ritchie

Department of Physical and Inorganic Chemistry,
University of Western Australia, Nedlands, Western Australia 6009

When calculating the shape of a polarization curve in the vicinity of its limiting current, it has been assumed in a number of important papers and texts (1-3) that the exchange current density is independent of the polarization current.

In the particular case where the electrode reaction is the reduction of MZ^+ to M , and Tafel behaviour may be assumed, the relevant equations for the charge transfer and diffusion overpotentials (η_c and η_d) are

$$\eta_c = \{RT/(1-\alpha)zF\} \ln(i_0/i) \quad [1]$$

$$\eta_d = \{RT/zF\} \ln\{1-(i/i_d)\} \quad [2]$$

where the symbols have their usual meanings. The total overpotential is then assumed to be given by

$$\eta = \eta_c' + \eta_d \quad [3]$$

where η_c' is the charge transfer overpotential in the absence of any diffusion control.

However, when a slow transport step is present in the overall electrode reaction, the surface concentration C_s is no longer equal to the bulk concentration C_b , and so the exchange current density is no longer equal to i_0' , the value corresponding to pure charge transfer control. In general, the exchange current density is a function of the surface concentration

$$i_0 = \phi_i C_s^\alpha \quad [4]$$

where ϕ_i is the standard exchange current density. If the rate of the electrode reaction is partially governed by diffusion,

the surface concentration is given by

$$C_s = C_b \{1-(i/i_d)\} \quad [5]$$

Thus i_0 is a function of i and Eq. (3) is invalid.

Since correct treatments of the problem have already been given by Breiter and Clamroth (4) for the particular case of the hydrogen overvoltage, and by Vetter (5) for the general case, it seems likely that the assumption of the independence of i_0 on i has been made for convenience in the belief that the error incurred will not be large. The purpose of this note is to draw attention to the assumption before it becomes widely accepted since, as will be shown, the errors associated with it need not be negligible.

Firstly we note that

$$i_0' = \phi_i C_b^\alpha \quad [6]$$

Combining equations [1], [2], [4], [5] and [6] we get for the total overpotential

$$\eta = \eta_c + \eta_d = \eta_c' + \{\eta_d/(1-\alpha)\} \quad [7]$$

In Fig. 1 we compare a polarization curve which has been calculated according to Eq. [7] (solid line) with one which has been calculated according to Eq. [3] (dashed line). The parameters chosen for these calculations were the same as those used by Stern and Geary in their paper (1); viz $\alpha = 0.41$, $i_d = 5 \times 10^{-3} \text{ A cm}^{-2}$ and $i_0' = 1 \times 10^{-6} \text{ A cm}^{-2}$.

From Eqs. [3] and [7] it can be seen that the error in η , $\Delta\eta$, incurred by not allowing for the variation of i_0 is given by

$$\Delta\eta = \alpha\eta_d/(1-\alpha) \quad [8]$$

The magnitude of $\Delta\eta$ can be seen to increase with η_d and hence with the polarization current. For the values used in Fig. 1, the error incurred in assuming that

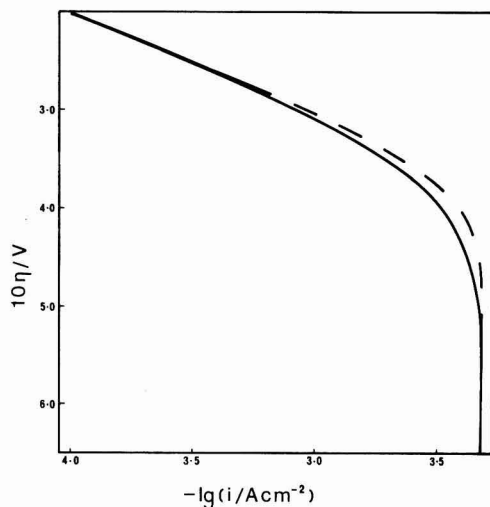
Key words: overpotential, diffusion, charge-transfer.

Fig. 1. A plot of the total overpotential against the logarithm of the current density assuming $\alpha = 0.41$ and $i_d = 5 \times 10^{-3} \text{ A cm}^{-2}$. The dotted line is from Stern and Geary (1) and assumes a value of i_0 of $10^{-6} \text{ A cm}^{-2}$. The solid line is the corresponding plot allowing for the variation of i_0 with i .

i_0 is independent of i is about 70% of η_d . The maximum error in the current, which occurs near the knee of the curve, is about 10%. These errors, which increase with increasing α , are sufficiently large to warrant the use of equation [7] rather than equation [3].

REFERENCES

1. M. Stern and A. L. Geary, This Journal, **104**, 56 (1957).
2. J. O'M. Bockris and A. K. N. Reddy, "Modern Electrochemistry," p 1371, Plenum Press, New York (1973).
3. J. O'M. Bockris and S. Srinivasan, "Fuel Cells: Their Electrochemistry," p. 181, McGraw-Hill Book Co., New York (1969).
4. M. Breiter and R. Clamroth, Z. Elektrochem, **58**, 483 (1954).
5. K. J. Vetter, "Electrochemical Kinetics: Theoretical Aspects," p 342, Academic Press, New York (1967).



Manuscript submitted Sept. 19, 1978;
revised manuscript received March 22, 1979.

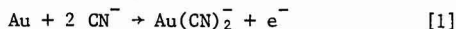
Electron Stoichiometry of Anodic Dissolution of Gold in Aqueous Alkaline Cyanide

D. W. Kirk,* F. R. Foulkes,** and W. F. Graydon

*Department of Chemical Engineering and Applied Chemistry,
University of Toronto, Toronto, Ontario, Canada M5S 1A4*

In an earlier paper (1), it was shown by the use of slow anodic potential sweep measurements that the electrochemical dissolution of gold in de-oxygenated aqueous alkaline cyanide solutions was characterized by the presence of three current peaks. These peaks were shown to correspond to three potential regions of enhanced gold dissolution rates. These current peaks also had been observed by other workers (2,3,4,5); but, no attempts had been made to determine electron stoichiometry, which was assumed to be 1 or 2, depending on the peak.

By means of weight loss measurements at fixed potentials it was concluded (1) that the reactions in the three peak regions corresponded to a single overall dissolution process, namely



Coulometric analyses indicated that the values of n , the number of moles of electrons passed per mole of gold dissolved, were 0.85, 0.95, and 1.05 for peaks 1, 2, and 3, respectively.

In order to explain the fact that the observed n values for peaks 1 and 2 were less than unity, it was suggested that, in addition to the main electrochemical reaction [1], some concurrent chemical dissolution process also may have been taking place, which tended to lower the apparent values of n . In the case of peak 3, it was readily shown that the n value was slightly greater than unity on account of the onset of some gold oxidation to gold (III) oxide, which begins to form at potentials just anodic to the peak potential for peak 3.

Although chemical gold dissolution in de-oxygenated alkaline cyanide has not previously been reported, such dissolution would be expected to proceed independently of electrochemical dissolution provided that the gold substrate be neither under cathodic protection nor protected by an impervious anodic oxide film. For strict additivity of the two dissolution processes, the absence

of competition for sites also is required. Such additivity between a chemical and electrochemical process has been long recognized in the electrochemical behaviour of zinc. In the present work with gold, anodic currents begin to flow at potentials more positive than about -0.90 V vs S.C.E.* Since all three peaks occur at potentials more positive than this, cathodic protection can be ruled out. Likewise, interference from the formation of gold (III) oxide films would be expected only at potentials more positive than the thermodynamic formation potential of gold (III) oxide, which occurs in the vicinity of peak 3. If the chemical dissolution process is independent of the electrochemical process, and is the only additional secondary process, subtraction of the chemical weight loss for the appropriate time, concentration, and surface area from the total measured weight loss during the electrochemical measurement should yield an n value reflecting only the electrochemical dissolution.

Chemical dissolution rates were determined by measuring the weight losses of gold foil electrodes (99.99% purity) suspended in alkaline cyanide electrolyte solutions. The gold foil was given the same electrochemical cleaning pretreatment as that described previously for the electrochemical dissolution experiments (1). The solutions were prepared from analytical grade potassium hydroxide and potassium cyanide, using doubly distilled water. De-oxygenation was effected by continuous bubbling of oxygen-free nitrogen. To test for complete removal of oxygen, additional experiments were carried out using oxygen-free nitrogen which had been scrubbed with a solution of vanadous chloride. No significant differences in the weight losses were observed using this procedure.

The following sample calculation will clarify the method used to compute the chemically corrected n values: In 0.10 M KOH + 0.10 M KCN solution

* All potentials are against S.C.E.

*Electrochemical Society Student Member.

**Electrochemical Society Active Member.

Key words: metal, anode, potential, dissolution.

at -0.680 V the passage of 0.07258 C ($=7.522 \cdot 10^{-7}$ F) over a period of 5.00 minutes resulted in a weight loss of $1.80 \cdot 10^{-4}$ g from a 2.73 cm² gold foil electrode. The rate of chemical dissolution under the same conditions of temperature and concentration was found to be $4.00 \cdot 10^{-8}$ g \cdot s⁻¹ \cdot cm⁻², which corresponds to a chemical weight loss of $3.28 \cdot 10^{-5}$ g for an electrode of the same area and dissolution time. Therefore the corrected electrochemical weight loss was $(18.0-3.28) \times 10^{-5} = 14.72 \cdot 10^{-5}$ g or $7.473 \cdot 10^{-7}$ mol of gold, and the corrected n value is $7.552 \cdot 10^{-7} \text{ F} \div 7.473 \cdot 10^{-7} \text{ mol} = 1.01 \text{ F} \cdot \text{mol}^{-1}$. The uncorrected value is $0.823 \text{ F} \cdot \text{mol}^{-1}$. Because the chemical dissolution rate was found to be a function of cyanide concentration, hydroxide concentration, temperature, and the surface state of the gold, the chemical correction for each electrochemical datum was matched with respect to concentrations and temperature.

The gold dissolution data with and without the chemical weight loss corrections are presented in Table I. Approximately fifty measurements were made in each of the three peak regions to determine average n values. Data obtained at potentials more positive than the reversible potential for gold (III) oxide formation (about $+0.30$ V) were not used in determining the average n value for peak 3 on account of interference from the formation of gold (III) oxide as discussed above. The results clearly show that $n=1$ for the three peak regions, and that the chemical dissolution accounts for nearly all the deviation from unity previously observed in the electron stoichiometry. There is no significant difference between the mean value of n calculated for each peak region, and an overall value of 1.03 ± 0.02 is obtained at the 95% confidence level. The slightly positive bias which still remains (Table I) is attributed to slight differences in the nature of the gold surface in chemical and electrochemical dissolution experiments.

It can be concluded that the electrochemical dissolution of gold in alkaline cyanide is clearly a one electron transfer reaction throughout the potential region -0.90 to $+0.30$ V. Furthermore, throughout this potential domain only a one electron transfer electrochemical process and chemical dissolution occur. The chemical process may occur as a result of trace oxygen contamination (6): $2\text{Au} + 4\text{CN}^- + \frac{1}{2}\text{O}_2 + \text{H}_2\text{O} \rightarrow 2\text{Au}(\text{CN})_2^- + 2\text{OH}^-$ [2] Alternatively, an oxygen-free process such as the following (1) may be involved: $\text{Au} + \text{HCN} + \text{CN}^- \rightarrow \frac{1}{2}\text{H}_2 + \text{Au}(\text{CN})_2^-$ [3] A more detailed study of this process is currently underway.

Publication costs of this article were assisted by the University of Toronto.

Table I
Number of Faradays per mole of
gold dissolved in aqueous alkaline
cyanide. Temperature = 23.5°C

Potential (V vs S.C.E.)	Faradays per mole of gold dissolved	
	Without Chemical Correction*	With Chemical Correction*
Peak 1		
-0.90	0.94 ± 0.36	1.02 ± 1.9
-0.80	0.80 ± 0.60	1.10 ± 2.4
-0.75	0.89 ± 0.35	0.96 ± 0.37
-0.70	0.79 ± 0.13	1.05 ± 0.40
-0.68	0.82 ± 0.05	0.97 ± 0.40
-0.66	0.81 ± 0.72	0.99 ± 0.89
-0.65	0.85 ± 0.11	1.01 ± 0.10
-0.63	0.87 ± 0.17	1.10 ± 0.21
-0.60	0.92 ± 0.20	1.01 ± 0.23
Average	$0.85 \pm 0.02^{**}$	$1.03 \pm 0.06^{**}$
Peak 2		
-0.1	0.91 ± 0.21	1.02 ± 0.10
0	0.94 ± 0.14	1.01 ± 0.08
+0.05	0.95 ± 0.05	0.96 ± 0.10
+0.10	0.98 ± 0.04	1.16 ± 0.18
+0.15	0.95 ± 1.52	1.29 ± 2.2
Average	$0.95 \pm 0.02^{**}$	1.01 ± 0.03
Peak 3		
+0.20	1.01 ± 0.07	1.02 ± 0.07
+0.25	1.13 ± 0.72	1.28 ± 0.37
+0.30	1.03 ± 0.06	1.04 ± 0.06
Average	$1.04 \pm 0.04^{**}$	$1.07 \pm 0.06^{**}$
Above E° for Au (III)		
+0.30	1.04 ± 0.11	-
+0.38	1.07 ± 0.07	-
+0.40	1.45 ± 0.17	-
+0.50	3.11	-
+0.60	2.65	-
+0.80	3.10	-

* 95% confidence limits

** 95% confidence limits based on all measurements in peak range.

ACKNOWLEDGMENT

Financial assistance from the National Research Council of Canada is gratefully acknowledged.

REFERENCES

1. D.W. Kirk, F.R. Foulkes, and W.F. Graydon J. Electrochem. Soc., **125**, 1436 (1978).
 2. K.J. Cathro and D.F.A. Koch, *ibid*, **111**, 1416, (1964).
 3. D.M. MacArthur, *ibid*, **119**, 672 (1972).
 4. J.D.E. McIntyre and W.F. Peck, *ibid*, **123**, 1800 (1976).
 5. E.T. Eisenmann, *ibid*, **125**, 717 (1978).
 6. F. Habashi, Bureau of Mines and Geology, State of Montana, Bulletin 59, (1967).
- Manuscript submitted May 15, 1979; revised manuscript received July 30, 1979.



The Effects of Surface Additives on the Performance of Lithium-Aluminum Electrodes

W. Cheng¹

Department of Chemical Engineering, Stanford University, Stanford, California 94305

(1979 F. M. Becket Memorial Award Report)

ABSTRACT

Investigations of the effect of surface additives on the performance of lithium-aluminum alloy electrodes were conducted. Predeposition of 4.48×10^{-7} mole/cm² of indium or magnesium on aluminum wire electrodes led to improved lithium utilization during early cycles but lower capacity retention. The higher lithium utilization was attributed to the more dendritic surfaces formed by the addition of In and Mg. Upon discharge, the higher lithium extraction caused greater depletion of the β -phase LiAl, which held the electrode radial structure together. This in turn led to faster electrode attrition and lower capacity retention. Results of early cycles confirmed the importance of surface effects.

Lithium-aluminum alloy electrodes have shown a great deal of promise for meeting the performance requirements of negative electrodes in molten salt secondary batteries. The lithium-aluminum phase diagram at 423°C (Fig. 1) (1) shows that from 0 to 9.2 atomic percent (a/o) lithium, a solid solution, the α -phase exists; the β -phase is from 46.8 to 56 a/o lithium, and the γ -phase is from 60.3 to 61.7 a/o lithium. In the two-phase region between α and β , the potential is a constant 297 mV anodic to (more positive than) pure lithium. The large concentration range ensures high power density and a steady potential for the LiAl anode. In an effort to improve electrode performance, ternary systems are being investigated. Melendres (2) has shown that incorporation of 5-19 a/o magnesium into the LiAl electrode, led to a marked morphological change which improved the structural stability of the electrodes upon cycling. Visser (3) tested the cycle lives of engineering-type LiAl electrodes with various metal additives, tin, lead, copper, and indium; while tin, lead, and copper showed no improvement, the electrode with 3.9 weight percent (w/o) indium showed superior lithium retention capacity over a large number of cycles. Photomicrographic examination of the electrodes showed the LiAlIn alloy to be much more dendritic, and it was postulated that this led to the improved retention. The purpose of this investigation was to test the hypothesis that structural improvement by the incorporation of magnesium and indium is indeed a surface effect. This has been done by testing LiAl electrodes with the ternary component on only the electrode surface.

Experimental

Lithium chloride (99% minimum assay) and potassium chloride (99.8 minimum assay), obtained from BDH Chemicals Limited, Poole, Dorset, were used to prepare the LiCl-KCl eutectic (melting point 352°C) (4). The mixture of 59 mole percent (m/o) LiCl and 41 m/o KCl was heated under vacuum for several

days to remove the water of hydration. The anhydrous mixture was then melted, and constant potential electrolysis at 0.2V anodic of α/β LiAl was carried out to remove inorganic impurities, using an aluminum cathode and a graphite anode.

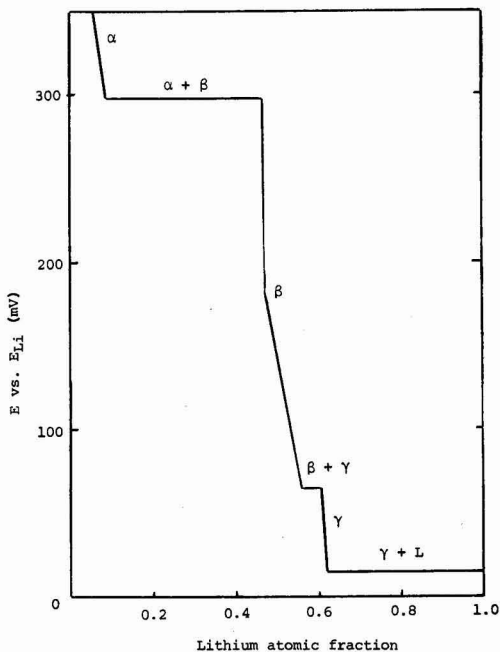


Fig. 1. Potential-composition diagram for the lithium-aluminum system at 423°C (1).

¹ Research and study conducted under the supervision of Professor Douglas Inman at Imperial College, London.

The additives, MgCl_2 (Hopkins & Williams Limited, Essex, England) and InCl_3 (BDH Chemicals Limited) were dehydrolized by first reacting with 2,2 dimethoxypropane (Aldrich Chemicals Company) followed by heating under vacuum (5).

To minimize contact with air, all cell assembling operations were performed inside a nitrogen dry box, and an argon blanket filled the cell during experiments. A simplified schematic of the cell is shown in Fig. 2. It consists of a counterelectrode of α/β LiAl, a reference electrode of α/β LiAl, electrochemically prepared, and a working electrode. (Typically, three working electrodes were used in each experiment.) The counterelectrode was prepared by packing lithium metal (99% purity, BDH Chemicals) into an aluminum shell, 1/2 in. OD, 1 in. long, and placing the shell in contact with molten LiCl-KCl eutectic. Lithium, being a liquid at this temperature, readily alloyed with the aluminum. 99.9% pure aluminum, diameter 0.74 mm (BDH Chemicals) was used for the working electrodes and as starting material for the reference electrode.

In all experiments the working electrode was dipped 1 cm into the melt. The level was indicated by a notch in the wire. A small inner beaker was used to contain the melt in which the additive (InCl_3 or MgCl_2) was dissolved. A thin glass membrane, permeable to lithium ions, but not to indium or magnesium ions, separated the inner beaker from the main beaker. The emf's of In(III)/In(O) and Mg(II)/Mg(O) were respectively 2.0V and 0.42V anodic of α/β LiAl (4). It was therefore possible to predeposit Mg and In on the aluminum working electrodes without forming LiAl alloys in the process. Predeposition of magnesium was carried out at +0.2V of α/β LiAl, and that of indium was at +0.5V of α/β LiAl. A Wenking control amplifier, Model PCA 72L, was used for constant potential electrolysis. The amount of additives deposited was measured by a Bentham Hi-Tek Gated Integrator and DVM. After predeposition, the working electrodes were transferred to the main beaker (again 1 cm in the melt) for cycling tests.

The melt temperature was maintained at about 420°C. The electrodes were subjected to repeated galvanostatic (constant current) charging and discharging at a current density of 215 mA/cm². The cut-off voltages were -0.15 (of α/β LiAl) on charging, and +0.15 (of α/β LiAl) on discharging. The current was supplied by an Advance regulated d-c power source, Type PP1. When the voltage reached the prescribed cut-off point, the polarity was manually reversed. A Servoscribe chart recorder Type RE 511.20 (Goerz Electro) was used to record the potential variation.

Results and Discussion

Figure 3 shows the charging and discharging curves of an initially pure aluminum electrode. On the first charge, simple calculation showed that the entire electrode was completely converted to β -phase LiAl. This meant that at the applied current density of 215 mA/cm², the rate of formation of β -phase LiAl was not controlled either by slow diffusion or reaction kinetics. On the contrary, the lithium utilization upon discharging was not 100%; James (6) suggested that this was due to diffusion limitations. Similar first cycle curves were observed with electrodes that had been predeposited with additives.

Figure 4 shows the charging and discharging curves for the three electrodes: (a) initially pure aluminum, (b) pure aluminum initially charged with 1.04×10^{-7} moles of magnesium (compared to 4.3×10^{-4} moles of aluminum in the entire electrode), and (c) pure aluminum initially charged with 1.04×10^{-7} moles of indium. Although the amount of each additive was small, its concentration on the surface could be quite

² The current density is based on the initial external electrode area. Since the electrode porosity changed with each cycle, it was not possible to know the exact surface area.

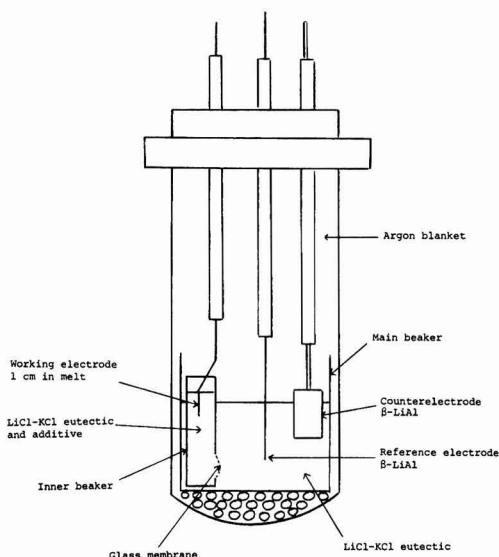


Fig. 2. Schematic of the cell

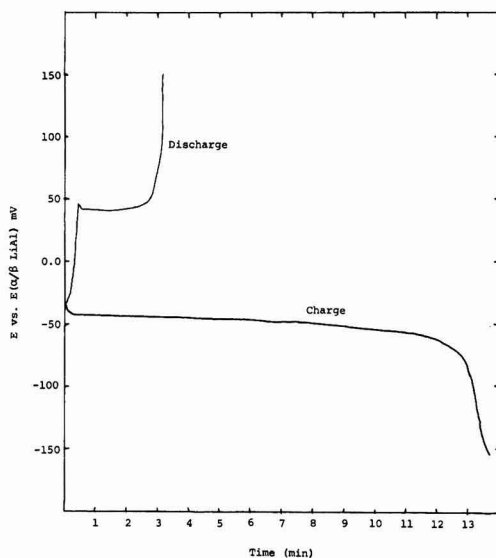


Fig. 3. First cycle charging and discharging curves of initially pure Al electrode.

high. Both the addition of Mg and In led to higher charging and discharging overpotentials. However, the ternary electrodes also had higher lithium utilizations—utilization being defined as the ratio of the amount of lithium discharged to the theoretical amount upon complete conversion from β -LiAl to α -LiAl. Examination of the electrodes at the end of the cycle tests showed both the LiAlMg and LiAlIn electrodes to have rougher surfaces than the LiAl electrode. Thus the higher surface area, accompanying the more (micro-) dendritic electrode could have explained the higher utilization of the ternary electrodes. Also evident from Fig. 4 is the presence of additional plateaus on the discharge curves of LiAlMg and LiAlIn systems, indicating the formation of extra phases involving Mg and

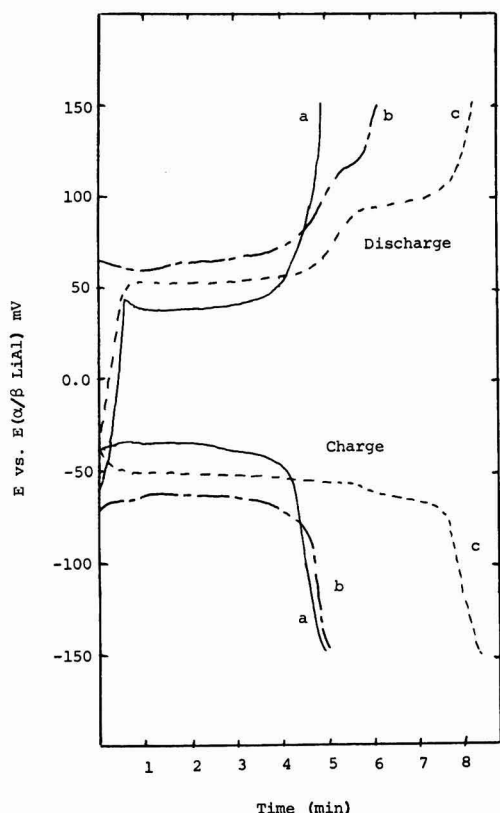


Fig. 4. Charging and discharging behavior of (a) initially pure Al electrodes, (b) electrode predeposited with 1.04×10^{-7} moles Mg, (c) electrode predeposited with 1.04×10^{-7} moles In.

In. No attempts were made to identify the composition of the new phases. Melendres (2) has identified the presence of LiMgAl_2 and Li_2AlMg compounds in his work. The extra plateaus gradually disappeared with repeated cycling. This was probably due to the dilution of the additives on the surface, either by migration into the electrode interior, or dissolution into the melt.

A plot of lithium utilization vs. the number of cycles is shown in Fig. 5. In the first few cycles the utilization rose to a maximum, reflecting the favorable changes in the electrode, i.e., increasing porosity. The utilization then declined with each additional cycle. The reason for the decline was not clear; it could be due to the loss of electrode material by the breaking of the dendrites, or to the accumulation of impurities such as oxides on the surface, thereby reducing the available aluminum.³ More work is needed to understand the decaying mechanism. As can be seen, the LiAlIn electrode exhibited the highest utilization in the first 18 cycles. The LiAlMg electrode had greater utilization than the LiAl for up to the 15th cycle. However, the utilization of the ternary electrodes decayed more rapidly than that of the LiAl electrode which remained nearly constant up to about the 20th cycle.

The higher capacity retention of the LiAl electrode may well be due to its lower utilization. As explained by Melendres (7), the radial structure of the electrode

³ Although argon was constantly circulated around the melt, the cell was not completely leak-proof and, in time, oxides could have accumulated.

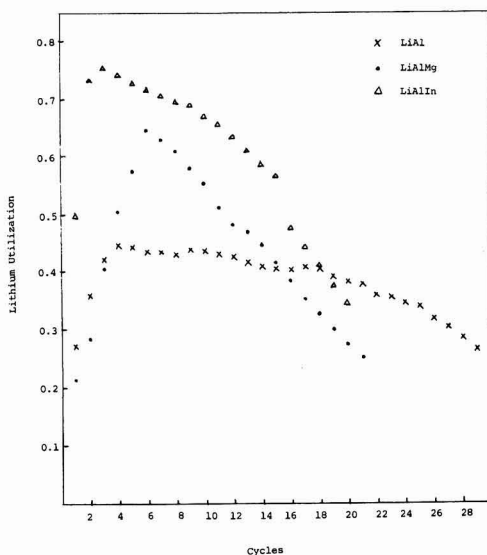


Fig. 5. Lithium utility as a function of the number of charge/discharge cycles.

is held together by the β -phase, without which the electrode would simply fall apart. It follows then that the more lithium extracted during the discharge, the weaker the electrode becomes and therefore the faster it will erode. This form of attrition would be greatly reduced by the use of engineering electrodes (3) in which the electrode material is wrapped in a zirconia fabric.

The long-term effect of the surface additives could not be accurately assessed because it was not certain that the additives remained on the surface throughout so many cycles. It is more likely that the additives migrated into the bulk of the electrode, or dissolved in the melt, as shown by the gradual disappearance of the additional discharge plateaus. Electrodes made entirely from LiAlIn and LiAlMg alloys would be more suitable for long-term tests. However, the results of early cycles confirmed that surface modification by the incorporation of Mg and In improved electrode performance.

Conclusion

Predeposition of 4.48×10^{-7} mole/cm² of indium and magnesium on aluminum wire electrodes led to improved lithium utilization during early cycles. Examination of the electrodes after the test showed the ternary electrodes to be more dendritic. The higher surface area was believed to be the key to the improvement of electrode performance. The retention capacity of ternary electrodes was lower than the binary LiAl . This might be caused by the higher utilization since higher lithium extraction depleted the β -phase LiAl which held the electrode radial structure together.

Engineering electrodes which utilize materials such as zirconia fabric to contain the electrode material would be more suitable to assess the long-term performance of ternary electrodes. However, the short-term results from the wire electrodes indicate that the improved electrode performance resulting from the addition of In and Mg is mainly a surface effect.

Acknowledgments

The author would like to express his sincere gratitude to the F. M. Becket Committee and the Electrochemical Society for providing the scholarship and

thus the opportunity for this work, and to Dr. D. Inman for providing the facilities and accommodation at Imperial College. I am especially grateful to Mr. Y. S. Fung for allowing me to use his apparatus and for his invaluable supervision.

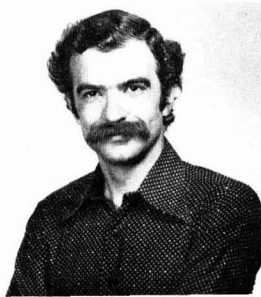
REFERENCES

1. C. J. Wen, W. Weppner, B. A. Boukamp, and R. A. Huggins, *This Journal*, **126**, 2258 (1979).
2. C. A. Melendres, S. Siegel, and J. Settle, *ibid.*, **125**, 1886 (1978).
3. D. R. Visser, K. E. Anderson, and W. R. Frost, Abstract 42, p. 115, The Electrochemical Society Extended Abstracts, Las Vegas, Nevada, Oct. 17-22, 1976.
4. J. A. Plambeck, in "Encyclopedia of the Elements, Vol. X, Fused Salt Systems," A. J. Bard, Editor, Marcel Dekker, Inc., New York (1976).
5. F. A. Cotton and G. Wilkinson, "Advanced Inorganic Chemistry," 3rd ed., p. 465, John Wiley & Son Inc., New York (1972).
6. S. D. James, *Electrochim. Acta*, **21**, 159 (1976).
7. C. A. Melendres and C. C. Sy, *This Journal*, **125**, 727 (1978).

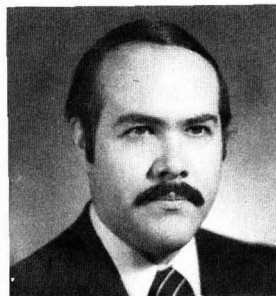
Young Authors' Awards for 1978



C.-H. Tsang



D. A. Antoniadis



A. G. Gonzalez

The winners of the Young Authors' Prizes were announced at the Awards and Recognition Session held on Tuesday afternoon, October 26, during the Los Angeles, California, Meeting of The Electrochemical Society.

Chi-Hwa Tsang, currently at the University of Pennsylvania, won \$200 for his paper "Mass Transfer to an Impinging Jet Electrode," which appeared in the September 1978 issue of the *Journal*.

Dimitri A. Antoniadis, Assistant Professor at M.I.T., and Adalberto G. Gonzalez, Professor at the Metropolitan University of Mexico, each won \$200 for their paper entitled "Boron in Near-Intrinsic <100> and <111> Silicon under Inert and Oxidizing Ambients—Diffusion and Segregation," which appeared in the May 1978 issue of the *Journal*.

Mr. Tsang is a native of Taiwan, China. He received his B.S.E. degree in chemical engineering from National Cheng-Kung University at Tainan, Taiwan in 1974 and an M.S. in chemical engineering from Clarkson Col-

lege of Technology in 1978. Mr. Tsang is currently working for his Ph.D. in the Laboratory for Research on the Structure of Matter and the Department of Materials Science and Engineering at the University of Pennsylvania. Mr. Tsang's paper is a result of his M.S. thesis research under Professor D.T. Chin.

While Mr. Tsang has a continued interest in electrode processes/kinetics, his current Ph.D. research is in investigating the catalytic properties of transition metal-noble metal alloys.

Dr. Antoniadis was born in Athens, Greece. He received his B.S. in physics from the University of Athens in 1970 and his Ph.D. in electrical engineering from Stanford University in 1976, where he remained as Research Associate and Instructor. Since 1978 he has been an Assistant Professor at M.I.T. He is a member of The Electrochemical Society and of IEEE.

Dr. Antoniadis' research interests are in the area of characterization, modeling, and numerical simulation of semi-

conductor device fabrication and operation. He is a primary author of the computer program SUPREM (Stanford University Process Engineering Models).

Dr. Gonzalez was born in Tijuana, Mexico. He received his B.S. degree in physics from the National University of Mexico in 1971, and the M.S.E.E. degree from Stanford University in 1972. He finished his Ph.D. research work at Stanford in 1977. Dr. Gonzalez joined the Department of Electronic Engineering at the Metropolitan University of Mexico, Mexico City, in 1978. He is currently working as a full-time professor and is in charge of the Mini and Microcomputer Laboratory. He is presently directing a joint government/industry sponsored project on the development of microcomputer-controlled communications equipment.

Dr. Gonzalez's general research interests include the development of hardware and software for industrial applications, using microprocessors. He has a very strong interest in bipolar and MOS transistor simulation and optimization.

Nominations Invited for Edward Goodrich Acheson Award and Prize

The Edward Goodrich Acheson Award and Prize was established in 1928 to recognize a person who, in the judgment of the directors of the Society, has made contributions to the advancement of any of the objects, purposes, or activities of The Electrochemical Society—as to merit the award. Such contributions may consist of, but shall not be limited to, (a) a discovery pertaining to electrochemistry, electro-metallurgy, or electrothermics, (b) an invention of a plan, process, or device, or research evidenced by a paper embodying information useful, valuable, or significant in the theory or practice of electrochemistry, electrometallurgy, or electrothermics, and/or (c) distinguished services rendered to the Society.

The Award consists of a gold medal, a bronze replica, and two thousand

dollars (\$2000). The following have received the Award:

1929—Edward G. Acheson
1931—Edwin F. Northrup
1933—Colin Garfield Fink
1935—Frank J. Tone
1937—Frederick M. Becket
1939—Francis C. Frary
1942—Charles F. Burgess
1944—William Blum
1946—H. Jermain Creighton
1948—Duncan A. MacInnes
1951—George W. Vinal
1953—J. W. Marden
1954—George W. Heise
1956—Robert M. Burns
1958—William J. Kroll
1960—Henry B. Linford
1962—C. L. Faust
1964—Earl A. Gulbransen

1966—Warren C. Vosburgh
1968—Francis L. LaQue
1970—Samuel Ruben
1972—Charles W. Tobias
1974—Cecil V. King
1976—N. Bruce Hannay
1978—David A. Vermilyea

Nominations for the next Award to be presented at the Fall Meeting of the Society in 1980 in Hollywood, Florida, are invited. Nominees do not have to be members of the Society to be considered. Furthermore, there are no distinctions, restrictions, or reservations regarding age, sex, race, citizenship, or place of origin or residence.

Please send nominations with supporting documents to Fritz G. Will, General Electric, R&D Center, P.O. Box 8, Schenectady, New York 12301 by March 1, 1980.

ECS Membership Statistics

The following three tables give a breakdown of membership as of Oct. 1, 1979.

Table I. ECS Membership by Sections

Section	1977	1978	1979
Boston	287	291	374
Chicago	214	237	265
Cleveland	140	144	154
Columbus	84	82	91
Detroit	127	113	138
Indianapolis	39	33	30
Metropolitan New York	667	639	687
Midland	28	29	34
National Capital Area	182	167	175
Niagara Falls	79	84	151
North Texas	149	147	178
Ontario-Quebec	187	158	163
Pacific Northwest	67	93	102
Philadelphia	222	217	229
Pittsburgh	132	122	149
Rocky Mountain	67	89	106
San Francisco	391	425	495
South Texas	69	56	45
Southern California-Nevada	286	279	304
Non-Section	882	1199	1028
Subtotal—In Good Standing	4299	4604	4898
Delinquents (Active and Student)	325	323	362
TOTAL	4624	4927	5260

Table II. ECS Membership by Divisions*

Division	1977	1978	1979
Battery	1317	1370	1478
Corrosion	1287	1311	1309
Dielectrics and Insulation	962	1020	1025
Electrodeposition	1179	1177	1161
Electronics	2398	2375	2363
General Materials and Processes	1548	1523	1394
Semiconductors	1777	1788	1948
Luminescence	554	511	460
Electrothermics and Metallurgy	863	873	804
Industrial Electrolytic	693	698	712
Organic and Biological Electrochemistry	599	625	613
Physical Electrochemistry	1550	1618	1647
Energy Technology Group	—	205	813

* A member may be included in the count of several Divisions.

Table III. ECS Membership by Grade

	1977	1978	1979	1979/1978 % Increase
Active	3701	3958	4208	6.32
Member Reps. of Contributing Companies	135	127	142	11.81
Emeritus	114	116	117	.86
Life	47	49	51	4.08
Honorary	9	13	14	7.69
Subtotal Active in Good Standing	4006	4263	4532	6.31
Delinquent	258	267	312	16.85
Total Active on Record	4264	4530	4844	6.93
Students and Associates	293	341	366	7.33
Delinquent	67	56	50	(10.71)
Total Students and Associates	360	397	416	4.79
Total Individual Members	4624	4927	5260	6.76

NEW MEMBERS

It is a pleasure to announce the following new members of The Electrochemical Society as recommended by the Admissions Committee and approved by the Board of Directors in October 1979.

Active Members

Auciello, O., Downsview, Ont., Canada
 Buoncristiani, A. M., Newport News, Va.
 Caro, P., Meudon, France
 Clark, K. G., Riddings, Derby, England
 Coury, A. G., St. Paul, Mn.
 Douglas, D. L., Palo Alto, Ca.
 Ess, J. M., Dallas, Tx.
 Feit, E. D., N. Indianantic, Fl.
 Gibney, A., Monroeville, Pa.
 Griffin, T. E., Bethesda, Md.
 Holmstrom, B., Goteborg, Sweden
 Lapham, J., Westford, Ma.
 Mehta, J. R., St. Paul, Mn.
 Miller, R. J., Hopewell Junction, N.Y.
 Morrison, R. P., Wayne, Pa.
 Nicolet, M. A., Pasadena, Ca.
 Nordemann, J. M., Montevideo, Uruguay
 Perrymore, L., Dallas, Tx.
 Reddy, S. N. S., Naperville, Ill.
 Shia, G. A., Bridgeport, Pa.
 Stiefbold, D. R., Chandler, Az.
 Ulatowski, C. P., Framingham, Ma.
 Washburn, J. W., Tulsa, Ok.
 Westbrook, P. M., Mesquite, Tx.
 White, H. W., Columbia, Mo.
 Widder, G. A., Dallas, Tx.
 Yeh, H. L., Suffern, N.Y.

Student Members

Batts, A. L., Evanston, Ill.
 Bliss, D. F., Watertown, Ma.
 Casselberry, R. L., Jr., Newark, De.
 Chan, W. K., Stony Brook, N.Y.
 Chopelas, A., Los Angeles, Ca.
 Deininger, P., College Station, Tx.
 Free, W. M., Newark, De.
 Gotz, R., Lausanne, Switzerland
 Gross, K. T., Pearl Harbor, Hi.
 Landauer, A., Stanford, Ca.
 Lester, P. A., University Park, Pa.
 Manchanda, L., New Delhi, India
 McIntyre, G. L., Newark, De.
 Meier, T. J., Cincinnati, Oh.
 Parks, J., Golden, Co.
 Sriram, S., Cincinnati, Oh.
 Tellefson, K., Ottawa, Ont., Canada
 Yin, S.-Y., Los Angeles, Ca.

Reinstatement

O'Malley, R. F., Chestnut Hill, Ma.

Member Representatives

Barlow, G. A., Molycorp, Inc.
 Heym, G. E., Marston Excelsior (Bermuda) Ltd.
 McIlvaine, B., Philips Laboratories

Notice to Subscribers

Your subscription to the JOURNAL OF THE ELECTROCHEMICAL SOCIETY will expire on December 31, 1979. Avoid missing any issue. A subscription renewal card invoice and return envelope have been mailed to all subscribers. To insure proper handling, mail your check for \$80.00 with the completed card invoice in the envelope provided. [Subscribers located outside the Continental United States and Canada must add \$5.00 to the subscription price for postage (\$85.00), and payment must be made by money order or check in U.S. Funds.]

NEWS ITEM

Third International Meeting
on Solid Electrolytes

The Third International Meeting on Solid Electrolytes, "Solid State Ionics and Galvanic Cells," will be held Sept. 15-19, 1980 at the Sasakawa Hall, Mita, Minato-ku, Tokyo, Japan.

The meeting will deal with experimental, theoretical, and applied aspects of solid ion conductors as well as mixed ionic-electronic conductors.

For further details, contact the meeting chairman, Dr. T. Takahashi, Department of Applied Chemistry, Faculty of Engineering, Nagoya University, Chikusa-ku, Nagoya 464, Japan.

ADVERTISERS' INDEX

ASI, Inc.	494C
IBM Corp.	492C
NCR	493C
Princeton Applied Research Corp.	496C
Plenum	495C
Univ. of Pennsylvania	490C
Westinghouse	491C

Young Authors' Awards for 1978 ..	487C
Acheson Award and Prize	487C
ECS Membership Statistics	488C
New Members	488C
Notice to Subscribers	488C
News Item	489C
Position Wanted	489C
Nominations for ECS Award in Solid State Science and Technology	489C
ECS Summer Fellowship Awards to be Granted	489C
Positions Available	490C
New Books	490C
Book Reviews	490C-493C
Call for Papers—Hollywood, Florida, Meeting	503C-508C

POSITION WANTED

Please address replies to the box number shown, c/o The Electrochemical Society, Inc., P.O. Box 2071, Princeton, N. J. 08540.

Doctorate in Electroanalytical Chemistry—Desires position in industry or academic institution. Experienced in polarography, chronopotentiometry cyclic voltammetry, anodic stripping voltammetry, etc. Have also worked on corrosion inhibitors by the galvanostatic method. Reply Box C-214.

Nominations Solicited for Fifth Electrochemical
Society Award in Solid State Science
and Technology

Nominations are solicited by the Honors and Awards Committee for the Solid State Science and Technology Award. Since establishment of the biennial award in 1972, the recipients have been the following:

1973 William G. Pfann	1977 Robert N. Hall
1975 Harry C. Gatos	1979 Morton B. Panish

The next award will be presented at the Spring 1981 Meeting of the Society.

The recipient of this Award must have made distinguished contributions to the field of solid state science. He need not be a member of the Society, and there are no restrictions regarding age, sex, race, citizenship, or place of origin.

The Award consists of a silver medal together with a bronze replica and the sum of \$1500. The recipient will deliver an address to the Society on a subject related to the contributions for which the Award is presented.

This is one of the Society's most prestigious awards, and we urge all members of the Society to give serious consideration to possible candidates. Please send nominations, with supporting documents, to Don W. Shaw, Texas Instruments, Inc., P.O. Box 225936, MS-145, Dallas, Texas 75265. The supporting documents need not be lengthy, and may consist of a half-page description of the contributions made, a half-page biography, and a list of publications of the candidate. If the paper titles are not included in the publication list, please identify the most outstanding papers. If the Committee needs more information, the nominator will be contacted. If possible, please submit the nominations by March 1, 1980 to facilitate consideration by the Committee. Nominations close at the opening of the Spring 1980 Meeting.

Summer Fellowship Award Program
of The Electrochemical Society

The Board of Directors of The Electrochemical Society has voted to allocate \$4,500 for summer fellowships in 1980. The Award subcommittee shall have the discretion of deciding the number of recipients and the amount granted to each, within the limits of the appropriation.

The purpose of the award is to assist a student in continuing his/her graduate work during the summer months in a field of interest to The Electrochemical Society. According to the rules for the Society Summer Fellowship Program, if one award is given, it shall be called the Edward G. Weston Fellowship Award; if two awards are given, the second one shall be designated the Colin Garfield Fink Fellowship Award; if more than two are given, the third award shall be called the Joseph W. Richards Fellowship Award.

Candidate's qualifications: "The award shall be made without regard to sex, citizenship, race, or financial need. It shall be made to a graduate student pursuing work between the degree of B.S. and Ph.D., in a college or university in the United States or Canada, and who will continue their studies after the summer period. A previous holder of an award is eligible for reappointment."

Qualified graduate students are invited to apply for these fellowship awards. Applicants must complete an application form and supply the following information:

1. A brief statement of educational objectives.
2. A brief statement of the thesis research problem including objectives, work already accomplished, and work planned for the summer of 1980.
3. A transcript of undergraduate and graduate academic work.
4. Two letters of recommendation, one of which should be from the applicant's research adviser.
5. Successful recipients of fellowships shall agree not to hold other appointments or other fellowships during the summer of 1980.

Application forms are available from the Chairman of the Fellowship Awards Subcommittee, to whom completed applications and letters of recommendation should be sent: Professor Keith Prater, Ultra Energy, Inc., 1164 15th Street West, North Vancouver, British Columbia, Canada V7P 1M9.

Deadline for receipt of completed applications will be January 1, 1980, and award winners will be announced on May 1, 1980.

NATO ADVANCED STUDY INSTITUTE ON CHEMICALLY SENSITIVE ELECTRONIC DEVICES

A NATO Advanced Study Institute on Chemically Sensitive Electronic Devices will be held at the Peddie School, Hightstown, N.J. from 9 June to 21 June 1980. The fundamental principles of transducer action for chemical sensors, the resulting device physics and selected areas of application will be presented in a series of lectures by: P. Bergveld and G. A. Bootsma, Twente Technical University; P. Buck, University of North Carolina; G. Farrington, General Electric; M. Green, Imperial College; T. Matsuo of Tohoku University; I. Lundström of Lin Kärping University; I. Lauks and J. N. Zemel, University of Pennsylvania; S. Pace, Stauffer Chemical. This course is primarily intended for the young researcher at the post doctoral level but consideration will be given to anyone in the process of initiating research in these areas. The student body will be sought from a broad range of disciplines such as: electrical engineering, chemistry and chemical engineering, physics, material science and biomedical science and engineering. Limited travel and living assistance is available. Special arrangements are being made to provide low cost travel to and from the Peddie School. For further information and applications write to either:

J. N. Zemel
University of Pennsylvania
Moore School/D2
200 S. 33rd Street
Philadelphia, Pa. 19104
U.S.A.

P. Bergveld
Twente University of Tech.
Dept. of Electrical Eng'g
P.O. Box 217
Enschede, Netherlands

POSITIONS AVAILABLE

RESEARCH SCIENTIST Corrosion Science Electrochemistry Metallurgy Physics

This senior position in the FONTANA CORROSION CENTER will be of interest to persons who hold a Ph.D. degree in metallurgy, physics, physical chemistry, or corrosion science, and who have an established record of scientific research. The successful applicant will direct research on a wide variety of fundamental and applied problems.

Interested persons should send resumes and the names of three referees to Prof. D. D. Macdonald, Director

FONTANA CORROSION CENTER
Dept. of Metallurgical Engineering
The Ohio State University
116 West 19th Avenue
Columbus, Ohio 43210

An equal opportunity/affirmative
action employer

Faculty Position — Extractive (Chemical) Metallurgy—Henry Krumb School of Mines, Columbia University, seeks applicants for a full-time position (assistant, associate, or full professor, depending on qualifications of applicant) for teaching and research in extractive metallurgy. Applicants should possess a doctoral degree and show evidence of knowledge and experience in areas of pyrometallurgy, heat and mass transfer applied to metal extraction, design, and mathematical modelling of processes. Those interested should write to Prof. H. H. Kellogg, Henry Krumb School of Mines, Columbia University, New York, N.Y. 10027, and enclose a brief vita. Columbia University is an equal opportunity/affirmative action employer.

NEW BOOKS

Active and Passive Thin Film Devices, edited by T. J. Coutts.

1978, Academic Press, Inc., 111 Fifth Ave., New York, NY 10003. 858 pages, bound.

This book provides a comprehensive account of the properties of thin films, the theories of thin film phenomena, and their wide range of applications. The properties of each type of device are discussed by experts in the field, covering both general properties and those specific to the material and to the method of preparation. Similarly, the applications are considered in terms of those which exploit preparational properties or those which simply exploit the small sizes obtainable with films. In addition, for many of the active devices the background theory necessary for understanding the physical operation is given.

Intergranular Corrosion of Stainless Alloys.

1978, ASTM, 1916 Race St., Philadelphia, PA 19103. 257 pages, bound. \$24.00.

The volume opens with a keynote paper that suggests a unified testing system for all stainless alloys. There are eight other papers dominated by three themes: the state of the art in testing austenitic stainless steels; intergranular corrosion testing of stainless steels for nuclear systems; and evaluation tests for ferritic stainless steels.

Ferritic Steels for Fast Reactor Steam Generators, edited by S. F. Pugh and E. A. Little.

1978, British Nuclear Energy Society. Distributed by Thomas Telford, Ltd., P.O. Box 101 26-34, Old St., London EC1P 1JH, England. 2 volumes (507 pages), paper. \$100.00.

The 80 papers delivered at this conference were presented in five technical sessions and a general discussion. The sessions were: introductory; physical metallurgy and mechanical properties; behavior in sodium; waterside corrosion; welding and manufacture. Among the papers are: design codes for fast reactor steam generators; the physical metallurgy of chromiummolybdenum steels for fast reactor boilers; mechanical properties data on 9% Cr steels; corrosion of ferritic steels in flowing sodium; tribology of ferritic steels in sodium; review of waterside performance of 9Cr1Mo boiler tube material; oxidation of ferritic steels in steam; concept for fabrication of a fast reactor steam generator; residual stresses in 2¼ Cr1Mo welds.

Introduction to Microelectronics, 2nd ed., by D. Roddy.

1978, Pergamon Press, Maxwell House, Fairview Park, Elmsford, NY 10523. 216 pages, paper. \$10.00.

Since the introduction of the transistor, the electronic properties of solids in general and semiconductors in particular have been exploited at a remarkable rate. In this book only those devices and circuits which are reasonably well established in practical applications are described. In this second edition, a new chapter on semiconductor memories has been included. Some of the existing chapters have been expanded to include details of the developments which appear to be most important. The book uses SI/metric units.

Chemical Coatings Conference.

1978, National Paint & Coatings Assoc., Inc., 1500 Rhode Island Ave., N.W., Washington, DC 20005. Five parts: Powder Coatings, 167 pages, \$15.00; Water-Borne Coatings, 142 pages, \$15.00; Radiation Cured Coatings, 126 pages, \$10.00; High Solids Coatings, 66 pages, \$10.00; Electrocoating, 91 pages, \$10.00. Paper. \$40.00 Set.

These volumes include 18 papers on powder coatings, 13 on water-borne coatings, six on high solids, seven on radiation curing, and seven on electrocoating. Among the individual papers are: the powder coatings market; new applications and powder-handling equipment; conversion to water-reducible paint; future water-borne coatings; high solids, low energy—is there compatibility?; experience with high solids coatings for major appliances; electron beam equipment; graphics-metal decoration; effects of energy, ecology, and economics on electrocoating; automotive electrocoat.

Except where noted, these books have been prepared by the staff of The Engineering Societies Library, and were selected for inclusion in the *Journal* by Dr. Daniel Cubicciotti of Stanford Research Institute. The Electrochemical Society does not have copies available for sale or loan. Orders for the books should be forwarded directly to the publishers.

BOOK REVIEWS

"Proceedings of the International Symposium on Atomic, Molecular, and Solid-State Theory, Collision Phenomena, and Computational Methods," International Journal of Quantum Chemistry, Vol. XIII, Quantum Chemistry Symposium No. 12, 1978, edited by P.-O. Löwdin. Published by John Wiley and Sons, Inc., New York (1978). 550 + xvi pages, \$30.00.

This volume contains the proceedings of the Eighteenth Sanibel Symposia, which, for the first time, was not held on Sanibel Island. The conference was held at Flagler Beach, Florida, during the period March 12-18, 1978, and was arranged by the University of Florida in collaboration with Uppsala University in Sweden.

The proceedings consists of 45 invited and contributed papers varying in length from 1 to 28 pages. The topics covered include graph theoretical and/or numerical applications to various current atomic and molecular problems in quantum chemistry and solid-state theory. The following areas that are discussed would be of particular interest to readers of **This Journal**: Coulombic interactions in polymer theory, ab initio cluster-type calculation for a single hydrogen impurity in a nickel crystal, magnetic impurities and the Kondo effect, force fields in d-band metals, molecular model of impurity bands in semiconductors, localized electronic states near dislocations in Mo, valence bond dissociation energies of diatomic intermetallic compounds, x-ray band spectra calculations of V metal, and Green's function methods for point defects, surfaces, and interfaces in solids.

Problems related to intermolecular interactions are discussed for the following systems: Infrared spectra of the hydrogen bond, oxopyridine-water interactions, and group function application to two interacting, rigid HF molecules.

The figures and diagrams are clearly and attractively displayed throughout the volume. The references in most of the articles are current through 1978. In his introductory remarks, the editor hopes that the proceedings will "reflect the current status of the research in quantum chemistry and solid-state theory on an international level." To this end, the volume succeeds as it represents an excellent collection of high quality articles. Even though most of the papers do not involve solid-state theory, these proceedings would, nevertheless, be a definite asset to anyone who is interested in the state-of-the-art computational methods as applied to the solid state.

Zvi C. Kornblum
The Cooper Union
New York, New York

"Principles of Metal Surface Treatment and Protection," by D. R. Gabe, 2nd ed., published by Pergamon Press, Elmsford, New York (1978). 208 pages, \$11.00.

This is volume 28 of the International series on Materials Science and Technology published by Pergamon. It is designed primarily for those interested in an overview of the topic. From an initial chapter on "Protection" it surveys electrodeposition and coating techniques (hot dip, diffusion, nonmetallic and metallic, oxide, and conversion), as well as testing and selection of ap-



Engineers

The Westinghouse Advanced Technology Laboratories are the center for research and development for the Defense and Electronic Systems Center.

The advanced technology responsibilities in integrated electronics, solid state, electromagnetic and applied sciences are combined to facilitate the interchange of information in the development of the techniques that form the basis for the Westinghouse advanced systems.

Immediate openings exist in these laboratories for persons with appropriate degree and 2 to 10 years experience in the following areas:

Computer Aided Technology Systems

Integrated approaches to automated product design and manufacturing of IC'S.

Integrated Circuits & VLSI R&D

Digital IC Design—advanced high speed MOS and bipolar digital devices and circuits and CAD techniques.

Analog IC Design—advanced devices and circuits including A/D's and IF/RF amplifiers.

Digital Architecture—high speed circuits for signal and data processing circuits.

Silicon Processing—definition/development of chemical and electron beam processes for the production of VHSIC devices and circuits.

ATL is located in suburban Baltimore within easy access to the educational and cultural facilities of the Baltimore and Washington metropolitan areas. Also, you will participate in a very generous employee benefit program.

Please send resume, stating present salary, to:

J. C. Higinbotham, Dept. 613
Westinghouse
P.O. Box 1693
Baltimore, MD. 21203

An Equal Opportunity Employer

Westinghouse

CHANGES OF ADDRESS
SHOULD BE PROMPTLY
REPORTED.

ATTACH
LABEL
HERE

Change of Address

To change your address, place address label here for proper identification. Print your NEW address below.

Mail to the Circulation
Department, The Electro-
chemical Society, Inc.,
P. O. Box 2071, Prince-
ton, N.J. 08540.

name

address

city

state

zip code

Chemist and Chemical Engineer for Plating Operations at IBM, East Fishkill, NY

Challenging, Excellent Career Opportunities in State-of-the-Art Technology:

PROCESS CHEMICAL ENGINEER/PLATING WITH LEADERSHIP SKILLS—

EXPERIENCED in process development, optimization, and process control in microelectronics technology, including at least five years in electroless and electroplating operations. Demonstrated ability to provide technical direction in complex, diverse plating operation required.

ELECTROLESS PLATING DEVELOPMENT CHEMIST—

EXPERIENCED, a minimum of five years, in developing and operating electroless plating baths. Theoretical and practical knowledge of plating bath chemistry formulation and control required; knowledge of metallurgical analysis of plated films desirable.

Scenic Mid-Hudson Site,

approximately 60 miles north of NYC, is one of IBM's largest. Comprises one of the most sophisticated facilities in the world for manufacture of integrated circuits.

Outstanding Benefits

include medical, dental, retirement plans and tuition refund.

Send Resume Today

to Michael A. DiMeglio, Employment Manager, Dept. JE1, IBM Corporation, Route 52, Hopewell Junction, NY 12533.



An Equal Opportunity Employer

appropriate coatings. A short section on the theory of corrosion protection followed by an extremely short appendix on the calculation on economic benefits concludes the book.

It is an excellent introduction to the topic for technicians and even for senior personnel who can further extend their knowledge by the lengthy lists of references.

Julius Klerer
The Cooper Union
New York, New York

"Principles of Photochemistry," by J. A. Barltrop and J. D. Coyle, published by John Wiley & Sons, Inc., New York (1979). 207 pages, \$12.50.

This is a well written, terse coverage of the field of photochemistry applied to organic molecules. It presupposes a familiarity with quantum mechanics and reaction mechanics and, as such, is designed for the honors college senior to postgraduate student. Forty-two problems at the end of the book test the readers' diligence. For the person in the field, it might prove to be a succinct review and for those senior personnel wishing to obtain an overview of the field, it would be an excellent and thorough introduction.

Julius Klerer
The Cooper Union
New York, New York

"Adhesion of Solids," by B. V. Deryagin, N. A. Krotova, and V. P. Smilga. Published by Plenum Press, New York, NY (1978). 457 pages; \$49.50.

This book represents a major and significant contribution by the authors to the field of adhesion. The present edition is the English translation of the original Russian text published in Moscow in 1973. The phenomenon of adhesion is ubiquitous in nature and recently there have been a number of symposia and symposium proceedings volumes covering various aspects of adhesion. Although there are many proceedings volumes or edited works (chapters written by different authors), the field of adhesion generally suffers from the paucity of monographs covering in detail the subtopics in the broad spectrum of adhesion. So, in the light of this fact, the present volume should be a most welcome addition to the adhesion literature.

The senior author (B. V. Deryagin) has been a very productive researcher and a prolific writer during his long and illustrious research career. He is internationally acclaimed for his many seminal research works in the general field of surface and colloid science and has contributed a great deal in the area of adhesion.

The book starts with an interesting Foreword by David Tabor, a renowned authority in the general area of surface science. As this monograph presents and summarizes the work of Professor Deryagin and his associates over the past 40 years, so it's natural that the

emphasis is on the role of electrostatic attractive forces in adhesion, as Deryagin's school has been the main proponent of the electrostatic theory of adhesion and electro-adhesion phenomena, and they have argued in this book the importance of electrostatics in adhesion with skill and vigor. However, in addition to the emphasis on the role of electric charge separation at the interface, other aspects of adhesion are described as well, particularly the role of diffusion in the adhesion of polymers.

This book is divided into nine chapters, and an interesting and informative Introduction precedes the main body of the text. There is a Conclusion section at the end of the text followed by a long (about 50 pages) Appendix in which, among other items, methods of adhesiometry, various kinds of adhesiometers, and effect of double layer on the electrostatic component of adhesion are discussed.

Among the many topics discussed in this monograph include: phenomena associated with the breaking of adhesive joints, such as fast-electron emission, luminescence, gas discharge, and radio-wave emission; adhesion of semiconductors from the standpoint of the electrical effects involved in surface modifications; adhesive properties of many other materials including dusts and powders, compatible and incompatible polymers, and surface coatings; and friction processes in relation to adhesion. It should be added that in addition to the theoretical treatments, the experimental tools and apparatuses are carefully delineated.

There is a bibliography at the end of each chapter and as this book was originally addressed to the Russian audience, except for a few references, it is a review of the work carried out in the Soviet Union by Professor Deryagin and his associates.

All in all, this is an important book in the field of adhesion and the authors should be thanked for sharing their work with the adhesion community in a coherent fashion. This book should grace the library shelves and should be a valuable acquisition to personal collections of those who consider themselves as serious "students" of the fascinating world of adhesion science.

K. L. Mittal

IBM Corporation
Hopewell Junction, New York

Book Reviewers Needed

The Electrochemical Society needs competent individuals to review books for the Journal.

Any Society member who wishes to volunteer his services should send his name, address, and field of competence to the attention of the Book Review Editor, Dr. Julius Klerer, c/o The Electrochemical Society, P.O. Box 2071, Princeton, N.J. 08540

ENGINEERING

LSI/VLSI Professional Opportunities

At NCR Microelectronics you'll be part of a far-sighted R&D enterprise.

If you like being involved in long range state-of-the-art investigations as well as designs of custom chips for specific requirements, here is an opportunity to join a creative R&D organization that has NCR's powerful resources behind it.

At NCR Microelectronics in Miamisburg, Ohio, much of the work we are doing in memories and microprocessor capabilities is exploratory in nature. Still, we have been manufacturing MOS semiconductors for NCR's needs for many years. Our well developed processing capability is unsurpassed. We are a leader in LSI design, non-volatile memory technique and deeply involved in VLSI development. All of this to help create the most cost-effective, computerized systems for NCR's world market.

We are expanding. We have immediate growth and promotion-created openings at all levels for engineers and scientists with BS/MS/PhD degrees in Electrical Engineering, Solid State Physics, or other compatible professional engineering disciplines. Your professional efforts can be extended in Advanced Development, Process Development or Engineering. Memory and Systems Design as well as Circuit Design and QA engineering. Salaries are fully commensurate with appropriate experience. Benefits, including relocation assistance to one of the most attractive and affordable areas of the midwest, are what you would expect from the world's second largest computer company.

If you have the qualifications we are looking for, then let's explore for mutual interests. Send your resume to: T. F. Wade, Dept. M-113 NCR Microelectronics, 8181 Byers Road, Miamisburg, Ohio 45342.

NCR
Complete Computer Systems

An Equal Opportunity Employer

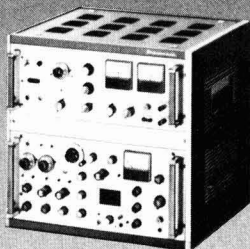
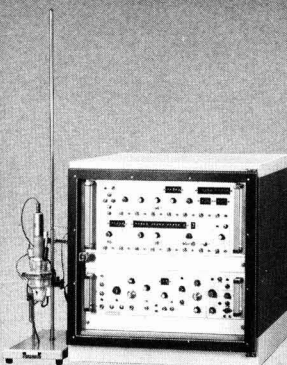
IF YOU'RE SERIOUS ABOUT ELECTROCHEMISTRY...

YOU SHOULD BE USING TACUSSEL EQUIPMENT.

With over 30 years of experience in developing and producing electrochemical instrumentation, Tacussel products have earned the respect and reputation for high quality, sophisticated instruments to meet your electrochemical needs. That's why Tacussel equipment is so widely used.

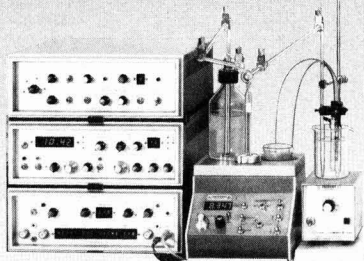
POTENTIOSTATS

A wide variety of different models are available to meet the requirements of every electrochemical laboratory. These potentiostats are widely used for plotting of current/voltage curves of electrochemical systems, potentiokinetic studies, polarography and programmed voltammetry. Power ranges vary from 2 watts to 20 kilowatts with rise times of 50 nanoseconds to 10 seconds.



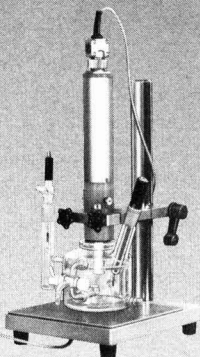
POLAROGRAPHIC SYSTEMS

A unique research system is available, which allows you to control a variety of electrochemical studies such as cyclic voltammetry, chronoamperometry, chronocoulometry, electrode kinetics, etc., as well as a versatile pulse polarographic analyzer for routine applications and a simple D.C. instrument for educational purposes.



TITRATION

A number of systems for potentiometric, coulometric, and conductometric titrations are available — from simple, quality control type systems to sophisticated computer-compatible research instruments.



ROTATING ELECTRODES

A rotating disc electrode is available for carrying out voltammetric techniques in chemical research and analysis. Also available is a rotating ring and disc electrode designed for the study of electrode processes and for determining kinetic characteristics of homogeneous or heterogeneous reaction.

Other equipment includes pH meters, ion meters, millivolt meters, conductivity meters, electrodes, corrosion instruments, current measurement instruments and industrial electrochemical instruments.

For a brief description of the Tacussel product line, write or call for their mini-catalog, or ask for detailed information on a specific product.

Tacussel products are available in the United States exclusively through

ASI

ASTRA SCIENTIFIC INTERNATIONAL, INC.

P.O. BOX 2004/SANTA CLARA, CALIFORNIA 95051/TELEPHONE (408) 244-3040/TELEX 348-399

Current Titles in Electrochemistry

Modern Aspects of Electrochemistry Number 13

edited by **B. E. Conway**
University of Ottawa, Canada
and **J. O'M. Bockris**
Texas A&M University

praise for the series

"All the topics are of importance and current interest, and the reviews are timely and welcome, well written and documented."

—*ASLIB*

Topics covered in this volume include electrolyte solutions, the state of solvent molecules at electrode surfaces, changed colloid interfaces, surface chemistry of oxide electrodes, and electrochemistry and bio-electrochemistry charge transfer complexes. approx. 300 pp., 1979, \$42.50

Water

A Comprehensive Treatise Volume 6 Recent Advances

edited by **Felix Franks**
University of Cambridge, England

This work examines recently developed aspects of the physics and chemistry of water and aqueous systems, emphasizing the role of water in determining the properties of aqueous solutions or solid hydrates, and modern techniques for studying aqueous systems. 470 pp., illus., 1979, \$45.00

Photoelectrochemistry

by **Yu. Ya. Gurevich** and **Yu. V. Pleskov**
Academy of Sciences of the USSR, Moscow
and **Z. A. Rotenberg**
translated from Russian by **H. Wroblowa**
Case Western Reserve University
translation edited by **H. Wroblowa** and **B. E. Conway**

Photoelectrochemistry presents the theory of photoemission in a novel and accessible fashion that does not require familiarity with quantum mechanics. Special emphasis is given to photoemission, electrochemical, and radiation-chemical problems. approx. 260 pp., illus., 1979, \$39.50

The Comprehensive Treatise of Electrochemistry

Volume 1

edited by **J. O'M. Bockris**
Texas A&M University
B. E. Conway
University of Ottawa, Canada
Ernest Yeager
Case Western Reserve University
and **Ralph E. White**
Texas A&M University

The first truly comprehensive treatise on electrochemistry, this volume presents contributions by preeminent experts in the field today. Topics covered include the ionic double layer structure without specific adsorption, potentials of zero charge, insulator/electrolyte interface, and the adsorption of organic molecules. approx. 475 pp., illus., 1979, \$49.50

Surface Contamination Genesis, Detection, and Control

edited by **K. L. Mittal**
IBM Corporation, Hopewell Junction, New York
in two volumes

Surface Contamination consolidates a wide range of current research and developmental activities relating to surface contamination and cleaning. General aspects discussed include techniques for cleaning, monitoring surface cleanliness, and the ramifications of surface contaminations in adhesions.

Volume 1: approx. 500 pp., 1979, \$39.50

Volume 2: approx. 550 pp., 1979, \$39.50

two volume set: \$70.00

Solution Chemistry of Surfactants

edited by **K. L. Mittal**
IBM Corporation, Hopewell Junction, New York
in two volumes

Solution Chemistry of Surfactants presents comprehensive coverage by top authorities in the field of theoretical, as well as practical, aspects of adsorption and aggregation behavior of surfactants.

Volume 1: 544 pp., 1979, \$45.00

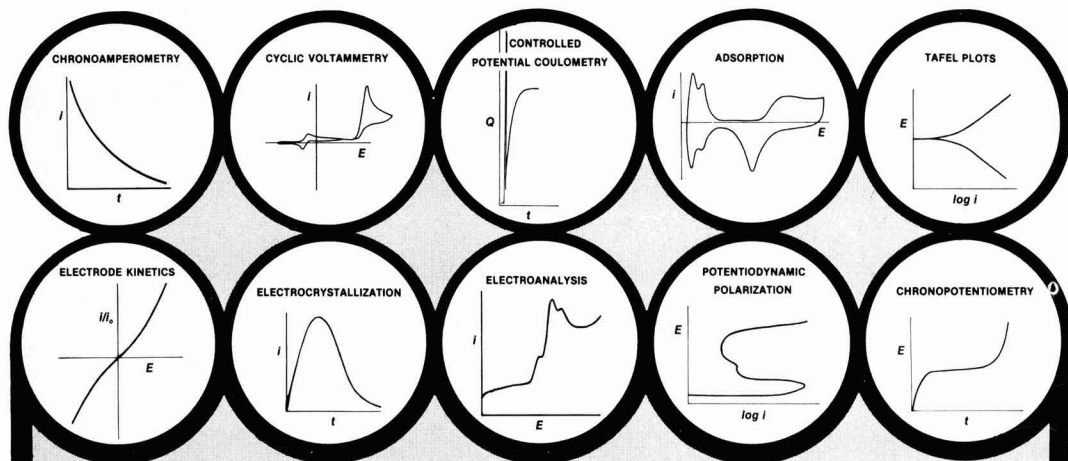
Volume 2: 462 pp., 1979, \$39.50

two volume set: \$75.00

Prices slightly higher outside the U.S.



PLENUM PUBLISHING CORPORATION
227 West 17th Street, New York, N.Y. 10011



When only the best will do.

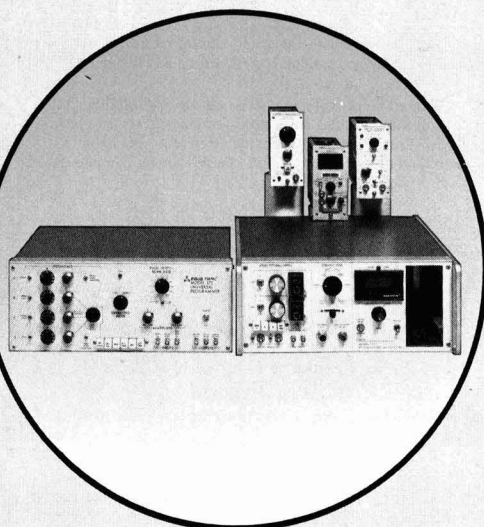
Potentiostats, Plug-Ins and Programmers from EG&G PRINCETON APPLIED RESEARCH

Model 173 Potentiostat

A superior potentiostat for both basic and applied research. Its ± 100 V compliance voltage, ± 1 Amp capability and $3 \mu\text{s}$ rise time make it ideal for the most crucial studies.

Model 173 Plug-Ins

Use the Model 173 with the **Model 176 Current to Voltage Converter** for energy and battery studies. Plug in the 5-decade **Model 376 Logarithmic Current Converter** when corrosion investigations require tracking of widely varying currents. Or go with a high precision, high accuracy **Model 179 Digital Coulometer** for synthesis and assays...applications where every coulomb counts.



Model 175 Universal Programmer

The perfect complement to the 173 Potentiostat. Program ramps, triangles, pulses, steps—symmetric or not. This programmer has completely independent potential controls, scan slopes, pulse duration and pulse amplitudes for maximum flexibility.

For more information on our superior electrochemical instrumentation, write or call EG&G PRINCETON APPLIED RESEARCH, P. O. Box 2565, Princeton, NJ 08540; 609/452-2111.



EG&G

PRINCETON APPLIED RESEARCH

P. O. BOX 2565 • PRINCETON, NJ 08540 • 609/452-2111 • TELEX: 843409

522

THE ELECTROCHEMICAL SOCIETY

BOOKS IN PRINT

Monograph Series

The following hardbound volumes are sponsored by The Electrochemical Society, Inc. and published by John Wiley & Sons, Inc. Members who wish to receive a discount must send their orders to the Society Headquarters, P.O. Box 2071, Princeton, N.J. 08540. The books will be shipped by John Wiley & Sons, Inc. Invoices for the cost of the volume plus postage and handling will be sent by Society Headquarters. Terms: Payment upon receipt of invoice. All prices are subject to change without notice.

Corrosion Handbook, edited by Herbert H. Uhlig (1948). 1188 pages, \$42.95.

Arcs in Inert Atmospheres and Vacuum, edited by W. E. Kuhn. A 1956 Spring Symposium (1956). 188 pages, \$13.95.

The Stress Corrosion of Metals, by Hugh I. Logan (1966). 306 pages, \$27.95.

The Corrosion of Light Metals, by H. P. Godard, W. B. Jepson, M. R. Bothwell, and R. L. Kane (1967). 360 pages, \$24.95.

High-Temperature Materials and Technology, edited by I. E. Campbell and E. M. Sherwood (1967). 1022 pages, \$48.75.

Alkaline Storage Batteries, by S. Uno Falk and Alvin J. Salikind (1969). 656 pages, \$49.50.

The Primary Battery, Volume I, edited by George W. Helse and N. Corey Cahoon (1971). 500 pages, \$42.95.

Handbook on Corrosion Testing and Evaluation, edited by W. H. Ailor (1971). 873 pages, \$62.50.

Modern Electroplating, edited by Frederick A. Lowenheim. Third Edition (1974). 801 pages, \$37.95.

Marine Corrosion, by Francis L. LaQue (1975). 332 pages, \$27.50.

The Primary Battery, Volume II, edited by George W. Helse and N. Corey Cahoon (1975). 528 pages, \$42.95.

Lead-Acid Batteries, by Hans Bode (1977). 387 pages, \$33.00.

Thin Films—Interdiffusion and Reactions, edited by J. M. Poate, K. N. Tu, and J. W. Mayer (1978). 576 pages, \$37.50.

Society Published Monograph Series

The following hardbound proceedings volume is sponsored by and published by The Electrochemical Society, Inc. It should be ordered from: The Electrochemical Society, Inc., P.O. Box 2071, Princeton, N.J. 08540. Remittance must accompany order for this volume.

Passivity of Metals (Proceedings of The Fourth International Symposium on Passivity). R. P. Frankenthal and J. Kruger, Editors. A 1977 symposium. 1078 pages, \$65.00.

12/79

OUT-OF-PRINT SOCIETY VOLUMES

The following volumes sponsored or published by The Electrochemical Society, Inc. are now out-of-print. Xerographic copies* or reprint of these volumes are available.

* **Vapor Plating**. C. F. Powell, I. E. Campbell, and B. W. Gonser, Editors. A 1955 symposium. 158 pages.

* **The Structure of Electrolytic Solutions**. W. J. Hamer, Editor. A 1957 symposium. 441 pages.

* **Technology of Columbium (Niobium)**. B. W. Gonser and E. M. Sherwood, Editors. A 1958 symposium. 120 pages.

* **Surface Chemistry of Metals and Semiconductors**. H. C. Gatos, J. W. Faust, Jr., and W. J. La Fleur, Editors. A 1959 symposium. 526 pages.

* **Electrode Processes**, First Conference. E. Yeager, Editor. A 1959 symposium. 374 pages.

* **Mechanical Properties of Intermetallic Compounds**. J. H. Westbrook, Editor. A 1959 symposium. 435 pages.

* **Zirconium and Its Alloys**. J. P. Pemsler, E. C. W. Perryman, and W. W. Smeltzer, Editors. A 1965 symposium. 205 pages.

† **Measurement Techniques for Thin Films**. B. Schwartz and N. Schwartz, Editors. 1965 and 1966 symposia. 347 pages.

† **Electrode Processes**, Second Conference. E. Yeager, H. Hoffman, and E. Eisenmann, Editors. A 1966 symposium. 190 pages.

* **Electrolytic Rectification and Conduction Mechanisms in Anodic Oxide Films**. P. F. Schmidt and D. M. Smyth, Editors. A 1967 symposium. 230 pages.

* **Electrets and Related Electrostatic Charge Storage Phenomena**. L. M. Baxt and M. M. Perlman, Editors. A 1967 symposium. 150 pages.

* **Dielectrophoretic and Electrophoretic Deposition**. E. F. Pickard and H. A. Pohl, Editors. A 1967 symposium. 138 pages.

* **Electron and Ion Beam Science and Technology**, Third International Conference. R. Bakish, Editor. A 1968 symposium. 725 pages.

* **Optical Properties of Dielectric Films**. N. Axelrod, Editor. A 1968 symposium. 325 pages.

* **Thin Film Dielectrics**. F. Vratny, Editor. A 1968 symposium. 680 pages.

* **Ohmic Contacts to Semiconductors**. B. Schwartz, Editor. A 1968 symposium. 356 pages.

* **Semiconductor Silicon**. R. R. Haberecht and E. L. Kern, Editors. A 1969 symposium. 750 pages.

* **Chemical Vapor Deposition**, Second International Conference. J. M. Blocher, Jr. and J. C. Withers, Editors. A 1970 symposium. 872 pages.

* **Semiconductor Silicon 1973**. H. R. Huff and R. R. Burgess, Editors. A 1973 symposium. 936 pages.

* **High Temperature Oxidation of Metals**. By P. Kofstad. The Corrosion Monograph Series. 340 pages.

* **Chemical Vapor Deposition**, Fourth International Conference. G. F. Wakefield and J. M. Blocher, Jr., Editors. A 1973 symposium. 595 pages.

* **Electrets, Charge Storage and Transport in Dielectrics**. M. M. Perlman, Editor. A 1973 symposium. 675 pages.

* **Fine Particles**. W. E. Kuhn and J. Ehretsmann, Editors. A 1974 symposium. 352 pages.

* **Corrosion Problems in Energy Conversion and Generation**. C. S. Tedmon, Editor. A 1974 symposium. 484 pages.

* **Electrocatalysis**. M. W. Breiter, Editor. A 1974 symposium. 378 pages.

* Order from University Microfilms, Inc., 300 North Zeeb Street, Ann Arbor, Mich. 48103. Specify an Electrochemical Society volume.

† Order from Johnson Reprint Co., 355 Chestnut St., Norwood, N.J. 07648. Specify an Electrochemical Society volume.

9/79

Announcement

To decrease costs and improve the use of the annual and decennial indexes, the author-chosen random key words is being abandoned starting in 1978. Instead, the following Standard Key-Descriptor List will be used. Each author should follow the instructions below for the proper selection.

Standard Key-Descriptor List

A selection of no more than four standard key-descriptors from the attached list is required for each JOURNAL article. These descriptors are used for the yearly and decennial indexes.

These descriptors are divided into four classes: Material, Component or System, Electrical or Optical Phenomena and Techniques, Chemical or Physical or Other Phenomena and Techniques. The author should tend to select one descriptor from each of these classes with a maximum of four. Avoid selection of all descriptors from a single class. Words appearing in the title should be avoided since they are the prime source of other important descriptors.

The key-descriptors are purposefully general in order to control the over-all size of the JOURNAL index and thereby reduce costs. Specificity is determined by the author in the judicious choice of the article title.

Standard Key-Descriptors

I	II	III	IV
"Material"	Component, System	Electrical/Optical Phenomena-Techniques	Chemical/Physical/Other Phenomena-Techniques
Abrasive Acid Additives Adhesives Addresses Aerosol Air Alloy Amalgam Amorphous Anion Atmosphere	Amplifier Anode	Acoustics Antiferroelectricity	Absorption Activation Activity Coeff. Additive Adsorption Allotrophy Analysis Anneal Association Azcotropes
	Battery		Biological Boiling Bonding
Carbon Cations Ceramics Chelates Cleaners Coatings Colorants Composites	Capacitor Cathode Cell Circuits Coils Computer Connectors Contacts Couplers Cryotrons	Capacitance Candoluminescence Cathodoluminescence Charge Chemiluminescence Coercive Force Conductance Current Current Density Current Efficiency Crystallography	Catalysis Chelation Chemisorption Chromatography Chronopotentiometry Coagulation Condensation Conduction Contamination Convection Cooling Corrosion Cracking Crystallization CVD
Defects Dendrite Dielectrics	Diodes	Depolarization Discharge	Deposition Desorption Dialysis Diffraction Diffusion Dipole Discharge Dissolution Dissociation Doping DTA
Electret Electrolyte Electron Emulsion Environment Eutectic	Electrode	Electroluminescence Electrostatics Ellipsometry EPR ESCA ESR	Economics Effusion Electrodeposition Electrodialysis Electroless Electrolysis

I	II	III	IV
<u>"Material"</u>	<u>Component, System</u>	<u>Electrical/Optical Phenomena-Techniques</u>	<u>Chemical/Physical/Other Phenomena-Techniques</u>
			Electromachining Electromigration Electroosmosis Electrophoresis Embrittlement EMF Energy Conversion Energy Storage Energy Transfer Enthalpy Entropy Epitaxy Equilibrium Etching Evaporation Extraction
Films Finishes Free Radicals Fuels Fused Salts	Filters Fuel Cell Fuses	FEM Ferroelectricity Ferromagnetism FIM Fluorescence	Failure Fission Free Energy Fusion
Gas Glass	Gates (elec)		Gettering Growth
			Heat Capacity Heteroepitaxy Hydrolysis
Impurity Inorganic Insulator Interfaces	Integrated Circuits	Impedance Incandescence Infrared Interferometry	Inhibition Ion Exchange Ion Implantation Isomerization
Junctions			
	Kystrons		Kinetics
Liquid Lubricants	Lasers	LEED Luminescence	Levitation
Membrane Metals	Magnetrons Masers Mixers Multivibrators	Magnetism Microwave Mobility	Machinery Masking Mass Spectroscopy Mass Transport Mechanics Melting Migration
	Neuristors	Nuclear Particles	Nuclear Reactions Nucleation
Oils Organic	Orthicons Oscillators	Optics	Osmosis Overvoltage Oxidation
Particles Particles, Nuclear Plastics Poisons Polymers	Photocathode Photodiode Plasmas	Paramagnetism Photoconductivity Photoelectricity Photoluminescence Photovoltaic Phosphorescence Piezoelectricity Potential Power Pyroelectricity	Passivity pH Phases Phase Transformation Polarization Polarography Pollution Polymerization Pressure

I	II	III	IV
<u>"Material"</u>	<u>Component, System</u>	<u>Electrical/Optical Phenomena-Techniques</u>	<u>Chemical/Physical/Other Phenomena-Techniques</u>
			Quantum Theory
Refractories Rubber	Rectifiers Relays Resistor Resonators	Radiofrequency Reflectance Refraction Resistivity RHEED	Radioactivity Reduction Relativity Reliability
Semiconductor Slag Solids Solvents Surfaces	Seals Separators Switches	SEM Solar Spectra Superconductivity	Solidification Solubility Solvation Spalling Sputtering Sublimation Sulfidation Stress-Strain Stoichiometry Synthesis
	Terminals Transducers Transistors Triodes Tubes	Thermionic Emission Thermodynamics Thermoelectricity Thermoluminescence Transmittance	Tafel Slope Topography Transients Transport Trapping Tunneling
		Ultraviolet	
	Vidicon	Visible	Vacuum Valence Vaporization Voltammetry
Water Whiskers Wood		Work Function	
		X-Rays	

APPLICATION FOR ADMISSION

TO

The Electrochemical Society, Inc.

Return completed application to:

Secretary
The Electrochemical Society, Inc.
 Post Office Box 2071, Princeton, New Jersey 08540
 609-924-1902

For office use only

Notice of Ackn. _____

recap _____ \$ _____

Checked: _____

Approved: _____

To the Board of Directors of The Electrochemical Society, Inc:

Name: _____

Address: _____

Please print complete
 name and address
 as it should
 appear on mailings.

Business Telephone: (include area code) _____

I hereby make application for admission to The Electrochemical Society, Inc., as a _____ member, and enclose the amount of \$ _____ covering the first year's dues. (Please see reverse side for proper class of membership and dues applying thereto, noting the options with regard to the date of election and active life membership and the credit available for nonmember meeting registration.)

1. Date of Birth: _____ (month) _____ (day) _____ (year)

2. Please check LOCAL SECTION with which you wish to affiliate:

- | | | | | |
|---|---|--|---|---|
| <input type="checkbox"/> Boston (05) | <input type="checkbox"/> Detroit (25) | <input type="checkbox"/> Natl. Capital Area (45) | <input type="checkbox"/> Pacific Northwest (65) | <input type="checkbox"/> San Francisco (85) |
| <input type="checkbox"/> Chicago (10) | <input type="checkbox"/> Indianapolis (30) | <input type="checkbox"/> Niagara Falls (50) | <input type="checkbox"/> Philadelphia (70) | <input type="checkbox"/> So. Calif.-Nevada (90) |
| <input type="checkbox"/> Cleveland (15) | <input type="checkbox"/> Metropolitan N.Y. (35) | <input type="checkbox"/> North Texas (55) | <input type="checkbox"/> Pittsburgh (75) | <input type="checkbox"/> None (99) |
| <input type="checkbox"/> Columbus (20) | <input type="checkbox"/> Midland (Mich.) (40) | <input type="checkbox"/> Ontario-Quebec (60) | <input type="checkbox"/> Rocky Mountain (80) | |

3. Please indicate your DIVISIONAL and GROUP interests, noting your primary interest(s) with the number 1 and secondary interest(s) with the number 2.

- | | | |
|--|---|---|
| <input type="checkbox"/> Battery (AO) | <input type="checkbox"/> Electronics (EO) | <input type="checkbox"/> Energy Technology Group (GO) |
| <input type="checkbox"/> Corrosion (BO) | <input type="checkbox"/> check specific interest(s) below | <input type="checkbox"/> Industrial Electrolytic (IO) |
| <input type="checkbox"/> Dielectrics and Insulation (CO) | <input type="checkbox"/> General Materials and Processes (E1) | <input type="checkbox"/> Organic and Biological |
| <input type="checkbox"/> Electrodeposition (DO) | <input type="checkbox"/> Luminescence (E2) | <input type="checkbox"/> Electrochemistry (FO) |
| | <input type="checkbox"/> Semiconductors (E3) | <input type="checkbox"/> Physical Electrochemistry (JO) |
| | <input type="checkbox"/> Electrothermics and Metallurgy (HO) | |

4. Education:

Institution	Dates Attended	Major Subject	Degree Earned
-------------	----------------	---------------	---------------

5. Work Experience:

Name of Employer (current, followed by previous)	Dates	Position
--	-------	----------

6. The Society's Constitution provides that two Active Members of the Society (who can substantiate the above record) must recommend you for admission to membership. It will facilitate the handling of your application if you are able to have your references sign this application form; if this is not convenient, please list their names and addresses. On a student application, only a single faculty member recommendation with signature (including title and institution) is required.

Name (please print)	Signature	Address
---------------------	-----------	---------

Name (please print)	Signature	Address
---------------------	-----------	---------

The undersigned certifies that the above statements are correct and agrees, if elected to the Society, to be governed by its Constitution and Bylaws and to promote the objects of the Society as stated in its Constitution.

Date _____ 19 ____

(Signature)

EXTRACTS FROM THE CONSTITUTION AND BYLAWS

CONSTITUTION—Article II

Membership

Section 1. The individual membership shall consist of Active, Honorary and Emeritus Members. The Board of Directors may from time to time authorize other classifications of membership as defined in the Bylaws of the Society.

(Active Member—Annual Dues \$40.00)

Active Member

Section 2. An Active Member shall be interested in electrochemistry or allied subjects and possess a Bachelor's degree, or its equivalent, in engineering or natural science. In lieu of a Bachelor's degree, or its equivalent, any combination of years of undergraduate study and years of relevant work experience in electrochemistry or allied subjects adding to at least seven years shall be required. Election to Active Membership shall require the recommendation of two Active Members in good standing.

BYLAWS—Article II

Non-Voting Membership

(Student Member—Annual Dues \$4.00)

Student Member

Section 1. Student Member. A Student Member shall be a full-time undergraduate or graduate student registered for a degree in natural science or engineering. The applicant for Student Membership shall be recommended by a member of the faculty of the school. Upon graduation with a Bachelor's degree or equivalent in natural science or engineering, the Student Member may apply for Active Membership. The application shall be approved by two Active Members of the Society in good standing. If the Student Member enters graduate school as a full-time student, the person may choose to apply for Active Membership or remain a Student Member.

BYLAWS—Article XXI

Dues and Fees

Dues

Section 1. The annual dues for Active Members shall be forty dollars. The annual dues for Student Members shall be four dollars. Each member shall receive the JOURNAL OF THE ELECTROCHEMICAL SOCIETY.

Date of Election

Section 2. When individuals are elected to membership, they must elect to initiate their membership as of January 1 or July 1 of the year of election; or, if elected during the last quarter, January 1 of the year following election. In the case of a July 1 election for starting membership, dues will be prorated.

Active Life Membership

Section 3. Any Active Member who shall pay in one lump sum the amount equivalent to two-thirds of the remaining dues to age sixty-five at the time of payment, but not less than an amount of 5 years of full dues, shall be exempt from payment of any further dues and shall be considered an Active Member during the remainder of his or her life.

Nonmember Meeting Registration Credit

BOARD OF DIRECTORS ACTION OF OCTOBER 9, 1960

If application for new membership is received within four months of the payment of nonmember registration at a Society Meeting by the applicant, the difference between the nonmember and member registration fees shall be credited toward the first year's dues.

CONSTITUTION—Article III

Admission and Dismissal of Members

Section 1. Application for individual membership shall be in writing on a form adopted by the Board of Directors.

Section 2. The Admissions Committee shall be a rotating committee consisting of three members. One member shall be appointed each year by the President with the approval of the Board of Directors for a term of three years to replace the outgoing member. This Committee shall receive from the Secretary all properly executed and properly recommended applications for admission which he has received from persons desirous of becoming members of the Society. It shall be the duty of this Committee, after examining the credentials of applicants, to make appropriate recommendation to the Board as to approval or rejection of the applications. Unanimous approval of an applicant by this Committee shall be required before the candidate's name may be submitted to the Board of Directors for election. The election to membership shall be by a mail vote of the Board of Directors. The candidate shall be considered elected two weeks after the date the proposed membership list is mailed to the Board if no negative votes have been received by the Secretary. If a candidate receives one negative vote, his application shall then be considered and voted upon at the next meeting of the Board of Directors. Two negative votes cast at this meeting shall exclude a candidate. The Board of Directors may refuse to elect a candidate who, in its opinion, is not qualified for membership. The names of those elected shall be announced to the Society. Duly elected candidates shall have all the rights and privileges of membership as soon as their entrance fee, if any, and dues for the current year have been paid.

Section 3. A member desiring to resign shall send a written resignation to the Office of the Society.

Section 4. Upon the written request of ten or more Active Members that, for cause stated therein, a member be dismissed, the Board of Directors shall consider the matter and, if there appears to be sufficient reason, shall advise the accused of the charges against him. He shall then have the right to present a written defense, and to appear in person before a meeting of the Board of Directors, of which meeting he shall receive notice at least twenty days in advance. Not less than two months after such meeting the Board of Directors shall finally consider the case and, if in the opinion of the majority of the Board of Directors a satisfactory defense has not been made and the accused member has not in the meantime tendered his resignation he shall be dismissed from the Society.

Section 7. The entrance fee, if any, annual dues and any other payments to be made by the members of the Society shall be paid in accordance with regulations set forth in the Bylaws.

Section 8. Any member delinquent in dues after April 1 shall not receive the Society's publications and will not be allowed to vote in any Society election until such dues are paid. All members in arrears for one year after April 1 shall lose their membership status and can be reinstated only by action of the Board of Directors.

Call for Papers

158th Meeting, Hollywood, Florida, October 5-10, 1980

Divisions which have scheduled sessions are listed on the overleaf, along with symposium topics.

1. Symposium Papers.

Authors desiring to contribute papers to a symposium listed on the overleaf should check first with the symposium chairman to ascertain appropriateness of the topic.

2. General Session Papers.

Each of the Society Divisions or Group which will meet in Hollywood, Florida, can plan a general session. If your paper does not fit readily into a planned symposium, you should specify "General Session."

3. To Submit a Meeting Paper.

Each author who submits a paper for presentation at a Society Meeting must do three things:

A—Submit one original 75-word abstract of the paper on the attached form or a facsimile thereof. **Deadline for receipt of 75-word abstract is May 1, 1980.**

B—Submit original and one copy of an Extended Abstract of the paper. **Deadline for receipt of Extended Abstract is June 1, 1980.** See (6) below for details.

C—Determine whether the meeting paper is to be submitted to the Society Journal for publication. See (7) below for details.

Send all material to The Electrochemical Society, Inc., P.O. Box 2071, Princeton, N.J. 08540.

Unless the 75-word and required Extended Abstracts are received at Society Headquarters by stated deadlines, the papers will not be considered for inclusion in the program.

4. To Submit a Recent News Paper.

Recent News Papers and Extended Recent News Papers are invited for this meeting. Each author must submit one of the following items to the Session Chairman:

A—Triplicate copies of a 75-word abstract of a Recent News Paper, for a 10-minute presentation. **Deadline for receipt is August 25, 1980.**

B—Triplicate copies of a 75-word abstract and, also, a 200-300 word abstract of an Extended Recent News Paper, for a 20-minute presentation. **Deadline for receipt is August 15, 1980.**

Send all material to the appropriate Session Chairman listed, for Recent News Papers only.

5. Meeting Paper Acceptance.

Notification of acceptance for meeting presentation, along with scheduled time, will be mailed to authors with general instructions no earlier than two months before the meeting. Those authors who require more prompt notification are requested to submit with their abstracts a self-addressed postal card with full author-title listing on the reverse.

6. Extended Abstract Volume Publication.

All scheduled papers will be published in the EXTENDED ABSTRACTS volume of the meeting. The volume is published by photo-offset directly from typewritten copy submitted by the author. Therefore, special care should be given to the following instructions to insure legibility.

A—Abstracts are to be from 500 to 1000 words in length and should not exceed two pages, single spaced. The abstract should contain to whatever extent practical all significant experimental data to be presented during oral delivery.

B—Abstracts should be typed single spaced on the typing guide forms which are sent to each author after the submission of a short abstract. If it is necessary to use white bond paper, it should be 8½ x 11 inches with 1¼ inch margins on all sides. Submit all copy in black ink. Do not use handwritten corrections.

C—Title of paper should be in capital letters. Author(s) name and affiliation and address should be typed immediately below in capital and lower case

letters. Please include zip code in address. It is not necessary to designate paper as "Extended Abstract" or to quote the divisional symposium involved.

D—If figures, tables, or drawings are used, they should follow the body of the text and should not exceed one page. Submit only the important illustrations and avoid use of halftones. Lettering and symbols should be no smaller than ⅛ inch in size. Figure captions should be typed beneath the figure and be no wider than the figure. Table titles should be typed above and the same width as the table.

E—Mail original and one copy of the abstract to: The Electrochemical Society, Inc., P.O. Box 2071, Princeton, N.J. 08540, unfolded.

Abstracts exceeding the stipulated length will be returned to author for condensation and retyping.

7. Manuscript Publication in Society Journal.

All meeting papers upon presentation become the property of The Electrochemical Society, Inc. However, presentation incurs no obligation to publish. If publication in *Journal* is desired, papers should be submitted as promptly as possible in full manuscript form in order to be considered. If publication elsewhere after presentation is desired, written permission from Society Headquarters is required.

Hollywood, Florida, Meeting Symposia Plans—Fall 1980

October 5-10, 1980

- a.) For receipt no later than May 1, 1980, submit a 75-word abstract of the paper to be delivered on the enclosed form.
 b.) For receipt no later than June 1, 1980, submit two copies of an extended abstract, 500-1000 words.
 c.) Send all abstracts to The Electrochemical Society, Inc., P.O. Box 2071, Princeton, N.J. 08540, with the exception of Recent News Papers. See details on preceding page.

BATTERY

Characteristics of Fuel Cell and Battery Electrodes

This symposium will focus on recent advances in the development of fuel cell and battery electrodes that may lead to a better understanding of electrode characteristics both from a theoretical and practical viewpoint. It will include characteristics of solid, liquid, and porous electrodes which are used in fuel cells, primary, and secondary batteries. Papers are requested covering the following topics: 1. the correlation between fundamental electrochemical parameters and design characteristics for both practical and model electrodes; 2. materials selection, component optimization, and electrode construction techniques for efficient, low cost electrodes; 3. electrocatalysis on platinum, platinum alloy, supported, and non-noble metal catalysts; 4. the effects of surface properties and charge transport on the charge and discharge characteristics of primary and secondary battery electrodes; 5. the properties of high current density electrodes for use in high power density battery systems and high temperature fuel cells; and 6. the design of novel electrodes, electrode-separator, and electrode-matrix packages for energy storage or energy conversion devices.

Suggestions and inquiries should be sent to the Symposium Chairman: A. A. Adams, U.S. Army MERADCOM, Electrochemical Division (DRDME-EC), Fort Belvoir, Va. 22060.

Lithium Battery

This symposium will include papers dealing with experimental and theoretical aspects of lithium cells and batteries for the conversion and storage of electrical energy. Emphasis will be placed on recent advances and new systems of high specific energy and/or high specific power batteries and in particular their safety during use and storage. Papers dealing with secondary cells will be of great interest. Appropriate systems will include those using inorganic electrolytes, organic electrolytes, high temperature electrolytes, solid electrolytes, and novel types. Subjects of special interest are: 1. electrode kinetics and mechanisms; 2. electrolytes composition and their role in cell performance; 3. identification of discharge products and their influence on cell performance; 4. battery systems' performance as a function of temperature before and after storage; 5. chemical and electrochemical intracell reactions; 6. identification of causes for safety hazards during use and/or storage; 7. heat generation in the battery during use and thermal management techniques; and 8. innovative methods in terms of cell components and design principles for safe operation.

Suggestions and inquiries should be sent to the Symposium Chairman: H. V. Venkatasetty, Honeywell Corporate Material Science Ctr., 10701 Lyndale Ave., S. Bloomington, Minn. 55420.

Rechargeable Alkaline Zinc Electrodes

This symposium will focus on recent advances in zinc electrode technology used in rechargeable batteries, both in vented and sealed cell types. Systems of interest include zinc-nickel oxide, zinc-silver oxide, etc.

Both basic and applied papers are being solicited. Suitable topics would include: 1. porous electrode modeling; 2. electrode kinetics and solution chemistry; 3. shape change and dendrite control; 4. electrolyte distribution and gassing phenomena; 5. separator technology; 6. optimization of electrodes and battery designs; 7. charging techniques; 8. post-test analyses; 9. performance in electric vehicle type batteries; and 10. economic and manufacturing considerations.

The publication of a proceedings volume is being considered. Suggestions and inquiries should be sent to the Symposium Chairman: E. G. Gagnon, General Motors Corp., Research Laboratory, Electrochemistry Dept., Warren, Mich. 48090.

Uninterruptible Power Supplies

This symposium will include theoretical and experimental methods of all aspects of uninterruptible power systems, related battery systems, computer applications, and economics. Papers are solicited in these areas. Possible subjects of interest are: 1. maintenance-free batteries for UPS; 2. economics of battery UPS; 3. battery maintenance and safety; 4. high-rate battery design; 5. single-phase UPS; 6. battery parameter trade-offs for UPS; 7. forward-transfer UPS; 8. UPS computer applications; 9. UPS process control application; 10. battery diagnostic instrumentation; 11. modern battery charging methods; and 12. power factor improvement in UPS.

Suggestions and inquiries should be sent to the Symposium Chairman: J. J. Kelley, ESB Inc., 19 West College Ave., Yardley, Pa. 19067.

General Session

Recently developed test methods and analytical procedures which assist in the characterization of battery components—electrodes, electrolytes, separators, etc.—will be the subject of the general session. Papers describing the application of analytical techniques and equipment such as optical and electron microscopy, x-ray diffraction and fluorescence, spectroscopy, and voltammetry to battery related materials are solicited.

Results obtained in bench, field, and fleet testing of cells and batteries for various applications will also be considered. Correlation of laboratory test results with field test results would be of particular interest.

Suggestions and inquiries should be sent to the Session Chairman: J. R. Pierson, Globe-Union, Inc., P.O. Box 591, Milwaukee, Wis. 53201.

BATTERY/CORROSION/ELECTROTHERMICS AND METALLURGY/ENERGY TECHNOLOGY

Molten Carbonate Fuel Cell Technology

This symposium will deal with all aspects of development of molten carbonate fuel cell technology. Invited presentations will discuss the status of cell and stack development and of power plant design. Papers dealing with the following areas will be entertained: 1. fundamental research on cell-related phenomena such as ion transport or electrochemical kinetics; 2. materials for molten carbonate fuel cells and stacks; 3. cell and stack development including design, performance, modeling, life, operability, etc.; 4. power plant design and characteristics; and 5. related areas, such as fuels processing or cleanup for molten carbonate fuel cells.

Suggestions and inquiries should be sent to the Symposium Co-Chairmen: J. P. Ackerman, Argonne National Laboratory, 9700 South Cass Ave., Argonne, Ill. 60439; E. J. Cairns, University of California, Lawrence Berkeley Laboratory, Berkeley, Calif. 94720; or L. Grantham, Rockwell International, Canoga Park, Calif. 91304.

BATTERY/CORROSION/ENERGY TECHNOLOGY

Energy Storage for Solar Applications

This symposium will include papers dealing with technology requirements for com-

ponent systems, development, and economic assessment of storage technologies for solar systems. Appropriate topics include: 1. chemical and electrochemical storage technologies for solar thermal, ocean thermal, power tower, photovoltaic, and photogalvanic applications; 2. technology development of photochargeable batteries; 3. other photochemical storage technologies; 4. results of laboratory evaluations, advanced system tests, and application experiments, materials problems; 5. recent development of batteries, fuel cells, and other electrochemical systems; 6. design of storage/solar systems; and 7. technical, economic, and social barriers to commercialization.

Suggestions and inquiries should be sent to the Symposium Co-Chairmen: A. R. Landgrebe, U.S. Dept. of Energy, Energy Storage Systems, 600 E. St. NW, Room 414, Washington, D.C. 20545; R. H. Muller, University of California, Lawrence Berkeley Laboratory, Bldg. 62, Berkeley, Calif. 94720; or R. Clark, Sandia Laboratories, Albuquerque, N.M. 87115; or P. Russell, Solar Energy Research Institute, 1536 Cole Blvd., Golden, Colo. 80401.

CORROSION

Corrosion in Organic Solvents

This symposium will include papers which deal with all aspects of corrosion in organic media. These aspects could include: 1. morphology of corrosion processes in organic media; 2. effect of specific functional groups—acids, alcohols, etc.; 3. corrosion kinetics; 4. mass transport influence on corrosion process; 5. electrochemical techniques including cell design, reference electrode selection, etc.; and 6. inhibitors used to affect corrosion rates.

The overall scope of the symposium should include both theoretical and applied aspects of the subject.

Suggestions and inquiries should be sent to the Symposium Chairman: J. R. Ambrose, Dept. of Materials Science and Engineering, University of Florida, Gainesville, Fla. 32611.

International Symposium on Atmospheric Corrosion

Papers concerning all phases of atmospheric corrosion and its testing and evaluation are being solicited. Areas of interest include laboratory, service, and environmental testing and may range from fundamental studies to engineering problems. Papers on statistical treatment of data, evaluation criteria, and theoretical considerations are desired, as well as those concerned with recording and retrieval of data and environmental and weather factors.

Of particular interest are papers tabulating long-term atmospheric test results from established test sites throughout the world for all metals. Effects of plating, conversion coats, anodizing, and cladding are appropriate subjects. Results of attempts to correlate laboratory and field testing may be reported.

The publication of a proceedings volume as part of the Corrosion Monograph Series is being considered.

Suggestions and inquiries should be sent to the Symposium Chairman: W. H. Ailor, Reynolds Metals Co., Metallurgical Research Div., Richmond, Va. 23261.

General Session

Papers on all aspects of low and high temperature corrosion will be considered. Experimental techniques for the study of corrosion phenomena are also of interest.

Suggestions and inquiries should be sent to the Session Chairman: K. Nobe, University of California, Boelter Hall 5405, Los Angeles, Calif. 90024.

CORROSION/DIELECTRICS AND INSULATION/ELECTRONICS/ELECTROTHERMICS AND METALLURGY/ENERGY TECHNOLOGY

Materials and New Processing Technologies for Photovoltaics

This symposium will deal with all aspects of the materials, processing, and characterization of photovoltaic devices, with the exception of amorphous silicon photovoltaics which will be covered in another symposium. Papers are especially solicited on fabrication techniques, including junction formation, metallization, and antireflection coating, on low cost silicon, novel thin film materials, encapsulation and packaging technologies and materials, failure mechanisms, and on modeling and characterization techniques. Papers on both concentrator and flat panel photovoltaics will be welcome.

A proceedings volume for this symposium is planned. Papers for this volume must be provided, in camera-ready copy form, at the time of presentation.

Suggestions and inquiries should be sent to the Symposium Co-Chairmen: J. Amick, Exxon Research and Engineering, P.O. Box 8, Linden, N.J. 07036; P. Rai-Choudhury, Westinghouse Research Laboratories, Pittsburgh, Pa. 15235; or E. Sirtl, Hellotronic GmbH, Postfach 1129, D-8263 Burghausen, Germany.

CORROSION/ELECTRONICS/ENERGY TECHNOLOGY/PHYSICAL ELECTROCHEMISTRY

Materials Problems in Photoelectrochemical Devices

Papers will be accepted on any aspect of the development of photochemical converters which stresses the solution to normal and photocorrosion.

Suggestions and inquiries should be sent to the Symposium Co-Chairmen: J. O'M. Bockris, Dept. of Chemistry, Texas A & M University, College Station, Texas 77843; R. L. White, Stanford University, Electronics Laboratories, Stanford, Calif. 94305; or K. Nobe, University of California, Boelter Hall 5405, Los Angeles, Calif. 90024.

DIELECTRICS AND INSULATION

General Session

Papers which deal with all aspects of dielectric materials including their preparation, characterization, interactions, and uses and whose subject matter is not covered by the special symposia, are invited to be submitted to this session.

Suggestions and inquiries should be sent to the Session Co-Chairmen: G. C. Schwartz, IBM Corp., Data Systems Div., Zip 461, Hopewell Junction, N.Y. 12533; or R. G. Frieser, IBM Corp., Data Systems Div., Zip 41A, Hopewell Junction, N.Y. 12533.

DIELECTRICS AND INSULATION/ELECTRONICS

Dielectric Isolation for VLSI and Other Devices

This symposium's aim is to focus on all aspects of dielectric isolation for device application. Priority will be placed on recent advances, both theoretical and experimental. Suggested topics are: 1. oxidation modeling (two dimensional oxidation, high pressure oxidation, HCl oxides); 2. isolation process schemes (isoplanar, LOCOS, OXIM, ROX, IOP, DGI, porous Si, total isolation, SOS); 3. process methods (thermal oxidation, high pressure oxidation, CVD, etc.); 4. geometry aspects (bird's beak modeling, planarization techniques); 5. physical/chemical/electrical characterization methods and results (stress and defect analysis in and around isolation areas, interrelationship between stress/defects and process/materials aspects, proximity effects, dopant/diffusion effects, enhanced or retarded diffusion effects); and 6. device fabrication and analysis (density aspects, device performance improvements, new device capabilities, reliability).

Suggestions and inquiries should be sent to the Symposium Co-Chairmen: H. B. Pogue, IBM Corp., Data Systems Div., Hopewell Junction, N.Y. 12533; or R. Kumar, Burroughs Corp., Components Group, Technology Ctr., 16701 W. Bernardo Dr., San Diego, Calif. 92127.

Fiber Optics: Materials and Devices

This symposium will be devoted to topics relevant to the components and materials associated with fiber optic systems. Topics concerning optical fibers, optical sources, optical detectors, and integrated optics will be included in order to provide the widest basis for interest and discussion.

Papers are solicited on the following topics: 1. process control; 2. relations between fiber properties and process parameters; 3. new materials systems and novel processes; 4. drawing conditions and their effects on fiber properties, particularly strength; 5. fundamental understanding of reactions and processes; and 6. materials and process requirements to be expected in future optical communications systems.

Papers dedicated to the study of injection lasers, light-emitting diodes and detectors for fiber optic systems are desired. Topics include: 1. materials growth systems; 2. new material systems; 3. materials properties and their relation to device performance; 4. new device structures; 5. device fabrication technology; 6. device properties necessary for optimum system design; 7. device packaging and technology problems. Review papers on selected topics will be presented, and if sufficient interest is apparent, a proceedings volume will be published.

Suggestions and inquiries should be sent to the Symposium Co-Chairmen: M. I. Cohen, Bell Laboratories, Room 8D-325, Murray Hill, N.J. 07974; or M. DiDomenico, Laboratories, Room 2D-354, Murray Hill, N.J. 07974.

Ionic and Electronic Conduction in Glasses

Papers are solicited on ionic and electronic conduction phenomena in glasses. Of particular interest are papers relating structure to conduction processes and mechanisms. Glasses are taken to include amorphous thin films as well as bulk materials. Suggested topics include electrode/glass reactions, charge injection, influence of impurities, heat-treatment, and radiation. Field effects include low and high field behavior and onset of breakdown. Also of interest are application-oriented papers treating, for example, nonlinear conduction, stress generation, optical properties, and electrochemical behavior.

Suggestions and inquiries should be sent to the Symposium Chairman: D. B. Dove, IBM Corp., Thomas J. Watson Research Ctr., P.O. Box 218, Yorktown Heights, N.Y. 10598.

Resist and Patterning Technology

A symposium will be held to discuss various aspects of the micro lithographic processes and materials used in the fabrication of integrated circuits, printed circuit boards, information storage devices, and other novel applications such as microengraving and biological patterning. Of special interest are new organic and inorganic resist materials and emerging lithographic techniques associated with the processing of submicron structures.

Original work or substantial review papers are solicited for the following topics: 1. resists: organic and inorganic materials for photon, x-ray, electron, and ion source exposure, chemistry, adhesion, characterization, processing techniques (coating, exposure, development, baking, stripping); 2. printing: contact (vacuum, conformable), proximity and projection (normal and deep u.v.), x-ray, laser, holographic, synchrotron, electron and ion beam, resistless direct radiation patterning; test structures for evaluating misregistration optically or electrically; micro lithography: lifts, printed circuit; etching: solution, vapor phase, plasma, and ion assisted techniques applied to metals and organic and inorganic dielectrics including radiation-sensitive materials, patterning associated contamination; 4. masks: materials, fabrication, inspection, cleaning, degradation, repair; 5. modeling image formation; 6. resists: resist processing techniques, limitations of optical lithography; and 6. device results: high resolution devices and structures that exemplify the application of advanced micro lithographic techniques.

The publication of a proceedings volume is being considered. It suggests that authors should have camera-ready copies of their papers for inclusion in a proceedings volume at the time of submission of the extended abstract.

Suggestions and inquiries, as well as comments on the structure of this symposium, should be sent to the Symposium Co-Chairmen: A. M. Voshchenko, Bell Laboratories, Crawford Corner Rd., Holmdel, N.J. 07733;

or M. Hatzakis, IBM Corp., Thomas J. Watson Research Ctr., P.O. Box 218, Yorktown Heights, N.Y. 10598.

Thin Films of Tunneling Dimensions

The purpose of this symposium is to promote a dialogue between those scientists interested in thin film surface physics and in the physics of interfacial layers and those working in the field of tunneling device physics. Papers of interest will focus on the properties and applications of thin films of tunneling dimensions. Examples of suitable topics include: 1. chemical and physical properties: film preparation, growth, deposition, multilayered structures—film characterization, defects, film uniformity, tunneling phenomena, electronic and electrical behavior of interfaces; and 2. applications: superconductive tunneling, solar cells, interfacial layer devices, novel tunneling devices.

A number of invited papers will be presented and contributed papers are solicited. The publication of a proceedings volume is being considered.

Suggestions and inquiries should be sent to the Symposium Co-Chairmen: J. Shewchun, Dept. of Engineering Physics, McMaster University, Institute of Materials Research, Hamilton, Ont., Canada L8S 4M1; or S. I. Raider, IBM Corp., Thomas J. Watson Research Ctr., P.O. Box 218, Yorktown Heights, N.Y. 10598.

DIELECTRICS AND INSULATION/ELECTRONICS/ELECTROTHERMICS AND METALLURGY

Defects and Transport in Semiconductors and Dielectrics

This is the fourth in a series of jointly sponsored symposia on the defect chemistry of nonmetallic solids. This symposium will deal with the generation and interactions of defects, charge transport, and the related properties of semiconductors and insulators. Both experimental and theoretical papers are solicited. Subjects within the scope of the symposium include isolated point defects, impurity centers, defect associates, and defect ordering in dielectric materials and in elemental and compound semiconductors, as well as surface effects including insulator to metal, insulator to semiconductor, and insulator to insulator phenomena. Experimental results are invited which involve such techniques as electrical conductivity, resonance techniques, optical methods including laser techniques, phase diagram determination, preparation of crystals and films containing controlled deviations from stoichiometry, dielectric breakdown, and mobility determinations.

Suggestions and inquiries should be sent to the Symposium Co-Chairmen: D. M. Smyth, Materials Research Ctr., Lehigh University, Bethlehem, Pa. 18080; or R. Reisner, IBM Corp., Thomas J. Watson Research Ctr., P.O. Box 218, Yorktown Heights, N.Y. 10598; or J. B. Wagner, Jr., Center for Solid State Science, Arizona State University, Tempe, Ariz. 85281.

ELECTRODEPOSITION

General Session

Original papers dealing with theoretical and applied aspects of electrodeposition and metal finishing that do not come under the special symposia are invited for this session.

Suggestions and inquiries should be sent to the Session Chairman: R. Sard, Oxy Metal Industries, 21441 Hoover Rd., Warren, Mich. 48089.

ELECTRODEPOSITION/PHYSICAL ELECTROCHEMISTRY

Electrocrystallization

The purpose of this symposium is to provide a forum for active workers in nucleation, phase formation, crystallization, and deposition on electrodes to make original fundamental contributions to these and related aspects of electrocrystallization. A number of invited papers are expected to be presented by international experts. Papers are solicited in the following areas: 1. stochastic nature of two-dimensional and three-dimensional nucleation and growth processes; 2. statistical aspects of crystal growth and metal deposition; 3. adsorption and other initial stages of deposition; 4. under and overpotential deposition; 5. factors

that influence the formation and growth of thick deposits and their relationship to passivation processes; 6. the atomic and micro structure of electrodeposits and their relationships to pertinent properties; 7. chemically modified surfaces; and 8. theoretical developments and computer simulation studies.

Suggestions and inquiries should be sent to the Symposium Co-Chairmen: R. G. Barris, Dept. of Chemistry, Carleton University, Ottawa, Ont., Canada K1S 5B6; or R. Weil, Dept. of Materials and Metallurgical Engineering, Stevens Institute of Technology, Castle Point Station, Hoboken, N.J. 07030.

ELECTRONICS

Semiconductors

Annealing of Semiconductors

This symposium will include invited and contributed papers on a variety of topics related to the annealing of defects in single crystal and polycrystalline semiconductors. The defects may have been introduced during growth, by high temperature processing, ion implantation, neutron transmutation doping, and any other means. Because of the current widespread interest in laser and electron beam annealing it is expected that these and other localized annealing techniques will be emphasized. However, the organizers of the symposium encourage abstracts on the latest advances in conventional thermal annealing and on economic comparisons of the newly developed localized methods with more conventional ones. Abstracts on other topics such as the impact of high temperature annealing on device, thin film, and metallization technology, basic electronic and ionic mechanisms of annealing, ultrarapid melting and recrystallization phenomena associated with pulsed laser annealing, transmutation doping, the effects of grain boundaries on annealing processes in polycrystalline materials, novel measurement techniques will be welcomed.

Suggestions and inquiries should be sent to the Symposium Co-Chairmen: R. F. Wood or R. T. Young, Oak Ridge National Laboratory, Solid State Div., Oak Ridge, Tenn. 37830.

Electron Microscopy of Semiconductors

This symposium will be devoted to the applications of electron microscopy in understanding semiconductor materials and correlating material characteristics with device performance. A few invited speakers will present overviews on the following topics: 1. structural characterization of defects and their influence on device performance; 2. determination of local chemistry via electron energy loss spectroscopy and energy dispersive x-ray analysis; 3. grain boundary structure in polycrystalline semiconductors; and 4. structure and properties of amorphous semiconductors. Abstracts covering original research on various topics where electron microscopy has been a valuable tool in evaluating materials or solving material problems are also solicited for a twenty minute oral presentation.

The publication of a proceedings volume is being considered. Suggestions and inquiries should be sent to the Symposium Co-Chairmen: S. Mahajan, Bell Laboratories, Murray Hill, N.J. 07974; or M. S. Abrahams, RCA Laboratories, Princeton, N.J. 08540.

Semiconductor Materials and Technologies for High Speed Logic

This symposium will be concerned with all semiconductor materials and technologies appropriate to high speed integrated logic excepting those related to Josephson junctions. Invited and contributed papers in the following areas are planned: 1. advanced silicon materials appropriate for high speed logic such as silicon-on-sapphire; 2. GaAs materials preparation including crystal growth, heteroepitaxy, LPE, VPE, MBE, and implantation; 3. other theoretically promising material candidates such as InP, Ge, ternaries, and quaternaries; 4. advanced processing techniques, e.g., self-aligned/short gate techniques; 5. improved dielectric and passivation systems; and 6. studies relating processing technology to yield, reliability, radiation hardness, and/or ease of fabrication.

Suggestions and inquiries should be sent to the Symposium Co-Chairmen: M. R. Namoridi, Texas Instruments, Inc., Central

Research Laboratories, M/S 118, P.O. Box 225936, Dallas, Texas 75265; or E. B. Stoneham, Hewlett-Packard, Santa Rosa Div., 1400 Fountain Grove Pkwy., Santa Rosa, Calif. 95404.

Semiconductors and New Electronic Technologies General Session

Original papers are requested on elemental and compound semiconductors including materials of interest in electronic devices. Areas to be covered include: 1. preparation and characterization of single crystalline, polycrystalline, and amorphous semiconductor materials in bulk form or as thin films; 2. preparation by growth and deposition techniques; 3. characterization by destructive and nondestructive diagnostic techniques; 4. advances in techniques to modify their electronic properties and device processing characteristics; 5. characterization and elimination of defects generated during material preparation and device fabrication; 6. materials possessing high electrical conductivity and thermal stability for VLSI applications; 7. preparation and properties of insulating and passivating layers for device applications; 8. metallization processes for interconnections and semiconductor contacts; 9. novel materials and devices in fabrication and processing of silicon integrated circuits, solar cells, power devices, laser diodes, and LEDs; 10. new developments in wet and dry processes employed in the fabrication of active and passive electronic devices; 11. micro lithographic techniques for patterning of thin films and small structures by optical, x-ray, E-beam, and ion-beam methods; 12. selective etching and deposition of thin films by physical and chemical techniques involving sputtering, plasma, reactive ion etching, evaporation, plating, and chemical solutions; 13. novel resist materials and processes for lithographic applications; 14. masking films for selective etching and deposition; 15. isotropic and anisotropic etching of bulk crystalline and amorphous materials; and 16. fabrication of three-dimensional device microstructures useful in instrumentation and biomedical applications. Suggestions and inquiries should be sent to the Session Chairmen: E. Bassous, IBM Corp., Thomas J. Watson Research Ctr., P.O. Box 218, Yorktown Heights, N.Y. 10598.

Recent News Papers Session

Recent News Papers and Extended Recent News Papers consisting of topics covered by the symposia and sessions being sponsored or cosponsored by the Electronics Division are invited for presentation.

Suggestions and inquiries should be sent to the Session Chairman: W. A. Pliskin, IBM Corp., Dept. 175, Zip 462, Route 52, Hopewell Junction, N.Y. 12533. A special Call for Recent News Papers will appear in the June, July, and August 1980 issues of the JOURNAL.

ELECTRONICS/ELECTROTHERMICS AND METALLURGY

Process and Use Related Radiation Effects in Electronic Devices

Ionizing radiation and its influence on electronic materials, devices, and circuits is the subject of this symposium. Radiation effects arising from device processing or from device operation in environments where ionizing radiation is present are to be discussed. Papers which deal with these topics on a fundamental or applied level are solicited for this symposium. State-of-the-art reviews or investigations into specific topics are both acceptable. Suggested areas for contributed papers are: process induced radiation damage and its influence on device stability; alpha particle or cosmic ray induced soft failures in high density circuits; and radiation-hardening of high density or high performance integrated circuits.

Papers discussing damage mechanisms, device/circuit stability, and their measurement and characterization will be considered. Studies of materials, processes, or devices which impact the stability of such devices or circuits are also solicited. The publication of a proceedings volume is being considered.

Suggestions and inquiries should be sent to the Symposium Co-Chairmen: J. M. Aitken, IBM Corp., Thomas J. Watson Research Ctr., P.O. Box 218, Yorktown Heights, N.Y. 10598; or T. May, Intel Corp., 3585 SW 198th Ave., Aloha, Ore. 97005.

ELECTRONICS/ENERGY TECHNOLOGY

Properties and Preparation of Amorphous Silicon for Electronic Devices

This symposium will consist of state-of-the-art invited papers and contributed presentations on application related aspects of the deposition, characterization, and understanding of amorphous silicon based films. Contributions are sought on photovoltaic and photoconductive response (e.g., solar cells, detectors), novel device configurations (e.g., stacked cells, arrays), the role of additives (e.g., H, F, O, dopants), diagnostics of preparative plasmas (e.g., mass spectroscopy, optical spectroscopy), and new preparation or characterization techniques. Papers on electronic properties as they pertain to possible devices will also be considered.

Suggestions and inquiries should be sent to the Symposium Co-Chairmen: H. C. Gobrecht, IBM Corp., Thomas J. Watson Research Ctr., P.O. Box 218, Yorktown Heights, N.Y. 10598; or D. E. Carlson, RCA Laboratories, Princeton, N.J. 08540.

ELECTROTHERMICS AND METALLURGY

Science and Technology of Halide Lamps and Lasers

This symposium will be devoted to the fundamental and applied aspects of the high temperature halide chemistry in lamps (incandescent and discharge) and lasers. Topics of interest include: 1. chemical effects of gaseous and condensed phase halides in discharges and in temperature gradients; 2. high temperature metal halide reaction kinetics and thermodynamics; 3. phase equilibria, vaporization phenomena, complex molecules; 4. tungsten halogen lamps; 5. chemistry; 6. transport cycles; 7. halide-electrode-wall interactions; 7. electrode reactions; and 8. impurity effects.

Suggestions and inquiries should be sent to the Symposium Chairman: E. G. Zubler, General Electric Co., Lighting Research and Technical Service Operation, Nela Park, Cleveland, Ohio 44112.

ENERGY TECHNOLOGY

Fuels from Nonfossil Energy Storage Systems

This symposium will deal with processes to produce hydrogen based on nonfossil energy storage systems such as fusion and solar energy. Processes to be considered include high temperature electrolysis, thermochemical, and thermochemical/hybrid processes. Primary emphasis will be placed on experimental results including materials for electrodes and electrolytes, chemical reactions, and so on. Papers dealing with fundamentals (thermodynamics, chemistry, etc.) will also be considered as well as papers dealing with theory and modeling of processes and components. The symposium will consist of invited and contributed papers.

Suggestions and inquiries should be sent to the Symposium Co-Chairmen: J. A. Fillo, Brookhaven National Laboratory, Bldg. 129, Upton, N.Y. 11973; or M. Bowman, University of California, Los Alamos Scientific Laboratory, P.O. Box 1663, Los Alamos, N.M. 87545.

General Session

Papers are solicited in all areas on energy technology not covered by concurrent symposia. Of particular interest are electrochemical aspects of power sources and converters, as well as of energy distribution, storage, and conservation. Power sources include fossil and biomass, nuclear, geo and ocean thermal, and solar. Storage includes specific applications, such as power sources and fuels for individual transportation, or fuels for transmission in pipelines, are also solicited.

Suggestions and inquiries should be sent to the Session Co-Chairmen: A. J. Nozik, Solar Energy Research Institute, 2500 N. 15th St., Golden, Colo. 80401; or J. McCrean, Brookhaven National Laboratory, Upton, N.Y. 11973.

ENERGY TECHNOLOGY/INDUSTRIAL ELECTROLYTIC/PHYSICAL ELECTROCHEMISTRY

Ion Exchange: Transport and Interfacial Properties

This symposium will emphasize the processes and properties of materials broadly de-

finer as ion exchangers and ionic conductors. Papers should pertain to interfacial material transport, analogous to "electrodes" and to bulk transport, analogous to "ionics". Materials might be typical synthetic organic polymer solids, but could include free-standing liquids, liquids in inert supports, liquids in gelled binders, single crystals, pressed pellets, and composites. Materials need not be in the form of membranes. Contacting media might be electrolytes but could also be ion-generating metals, inert metals, or other conductors. Specific topics include: 1. macroscopic models, equations of motion, interfacial potential theory, reconciliation of models with thermodynamic theories; 2. microscopic models for thermodynamic and transport properties, structural factors in relation to single ion partitioning, salt extraction, ion pairing, activity coefficients, and mobilities; 3. experimental methods for measuring electrical properties, transient and steady-state ionic and electroneutral species transport, comparison of models and experiments, analysis of interfacial transport, kinetics, adsorption, blocked vs. nonblocked interfaces; 4. applications of spectroscopic, diffraction, magnetic, and other nonelectrical methods to structure and dynamic properties; 5. synthesis, fabrication, and characterization of new materials for ion exchanger and ion exchanging membrane applications—stability of materials; and 6. progress in devices, device concepts, and device applications using ion exchanging materials.

Suggestions and inquiries should be sent to the Symposium Co-Chairmen: R. P. Buck, Dept. of Chemistry, University of North Carolina, Chapel Hill, N.C. 27514; R. S. Yeo, The Continental Group, Inc., Energy Systems Laboratory, 10432 N. Tantau Ave., Cupertino,

Calif. 95014; or M. M. Dorio, General Electric Co., Nela Park #3400, Cleveland, Ohio 44112.

INDUSTRIAL ELECTROLYTIC

Regeneration of Chemicals

This symposium will explore new developments in the use of electrolysis to regenerate chemicals which have been previously decomposed, contaminated, or diluted in an industrial process. Regeneration can occur simultaneously with consumption (one-stage process) or after consumption (two-stage or multistage process). Papers are invited in the fields of 1. organosynthesis, 2. redox reactions, 3. waste treatment, 4. etching, 5. electroplating, 6. inorganic synthesis, 7. leaching, and 8. polymerization, etc.

Suggestions and inquiries should be sent to the Symposium Chairman: K. H. Oehr, B. C. Research, 3650 Westbrook Mall, Vancouver, B.C., Canada V6S 2L2.

Separators

This symposium will consist of invited and contributed papers dealing with critical problems and new developments in separators in industrial electrolytic processes. Two major areas of interest are the chlor-alkali and battery fields. For the former, papers on both ion exchange membranes and porous diaphragms are solicited. Areas of battery separators which will be of interest are new developments for ambient and high temperature secondary batteries. Research in primary batteries and miscellaneous separator topics will be considered if

interest warrants. Topics suitable for presentation will include: 1. chlor-alkali membrane cells, including new applications; 2. progress in porous separators; 3. high temperature battery ceramics, others; and 4. porous battery separators. The publication of the proceedings volume is being considered. Suggestions and inquiries should be sent to the Symposium Chairman: M. M. Dorio, General Electric Co., Nela Park #3400, Cleveland, Ohio 44112.

PHYSICAL ELECTROCHEMISTRY

Third International Symposium on Molten Salts

This symposium will stress two major topics of importance to molten salt chemistry and technology, molten salts in energy conversion and conservation and fundamental aspects of molten salt chemistry.

Topics suitable for the symposium include: 1. applications of molten salts in batteries and fuel cells; 2. applications in solar energy storage; 3. uses of molten salts in coal and oil shale conversion; 4. catalytic properties of molten salt media; 5. advances in electrochemistry and spectroscopy of molten salt solutions; and 6. thermodynamic and transport properties of melt systems.

Suggestions and inquiries should be sent to the Symposium Co-Chairmen: G. Mamantov, Dept. of Chemistry, University of Tennessee, Knoxville, Tenn. 37916; S. J. Yosim, Atomics International, 8900 DeSoto Ave., Canoga Park, Calif. 91304; or M. Blander, Argonne National Laboratory, Argonne, Ill. 60439.

-
- a.) For receipt no later than May 1, 1980, submit a 75-word abstract of the paper to be delivered on the enclosed form.
 b.) For receipt no later than June 1, 1980, submit two copies of an extended abstract, 500-1000 words.
 c.) Send all abstracts to The Electrochemical Society, Inc., P.O. Box 2071, Princeton, N.J. 08540, with the exception of Recent News Papers. See details on preceding page.
-

Use overleaf in submitting your abstract for
 The 1980 Fall Meeting
 of
 The Electrochemical Society, Inc.
 to be held at
 The Diplomat
 Hollywood, Florida
 October 5-10, 1980

75-Word Abstract Form

(Deadline for receipt—May 1, 1980)

HOLLYWOOD, FLORIDA, MEETING—OCTOBER 5-10, 1980

Submit to: The Electrochemical Society, Inc.
P.O. Box 2071, Princeton, N.J. 08540

Schedule for _____ of _____
Symposium ECS Division

Abstract No. _____
(do not write in this space)

(Title of paper) _____

(Authors) (Underline name of author presenting paper) _____

(Business Affiliation and Address) _____

(ZIP Code)

(Tel. No.)

(Type abstract in this area—double spaced.)

Do you require any audiovisual equipment?

- ☐ 35 mm (2 x 2 in.) slide projector
☐ Vu-Graph
☐ other (specify)

Is a full length paper on this work to be
submitted for Society Journal publication?

☐ Yes ☐ No

Papers presented before a Society technical meeting become the property of the Society and may not be published elsewhere without written permission of the Society. Papers presented at Society technical meetings must be authored by a member or sponsored by an active member.

Insert name of Society member author or sponsor

1979—Volume 126
Author and Subject Index
Journal of the Electrochemical Society



The Computer-Derived 1978 Journal Index

The Publication Committee of the Society recommended the use of a computer-derived index in 1968, and this practice is planned to be continued. This index is published two months earlier than the usual index and makes possible indexing more information than before. These indices refer only

to *Journal* articles, reviews, brief communications, discussions, and news and reviews listed in the contents pages. They do not include meeting papers, abstracts, and news items. These indices were prepared for the *Journal* by the Institute for Scientific Information®, Philadelphia, Pennsylvania.

Using the Index

1. Given any author, go directly to his name in the author and title index to find the full paper title with a page citation or, if he is a secondary author, to find a cross-reference to a primary author.
2. Given any topic, go to the subject index and search for the key word itself.
3. For a detailed explanation of symbols and abbreviations, see the sample pages before the individual author and title index and the subject index.
4. Chemical formulae cannot be reproduced directly because the conventional computer printout appears in capital letters only. For example, B13 could be three atoms of bismuth or boron triiodide. To avoid this am-

biguity, an attempt has been made to write out chemical formulae.

5. In the author index, an author is always listed with all available initials, which for lack of space sometimes can mean omission of one or two letters from the end of his last name. This truncation is indicated by a period at the end of the last name.

The Publication Committee will appreciate comments on the usefulness and accuracy of this index.

NEWTON SCHWARTZ
Chairman
Publication Committee

JOURNAL ARTICLE AUTHOR AND TITLE INDEX

To locate a full description of a source item, look up the primary author. Under a given name, journal articles of primary authorship are described first. Items of secondary authorship follow. These are cross-referenced to the primary author whose name follows the word SEE.

	Primary Author	Issue Number	Volume	Page
	CRAMER SD		N6	126 891
Article Title	ESTIMATION OF THE SLOPE OF POLARIZATION CURVES IN THE VICINITY OF THE CORROSION POTENTIAL			
	CREVECOE.C SEE DEWIT HJ		126	779
	CRIPPA PR SEE BARALDI P		126	1207
	CROSET M DIAZ J	DIEUMEGA.D	MERCANDA.LM	N9 126 1543
	INFLUENCE OF CURRENT DENSITY ON THE COMPOSITION OF GAAS ANODIC OXIDE FILMS			
	CUBICCIO.D LAU KH		N5	126 771
	THERMODYNAMICS OF VAPORIZATION OF ZRL4 FROM SUBSTOICHIOMETRIC SOLID ZIRCONIUM IODIDES			
Secondary Author(s)	CUBICCIO.D LAU KH		N10	126 1723
	KINETICS OF OXIDATION OF YTTRIA HOT-PRESSED SILICON NITRIDE			
	CUBICCIO.D SEE LAU KH		126	490
	CURRAN JS GISSLER W		N1	126 56
Cross Referenced	DIFFERENT PHOTOELECTROCHEMICAL BEHAVIOR OF SINTERED AND FLAME-OXIDIZED FE2O3			
Secondary Author	CURRIE JE SEE CONWAY BE		126	985
	CZAKONAG.I SEE LEIDHEIS.H		126	204
	CZAKONAG.I SEE LEIDHEIS.H		126	391
	DABROWIA.JC SANTILLO FS		N12	126 2091
Primary Author	REDOX PROPERTIES OF BLEOMYCIN AND TALLYSOMYCIN AND A SERIES OF THEIR METALLODERIVATIVES			

- ABBOTT RE SEE BLANK M 126 1471
 ABDOLAHAM AA SEE ELHAGHY SM 126 171
 ABRAHAM KM SEE RAINH SP 126 523
 ADACHI N SEE MATSUSHI K 126 1268
 ADAMS AA FOLEY RT N5 126 775
- ELECTROCHEMICAL BEHAVIOR OF LOW MOLECULAR WEIGHT HYDROCARBONS IN TRIFLUOROMETHANESULFONIC ACID MONOMERATE
 ADAMS AC CAPIO CD HASZKO SE PARISI GE POVLONET EI ROBINSON M N2 126 313
- HIGH TEMPERATURE DEPOSITION AND EVALUATION OF PHOSPHORUS-DOPED OR BORON-DOPED SILICON DIOXIDE FILMS
 ADAMS AC MURAKA R N2 126 334
- MEASURING THE PHOSPHORUS CONCENTRATION IN DEPOSITED PHOSPHOSILICATE FILMS
 ADAMS AC CAPIO CD N6 126 1042
- DEPOSITION OF SILICON DIOXIDE FILMS AT REDUCED PRESSURE
 ADAMS AC SCHINKE DP CAPIO CD N9 126 1539
- EVALUATION OF THE PRISM COUPLER FOR MEASURING THE THICKNESS AND REFRACTIVE INDEX OF DIELECTRIC FILMS ON SILICON SUBSTRATES
 ADAMS AC SEE MURAKA SP 126 996
 AGARWAL AK SEE PEDHARJE SP 126 701
 AGARWAL VK SEE SHARMA SD 126 325
 ALKIRE R SIFARI D N1 126 15
- LOCATION OF CATHODIC REACTION DURING LOCALIZED CORROSION
 ALKIRE R LU PY N12 126 218
- EFFECT OF HYDROGEN EVOLUTION ON CURRENT DISTRIBUTION DURING ELECTRODEPOSITION AT VERTICAL ELECTRODES
 ALKIRE RC SEE BECK TR 126 1662
 ALKIRE RC SEE GOAL POWER SOURCES 126 2125
 AMES A SEE HOFFMAN A 126 603
 ANDHARE PN SEE KESAVAN R 126 642
 ANDHARE PN SEE TOPICH JA 126 2274
 ANDRESEN RE N2 126 328
- SOLUBILITY OF OXYGEN AND SULFUR DIOXIDE IN MOLTEIN SODIUM SULFATE AND CARBON DIOXIDE IN MOLTEIN SODIUM CARBONATE
 ANG POP SEE SARMEHLS AF 126 1831
 ANGLELL J SEE SHAFER M 126 1625
 ANTONIADOU D RODONI M DUTTON RN N11 126 1939
- PURITY REDISTRIBUTION IN SiO₂-Si DURING OXIDATION - NUMERICAL SOLUTION INCLUDING INTERFACIAL FLUXES
 ANTONIADOU D SEE LEE HC 126 2001
 ARAI M SEE KASAHARA J 126 1597
 ARVIA AJ SEE CORCOVA R 126 1172
 ARVIA AJ SEE FOLMER ME 126 257
 ARVIA AJ SEE FOLMER ME 126 592
 ARVIA AJ SEE LEZNA R 126 2140
 ARVIA AJ SEE PODESTA JJ 126 1363
 ARVIA AJ SEE TRIACA WE 126 218
 ARVIA AJ SEE ZERBINO JO 126 93
 ATUNG S WEST K JACOBSEN T N8 126 1311
- DYNAMIC ASPECTS OF SOLID SOLUTION CATHODES FOR ELECTROCHEMICAL POWER SOURCES
 ATUNG S SEE JACOBSEN T 126 2169
 ATODA N SEE KOMURO M 126 483
 AUGUSTYN J SEE KUDDELMG 126 1656
 AUGUSTYN J SEE STALDER C 126 2007
 AWAKURA Y EBATA A KONO D N1 126 23
- DISTRIBUTION OF LOCAL CURRENT DENSITIES DURING COPPER ELECTRODEPOSITION ON A PLANE VERTICAL CATHODE
 BACON FT N1 126 C 7
- FUEL CELL - SOME THOUGHTS AND RECOLLECTIONS
 BADZALAM JJ SEE DEUGHERA A 126 1902
 BAGLIN JEE HEUBLE FM N2 126 277
- EPITAXIAL RELATIONS IN FILMS OF CR₂PT₃ AND CRPT ON SAPPHIRE
 BAILEY JM RITCHEE IM N12 126 2285
- CALCULATION OF POLARIZATION CURVES IN THE VICINITY OF THE LIMITING CURRENT
 BAILY MG SEE SHAFER M 126 911
 BAILY F CONENOLD G MIKILAJC J N9 126 1604
- SIMPLIFIED THEORY OF REACTIVE CLOSE-SPACED VAPOR TRANSPORT
 BAIZER MM SEE MALLCHER R 126 404
 BALIGA BJ GHANSHI SK N1 126 135
- PLANAR DIFFUSION IN GALLIUM ARSENIDE FROM TINDOPED OXIDES
 BALIGA BJ N1 126 138
- DOPANT DISTRIBUTION IN SILICON LIQUID PHASE EPITAXIAL LAYERS - MELTBATH EFFECTS
 BALIGA BJ N2 126 292
- DEEP PLANAR GALLIUM AND ALUMINUM DIFFUSION IN SILICON
 BALIG P SEE SINGH BR 126 1288
 BALIG P SEE WILHELM SM 126 419
 BALOG M SCHIEBER M MECHAN M PATAL S N7 126 1203
- CHARACTERISTICS OF GROWTH OF FILMS OF ZIRCONIUM AND HAFNIUM OXIDES XZRO₂·HFO₂ BY THERMAL DECOMPOSITION OF ZIRCONIUM AND HAFNIUM BETA-DICARBOXYLATE COMPLEXES IN THE PRESENCE AND ABSENCE OF OXYGEN
 BANDY SG SEE SANKARAN R 126 1241
 BANAL NP SEE LOVBERG M 126 985
 BARALDI P CAPELLET R CRIPPA PR ROMEO N N7 126 1207
- ELECTRICAL CHARACTERISTICS AND ELECTRET BEHAVIOR OF MELANIN
 BARD AJ SEE FREIDLIN RA 126 1892
 BARD AJ SEE KHL PA 126 598
 BARD AJ SEE KOHL PA 126 598
 BARD AJ SEE KOHL PA 126 603
 BARD AJ SEE LUTHER JD 126 414
 BARD AJ SEE NOUFI RN 126 949
 BARD AJ SEE REICHMAN B 126 583
 BARD AJ SEE REICHMAN B 126 2133
 BARNES JJ DELASTI JM DEAL BE N10 126 1779
- LOW TEMPERATURE DIFFERENTIAL OXIDATION FOR DOUBLE POLYSILICON VLSI DEVICES
 BARNES RJ SEE THIEL FA 126 1272
 BARRADAS R4 SEE PORTER JD 126 1693
 BARYCKA T TETERCH H ZNANIKOW Z N2 126 345
- SODIUM HYDROXIDE SOLUTION SHOWS SELECTIVE ETCHING OF BORON-DOPED SILICON
 BARKAL M SEE KNOBLER R 126 1853
 BAYLIS BKW HUANG CC SCHLESIN M N3 126 394
- STUDY OF THE PRODUCTS OF ULTRAVIOLET IRRADIATION OF PALLADIUM-CONTAINING CATALYSTS FOR ELECTROLESS METAL DEPOSITION
 BAYLIS BKW HEDGECOCK NE SCHLESIN M VANMEIJNA N10 126 1071
- PROTON BACKSCATTERING ANALYSIS OF THE POLY-CATALYST ON GLASS USED IN ELECTROLESS DEPOSITION
 BECK TR LIN KF N2 126 252
- SURFACE STRESS CURVES FOR PLATINUM
 BECK TR ALKIRE RC N10 126 1602
- OCCURRENCE OF SALT FILMS DURING INITIATION AND GROWTH OF CORROSION PITS
 BECKER ME SEE FRANKENBERG 126 1718
 BELANGER G SEE SUGIMOTO K 126 535
 BENGALI A NOBE K N7 126 1118
- ELECTRODISOLUTION KINETICS OF NICKEL IN CONCENTRATED ACIDIC CHLORIDE SOLUTIONS
 BENSON DN SEE H M 126 965
 BERKENBLUM SE REISMAN A 126 1004
 BERKENBLUM SE REISMAN A 126 1406
 BERKOWITZ HL LUR RA N9 126 1479
- ERRORS IN RESISTIVITIES CALCULATED BY MULTILAYER ANALYSIS OF SPREADING RESISTANCES
 BEZILLA BM MALDY JT N4 126 579
- LOW TEMPERATURE STUDIES OF ELECTROCHEMICAL KINETICS - 3. USE OF CONCENTRATION STUDIES IN DETERMINING THE RATES, MECHANISMS, AND APPARENT RATE CONSTANTS OF ELECTROHYDRODYNAMIC REACTIONS
 BHAR TN LAMB GW N9 126 1514
- EFFECT OF PROCESSING PARAMETERS ON THE PULSE ELECTROPLATED AU COATING
 BHARGAVA RN SEE FITZPATRICK 126 341
 BHILL VS SEE FRITZ EM 126 683
 BHILLA KL SEE KESAVAN R 126 642
 BHILLA KL SEE TOPICH JA 126 2274
 BIEFELD R JOHNSON RT N1 126 1
- IONIC CONDUCTIVITY OF LI2C-BASED MIXED XIDES AND THE EFFECTS OF MOISTURE AND LEAD ON THEIR ELECTRICAL AND STRUCTURAL PROPERTIES
 BIEFELD RM JOHNSON RT KARNOSK MN N5 126 618
- IONIC CONDUCTIVITY AND PHASE DIAGRAM OF THE CuBr-AGL SYSTEM
 BINDRA P CLOUSER SJ YEAGER E N9 126 1631
- PLATINUM DISSOLUTION IN CONCENTRATED PHOSPHORIC ACID
 BIRD GR SEE SHENIZU S 126 273
 BIRKES LA SEE VERNON SM 126 703
 BLANK M SGO L ABBETT RE N9 126 1471
- IONIC PERMEABILITY OF ADSORBED MEMBRANE PROTEIN MONOLAYERS
 BLATTNER RJ SEE TSAI WY 126 98
 BLONDEAU G FROELICH M FROMENT M GOFF AHL DYER CK N4 126 586
- BREAKDOWN AND EFFICIENCY OF ANODIC OXIDE GROWTH ON TITANIUM
 BLONDEAU G FROELICH M FROMENT M GOFF AHL ZERBINO J N5 126 1592
- INFLUENCE OF COPPER ADDITION ON OPTICAL PROPERTIES OF TiO₂
 BLUMENTHAL RM SEE DIRSHTE RT 126 264
 BOMHE G SEE KNOBLER R 126 1853
- CPA ETCHING IN A DIODE SYSTEM
 BONINO F SEE DIPIETRI B 126 729
 BOMNET M SEE DUCHEMIN JP 126 1134
 BONNETI A HADATE M BIEDA F N2 126 248
- ELECTROCHEMICAL STUDIES ON IONIC NITRIDE SOLUTIONS IN MOLTEIN SALTS
 BORREGO JM SEE PANDE K 126 300
 BORKAMP BA SEE WEN CJ 126 2258
 BOWEN W DEY AN N11 126 2335
- PRIMARY Li-SOCL₂ CELLS - 9. CYCLIC VOLTAMMETRIC AND COLUMETRIC STUDIES OF SOCL₂ REDUCTION
 BOYD GO SEE MOHAPATRA SK 126 805
 BRACKEN RC SEE MCGUIRE GE 126 1075
 BRAUN M NOBE K N10 126 1666
- ELECTRODISOLUTION KINETICS OF COPPER IN ACIDIC CHLORIDE SOLUTIONS
 BRANSTEE J VALLET CE N6 126 960
- MIGRATIONAL POLARIZATION IN HIGH CURRENT DENSITY MOLTEIN SALT BATTERY AND FUEL CELL ANALOGS
 BRANSTEE J SEE VALLET CE 126 527
 BREDA F SEE BONDI PA 126 248
 BROOKER MH N12 126 2295
- KINETIC STABILITY OF NITRATE ION IN MOLTEIN NITRATE BY RAMAN SPECTROSCOPIC STUDIES OF G-18-ENRICHED KNO₃
 BROWN JR SEE JOH DY 126 1731
 BRUCKENS S MARTINCH N7 126 1307
- CLOSE FORM EXPRESSION FOR THE PRIMARY RESISTANCE AT A RING ELECTRODE
 BRUCKENS S SEE KANZAKI Y 126 437
 BRUCKENS S SEE TOSUDA K 126 431
 BRUNNER SO SEE RAUH RD 126 523
 BRUNDADE D SEE ROLISON DR 126 407
 BRYANT W N11 126 1899
- IMPORTANCE OF PHYSICAL STRUCTURE TO THE CAPACITY OF POROUS JELLY ELECTRODES
 BUCKLEY ON BURKE LD MCINTYRE JD N12 126 2171
- ELECTROCHROMISM IN ANODIC IRIDIUM FILMS - 2. PH EFFECTS ON CORROSION STABILITY AND THE MECHANISM OF COLORATION AND BLEACHING
 BUEHLER RG SEE PHILLIPS WE 126 1979
- EFFECT OF PHOSPHORIC ACID ON THE POSITIVE ELECTRODE IN THE LEAD-ACID BATTERY - 2. CONSTANT POTENTIAL CORROSION STUDIES
 BULLOCK KH N11 126 1848
- EFFECT OF PHOSPHORIC ACID ON THE POSITIVE ELECTRODE IN THE LEAD-ACID BATTERY - 3. MECHANISM
 BURKE LD SEE BUCKLEY ON 126 2171
 BUTLER MA N2 126 338
- AGING EFFECTS IN DEFECT-DOPED SEMICONDUCTING ELECTRODES
 BUTLER SR SEE ROHATGE A 126 143
 BUTLER SR SEE ROHATGE A 126 149
 BYERS MA PERONE SP N5 126 720
- COMPUTERIZED PATTERN RECOGNITION APPLIED TO Ni-CD CELL LIFE PREDICTION
 CAPELLET R SEE BARALDI P 126 1207
 CAPIO CD SEE ADAMS AC 126 313
 CAPIO CD SEE ADAMS AC 126 1042
 CAPIO CD SEE ADAMS AC 126 1539
 CARDIES JM SEE MURPHY DW 126 349
 CARDIES JM SEE MURPHY DW 126 497
 CARLSON DE HAGEE CW TRIANO AR N6 126 686
- EFFECT OF HYDROGEN CONTENT ON THE PHOTOVOLTAIC PROPERTIES OF AMORPHOUS SILICON
 CARMICHAEL NR FLENGAS SN N12 126 2098
- MOLAR VOLUME AND ELECTRICAL CONDUCTIVITY MEASUREMENTS IN THE TERNARY MOLTEIN SALT SYSTEM NaCl-CsCl-NaClO₄ - 1. MOLAR VOLUMES
 CARMICHAEL NR FLENGAS SN N12 126 2104
- MOLAR VOLUME AND ELECTRICAL CONDUCTIVITY MEASUREMENTS IN THE TERNARY MOLTEIN SALT SYSTEM NaCl-CsCl-NaClO₄ - 2. ELECTRICAL CONDUCTIVITIES
 CARMICHAEL NR FLENGAS SN N12 126 2104
- DENSITY, ELECTRIC CONDUCTIVITY, AND VISCOSITY OF SEVERAL N-ALKYLPYRIDINIUM HALIDES AND THEIR MIXTURES WITH ALUMINUM CHLORIDE
 CAPIO RA KING LA KING LA LINDSTRAE NARDI JC HUSSEY CL N10 126 1644
- CONDUCTIVITIES OF ALCL₃-RICH MOLTEIN ALCL₃-LiCl MIXTURES
 CAPIO RA SEE HUSSEY CL 126 1029
 CARLHUTTE JR SEE MURPHY EP 126 284
 CARUSO R SEE LUCIA C 126 637
 CATHART JC SEE PAWEL RE 126 1105
 CECILON P SEE PUCCIARELLI F 126 972
 CHAKRABARTY SC SEE IN JC 126 69
 CHAN ML SEE FLETCHER AN 126 1494
 CHAN SA SEE REISMAN A 126 1004
 CHAN SA SEE REISMAN A 126 1496
 CHANDLER TC FAUST JN HILBERON RE N12 126 2216
- DEBRIS-INDUCED EFFECTS FROM SPIN-ON DIFFUSION SOURCES
 CHANG CC SEE MURAKA SP 126 996
 CHANG CC SEE MURAKA SP 126 1095
 CHAO CY SEE SMALOWS G 126 2038
 CHANG HE SEE PEDNEKAR S 126 701
 CHANG HE SEE PEDNEKAR S 126 701
 CHEN Y SEE VISWANATH K 126 398
 CHEN Y SEE HELBERT JN 126 694
 CHEN M WINKIEWICZ VJ LEE K N11 126 1546
- ETCHING SILICON WITH FLUORINE GAS
 CHENG W N12 126 483
- BECKETT F M AWARD REPORT - EFFECTS OF SURFACE ADDITIVES ON THE PERFORMANCE OF LITHIUM-ALUMINUM ELECTRODES
 CHIANELL RR SEE JACOBSON AJ 126 2277
 CHIANELL RR SEE WALES CP 126 2260
 CHIANG KL SEE LUCIA C J SCHWETZ MF N12 126 997
- OPTICAL EVALUATION OF POLYCRYSTALLINE SILICON SURFACE ROUGHNESS
 CHIANG SH SEE SAVINELL RF 126 357
 CHIN DT YEO RS MCGREEN J SRINIVAS S N12 126 713
- ELECTROCHEMICALLY REGENERATIVE HYDROGEN-CHLORINE ENERGY STORAGE SYSTEM - STUDY OF MASS AND HEAT BALANCES
 CHIN DT VENKATES S N11 126 1908
- STUDY OF ALTERNATING VOLTAGE MODULATION ON THE POLARIZATION OF MILD STEEL
 CHIU TL SEE HUFF HR 126 1142
 CHOI KW YAO NP N8 126 1321
- HEAT TRANSFER IN LEAD-ACID BATTERIES DESIGNED FOR ELECTRIC-OR DIESEL PROPULSION APPLICATIONS
 CHOI MS SEE RHINES FN 126 1061
 CHRISTIAN PA SEE MURPHY DW 126 497
 CIGADA A SEE HAZZA B 126 2075
 CLEAK NJ SEE CORNER GA 126 1339
 CLOUSER SJ SEE BIODRA P 126 1631
 CLOUSER SJ SEE ROBBINS DJ 126 1213
 COCKAYNE B SEE ROBBINS DJ 126 1213
 COCKAYNE B SEE ROBBINS DJ 126 1556
 COCKS PH SEE WONG D 126 111
 COLEMAN JP SEE SAVINELL RF 126 357
 COHEN LH SEE KLEMENT M 126 1403
 COHEN M MITCHELL D NASHIMOTO K N3 126 442
- COMPOSITION OF ANODICALLY FORMED IRON OXIDE FILMS
 COHEN M SEE OLMEAD AM 126 2167
 COHEN RL KOCH FB SCHONBEIN L WEST KW N9 126 1608
- CHARACTERIZATION OF COBALT-HARDENED GOLD ELECTRODEPOSITS BY MOSSBAUER SPECTROSCOPY - 1. STATE OF COBALT IN THE AS-DEPOSITED MATERIAL
 CORNEJO SG SEE BAILY F 126 1694
 COLSON JC SEE JALLOULI EM 126 2254
 COLTON CK SEE LERNER H 126 337
 COLTON CK SEE LERNER H 126 337
 COLTON CK SEE RHEINIC L 126 1087
 CONNELL RG SEE MARINES FN 126 1061
 CONWAY BE CURRIE JE N6 126 985
- SIGNIFICANCE OF EFFECTS OF HIGH PRESSURE ON KINETICS OF ELECTRODE REACTIONS - 1. APPLICATIONS TO TRANSITION STATES IN HYDROGEN EVOLUTION REACTION MECHANISMS
 COOPER CF SEE HELBERT JN 126 694
 COOPER CF SEE HELBERT JN 126 131
 CORRODA R MARTINS RE ARVIA AJ N7 126 1172
- MULTIPLICITY OF ANODIC AND CATHODIC CURRENT PEAKS OBSERVED DURING POTENTIODYNAMIC PERTURBATIONS OF GOLD-SODIUM HYDROXIDE SOLUTION INTERFACES
 CORNER GA GRANT B CLEAK NJ N8 126 1339
- EXPLANATION OF THE ELECTROCHROMISM OF LUTETIUM DIPHthalocYANINE
 COSANDEY M ERMENEGOFF P N9 126 1601
- GASEOUS COMPLEXES OF GADOLINIUM CHLORIDE WITH

[illegible]

- AG-AGCL SYSTEM
GUALTIERI G. SEE SCHWARTZ G. 126 1737
GUARNIERI C. SEE LEE V. 126 1533
GUPTA N. TENNENBERG J. 126 1533
- FAILURE ANALYSIS OF BETA-98-ALUMINA MEMBRANES
TAKEN FROM SODIUM-SULFUR CELLS
GUR TM HUGGINS RA N 126 1451
- DECOMPOSITION OF NITRIC OXIDE ON ZIRCONIA IN A
SOLID-STATE ELECTROCHEMICAL CELL
GUTIERREZ AR SEE HIRAKAWA H 126 860
GUTZLER DE N 126 571
- EFFICIENCY OF Y2O3-TB UNDER LOW ENERGY
ELECTRON BOMBARDMENT
HABERLE K FROSCHELE E N 126 878
- WORK FUNCTION DIFFERENCE IN THE AL-SiO₂-Si
SYSTEM WITH REACTIVELY SPUTTERED SiO₂
HACKERMAN N SEE DELINCK F W 126 732
HACKERMAN N SEE WILHELM SM 126 419
HADATE M SEE BONKAI A 126 248
HADEISHI T KIMURA H N 126 1988
- DIRECT MEASUREMENTS OF CONCENTRATION OF TRACE
ELEMENTS IN GAS CRYSTALS BY ZEEMAN ATOMIC
ABSORPTION SPECTROSCOPY
HALLONER HC WHITE DA BAIZER MM N 126 404
- ELECTROCHEMICAL AND SECULAR SYNTHESIS OF
DERIVATIVES OF O-CARBOXYMETHYLARSONIC ACID
HALLER I FEDER R HATZKINS M SPILLER E N 126 154
- COPOLYMERS OF METHYL METHACRYLATE AND
METHACRYLIC ACID AND THEIR METAL SALTS AS
RADIATION SENSITIVE RESISTS
HAMBY C HOOVER NJ WIRKALA J ZAHNLE D N 126 2110
- CONCENTRATION CHANGES IN POROUS ZN ELECTRODES
DURING CYCLING
HAMPTON RE SEE STEIN H J 126 1750
HARRA N SUGIMOTO K N 126 1328
- STUDY OF THE PASSIVATION FILMS ON Fe-Cr ALLOYS
BY MODULATION SPECTROSCOPY
HARRADA S SEE OHMA Y 126 1531
HARUO T SEE MATSUHISHI K 126 1260
HARNACK PM SEE FITZPATRICK DJ 126 341
HARRIS LA GERSTNER M WILSON RH N 126 850
- CHARACTERIZED SEMICONDUCTOR ELECTRODES +2
ROOM TEMPERATURE DIFFUSION IN A SINGLE CRYSTAL
RUTILE ELECTRODE
HARRIS LA SEE WILSON RH 126 844
HARRISBAR NR SEE PORTER RA 126 460
HASE T SEE KOIKE J 126 1008
HASHTADT K SEE COHEN K 126 442
HASZKO SE SEE ADAMI K 126 313
HATTORI T N 126 1789
- THERMAL OXIDATION OF SILICON IN NET O₂-TE
MIXTURES AT 1200-DEGREES-C
HATZKINS M SEE HALLER I 126 154
HATZKINS M SEE SHAW JM 126 1026
HAYASHI I SEE MATSUI J 126 664
HAYASHI S SEE TAKAHASHI T 126 1654
HAYNES R N 126 881
- QUANTITY OF METAL DEPOSITED IN PULSED PLATING
VS DIRECT CURRENT PLATING
HAYNES R N 126 1633
- PULSE PLATING VS DIRECT CURRENT PLATING -
PERMEATION RATES OF HYDROGEN
HEARN E SEE PAZ D 126 1754
HEATH DE SEE PIETZEL RD 126 1274
HEATH DE SEE PINNELL RM 126 1798
HEDEGOCNEE SEE BAYLIS BKW 126 1671
HEERMAN L SEE DOLANES AW 126 347
HEINE K SEE KONIG L 126 296
HELBERT JN COOK CF CHEN CY PITTMAN CU N 126 694
- ELECTRON BEAM AND X-RAY RESIST BEHAVIOR OF
POLYMETHACRYLATE-LITHIUM
HELLER A SEE HILLER B 126 1483
HELLER A SEE PARKINSON DA 126 954
HELLER A SEE SHABDE SN 126 2279
HENGNER CH SEE WANG R 126 83
HERND SP SEE FITZPATRICK DJ 126 341
HESS KL SEE MANASEVICH BJ 126 2031
HEURLE FMD SEE BAGIN JEE 126 277
HEYNE L SEE DENIGELSD J 126 242
HEYROVSKY M SEE PUCCARELLI 126 972
HEZE K SEE ZEITLER HU 126 1430
HILDRON RB SEE CHANDLER TC 126 2216
- MODEL CALCULATIONS OF THE THERMODYNAMIC
PROPERTIES OF GASEOUS METAL HALIDES
HILDRON DL SEE LAU KH 126 490
HINE F HASTON M NODA T YOSHIDA T N 126 1439
- ELECTROCHEMICAL BEHAVIOR OF THE OXIDE-COATED
METAL ANODES
HIRAKAWA H GUTIERREZ AR N 126 860
- ELECTRON BEAM-INDUCED REACTIONS OF
ORTHOPHTHALQUINONE-DIAZIDE-SULFONYL
DERIVATIVES IN PHENOLIC-TYPE RESINS
HIRIBE K IWAMATSU S N 126 1426
- ELECTROSTATIC TECHNIQUE FOR PURIFYING
PHOTORESISTS
HO CP PLUMMER JD N 126 1516
- SI-SiO₂ INTERFACE OXIDATION KINETICS -
PHYSICAL MODEL FOR THE INFLUENCE OF HIGH
SUBSTRATE DOPING LEVELS +1, THEORY
HO CP PLUMMER JD N 126 1523
- SI-SiO₂ INTERFACE OXIDATION KINETICS -
PHYSICAL MODEL FOR THE INFLUENCE OF HIGH
SUBSTRATE DOPING LEVELS +2, COMPARISON WITH
EXPERIMENT AND DISCUSSION
HOARE JP N 126 190
- MECHANISMS OF CHROMIUM ELECTRODEPOSITION
HOARE JP N 126 1502
- SOME ASPECTS OF THE REDUCTION OF OXYGEN AT A
PLATINUM-ORGANIC ALLOY DIAPHRAGM
HOFFMAN A N 126 803
- CONDUCTION AND REDUCTION IN ANODECALLY FORMED
LAYERS OF SILVER BROMIDE
HOJKA HM ZAHN M MURTHY NK N 126 795
- VALIDITY OF MAGNER THEORY OF ELECTROPOLESHING
HOLLAHAN JR N 126 930
- DEPOSITION OF PLASMA SILICON OXIDE THIN FILMS
IN A PRODUCTION PLASMA REACTOR
HOLLAN L TRANCHARD JC HENNING R N 126 855
- INTERPRETATION OF SELECTIVE ETCHING OF III-V
COMPOUNDS ON THE BASIS OF SEMICONDUCTOR
ELECTROCHEMISTRY
HOLMES RM SEE DEY AN 126 1637
HOLMA V HARADA S KAJI T N 126 1531
- LSI SURFACE LEVELING BY RF SPUTTER ETCHING
HOODER NJ SEE HANBY DC 126 2110
HOODER NJ SEE NOVOTNY V 126 925
HOPPER NA SEE NOVOTNY V 126 2211
HORKANS J N 126 1861
- ROLE OF BUFFERS AND ANIONS IN NiFe
ELECTRODEPOSITION
HOSHINA T SEE OHNO K 126 1675
HOTIET F SEE THEETEN JB 126 450
HOWEL HJ SEE VERNON SM 126 703
HOWELLS BF SEE KATZ LE 126 1622
HOWES NJ SEE MUMFORD SD 126 1047
HSU L GELAS A SKINNER FJ FUNT BL N 126 635
- REDOX REACTIONS OF S2O8²⁻ WITH CUX²⁺ AND PEXIC²⁺
AT THE ROTATING RING DISK ELECTRODE
HSU YS GHANDHI SK N 126 1434
- PREPARATION AND PROPERTIES OF ARSENIC-DOPED
TiN OXIDE FILMS
HOSHINA T SEE BAYLIS BKW 126 354
HUANG CC SEN RK YEAGER E N 126 786
- OXYGEN REDUCTION ON PLATINUM IN 85-PERCENT
ORTHOPHOSPHORIC ACID
HUANG MD MESCHI DJ SEARCY AW N 126 1625
- THERMODYNAMIC PROPERTIES OF SES GAS
HUFF RH CHIU TL N 126 1142
- MINORITY-CARRIER LIFETIME - CORRELATION WITH
IC PROCESS PARAMETERS
HUGGINS RA SEE GUR TM 126 1007
HUGGINS RA SEE WEN CJ 126 2258
HUSSEY CL KING LA CARPIO RA N 126 1029
- ELECTROCHEMISTRY OF COPPER IN A ROLM
TEMPERATURE ACTIVE CHLOROALUMINATE MELT
HUSSEY CL SEE CARPIO RA 126 1644
HUYGHE O SEE DUCHEMIN JP 126 1134
HYDER SB SEE SANKARAN R 126 1241
IIDA Y SEE SASAKI Y 126 1948
- CHLOROMETHYLATED POLYSTYRENE AS A DRY ETCHING-
RESISTANT NEGATIVE RESIST FOR SUBMICRON
TECHNOLOGY
IMAMURA Y JASTRZEBSKI L GATOS HC N 126 1381
- DEFECT STRUCTURE AND ELECTRONIC
CHARACTERISTICS OF GAS LAYERS GROWN BY
ELECTROLYTIC AND THERMAL LIFE
INAH S SEE KOIKE J 126 1008
ISHIKAWA T SEE NAKAYAMA H 126 1301
ISHIZAKA A SEE IWATA S 126 110
- ISLAM N SINGH KP KUMAR S N 126 1676
- DENSITY, ELECTRICAL CONDUCTIVITY, AND
VISCOSITY OF MANGANESE(II) CHLORIDE AND TETRA-
N-BUTYLAMMONIUM HALIDES
ISOMAE S TANAKI Y YAJIMA A NABA M N 126 1014
- DISLOCATION GENERATION AT SI3N4 FILM/ SiO₂
SILICON SUBSTRATES AND VISCOELASTIC BEHAVIOR
OF SiO₂ FILMS
ISOMAE S SEE TANAKI Y 126 1071
ITOGAWA K N 126 691
- PROPERTIES OF SiN-DOPED INDIUM OXIDE COATINGS
DEPOSITED ON POLYESTER FILM BY HIGH RATE
REACTIVE SPUTTERING
IVES MB SEE ZARIN M 126 470
IWATA S TANAKI Y N 126 1078
- METHOD FOR REDUCING THE THERMAL AND ELECTRON
TRAPPING DENSITY IN THE HOLE SIDE FILMS
IWAMATSU S SEE HIRIBE K 126 1426
IWASAKI H SEE MIZUKAWA Y 126 1370
IWATA S ISHIZAKA A YAHAMOTO H N 126 110
- CORROSION TEST FOR METALLIZATION FOR PLASTIC-
ENCAPSULATED ICS
JACKSON LO SEE DEVRIES LE 126 993
JACOBI KT RAO DB N 126 1642
- SOLID-STATE PROBE FOR SO2-SO3 BASED ON Na2SO4-
I ELECTROLYTE
JACOBSEN T WEST K ATLUNG S THOMPSON AW N 126 2109
- ELECTROCHEMICAL POTENTIAL SPECTROSCOPY - NEW
ELECTROCHEMICAL SUBSTRATE
JACOBSEN T SEE ATLUNG S 126 1311
JACOBSON AJ WHITTING MS RICH SM N 126 887
- NEW IRON SULFUR CATHODES FOR NONAQUEOUS
LITHIUM BATTERIES
JACOBSON AJ CHANELL RR WHITTING MS N 126 2277
- AMORPHOUS MOLYBDENUM DISULFIDE CATHODES
JAEGER CA N 126 2205
- ELECTROCHEMICAL BEHAVIOR OF ORGANIC
SEMICONDUCTING AND CONDUCTING ELECTRODES IN
AQUEOUS MEDIA
JAIN GC PRASAD A CHAKRAVARTY BC N 126 89
- MECHANISM OF THE ANODIC OXIDATION OF SI AT
CONSTANT VOLTAGE
JAIN K KUMAR N MEHENDRU PC N 126 1558
- ELECTRICAL AND DIELECTRIC PROPERTIES OF
POLYVINYL BUTYRAL +1, STUDIES OF CHARGE
STORAGE MECHANISM
JAKLEVIC RC N 126 1548
- SOLID-STATE ANODIZATION OF ALUMINUM BY VAPOR
INFUSION
JALLOULI EM LARPIN JP LAMBERTI M CLESON JC N 126 2254
- Fe-Cr-AL ALLOY, HIGH TEMPERATURE CORROSION IN
SULFUR VAPOR
JAMES SD SEE DEVRIES LE 126 993
JANJAN MB SEE LEROY RL 126 1674
JANSEN SM TSEUNG ACC N 126 1353
- POTENTIOSTATIC PULSE STUDY OF OXYGEN EVOLUTION
ON TEFION-BONDED NICKEL-COBALT OXIDE
ELECTRODES
JASINSKI W N 126 167
- GROWTH OF CATHODIC NORMAL-HEPTYLVIOLGOLIN
RADICAL CATION FILMS
JASTRZEBSKI L LAGOWSKI J GATOS HC N 126 260
- QUANTITATIVE DETERMINATION OF THE CARBON
CONCENTRATION DISTRIBUTION IN SEMICONDUCTORS
BY SCANNING IR-ABSORPTION - SI
JASTRZEBSKI L LAGOWSKI J GATOS HC N 126 2231
- OUTDIFFUSION OF RECOMBINATION CENTERS FROM THE
SUBSTRATE TO THE FILM LAYERS - GAAS
JASTRZEBSKI L SEE IMAMURA Y 126 1381
JOH DY GRANNER BW BROWN ND N 126 1731
- EFFECTS OF D AND A MODEL FOR SILICON OXIDE
GROWTH UNDER A DEPOSITED THIN FILM ON SILICON
DURING POSTDEPOSITION HIGH TEMPERATURE
ANNEALING
JOHANNES JS SEE FJELBY FA 126 793
JOHNSON RT SEE DIEFFEL RM 126 116
JOHNSON RT SEE DIEFFEL RM 126 818
JONES KM SEE ROHATGI A 126 143
JORDAN J SEE SCHELLER FN 126 988
JORME J SEE KIM J K 126 1537
JOW T WAGNER JB N 126 1963
- EFFECT OF DISPERSED ALUMINA PARTICLES ON THE
ELECTRICAL CONDUCTIVITY OF CUPROUS CHLORIDE
JUNGE C MOLLER W N 126 1294
- EFFECT OF DIAZO AND CHROMATE SENSITIZERS ON
THE ACCURACY AND ADHERENCE OF PHOTODEPOSITED
PHOSPHOR LINES IN COLOR TV TUBES
KADISH KM SEE SCHELLER FN 126 988
KAGAMI A SEE KOIKE J 126 1002
KAJ I SEE HOMMA Y 126 1531
KAMEJIMA J SEE MATSUI J 126 664
KAMINS TI N 126 833
- RESISTIVITY OF LPCVD POLYCRYSTALLINE-SILICON
FILMS
KAMINS TI N 126 838
- OXIDATION OF PHOSPHOR-DOPED LOW PRESSURE AND
ATMOSPHERIC PRESSURE CVD POLYCRYSTALLINE-
SILICON FILMS
KAMINS TI SEE MANURAM MM 126 1019
KAMINS TI SEE REIF R 126 644
KAMINS TI SEE REIF R 126 653
KAMLOTT GW SEE SCHWARTZ GP 126 1737
KAND T SEE WANGHZ H 126 305
KANOKI I SEE KANZAKI K 126 1024
KANZAKI Y BRUCKENS S N 126 437
- SINUSOIDAL HYDRODYNAMIC VOLTAMMETRY AT A
ROTATING DISK ELECTRODE +2, EXPERIMENTAL TEST
OF THE ELECTRON TRANSFER THEORY
KANONOKI NR SEE DIEFFEL RM 126 818
KASAHARA J ARAI M WATANABE N N 126 1997
- EFFECT OF AEROSOL PARTICLE PRESSURE ON CARLESS
ANNEAL OF ION-IMPLANTED GAAS
KASANO H FURUHATA Y N 126 1567
- MORPHOLOGY CONTROL OF NPO5014 SINGLE CRYSTALS
GROWN FROM POLYPHOSPHORIC ACIDS
KATAN T RYGE G N 126 903
- CORROSION PENETRATION IN CREVICES OF DENTAL
AMALGAM
KATAN T SAVORY JR PERKINS J N 126 1635
- OBSERVATIONS OF AN OPERATING ZINC-PORRE
ELECTRODE
KATZ LE HOWELLS BF N 126 1622
- LOW TEMPERATURE, HIGH PRESSURE STEAM OXIDATION
OF SILICON
KAUFMAN FB SEE REISHAN A 126 1406
KAUFMAN L SEE SCHMID F 126 935
KANAKATSU S SEE KUROSU M 126 483
KEDDAR M SEE GABRIELLC 126 989
- ANODIC DISSOLUTION AND PASSIVATION OF TITANIUM
IN ACIDIC MEDIA +1, CHLORIDE SOLUTIONS
KELNER G SEE PHATAK SB 126 287
KESAVAN R ANDHARE PN BHOLA KL SINGH DV N 126 642
- ENHANCEMENT OF LATERAL P-N-P CURRENT GAIN BY
GETTERING
KESAVAN R SEE TOPICH JA 126 274
KHATTAK CP SEE SCHMID F 126 935
KIBLER FC SEE CARPIO RA 126 1050
KIM JT JORNE J N 126 1937
- MASS TRANSFER TO A ROTATING HEMISPHERE IN THE
LAMINAR FLOW REGION
KIM KM N 126 875
- INTERFACE MORPHOLOGICAL INSTABILITY IN
CZCHROMALSI SILICON CRYSTAL GROWTH FROM
HEAVILY B-DOPED MELT
KIMIZUKA N SEE TAKAYAMA E 126 2012
KIMURA H SEE HADEISHI T 126 1988
KING LA SEE CARPIO RA 126 1044
KING LA SEE CARPIO RA 126 1650
KING LA SEE HUSSEY CL 126 1029
- ELECTRON STOICHIOMETRY OF ANODIC DISSOLUTION
OF GOLD IN AQUEOUS ALKALINE CYANIDE
KIRKADY JS SEE PRYFT EM 126 673
KIRKADY JS SEE PRYFT EM 126 683
KITAGAWA M SEE SARAJE J 126 2226
KITAHORI T YONEDA Y KITAMURA K OKUYAMA H N 126 2287
- POLYMERS CONSTITUTED BY METHYL METHACRYLATE-
METHACRYLIC ACID, AND METHACRYLOYL CHLORIDE AS
A POSITIVE ELECTRON RESIST
KITAMURA K SEE KITAKOJU T 126 1881
KLEITZ M SEE FARRY P 126 2183
KLEBENT W N 126 1403
- SOLID-SOLID TRANSITION TEMPERATURES IN PEP2
FROM DIFFERENTIAL THERMAL ANALYSES UNDER
HYDROSTATIC PRESSURES LESS-THAN-EQUAL-TO 6
KB
KNODLER R BAKAL M BOHME G N 126 1853
- PERFORMANCE OF LiAl-FES CELLS WITH NEGATIVE
ELECTRODES PREPARED BY A POWDER-METALLURGICAL
METHOD
KNOTER ML SEE GINLEY DS 126 2163

- NITRIDE 126 334
MURAKA SP. SEE ADAMS AC 126 334
MURKAT A GATOS HC N12 126 2240
- EFFECT OF MICROSCOPIC GROWTH RATE ON OXYGEN
MICROSEGREGATION AND SWELL DEFECT DISTRIBUTION
IN COCHROMALIC-DRIVEN SILICON
MURPHY DB CARIDES JN N3 126 349
- LOW VOLTAGE BEHAVIOR OF LITHIUM-METAL
DIOXALCOGENE TOPOCHEMICAL CELLS
MURPHY DW CHRISTIAN-PA DISALVO FJ CARIDES JN
N3 126 497
- VANADIUM OXIDE CATHODE MATERIALS FOR SECONDARY
LITHIUM CELLS
MURRAY RM SEE ROBINSON DR 126 407
MURRAY RM SEE WIER LL 126 617
MURPHY MK SEE HUKA HM 126 795
NAGAT H N8 126 1400
- SIMPLE ANALYSIS OF VAPOR PHASE GROWTH - CITING
AN INSTANCE OF GAXINI-RAS
NAGY K SEE FIEJOLY TA 126 793
NAGY Z N7 126 1148
- THEORY OF THE GALVANOSTATIC DOUBLE PULSE
TECHNIQUE FOR THE INVESTIGATION OF FAST
ELECTRODE REACTIONS
NAIK JK TIEN YZ N4 126 562
- ELECTRICAL CONDUCTION IN Nb2O5-DOPED CERUM
DIOXIDE
NAKAHARA S N7 126 1123
- STEREODIFFRACTION METHOD FOR STUDYING THE
INCORPORATION OF ORGANIC MOLECULES IN
ELECTRODEPOSITED FILMS
NAKAI J SEE MORITANI A 126 1191
NAKAI J SEE OSAMURA K 126 1992
NAKAMURA H SEE TATE M 126 822
NAKAMURA S 126 1370
NAKATA H SEE YAMAZAKI T 126 1794
NAKAYAMA H SHINDO N ISHIZAKA T N7 126 1301
- ORGANIC COMPOUNDS INDUCING THE ROOM
TEMPERATURE INSTABILITIES OF P-CANNEL SILICON
GATE MOS TRANSISTORS
NAKAYAMA H SEE OSADA Y 126 1261
NANDA M SEE ISHIOE S 126 1014
NARAYANA-GH RUSTOMJI SH N5 126 809
- STUDY OF ANNEALING-INDUCED LATTICE DEFECTS IN
P-DOPED CODE BY TRANSMISSION ELECTRON
MICROSCOPY
NARAI JC SEE CARPIO RA 126 1644
NARULA ML SEE RAMANARATA 126 1360
NEHRIDIS-Y FINKMAN E N5 126 768
- ANODIC OXIDE FILMS ON HGI-XCDXTE
NEWMAN J SEE GORDON BA 126 894
NEWMAN J SEE LAU CG 126 2150
NEWMAN J SEE PIERINI P 126 1348
NEWMAN J SEE POLLARD R 126 1713
NGUYEN TH FOLEY RT N11 126 1955
- MECHANISM OF PITTING OF ALUMINUM
NICHOLSON-MM PIZZARELLA F N9 126 1490
- CHARGE TRANSFER IN OXIDATION PRODUCT OF
LUTETIUM DIHYDROXYNANE
NISHITANI R SEE MIZOKAWA Y 126 1370
NISHITANI Y ADACHI T N12 126 2269
- CHEMICAL ETCHING OF INP BY H2O2-H2SO4-H2O
SOLUTION
NISSEN DA N2 126 176
- STUDY OF THE ANODE-ELECTROLYTE INTERFACE IN A
THERMAL BATTERY
NOBE K SEE BENGALI A 126 1118
NOBE K SEE BRAUN M 126 1686
NOBE T SEE PINE P 126 1495
NOUFI RN KOHL PA ROGERS JN WHITE JM
BARD AJ N6 126 949
- SEMICONDUCTOR ELECTRODES -19. INVESTIGATION OF
S-SUBSTITUTION IN SINGLE CRYSTAL CO AND
COS PHOTOELECTRODES BY ELECTRON SPECTROSCOPY
NOVAK DM N5 126 6209
- CL-ION AND OXIDE FILM COVERAGE EFFECTS IN
ANODIC CL2 EVOLUTION KINETICS
NOVOITY V HOPPER MA N6 126 925
- TRANSIENT CONDUCTION OF WEAKLY DISSOCIATING
SPECIES IN DIELECTRIC FLUIDS
NOVOITY V HOPPER MA N12 126 2211
- OPTICAL AND ELECTRICAL CHARACTERIZATION OF
ELECTROPHORETIC DISPLAYS
NOWICK AS SEE TULLER NL 126 209
NOWICK AS SEE WANG DY 126 1155
NOWICK AS 126 1166
NOZAKI T SEE ENDO Y 126 1422
ODAKA T SEE OSADA Y 126 31
ODAKA Y SEE OSADA Y 126 31
ODGEN CA SEE WALESH G 126 1087
ODGEN CA SEE RALEIGH DO 126 1093
OHGUSHI T SEE TAKASHI T 126 1270
OHNO H N11 126 1975
- DETERIORATION OF LUMINESCENCE EFFICIENCY OF
ZNS PHOSPHORS DUE TO SURFACE OXIDATION BY
THERMAL DECOMPOSITION OF AMMONIUM DICROMATE
OHWADA K SEE EHARA K 126 2249
OHWA J SEE HIRATA K 126 1439
OHWAIRA S SEE SUZUKI K 126 1024
OKUYAMA H SEE TAKAHASHI T 126 1681
OLAHAM B SEE GOTT P 126 50
OLMEDO AM COHEN M N12 126 2167
- COMPOSITION OF ANODICALLY FORMED IRON OXIDE
FILMS
OLSON C N11 126 1885
- TRICKLE BED ELECTROCHEMICAL REACTIONS
OLSON B SEE SHAFER M 126 1625
OMABE K SEE HASEGUTI J 126 664
ONO H TANGO M N3 126 504
- NEW TECHNOLOGY FOR TAPERED WINDOWS IN
INSULATING FILMS
ORD JL LUSHKIN EV N6 126 1374
- OPEN-CIRCUIT TRANSIENT ANALYSIS OF THE ANODIC
OXIDATION OF TUNGSTEN AND NIOBIUM
ORHOND DW N11 126 142
- DIELECTRIC BREAKDOWN OF SILICON DIOXIDE THIN
FILM CAPACITORS USING POLYCRYSTALLINE SILICON
AND ALUMINUM ELECTRODES
OSA T SEE MATSUE T 126 500
OSADA Y NAKAYAMA H SHINDO N OKADA F
OGATA Y N1 126 31
- GROWTH AND STRUCTURE OF SILICON FIBERS
OSAMURA K NAKAJIMA K MURAKAMI Y
N11 126 1992
- EXPERIMENTS AND CALCULATION OF THE AL-0A-SB
TERNARY PHASE DIAGRAM
OTA Y N10 126 1761
- N-TYPE DOPING TECHNIQUES IN SILICON-MOLECULAR
BEAM EPITAXY BY SIMULTANEOUS ARSENIC
IMPLANTATION AND BY ANTIMONY EVAPORATION
OUTLAW RA SEE SCHMIDT FA 126 1811
OVERSLEIGH C SEE SCHODDINA-J 126 709
OWEN D SEE MCINTYRE NS 126 750
OWEN DG SEE SHOESMITH DW 126 911
OZARA S N12 126 106
- DETERMINATION OF SELF-CONCENTRATION QUENCHING
MECHANISMS OF RARE EARTH LUMINESCENCE FROM
INTENSITY MEASUREMENTS ON POWDERED FHCSPCR
SCREENS
PANDE K REEP D SRIVASTAVA T N12 126 300
BORRERO JM GHANDHI SM 126 313
- DEVICE QUALITY POLYCRYSTALLINE GALLIUM
ARSENIDE ON GERMANIUM-MOLYBDENUM SUBSTRATES
PARISI GI SEE ADAMS AC 126 313
PARKINSOBA HELLER A MILLER B N6 126 954
- EFFECTS OF CATIONS ON THE PERFORMANCE OF THE
PHOTOGALVANE IN THE H-GAS-H2S-CH2S-H2O-HC-
SEMICONDUCTOR LIQUID JUNCTION SOLAR CELL
PARTIN DL WILNES AG VASSAMIL LF N6 126 1581
- EFFECT OF SURFACE PREPARATION AND HEAT-
TREATMENT ON HOLE DIFFUSION LENGTHS IN VPL
GAS AND GAS-0D0.4
PARTIN DL WILNES AG VASSAMIL LF N6 126 1584
- MOL DIFFUSION LENGTHS IN VPE GAS-
AND-0D0.4 TREATED WITH TRANSITION METALS
PATAI S SEE BALOG M 126 1203
PAVINOVC M VITRAVAGOV N12 126 2282
- DETERMINATION OF ELECTROLESS COPPER DEPOSITION
RATE FROM POLARIZATION DATA IN THE VICINITY OF
THE MIXED POTENTIAL
PAVLU D RUEVSKI S N7 126 1100
- THERMOPOLARIZATION OF THE LEAD DIOXIDE PLATE OF
LEAD ACID BATTERIES
PANEL RE CATHART JR MCKEE RA N7 126 1105
- KINETICS OF OXIDATION OF ZIRCALOY-4 IN STEAM
AT HIGH TEMPERATURES
PANEL RE N7 126 1111
- OXYGEN DIFFUSION IN THE OXIDE AND ALPHA PHASES
DURING THE REACTION OF ZIRCALOY-4 WITH STEAM FROM
1000-DEGREE-C TO 1500-DEGREE-C
PAZ D HEARN E FAYC E N10 126 1754
- POCL3 AND BORON GETTERING OF LSI SILICON
DEVICES - SIMILARITIES AND DIFFERENCES
PEARCE CB ZALCZAK VJ N8 126 1436
- NEW APPROACH TO LATTICE DAMAGE GETTERING
PERKINS G SEE RAOH RD 126 523
PEAVEY J SEE PINTCHOV F 126 1475
PEDEFERR P SEE MAZZA B 126 2028
PEDERNAK SP AGRAWAL AK CHAUNG HE STAEHLER M
N4 126 701
- TRANSGRANULAR CRACKING OF COPPER IN 1P NANC2
SOLUTION
PELED E N12 126 2647
- ELECTROCHEMICAL BEHAVIOR OF ALKALI AND
ALKALINE EARTH METALS IN AQUEOUS LATTICE
SYSTEMS - SOLID ELECTROLYTE INTERPASE MODEL
PERKINS J SEE KATAT T 126 1835
PERKINS RA SEE LEVITS NB 126 544
PERONE SP SEE BERRY WA 126 720
PERNAULT GG N2 126 199
- ROLE OF HYDRIDES IN THE EQUILIBRIUM OF
ALUMINUM IN AQUEOUS SOLUTIONS
PETERS DA DECKERT CA N5 126 883
- REMOVAL OF PHOTORESIST FILM RESIDUES FROM
WAFER SURFACES
PHATAK SB KELLNER G N2 126 287
- MATERIAL-SELECTIVE CHEMICAL ETCHING IN THE
SYSTEM INGAAS-IMP
PHILLIPS BE KOYAMA R BUEHLER NG N11 126 1970
- SUPPRESSION OF MEASUREMENT INTERFERENCE FROM
INTERFACE STATES AND MOBILE IONS IN THERMAL
STIMULATED CURRENT MEASUREMENTS IN AN MOS
CAPACITOR
PHIPPS PBP SEE RICE DW 126 1459
PIATTI RCY SEE PODESTA JJ 126 1363
PIESINI R NERMAN J N8 126 1348
- POTENTIAL DISTRIBUTION FOR DISK ELECTRODES IN
ASYMMETRIC CYLINDRICAL CELLS
PIETSCH SJ SEE LANGER SH 126 1189
PIGNATTEL G QUEIROLO G N10 126 1505
- AES STUDY OF BORON DIFFUSION IN SILICON FROM A
BORON NITRIDE SOURCE WITH HYDROGEN INJECTION
PINNEL MR TOMPKINS HG HEATH DE N7 126 1274
- OXIDATION OF NICKEL AND NICKEL-GOLD ALLOYS IN
A1 AT 90-DEGREE-C-150-DEGREE-C
PINNEL MR TOMPKINS HG HEATH DE N10 126 1798
- OXIDATION KINETICS OF COPPER FROM GOLD ALLOY
SOLUTION AT 90-DEGREE-C-150-DEGREE-C
PINTCHOV F PRICE JB TOBIN PJ PEAVEY J
KOBOLD K N8 126 1428
- THERMAL CHARACTERISTICS OF THE M2S24-202
SILICON WAFER CLEANING SOLUTION
PIRON D SEE SUKIMOTO K 126 535
PITTMAN CU SEE HELBERT JA 126 694
PIZZARELLA F SEE NICHOLSON-MM 126 1490
PLAMBECK JA SEE LOVINGSBY D 126 985
PILCHER V SEE DEUGIERA-A 126 1902
PLUMER JD SEE HO CP 126 1516
PLUMER JD SEE HO CP 126 1523
- POTENTIOSTATIC CURRENT OSCILLATIONS AT IRON-
SULFURIC ACID SOLUTION INTERFACES
POLAN NM POPPMEIER JR PRYOR NJ N7 126 1299
- MECHANICALLY ASSISTED DEZINCIFICATION OF CU-ZN
ALLOYS DURING STRESS CORROSION IN AMMONIACAL
SOLUTIONS
POLLARD R NEWMAN J N10 126 1713
- TRANSPORT EQUATIONS FOR A MIXTURE OF 2 BINARY
MOLTEN SALTS IN A POROUS ELECTRODE
POPPELMEIER JM SEE POLAN NM 126 1299
PORTER JD FLETCHER S BARRADAS RG N10 126 1693
- EPOXIDE DIMERS FORMED ELECTROCHEMICALLY FROM
PHENYLALDOL IN ALKALINE SOLUTION - KINETIC AND
STRUCTURAL ANALYSIS
PORTER RA HARSHBARGER N3 126 460
- GAS ROTATIONAL TEMPERATURE IN AN RF PLASMA
POVLONIA EI SEE ADAMS AC 126 313
POWERS JM SEE RODGARE HM 126 1905
PRASAD A SEE JAIN GC 126 89
PRICE JB GOLDMAN J N11 126 2033
- SILICON EPITAXIAL INTERFACE MIGRATION
PRICE JB SEE PINTCHOV F 126 1428
PRINAK V MONAHAN E N12 126 2196
- GLOW DISCHARGE TUBE GLASS ELECTRODES
PROCHAZKA S SEE DUBIN RR 126 2156
PROPP R YOUNG L N4 126 624
- ADHESION, DUCTILITY, AND FRACTURE OF ANODIC
OXIDE FILMS ON TANTALUM
PRYOR NJ SEE POLAN NM 126 1295
- PUCCIARE F CECSON P HEYROVSK M N8 126 972
- ELECTROLYTIC OXIDATION OF MOLYBDENIC
AND THE EFFECT OF LIGHT
QUEIROLO G SEE JACOB T 126 1805
RABAGO F SEE GAUTRON J 126 1868
RABOCCI T SEE THACA WE 126 218
RALEIGH DO WHITE JT ODGEN CA N7 126 1087
- ANODIC CORROSION RATE MEASUREMENTS IN LiCl-KCl
EUTECTIC -1. ELECTROCHEMICAL CONSIDERATIONS
RALEIGH DO WHITE JT ODGEN CA N7 126 1093
- ANODIC CORROSION RATE MEASUREMENTS IN LiCl-KCl
EUTECTIC -2. RESULTS ON NICKEL-NIOBENUM-
AND STAINLESS STEEL
RAMANARATA NA NARULA M MORRELL WL N8 126 1360
- MEASUREMENT OF OXYGEN CHEMICAL POTENTIALS WITH
A CALCIUM FLUORIDE SOLID ELECTROLYTE
RAO P SEE JACOB T 126 1842
RAO PVV SEE GALGALI RK 126 725
RAPD RA SEE REDDY SN 126 2023
RAUH RD ABRAHAM KR PEARSON GF SURPRENA JC
BRUNNER SB N4 126 523
- LITHIUM-DISSOLVED SULFUR BATTERY WITH AN
ORGANIC ELECTROLYTE
RAZOUK RR DEAL BE N9 126 1573
- DEPENDENCE OF INTERFACE STATE DENSITY ON
SILICON THERMAL OXIDATION PROCESS VARIABLES
RE J SEE MAZZA B 126 2075
REDDY SN RAPP RA N11 126 2023
- ELECTRONIC CONDUCTION IN THE BAF2 SOLID
ELECTROLYTE
REEP D SEE PANDE K 126 300
REHDOFF CH SEE MICROFILM RL 126 1563
REICHMAN B BARD AJ N4 126 583
- ELECTROCHEMICAL PROCESS AT W3 ELECTRODES
PREPARED BY VACUUM EVAPORATION AND ANODIC
OXIDATION OF W
REICHMAN B BARD AJ N12 126 2133
- SEMICONDUCTOR ELECTRODES -22. ELECTROCHROMISM
AND PHOTOELECTROCHEMISTRY AT W3 LAYERS
PREPARED BY THERMAL AND ANODIC OXIDATION OF W
REIF R KAMINS TI SARASWAT KC N6 126 644
- MODEL FOR DOPANT INCORPORATION INTO GROWING
SILICON EPITAXIAL FILMS -1. THEORY
REIF R KAMINS TI SARASWAT KC N4 126 653
- MODEL FOR DOPANT INCORPORATION INTO GROWING
SILICON EPITAXIAL FILMS -2. COMPARISON OF
THEORY AND EXPERIMENT
REISSMAN A BERKENBL M ZIRINSKY S CHAN SA
KAUFMAN FB N6 126 1004
- ETCHING OF CRYSTALLOGRAPHICALLY DETERMINED
ORIFICES IN SAPPHIRE
REISSMAN A BERKENBL M CHAN SA KAUFMAN FB
GREEN DC N8 126 1406
- CONTROLLED ETCHING OF SILICON IN CATALYZED
ETHYLENEDIAMINE-PYROCATALYTIC-WATER SOLUTIONS
REMAUD R SEE LEROY M 126 1674
REMER J WOODARD KE N7 126 6263
- REPORT OF THE ELECTROLYTIC INDUSTRIES FOR THE
YEAR 1978
REVEZ AG N1 126 122
- ROLE OF HYDROGEN IN SiO2 FILMS ON SILICON
REVEZ AG N3 126 502
- INITIAL OXIDATION RATE OF SILICON
RHINES FN CONNELL RG CHOI MS N6 126 1061
- MICROSTRUCTURAL EVOLUTION OF THE INNER LAYER
OF THE HIGH TEMPERATURE OXIDE SCALE ON NICKEL
RICE DW PHIPPS PBP TREMURRE-A N9 126 1459
- ATMOSPHERIC CORROSION OF COBALT
RICE DW SEE SHAFER M 126 887
RIDEOUT VL SEE SILVESTRA-VJ 126 1335
RITCHIE IM SEE BAILEY JN 126 2285
ROBBINS DJ COCKAYNE B GLASPER JL LENT B
N7 126 1213
- TEMPERATURE DEPENDENCE OF RARE-EARTH ACTIVATED
GARNET PHOSPHORS -1. INTENSITY AND LIFETIME
MEASUREMENTS ON UNDOPED AND CE-DOPED Y3Al5O12
ROBBINS DJ COCKAYNE B GLASPER JL LENT B
N7 126 1221
- TEMPERATURE DEPENDENCE OF RARE-EARTH ACTIVATED
GARNET PHOSPHORS -2. COMPARATIVE STUDY OF
Ce3+, Eu3+, Tb3+, and Gd3+ IN Y3Al5O12
ROBBINS DJ N9 126 1550
- EFFECTS OF CRYSTAL FIELD AND TEMPERATURE ON
THE PHOTOLUMINESCENCE EXCITATION EFFICIENCY OF
Ce3+ IN YAG
ROBBINS DJ COCKAYNE B LENT B GLASPER JL
N9 126 1556
- RELATIONSHIP BETWEEN CONCENTRATION AND
EFFICIENCY IN RARE EARTH ACTIVATED PHOSPHORS

- ROBINSON M SEE ADAMS AC 126 313
RODDIN M SEE ANTONIAC-DA 126 1939
ROEDEL RJ VONNEIDER AR CARUSO R DAWSON LR N4 126 637
EFFECT OF DISLOCATIONS IN GAL-KALAS-SI LIGHT-EMITTING DIODES 126 949
ROGERS JM SEE MOUFFI RN
ROHATGI A BUTLER SR FEIGL FJ KRAMER HW N1 126 143
CHLORINE INCORPORATION IN HCL OXIDES
ROHATGI A BUTLER SR FEIGL FJ N1 126 149
MOBILE SODIUM ION PASSIVATION IN HCL OXIDES
ROTHMAN P SEE GALLOWAY KF 126 2245
ROUSSEL DR KUD K UMANA M ERUNJADA D
PROPERTIES OF RUO-CHN WORKING ELECTRODES IN NONAQUEOUS SOLVENTS 126 407
RONEA N SEE BARALDI P 126 1207
RUDTALR HM POWERS JP N11 126 1905
COMPARISON OF ZETA-POTENTIAL OF SYNTHETIC FLUORAPATITE OBTAINED BY STEPNISE AND CONTINUOUS METHODS OF STREAMING
ROSENDA-GM SEE DRAKE KC 126 1387
ROSMER DL SEE KOHL FJ 126 1054
RCSA RN N1 126 67
STRUCTURE SENSITIVITY IN THE ELECTROCATALYTIC PROPERTIES OF Pt α -HYDROGEN ADSORPTION ON LOW INDEX SINGLE CRYSTALS AND THE KLE OF STEPS
RCSA RN N1 126 78
STRUCTURE SENSITIVITY IN ELECTROCATALYTIC PROPERTIES OF Pt α -OXYGEN REDUCTION ON LOW INDEX SINGLE CRYSTALS AND THE MOLE OF STEPS
ROTH J SEE WITTMER M 126 1247
ROTHMAN LB SEE SCHWARTZ GC 126 464
ROY AS SEE FAHMY TZ 126 986
RUBINSTEIN I GILEAEI E N8 126 1360
HIGH ELECTROLYTIC CONDUCTIVITY IN SOLILO BROMINE
RUEVSKI S SEE PAVLEV C 126 1100
RUMERY TE SEE SHESMITH D 126 911
RUSTONJI SH SEE NARAYANA-GH 126 809
RUUT TC SEE FULSON JC 126 1650
RYAN TG SEE LORENZO JP 126 118
RYGE C SEE KATAN T 126 903
RYZMAN K SEE KATAN T 126 1467
SABACKY BJ EVANS JW N7 126 1176
ELECTRODEPOSITION OF METALS IN FLUORIDIZED BED ELECTRODES +1. MATHEMATICAL MODEL
SABACKY BJ EVANS JW N7 126 1180
ELECTRODEPOSITION OF METALS IN FLUORIDIZED BED ELECTRODES +2. EXPERIMENTAL INVESTIGATION OF COPPER ELECTRODEPOSITION AT HIGH CURRENT DENSITY
SAKAMOTO M SEE YANAKANA H 126 1415
SAKELLAR-GP FRANCIS GA N11 126 1928
ELECTROCHEMICAL REACTOR ANALYSIS - SELECTIVITY OF MULTIPLE COUPLED REACTIONS
SAKUNA K SEE EHARA K 126 2249
SAKURAI T SERIKAWA T N7 126 1257
LIFT-OFF METALLIZATION OF SPUTTERED AL ALLOY FILMS
SALAMA AM N1 126 114
COPPER PRECIPITATION EFFECTS IN SILICON USED IN SOLAR CELLS
SAMBELLS AF ANG PGP N10 126 1831
ENHANCED PHOTOEFFECTS AT N-TYPE IRON OXIDE ELECTRODES BY ELECTROCATALYSIS AND PEROXIDE EFFECTS
SAMSON RN SEE DAKIN TB 126 C 55
SANDHU JS SEE MUKTANI JS 126 1084
SANKARAN R N5 126 797
VAPOR PHASE EPITAXIAL GROWTH OF SN-GE2 GAAS
SANKARAN R HYDER SB BANDY SJ N7 126 1241
SELECTIVE INSITU VAPOR ETCH AND GROWTH OF GAAS
SANTILLO FS SEE DABROWIAJC 126 2091
SANTORO GJ SEE KOHL FJ 126 1054
SARAJE J KITAGAWA R TANAKA T N12 126 2226
EFFECT OF EXCESS COMPONENT ELEMENT DURING LPE ON ELECTRICAL PROPERTIES OF COTE
SARASWAT KC SEE MAHMOUD HN 126 1019
SARASWAT KC SEE REIF R 126 444
SARASWAT KC SEE REIF R 126 453
SARIN VK LINDSTEDT-JN N7 126 1281
EFFECT OF LTA PHASE ON THE PROPERTIES OF CVD TIC-CLCATED CEMENTED CARBIDE CUTTING TOOLS
SASAKI Y UEDA S N8 126 1432
PHOSPHORATION OF ZINC AND ITS DIFFUSION COEFFICIENTS
SASAKI Y UEDA S N11 126 1948
HIGH TEMPERATURE PHOSPHORATION OF NICKEL-CHROMIUM ALLOYS IN PHOSPHORUS VAPOR
SAVHNEH RF SEE GALASSO RT CHIANG SH COETZEE JF N3 126 357
DISCHARGE CHARACTERISTICS OF A SOLUBLE IRON-TITANIUM BATTERY SYSTEM
SAVORY JR SEE KATAN T 126 1835
SCHROEDT-JE SEE FOSTER LN
SCHELLER FW KUZNETSOV-BA KADIS-KM JORDAN JN N6 126 988
ELECTRODE KINETICS OF HERE AND ELECTROTRANSFER MECHANISMS OF HERE AND HEMOPROTEINS
SCHERER G SEE LEE Y 126 847
SCHERER G SEE LEE Y 126 1537
SCHIEDER M SEE BALOG M 126 1203
SCHINNEL DG N3 126 479
DEFECT ETCH FOR 1100 SILICON EVALUATION
SCHINKE DP SEE ADAMS AC 126 1539
SCHLAIRK-CR GOEBEL F NARINIC N N4 126 513
DISCHARGE REACTION MECHANISMS IN LI-SOCL2 CELLS
SCHLAIRK-CR SEE HILES NH 126 2168
SCHLESING-NR SEE BAYLES BKW 126 394
SCHLESING-NR SEE BAYLES BKW 126 1071
SCHLOTTE-BJ FLEISCHBAUM YARNELL CF N6 126 991
PASTE MIXING AND CURING OF TETRABASIC LEAD SULFATE PLATES FOR THE LEAD-ACID BATTERY
SCHMID F KHATTAK CP DIGGES TG KAUFMAN L N6 126 935
ORIGIN OF SIC IMPURITIES IN SILICON CRYSTALS GROWN FROM THE MOLT IN VACUUM
SCHMIDT FA OUTLAW RA LUNDE BK N10 126 1811
ELECTROTRANSPORT PURIFICATION OF THORIUM UNDER LOW PRESSURE CONDITIONS
SCHNEIDER LN SEE COHEN LR 126 1608
SCHODMAJZ J WAPENAR RE OVERSLUG G N5 126 709
FLUORIDE-CONDUCTING SOLID ELECTROLYTES IN GALVANIC CELLS
SCHODMAJZ J WAPENAR RE N12 1385
IONIC CONDUCTIVITY OF PBI-XALF26X
SCHODMAJZ J SEE BAPENAR RE 126 667
SCHOPEN TJ SEE SCHWARTZ GC 126 464
SCHWARTZ B SEE SCHWARTZ GC 126 1737
SCHWARTZ GC ROTHMAN LB SCHOPEN TJ N3 126 464
COMPETITIVE MECHANISMS IN REACTIVE ION ETCHING IN A CFA PLASMA
SCHWARTZ GP GUALTIERO-GJ KAMMLOT GW SCHWARTZ B N10 126 1737
X-RAY PHOTOELECTRON SPECTROSCOPY STUDY OF NATIVE OXIDES ON Cu
SCHWETTER-FN SEE CHANG LR 126 2267
SCHWIT AC SEE MACDONALD-DD
SCOTT AC SEE MACDONALD-DD
SCOSATI B VOSS RA LAZZARI M N4 126 699
CYCLABLE COPPER SOLID-STATE CELL BASED ON INTERCALATION ELECTRODES
SCOSATI B SEE DIPIETRO E 126 729
SEARCY AM SEE HUANG HO 126 1825
SEN RK SEE HUANG JC 126 786
SERIKATA T SEE SAKURAI T 126 1257
SHABDE SN, HELLIMELK N12 126 2279
ARSENIC DIFFUSION THROUGH THIN OXIDES
SHAWER NW FIAT RA ULSON B LAPLACA SJ ANGIELLO J N9 126 1625
PREPARATION AND CHARACTERIZATION OF RUTHENIUM DIOXIDE CRYSTALS
SHAWER NW SEE MCQUIRE GE 126 1075
SHARMA SD MEHROTRA K AGRAWAL VK N2 126 325
GROWTH AND POLYTYPISM IN VAPOR-GROWN MIXED CADMIUM SULFIDE CRYSTALS
SHARMA SP THOMAS JH N7 126 1261
FILM GROWTH OF SUBSTRATE MATERIAL DIFFUSING THROUGH A NOBLE METAL CONTACT
SHARMA SP SEE TADOKA T 126 445
SHAW JH HATZAKIS M N11 126 2026
DEVELOPER TEMPERATURE EFFECTS ON E-BEAM AND OPTICALLY EXPOSED POSITIVE PHOTORESIST
SHEPHERD LT SEE LAI JH 126 696
SHIBATA Y SEE MATSUSHI-K 126 2268
SHIBUZI S BIRIO GR N2 126 273
CHEMICAL MECHANISMS IN PHOTORESIST SYSTEMS -3. CROSSLINKING AND RECIPROCALITY FAILURE IN BISAZIDE RESIST
SHINDO M SEE NAKAYAMA H 126 1301
SHINDO M SEE OKADA Y 126 371
SHINTANI A SEE TANAKI Y 126 221
SHOESMITH-D RUMMERY TE BAILEY MG OWEN DG N10 911
ELECTROCRYSTALLIZATION OF PYRITE AND MARCASITE ON STAINLESS STEEL SURFACES
SHOENEL JH SEE KAWKONE S 126 401
SIGESLE-PPF SEE VIEGOW-GF 126 1792
SIITARI D SEE ALKIRE R 126 15
SILVESTRY-VJ RIDEOUT VL MANICALLV N8 126 1335
AL COVERAGE OF SURFACE STEPS AT SI02 INSULATED POLYCRYSTALLINE Si BOUNDARIES - AL EVAPORATION IN VACUUM AND LOW PRESSURE AIR
SIMMONS GW VERTES A VARSANYI ML LEIDENHIS-H N2 126 187
EMISSION MESSBAUER STUDIES OF ANODICALLY FORMED COO2
SIMON BR BALK P N7 126 1288
THERMAL OXIDATION OF SILICON IN O2-TRICHLOROETHYLENE
SINGH DV SEE KESAVAN R 126 642
SINGH DV SEE TOPICH JA 126 2274
SINGH KP SEE ISLAN R 126 1876
SINGH R N6 126 1081
DETERMINATION OF ELECTRON AFFINITY OF IN2O3 FROM ITS HETEROJUNCTION PHOTOVOLTAIC PROPERTIES
SINGHAG-D SEE MAZZA B 126 2075
SKINNER JP SEE HOU L 126 935
SMELTZER WN SEE FRYT EN 126 673
SMELTZER WN SEE FRYT EN 126 683
SMELTZER WN SEE LOCKHIE-AV 126 574
SHIALEK JL GOELHITL-FA STOTT FH WOOD GC N12 126 2275
RELATIONSHIP BETWEEN OXIDE GRAIN MORPHOLOGY AND GROWTH MECHANISMS FOR FE-CR-AL AND FE-CR-AL-TI ALLOYS
SMAILDOWS S CHAO C CHAUNG HE STAEHLER R N11 126 2038
EFFECT OF SULFUR SEGREGATION ON INTERGRANULAR CORROSION OF NICKEL IN DILUTE SULFURIC ACID SOLUTIONS
SMITH DJ SEE YOUNG L 126 765
SMITH DJ SEE YOUNG L 126 772
SMITH P SEE SMITH T 126 799
SMITH T SMITH P MANSFELD F N5 126 799
ELLIPSOmetry INTERPRETATION FOR ELECTROCHEMISTRY
SMITH TE SEE HURAKA SP 126 1951
SOELDMER JS SEE LERNER H 126 237
SOELDMER JS SEE MARINIC LC 126 43
SOELDMER JS SEE MARINIC LC 126 1687
SOOL L SEE BLANK M 126 1471
SPILLER E SEE HALLER I 126 154
SPRINGEN SE SEE KARASS R 126 331
SRINIVAS S SEE CHEN DT 126 713
SRIVASTAVA A SEE PANDE K 126 200
STACH J SEE MONKOWSKJ J 126 1129
STACH J SEE PEDERSEN SP 126 701
STAEHLER RW SEE SMAILDOWS S 126 2038
STAKEBAK-JL N3 126 495
TEMPERATURE DEPENDENCE OF THE REACTION OF HYDROGEN WITH HIGHLY REACTIVE URANIUM POWDERS
STAKEBAK-JL N9 126 1596
KINETICS FOR THE REACTION OF HYDROGEN WITH URANIUM POWDER
STALDER C AUGUSTYNS-J N11 126 2007
PHOTOASSISTED OXIDATION OF WATER AT BERYLLIUM-DOPED POLYCRYSTALLINE TiO2 ELECTRODES
STANLEY-RJ GARY RA N6 126 981
IDENTIFICATION OF THE HYDROLYSIS PRODUCTS IN THIONYL CHLORIDE
STEARNS CA SEE KOHL FJ 126 1054
STEIN HJ WELLS VA HAMPY RE N10 126 1755
PROPERTIES OF PLASMA-DEPOSITED SILICON NITRIDE
STOEF FC SEE MOHAPATRA-SK 126 895
STOTT FH SEE GOELHITL-FA 126 1035
STOTT FH SEE SHIALEK JL 126 2275
STREETSMA-JG SEE TSUI MY 126 98
SUGIMOTO K BELANGER G PIRON DL N4 126 535
CHANGES IN THE NIDBIUM ELECTRODE SURFACE INDUCED BY STRONG CATHODIC POLARIZATION
SUGIMOTO K SEE HARA N 126 1328
SUNPENA-JK SEE RAHM RD 126 523
SUSSMAN A N1 126 85
INITIATION OF OPERATING DEFECTS IN THIN FILM NEMATIC LIQUID CRYSTAL DISPLAYS
SUZUKI K OKUDAIRA S KANOHATA I N6 126 1024
RULES OF IONS AND NEUTRAL ACTIVE SPECIES IN MICROWAVE PLASMA ETCHING
SUZUKI Y SEE YAMAKI T 126 1794
SMITTE L SEE MONG D 126 11
SZPAK S GABRIEL CJ N11 126 1514
ZN-KOH SYSTEM - SOLUTION-PRECIPITATION PATH FOR ANODIC ZN FORMATION
TABE M NAKAMURA H N5 126 622
ADSORBED LAYER MODEL FOR AUTOPOLING MECHANISM IN SILICON EPITAXIAL GROWTH
TADOKA T SEE MAZZA B 126 2075
TACCONI MRD SEE FOLGHER ME 126 257
TACCONI MRD SEE FOLGHER ME 126 2592
TACCONI MRD SEE LELAND R 126 2145
TADA T N9 126 1635
CROSSLINKED POLY(2,2,2-TRICHLOROETHYL METHACRYLATE) AS A HIGHLY SENSITIVE POSITIVE ELECTRON RESIST
TADA T N10 126 1829
POLYTRIFLUOROETHYL ALPHA-CHLOROACRYLATE AS A HIGHLY SENSITIVE POSITIVE ELECTRON RESIST
TAFT E CORDES L N1 126 131
OPTICAL EVIDENCE FOR A SILICON-SILICON OXIDE INTERLAYER
TAFT EA N10 126 1728
FILMS FROM THE LOW TEMPERATURE OXIDATION OF SILANE
TAKAHASHI Y YAMAMOTO C TANADA S HAYASHI S N10 126 1654
SOLID-STATE IONICS - HIGH COPPER ION CONDUCTIVITY OF THE ACTIVATED CUCI-CUCL RECL
TAKAHASHI Y YAMADA O N12 126 2206
LUMINESCENCE OF TERBIUM-SYTERATED ALKALI RARE EARTH METAPHOSPHATE GLASSES
TAKASHI T YUSA A OHSUGHI T N10 126 1720
DETERMINATION OF THE SURFACE ROUGHNESS OF PASSIVE FILM BY GAS ADSORPTION TECHNIQUES
TAKAYAMA E KIMIZUKA N N11 126 2012
MODIFIED MIXED-GAS FLOW METHOD FOR CONTROLLING THE OXYGEN PARTIAL PRESSURE IN A FURNACE BELOW 1100-DEGREES-C
TAKENOUTI Y SEE GABRIEL-C 126 989
TANAKI Y ISOMAE S SHINTANI A MAKI M N12 126 2271
GE-DEPOSED Si3N4 FILM
TANAKI Y SEE ISOMAE S 126 1014
TANAKA T SEE TANAKI Y 126 1282
TANGO H SEE ONO H 126 504
TARUI Y SEE IWANATSU S 126 1078
TENG TC N5 126 870
INVESTIGATION OF THE APPLICATION OF POROUS SILICON LAYERS TO THE DIELECTRIC ISOLATION OF INTEGRATED CIRCUITS
TENNENH-GJ SEE GUPTA NK 126 1451
TERAI Y SEE ENDO T 126 1242
TEERTCH H SEE TARTYCK I 126 345
THEETEN JB HOTTIER F N3 126 450
INSITU SURFACE ANALYSIS OF THE VAPOR PHASE EPITAXY OF GAAS
THIEL PA BARNS LR N7 126 1272
ETCHING AND X-RAY DIFFRACTION STUDIES OF THE 111-A-FACES AND 111-B-FACES OF GAXIN1-XPYAS1-Y CRYSTALS
THOMAS JH SHARMA SP N3 126 445
HIGH TEMPERATURE FILM FORMATION ON COBALT-HARDENED GOLD
THOMAS JH GODDARD AP N10 126 1766
AES AND XPS STUDIES OF SEMI-INSULATING POLYCRYSTALLINE SILICON XPSO2 LAYERS
THOMAS JH SEE SHARMA SP 126 1261
THOMPSON AH N4 126 608
ELECTROCHEMICAL POTENTIAL SPECTROSCOPY - NEW ELECTROCHEMICAL MEASUREMENT
THOMPSON AH SEE JACOBSEN T 126 2169
THOMPSON AH SEE JACOBSEN T 126 2107
THOMPSON GE WOOD GC N11 126 2042
IRREGULAR ANODIC FILM FORMATION ON ALUMINUM
THOMPSON FL DOERRIES ER N10 126 1699
NEGATIVE ELECTRON RESISTES FOR DIRECT DEVICE LITHOGRAPHY -1. INITIAL MATERIAL SURVEY
THOMPSON FL YAU L DOERRIES ER N10 126 1703
NEGATIVE ELECTRON RESISTES FOR DIRECT DEVICE LITHOGRAPHY -2. POLY(2,2,2-TRICHLOROETHYL METHACRYLATE)-CO-3-CHLOROTERENE - LITHOGRAPHIC PERFORMANCE
TIEN TY SEE MAIK IK 126 562
TILAK BV N8 126 1343
KINETICS OF CHLORINE EVOLUTION - COMPARATIVE STUDY
TITANI S SEE PANDE K 126 300
TODIN PJ SEE PINCHOFF P 126 1428
TOKUDA K BRUCKENSS-N N3 126 431
SINUSOIDAL HYDRODYNAMIC VOLTAMMETRY AT THE

- ROTATING DISK ELECTRODE +1. THEORY OF ELECTRON
TRANSFER KINETICS
TOMKINS H N9 126 1505
- POTENTIAL DISTRIBUTION AT THE TiO2 AQUEOUS
ELECTROLYTE INTERFACE
TOMKINS H N12 126 2220
- RELAXATION SPECTRUM ANALYSIS OF SEMICONDUCTOR-
ELECTROLYTE INTERFACE-TiO2
TOMKINS H6 SEE PINNELL MR 126 1274
TOMPKINS HG SEE PINNELL MR 126 1798
TOPICH JA KESAVAN R ANDHARE PN BHOLA KL
SINGH OV N12 126 2274
- ENHANCEMENT OF LATERAL P-N-P CURRENT GAIN BY
GETTERING
TODONAGA R SEE KOIKE J 126 1008
- TRACY CE 126 1008
- MICROMETHOD FOR REFRACTIVE INDEX DETERMINATION
OF THIN FILMS USING LIQUID STANDARDS
TRANCHAR JC SEE HOLLAN L 126 855
TRENDAURE R SEE PRICE DB 126 1459
TRESSLER RE SEE MONKOWSK-J 126 1219
- TRIACA WE RABOCKAI T ARVIA AJ N2 126 218
- KINETICS AND MECHANISM OF ADSORBED ETHYLENE
ELECTROOXIDATION ON PLATINIZED PLATINUM UNDER
POTENTIODYNAMIC CONDITIONS
TRIAND AR SEE CARLSON DE 126 688
- TRIOBLEUR H SEE GAUTRON J 126 1868
- TSAI KC SEE LITTAUER EL 126 1924
- TSAI MY STREETMA BG BLATTNER RJ EVANS CA
N1 126 98
- STUDY OF SURFACE CONTAMINATION PRODUCED DURING
HIGH DOSE ION IMPLANTATION
TSUNG ACC SEE JASEM SM 126 1353
- TULLER HL NOWICK AS N2 126 209
- DEFECT STRUCTURE AND ELECTRICAL PROPERTIES OF
NONSTOICHIOMETRIC CeO2 SINGLE CRYSTALS
TWU B N9 126 1589
- PROCESS MONITOR OF RESIDUAL FILMS BY
ELLIPSOMETRY
UDAPA MK SEE GALGALI RK 126 725
UEDA S SEE SASAKI Y 126 1432
UEDA S SEE SASAKI Y 126 1948
- UMANA N SEE ROLISON DR 126 407
- UMEZAWA Y YAMAKURA T N4 126 705
- NONIIC PORPHYRIN ELECTRODE FOR A POSSIBLE WET
SOLAR CELL
UNO J SEE YAMAZAKI T 126 1794
- VADIMSKY RG FRANKENT RP THOMPSON DE
N11 126 2017
- RU AND RUO2 AS ELECTRICAL CONTACT MATERIALS -
PREPARATION AND ENVIRONMENTAL INTERACTIONS
VALLET CE BRAUNSTE J N4 126 527
- STEADY-STATE COMPOSITION PROFILES IN MIXED
MOLTEN SALT ELECTROCHEMICAL DEVICES +2. MOLTEN
CARBONATE FUEL CELL ANALOGS
VALLET CE SEE BRAUNSTE J 126 960
- VANBUREN FR DEWIT JHM N10 126 1817
- THERMOELECTRIC POWER OF LAI-XSRKOD3-Y
VANIJING-A SEE BAYLES BKW 126 1671
- VARSANYI ML SEE LEIDHEIS-H 126 204
VARSANYI ML SEE LEIDHEIS-H 126 391
VARSANYI ML SEE SIMMONS GN 126 187
VASSAMIL-LP SEE PARTIN DL 126 1581
VASSAMIL-LP SEE PARTIN DL 126 1584
VENKATES-S SEE CHEN DT 126 1908
- VERMILY-DA N3 126 C 81
- SOCIAL CHANGE AND FUTURE ECONOMIC GROWTH
VERNON SM BLAKESLEAE HOVEL HJ N4 126 703
- SOLAR CELLS ON LARGE-GRAIN GAAS THIN FILMS
VERTES A SEE LEIDHEIS-H 126 204
VERTES A SEE LEIDHEIS-H 126 391
VERTES A SEE SIMMONS GN 126 187
- VIEBEGW-FG SIEGELS-PF N10 126 1792
- MODEL TO EXPLAIN THE ELECTRICAL BEHAVIOR OF P-
TYPE SILICON SURFACES AFTER A CHEMICAL
TREATMENT
VILCHE JR SEE FOLQUER ME 126 257
- VISHNAT-K CHEM HY N3 126 398
- MASS TRANSFER ASPECTS OF ELECTROLYSIS BY
PERIODIC CURRENTS
VITKAVAG-D SEE PRANDOVIC H 126 2282
- VONKHOA AR SEE ROEDER RJ 126 637
- VOSO MA SEE SCRODATI B 126 699
- VOSSSEN JL N2 126 319
- GLOW DISCHARGE PHENOMENA IN PLASMA ETCHING AND
PLASMA DEPOSITION
WADA T SEE YAMAKURA H 126 1415
- WAGENKNE-JH N6 126 563
- STERESELECTIVE ANODIC CLEAVAGE OF 4,4'-
DIHYDROXYHYDROBENZIN
WAGNER JB SEE JOH T 126 1003
- WAGNER S SEE MOHAPATRA-SK 126 805
- WALES CP N3 126 351
- CUPRIC OXALATE CATHODES FOR SEAWATER CELLS
WALES CP CHIANELL-RR N6 126 990
- DYNAMIC X-RAY DIFFRACTION
WANG DNK SEE MURAKA SP 126 1951
- WANG DY NOWICK AS N7 126 1155
- CATHODIC AND ANODIC POLARIZATION PHENOMENA AT
PLATINUM ELECTRODES WITH DOPED CeO2 AS
ELECTROLYTE +1. STEADY-STATE OVERPOTENTIAL
WANG DY NOWICK AS N7 126 1166
- CATHODIC AND ANODIC POLARIZATION PHENOMENA AT
PLATINUM ELECTRODES WITH DOPED CeO2 AS
ELECTROLYTE +2. TRANSIENT OVERPOTENTIAL AND A-C
IMPEDANCE
WANG R HENAGER CH N1 126 63
- ARC-PLASMA-SPRAYED RUTILE ANODES FOR
PHOTOELECTROLYSIS OF WATER
WAPENAR KE SEE SCHONNA-J N4 126 667
- IONIC CONDUCTIVITY OF FLUORITE-STRUCTURED
SOLID SOLUTIONS OF COMPOSITION -
CaF2-SrF2-BaF2-2CeF3
WAPENAR KE SEE SCHONNA-J 126 709
- WAPENAR KE SEE SCHONNA-J 126 1385
- WATANABE N SEE KASAHARA J 126 1997
- WANDERL S SHADEL JN N3 126 401
- ELECTROCHEMICAL REDUCTION OF BENZYL CHLORIDE
IN THE PRESENCE OF CARBON DIOXIDE
WEEKS MC SEE YARNELL CF 126 7
- WEIL R SEE FEIGENBA-H 126 2085
- WELLS VA SEE STEIN PJ 126 1750
- WEN CJ BOUKAMP BA HUGGINS RA WEPNER W
N12 126 2258
- THERMODYNAMIC AND MASS TRANSPORT PROPERTIES OF
LiAl N10 126 1823
- FLASH EVAPORATED FILMS OF INDIUM-DOPED CdS AND
COSSEX-L-X 126 2075
- WENGER D SEE NAZZA B 126 908
- WENTRICK P SEE MACDONALD-DD 126 1618
- WENTRICK P SEE MACDONALD-DD 126 2258
- WEST A SEE ATUNG S 126 1311
- WEST K SEE JACOBSEN T 126 2169
- WEST KA SEE COHEN RL 126 1608
- WHITE CA SEE HALLCHER RC 126 404
- WHITE JM SEE NOUF R 126 949
- WHITE JT SEE RALEIGH DG 126 1087
- WHITE JT SEE RALEIGH DG 126 1093
- WHITTING MS SEE JACOBSON AJ 126 887
- WHITTING MS SEE JACOBSON AJ 126 2277
- WIEAK JP SEE MARASSI R 126 231
- WIER LM MURRAY RN N4 126 617
- CHEMICALLY MODIFIED ELECTRODES +8. INTERACTION
OF AQUEOUS RuCl3 WITH NATIVE AND SILANIZED
SnO2 ELECTRODES
WIJNHOEDIC SEE DEWIT HJ 126 779
- WIJNHELM M N5 126 C207
- ELECTRON INJECTION FROM SEMICONDUCTOR
ELECTRODES IN LIQUID AMMONIA
WIJNHELM SM YUN KS BALLENGE-LW HACKERMAN
N3 126 419
- SEMICONDUCTOR PROPERTIES OF IRON OXIDE
ELECTRODES
WILL FG N1 126 36
- BROMINE DIFFUSION THROUGH NAFION
PERFLUORINATED ION EXCHANGE MEMBRANES
WILLIAMS LF N4 126 560
- DEPOSITION OF COPPER IMPURITIES INTO ZINC
PLATE
WILLIAMS R SEE MU P 126 1982
- WILLINGGE N9 126 1510
- FLOAT CURRENT OF STATIONARY BATTERIES
WILSON RH HARRIS LA GERSTNER ME N5 126 844
- CHARACTERIZED SEMICONDUCTOR ELECTRODES +1.
EFFECT OF PROCESSING VARIABLES ON THE
PHOTOELECTROCHEMICAL PROPERTIES OF SINGLE
CRYSTAL TiO2 BRITILE
WILSON RH N7 126 1187
- ANALYSIS OF CHARGE TRANSFER AT PHOTOEXCITED
CdS ELECTRODES WITH Na2S IN THE ELECTROLYTE
WILSON RH SEE HARRIS LA 126 850
- WINDISCH-H MARK P N4 126 627
- MODEL FOR THE OPERATION OF A THIN-FILM SENS
CONDUCTANCE-MODULATION CARBON MONOXIDE SENSOR
WIRKALA J SEE HANBY DC 126 2110
- WITT AF SEE MARTIN EP 126 284
- WITTNER M RCTH J MAYER JW N7 126 1247
- INFLUENCE OF NOBLE GAS ATOMS ON THE EPITAXIAL
GROWTH OF IMPLANTED AND SPUTTERED AMORPHOUS
SILICON
WONG D SWETTE L COCKS FH N1 126 11
- ALUMINUM CORROSION IN UNINHIBITED ETHYLENE
GLYCOL-WATER SOLUTIONS
WOOD GC SEE GOLIGHTL-PA 126 1035
- WOOD GC SEE SWALLEK JL 126 2275
- WOOD GC SEE THOMPSON GE 126 2042
- WOODARD KE SEE RENNER J 126 C243
- WORELL WL SEE RAMANARATA 126 1360
- WU CP DOUGLAS EC MUELLER CW WILLIAMS R
N11 126 1582
- TECHNIQUES FOR LAPPING AND STAINING ION-
IMPLANTED LAYERS
WUOL F SEE MOHAPATRA-SK 126 805
- YAJIMA A SEE ISOWAE S 126 1014
- YAMADA D SEE TAKAHASHI-T 126 2206
- YAMADA S SEE TAKAHASHI-T 126 1654
- YAMAMOTO H KAND T N2 126 305
- ENHANCEMENT OF CATHODOLUMINESCENCE EFFICIENCY
OF RARE EARTH ACTIVATED Y2O3 BY TRIS OR PR3
YAMAMOTO H SEE IWATA S 126 110
- YAMAMOTO C SEE TAKAHASHI-T 126 1954
- YAMAMURA T SEE UMEZAWA Y 126 705
- YAMAMURA H WADA T KUDOH O SAMAMOTO N
N8 126 1415
- POLYSILICON INTERCONNECTION TECHNOLOGY FOR IC
DEVICE
YAMAZAKI T SUZUKI Y UNO J NAKATA H
N10 126 1794
- REVERSAL ETCHING OF CHROMIUM FILM IN GAS
PLASMA
YAO NP SEE CHOI KN 126 1321
- YARNELL CF WEEKS MC N1 126 7
- OXIDATION OF TETRABASIC LEAD SULFATE TO LEAD
DIOXIDE IN THE POSITIVE PLATE OF THE LEAD-ACID
BATTERY
YARNELL CF SEE SCHLOTTE-WJ 126 991
- YASUDA M SEE HINE F 126 1439
- YASUDAGY Y SEE ENDO Y 126 1422
- YAU L SEE THOMPSON FL 126 1703
- YEAGER E SEE BINDRA P 126 1631
- YEAGER E SEE HUANG JC 126 786
- YEH LSR SEE DAMJANCVA 126 555
- YEO RS MCBREEN J N10 126 1682
- TRANSPORT PROPERTIES OF NAFION MEMBRANES IN
ELECTROCHEMICALLY REGENERATIVE HYDROGEN-
HALOGEN CELLS
YEO RS SEE CHIN DT 126 713
- YONEDA Y SEE KITAHAKU-T 126 1881
- YOSHIDA T SEE HINE F 126 1435
- YOUNG L SMITH DJ N5 126 765
- MODELS FOR IONIC CONDUCTION IN AMMONIC OXIDE
FILMS
YOUNG L SMITH DJ N11 126 1972
- OPEN-CIRCUIT TRANSIENT METHOD OF INVESTIGATING
IONIC CONDUCTION IN AMMONIC OXIDE FILMS - ITS
RELATION TO OTHER TECHNIQUES
YOUNG L SEE PROPP H 126 424
- YUN KS SEE WILHELM SM 126 419
- YUSA A SEE TAKASHI T 126 1720
- ZAINLD K SEE HANBY DC 126 2110
- ZAKZOU AKM N10 126 1771
- DEPENDENCE OF THE S2O2 DEFECT DENSITY ON BOTH
THE APPLIED ELECTRIC FIELD AND THE OXIDE
THICKNESS
ZALECKAS VJ SEE PEARCE CW 126 1436
- ZAMIN H IVES MB N3 126 470
- ANODIC OXIDATION OF NICKEL IN H2SO4
SOLUTION
ZAMIN H SEE HOKHA HM 126 795
- ZETTLER HU NIEKE EK N8 126 1430
- OPTIMIZATION OF EXPOSURE AND DEVELOPMENT
PARAMETERS FOR ELECTRON-BEAM-WRITTEN PMMA
STRUCTURES
ZERBINO J SEE BLONDEAU G 126 1592
- ZERBINO JO ARVIA AJ N1 126 93
- POTENTIODYNAMIC BEHAVIOR OF IRIUM IN
DIFFERENT ACID SOLUTIONS
ZERBINO JO SEE FOLQUER ME 126 592
- ZETARUK DG SEE MCINTYRE NS 126 750
- ZIRINSKY S SEE REISMAN A 126 1004
- ZNANIKOW-Z SEE GARYKA T 126 345

JOURNAL ARTICLE SUBJECT INDEX

TO FIND ARTICLES ON A SPECIFIC TOPIC:

1. Locate any one of the words (Primary Terms) that describes the topic. If you want every title that includes primary term, select only the articles marked with an arrow (>). This eliminates unnecessary lookups.
2. To narrow selection, use any of the other words (Co-Terms) listed below that Primary Term. When using co-terms, always disregard arrows.
3. Two word terms occur when they are generally used together to describe a single concept (e.g. heat-transfer). This simplifies multiple co-term lookup.
4. The PAGE NO. refers to the beginning page in the Journal on which the article containing the keyword appears.

	PRIMARY TERM CO-TERM	PAGE NO.
	ELECTROCATALYSIS	
PRIMARY TERM <i>This word is selected from the contents of one or more articles.</i>	ACRYLIC ACID - - - - -	939
	ANION INFLUENCE ->	2140
	ANODIC ACTIVATION>	78
	AUGER SPECTROSCO.>	67
		78
	CHLORINE EVOLUTI.>	1189
	ELECTRON DIFFRAC.	67
	ELECTROOXIDATION >	218
	ELECTROSORPTION -	2140
	ETHYLENE - - - - -	218
	HYDROGEN ABSORPT.	67
	HYDROGEN MONOLAY.	2140
	HYDROGEN PEROXIDE>	1831
	IRON OXIDE - - - - -	"
	N-TYPE - - - - -	"
	OXYGEN MONOLAYER	2140
	OXYGEN REDUCTION	78
	PHOTOANODE - - - - -	1831
	PLATINUM - - - - -	67
		78
		218
		2140
	POLYMERIZATION -	939
	POTENTIODYNAMICS	218
	REDOX - - - - -	939
	RING DISK ELECTR.	"

PRIMARY TERM
This word is selected from the contents of one or more articles.

CO-TERM
These words also were selected from the contents of articles about "ELECTROCATALYSIS".

Co-term identical to Co-term "PLATINUM" above.

To find all articles concerned with "ELECTROCATALYSIS" check only entries with this mark.

Ditto marks indicate same page.

To find articles concerning "ELECTROCATALYSIS" and "PLATINUM" check all entries under Co-term "PLATINUM"

PRIMARY TERM CO-TERM	PAGE NO.	PRIMARY TERM CO-TERM	PAGE NO.	PRIMARY TERM CO-TERM	PAGE NO.	PRIMARY TERM CO-TERM	PAGE NO.
A-C IMPEDENCE		ACTIVATION ENERGY (CONTO)		ALKALINE SOLUTION (CONTO)		ALUMINUM BROMIDE	
CERIUM DIOXIDE ->1166		POTENTIOSTATIC - 1353		PHTHALIMIDE - - - 1693		AROMATIC HYDROCA. >1474	
PLATINUM ELECTRO. - "		PULSE - - - - - "		REACTION ORDER - 541		CYCLIC VOLTAMME. - "	
POLARIZATION - - - "		TEFLON BONDED - - - "		REDUCTION - - - 1693		POTASSIUM BROMIDE - "	
TRANSIENT DECAY - - - "				STRUCTURAL ANALY. - "		SURFACE PROCESSES - "	
		ACTIVATOR		ZINC ELECTRODE - 541			
ABSORPTION SPECT.		BACKSCATTERING ->1671				ALUMINUM CHLORIDE	
CERIUM - - - - ->1550		CONCENTRATION - -> 106		ALLOY		CONDUCTIVITY - ->1644	
CRYSTAL FIELD - - - "		ELECTROLESS - - 1671		ALUMINUM - - - - -> 574		- - - - ->1650	
GARNET PHOSPHORS - "		GLASS SUBSTRATE - "		BUBBLE DYNAMICS - "		CVD - - - - ->1601	
PHOTOLUMINESCENCE - "		LUMINESCENCE - - 106		ELECTRODEPOSITION >2162		DENSITY - - - - - 1644	
TEMPERATURE RANGE - "		METAL DEPOSITION 1671		ELECTROPOLISHING 574		FUSED SALT - - - - - "	
		PALLADIUM - - - - - "		FOIL - - - - - 2162		- - - - - 1650	
ABUSE TOLERANCE		POWDERED PHOSPHOR 106		FUSED SALT - - - - - "		GADOLINIUM CHLOR. 1601	
BATTERY - - - - ->1637		QUENCHING MECHAN. - "		GASEOUS DISCHARGE 574		GASEOUS COMPLEX - - - "	
DTA - - - - - - - - - "		RADIATION - - - - - "		GROOVE SPACING - - - "		HALIDE - - - - - 1644	
LITHIUM - - - - - - - - - "		RARE EARTH - - - - - "		IRON PLATINUM - - - 2162		IRON CHLORIDE - - - 1601	
SULFUR DIOXIDE - - - - - "				NICKEL - - - - - 574		LITHIUM CHLORIDE 1650	
		ACTIVITY COEFFIC.		PREPARATION - - - 2162		N-ALKYLPYRIDINIUM 1644	
AC ADMITTANCE		LITHIUM NITRIDE -> 248		SURFACE MORPHOLO. 574		TRANSPORT - - - - - "	
INTERFACE - - - - -> 424		MOLTEN SALT - - - - - "				VISCOSITY - - - - - "	
PLATINUM - - - - - - - - - "		NITRIDE SOLUTION - - - "		ALTERNATING VOLT.			
ROTATING DISK - - - - - "				CORROSION POTENT. >1908		ALUMINUM COVERAGE	
SULFURIC ACID - - - - - "		ADHESION		FARADAIC RECTIFI. - "		ARGON - - - - - ->1335	
SWEEP FREQUENCY - - - - - "		ANODIC OXIDE FILM > 624		MILD STEEL - - - - - "		CVD - - - - - - - - - "	
		DUCTILITY - - - - - "		PASSIVATION - - - - - "		EVAPORATION - - - - - "	
ACCEPTER HYPOTHE.		FRACTURE - - - - - "		POLARIZATION - - - - - "		INSULATION - - - - - "	
ELECTROPOLISHING > 795		TANTALUM - - - - - "				POLYSILICON - - - - - "	
TANTALUM - - - - - - - - - "				ALUMINA		PRESSURE VARIATI. - "	
WAGNERS THEORY - - - - - "		ADSORPTION		CUPROUS CHLORIDE >1963		SILICON DIOXIDE - - - "	
		CELL KINETICS - -> 608		DISPERSED ALUMINA - "			
ACETONITRILE		HIGHLY REACTIVE -> 495		GROWTH MECHANISM >1035		ALUMINUM DIFFUSI.	
EFFICIENCY - - - - -> 603		HYDROGEN - - - - - "		ION CONDUCTIVITY 1963		MASKING STRUCTURE > 292	
ELECTRODE BEHAVI. >1892		LITHIUM BATTERY - 608		OXIDE MORPHOLOGY 1035		PLANAR GALLIUM - - - "	
FERRIC OXIDE - - - - - "		PHASE DIAGRAM - - - "		YTTRIUM - - - - - - - - - "		SILICON - - - - - - - - - "	
FLATBAND POTENTI. > 598		POTENTIAL - - - - - "					
GAAS - - - - - - - - -> 59		REACTIVITY - - - - - 495		ALUMINUM		ALUMINUM FLUORIDE	
- - - - - 603		SPECTROSCOPY - - - 608		ALLOY - - - - - - -> 574		DEFECT INTERACTI. >1385	
INDIUM PHOSPHIDE 598		TEMPERATURE DEPE. 495		ANODIC BEHAVIOR >1659		FLUORITE - - - - - - - - - "	
LIQUID JUNCTION - 603		TITANIUM DISULFI. 608		ANODIC FILM - - ->2042		IONIC CONDUCTIVI. - "	
N-TYPE - - - - - - - - - 59		URANIUM POWDER - 495		ANGDIZATION - - -> 779		IONIC MOTION - - - - - "	
N-TYPE CONDUCTION 1892		VOLTAGE STEPS - - - 608		ANTIMONY - - - - ->1548		LEAD - - - - - - - - - - - "	
P-TYPE - - - - - - - - - 59				AQUEOUS SOLUTION > 199		SOLID ELECTROLYTE - "	
PHOTOELECTROCHEM.		AGING EFFECTS		BUBBLE DYNAMICS - 574			
598		DEFECT DOPING - -> 338		CAPACITOR - - - - -> 162		ALUMINUM OXIDE	
PHOTOVOLTAIC CELL 603		ELECTROMIGRATION - "		CHLORIDE ION - - - 1659		ALUMINUM POWDER ->1304	
REGENERATIVE CELL - - - - - "		ENERGY CONVERSION - "		CORROSION - - - - -> 11		COMPOSITE SYSTEM - "	
SEMICONDUCTOR - - - 59		SEMICONDUCTOR - - - "		DIELECTRIC BREAK. 162		DISORDERED SYSTEM - "	
- - - - - 598				DTA - - - - - - - - - 1992			
SINGLE CRYSTAL - - - - - 603		AGING KINETICS		ELECTROPOLISHING 574		ALUMINUM PITTING	
SURFACE EFFECT - 59		OXYGEN MONOLAYER > 592		ETHYLENE GLYCOL - 11		CHLORIDE PITTING >1855	
		PERTURBATION PRO. - "		FILM FORMATION - 2042		COMPLEX ION - - - - - "	
		PLATINUM - - - - - - - - - "		GALLIUM - - - - - 1992		PIT INITIATION - - - - - "	
ACID MEDIUM		POTENTIAL DYNAMICS - "					
CHARGE CAPACITY -> 93		AGITATION		GASEOUS DISCHARGE 574		ALUMINUM POWDER	
HYDROXIDE-TYPE - - - - - "		DEFECT - - - - - -> 479		GROOVE SPACING - - - "		ALUMINUM OXIDE ->1304	
IRIDIUM - - - - - - - - - "		ETCH - - - - - - - - - - - "		HYDRIDE FORM - - - 199		COMPOSITE SYSTEM - "	
THIN FILM - - - - - - - - - "		SELLO ETCH - - - - - "		IMPEDENCE - - - - - 779		DISORDERED SYSTEM - "	
		SILICON EVALUATI. - "		LIGAND ASSOCIATI. 1992		LITHIUM - - - - - ->1853	
ACID SULFATE		ULTRASONIC - - - - - "		NICKEL - - - - - - - - - 574		METAL SULFIDE - - - - - "	
ANODIC DISSOLUTI. > 95		AIR ENVIRONMENT		NITRATE ION - 1659		NEGATIVE ELECTRO. - "	
CORROSION RATE - - - - - "		NICKEL GOLD ALLOY >1274		OXIDE CHARGE DEN. > 878		POWDER ELECTRODE - "	
GOLD - - - - - - - - - - - "		OXIDE FILM GROWTH - "		PASSIVITY - - - - - 1659		RECHARGEABLE CELL - "	
OXYGEN EVOLUTION - - - - - "		UNALLOYED NICKEL - "		PH - - - - - - - - - 199			
PH - - - - - - - - - - - - - "				PHASE DIAGRAM - - - 1992		ALUMINUM SOLUBIL.	
		ALCOHOL		PITTING POTENTIAL 1659		BARIUM TITANATE -> 165	
ACIDIC CHLORIDE		INDUCED INSTABIL. >1301		POLYSILICON - - - 162		CONDUCTIVITY - - - - - "	
ANODIC DISSOLUTI. >1666		KETONE - - - - - - - - - - - "		POTENTIAL - - - - - 199		THERMISTOR - - - - - "	
COPPER - - - - - - - - - - - "		SILICON GATE MOS - - - "		RELAXATION TIME - 779			
CORROSION - - - - - - - - - - - "				SALT SOLUTION - - - 199		AMALGAM CORROSION	
DISSOLUTION KINE. - - - - - "		ALKALI METAL		SILICON - - - - - 878		CAPILLARY PORE -> 903	
ELECTRODISSOLUTI. >1118		ALKALINE METAL ->2047		SILICON DIOXIDE - 162		CREVICE CORROSION - "	
NICKEL - - - - - - - - - - - "		NONAQUEOUS BATTE. - "		- 878		DENTAL AMALGAM - - - - - "	
		SOLID ELECTROLYTE - "		SOLAR COLLECTOR - 11			
ACIDIC SULFATE				STOICHIOMETRY - 779		AMBIENT PRESSURE	
ANODIC DISSOLUTI. >2064		ALKALI RARE EARTH		SURFACE MORPHOLO. 574		CARBON - - - - - ->1422	
CHLORIDE SOLUTION - - - - - "		CESIUM COACTIVAT. >2206		TERNARY PHASE - - 1992		CARBON MONOXIDE - - - "	
CORROSION - - - - - - - - - - - "		GLASSY PHOSPHORS - - - "		TUNNELING - - - - - 1548		EQUILIBRIUM - - - - - "	
DEOXYGENATED SOL. - - - - - "		LUMINESCENCE - - - - - "		VAPOR INFUSION - - - "		OXYGEN - - - - - - - - - - - "	
PASSIVATION - - - - - - - - - - - "		METAPHOSPHATE - - - - - "		WORK FUNCTION - - - 878		SILICON - - - - - - - - - - - "	
TITANIUM - - - - - - - - - - - "		TERBIUM ACTIVATI. - "					
ACRYLIC ACID				ALUMINUM ALLOY		AMMONIA	
ELECTROCATALYSIS > 939		ALKALINE METAL		CORROSION TEST -> 110		BREATH TEST - - -> 883	
POLYMERIZATION - - - - - "		ALKALI METAL - ->2047		INTEGRATED CIRCU. - "		CLEANING - - - - - - - - - "	
REDOX - - - - - - - - - - - - - "		NONAQUEOUS BATTE. - "		LIFT-OFF METALLI. >1257		HYDROGEN PEROXIDE - - - "	
RING DISK ELECTR. - - - - - "		SOLID ELECTROLYTE - "		METALLIZATION - - 110		PHOTORESIST FILM - - - - - "	
				PLASTIC ENCAPSUL. - "		STRIPPING - - - - - - - - - - - "	
				SPUTTER DEPOSITI. 1257		WAFER SURFACE - - - - - "	
ACTIN							
IONIC PERMEABILI. >1471		ALKALINE SOLUTION		ALUMINUM ARSENIDE		AMMONIA GAS	
MEMBRANE PROTEINS - - - - - "		CATALYTIC DECOMP. >1924		DIODE - - - - - - - - -> 637		DIELECTRIC FILM -> 996	
POLAROGRAPHY - - - - - - - - - "		CURRENT DENSITY -> 541		DISLOCATION - - - - - "		OXIDATION RESIST. - "	
SPECTRIN - - - - - - - - - - - "		EPOXIDE DIMERS ->1693		GAAS - - - - - - - - - - - "		SILICON OXYNITRI. - "	
		EQUILIBRIUM POTE. 541		GALLIUM - - - - - - - - - - - "		THERMAL NITRIDAT. - "	
ACTIVATION ENERGY		FUEL CELL - - - - - 1924		LIGHT-EMITTING			
NICKEL COBALT OX. >1353		KINETIC ANALYSIS 1693		QUANTUM EFFICIEN. - "		AMMONIACAL SOLUT.	
OXYGEN EVOLUTION - - - - - "		PERHYDROXYL ION - 1924		SILICON - - - - - - - - - - - "		COPPER ZINC - - - ->1299	

PRIMARY TERM CO-TERM	PAGE NO.	PRIMARY TERM CO-TERM	PAGE NO.	PRIMARY TERM CO-TERM	PAGE NO.	PRIMARY TERM CO-TERM	PAGE NO.
AMMONIACAL SOLUT. (CONTD)		ANODE (CONTD)		ANODIC FILM (CONTD)		ANODIC STABILITY (CONTD)	
DEZINCIFICATION - 1299		PHOTOCONDUCTIVITY 972		SILVER OXIDE - - - - - 725		TANTALUM - - - - - 507	
STRESS CORROSION - "		PHOTOCURRENT - - - 419		XPS - - - - - 1370		TETRAHYDROFURAN - "	
AMMONIUM DICHROM.		PLATINUM - - - - - 555					
LUMINESCENCE - ->1975		SEMICONDUCTOR - - 419		ANODIC FORMATION		ANODIC ZINC OXIDE	
OXIDATION - - - - - "		THIOCYANATE - - - 972		COMPOSITION - - ->2167		CRYSTALLITE GROW->1914	
PHOSPHOR LUMINES.		ANODE MATERIAL		IRON OXIDE FILM - "		NUCLEATION - - - - - "	
THERMAL DECOMPOS.		LITHIUM BORON - -> 866				SOLUTION PRECIPIT.	
ZINC SULFIDE - - - - - "		MOLTEN SALT BATT.		ANODIC OXIDATION		ZINC OXIDE FILM - "	
		THERMAL ANALYSIS - "		BANDGAP SHIFT - ->1592			
AMORPHOUS SEMICO.				BORATE BUFFER - -> 187		ANODIZATION	
DEPOSITION - - - - -> 688		ANODE MECHANISM		- - - - -> 442		ALUMINUM - - - - -> 779	
HYDROGEN CONTENT - "		CALCIUM ANODE - -> 176		CADMIUM TELLURIDE> 768		- - - - ->1548	
MASS SPECTROMETRY - "		FUSED SALT - - - - -		CARRIER CONCENTR.> 118		BISMUTH TRITELLU.>1191	
PHOTOVOLTAIC PRO.		LITHIUM CHLORIDE - "		COBALT DIOXIDE - 187		CIRCUIT - - - - ->1718	
SILICON - - - - - - - - - "		OVERVOLTAGE - - - - -		COMPOSITION - - - 442		CONDUCTION - - -> 803	
		THERMAL BATTERY - "		CONSTANT VOLTAGE > 89		CORROSION - - - - - 1718	
AMORPHOUS SILICON				COPPER DOPING - - 1592		DENDRITE - - - - - "	
ARGON - - - - - - - - ->1247		ANODIC		CURRENT DENSITY ->1268		ELLIPSONOMETRY - - 1191	
EPITAXIAL GROWTH - "		BLEACHING - - - ->2171		- - - - ->1543		FILM FORMATION - 1718	
KRYPTON - - - - - - - - - "		COLORATION - - - - -		DIABETES - - - - -> 43		GALLIUM SELENIDE 1191	
NEON - - - - - - - - - - - "		CORROSION STABIL.		DIELECTRICS - - ->1374		GOLD METALLIZATI. 1718	
		ELECTROCHROMISM - "		ELECTROCHROMISM -> 583		IMPEDENCE - - - - - 779	
ANALYTIC SOLUTION		IRIDIUM OXIDE - - -		- - - - ->2133		KEIL SALOMON - - -> 544	
FOURIER ANALYSIS >2081		MECHANISM - - - - -		ELLIPSONOMETRY - - 1374		LAYER PERIODICITY 1191	
LINEAR POLARIZAT. - "		PH - - - - - - - - - - - "		FILM GROWTH - - -> 470		LAYERED SEMICOND. - "	
PASSIVE FILM - - - - - "				FILM STRUCTURE - 583		OXYGEN ISOTOPE - 544	
POTENTIAL DISTRI. - "				FLAKE POTENTIAL - 470		REDUCTION - - - - - 803	
SCRATCH - - - - - - - - - "				GAAS - - - - - - - - - 1268		RELAXATION TIME 779	
		ANODIC ACTIVATION		- - - - - 1543		SILVER BROMIDE - 803	
ANGLE LAPPING		AUGER SPECTROSCOP.> 78		GLUCOSE SENSOR - 43		STICHIOMETRY - - 779	
ION IMPLANTATION >1982		ELECTROCATALYSIS - "		- - - - ->1687		TUNNELING - - - - - 1548	
JUNCTION DEPTH - - - - - "		OXYGEN REDUCTION - "		HALL DATA - - - - - 118		VANADIUM - - - - - 544	
STAINING - - - - - - - - - "		PLATINUM - - - - - "		IMPLANTATION - - 43		VAPOR INFUSION - 1548	
		SINGLE CRYSTAL - - -		INDIUM PHOSPHIDE 118		WATER - - - - - - - - - 1718	
		STRUCTURE SENSIT. - "		INHIBITION - - - 1687			
ANION INFLUENCE		ANODIC BEHAVIOR		ION IMPLANTATION 118		ANTIMONY	
ELECTROCATALYSIS >2140		ALUMINUM - - - ->1659		ION SCATTERING - 1543		ALUMINUM - - - - ->1992	
ELECTROSORPTION - - - - - "		CHLORIDE ION - - - - -		IRON OXIDE FILM - 442		CRYSTAL GROWTH -> 875	
HYDROGEN MONOLAY. - "		NITRATE ION - - - - -		KREBS-RINGER - - 43		CZOCHELSKI - - - - -	
OXYGEN MONOLAYER - - - - -		PASSIVITY - - - - -		- - - - - 1687		DOPED MELT - - - - -	
PLATINUM - - - - - - - - - "		PITTING POTENTIAL - "		LINEAR POTENTIAL 43		DTA - - - - - - - - - 1992	
SULFURIC ACID - - - - - "				MERCURY - - - - - 768		GALLIUM - - - - - - - - -	
		ANODIC CORROSION		MOSSBAUER SPECTR. 187		INSTABILITY - - - - - 875	
ANNEAL		EUTECTIC - - - ->1087		NATIVE OXIDE - - 768		LIQUID ASSOCIATI. 1992	
CHANNELING - - - - -> 277		- - - - ->1093		NICKEL - - - - - 470		MORPHOLOGY - - - 875	
CHROMIUM - - - - - - - - - "		FUSED SALT - - - - - 1087		NIOBIUM - - - - - 1374		PHASE DIAGRAM - - 1992	
DIFFACTION - - - - - - - - -		- - - - - 1093		OPEN CIRCUIT - - - - -		SILICON CRYSTAL - 875	
EPITAXIAL RELATI. - "		LITHIUM CHLORIDE 1087		OPTICAL PROPERTY 1592		TERNARY PHASE - - 1992	
PLATINUM - - - - - - - - - "		- - - - - 1093		PARABOLIC GROWTH 89			
SAPPHIRE - - - - - - - - - "		POTASSIUM CHLORI. 1087		PASSIVATION TIME 1268		ANTIMONY EVAPORA.	
		- - - - - 1093		PASSIVE FILM - - 442		ARSENIC - - - - ->1761	
ANNEALING		SULFIDATION - - - - -		PHOTOELECTROCHEM. 2133		DOPING - - - - - - - - -	
C-V CURVE - - - - ->1078		VOLTAMMETRY - - - 1087		PLATINUM ELECTRO. 43		EPITAXY - - - - - - - - -	
CADMIUM TELLURIDE> 809		- - - - - 1093		REACTION RATE - - 583		ION IMPLANTATION - "	
CAPACITANCE - - - - ->1731		ANODIC DISCHARGE		SILICON - - - - - 89		MOLECULAR BEAM - "	
CHARGE DENSITY - - ->1573		FELTMETAL - - - -> 993		SILURIC ACID - - 470		SILICON - - - - - - - - -	
CORONA CHARGING - 1078		LITHIUM BORON - - -		TAFEL SLOPE - - - 1374		ULTRAHIGH VACUUM - "	
DEFECT ISOTHERM - 809		MOLTEN SALT - - - - -		TELLURIUM DIOXIDE 768			
DEPTH PROFILE - - ->1737		VOLTAGE REGULATI. - "		THERMAL OXIDATION 2133		APPLICATION	
ELECTRON MICROSC.				TITANIUM DIOXIDE 1592		FUEL CELL - - - - -> 7C	
GAAS - - - - - - - - - 1737		ANODIC DISSOLUTI.		TRANSIENT ANALYS. 1374		HISTORY - - - - - - - - -	
HIGH TEMPERATURE 1731		ACID SULFATE - - -> 95		TUNGSTEN - - - - - 583		APPLIED POLARIZA.	
HYDROGENATION - - ->1750		ACIDIC CHLORIDE ->1666		TUNGSTEN TRIOXIDE 583		COPPER ZINC - - ->2057	
INTERFACE STATE - 1573		ACIDIC SULFATE ->2064		- - - - - 2133		ELECTRODE POTENT. - "	
LATTICE DEFECT - - 809		CHLORIDE SOLUTION - -		UREA - - - - - - - - - 1687		GALVANIC CORROSI. - "	
OXIDE - - - - - - - - - 1737		COPPER - - - - - - - - - 1666		VACUUM EVAPORATI. 583		NUMERICAL ANALYS. - "	
OXIDE FILM GROWTH 1731		CORROSION - - - - - - - 2064				SOLUTION DEPTH - - - - -	
PHOSPHORUS DOPING 1078		CORROSION RATE - 95		ANODIC OXIDE			
PLASMA DEPOSITION 1750		DEOXYGENATED SOL. 2064		ANODIC FILM - - ->1370		APROTIC SOLVENT	
REOXIDATION - - - - - 1731		DISSOLUTION KINE. 1666		DEPTH PROFILE - - -		CHEMILUMINESCENCE> 414	
SILICON DIOXIDE - 1078		GOLD - - - - - - - - - 95		ELLIPSONOMETRY - -> 986		ELECTROGENERATED - "	
- - - - - 1573		IRON - - - - - - - - ->2150		GAAS - - - - - - - - - 1370		ENERGY CONVERSION - "	
SILICON NITRIDE - 1750		OXYGEN EVOLUTION 95		PASSIVATION - - - - -		PHOTOINDUCED - - -	
SILICON OXIDE - 1731		PASSIVATION - - - 2064		SUBSTRATE CONSTA. 986		SEMICONDUCTOR - - -	
THERMAL OXIDATION 1573		PH - - - - - - - - - 95		TITANIUM - - - - - - -		VP CONVERSION - - -	
TITANIUM DIOXIDE 1731		POTENTIAL DISTRI. 2150		XPS - - - - - - - - - 1370			
TRAPPING DENSITY 1078		SULFURIC ACID - - -				AQUEOUS BASE	
XPS - - - - - - - - - 1737		TITANIUM - - - - - 2064		ADHESION - - - - -> 624		OXIDATION - - - - -> 983	
ANODE				DIELECTRICS - - -> 766		P-HYDROXYBENZALD. -	
CONSTANT CURRENT > 555		ANODIC FILM		DUCTILITY - - - - - 624		STEEL ANODE - - - - -	
CONSTANT POTENTI.> 360		ALUMINUM - - - ->2042		FRACTURE - - - - - - -		STERESELECTIVITY - "	
- - - - - 555		ANODIC OXIDE - - ->1370		IONIC CONDUCTION 765			
CORROSION - - - - - 360		BLEACHING - - - -> 742		>1972		AQUEOUS ELECTROL.	
CRYSTAL GROWTH - - - - -		COBALT SULFATE - -> 725		SELF DISCHARGE - -		DARK POTENTIAL ->1868	
CYCLIC CORROSION > 365		COLORATION - - - - - 742		TANTALUM - - - - - 624		FLATBAND POTENTI. - "	
DEEP DISCHARGE - - - - -		CORROSION STABIL. -		TANTALUM PENTOXI. 765		GROUP II-VI COMP. - "	
ELECTROOXIDATION > 972		DEPTH PROFILE - - 1370				IODINE DOPING - - -	
IRON OXIDE - - - - -> 419		ELECTROCHROMISM - 742				LIGHT ABSORPTION - "	
LEAD ACID BATTERY 360		FILM FORMATION - 2042				OPTICAL ABSORPTI. - "	
- - - - - 365		GAAS - - - - - - - - - 1370				ZINC SELENIDE - - - - -	
LEAD DIOXIDE - - - - -		GRID CORROSION - 725		ANODIC STABILITY			
LIGHT EFFECT - - - - - 972		IRIDIUM OXIDE - 742		COLD-ROLLED STEEL> 507		AQUEOUS MEDIA	
OXIDE FILM GROWTH 555		LEAD ACID BATTERY 725		CORROSION RESIST. -		CONDUCTING ELECT.>205C	
PH DEPENDENT - - - - -		PASSIVATION - - - 1370		HEXAFLUOROCARSEN. -		ORGANOMETALLICS - "	
PHOSPHORIC ACID - 360				LITHIUM - - - - - - - - -		SEMICONDUCTOR - - - - -	
				LITHIUM BATTERY - - -			

PRIMARY TERM CO-TERM	PAGE NO.	PRIMARY TERM CO-TERM	PAGE NO.	PRIMARY TERM CO-TERM	PAGE NO.	PRIMARY TERM CO-TERM	PAGE NO.
AQUEOUS OXIDATION		ATOMIC ABSORPTION		BARIUM FLUORITE (CONTD)		BORATE BUFFER	
INCONNEL 600 --> 750		GAAS CRYSTAL -->1988		SOLID SOLUTION -- 667		ANODIC OXIDATION > 187	
NUCLEAR REACTOR -- "		SPECTROSCOPY -- "		STRONTIUM FLUORITE -- "		COBALT DIOXIDE --> 442	
XPS -- -- -- -- -- "		TRACE ELEMENT -- "		URANIUM FLUORITE -- "		COMPOSITION -- -- 442	
AQUEOUS SOLUTION		ZEEMAN TECHNIQUE -- "		BARIUM TITANATE		IRON OXIDE FILM -- "	
ALUMINUM -- -- --> 199		AUGER SPECTROSC.		ALUMINUM SOLUBIL.> 165		MOSSBAUER SPECTR. 187	
ETCHING -- -- -->1406		ANODIC ACTIVATION> 78		CONDUCTIVITY -- -- "		PASSIVE FILM -- -- 442	
ETHYLENEDIAMINE -- "		BORON DIFFUSION -->1805		THERMISTOR -- -- -- "		PLATINUM ELECTRO. 187	
HYDRIDE FORM -- -- 199		BORON NITRIDE -- -- "		BATTERY		BORON DIFFUSION	
PH -- -- -- -- -- "		BORON RICH LAYER -- "		ABUSE TOLERANCE -->1637		AUGER SPECTROSCOP. >1805	
POTENTIAL -- -- -- -- "		CADMIUM SELENIDE > 949		DTA -- -- -- -- -- "		BORON NITRIDE -- -- "	
PYROCATECHOL -- -- 1406		CADMIUM SULFIDE -- -- "		LITHIUM -- -- -- -- -- "		BORON RICH LAYER -- "	
SALT SOLUTION -- -- 199		CORROSION -- -- --> 547		SULFUR DIOXIDE -- -- "		DEPTH PROFILE -- -- "	
SILICON -- -- -- -- 1406		CVD -- -- -- -- -->1766		BENZAL CHLORIDE		HYDROGEN INJECT. -- "	
AQUEOUS SYSTEM		DEPTH PROFILE -- -- 1805		CARBON DIOXIDE --> 401		SILICON -- -- -- -- -- "	
HIGH TEMPERATURE > 908		ELECTROCATALYSIS > 67		DIMETHYLFORMAMIDE -- "		BORON DOPING	
REFERENCE ELECTR. -- "		ELECTRON DIFFRAC. 78		REDUCTION MECHAN. -- "		CVD -- -- -- -- --> 313	
THERMAL CELL -- -- "		ELLIPSOmetry -- --> 450		BERYLLIUM DOPING		DEPOSITION -- -- -- "	
ARC PLASMA SPRAY.		ENERGY CONVERSION 949		PHOTOELECTROLYSIS>2007		DIELECTRICS -- -- -- "	
CERAMICS -- -- --> 83		GAAS -- -- -- -- -- 450		QUANTUM EFFICIEN. -- "		OPAPANT DISTRIBUT.> 138	
PHOTOELECTROLYSIS -- "		HYDROGEN ABSORPT. 67		ETCHING -- -- -- -- --> 345		LPE -- -- -- -- -- 138	
RUTILE ANODE -- -- "		HYDROGEN INJECT. 1805		MELTBACK -- -- -- -- "		PHOSPHORUS DOPING 313	
TITANIUM DIOXIDE -- "		IN SITU -- -- -- -- 450		PHOTOCHEMISTRY -- "		SILICON -- -- -- -- -- 138	
ARGON		ION IMPLANTATION > 98		SODIUM SULFUR -- 1451		SILICON DIOXIDE -- 313	
ALUMINUM COVERAGE>1335		IRON -- -- -- -- -- 547		SODIUM-22 LABEL -- 1513		SODIUM HYDROXIDE 345	
AMORPHOUS SILICON>1247		LEED -- -- -- -- -- 450		BIRGE-SPICER		BORON GETTERING	
CVD -- -- -- -- -- 1335		OXIDATION -- -- -- -- 547		DISSOCIATION -- -->1396		LSI DEVICE -- -- -->1754	
EPITAXIAL GROWTH 1247		OXYGEN CONCENTRA. 1766		METAL HALIDE GAS -- "		OXYCHLORIDE -- -- -- "	
EVAPORATION -- -- 1335		OXYGEN REDUCTION 78		MODEL CALCULATION -- "		PHOSPHORUS -- -- -- "	
INSULATION -- -- -- "		PALLADIUM -- -- -- 547		THERMOCHEMISTRY -- "		PIPE YIELD -- -- -- "	
KRYPTON -- -- -- -- 1247		PASSIVE OXIDE -- -- -- "		BISAZIDE RESIST		SILICON -- -- -- -- -- "	
NEON -- -- -- -- -- "		PHOTOELECTRICITY 949		CROSSLINKING -- --> 273		BORON NITRIDE	
POLYSILICON -- -- 1335		PLATINUM -- -- -- -- 67		PHOTORESIST SYST. -- "		AUGER SPECTROSCOP.>1805	
PRESSURE VARIATI. -- "		POLYSILICON -- -- 1766		RECIPROCITY FAIL. -- "		BORON DIFFUSION -- "	
SILICON DIOXIDE -- -- "		RHEED -- -- -- -- -- 450		BISMUTH TRITELLU.		BORON RICH LAYER -- "	
AROMATIC HYDROCA.		SEMICONDUCTOR -- -- 949		ANODIZATION -- -->1191		CVD -- -- -- -- -->1951	
ALUMINUM BROMIDE >1474		SEMIINSULATION -- 1766		ELLIPSOmetry -- -- "		DEPTH PROFILE -- -- 1805	
CYCLIC VOLTAMMET. -- "		SILICON -- -- -- -- 1805		GALLIUM SELENIDE -- "		GROWTH PARAMETER 1951	
POTASSIUM BROMIDE -- "		SINGLE CRYSTAL -- 67		LAYER PERIODICITY -- "		HYDROGEN INJECT. 1805	
SURFACE PROCESSES -- "		STRUCTURE SENSIT. 67		AYER PERIODICITY -- "		PHOSPHOR DOPING -- 1951	
ARSENIC		SURFACE ANALYSIS 450		AYER PERIODICITY -- "		SILICON -- -- -- -- -- 1805	
ANTIMONY EVAPORA.>1761		SURFACE CONTAMIN. 98		BISULFATE CATALY.		BORON REDISTRIBU.	
DOPING -- -- -- -- -- "		THIN FILM -- -- -- 547		CATHODE FILM -- --> 190		DIFFUSION MODEL -->2001	
EPIITAXY -- -- -- -- -- "		VPE -- -- -- -- -- 450		CHROMIUM -- -- -- -- "		THERMAL OXIDATION -- "	
ION IMPLANTATION -- "		XPS -- -- -- -- -- 547		ELECTRODEPOSITION -- "		BORON RICH LAYER	
MOLECULAR BEAM -- "		-- -- -- -- -- 1766		POLYCHROMEATE -- -- "		AUGER SPECTROSCOP.>1805	
SILICON -- -- -- -- -- "		AUSTENITIC		BITHIAZOLE		BORON DIFFUSION -- "	
ULTRAHIGH VACUUM -- "		CORROSION -- -- --> 374		BLEOMYCIN -- -- -->2091		BORON NITRIDE -- -- "	
ARSENIC DESORPTI.		DUPLEX 308 -- -- -- "		CYCLIC VOLTAMMET. -- "		DEPTH PROFILE -- -- 1805	
AUTODOPING -- -- --> 822		INTERGRANULAR -- -- "		METAL COMPLEX -- -- "		HYDROGEN INJECT. -- "	
EPITAXIAL GROWTH -- "		MICROSTRUCTURE -- -- "		POLAROGRAPHY -- -- "		SILICON -- -- -- -- -- "	
SILANE -- -- -- -- -- "		PHASE TRANSFORMA. -- "		PYRIMIDINE -- -- -- "		BREATH TEST	
SILICON -- -- -- -- -- "		PITTING -- -- -- -- "		REDUX -- -- -- -- -- "		AMMONIA -- -- -- --> 883	
ARSENIC DOPING		STAINLESS STEEL -- -- "		TALLYSCMYCIN -- -- "		CLEANING -- -- -- -- "	
CONDUCTIVITY -- -->1434		AUTODOPING		BLEACHING		HYDROGEN PEROXIDE -- "	
CVD -- -- -- -- -- -- "		ARSENIC DESORPTI.> 822		ANODIC -- -- -- -- -->2171		PHOTORESIST FILM -- "	
OXIDE FILM -- -- -- -- "		EPITAXIAL GROWTH -- "		ANODIC FILM -- -- --> 742		STRIPPING -- -- -- -- "	
TIN OXIDE -- -- -- -- -- "		SILANE -- -- -- -- -- "		COLORATION -- -- -- "		WAFER SURFACE -- -- -- "	
ARSENIC PRESSURE		SILICON -- -- -- -- -- "		-- -- -- -- -- 2171		BROMINE DIFFUSION	
CAPLESS ANNEAL -->1997		BACKSCATTERING		CORROSION STABIL. 742		DIFFUSION COEFFI.> 36	
GAAS -- -- -- -- -- -- "		ACTIVATOR -- -- -->1671		ELECTROCHROMISM -- 742		ION EXCHANGE -- -- -- "	
ION IMPLANTATION -- "		ELECTROLESS -- -- -- "		IRIDIUM OXIDE -- -- 742		NAFION MEMBRANE -- -- "	
ARSINE GAS		GLASS SUBSTRATE -- -- "		MECHANISM -- -- -- -- "		BUBBLE DYNAMICS	
DEVICE QUALITY --> 300		METAL DEPOSITION -- -- "		PH -- -- -- -- -- -- "		ALLOY -- -- -- -- --> 574	
EPIITAXY -- -- -- -- -- "		PALLADIUM -- -- -- -- "		BLEOMYCIN		ALUMINUM -- -- -- -- -- "	
GAAS -- -- -- -- -- -- "		BANDGAP SHIFT		BITHIAZOLE -- -- -->2091		ELECTROPOLISHING -- "	
GERMANIUM -- -- -- -- -- "		ANODIC OXIDATION >1592		CYCLIC VOLTAMMET. -- "		GASEOUS DISCHARGE -- "	
MOLYBDENUM -- -- -- -- -- "		COPPER DOPING -- -- -- "		METAL COMPLEX -- -- -- "		GROOVE SPACING -- -- -- "	
TRIMETHYLGALLIUM -- "		OPTICAL PROPERTY -- -- "		POLAROGRAPHY -- -- -- "		NICKEL -- -- -- -- -- -- "	
ATMOSPHERE		TITANIUM DIOXIDE -- -- "		PYRIMIDINE -- -- -- -- "		SURFACE MORPHOLO. -- "	
DOPING -- -- -- -- -->1785		BARIUM CHLOROSIL.		REDUX -- -- -- -- -- -- "		BUFFER CAPACITY	
HELIUM-HYDROGEN -- "		EUROPIUM -- -- -- -->1734		TALLYSCMYCIN -- -- -- "		CURRENT EFFICIEN.>1861	
HETEROEPIITAXY -- -- "		HIGH QUENCHING -- -- -- "		BLUE LIGHT EMISS.		ELECTRODEPOSITION -- "	
SILICON GROWTH -- -- -- "		PHOSPHORS -- -- -- -- -- "		GALLIUM -- -- -- -- --> 341		HYDROGEN EVOLUTI. -- "	
ATMOSPHERIC CORR.		PHOTOLUMINESCENCE -- -- "		LUMINESCENCE -- -- -- -- "		NICKEL IRON ALLOY -- -- "	
FABRICATION METH.>1533		TEMPERATURE -- -- -- -- -- "		SOLUTICN GROWTH -- -- "		BULK PHASE	
OXIDATION -- -- -- -- -- "		BARIUM FLUORIDE		ZINC SELENIDE -- -- -- -- "		EMF -- -- -- -- -->1467	
PERMALLOY FILM -- -- -- "		ELECTRONIC CONDU.>2023				MOLTEN SALT -- -- -- -- "	
ATMOSPHERIC EFEE.		SOLID ELECTROLYTE -- "				SILVER CHLORIDE -- -- -- "	
COBALT -- -- -- -- -->1459		BARIUM FLUORITE				SODIUM CHLORIDE -- -- -- "	
CORROSION -- -- -- -- -- "		CALCIUM FLUORITE > 667				SURFACE TENSION -- -- -- "	
OXYHYDROXIDE -- -- -- -- "		CESIUM FLUORITE -- -- -- "					
		DEFECT INTERACTI. -- -- "					
		IONIC CONDUCTIVI. -- -- "					

PRIMARY TERM CO-TERM	PAGE NO.	PRIMARY TERM CO-TERM	PAGE NO.	PRIMARY TERM CO-TERM	PAGE NO.	PRIMARY TERM CO-TERM	PAGE NO.
C-V CURVE		CAPACITY (CONTO)		CARBOXYLATION (CONTO)		CATHOLYTE (CONTO)	
ANNEALING - - ->1078		LITHIUM BATTERY - 523		SYNTHESIS - - - - 404		OPEN PAN STUDY - 1496	
CORONA CHARGING - "		ORGANIC ELECTROL. - "		TARTRONIC ACID - "		REDUCTION - - - - "	
PHOSPHORUS DOPING - "		RATE CAPABILITY - "				THERMAL BATTERY - "	
SILICON DIOXIDE - "		SECONDARY BATTERY - "		CARRIER CONCENTR.			
TRAPPING DENSITY - "		SYSTEM STABILITY - "		ANODIC OXIDATION > 118		CATION ABSORPTION	
		TETRAHYDROFURAN - "		CERIUM DIOXIDE -> 562		ENERGY CONVERSION> 954	
CADMIUM HALIDE				DOPING - - - - - "		PHOTOANODE - - - - "	
CRYSTALLOGRAPHY -> 325		CAPILLARY PORE		ELECTRICAL CONDU. - "		PHOTOELECTROCHEM. - "	
DIFFRACTION - - - - "		AMALGAM CORROSION> 903		HALL DATA - - - - 118		RUTHENIUM - - - - "	
MIXED CRYSTALS - - - - "		CREVICE CORROSION - "		INDIUM PHOSPHIDE - "		SOLAR CELL - - - - "	
POLYTYPISM - - - - "		DENTAL AMALGAM - - - - "		ION IMPLANTATION - "		SURFACE TREATMENT - "	
VAPOR GROWN - - - - "				IR ABSORPTION -> 260			
		CAPLESS ANNEAL		NIOBIUM PENTOXIDE 562		CATION FILM	
CADMIUM SELENIDE		ARSENIC PRESSURE >1997		SEMICONDUCTOR - - 260		DISPLAY DEVICE -> 167	
AUGER SPECTROSCO.> 949		GAAS - - - - - "		SILICON - - - - - "		GOLD SUBSTRATE - - - - "	
CADMIUM SULFIDE - - - - "		ION IMPLANTATION - "				N-HETHTYLVIOLGEN - - - - "	
ENERGY CONVERSION - "				CATALYST			
PHOTOELECTRICITY - - - - "		CARBON		DEPOSITION - - - -> 394		CATION RADIUS	
SEMICONDUCTOR - - - - "		AMBIENT PRESSURE >1422		ELECTROLESS - - - - "		CATHOLYTE - - - ->1496	
XPS - - - - - - - - - - "		CARBON MONOXIDE - - - - "		PALLADIUM - - - - - "		MOLTEN NITRATE - - - - "	
		CATHODE - - - - ->2052		UV IRRADIATED - - - - "		NITRATE SALT - - - - "	
CADMIUM SULFIDE		CHROMIUM STEEL ->2173				OPEN PAN STUDY - - - - "	
AUGER SPECTROSCO.> 949		EQUILIBRIUM - - - - 1422		CATALYTIC DECOMP.		REDUCTION - - - - - "	
CADMIUM SELENIDE - - - - "		LITHIUM - - - - - 2052		ALKALINE SOLUTION>1924		THERMAL BATTERY - - - - "	
CHARGE TRANSFER ->1187		NIGBIUM - - - - - 2173		FUEL CELL - - - - - "			
ENERGY CONVERSION 949		OXIDATION RESIST. - - - - "		PERHYDRCXYL ION - - - - "		CELL KINETICS	
FLASH EVAPORATION>1820		OXYGEN - - - - - 1422				ADSORPTION - - - -> 608	
INDIUM DOPING - - - - "		SILICON - - - - - 2052		CATHODE		LITHIUM BATTERY - - - - "	
MOBILITY - - - - - "		THIONYL CHLORIDE 2052		CARBON - - - - ->2052		PHASE DIAGRAM - - - - "	
PHOTOELECTRICITY 949		TITANIUM - - - - - 2173		CONVECTION - - - -> 23		POTENTIAL - - - - - "	
SEMICONDUCTOR - - - - "		ZIRCONIUM - - - - - "		COPPER - - - - - "		SPECTROSCOPY - - - - "	
SODIUM MONOSULFI. 1187				CUPRIC OXALATE -> 351		TITANIUM DISULFI. - - - - "	
XPS - - - - - - - - - - 949		CARBON DIOXIDE		CURRENT DENSITY - 23		VOLTAGE STEPS - - - - "	
		BENZAL CHLORIDE -> 401		ELECTRODEPOSITION - - - - "			
CADMIUM TELLURIDE		DIMETHYLFORMAMIDE - - - - "		HOST LATTICE - - - ->1311		CELL MEMBRANE	
ANNEALING - - - -> 809		FURNACE - - - - ->2012		IRON SULFUR - - - -> 887		BETA-ALUMINA - - - ->1451	
ANODIC OXIDATION > 768		GAS FLOW METHOD - - - - "		LITHIUM - - - - - 2052		ELECTRODE SHAPE - - - - "	
DEFECT ISOTHERM - 809		GAS SOLUBILITY -> 328		LITHIUM BATTERY - 887		FAILURE ANALYSIS - - - - "	
ELECTRON MICROSC. - - - - "		HYDROGEN - - - - - 2012		LITHIUM CELL -> 497		SODIUM SULFUR - - - - "	
LATTICE DEFECT - - - - "		LOWER TEMPERATURE - - - - "		MASS TRANSPORT - 23			
MERCURY - - - - - 768		MOLTEN SALT - - - - 328		NONAQUEOUS CELL - 887		CERAMICS	
NATIVE OXIDE - - - - - "		OXYGEN - - - - - 2012		PLANE VERTICAL - 23		ARC PLASMA SPRAY.> 83	
TELLURIUM DIOXIDE - - - - "		OXYGEN PRESSURE - 2012		POTASSIUM IRON S. 887		CONTAINER MATERI.>2156	
		PRESSURE CONTROL - - - - "		POWER SOURCE - 1311		CORROSION - - - ->1723	
CALCIA		REDUCTION MECHAN. 401		SEAWATER CELL - 351		DTA - - - - -> 1	
CERIUM DIOXIDE -> 264		SODIUM CARBONATE 328		SECONDARY BATTERY 497		HOT-PRESSED - 1723	
IONIC CONDUCTIVI. - - - - "		SULFUR DIOXIDE - - - - "		SOLID SOLUTION - 1311		IONIC CONDUCTIVI. - 1	
YTTRIA - - - - - - - - - - "		WUSTITE PHASE - - 2012		THIONYL CHLORIDE 2052		LITHIUM OXIDE - - - - "	
				VANADIUM OXIDE - 497		MOISTURE CONTENT - - - - "	
CALCIUM ANODE		CARBON IMPURITY		CATHODE FILM		OXIDATION KINETI. 1723	
ANODE MECHANISM -> 176		HEAT EXCHANGER -> 935		BISULFATE CATALY.> 190		PHOTOELECTROLYSIS 83	
FUSED SALT - - - - - "		MOLYBDENUM RETAI. - - - - "		CHROMIUM - - - - - "		PHYSICAL PROPERT. 1	
LITHIUM CHLORIDE - - - - "		SILICON CRYSTAL - - - - "		ELECTRODEPOSITION - - - - "		REFRACTORIES - - 1723	
OVERVOLTAGE - - - - - "				POLYCHROMATE - - - - "		RUTILE ANODE - - - - 83	
THERMAL BATTERY - - - - "		CARBON MONOXIDE				SILICON CARBIDE - 2156	
		AMBIENT PRESSURE >1422		CATHODE RAY		SILICON NITRIDE - 1723	
CALCIUM FLUORIDE		CARBON - - - - - "		CERIUM - - - - ->1556		SINTERING - - - - 2156	
CHEMICAL POTENTI.>1360		CONDUCTANCE MODU.> 627		CONCENTRATION - - - - "		SODIUM SULFUR - - - - "	
MEASUREMENT - - - - - "		EQUILIBRIUM - - - - 1422		EFFICIENCY - - - - - "		TITANIUM DIOXIDE 83	
OXYGEN - - - - - - - - - - "		OXYGEN - - - - - "		GADOLINIUM - - - - - "		YTTRIUM - - - - - 1723	
SOLID ELECTROLYTE - - - - "		SENSOR - - - - - 627		GARNET PHOSPHORS - - - - "			
		SILICON - - - - - 1422		TERBIUM - - - - - "		CERIUM	
CALCIUM FLUORITE		THIN FILM - - - - 627				ABSORPTION SPECT.>1550	
BARIUM FLUORITE -> 667		TIN OXIDE - - - - - "		CATHODIC POLARIZ.		CATHODE RAY - - ->1556	
CESIUM FLUORITE - - - - "				NIOBIUM ELECTRODE> 535		CONCENTRATION - - - - "	
DEFECT INTERFACIAL		CARBON STEEL		POTASSIUM HYDROX. - - - - "		CRYSTAL FIELD - - - 1550	
IONIC CONDUCTIVI. - - - - "		ELECTRODEPOSITION> 911		SURFACE CHANGE - - - - "		EFFICIENCY - - - - 1556	
SOLID SOLUTION - - - - - "		HYDROGEN SULFIDE - - - - "		XPS - - - - - - - - - - "		GADOLINIUM - - - - - "	
STRONTIUM FLUORI. - - - - "		MARCASITE - - - - - "				GARNET PHOSPHORS 1550	
URANIUM FLUORITE - - - - "		PYRITE - - - - - - - - - - "				1556	
				CATHODIC REACTION		PHOTOLUMINESCENCE 1550	
CALCIUM NITRATE		CARBON TETRAFLUO.		CREVICE CORROSION> 15		TEMPERATURE RANGE - - - - "	
HYDRATED METALS -> 985		COMPETATIVE MECH.> 464		CURRENT DISTRIBU. - - - - "		TERBIUM - - - - - 1556	
NUCLEATION - - - - - "		ETCHING - - - - - - - - - - "		MATHEMATICAL MOD. - - - - "			
THALLIUM - - - - - - - - - - "		- - - - ->1419		PITTING - - - - - - - - - - "			
		HYDROGEN - - - - - "				CERIUM DIOXIDE	
CAPACITANCE		ION ASSISTANCE - 464		CATHODOLUMINESCE.		A-C IMPEDENCE - ->1166	
ANNEALING - - - ->1731		REACTIVE ION ETCH 1419		ELECTRON BOMBARD.> 571		CALCIA - - - - - - - -> 264	
FLATBAND POTENTI.>1506		SILICON DIOXIDE - 464		HOST SENSITIZATI.> 305		CARRIER CONCENTR.> 562	
HIGH TEMPERATURE 1731		- 1419		LANTHANUM OXSUL. 571		DEFECT STRUCTURE > 209	
MOTT-SCHOTTKY - - 1505		CARBONATE		LOW ENERGY - - - - - "		DOPING - - - - - - - - 562	
OXIDE FILM GROWTH 1731		COMPOSITION PROF.> 527		NONRADIATIVE PRO. 305		ELECTRICAL CONDU. - - - - "	
POTENTIAL DISTRI. 1505		FUEL CELL - - - - - "		PHOSPHORS - - - - - 571		EXCHANGE CURRENT >1155	
REOXIDATION - - - - 1731		MOLTEN SALT - - - - - "		PRASEODYMIUM - 305		IONIC CONDUCTIVI. 264	
SILICON OXIDE - - - - "		STEADY STATE EQU. - - - - "		TERBIUM - - - - - - - - 571		NIOBIUM PENTOXIDE 562	
TITANIUM DIOXIDE 1505				- - - - - - - - - - 305		NONSTOICHIOMETRY 209	
1731				TRAPPING - - - - - - - - 571		OVERPOTENTIAL - - 1155	
CAPACITOR		CARBON TETRAFLUO.		XPS - - - - - - - - - - 571		OXIDE SEMICONDC. 209	
ALUMINUM - - - -> 162		DIOIDE SYSTEM - -> 226		YTTRIUM OXSULFI. 305		PLATINUM ELECTRO. 1155	
DIELECTRIC BREAK. - - - - "		PLASMA ETCHING - - - - "		YTTRIUM OXSULFI. 571		1166	
POLYSILICON - - - - - "		REACTIVE SPUTTER. - - - - "				POINT DEFECT - - - - 209	
SILICON DIOXIDE - - - - "				CATHOLYTE		POLARIZATION - - - - 1155	
		CARBOXYLATION		CATION RADIUS - ->1496		- - - - - 1166	
CAPACITY		DERIVATIVE - - - -> 404		MOLTEN NITRATE - - - - "		THERMOGRAVIMETRY 209	
DISSOLVED SULFUR > 523		O-CARBOXYMETHYL - - - - "		NITRATE SALT - - - - - "		TRANSIENT DECAY - 1166	
		REDUCTION - - - - - - - - - - "					

PRIMARY TERM CO-TERM	PAGE NO.	PRIMARY TERM CO-TERM	PAGE NO.	PRIMARY TERM CO-TERM	PAGE NO.	PRIMARY TERM CO-TERM	PAGE NO.
CERIUM DICHIDE (CONTO)		CHEMICAL EQUILIB.		CHLORINE INCORPO.		CHRONOAMPEROMETRY (CONTO)	
YTTRIA - - - - -	264	COMBUSTION GASES >1054		HYDROCHLORIC ACID > 143		POTASSIUM CHLORIDE 1902	
CERIUM DOPING		DEPOSITION - - -	"	OXIDATION - - - -	"	POTENTIOMETRY - - - 1029	
DECAY PROCESS - ->1213		HOT CORROSION - -	"	PLANAR DEVICE - -	"	CHRONOCOULOMETRY	
EUROPIUM DOPING >1221		SODIUM SULFATE - -	"	SILICON - - - - -	"	ELECTROHYDROLYSE > 579	
GADOLINIUM DOPING		CHEMICAL ETCHING		CHLORINE OXIDATI.		ETHYL CINNAMATE - -	"
GARNET PHOSPHORS	1213	CLEANING PROCESS >1581		DIOXIDE AMBIENCE >1288		LOW TEMPERATURE - -	"
1221		EPITAXIAL LAYER > 287		OXIDATION KINETI. >1789		METHYL CINNAMATE - -	"
RARE EARTH ACTIV.	1213	GAAS - - - - - 1581		SILICON DIOXIDE - 1288		REACTION ORDER - -	"
1221		HEAT TREATMENT - -	"	- 1789			
TERBIUM DOPING - -	"	HOLE DIFFUSION L.	"	STACKING FAULT - -	"	CIRCUIT	
THERMAL DEPENDEN.	1213	HYDROCHLORIC ACID 287		THERMAL OXIDATION 1288		ANODIZATION - - ->1718	
1221		INDIUM PHOSPHIDE	"	1789		CORROSION - - - -	"
		MATERIAL SELEC.	"	TRICHLOROETHYLENE	"	DENORITE - - - -	"
CESIUM		PHOSPHORIC ACID - -	"			FILM FORMATION - -	"
DEPTH PROFILE - -> 660				CHLOROACRYLATE		GOLD METALLIZATI.	"
DOPANT - - - - -	"	CHEMICAL POTENTI.		ELECTRON BEAM - ->1829		WATER - - - - -	"
GAAS - - - - -	"	CALCIUM FLUORIDE >1360		INTEGRATED CIRCU.	"	CLEANING	
ION SELECTIVE - -> 347		MEASUREMENT - - -	"	MOLECULAR ORBITAL	"	AMMONIA - - - - -> 883	
MASS SPECTROMETRY 660		OXYGEN - - - - -	"	POLYMER - - - - -	"	BREATH TEST - - -	"
POTASSIUM - - - - - 347		SOLID ELECTROLYTE	"	POSITIVE RESIST - -	"	HYDROGEN PEROXIDE	"
PVC MATRIX - - -	"	CHEMICAL TREATME.		TRIFLUOROETHYL - -	"	PHOTORESIST FILM	"
SECONDARY ION - -	660	CONDUCTIVITY - ->1792				STRIPPING - - - -	"
SILICON - - - - -	"	ELECTRICAL MEASU.	"	CHLOROALUMINATE		WAFER SURFACE - -	"
ULTRAHIGH VACUUM	"	HYDROGEN DIFFUSI.	"	CHRONOAMPEROMETRY >1029			
ZINC FERROCYNANIDE 347		P-TYPE - - - - -	"	COPPER - - - - -	"	CLEANING PROCESS	
		RESISTIVITY SHIFT	"	DISK ELECTRODE	"	CHEMICAL ETCHING >1581	
CESIUM COACTIVAT.		SILICON SURFACE - -	"	FUSED SALT - - -	"	GAAS - - - - -	"
ALKALI RARE EARTH >2206				POTENTIOMETRY - -	"	HEAT TREATMENT - -	"
GLASSY PHOSPHORS		CHEMILUMINESCENCE				HOLE DIFFUSION L.	"
LUMINESCENCE - -	"	APROTIC SOLVENT -> 414		CHLOROMETHYLATED		CLEANING SOLUTION	
METAPHOSPHATE - -	"	ELECTROGENERATED	"	DRY ETCHING - - ->1628		HYDROGEN PEROXIDE >1428	
TERBIUM ACTIVATI.	"	ENERGY CONVERSION	"	NEGATIVE RESIST - -	"	OXIDATION - - - -	"
		PHOTOINDUCED - -	"	POLYSTYRENE - - -	"	SILICON WAFER - -	"
CESIUM FLUORITE		SEMICONDUCTOR - -	"	SUBMICRON TECHNO.	"	SULFURIC ACID - -	"
BARIUM FLUORITE -> 667		VP CONVERSION - -	"				
CALCIUM FLUORITE	"	CHEMISORPTION		CHLOROSILCXANE		CLOSE SPACING	
DEFECT INTERACTI.	"	RUTHENIUM TRICHL. > 617		HYDROCHLORIC ACID >1081		ENTHALPY - - - ->1604	
IONIC CONDUCTIVI.	"	SURFACE WAVE - -	"	SILICON OXIDE - -	"	VAPOR TRANSPORT - -	"
SOLID SOLUTION - -	"	TIN DIOXIDE - - -	"				
STRONTIUM FLUORI.	"	XPS - - - - -	"	CHROMATE		CLOSED FORM	
URANIUM FLUORITE	"			CHLORIDE SOLUTION > 385		PRIMARY RESISTAN. >1307	
CHANNELING		CHLORALUMINATE		CREVICE CORROSION	"	RING ELECTRODE - -	"
ANNEAL - - - - -> 277		ELECTROOXIDATION > 231		INHIBITION - - -	"		
CHROMIUM - - - -	"	MELT COMPOSITION	"	IRON - - - - -	"		
DIFFRACTION - - -	"	MOLTEN SALT BATT.	"			COAL CHAR	
EPITAXIAL RELATI.	"	SULFUR - - - - -	"	CHROMATE SENSITI.		FERROUS SULFIDE -> 894	
PLATINUM - - - -	"			COLOR TV TUBE - ->1294		GASIFICATION - - -	"
SAPPHIRE - - - -	"	CHLORIDE ION		DIAZO SENSITIZER	"	IRON ALLOY - - -	"
		ALUMINUM - - - ->1659		PHOSPHOR DEPOSIT.	"	SULFIDATION - - -	"
CHARGE CAPACITY		ANODIC BEHAVIOR - -	"	CHROMIUM			
ACID MEDIUM - - -> 93		DISSOLUTION - - -> 919		ANNEAL - - - - -> 277		COBALT	
HYDROXIDE-TYPE - -	"	NICKEL OXIDE FILM	"	BISULFATE CATALY. > 190		ATMOSPHERIC EFPE. >1459	
IRIDIUM - - - - -	"	NITRATE ION - - - 1659		CATHODE FILM - - -	"	COBALT HARDENED -> 391	
THIN FILM - - - -	"	PASSIVATION - - - 919		CHANNELING - - - 277		COBALT OXYHYDROX.	"
CHARGE DENSITY		PASSIVITY - - - - 1659		DEGRADATION - - ->1047		CORROSION - - - - 1459	
ANNEALING - - - ->1573		PIT INITIATION - 919		DIFFRACTION - - - 277		GAAS - - - - ->1584	
INTERFACE STATE - -	"	PITTING POTENTIAL 1659		ELECTRODEPOSITION 190		GAASP - - - - -	"
SILICON DIOXIDE - -	"			EPITAXIAL RELATI.	"	GOLD ELECTRODEPO. 391	
THERMAL OXIDATION	"	CHLORIDE PITTING		ETCHING - - - - ->1075		HOLE DIFFUSION L. 1584	
		ALUMINUM PITTING >1855		IMPACT EROSION - 1047		MOSSBAUER SPECTR. 391	
CHARGE STORAGE		COMPLEX ION - - -	"	INTERDIFFUSION - -	"	NICKEL - - - - - 1584	
DIELECTRIC PROPE. >1958		PIT INITIATION - -	"	METALLIZATION - -	"	OXYHYDROXIDE - - -> 1459	
ELECTRICAL PROPE.	"			PHOTOLITHOGRAPHY 1075		VPE - - - - - 1584	
POLARIZATION - - -	"	CHLORIDE SOLUTION		PHOTOMASK COATING	"		
POLYVINYL BUTYRAL	"	ACIDIC SULFATE ->2064		PLATINUM - - - - 277		COBALT CONCENTRA.	
CHARGE TRANSFER		ANODIC DISSOLUTI.	"	- - - - - 1047		CORROSION SUPPRE. > 944	
CADMIUM SULFIDE ->1187		CHROMATE - - - - -> 385		POLYCHROMATE - - 190		LIGHT INTENSITY - -	"
DIGITAL SIMULATI. >1011		CORROSION - - - - 2064		SAPPHIRE - - - - 277		PHOTOANODE - - -	"
ETCHING - - - - -> 855		CREVICE CORROSION 385		SILICON - - - - - 1047		SULFATE CONCENTR.	"
GAAS ELECTRODE - -	"	DEOXYGENATED SOL. 2064		SILVER - - - - -	"	TITANIUM DIOXIDE	"
GROUP III-V COMP.	"	INHIBITION - - - 385		THIN FILM - - - - 1075			
HOLE INJECTION - 1011		IRON - - - - -	"	CHROMIUM FILM		COBALT DIOXIDE	
ILLUMINATED - - -	"	PASSIVATION - - - 2064		GAS PLASMA - - ->1794		ANODIC OXIDATION > 187	
LIQUID JUNCTION - -	"	TITANIUM - - - -	"	MOS-LSI PROCESS - -	"	BORATE BUFFER - -	"
PHOTOANODE - - -	"			PHOTOMASK - - - -	"	MOSSBAUER SPECTR.	"
PHOTOEFFECT - - - 855		CHLORINATION		REVERSAL ETCHING	"	PLATINUM ELECTRO.	"
REDOX - - - - -	"	CYCLODEXTRIN - -> 500					
SEMICONDUCTOR - - 1011		MODIFIED ELECTRO.	"	CHROMIUM STEEL		COBALT HARDENED	
SODIUM MONOSULFI. 1187		SELECTIVITY - - -	"	CARBON - - - - ->2173		COBALT - - - - -> 391	
SOLAR CELL - - - 1011		CHLORINE		NIOBIUM - - - - -	"	COBALT OXYHYDROX.	"
CHARGE TRANSPORT		EVOLUTION KINETI. >209C		OXIDATION RESIST.	"	ELECTRODEPOSITION > 445	
DIPHETHALOCYANINE >1490		OXIDE FILM - - -	"	TITANIUM - - - -	"	FILM FORMATION - -	"
ELECTROCHROMISM - -	"	PLATINUM ELECTRO.	"	ZIRCONIUM - - - -	"	GOLD - - - - -	"
OXIDATION PRODUCT	"					GOLD ELECTRODEPO. 391	
CHEMICAL DIFFUSI.		CHLORINE EVOLUTI.		CHRONOAMPEROMETRY		>1608	
IRON SULFIDE - - -> 673		DESORPTION - - ->1343		CHLOROALUMINATE ->1029		HIGH TEMPERATURE 445	
NONSTOICHIOMETRY	"	ELECTROCATALYSIS >1189		COPPER - - - - -	"	MOSSBAUER SPECTR. 391	
POINT DEFECT - - -	"	RUTHENIUM - - - -	"	DISK ELECTRODE - -	"	1608	
		STOICHIOMETRY - - 1343		FUSED SALT - - - -	"		
		TAPEL SLOPE - - -	"			COBALT MONOXIDE	
		TITANIUM OXIDE - 1189		LEAD CHLORIDE - - -	"	ELECTROTRANSPORT > 760	
		TITANIUM SUPPORT.	"	LEAD SULFIDE - - -	"	OXIDATION THEORY - -	"
				OXIDATION - - - -	"	POINT DEFECT - - -	"
						TRANSITION METAL	"

PRIMARY TERM CO-TERM	PAGE NO.	PRIMARY TERM CO-TERM	PAGE NO.	PRIMARY TERM CO-TERM	PAGE NO.	PRIMARY TERM CO-TERM	PAGE NO.
COBALT OXIDE		COMPLEX ION MODEL (CONTD)		CONDUCTIVITY (CONTD)		CONVECTIVE DIFFU. (CONTD)	
ELECTRODE MATERIA. >1817		TERNARY SYSTEM - 2098		N-ALKYLPYRIDINIUM 1644		ROTATING DISK - - 431	
LANTHANUM STRONT. "				OXIDE FILM - - - 1434		SINUSOIDAL - - - 431	
POWER - - - - - "		COMPOSITE SYSTEM		P-TYPE - - - - - 1792		VOLTAMMETRY - - - 431	
THERMOELECTRICITY "		ALUMINUM OXIDE ->1304		RESISTIVITY SHIFT "			
COBALT OXYHYDROX.		ALUMINUM POWDER "		SILICON SURFACE - "			
COBALT - - - - -> 391		DISORDERED SYSTEM "		TERNARY SYSTEM - 2098			
COBALT HARDENED - "				2104			
GOLD ELECTRODEPO. "		COMPOSITION		THERMISTOR - - - 165		COPOLYMER	
MOSSBAUER SPECTR. "		ANODIC FORMATION >2167		TIN OXIDE - - - - 1434		LITHOGRAPHY - - -> 154	
COBALT SULFATE		ANODIC OXIDATION > 442		TRANSITION TEMPE. 2144		METHACRYLIC ACID "	
ANODIC FILM - - -> 725		BORATE BUFFER - - "		TRANSPORT - - - - 1644		METHYL METHACRYL. "	
GRID CORROSION - "		IRON OXIDE FILM - "		VISCOSITY - - - - - "		POSITIVE RESIST - "	
LEAD ACID BATTERY		2167				RADIATION SENSIT. "	
SILVER OXIDE - - - "		PASSIVE FILM - - 442		CONNECTOR			
CODEPOSITION		COMPOSITION PROF.		COPPER - - - - ->1798		COPPER	
COPPER - - - - -> 566		CARBONATE - - - -> 527		DIFFUSION - - - - - "		ACIDIC CHLORIDE ->1666	
DIFFUSION CONTROL		FUEL CELL - - - - - "		GOLD ALLOY - - - - - "		ANODIC DISSOLUTI. "	
ROTATING DISK - - - "		MOLTEN SALT - - - - - "		OXIDATION KINETI. "		CATHODE - - - - -> 23	
ZINC - - - - - - - "		STEADY STATE EQU. "		RELIABILITY - - - - - "		CHLORALUMINATE ->1029	
COLD PLASTIC DEF.		CONCENTRATION		CONSTANT CURRENT		CHRONOAMPEROMETRY "	
CORROSION - - - - ->2075		ACTIVATOR - - - - -> 106		ANODE - - - - -> 555		CODEPOSITION - - -> 566	
PITTING RESISTAN. "		CATHODE RAY - - ->1556		CONSTANT POTENTI. "		CONNECTOR - - - ->1798	
SALT SOLUTION - - - "		CERUM - - - - - - - "		OXIDE FILM GROWTH "		CONVECTION - - - - 23	
STAINLESS STEEL - - "		CONVECTION - - ->2110		PH DEPENDENT - - - "		CORROSION - - - - 1666	
		CYCLING - - - - - - "		PLATINUM - - - - - "		CRACKING - - - -> 701	
		EFFICIENCY - - - - 1556				CURRENT DENSITY - 23	
COLD-ROLLED STEEL		ELECTROOSMOSIS - 2110		CONSTANT POTENTI.		CVD - - - - - - ->1425	
ANODIC STABILITY > 507		GADOLINIUM - - - - 1556		ANODE - - - - -> 360		CYCLABLE CELL -> 699	
CORROSION RESIST. "		GARNET PHOSPHORS "		- - - - -> 555		DEPOSITION - - ->2167	
HEXAFLUOROARSENA. "		LUMINESCENCE - - 106		CONSTANT CURRENT "		DIFFUSION - - - - 1798	
LITHIUM - - - - - - "		POWDERED PHOSPHOR "		CORROSION - - - - 360		DIFFUSION CONTROL 566	
LITHIUM BATTERY - - "		QUENCHING MECHAN. "		CRYSTAL GROWTH - "		DISK ELECTRODE - 1029	
TANTALUM - - - - - "		RADIATION - - - - - "		LEAD ACID BATTERY "		DISSOLUTION KINE. 1666	
TETRAHYDROFURAN - "		RARE EARTH - - - - - "		OXIDE FILM GROWTH 555		ELECTRODE - - - - 699	
		TERBIUM - - - - - 1556		PH DEPENDENT - - - "		ELECTRODEPOSITION 23	
		ZINC ELECTRODE - 2110		PHOSPHORIC ACID - 360		ELECTROLESS - - -> 2167	
COLOR TV PICTURE				PLATINUM - - - - - 555		FUSED SALT - - - - 1029	
GAS DISCHARGE ->1008		CONDUCTANCE				GLASSY LAYER - - - 1425	
PHOSPHORS - - - - - "		DIFFUSION - - - ->1682		CONSTANT VOLTAGE		GOLD ALLOY - - - - 1798	
ULTRAVIOLET EXCT. "		ELECTRON EXCHANGE>1827		ANODIC OXIDATION > 89		INTERCALATION - - 699	
COLOR TV TUBE		FUEL CELL - - - - - 1682		PARABOLIC GROWTH "		MASS TRANSPORT - 23	
CHROMATE SENSITI.>1294		HALOGEN - - - - - - "		SILICON - - - - - - "		OXIDATION - - - - 1425	
DIAZO SENSITIZER		HYDROGEN - - - - - - "				OXIDATION KINETI. 1798	
PHOSPHOR DEPOSIT. "		NAFION MEMBRANE - "		CONTACT MATERIAL		PASSIVITY - - - - 1425	
		POLYMER - - - - - - - "		CONTACT RESISTAN.>2017		PLANE VERTICAL - 23	
COLORATION		SILICA SURFACE - 1827		RUTHENIUM - - - - - "		POTENTIOMETRY - 1029	
ANODIC - - - - ->2171		THERMALLY GROWN - "		RUTHENIUM DIOXIDE "		RELIABILITY - - - 1798	
ANODIC FILM - - -> 742		TRANSPORT PROPER. 1682		SULFIDATION - - - - - "		ROTATING DISK - 566	
BLEACHING - - - - - "						SODIUM NITRIDE 701	
		CONDUCTANCE MODU.		CONTACT RESISTAN.		SOLID-STATE CELL 699	
CORROSION STABIL. 742		CARBON MONOXIDE -> 627		CONTACT MATERIAL >2017		STRESS CORROSION 701	
2171		SENSOR - - - - - - - "		RUTHENIUM - - - - - "		TRANSGRANULAR - - "	
ELECTROCHROMISM - 742		THIN FILM - - - - - "		RUTHENIUM DIOXIDE "		ZINC - - - - - - - 566	
2171		TIN OXIDE - - - - - - "		SULFIDATION - - - - - "			
IRIDIUM OXIDE - - 742		CONDUCTING ELECT.		CONTAINER MATERI.		COPPER BROMIDE	
2171		AQUEOUS MEDIA ->205C		CERAMICS - - - - ->2156		IONIC CONDUCTIV.> 818	
MECHANISM - - - - - "		ORGANOMETALLICS - "		CORROSION - - - - - "		PHASE DIAGRAM - - "	
PH - - - - - - - - - "		SEMICONDUCTOR - - - "		SILICON CARBIDE - "		SILVER IODIDE - - - "	
COMBUSTION GASES				SINTERING - - - - - "			
CHEMICAL EQUILIB.>1054		CONDUCTION		SODIUM SULFUR - - - "		COPPER DEPOSITION	
DEPOSITION - - - - - "		ANODIZATION - - -> 803				CURRENT DISTRIBU.>2118	
HOT CORROSION - - - "		ELECTROLYSIS - - ->1368		CONTAMINATION		ELECTRODEPOSITION "	
SODIUM SULFATE - - - "		REDUCTION - - - - 803		CURRENT DENSITY -> 54		ELECTROLESS - - -> 171	
		SILVER BROMIDE - - "		ELECTROLYSIS - - - "		GALVANIC CELL - - - "	
COMPETITIVE MECH.		SOLID BROMINE - - 1368		GLOW DISCHARGE -> 319		GAS LIFT - - - - - 2118	
CARBON TETRAFLUC.> 464				NONFARADAY - - - 54		HYDROGEN EVOLUTI. "	
ETCHING - - - - - - - "		CONDUCTIVITY		PLASMA DEPOSITION 319		MATHEMATICAL MOD. "	
ION ASSISTANCE - - - "		ALUMINUM CHLORIDE>1644		PLASMA ETCHING - - "		OXIDATION - - - - 171	
SILICON DIOXIDE - - - "		>1650		RADIATION DAMAGE "		REDUCTION - - - - - "	
		ALUMINUM SOLUBIL.> 165		SPUTTERING - - - - - "		VERTICAL ELECTRO. 2118	
COMPETING REACTI.		ARSENIC DOPING ->1434		WATER - - - - - - - 54			
MULTIPLE REACTIO.>1928		BARIUM TITANATE - 165				COPPER DOPING	
POROUS ELECTRODE "		CHEMICAL TREATME.>1792		CONVECTION		ANODIC OXIDATION >1592	
REACTOR ANALYSIS "		COMPLEX - - - - ->2104		CATHODE - - - - -> 23		BANDGAP SHIFT - - - "	
		COMPLEX ION MODEL>2098		CONCENTRATION ->2110		COPPER PRECIPITA.> 114	
COMPLEX		CVD - - - - - - - 1434		COPPER - - - - - - 23		OPTICAL PROPERTY 1592	
CONDUCTIVITY - - ->2104		DENSITY - - - - - 1644		CURRENT DENSITY - - "		POINT DEFECT - ->2183	
FUSED SALT - - - - - "		ELECTRICAL MEASU. 1792		CYCLING - - - - - 2110		SILICON WAFER - - - 114	
MEASUREMENT - - - - - "		FUSED SALT - - - - 1644		DIFFUSION - - - ->2173		SOLAR CELL - - - - - "	
MOLAR VOLUME - - - - - "		- - - - - 1650		ELECTRODEPOSITION 23		SWEEP VOLTAMMETRY 2183	
TERNARY SYSTEM - - - "		- - - - - 2098		ELECTROOSMOSIS - 2110		TITANIUM DIOXIDE 1592	
		- - - - - 2104		MASS TRANSPORT - 23		VALENCE CHANGE - 2183	
COMPLEX ION		GLASS - - - - - - ->2144		MIGRATION - - - - 1713		ZIRCONIA - - - - - "	
ALUMINUM PITTING >1855		HALIDE - - - - - - 1644		MOLTEN SALT - - - - - "			
CHLORIDE PITTING "		HYDRATE MELT - - 2144		PLANE VERTICAL - 23		COPPER ELECTRODE.	
PIT INITIATION - - - "		HYDROGEN DIFFUSI. 1792		POROUS ELECTRODE 1713		CURRENT DENSITY ->1180	
		LITHIUM CHLORIDE 1650		TRANSPORT EQUATI. "		ELECTRODEPOSITION "	
COMPLEX ION MODEL		MEASUREMENT - - - 2098		ZINC ELECTRODE - 2110		FLUIDIZED ELECTR. "	
CONDUCTIVITY - - ->2098		- - - - - 2104					
FUSED SALT - - - - - "		MIXED ALKALI EFF. 2144		CONVECTIVE DIFFU.		COPPER ION CONDU.	
MEASUREMENT - - - - - "		MOLAR VOLUME - - - 2098		ELECTRON TRANSFER> 431		CUPROUS CHLORIDE >1654	
MOLAR VOLUME - - - - - "		- - - - - 2104		> 437		CUPROUS IODIDE - - - "	
				HYDRODYNAMICS - - - 431		RUBIDIUM CHLORIDE "	
				- - - 437		SOLID ELECTROLYTE "	
						X-RAY DIFFRACTION "	

PRIMARY TERM CO-TERM	PAGE NO.	PRIMARY TERM CO-TERM	PAGE NO.	PRIMARY TERM CO-TERM	PAGE NO.	PRIMARY TERM CO-TERM	PAGE NO.
COPPER PRECIPITA.		CORROSION FILM		CRYSTAL FIELD (CONTO)		CURRENT DISTRIBU. (CONTO)	
COPPER DOPING -> 114		LEAD ACID BATTERY>1648		CERIUM - - - - -> 1550		VERTICAL ELECTRO. 2118	
SILICON WAFER - - -	"	PHOSPHORIC ACID -	"	GARNET PHOSPHORS	"	CURRENT EFFICIEN.	
SOLAR CELL - - -	"	POSITIVE ELECTRO.	"	PHOTOLUMINESCENCE	"	BUFFER CAPACITY ->1861	
COPPER ZINC		CORROSION POTENT.		TEMPERATURE RANGE	"	ELECTRODEPOSITION	"
AMMONIACAL SOLUT.>1299		ALTERNATING VOLT.>1908		CRYSTAL GROWTH		HYDROGEN EVOLUT.	"
APPLIED POLARIZA.>2057		FARADAIC RECTIFI.	"	ANODE - - - - -> 360		NICKEL IRON ALLOY	"
DEZINCIFICATION - 1299		LINEAR POLARIZAT.> 891		ANTIMONY - - - -> 875			
ELECTRODE POTENT. 2057		MILD STEEL - - - 1908		CONSTANT POTENTI. 360			
GALVANIC CORROSI.	"	NUMERICAL METHODS 891		CORROSION - - - -	"	CURRENT GAIN	
NUMERICAL ANALYS.	"	PASSIVATION - - - 1908		CZOCHEWSKI - - -	875	EMITTER EFFICIEN.> 642	
SOLUTION DEPTH -	"	POLARIZATION - - -	"	DOPED MELT - - -	"	GETTERING - - - -	"
STRESS CORROSION 1299		THREE POINT - - - 891		INSTABILITY - - -	"	P-N-P - - - - -	"
CORONA CHARGING		CORROSION RATE		LEAD ACID BATTERY 360		PHOSPHORUS PENTO.	"
ANNEALING - - - ->1078		ACID SULFATE -> 95		MORPHOLOGY - - - 875		TRANSISTOR - - -	"
C-V CURVE - - - -	"	ANODIC DISSOLUTI.	"	OPTIMUM CONDITION>1625		CURRENT OSCILLAT.	
PHOSPHORUS DOPING	"	GOLD - - - - -	"	PHOSPHORIC ACID - 360		CORROSION - - - ->1363	
SILICON DIOXIDE -	"	OXYGEN EVOLUTION	"	RUTHENIUM DIOXIDE 1625		IRON - - - - -	"
TRAPPING DENSITY	"	PH - - - - -	"	SILICON CRYSTAL - 875		PASSIVITY - - - -	"
				THERMAL EXPANSION 1625		SULFURIC ACID - -	"
CORROSION		CORROSION RESIST.		CRYSTALLITE GROW.		CURRENT PEAK	
ACIDIC CHLORIDE ->1666		ANODIC STABILITY> 507		ANODIC ZINC OXIDE>1914		ELECTROSPRATION -> 257	
ACIDIC SULFATE ->2064		COLD-ROLLED STEEL	"	NUCLEATION - - -	"	HYDROGEN ADATOM -	"
ALUMINUM - - - -> 11		HEXAFLUOROARSEN.	"	SOLUTION PRECIP.	"	PERTURBATIONS - -	"
ANODE - - - - -> 360		LITHIUM - - - - -	"	ZINC OXIDE FILM -	"	PLATINUM - - - -	"
ANODIC DISSOLUTI. 1666		LITHIUM BATTERY -	"			POTENTIAL - - - -	"
2064		TANTALUM - - - -	"	CRYSTALLOGRAPHY			
ANODIZATION - - ->1718		TETRAHYDROFURAN -	"	CADMIUM HALIDE -> 325		CUTTING TOOLS	
ATMOSPHERIC EFPE.>1459				DIFRACTION - - -	"	CVD COATING - - ->1281	
AUGER SPECTROSCO.> 547		CORROSION STABIL.		MIXED CRYSTALS -	"	ETA PHASE - - - -	"
AUSTENITIC - - - -> 374		ANODIC - - - - ->2171		POLYTYPISM - - -	"	TITANIUM CARBIDE	"
CERAMICS - - - ->1723		ANODIC FILM - - -> 742		VAPOR GROWN - - -	"	TOUGHNESS BEHAVI.	"
- - - ->2156		BLEACHING - - - -	"				
CHLORIDE SOLUTION 2064		- - - - - 2171		CUPRIC OXALATE		CVD	
CIRCUIT - - - - - 1718		COLORATION - - - 742		CATHODE - - - - -> 351		ALUMINUM CHLORIDE>1601	
COBALT - - - - - 1459		- - - - - 2171		SEAWATER CELL - -	"	ALUMINUM COVERAGE>1335	
COLD PLASTIC DEF.>2075		ELECTROCHROMISM - 742				ARGON - - - - -	"
CONSTANT POTENTI. 360		- - - - - 2171		CUPROUS CHLORIDE		ARSENIC DOPING ->1434	
CONTAINER MATERI. 2156		IRIDIUM OXIDE - - 742		ALUMINA - - - - ->1963		AUGER SPECTROSCO.>1766	
COPPER - - - - - 1666		- - - - - 2171		COPPER ION CONDU.>1654		BORON DOPING -> 313	
CRYSTAL GROWTH - 360		MECHANISM - - - -	"	CUPROUS IODIDE -	"	BORON NITRIDE ->1951	
CURRENT OSCILLAT.>1363		PH - - - - -	"	DISPERSED ALUMINA 1963		CONDUCTIVITY - - 1434	
DENDRITE - - - - 1718		CORROSION SUPPRE.		ION CONDUCTIVITY	"	COPPER - - - - ->1425	
DECRYGENATED SOL. 2064		COBALT CONCENTRA.> 944		RUBIDIUM CHLORIDE 1654		DEPOSITION - - - 313	
DISSOLUTION KINE. 1666		LIGHT INTENSITY -	"	SOLID ELECTROLYTE	"	DEPOSITION RATE ->1042	
DUPLEX 308 - - - - 374		PHOTOANODE - - -	"	X-RAY DIFFRACTION	"	DIELECTRICS - - - 313	
ENVIRONMENT - - ->2159		SULFATE CONCENTR.	"			- - -> 334	
ETHYLENE GLYCOL - 11		TITANIUM DIOXIDE	"	CUPROUS IODIDE		- - ->1728	
FILM FORMATION - 1718				COPPER ION CONDU.>1654		DOPANT INCORPORA.> 644	
FLOW CONTROL - - 2159		CORROSION TEST		CUPROUS CHLORIDE	"	EPITAXIAL FILM - 644	
GOLD METALLIZATI. 1718		ALUMINUM ALLOY -> 110		RUBIDIUM CHLORIDE	"	EVAPORATION - - - 1335	
HOT-PRESSED - - - 1723		INTEGRATED CIRCU.	"	SOLID ELECTROLYTE	"	GADOLINIUM CHLOR. 1601	
INTERGRANULAR - 374		METALLIZATION - -	"	X-RAY DIFFRACTION	"	CALLIUM ANTIMONI.>2031	
IRON - - - - - 547		PLASTIC ENCAPSUL.	"			GAZEUS COMPLEX - 1601	
- - - - - 1363				CURRENT DENSITY		GLASSY LAYER - - 1425	
LEAD ACID BATTERY 360		COULOMETRY		ALKALINE SOLUTION> 541		GROWTH MECHANISM> 31	
MATHEMATICAL MOD.>1662		CYCLIC VOLTAMMET.>2035		ANODIC OXIDATION>1268		GROWTH PARAMETER 1951	
MICROSTRUCTURE - 374		LITHIUM - - - - -	"	- - - - ->1543		INFRARED ABSORPT. 1728	
NICKEL - - - - ->2038		REDUCTION - - - -	"	CATHODE - - - - -> 23		INSULATION - - - 1335	
OXIDATION - - - - 547		SULFUR OXYCHLORI.	"	CONTAMINATION -> 54		INTEGRATED CIRCU. 334	
OXIDATION KINETI. 1723				CONVECTION - - - 23		1042	
OXYHYDROXIDE - - 1459		CRACKING		COPPER - - - - -	"	ION IMPLANTATION>1019	
PALLADIUM - - - - 547		COPPER - - - - -> 701		COPPER ELECTRODE->1180		IRON CHLORIDE - - 1601	
PASSIVATION - - - 2064		SODIUM NITRITE -	"	ELECTRODEPOSITION 23		LOW PRESSURE - -> 833	
PASSIVE OXIDE - - 547		STRESS CORROSION	"	- - - - - 1180		- - - 1019	
PASSIVITY - - - - 1363		TRANSGRANULAR - -	"	ELECTROLYSIS - - 54		LOW TEMPERATURE - 1728	
PERMEATION - - - 2159				EQUILIBRIUM POTE. 541		METALORGANICS - - 2031	
PHASE TRANSFORMA. 374		CREVICE CORROSION		FLUIDIZED ELECTR. 1180		OXIDATION - - - -> 838	
PHOSPHORIC ACID - 360		AMALGAM CORROSION> 903		GAAS - - - - - 1268		- - - - - 1425	
PIT GROWTH - - - 1662		CAPILLARY PORE - -	"	- - - - - 1543		MASS TRANSPECT. 23	
PIT INITIATION - -	"	CATHODIC REACTION> 15		ION SCATTERING - -	"	MULTILAYER ANALY.>1479	
PITTING - - - - 374		CHLORIDE SOLUTION> 385		- - - - - 23		OXIDE FILM - - - - 1728	
PITTING RESISTAN. 2075		CHROMATE - - - -	"	NONFARADAY - - 54		OXYGEN CONCENTRA. 1766	
POLYMER - - - - - 2159		CURRENT DISTRIBU. 15		PASSIVATION TIME 1268		PASSIVITY - - - - 1425	
REFRACTORIES - - 1723		DENTAL AMALGAM - 903		PLANE VERTICAL - 23		PHOSPHOR DOPING - 1951	
SALT FILM - - - - 1662		INHIBITION - - - 385		REACTION ORDER - 541		PHOSPHORUS - - - 334	
SALT SOLUTION - - 2075		IRON - - - - -	"	RESISTIVITY - - - 1479		PHOSPHORUS DOPING 313	
SILICON CARBIDE - 2156		MATHEMATICAL MOD. 15		SPREADING RESIST.	"	- - - - - 833	
SILICON NITRIDE - 1723		PITTING - - - - -	"	WATER - - - - - 54		- - - - - 838	
SINTERING - - - - 2156		CROSSLINKED TYPE		ZINC ELECTRODE - 541		- - - - - 1019	
SODIUM SULFUR - -	"	ELECTRON RESIST ->1635		CURRENT DISTRIBU.		- - - - - 1042	
SOLAR COLLECTOR - 11		HOMOPOLYMER - - -	"	CATHODIC REACTION> 15		PHOSPHOSILICATE - 334	
STAINLESS STEEL - 374		INTEGRATED CIRCU.	"	COPPER DEPOSITION>2118		POLYMERIZATION - 1728	
- - - - - 2075		METHACRYLATE - -	"	CREVICE CORROSION 15		POLYSILICON - - - 1335	
SULFUR SEGREGATI. 2038		2,2,2-TRICHLORIDE.	"	CYLINDRICAL CELL>1348		- - - - - 1766	
SULFURIC ACID - - 1363				DISK ELECTRODE -	"	POLYSILICON FILM 833	
- - - - - 2038		CROSSLINKING		ELECTRODEPOSITION 2118		- - - - - 838	
THIN FILM - - - - 547		BISAZIDE RESIST -> 273		GAS LIFT - - - -	"	PRESSURE REDUCTI. 1042	
TITANIUM - - - - 2064		PHOTORESIST SYST.	"	HYDROGEN EVOLUT.	"	PRESSURE VARIATI. 1335	
TRACE GAS - - - - 2159		RECIPROCITY FAIL.	"	MATHEMATICAL MOD. 15		RESISTIVITY - - - 833	
TRANSPORT LAW - 1662				- - - - - 2118		SEMICONDUCTOR - - 2031	
WATER - - - - - 1718		CRYSTAL FIELD		PITTING - - - - - 15		SEMIINSULATION - 1766	
XPS - - - - - 547		ABSORPTION SPECT.>1550		RESISTANCE - - - 1348		SILANE - - - - - 1728	
YTRIUM - - - - - 1723						SILICON - - - - - 644	

PRIMARY TERM CO-TERM	PAGE NO.	PRIMARY TERM CO-TERM	PAGE NO.	PRIMARY TERM CO-TERM	PAGE NO.	PRIMARY TERM CO-TERM	PAGE NO.
CVD (CONTO)		DECAY PROCESS (CONTO)		DENSITY (CONTO)		DEVELOPER TEMPER. (CONTO)	
SILICON - - - - -	653	RARE EARTH ACTIV. 1213		N-ALKYLPYRIDINIUM 1644		ELECTRON BEAM - - -	2026
SILICON DIOXIDE - -	313	THERMAL DEPENDEN. "		TRANSPORT - - - - "		LINE EDGE PROFILE "	
- - - - -	1042			VISCOSITY - - - - "		OPTICAL EXPOSURE "	
- - - - -	1335	DECOMPOSITION		DENTAL AMALGAM		PHOTORESIST - - - "	
SILICON FIBER - - -	31	EFFUSION - - - - -> 490		AMALGAM CORROSION> 903		POSITIVE DIAZO - - "	
SILICON FILM - - -	1019	NITRIC OXIDE - - ->1067		CAPILLARY PORE - -		DEVELOPING TIME	
TIN OXIDE - - - - -	1434	POTASSIUM SULFATE 490		CREVICE CORROSION "		ELECTRON BEAM - - ->1430	
WHISKERS - - - - -	31	REDUCING CONDITI. 1067				LINE WIDTH - - - - "	
XPS - - - - -	1766	SCANDIA DOPING - -		DEOXYGENATED SOL.		POLYMETHYLMETHAC. "	
		VAPORIZATION - - - 490		ACIDIC SULFATE ->2064		RESIST - - - - -	
CVD COATING		ZIRCONIA - - - - - 1067		ANODIC DISSOLUTION "		SLOPE ANGLE - - - - "	
CUTTING TOOLS - ->1281				CHLORIDE SOLUTION "			
ETA PHASE - - - - -	"	DEEP DISCHARGE		CORROSION - - - - "		DEVELOPMENT RATE	
TITANIUM CARBIDE "	"	ANODE - - - - -> 365		PASSIVATION - - - - "		DEVELOPER TEMPER.>2026	
TOUGHNESS BEHAVI. "	"	CYCLIC CORROSION "		TITANIUM - - - - -		ELECTRON BEAM - - -	
		LEAD ACID BATTERY "				LINE EDGE PROFILE "	
		LEAD DIOXIDE - - -		DEPOLARIZATION		OPTICAL EXPOSURE "	
CYCLABLE CELL		DEFECT		ELECTRET BEHAVIOR>1207		PHOTORESIST - - -	
COPPER - - - - -> 699		AGITATION - - - -> 479		MELANIN - - - - -		POSITIVE DIAZO - - "	
ELECTRODE - - - - -	"	ETCH - - - - -					
INTERCALATION - - -	"	SELDO ETCH - - - -		DEPOSITION		DEVICE QUALITY	
SOLID-STATE CELL "	"	SILICON EVALUATI. "		AMORPHOUS SEMICO.> 688		ARSINE GAS - - - -> 300	
		ULTRASONIC - - - -		BORN DCPING - - -> 313		EPITAXY - - - - -	
CYCLIC CCRROSION				CATALYST - - - - -> 394		GAAS - - - - -	
ANODE - - - - -> 365		DEFECT DENSITY		CHEMICAL EQUILIB.1054		GERMANIUM - - - - -	
DEEP DISCHARGE - -	"	ELECTRIC FIELD ->1771		COMBUSTION GASES "		MOLYBDENUM - - - -	
LEAD ACID BATTERY "	"	LIQUID CRYSTAL - -		COPPER - - - - ->2167		TRIMETHYLGALLIUM "	
LEAD DICIDE - - -	"	OXIDE THICKNESS - -		CVD - - - - -	313		
		SILICON DIOXIDE - -		DIELECTRICS - - - -		DEZINCIFICATION	
				ELECTROLESS - - - -	394	AMMONIACAL SOLUT.>1299	
CYCLIC VOLTAMMET.		DEFECT DOPING		HOT CORROSION - - -	2167	COPPER ZINC - - - -	
ALUMINUM BROMIDE >1474		AGING EFFECTS - -> 338		HYDROGEN CONTENT "	1054	STRESS CORROSION "	
AROMATIC HYDROCA. "	"	ELECTROMIGRATION "		MASS SPECTROMETRY "	688		
BITHIAZOLE - - - ->2091		ENERGY CONVERSION "		PALLADIUM - - - - -	394	DIABETES	
BLEOMYCIN - - - - -	"	SEMICONDUCTOR - - -		PHOSPHORUS DOPING "	313	ANODIC OXIDATION > 43	
CGULOMETRY - - - ->2035				PHOTOVOLTAIC PRO. "	688	IMPLANTATION - - -	
IMPEDENCE - - - -> 989		DEFECT GENERATION		SILICON - - - - -		KREBS-RINGER - - -	
LITHIUM - - - - -	2035	LIQUID CRYSTAL -> 85		SILICON DIOXIDE - -	313	LINEAR POTENTIAL "	
METAL COMPLEX "	2091	NEMATIC DISPLAY - -		SODIUM SULFATE - - -	1054	PLATINUM ELECTRO. "	
POLAROGRAPHY - - -	"			UV IRRADIATED - - -	394		
POTASSIUM BROMIDE 1474		DEFECT INTERACTI.				DIAPHRAGM	
PYRIMIDINE - - - -	2091	ALUMINUM FLUORIDE>1385		DEPOSITION RATE		OXYGEN REDUCTION >1502	
REDOX - - - - -	"	BARIUM FLUORITE -> 667		CVD - - - - ->1042		PLATYUM-OXYGEN - -	
REDUCTION - - - -	2035	CALCIUM FLUORITE "		INTEGRATED CIRCU. "		POLARIZATION - - -	
RESISTIVE CAPACI. 989		CESIUM FLUORITE - -		PHOSPHORUS DOPING "			
SMALL AMPLITUDE - -	"	FLUORITE - - - - - 1385		PLANAR REACTOR -> 930		DIAZIDE-S-SULFON.	
SULFUR OXYCHLORID. 2035		IONIC CONDUCTIVI. 667		PLASMA - - - - -		ELECTRON BEAM - -> 860	
SURFACE PROCESSES 1474		1385		PRESSURE REDUCTI. 1042		EPR - - - - -	
TALLYSCMYCIN - - -	2091	IONIC MOTION - - -		SILICON DIOXIDE - -		MASS SPECTROSCOPY "	
VOLTAMMGRAM - - - -	989	LEAD - - - - -		SILICON OXIDE - - -	930	O-NAPHTHOQUINONE "	
		SOLID ELECTROLYTE "				PHENOLIC-TYPE - - -	
CYCLING		SOLID SOLUTION - 667		DEPTH PROFILE		RESIN - - - - -	
CONCENTRATION - ->2110		STRONTIUM FLUORI. "		ANNEALING - - - ->1737			
CONVECTION - - - - -	"	URANIUM FLUORITE "		ANODIC FILM - - ->1370		DIAZO SENSITIZER	
ELECTROCMOSIS - - -	"			ANODIC OXIDE - - -		CHROMATE SENSITI.>1294	
ZINC ELECTRODE - - -	"	DEFECT ISOTHERM		AUGER SPECTROSCO.>1805		COLORYIN TUBE - - -	
		ANNEALING - - - -> 809		BORON DIFFUSION "		PHOSPHOR DEPOSIT. "	
CYCLODEXTRIN		CADMIUM TELLURIDE "		BORON NITRIDE - - -			
CHLORINATION - -> 500		ELECTRON MICROSC. "		BORON RICH LAYER "		DICHALCOGENIDE	
MODIFIED ELECTRO. "	"	LATTICE DEFECT - -		CESIUM - - - - -> 660		INTERCALATION - -> 349	
SELECTIVITY - - - -	"			DDPANT - - - - -		LITHIUM - - - - -	
		DEFECT STRUCTURE		GAAS - - - - -	1370	LOW VOLTAGE BEHA. "	
CYLINDRICAL CELL		CERIUM DIOXIDE -> 209		- - - - -	1737	SECONDARY BATTERY "	
CURRENT DISTRIBUTU.>1348		DOPING - - - - ->1381		HYDROGEN INJECTI. 1805		TOPOCHEMICAL CELL "	
DISK ELECTRODE - - -	"	ELECTROEPITAXY "		MASS SPECTROMETRY 660		DIELECTRIC BREAK.	
RESISTANCE - - - - -	"	ELECTRONIC CHARA. "		OXIDE - - - - -	1737	ALUMINUM - - - -> 162	
		GAAS - - - - -		PASSIVATION - - - -	1370	CAPACITOR - - - - -	
CZOCHEALSKI		NONSTOICHIOMETRY 209		SECONDARY ION - - -	660	POLYSILICON - - - -	
ANTIMONY - - - -> 875		OXIDE SEMICONDC. "		SILICON - - - - -	1805	SILICON DIOXIDE - -	
CRYSTAL GROWTH - -	"	POINT DEFECT - - -		ULTRAHIGH VACUUM 660		DIELECTRIC FILM	
DOPED MELT - - - -	"	THERMAL LPE - - - 1381		XPS - - - - -	1370	AMMONIA GAS - - -> 996	
GALLIUM DOPING -> 284		THERMOGRAVIMETRY 209		- - - - -	1737	FILM THICKNESS ->1539	
GERMANIUM - - - - -	"	DEGRADATION		DERIVATIVE		OXIDATION RESIST. 996	
HEAT PIPE - - - - -	"	CHROMIUM - - - ->1047		CARBOXYLATION - -> 404		POLYIMIDE - - - -> 269	
INSTABILITY - - - -	875	IMPACT DIODE - - -		O-CARBOXYMETHYL "		PRISM COUPLER - - -	1539
INTEGRATED CIRCU.>1142		INTERDIFFUSION - -		REDUCTION - - - - -		REFRACTIVE INDEX "	
LIFETIME - - - - -	"	METALLIZATION - - -		SYNTHESIS - - - - -		SILICON DIOXIDE - -	
MINORITY CARRIER "	"	PLATINUM - - - - -		TARTRONIC ACID - -		SILICON OXYNITRIF. 996	
MORPHOLOGY - - - -	875	SILICON - - - - -				SILICON SUBSTRATE 1539	
RADIAL HEAT GRAD. 284		SILVER - - - - -		DESORPTION		SPUN-ON FILM - - -	269
SEGREGATION - - - -	"			CHLORINE EVCLUTI.>1343		THERMAL NITRIDAT. 996	
SILICON - - - - -	1142	DENDRITE		STOICHIOMETRY - - -		THICKNESS PROFILE 269	
SILICON CRYSTAL - 875		ANGDIZATION - - ->1718		TAFEL SLOPE - - - -		THIN FILM - - - - -	
SYMMETRY - - - - -	284	CIRCUIT - - - - -					
THERMAL PROCESSI. 1142		CORROSION - - - - -		DESTRUCTIVE EFFE.		DIELECTRIC FLUID	
		FILM FORMATION - -		GLASS ELECTRODE ->2196		DISSOCIATION - -> 925	
DARK POTENTIAL		GOLD METALLIZATI. "		GLOW TUBE - - - - -		STEADY STATE CON. "	
AQUEOUS ELECTROL.>1868		WATER - - - - -		IONIC CONDUCTIVI. "		SURFACTANT - - - -	
FLATBAND POTENTI. "	"	DENSITY		DEVELOPER TEMPER.		TRANSIENT CONDCU. "	
GROUP II-VI COMP. "	"	ALUMINUM CHLORIDE>1644		DEVELOPMENT RATE >2026			
IODINE DOPING - - -	"	CONDUCTIVITY - - -				DIELECTRIC ISOLA.	
LIGHT ABSORPTION "	"	FUSED SALT - - - -				INTEGRATED CIRCU.> 870	
OPTICAL ABSORPTI. "	"	HALIDE - - - - -					
ZINC SELENIDE - - -	"						

PRIMARY TERM CO-TERM	PAGE NO.	PRIMARY TERM CO-TERM	PAGE NO.	PRIMARY TERM CO-TERM	PAGE NO.	PRIMARY TERM CO-TERM	PAGE NO.
DIELECTRIC ISOLA. (CONTO)		DIFFUSION COEFFI. (CONTO)		DISCHARGE REACTI.		DOPANT DISTRIB.	
SILICON ANODIZAT. 870		PHOSPHODATION -->1432		LITHIUM ANODE --> 513		BORON DOPING --> 138	
SILICON POROSITY "		TRANSPORT EQUATI.> 988		PRIMARY CELL -- "		LPE -- -- -- -- "	
		ZINC -- -- -- -- 1432		SOLUBLE CATHODE -- "		MELTBACK -- -- -- "	
		ZINC PHOSPHIDE -- "		THIONYL CHLORIDE -- "		SILICON -- -- -- -- "	
DIELECTRIC PROPE.							
CHARGE STORAGE -->1958		DIFFUSION CONTROL		DISK ELECTRODE		DOPANT EFFECT	
ELECTRICAL PROPE.		CODEPOSITION --> 566		CHLOROALUMINATE -->1029		OXIDATION KINETI.>1516	
POLARIZATION -- "		COPPER -- -- -- -- "		CHRONOAMPEROMETRY "		>1523	
POLYVINYL BUTYRAL "		ROTATING DISK -- "		COPPER -- -- -- -- "		PHYSICAL MODEL -- "	
		ZINC -- -- -- -- "		CURRENT DISTRIBU.>1348		POINT DEFECT -- -- 1516	
DIELECTRICS				CYLINDRICAL CELL "		POINT EFFECT -- -- 1523	
ANODIC OXIDATION >1374		DIFFUSION MODEL		FUSED SALT -- -- -- 1029		SILICON DIOXIDE -- 1516	
ANODIC OXIDE FILM> 765		BORON REDISTRIBU.>2001		PHOTOCORROSION -->1483		-- 1523	
BORON DOPING --> 313		THERMAL OXIDATION "		PHOTON FLUX -- -- -- 1029			
CVD -- -- -- --> 334				POTENTIOMETRY -- -- -- 1483		DOPANT INCORPORA.	
-- -- -- -->1728		DIFFUSION PROCESS		REDOX -- -- -- -- 1348		CVD -- -- -- --> 644	
DEPOSITION -- -- -- 313		GAAS -- -- -- --> 135		RESISTANCE -- -- -- 1029		-- -- -- --> 653	
ELLIPSCIMETRY -- -- 1374		PHOSPHORUS DIFFU.>1252				EPITAXIAL FILM -- 644	
INFRARED ABSORPT. 1728		PHOSPHORUS DOPING "		DISLOCATION		-- -- -- -- 653	
INTEGRATED CIRCU. 334		PLANAR DIFFUSION 135		ALUMINUM ARSENIDE> 637		SILICON -- -- -- -- 644	
IONIC CONDUCTION 765		PLANAR JUNCTION -- "		DIODE -- -- -- -- "		-- -- -- -- 653	
LOW TEMPERATURE -- 1728		SILICA FILM -- -- 1252		FILM EDGE -- -- -->1014			
NIOBUM -- -- -- -- 1374		SILICON DIOXIDE -- 135		GAAS -- -- -- -- 637		DOPED MELT	
OPEN CIRCUIT -- -- "		TIN DOPING -- -- "		GALLIUM -- -- -- -- "		ANTIMONY -- -- -- --> 875	
OXIDATION -- -- -- 1728				LIGHT-EMITTING -- "		CRYSTAL GROWTH -- "	
PHOSPHORUS -- -- -- 334		DIGITAL SIMULATI.		QUANTUM EFFICIEN. "		CZOCHELSKI -- -- -- "	
PHOSPHORUS DOPING 313		CHARGE TRANSFER -->1011		SILICON -- -- -- -- "		INSTABILITY -- -- -- "	
PHOSPHOSILICATE -- 334		HOLE INJECTION -- -- "		SILICON DIOXIDE -- 1014		MORPHOLOGY -- -- -- "	
POLYMERIZATION -- 1728		ILLUMINATED -- -- "		SILICON NITRIDE -- "		SILICON CRYSTAL -- "	
SILANE -- -- -- -- "		LIQUID JUNCTION -- "		VISCOELASTICITY -- "			
SILICON DIOXIDE -- 313		PHOTOANODE -- -- "					
TAPEL SLOPE -- -- 1374		SEMICONDUCTOR -- -- "		DISORDERED SYSTEM		DOPING	
TANTALUM PENTOXI. 765		SOLAR CELL -- -- "		ALUMINUM OXIDE -->1304		ANTIMONY EVAPORA.>1761	
TRANSIENT ANALYS. 1374				ALUMINUM POWDER -- "		ARSENIC -- -- -- -- "	
TUNGSTEN -- -- -- -- "		DIMETHYLFORMAMIDE		COMPOSITE SYSTEM "		ATMOSPHERE -- -- -->1785	
		BENZAL CHLORIDE --> 401				CARRIER CONCENTR.> 562	
DIFFRACTICIMETRY		CARBON DIOXIDE -- "		DISPERSED ALUMINA		CERIUM DIOXIDE -- "	
DOUBLE CRYSTAL --> 664		REDUCTION MECHAN. "		ALUMINA -- -- -- -->1963		DEFECT STRUCTURE >1381	
GROUP III-V COMP. "				CUPROUS CHLORIDE "		ELECTRICAL CONDU. 562	
INDIUM PHOSPHIDE "		DIODE		ION CONDUCTIVITY "		ELECTROEPITAXY -- 1381	
INGAPAS -- -- -- -- "		ALUMINUM ARSENIDE> 637				ELECTRONIC CHARA. "	
LATTICE MISMATCH -- "		DISLOCATION -- -- -- "		DISPLAY DEVICE		EPITAXY -- -- -- -- 1761	
LPE -- -- -- -- -- "		GAAS -- -- -- -- -- "		CATION FILM -- -- --> 167		GAAS -- -- -- -- 1381	
QUARTERNARY -- -- -- "		GALLIUM -- -- -- -- -- "		ELECTRICAL CHARA.>2211		HELIUM-HYDROGEN -- 1785	
		LIGHT-EMITTING -- -- "		ELECTROPHORESIS -- "		HETEROEPITAXY -- -- "	
DIFFRACTION		QUANTUM EFFICIEN. "		GOLD SUBSTRATE -- 167		ION IMPLANTATION 1761	
ANNEAL -- -- -- --> 277		SILICON -- -- -- -- -- "		N-HEPTYLVIOLOGEN -- -- -->1779		LOW TEMPERATURE -- "	
CADMIUM HALIDE --> 325				OPTICAL CHARACTER 2211		MOLECULAR BEAM -- 1761	
CHANNELING -- -- -- 277		DIODE SYSTEM		TITANIUM DIOXIDE "		NIOBUM PENTOXIDE 562	
CHROMIUM -- -- -- -- "		CARBON TETRAFLUOR.> 226				OXIDATION -- -- -- -- 1779	
CRYSTALLOGRAPHY -- 325		PLASMA ETCHING -- "		DISSOCIATION		POLYSILICON -- -- -- "	
EPITAXIAL RELATI. 277		REACTIVE SPUTTER. "		BIRGE-SPONER -- -->1396		SILICON -- -- -- -- 1761	
MIXED CRYSTALS -- 325				DIELECTRIC FLUID > 925		SILICON GROWTH -- 1785	
PLATINUM -- -- -- -- 277		DIOXIDE AMBIENCE		MASS SPECTROSCOPY>1825		THERMAL LPE -- -- -- 1381	
POLYTYPISM -- -- -- 325		CHLORINE OXIDATI.>1288		METAL HALIDE GAS 1396		ULTRAHIGH VACUUM 1761	
SAPPHIRE -- -- -- -- 277		SILICON DIOXIDE -- "		MODEL CALCULATION "		VLSI DEVICE -- -- -- 1779	
VAPOR GROWN -- -- -- 325		THERMAL OXIDATION "		SELENIUM SULFIDE 1825			
				STEADY STATE CON. 925		DOPING PROFILE	
DIFFUSING SPECIES		DIPHthalocyanine		SURFACTANT -- -- -- -- "		GAAS -- -- -- -- --> 296	
HIGH TEMPERATURE >1948		CHARGE TRANSPORT >1490		THERMOCHEMISTRY -- 1396		GROWTH PROCESS -- "	
NICKEL CHROMIUM -- "		ELECTROCHROMISM -->1339		THERMODYNAMICS -- 1825		LPE -- -- -- -- -- -- "	
PHOSPHODATION -- -- "		1490		TRANSIENT CONDUCT. 925		MOBILITY PROFILE -- "	
PHOSPHORUS VAPOR "		LUTETIUM -- -- -- -- 1339		VAPORIZATION -- -- -- 1825		TIN -- -- -- -- -- -- "	
		OXIDATION PRODUCT 1490					
DIFFUSION		OXIDATION STATE -- 1339		DISSOLUTION		DOUBLE CRYSTAL	
CONDUCTANCE -- -- -->1682				CHLORIDE ION -- --> 919		DIFFRACTICIMETRY --> 664	
CONNECTOR -- -- -->1798		DIRECT CURRENT		FICKS LAW -- -- --> 634		EPITAXIAL LAYER -->1228	
CONVECTION -- -- -->1713		HYDROGEN PERMEAT.>1633		MOLTEN SILICON -- "		GROUP III-V COMP. 664	
COPPER -- -- -- -- 1798		METAL QUANTITY --> 881		NICKEL OXIDE FILM 919		INDIUM PHOSPHIDE "	
ELLIPSCIMETRY --> 242		PLATING -- -- -- -- 1633		PASSIVATION -- -- -- "		INGAPAS -- -- -- -- "	
FUEL CELL -- -- -- -- 1682		PLATING CYCLE -- -- 881		PIT INITIATION -- -- "		LATTICE MISMATCH "	
GOLD ALLOY -- -- -- -- 1798		PULSED PLATING -- -- 1633		SILICON CARBIDE -- 634		LPE -- -- -- -- -- -- "	
HALOGEN -- -- -- -- 1682						PENDELLOSUNG -- -- 1228	
HYDROGEN -- -- -- -- "				DISSOLUTION KINE.		QUARTERNARY -- -- -- 664	
HYDROGEN PROTON --> 850		DISCHARGE		ACIDIC CHLORIDE -->1666		STRAIN DISTRIBUT. 1228	
INTERFACE POTENT. 242		LITHIUM -- -- -- -->2168		ANODIC DISSOLUTI. "		X-RAY DIFFRACTION "	
IONIC CONDUCTOR -- "		REACTION MECHAN. "		COPPER -- -- -- -- -- "			
MIGRATION -- -- -- 1713		THIONYL CHLORIDE "		CORROSION -- -- -- -- "		DOUBLE PULSE	
MOLTEN SALT -- -- -- "						FAST ELECTRODE -->1148	
NAFION MEMBRANE -- 1682		DISCHARGE CAPACI.		DISSOLVED SULFUR		GALVANOSTATICS -- "	
OXIDATION KINETI. 1798		PHYSICAL STRUCTU.>1899		CAPACITY -- -- -- --> 523		OVERPOTENTIAL -- -- "	
PHOTOELECTROCHEM. 850		POROUS IRON ELEC. "		LITHIUM BATTERY -- "			
POLYMER -- -- -- -- 1682		POWDER REDUCTION "		ORGANIC ELECTROL. "		DRY ETCHING	
POROUS ELECTRODE 1713		SINTERING -- -- -- -- "		RATE CAPABILITY -- "		CHLOROMETHYLATED >1628	
RELIABILITY -- -- -- 1798				SECONDARY BATTERY -- "		NEGATIVE RESIST -- "	
ROTATING ELECTRO. 242		DISCHARGE CHARAC.		SYSTEM STABILITY -- "		POLYSTYRENE -- -- -- "	
-- -- -- -- -- "		FLUORIDE -- -- -- --> 709		TETRAHYDROFURAN -- "		SUBMICRON TECHNO. "	
SILVER SALT SOLU. "		GALVANIC CELL -- -- "					
TITANIUM DIOXIDE 850		SOLID ELECTROLYTE -- "		DOPANT		DTA	
TRANSPORT EQUATI. 1713				CESIUM -- -- -- --> 660		ABUSE TOLERANCE -->1637	
TRANSPORT PROPER. 1682		DISCHARGE DATA		DEPTH PROFILE -- -- --> 1992		ALUMINUM -- -- -- --> 1992	
		IRON -- -- -- --> 357		GAAS -- -- -- -- -- "		ANTIMONY -- -- -- -- "	
DIFFUSION COEFFI.		SECONDARY BATTERY		MASS SPECTROMETRY -- "		BATTERY -- -- -- -- 1637	
BROMINE DIFFUSION> 36		SOLUBLE SYSTEM -- "		SECONDARY ION -- -- -- "		CERAMICS -- -- -- --> 1	
ION EXCHANGE -- -- -- "		TITANIUM -- -- -- -- -- "		SILICON -- -- -- -- -- "		EQUILIBRIUM -- -- -->1403	
NAFION MEMBRANE -- "				ULTRAHIGH VACUUM -- "		GALLIUM -- -- -- -- -- 1992	

PRIMARY TERM CO-TERM	PAGE NO.	PRIMARY TERM CO-TERM	PAGE NO.	PRIMARY TERM CO-TERM	PAGE NO.	PRIMARY TERM CO-TERM	PAGE NO.
DTA (CONTO)		ELECTRICAL MEASU.		ELECTROCHROMISM (CONTO)		ELECTRODEPOSITION (CONTO)	
HYDROSTATIC PRES. 1403		CHEMICAL TREATME. >192		TUNGSTEN TRIOXIDE 583		PREPARATION - - - - - 2162	
IONIC CONDUCTIVI. 1		CONDUCTIVITY - - - - - "		2133		PYRITE - - - - - 911	
LEAD FLUORIDE - - - 1403		HYDROGEN DIFFUSI. "		VACUUM EVAPORATI. 583		SACCHARIN - - - - - 2085	
LIQUID ASSOCIATI. 1992		P-TYPE - - - - - "				STEREO MICROSCOPY 1123	
LITHIUM - - - - - 1637		RESISTIVITY SHIFT "		ELECTROCRYSTALLI.		SURFACE STRESS - 2085	
LITHIUM OXIDE - - - 1		SILICON SURFACE - - - "		ELECTRODEPOSITION >2085		THERMAL PREPARAT. 204	
MOISTURE CONTENT "				EPITAXY - - - - - "		TIN NICKEL ALLOY "	
PHASE DIAGRAM - - - 1992		ELECTRICAL PROPE.		NICKEL - - - - - "		VERTICAL ELECTRO. 2118	
PHASE TRANSITION 1403		CHARGE STORAGE - >1958		PASSIVATION - - - - - "			
PHYSICAL PROPERT. 1		DIELECTRIC PROPE. "		SACCHARIN - - - - - "		ELECTRODISSOLUTI.	
SULFUR DIOXIDE - - 1637		POLARIZATION - - - - - "		SURFACE STRESS - - - - - "		ACIDIC CHLORIDE - >1118	
TERNARY PHASE - - - 1992		POLYVINYL BUTYRAL "				NICKEL - - - - - "	
				ELECTRODE			
DUCTILITY		ELECTROANALYSIS		COPPER - - - - - > 699		ELECTROEPITAXY	
ADHESION - - - - - > 624		ELECTROLYTE CONC. > 50		CYCLABLE CELL - - - - - "		DEFECT STRUCTURE >1381	
ANODIC OXIDE FILM "		SEMIINTEGRATION - - - - - "		INTERCALATION - - - - - "		DOPING - - - - - "	
FRACTURE - - - - - "		SUPPORTING ELECT. "		SOLID-STATE CELL "		ELECTRONIC CHARA. "	
TANTALUM - - - - - "		VOLTAMMETRY - - - - - "				GAAS - - - - - "	
				ELECTRODE BEHAVI.		THERMAL LPE - - - - - "	
DUPLEX 308		ELECTROCAPILLARY		ACETONITRILE - - - >1892			
AUSTENITIC - - - - - > 374		EXTENSOMETER - - - > 252		FERRIC OXIDE - - - - - "		ELECTROGENERATED	
CORROSION - - - - - "		PLATINUM - - - - - "		N-TYPE CONDUCTION "		APROTIC SOLVENT - > 414	
INTERGRANULAR - - - - - "		SALT SOLUTION - - - - - "				CHEMILUMINESCENCE "	
MICROSTRUCTURE - - - - - "		SURFACE STRESS - - - - - "		ELECTRODE KINETI.		ENERGY CONVERSION "	
PHASE TRANSFORMA. "				ELECTRON TRANSFER > 988		PHOTOINDUCED - - - - - "	
PITTING - - - - - "		ELECTROCATALYSIS		HENE - - - - - "		SEMICONDUCTOR - - - - - "	
STAINLESS STEEL - - - - - "		ACRYLIC ACID - - - > 939		HEMOPROTEIN - - - - - "		VP CONVERSION - - - - - "	
		ANION INFLUENCE - >2140					
ECONOMIC GROWTH		ANODIC ACTIVATION > 78		ELECTRODE MATERI.		ELECTROHYDRODINE	
FUTURE - - - - - > 81C		AUGER SPECTROSCOP. > 67		COBALT OXIDE - - - >1817		CHRONOCOLOMETRY > 579	
SOCIAL CHANGE - - - - - "		78		LANTHANUM STRONT. "		ETHYL CINNAMATE - - - - - "	
		CHLORINE EVOLUTI. >1189		POWER - - - - - "		LOW TEMPERATURE - - - - - "	
EFFICIENCY		ELECTRON DIFFRAC. 67		THERMOELECTRICITY "		METHYL CINNAMATE "	
ACETONITRILE - - - > 603		ELECTROOXIDATION > 218				REACTION ORDER - - - - - "	
CATHODE RAY - - - >1556		ELECTROSORPTION - 2140		ELECTRODE MODEL			
CERIUM - - - - - "		ETHYLENE - - - - - 218		POROUS ELECTRODE >1835		ELECTROLESS	
CONCENTRATION - - - - - "		HYDROGEN ABSORPT. 67		REACTION PROFILE "		ACTIVATOR - - - - - >1671	
GAAS - - - - - 603		HYDROGEN MONOLAY. 2140		SURFACE MORPHOLO. "		BACKSCATTERING - - - - - "	
GADOLINIUM - - - - - 1556		HYDROGEN PEROXIDE >1831		ZINC PCRE ELECTR. "		CATALYST - - - - - > 394	
GARNET PHOSPHORS "		IRON OXIDE - - - - - "				COPPER - - - - - >2167	
LIQUID JUNCTION - 603		N-TYPE - - - - - - - - - - -		ELECTRODE POTENT.		COPPER DEPOSITION > 171	
PHOTOVOLTAIC CELL "		OXYGEN MONOLAYER 2140		APPLIED POLARIZA. >2057		DEPOSITION - - - - - 394	
REGENERATIVE CELL "		OXYGEN REDUCTION 78		COPPER ZINC - - - - - "		- - - - - 2167	
SINGLE CRYSTAL - - - - - "		PHOTOANODE - - - - - 1831		GALVANIC CORROSI. "		GALVANIC CELL - - - - - 171	
TERBIUM - - - - - 1556		PLATINUM - - - - - 67		NUMERICAL ANALYS. "		GLASS SUBSTRATE - 1671	
		- - - - - 78		SOLUTION DEPTH - - - - - "		METAL DEPOSITION "	
		- - - - - 218				OXIDATION - - - - - 171	
EFFLUENT GAS		- - - - - 2140		ELECTRODE SHAPE		PALLADIUM - - - - - 394	
EQUILIBRIUM - - - > 827		POLYMERIZATION - 939		BETA-ALUMINA - - - >1451		- - - - - 1671	
GERMANIUM - - - - - "		POTENTIODYNAMICS 218		CELL MEMBRANE - - - - - "		REDUCTION - - - - - 171	
OXYGEN SOLUBILITY "		REDOX - - - - - 939		FAILURE ANALYSIS "		UV IRRADIATED - - - - - 394	
		RING DISK ELECTR. "		SODIUM SULFUR - - - - - "			
EFFUSION		RUTHENIUM - - - - - 1189				ELECTROLYSIS	
DECOMPOSITION - - - > 490		SINGLE CRYSTAL - 67		ELECTRODEPOSITION		CONDUCTION - - - - - >1368	
POTASSIUM SULFATE - - - - - "		78		ALLOY - - - - - >2162		CONTAMINATION - - - - - 54	
SOLID PHASE - - - > 771		STRUCTURE SENSIT. 67		BISULFATE CATALY. > 190		CURRENT DENSITY - - - - - "	
VAPORIZATION - - - 490		78		BUFFER CAPACITY >1861		MASS TRANSFER - - - > 398	
ZIRCONIUM IODIDE - - - 771		SULFURIC ACID - - 2140		CARBON STEEL - - - > 911		NONFARADAY - - - - - 54	
		TITANIUM OXIDE - 1189		CATHODE - - - - - > 23		PERIODIC CURRENT 398	
		TITANIUM SUPPORT. "		CATHODE FILM - - - 190		ROTATING DISK - - - - - "	
ELECTRET				CHROMIUM - - - - - "		SOLID BROMINE - - - 1368	
HETEROCHARGE - - - >1708		ELECTROCHEMICAL		COBALT HARDENED - > 445		WATER - - - - - 54	
MEMBRANE - - - - - "		POTENTIAL - - - - - >2169		CONVECTION - - - - - 23			
POLARIZATION - - - - - "		SPECTROSCOPY - - - - - "		COPPER - - - - - "		ELECTROLYTE	
POLYSTYRENESULFO. "						INDUSTRY REPORT - >243C	
POLYVINYL ALCOHOL "		ELECTROCHROME		COPPER DEPOSITION >2118			
POTASSIUM - - - - - "		PHOSPHOTUNGSTIC > 805		COPPER ELECTRODE >1180		ELECTROLYTE CONC.	
SODIUM - - - - - "		PROTON CONDUCTION "		CURRENT DENSITY - 23		ELECTROANALYSIS - > 50	
		TUNGSTEN TRIOXIDE "		- - - - - 1180		SEMIINTEGRATION - - - - - "	
ELECTRET BEHAVIOR		ZIRCONIUM PHOSPH. "		CURRENT DISTRIBU. 2118		SUPPORTING ELECT. "	
DEPOLARIZATION - >1207				CURRENT EFFICIEN. 1861		VOLTAMMETRY - - - - - "	
MELANIN - - - - - "		ELECTROCHROMISM		ELECTROCRYSTALLI. >2085			
		ANODIC - - - - - >2171		EPITAXY - - - - - 2085		ELECTROLYTE FLOW	
ELECTRIC FIELD		ANODIC FILM - - - > 742		FILM FORMATION - 445		ELECTRIC VEHICLE >1321	
DEFECT DENSITY - >1771		ANODIC OXIDATION > 583		FLUIDIZED ELECTR. >1176		HEAT TRANSFER - - - - - "	
LIQUID CRYSTAL - - - - - "		>2133		1180		LEAD ACID BATTERY "	
OXIDE THICKNESS - - - - - "		BLEACHING - - - - - 742		FOIL - - - - - 2162		PROPULSION - - - - - "	
SILICON DIOXIDE - - - - - "		- - - - - 2171		FUSED SALT - - - - - "			
		CHARGE TRANSPORT >1490		GAS LIFT - - - - - 2118		ELECTROLYTE SALT	
ELECTRIC VEHICLE		COLORATION - - - 742		GOLD - - - - - 445		ENERGY CONVERSION >1445	
ELECTROLYTE FLOW >1321		- - - - - 2171		HIGH TEMPERATURE "		HERMETIC D-CELL - - - - - "	
HEAT TRANSFER - - - - - "		CORROSION STABIL. 742		HYDROGEN EVOLUTI. 1861		LITHIUM BORON CH. "	
LEAD ACID BATTERY "		2171		2118		THIONYL CHLORIDE "	
PROPULSION - - - - - "		DIPHthalOCYANINE >1339		HYDROGEN SULFIDE 911			
		1490		IRON PLATINUM - - - 2162		ELECTROMIGRATION	
ELECTRICAL CHARA.		FILM STRUCTURE - 583		MARCASITE - - - - - 911		AGING EFFECTS - - - > 338	
DISPLAY DEVICE - >2211		IRIDIUM OXIDE - - - 742		MASS TRANSPORT - 23		DEFECT DOPING - - - - - "	
ELECTROPHORESIS "		- - - - - 171		MATHEMATICAL MOD. 1176		ENERGY CONVERSION "	
OPTICAL CHARACTER "		LUTETIUM - - - - - 1339		2118		SEMICONDUCTOR - - - - - "	
TITANIUM DIOXIDE "		MECHANISM - - - - - 2171		MOSSBAUER SPECTR. > 204			
		OXIDATION PRODUCT 1490		NICKEL - - - - - 2085		ELECTRON AFFINITY	
ELECTRICAL CONDU.		OXIDATION STATE - 1339		NICKEL IRON ALLOY 1861		INDIUM SESQUIOXIDE >1081	
CARRIER CONCENTR. > 562		PH - - - - - 2171		ORGANIC INCLUSION 1123		OXIDE SEMICONDUCT. "	
CERIUM DIOXIDE - - - - - "		PHOTOELECTROCHEM. 2133		PASSIVATION - - - 2085		PHOTOVOLTAIC PRO. "	
DOPING - - - - - "		REACTION RATE - - 583		PLANE VERTICAL - 23			
NIOBIUM PENTOXIDE "		THERMAL OXIDATION 2133		POLYCHROMATE - - - 190			

PRIMARY TERM CO-TERM	PAGE NO.	PRIMARY TERM CO-TERM	PAGE NO.	PRIMARY TERM CO-TERM	PAGE NO.	PRIMARY TERM CO-TERM	PAGE NO.
ELECTRON BEAM CHLOROACRYLATE ->1829		ELECTRON TRANSFER (CONTO) HEMOPROTEIN - - - 988		ELECTROTRANSPORT (CONTO) PURIFICATION - - - 1811		ENERGY STORAGE HYDROGEN-CHLORINE> 713	
DEVELOPER TEMPER.>2026		HYDRODYNAMICS - - - 431		THORIUM - - - - - "		MASS HEAT BALANCE - - - "	
DEVELOPING TIME ->1430		ROTATING DISK - - - 437		TRANSITION METAL 760		REGENERATION - - - "	
DEVELOPMENT RATE 2026		SINUSOIDAL - - - 437		ELLIPSONOMETRY		STOICHIOMETRY - - - "	
DIAZIDE-S-SULFON.> 860		ELECTRONIC CHARG. DEFECT STRUCTURE >1381		ANODIC OXIDATION >1374		ENTHALPY	
ELECTRON RESIST ->1699		DOPING - - - - - "		ANODIC OXIDE - -> 986		CLOSE SPACING - ->1604	
EPR - - - - - 860		ELECTRODEPOSITAX - - - "		ANODIZATION - - ->1191		VAPOR TRANSPORT - - - "	
GLYCIDYL METHACR. 1699		GAAS - - - - - - - "		AUGER SPECTROSCOP.> 450		ENVIRONMENT	
HALOSTYRENE - - - - - "		THERMAL LPE - - - - - "		BISMUTH TRITELLU. 1191		CORROSION - - - - ->2159	
INTEGRATED CIRCU. 1829		ELECTRONIC CONDU. BARIUM FLUORIDE ->2023		DIELECTRICS - - - - - 1374		FLOW CONTROL - - - - - "	
LINE EDGE PROFILE		SOLID ELECTROLYTE "		DIFFUSION - - - - -> 242		PERMEATION - - - - - "	
LINE WIDTH - - - - - 1430		ELECTROOSMOSIS CONCENTRATION - ->2110		GAAS - - - - - - ->1589		POLYMER - - - - - - - "	
LITHOGRAPHY - - - - -> 694		CONVECTION - - - - - "		GALLIUM PHOSPHIDE "		TRACE GAS - - - - - - - "	
- - - - - 1699		CYCLING - - - - - - - "		GALLIUM SELENIIDE 1191		EPITAXIAL FILM	
MASS SPECTROSCOPY 860		ZINC ELECTRODE - - - - - "		IN SITU - - - - - - - 450		CVD - - - - - - - -> 644	
MOLECULAR ORBITAL 1829		ELECTROOXIDATION ANODE - - - - - -> 972		INTERFACE POTENT. 242		- - - - - - - -> 653	
NEGATIVE - - - - - 1699		CHLORALUMINATE -> 231		IONIC CONDUCTOR - - - - - "		DOPANT INCORPORA. 644	
O-NAPHTHOQUINONE - 860		ELECTROCATALYSIS > 218		LAYER PERIODICITY 1191		653	
OPTICAL EXPOSURE 2026		ETHANE - - - - - -> 775		LAYERED SEMICOND. "		SILICON - - - - - 644	
PHENOLIC-TYPE - - - 860		ETHYLENE - - - - - 218		LEED - - - - - - - 450		- - - - - 653	
PHOTORESIST - - - - 2026		FUEL CELL - - - - - 775		NIOBIUM - - - - - 1374		EPITAXIAL GROWTH	
POLYMER - - - - - 694		LIGHT EFFECT - - - 972		OPEN CIRCUIT - - - - - "		AMORPHOUS SILICON>1247	
- - - - - 1829		MELT COMPOSITION 231		OPTICAL LAYER - -> 131		ARGON - - - - - - - "	
POLYMER RESIST - 1699		METHANE - - - - - 775		PROCESS CONTROL - 1589		ARSENIC DESORPTI.> 822	
POLYMETHACRYLONI. 694		MOLTEN SALT BATT. 231		RESIDUAL FILM - - - - - "		AUTODOPING - - - - - "	
POLYMETHYLMETHAC. 1430		N-BUTANE - - - - - 775		RHEED - - - - - - - 450		FILM THICKNESS ->2033	
POSITIVE DIAZO - - - 2026		PHOTOCONDUCTIVITY 972		ROTATING ELECTRO. 242		INTERFACE MIGRAT. "	
POSITIVE RESIST 1829		PLATINUM - - - - - 218		SILICON DIOXIDE - 131		KRYPTON - - - - - - - 1247	
RESIN - - - - - - - 860		POTENTIODYNAMICS "		SILICON INTERFACE "		NEON - - - - - - - - - "	
RESIST - - - - - - - 694		PROPANE - - - - - 775		SILVER SALT SOLU. 242		SILANE - - - - - - - 822	
- - - - - 1430		SULFUR - - - - - 231		STRESS-STRAIN - - - 131		SILICON - - - - - - - "	
SLOPE ANGLE - - - - - "		THIOCYANATE - - - 972		SUBSTRATE CONSTA. 986		- - - - - - - - 2033	
TRIFLUOROETHYL - 1829		TRIFLUOROMETHANE 775		SUBSTRATE ANALYSIS 450		EPITAXIAL LAYER	
X-RAY - - - - - - - 694		ELECTROPHORESIS DISPLAY DEVICE ->2211		TAFEL SLOPE - - - - 1374		CHEMICAL ETCHING > 287	
ELECTRON BOMBARD. CATHODOLUMINESC.> 571		ELECTRICAL CHARG. "		TITANIUM - - - - - 986		DOUBLE CRYSTAL ->1228	
LANTHANUM OXYSL. "		OPTICAL CHARACTER "		TRANSIENT ANALYS. 1374		HYDROCHLORIC ACID 287	
LOW ENERGY - - - - - "		TITANIUM DIOXIDE "		TRANSPARENT OXIDE 799		INDIUM PHOSPHIDE "	
PHOSPHORS - - - - - "		ELECTROPOLISHING ACCEPTER HYPOTHE.> 795		TUNGSTEN - - - - - 1374		MATERIAL SELECTI. "	
TERBIUM - - - - - - - "		ALLOY - - - - - -> 574		UNIFORM OXIDE - - - 799		PENDELLING - - - - - 1228	
XPS - - - - - - - - - "		ALUMINUM - - - - - "		VPE - - - - - - - - - 450		PHOSPHORIC ACID 287	
YTRITIUM OXYSULFI. "		BUBBLE DYNAMICS - - - "		EMF		STRAIN DISTRIBUT. 1228	
ELECTRON DIFFRAC. AUGER SPECTROSCOP.> 67		GASEOUS DISCHARGE - - - "		BULK PHASE - - - ->1467		X-RAY DIFFRACTION "	
ELECTROCATALYSIS "		GROOVE SPACING - - - - - "		MOLTEN SALT - - - - - "		EPITAXIAL LAYERS	
HYDROGEN ABSORPT. "		NICKEL - - - - - - - - - "		NERNST - - - - - ->1456		GAAS EPILAYER - ->1134	
PLATINUM - - - - - - - "		SURFACE MORPHOLO. TANTALUM - - - - - 795		SILVER CHLORIDE - 1467		LOW PRESSURE - - - - - "	
SINGLE CRYSTAL - - - - - "		WAGNERS THEORY - - - - - "		SODIUM CHLORIDE - - - "		PYROLYSIS - - - - - - - "	
STRUCTURE SENSIT. "		ELECTROSORPTION ANION INFLUENCE ->2140		SURFACE TENSION - - - "		EPITAXIAL RELATI.	
ELECTRON EXCHANGE		CURRENT PEAK - -> 257		ZINC ELECTRODE - 1456		ANNEAL - - - - - -> 277	
CONDUCTANCE - - ->1827		ELECTROCATALYSIS 2140		ZINC HYDROXIDE - - - "		CHANNELING - - - - - "	
SILICA SURFACE - - - - - "		FILM FORMATION ->1172		EMISSION SPECTRUM		CHROMIUM - - - - - - - "	
THERMALLY GROWN - - - - - "		GOLD ELECTRODE - - - - - "		GLOW DISCHARGE - -> 460		DIFFRACTION - - - - - "	
ELECTRON INJECTI. LIQUID AMMONIA ->207C		HYDROGEN ADATOM 257		NITROGEN - - - - - - - "		PLATINUM - - - - - - - "	
SEMICONDUCTOR - - - - - "		HYDROGEN MONOLAYER 2140		PLASMA TEMPERATU. "		SAPPHIRE - - - - - - - - - "	
SOLVATED ELECTRON - - - - - "		OXYGEN MONOLAYER "		RF PLASMA - - - - - - - "		ANTIMONY EVAPORA.>1761	
ELECTRON MICROSC. ANNEALING - - - -> 809		PERTURBATIONS - - - 257		ROTATIONAL TEMPE. "		ARSENIC - - - - - - - - - "	
CADMIUM TELLURIDE "		PLATINUM - - - - - 2140		EMITTER EFFICIEN. CURRENT GAIN - -> 642		ARSINE GAS - - - -> 300	
DEFECT ISOTHERM - - - - - "		POTENTIAL - - - - - 257		GETTERING - - - - - - - "		DEVICE QUALITY - - - - - "	
ELECTRODEPOSITION>1123		POTENTIAL PERTUR. 1172		P-N-P - - - - - - - - - "		DOPING - - - - - - - - 1761	
LATTICE DEFECT - 809		SODIUM HYDROXIDE "		PHOSPHORUS PENTC. "		ELECTROCRYSTALLI.>2085	
ORGANIC INCLUSION 1123		SULFURIC ACID - - 2140		TRANSISTOR - - - - - - - "		ELECTRODEPOSITION "	
STEREOMICROSCOPY "		ELECTROSTATICS FILTRATION - - - ->1426		ENERGY CONVERSION		GAAS - - - - - - - - 300	
ELECTRON RESIST CROSSLINKED TYPE >1635		MICROMINUTIRIZAT. "		AGING EFFECTS - -> 338		GERMANIUM - - - - - - - "	
ELECTRON BEAM - ->1699		PHOTOLITHOGRAPHY "		APROTIC SOLVENT -> 414		ION IMPLANTATION 1761	
GLYCIDYL METHACR. - - - - - "		PHOTORESIST - - - - - "		AUGER SPECTROSCOP.> 949		MOLECULAR BEAM - - - - - "	
- - - - ->1703		PLASMA ETCHING - - - - - "		CADMIUM SELENIIDE "		MOLYBDENUM - - - - - 300	
HALCSTYRENE - - - 1699		ELECTROTRANSPORT COBALT MONOXIDE -> 760		CADMIUM SULFIDE - - - "		NICKEL - - - - - - - 2085	
HOMOPLYMER - - - - 1635		HIGH RESISTANCE ->1811		CATION ABSORPTION> 954		PASSIVATION - - - - - - - "	
INTEGRATED CIRCU. - - - - - "		LOW PRESSURE - - - - - "		CHEMILUMINESCENCE 414		SACCHARIN - - - - - - - "	
LITHOGRAPHY - - - - 1699		MICROGRAVITY - - - - - "		DEFECT DOPING - - - 338		SILICON - - - - - - - 1761	
- - - - - 1703		OXIDATION THEORY 760		ELECTROGENERATED 414		SURFACE STRESS - 2085	
METHACRYLATE - - - 1635		POINT DEFECT - - - - - "		ELECTROLYTE SALT >1445		TRIMETHYLGALLIUM 300	
MONODISPERSE - -> 696				ELECTROMIGRATION 338		ULTRAHIGH VACUUM 1761	
NEGATIVE - - - - - - - "				HERMETIC O-CELL - 1445		EPPOXIDE DIMERS	
- - - - - 1699				LITHIUM BORN CH. - - - "		ALKALINE SOLUTION>1693	
POLYMER RESIST - - - - - "				PHOTOANODE - - - - - 954		KINETIC ANALYSIS "	
- - - - - 1703				PHOTOELECTRICITY 949		PHTHALIMIDE - - - - - "	
POLYSTYRENE - - - - 696				PHOTOELECTROCHEM. 954		REDUCTION - - - - - - - "	
WAFER FABRICATION 1703				PHOTOINDUCED - - - 414		STRUCTURAL ANALY. "	
2,2,2-TRICHLOROE. 1635				RUTHENIUM - - - - - 954		EPR	
ELECTRON TRANSFER CONVECTIVE DIFFU.> 431				SEMICONDUCTOR - - - 338		DIAZIDE-5-SULFON.> 860	
- - - - -> 437				- - - - - 414		ELECTRON BEAM - - - - - "	
ELECTRODE KINETI.> 988				SOLAR CELL - - - - - 954		MASS SPECTROSCOPY "	
HEME - - - - - - - - - "				SURFACE TREATMENT "		O-NAPHTHOQUINONE - - - - - "	
				THIONYL CHLORIDE 1445		PHENOLIC-TYPE - - - - - "	
				VP CONVERSION - - - 414		RESIN - - - - - - - - - - - "	
				XPS - - - - - - - - - 949			

PRIMARY TERM CO-TERM	PAGE NO.	PRIMARY TERM CO-TERM	PAGE NO.	PRIMARY TERM CO-TERM	PAGE NO.	PRIMARY TERM CO-TERM	PAGE NO.
EQUILIBRIUM		ETHYLENE GLYCOL (CONTO)		FERRIC OXIDE		FLATBAND POTENTI.	
AMBIENT PRESSURE >1422		SOLAR COLLECTOR - 11		ACETONITRILE - ->1892		ACETONITRILE - -> 598	
CARBON - - - - - "				ELECTRODE BEHAVI.		AQUEOUS ELECTROLYTE >1868	
CARBON MONOXIDE - -		ETHYLENEDIAMINE		FLAME OXIDATION -> 56		CAPACITANCE - - ->1505	
DTA - - - - - >1403		AQUEOUS SOLUTION >1406		N-TYPE CONDUCTION 1892		DARK POTENTIAL - 1868	
EFFLUENT GAS - -> 827		ETCHING - - - - - "		PHOTOCURRENT - - - 56		GROUP II-VI COMP. "	
GERMANIUM - - - - - "		PYROCATECHOL - - -		PULSED ILLUMINAT. "		INDIUM PHOSPHIDE 598	
HYDROSTATIC PRES. 1403		SILICON - - - - - "		SINTERING - - - - - "		IODINE DOPING - - 1868	
LEAD FLUORIDE - - -				SOLAR CELL - - - - - "		LIGHT ABSORPTION "	
OXYGEN - - - - - 1422		EUROPIUM				MOTT-SCHOTTKY - - 1505	
OXYGEN SOLUBILITY 827		BARIUM CHLOROSIL >1734		FERROUS SULFIDE		OPTICAL ABSORPTI. 1868	
PHASE TRANSITION 1403		HIGH QUENCHING - - "		COAL CHAR - - - -> 894		PHOTOELECTROCHEM. 598	
SILICON - - - - - 1422		PHOSPHORS - - - - - "		GASIFICATION - - - "		POTENTIAL DISTRI. 1505	
		PHOTOLUMINESCENCE "		IRON ALLOY - - - - - "		SEMICONDUCTOR - - 598	
		TEMPERATURE - - - - "		SULFIDATION - - - - - "		SINGLE CRYSTAL - -	
EQUILIBRIUM PCTE.						TITANIUM DIOXIDE 1505	
ALKALINE SOLUTION > 541		EUROPIUM DOPING		FICKS LAW		ZINC SELENIDE - - 1868	
CURRENT DENSITY - - "		CERIUM DOPING - ->1221		DISSOLUTION - - -> 634			
REACTION ORDER - - -		GADOLINIUM DOPING "		MOLTEN SILICON - - -		FLOAT CURRENT	
ZINC ELECTRODE - - -		GARNET PHOSPHORS "		SILICON CARBIDE - - -		STATIONARY BATTE. >1510	
		RARE EARTH ACTIV. "					
EQUIVALENT CIRCU.		TERBIUM DOPING - -		FILM EDGE		FLOW CONTROL	
IMPEDANCE PARAM. >1082		THERMAL DEPENDEN. "		DISLOCATION - - ->1014		CORROSION - - - ->2159	
PSEUDOINDUCTANCE "				SILICON DIOXIDE - - -		ENVIRONMENT - - - -	
		EUTECTIC		SILICON NITRIDE - - -		PERMEATION - - - - -	
ETA PHASE		ANODIC CORROSION >1087		VISCOELASTICITY - - -		POLYMER - - - - - "	
CUTTING TOOLS - ->1281		FUSED SALT - - - - 1087				TRACE GAS - - - - - "	
CVD COATING - - - - -		- - - - 1093		FILM FORMATION			
TITANIUM CARBIDE - - -		LITHIUM CHLORIDE 1087		ALUMINUM - - - - ->2042		FLOW-THROUGH	
TOUGHNESS BEHAVI. "		- - - - 1093		ANODIC FILM - - - - -		GASEOUS REACTANTS >1885	
		POTASSIUM CHLORIDE 1087		ANODIZATION - ->1718		REACTOR - - - - - "	
ETCH		- - - - 1093		CIRCUIT - - - - - "		TRICKLE BED ELEC. "	
AGITATION - - - -> 479		SULFIDATION - - - - -		COBALT HARDENED -> 445			
DEFECT - - - - - "		VOLTAMMETRY - - - 1087		CORROSION - - - - - 1718		FLUIDIZED ELECTR.	
SELLO ETCH - - - - -		- - - - 1093		DENDRITE - - - - - "		COPPER ELECTRODE >1180	
SILICON EVALUATI. "				ELECTRODEPOSITION 445		CURRENT DENSITY - -	
ULTRASONIC - - - - -				ELECTROSCORPTION >1172		ELECTRODEPOSITION >1176	
		EVAPORATION		GOLD - - - - - 445		- - - - 1180	
ETCHING		ALUMINUM COVERAGE >1335		GOLD ELECTRODE - 1172		MATHEMATICAL MOD. 1176	
AQUEOUS SOLUTION >1406		ARGON - - - - - "		GOLD METALLIZATI. 1718			
BORON DOPING - -> 345		CVD - - - - - "		HIGH TEMPERATURE 445		FLUORAPATITE	
CARBON TETRAFLUOR. > 464		INSULATION - - - - -		POTENTIAL PERTURB. 1172		STREAMING POTENT. >1905	
- - - - - >1419		POLYSILICON - - - - -		SODIUM HYDROXIDE - -		ZETA POTENTIAL - - -	
CHARGE TRANSFER -> 855		PRESSURE VARIATI. "		WATER - - - - - 1718			
CHROMIUM - - - - - >1075		SILICON DIOXIDE - - -				FLUORIDE	
COMPETITIVE MECH. 464				FILM GROWTH		DISCHARGE CHARAC. > 709	
ETHYLENEDIAMINE - 1406		EVOLUTION KINETI.		ANODIC OXIDATION > 470		GALVANIC CELL - - -	
GAAS ELECTRODE - 855		CHLORINE - - - ->209C		FLADE POTENTIAL - - -		SOLID ELECTROLYTE "	
GROUP III-V COMP. "		OXIDE FILM - - - - -		MATHEMATICAL MOD. >1261			
HYDROGEN - - - - - 1419		PLATINUM ELECTRO. "		NICKEL - - - - - 470		FLUORINE GAS	
ION ASSISTANCE - 464				NOBLE METAL LAYER 1261		INDUCTION PERIOD >1946	
MASKING - - - - ->1004		EXCHANGE CURRENT		SUBSTRATE DIFFUS. "		MICROCIRCUIT - - -	
ORIFICE SIZE - - - -		CERIUM DIOXIDE ->1155		SULFURIC ACID - - 470		SILICON ETCH - - - -	
PHOTODETECT - - - 855		OVERPOTENTIAL - - -					
PHOTOLITHOGRAPHY 1075		PLATINUM ELECTRO. "		FILM STRUCTURE		FLUORITE	
PHOTOMASK COATING - -		POLARIZATION - - - -		ANODIC OXIDATION > 583		ALUMINUM FLUORIDE >1385	
PYROCATECHOL - - 1406		EXTENSOMETER		ELECTROCHROMISM - -		DEFECT INTERACTI. "	
REACTIVE ION ETCH 1419		ELECTROCAPILLARY > 252		REACTION RATE - - -		IONIC CONDUCTIVI. "	
REDOX - - - - - 855		PLATINUM - - - - - "		ROSENTHAL TRIOXIDE "		IONIC MOTION - - -	
SAPPHIRE - - - - - 1004		SALT SOLUTION - - - -		VACUUM EVAPORATI. "		LEAD - - - - - "	
SILICON - - - - - 345		SURFACE STRESS - - -				SOLID ELECTROLYTE "	
- - - - - 1406				FILM THICKNESS			
SILICON DIOXIDE - 464		FABRICATION		DIELECTRIC FILM ->1539		FOIL	
- - - - - 1419		INTEGRATED CIRCU. >1415		EPITAXIAL GROWTH >2033		ALLOY - - - - ->2162	
SODIUM HYDROXIDE 345		MOS-LSI - - - - - "		INTERFACE MIGRAT. "		ELECTRODEPOSITION "	
THIN FILM - - - - - 1075		POLYSILICON - - - - -		PRISM COUPLER - 1539		FUSED SALT - - - - -	
				REFRACTIVE INDEX "		IRON PLATINUM - - -	
ETCHING DEFECT				SILICON - - - - - 2033		PREPARATION - - - -	
GROUP III-IV ALL. >1272		FABRICATION METH.		SILICON DIOXIDE - 1539			
INDIUM PHOSPHIDE "		ATMOSPHERIC CORR. >1533		SILICON SUBSTRATE - -		FOURIER ANALYSIS	
X-RAY DIFFRACTION "		OXIDATION - - - - - "				ANALYTIC SOLUTION >2081	
111-A FACE - - - - -		PERMALLOY FILM - - -		FILTRATION		LINEAR POLARIZAT. "	
111-B FACE - - - - -				ELECTROSTATICS ->1426		PASSIVE FILM - - -	
		FAILURE ANALYSIS		MICROMINIATURIZAT. "		POTENTIAL DISTRI. "	
ETHANE		BETA-ALUMINA - ->1451		PHOTOLITHOGRAPHY "		SCRATCH - - - - - "	
ELECTROCYCLIZATION > 775		CELL MEMBRANE - - -		PHOTORESIST - - - -			
FUEL CELL - - - - - "		ELECTRODE SHAPE - -		PLASMA ETCHING - - -		FRACTURE	
METHANE - - - - - "		SODIUM SULFUR - - - -				ADHESION - - - - -> 624	
N-BUTANE - - - - - "				FLADE POTENTIAL		ANODIC OXIDE FILM "	
PROPANE - - - - - "		FARADAIC RECTIFI.		ANODIC OXIDATION > 470		DUCTILITY - - - - -	
TRIFLUOROMETHANE "		ALTERNATING VOLT. >1908		FILM GROWTH - - - - -		TANTALUM - - - - - "	
		CORROSION POTENT. "		NICKEL - - - - - "			
ETHYL CINNAMATE		MILD STEEL - - - - -		SULFURIC ACID - - -			
CHRONOCOLUMETRY > 579		PASSIVATION - - - - -				FUEL CELL	
ELECTROHYDRODYNAMIC		POLARIZATION - - - -		FLAME OXIDATION		ALKALINE SOLUTION >1924	
LOW TEMPERATURE - -		FAST ELECTRODE		FERRIC OXIDE - -> 56		APPLICATION - - -> 7C	
METHYL CINNAMATE - -		DOUBLE PULSE - ->1148		PHOTOCURRENT - - -		CARBONATE - - -> 527	
REACTION ORDER - - -		GALVANOSTATICS - - -		PULSED ILLUMINAT. "		CATALYTIC DECOMP. 1924	
		OVERPOTENTIAL - - - -		SINTERING - - - - - "		COMPOSITION PROF. 527	
ETHYLENE				SOLAR CELL - - - - -		CONDUCTANCE - - ->1682	
ELECTROCATALYSIS > 218		FELTMETAL				DIFFUSION - - - - -	
ELECTROOXIDATION "		ANODIC DISCHARGE > 993		FLASH EVAPORATION		ELECTROOXIDATION > 775	
PLATINUM - - - - - "		LITHIUM BORON - - - -		CADMIUM SULFIDE ->1820		ETHANE - - - - - "	
POTENTIAL DYNAMICS "		MOLTEN SALT - - - - -		INDIUM DOPING - - - -		HALOGEN - - - - - 1682	
		VOLTAGE REGULATI. "		MOBILITY - - - - - "		HISTORY - - - - - 7C	
ETHYLENE GLYCOL						HYDROGEN - - - - - 1682	
ALUMINUM - - - - -> 11						LITHIUM CHLORIDE > 960	
CORROSION - - - - - "						METHANE - - - - - 775	

PRIMARY TERM CO-TERM	PAGE NO.	PRIMARY TERM CO-TERM	PAGE NO.	PRIMARY TERM CO-TERM	PAGE NO.	PRIMARY TERM CO-TERM	PAGE NO.
FUEL CELL (CONTO)		GAAS (CONTO)		GAAS EPILAYER		GALVANIC CELL (CONTO)	
MIGRATION POLARA. 960		ARSENIC PRESSURE >1997		EPITAXIAL LAYERS >1134		OXIDATION - - - - 171	
MOLTEN CARBONATE "		ARSINE GAS - - - - 300		LOW PRESSURE - - "		REDUCTION - - - - "	
MOLTEN SALT - - - 527		AUGER SPECTROSCO.> 450		PYROLYSIS - - - - "		SOLID ELECTROLYTE 709	
MOLTEN SALT BATT. 960		CAPLESS ANNEAL - 1997					
N-BUTANE - - - - 775		CESIUM - - - - -> 660		GAAS GROWTH		GALVANIC CORROSI.	
NAFION MEMBRANE - 1682		CHEMICAL ETCHING >1581		VAPOR ETCH - - ->1241		APPLIED POLARIZA.>2057	
PERHYDROXYL ION - 1924		CLEANING PROCESS "				COPPER ZINC - - - "	
POLYMER - - - - - 1682		COBALT - - - - ->1584		GAAS OXIDE		ELECTRODE POTENT. "	
POTASSIUM CHLOR. 960		CURRENT DENSITY - 1268		INERT ELECTROLYTE>1235		NUMERICAL ANALYS. "	
PROPANE - - - - - 775		DETECT STRUCTURE >1381		INTERFACE STATE - "		SOLUTION DEPTH - "	
STEADY STATE EQU. 527		DEPTH PROFILE - - - 660					
TRANSPORT PROPER. 1682		- - - - - 1370		GAASP		GALVANOSTATICS	
TRIFLUOROMETHANE 775		- - - - - 1737		COBALT - - - - ->1584		DOUBLE PULSE - ->114	
		DEVICE QUALITY - 300		GAAS - - - - - "		FAST ELECTRODE - "	
FURNACE		DIFFUSION PROCESS> 135		HOLE DIFFUSION L. "		OVERPOTENTIAL - - "	
CARBON DIOXIDE ->2012		DIOLE - - - - - 637		NICKEL - - - - - "		GARNET PHOSPHORS	
GAS FLOW METHOD - "		DISLOCATION - - - "		VPE - - - - - "		ABSORPTION SPECT.>1550	
HYDROGEN - - - - - "		DOPANT - - - - - 660				CATHODE RAY - ->1556	
LOWER TEMPERATURE "		DOPING - - - - - 1381		GADOLINIUM		CERIUM - - - - - 1550	
OXYGEN PRESSURE - "		DOPING PROFILE -> 296		CATHODE RAY - - ->1556		- - - - - 1556	
PRESSURE CONTROL - "		EFFICIENCY - - - 603		CERIUM - - - - - "		CERIUM DOPING ->1213	
WUSTITE PHASE - - - "		ELECTROEPITAXY - 1381		CONCENTRATION - - "		- - - - ->1221	
		ELECTRONIC CHARA. "		EFFICIENCY - - - "		CONCENTRATION - - 1556	
FUSED SALT		ELLIPSONOMETRY - - 450		GARNET PHOSPHORS		CRYSTAL FIELD - - 1550	
ALLOY - - - - ->2162		- - - - ->1589		TERBIUM - - - - - "		DECAY PROCESS - - 1213	
ALUMINUM CHLORIDE>1644		EPITAXY - - - - - 300				EFFICIENCY - - - 1556	
>1650		GAASP - - - - - 1584		GADOLINIUM CHLOR.		EUROPIUM DOPING - 1221	
ANODE MECHANISM -> 176		GALLIUM - - - - - 637		ALUMINUM CHLORIDE>1601		GADOLINIUM - - - 1556	
ANODIC CORROSION >1087		GALLIUM PHOSPHIDE 1589		CVD - - - - - "		GADOLINIUM DOPING 1221	
>1093		GERMANIUM - - - 300		GASEOUS COMPLEX - "		PHOTOLUMINESCENCE 1550	
CALCIUM ANODE - - 176		GROWTH PROCESS - 296		IRON CHLORIDE - - "		RARE EARTH ACTIV. 1213	
CHLOROALUMINATE ->1029		HEAT TREATMENT - 1581				1221	
CHRONAMPEROMETRY "		HOLE DIFFUSION L. "		GADOLINIUM DOPING		TEMPERATURE RANGE 1550	
>1902		- - - - - 1584		CERIUM DOPING ->1221		TERBIUM - - - - - 1556	
COMPLEX - - - - ->2104		IN SITU - - - - - 450		EUROPIUM DOPING - "		- - - - - "	
COMPLEX ION MODEL>2098		ION IMPLANTATION 1997		GARNET PHOSPHORS		TERBIUM DOPING - 1221	
CONDUCTIVITY - - 1644		ION SCATTERING - 1543		RARE EARTH ACTIV. "		THERMAL DEPENDEN. 1213	
- - - - - 1650		LARGE GRAIN - -> 703		TERBIUM DOPING - "		1221	
- - - - - 2098		LEED - - - - - 450		THERMAL DEPENDEN. "			
- - - - - 2104		LIGHT-EMITTING - 637					
COPPER - - - - - 1029		LIQUID JUNCTION - 603		GALLIUM		GAS ADSORPTION	
DENSITY - - - - - 1644		LPE - - - - - 296		ALUMINUM - - - ->1992		PASSIVE FILM - ->1720	
DISK ELECTRODE - 1029		MASS SPECTROMETRY 660		ALUMINUM ARSENIDE> 637		SURFACE ROUGHNESS "	
ELECTRODEPOSITION 2162		MOBILITY PROFILE 296		ANTIMONY - - - - - 1992			
EUTECTIC - - - - 1087		MOLYBDENUM - - - 300		BLUE LIGHT EMISS.> 341		GAS DISCHARGE	
FOIL - - - - - 1093		N-TYPE - - - - - 59		DIOLE - - - - - 637		COLOR TV PICTURE >1008	
GLASS FORMING ->1876		NICKEL - - - - - 1584		DISLOCATION		PHOSPHORS - - - - "	
HALIDE - - - - - 1644		OXIDE - - - - - 1737		DTA - - - - - 1992		ULTRAVIOLET EXCI. "	
IRON PLATINUM - - 2162		P-TYPE - - - - - 59		GAAS - - - - - 637			
LEAD CHLORIDE - 1902		PASSIVATION - - 1370		INDIUM ARSENIDE ->1400		GAS FLOW METHOD	
LEAD SULFIDE - - -		PASSIVATION TIME 1268		LIGHT-EMITTING - 637		CARBON DIOXIDE ->2012	
LITHIUM CHLORIDE 176		PHOTOELECTROCHEM. 59		LIQUID ASSOCIATI. 1992		FURNACE - - - - - "	
1087		PHOTOVOLTAIC CELL 603		LUMINESCENCE - - 341		HYDROGEN - - - - - "	
1093		PLANAR DIFFUSION 135		MIXED CRYSTAL PH. 1400		LOWER TEMPERATURE "	
1650		PLANAR JUNCTION - "		PHASE DIAGRAM - - 1992		OXYGEN PRESSURE - "	
MANGANESE CHLOR. 1876		PROCESS CONTROL - 1589		QUANTUM EFFICIEN. 637		PRESSURE CONTROL "	
MEASUREMENT - - - 2098		QUANTUM EFFICIEN. 637		SILICON - - - - - "		WUSTITE PHASE - - "	
- - - - - 2104		REGENERATIVE CELL 603		SOLUTION GROWTH - 341			
MOLAR VOLUME - - 2098		RESIDUAL FILM - - 1589		SOURCE GAS PHASE 1400		GAS INSULATION	
- - - - - 2104		RHEED - - - - - 450		TERNARY PHASE - - 1992		INSULATION - - -> 550	
MOLTEN SALT - - - 1876		SECONDARY ION - 660		THERMODYNAMICS - 1400		LIQUID INSULATION "	
N-ALKYLPYRIDINIUM 1644		SEMICONDUCTOR - - 59		VPE - - - - - "		SOLID INSULATION "	
OVERVOLTAGE - - - 176		SILICON - - - - - 637		ZINC SELENIDE - - 341			
OXIDATION - - - - 1902		- - - - - 660				GAS LIFT	
POTASSIUM CHLOR. 1087		SILICON DIOXIDE - 135		GALLIUM ANTIMONI.		COPPER DEPOSITION>2118	
1902		SINGLE CRYSTAL - 603		CVD - - - - - ->2031		CURRENT DISTRIB. "	
POTENTIOMETRY - - 1029		SOLAR CELL - - - 703		METALORGANICS - - "		ELECTRODEPOSITION "	
PREPARATION - - - 2162		SURFACE ANALYSIS 450		SEMICONDUCTOR - - "		HYDROGEN EVOLUTI.	
SULFIATION - - - 1093		SURFACE EFFECT - 59				MATHEMATICAL MOD.	
TBA CHLORIDE - - - 1876		THERMAL LPE - - - 1381		GALLIUM DOPING		VERTICAL ELECTRO. "	
TBA IODIDE - - - -		THIN FILM - - - 703		CZOCHELSKI - - -> 284			
TERNARY SYSTEM - 2098		TIN - - - - - 296		GERMANIUM - - - - "		GAS PLASMA	
- - - - - 2104		TIN DOPING - - - 135		HEAT PIPE - - - - "		CHROMIUM FILM - ->1794	
TETRA-N-BUTYLAMM. 1876		- - - - -> 797		RADIAL HEAT GRAD. "		MOS-LSI PROCESS - "	
THERMAL BATTERY - 176		TRIMETHYLGALLIUM 300		SEGREGATION - - - "		PHOTOMASK - - - - "	
TRANSPORT - - - 1644		ULTRAHIGH VACUUM 660		SYMMETRY - - - - - "		REVERSAL ETCHING "	
TRANSPORT PROPER. 1876		VPE - - - - - 450					
VISCOSITY - - - - 1644		- - - - - 797		GALLIUM PHOSPHIDE		GAS SOLUBILITY	
VOLTAMMETRY - - - 1087		- - - - - 1584		ELLIPSONOMETRY ->1589		CARBON DIOXIDE -> 328	
- - - - - 1093		XPS - - - - - 1370		GAAS - - - - - "		MOLTEN SALT - - - "	
		- - - - - 1737		PROCESS CONTROL - "		OXYGEN - - - - - "	
				RESIDUAL FILM - - "		SODIUM CARBONATE "	
						SULFUR DIOXIDE - "	
FUTURE		GAAS CRYSTAL		GALLIUM SELENIDE			
ECONOMIC GROWTH -> 81C		ATOMIC ABSORPTION>1988		ANODIZATION - - ->1191		GASEOUS COMPLEX	
SOCIAL CHANGE - - - "		SPECTROSCOPY - - -		BISMUTH TRITELL. "		ALUMINUM CHLORIDE>1601	
		TRACE ELEMENT - - -		ELLIPSCMETRY - - -		CVD - - - - ->1601	
GAAS		ZEEMAN TECHNIQUE "		LAYER PERIODICITY "		GADOLINIUM CHLOR.	
ACETONITRILE - - -> 59				LAYERED SEMICOND. "		IRON CHLORIDE - - -	
- - - - - 603		GAAS ELECTRODE					
ALUMINUM ARSENIDE> 637		CHARGE TRANSFER -> 855		GALVANIC CELL		GASEOUS DISCHARGE	
ANNEALING - - - - ->1737		ETCHING - - - - - "		COPPER DEPOSITION> 171		ALLOY - - - - -> 574	
ANODIC FILM - - ->1370		GROUP III-V COMP. "		DISCHARGE CHARAC.> 709		ALUMINUM - - - - -	
ANODIC OXIDATION >1268		PHOTOEFFECT - - - "		ELECTROLESS - - - 171		BUBBLE DYNAMICS -	
- - - - ->1543		REDOX - - - - - "		FLUORIDE - - - - - 709		ELECTROPOLISHING "	
ANODIC CXIDE - - - 1370						GROOVE SPACING - -	

PRIMARY TERM CO-TERM	PAGE NO.	PRIMARY TERM CO-TERM	PAGE NO.	PRIMARY TERM CO-TERM	PAGE NO.	PRIMARY TERM CO-TERM	PAGE NO.
GASEOUS DISCHARGE (CONTD)		GLOW TUBE (CONTD)		GRID CORROSION (CONTD)		HALOGEN (CONTD)	
NICKEL - - - - - 574		IONIC CONDUCTIVITY 2196		SILVER OXIDE - - - 725		POLYMER - - - - - 1682	
SURFACE MORPHOLOGY - - - - -						TRANSPORT PROPER. - - - - -	
GASEOUS REACTANTS		GLUCOSE OXIDATION		GROOVE SPACING		HALOSTYRENE	
FLOW-THROUGH - - - - - 1885		KINETIC PHENOMENA - - - 237		ALLOY - - - - - 574		ELECTRON BEAM - - - 1699	
REACTOR - - - - -		KREBS-RINGER - - -		ALUMINUM - - - - -		ELECTRON RESIST - - -	
TRICKLE BED ELEC. - - - - -		MASS TRANSPORT - - -		BUBBLE DYNAMICS - - -		GLYCIDYL METHACR. - - -	
		PLATINUM ELECTRO. - - -		ELECTROPOLISHING - - -		LITHOGRAPHY - - - - -	
GASIFICATION				GASEOUS DISCHARGE		NEGATIVE - - - - -	
COAL CHAR - - - - - 394		GLUCOSE SENSOR		NICKEL - - - - -		POLYMER RESIST - - -	
FERROUS SULFIDE - - - - -		ANODIC OXIDATION - - - 43		SURFACE MORPHOLOGY - - -			
IRON ALLOY - - - - -		>1687					
SULFIDATION - - - - -		DIABETES - - - - - 43		GROUP II-VI COMP.		HEAT EXCHANGER	
		IMPLANTATION - - - - -		AQUEOUS ELECTROLYTE - - - 1868		CARBON IMPURITY - - - 935	
GERMANIUM		INHIBITION - - - - - 1687		DARK POTENTIAL - - -		MOLYBDENUM RETAIN. - - -	
ARSINE GAS - - - - - 300		KREBS-RINGER - - - 43		FLATBAND POTENTIAL - - -		SILICON CRYSTAL - - -	
CZOCHEWSKI - - - - - 284		LINEAR POTENTIAL - - - 43		IODINE DOPING - - - - -			
QUALITY - - - - - 300		PLATINUM ELECTRO. - - -		LIGHT ABSORPTION - - -		HEAT PIPE	
EFFLUENT GAS - - - - - 327		UREA - - - - - 1687		OPTICAL ABSORPTION - - -		CZOCHEWSKI - - - - - 284	
EPITAXY - - - - - 300				ZINC SELENIUM - - - - -		GALLIUM DOPING - - -	
EQUILIBRIUM - - - - - 827						GERMANIUM - - - - -	
GAAS - - - - - 300		GLYCIDYL METHACR.		GROUP III-IV ALL.		RADIAL HEAT GRAD. - - -	
GALLIUM DOPING - - - 284		ELECTRON BEAM - - - 1699		ETCHING DEFECT - - - 1272		SEGREGATION - - - - -	
HEAT PIPE - - - - -		ELECTRON RESIST - - -		INDIUM PHOSPHIDE - - -		SYMMETRY - - - - -	
MOLYBDENUM - - - - - 300		>1703		X-RAY DIFFRACTION - - -			
OXYGEN SOLUBILITY 827		HALOSTYRENE - - - - - 1699		111-A FACE - - - - -		HEAT TRANSFER	
RADIAL HEAT GRAD. 284		LITHOGRAPHY - - - - -		111-B FACE - - - - -		ELECTRIC VEHICLE - - - 1321	
SEGREGATION - - - - -		>1703				ELECTROLYTE FLOW - - -	
SYMMETRY - - - - -		NEGATIVE - - - - - 1699		GROUP III-V COMP.		LEAD ACID BATTERY - - -	
TRIMETHYLGALLIUM 300		POLYMER RESIST - - -		CHARGE TRANSFER - - - 855		PURIFICATION - - - - -	
		>1703		DIFFRACTIONOMETRY - - - 664			
GETTERING		WAFER FABRICATION - - -		DOUBLE CRYSTAL - - -		HEAT TREATMENT	
CURRENT GAIN - - - - - 642				ETCHING - - - - - 855		CHEMICAL ETCHING - - - 1581	
EMITTER EFFICIENCY - - -		GOLD		GAAS ELECTRODE - - -		CLEANING PROCESS - - -	
LASER - - - - - 1436		ACID SULFATE - - - - - 95		INDIUM PHOSPHIDE 664		GAAS - - - - -	
LATTICE DAMAGE - - - - -		ANODIC DISSOLUTION - - -		INGAPAS - - - - -		SOLE DIFFUSION L. - - -	
P-N-P - - - - - 642		COBALT HARDENED - - - 445		LATTICE MISMATCH - - -			
PHOSPHORUS PENTO. - - -		CORROSION RATE - - - 95		LPE - - - - -		HELIUM-HYDROGEN	
SILICON WAFER - - - 1436		ELECTRODEPOSITION 445		PHOTODEFFECT - - - - - 855		ATMOSPHERE - - - - - 1785	
TRANSISTOR - - - - - 642		FILM FORMATION - - -		QUARTERNARY - - - - - 664		DOPING - - - - -	
		HIGH TEMPERATURE - - -		REDOX - - - - - 855		HETEROEPITAXY - - -	
GLASS		OXYGEN EVOLUTION 95				SILICON GROWTH - - -	
CONDUCTIVITY - - - 2144		PH - - - - -		GROWTH MECHANISM			
HYDRATE MELT - - - - -				ALUMINA - - - - - 1035		HEME	
MIXED ALKALI EFF. - - -		GOLD ALLOY		CVD - - - - - 31		ELECTRODE KINETICS - - - 988	
TRANSITION TEMPE. - - -		CONNECTOR - - - - - 1798		OXIDE MICROPHYSICS 1035		ELECTRON TRANSFER - - -	
		COPPER - - - - -		SILICON FIBER - - - 31		HEMOGLOBIN - - - - -	
GLASS ELECTRODE		DIFFUSION - - - - -		WHISKERS - - - - -			
DESTRUCTIVE EFFECTS - - - 2196		OXIDATION KINETICS - - -		YTTRIUM - - - - - 1035		HEMOGLOBIN	
GLOW TUBE - - - - -		RELIABILITY - - - - -				ELECTRODE KINETICS - - - 988	
IONIC CONDUCTIVITY - - -				GROWTH PARAMETER		ELECTRON TRANSFER - - -	
		GOLD COATING		BORON NITRIDE - - - 1951		HEME - - - - -	
GLASS FORMING		LITHOGRAPHY - - - - - 1514		CVD - - - - -			
FUSED SALT - - - - - 1876		PROCESSING - - - - -		PHOSPHOR DOPING - - -		HERMETIC D-CELL	
MANGANESE CHLORIDE - - -		PULSE ELECTROPLATING - - -				ELECTROLYTE SALT - - - 1445	
MOLTEN SALT - - - - -				GROWTH PROCESS		ENERGY CONVERSION - - -	
TBA CHLORIDE - - - - -		GOLD ELECTRODE		DOPING PROFILE - - - 296		LITHIUM BORON CH. - - -	
TBA IODIDE - - - - -		ELECTRODEPOSITION - - - 1172		GAAS - - - - -		THIANYL CHLORIDE - - -	
TETRA-N-BUTYLAM. - - -		FILM FORMATION - - -		LPE - - - - -			
TRANSPORT PROPER. - - -		POTENTIAL PERTURB. - - -		MOBILITY PROFILE - - -		HETEROCHARGE	
		SODIUM HYDROXIDE - - -		TIN - - - - -		ELECTRET - - - - - 1708	
GLASS SUBSTRATE						MEMBRANE - - - - -	
ACTIVATOR - - - - - 1671		GOLD ELECTRODEPOSITION		HAFNIUM DIKETONE		POLARIZATION - - - - -	
BACKSCATTERING - - - - -		COBALT - - - - - 391		HAFNIUM DIOXIDE - - - 1203		POLYSTYRENESULFON. - - -	
ELECTROLESS - - - - -		COBALT HARDENED - - -		THERMAL DECOMPOS. - - -		POLYVINYL ALCOHOL - - -	
METAL DEPOSITION - - -		>1608		THIN FILM GROWTH - - -		POTASSIUM - - - - -	
PALLADIUM - - - - -		COBALT OXYHYDROX. 391		ZIRCONIUM DIKETONE - - -		SODIUM - - - - -	
		MOSSBAUER SPECTR. 1608		ZIRCONIUM DIOXIDE - - -			
GLASSY LAYER						HETEROEPITAXY	
COPPER - - - - - 1425		GOLD METALLIZATION		HAFNIUM DIOXIDE		ATMOSPHERE - - - - - 1785	
CVD - - - - -		ANODIZATION - - - - - 1718		HAFNIUM DIKETONE - - - 1203		DOPING - - - - -	
OXIDATION - - - - -		CIRCUIT - - - - -		THERMAL DECOMPOS. - - -		HELIUM-HYDROGEN - - -	
PASSIVITY - - - - -		CORROSION - - - - -		THIN FILM GROWTH - - -		SILICON GROWTH - - -	
		DENDRITE - - - - -		ZIRCONIUM DIKETONE - - -			
GLASSY PHOSPHORS		FILM FORMATION - - -		ZIRCONIUM DIOXIDE - - -		HEXACYANOFERRATE	
ALKALI RARE EARTH - - - 2206		WATER - - - - -				OXIDE FILM - - - - - 732	
CESIUM COACTIVATOR - - -				HALIDE		PASSIVE IRON - - - - -	
LUMINESCENCE - - - - -		GOLD SUBSTRATE		ALUMINUM CHLORIDE - - - 1644		SEMICONDUCTOR - - - - -	
METAPHOSPHATE - - - - -		CATION FILM - - - - - 167		CONDUCTIVITY - - - - -		TAFEL SLOPE - - - - -	
TERBIUM ACTIVATOR - - -		DISPLAY DEVICE - - -		DENSITY - - - - -			
		N-HEPTYLVIOLOGEN - - -		FUSED SALT - - - - -		HEXAFLUOROARSEN. - - -	
GLOW DISCHARGE				N-ALKYLPIRIDINIUM - - -		ANODIC STABILITY - - - 507	
CONTAMINATION - - - - - 319		GRAIN STRUCTURE		TRANSPORT - - - - -		COLD-ROLLED STEEL - - -	
EMISSION SPECTRUM - - - 460		MICROSTRUCTURE - - - 1061		VISCOSITY - - - - -		CORROSION RESIST. - - -	
NITROGEN - - - - -		NICKEL - - - - -				LITHIUM - - - - - 181	
PLASMA DEPOSITION 319		OXIDATION - - - - -		HALL DATA		>507	
PLASMA ETCHING - - - - -				ANODIC OXIDATION - - - 118		LITHIUM BATTERY - - - - -	
PLASMA TEMPERATURE 460		GRID CORROSION		CARRIER CONCENTR. - - -		ORGANIC PRODUCT - - - 181	
RADIATION DAMAGE 319		ANODIC FILM - - - - - 725		INDIUM PHOSPHIDE - - -		SOLID CORROSION - - -	
RF PLASMA - - - - - 460		COBALT SULFATE - - -		ION IMPLANTATION - - -		TANTALUM - - - - - 507	
ROTATIONAL TEMPE. - - -		LEAD ACID BATTERY - - -				TETRAHYDROFURAN - - - 181	
SPUTTERING - - - - - 319				HALOGEN		>507	
GLOW TUBE				CONDUCTANCE - - - - - 1682			
DESTRUCTIVE EFFECTS - - - 2196				DIFFUSION - - - - -		HIGH FIELD	
GLASS ELECTRODE - - - - -				FUEL CELL - - - - -		INTERFACE ROLE - - - 2188	
				HYDROGEN - - - - -		IONIC CONDUCTION	
				NAFION MEMBRANE - - -		THIN FILM - - - - -	

PRIMARY TERM CO-TERM	PAGE NO.	PRIMARY TERM CO-TERM	PAGE NO.	PRIMARY TERM CO-TERM	PAGE NO.	PRIMARY TERM CO-TERM	PAGE NO.
HIGH PRESSURE		HOT SENSITIZATI. (CONTD)		HYDROGEN (CONTD)		HYDROGEN SULFIDE	
HYDROGEN EVOLUTI. > 985		PRASEODYMIUM - - - - - 305		URANIUM POWDER - - - - - 495		CARBON STEEL - - - - - 911	
LOW TEMPERATURE - >1822		TERBIUM - - - - - "		- - - - - 1596		ELECTRODEPOSITION - - - - - "	
OXIDE FILM GROWTH - - - - - "		TRAPPING - - - - - "		WUSTITE PHASE - - - - - 2012		MARCASITE - - - - - "	
REACTION MECHAN. 985		YTTRIUM OXISULFI. - - - - - "				PYRITE - - - - - "	
SILICON - - - - - 1822				HYDROGEN ABSORPT.			
STEAM OXIDATION - - - - - "		HOT CORROSION		AUGER SPECTROSC. > 67		HYDROGEN-CHLORINE	
TRANSITION STATES 985		CHEMICAL EQUILIB. >1054		ELECTROCATALYSIS - - - - - "		ENERGY STORAGE - - - - - 713	
		COMBUSTION GASES - - - - - "		ELECTRON DIFFRAC. - - - - - "		MASS HEAT BALANCE - - - - - "	
HIGH QUENCHING		DEPOSITION - - - - - "		PLATINUM - - - - - "		REGENERATION - - - - - "	
BARIUM CHLOROSIL. >1734		SODIUM SULFATE - - - - - "		SINGLE CRYSTAL - - - - - "		STOICHIOMETRY - - - - - "	
EUROPIUM - - - - - "				STRUCTURE SENSIT. - - - - - "			
PHOSPHORS - - - - - "		HOT-PRESSED				HYDROGENATION	
PHOTOLUMINESCENCE - - - - - "		CERAMICS - - - - - >1723		HYDROGEN ADATOM		ANNEALING - - - - - >1750	
TEMPERATURE - - - - - "		CORROSION - - - - - "		CURRENT PEAK - - - - - > 257		PLASMA DEPOSITION - - - - - "	
		OXIDATION KINETI. - - - - - "		ELECTROSORPTION - - - - - "		SILICON NITRIDE - - - - - "	
HIGH RATE		REFRACTORIES - - - - - "		PERTURBATIONS - - - - - "			
INDIUM OXIDE - - - - - 691		SILICON NITRIDE - - - - - "		PLATINUM - - - - - "		HYDROLYSIS	
POLYESTER FILM - - - - - "		YTTRIUM - - - - - "		POTENTIAL - - - - - "		IMPURITY - - - - - > 981	
REACTIVE SPUTTER. - - - - - "						LIQUID CATHOLYTE - - - - - "	
TIN DOPING - - - - - "						LITHIUM BATTERY - - - - - "	
						THIONYL CHLORIDE - - - - - "	
HIGH RESISTANCE		HYDRATE MELT		HYDROGEN CONTENT		HYDROSTATIC PRES.	
ELECTROTRANSPORT >1811		CONDUCTIVITY - - - - - >2144		AMORPHOUS SEMICO. > 688		DTA - - - - - >1403	
LOW PRESSURE - - - - - "		GLASS - - - - - "		DEPOSITION - - - - - "		EQUILIBRIUM - - - - - "	
MICROGRAVITY - - - - - "		MIXED ALKALI EFF. - - - - - "		MASS SPECTROMETRY - - - - - "		LEAD FLUORIDE - - - - - "	
PURIFICATION - - - - - "		TRANSITION TEMPE. - - - - - "		PHOTOVOLTAIC PRO. - - - - - "		PHASE TRANSITION - - - - - "	
THORIUM - - - - - "				SILICON - - - - - "			
HIGH TEMPERATURE		HYDRATED METALS		HYDROGEN DIFFUSI.		HYDROXIDE-TYPE	
ANNEALING - - - - - >1731		CALCIUM NITRATE - - - - - 985		CHEMICAL TREATME. >1792		ACID MEDIUM - - - - - > 93	
AQUEOUS SYSTEM - - - - - 908		NUCLEATION - - - - - "		CONDUCTIVITY - - - - - "		CHARGE CAPACITY - - - - - "	
CAPACITANCE - - - - - 1731		THALLIUM - - - - - "		ELECTRICAL MEASU. - - - - - "		IRIDIUM - - - - - "	
COBALT HARDENED - - - - - 445				P-TYPE - - - - - "		THIN FILM - - - - - "	
DIFFUSING SPECIES >1948		HYDRIDE FORM		RESISTIVITY SHIFT - - - - - "			
ELECTRODEPOSITION 445		ALUMINUM - - - - - > 199		SILICON SURFACE - - - - - "			
FILM FORMATION - - - - - "		AQUEOUS SOLUTION - - - - - "					
GOLD - - - - - "		PH - - - - - "		HYDROGEN EFFECT		ILLUMINATED	
NICKEL CHROMIUM - 1948		POTENTIAL - - - - - "		SILICON DIOXIDE - - - - - 122		CHARGE TRANSFER - - - - - >1011	
OXIDATION KINETI. >1105		SALT SOLUTION - - - - - "		SILICON INTERFACE - - - - - "		DIGITAL SIMULATI. - - - - - "	
OXIDE FILM GROWTH 1731				THERMAL OXIDATION - - - - - "		HOLE INJECTION - - - - - "	
PARABOLIC KINETI. 1105		HYDROCHLORIC ACID				LIQUID JUNCTION - - - - - "	
PHOSPHIDATION - - - - - 1948		CHEMICAL ETCHING > 287		HYDROGEN EVOLUTI.		PHOTOANODE - - - - - "	
PHOSPHORUS VAPOR - - - - - "		CHLORINE INCORPO. > 143		BUFFER CAPACITY - - - - - >1861		SEMICONDUCTOR - - - - - "	
REFERENCE ELECTR. 908		CHLOROSILOXANE - - - - - >1081		COPPER DEPOSITION >2118		SOLAR CELL - - - - - "	
REOXIDATION - - - - - 1731		EPITAXIAL LAYER - - - - - 287		CURRENT DISTRIBU. - - - - - "			
SILICON OXIDE - - - - - "		INDIUM PHOSPHIDE - - - - - "		CURRENT EFFICIEN. 1861		IMPATT DIODE	
THERMAL CELL - - - - - 908		MATERIAL SELECT. - - - - - "		ELECTRODEPOSITION - - - - - "		CHROMIUM - - - - - >1047	
TITANIUM DIOXIDE 1731		MOBILE SODIUM - - - - - > 149				DEGRADATION - - - - - "	
ZIRCALOXY OXIDI. 1105		OXIDATION - - - - - 149				INTERDIFFUSION - - - - - "	
		PASSIVATION - - - - - "				METALLIZATION - - - - - "	
		PHASE SEPARATION >1129				PLATINUM - - - - - "	
		PHOSPHORIC ACID - - - - - 287				SILICON - - - - - "	
		PLANAR DEVICE - - - - - 143				SILVER - - - - - "	
		SILICON - - - - - "					
		SILICON DIOXIDE - - - - - 149				IMPEDENCE	
		SILICON OXIDE - - - - - 1081				ALUMINUM - - - - - > 779	
		- - - - - 1129				ANODIZATION - - - - - "	
		SODIUM NEUTRALIZ. 149				CYCLIC VOLTAMMET. > 989	
		SODIUM PASSIVATI. 1129				INTEGRATED ELECT. > 793	
						ION SELECTIVE EL. - - - - - "	
						RELAXATION TIME - - - - - 779	
						RESISTIVE CAPACIT. 989	
						SMALL AMPLITUDE - - - - - "	
						SOLID-STATE - - - - - 793	
						STOICHIOMETRY - - - - - 779	
						VOLTAMMOGRAM - - - - - 989	
						IMPEDANCE PARAM.	
						EQUIVALENT CIRCU. >1082	
						PSEUDOINDUCTANCE - - - - - "	
						IMPLANTATION	
						ANODIC OXIDATION > 43	
						DIABETES - - - - - "	
						GLUCOSE SENSOR - - - - - "	
						KREBS-RINGER - - - - - "	
						LINEAR POTENTIAL - - - - - "	
						PLATINUM ELECTRO. - - - - - "	
						IMPURITY	
						HYDROLYSIS - - - - - > 981	
						LIQUID CATHOLYTE - - - - - "	
						LITHIUM BATTERY - - - - - "	
						THIONYL CHLORIDE - - - - - "	
						IMPURITY REDISTR.	
						IMPURITY SEGREGA. >1939	
						INTERFACIAL FLUX - - - - - "	
						MOVING BOUNDARY - - - - - "	
						NUMERICAL SOLUTI. - - - - - "	
						SILICON OXIDATION - - - - - "	
						IMPURITY SEGREGA.	
						IMPURITY REDISTR. >1939	
						INTERFACIAL FLUX - - - - - "	
						MOVING BOUNDARY - - - - - "	
						NUMERICAL SOLUTI. - - - - - "	
						SILICON OXIDATION - - - - - "	

PRIMARY TERM CO-TERM	PAGE NO.	PRIMARY TERM CO-TERM	PAGE NO.	PRIMARY TERM CO-TERM	PAGE NO.	PRIMARY TERM CO-TERM	PAGE NO.
IN SITU		INGAPAS (CONTO)		INTERCALATION (CONTO)		ION BEAM (CONTO)	
AUGER SPECTROSCOP. >	450	QUARTERNARY - - -	664	TOPOCHEMICAL CELL	349	POLYDIMETHYLSILO. >	483
ELLIPSCOMETRY - - -	"					POLYMETHYLMETACR. >	"
GAAS - - - - -	"	INHIBITION		INTERDIFFUSION		RADIATION YIELD - -	"
LEED - - - - -	"	ANODIC OXIDATION >	1687	CHROMIUM - - - ->	1047	RESIST MATERIAL - -	"
REED - - - - -	"	CHLORIDE SOLUTION >	385	DEGRADATION - - -	"		
SURFACE ANALYSIS	"	CHROMATE - - - -	"	IMPATT DIODE - - -	"	ION CONDUCTIVITY	
VPE - - - - -	"	CREVICE CORROSION	"	METALLIZATION - -	"	ALUMINA - - - - ->	1963
		GLUCOSE SENSOR -	1687	PLATINUM - - - - -	"	CUPROUS CHLORIDE	"
INCONEL 600		IRON - - - - -	385	SILICON - - - - -	"	DISPERSED ALUMINA	"
AQUEOUS OXIDATION >	750	KREBS-RINGER - -	1687	SILVER - - - - -	"		
NUCLEAR REACTOR -	"	PLATINUM ELECTRO.	"			ION EXCHANGE	
XPS - - - - -	"	UREA - - - - -	"			BROMINE DIFFUSION >	36
				INTERFACE		DIFFUSION COEFFI. -	"
INDIUM ARSENIIDE		INSTABILITY		AC ADMITTANCE - ->	424	NAFION MEMBRANE -	"
GALLIUM - - - - ->	1400	ANTIMONY - - - ->	875	PLATINUM - - - - -	"		
MIXED CRYSTAL PH. >	"	CRYSTAL GROWTH -	"	ROTATING DISK - -	"	ION IMPLANTATION	
SOURCE GAS PHASE	"	CZOCHELSKI - - -	"	SULFURIC ACID - -	"	ANGLE LAPPING - ->	1982
THERMODYNAMICS	"	DOPED MELT - - -	"	SWEET FREQUENCY -	"	ANODIC OXIDATION >	118
VPE - - - - -	"	MORPHOLOGY - - -	"			ANTIMONY EVAPORA. >	1761
		SILICON CRYSTAL -	"	INTERFACE MIGRAT.		ARSENIC - - - - -	"
INDIUM DOPING				EPITAXIAL GROWTH >	2033	ARSENIC PRESSURE >	1997
CADMIUM SULFIDE ->	1820	INSULATING FILM		FILM THICKNESS - -	"	AUGER SPECTROSCOP. >	98
FLASH EVAPORATION	"	NEW TECHNOLOGY ->	504	SILICON - - - - -	"	CAPLESS ANNEAL -	1997
MOBILITY - - - - -	"	TAPER ETCHING - -	"			CARRIER CONCENTR.	118
		TAPERED WINDOW -	"	INTERFACE POTENT.		CVD - - - - ->	1019
INDIUM OXIDE				DIFFUSION - - - ->	242	DOPING - - - - -	1761
HIGH RATE - - - ->	691	INSULATION		ELLIPSCOMETRY - -	"	- - - - ->	1779
POLYESTER FILM -	"	ALUMINUM COVERAGE >	1335	IONIC CONDUCTOR -	"	EPITAXY - - - - -	1761
REACTIVE SPUTTER. >	"	ARGON - - - - -	"	ROTATING ELECTRO.	"	GAAS - - - - -	1997
TIN DOPING - - - -	"	CVD - - - - -	"	SILVER SALT SOLU.	"	HALL DATA - - - -	118
		EVAPORATION - - -	"			INDIUM PHOSPHIDE	"
INDIUM PHOSPHIDE		GAS INSULATION ->	55C	INTERFACE ROLE		JUNCTION DEPTH -	1982
ACETONITRILE - ->	598	LIQUID INSULATION	"	HIGH FIELD - - ->	2188	LOW PRESSURE - -	1019
ANODIC OXIDATION >	118	POLYSILICON - - -	1335	IONIC CONDUCTION	"	LOW TEMPERATURE -	1779
CARRIER CONCENTR. >	"	PRESSURE VARIAT.	"	THIN FILM - - - -	"	MOLECULAR BEAM -	1761
CHEMICAL ETCHING >	287	SILICON DIOXIDE -	"			OXIDATION - - - -	1779
DIFRACTOMETRY >	664	SOLID INSULATION	55C	INTERFACE STATE		PHOSPHORUS DOPING	1019
DOUBLE CRYSTAL -	"			ANNEALING - - - ->	1573	POLYSILICON - - -	1779
EPITAXIAL LAYER -	287	INTEGRATED CIRCU.		CHARGE DENSITY -	"	SILICON - - - - -	1761
ETCHING DEFECT ->	1272	ALUMINUM ALLOY ->	110	GAAS OXIDE - - ->	1235	SILICON FILM - - -	1019
FLATBAND POTENTI.	598	CHLOROACRYLATE ->	1829	INERT ELECTROLYTE	"	STAINING - - - -	1982
GROUP III-IV ALL.	1272	CORROSION TEST -	110	INTERFERENCE ->	1979	SURFACE CONTAMIN.	98
GROUP III-V COMP.	664	CROSSLINKED TYPE >	1335	MOBILE ION - - -	"	ULTRAHIGH VACUUM	1761
HALL DATA - - - -	118	CVD - - - - ->	334	MOS CAPACITOR - -	"	VLSI DEVICE - - -	1779
HYDROCHLORIC ACID	287	- - - - ->	1042	SILICON - - - - -	"		
INGAPAS - - - - -	664	CZOCHELSKI - - ->	1142	SILICON DIOXIDE -	1573	ION ROLE	
ION IMPLANTATION	118	DEPOSITION RATE -	1042	THERMAL OXIDATION	"	MICROWAVE - - - ->	1024
LATTICE MISMATCH	664	DIELECTRIC ISOLA. >	870			NEUTRAL SPECIES -	"
LPE - - - - -	"	DIELECTRICS - - -	334	INTERFACIAL FLUX		PLASMA ETCHING -	"
MATERIAL SELECT.	287	ELECTRON BEAM -	1829	IMPURITY REDISTR. >	1939	SILICON - - - - -	"
PHOSPHORIC ACID -	"	ELECTRON RESIST -	1635	IMPURITY SEGREGA.	"		
PHOTOELECTROCHEM.	598	FABRICATION - ->	1415	MOVING BOUNDARY -	"	ION SCATTERING	
QUARTERNARY - - -	664	HOMOPOLYMER - - -	1635	NUMERICAL SOLUT.	"	ANODIC OXIDATION >	1543
SEMICONDUCTOR - -	598	LIFETIME - - - -	1142	SILICON OXIDATION	"	CURRENT DENSITY -	"
SINGLE CRYSTAL -	"	LIQUID STANDARD ->	103			GAAS - - - - -	"
X-RAY DIFFRACTION	1272	METALLIZATION -	110	INTERFERENCE			
111-A FACE - - -	"	METHACRYLATE - -	1635	INTERFACE STATE ->	1979	ION SELECTIVE	
111-B FACE - - -	"	MINORITY CARRIER	1142	MOBILE ION - - -	"	CESIUM - - - - ->	347
		MOLECULAR ORBITAL	1829	MOS CAPACITOR - -	"	POTASSIUM - - - -	"
INDIUM SESQUIOXI.		MOS - - - - ->	20C	SILICON - - - - -	"	PVC MATRIX - - -	"
ELECTRON AFFINITY >	1081	MOS-LSI - - - -	1415			ZINC FERROCYNIDE	"
OXIDE SEMICONDUCT.	"	PASSIVATION LAYER	103	INTERGRANULAR			
PHOTOVOLTAIC PRO.	"	PHOSPHORUS - - -	334	AUSTENITIC - - - ->	374	ION SELECTIVE EL.	
		PHOSPHORUS DOPING	1042	CORROSION - - - -	"	IMPEDENCE - - - ->	793
INDUCED INSTABIL.		PHOSPHOSILICATE -	334	DUPLEX JOB - - - -	"	INTEGRATED ELECT.	"
ALCOHOL - - - - ->	1301	PLASTIC ENCAPSUL.	110	MICROSTRUCTURE	"	SOLID-STATE - - -	"
KETONE - - - - -	"	POLYMER - - - - -	1829	PHASE TRANSFORMA.	"		
SILICON GATE MOS	"	POLYSILICON - - -	1415	PITTING - - - - -	"	IONIC CONDUCTION	
		POSITIVE RESIST -	1829	STAINLESS STEEL -	"	ANODIC OXIDE FILM >	765
INDUCTION PERIOD		PRESSURE REDUCT.	1042			>	1972
FLUORINE GAS - ->	1946	REFRACTIVE INDEX	103	IODINE		DIELECTRICS - - -	765
MICROCIRCUIT - -	"	SEMICONDUCTOR - -	20C	POLLUTION CONTROL >	1842	HIGH FIELD - - ->	2188
SILICON ETCH - - -	"	SILICON - - - - -	"	SODIUM SULFATE - -	"	INTERFACE ROLE -	"
		- - - - -	1142	SOLID-STATE PROBE	"	SELF DISCHARGE -	1972
INDUSTRY REPORT		SILICON ANODIZAT.	870	SULFUR DIOXIDE -	"	TANTALUM PENTOXI.	765
ELECTROLYTE - - ->	243C	SILICON DIOXIDE -	1042	SULFUR PROBE - -	"	THIN FILM - - - -	2188
		SILICON POROSITY	870	SULFUR TRIOXIDE -	"		
INERT ELECTROLYTE		THERMAL PROCESSI.	1142			IONIC CONDUCTIVI.	
GAAS OXIDE - - - -	>1235	TRANSPARENT FILM	103	IODINE DOPING		ALUMINUM FLUORIDE >	1385
INTERFACE STATE -	"	TRIFLUOROETHYL -	1829	AQUEOUS ELECTROL. >	1868	BARIUM FLUORITE ->	664
		2,2,2-TRICHLOROE.	1635	DARK POTENTIAL -	"	CALCIA - - - - ->	267
INFRARED ABSORPT.				FLATBAND POTENTI.	"	CALCIUM FLUORITE	> 1
CVD - - - - ->	1728	INTEGRATED ELECT.		GROUP II-VI COMP.	"	CERAMICS - - - -	667
DIELECTRICS - - -	"	IMPEDENCE - - ->	793	LIGHT ABSORPTION	"	CERIUM DIOXIDE -	266
LOW TEMPERATURE	"	ION SELECTIVE EL.	"	OPTICAL ABSORPTI.	"	CESIUM FLUORITE -	617
OXIDATION - - - -	"	SOLID-STATE - - -	"	ZINC SELENIDE - -	"	COPPER BROMIDE ->	868
POLYMERIZATION -	"					DEFECT INTERACTI.	667
SILANE - - - - -	"	INTERCALATION		ION ASSISTANCE		1385	
		COPPER - - - - ->	699	CARBON TETRAFLUO. >	464	DESTRUCTIVE EFEE >	2196
INGAPAS		CYCLABLE CELL - -	"	COMPETATIVE MECH.	"	DTA - - - - -	1
DIFRACTOMETRY ->	664	DICHALCOGENIDE ->	349	ETCHING - - - - -	"	FLUORITE - - - - -	1385
DOUBLE CRYSTAL -	"	ELECTRODE - - - -	699	SILICON DIOXIDE -	"	GLASS ELECTRODE -	2196
GROUP III-V COMP.	"	LITHIUM - - - - -	349			GLOW TUBE - - - -	"
INDIUM PHOSPHIDE	"	LOW VOLTAGE BEHA.	"	ION BEAM		IONIC MOTION - -	1385
LATTICE MISMATCH	"	SECONDARY BATTERY	"	LITHOGRAPHY - - ->	483	LEAD - - - - -	"
LPE - - - - -	"	SOLID-STATE CELL	699	PATTERN DUPLICAT.	"	LITHIUM OXIDE - -	1

PRIMARY TERM CO-TERM	PAGE NO.	PRIMARY TERM CO-TERM	PAGE NO.	PRIMARY TERM CO-TERM	PAGE NO.	PRIMARY TERM CO-TERM	PAGE NO.
IONIC CONDUCTIVITY. (CONTD)		IRON CHLORIDE		KREBS-RINGER (CONTD)		LEAD (CONTD)	
MOISTURE CONTENT		ALUMINUM CHLORIDE>1601		GLUCOSE OXIDATION> 237		SOLID ELECTROLYTE 1385	
PHASE DIAGRAM --	818	CVD --	"	GLUCOSE SENSOR --	43		
PHYSICAL PROPERTY.	1	GADOLINIUM CHLOR. "	"	IMPLANTATION --	1687	LEAD ACID BATTERY	
SILVER IODIDE --	818	GASEOUS COMPLEX --	"	INIBITION --	1687	ANODE -- -- -- --> 360	
SOLID ELECTROLYTE 1385				KINETIC PHENOMENA	237	ANODIC FILM -- --> 725	
SOLID SOLUTION --	667	IRON CHROMIUM		LINEAR POTENTIAL	43	COBALT SULFATE --	
STRONTIUM FLUORIDE.	"	MODULATION SPECT.>1328		MASS TRANSPORT --	237	CONSTANT POTENTI. 360	
URANIUM FLUORIDE "	"	PASSIVATION FILM "	"	PLATINUM ELECTRO. 43		CORROSION -- -- "	
YTTRIA -- -- -- --	264			237		CORROSION FILM -->1848	
		IRON OXIDE		1687		CRYSTAL GROWTH -- 360	
IONIC CONDUCTOR		ANODE -- -- -- --> 419		UREA -- -- -- --	"	CYCLIC CORROSION 365	
DIFFUSION -- -- --> 242		ELECTROCATALYSIS >1831				DEEP DISCHARGE --	
ELLIPSCOMETRY --	"	HYDROGEN PEROXIDE "	"	KRYPTON		ELECTRIC VEHICLE >1321	
INTERFACE POTENT.	"	N-TYPE -- -- -- --	"	AMORPHOUS SILICON>1247		ELECTROLYTE FLOW "	
ROTATING ELECTRO. "	"	PHOTOANODE -- --	"	ARGON -- -- -- --	"	GRID CORROSION -- 725	
		PHOTOCURRENT -- 419		EPITAXIAL GROWTH "		HEAT TRANSFER --> 1321	
SILVER SALT SOLU. "	"	SEMICONDUCTOR -- "	"	NEON -- -- -- --	"	LEAD DIOXIDE --> 7	
						365	
IONIC MODEL		IRON OXIDE FILM		LAMINAR FLOW		LEAD DIOXIDE PLA.>1100	
LANTHANIDE METAL >1387		ANODIC FORMATION >2167		LIMITING CURRENT >1937		LEAD SULFATE -- --	7
METAL HALIDE GAS "		ANODIC OXIDATION > 442		MASS TRANSFER -- "		-- -- -- --> 991	
MOLECULAR STRUCT. "		BORATE BUFFER -- "		ROTATING HEMISP. "		OXIDATION -- -- "	7
TRANSITION METAL "		COMPOSITION -- --				PHOSPHORIC ACID -- 360	
VIBRATIONAL FREQ. "		-- -- 2167		LANTHANIDE METAL		-- 1848	
		PASSIVE FILM -- 442		IONIC MODEL -- -->1387		POSITIVE ELECTRO. "	
IONIC MOTION				METAL HALIDE GAS "		POSITIVE PLATE -- 7	
ALUMINUM FLUORIDE>1385		IRON PLATINUM		MOLECULAR STRUCT. "		PROPULSION -- -- 1321	
DEFECT INTERACTI. "		ALLOY -- -- -- -->2162		TRANSITION METAL "		SILVER OXIDE -- -- 725	
FLUORITE -- -- --	"	ELECTRODEPOSITION "		VIBRATIONAL FREQ. "		SULFURIC ACID -- 7	
IONIC CONDUCTIVI. "		FOIL -- -- -- --	"			THERMOPASSIVATION 1100	
LEAD -- -- -- --	"	FUSED SALT -- --	"	LANTHANUM OXYSUL.		WATER PASTE -- -- 991	
SOLID ELECTROLYTE "		PREPARATION -- --	"	CATHODOLUMINESC.> 571			
				ELECTRON BOMBARD. "		LEAD CHLORIDE	
IONIC PERMEABILI.		IRON SULFIDE		LOW ENERGY -- --	"	CHRONOAMPEROMETRY>1902	
ACTIN -- -- -- -->1471		CHEMICAL DIFFUSI.> 673		PHOSPHORS -- -- --	"	FUSED SALT --	
MEMBRANE PROTEINS "		IRON -- -- -- --> 683		TERBIUM -- -- -- --	"	LEAD SULFIDE -- --	
POLAROGRAPHY --	"	NONSTOICHIOMETRY 673		XPS -- -- -- --	"	OXIDATION -- -- --	
SPECTRIA -- -- --	"	POINT DEFECT -- "		YTTRIUM OXSULFI. "		POTASSIUM CHLORI. "	
		SCALE -- -- -- -- 683					
IR ABSORPTION		SULFIDATION -- --	"	LANTHANUM STRONT.		LEAD DIOXIDE	
CARRIER CONCENTR.> 260				COBALT OXIDE -- -->1817		ANODE -- -- -- --> 365	
SEMICONDUCTOR --	"	IRON SULFUR		ELECTRODE MATERI. "		CYCLIC CORROSION "	
SILICON -- -- -- --	"	CATHODE -- -- -- --> 887		POWER -- -- -- --	"	DEEP DISCHARGE --	
		LITHIUM BATTERY --	"	THERMOELECTRICITY "		LEAD ACID BATTERY> 7	
IRIDIUM		NONAQUEOUS CELL --	"			365	
ACID MEDIUM -- --> 93		POTASSIUM IRON S. "		LARGE GRAIN		LEAD SULFATE -- --	7
CHARGE CAPACITY --	"			GAAS -- -- -- --> 703		OXIDATION -- -- --	
HYDROXIDE-TYPE --	"	ISOTOPE SEPARATI.		SOLAR CELL -- --	"	POSITIVE PLATE --	
THIN FILM -- -- --	"	UNDERVOLTAGE -->2045		THIN FILM -- -- --	"	SULFURIC ACID -- --	
IRIDIUM OXIDE		JUNCTION DEPTH		LASER		LEAD DIOXIDE PLA.	
ANODIC -- -- -- -->2171		ANGLE LAPPING -->1982		GETTERING -- -- -->1436		LEAD ACID BATTERY>1100	
ANODIC FILM -- --> 742		ION IMPLANTATION "		LATTICE DAMAGE --		THERMOPASSIVATION "	
BLEACHING -- -- --	"	STAINING -- -- --	"	SILICON WAFER -- --	"		
						LEAD FLUORIDE	
COLORATION -- -- --	2171	JUNCTION POTENTI.		LATTICE DAMAGE		OTA -- -- -- -->1403	
-- -- -- -- 2171		POTASSIUM CHLORI.>1618		GETTERING -- -- -->1436		EQUILIBRIUM -- --	"
CORROSION STABIL. 742		SILVER -- -- -- --	"	LASER -- -- -- --	"	HYDROSTATIC PRES. "	
2171		SILVER CHLORIDE --	"	SILICON WAFER -- --	"	PHASE TRANSITION "	
ELECTROCHROMISM -- 742		THERMAL LIQUID --	"				
-- 2171		THERMOCELL -- --	"	LATTICE DEFECT		LEAD SULFATE	
MECHANISM -- -- --	"	TRANSPORT ENTROPY "		ANNEALING -- -- --> 809		LEAD ACID BATTERY> 7	
PH -- -- -- --	"			CADMIUM TELLURIDE "		-- -- -- --> 991	
		KEIL SALOMON		DEFECT ISOTHERM --		OXIDATION -- -- --	
IRON		ANODIZATION -- --> 544		ELECTRON MICROSC.		POSITIVE PLATE --	
ANODIC DISSOLUTION>2150		OXYGEN ISOTOPE --	"			SULFURIC ACID -- --	
AUGER SPECTROSCO.> 547		VANADIUM -- -- -- --	"	LATTICE MISMATCH		WATER PASTE -- -- 991	
CHLORIDE SOLUTION> 385				DIFRACTOMETRY --> 664			
CHROMATE -- -- --	547	KETONE		DOUBLE CRYSTAL --	"	LEAD SULFIDE	
CORROSION -- -- -->1363		ALCOHOL -- -- -- -->1301		GROUP III-V COMP. "		CHRONOAMPEROMETRY>1902	
		INDUCED INSTABIL. "		INDIUM PHOSPHIDE "		FUSED SALT -- -- --	
CREVICE CORROSION 385		SILICON GATE MOS --	"	INGAPAS -- -- -- --	"	LEAD CHLORIDE -- --	
CURRENT OSCILLAT. 1363				LPE -- -- -- --	"	OXIDATION -- -- --	
DISCHARGE DATA --> 357		KINETIC ANALYSIS		QUATERNARY -- -- --	"	POTASSIUM CHLORI. "	
INIBITION -- -- -- 385		ALKALINE SOLUTION>1693					
IRON SULFIDE -- --> 683		EPoxide DIMERS --	"	LAYER PERIODICITY		LEED	
OXIDATION -- -- -- 547		PHTHALIMIDE -- --	"	ANODIZATION -- -->1191		AUGER SPECTROSCO.> 450	
PALLADIUM -- -- --	"	REDUCTION -- -- --	"	BISMUTH TRITELLU. "		ELLIPSCOMETRY -- --	
PASSIVE OXIDE -- --	"	STRUCTURAL ANALY. "	"	ELLIPSCOMETRY -- --	"	GAAS -- -- -- --	"
PASSIVITY -- -- -- 1363				GALLIUM SELENIDE "		IN SITU -- -- -- --	"
POTENTIAL DISTRI. 2150		KINETIC PHENOMENA		LAYERED SEMICOND. "		RHEED -- -- -- --	"
SCALE -- -- -- -- 683		GLUCOSE OXIDATION> 237		ANODIZATION -- -->1191		SURFACE ANALYSIS "	
SECONDARY BATTERY 357		KREBS-RINGER -- --	"	BISMUTH TRITELLU. "		VPE -- -- -- --	"
SOLUBLE SYSTEM --		MASS TRANSPORT --	"	ELLIPSCOMETRY -- --	"		
SULFIDATION -- -- -- 683		PLATINUM ELECTRO. "	"	GALLIUM SELENIDE "		LIFE TEST	
SULFURIC ACID -- -- 1363				LAYER PERIODICITY "		OXIDE COATING -- -->1439	
		KINETIC STABILITY				PERCHLORIC ACID --	
THIN FILM -- -- -- 2150		NITRATE ION -- -->2095		LEAD		POLARIZATION -- --	
TITANIUM -- -- -- -- 357		OXYGEN EXCHANGE --	"	ALUMINUM FLUORIDE>1385		SODIUM CHLORIDE --	
XPS -- -- -- -- 547		POTASSIUM NITRATE "		DEFECT INTERACTI. "		TITANIUM ANODE --	
		RAMAN SPECTROSCO. "		FLUORITE -- -- --	"		
IRON ALLCY		KREBS-RINGER		IONIC CONDUCTIVI. "		LIFETIME	
COAL CHAR -- -- --> 894		ANODIC OXIDATION > 43		IONIC MOTION -- --	"	CZCHRSLSKI -- -->1142	
FERROUS SULFIDE --	"	-- -- -- -->1687				INTEGRATED CIRCU. "	
GASIFICATION -- --	"	DIABETES -- -- -- 43					
SULFIDATION -- -- --	"						

PRIMARY TERM CO-TERM	PAGE NO.	PRIMARY TERM CO-TERM	PAGE NO.	PRIMARY TERM CO-TERM	PAGE NO.	PRIMARY TERM CO-TERM	PAGE NO.
LIFETIME (CONTD)		LIQUID CATHOLYTE (CONTD)		LITHIUM BATTERY (CONTD)		LITHOGRAPHY (CONTD)	
MINORITY CARRIER 1142		THIONYL CHLORIDE 981		ORGANIC ELECTROL. 523		PROCESSING - - - 1514	
NICKEL CADMIUM -> 720				729		PULSE ELECTROPLA. "	
PATTERN RECOGNIT. "		LIQUID CRYSTAL		PHASE DIAGRAM - - 608		RADIATION SENSIT. 154	
SILICON - - - - - 1142		DEFECT DENSITY ->1771		POTASSIUM IRON S. 887		RADIATION YIELD - 483	
THERMAL PROCESSI. "		DEFECT GENERATION> 85		POTENTIAL - - - - - 608		RESIST - - - - - 694	
LIFT-OFF METALLI.		ELECTRIC FIELD - 1771		RATE CAPABILITY - 523		RESIST MATERIAL - 483	
ALUMINUM ALLOY ->1257		NEUMATIC DISPLAY - 85		SECONDARY BATTERY "		WAFER FABRICATION 1703	
SPUTTER DEPCOSITI. "		OXIDE THICKNESS - 1771		SPECTROSCOPY - - 608		X-RAY - - - - - 694	
		SILICON DIOXIDE - "		SYSTEM STABILITY 523			
LIGHT ABSORPTION				TANTALUM - - - - - 507		LONG TERM TESTING	
AQUEOUS ELECTROL.>1868		LIQUID INSULATION		TETRAHYDROFURAN - "		TIME VARIATION ->1674	
DARK PCTENTIAL - "		GAS INSULATION -> 55C		523		WATER ELECTROLYZ. "	
FLATBAND POTENTI. "		INSULATION - - - - "		THIONYL CHLORIDE 981			
GROUP II-VI COMP. "		SOLID INSULATION "		TITANIUM DISULFI. 608		LOW ENERGY	
IODINE DOPING - - "				VOLTAGE STEPS - - "		CATHODOLUMINESCE.> 571	
OPTICAL ABSORPTI. "		LIQUID JUNCTION				ELECTRON BOMBARD. "	
ZINC SELENIIDE - - "		ACETONITRILE - -> 603		LITHIUM BORON		LANTHANUM OXSULF. "	
		CHARGE TRANSFER ->1011		ANODE MATERIAL -> 866		PHOSPHORS - - - - "	
LIGHT EFFECT		DIGITAL SIMULATI. "		ANODIC DISCHARGE > 993		TERBIUM - - - - - "	
ANODE - - - - -> 972		EFFICIENCY - - - - 603		FELTMETAL - - - - "		XPS - - - - - "	
ELECTROOXIDATION "		GAAS - - - - - "		MOLTEN SALT - - - - "		YTIPIUM OXSULFI. "	
PHOTOCNDUCTIVITY "		HOLE INJECTION - 1011		MOLTEN SALT BATT. 866			
THIOCYANATE - - - "		ILLUMINATED - - - "		THERMAL ANALYSIS "		LOW PRESSURE	
		PHOTOANODE - - - "		VOLTAGE REGULATI. 993		CVD - - - - -> 833	
LIGHT INTENSITY		PHOTOVOLTAIC CELL 603				- - - - ->1019	
COBALT CONCENTRA.> 944		REGENERATIVE CELL "		LITHIUM BORON CH.		ELECTROTRANSPORT >1811	
CORROSION SUPPRE. "		SEMICONDUCTOR - - 1011		ELECTROLYTE SALT >1445		EPITAXIAL LAYERS >1134	
PHOTOANODE - - - "		SINGLE CRYSTAL - 603		ENERGY CONVERSION "		GAAS EPI-LAYER - - "	
SULFATE CONCENTR. "		SOLAR CELL - - - 1011		HERMETIC D-CELL - "		HIGH RESISTANCE - 1811	
TITANIUM DIOXIDE "				THIONYL CHLORIDE "		ION IMPLANTATION 1019	
		LIQUID STANDARD				MICROGRAVITY - - 1811	
LIGHT-EMITTING		INTEGRATED CIRCU.> 103		LITHIUM CELL		PHOSPHORUS DOPING 833	
ALUMINUM ARSENIDE> 637		PASSIVATION LAYER "		CATHODE - - - - -> 497		1019	
DIODE - - - - - "		REFRACTIVE INDEX "		SECONDARY BATTERY "		POLYSILICON FILM 833	
DISLOCATION - - - "		TRANSPARENT FILM "		VANADIUM OXIDE - "		PURIFICATION - - 1811	
GAAS - - - - - "						PYROLYSIS - - - 1134	
CALCIUM - - - - - "		LITHIUM		LITHIUM CHLORIDE		RESISTIVITY - - - 833	
QUANTUM EFFICIEN. "		ABUSE TOLERANCE ->1637		ALUMINUM CHLORIDE>1650		SILICON FILM - 1019	
SILICON - - - - - "		ALUMINUM POWDER ->1853		ANODE MECHANISM -> 176		THORIUM - - - - - 1811	
		ANODIC STABILITY > 507		ANODIC CORROSION >1087			
LIMITING CURRENT		BATTERY - - - - - 1637		>1093		LOW TEMPERATURE	
LAMINAR FLOW - ->1937		CARBON - - - - ->2052		CALCIUM ANODE - - 176		CHRONOCOULOMETRY > 579	
MASS TRANSFER - - "		CATHODE - - - - - "		CONDUCTIVITY - - 1650		CVD - - - - ->1728	
ROTATING HEMISP. "		COLD-ROLLED STEEL 507		EUTECTIC - - - - - 1087		DIELECTRICS - - - "	
		CORROSION RESIST. "		- - - - - 1093		DOPING - - - - ->1779	
LINE EDGE PROFILE		COULOMETRY - - ->2035		FUEL CELL - - - -> 960		ELECTROHYDRODIME. 579	
DEVELOPER TEMPER.>2026		CYCLIC VOLTAMMET. "		FUSED SALT - - - 176		ETHYL CINNAMATE - "	
DEVELOPMENT RATE "		DICHALCOGENIDE -> 349		- - - - - 1087		HIGH PRESSURE ->1822	
ELECTRON BEAM - - "		DISCHARGE - - ->2168		- - - - - 1093		INFRARED ABSORPT. 1728	
OPTICAL EXPOSURE "		DTA - - - - - 1637		- - - - - 1650		ION IMPLANTATION 1779	
PHOTORESIST - - - "		HEXAFLUOROARSENA.> 181		MIGRATION POLAR. 960		METHYL CINNAMATE 579	
POSITIVE DIAZO - - "		INTERCALATION - - 349		MOLTEN CARBONATE "		OXIDATION - - - 1728	
		LITHIUM BATTERY - 507		MOLTEN SALT BATT. "		- - - - - 1779	
LINE WIDTH		LOW VOLTAGE BEHA. 349		OVERVOLTAGE - - 176		OXIDE FILM GROWTH 1822	
DEVELOPING TIME ->1430		METAL SULFIDE - 1853		POTASSIUM CHLORI. 960		POLYMERIZATION - 1728	
ELECTRON BEAM - - "		NEGATIVE ELECTRO. "		1087		POLYSILICON - - 1779	
POLYMETHYLMETHAC. "		ORGANIC PRODUCT - 181		1093		REACTION ORDER - 579	
RESIST - - - - - "		POWDER ELECTRODE 1853		SULFIDATION - - - "		SILANE - - - - - 1728	
SLOPE ANGLE - - - "		REACTION MECHAN. 2168		THERMAL BATTERY - 176		SILICON - - - - - 1822	
		RECHARGEABLE CELL 1853		VOLTAMMETRY - - - 1087		STEAM OXIDATION - "	
LINEAR POLARIZAT.		REDUCTION - - - 2035		- - - - - 1093		WLSI DEVICE - - - 1779	
ANALYTIC SOLUTION>2081		SECONDARY BATTERY 349		LITHIUM NITRIDE		LOW VOLTAGE BEHA.	
CORROSION POTENT.> 891		SOLID CORROSION - 181		ACTIVITY COEFFIC.> 248		DICHALCOGENIDE -> 349	
FOURIER ANALYSIS 2081		SULFUR DIOXIDE - 1637		MOLTEN SALT - - - "		INTERCALATION - - "	
NUMERICAL METHODS 991		SULFUR OXYCHLORI. 2035		NITRIDE SOLUTION "		LITHIUM - - - - - "	
PASSIVE FILM - - 2081		TANTALUM - - - - 507				SECONDARY BATTERY "	
POTENTIAL DISTRI. "		TETRAHYDROFURAN - 181		LITHIUM OXIDE		TOPOCHEMICAL CELL "	
SCRATCH - - - - - "		507		CERAMICS - - - -> 1			
THREE POINT - - - 891		THIONYL CHLORIDE 2052		DTA - - - - - "		LOWER TEMPERATURE	
		2168		IONIC CONDUCTIVI. "		CARBON DIOXIDE ->2012	
LINEAR POTENTIAL		TOPOCHEMICAL CELL 349		MOISTURE CONTENT "		FURNACE - - - - - "	
ANODIC OXIDATION > 43				PHYSICAL PROPERT. "		GAS FLOW METHOD - "	
DIABETES - - - - - "		LITHIUM ANODE				HYDROGEN - - - - - "	
GLUCOSE SENSOR - "		DISCHARGE REACT.> 513		LITHOGRAPHY		OXYGEN PRESSURE - "	
IMPLANTATION - - - "		PRIMARY CELL - - - "		COPOLYMER - - - -> 154		PRESSURE CONTROL "	
KREBS-RINGER - - - "		SOLUBLE CATHODE - "		ELECTRON BEAM -> 694		WUSTITE PHASE - - "	
PLATINUM ELECTRO. "		THIONYL CHLORIDE "		- - - - ->1699			
				ELECTRON RESIST - "		LPE	
LIQUID AMMONIA		LITHIUM BATTERY		->1703		BORON DOPING - -> 138	
ELECTRON INJECTI.>207C		ADSORPTION - - -> 608		GLYCIDYL METHACR. 1699		DIFFRACTIONMETRY-> 664	
SEMICONDUCTOR - - "		ANODIC STABILITY > 507		1703		DOPANT DISTRIBUT. 138	
SOLVATED ELECTRON "		CAPACITY - - - - - 523		GOLD COATING - ->1514		DOPING PROFILE -> 296	
LIQUID ASSOCIATI.		CATHODE - - - - -> 887		HALOSTYRENE - - 1699		DOUBLE CRYSTAL - 664	
ALUMINUM - - - - ->1992		CELL KINETICS - - 608		ION BEAM - - - - -> 483		GAAS - - - - - 296	
ANTIMONY - - - - - "		COLD-ROLLED STEEL 507		METHACRYLIC ACID 154		GROUP III-V COMP. 664	
DTA - - - - - "		CORROSION RESIST. "		METHYLMETHACRYL. "		GROWTH PROCESS 296	
GALLIUM - - - - - "		DISSOLVED SULFUR 523		NEGATIVE - - - - - 1699		INDIUM PHOSPHIDE 664	
PHASE DIAGRAM - - "		HEXAFLUOROARSENA. 507		PATTERN DUPLICAT. 483		INGAPAS - - - - - "	
TERNARY PHASE - - "		HYDROLYSIS - -> 981		POLYDIMETHYLSILC. "		LATTICE MISMATCH - "	
		IMPURITY - - - - - 694		POLYMER - - - - - 694		MELTBACK - - - - - 138	
LIQUID CATHOLYTE		IRON SULFUR - - - 887		POLYMER RESIST - 1699		MOBILITY PROFILE 296	
HYDROLYSIS - - -> 981		LIQUID CATHOLYTE 981		- 1703		QUARTERNARY - - 664	
IMPURITY - - - - - "		LITHIUM - - - - - 507		POLYMETHACRYLONI. 694		SILICON - - - - - 138	
LITHIUM BATTERY - - "		METALLIC OXSALT > 729		POLYMETHYLMETACR. 483		TIN - - - - - 296	
		NONAQUEOUS CELL - 887		POSITIVE RESIST - 154			

PRIMARY TERM CO-TERM	PAGE NO.	PRIMARY TERM CO-TERM	PAGE NO.	PRIMARY TERM CO-TERM	PAGE NO.	PRIMARY TERM CO-TERM	PAGE NO.
LSI DEVICE		MASS SPECTROSCOPY (CONTD)		MEMBRANE		METHACRYLATE (CONTD)	
BORON GETTERING ->1754		VAPORIZATION - - - 1825		ELECTRET - - - ->1708		2,2,2-TRICHLOROE. 1635	
ORGANIC RESIST ->1531				HETEROCHARGE - - - "			
OXYCHLORIDE - - - 1754		MASS TRANSFER		POLARIZATION - - - "		METHACRYLIC ACID	
PHOSPHORUS - - - - "		ELECTROLYSIS - -> 398		POLYSTYRENESULF. "		COPOLYMER - - - -> 154	
PIPE YIELD - - - - "		LAMINAR FLOW - ->1937		POLYVINYL ALCOHOL "		LITHOGRAPHY - - - - "	
SILICON - - - - - "		LIMITING CURRENT "		POTASSIUM - - - - - "		METHACRYLOYL CHL.>1881	
SILICON DIOXIDE - 1531		PERIODIC CURRENT 398		SODIUM - - - - - "		METHYL METHACRYL. 154	
SPUTTER ETCH - - - "		ROTATING DISK - - - "				POLYMER MIXTURE - 1881	
		ROTATING HEMISPHER. 1937				POSITIVE RESIST - 154	
LUMINESCENCE				MEMBRANE PROTEINS		RADIATION SENSIT. 154	
ACTIVATOR - - - -> 106		MASS TRANSPORT		ACTIN - - - - ->1471			
ALKALI RARE EARTH>2206		CATHODE - - - -> 23		IONIC PERMEABIL. "			
AMMONIUM DICHROM.>1975		CONVECTION - - - - "		POLAROGRAPHY - - - "			
BLUE LIGHT EMISS.> 341		COPPER - - - - - "		SPECTRIN - - - - - "			
CESIUM COACTIV. 2206		CURRENT DENSITY - - - "				METHACRYLOYL CHL.	
CONCENTRATION - - - 106		ELECTRODEPOSITION "		MERCURY		METHACRYLIC ACID >1881	
GALLIUM - - - - - 341		GLUCOSE OXIDATION> 237		ANGIIC OXIDATION > 768		METHYL METHACRYL. "	
GLASSY PHOSPHORS 2206		KINETIC PHENOMENA "		CADMIUM TELLURIDE "		POLYMER MIXTURE - "	
METAPHOSPHATE - - - "		KREBS-RINGER - - - "		NATIVE OXIDE - - - "		POSITIVE RESIST - "	
OXIDATION - - - - 1975		PLANE VERTICAL - 23		TELLURIUM DIOXIDE "			
PHOSPHOR LUMINES.		PLATINUM ELECTRO. 237				METHANE	
POWDERED PHOSPHOR 106				METAL COMPLEX		ELECTROOXIDATION > 775	
QUENCHING MECHAN. "		MATERIAL SELECT.		BITHIAZOLE - - - ->2091		ETHANE - - - - - "	
RADIATION - - - - - "		CHEMICAL ETCHING > 287		BLEOMYCIN - - - - - "		FUEL CELL - - - - - "	
RARE EARTH - - - - - "		EPITAXIAL LAYER - - - "		CYCLIC VOLTAMMET. "		N-BUTANE - - - - - "	
SOLUTION GROWTH - 341		HYDROCHLORIC ACID "		POLAROGRAPHY - - - "		PROPANE - - - - - "	
TERBIUM ACTIVATI. 2206		INDIUM PHOSPHIDE "		PYRIMIDINE - - - - - "		TRIFLUOROMETHANE "	
THERMAL DECOMPOS. 1975		PHOSPHORIC ACID - - - "		REDOX - - - - - "			
ZINC SELENIDE - - - 341				TALLYSCMYCIN - - - "			
ZINC SULFIDE - - - 1975						METHYL CINNAMATE	
		MATHEMATICAL MOD.		METAL DEPOSITION		CHRONOCULOMETRY > 579	
LUTETIUM		CATHODIC REACTION> 15		ACTIVATOR - - - ->1671		ELECTROHYDRODIME. "	
DIPHthalocYANINE >1339		COPPER DEPOSITION>2118		BACKSCATTERING - - - "		ETHYL CINNAMATE - "	
ELECTROCHROMISM - - - "		CORROSION - - - ->1662		ELECTROLESS - - - - "		LOW TEMPERATURE - "	
OXIDATION STATE - - - "		CREVICE CORROSION 15		GLASS SUBSTRATE - - - "		REACTION ORDER - - - "	
		CURRENT DISTRIBU. "		MATHEMATICAL MOD.>2125			
		2118		MULTIPLE REACTIO. "		METHYL METHACRYL.	
MANGANESE CHLORI.		ELECTRODEPOSITION>1176		PALLADIUM - - - - 1671		COPOLYMER - - - -> 154	
FUSED SALT - - - ->1876		2118		POROUS CATHODE - 2125		LITHOGRAPHY - - - - "	
GLASS FORMING - - - "		FILM GROWTH - - ->1261				METHACRYLIC ACID "	
MOLTEN SALT - - - - - "		FLUIDIZED ELECTRO. 1176		METAL HALIDE GAS		>1881	
TBA CHLORIDE - - - - "		GAS LIFT - - - - 2118		BIRGE-SPONER - ->1396		METHACRYLOYL CHL.	
TBA IODIDE - - - - - "		HYDROGEN EVOLUTI. "		DISSOCIATION - - - - "		POLYMER MIXTURE - "	
TETRA-N-BUTYLAMM. "		METAL DEPOSITION >2125		IONIC MODEL - - ->1387		POSITIVE RESIST - 154	
TRANSPERT PROPER. "		MULTIPLE REACTIO. "		LANTHANIDE METAL "		RADIATION SENSIT. 154	
		NOBLE METAL LAYER 1261		MODEL CALCULATION 1396			
MANGANESE PORPHY.		PIT GROWTH - - - - 1662		MOLECULAR STRUCT. 1387		MICROCIRCUIT	
PHOTOELECTROCHEM. > 705		PIT INITIATION - - - "		THERMOCHEMISTRY - 1396		FLUORINE GAS - ->1946	
PLATINUM ELECTRO. "		PITTING - - - - - 15		TRANSITION METAL 1387		INDUCTION PERIOD "	
WET SOLAR CELL - - - "		POROUS CATHODE - 2125		VIBRATIONAL FREQ. "		SILICON ETCH - - - "	
		SALT FILM - - - - 1662					
MARCASITE		SUBSTRATE DIFFUS. 1261		METAL QUANTITY		MICROGRAVITY	
CARBON STEEL - - -> 911		TRANSPORT LAW - 1662		DIRECT CURRENT -> 881		ELECTROTRANSPORT >1811	
ELECTRODEPOSITION "		VERTICAL ELECTRO. 2118		PLATING CYCLE - - - "		HIGH RESISTANCE - - - "	
HYDROGEN SULFIDE "				PULSED PLATING - - - "		LOW PRESSURE - - - - "	
PYRITE - - - - - - - "						PURIFICATION - - - - "	
		MEASUREMENT				THORIUM - - - - - "	
MASKING		CALCIUM FLUORIDE >1360		METAL SULFIDE			
ETCHING - - - - ->1004		CHEMICAL POTENT. "		ALUMINUM POWDER ->1853			
ORIFICE SIZE - - - - - "		COMPLEX - - - - ->2104		LITHIUM - - - - - "		MICROMINUTRIZAT.	
SAPPHIRE - - - - - - - "		COMPLEX ION MODEL>2098		NEGATIVE ELECTRO. "		ELECTROSTATICS ->1426	
		CONDUCTIVITY - - - - "		POWDER ELECTRODE "		FILTRATION - - - - - "	
MASKING STRUCTURE		- - - 2104		RECHARGEABLE CELL "		PHOTOLITHOGRAPHY "	
ALUMINUM DIFFUSI.> 292		FUSED SALT - - - 2098				PHOTORESIST - - - - "	
PLANAR GALLIUM - - - "		- - - 2104		METALLIC CRYSTAL		PLASMA ETCHING - - - "	
SILICON - - - - - - - "		MOLAR VOLUME - - - 2098		LITHIUM BATTERY -> 729			
		- - - 2104		ORGANIC ELECTROL. "			
MASS HEAT BALANCE		OXYGEN - - - - - 1360				MICROSTRUCTURE	
ENERGY STORAGE -> 713		SOLID ELECTROLYTE "		METALLIZATION		AUSTENITIC - - - -> 374	
HYDROGEN-CHLORINE "		TERNARY SYSTEM - 2098		ALUMINUM ALLOY -> 110		CORROSION - - - - - "	
REGENERATION - - - - "		- 2104		CHROMIUM - - - ->1047		DUPLEX 308 - - - - - "	
STOICHIOMETRY - - - - "				CORROSION TEST - 110		GRAIN STRUCTURE->1061	
		MECHANISM		DEGRADATION - - - 1047		INTERGRANULAR - - - 374	
MASS SPECTROMETRY		ANGIIC - - - - ->2171		IMPACT DIODE - - - - "		NICKEL - - - - - 1061	
AMORPHOUS SEMICC.> 688		BLEACHING - - - - - "		INTEGRATED CIRCU. 110		OXIDATION - - - - - "	
CESIUM - - - - - -> 660		COLORATION - - - - - "		INTERDIFFUSION - 1047		PHASE TRANSFORMA. 374	
DEPOSITION - - - - - 688		CORROSION STABIL. "		PLASTIC ENCAPSUL. 110		PITTING - - - - - - - "	
DEPTH PROFILE - - - 660		ELECTROCHROMISM - - - "		PLATINUM - - - - - 1047		STAINLESS STEEL - - - "	
DOPANT - - - - - - - "		IRIDIUM OXIDE - - - - "		SILICON - - - - - - - "			
GAAS - - - - - - - - - "		PH - - - - - - - - - "		SILVER - - - - - - - - "		MICROWAVE	
HYDROGEN CONTENT 688						ION ROLE - - - - ->1024	
PHOTOVOLTAIC PRO. "		MELANIN		METALORGANICS		NEUTRAL SPECIES - - - "	
SECONDARY ION - - - 660		DEPOLARIZATION ->1207		CVD - - - - - - - ->2031		PLASMA ETCHING - - - "	
SILICON - - - - - - - "		ELECTRET BEHAVIOR "		GALLIUM ANTIMONI. "		SILICON - - - - - - - "	
- - - - - - - - - 688				SEMICONDUCTOR - - - "			
ULTRAHIGH VACUUM 660		MELT COMPOSITION				MIGRATION	
MASS SPECTROSCOPY		CHLORALUMINATE -> 231		METAPHOSPHATE		CONVECTION - - - ->1713	
DIAZIDE-S-SULFON.> 860		ELECTROOXIDATION "		ALKALI RARE EARTH>2206		DIFFUSION - - - - - "	
DISSOCIATION - - ->1825		MOLTEN SALT BATT. "		CESIUM COACTIV. "		MOLTEN SALT - - - - - "	
ELECTRON BEAM - - - 860		SULFUR - - - - - - - "		GLASSY PHOSPHORS "		POROUS ELECTRODE "	
EPR - - - - - - - - - "				LUMINESCENCE - - - - "		TRANSPORT EQUATI. "	
D-NAPHTHOQUINONE - - - "		MELTBACK		TERBIUM ACTIVATI. "			
PHENOLIC-TYPE - - - - "		BORON DOPING - -> 138				MIGRATION POLARA.	
RESIN - - - - - - - - - "		DOPANT DISTRIBUT. "		METHACRYLATE		FUEL CELL - - - -> 960	
SELENIUM SULFIDE 1825		LPE - - - - - - - - - "		CRCSSLINKED TYPE >1635		LITHIUM CHLORIDE - - - "	
THERMODYNAMICS - - - "		SILICON - - - - - - - "		ELECTRON RESIST - - - "		MOLTEN CARBONATE "	
				HOMOPOLYMER - - - - - "		MOLTEN SALT BATT. "	
				INTEGRATED CIRCU. "		POTASSIUM CHLORI. "	

PRIMARY TERM CO-TERM	PAGE NO.	PRIMARY TERM CO-TERM	PAGE NO.	PRIMARY TERM CO-TERM	PAGE NO.	PRIMARY TERM CO-TERM	PAGE NO.
MILD STEEL		MOLECULAR BEAM (CONTD)		MOLYBDENUM RETAI.		N-ALKYLPYRIDINIUM	
ALTERNATING VOLT.>1908		EPITAXY - - - - -	1761	CARBON IMPURITY -> 935		ALUMINUM CHLORIDE>1644	
CORROSION POTENT. "		ION IMPLANTATION "		HEAT EXCHANGER - "		CONDUCTIVITY - - - "	
FARADAIC RECTIFI. "		SILICON - - - - -		SILICON CRYSTAL - "		DENSITY - - - - - "	
PASSIVATION - - - "		ULTRAHIGH VACUUM "				FUSED SALT - - - - "	
POLARIZATION - - - "				MONOCRYSTAL		HALIDE - - - - - "	
		MOLECULAR DBITAL		BETA-ALUMINA - ->1513		TRANSPORT - - - - "	
MINORITY CARRIER		CHLOROACRYLATE ->1829		RADIOCHEMISTRY - "		VISCOSITY - - - - - "	
CZOCHELSKI - - ->1142		ELECTRON BEAM - -		SODIUM-22 LABEL - "			
INTEGRATED CIRCU.		INTEGRATED CIRCU. "				N-BUTANE	
LIFETIME - - - - -		POLYMER - - - - -		MONODISPERSE		ELECTROOXIDATION > 775	
SILICON - - - - -		POSITIVE RESIST - "		ELECTRON RESIST -> 696		ETHANE - - - - - "	
THERMAL PROCESSI. "		TRIFLUOROETHYL - "		NEGATIVE - - - - -		FUEL CELL - - - - - "	
				POLYSTYRENE - - - -		METHANE - - - - - "	
MIXED ALKALI EFF.		MOLECULAR STRUCT.		MORPHOLOGY		PROPANE - - - - - "	
CONDUCTIVITY - ->2144		IONIC MODEL - - ->1387		ANTIMONY - - - -> 875		TRIFLUOROMETHANE "	
GLASS - - - - -		LANTHANIDE METAL "		CRYSTAL GROWTH - "			
HYDRATE MELT - - -		METAL HALIDE GAS "		CZOCHELSKI - - - -		N-HEPTYLVIOLOGEN	
TRANSITION TEMPE. "		TRANSITION METAL "		DOPED MELT - - - -		CATION FILM - - -> 167	
		VIBRATIONAL FREQ. "		INSTABILITY - - - -		DISPLAY DEVICE - "	
MIXED CRYSTAL PH.				SILICON CRYSTAL - "		GOLD SUBSTRATE - "	
GALLIUM - - - ->1400		MOLTEN CARBONATE					
INDIUM ARSENIDE - "		FUEL CELL - - - -> 960		MORPHOLOGY CONTR.		N-TYPE	
SOURCE GAS PHASE "		LITHIUM CHLORIDE "		NEODYMIUM PENTAP.>1567		ACETONITRILE - -> 59	
THERMODYNAMICS -		MIGRATION POLARA. "		POLYMERIZATION - "		ELECTROCATALYSIS >1831	
VPE - - - - -		MOLTEN SALT SAT. "		POLYPHOSPHORIC A. "		GAAS - - - - - 59	
		POTASSIUM CHLORI. "		SINGLE CRYSTAL - "		HYDROGEN PEROXIDE 1831	
MIXED CRYSTALS						IRON OXIDE - - - -	
CADMIUM HALIDE -> 325		MOLTEN NITRATE				P-TYPE - - - - - 59	
CRYSTALLOGRAPHY -		CATHOLYTE - - ->1496		MOS		PHOTOANODE - - - 1831	
DIFFRACTION - - - -		CATION RADIUS - - -		INTEGRATED CIRCU.> 20C		PHOTOELECTROCHEM. 59	
POLYTYPISM - - - -		NITRATE SALT - - -		SEMICONDUCTOR - - -		SEMICONDUCTOR - - -	
VAPOR GROWN - - - -		OPEN PAN STUDY - "		SILICON - - - - -		SURFACE EFFECT - -	
		REDUCTION - - - -					
MOBILE ION		THERMAL BATTERY - -		MOS CAPACITOR		N-TYPE CONDUCTION	
INTERFACE STATE ->1979				INTERFACE STATE ->1979		ACETONITRILE - ->1892	
INTERFERENCE - - -		MOLTEN SALT		INTERFERENCE - - -		ELECTRODE BEHAVI. "	
MOS CAPACITOR - - -		ACTIVITY COEFFIC.> 248		MOBILE ION - - - -		FERRIC OXIDE - - -	
SILICON - - - - -		ANODIC DISCHARGE > 993		SILICON - - - - -			
		BULK PHASE - - ->1467				NAFION MEMBRANE	
MOBILE SODIUM		CARBON DIOXIDE -> 328		MOS-LSI		BROMINE DIFFUSION> 36	
HYDROCHLORIC ACID> 149		CARBONATE - - -> 527		FABRICATION - - ->1415		CONDUCTANCE - - ->1682	
OXIDATION - - - - -		COMPOSITION PROF. "		INTEGRATED CIRCU. "		DIFFUSION - - - - -	
PASSIVATION - - - -		CONVECTION - - ->1713		POLYSILICON - - - -		DIFFUSION COEFFICI. 36	
SILICON DIOXIDE - -		DIFFUSION - - - -				FUEL CELL - - - - - 1682	
SODIUM NEUTRALIZ. "		EMF - - - - - 1467		MOS-LSI PROCESS		HALOGEN - - - - -	
		FELTMETAL - - - - 993		CHROMIUM FILM - ->1794		HYDROGEN - - - - -	
MOBILITY		FUEL CELL - - - - 527		GAS PLASMA - - - -		ION EXCHANGE - - - 36	
CADMIUM SULFIDE ->1820		FUSED SALT - - ->1876		PHOTOMASK - - - -		POLYMER - - - - - 1682	
FLASH EVAPORATION "		GAS SOLUBILITY - 328		REVERSAL ETCHING "		TRANSPORT PROPER. "	
INDIUM COPING - - -		GLASS FORMING - 1876					
		LITHIUM BORON - 993		MOSSBAUER SPECTR.		NATIVE OXIDE	
MOBILITY PROFILE		LITHIUM NITRIDE - 248		ANODIC OXIDATION > 187		ANODIC OXIDATION > 768	
DOPING PROFILE -> 296		MANGANESE CHLORI. 1876		BORATE BUFFER - - -		CADMIUM TELLURIDE "	
GAAS - - - - -		MIGRATION - - - - 1713		COBALT - - - - -> 391		MERCURY - - - - -	
GROWTH PROCESS - -		NITRIDE SOLUTION 248		COBALT DIOXIDE - 187		TELLURIUM DIOXIDE "	
LPE - - - - -		OXYGEN - - - - - 328		COBALT HARDENED - 391			
TIN - - - - -		POROUS ELECTRODE 1713		COBALT CXYHYDROX. 391		NEGATIVE	
		SILVER CHLORIDE - 1467		ELECTRODEPOSITION> 204		ELECTRON BEAM - ->1699	
MODEL CALCULATION		SODIUM CARBONATE 328		GOLD ELECTRODEPC. 391		ELECTRON RESIST -> 696	
BIRGE-SPONER - ->1396		SODIUM CHLORIDE - 1467		STEADY STATE EQU. 527		GLYCIDYL METHACR. "	
DISSOCIATION - - -		SULFUR DIOXIDE - 328		SURFACE TENSION - 1467		HALOSTYRENE - - -	
METAL HALIDE GAS "		TBA CHLORIDE - 1876		THERMAL PREPARAT. 204		LITHOGRAPHY - - - -	
THERMOCHEMISTRY -		TBA IODIDE - - - -		TIN NICKEL ALLOY "		MONODISPERSE - - 696	
MODIFIED ELECTRO.		TETRA-N-BUTYLAM. "				POLYMER RESIST - 1699	
CHLORINATION - - -> 500		TRANSPORT EQUIV. 1713		MOTT-SCHOTTKY		POLYSTYRENE - - - 696	
CYCLODEXTRIN - - -		TRANSPORT PROPER. 1876		CAPACITANCE - - ->1505			
SELECTIVITY - - - -		VOLTAGE REGULATI. 993		FLATBAND POTENTI. "		NEGATIVE ELECTRO.	
				POTENTIAL DISTRI. "		ALUMINUM POWDER ->1853	
MODULATION SPECT.		MOLTEN SALT BATT.		TITANIUM DIOXIDE "		LITHIUM - - - - -	
IRON CHROMIUM - ->1328		ANODE MATERIAL -> 866				METAL SULFIDE - - -	
PASSIVATION FILM "		CHLORALUMINATE -> 231		MOVING BOUNDARY		POWDER ELECTRODE "	
		ELECTROOXIDATION "		IMPURITY REDISTR.>1939		RECHARGEABLE CELL "	
MOISTURE CONTENT		FUEL CELL - - -> 960		IMPURITY SEGREGA. "			
CERAMICS - - - - -> 1		LITHIUM BORON - 866		INTERFACIAL FLUX "		NEGATIVE RESIST	
OTA - - - - -		LITHIUM CHLORIDE 960		NUMERICAL SOLUTI. "		CHLOROMETHYLATED >1628	
IONIC CONDUCTIVI. "		MELT COMPOSITION 231		SILICON OXIDATION "		DRY ETCHING - - - -	
LITHIUM OXIDE - - -		MIGRATION POLARA. 960				POLYSTYRENE - - - -	
PHYSICAL PROPERT. "		MOLTEN CARBONATE "		MULTILAYER ANALY.		SUBMICRON TECHNOL. "	
		POTASSIUM CHLORI. "		CURRENT DENSITY ->1479			
MOLAR VOLUME		SULFUR - - - - - 231		RESISTIVITY - - - -		NEMATIC DISPLAY	
COMPLEX - - - - ->2104		THERMAL ANALYSIS 866		SPREADING RESIST. "		DEFECT GENERATION> 85	
COMPLEX ION MODEL>2098						LIQUID CRYSTAL - -	
CONDUCTIVITY - - -		MOLTEN SILICON		MULTIPHASE DIFFU.			
- - - 2104		DISSOLUTION - - -> 634		OXYGEN DIFFUSION >1111		NEODYMIUM PENTAP.	
FUSED SALT - - - - 2098		FICKS LAW - - - - -		ZIRCALOY-4 - - - -		MORPHOLOGY CONTR.>1567	
- - - 2104		SILICON CARBIDE - -				POLYMERIZATION - -	
MEASUREMENT - - - 2098				MULTIPLE REACTIO.		POLYPHOSPHORIC A. "	
- - - 2104				COMPETING REACTI.>1928		SINGLE CRYSTAL - - -	
TERNARY SYSTEM - 2098		MOLYBDENUM		MATHEMATICAL MOD.>2125			
- - - 2104		ARSINE GAS - - -> 300		METAL DEPOSITION "		NEON	
		DEVICE QUALITY - -		POROUS CATHODE - - -		AMORPHOUS SILICON>1247	
MOLECULAR BEAM		EPITAXY - - - - -		POROUS ELECTRODE 1928		ARGON - - - - -	
ANTIMONY EVAPORA.>1761		GAAS - - - - -		REACTOR ANALYSIS "		EPITAXIAL GROWTH "	
ARSENIC - - - - -		GERMANIUM - - - -				KRYPTON - - - - -	
DOPING - - - - -		TRIMETHYLGALLIUM "					

PRIMARY TERM CO-TERM	PAGE NO.	PRIMARY TERM CO-TERM	PAGE NO.	PRIMARY TERM CO-TERM	PAGE NO.	PRIMARY TERM CO-TERM	PAGE NO.
NERNST		NIOBIUM ELECTRODE		NUCLEAR REACTOR		OPTICAL PROPERTY (CONTD)	
EMF - - - - -	->1456	CATHODIC POLARIZ.>	535	AQUEOUS OXIDATION>	750	COPPER DOPING - -	1592
ZINC ELECTRODE -	"	POTASSIUM HYDROX.	"	INCONEL 600 - -	"	TITANIUM DIOXIDE	"
ZINC HYDROXIDE -	"	SURFACE CHANGE -	"	XPS - - - - -	"		
		XPS - - - - -	"			OPTIMUM CONDITION	
NEUTRAL SPECIES				NUCLEATION		CRYSTAL GROWTH ->	1625
ION ROLE - - - -	->1024	NIOBIUM PENTOXIDE		ANODIC ZINC OXIDE>	1914	RUTHENIUM DIOXIDE	"
MICROWAVE - - -	"	CARRIER CONCENTR.>	562	CALCIUM NITRATE ->	985	THERMAL EXPANSION	"
PLASMA ETCHING -	"	CERIUM DIOXIDE -	"	CRYSTALLITE GROW.	1914		
SILICON - - - - -	"	DOPING - - - - -	"	HYDRATED METALS -	985	ORGANIC ELECTROL.	
		ELECTRICAL CONDU.	"	SOLUTION PRECIPIT.	1914	CAPACITY - - - -	-> 523
NEW TECHNOLOGY				THALLIUM - - - -	985	DISSOLVED SULFUR	"
INSULATING FILM ->	504	NITRATE ION		ZINC OXIDE FILM -	1914	LITHIUM BATTERY -	"
TAPER ETCHING -	"	ALUMINUM - - - -	->1659			- - - - -	-> 729
TAPERED WINDOW -	"	ANODIC BEHAVIOR -	"	NUMERICAL ANALYS.		METALLIC OXSALT	"
		CHLORIDE ION - -	"	APPLIED POLARIZA.>	2057	RATE CAPABILITY -	523
NICKEL		KINETIC STABILITY>	2095	COPPER ZINC - - -	"	SECONDARY BATTERY	"
ACIDIC CHLORIDE ->	1118	OXYGEN EXCHANGE -	"	ELECTRODE POTENT.	"	SYSTEM STABILITY	"
ALLOY - - - - -	-> 574	PASSIVITY - - - -	1659	GALVANIC CORROSI.	"	TETRAHYDROFURAN -	"
ALUMINUM - - - -	"	PITTING POTENTIAL	"	SOLUTION DEPTH -	"		
ANODIC OXIDATION >	470	POTASSIUM NITRATE	2095			ORGANIC INCLUSION	
BUBBLE DYNAMICS -	574	RAMAN SPECTROSCO.	"	NUMERICAL METHODS		ELECTRODEPOSITION>	1123
COBALT - - - - -	->1584			CORROSION PCTENT.>	891	ELECTRON MICROSC.	"
CORROSION - - - -	->2038	NITRATE SALT		LINEAR POLARIZAT.	"	STEREOMICROSCOPY	"
ELECTROCRYSTALLI.>	2085	CATHOLYTE - - - -	->1496	THREE POINT - - -	"		
ELECTRODEPOSITION	"	CATION RADIUS - -	"			ORGANIC PRODUCT	
ELECTRODISSOLUT.	1118	MOLTEN NITRATE -	"	NUMERICAL SOLUTI.		HEXAFLUOROARSEN.>	181
ELECTROFOLISHING	574	OPEN PAN STUDY -	"	IMPURITY REDISTR.>	1939	LITHIUM - - - - -	"
EPITAXY - - - - -	-> 2085	REDUCTION - - - -	"	IMPURITY SEGREGA.	"	SOLID CORROSION -	"
FILM GROWTH - - -	-> 470	THERMAL BATTERY -	"	INTERFACIAL FLUX	"	TETRAHYDROFURAN -	"
FLADE POTENTIAL -	"			MOVING BOUNDARY -	"		
GAAS - - - - -	-> 1584	NITRIC OXIDE		SILICON OXIDATION	"	ORGANIC RESIST	
GAASP - - - - -	"	DECOMPOSITION - -	->1067			LSI DEVICE - - - -	->1531
GASEOUS DISCHARGE	574	REDUCING CONDITI.	"	O-CARBOXYMETHYL		SILICON DIOXIDE -	"
GRAIN STRUCTURE ->	1061	SCANDIA DOPING -	"	CARBOXYLATION - -	-> 404	SPUTTER ETCH - -	"
GROOVE SPACING -	574	ZIRCONIA - - - -	"	DERIVATIVE - - -	"		
HOLE DIFFUSION L.	1584			REDUCTION - - -	"	ORGANOMETALLICS	
MICROSTRUCTURE -	1061	NITRIDE SOLUTION		SYNTHESIS - - -	"	AQUEOUS MEDIA - -	->205C
OXIDATION - - - -	"	ACTIVITY COEFFIC.>	248	TARTRONIC ACID -	"	CONDUCTING ELECT.	"
PASSIVATION - - -	-> 2085	LITHIUM NITRIDE -	"			SEMICONDUCTOR - -	"
SACCHARIN - - - -	"	MOLTEN SALT - - -	"	O-NAPHTHOQUINONE			
SULFUR SEGREGATI.	2038			DIAZIDE-S-SULFON>	860	ORIFICE SIZE	
SULFURIC ACID - -	-> 470	NITROGEN		ELECTRON BEAM - -	"	ETCHING - - - - -	->1004
- - - - -	-> 2038	EMISSION SPECTRUM>	460	EPR - - - - -	"	MASKING - - - - -	"
SURFACE MORPHOLO.	574	GLOW DISCHARGE -	"	MASS SPECTROSCOPY	"	SAPPHIRE - - - - -	"
SURFACE STRESS -	2085	PLASMA TEMPERATU.	"	PHENOLIC-TYPE -	"		
VPE - - - - -	-> 1584	RF PLASMA - - -	"	RESIN - - - - -	"	ORTHOPHOSPHORIC	
		ROTATIONAL TEMPE.	"			OXYGEN REDUCTION >	786
NICKEL CADMIUM				OPEN CIRCUIT		PARALLEL MECHAN.	"
LIFETIME - - - -	-> 720	NOBLE METAL LAYER		ANODIC OXIDATION >	1374	PLATINUM - - - -	"
PATTERN RECOGNIT.	"	FILM GROWTH - - -	->1261	DIELECTRICS - - -	"	VOLTAMMETRY - - -	"
		MATHEMATICAL MOD.	"	ELLIPSEMETRY - -	"		
NICKEL CHROMIUM		SUBSTRATE DIFFUS.	"	NIOBIUM - - - -	"	OVERPOTENTIAL	
DIFFUSING SPECIES>	1948			TAFEL SLOPE - - -	"	CERIUM IOXIDE ->	1155
HIGH TEMPERATURE	"	NONAQUEOUS BATTE.		TRANSIENT ANALYS.	"	DOUBLE PULSE - -	->1148
PHOSPHICATION - -	"	ALKALI METAL - -	->2047	TUNGSTEN - - - -	"	EXCHANGE CURRENT	1155
PHOSPHORUS VAPOR	"	ALKALINE METAL	"			FAST ELECTRODE -	1148
		SOLID ELECTROLYTE	"	OPEN PAN STUDY		GALVANOSTATICS -	"
NICKEL COBALT CX.				CATHOLYTE - - - -	->1496	PLATINUM ELECTRO.	1155
ACTIVATION ENERGY>	1353	NONAQUEOUS CELL		CATION RADIUS - -	"	POLARIZATION - -	"
OXYGEN EVOLUTION	"	CATHODE - - - - -	-> 887	MOLTEN NITRATE -	"		
POTENTIOSTATIC -	"	IRON SULFUR - - -	"	NITRATE SALT - - -	"	OVERVOLTAGE	
PULSE - - - - -	"	LITHIUM BATTERY -	"	REDUCTION - - - -	"	ANODE MECHANISM ->	176
TEFLON BONDED - -	"	POTASSIUM IRON S.	"	THERMAL BATTERY -	"	CALCIUM ANODE - -	"
						FUSED SALT - - -	"
NICKEL GOLD ALLOY		NONAQUEOUS SOLVE.		OPTICAL ABSORPTI.		LITHIUM CHLORIDE	"
AIR ENVIRONMENT ->	1274	RUTHENIUM OXIDE ->	407	AQUEOUS ELECTROL.>	1868	THERMAL BATTERY -	"
OXIDE FILM GROWTH	"	WORKING ELECTRODE	"	DARK POTENTIAL -	"		
UNALLOYED NICKEL	"	XPS - - - - -	"	FLATBAND POTENTI.	"	OXIDATION	
				GROUP II-VI COMP.	"	AMMONIUM DICHROM.>	1975
NICKEL IRON ALLOY		NONAQUEOUS SYSTEM		IODINE DOPING - -	"	AQUEOUS BASE - -	-> 983
BUFFER CAPACITY ->	1861	TERNARY SYSTEM ->	990	LIGHT ABSORPTION	"	ATMOSPHERIC CORR.>	1533
CURRENT EFFICIEN.	"	X-RAY DIFFRACTION	"	ZINC SELENIDE - -	"	AUGER SPECTROSCOP.	547
ELECTRODEPOSITION	"					CHLORINE INCORPO.>	143
HYDROGEN EVOLUTI.	"	NONFARADAY		OPTICAL CHARACTER		CHRONOAMPEROMETRY>	1902
		CONTAMINATION - -	-> 54	DISPLAY DEVICE - -	->2211	CLEANING SOLUTION>	1428
NICKEL OXIDE FILM		CURRENT DENSITY -	"	ELECTRICAL CHARA.	"	COPPER - - - - -	->1425
CHLORIDE ION - -	-> 919	ELECTROLYSIS - -	"	ELECTROPHORESIS -	"	COPPER DEPOSITION>	171
DISSOLUTION - - -	"	WATER - - - - -	"	TITANIUM DIOXIDE	"	CORROSION - - - -	547
PASSIVATION - - -	"					CVD - - - - -	-> 838
PIT INITIATION - -	"	NONRADIATIVE PRO.		OPTICAL EXPOSURE		- - - - -	-> 1425
		CATHODOLUMINESCE.>	305	DEVELOPER TEMPER.>	2026	- - - - -	->1728
NIOBIUM		HOT SENSITIZATI.	"	DEVELOPMENT RATE	"	DIELECTRICS - - -	"
ANODIC OXIDATION >	1374	PRASEODYMIUM - -	"	ELECTRON BEAM - -	"	DOPING - - - - -	->1779
CARBON - - - - -	->2173	TERBIUM - - - - -	"	LINE EDGE PROFILE	"	ELECTROLESS - - -	171
CHROMIUM STEEL -	"	TRAPPING - - - -	"	PHOTORESIST - - -	"	FABRICATION METH.	1533
DIELECTRICS - - -	-> 1374	YTTRIUM OXISULF.	"	POSITIVE DIAZO -	"	FUSED SALT - - -	1902
ELLIPSEMOMETRY -	"					GALVANIC CELL - -	171
OPEN CIRCUIT - -	"			OPTICAL LAYER		GLASSY LAYER - -	1425
OXIDATION RESIST.	2173	NONSTOICHIOMETRY		ELLIPSEMOMETRY ->	131	GRAIN STRUCTURE ->	1061
TAFEL SLOPE - - -	-> 1374	CERIUM DIOXIDE ->	209	SILICON DIOXIDE -	"	HYDROCHLORIC ACID	143
TITANIUM - - - -	-> 2173	CHEMICAL DIFFUS.>	673	SILICON INTERFACE	"	- - - - -	> 149
TRANSIENT ANALYS.	1374	DEFECT STRUCTURE	209	STRESS-STRAIN - -	"	HYDROGEN PEROXIDE	1428
TUNGSTEN - - - -	"	IRON SULFIDE - - -	673			INFRARED ABSORPT.	1728
ZIRCONIUM - - - -	-> 2173	OXIDE SEMICONDU.	209	OPTICAL PROPERTY		ION IMPLANTATION	1779
		POINT DEFECT - -	"	ANODIC OXIDATION >	1592	IRON - - - - -	-> 547
				BANDGAP SHIFT - -	"	LEAD ACID BATTERY>	7
		THERMOGRAVIMETRY	209				

PRIMARY TERM CO-TERM	PAGE NO.	PRIMARY TERM CO-TERM	PAGE NO.	PRIMARY TERM CO-TERM	PAGE NO.	PRIMARY TERM CO-TERM	PAGE NO.
OXIDATION (CONTD)		OXIDATION THEORY (CONTD)		OXYGEN (CONTD)		P-TYPE	
LEAD CHLORIDE - - -	1902	TRANSITION METAL	760	SULFUR DIOXIDE - -	328	ACETONITRILE - - -	59
LEAD DIOXIDE - - -	7					CHEMICAL TREATME.	>1792
LEAD SULFATE - - -	"					CONDUCTIVITY - -	"
LEAD SULFIDE - - -	1902	OXIDE		OXYGEN CONCENTRA.		ELECTRICAL MEAS.	"
LOW TEMPERATURE - -	1728	ANNEALING - - -	>1737	AUGER SPECTROSC.	>1766	GAAS - - - - -	59
LUMINESCENCE - - -	1779	DEPTH PROFILE - -	"	CVD - - - - -	"	HYDROGEN DIFFUSI.	1792
LUMINESCENCE - - -	1975	GAAS - - - - -	"	POLYSILICON - - -	"	N-TYPE - - - - -	59
MICROSTRUCTURE - -	1061	XPS - - - - -	"	SEMIINSULATION -	"	PHOTOELECTROCHEM.	"
MOBILE SODIUM - - -	149			XPS - - - - -	"	RESISTIVITY SHIFT	1792
NICKEL - - - - -	1061	OXIDE CHARGE DEN.				SEMICONDUCTOR - -	59
P-HYDROXYBENZALD.	983	ALUMINUM - - - -	> 878	OXYGEN DIFFUSION		SILICON SURFACE -	1792
PALLADIUM - - - -	547	SILICON - - - - -	"	MULTIPHASE DIFFU.	>1111	SURFACE EFFECT -	59
PASSIVATION - - -	149	SILICON DIOXIDE -	"	ZIRCALCY-4 - - -	"		
PASSIVE OXIDE - - -	547	WORK FUNCTION - -	"				
PASSIVITY - - - -	1425						
PERMALLOY FILM - -	1533	OXIDE COATING					
PHOSPHOR LUMINES.	1975	LIFE TEST - - - -	>1439	ACID SULFATE - - -	95	PALLADIUM	
PHOSPHORUS DOPING	838	PERCHLORIC ACID -	"	ACTIVATION ENERGY	>1353	ACTIVATOR - - - -	>1671
PLANAR DEVICE - - -	143	POLARIZATION - -	"	ANODIC DISSOLUTI.	95	AUGER SPECTROSC.	> 547
POLYMERIZATION - -	1728	SODIUM CHLORIDE -	"	CORROSION RATE - -	"	BACKSCATTERING -	1671
POLYSILICON - - -	1779	TITANIUM ANODE - -	"	GOLD - - - - -	"	CATALYST - - - -	> 394
POLYSILICON FILM	838			NICKEL COBALT OX.	1353	CORROSION - - - -	547
POSITIVE PLATE - -	7	OXIDE FILM		PH - - - - -	95	DEPOSITION - - -	394
POTASSIUM CHLORID.	1902	ARSENIC DOPING -	>1434	POTENTIOSTATIC -	1353	ELECTROLESS - -	1671
REDUCTION - - - -	171	CHLORINE - - - -	>209C	PULSE - - - - -	"	GLASS SUBSTRATE -	1671
SILANE - - - - -	1728	CONDUCTIVITY - -	1434	TEFLON BONDED - -	"	IRON - - - - -	547
SILICON - - - - -	143	CVD - - - - -	"			METAL DEPOSITION	1671
SILICON DIOXIDE - -	149	EVOLUTION KINETI.	209C	OXYGEN EXCHANGE		OXIDATION - - - -	547
SILICON WAFER - - -	1428	HEXACYANOFERRATE	> 732	KINETIC STABILITY	>2095	PASSIVE OXIDE - -	"
SODIUM NEUTRALIZ.	149	PASSIVE IRON - -	"	NITRATE ION - - -	"	THIN FILM - - -	"
STEEL ANODE - - -	983	PLATINUM ELECTRO.	209C	POTASSIUM NITRATE -	"	UV IRRADIATED - -	394
STERESELECTIVITY -	"	SEMICONDUCTOR - -	732	RAMAN SPECTROSC.	"	XPS - - - - -	547
SULFURIC ACID - -	7	TAFEL SLOPE - - -	"				
- - - - -	1428	TIN OXIDE - - - -	1434	OXYGEN ISOTOPE		PARABOLIC GROWTH	
THERMAL DECOMPOS.	1975			ANODIZATION - - -	> 544	ANODIC OXIDATION	> 89
THIN FILM - - - -	547	OXIDE FILM GROWTH		KEIL SALOMON - - -	"	CONSTANT VOLTAGE	"
VLSI DEVICE - - -	1779	AIR ENVIRONMENT -	>1274	VANADIUM - - - -	"	SILICON - - - - -	"
XPS - - - - -	547	ANNEALING - - -	>1731				
ZINC SULFIDE - - -	1975	ANODE - - - - -	> 555	OXYGEN MONOLAYER		PARABOLIC KINETI.	
		CAPACITANCE - - -	1731	AGING KINETICS - -	> 592	HIGH TEMPERATURE	>1105
		CONSTANT CURRENT	555	ANION INFLUENCE -	>2140	OXIDATION KINETI.	"
		CONSTANT POTENTI.	"	ELECTROCATALYSIS	"	ZIRCALOXY OXIDATI.	"
OXIDATION KINETI.		HIGH PRESSURE - -	>1822	ELECTROSORPTION -	"		
CERAMICS - - - -	>1723	HIGH TEMPERATURE	1731	HYDROGEN MONOLAY.	"	PARALLEL MECHAN.	
CHLORINE OXIDATI.	>1789	LOW TEMPERATURE -	1822	PERTURBATION PRO.	592	ORTHOPHOSPHORIC	> 786
CONNECTOR - - - -	>1798	NICKEL GOLD ALLOY	1274	PLATINUM - - - -	2140	OXYGEN REDUCTION	"
COPPER - - - - -	"	PH DEPENDENT - -	555	POTENTIALDYNAMICS	592	PLATINUM - - - -	"
CORROSION - - - -	1723	PLATINUM - - - -	"	SULFURIC ACID - -	2140	VOLTAMMETRY - - -	"
DIFFUSION - - - -	1798	REOXIDATION - - -	1731				
DOPANT EFFECT - - -	>1516	SILICON - - - - -	1822	OXYGEN PRESSURE		PASSIVATION	
- - - - -	>1523	SILICON OXIDE - -	1731	CARBON DIOXIDE - -	>2012	ACIDIC SULFATE -	>2064
GOLD ALLCY - - - -	1798	STEAM OXIDATION -	1822	FURNACE - - - -	"	ALTERNATING VOLT.	>1908
HIGH TEMPERATURE	1105	TITANIUM DIOXIDE	1731	GAS FLOW METHOD -	"	ANODIC DISSOLUTI.	2064
HOT-PRESSED - - -	1723	UNALLOYED NICKEL	1274	HYDROGEN - - - -	"	ANODIC FILM - - -	>1370
PARABOLIC KINETI.	1105			LOWER TEMPERATURE	"	ANODIC OXIDE - -	"
PHYSICAL MODEL - -	1523	OXIDE MORPHOLOGY		PRESSURE CONTROL	"	CHLORIDE ION - -	> 919
POINT DEFECT - - -	1516	ALUMINA - - - -	>1035	WUSTITE PHASE - -	"	CHLORIDE SOLUTION	2064
POINT EFFECT - - -	1523	GROWTH MECHANISM	"			CORROSION - - - -	"
REFRACTORIES - - -	1723	YTRIUM - - - - -	"			CORROSION POTENT.	1908
RELIABILITY - - -	1798			OXYGEN REDUCTION		DEOXYGENATED SOL.	2064
SILICON DIOXIDE - -	1516	OXIDE SEMICONDUCT.		ANODIC ACTIVATION	> 78	DEPTH PROFILE - -	1370
- - - - -	1523	CERUM DIOXIDE - -	> 209	AUGER SPECTROSC.	"	DISSOLUTION - - -	919
SILICON NITRIDE - -	1723	DEFECT STRUCTURE	"	DIAPHRAGM - - -	>1502	ELECTROCRYSTALL.	>2085
STACKING FAULT - -	1789	ELECTRON AFFINITY	>1081	ELECTROCATALYSIS	78	ELECTRODEPOSITION	"
THERMAL OXIDATION	"	INDIUM SESQUIOXI.	209	ORTHOPHOSPHORIC	> 786	EPITAXY - - - -	"
TRICHLOROETHYLENE	"	NONSTOICHIOMETRY	209	PARALLEL MECHAN.	"	FARADAIC RECTIFI.	1908
YTRIUM - - - - -	1723	PHOTOVOLTAIC PRO.	1081	PHOSPHORIC ACID	>1631	GAAS - - - - -	1370
ZIRCALOXY OXIDATI.	1105	POINT DEFECT - -	209	PLATINUM - - - -	786	HYDROCHLORIC ACID	> 149
		THERMOGRAVIMETRY	"	PLATINUM DISSOLU.	1631	MILD STEEL - - -	1908
				PLATINUM-OXYGEN	1502	MOBILE SODIUM - -	149
OXIDATION PRODUCT		OXIDE THICKNESS		POLARIZATION - -	"	NICKEL - - - - -	2085
CHARGE TRANSPORT	>1490	DEFECT DENSITY -	>1771	SINGLE CRYSTAL - -	78	NICKEL OXIDE FILM	919
DIPHTHALOCYANINE	"	ELECTRIC FIELD -	"	STRUCTURE SENSIT.	"	OXIDATION - - - -	149
ELECTROCHROMISM -	"	LIQUID CRYSTAL -	"	VOLTAAMMETRY - - -	786	PIT INITIATION -	919
		SILICON DIOXIDE -	"			POLARIZATION - -	1908
OXIDATION RATE				OXYGEN SOLUBILITY		SACCHARIN - - - -	2085
SILICON - - - - -	> 502	OXYCHLORIDE		EFFLUENT GAS - - -	> 827	SILICON DIOXIDE -	149
		BORON GETTERING	>1754	EQUILIBRIUM - - -	"	SODIUM NEUTRALIZ.	"
OXIDATION RESIST.		LSI DEVICE - - -	"	GERMANIUM - - - -	"	SURFACE STRESS -	2085
AMMONIA GAS - - -	> 996	PHOSPHORUS - - -	"			TITANIUM - - - -	2064
CARBON - - - - -	>2173	PIPE YIELD - - -	"			XPS - - - - -	1370
CHROMIUM STEEL - -	"	SILICON - - - - -	"				
DIELECTRIC FILM - -	996						
NIOBIUM - - - - -	2173	OXYGEN					
SILICON OXYNITRIT.	996	AMBIENT PRESSURE	>1422				
THERMAL NITRIDAT.	"	CALCIUM FLUORIDE	>1360				
TITANIUM - - - - -	2173	CARBON - - - - -	1422				
ZIRCONIUM - - - -	"	CARBON DIOXIDE -	> 328				
		CARBON MONOXIDE -	1422				
OXIDATION STATE		CHEMICAL POTENTI.	1360				
DIPHTHALOCYANINE	>1339	EQUILIBRIUM - - -	1422				
ELECTROCHROMISM -	"	GAS SOLUBILITY -	328				
LUTETIUM - - - -	"	MEASUREMENT - -	1360				
		MOLTEN SALT - - -	328				
OXIDATION THEORY		SILICON - - - - -	1422				
COBALT MONOXIDE -	> 760	SODIUM CARBONATE	328				
ELECTROTRANSPORT	"	SOLID ELECTROLYTE	1360				
POINT DEFECT - - -	"						

PRIMARY TERM CO-TERM	PAGE NO.	PRIMARY TERM CO-TERM	PAGE NO.	PRIMARY TERM CO-TERM	PAGE NO.	PRIMARY TERM CO-TERM	PAGE NO.
PASSIVE FILM		PERTURBATIONS		PHOSPHOR LUMINES.		PHOSPHORUS PENTO. (CONTO)	
ANALYTIC SOLUTION>2081		CURRENT PEAK --> 257		AMMONIUM DICHROM.>1975		P-N-P - - - - -	642
ANODIC OXIDATION > 442		ELECTROSORPTION - "		LUMINESCENCE - - -		TRANSISTOR - - -	"
BORATE BUFFER - - -	"	HYDROGEN ADATOM - "		OXIDATION - - - - -			
COMPOSITION - - - -	"	PLATINUM - - - - -		THERMAL DECOMPOS. -		PHOSPHORUS VAPOR	
FOURIER ANALYSIS 2081		POTENTIAL - - - - -		ZINC SULFIDE - - - -		DIFFUSING SPECIES>1948	
GAS ADSORPTION ->1720						HIGH TEMPERATURE -	"
IRON OXIDE FILM - 442		PH		PHOSPHOR PARTICLE		NICKEL CHROMIUM -	"
LINEAR POLARIZAT. 2081		ACID SULFATE --> 95		SCREEN WEIGHT ->1563		PHOSPHIDATION - - -	
POTENTIAL DISTRI. "		ALUMINUM - - - -> 199		VOID TRANSMISSION "			
SCRATCH - - - - -	"	ANODIC - - - ->2171		WEIGHT OPTIMIZAT. "		PHOSPHOSILICATE	
SURFACE ROUGHNESS 1720		ANODIC DISSOLUTION. 95				CVD - - - - -> 334	
		AQUEOUS SOLUTION 199		PHOSPHORIC ACID		DIELECTRICS - - -	"
PASSIVE IRON		BLEACHING - - - 2171		ANODE - - - - -> 360		INTEGRATED CIRCU. -	"
HEXACYANOFERRATE > 732		COLORATION - - -		CHEMICAL ETCHING > 287		PHOSPHORUS - - - -	"
OXIDE FILM - - - -	"	CORROSION RATE - 95		CONSTANT POTENTI. 360			
SEMICONDUCTOR - - -	"	CORROSION STABIL. 2171		CORROSION - - - - -		PHOSPHOTUNGSTIC	
TAFEL SLOPE - - - -	"	ELECTROCHROMISM -		CORROSION FILM ->1848		ELECTROCHROME -> 805	
		GOLD - - - - - 95		CRYSTAL GROWTH - 360		PROTON CONDUCTION "	
PASSIVE OXIDE		HYDRIDE FORM - - 199		EPITAXIAL LAYER - 287		TUNGSTEN TRIOXIDE "	
AUGER SPECTROSCOP. > 547		IRIDIUM OXIDE - 2171		HYDROCHLORIC ACID "		ZIRCONIUM PHOSPH. "	
CORROSION - - - - -	"	MECHANISM - - - -		INDIUM PHOSPHIDE "			
IRON - - - - - - -	"	OXYGEN EVOLUTION 95		LEAD ACID BATTERY 360		PHOTOANODE	
OXIDATION - - - - -	"	POTENTIAL - - - - 199		MATERIAL SELECTI. 287		CATION ABSORPTION> 954	
PALLADIUM - - - - -	"	SALT SOLUTION - - -		OXYGEN REDUCTION >1631		CHARGE TRANSFER >1011	
THIN FILM - - - - -	"			PLATINUM DISSOLU. "		COALIT. CONCENTRA-> 944	
XPS - - - - - - -	"	PH DEPENDENT		POSITIVE ELECTRO. 1848		CORROSION SUPPRE. "	
		ANODE - - - - -> 555				DIGITAL SIMULATI. 1011	
PASSIVITY		CONSTANT CURRENT "		PHOSPHORS		ELECTROCATALYSIS >1831	
ALUMINUM - - - ->1659		CONSTANT POTENTI. "		BARIUM CHLOROSIL.>1734		ENERGY CONVERSION 954	
ANODIC BEHAVIOR - "		OXIDE FILM GROWTH "		CATHODOLUMINESCENCE> 571		HOLE INJECTION - 1011	
CHLORIDE ION - - - -	"	PLATINUM - - - - -		COLOR TV PICTURE >1008		HYDROGEN - - - ->2163	
COPPER - - - - ->1425				ELECTRON BOMBARD. 571		HYDROGEN PEROXIDE 1831	
CORROSION - - - - ->1363		PHASE DIAGRAM		EUROPIUM - - - - 1734		ILLUMINATED - - - 1011	
CURRENT OSCILLAT. "		ADSORPTION - - -> 608		GAS DISCHARGE - - 1008		IRON OXIDE - - - 1831	
CVD - - - - - 1425		ALUMINUM - - - ->1992		HIGH QUENCHING - 1734		LIGHT INTENSITY - 944	
GLASSY LAYER - - - -	"	ANTIMONY - - - - -		LANTHANUM OXYSUL. 571		LIQUID JUNCTION 1011	
IRON - - - - - 1363		CELL KINETICS - - 608		LOW ENERGY - - -		N-TYPE - - - - - 1831	
NITRATE ION - - - - 1659		COPPER BROMIDE -> 818		PHOTOLUMINESCENCE 1734		PHOTOELECTROCHEM. 954	
OXIDATION - - - - - 1425		DTA - - - - - 1992		TEMPERATURE - - -		RUTHENIUM - - - -	
PITTING POTENTIAL 1659		GALLIUM - - - - -		TERBIUM - - - - - 571		RUTILE LATTICE - 2163	
SULFURIC ACID - - 1363		IONIC CONDUCTIVITY. 818		ULTRAVIOLET EXCI. 1008		SEMICONDUCTOR - - 1011	
		LIQUID ASSOCIATI. 1992		XPS - - - - - 571		SOLAR CELL - - - 1011	
PATTERN DUPLICAT.		LITHIUM BATTERY - 608		YTIUM OXYSULFI. "		SULFATE CONCENTR. 944	
ION BEAM - - - -> 483		POTENTIAL - - - -				SURFACE TREATMENT 954	
LITHOGRAPHY - - - -	"	SILVER IODIDE - - 818		PHOSPHORUS		TITANIUM DIOXIDE 944	
POLYDIMETHYLSILO. "		SPECTROSCOPY - - 608		BORON GETTERING ->1754		2163	
POLYMETHYLMETAC. "		TERNARY PHASE - 1992		CVD - - - - -> 334			
RADIATION YIELD - -	"	TITANIUM DISULFI. 608		DIELECTRICS - - -		PHOTOCONDUCTIVITY	
RESIST MATERIAL - -	"	VOLTAGE STEPS - -		INTEGRATED CIRCU. -		ANODE - - - - -> 972	
				LSI DEVICE - - - 1754		ELECTROOXIDATION "	
PATTERN RECOGNIT.		PHASE SEPARATION		OXYCHLORIDE - - -		LIGHT EFFECT - - -	
LIFETIME - - - -> 720		HYDROCHLORIC ACID>1129		PHOSPHOSILICATE - 334		THIOCYANATE - - -	
NICKEL CADMIUM - -	"	SILICON OXIDE - - -		PIPE YIELD - - - 1754			
		SODIUM PASSIVATI. "		SILICON - - - - -		PHOTOCORROSION	
PENDELLOSUNG						DISK ELECTRODE ->1483	
DOUBLE CRYSTAL ->1228		PHASE TRANSFORMA.		PHOSPHORUS DIFFU.		PHOTON FLUX - - -	
EPITAXIAL LAYER - -	"	AUSTENITIC - - -> 374		DIFFUSION PROCESS>1252		REDOX - - - - - - -	
STRAIN DISTRIBUT. "		CORROSION - - - -		PHOSPHORUS DOPING "			
X-RAY DIFFRACTION "		DUPLEX 308 - - -		SILICA FILM - - - -		PHOTOCURRENT	
		INTERGRANULAR - -				ANODE - - - - -> 419	
PERCHLORIC ACID		MICROSTRUCTURE -		PHOSPHORUS DOPING		FERRIC OXIDE - - -> 56	
LIFE TEST - - - ->1439		PITTING - - - - -		ANNEALING - - - ->1078		FLAME OXIDATION - "	
OXIDE COATING - - -	"	STAINLESS STEEL -		BORON DOPING - -> 313		IRON OXIDE - - - 419	
POLARIZATION - - -	"			C-V CURVE - - - - 1078		PHOTOELECTRODE -> 475	
SODIUM CHLORIDE - -	"	PHASE TRANSITION		CORONA CHARGING -		PULSED ILLUMINAT. 56	
TITANIUM ANODE - -	"	DTA - - - - ->1403		CVD - - - - - 313		SEMICONDUCTOR - - 419	
		EQUILIBRIUM - - -		- - - - -> 833		SINTERING - - - - 56	
PERHYDROXYL ION		HYDROSTATIC PRES. "		- - - - -> 838		SOLAR CELL - - - -	
ALKALINE SOLUTION>1924		LEAD FLUORIDE - -		- - - - ->1019		SUBBANDGAP ILLUM. 475	
CATALYTIC DECOMP. "				- - - - ->1042		TITANIUM OXIDE - -	
FUEL CELL - - - - -	"	PHENOLIC-TYPE		DEPOSITION - - - 313			
		DIAZIDE-S-SULFON.> 860		DEPOSITION RATE - 1042		PHOTOEFFECT	
PERIODIC CURRENT		ELECTRON BEAM - -		DIELECTRICS - - - 313		CHARGE TRANSFER -> 855	
ELECTROLYSIS - -> 398		EPR - - - - - - -		DIFFUSION PROCESS>1252		ETCHING - - - - -	
MASS TRANSFER - - -	"	MASS SPECTROSCOPY "		INTEGRATED CIRCU. 1042		GAS ELECTRODE - -	
ROTATING DISK - - -	"	O-NAPHTHOQUINONE "		ION IMPLANTATION 1019		GROUP III-V COMP. "	
		RESIN - - - - - -		LOW PRESSURE - - - 833		REDOX - - - - - - -	
PERMALLOY FILM				- - - - - 1019			
ATMOSPHERIC CORR.>1533		PHOSPHIDATION		OXIDATION - - - - 838		PHOTOELECTRICITY	
FABRICATION METH. "		DIFFUSING SPECIES>1948		PHOSPHORUS DIFFU. 1252		AUGER SPECTROSCOP. > 949	
OXIDATION - - - - -	"	DIFFUSION COEFFI.>1432		POLYSILICON FILM 833		CADMIUM SELENIDE "	
		HIGH TEMPERATURE 1948		PRESSURE REDUCTI. 1042		CADMIUM SULFIDE -	
PERMEATION		NICKEL CHROMIUM -		RESISTIVITY - - - 833		ENERGY CONVERSION "	
CORROSION - - - ->2159		PHOSPHORUS VAPOR "		SILICA FILM - - - 1252		SEMICONDUCTOR - -	
ENVIRONMENT - - - -	"	ZINC - - - - - 1432		SILICON DIOXIDE - 313		XPS - - - - - - -	
FLOW CONTROL - - -	"	ZINC PHOSPHIDE - "					
POLYMER - - - - -	"					PHOTOELECTROCHEM.	
TRACE GAS - - - - -	"	PHOSPHOR DEPOSIT.				ACETONITRILE - -> 59	
		CHROMATE SENSITI.>1294				- - - - -> 598	
PERTURBATION PRO.		COLOR TV TUBE - -				ANODIC OXIDATION >2133	
AGING KINETICS -> 592		DIAZO SENSITIZER >1078				CATION ABSORPTION> 954	
OXYGEN MONOLAYER "				PHOSPHORUS PENTO.		DIFFUSION - - - -> 850	
PLATINUM - - - - -	"	PHOSPHOR DOPING		CURRENT GAIN - -> 642		ELECTROCHROMISM - 2133	
POTENTIAL DYNAMICS "		BORON NITRIDE ->1951		EMITTER EFFICIEN. "		ENERGY CONVERSION 954	
		CVD - - - - - - -		GETTERING - - - - -		FLATBAND POTENTI. 598	
		GROWTH PARAMETER "					

PRIMARY TERM CO-TERM	PAGE NO.	PRIMARY TERM CO-TERM	PAGE NO.	PRIMARY TERM CO-TERM	PAGE NO.	PRIMARY TERM CO-TERM	PAGE NO.
PHOTOELECTROCHEM. (CONTD)		PHOTORESIST FILM		PITTING POTENTIAL		PLATING	
GAAS - - - - -	59	AMMONIA - - - - -	883	ALUMINUM - - - - -	>1659	DIRECT CURRENT - - -	>1633
HYDROGEN PROTON -	850	BREATH TEST - - -	"	ANODIC BEHAVIOR -	"	HYDROGEN PERMEAT. -	"
INDIUM PHOSPHIDE	598	CLEANING - - - - -	"	CHLORIDE ION - - -	"	PULSED PLATING - - -	"
MANGANESE PORPHYR>	705	HYDROGEN PEROXIDE	"	NITRATE ION - - -	"		
N-TYPE - - - - -	59	STRIPPING - - - - -	"	PASSIVITY - - - - -	"	PLATING CYCLE	
P-TYPE - - - - -	"	WAFER SURFACE - - -	"			DIRECT CURRENT - - -	> 881
PHOTOANODE - - -	954			PITTING RESISTAN.		METAL QUANTITY - - -	"
PLATINUM ELECTRO.	705	PHOTORESIST SYST.		COLD PLASTIC DEF.>	2075	PULSED PLATING - - -	"
RUTHENIUM - - - -	954	BISAZIDE RESIST ->	273	CORROSION - - - - -	"		
SEMICONDUCTOR - -	59	CROSSLINKING - - -	"	SALT SOLUTION - - -	"		
- - - - -	598	RECIPROCITY FAIL. -	"	STAINLESS STEEL - -	"	PLATINUM	
SINGLE CRYSTAL - -	"					AC ADMITTANCE - - -	> 424
SOLAR CELL - - -	954	PHOTOVOLTAIC CELL		PLANAR DEVICE		AGING KINETICS - - -	> 592
SURFACE EFFECT -	59	ACETONITRILE - - -	603	CHLORINE INCORPOR.>	143	ANION INFLUENCE ->	2140
SURFACE TREATMENT	954	EFFICIENCY - - - -	"	HYDROCHLORIC ACID	"	ANNEAL - - - - -	> 277
THERMAL OXIDATION	2133	GAAS - - - - -	"	OXIDATION - - - - -	"	ANODE - - - - -	> 555
TITANIUM DIOXIDE	850	LIQUID JUNCTION -	"	SILICON - - - - -	"	ANODIC ACTIVATION>	78
TUNGSTEN TRIOXIDE	2133	REGENERATIVE CELL	"			AUGER SPECTROSCOP.>	67
WET SOLAR CELL -	705	SINGLE CRYSTAL - - -	"	PLANAR DIFFUSION		CHANNELING - - - -	277
				DIFFUSION PROCESS>	135	CHROMIUM - - - - -	"
PHOTOELECTRODE		PHOTOVOLTAIC PRO.		GAAS - - - - -	"	- - - - -	>1047
PHOTOCURRENT - ->	475	AMORPHOUS SEMICO.>	688	PLANAR JUNCTION -	"	CONSTANT CURRENT	555
SUBBAND GAP ILLUM.	"	DEPOSITION - - - -	"	SILICON DIOXIDE -	"	CONSTANT POTENTI. -	"
TITANIUM OXIDE - -	"	ELECTRON AFFINITY>	1081	TIN DOPING - - - -	"	CURRENT PEAK - - -	> 257
		HYDROGEN CONTENT	688			DEGRADATION - - -	> 1047
PHOTOELECTROLYSIS		INDIUM SESQUIOXID.	1081	PLANAR GALLIUM		DIFFRACTION - - - -	> 277
ARC PLASMA SPRAY.>	83	MASS SPECTROMETRY	688	ALUMINUM DIFFUSI.>	292	ELECTROCAPILLARY >	252
BERYLLIUM DOPING >	2007	OXIDE SEMICONDUCT.	1081	MASKING STRUCTURE	"	ELECTROCATALYSIS	67
CERAMICS - - - - -	13	SILICON - - - - -	688	SILICON - - - - -	"	- - - - -	78
QUANTUM EFFICIEN.	2007					- - - - -	> 218
RUTILE ANODE - - -	83	PHTHALIMIDE		PLANAR JUNCTION		ELECTRON DIFFRAC.	67
TITANIUM DIOXIDE -	"	ALKALINE SOLUTION>	1693	DIFFUSION PROCESS>	135	ELECTROOXIDATION	218
- - - - -	2007	EPOXIDE DIMERS - -	"	GAAS - - - - -	"	ELECTROSORPTION -	257
WATER OXIDATION -	"	KINETIC ANALYSIS	"	PLANAR DIFFUSION	"	- - - - -	2140
		REDUCTION - - - -	"	SILICON DIOXIDE -	"	EPITAXIAL RELATI.	277
PHOTOINDUCED		STRUCTURAL ANALY.	"	TIN DOPING - - - -	"	ETHYLENE - - - - -	218
APROTIC SOLVENT ->	414					EXTENSOMETER - - -	252
CHEMILUMINESCENCE	"	PHYSICAL MODEL		PLANAR REACTOR		HYDROGEN ABSORPT.	67
ELECTROGENERATED	"	DUPANT EFFECT - ->	1523	DEPOSITION RATE ->	930	HYDROGEN ADATOM -	257
ENERGY CONVERSION	"	OXIDATION KINETI.	"	PLASMA - - - - -	"	HYDROGEN MONOLAY.	2140
SEMICONDUCTOR - -	"	POINT EFFECT - - -	"	SILICON OXIDE - - -	"	IMPATT DIODE - - -	1047
VP CONVERSION - -	"	SILICON DIOXIDE - -	"			INTERDIFFUSION - -	"
				PLANE VERTICAL		INTERFACE - - - - -	424
PHOTOLITHOGRAPHY		PHYSICAL PROPERTY.		CATHODE - - - - -	> 23	METALLIZATION - -	> 1047
CHROMIUM - - - - -	>1075	CERAMICS - - - - -	1	CONVECTION - - - -	"	ORTHOPHOSPHORIC >	786
ELECTROSTATICS ->	1426	DTA - - - - -	"	COPPER - - - - -	"	OXIDE FILM GROWTH	555
ETCHING - - - - -	1075	IONIC CONDUCTIVI.	"	CURRENT DENSITY -	"	OXYGEN MONOLAYER	592
FILTRATION - - - -	1426	LITHIUM OXIDE - - -	"	ELECTRODEPOSITION	"	- - - - -	2140
MICROMINITURIZAT.	"	MOISTURE CONTENT	"	MASS TRANSPORT -	"	OXYGEN REDUCTION	78
PHOTOMASK COATING	1075					- - - - -	786
PHOTORESIST - - -	1426	PHYSICAL STRUCTU.		PLASMA		PARALLEL MECHAN.	"
PLASMA ETCHING - -	"	DISCHARGE CAPACI.>	1899	DEPOSITION RATE ->	930	PERTURBATION PRO.	592
THIN FILM - - - -	1075	POROUS IRON ELEC.	"	PLANAR REACTOR -	"	PERTURBATIONS - -	257
		POWDER REDUCTION	"	SILICON OXIDE - - -	"	PH DEPENDENT - - -	555
PHOTOLUMINESCENCE		SINTERING - - - - -	"			POTENTIAL - - - - -	257
ABSORPTION SPECT.>	1550			PLASMA DEPOSITION		POTENTIODYNAMICS	218
BARIUM CHLOROSIL.>	1734	PIPE YIELD		ANNEALING - - - -	>1750	- - - - -	592
CERIUM - - - - -	1550	BORON GETTERING ->	1754	CONTAMINATION ->	319	ROTATING DISK - - -	444
CRYSTAL FIELD - - -	"	LSI DEVICE - - - -	"	GLOW DISCHARGE - -	"	SALT SOLUTION - - -	252
EUROPIUM - - - - -	1734	OXYCHLORIDE - - -	"	HYDROGENATION - -	1750	SAPPHIRE - - - - -	277
GARNET PHOSPHORS	1550	PHOSPHORUS - - - -	"	PLASMA ETCHING - -	319	SILICON - - - - -	1047
HIGH QUENCHING -	1734	SILICON - - - - -	"	RADIATION DAMAGE	"	SILVER - - - - -	"
PHOSPHORS - - - -	"			SILICON NITRIDE -	1750	SINGLE CRYSTAL - -	67
TEMPERATURE - - -	"	PIT GROWTH		SPUTTERING - - - -	319	- - - - -	78
TEMPERATURE RANGE	1550	CORROSION - - - -	>1662			STRUCTURE SENSIT.	67
		MATHEMATICAL MOD.	"	PLASMA ETCHING		- - - - -	78
PHOTOMASK		PIT INITIATION - - -	"	CARBONTETRAFLUOR.>	226	SULFURIC ACID - - -	424
CHROMIUM FILM - ->	1794	SALT FILM - - - - -	"	CONTAMINATION ->	319	- - - - -	2140
GAS PLASMA - - - -	"	TRANSPORT LAW - -	"	DIODE SYSTEM - - -	226	SURFACE STRESS - -	252
MOS-LSI PROCESS -	"			ELECTROSTATICS ->	1426	SWEEP FREQUENCY -	424
REVERSAL ETCHING	"			FILTRATION - - - -	"	VOLTAMMETRY - - - -	786
				GLOW DISCHARGE -	319		
PHOTOMASK COATING		PIT INITIATION		ION ROLE - - - - -	>1024	PLATINUM DISSOLU.	
CHROMIUM - - - - -	>1075	ALUMINUM PITTING >	1855	MICROMINITURIZAT.	1426	OXYGEN REDUCTION >	1631
ETCHING - - - - -	"	CHLORIDE ION - - -	919	MICROWAVE - - - -	1024	PHOSPHORIC ACID -	"
PHOTOLITHOGRAPHY	"	CHLORIDE PITTING	1855	NEUTRAL SPECIES -	"		
THIN FILM - - - -	"	COMPLEX ION - - -	"	PHOTOLITHOGRAPHY	1426	PLATINUM ELECTRO.	
		CORROSION - - - -	>1662	PHOTORESIST - - -	"	A-C IMPEDENCE - ->	1166
PHOTON FLUX		DISSOLUTION - - -	919	PLASMA DEPOSITION	319	ANODIC OXIDATION >	43
DISK ELECTRODE ->	1483	MATHEMATICAL MOD.	1662	RADIATION DAMAGE	"	- - - - -	> 187
PHOTOCORROSION -	"	NICKEL OXIDE FILM	919	REACTIVE SPUTTER.	226	SILICON - - - - -	>1687
REDOX - - - - -	"	PASSIVATION - - -	"	SILICON - - - - -	1024	BORATE BUFFER - - -	187
		PIT GROWTH - - - -	1662	SPUTTERING - - - -	319	CERTUM DIOXIDE ->	1155
		SALT FILM - - - - -	"			- - - - -	1166
		TRANSPORT LAW - -	"	PLASMA TEMPERATU.		CHLORINE - - - - -	>209C
PHOTORESIST				EMISSION SPECTRUM>	460	COBALT DIOXIDE -	187
DEVELOPER TEMPER.>	2026	PITTING		GLW DISCHARGE - -	"	DIABETES - - - - -	43
DEVELOPMENT RATE	"	AUSTENITIC - - - -	> 374	NITROGEN - - - - -	"	EVOLUTION KINETI.	209C
ELECTRON BEAM - -	"	CATHODIC REACTION>	15	RF PLASMA - - - -	"	EXCHANGE CURRENT	1155
ELECTROSTATICS ->	1426	CORROSION - - - -	"	ROTATIONAL TEMPE.	"	GLUCOSE OXIDATION>	237
FILTRATION - - - -	"	CREVICE CORROSION	15			GLUCOSE SENSOR -	43
LINE EDGE PROFILE	2026	CURRENT DISTRIB.	"	PLASTIC ENCAPSUL.		- - - - -	1687
MICROMINITURIZAT.	1426	DUPLEX 308 - - - -	374	ALUMINUM ALLOY ->	110	IMPLANTATION - - -	43
OPTICAL EXPOSURE	2026	INTERGRANULAR - -	"	CORROSION TEST - -	"	INHIBITION - - - -	1687
PHOTOLITHOGRAPHY	1426	MATHEMATICAL MOD.	15	INTEGRATED CIRCU.	"	KINETIC PHENOMENA	237
PLASMA ETCHING - -	"	MICROSTRUCTURE -	374	METALLIZATION - -	"		
POSITIVE DIAZO -	2026	PHASE TRANSFORMA.	"				
		STAINLESS STEEL -	"				

PRIMARY TERM CO-TERM	PAGE NO.	PRIMARY TERM CO-TERM	PAGE NO.	PRIMARY TERM CO-TERM	PAGE NO.	PRIMARY TERM CO-TERM	PAGE NO.
PLATINUM ELECTRO. (CONTD)		POLLUTION CONTROL		POLYMETHACRYLON. (CONTD)		POLYVINYL BUTYRAL (CONTD)	
KREBS-RINGER - - -	43	IODINE - - - - -	>1842	RESIST - - - - -	694	ELECTRICAL PROPE. 1958	
- - - 237		SODIUM SULFATE - -	"	X-RAY - - - - -	"	POLARIZATION - - -	"
- - - 1687		SOLID-STATE PROBE -	"				
LINEAR POTENTIAL	43	SULFUR DIOXIDE - -	"	POLYMETHYLMETACR.		POROUS CATHODE	
MANGANESE PORPHY. >	705	SULFUR PROBE - - -	"	ION BEAM - - - - -	> 483	MATHEMATICAL MOD. >	2125
MASS TRANSPORT	237	SULFUR TRIOXIDE - -	"	LITHOGRAPHY - - -	"	METAL DEPOSITION	"
MOSSBAUER SPECTR.	187			PATTERN DUPLICAT.	"	MULTIPLE REACTIO.	"
OVERPOTENTIAL - - -	1155	POLYCHROMATE		POLYDIMETHYLSILC.	"		
OXIDE FILM - - - 209C		BISULFATE CATALY. >	190	RADIATION YIELD - -	"	POROUS ELECTRODE	
PHOTOELECTROCHEM.	705	CATHODE FILM - - -	"	RESIST MATERIAL - -	"	COMPETING REACTI. >	1928
POLARIZATION - - -	1155	CHROMIUM - - - - -	"			CONVECTION - - - >	1713
- - - 1166		ELECTRODEPOSITION	"			DIFFUSION - - - -	"
TRANSIENT DECAY - -	"			POLYMETHYLMETHAC.		ELECTRODE MODEL - -	>1835
UREA - - - - - 1687		POLYDIMETHYLSILO.		DEVELOPING TIME - -	>1430	MIGRATION - - - - -	1713
WET SOLAR CELL - -	705	ION BEAM - - - - -	> 483	ELECTRON BEAM - - -	"	MOLTEN SALT - - - -	"
		LITHOGRAPHY - - -	"	LINE WIDTH - - - -	"	MULTIPLE REACTIO.	1928
PLATINUM-CRYSTAL		PATTERN DUPLICAT.	"	RESIST - - - - -	"	REACTION PROFILE	1835
DIAPHRAGM - - - - -	>1502	POLYMETHYLMETACR.	"	SLOPE ANGLE - - - -	"	REACTOR ANALYSIS	1928
OXYGEN REDUCTION - -	"	RADIATION YIELD - -	"			SILVER CHLORIDE - -	> 965
POLARIZATION - - -	"	RESIST MATERIAL - -	"	POLYPHOSPHORIC A.		SINGLE PORE ELEC.	"
				MORPHOLOGY CONTR. >	1567	SOLUBLE REACTANT	"
POINT DEFECT		POLYESTER FILM		NEODYMIUM PENTAP.	"	SURFACE MORPHOLO.	1835
CERIUM DIOXIDE - - -	> 209	HIGH RATE - - - - -	> 691	POLYMERIZATION - -	"	TRANSPORT EQUATI.	1713
CHEMICAL DIFFUSI. >	673	INDIUM OXIDE - - -	"	SINGLE CRYSTAL - -	"	ZINC PORE ELECTR.	1835
COBALT MONOXIDE - -	> 760	REACTIVE SPUTTER.	"				
COPPER DOPING - - -	>2183	TIN DOPING - - - -	"	POLYSILICON		POROUS IRON ELEC.	
DEFECT STRUCTURE	209			ALUMINUM - - - - -	> 162	DISCHARGE CAPACI. >	1899
DOPANT EFFECT - - -	>1516	POLYIMIDE		ALUMINUM COVERAGE >	1335	PHYSICAL STRUCTU.	"
ELECTROTRANSPORT	760	DIELECTRIC FILM - -	> 269	ARGON - - - - -	"	POWDER REDUCTION	"
IRON SULFIDE - - -	673	SPUN-ON FILM - - -	"	AUGER SPECTROSCG. >	1766	SINTERING - - - - -	"
NONSTOICHIOMETRY	209	THICKNESS PROFILE	"	CAPACITOR - - - - -	162		
- - - 673		THIN FILM - - - - -	"	CVD - - - - -	1335		
OXIDATION KINETI.	1516			- - - - -	1766	POSITIVE DIAZO	
OXIDATION THEORY	760	POLYMER		DIELECTRIC BREAK.	162	DEVELOPMENT TEMPER. >	2026
OXIDE SEMICONDUCT.	209	CHLOROACRYLATE - -	>1829	DOPING - - - - -	>1779	DEVELOPMENT RATE	"
SILICON DIOXIDE - -	1516	CONDUCTANCE - - -	>1682	EVAPORATION - - -	1335	ELECTRON BEAM - -	"
SWEEP VOLTAMMETRY	2183	CORROSION - - - -	>2159	FABRICATION - - -	>1415	LINE EDGE PROFILE	"
THERMOGRAVIMETRY	209	DIFFUSION - - - -	1682	INSULATION - - - -	1335	OPTICAL EXPOSURE	"
TRANSITION METAL	760	ELECTRON BEAM - - -	> 694	INTEGRATED CIRCU.	1415	PHOTORESIST - - -	"
VALENCE CHANGE - -	2183	- - - 1829		ION IMPLANTATION	1779		
ZIRCONIA - - - - -	"	ENVIRONMENT - - -	2159	LOW TEMPERATURE - -	"	POSITIVE ELECTRO.	
		FLOW CONTROL - - -	"	MOS-LSI - - - - -	1415	CORROSION FILM - -	>1848
POINT EFFECT		FUEL CELL - - - -	1682	OXIDATION - - - - -	1779	LEAD ACID BATTERY	"
DOPANT EFFECT - - -	>1523	HALOGEN - - - - -	"	OXYGEN CONCENTRA.	1766	PHOSPHORIC ACID - -	"
OXIDATION KINETI.	"	HYDROGEN - - - -	"	PRESSURE VARIATI.	1335		
PHYSICAL MODEL - -	"	INTEGRATED CIRCU.	1829	SEMIINSULATION - -	1766	POSITIVE PLATE	
SILICON DIOXIDE - -	"	LITHOGRAPHY - - -	694	SILICON DIOXIDE - -	162	LEAD ACID BATTERY >	7
		MOLECULAR ORBITAL	1829	- - - - -	1335	LEAD DIOXIDE - - -	"
POLARIZATION		MOLECULAR ORBITAL	1829	VLSI DEVICE - - - -	1779	LEAD SULFATE - - -	"
A-C IMPEDENCE - - -	>1166	PERMEATION - - - -	2159	XPS - - - - -	1766	OXIDATION - - - - -	"
ALTERNATING VOLT. >	1908	POLYMETHACRYLON.	694			SULFURIC ACID - - -	"
CERIUM DIOXIDE - -	>1155	POSITIVE RESIST - -	1829	POLYSILICON FILM			
- - - 1166		RESIST - - - - -	694	CVD - - - - -	> 833	POSITIVE RESIST	
CHARGE STORAGE - -	>1958	TRACE GAS - - - -	2159	- - - - -	> 838	CHLOROACRYLATE - -	>1829
CORROSION POTENT.	1908	TRANSPORT PROPER.	1682	LOW PRESSURE - - -	833	COPOLYMER - - - - -	> 154
DIAPHRAGM - - - -	>1502	TRIFLUOROETHYL - -	1829	OXIDATION - - - -	838	ELECTRON BEAM - - -	> 1829
DIELECTRIC PROPE.	1958	X-RAY - - - - -	694	PHOSPHORUS DOPING	833	INTEGRATED CIRCU.	"
ELECTRET - - - - -	>1708			- - - - -	838	LITHOGRAPHY - - -	154
ELECTRICAL PROPE.	1958	POLYMER MIXTURE		RESISTIVITY - - -	833	METHACRYLIC ACID - -	>1881
EXCHANGE CURRENT	1155	METHACRYLIC ACID >	1881	POLYSTYRENE		METHACRYLOYL CHL.	"
FARADAIC RECTIFI.	1908	METHACRYLOYL CHL.	"	CHLORDIMETHYLATED >	1628	METHYL METHACRYL.	154
HETEROCARGE - - -	1708	METHYL METHACRYL.	"	DRY ETCHING - - -	"	- - - - -	1881
LIFE TEST - - - - -	>1439	POSITIVE RESIST - -	"	ELECTRON RESIST - -	> 696	MOLECULAR ORBITAL	1829
MEMBRANE - - - - -	1708	ELECTRON BEAM - -	>1699	MONODISPERSE - - -	"	POLYMER - - - - -	"
MILD STEEL - - - -	1908	ELECTRON RESIST - -	>1703	NEGATIVE - - - - -	"	POLYMER MIXTURE - -	1881
OVERPOTENTIAL - - -	1155	GLYCIDYL METHACR.	1699	NEGATIVE RESIST - -	1628	RADIATION SENSIT.	154
OXIDE COATING - - -	1439	- - - 1703		SUBMICRON TECHNG.	"	TRIFLUOROETHYL - -	1829
OXYGEN REDUCTION	1502	HALOSTYRENE - - -	1699	POLYSTYRENESULFO.			
PASSIVATION - - - -	1908	LITHOGRAPHY - - -	"	ELECTRET - - - - -	>1708	POTASSIUM	
PERCHLORIC ACID - -	1439	- - - 1703		HETEROCARGE - - -	"	CESIUM - - - - -	> 347
PLATINUM ELECTRO.	1155	NEGATIVE - - - - -	1699	MEMBRANE - - - - -	"	ELECTRET - - - - -	>1708
- - - 1166		WAFER FABRICATION	1703	POLARIZATION - - -	"	HETEROCARGE - - -	"
PLATINUM-OXYGEN - -	1502			POLYVINYL ALCOHOL	"	ION SELECTIVE - - -	347
POLYSTYRENESULFO.	1708	POLYMERIZATION		POTASSIUM - - - - -	"	MEMBRANE - - - - -	> 1708
POLYVINYL ALCOHOL	"	ACRYLIC ACID - - -	> 939	SODIUM - - - - -	"	POLARIZATION - - -	"
POLYVINYL BUTYRAL	1958	CVD - - - - -	>1728			POLYSTYRENESULFO.	"
POTASSIUM - - - - -	1708	DIELECTRICS - - -	"	POLYTYPISM		POLYVINYL ALCOHOL	"
- - - - -	"	ELECTROCATALYSIS	939	CADMIUM HALIDE - -	> 325	PVC MATRIX - - - -	347
SODIUM CHLORIDE - -	1439	INFRARED ABSORPT.	1728	CRYSTALLOGRAPHY -	"	SODIUM - - - - -	> 1708
TITANIUM ANODE - -	"	LOW TEMPERATURE - -	"	DIFRACTION - - - -	"	ZINC FERROCYNANTE	347
TRANSIENT DECAY - -	1166	MORPHOLOGY CONTR. >	1567	MIXED CRYSTALS - -	"		
		NEODYMIUM PENTAP.	"	VAPOR GROWN - - -	"	POTASSIUM BROMIDE	
POLAROGRAPHY		OXIDATION - - - - -	1728			ALUMINUM BROMIDE >	1474
ACTIN - - - - -	>1471	POLYPHOSPHORIC A.	1567	POLYVINYL ALCOHOL		AROMATIC HYDROCA.	"
BITHIAZOLE - - - -	>2091	REDOX - - - - -	939	ELECTRET - - - - -	>1708	CYCLIC VOLTAMMET.	"
BLEOMYCIN - - - -	"	RING DISK ELECTR.	"	HETEROCARGE - - -	"	SURFACE PROCESSES	"
CYCLIC VOLTAMMET.	"	SILANE - - - - -	1728	MEMBRANE - - - - -	"		
IONIC PERMEABILI.	1471	SINGLE CRYSTAL - -	1567	POLARIZATION - - -	"	POTASSIUM CHLORI.	
MEMBRANE PROTEINS	"			POLYSTYRENESULFO.	"	ANODIC CORROSION >	1087
METAL COMPLEX - - -	2091	POLYMETHACRYLON.		POTASSIUM - - - - -	"	- - - - -	>1093
PYRIMIDINE - - - -	"	ELECTRON BEAM - -	> 694	SODIUM - - - - -	"	EUTECTIC - - - - -	1087
REDOX - - - - -	"	LITHOGRAPHY - - -	"			- - - - -	1093
SPECTRIN - - - - -	1471	POLYMER - - - - -	"	POLYVINYL BUTYRAL		FUEL CELL - - - - -	> 960
TALLYSONYCIN - - -	2091			CHARGE STORAGE - -	>1958	FUSED SALT - - - -	1087
				DIELECTRIC PROPE.	"	- - - - -	> 1093

PRIMARY TERM CO-TERM	PAGE NO.	PRIMARY TERM CO-TERM	PAGE NO.	PRIMARY TERM CO-TERM	PAGE NO.	PRIMARY TERM CO-TERM	PAGE NO.
POTASSIUM CHLORIDE (CONTD)		POTENTIOMETRY (CONTD)		PRISM COUPLER (CONTD)		PYRITE (CONTD)	
FUSED SALT - - - - -	1902	CHRONOAMPEROMETRY 1029		FILM THICKNESS - 1539		ELECTRODEPOSITION 911	
JUNCTION POTENTIAL >1618		COPPER - - - - -	"	REFRACTIVE INDEX - "		HYDROGEN SULFIDE - "	
LEAD CHLORIDE - - - - -	1902	DISK ELECTRODE - - - - -	"	SILICON DIOXIDE - "		MARCASITE - - - - -	"
LEAD SULFIDE - - - - -	"	FUSED SALT - - - - -	"	SILICON SUBSTRATE - "			
LITHIUM CHLORIDE 960		POTENTIOSTATIC		PROCESS CONTROL		PYROCATHECOL	
1087		ACTIVATION ENERGY >1353		ELLIPSEMETER - ->1589		AQUEOUS SOLUTION >1406	
1093		NICKEL COBALT OX. - - - - -	"	GAAS - - - - -	"	ETCHING - - - - -	"
MIGRATION POLAR. 960		OXYGEN EVOLUTION - - - - -	"	GALLIUM PHOSPHIDE - "		ETHYLENEDIAMINE - - - - -	"
MOLTEN CARBONATE - - - - -	"	PULSE - - - - -	"	RESIDUAL FILM - - - - -	"	SILICON - - - - -	"
MOLTEN SALT BATT. - - - - -	"	TEFLON BONDED - - - - -	"				
OXIDATION - - - - -	1902			PROCESSING		PYROLYSIS	
SILVER - - - - -	1618	POWDER ELECTRODE		GOLD COATING - ->1514		EPITAXIAL LAYERS >1134	
SILVER CHLORIDE - - - - -	"	ALUMINUM POWDER ->1853		LITHOGRAPHY - - - - -		GAAS EPILAYER - - - - -	"
SULFIDATION - - - - -	1093	LITHIUM - - - - -	"	PULSE ELECTROPLA. - "		LOW PRESSURE - - - - -	"
THERMAL LIQUID - 1618		METAL SULFIDE - - - - -	"				
THERMOCELL - - - - -	"	NEGATIVE ELECTRO. - - - - -	"	PROCESSING VARIA.		QUANTUM EFFICIEN.	
TRANSPORT ENTROPY - - - - -	"	RECHARGEABLE CELL - - - - -	"	REDUCTION ETCHING > 844		ALUMINUM ARSENIDE > 637	
VOLTAMMETRY - - - - -	1087			SEMICONDUCTOR - - - - -	"	BERYLLIUM DOPING >2007	
- - - - -	1093	POWDER REDUCTION		TITANIUM DIOXIDE - "		DIOIDE - - - - -	637
		DISCHARGE CAPACIT. >1899				DISLOCATION - - - - -	"
POTASSIUM HYDROX.		PHYSICAL STRUCT. - - - - -	"	PROPANE		GAAS - - - - -	"
CATHODIC POLARIZ. > 535		POROUS IRON ELEC. - - - - -	"	ELECTROOXIDATION > 775		GALLIUM - - - - -	"
NIOBIUM ELECTRODE - - - - -	"	SINTERING - - - - -	"	ETHANE - - - - -	"	LIGHT-EMITTING - - - - -	"
SURFACE CHANGE - - - - -	"			FUEL CELL - - - - -	"	PHOTOELECTROLYSIS 2007	
XPS - - - - -	"	POWDERED PHOSPHOR		METHANE - - - - -	"	SILICON - - - - -	637
		ACTIVATOR - - - - -	106	N-BUTANE - - - - -	"	TITANIUM DIOXIDE 2007	
POTASSIUM IRON S.		CONCENTRATION - - - - -	"	TRIFLUOROMETHANE - "		WATER OXIDATION - - - - -	"
CATHODE - - - - -	887	LUMINESCENCE - - - - -	"				
IRON SULFUR - - - - -	"	QUENCHING MECHAN. - - - - -	"	PROPULSION		QUARTERNARY	
LITHIUM BATTERY - - - - -	"	RADIATION - - - - -	"	ELECTRIC VEHICLE >1321		DIFFRACTIONOMETRY -> 664	
NONAQUEOUS CELL - - - - -	"	RARE EARTH - - - - -	"	ELECTROLYTE FLOW - "		DOUBLE CRYSTAL - - - - -	"
				HEAT TRANSFER - - - - -	"	GROUP III-V COMP. - - - - -	"
POTASSIUM NITRATE				LEAD ACID BATTERY - - - - -	"	INDIUM PHOSPHIDE - - - - -	"
KINETIC STABILITY >2095		POWER				INGAPAS - - - - -	"
NITRATE ION - - - - -	"	COBALT OXIDE - ->1817		PROTON CONDUCTION		LATTICE MISMATCH - - - - -	"
OXYGEN EXCHANGE - - - - -	"	ELECTRODE MATERI. - - - - -	"	ELECTROCHROME - -> 805		LPE - - - - -	"
RAMAN SPECTROSCOP. - - - - -	"	LANTHANUM STRONT. - - - - -	"	PHOSPHOTUNGSTIC - - - - -	"	QUENCHING MECHAN.	
		THERMOELECTRICITY - - - - -	"	TUNGSTEN TRIOXIDE - - - - -	"	ACTIVATOR - - - - -	106
POTASSIUM SULFATE				ZIRCONIUM PHOSPH. - - - - -	"	CONCENTRATION - - - - -	"
DECOMPOSITION - -> 490		POWER SOURCE				LUMINESCENCE - - - - -	"
EFFUSION - - - - -	"	CATHODE - - - - -	1311	PSEUDOINDUCTANCE		POWDERED PHOSPHOR - - - - -	"
VAPORIZATION - - - - -	"	HOST LATTICE - - - - -	"	EQUIVALENT CIRCU. >1082		RADIATION - - - - -	"
		SOLID SOLUTION - - - - -	"	IMPEDENCE PARAM. - - - - -	"	RARE EARTH - - - - -	"
POTENTIAL							
ADSORPTION - - - - -	608	PRASEODYMIUM		PULSE		RADIAL HEAT GRAD.	
ALUMINUM - - - - -	199	CATHODOLUMINESC. > 305		ACTIVATION ENERGY >1353		CZOCHELSKI - - - - -	284
AQUEOUS SOLUTION - - - - -	"	HOST SENSITIZATI. - - - - -	"	NICKEL COBALT OX. - - - - -	"	GALLIUM DOPING - - - - -	"
CELL KINETICS - - - - -	608	NONRADIATIVE PRO. - - - - -	"	OXYGEN EVOLUTION - - - - -	"	GERMANIUM - - - - -	"
CURRENT PEAK - - - - -	257	TERBIUM - - - - -	"	POTENTIOSTATIC - - - - -	"	HEAT PIPE - - - - -	"
ELECTROCHEMICAL ->2169		TRAPPING - - - - -	"	TEFLON BONDED - - - - -	"	SEGREGATION - - - - -	"
ELECTRODEPOSITION - 257		YTTRIUM OXISULF. - - - - -	"			SYMMETRY - - - - -	"
HYDRIDE FORM - - - - -	199			PULSE ELECTROPLA.			
HYDROGEN ADATOM - 257		PREPARATION		GOLD COATING ->1514		RADIATION	
LITHIUM BATTERY - 608		ALLOY - - - - -	2162	LITHOGRAPHY - - - - -	"	ACTIVATOR - - - - -	106
PERTURBATIONS - - 257		ELECTRODEPOSITION - - - - -	"	PROCESSING - - - - -	"	CONCENTRATION - - - - -	"
PH - - - - -	199	FOIL - - - - -	"			LUMINESCENCE - - - - -	"
PHASE DIAGRAM - - - - -	608	FUSED SALT - - - - -	"	PULSED ILLUMINAT.		POWDERED PHOSPHOR - - - - -	"
PLATINUM - - - - -	257	IRON PLATINUM - - - - -	"	FERRIC OXIDE - -> 56		QUENCHING MECHAN. - - - - -	"
SALT SOLUTION - - - - -	199			FLAME OXIDATION - - - - -	"	RARE EARTH - - - - -	"
SPECTROSCOPY - - - - -	608	PRESSURE CONTROL		PHOTOCURRENT - - - - -	"		
- - - - -	2169	CARBON DIOXIDE ->2012		SINTERING - - - - -	"	RADIATION DAMAGE	
TITANIUM DISULF. 608		FURNACE - - - - -	"	SOLAR CELL - - - - -	"	CONTAMINATION - -> 319	
VOLTAGE STEPS - - - - -	"	GAS FLOW METHOD - - - - -	"			GLOW DISCHARGE - - - - -	"
		HYDROGEN - - - - -	"	PULSED PLATING		PLASMA DEPOSITION - - - - -	"
POTENTIAL DISTRI.		LOWER TEMPERATURE - - - - -	"	DIRECT CURRENT -> 881		PLASMA ETCHING - - - - -	"
ANALYTIC SOLUTION >2081		OXYGEN PRESSURE - - - - -	"	->1633		SPUTTERING - - - - -	"
ANODIC DISSOLUTION >2150		WUSTITE PHASE - - - - -	"	HYDROGEN PERMEAT. - - - - -	"	RADIATION SENSIT.	
CAPACITANCE - ->1505				METAL QUANTITY - 881		COPOLYMER - - - - -	154
FLATBAND POTENTI. - - - - -	"	PRESSURE REDUCTI.		PLATING - - - - -	1633	LITHOGRAPHY - - - - -	"
FOURIER ANALYSIS 2081		CVD - - - - -	1042	PLATING CYCLE - - - - -	881	METHACRYLIC ACID - - - - -	"
IRON - - - - -	2150	DEPOSITION RATE - - - - -	"			METHYL METHACRYL. - - - - -	"
LINEAR POLARIZAT. 2081		INTEGRATED CIRCU. - - - - -	"	PURIFICATION		POSITIVE RESIST - - - - -	"
MOTT-SCHOTTKY - - 1505		PHOSPHORUS DOPING - - - - -	"	ELECTROTRANSPORT >1811			
PASSIVE FILM - - - - -	2081	SILICON DIOXIDE - - - - -	"	HIGH RESISTANCE - - - - -	"	RADIATION YIELD	
SCRATCH - - - - -	"			LOW PRESSURE - - - - -	"	ION BEAM - - - - -	483
SULFURIC ACID - 2150		PRESSURE VARIATI.		MICROGRAVITY - - - - -	"	LITHOGRAPHY - - - - -	"
TITANIUM DIOXIDE 1505		ALUMINUM COVERAGE >1335		THORIUM - - - - -	"	PATTERN DUPLICAT. - - - - -	"
		ARGON - - - - -	"			POLYDIMETHYLSILO. - - - - -	"
POTENTIAL PERTUR.		CVD - - - - -	"	PVC MATRIX		POLYMETHYLMETACR. - - - - -	"
ELECTROSORPTION ->1172		EVAPORATION - - - - -	"	CESIUM - - - - -	347	RESIST MATERIAL - - - - -	"
FILM FORMATION - - - - -	"	INSULATION - - - - -	"	ION SELECTIVE - - - - -	"		
GOLD ELECTRODE - - - - -	"	POLYSILICON - - - - -	"	POTASSIUM - - - - -	"	RADIOCHEMISTRY	
SODIUM HYDROXIDE - - - - -	"	SILICON DIOXIDE - - - - -	"	ZINC FERROCYANIDE - - - - -	"	BETA-ALUMINA - ->1513	
						MONOCRYSTAL - - - - -	"
POTENTIODYNAMICS		PRIMARY CELL		PYRIMIDINE		SODIUM-22 LABEL - - - - -	"
AGING KINETICS -> 592		DISCHARGE REACTI. > 513		BITHIAZOLE - - ->2091			
ELECTROCATALYSIS > 218		LITHIUM ANODE - - - - -	"	BLEEDING - - - - -	"	RAMAN SPECTROSCOP.	
ELECTROOXIDATION - - - - -	"	SOLUBLE CATHODE - - - - -	"	CYCLIC VOLTAMMET. - - - - -	"	KINETIC STABILITY >2095	
ETHYLENE - - - - -	"	THIONYL CHLORIDE - - - - -	"	METAL COMPLEX - - - - -	"	NITRATE ION - - - - -	"
OXYGEN MONOLAYER 592				POLAROGRAPHY - - - - -	"	OXYGEN EXCHANGE - - - - -	"
PERTURBATION PRO. - - - - -	"	PRIMARY RESISTAN.		REDUX - - - - -	"	POTASSIUM NITRATE - - - - -	"
PLATINUM - - - - -	218	CLOSED FORM - ->1307		TALLYSCMYCIN - - - - -	"		
- - - - -	592	RING ELECTRODE - - - - -	"				
POTENTIOMETRY		PRISM COUPLER		PYRITE		RARE EARTH	
CHLOROALUMINATE ->1029		DIELECTRIC FILM ->1539		CARBON STEEL - -> 911		ACTIVATOR - - - - -	106

PRIMARY TERM CO-TERM	PAGE NO.	PRIMARY TERM CO-TERM	PAGE NO.	PRIMARY TERM CO-TERM	PAGE NO.	PRIMARY TERM CO-TERM	PAGE NO.
RARE EARTH (CONTO)		RECHARGEABLE CELL		REFRACTORIES (CONTO)		RESISTIVITY SHIFT (CONTO)	
CONCENTRATION - - - -	106	ALUMINUM POWDER ->1853		HOT-PRESSED - - - -	1723	CONDUCTIVITY - - - -	1792
LUMINESCENCE - - - -	"	LITHIUM - - - -	"	OXIDATION KINETI. - -	"	ELECTRICAL MEASU. -	"
POWDERED PHOSPHOR - -	"	METAL SULFIDE - - -	"	SILICON NITRIDE - - -	"	HYDROGEN DIFFUSI. -	"
QUENCHING MECHAN. - -	"	NEGATIVE ELECTRO. -	"	YTTRIUM - - - - - - -	"	P-TYPE - - - - - - -	"
RADIATION - - - - - -	"	POWDER ELECTRODE - -	"			SILICON SURFACE - -	"
RARE EARTH ACTIV.		RECIPROCITY FAIL.		REGENERATION		REVERSAL ETCHING	
CERIUM DOPING - ->1213		BISAZIDE RESIST -> 273		ENERGY STORAGE -> 713		CHROMIUM FILM - ->1794	
DECAY PROCESS - ->1221		CROSSLINKING - - - -	"	HYDROGEN-CHLORINE - -	"	GAS PLASMA - - - -	"
EUROPIUM DOPING - 1221		PHOTORESIST SYST. - -	"	MASS HEAT BALANCE - -	"	MOS-LSI PROCESS - -	"
GADOLINIUM DOPING - -	"			STOICHIOMETRY - - - -	"	PHOTOMASK - - - - -	"
NARCT PHOSPHORS - 1221		REDOX		REGENERATIVE CELL		RF PLASMA	
TERBIUM DOPING - - -	"	ACRYLIC ACID - -> 939		ACETONITRILE - -> 603		EMISSION SPECTRUM> 460	
THERMAL DEPENDEN. 1213		BITHIAZOLE - ->2091		EFFICIENCY - - - - -	"	GLOW DISCHARGE - -	"
	1221	BLEDMYCIN - - - - -	"	GAAS - - - - - - - -	"	NITROGEN - - - - -	"
		CHARGE TRANSFER -> 855		LIQUID JUNCTION - - -	"	PLASMA TEMPERATU. -	"
		CYCLIC VOLTAMMET. 2091		PHOTOVOLTAIC CELL - -	"	ROTATIONAL TEMPE. -	"
		DISK ELECTRODE ->1483		SINGLE CRYSTAL - - - -	"		
RATE CAPABILITY		ELECTROCATALYSIS 939					
CAPACITY - - - - -> 523		ETCHING - - - - - - -	855	RELAXATION TIME			
DISSOLVED SULFUR - -	"	GAAS ELECTRODE - - -	"	ALUMINUM - - - -> 779		RHEED	
LITHIUM BATTERY - - -	"	GROUP III-V COMP. - -	"	ANODIZATION - - - -	"	AUGER SPECTROSCO. > 450	
ORGANIC ELECTROL. - -	"	METAL COMPLEX - 2091		IMPEDENCE - - - - -	"	ELLIPSPOMETRY - - -	"
SECONDARY BATTERY - -	"	PHOTOCORROSION - 1483		STOICHIOMETRY - - - -	"	GAAS - - - - - - - -	"
SYSTEM STABILITY - -	"	PHOTOEFFECT - - - -	855			IN SITU - - - - - -	"
TETRAHYDROFURAN - -	"	PHOTON FLUX - - - -	1483	RELIABILITY		LEED - - - - - - - -	"
		POLAROGRAPHY - - - -	2091	CONNECTOR - - - ->1798		SURFACE ANALYSIS -	"
REACTION KINETICS		POLYMERIZATION - 939		COPPER - - - - - - -	"	VPE - - - - - - - -	"
HYDROGEN - - - ->1596		PYRIMIDINE - - - -	2091	DIFFUSION - - - - -	"		
URANIUM POWDER - - -	"	RING DISK ELECTR. 939		GOLD ALLOY - - - - -	"	RING DISK ELECTR.	
		TALLYSDMYCIN - - 2091		OXIDATION KINETI. - -	"	ACRYLIC ACID - -> 939	
REACTION MECHAN.						ELECTROCATALYSIS -	"
DISCHARGE - - - ->2168		REDUCING CONDITI.		REOXIDATION		POLYMERIZATION - -	"
HIGH PRESSURE - -> 985		DECOMPOSITION - ->1067		ANNEALING - - - ->1731		REDOX - - - - - - -	"
HYDROGEN EVOLUTI. - -	"	NITRIC OXIDE - - - -	"	CAPACITANCE - - - -	"		
LITHIUM - - - - - - -	2168	SCANDIA DOPING - - -	"	HIGH TEMPERATURE - -	"	RING ELECTRODE	
THIONYL CHLORIDE - -	"	ZIRCONIA - - - - - -	"	OXIDE FILM GROWTH - -	"	CLOSED FORM - - ->1307	
TRANSITION STATES 985				SILICON OXIDE - - - -	"	PRIMARY RESISTAN. -	"
		REDUCTION		TITANIUM DIOXIDE - -	"		
REACTION ORDER		ALKALINE SOLUTION>1693				ROTATING DISK	
ALKALINE SOLUTION> 541		ANODIZATION - -> 803		RESIDUAL FILM		AC ADMITTANCE - -> 424	
CHRONOCULOMETRY > 579		CARBOXYLATION -> 404		ELLIPSPOMETRY - ->1589		CODEPOSITION - -> 566	
CURRENT DENSITY - 541		CATHOLYTE - - - ->1496		GAAS - - - - - - - -	"	CONVECTIVE DIFFU. > 431	
ELECTROHYDRODIME. 579		CATION RADIUS - - - -	"	GALLIUM PHOSPHIDE - -	"	COPPER - - - - - - -	566
EQUILIBRIUM POTE. 541		CONDUCTION - - - -	803	PROCESS CONTROL - - -	"	DIFFUSION CONTROL -	"
ETHYL CINNAMATE - 579		COPPER DEPOSITION> 171				ELECTROLYSIS - -> 398	
LOW TEMPERATURE - - -	"	COULOMETRY - - - ->2035		RESIN		ELECTRON TRANSFER 431	
METHYL CINNAMATE - -	"	CYCLIC VOLTAMMET. - -	"	DIAZIDE-S-SULFON.> 860			437
ZINC ELECTRODE - 541		DERIVATIVE - - - - -	404	ELECTRON BEAM - - - -	"	HYDRODYNAMICS - - -	431
		ELECTROGLASS - - - -	171	EPR - - - - - - - -	"		437
REACTION PROFILE		EPOXIDE DIMERS - 1693		MASS SPECTROSCOPY - -	"	INTERFACE - - - - -	424
ELECTRODE MODEL ->1835		GALVANIC CELL - - - -	171	O-NAPHTHOQUINONE - -	"	MASS TRANSFER - - -	398
POROUS ELECTRODE - -	"	KINETIC ANALYSIS 1693		PHENOLIC-TYPE - - -	"	PERIODIC CURRENT -	"
SURFACE MORPHOLO. - -	"	LITHIUM - - - - - - -	2035	RESIST		PLATINUM - - - - -	424
ZINC PORE ELECTR. - -	"	MOLTEN NITRATE - 1496		DEVELOPING TIME ->1430		SINUOIDAL - - - - -	431
		NITRATE SALT - - - -	"	ELECTRON BEAM - -> 694			437
REACTION RATE		O-CARBOXYMETHYL - 404		EPR - - - - - - - -	1430	SULFURIC ACID - - -	424
ANODIC OXIDATION > 583		OPEN PAN STUDY - 1496		LINE WIDTH - - - - -	1430	SWEEP FREQUENCY - -	"
ELECTROCHROMISM - -	"	OXIDATION - - - - - -	171	LITHOGRAPHY - - - - -	694	VOLTAMMETRY - - - -	431
FILM STRUCTURE - - -	"	PHTHALIMIDE - - - -	1693	POLYMER - - - - - - -	"		437
TUNGSTEN TRIOXIDE - -	"	SILVER BROMIDE - 803		POLYMETHACRYLONI. -	"	ZINC - - - - - - - -	566
VACUUM EVAPORATI. - -	"	STRUCTURAL ANALY. 1693		POLYMETHYLMETHAC. 1430			
		SULFUR OXYCHLORID. 2035		SLOPE ANGLE - - - - -	"	ROTATING ELECTRO.	
REACTIVE ION ETCH		SYNTHESIS - - - - - -	404	X-RAY - - - - - - -	694	DIFFUSION - - - -> 242	
CARBON TETRAFLUO.>1419		TARTRONIC ACID - - -	"				- - -> "
ETCHING - - - - - - -	"	THERMAL BATTERY - 1496		RESIST MATERIAL		ELLIPSPOMETRY - - -	"
HYDROGEN - - - - - -	"			ION BEAM - - - -> 483		INTERFACE POTENT. -	"
SILICON DIOXIDE - - -	"	REDUCTION ETCHING		LITHOGRAPHY - - - -	"	IONIC CONDUCTOR - -	"
		PROCESSING VARIA.> 844		PATTERN DUPLICAT. - -	"	ROTATING ELECTRO. -	"
REACTIVE SPUTTER.		SEMICONDUCTOR - - -	"	POLYDIMETHYLSILO. - -	"		"
CARBONTETRAFLUOR.> 226		TITANIUM DIOXIDE - -	"	POLYMETHYLMETACR. -	"	SILVER SALT SOLU. -	"
DIODE SYSTEM - - - -	"			RADIATION YIELD - - -	"		
HIGH RATE - - - -> 691		REDUCTION MECHAN.					
INDIUM OXIDE - - - -	"	BENZAL CHLORIDE -> 401		RESISTANCE		ROTATING HEMISP. -	"
PLASMA ETCHING - 226		CARBON DIOXIDE - - -	"	CURRENT DISTRIBUTU.>1348		LAMINAR FLOW - ->1937	
POLYESTER FILM - 691		DIMETHYLFORMAMIDE -	"	CYLINDRICAL CELL - -	"	LIMITING CURRENT - -	"
TIN DOPING - - - - -	"			DISK ELECTRODE - - -	"	MASS TRANSFER - - -	"
REACTIVITY		REFERENCE ELECTR.					
ABSORPTION - - - -> 495		AQUEOUS SYSTEM -> 908		RESISTIVE CAPACI.		ROTATIONAL TEMPE.	
HIGHLY REACTIVE - -	"	HIGH TEMPERATURE - -	"	CYCLIC VOLTAMMET.> 989		EMISSION SPECTRUM> 460	
HYDROGEN - - - - - -	"	THERMAL CELL - - - -	"	IMPEDENCE - - - - -	"	GLOW DISCHARGE - -	"
TEMPERATURE DEPE. - -	"			SMALL AMPLITUDE - - -	"	NITROGEN - - - - -	"
URANIUM POWDER - - -	"	REFRACTIVE INDEX		VOLTAMMGRAM - - - -	"	PLASMA TEMPERATU. -	"
		DIELECTRIC FILM ->1539				RF PLASMA - - - - -	"
REACTOR		FILM THICKNESS - - -	"	RESISTIVITY			
FLOW-THROUGH - ->1885		INTEGRATED CIRCU.> 103		CURRENT DENSITY ->1479		RUBIDIUM CHLORIDE	
GASEOUS REACTANTS - -	"	LIQUID STANDARD - - -	"	CVD - - - - - - - -	> 833	COPPER ION CONDU.>1654	
TRICKLE BED ELEC. - -	"	PASSIVATION LAYER - -	"	LOW PRESSURE - - - -	"	CUPROUS CHLORIDE -	"
		PRISM COUPLER - - 1539		MULTILAYER ANALY. 1479		CUPROUS IODIDE - -	"
REACTOR ANALYSIS		SILICON DIOXIDE - - -	"	POLYSILICON FILM - -	"	SOLID ELECTROLYTE -	"
COMPETING REACTI.>1928		SILICON SUBSTRATE - -	"	SPREADING RESIST. 1479		X-RAY DIFFRACTION -	"
MULTIPLE REACTI. - -	"	TRANSPARENT FILM 103					
POROUS ELECTRODE - -	"			RESISTIVITY SHIFT			
		REFRACTORIES		CHEMICAL TREATME.>1792			
		CERAMICS - - - ->1723					
		CORROSION - - - - -	"				

PRIMARY TERM CO-TERM	PAGE NO.	PRIMARY TERM CO-TERM	PAGE NO.	PRIMARY TERM CO-TERM	PAGE NO.	PRIMARY TERM CO-TERM	PAGE NO.
RUTHENIUM		SCANDIA DOPING (CONTD)		SEMICONDUCTOR (CONTD)		SILICON (CONTD)	
CATION ABSORPTION>	954	ZIRCONIA - - - - -	1067	ELECTROMIGRATION	338	AUTODOPING - - - - -	822
CHLORINE EVOLUTI.>	1189	SCRATCH		ELECTRON INJECTI.>	207C	BORON DIFFUSION -	1805
CONTACT MATERIAL >	2017	ANALYTIC SOLUTION>	2081	ENERGY CONVERSION	338	BORON DOPING - ->	138
CONTACT RESISTAN.	"	FOURIER ANALYSIS	"		414	BORON - - - - -	345
ELECTROCATALYSIS	1189	LINEAR POLARIZAT.	"	FLATBAND POTENTI.	598	BORON GETTERING ->	1754
ENERGY CONVERSION	954	PASSIVE FILM - - -	"	GAAS	59	BORON NITRIDE - -	1805
PHOTOANODE - - - -	"	POTENTIAL DISTRI.	"	GALLIUM ANTIMONI.	2031	BORON RICH LAYER	"
PHOTOELECTROCHEM.	"			HEXACVANOFERRATE	732	CARBON - - - - -	1422
RUTHENIUM DIOXIDE	2017	SCREEN WEIGHT		HOLE INJECTION	1011	CARBON MONOXIDE -	"
SOLAR CELL - - - -	954	PHOSPHOR PARTICLE>	1563	ILLUMINATED - - -	"	CARRIER CONCENTR.>	260
SULFIDATION - - - -	2017	VOID TRANSMISSION	"	INDIUM PHOSPHIDE	598	CESIUM - - - - -	660
SURFACE TREATMENT	954	WEIGHT OPTIMIZAT.	"	INTEGRATED CIRCU.>	20C	CHLORINE INCORPO.>	143
TITANIUM OXIDE - -	1189	SEAWATER CELL		IR ABSORPTION - -	260	CHROMIUM - - - - -	1047
TITANIUM SUPPORT.	"	CATHODE - - - - -	351	IRON OXIDE - - - -	419	CONSTANT VOLTAGE	89
		CUPRIC OXALATE - -	"	LIQUID AMMONIA	207C	CVD - - - - -	644
RUTHENIUM DIOXIDE				LIQUID JUNCTION	1011	- - - - -	653
CONTACT MATERIAL >	2017	SECONDARY BATTERY		METALORGANICS - -	2031	CZOCHEKRSKI - - -	1142
CONTACT RESISTAN.	"	CAPACITY - - - - -	523	MOS - - - - -	20C	DEGRADATION - - -	1047
CRYSTAL GROWTH ->	1625	CATHODE - - - - -	497	N-TYPE - - - - -	59	DEPOSITION - - -	688
OPTIMUM CONDITION	"	DICHALCOGENIDE ->	349	ORGANOMETALLICS -	205C	DEPTH PROFILE - -	660
RUTHENIUM - - - - -	2017	DISCHARGE DATA ->	357	OXIDE FILM - - - -	732	DIOXIDE - - - - -	1805
SULFIDATION - - - -	"	DISSOLVED SULFUR	523	OXIDE TYPE - - - -	59	DILLOCATION - - - -	59
THERMAL EXPANSION	1625	INTERCALATION - -	349	PASSIVE IRON - - -	732	DOPANT - - - - -	660
		IRON - - - - -	357	PHOTOANODE - - - -	1011	DOPANT DISTRIBUT.	138
RUTHENIUM OXIDE		LITHIUM - - - - -	349	PHOTOCURRENT - -	419	DOPANT INCORPORA.	644
NONAQUEOUS SOLVE.>	407	LITHIUM BATTERY -	523	PHOTOELECTRICITY	949	DOPANT - - - - -	653
WORKING ELECTRODE	"	LITHIUM CELL - - -	457	PHOTOELECTROCHEM.	59	DOPING - - - - -	1761
XPS - - - - -	"	LOW VOLTAGE BEHA.	349		598	EPITAXIAL FILM -	644
		ORGANIC ELECTROL.	523	PHOTOINDUCED - -	414	- - - - -	653
RUTHENIUM TRICHL.		RATE CAPABILITY -	"	PROCESSING VARIA.>	844	EPITAXIAL GROWTH	822
CHEMISORPTION - ->	617	SOLUBLE SYSTEM -	357	REDUCTION ETCHING	"	- - - - -	2033
SURFACE WAVE - - -	"	SYSTEM STABILITY	523	SILICON - - - - -	20C	EPITAXY - - - - -	1761
TIN DIOXIDE - - - -	"	TETRAHYDROFURAN -	"	- - - - -	260	EQUILIBRIUM - - -	1422
XPS - - - - -	"	TITANIUM - - - - -	357	SINGLE CRYSTAL - -	598	ETCHING - - - - -	345
		TOPOCHEMICAL CELL	349	SOLAR CELL - - - -	1011	- - - - -	1406
RUTILE ANODE		VANADIOUS OXIDE -	497	SOLVATED ELECTRON	207C	ETHYLENEDIAMINE -	"
ARC PLASMA SPRAY.>	83			SURFACE EFFECT -	59	FILM THICKNESS -	2033
CERAMICS - - - - -	"	SECONDARY ION		TAFEL SLOPE - - -	732	GAAS - - - - -	637
PHOTOELECTROLYSIS	"	CESIUM - - - - -	660	TITANIUM DIOXIDE	844	- - - - -	660
TITANIUM DIOXIDE	"	DEPTH PROFILE - -	"	VP CONVERSION - -	414	GALLIUM - - - - -	637
		DOPANT - - - - -	"	XPS - - - - -	949	GOLD MERCURY ->	1084
RUTILE LATTICE		GAAS - - - - -	"	SEMIINSULATION		HIGH PRESSURE ->	1822
HYDROGEN - - - - -	2163	MASS SPECTROMETRY	"	AUGER SPECTROSCO.>	1766	HYDROCHLORIC ACID	143
PHOTOANODE - - - -	"	SILICON - - - - -	"	CVD - - - - -	"	HYDROGEN CONTENT	688
TITANIUM DIOXIDE	"	ULTRAHIGH VACUUM	"	OXYGEN CONCENTRA.	"	HYDROGEN INJECT.	1805
				POLYSILICON - - -	"	IMPACT DIODE - -	1047
SACCHARIN		SEGREGATION		XPS - - - - -	"	INTEGRATED CIRCU.>	20C
ELECTROCRYSTALLI.>	2085	CZOCHEKRSKI - - ->	284	SEMIINTEGRATION		- - - - -	1142
ELECTRODEPOSITION	"	GALLIUM DOPING -	"	ELECTROANALYSIS ->	50	INTERDIFFUSION -	1047
EPITAXY - - - - -	"	GERMANIUM - - - -	"	ELECTROLYTE CONC.	"	INTERFACE MIGRAT.	2033
NICKEL - - - - -	"	HEAT PIPE - - - -	"	SUPPORTING ELECT.	"	INTERFACE STATE ->	1979
PASSIVATION - - - -	"	RADIAT. HEAT GRAD.	"	VOLTAMMETRY - - -	"	INTERFERENCE - -	"
SURFACE STRESS - -	"	SYMMETRY - - - - -	"			ION IMPLANTATION	1761
				SENSOR		ION ROLE - - - - -	1024
SALT FILM		SELECTIVITY		CARBON MONOXIDE ->	627	IR ABSORPTION - -	260
CORROSION - - - - -	1662	CHLORINATION - - ->	500	CONDUCTANCE MODU.	"	LIFETIME - - - - -	1142
MATHEMATICAL MOD.	"	CYCLODEXTRIN - -	"	THIN FILM - - - -	"	LIGHT-EMITTING -	132
PIT GROWTH - - - -	"	MODIFIED ELECTRO.	"	TIN OXIDE - - - - -	"	LOW TEMPERATURE -	822
PIT INITIATION - - -	"					LPE - - - - -	138
TRANSPORT LAW - - -	"			SILANE		LSI DEVICE - - - -	1754
				ARSENIC DESORPTI.>	822	MASKING STRUCTURE	292
SALT SOLUTION		SELENIUM SULFIDE		AUTODOPING - - - -	"	MASS SPECTROMETRY	660
ALUMINUM - - - - -	199	DISSOCIATION - ->	1825	CVD - - - - -	1728	- - - - -	688
AQUEOUS SOLUTION	"	MASS SPECTROSCOPY	"	DIELECTRICS - - - -	"	MELTBACK - - - - -	138
COLD PLASTIC DEF.>	2075	THERMODYNAMICS -	"	EPITAXIAL GROWTH	822	METALLIZATION -	1047
CORROSION - - - - -	"	VAPORIZATION - - -	"	INFRARED ABSORPT.	1728	MICROWAVE - - - -	1024
ELECTROCAPILLARY >	252			ION TEMPERATURE -	"	MINORITY CARRIER	1142
EXTENSOMETER - - -	"	SELF DISCHARGE		OXIDATION - - - - -	"	MOBILE ION - - - -	1979
HYDRIDE FORM - - -	199	ANODIC OXIDE FILM>	1972	POLYMERIZATION - -	"	MOLECULAR BEAM -	1761
PH - - - - -	"	IONIC CONDUCTION	"	SILICON - - - - -	822	MOS - - - - -	20C
PITTING RESISTAN.	2075					MOS CAPACITOR -	1979
PLATINUM - - - - -	199	SELLO ETCH		SILICA FILM		NEUTRAL SPECIES	1024
POTENTIAL - - - - -	"	AGITATION - - - - -	479	DIFFUSION PROCESS>	1252	OXIDATION - - - -	143
STAINLESS STEEL -	2075	DEFECT - - - - -	"	PHOSPHORUS DIFFU.	"	OXIDATION RATE ->	502
SURFACE STRESS -	252	ETCH - - - - -	"	PHOSPHORUS DOPING	"	OXIDE CHARGE DEN.	878
		SILICON EVALUATI.	"			OXIDE FILM GROWTH	1822
SAPPHIRE		ULTRASONIC - - -	"	SILICA SURFACE		OXYCHLORIDE - - -	1754
ANNEAL - - - - -	277	SEMICONDUCTOR		CONDUCTANCE - - ->	1827	OXYGEN - - - - -	1422
CHANNELING - - - -	"	ACETONITRILE - ->	59	ELECTRON EXCHANGE	"	PARABOLIC GROWTH	89
CHROMIUM - - - - -	"	- - - - -	598	THERMALLY GROWN -	"	PHOSPHORUS - - -	1754
DIFFRACTION - - - -	"	AGING EFFECTS - ->	338			PHOTOVOLTAIC PRO.	688
EPITAXIAL RELATI.	"	ANODE - - - - -	419	SILICON		PIPE YIELD - - - -	1754
ETCHING - - - - -	1004	APROTIC SOLVENT ->	414	ALUMINUM - - - - -	878	PLANAR DEVICE - -	143
MASKING - - - - -	"	AQUEOUS MEDIA ->	205C	ALUMINUM ARSENIDE>	637	PLANAR GALLIUM -	292
ORIFICE SIZE - - - -	"	AUGER SPECTROSCO.>	949	ALUMINUM DIFFUSI.>	292	PLASMA ETCHING -	1024
PLATINUM - - - - -	277	CADMIUM SELENIDE	"	AMBIENT PRESSURE >	1422	PLATINUM - - - - -	1047
		CADMIUM SULFIDE -	"	AMORPHOUS SEMICO.>	688	PYROCATTECHOL -	1406
SCALE		CARRIER CONCENTR.>	260	ANODIC OXIDATION >	89	QUANTUM EFFICIEN.	637
IRON - - - - -	683	CHARGE TRANSFER >	1011	ANTIMONY EVAPORA.>	1761	SECONDARY ION -	660
IRON SULFIDE - - - -	"	CHEMILUMINESCENCE	414	AQUEOUS SOLUTION >	1406	SEMICONDUCTOR -	20C
SULFIDATION - - - -	"	CONDUCTING ELECT.	205C	ARSENIC - - - - -	1761	- - - - -	260
		CVD - - - - -	2031	ARSENIC DESORPTI.>	822	SILANE - - - - -	822
SCANDIA DOPING		DEFECT DOPING - -	338	AUGER SPECTROSCO.>	1805	SILICON DIOXIDE -	878
DECOMPOSITION - ->	1067	DIGITAL SIMULATI.	1011			SILVER - - - - -	1047
NITRIC OXIDE - - - -	"	ELECTROGENERATED	414			SODIUM HYDROXIDE	345
REDUCING CONDITI.	"						

PRIMARY TERM CO-TERM	PAGE NO.	PRIMARY TERM CO-TERM	PAGE NO.	PRIMARY TERM CO-TERM	PAGE NO.	PRIMARY TERM CO-TERM	PAGE NO.
SILICON (CONTD)		SILICON DIOXIDE (CONTD)		SILICON OXIDE (CONTD)		SILVER OXIDE (CONTD)	
STEAM OXIDATION - 1822		PLANAR JUNCTION - 135		CAPACITANCE - - - 1731		GRID CORROSION - 725	
THERMAL PROCESS - 1142		POINT DEFECT - - 1516		CHLOROSILOXANE ->1081		LEAD ACID BATTERY "	
ULTRAHIGH VACUUM 660		POINT EFFECT - - 1523		DEPOSITION RATE -> 930			
WORK FUNCTION - - 878		POLYSILICON - - - 162		HIGH TEMPERATURE 1731		SILVER SALT SOLU.	
- - - 1084		- - - 1335		HYDROCHLORIC ACID 1081		DIFFUSION - - - -> 242	
		PRESSURE REDUCT. 1042		>1129		ELLIPSONOMETRY - - "	
SILICON ANODIZAT.		PRESSURE VARIAT. 1335		OXIDE FILM GROWTH 1731		INTERFACE POTENT. "	
DIELECTRIC ISOLA.> 870		PRISM COUPLER - - 1539		PHASE SEPARATION 1129		IONIC CONDUCTOR "	
INTEGRATED CIRCU. "		REFRACTIVE ION ETCH 1419		PLANAR REACTOR - 930		ROTATING ELECTRO. "	
SILICON POROSITY "		REFRACTIVE INDEX 1539		PLASMA - - - - "			
		SILICON - - - - 878		REDUCTION - - - 1731			
		SILICON INTERFACE 122		SODIUM PASSIVAT. 1129		SINGLE CRYSTAL	
SILICON CARBIDE		131		TITANIUM DIOXIDE 1731		ACETONITRILE - -> 598	
CERAMICS - - - ->2156		SILICON NITRIDE - 1014				- -> 603	
CONTAINER MATERI. "		SILICON SUBSTRATE 1539		SILICON CXYNITRI.		ANODIC ACTIVATION> 78	
CORROSION - - - - "		SODIUM NEUTRALIZ. 149		AMMONIA GAS - - -> 996		AUGER SPECTROSCOP. > 67	
DISSOLUTION - - -> 634		SPUTTER ETCH - - 1531		DIELECTRIC FILM - "		EFFICIENCY - - - 603	
FICKS LAW - - - - "		STACKING FAULT - 1789		OXIDATION RESIST. "		ELECTROCATALYSIS 67	
MOLTEN SILICON - "		STRESS-STRAIN - - 131		THERMAL NITRIDAT. "		78	
SINTERING - - - - 2156		THERMAL OXIDATION 122				ELECTRON DIFFRAC. 67	
SODIUM SULFUR - - - "		1288		SILICON POROSITY		FLATBAND POTENTI. 598	
		1573		DIELECTRIC ISOLA.> 870		GAAS - - - - 603	
SILICON CRYSTAL		1789		INTEGRATED CIRCU. "		HYDROGEN ABSORPT. 67	
ANTIMONY - - - -> 875		TIN DOPING - - - 135		SILICON ANODIZAT. "		INDIUM PHOSPHIDE 598	
CARBON IMPURITY -> 935		TRAPPING DENSITY 1078				LIQUID JUNCTION - 603	
CRYSTAL GROWTH - 875		TRICHLOROETHYLENE 1789		SILICON SUBSTRATE		MORPHOLOGY CONTR.>1567	
CZOCHEWSKI - - - - "		VISCOELASTICITY - 1014		DIELECTRIC FILM ->1539		NEODYMIUM PENTAP. "	
DOPED MELT - - - - "		WORK FUNCTION - - 878		FILM THICKNESS - "		OXYGEN REDUCTION 78	
HEAT EXCHANGER - 935				PRISM COUPLER - - "		PHOTOELECTROCHEM. 598	
INSTABILITY - - - 875		SILICON ETCH		REFRACTIVE INDEX "		PHOTOVOLTAIC CELL 603	
MOLYBDENUM RETAI. 935		FLUORINE GAS - ->1946		SILICON DIOXIDE - "		PLATINUM - - - - 67	
MORPHOLOGY - - - 875		INDUCTION PERIOD "				- - - - 78	
		MICROCIRCUIT - - "		SILICON SURFACE		POLYMERIZATION - 1567	
SILICON DIOXIDE				CHEMICAL TREATME.>1792		POLYPHOSPHORIC A. "	
ALUMINUM - - - -> 162		SILICON EVALUATI.		CONDUCTIVITY - - "		REGENERATIVE CELL 603	
- - - -> 878		AGITATION - - - -> 479		ELECTRICAL MEASU. "		SEMICONDUCTOR - - 598	
ALUMINUM COVERAGE>1335		DEFECT - - - - - "		HYDROGEN DIFFUS. "		STRUCTURE SENSIT. 67	
ANNEALING - - ->1078		ETCH - - - - - "		P-TYPE - - - - - "		78	
- - - ->1573		SELLO ETCH - - - "		RESISTIVITY SHIFT "			
ARGON - - - - - 1335		ULTRASONIC - - - "					
BORON DOPING - - -> 313				SILICON WAFER		SINGLE PORE ELEC.	
C-V CURVE - - - - 1078		SILICON FIBER		CLEANING SOLUTION>1428		POROUS ELECTRODE > 965	
CAPACITOR - - - - 162		CVD - - - - - -> 31		COPPER DOPING -> 114		SILVER CHLORIDE - "	
CARBON TETRAFLUO.> 464		GROWTH MECHANISM "		COPPER PRECIPITA. "		SOLUBLE REACTANT "	
- - - ->1419		WHISKERS - - - - "		GETTERING - - ->1436			
CHARGE DENSITY - 1573				HYDROGEN PEROXIDE 1428		SINTERING	
CHLORINE OXIDATI.>1288		SILICON FILM		LASER - - - - - 1436		CERAMICS - - - ->2156	
- - - ->1789		CVD - - - - - ->1019		LATTICE DAMAGE - "		CONTAINER MATERI. "	
COMPETATIVE MECH. 464		ION IMPLANTATION "		OXIDATION - - - 1428		CORROSION - - - - "	
CORONA CHARGING - 1078		LOW PRESSURE - - "		SOLAR CELL - - - 114		DISCHARGE CAPACI.>1899	
CVD - - - - - 313		PHOSPHORUS DOPING "		SULFURIC ACID - 1428		FERRIC OXIDE -> 56	
- - - - ->1042						FLAME OXIDATION - "	
- - - - - 1335		SILICON GATE MOS		SILVER		PHOTOCURRENT - - "	
DEFECT DENSITY ->1771		ALCOHOL - - - ->1301		CHROMIUM - - - ->1047		PHYSICAL STRUCTU. 1899	
DEPOSITION - - - 313		INDUCED INSTABIL. "		DEGRADATION - - - "		POROUS IRON ELEC. "	
DEPOSITION RATE - 1042		KETONE - - - - - "		IMPATT CLODE - - - "		POWDER REDUCTION "	
DIELECTRIC BREAK. 162				INTERDIFFUSION - "		PULSED ILLUMINAT. 56	
DIELECTRIC FILM ->1539		SILICON GROWTH		JUNCTION POTENTI.>161		SILICON CARBIDE - 2156	
DIELECTRICS - - - 313		ATMOSPHERE - - ->1785		METALLIZATION - 1047		SODIUM SULFUR - - - 56	
DIFFUSION PROCESS> 135		DOPING - - - - - "		PLATINUM - - - - "		SOLAR CELL - - - - 56	
DIOXIDE AMBIENCE 1288		HELIUM-HYDROGEN - "		POTASSIUM CHLORI. 1618			
DISLOCATION - - - 1014		HETEROEPI TAXY - - "		SILICON - - - - 1047		SINUSOIDAL	
DOPANT EFFECT - ->1516				SILVER CHLORIDE - 1618		CONVECTIVE DIFFU.> 431	
- - - ->1523		SILICON INTERFACE		THERMAL LIQUID - - "		- -> 437	
ELECTRIC FIELD - 1771		ELLIPSONOMETRY - -> 131		THERMOCELL - - - - "		ELECTRON TRANSFER 431	
ELLIPSONOMETRY -> 131		HYDROGEN EFFECT -> 122		TRANSPERT ENTROPY "		437	
ETCHING - - - - 464		OPTICAL LAYER - - 131				HYDRODYNAMICS - - 431	
- - - - 1419		SILICON DIOXIDE - 122		SILVER BROMIDE		- - - 437	
EVAPORATION - - - 1335		- - - 131		ANODIZATION - - -> 803		ROTATING DISK - - 431	
FILM EDGE - - - 1014		STRESS-STRAIN - - "		CONDUCTION - - - - "		- - - 437	
FILM THICKNESS - 1539		THERMAL OXIDATION 122		REDUCTION - - - - - "		VOLTAMMETRY - - - 431	
GAAS - - - - - 135						- - - 437	
HYDROCHLORIC ACID> 149		SILICON NITRIDE		SILVER CHLORIDE		SLOPE ANGLE	
HYDROGEN - - - - 1419		ANNEALING - - - ->1750		BULK PHASE - - - ->1467		DEVELOPING TIME ->1430	
HYDROGEN EFFECT -> 122		CERAMICS - - - ->1723		EMF - - - - - - - "		ELECTRON BEAM - - "	
INSULATION - - - 1335		CORROSION - - - - "		JUNCTION POTENTI.>1618		LINE WIDTH - - - - "	
INTEGRATED CIRCU. 1042		DISLOCATION - - ->1014		MOLTEN SALT - - - 1467		POLYMETHYLMETHAC. "	
INTERFACE STATE - 1573		FILM EDGE - - - - "		POROUS ELECTRODE > 965		RESIST - - - - - "	
ION ASSISTANCE - 464		HOT-PRESSED - - 1723		POTASSIUM CHLORI. 1618			
LIQUID CRYSTAL - 1771		HYDROGENATION - 1750		SILVER - - - - - "		SMALL AMPLITUDE	
LSI DEVICE - - ->1531		OXIDATION KINETI. 1723		SINGLE PORE ELEC. 965		CYCLIC VOLTAMMETR.> 989	
MOBILE SODIUM - - 149		PLASMA DEPOSITION 1750		SODIUM CHLORIDE - 1467		IMPEDENCE - - - - "	
OPTICAL LAYER - - 131		REFRACTORIES - - 1723		SOLUBLE REACTANT 965		RESISTIVE CAPACI. "	
ORGANIC RESIST - 1531		SILICON DIOXIDE - 1014		SURFACE TENSION - 1467		VOLTAMMOGRAM - - - "	
OXIDATION - - - - 149		VISCOELASTICITY - "		THERMAL LIQUID - 1618			
OXIDATION KINETI. 1516		YTTRIUM - - - - - 1723		THERMOCELL - - - - "		SOCIAL CHANGE	
1523				TRANSPORT ENTROPY "		ECONOMIC GROWTH -> 81C	
1789		SILICON OXIDATION				FUTURE - - - - - "	
OXIDE CHARGE DEN. 878		IMPURITY REDISTR.>1939		SILVER IODIDE		SODIUM	
OXIDE THICKNESS - 1771		IMPURITY SEGREGA. "		COPPER BROMIDE -> 818		ELECTRET - - - ->1708	
PASSIVATION - - - 149		INTERFACIAL FLUX "		IONIC CONDUCTIVI. "		HETEROCHARGE - - - "	
PHOSPHORUS DOPING 313		MOVING BOUNDARY - "		PHASE DIAGRAM - - - "		MEMBRANE - - - - - "	
- - - 1042		NUMERICAL SOLUTI. "				POLARIZATION - - - "	
1078				SILVER OXIDE		POLYSTYRENESULFO. "	
PHYSICAL MODEL - 1523		SILICON OXIDE		ANODIC FILM - - -> 725			
PLANAR DIFFUSION 135		ANNEALING - - - ->1731		COBALT SULFATE - - - "			

PRIMARY TERM CO-TERM	PAGE NO.	PRIMARY TERM CO-TERM	PAGE NO.	PRIMARY TERM CO-TERM	PAGE NO.	PRIMARY TERM CO-TERM	PAGE NO.
SODIUM (CONTD)		SOLAR CELL (CONTD)		SOLUBLE CATHODE (CONTD)		STACKING FAULT (CONTD)	
POLYVINYL ALCOHOL 1708		PHOTOANODE -- -- 1011		THIONYL CHLORIDE 513		THERMAL OXIDATION 1789	
POTASSIUM -- -- -- "		PHOTOCURRENT -- -- 56				TRICHLOROETHYLENE "	
SODIUM CARBONATE		PHOTOELECTROCHEM. 954		SOLUBLE REACTANT		STAINING	
CARBON DIOXIDE --> 328		PULSED ILLUMINAT. 56		POROUS ELECTRODE > 965		ANGLE LAPPING --> 1982	
GAS SOLUBILITY -- -- "		RUTHENIUM -- -- -- 954		SILVER CHLORIDE -- -- "		ION IMPLANTATION -- -- "	
MOLTEN SALT -- -- -- "		SEMICONDUCTOR -- -- 1011		SINGLE PORE ELEC. -- -- "		JUNCTION DEPTH -- -- "	
OXYGEN -- -- -- -- "		SILICON WAFER -- -- 114					
SULFUR DIOXIDE -- -- "		SINTERING -- -- -- 56		SOLUBLE SYSTEM		STAINLESS STEEL	
		SURFACE TREATMENT 954		DISCHARGE DATA --> 357		AUSTENITIC -- -- --> 374	
SODIUM CHLORIDE		THIN FILM -- -- -- 703		IRON -- -- -- -- -- "		COLD PLASTIC DEF.>2075	
BULK PHASE -- -- -->1467		SOLAR COLLECTOR		SECONDARY BATTERY -- -- "		CORROSION -- -- -- 374	
EMF -- -- -- -- -- "		ALUMINUM -- -- --> 11		TITANIUM -- -- -- -- -- "		----- 2075	
LIFE TEST -- -- -->1439		CORROSION -- -- -- "				DUPLEX 308 -- -- -- 374	
MOLTEN SALT -- -- -- 1467		ETHYLENE GLYCOL -- -- "		SOLUTION DEPTH		INTERGRANULAR -- -- -- "	
OXIDE COATING -- -- 1439				APPLIED POLARIZA.>2057		MICROSTRUCTURE -- -- -- "	
PERCHLORIC ACID -- -- "		SOLID BROMINE		COPPER ZINC -- -- -- "		PHASE TRANSFORMA. -- -- -- "	
POLARIZATION -- -- -- "		CONDUCTION -- -- -->1368		ELECTRODE POTENT. -- -- -- "		PITTING -- -- -- -- -- "	
SILVER CHLORIDE -- 1467		ELECTROLYSIS -- -- -- "		GALVANIC CORROSI. -- -- -- "		PITTING RESISTAN. 2075	
SURFACE TENSION -- -- -- "				NUMERICAL ANALYS. -- -- -- "		SALT SOLUTION -- -- -- -- "	
TITANIUM ANODE -- 1439							
SODIUM HYDROXIDE		SOLID CORROSION		SOLUTION GROWTH		STATIONARY BATTE.	
BORON DOPING -- -- --> 345		HEXAFLUOROARSEN.> 181		BLUE LIGHT EMISS.> 341		FLOAT CURRENT -- -->1510	
ELECTROSORPTION -->1172		LITHIUM -- -- -- -- -- "		GALLIUM -- -- -- -- -- "			
ETCHING -- -- -- -- -- 345		ORGANIC PRODUCT -- -- -- "		LUMINESCENCE -- -- -- "		STEADY STATE CON.	
FILM FORMATION -- 1172		TETRAHYDROFURAN -- -- -- "		ZINC SELENIDE -- -- -- "		DIELECTRIC FLUID > 925	
GOLD ELECTRODE -- -- -- "						DISSOCIATION -- -- -- "	
POTENTIAL PERTUR. -- -- -- "		SOLID ELECTROLYTE		SOLUTION PRECIPIT.		SURFACTANT -- -- -- -- "	
SILICON -- -- -- -- -- 345		ALKALI METAL -- -- -->2047		ANODIC ZINC OXIDE>1914		TRANSIENT CONDUCT. -- -- -- "	
SODIUM MONOSULFID.		ALKALINE METAL -- -- -- "		CRYSTALLITE GROW. -- -- -- "			
CADMIUM SULFIDE -->1187		ALUMINUM FLUORIDE>1385		NUCLEATION -- -- -- -- -- "		STEADY STATE EQU.	
CHARGE TRANSFER -- -- -- "		BARIUM FLUORIDE -->2023		ZINC OXIDE FILM -- -- -- "		CARBONATE -- -- -- --> 527	
		CALCIUM FLUORIDE >1360				COMPOSITION PROF. -- -- -- "	
SODIUM NEUTRALIZ.		CHEMICAL POTENTI. -- -- -- "		SOLVATED ELECTRON		FUEL CELL -- -- -- -- -- "	
HYDROCHLORIC ACID> 149		COPPER ION CONDU.>1654		ELECTRON INJECTI.>207C		MOLTEN SALT -- -- -- -- -- "	
MOBILE SODIUM -- -- -- "		CUPROUS CHLORIDE -- -- -- "		LIQUID AMMONIA -- -- -- "			
OXIDATION -- -- -- -- -- "		CUPROUS IODIDE -- -- -- "		SEMICONDUCTOR -- -- -- -- -- "		STEAM OXIDATION	
PASSIVATION -- -- -- -- -- "		CUPROUS INTERACTI. 1385				HIGH PRESSURE -- -->1822	
SILICON DIOXIDE -- -- -- "		DISCHARGE CHARAC.> 709		SOURCE GAS PHASE		LOW TEMPERATURE -- -- -- "	
		ELECTRONIC CONDU. 2023		GALLIUM -- -- -- -- -->1400		OXIDE FILM GROWTH -- -- -- "	
SODIUM NITRITE		FLUORIDE -- -- -- -- -- 709		INDIUM ARSENIDE -- -- -- "		SILICON -- -- -- -- -- -- "	
COPPER -- -- -- -- --> 701		FLUORITE -- -- -- -- -- 1385		MIXED CRYSTAL PH. -- -- -- "			
CRACKING -- -- -- -- -- "		GALVANIC CELL -- -- -- 709		THERMODYNAMICS -- -- -- -- -- "		STEEL ANODE	
STRESS CORROSION -- -- -- "		IONIC CONDUCTIVI. 1385		VPE -- -- -- -- -- -- -- "		AQUEOUS BASE -- -- --> 983	
TRANSGRANULAR -- -- -- -- -- "		IONIC MOTION -- -- -- -- -- "				OXIDATION -- -- -- -- -- -- "	
		LEAD -- -- -- -- -- -- -- "		SPECTRIN		P-HYDROXYBENZALD. -- -- -- "	
SODIUM PASSIVATI.		MEASUREMENT -- -- -- 1360		ACTIN -- -- -- -- -->1471		STERESELECTIVITY -- -- -- -- -- "	
HYDROCHLORIC ACID>1129		NONAQUEOUS BATTE. 2047		IONIC PERMEABILI. -- -- -- "			
PHASE SEPARATION -- -- -- "		OXYGEN -- -- -- -- -- 1360		MEMBRANE PROTEINS -- -- -- "		STEREOMICROSCOPY	
SILICON OXIDE -- -- -- -- -- "		RUBIDIUM CHLORIDE 1654		POLAROGRAPHY -- -- -- -- -- "		ELECTRODEPOSITION>1123	
		X-RAY DIFFRACTION -- -- -- "				ELECTRON MICROSC. -- -- -- "	
SODIUM SULFATE				SPECTROSCOPY		ORGANIC INCLUSION -- -- -- -- -- "	
CHEMICAL EQUILIB.>1054		SOLID INSULATION		ADSORPTION -- -- -- --> 608			
COMBUSTION GASES -- -- -- "		GAS INSULATION -- -- --> 55C		ATOMIC ADSORPTION>1988		STERESELECTIVITY	
DEPOSITION -- -- -- -- -- "		INSULATION -- -- -- -- -- "		CELL KINETICS -- -- -- -- -- 608		AQUEOUS BASE -- -- --> 983	
HOT CORROSION -- -- -- -- -- "		LIQUID INSULATION -- -- -- -- -- "		ELECTROCHEMICAL -->2169		OXIDATION -- -- -- -- -- -- "	
IODINE -- -- -- -- -->1842				GAAS CRYSTAL -- -- -- -- -- 1988		P-HYDROXYBENZALD. -- -- -- -- -- "	
POLLUTION CONTROL -- -- -- -- -- "		SOLID PHASE		LITHIUM BATTERY -- -- -- -- -- 608		STEEL ANODE -- -- -- -- -- -- "	
SOLID-STATE PROBE -- -- -- -- -- "		EFFUSION -- -- -- --> 771		PHASE DIAGRAM -- -- -- -- -- "			
SULFUR DIOXIDE -- -- -- -- -- "		VAPORIZATION -- -- -- -- -- 771		POTENTIAL -- -- -- -- -- -- -- "		STOICHIOMETRY	
SULFUR PROBE -- -- -- -- -- "		ZIRCONIUM IODIDE -- -- -- -- -- "				ALUMINUM -- -- -- -- --> 779	
SULFUR TRIOXIDE -- -- -- -- -- "				TITANIUM DISULFID. 608		ANGORIZATION -- -- -- -- -- -- "	
SODIUM SULFUR		SOLID SOLUTION		TRACE ELEMENT -- -- -- -- -- 1988		CHLORINE EVOLUTI.>1343	
BETA-ALUMINA -- -- -->1451		BARIUM FLUORITE --> 667		VOLTAGE STEPS -- -- -- -- -- 608		DESORPTION -- -- -- -- -- -- "	
CELL MEMBRANE -- -- -- -- -- "		CALCIUM FLUORITE -- -- -- -- -- "		ZEEMAN TECHNIQUE 1988		ENERGY STORAGE --> 713	
CERAMICS -- -- -- -- -->2156		CATHODE -- -- -- -- -->1311				HYDROGEN-CHLORINE -- -- -- -- -- "	
CONTAINER MATERIAL. -- -- -- -- -- "		CESIUM FLUORITE -- 667		SPREADING RESIST.		IMPEDENCE -- -- -- -- -- 779	
CORROSION -- -- -- -- -- -- -- "		DEFECT INTERACTI. -- -- -- -- -- "		CURRENT DENSITY -->1479		MASS HEAT BALANCE 713	
ELECTRODE SHARD -- 1451		HOST LATTICE -- -- -- 1311		MULTILAYER ANALY. -- -- -- -- -- "		REGENERATION -- -- -- -- -- -- "	
FAILURE ANALYSIS -- -- -- -- -- "		IONIC CONDUCTIVI. 667		RESISTIVITY -- -- -- -- -- -- -- "		RELAXATION TIME -- -- -- 779	
SILICON COMPOUND -- 2156		POWER SOURCE -- -- -- 1311				TAFEL SLOPE -- -- -- -- -- 1343	
SINTERING -- -- -- -- -- -- -- "		STRONTIUM FLUORI. 667		SPUN-ON FILM			
		URANIUM FLUORITE -- -- -- -- -- "		DIELECTRIC FILM --> 269		STRAIN DISTRIBUT.	
SODIUM-22 LABEL				POLYIMIDE -- -- -- -- -- -- -- "		DOUBLE CRYSTAL -->1228	
BETA-ALUMINA -- -- -->1513		SOLID-STATE		THICKNESS PROFILE -- -- -- -- -- "		EPITAXIAL LAYER -- -- -- -- -- -- "	
MONOCRYSTAL -- -- -- -- -- -- -- "		IMPEDENCE -- -- -- --> 793		THIN FILM -- -- -- -- -- -- -- "		PENDELLOSUNG -- -- -- -- -- -- "	
RADIOCHEMISTRY -- -- -- -- -- -- -- "		INTEGRATED ELEC. -- -- -- -- -- "				X-RAY DIFFRACTION -- -- -- -- -- "	
		ION SELECTIVE EL. -- -- -- -- -- "		SPUTTER DEPOSITI.			
SOLAR CELL				ALUMINUM ALLOY -->1257		STREAMING POTENT.	
CATION ABSORPTION> 954		SOLID-STATE CELL		LIFT-OFF METALLI. -- -- -- -- -- "		FLUORAPATITE -- -- -->1905	
CHARGE TRANSFER -->1011		COPPER -- -- -- -- --> 699				ZETA POTENTIAL -- -- -- -- -- -- "	
COPPER DOPING --> 114		CYCLABLE CELL -- -- -- -- -- "		SPUTTER ETCH		STRESS CORROSION	
COPPER PRECIPITA. -- -- -- -- -- "		ELECTRODE -- -- -- -- -- -- -- "		LSI DEVICE -- -- -->1531		AMMONIACAL SOLUT.>1299	
DIGITAL SIMULATI. 1011		INTERCALATION -- -- -- -- -- -- -- "		ORGANIC RESIST -- -- -- -- -- -- -- "		COPPER -- -- -- -- --> 701	
ENERGY CONVERSION 954				SILICON DIOXIDE -- -- -- -- -- -- -- "		COPPER ZINC -- -- -- -- -- 1299	
FERRIC OXIDE -- -- --> 56		SOLID-STATE PROBE				CRACKING -- -- -- -- -- 701	
FLAME OXIDATION -- -- -- -- -- "		IODINE -- -- -- -- -->1842		SPUTTERING		DEZINCIFICATION -- 1299	
GAAS -- -- -- -- --> 703		POLLUTION CONTROL -- -- -- -- -- "		CONTAMINATION -- -- --> 319		SODIUM NITRITE -- -- -- 701	
HOLE INJECTION -- -- -- -- -- 1011		SODIUM SULFATE -- -- -- -- -- -- -- "		GLOW DISCHARGE -- -- -- -- -- -- -- "		TRANSGRANULAR -- -- -- -- -- -- "	
ILLUMINATED -- -- -- -- -- -- -- "		SULFUR DIOXIDE -- -- -- -- -- -- -- "		PLASMA DEPOSITION -- -- -- -- -- -- -- "			
LARGE GRAIN -- -- -- -- -- 703		SULFUR PROBE -- -- -- -- -- -- -- "		PLASMA ETCHING -- -- -- -- -- -- -- "		STRESS-STRAIN	
LIQUID JUNCTION -- 1011		SULFUR TRIOXIDE -- -- -- -- -- -- -- "		RADIATION DAMAGE -- -- -- -- -- -- -- "		ELLIPSOmetry -- -- -- --> 131	
PHOTOANODE -- -- -- 954						OPTICAL LAYER -- -- -- -- -- -- "	
		SOLUBLE CATHODE		STACKING FAULT		SILICON DIOXIDE -- -- -- -- -- -- "	
		DISCHARGE REACTI.> 513		CHLORINE OXIDATI.>1789		SILICON INTERFACE -- -- -- -- -- -- "	
		LITHIUM ANODE -- -- -- -- -- -- -- "		OXIDATION KINETI. -- -- -- -- -- -- -- "			
		PRIMARY CELL -- -- -- -- -- -- -- "		SILICON DIOXIDE -- -- -- -- -- -- -- "			

PRIMARY TERM CO-TERM	PAGE NO.	PRIMARY TERM CO-TERM	PAGE NO.	PRIMARY TERM CO-TERM	PAGE NO.	PRIMARY TERM CO-TERM	PAGE NO.
STRIPPING		SULFUR DIOXIDE		SURFACE CHANGE (CONTO)		SYMMETRY (CONTO)	
AMMONIA - - - - ->	883	ABUSE TOLERANCE ->	1637	NIOBIUM ELECTRODE	535	RADIAL HEAT GRAD.	284
BREATH TEST - - -	"	BATTERY - - - - -	"	POTASSIUM HYDROX.	"	SEGREGATION - - -	"
CLEANING - - - - -	"	CARBON DIOXIDE ->	328	XPS - - - - -	"		
HYDROGEN PEROXIDE	"	DTA - - - - -	1637			SYNTHESIS	
PHOTORESIST FILM	"	GAS SOLUBILITY -	328	SURFACE CCNTAMIN.		CARBOXYLATION ->	404
WAFER SURFACE - -	"	IODINE - - - - ->	1842	AUGER SPECTROSCO.>	98	DERIVATIVE - - -	"
		LITHIUM - - - - -	1637	ION IMPLANTATION	"	O-CARBOXYMETHYL -	"
STRONTIUM FLUORIDE		MOLTEN SALT - - -	328			REDUCTION - - - -	"
BARIUM FLUORITE ->	667	OXYGEN - - - - -	"	SURFACE EFFECT		TARTRONIC ACID -	"
CALCIUM FLUORITE	"	POLLUTION CONTROL	1842	ACETONITRILE - ->	59		
CESIUM FLUORITE -	"	SODIUM CARBONATE	328	GAAS - - - - -	"	SYSTEM STABILITY	
DEFECT INTERACTI.	"	SODIUM SULFATE -	1842	N-TYPE - - - - -	"	CAPACITY - - - - ->	523
IONIC CONDUCTIVI.	"	SOLID-STATE PROBE	"	P-TYPE - - - - -	"	DISSOLVED SULFUR	"
SOLID SOLUTION	"	SULFUR PROBE - -	"	PHOTOELECTROCHEM.	"	LITHIUM BATTERY -	"
URANIUM FLUORITE	"	SULFUR TRIOXIDE -	"	SEMICONDUCTOR - -	"	ORGANIC ELECTROLY.	"
						RATE CAPABILITY -	"
STRUCTURAL ANALY.		SULFUR OXYCHLORIDE		SURFACE MORPHOLO.		SECONDARY BATTERY	"
ALKALINE SOLUTION>	1693	COULOMETRY - - ->	2035	ALLOY - - - - ->	574	TETRAHYDROFURAN -	"
EPOXIDE DIMERS -	"	CYCLIC VOLTAMMET.	"	ALUMINUM - - - -	"		
KINETIC ANALYSIS	"	LITHIUM - - - - -	"	BUBBLE DYNAMICS -	"	TAFEL SLOPE	
PHTHALIMIDE - - -	"	REDUCTION - - - -	"	ELECTRODE MODEL ->	1835	ANODIC OXIDATION >	1374
REDUCTION - - - -	"			ELECTROPOLISHING	574	CHLORINE EVOLUTI.>	1343
STRUCTURE SENSIT.		SULFUR PROBE		GASEOUS DISCHARGE	"	DESORPTION - - -	"
ANODIC ACTIVATION>	78	IODINE - - - - ->	1842	GROOVE SPACING -	"	DIELECTRICS - - -	1374
AUGER SPECTROSCO.>	67	POLLUTION CONTROL	"	NICKEL - - - - -	"	ELLIPSONOMETRY -	"
		SODIUM SULFATE -	"	POROUS ELECTRODE	1835	HEXACYANOFERRATE >	732
ELECTROCATALYSIS	67	SOLID-STATE PROBE	"	REACTION PROFILE	"	NIOBIUM - - - - -	1374
		SULFUR DIOXIDE -	"	ZINC PURE ELECTR.	"	OPEN CIRCUIT - - -	"
ELECTRON DIFFRAC.	67	SULFUR TRIOXIDE -	"			OXIDE FILM - - -	732
HYDROGEN ABSORPT.	"			SURFACE PROCESSES		PASSIVE IRON - - -	"
OXYGEN REDUCTION	78	SULFUR SEGREGATI.		ALUMINUM BROMIDE >	1474	SEMICONDUCTOR - -	"
PLATINUM - - - - -	67	CORROSION - - - ->	2038	AROMATIC HYDROCA.	"	STOICHIOMETRY - -	1343
		NICKEL - - - - -	"	CYCLIC VOLTAMMET.	"	TRANSIENT ANALYS.	1374
SINGLE CRYSTAL - -	67	SULFURIC ACID - -	"	POTASSIUM BROMIDE	"	TUNGSTEN - - - -	"
SUBBAND GAP ILLUM.		SULFUR TRIOXIDE		SURFACE ROUGHNESS		TALLY SOMYCIN	
PHOTOCURRENT - ->	475	IODINE - - - - ->	1842	GAS ADSORPTION ->	1720	BITHIAZOLE - - ->	2091
PHOTOELECTRODE -	"	POLLUTION CONTROL	"	PASSIVE FILM - - -	"	BLEOMYCIN - - - -	"
TITANIUM OXIDE - -	"	SODIUM SULFATE	"			CYCLIC VOLTAMMET.	"
		SOLID-STATE PROBE	"	SURFACE STRESS		METAL COMPLEX - -	"
SUBMICRON TECHNO.		SULFUR DIOXIDE -	"	ELECTROCAPILLARY >	252	POLAROGRAPHY - -	"
CHLOROMETHYLATED >	1628	SULFUR PROBE - -	"	ELECTROCRYSTALLI.>	2085	PYRIMIDINE - - -	"
DRY ETCHING - - -	"			ELECTRODEPOSITION	"	REDOX - - - - -	"
NEGATIVE RESIST -	"	SULFURIC ACID		EPITAXY - - - - -	"		
POLYSTYRENE - - -	"	AC ADMITTANCE - ->	424	EXTENSOMETER - -	252	TANTALUM	
		ANION INFLUENCE ->	2140	NICKEL - - - - -	2085	ACCEPTER HYPOTHE.>	795
SUBSTRATE CONSTA.		ANODIC DISSOLUTI.>	2150	PASSIVATION - - -	"	ADHESION - - - - ->	624
ANODIC OXIDE - ->	986	ANODIC OXIDATION >	470	PLATINUM - - - -	252	ANODIC OXIDE FILM	"
ELLIPSONOMETRY - -	"	CLEANING SOLUTION>	1428	SACCHARIN - - - -	2085	ANODIC STABILITY >	507
TITANIUM - - - - -	"	CORROSION - - - ->	1363	SALT SOLUTION - -	252	COLD-ROLLED STEEL	"
						CORROSION RESIST.	"
SUBSTRATE DIFFUS.		CURRENT OSCILLAT.	1363	SURFACE TENSION		DUCTILITY - - - -	624
FILM GROWTH - - ->	1261	ELECTROCATALYSIS	2140	BULK PHASE - - ->	1467	ELECTROPOLISHING	795
MATHEMATICAL MOD.	"	ELECTROSORPTION -	"	EMF - - - - -	"	FRACTURE - - - -	624
NOBLE METAL LAYER	"	FILM GROWTH - - -	470	MOLTEN SALT - - -	"	HEXAFLUOROARSEN.	507
		FLADE POTENTIAL -	"	SILVER CHLORIDE -	"	LITHIUM - - - - -	"
SUBSTRATE ROUGHN.		HYDROGEN MONOLAY.	2140	SODIUM CHLORIDE -	"	LITHIUM BATTERY -	"
ELLIPSONOMETRY - ->	799	HYDROGEN PEROXIDE	1428			TETRAHYDROFURAN -	"
TRANSPARENT OXIDE	"	INTERFACE - - - -	424	SURFACE TREATMENT		WAGNERS THEORY -	795
UNIFORM OXIDE - -	"	IRON - - - - -	1363	CATION ABSORPTION>	954		
				ENERGY CONVERSION	"	TANTALUM PENTOXI.	
SULFATE CONCENTR.		LEAD ACID BATTERY>	7	PHOTOANODE - - -	"	ANODIC OXIDE FILM>	765
COBALT CONCENTRA.>	944	LEAD DIOXIDE - -	"	PHOTOELECTROCHEM.	"	DIELECTRICS - - -	"
CORROSION SUPPRE.	"	LEAD SULFATE - -	"	RUTHENIUM - - - -	"	IONIC CONDUCTION	"
LIGHT INTENSITY -	"	NICKEL - - - - -	470	SOLAR CELL - - -	"		
PHOTOANODE - - -	"					TAPER ETCHING	
TITANIUM DIOXIDE	"			SURFACE WAVE		INSULATING FILM ->	504
		OXIDATION - - - -	7	CHEMISORPTION - ->	617	NEW TECHNOLOGY -	"
SULFIDATION				RUTHENIUM TRICHL.	"	TAPERED WINDOW -	"
ANODIC CORROSION >	1093	PASSIVITY - - - -	1363	TIN DIOXIDE - - -	"		
COAL CHAR - - - ->	894	PLATINUM - - - -	424	XPS - - - - -	"	TAPERED WINDOW	
CONTACT MATERIAL >	2017					INSULATING FILM ->	504
CONTACT RESISTAN.	"	POSITIVE PLATE -	7	SURFACTANT		NEW TECHNOLOGY -	"
EUTECTIC - - - - -	1093	POTENTIAL DISTRI.	2150	DIELECTRIC FLUID >	925	TAPER ETCHING - -	"
FERROUS SULFIDE -	894	ROTATING DISK - -	424	DISSOCIATION - -	"		
FUSED SALT - - - -	1093	ROTATING WAFER -	1428	STEADY STATE CON.	"	TARTRONIC ACID	
GASIFICATION - - -	894	SULFUR SEGREGATI.	2038	TRANSIENT CONDOC.	"	CARBOXYLATION - ->	404
IRON - - - - -	894	SWEEP FREQUENCY -	424			DERIVATIVE - - -	"
IRON ALLOY - - - -	894	SUPPORTING ELECT.		SWEEP FREQUENCY		O-CARBOXYMETHYL -	"
IRON SULFIDE - - -	683	ELECTROANALYSIS ->	50	AC ADMITTANCE - ->	424	REDUCTION - - - -	"
LITHIUM CHLORIDE	1093	ELECTROLYTE CONC.	"	INTERFACE - - - -	"	SYNTHESIS - - - -	"
POTASSIUM CHLORIDE	"	SEMI-TEGRATION -	"	PLATINUM - - - -	"		
RUTHENIUM - - - -	2017	VOLTAMMETRY - - -	"	ROTATING DISK - -	"	TBA CHLORIDE	
RUTHENIUM DIOXIDE	"			SULFURIC ACID - -	"	FUSED SALT - - ->	1876
SCALE - - - - -	683	SURFACE ANALYSIS				GLASS FORMING - -	"
VOLTAMMETRY - - -	1093	AUGER SPECTROSCO.>	450	SWEEP VOLTAMMETRY		MANGANESE CHLORIDE	"
		ELLIPSONOMETRY - -	"	COPPER DOPING - ->	2183	MOLTEN SALT - - -	"
SULFUR		GAAS - - - - -	"	POINT DEFECT - - -	"	TBA IODIDE - - -	"
CHLORALUMINATE ->	231	IN SITU - - - - -	"	VALENCE CHANGE -	"	TETRA-N-BUTYLAMM.	"
ELECTROOXIDATION	"	LEED - - - - -	"	ZIRCONIA - - - -	"	TRANSPORT PROPER.	"
MELT COMPOSITION	"	RHEED - - - - -	"				
MOLTEN SALT BATT.	"	VPE - - - - -	"	SYMMETRY		TBA IODIDE	
				CZOCHELSKI - - ->	284	FUSED SALT - - ->	1876
		SURFACE CHANGE		GALLIUM DOPING -	"	GLASS FORMING - -	"
		CATHODIC POLARIZ.>	535	GERMANIUM - - - -	"	MANGANESE CHLORIDE	"
				HEAT PIPE - - - -	"	MOLTEN SALT - - -	"

PRIMARY TERM CO-TERM	PAGE NO.	PRIMARY TERM CO-TERM	PAGE NO.	PRIMARY TERM CO-TERM	PAGE NO.	PRIMARY TERM CO-TERM	PAGE NO.
TBA IODIDE (CONTO)		TERNARY SYSTEM (CONTO)		THERMAL LIQUID (CONTO)		THERMOGRAVIMETRY	
TBA CHLORIDE -- 1876		FUSED SALT -- 2104		POTASSIUM CHLOR. 1618		CERIUM DIOXIDE -> 209	
TETRA-N-BUTYLAMM. "		MEASUREMENT -- 2098		SILVER -- -- --		DEFECT STRUCTURE "	
TRANSPORT PROPER. "		-- 2104		SILVER CHLORIDE --		NONSTOICHIOMETRY "	
		MOLAR VOLUME -- 2098		THERMOCELL -- --		OXIDE SEMI CONDUCT.	
TEFLON BONDED		2104		TRANSPORT ENTROPY		POINT DEFECT -- --	
ACTIVATION ENERGY>1353		NONAQUEOUS SYSTEM> 990					
NICKEL COBALT OX. "		X-RAY DIFFRACTION "		THERMAL LPE		THERMOPASSIVATION	
OXYGEN EVOLUTION "				DEFECT STRUCTURE >1381		LEAD ACID BATTERY>1100	
POTENTIOSTATIC --		TETRA-N-BUTYLAMM. "		DOPING -- -- --		LEAD DIOXIDE PLA. "	
PULSE -- -- -- --		FUSED SALT -->1876		ELECTROCEPATAXY --			
		GLASS FORMING -- "		ELECTRONIC CHARA. "		THICKNESS PROFILE	
TELLURIUM DIOXIDE		MANGANESE CHLOR. "		GAAS -- -- -- --		DIELECTRIC FILM -> 269	
ANODIC OXIDATION > 768		MOLTEN SALT -- --				POLYIMIDE -- -- --	
CADMIUM TELLURIDE "		TBA CHLORIDE -- --		THERMAL NITRIDAT.		SPUN-ON FILM -- --	
MERCURY -- -- -- --		TBA IODIDE -- --		AMMONIA GAS -- --> 996		THIN FILM -- -- -- --	
NATIVE CXIDE -- --		TRANSPORT PROPER. "		DIELECTRIC FILM --			
				OXIDATION RESIST. "		THIN FILM	
TEMPERATURE		TETRAHYDROFURAN		SILICON OXYNTRIST. "		ACID MEDIUM -- --> 93	
BARIUM CHLOROSIL>1734		ANODIC STABILITY > 507				AUGER SPECTROSCOP. > 547	
EUROPIUM -- -- -- --		CAPACITY -- -- --> 523		THERMAL OXIDATION		CARBON MONOXIDE -> 627	
HIGH QUENCHING --		COLD-ROLLED STEEL 507		ANNEALING -- -->1573		CARBON CAPACITY -- 93	
PHOSPHORS -- -- -- --		CORROSION RESIST. "		ANODIC OXIDATION >133		CHROMIUM -- -- -->1075	
PHOTOLUMINESCENCE "		DISSOLVED SULFUR 523		BORON REDISTRIBU.>2001		CONDUCTANCE MODUL. 627	
		HEXAFLUOROARSENA.> 181		CHARGE DENSITY -- 1573		CORROSION -- -- --> 547	
TEMPERATURE DEPE.		507		CHLORINE OXIDATI.>1288		DIELECTRIC FILM -> 269	
ADSORPTION -- --> 495		LITHIUM -- -- -- --		>1789		ETCHING -- -- -- --	
HIGHLY REACTIVE --		-- -- -- -- 507		DIFFUSION MODEL -- 2001		GAAS -- -- -- --> 1075	
HYDROGEN -- -- -- --		LITHIUM BATTERY --		DIOXIDE AMBIENCE 1288		HIGH FIELD -- -->2188	
REACTIVITY -- -- --		-- 523		ELECTROCHROMISM -- 2133		HYDROXIDE-TYPE -- 93	
URANIUM POWDER --		ORGANIC ELECTROL. --		HYDROGEN EFFECT -> 122		INTERFACE ROLE -- 2188	
		ORGANIC PRODUCT -- 181		INTERFACE STATE -- 1573		IONIC CONDUCTION "	
TEMPERATURE RANGE		RATE CAPABILITY -- 523		OXIDATION KINET. 1789		IRIDIUM -- -- -- -- 93	
ABSORPTION SPECT.>1550		SECONDARY BATTERY --		PHOTOELECTROCHEM. 2133		IRON -- -- -- -- 547	
CERIUM -- -- -- --		SOLID CORROSION -- 181		SILICON DIOXIDE -- 122		LARGE GRAIN -- 703	
CRYSTAL FIELD -- --		SYSTEM STABILITY 523		-- 1288		OXIDATION -- -- --> 547	
GARNET PHOSPHORS "		TANTALUM -- -- -- 507		-- 1573		PALLADIUM -- -- --	
PHOTOLUMINESCENCE "				-- 1789		PASSIVE OXIDE -- --	
		THALLIUM		SILICON INTERFACE 122		PHOTOLITHOGRAPHY 1075	
TERBIUM		CALCIUM NITRATE -> 985		STACKING FAULT -- 1789		PHOTOMASK COATING --	
CATHODE RAY -- -->1556		HYDRATED METALS --		TRICHLOROETHYLENE "		POLYIMIDE -- -- --> 269	
-- --> "		NUCLEATION -- -- --		TUNGSTEN TRIOXIDE 2133		SENSOR -- -- -- -- 627	
CATHODOLUMINESCE> 305						SOLAR CELL -- 703	
> 571		THERMAL ANALYSIS		THERMAL PREPARAT.		SPUN-ON FILM -- 269	
CERIUM -- -- -- -- 1556		ANODE MATERIAL --> 866		ELECTRODEPOSITION> 204		THICKNESS PROFILE "	
-- -- -- --		LITHIUM BORON -- --		MOSSBAUER SPECTR. "		TIN OXIDE -- -- --> 627	
CONCENTRATION -- --		MOLTEN SALT BATT. "		TIN NICKEL ALLOY		XPS -- -- -- -- 547	
-- -- -- --							
EFFICIENCY -- -- --		THERMAL BATTERY		THERMAL FDCCESSI.		THIN FILM GROWTH	
-- -- -- --		ANODE MECHANISM -> 176		CZOCHELSKI -- -->1142		HAFNIUM DIKETONA.>1203	
ELECTROGN BOMBARD. 571		CALCIUM ANODE -- --		INTEGRATED CIRCU. "		HAFNIUM DIOXIDE -- "	
GADOLINIUM -- -- 1556		CATHOLYTE -- -->1496		LIFETIME -- -- --		THERMAL DECOMPOS. --	
-- -- -- --		CATION RADIUS -- --		MINORITY CARRIER "		ZIRCONIUM DIKETO. "	
GARNET PHOSPHORS "		FUSED SALT -- 176		SILICON -- -- -- --		ZIRCONIUM DIOXIDE "	
		LITHIUM CHLORIDE "					
HOST SENSITIZATI. 305		MOLTEN NITRATE -- 1496		THERMALLY GROWN		THIOCYANATE	
LANTHANUM OXYSUL. 571		NITRATE SALT -- --		CONDUCTANCE -- -->1		ANODE -- -- -- --> 972	
LOW ENERGY -- --		OPEN PAN STUDY --		ELECTRON EXCHANGE "		ELECTROOXIDATION --	
NONRADIATIVE PRO. 305		OVERVOLTAGE -- -- 176		SILICA SURFACE --		LIGHT EFFECT -- --	
PHOSPHORS -- -- -- 571		REDUCTION -- -- -- 1496				PHOTOCONDUCTIVITY "	
PRASEODYMIUM -- 305				THERMISTOR			
TERBIUM -- -- -- -- 1556		THERMAL CELL		ALUMINUM SOLUBIL.> 165		THIONYL CHLORIDE	
-- -- -- --		AQUEOUS SYSTEM -> 908		BARIUM TITANATE --		CARBON -- -- -- -->2052	
TRAPPING -- -- -- 305		HIGH TEMPERATURE "		CONDUCTIVITY -- --		CATHODE -- -- -- --	
XPS -- -- -- -- 571		REFERENCE ELECTR. "				DISCHARGE -- -- -->2168	
YTRITIUM OXISULF. 305				THERMOCELL		DISCHARGE REACTI.> 513	
YTRITIUM OXSULF. 571		THERMAL DECOMPOS.		JUNCTION POTENTI.>1618		ELECTROLYTE SALT>1445	
		AMMONIUM DICHROM.>1975		POTASSIUM CHLOR. "		ENERGY CONVERSION "	
TERBIUM ACTIVATI.		HAFNIUM DIKETONA.>1203		SILVER -- -- -- --		HERMETIC O-CELL --	
ALKALI RARE EARTH>2206		HAFNIUM DIOXIDE -- "		SILVER CHLORIDE --		HYDROLYSIS -- --> 981	
CESIUM COACTIVAT. "		LUMINESCENCE -- 1975		THERMAL LIQUID --		IMPURITY -- -- --	
GLASSY PHOSPHORS "		OXIDATION -- -- --		TRANSPORT ENTROPY "		LIQUID CATHOLYTE --	
LUMINESCENCE -- --		PHOSPHOR LUMINES. "				LITHIUM -- -- -- -- 2052	
METAPHOSPHATE -- --		THIN FILM GROWTH 1203		THERMOCHEMISTRY		-- -- -- -- 2168	
		ZINC SULFIDE -- 1975		BIRGE-SPONER -->1396		LITHIUM ANODE -- 513	
TERBIUM DOPING		ZIRCONIUM DIKETO. 1203		DISSOCIATION -- --		LITHIUM BATTERY -- 981	
CERIUM DOPING -->1221		ZIRCONIUM DIOXIDE "		METAL HALIDE GAS "		LITHIUM BORON CH. 1445	
EUROPIUM DOPING --				MODEL CALCULATION "		PRIMARY CELL -- 513	
GADOLINIUM DOPING "		THERMAL DEPENDEN.				REACTION MECHAN. 2168	
GARNET PHOSPHORS "		CERIUM DOPING -->1213		THERMODYNAMICS		SOLUBLE CATHODE -- 513	
RARE EARTH ACTIV. "		-->1221		DISSOCIATION -->1825			
THERMAL DEPENDEN. "		DECAY PROCESS -- 1213		GALLIUM -- -- -- -->1400		THORIUM	
		EUROPIUM DOPING 1221		INDIUM ARSENIDE --		ELECTROTRANSFERT >1811	
TERNARY PHASE		GADOLINIUM DOPING "		MASS SPECTROSCOPY 1825		HIGH RESISTANCE -- "	
ALUMINUM -- -- -->1992		GARNET PHOSPHORS 1213		MIXED CRYSTAL PH. 1400		LOW PRESSURE -- --	
ANTIMONY -- -- -- --		1221		SELENIUM SULFIDE 1825		MICROGRAVITY -- --	
DTA -- -- -- -- --		RARE EARTH ACTIV. 1213		SOURCE GAS PHASE 1400		PURIFICATION -- --	
GALLIUM -- -- -- --		1221		VAPORIZATION -- -- 1825			
LIQUID ASSOCIATI.		TERBIUM DOPING -- "		VPE -- -- -- -- 1400		THREE POINT	
PHASE DIAGRAM -- --						CORROSION POTENT.> 891	
		THERMAL EXPANSION		THERMOELECTRICITY		LINEAR POLARIZAT. "	
TERNARY SYSTEM		CRYSTAL GROWTH ->1625		COBALT OXIDE -->1817		NUMERICAL METHODS "	
COMPLEX -- -- -- -->2104		OPTIMUM CONDITION "		ELECTRODE MATER. "			
COMPLEX ION MODEL>2098		RUTHENIUM DIOXIDE "		LANTHANUM STRONT. "		TIME VARIATION	
CONDUCTIVITY -- --				POWER -- -- -- --		LONG TERM TESTING>1674	
-- 2104		THERMAL LIQUID				WATER ELECTROLYZ. "	
FUSED SALT -- -- 2098		JUNCTION POTENTI.>1618					

PRIMARY TERM CO-TERM	PAGE NO.	PRIMARY TERM CO-TERM	PAGE NO.	PRIMARY TERM CO-TERM	PAGE NO.	PRIMARY TERM CO-TERM	PAGE NO.
TIN		TITANIUM DIOXIDE (CONTO)		TRANSISTOR		TRAPPING DENSITY	
DOPING PROFILE ->	296	OPTICAL PROPERTY	1592	CURRENT GAIN ->	642	ANNEALING - - ->	1078
GAAS - - - - -	"	OXIDE FILM GROWTH	1731	EMITTER EFFICIEN.	"	C-V CURVE - - -	"
GROWTH PROCESS -	"	PHOTOANODE - - -	944	GETTERING - - -	"	CORONA CHARGING	"
LPE - - - - -	"	- - - - -	2163	P-N-P - - - - -	"	PHOSPHORUS DOPING	"
MOBILITY PROFILE	"	PHOTOELECTROCHEM.	850	PHOSPHORUS PENTO.	"	SILICON DIOXIDE -	"
		PHOTOELECTROLYSIS	83				
TIN DIOXIDE			2007	TRANSITION METAL		TRICHLOROETHYLENE	
CHEMISORPTION ->	617	POTENTIAL DISTRI.	1505	COBALT MONOXIDE ->	760	CHLORINE OXIDATI.	>1789
RUTHENIUM TRICHL.	"	PROCESSING VARIA.	844	ELECTROTRANSPORT	"	OXIDATION KINETI.	"
SURFACE WAVE - -	"	QUANTUM EFFICIEN.	2007	IONIC MODEL - - ->	1387	SILICON DIOXIDE -	"
XPS - - - - -	"	REDUCTION ETCHING	844	LANTHANIDE METAL	"	STACKING FAULT -	"
		REOXIDATION - - -	1731	METAL HALIDE GAS	"	THERMAL OXIDATION	"
TIN DOPING		RUTILE ANODE - -	83	MOLECULAR STRUCT.	"		
DIFFUSION PROCESS	135	RUTILE LATTICE -	2163	OXIDATION THEORY	760	TRICKLE BED ELEC.	
GAAS - - - - -	"	SEMICONDUCTOR -	844	POINT DEFECT - -	"	FLOW-THROUGH -	>1885
- - - - ->	797	SILICON OXIDE - -	1731	VIBRATIONAL FREQ.	1387	GASEOUS REACTANTS	"
HIGH RATE - - ->	691	SULFATE CONCENTR.	944			REACTOR - - - - -	"
INDIUM OXIDE - -	"	WATER OXIDATION -	2007				
PLANAR DIFFUSION	135			TRANSITION STATES		TRIFLUOROETHYL	
PLANAR JUNCTION -	"	TITANIUM DISULFI.		HIGH PRESSURE ->	985	CHLOROACRYLATE ->	1829
POLYESTER FILM -	691	ADSORPTION - - ->	608	HYDROGEN EVOLUTI.	"	ELECTRON BEAM -	"
REACTIVE SPUTTER.	"	CELL KINETICS - -	"	REACTION MECHAN.	"	INTEGRATED CIRCU.	"
SILICON DIOXIDE -	135	LITHIUM BATTERY -	"			MOLECULAR ORBITAL	"
VPE - - - - -	797	PHASE DIAGRAM - -	"	TRANSITION TEMPE.		POLYMER - - - - -	"
		POTENTIAL - - - -	"	CONDUCTIVITY - ->	2144	POSITIVE RESIST -	"
TIN NICKEL ALLOY		SPECTROSCOPY - -	"	GLASS - - - - -	"		
ELECTRODEPOSITION	204	VOLTAGE STEPS - -	"	HYDRATE MELT - -	"	TRIFLUOROMETHANE	
MOSSBAUER SPECTR.	"			MIXED ALKALI EFF.	"	ELECTROOXIDATION	> 775
THERMAL PREPARAT.	"					ETHANE - - - - -	"
		TITANIUM OXIDE		TRANSPARENT FILM		FUEL CELL - - - -	"
TIN OXIDE		CHLORINE EVOLUTI.	>1189	INTEGRATED CIRCU.	103	METHANE - - - - -	"
ARSENIC DOPING ->	1434	ELECTROCATALYSIS	"	LIQUID STANDARD -	"	N-BUTANE - - - - -	"
CARBON MONOXIDE ->	627	PHOTOCURRENT - ->	475	PASSIVATION LAYER	"	PROPANE - - - - -	"
CONDUCTANCE MODU.	"	PHOTOELECTRODE -	"	REFRACTIVE INDEX	"		
CONDUCTIVITY - -	1434	RUTHENIUM - - - -	1189				
CVD - - - - -	"	SUBBANDGAP ILLUM.	475	TRANSPARENT OXIDE		TRIMETHYLGALLIUM	
OXIDE FILM - - -	"	TITANIUM SUPPORT.	1189	ELLIPSGMETRY - ->	799	ARSINE GAS - - ->	300
SENSOR - - - - -	627	CHLORINE EVOLUTI.	>1189	SUBSTRATE ROUGHN.	"	DEVICE QUALITY -	"
THIN FILM - - - -	"	ELECTROCATALYSIS	"	UNIFORM OXIDE - -	"	EPITAXY - - - - -	"
		RUTHENIUM - - - -	"			GAAS - - - - -	"
TITANIUM		TITANIUM OXIDE - -	"	TRANSPORT		GERMANIUM - - - -	"
ACIDIC SULFATE ->	2064			ALUMINUM CHLORIDE	>1644	MOLYBDENUM - - -	"
ANODIC DISSOLUTI.	"	TOPOCHEMICAL CELL		CONDUCTIVITY - -	"		
ANODIC OXIDE - ->	986	DICHALCOGENIDE ->	349	DENSITY - - - - -	"	TUNGSTEN	
CARBON - - - - -	>2173	INTERCALATION - -	"	FUSED SALT - - - -	"	ANODIC OXIDATION	>1374
CHLORIDE SOLUTION	2064	LITHIUM - - - - -	"	HALIDE - - - - -	"	DIELECTRICS - - -	"
CHROMIUM STEEL -	2173	LOW VOLTAGE BEHA.	"	N-ALKYLPYRIDINIUM	"	ELLIPSGMETRY - -	"
CORROSION - - -	2064	SECONDARY BATTERY	"	VISCOSITY - - - -	"	NIOBIUM - - - - -	"
DEOXYGENATED SOL.	"					OPEN CIRCUIT - -	"
DISCHARGE DATA ->	357	TOUGHNESS BEHAVI.		TRANSPORT ENTROPY		TAPEL SLOPE - - -	"
ELLIPSGMETRY - -	986	CUTTING TOOLS - ->	1281	JUNCTION POTENTI.	>1618	TRANSIENT ANALYS.	"
IRON - - - - -	357	CVD COATING - - -	"	POTASSIUM CHLORI.	"		
NIOBIUM - - - - -	2173	ETA PHASE - - - -	"	SILVER - - - - -	"	TUNGSTEN TRIOXIDE	
OXIDATION RESIST.	"	TITANIUM CARBIDE -	"	SILVER CHLORIDE -	"	ANODIC OXIDATION	> 583
PASSIVATION - - -	2064			THERMAL LIQUID -	"	- - - - ->	2133
SECONDARY BATTERY	357	TRACE ELEMENT		THERMOCELL - - -	"	ELECTROCHROME -	> 805
SOLUBLE SYSTEM -	"	ATOMIC ABSORPTION	>1988			ELECTROCHROMISM -	583
SUBSTRATE CONSTA.	986	GAAS CRYSTAL - -	"	TRANSPORT EQUATI.		- - - - -	2133
ZIRCONIUM - - - -	2173	SPECTROSCOPY - -	"	CONVECTION - - ->	1713	FILM STRUCTURE -	583
		ZEEMAN TECHNIQUE	"	DIFFUSION - - - -	"	PHOSPHOTUNGSTIC -	805
TITANIUM ANODE				DIFFUSION COEFFI.	> 988	PHOTOELECTROCHEM.	2133
LIFE TEST - - - -	>1439	TRACE GAS		MIGRATION - - - -	1713	PROTON CONDUCTION	805
OXIDE COATING - -	"	CORROSION - - - ->	2159	MOLTEN SALT - - -	"	REACTION RATE - -	583
PERCHLORIC ACID -	"	ENVIRONMENT - - -	"	POROUS ELECTRODE	"	THERMAL OXIDATION	2133
POLARIZATION - -	"	FLOW CONTROL - -	"			VACUUM EVAPORATI.	583
SODIUM CHLORIDE -	"	PERMEATION - - -	"	TRANSPORT LAW		ZIRCONIUM PHOSPH.	805
		POLYMER - - - - -	"	CORROSION - - - ->	1662		
TITANIUM CARBIDE				MATHEMATICAL MOD.	"	TUNNELING	
CUTTING TOOLS - ->	1281	TRANSGRANULAR		PIT GROWTH - - - -	"	ALUMINUM - - - ->	1548
CVD COATING - - -	"	COPPER - - - - ->	701	PIT INITIATION - -	"	ANODIZATION - - -	"
ETA PHASE - - - -	"	CRACKING - - - - -	"	SALT FILM - - - -	"	VAPOR INFUSION -	"
TOUGHNESS BEHAVI.	"	SODIUM NITRITE -	"				
		STRESS CORROSION	"	TRANSPORT PROPER.		ULTRAHIGH VACUUM	
TITANIUM DIOXIDE				CONDUCTANCE - - ->	1682	ANTIMONY EVAPORA.	>1761
ANNEALING - - - -	>1731	TRANSIENT ANALYS.		DIFFUSION - - - -	"	ARSENIC - - - - -	"
ANODIC OXIDATION	>1592	ANODIC OXIDATION	>1374	FUEL CELL - - - -	"	CESIUM - - - - ->	660
ARC PLASMA SPRAY.	83	DIELECTRICS - - -	"	FUSED SALT - - - -	>1876	DEPTH PROFILE - -	"
BANDGAP SHIFT - -	1592	ELLIPSGMETRY - -	"	GLASS FORMING - -	"	DOPANT - - - - -	"
BERYLLIUM DOPING	>2007	NIOBIUM - - - - -	"	HALOGEN - - - - -	1682	DOPING - - - - -	1761
CAPACITANCE - - -	>1505	OPEN CIRCUIT - -	"	HYDROGEN - - - -	"	EPITAXY - - - - -	"
- - - - -	1731	TAPEL SLOPE - - -	"	MANGANESE CHLORI.	1876	GAAS - - - - -	660
CERAMICS - - - -	83	TUNGSTEN - - - -	"	MOLTEN SALT - - -	"	ION IMPLANTATION	1761
COBALT CONCENTRA.	944	TRANSIENT CONDUCT.		NAFION MEMBRANE -	1682	MASS SPECTROMETRY	660
COPPER DOPING - -	1592	DIELECTRIC FLUID	> 925	POLYMER - - - - -	"	MOLECULAR BEAM -	1761
CORROSION SUPPRE.	944	DISSOCIATION - -	"	TBA CHLORIDE - - -	1876	SECONDARY ION - -	660
DIFFUSION - - - -	> 850	STEADY STATE CON.	"	TBA IODIDE - - - -	"	SILICON - - - - -	1761
DISPLAY DEVICE ->	2211	SURFACTANT - - -	"	TETRA-N-BUTYLAMM.	"		
ELECTRICAL CHARA.	"	TRANSIENT DECAY		TRAPPING		ULTRASONIC	
ELECTROPHORESIS	"	A-C IMPEDENCE - ->	1166	CATHODOLUMINESCE.	> 305	AGITATION - - - ->	479
FLATBAND POTENTI.	1505	CERIUM DIOXIDE -	"	HOT SENSITIZATI.	"	DEFECT - - - - -	"
HIGH TEMPERATURE	1731	PLATINUM ELECTRO.	"	NONRADIATIVE PRG.	"	ETCH - - - - -	"
HYDROGEN - - - -	>2163	POLARIZATION - -	"	PRASEODYMIUM - -	"	SELLO ETCH - - -	"
HYDROGEN PROTON -	850			TERBIUM - - - - -	"	SILICON EVALUATI.	"
LIGHT INTENSITY -	944			YTRIUM OXISULFI.	"		
MOTT-SCHOTTKY - -	1505					ULTRAVIOLET EXCI.	
OPTICAL CHARACTER	2211					COLOR TV PICTURE	>1008

PRIMARY TERM CO-TERM	PAGE NO.	PRIMARY TERM CO-TERM	PAGE NO.	PRIMARY TERM CO-TERM	PAGE NO.	PRIMARY TERM CO-TERM	PAGE NO.
ULTRAVIOLET EXCI. (CONTD)		VAPORIZATION (CONTD)		VOLTANMOGRAM (CONTD)		WORK FUNCTION (CONTD)	
GAS DISCHARGE - - - 1008		SELENIUM SULFIDE 1825		RESISTIVE CAPACI. 989		SILICON - - - - - 878	
PHOSPHORS - - - - "		SOLID PHASE - - - 771		SMALL AMPLITUDE - "		- - - - - 1084	
UNALLOYED NICKEL		THERMODYNAMICS - 1825				SILICON DIOXIDE - 878	
AIR ENVIRONMENT ->1274		ZIRCONIUM IODIDE 771		VP CONVERSION			
NICKEL GOLD ALLCY "				APROTIC SOLVENT -> 414		WORKING ELECTRODE	
OXIDE FILM GROWTH "		VERTICAL ELECTRO.		CHEMILUMINESCENCE "		NONAQUEOUS SOLVE-> 407	
		COPPER DEPOSITION>2118		ELECTROGENERATED "		RUTHENIUM OXIDE - "	
UNDERVOLTAGE		CURRENT DISTRIBUT. "		ENERGY CONVERSION "		XPS - - - - - "	
ISOTOPE SEPARATI.>2045		ELECTRODEPOSITION "		PHOTOINDUCED - - "			
		GAS LIFT - - - - "		SEMICONDUCTOR - - "		WUSTITE PHASE	
UNIFORM OXIDE		HYDROGEN EVOLUTI. "				CARBON DIOXIDE ->2012	
ELLIPSOmetry - -> 799		MATHEMATICAL MOD. "		VPE		FURNACE - - - - - "	
SUBSTRATE ROUGHN. "				AUGER SPECTROSCO.> 450		GAS FLOW METHOD - "	
TRANSPARENT OXIDE "		VIBRATIONAL FREQ.		COBALT - - - - ->1584		HYDROGENS - - - - "	
		IONIC MODEL - ->1387		ELLIPSOmetry - - 450		LOWER TEMPERATURE "	
URANIUM FLUORIDE		LANTHANIDE METAL "		GAAS - - - - - "		OXYGEN PRESSURE - "	
BARIUM FLUORITE -> 667		METAL HALIDE GAS "		- - - - -> 797		PRESSURE CONTROL "	
CALCIUM FLUORITE "		MOLECULAR STRUCT. "		- - - - - 1584			
CESIUM FLUORITE - "		TRANSITION METAL "		GAASP - - - - - "		X-RAY	
DEFECT INTERACTI. "				GALLIUM - - - - ->1400		ELECTRON BEAM - -> 694	
IONIC CONDUCTIVI. "		VISCOELASTICITY		HOLE DIFFUSION L. 1584		LITHOGRAPHY - - - - "	
SOLID SOLUTION - "		DISLOCATION - ->1014		IN SITU - - - - - 450		POLYMER - - - - - "	
STRONTIUM FLUORI. "		FILM EDGE - - - - "		INDIUM ARSENIDE - 1400		POLYMETHACRYLONI. "	
		SILICON DIOXIDE - "		LEED - - - - - 450		RESIST - - - - - "	
		SILICON NITRIDE - "		MIXED CRYSTAL PH. 1400			
URANIUM POWDER				NICKEL - - - - - 1584		X-RAY DIFFRACTION	
ADSORPTION - - -> 495		VISCOSITY		RHEOD - - - - - 450		COPPER ION CONDU.>1654	
HIGHLY REACTIVE - "		ALUMINUM CHLORIDE>1644		SOURCE GAS PHASE 1400		CUPROUS CHLORIDE - "	
HYDROGEN - - - - "		CONDUCTIVITY - - "		SURFACE ANALYSIS 450		CUPROUS IODIDE - "	
		DENSITY - - - - - "		THERMODYNAMICS - 1400		DOUBLE CRYSTAL ->1228	
REACTION KINETICS "		FUSED SALT - - - - "		TIN DOPING - - - 797		EPITAXIAL LAYER - "	
REACTIVITY - - - 495		HALIDE - - - - - "				ETCHING DEFECT ->1272	
TEMPERATURE DEPE. "		N-ALKYLPYRIDINIUM		WAFER FABRICATION		GROUP III-IV ALL. "	
		TRANSPORT - - - - "		ELECTRON RESIST ->1703		INDIUM PHOSPHIDE "	
UREA				GLYCIDYL METHACR. "		NONAQUEOUS SYSTEM> 990	
ANODIC OXIDATION >1687		VLSI DEVICE		LITHOGRAPHY - - - "		PENDELLOSUNG - - 1228	
GLUCOSE SENSOR - "		DOPING - - - - ->1779		POLYMER RESIST - "		RUBIDIUM CHLORIDE 1654	
INHIBITION - - - - "		ION IMPLANTATION "				SOLID ELECTROLYTE "	
KREBS-RINGER - - - "		LOW TEMPERATURE "		WAFER SURFACE		STRAIN DISTRIBUT. 1228	
PLATINUM ELECTRO. "		OXIDATION - - - - "		AMMONIA - - - - -> 883		TERNARY SYSTEM - 990	
		POLYSILICON - - - - "		BREATH TEST - - - "		111-A FACE - - - 1272	
UV IRRADIATED				CLEANING - - - - - "		111-B FACE - - - - "	
CATALYST - - - -> 394		VOID TRANSMISSION		HYDROGEN PEROXIDE "		XPS	
DEPOSITION - - - - "		PHOSPHOR PARTICLE>1563		PHOTORESIST FILM "		ANNEALING - - - ->1737	
ELECTROLESS - - - - "		SCREEN WEIGHT - - "		STRIPPING - - - - - "		ANODIC FILM - - ->1737	
PALLADIUM - - - - "		WEIGHT OPTIMIZAT. "				ANODIC OXIDE - - -	
				WAGNERS THEORY		AQUEOUS OXIDATION> 750	
VACUUM EVAPORATI.		VOLTAGE REGULATI.		ACCEPTER HYPOTHE.> 795		AUGER SPECTROSCO.> 547	
ANODIC OXIDATION > 583		ANGDIC DISCHARGE > 993		ELECTROPOLISHING "		-> 1766	
ELECTROCHROMISM - "		FELTMETAL - - - - "		TANTALUM - - - - - "		949	
FILM STRUCTURE - "		LITHIUM BORON - - - "				CADMIUM SELENIDE 949	
REACTION RATE - - -		MOLTEN SALT - - - - "		WATER		CADMIUM SULFIDE - "	
TUNGSTEN TRICXIDE "				ANODIZATION - - ->1718		CATHODIC POLARIZ.> 535	
				CIRCUIT - - - - - "		CATHODOLUMINESCE> 571	
VALENCE CHANGE		VOLTAGE STEPS		CONTAMINATION -> 54		CHEMI ADSORPTION ->	
COPPER DOPING - ->2183		ADSORPTION - - -> 608		CORROSION - - - - 1718		CORROSION - - - - 547	
POINT DEFECT - - - "		CELL KINETICS - - -		CURRENT DENSITY - 54		CVD - - - - - 1766	
SWEEP VOLTAMMETRY "		LITHIUM BATTERY - - "		DENDRITE - - - - 1718		DEPTH PROFILE - 1370	
ZIRCONIA - - - - - "		PHASE DIAGRAM - - -		ELECTROLYSIS - - 54		- 1737	
		POTENTIAL - - - - - "		FILM FORMATION - 1718		ELECTRON BOMBARD. 571	
VANADIUM		SPECTROSCOPY - - - "		GOLD METALLIZATI. "		ENERGY CONVERSION 949	
ANODIZATION - - -> 544		TITANIUM DISULFI. "		NONFARADAY - - - 54		GAAS - - - - - 1370	
KEIL SALOMON - - - "						- - - - - 1737	
OXYGEN ISOTOPE - - -		VOLTAMMETRY		WATER ELECTROLYZ.		INCONNEL 600 - - 750	
		ANODIC CORROSION >1087		LONG TERM TESTING>1674		IRGN - - - - - 547	
		->1093		TIME VARIATION - - "		LANTHANUM OXSULF. 571	
VANADIUM OXIDE		CONVECTIVE DIFFU.> 431				LOW ENERGY - - -	
CATHODE - - - - -> 497		-> 437		WATER OXIDATION		NIOBIUM ELECTRODE 535	
LITHIUM CELL - - - "		ELECTROANALYTE -> 50		BERYLLIUM DOPING >2007		NONAQUEOUS SOLVE-> 407	
SECONDARY BATTERY "		ELECTROLYTE CONC. "		PHOTOELECTROLYSIS "		NUCLEAR REACTOR - 750	
		ELECTRON TRANSFER 431		QUANTUM EFFICIENT. "		OXIDATION - - - - 547	
VAPOR ETCH-		437		TITANIUM DIOXIDE "		OXIDE - - - - - 1737	
GAAS GREWTH - - ->1241		EUTECTIC - - - - 1087				OXYGEN CONCENTRA. 1766	
		- - - - - 1093		WATER PASTE		PALLADIUM - - - - 547	
VAPOR GROWN		FUSED SALT - - - 1087		LEAD ACID BATTERY> 991		PASSIVATION - - - 1370	
CADMIUM HALIDE -> 325		- - - 1093		LEAD SULFATE - - - "		PASSIVE OXIDE - - 547	
CRYSTALLOGRAPHY - "		HYDRODYNAMICS - 431				PHOSPHORS - - - - 571	
DIFFRACTION - - - - "		- - - 437		WEIGHT OPTIMIZAT.		PHOTOELECTRICITY 949	
MIXED CRYSTALS - - -		LITHIUM CHLORIDE 1087		PHOSPHOR PARTICLE>1563		POLYSILICON - - - 1766	
POLYTYPISM - - - - "		1093		SCREEN WEIGHT - - -		POTASSIUM HYDROX. 535	
		ORTHOPHOSPHORIC -> 786		VOID TRANSMISSION "		RUTHENIUM OXIDE - 407	
VAPOR INFUSION		OXYGEN REDUCTION "				RUTHENIUM TRICHL. 617	
ALUMINUM - - - ->1548		PARALLEL MECHAN. "		WET SOLAR CELL		SEMICONDUCTOR - - 949	
ANODIZATION - - - - "		PLATINUM - - - - - "		MANGANESE PORPHY.> 705		SEMI INSULATION - 1766	
TUNNELING - - - - - "		POTASSIUM CHLORI. 1087		PHOTOELECTROCHEM. "		SURFACE CHANGE - 535	
		- 1093		PLATINUM ELECTRO. "		SURFACE WAVE - 617	
VAPOR TRANSPORT		ROTATING DISK - - 431				TERBIUM - - - - - 571	
CLOSE SPACING - ->1604		-> 437		WHISKERS		THIN FILM - - - - 547	
ENTHALPY - - - - - "		SEMI INTEGRATION - 50		CVD - - - - -> 31		TIN DIOXIDE - - - 617	
		SINUSOIDAL - - - 431		GROWTH MECHANISM "		WORKING ELECTRODE 407	
VAPORIZATION		- - - 437		SILICON FIBER - - -		YTRIUM OXSULFI. 571	
DECOMPOSITION - -> 490		SULFIDATION - - - 1093					
DISSOCIATION - ->1825		SUPPORTING ELECT. 50		WORK FUNCTION			
EFFUSION - - - - 490				ALUMINUM - - - -> 878		YTRIA	
- - - -> 771		VOLTANMOGRAM		GOLD MERCURY ->1084		CALCIA - - - - -> 264	
MASS SPECTROSCOPY 1825		CYCLIC VOLTAMMET.> 989		OXIDE CHARGE DEN. 878		CERIUM DIOXIDE -	
POTASSIUM SULFATE 490		IMPEDENCE - - - - "					

PRIMARY TERM CO-TERM	PAGE NO.	PRIMARY TERM CO-TERM	PAGE NO.	PRIMARY TERM CO-TERM	PAGE NO.	PRIMARY TERM CO-TERM	PAGE NO.
YTTRIA (CONTO)		ZINC (CONTO)		ZINC SELENIDE		ZIRCONIUM DIKETO.	
IONIC CONDUCTIVI. 264		PHOSPHIDATION - - - 1432		AQUEOUS ELECTROL. >1868		HAFNIUM DIKETONA. >1203	
YTTRIUM		ROTATING DISK - - - 566		BLUE LIGHT EMISS. > 341		HAFNIUM DIOXIDE - "	
ALUMINA - - - - ->1035		ZINC PHOSPHIDE - 1432		DARK POTENTIAL - 1868		THERMAL DECOMPOS. "	
CERAMICS - - - - ->1723				FLATBAND POTENTI. "		THIN FILM GROWTH "	
CORROSION - - - - -"				GALLIUM - - - - - 341		ZIRCONIUM DIOXIDE "	
GROWTH MECHANISM 1035		ZINC ELECTRODE		GROUP II-VI COMP. 1868		ZIRCONIUM DIOXIDE	
HOT-PRESSED - - - 1723		ALKALINE SOLUTION > 541		IODINE DOPING - - - "		HAFNIUM DIKETONA. >1203	
OXIDATION KINETI. "		CONCENTRATION - ->2110		LIGHT ABSORPTION "		HAFNIUM DIOXIDE - "	
OXIDE MORPHOLOGY 1035		CONVECTION - - - - -"		LUMINESCENCE - - - 341		THERMAL DECOMPOS. "	
REFRACTORIES - - 1723		CURRENT DENSITY - 541		OPTICAL ABSORPTI. 1868		THIN FILM GROWTH "	
SILICON NITRIDE - -"		CYCLING - - - - - 2110		SOLUTION GROWTH - 341		ZIRCONIUM DIKETO. "	
		ELECTROGROWTH - - -"					
YTTRIUM OXISULFI.		EMF - - - - - ->1456		ZINC SULFIDE			
CATHODOLUMINESC. > 305		EQUILIBRIUM POTE. 541		AMMONIUM DICHROM. >1975		ZIRCONIUM IODIDE	
HOT SENSITIZATI. "		NERNST - - - - - 1456		LUMINESCENCE - - - "		EFFUSION - - - -> 771	
NONRADIATIVE PRC. "		REACTION ORDER - 541		OXIDATION - - - - -"		SOLID PHASE - - - -"	
PRASEODYMIUM - - -"		ZINC HYDROXIDE - 1456		PHOSPHOR LUMINES. "		VAPORIZATION - - - -"	
TERBIUM - - - - -"				THERMAL DECOMPOS. "			
TRAPPING - - - - -"		ZINC FERRICYANIDE				ZIRCONIUM PHOSPH.	
YTTRIUM OXYSULFI.		CESIUM - - - - -> 347		ZIRCALOY OXIDATI.		ELECTROCHROME -> 805	
CATHODOLUMINESC. > 571		ION SELECTIVE - - -"		HIGH TEMPERATURE >1105		PHOSPHOTUNGSTIC -"	
ELECTRON BOMBARD. "		POTASSIUM - - - - -"		OXIDATION KINETI. "		PROTON CONDUCTION "	
LANTHANUM OXYSUL. "		PVC MATRIX - - - - -"		PARABOLIC KINETI. "		TUNGSTEN TRIOXIDE "	
LOW ENERGY - - - -"							
PHOSPHORS - - - - -"		ZINC HYDROXIDE		ZIRCALOY-4		111-A FACE	
TERBIUM - - - - -"		EMF - - - - - ->1456		MULTIPHASE DIFFU. >1111		ETCHING DEFECT ->1272	
XPS - - - - - - - -"		NERNST - - - - - -"		OXYGEN DIFFUSION "		GROUP III-IV ALL. "	
		ZINC ELECTRODE - -"				INDIUM PHOSPHIDE "	
ZEEMAN TECHNIQUE				ZIRCONIA		X-RAY DIFFRACTION "	
ATOMIC ABSORPTION >1988		ZINC OXIDE FILM		COPPER DOPING - ->2183		111-B FACE - - - -"	
GAAS CRYSTAL - - -"		ANODIC ZINC OXIDE >1914		DECOMPOSITION - ->1067			
SPECTROSCOPY - - -"		CRYSTALLITE GROW. "		NITRIC OXIDE - - - -"		111-B FACE	
TRACE ELEMENT - - -"		NUCLEATION - - - - -"		POINT DEFECT - - - 2183		ETCHING DEFECT ->1272	
		SOLUTION PRECIP. "		REDUCING CONDITI. 1067		GROUP III-IV ALL. "	
ZETA POTENTIAL				SCANDIA DOPING - - -"		INDIUM PHOSPHIDE "	
FLUORAPATITE - ->1905		ZINC PHOSPHIDE		SWEEP VOLTAMMETRY 2183		X-RAY DIFFRACTION "	
STREAMING POTENT. "		DIFFUSION COEFFI. >1432		VALENCE CHANGE - -"		111-A FACE - - - -"	
		PHOSPHIDATION - - -"					
ZINC		ZINC - - - - - - - -"		ZIRCONIUM		2,2,2-TRICHLORO.	
CODEPOSITION - -> 566		ZINC PORE ELECTR.		CARBON - - - - ->2173		CROSSLINKED TYPE >1635	
COPPER - - - - - - -"		ELECTRODE MODEL ->1835		CHROMIUM STEEL - -"		ELECTRON RESIST - -"	
DIFFUSION COEFFI. >1432		POROUS ELECTRODE "		NIOBIUM - - - - - -"		HOMOPOLYMER - - - -"	
DIFFUSION CONTROL 566		REACTION PROFILE "		OXIDATION RESIST. "		INTEGRATED CIRCU. "	
		SURFACE MORPHOLO. "		TITANIUM - - - - - -"		METHACRYLATE - - -"	



NOW AVAILABLE

PASSIVITY OF METALS

Edited by

ROBERT P. FRANKENTHAL

Bell Laboratories
Murray Hill, New Jersey

JEROME KRUGER

National Bureau of Standards
Washington, D.C.

(Proceedings of The Fourth International Symposium on Passivity)

This new volume in the Corrosion Monograph Series contains the proceedings of a symposium expressly designed to place passivity into its proper historical perspective and to provide the latest thinking and advances in the field. In 65 chapters contributed by 122 authors, with subject and author indexes, the book offers overviews of major theories and points of view, backgrounds of specific subject areas, and descriptions of the most recent advances in the field.

For those concerned with the corrosion of metals, alloys, and solid-state materials in both science and technology, this text will serve as the first comprehensive reference on passivity as well as a monographic treatment of the subject at the expert level.

Hardbound, xviii + 1077 pages

\$65.00 postpaid

Order with payment in U.S. funds from:

The Electrochemical Society, Inc.
P.O. Box 2071
Princeton, New Jersey 08540

THE ELECTROCHEMICAL SOCIETY, INC.

The Electrochemical Society is an international organization of individuals and companies concerned with or interested in materials sciences.

OBJECTIVES

1. The advancement of the theory and practice of electrochemistry, electrometallurgy, electrothermics, electronics, solid state, and allied subjects.
2. To encourage research and the reporting of such research for the dissemination of knowledge in the field of electrochemistry and solid state.
3. To insure the availability of adequate training in the field of electrochemistry for chemists, engineers, metallurgists, physicists, and solid-state investigators.

BENEFITS OF MEMBERSHIP

1. Assurance of keeping abreast of the latest scientific developments in your particular fields of interest.
2. Enjoyment of personal association with fellow scientists and engineers in the professions.
3. Opportunity to contribute to the advancement of the science and application of electrochemistry and solid state in your areas of interest.
4. Stimulation of interdisciplinary exchanges.

DIVISIONS

The activities of the Society are carried on by its nine Divisions and Group as follows:

Battery	Luminescence
Corrosion	Semiconductors
Dielectrics and Insulation	Electrothermics and Metallurgy
Electrodeposition	Energy Technology Group
Electronics	Industrial Electrolytic
General Materials and Processes	Organic and Biological Electrochemistry
	Physical Electrochemistry

SECTIONS

Local Sections of the Society have been organized in the following cities and regions:

Boston	North Texas
Chicago	Ontario-Quebec
Cleveland	Pacific Northwest
Columbus	Philadelphia
Detroit	Pittsburgh
Indianapolis	Rocky Mountain
Metropolitan New York	San Francisco
Midland (Michigan)	Southern California-Nevada
National Capital Area	

THE ELECTROCHEMICAL SOCIETY PATRON MEMBERS

Bell Laboratories

Murray Hill, N.J.

Dow Chemical Co.

Inorganic Chemicals Dept., Midland, Mich.

E. I. du Pont de Nemours and Co.

Plastic Products and Resins Department
Wilmington, Del.

Exxon Research and Engineering Company

Corporate Research
Advanced Energy Systems Laboratory,
Solid State Sciences Laboratory,
Linden, New Jersey
Engineering Technology Division
Florham Park, New Jersey

General Electric Co.

Battery Business Department, Gainesville, Fla.
Chemical Laboratory, Knolls Atomic Power Laboratory,
Schenectady, N.Y.
Lamp Div., Cleveland, Ohio
Materials & Process Laboratory, Large Steam
Turbine-Generator Dept., Schenectady, N.Y.

General Electric Co. (continued)

Research and Development Center,
Chemical Systems & Technology
Laboratory & Physical Chemistry Laboratory,
Signal Processing & Communication Laboratory,
Schenectady, N.Y.
Semiconductor Products Dept.,
Syracuse, N.Y.

International Business Machines Corp.

New York, N.Y.

The International Nickel Co., Inc.

New York, N.Y.

Olin Corporation

Chemicals Division
Charleston Technology Center
Charleston, Tennessee

Philips Research Laboratories

Eindhoven, Holland

Westinghouse Electric Corp.

Electronic Tube Div., Elmira, N.Y.
Lamp Div., Bloomfield, N.J.
Semiconductor Div., Youngwood, Pa.
Research Laboratories, Pittsburgh, Pa.

THE ELECTROCHEMICAL SOCIETY SUSTAINING MEMBERS

The Aerospace Corporation
Los Angeles, Calif.

Airco Industrial Gases
Murray Hill, N.J.

Airco Speer Carbon Graphite
St. Marys, Pa.

Allied Chemical Corp.
Industrial Chemicals Division
Solvay, N.Y.

Aluminum Co. of America
New Kensington, Pa.

Aluminum Co. of Canada, Ltd.
Montreal, P.Q., Canada

AMAX Inc.
New York, N.Y.

AMP Incorporated
Harrisburg, Pa.

Analog Devices, Inc.
Norwood, Mass.

Applied Materials, Inc.
Santa Clara, Calif.

Asahi Chemical Industry Canada, Ltd.
Toronto, Ontario, Canada

ASARCO, Inc.
South Plainfield, N.J.

BASF Wyandotte Corporation
Wyandotte, Mich.

Battelle Memorial Institute
Columbus, Ohio

Bell-Northern Research
Ottawa, Ont., Canada

Bethlehem Steel Corp.
Bethlehem, Pa.

Boeing Co.
Seattle, Wash.

The Borg-Warner Corp.
Roy C. Ingersoll Research Center
Des Plaines, Ill.

Brown, Boveri & Co., Ltd.
Research Center
Baden, Switzerland

Canadian Industries Ltd.
Montreal, P.Q., Canada

Carborundum Co.
Niagara Falls, N.Y.

Chrysler Corporation
Detroit, Michigan

Cominco Ltd.
Trail, B.C., Canada

The Continental Group, Inc.
Energy Systems Laboratory
Cupertino, Calif.

Corning Glass Works
Corning, N.Y.

Crawford & Russell Inc.
Stamford, Conn.

Diamond Shamrock Corp.
Painesville, Ohio

Dow Corning Corporation
Hemlock, Mich.

Duro-Test Corp.
North Bergen, N.J.

Eagle-Picher Industries, Inc.
Electronics Division
Joplin, Missouri

Eastman Kodak Co.
Rochester, N. Y.

Electric Power Research Institute
Palo Alto, California

Electrochemical Technology Corp.
Seattle, Wash.

Electrode Corporation
Chardon, Ohio

Eltra Corp.
Prestolite Div., Toledo, Ohio
C&D Batteries, Conshohocken, Pa.

Energy Development Associates,
A Gulf and Western Company
Madison Heights, Michigan

ESB Incorporated
Ray-O-Vac Div., Madison, Wisc.
Technology Center, Yardley, Pa.

SUSTAINING MEMBERS (CONTINUED)

Ever Ready Co. (Holdings) Ltd.
Whetstone, London, England

Exmet Corporation
Bridgeport, Conn.

Fairchild Camera & Instrument Corp.
Research and Development Laboratory
Palo Alto, Calif.

FMC Corp.
Inorganic Chemicals Div.
Buffalo, N.Y.

Ford Motor Co.
Dearborn, Mich.

General Motors Corporation
Delco Electronics Div., Kokomo, Ind.
Delco-Remy Div., Anderson, Ind.
Research Laboratories Div., Warren, Mich.

Globe Union, Inc.
Milwaukee, Wisc.

B. F. Goodrich Chemical Co.
Cleveland, Ohio

Gould Inc.
Gould Laboratories—
Electrical & Electronics Research
Energy Research
Rolling Meadows, Ill.
Gould Laboratories
Cleveland, Ohio

Great Lakes Carbon Corp.
New York, N.Y.

GTE Laboratories
Waltham, Mass.

GTE Sylvania Incorporated
Chemical & Metallurgical Division
Towanda, Pa.

The Harshaw Chemical Co.
Cleveland, Ohio

Heliotronic GmbH
Burghausen, Germany

Hewlett Packard Company
Loveland, Colo.

Hill Cross Co., Inc.
West New York, N.J.

Hochst-Uhde Corporation
Englewood Cliffs, New Jersey

Honeywell, Inc.
Power Sources Center
Horsham, Pa.

Hooker Chemical Corp.
Niagara Falls, N.Y. (2 memberships)

HP Associates
Palo Alto, Calif.

Hughes Research Laboratories
Div. of Hughes Aircraft Co.
Malibu, Calif.

Industrial Innovation Center
Tehran, Iran

**International Lead Zinc Research
Organization, Inc.**
New York, New York
**International Minerals and Chemical
Corporation**

Electrochemical Division
Orrington, Maine

Kaiser Aluminum & Chemical Corp.
Pleasanton, Ca.

Kaweck Berylo Industries, Inc.
Boyertown, Pa.

KW Battery Co.
Skokie, Ill.

Arthur D. Little, Inc.
Cambridge, Mass.

Lockheed Missiles & Space Co., Inc.
Research Laboratory
Palo Alto, Calif.

Mallory Battery Company
Tarrytown, N.Y. (2 memberships)

Marathon Battery Co.
Waco, Texas

Marston Bermuda
Hamilton, Bermuda

Matsumita Electric Industrial Co., Ltd.
Osaka, Japan

Mepco/Electra, Inc.
Columbia, S.C.

Microwave Associates, Inc.
Burlington, Mass.

Molycorp, Inc.
New York, N.Y.

Monsanto Company
St. Louis, Mo.

Motorola Inc.
Phoenix, Ariz.

M&T Chemicals Inc.
Detroit, Mich.

NIFE Jungner AB
Oskarshamn, Sweden

NL Industries, Inc.
New York, N.Y.

Noranda Research Centre
Pointe Claire, Quebec, Canada

Occidental Research Corporation
La Verne, California

Olin Corporation
Metals Research Laboratories
New Haven, Conn.

Owens-Illinois Inc.
Toledo, Ohio

Oxy Metal Industries Corp.
Warren, Mich.

Perkin-Elmer Corp.
Norwalk, Conn.

Phelps Dodge Refining Corp.
Maspeth, N.Y.

Philips Laboratories, Inc.
Briarcliff Manor, N.Y.

Poco Graphite, Inc.
Decatur, Texas

PPG Industries, Inc.
Chemical Div.
Pittsburgh, Pa.

Prototech Company
Newton Highlands, Mass.

RCA Corporation
Color Picture Tube Division
Lancaster, Pa.

Reynolds Metals Co.
Reduction Research Div.
Sheffield, Ala.

Rockwell International
El Segundo, Calif.

Sandia Laboratories
Albuquerque, N. M.

J. C. Schumacher Co.
Oceanside, Calif.

Shipley Company, Inc.
Newton, Massachusetts

Siemens Aktiengesellschaft
Munich, Germany

Signetics Corp.
Sunnyvale, Ca.

Siltec Corporation
Menlo Park, California

Sperry Research Center
Sudbury, Mass.

Sprague Electric Co.
North Adams, Mass.

Stackpole Carbon Co.
St. Marys, Pa.

**Standard Telecommunication
Laboratories Ltd.**
Essex, England

Stauffer Chemical Co.
Dobbs Ferry, N.Y.

St. Joe Minerals Corp.
Monaca, Pa.

Tektronix, Inc.
Beaverton, Oregon

Teletype Corp.
Skokie, Ill.

Texas Instruments Inc.
Attleboro, Mass.
Dallas, Texas

Tokyo Shibaura Electric Co., Ltd.
Toshiba Research and
Development Center

Kawasaki, Japan

Union Carbide Corp.
Battery Products Div.,
Corporate Research Dept.
New York, N.Y.

United States Steel Corp.
Research Laboratory
Monroeville, Pa.

Varian Associates
Palo Alto, Calif.

Wacker Chemitronic
Burghausen, Germany

Western Electric
Princeton, N.J.

Xerox Corporation
Webster Research Center
Rochester, N.Y.

Yardney Electric Corporation
Pawcatuck, Conn.

